

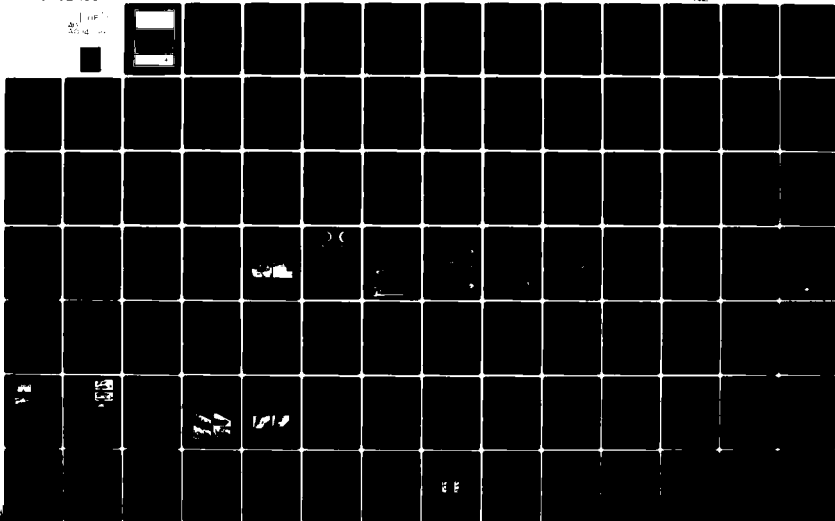
AD-A094 086 ADVISORY GROUP FOR AEROSPACE RESEARCH AND DEVELOPMENT--ETC F/G 20/4
SUBSONIC/TRANSONIC CONFIGURATION AERODYNAMICS.(U)

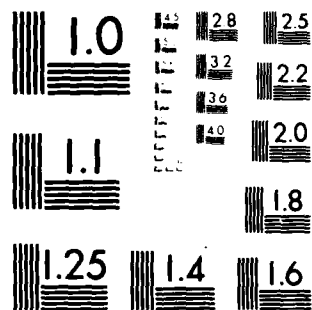
SEP 80

UNCLASSIFIED AGARD-CP-285

NL

1
2
3
4





MICROCOPY RESOLUTION TEST CHART
NATIONAL BUREAU OF STANDARDS 1963-A

AGARD-CP-285

AGARD-CP-285

AD A094086

AGARD

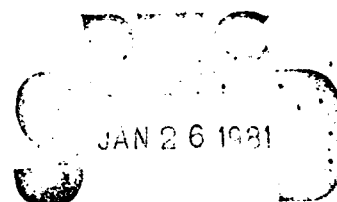
ADVISORY GROUP FOR AEROSPACE RESEARCH & DEVELOPMENT

7 RUE ANCELLE 92200 NEUILLY SUR SEINE FRANCE

AGARD CONFERENCE PROCEEDINGS No. 285

Subsonic/Transonic Configuration Aerodynamics

This document is a reproduction of the original document. It is not a translation of the original document.



A

NORTH ATLANTIC TREATY ORGANIZATION



DISTRIBUTION AND AVAILABILITY
ON BACK COVER

81 1 28 045

DDC FILE COPY

NORTH ATLANTIC TREATY ORGANIZATION
ADVISORY GROUP FOR AEROSPACE RESEARCH AND DEVELOPMENT
(ORGANISATION DU TRAITE DE L'ATLANTIQUE NORD)

⑪ Sep 80

12 | 449

AGARD Conference Proceedings No.285

SUBSONIC/TRANSONIC CONFIGURATION AERODYNAMICS .

Admission Fee
Name _____
Room No. _____
Date _____

Hist _____

A

Papers presented and discussions held at the Fluid Dynamics Panel Symposium held at the Hochschule Bundeswehr, Munich Neubiberg, Germany, 5-7 May 1980.

400043

—h

THE MISSION OF AGARD

The mission of AGARD is to bring together the leading personalities of the NATO nations in the fields of science and technology relating to aerospace for the following purposes:

- Exchanging of scientific and technical information;
- Continuously stimulating advances in the aerospace sciences relevant to strengthening the common defence posture;
- Improving the co-operation among member nations in aerospace research and development;
- Providing scientific and technical advice and assistance to the North Atlantic Military Committee in the field of aerospace research and development;
- Rendering scientific and technical assistance, as requested, to other NATO bodies and to member nations in connection with research and development problems in the aerospace field;
- Providing assistance to member nations for the purpose of increasing their scientific and technical potential;
- Recommending effective ways for the member nations to use their research and development capabilities for the common benefit of the NATO community.

The highest authority within AGARD is the National Delegates Board consisting of officially appointed senior representatives from each member nation. The mission of AGARD is carried out through the Panels which are composed of experts appointed by the National Delegates, the Consultant and Exchange Programme and the Aerospace Applications Studies Programme. The results of AGARD work are reported to the member nations and the NATO Authorities through the AGARD series of publications of which this is one.

Participation in AGARD activities is by invitation only and is normally limited to citizens of the NATO nations.

The content of this publication has been reproduced directly from material supplied by AGARD or the authors.

Published September 1980

Copyright © AGARD 1980
All Rights Reserved

ISBN 92-835-0276-0



*Printed by Technical Editing and Reproduction Ltd
Harford House, 7-9 Charlotte St, London, W1P 1HD*

EXECUTIVE SUMMARY

X
An important region of the flight envelope of military aircraft is the transonic regime where fighter aircraft must undergo agile maneuvers, and airlift aircraft must cruise efficiently. Unfortunately it is a speed regime where wind tunnel testing is difficult, and numerical computations are not yet fully viable. Most troublesome is that exact configuration optimization criteria are lacking. Unavoidably the optimization procedure has been an ad hoc procedure, depending on the intuitive skills of the aerodynamicist.

During the past decade, there has been significant progress in the development of transonic wind tunnel test techniques and computational methods. Employing these techniques, the aerodynamicist has developed many imaginative design concepts that have added to the optimization data base. It was the purpose of the symposium to review and assess these developments and project the future.

Twenty nine papers comprised the meeting with three invited review papers. There was a relatively even mixture of theoretical and experimental papers with many providing test/theory comparisons. Subject matter ranged from simple wing-fuselage interference for both fighter and airlift configurations to those involving additional components such as nacelle and pylons, powered jets, winglets, and most importantly stores and weapons.

The symposium was concluded by a Round Table discussion with invited introductory comments by Mr B.Haines (ARA), Mr P.Poisson-Quinton (ONERA), Dr W.Schmidt (Dornier), and Dr R.Whitcomb (NASA-Langley).

Despite the advanced state of computational fluid dynamics, there are still serious shortcomings as evidenced by the presentations. These include the inability to treat complex modern military configurations in satisfactory detail and with acceptable accuracy; and most importantly the need to incorporate the significant viscous interactions in an expedient manner.

There is finally the matter of developing guidelines and criteria to establish the optimum configuration. This is a difficult task, and undoubtedly will occupy our attention for many years. The optimal design must employ favorable interference with "performance synergism" between components in contrast to the neutral or zero interference much in evidence at the present symposium. In the latter, one proceeds from a given baseline configuration and seeks to eliminate local flow inefficiencies by shape improvements.

Configuration optimization with true favorable interference will surely be prominent at the next Fluid Dynamics Panel symposium that should be timely perhaps half a decade from the present symposium.

Dr H.YOSHIHARA
Prof. B.LASCHKA
Symposium Chairmen



AGARD FLUID DYNAMICS PANEL

Chairman: Dr K.J.Orlik-Rückemann
National Aeronautical Establishment
National Research Council
Montreal Road
Ottawa, Ontario K1A 0R6, Canada

Deputy Chairman: M.L'Ing. en Chef B.Monnerie
Chef de la Division d'Aérodynamique Appliquée
ONERA
29 Avenue de la Division Leclerc
92320 Châtillon, France

PROGRAM COMMITTEE MEMBERS

Pro Dr Ing.B.Laschka (Co-Chairman)
Institut für Stromungsmechanik
der Techn. Univers.
Bienroder Weg 3
D-3300 Braunschweig, Germany

Dr H. Yoshihara (Co-Chairman)
The Boeing Company
Mail Stop 41-18
P.O.Box 3999
Seattle, WA 98124, USA

Mr C.L.Bore
Head of Research (Kingston)
Kingston-Brough Division
of British Aerospace
Richmond Road
Kingston-upon-Thames, KT2 5Q
Surrey, UK

Mr R.O.Dietz
Sverdrup - ARO, Inc.
101 W. Lincoln Str.
Tullahoma, Tennessee 37388, USA

M. l'Ing. en Chef B.Monnerie
Chef de la Division d'Aérodynamique
Appliquée
ONERA
29 Avenue de la Division Leclerc
92320 Châtillon, France

Dr Ir.B.M.Spee
NLR
P.O.Box 90502
1006 BM Amsterdam, Netherlands

PANEL EXECUTIVE

Robert H.Rollins II
AGARD/NATO
7 rue Ancelle
92200 Neuilly sur Seine
France

CONTENTS

	Page
EXECUTIVE SUMMARY	iii
PANEL AND COMMITTEE MEMBERS	iv
	Reference
 <u>SESSION I – PREDICTION METHODS</u>	
APPLICATION OF TRANSONIC POTENTIAL CALCULATIONS TO AIRCRAFT AND WIND TUNNEL CONFIGURATIONS by J.E.Mercer and E.M.Murman	1
UNE METHODE VARIATIONNELLE D'ELEMENTS FINIS POUR LA RESOLUTION D'ECOULEMENTS TRANSSONIQUES TRIDIMENSIONNELS par Y.Vigneron, O.Brocard, J.Bousquet et T.Lejal	2
ETUDE PAR LA METHOD DES ELEMENTS FINIS DES INTERACTIONS VOILURE-FUSELAGE-NACELLE D'UN AVION DU TYPE FALCON A MACH = 0,79 par G.Heckmann	3
 <u>SESSION II – WEAPONS CARRIAGE</u>	
INCREASING THE VALUE OF AIRFORCES BY IMPROVING EXTERNAL STORE CONFIGURATION by C.L.Bore	4
PROSPECTS FOR EXPLOITING FAVOURABLE AND MINIMISING ADVERSE AERODYNAMIC INTERFERENCE IN EXTERNAL STORE INSTALLATIONS by A.B.Haines	5
EVALUATION OF AIRCRAFT INTERFERENCE EFFECTS ON EXTERNAL STORES AT SUBSONIC AND TRANSONIC SPEEDS by R.Deslandes	6
Paper 7 withdrawn	
STUDY OF TRANSONIC FLOW FIELDS ABOUT AIRCRAFT: APPLICATION TO EXTERNAL STORES by S.S.Stahara	8
 <u>SESSION III – CONFIGURATION OPTIMIZATION</u>	
AERODYNAMIC SUBSONIC/TRANSONIC AIRCRAFT DESIGN STUDIES BY NUMERICAL METHODS by W.Schmidt	9
DESIGN OF ADVANCED TECHNOLOGY TRANSONIC AIRFOILS AND WINGS by H.Sobieczky	10
INTERFERENCE ASPECTS OF THE A310 HIGH SPEED WING CONFIGURATION by J.A.Jupp	11
TRANSONIC WING TECHNOLOGY FOR TRANSPORT AIRCRAFT by G.Krenz and B.Ewald	12
DESIGN AND EXPERIMENTAL VERIFICATION OF A TRANSONIC WING FOR A TRANSPORT AIRCRAFT by G.Redeker, N.Schmidt and R.Müller	13
THE TALE OF TWO WINGS by E.Atraghji, L.Thornqvist and L.Torngren	14

	Reference
SOME PARTICULAR CONFIGURATION EFFECTS ON A THIN SUPERCRITICAL VARIABLE CAMBER WING by D.R.Holt and B.Probert	15
A CONSTRAINED INVERSE METHOD FOR THE AERODYNAMIC DESIGN OF THICK WINGS WITH GIVEN PRESSURE DISTRIBUTION IN SUBSONIC FLOW by J.M.J.Fray and J.W.Slooff	16
<u>SESSION IV – POWERED JET INTERACTION</u>	
JET-WING INTERACTION TO GIVE IMPROVED COMBAT PERFORMANCE by A.Vint	17
JET/WING INTERFERENCE FOR AN OVERWING ENGINE CONFIGURATION by R.A.Sawyer and M.P.Metcalf	18
INTERFERENCE EFFECTS OF CONCENTRATED BLOWING AND VORTICES ON A TYPICAL FIGHTER CONFIGURATION by W.Staudacher	19
ETUDE EXPERIMENTALE DE L'INTERACTION ENTRE UNE VOILURE D'AVION SUBSONIQUE RAPIDE ET UNE NACELLE DE MOTEUR A HAUT TAUX DE DILUTION par P.Levart	20
<u>SESSION V – MULTICOMPONENT INTERFERENCE</u>	
A WIND TUNNEL INVESTIGATION OF THE AERODYNAMIC CHARACTERISTICS OF FORWARD SWEEP WINGS by T.M.Weeks, G.C.Uhuad and R.Large	21
AN INVESTIGATION OF A SWEEP WING-BODY CONFIGURATION WITH DROOPED LEADING EDGE AT LOW AND TRANSONIC SPEEDS by G.Drougge	22
INTERACTION AERODYNAMIQUE ENTRE UN CANARD PROCHE ET UNE AILE EN FLECHE EN ECOULEMENT TRANSSONIQUE par Y.Brocard et V.Schmitt	23
SOME AERODYNAMIC INTERFERENCE EFFECTS THAT INFLUENCE THE TRANSONIC PERFORMANCE OF COMBAT AIRCRAFT by D.Treadgold and K.H.Wilson	24
DESIGN STUDY FOR THE INNER WING OF A TRANSONIC WING-BODY COMBINATION OF ASPECT RATIO 8 by N.Voogt and J.Th. van der Kolk	25
COMPLEX CONFIGURATION ANALYSIS AT TRANSONIC SPEEDS by C.W.Boppe and P.V.Aidala	26
THEORETICAL AND EXPERIMENTAL STUDIES OF AERODYNAMIC INTERFERENCE EFFECTS by I.H.Rettie	27
DATA BASE FOR THE PREDICTION OF INLET EXTERNAL DRAG by O.J.McMillan, E.W.Perkins and S.C.Perkins Jr	28
PHILOSOPHY AND RESULTS OF STEADY AND UNSTEADY TEST TECHNIQUES ON A LARGE SCALE TRANSPORT AIRCRAFT MODEL IN THE ONERA TRANSONIC TUNNEL S1 MA (Part 2 and Annex in French) by G.Anders, A.Giacchetto and A.Gravelle	29
ROUND TABLE DISCUSSION	RTD

APPLICATION OF TRANSONIC POTENTIAL CALCULATIONS TO AIRCRAFT AND WIND TUNNEL CONFIGURATIONS

by
Dr. John E. Mercer
and
Dr. Earll M. Murman
Flow Research Company
A Division of Flow Industries, Inc.
21414-68th Avenue South
Kent, Washington 98031
(206) 872-8500

SUMMARY

The computation of inviscid transonic flow modeled by the full-potential equation is presented for two geometrical configurations. The Jameson-Caughey finite-volume method is used to solve the governing equations in conservative form. The development of suitable computational meshes together with computed results are presented for a swept wing in a wind tunnel and for a wing-body configuration.

1. INTRODUCTION

During the past several years, inviscid, transonic-flow computational techniques have been developed to treat complex aircraft geometries. The developments have followed two complementary paths. One uses the modified transonic small-disturbance equation so that geometrical boundary conditions may be applied on a mean surface. This simplifies the mesh generation requirements and, hence, those techniques have proceeded the farthest in terms of geometrical complexity. The other uses the full-potential equation and hence is more accurate. However, the boundary conditions must be applied on the actual geometrical surface which requires the generation of a suitable mesh.

The most advanced transonic small-disturbance codes are extensions of the Bailey-Ballhaus¹ wing-body program. Mason et al.² improved upon these codes and incorporated a strip boundary layer for the wing. In a separate development, Boppe and Stern³ have extended the capability of the codes to handle complex geometrical features such as nacelles and winglets. These codes are useful for a wide variety of applications but they do have limitations on accuracy.⁴

The solution of the full-potential equation for transonic flow past complex geometrical configurations has advanced rapidly in recent years following the introduction in 1977 of the finite-volume technique by Jameson and Caughey.⁵ In their work, the authors presented an algorithm which solves the full-potential equation in conservative form for an arbitrary three-dimensional mesh in physical space consisting of six-sided volume elements. The restrictions on the volume element geometry are rather minimal, being only that the volume element size vary smoothly and that the six-sided cells are not too skew. The Jameson-Caughey finite-volume technique allows for mesh description and construction to be completely uncoupled from the construction of the finite-difference algorithm to solve the full-potential equation. Prior to the introduction of this technique, the solution of each new problem required an analytical transformation of the full-potential equation to the computational mesh and then construction of a suitable difference algorithm.

The solution of the full-potential equation in conservative form provides improved accuracy over the small-disturbance equation for many practical geometries. The potential flow assumption is limited in validity to flows with weak shocks, typically with normal shock Mach numbers below 1.3. In addition, a linearized wake assumption is assumed for vortex wakes.

Viscous effects must be included in the computational model for a complete description of the flow about a body. Various approaches are under study and will be reported at the upcoming AGARD Symposium on Computation of Viscous-Inviscid Interactions. The subject of this paper is limited to computation of inviscid transonic potential flow which provides the basis for more elaborate flow modeling.

Section 2 of this paper contains a review of the basic elements of the finite-volume technique introduced by Jameson and Caughey.⁵ A more detailed description may be found in that reference. In Section 3, the application of the method to the problem of flow past a swept wing in a rectangular wind tunnel is presented. An earlier version of this work is given by Mercer et al.⁶ Section 4 presents a computer code for wing-fuselage geometries and gives computed results for two configurations. This is an outgrowth of a cooperative project between Flow Research and Profs. Jameson and Caughey. Earlier results are reported in Reference 7. Finally, in Section 5, we discuss some limitations of the codes and some future extensions.

2. FINITE-VOLUME ALGORITHM

The finite-volume algorithm assumes that the six-sided elements comprising the mesh in the physical space can be transformed to cubes in the computational space. The map-

ping to each cube is assumed to be local so that transformations can be based on the physical values of the vertices of the six-sided elements. The location of the vertices (or mesh points) in physical space may be determined by any suitable procedure, and two specific examples are given in following sections. The mapped cubes have trilinear variations of coordinates ranging from $-\frac{1}{2}$ to $\frac{1}{2}$ (Figure 1), and the potential is assumed to vary trilinearly within each cell. With the coordinate variation assumption, the corresponding points in the physical space can be located from points in the computational space by the local trilinear mapping formula:

$$x = 8 \sum_{k=1}^8 x_k \left(\frac{1}{4} + X_k X \right) \left(\frac{1}{4} + Y_k Y \right) \left(\frac{1}{4} + Z_k Z \right), \quad (1)$$

where X_k , Y_k , and Z_k are the mapped vertices of the cubes ($\pm \frac{1}{2}$) and x_k represents the corresponding physical values. There are equivalent formulas for y , z , and ϕ , the velocity potential. With this mapping, continuity of x , y , z , and ϕ is preserved at the cell boundaries. The mapping also allows derivatives of the transformation and potential to be evaluated anywhere in the cell.

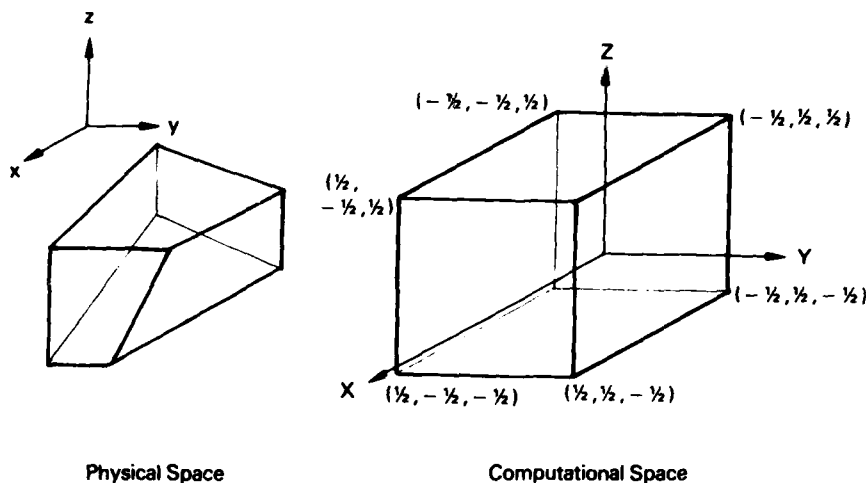


Figure 1. Mapping from Physical Space to Computational Space.

The flow equation that we wish to solve is the conservation relation:

$$\frac{\partial}{\partial x} (\rho u) + \frac{\partial}{\partial y} (\rho v) + \frac{\partial}{\partial z} (\rho w) = \frac{\partial}{\partial x^1} (\rho u^1) = 0 \quad (2)$$

The finite-volume algorithm is a conservative differencing scheme which satisfies the above equation using the cubical cells in the computational space. Density is computed from the isentropic relation:

$$\rho = \left\{ 1 + \frac{\gamma-1}{2} M_\infty^2 (1 - q^2) \right\}^{\frac{1}{\gamma-1}}, \quad (3)$$

where

$$q^2 = u^2 + v^2 + w^2. \quad (4)$$

The first step in the procedure is to determine the governing equation (Equation (2)) in computational space. The result is

$$\frac{\partial}{\partial X^1} (\rho h U^1) = 0, \quad (5)$$

where X^1 are the transformed coordinates (X , Y , and Z in Equation (1)), U^1 are the contravariant velocity components, and h is the determinant of the transformation matrix \tilde{H} with elements $\partial x^i / \partial X^j$. The contravariant velocity is defined by

$$U^i = g^{ij} \frac{\partial \phi}{\partial X^j} \equiv (\tilde{H}^T \tilde{H})^{-1} \frac{\partial \phi}{\partial X^j} \quad (6)$$

A differencing algorithm which conserves ϕU^1 on the cubical cells is derived by creating a set of secondary cells whose vertices lie at centers of the primary cubical cells. The flux quantity ϕU^1 is evaluated at the center of each primary cell (vertices of secondary cell, Figure 2). The flux computed at the corner is assumed to be constant over that portion of the secondary cell face that lies within the primary cell. If the global mapping is sufficiently smooth to allow a Taylor series expansion of the physical coordinates in terms of the computational coordinates, then the local linear truncation error terms for the flux will cancel and the flux conservation formula will be accurate to the second order.

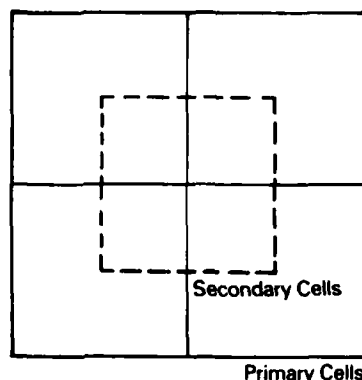


Figure 2. Primary and Secondary Cell in Computational Plane.

With this approach a problem arises in that the difference operator decouples odd and even points as shown in Figure 3. This results in a homogeneous solution where ϕ can be 1 at odd points and -1 at even points. This problem is overcome by displacing the flux evaluation point away from the vertices by adding a higher-order correction term. This displacement recouples the odd and even points and eliminates the homogeneous solution. For the simple case of the flux being given by ϕ_x , the displacement relation used by Jameson and Caughey is

$$\phi_x = \phi_{x_0} + \epsilon \phi_{xy_0}, \quad (7)$$

where the subscript o represents the center of the primary cell and ϵ can vary from 0 to $\frac{1}{2}$ where the cell height is assumed to be 1 (Figure 4). Computation of these recoupling terms requires time. Other methods involving averaging which do not require adding terms are currently under investigation by other researchers.

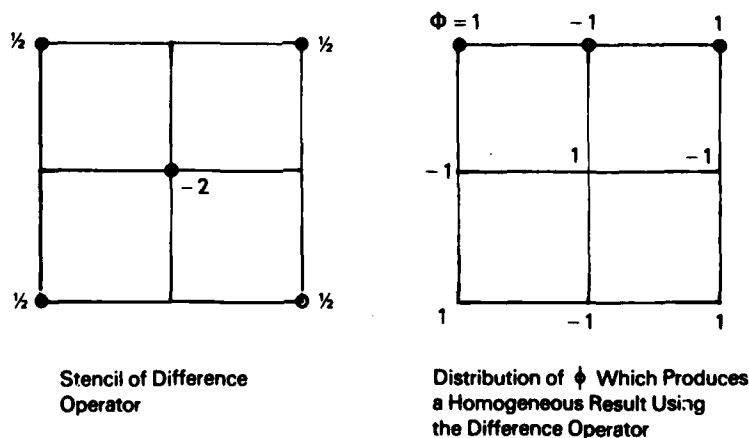


Figure 3. Decoupled Solution Arising from Difference Operator.

In regions where the flow is supersonic, upwind differencing is employed. This is accomplished by adding terms to the conservation equation which produce an upwind bias. The terms are selected such that the proper domain of dependence is used in the differencing. The effect of this is to produce a rotated difference operator of the form

$$\frac{\partial \phi}{\partial s} = \frac{U^1}{q_c} \frac{\partial \phi}{\partial X^1} \quad (8)$$

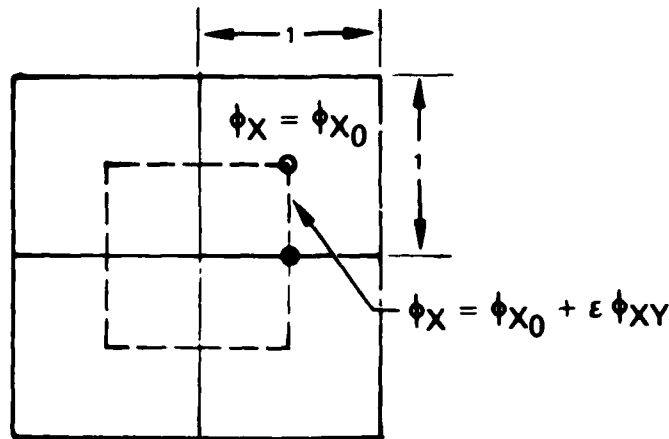


Figure 4. Shift in ϕ_X Used to Recouple Solutions.

where s is the streamwise direction, q_c is the contravariant velocity, and the first-order difference operators $\partial/\partial X^i$ are chosen to be in the upwind direction. The terms added to the flux equation are

$$P^i = -\mu |U^i| \rho_X^i, \quad (8)$$

where μ is a switching function:

$$\mu = \max \left\{ 0, (1 - a^2/q^2) \right\}.$$

and q/a is the local Mach number. The presence of these terms has the effect of adding artificial viscosity to the solution. This does require, however, that the mesh be smooth in the supersonic zone or the effect of the higher-order derivatives associated with the artificial viscosity will cause the solution to give erroneous results.

The last terms which have to be added to the equation are timelike derivatives which have the effect of embedding the steady-state equation in an artificial, time-dependent equation. The final equation that is solved is a discrete approximation to

$$\frac{\partial}{\partial X^i} \left(\rho h U^i + P^i \right) = \alpha \phi_{XT} + \beta \phi_{YT} + \gamma \phi_{ZT} + \delta \phi_T, \quad (9)$$

where the P^i are the upwind biasing terms in the supersonic zones. To make the flow direction timelike, as in the steady state, α , β , and γ are chosen and $\delta \phi_T$ is a damping factor.

The complete numerical scheme is outlined below.

- (1) Evaluate the contravariant velocity components and density at the centers of the primary cells.
- (2) Satisfy continuity on the secondary cells using the flux values calculated in step 1 plus the recoupling terms.
- (3) Add artificial viscosity in the supersonic zones to produce an upwind bias and enforce the entropy condition.
- (4) Add the time-dependent terms to embed the steady-state equation in a convergent, time-dependent process which evolves to the solution.

The numerical solution initially gives the values of ϕ at the grid points. The velocity is then calculated from gradients in the computational plane using the chain rule:

$$u_i = \frac{\partial \phi}{\partial x^i} = \frac{\partial X^j}{\partial x^i} \frac{\partial \phi}{\partial X^j}. \quad (10)$$

The grid point values of the velocity are calculated according to Equation (10) by central differencing (except at boundaries where one-sided differencing must be employed).

To obtain the velocity at an arbitrary prescribed point in physical space, the point is mapped to computational space where trilinear interpolation from the grid point velocities is used. One nontrivial advantage of interpolating in computational space is the Cartesian configuration of the grid which allows an easy search for the cell in which interpolation is to be made.

The main difficulty associated with developing a computer code based on the finite-volume algorithm is that of generating a grid system and incorporating boundary conditions. A desirable grid is one which conforms to all the solid boundaries. Boundary-conforming grids provide an accurate and convenient means of specifying boundary conditions. They also can be made very efficient in that the grid density can be readily controlled at the boundaries where the gradients of the flow parameters can vary most rapidly.

Since the finite-volume method only requires sets of coordinates corresponding to the corner points of the six-sided computational cells, there is no need to have a single mapping function to generate the grid. The procedure chosen is one that uses a sequence of rather simple transformations. The overall mapping is required to be smooth so that the higher-order effects of the transformations do not cause numerical instabilities, particularly in the vicinity of shocks. In Sections 3 and 4, two different grid systems are introduced for two different geometries.

3. COMPUTATION OF A SWEEPED WING IN A RECTANGULAR WIND TUNNEL

3.1 INTRODUCTION

Wind tunnel wall-interference effects are particularly severe at transonic speeds, and considerable effort is required to assess their magnitude, eliminate them, or correct for them if possible. Thus, there is a need for computational tools which can treat complex three-dimensional configurations in typical wind tunnels. The code described in this section was developed under sponsorship of the United States Air Force, Arnold Engineering Development Center, as part of a research project on adaptive-wall transonic wind tunnels. It is intended to be used as a numerical simulator for flow inside the wind tunnel so that studies may be performed to determine the required wall control and iteration procedures to use for such a tunnel. After such a tunnel is built, this code will be replaced by the real flow inside the wind tunnel. This same code may be used, however, to assess the severity of wall interference in a conventional wind tunnel. Such calculations might be incorporated in a suitable wall-correction technique.

The geometry to be computed is shown in Figure 5 together with the specified boundary conditions. The model consists of a swept wing in an infinitely long, rectangular cross-section wind tunnel. Either a normal velocity or pressure boundary condition may be prescribed on each wall.

3.2 GRID-GENERATION SCHEME

A boundary-conforming grid has been constructed consisting of planes parallel to the side walls which cut the wing parallel to the freestream. Within each plane a two-dimensional mapping is used following the suggestion of Caughey and Jameson.⁸ The detailed procedure is described below.

A Cartesian coordinate system is used for the physical space (Figure 5). In this system, x is in the direction of the undisturbed flow and z is in the spanwise direction. Planes normal to the top wall and parallel to the sidewall are generated with the spacing shown in Figure 6. On the planform, a uniform spacing is specified between

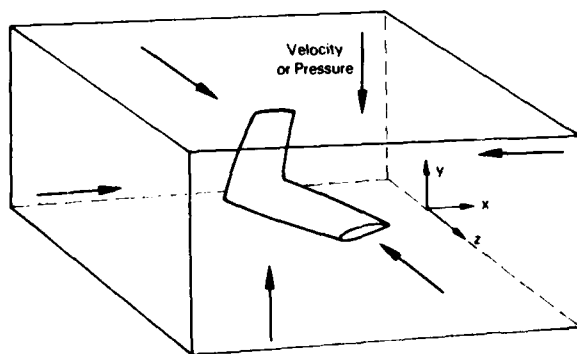


Figure 5. Geometry and Boundary Conditions Used for Wind Tunnel Code.

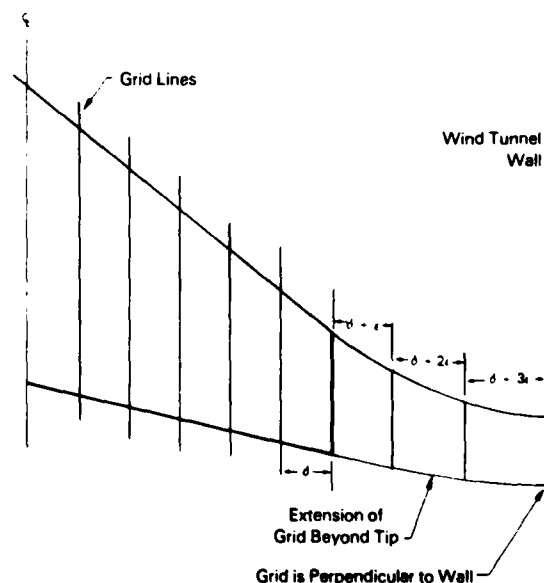


Figure 6. Z Grid Planes and Extension of Planform for Grid Generation.

the planes. Beyond the tip, the spacing is gradually increased or decreased by a small amount, ϵ , to avoid sudden increments in the grid spacing. Also the planform is artificially extended to the wall (as a porous slit) so that the two-dimensional mapping algorithm will remain constant. The extended planform boundaries are defined to be perpendicular to the wall so that the transformed coordinates will be orthogonal there. With the transformed coordinates orthogonal at the wall, the contravariant velocities are the same as the physical velocities except for a scale factor. Although this is not a requirement to specify boundary conditions, it does make the specification simpler.

There remains the task of obtaining a two-dimensional, boundary-conforming coordinate system for a physical x-y cut. The procedure is similar to that outlined by Caughey and Jameson.⁸ The desirable mesh in this cut is one which wraps around the wing section and follows the wake downstream (termed a "C" mesh). First, a wake position is assumed. For this the position downstream of the trailing edge is specified to vary as $A(\log \bar{x})/\bar{x}$ where the coefficient and nondimensionalization are chosen so that the wake leaves at the trailing edge at the bisector angle and the downstream trajectory behaves as a vortex at the quarter chord. It appears from numerical experimentation that the wake position assumed is not important so long as it leaves at the trailing bisector angle. The wake is not treated as a streamline, it is only a surface where the potential jump and sidewash shear occur. Thus, there is actually flow through the wake.

Once the wake is defined, the basic procedure is to use a transformation which unwraps the wing-wake and produces a mapping in which the wing-wake is one line and the tunnel walls are another. In this computational plane a simple Cartesian-grid distribution algorithm can be used which can be mapped back to the physical plane to obtain the cell corner-point coordinates. Figures 7 and 8 outline the procedure. First, the unwrapping point is located at the center of curvature of the wing-section leading edge. Next, a global scaling in x and a shift of origin to the center of curvature is made. Then a quadratic distortion in the y -direction is applied so that the upper wall is at π and the lower wall is at $-\pi$ in the intermediate coordinate system. This last transformation accounts for the global scaling factor used for x .

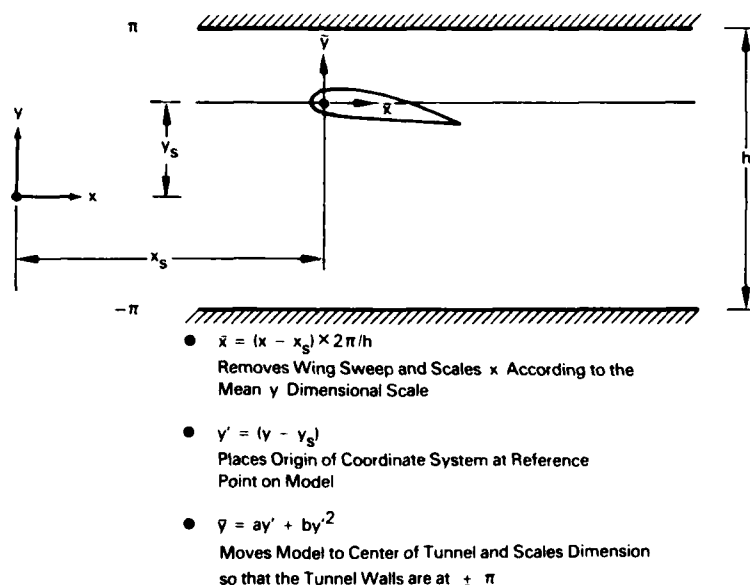


Figure 7. Origin Shift, X Scaling, and Y Distortion.

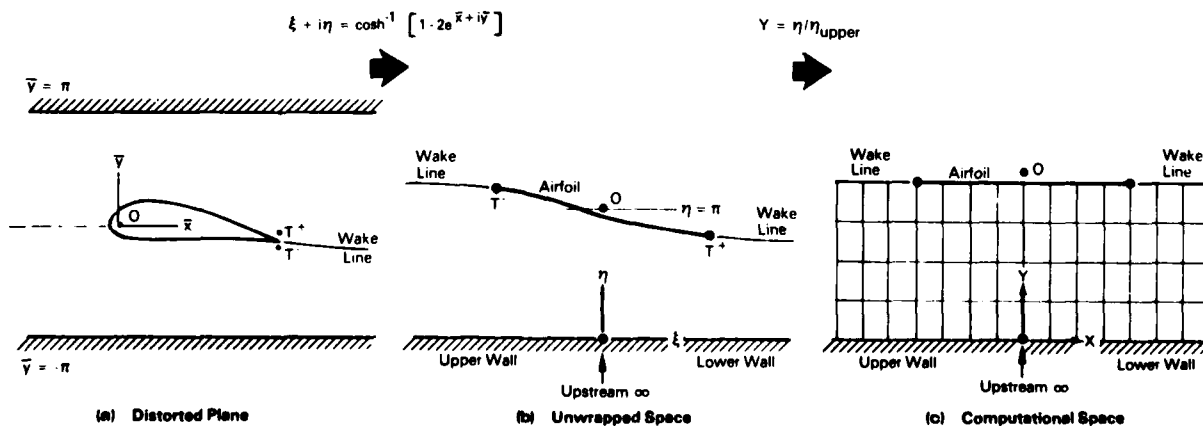


Figure 8. Sequential Mappings from Physical to Computational Space.

Next an unwrapping function is used:

$$\xi + i\eta = \cosh^{-1} [1 - 2e^{\bar{x}+i\bar{y}}] \quad (11)$$

This transformation makes the wing and wake appear as a slowly varying curve about $\eta = \pi$ in the ξ, η plane. Finally the ξ, η plane is sheared using

$$Y = \eta/\eta_{\text{wing-wake}}$$

This produces the desired parallel line representation of the wing-wake and tunnel wall shown in Figure 8. The remaining procedure is to distribute Cartesian grid lines in this space and transform the intersection points back to the physical plane by reversing the transformation procedure just described. Figure 9 shows a coarse grid generated by the procedure. The fine grid used for the final computation has four times as many divisions in each direction.

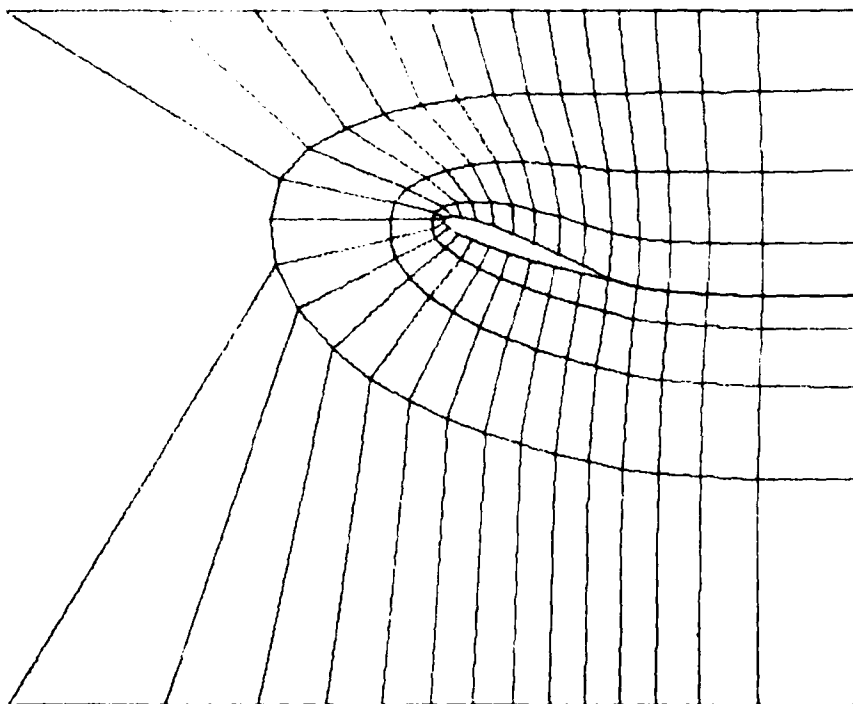


Figure 9. Sample Mesh of Wing in Wind Tunnel.

3.3 BOUNDARY CONDITIONS

The remaining task is to specify the boundary conditions. Upstream, the Mach number is specified. On the wing, the normal flow vanishes. On the wake, the jump in potential at the trailing edge is convected downstream and incorporated into the difference formulas such that the velocities normal and tangential to the wake are continuous. This last condition is a first-order approximation to specifying that there is no jump in pressure across the wake.

Two boundary conditions are employed on the walls. The first is a Neumann boundary condition where the normal velocity is specified as:

$$V_n = \frac{\partial \phi}{\partial n} \quad (12)$$

The second is a Dirichlet boundary condition where the wall pressure is specified as:

$$C_p = -2(u - U_\infty) \quad (13)$$

and

$$\phi = \int_{\text{along wall}} u \, dx \quad (14)$$

The expression for C_p is a small-perturbation approximation which should be accurate at the walls where the flow disturbances are small. Using the above two relations, the velocity potential ϕ can be derived from the pressure coefficient C_p .

The normal velocity or pressure is prescribed on a set of boundary-value grid points. This grid is specified independently of the computational grid so that maximum input flexibility can be achieved. Bilinear interpolation is used to obtain boundary conditions for the computational grid from the input values.

On the downstream plane, a velocity boundary condition is used. Since the potential used in the finite-volume algorithm is a perturbation, it is convenient to express the downstream condition in terms of a perturbation velocity

$$u_d = u_\infty + \delta u, \quad (15)$$

where

$$\delta u = \frac{1}{\rho_d A_d} \int_{\text{tunnel walls}} \rho V_n ds + \frac{\rho_\infty - \rho_d}{\rho_d} u_\infty, \quad (16)$$

ρ_d = downstream density,

A_d = tunnel cross-sectional area, and

V_n = normal velocity at wall (positive into tunnel).

Here it is assumed that the upstream and downstream cross-sectional tunnel areas are the same. This boundary condition conserves mass flux into the tunnel.

3.4 EXAMPLE CALCULATIONS AND CODE VALIDATION

In order to validate the code and illustrate its applications, various calculations have been performed and compared with theoretical, numerical, and experimental results. Theoretical and numerical results were used to validate the wind tunnel wall boundary capabilities. Suitable three dimensional experimental data with known normal flow or pressure values specified at the boundaries were not available at the time the calculations were performed. Therefore, a series of two-dimensional calculations was performed to compare with theoretical and numerical solutions. In this configuration an unswept wing which spanned the tunnel was used. The finite-volume code treats this configuration as a three-dimensional calculation, although the results are invariant spanwise.

Comparison with an exact, incompressible, potential-flow calculation is presented in Figure 10 for a Karman-Trefftz airfoil in a tunnel. The exact solution was obtained by calculating the free-air flow about the airfoil using analytical procedures. The normal component of velocity was calculated along a line parallel to the free stream and above (below) the airfoil as the upper (lower) tunnel wall boundary condition for the finite-volume-method computer calculation. The agreement at the airfoil surface and at the field points given in Figure 10 is excellent. Field-point comparisons along a vertical line from the leading edge was chosen to illustrate the accuracy of the calculations where the errors would be most noticeable. Maximum discretization error for the finite-volume method is expected near the leading edge where velocity gradients are largest. This comparison provides a validation for proper treatment of wall boundary conditions and for calculation of field-point velocities.

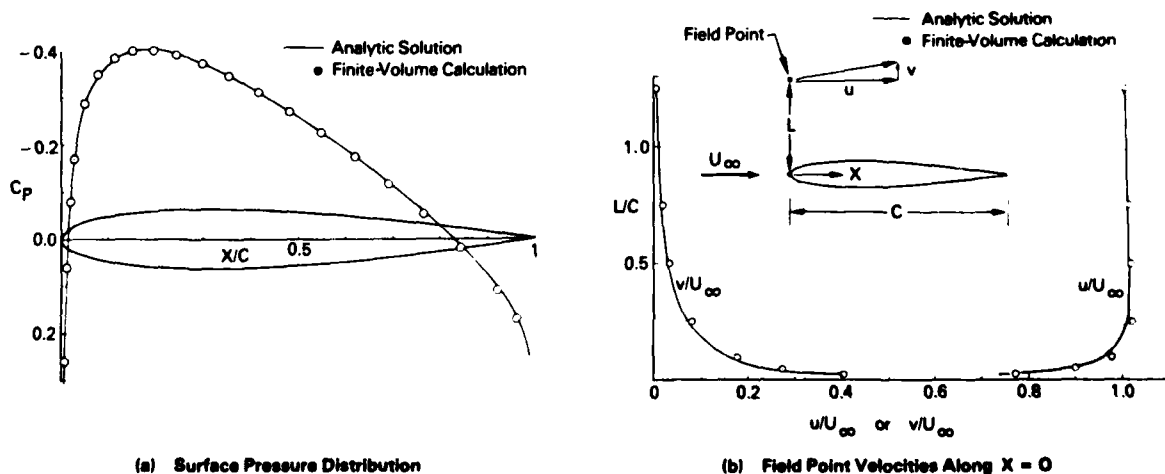


Figure 10. Incompressible Potential Flow about a Karman-Trefftz Airfoil.

To provide a transonic check case with tunnel walls, we calculated the two-dimensional flow about an NACA 0012 airfoil at a Mach number of 0.8 with solid tunnel walls (no normal flow) four chord lengths apart. Figure 11 shows a comparison of the finite-volume method to the small-disturbance method described by Murman, Bailey, and Johnson.⁹ Here again the agreement is quite good. The pressure levels are very close and the shock positions are within one grid spacing. The shock position of the full-potential equation is slightly upstream of the small-disturbance equation. These relative positions are expected due to the differences in the two equations being solved.

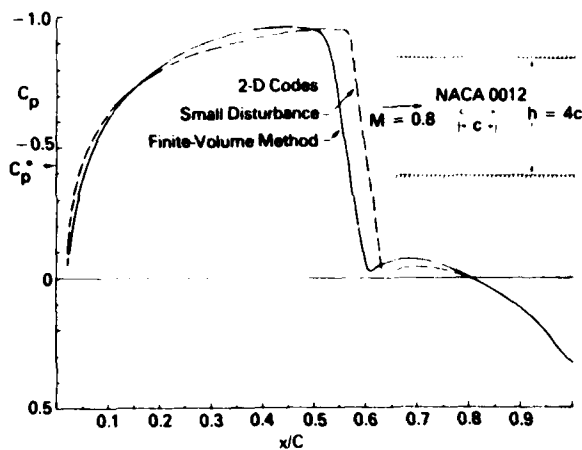


Figure 11. Calculation of the Transonic Flow about an NACA 0012 Airfoil in a Wind Tunnel.

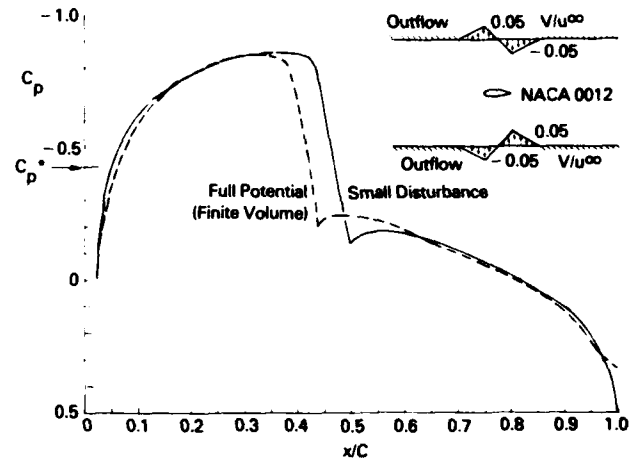


Figure 12. Calculation of the Transonic Flow about an NACA 0012 Airfoil in a Wind Tunnel with Flow Through the Walls.

Figure 12 shows the results for the same wind tunnel configuration but with outflow and inflow specified at the walls to relieve the blockage effect. Comparing Figure 12 with Figure 11 shows that the blockage has been reduced by the wall flow, confirming that the code is yielding the proper behavior. This calculation also provided a validation of the code's treatment of the downstream boundary condition according to Equation (15). The field-point velocities and densities calculated at the downstream boundary were found to satisfy Equation (15).

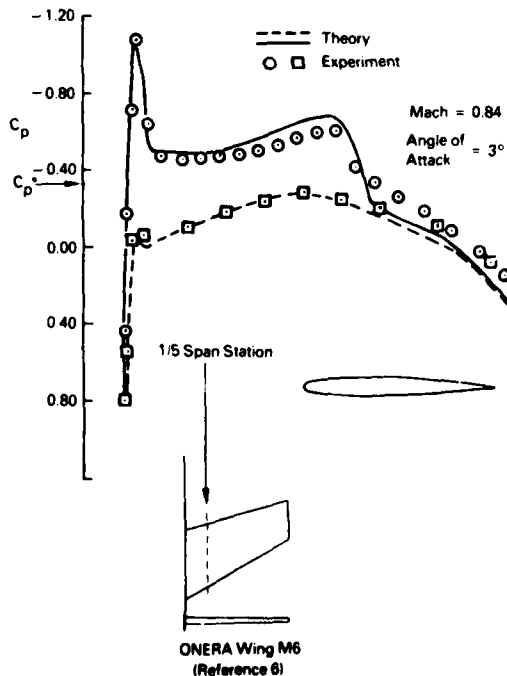


Figure 13. Finite-Volume Method and Wind Tunnel Results for Transonic Flow About a Swept Wing in Free Air.

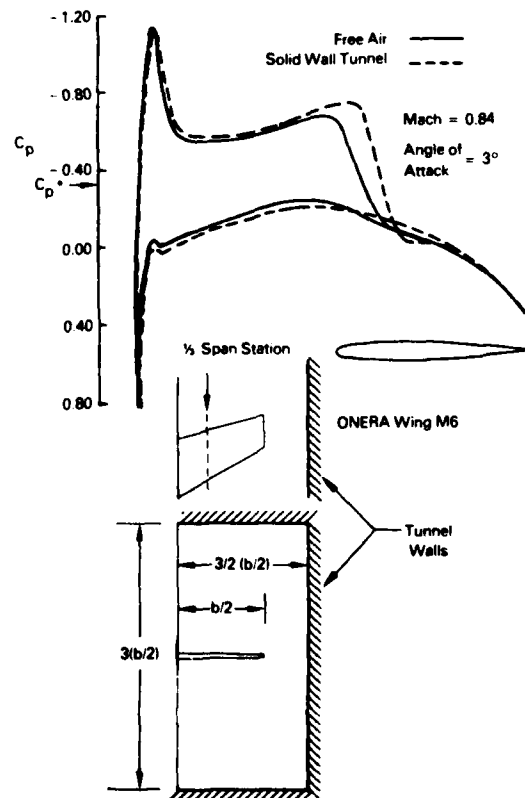


Figure 14. Effect of Solid Tunnel Walls on Free-Air Calculation of Figure 9.

Three-dimensional transonic calculations were made for the ONERA Wing M6, for which experimental data are given in Reference 10 for a slotted-wall tunnel that was simulating the free-air case. The comparison of the free-air calculation with data is shown in Figure 13. The calculation was repeated for solid tunnel walls, and the result is shown in Figure 14. No comparison with experiment is available for this calculation. However, the effects of the solid walls on the wing pressure distribution are in the direction one would expect. The lift coefficient for the wind tunnel flow increased about 20 percent above the free-air value. The shock position moved downstream and the strength increased because of the flow blockage.

4. WING-BODY CODE

4.1 INTRODUCTION

Aircraft design requires the prediction of flow past realistic wing-body-tail configurations with engines and other appendages. Such a complete configuration is currently beyond the capability of full-potential-equation computational techniques but can be treated by the more approximate small-disturbance theory.³ A significant step has been made during the past two years in a cooperative research program between Flow Research and Profs. Caughey and Jameson. Preliminary results were presented by Caughey and Jameson⁷ wherein two separate wing-body grid systems were studied.

One grid system uses a Joukowski transformation to map the noncircular fuselage to a slit with the wing extending outward. A grid system is then established with planes parallel to the freestream cutting the wing, and a parabolic C-type mesh is used within each plane. Results presented in Reference 7 revealed oscillations in the pressure distribution in the wing root area. Further analysis revealed that these were due to the fact that the parabolic-like grid system did not conform to the fuselage boundaries, which resulted in an irregular fuselage geometry in the computation. Although ways could be developed to modify this grid and overcome this problem, this approach was not undertaken because the other grid system appeared to provide better wing root-fuselage geometry modeling and did not suffer from the problem mentioned above. The problem noted became more severe for high- and low-mounted wings which are the typical configurations.

The other grid system introduced in Reference 7 uses a cylindrical-type system. Quasi-cylindrical shells surround the fuselage. The inner shell corresponds to the actual fuselage geometry and the outer shell to a cylinder on which the far-field boundary condition is applied. On each shell a parabolic C-type mesh, essentially identical to that described in the previous wind tunnel code, is used. This system provides excellent modeling in the wing root area and also provides more mesh points on the fuselage than the slit-type transformation. Two expected drawbacks from this system did not present any significant difficulties. For a closed body, the cylindrical system collapses to a line. In practice a very small cylindrical extension to the body is used and the results appear satisfactory. Also, since the system is a cylindrical-type one, the vertical mesh spacing above and below the wing increases with distance outward from the body. However, in practice, vertical mesh spacing near the wing tip is comparable for the cylindrical- and slit-type systems, with the result that the wing root mesh spacing is better.

The remainder of this section will describe the mesh system in more detail and explain some improvements which were necessary to make the earlier version, reported in Reference 7, more robust. Example calculations for a Learjet and an A-7 will be presented.

4.2 GRID GENERATION

The cylindrical computational surfaces are formed by first defining the fuselage surface as

$$r = R_f(x, \theta) \quad (17)$$

$$\text{where} \quad \theta = \tan^{-1} (y/z) \quad (18)$$

The coordinate system is shown in Figure 15 and the Cartesian axes are identical to the ones used for the wind tunnel. Next, a nondimensional radius is formed by

$$\bar{r} = \frac{r - R_f(x, \theta)}{R_c - R_f(x, \theta)} \quad (19)$$

Here R_c is the radius of the cylinder passing through the wing tip.

Within each constant \bar{r} surface, a parabolic C-type mesh system is used which is almost identical to the wind tunnel grid system described above. When the \bar{r} system is "unwrapped," the plane of symmetry passing through the body centerline is equivalent to the walls of the wind tunnel. One difference which must be accounted for is the location of the wing section between the "walls." In the wind tunnel problem, the wing section is approximately midway between the tunnel walls, and the quadratic transformation for y is sufficient to place the wing section midway between the computational boundaries. However, for a high- or low-mounted wing, the angular location of the wing section between the planes of symmetry often exceeds the valid range allowed for a quadratic transformation.

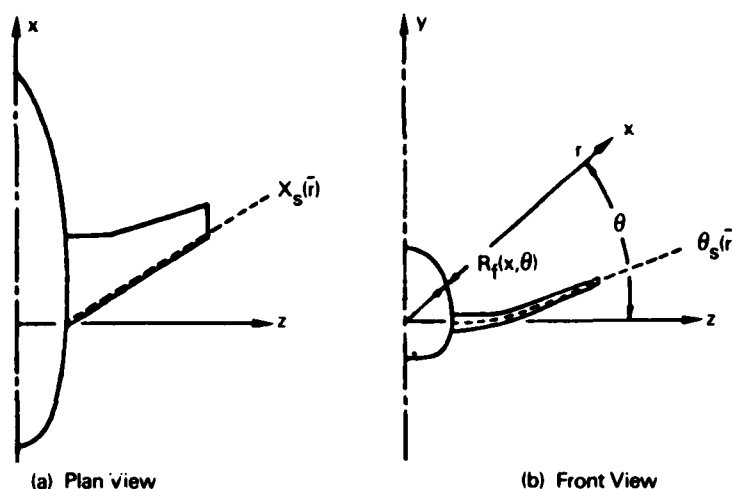


Figure 15. Coordinate System for Wing-Body Code.

An improvement which extends the range of angular displacement is to use an elliptical transformation

$$(\bar{y} - a)^2 + [2(\theta - \theta_s) - b]^2 = R^2, \quad (20)$$

where a , b , and R are selected to meet the constraints

$$\begin{aligned} \bar{y} &= +\pi \text{ at } \theta = +\pi/2, \\ \bar{y} &= -\pi \text{ at } \theta = -\pi/2, \text{ and} \\ \bar{y} &= 0 \text{ at } \theta = \theta_s. \end{aligned} \quad (21)$$

Here θ_s is the angular location of the center of curvature of the wing section formed by the intersection of the cylindrical grid surface and the wing. The factor 2 appears on the $\theta - \theta_s$ term so that the global scaling of the θ to \bar{y} transformation can be accounted for. This latter transformation allows the wing to be displaced from the centerline ($\theta = 0^\circ$) by as much as $+65.88^\circ$. This has been found to be adequate for all the test cases run so far. If still further displacements are required, an exponential transformation could be used. This function would always provide a unique mapping regardless of the amount of displacement from the centerline.

After the transformation to \bar{y} , \bar{x} space is done, the remaining transformations are identical to the wind tunnel grid. A wake trailing behind the wing section is assumed using the same relation as was used for the wind tunnel model. The two-dimensional wing sections are unwrapped and sheared so that the wing and wake form one line and the upper and lower intersection of the cylindrical surface with the centerplane form the other line. A Cartesian grid is then generated between the lines and the intersections of the grid lines and then transformed back to the physical space.

One additional transformation was found to be necessary to handle highly swept wing configurations. For swept wings that are highly tapered, the mesh system described above becomes very highly swept far upstream or downstream. This causes numerical instability problems. The reason that the mesh sweep increases upstream or downstream is that for each cylindrical surface the nondimensionalization used is based on the local wing chord. With a highly tapered wing the mesh lines advance upstream more rapidly at the root than at the tip. This adds to the basic sweep of the mesh system due to wing sweep. To overcome this problem, the grid points obtained by the transformations described so far were shifted according to:

$$x = x_{LE} + (x - x_{LE}) \left[1 + \left(\frac{C_R}{C} - 1 \right) \tanh^2 (x - x_{LE}) \right] \text{ for } x < x_{LE} \quad (22)$$

$$x = x_{TE} + (x - x_{TE}) \left[1 + \left(\frac{C_R}{C} - 1 \right) \tanh^2 (x - x_{TE}) \right] \text{ for } x > x_{TE} \quad (23)$$

where x_{LE} is the local wing leading edge, x_{TE} is the local wing trailing edge, C is the local wing section chord and C_R is the root section chord. These stretching functions have the effect of changing the local scaling from the local chord to the root chord far upstream and downstream of the wing. This removes much of the added sweep due to taper and provides the more stable computational grid.

4.3 BOUNDARY CONDITIONS

Boundary conditions for the wing-body code are similar to those for the wind tunnel code. The wake is treated in exactly the same fashion. Its position is assumed and made part of the airfoil definition. Continuity of longitudinal and normal components of velocity are enforced across the wake to approximate a shear surface without a pressure jump. Specifically, the wake is not assumed to be a streamline, just a free shear surface.

On the body and wing, no normal flow is allowed. Also, no normal flow is allowed at the upper and lower boundaries of the two-dimensional grids on the cylindrical surfaces since these lines correspond to the plane of symmetry. Flow normal to these lines on the cylindrical surface corresponds to cross flow which must be zero for symmetry reasons. Therefore, the flow on the two-dimensional surfaces looks just like the wind tunnel flow for a wing section in a solid wall tunnel.

Upstream, the Mach number and angle of attack are specified. Downstream, the perturbation velocity in the x-direction is assumed to vanish. This provides a first-order approximation to a return to freestream pressure. On the outer shell, all the perturbation velocity components are assumed to vanish. Of course the far field boundaries in the finite-volume algorithm are really at a finite distance from the configuration. This in itself introduces some error; however, comparisons with other analyses and wind tunnel data would indicate the effect to be small.

4.4 SAMPLE COMPUTATION

The wing-body code has been exercised for several representative configurations. Results have shown good agreement with other numerical techniques in their common range of validity. Two sample results are presented. The first example is a Learjet for which no wind tunnel data are available for comparison. The second configuration is a Navy attack aircraft (A-7) with a nonstandard supercritical wing which was designed for the configuration using numerical optimization techniques. The wing-body configuration was tested at NASA Ames Research Center to verify to new design goals and, hence, wind tunnel data is available for comparison. The redesigned wing configuration resulted from a design exercise to test transonic numerical design techniques.^{11,12}

Figure 16 shows a coarse computational grid on the Learjet. The final computational mesh has four times as many grid lines in each direction and is formed by dividing the mesh spacing shown in half and then in half again. Figure 17 shows the pressure distribution on the wing at a span station near the root and one near the tip. Wind tunnel data currently being processed should provide a good comparison.

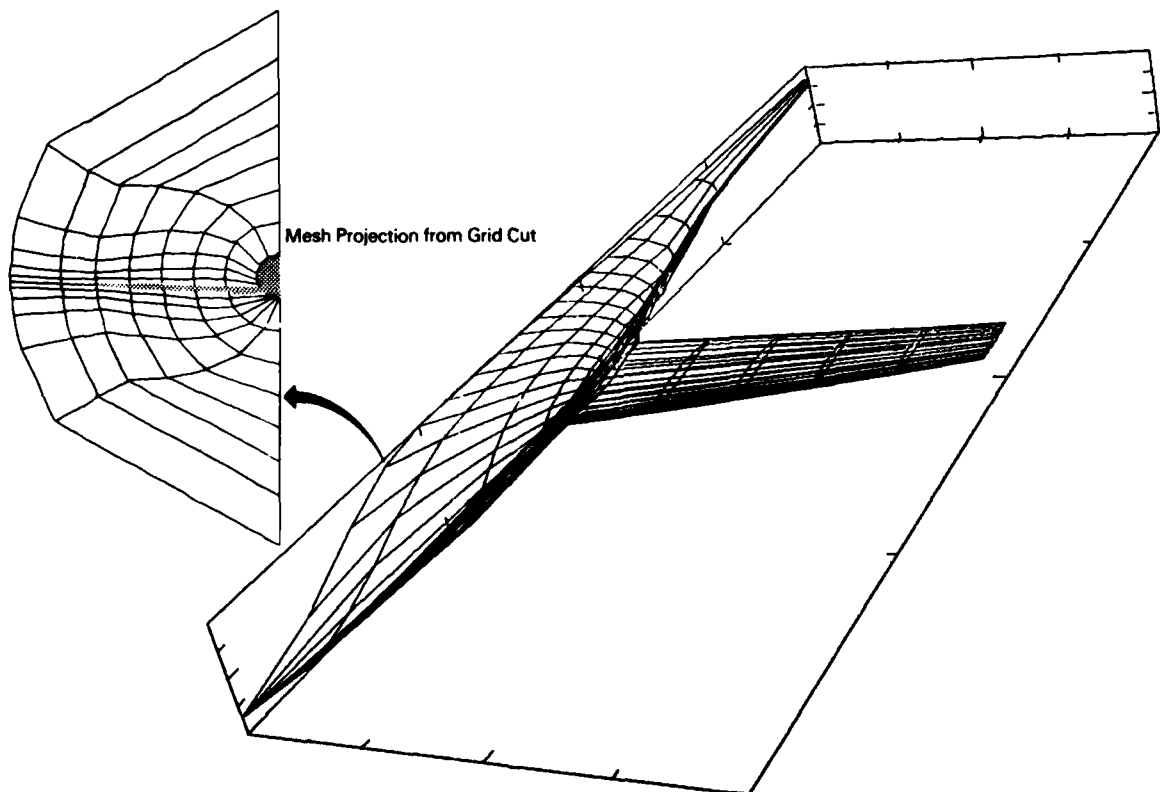


Figure 16. Coarse Grid on Learjet.

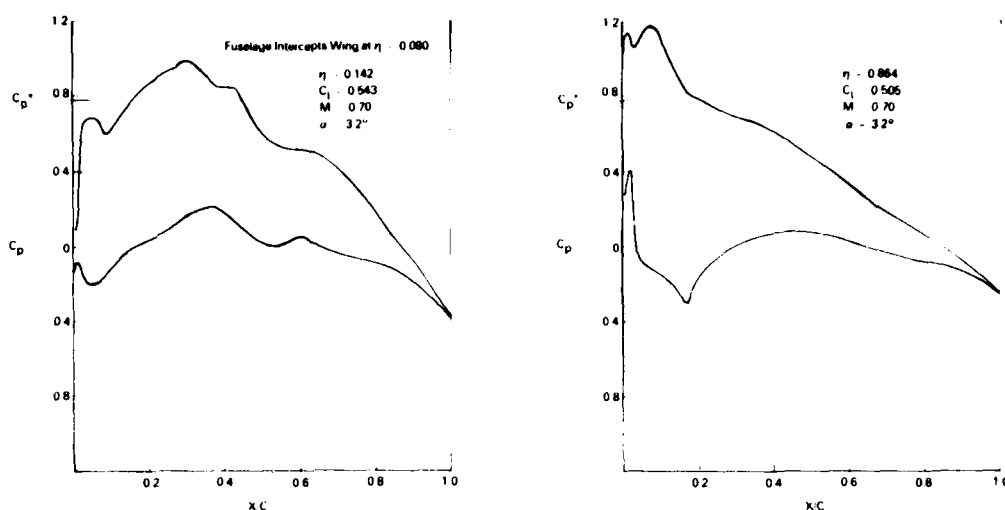


Figure 17. Cordwise Pressure Distribution on Learjet.

Figure 18 shows a comparison of wind tunnel data with the results from the wing-body finite-volume code and a wing-alone finite-volume code for the redesigned A-7 configuration. The first station shown on Figure 18 ($\eta = 0.146$) is close to the wing body juncture ($\eta = 0.12$). These results show the strong influence of the fuselage and the good agreement of the wing-body code with the wind tunnel data. Both the wing-body and wing-alone computer codes were run at the same angle of attack as the wind tunnel model; there was no attempt to match overall lift. Lower surface pressure agreement is excellent across the span. Upper surface pressures predicted by the code seem to be generally higher. This could be due to some viscous effect or possibly wall interference. The viscous effect due to shock-boundary layer interaction is quite noticeable near the tip, where the inviscid code predicts a stronger compression through the shock than was obtained by the experiment.

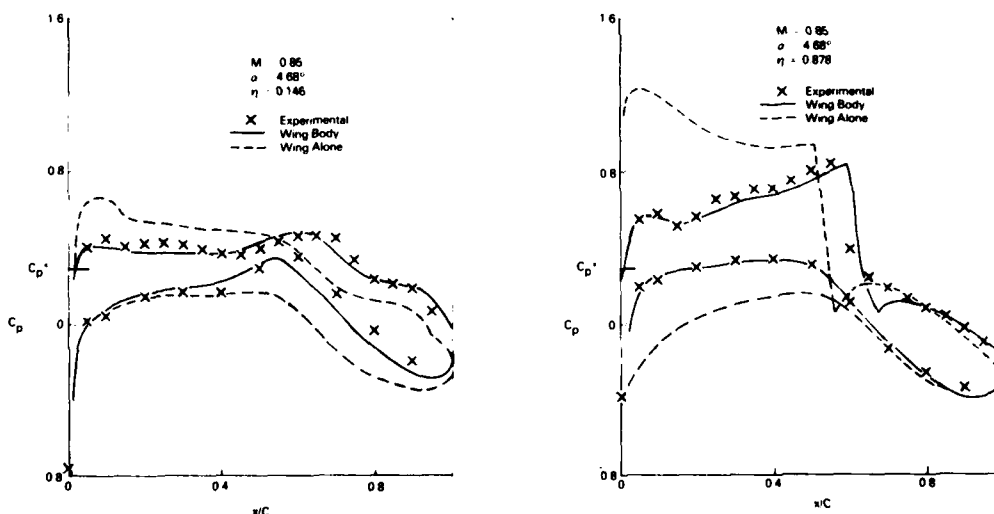


Figure 18. Comparison of Computed and Experimental Cordwise Pressure Distributions on Modified A-7 Model.

Figure 19 shows the effect of the fuselage on the spanwise loading. The results are nondimensionalized by the total lift coefficient so that the comparison shows the distribution effect. The presence of the fuselage tends to increase the loading inboard on the wing. The effect of the fuselage on the total lift is indicated on the figure. For an angle of attack of 4.68° , the fuselage reduced the total lift by 38 percent, from 0.485 for the wing-alone case to 0.300 for the wing-fuselage case.

5. DISCUSSION AND CONCLUSIONS

The finite-volume algorithm provides a very powerful basis to generate computer codes to solve the full-potential equations in conservation form about complex geometries. The two codes described in this paper show the fundamental process that needs to be followed in order to develop such codes. The accuracy of the results, when compared to other codes and experimental data for the two codes, attest to the range of applica-

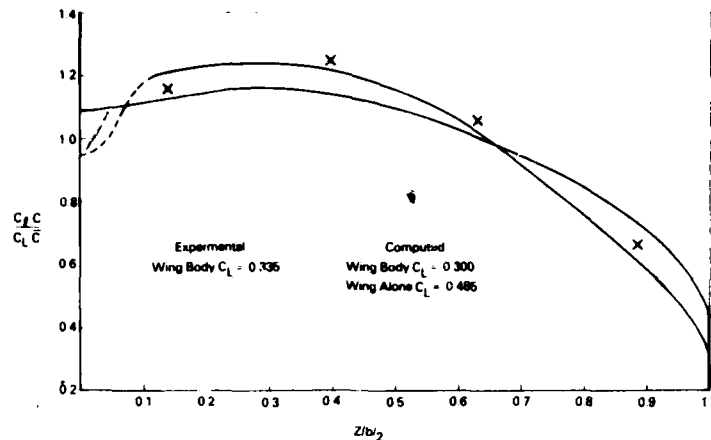


Figure 19. Effect of Fuselage on Computed Spanwise Loading of Modified A-7 Model.

tion of the algorithm. More work needs to be done to determine the restrictions which must be placed on the mesh generation. For example, this work uncovered that mesh sweep could destabilize the solution. The exact mechanism and limits on the sweep have not been fully studied. Furthermore, the smoothness of the mesh is known to place limits on the procedure, particularly in the vicinity of shocks. Again, the exact limits are unknown. Finally, two-dimensional computations have indicated that the aspect ratio of the mesh is important. These exact bounds are also unknown.

Although many of these limits have not yet been quantized, they have not proved to be real restrictions. The consequence of overstepping the bounds has so far been catastrophic, i.e., divergence. The main purpose of presenting them is to make potential program developers aware of where problems may occur should their codes suddenly diverge without apparent reason.

The two codes presented here have faced one or more of these difficulties during the course of their development. Their present status is such that they should run without difficulty on a wide variety of configurations. The wing-body code does represent a practical limit to what can be achieved using a single mesh-generation scheme. To include a tail, nacelles, etc., will require the marriage of more than one grid system. This will require combining special grid-generation algorithms, each best suited to a specific component on the configuration. Matching of flow parameters across common boundaries will have to be incorporated into the solution procedure.

One other consideration which has not been mentioned yet is that of computing time. Currently, both the wind tunnel program and the wing-body program require about 45 minutes of CDC 7600 time. Some bench mark runs have been made on the CRAY-1. From these tests, execution times of 8 to 9 minutes are expected. Improvements in execution speed on the CRAY machine are expected since the increased memory will allow the program to run totally in core without the need to store computational variables on disks. Still further improvements could be expected if the solvers were vectorized.

Long-term improvements in speed are expected from the new algorithms being developed. An order of magnitude improvement or better in speed has been indicated by some researchers using new algorithms such as multigrid. Near-term benefits have been demonstrated using such procedures as extrapolation. Work performed at Flow Research has shown that a 30 to 50 percent reduction in computing could be expected in general by applying this technique. More work is required to determine how robust this technique is.

Work currently in progress at Flow Research is addressed to short- and long-term development of general-configuration transonic codes. The goal is to achieve a general-configuration code which will provide designers with the most accurate results they can achieve outside of the wind tunnel.

REFERENCES

1. Bailey, F. R., and Ballhaus, W. F., "Comparisons of Computed and Experimental Pressures for Transonic Flows About Isolated Wings and Wing Fuselage Configurations," NASA SP-347, Part II, March 1975, pp. 1213-1232.
2. Mason, W., MacKenzie, D. A., Stern, M. A., and Johnson, J. K., "A Numerical Three-Dimensional Viscous Transonic Wing-Body Analysis and Design Tool," AIAA Paper 78-101, January 1978.
3. Boppe, E. W., and Stern, M. A., "Simulated Transonic Flows for Aircraft with Nacelles, Pylons, and Winglets," AIAA Paper 80-0130, January 1980.

4. Hinson, B. L., and Burdges, K. R., "An Evaluation of Three-Dimensional Transonic Codes Using New Correlation-Tailored Test Data," AIAA Paper 80-0003, January 1980.
5. Jameson, A., and Caughey, D. A., "A Finite Volume Method for Transonic Potential Flow Calculations," AIAA Paper 77-635 in Proceedings of AIAA 3rd Computational Fluid Dynamics Conference, June 1977, pp. 35-54.
6. Mercer, J. E., Geller, E. W., Johnson, M. L., and Jameson, A., "A Computer Code to Model Swept Wings in an Adaptive Wall Transonic Wind Tunnel," AIAA Paper 80-0156, January 1980.
7. Caughey, D. A., and Jameson, A., "Recent Progress in Finite-Volume Calculations for Wing-Fuselage Combinations," AIAA Paper 79-1513, July 1979.
8. Caughey, D. A., and Jameson, A., "Calculation of Transonic Potential Flow Fields About Complex Three-Dimensional Configurations," Transonic Flow Problems in Turbomachinery, Washington, D. C., Hemisphere Publishing, 1977, pp. 274-293.
9. Murman, E. M., Bailey, F. R., and Johnson, M. L., "TSFOIL-A Computer Code for 2-D Transonic Calculations Including Wind-Tunnel Wall Effects and Wave-Drag Evaluation," NASA SP-347, Part II, 1975, pp. 769-788.
10. Monnerie, B., and Charpin, F., "Essais de Buffeting d'une Aile en Fleche en Transsonique," 10e Colloque d'Aerodynamique Appliquee, Lille, November 1973.
11. Haney, H. P., Johnson, R. R., and Hicks, R. M., "Computational Optimization and Wind Tunnel Test of Transonic Wing Designs," AIAA Paper 79-0080, January 1979.
12. Haney, H. P., and Johnson, R. R., "Application of Numerical Optimization to the Design of Wings with Specified Pressure Distributions," NASA Contractor Report 3238, 1980.

ACKNOWLEDGMENT

The work reported here represents a cooperative effort between researchers at Flow Research and Profs. Jameson and Caughey. Dr. Wen-Huei Jou, Mr. Ed Geller and Ms. Margaret Johnson made significant contributions to the development of the codes. The work was done under the sponsorship of USAF/AEDC Contract No. F4D600-79-C-0001 and ONR Contract N00014-78-C-0079.

UNE METHODE VARIATIONNELLE D'ELEMENTS FINIS
POUR LA RESOLUTION D'ECOLEMENTS TRANSSONIQUES TRIDIMENSIONNELS

par : Y. VIGNERON* - O. BROCARD** - J. BOUSQUET* - T. LEJAL*

-==--§--==--

Société Nationale Industrielle Aérospatiale
 316, Route de Bayonne - BP 3153
 31060 Toulouse - France

RESUME

Il s'agit de présenter la méthode d'éléments finis développée à l'Aérospatiale pour la simulation numérique des écoulements transsoniques stationnaires non visqueux autour de géométries complexes, voilure avec fuselage par exemple. Dans cette méthode, l'écoulement aérodynamique est décrit par l'équation générale du potentiel, sous forme conservative. Pour résoudre cette équation, on utilise une formulation originale, basée sur une extension du principe variationnel de Bateman au cas transsonique. Cette formulation permet de réduire le nombre d'itérations nécessaire pour obtenir une solution. L'unicité de cette solution est assurée par l'emploi de viscosité artificielle, sous forme de densité "retardée". La discrétisation du problème s'effectue par une approximation isoparamétrique trilineaire sur des éléments hexaédraux. Dans le cas d'écoulements portants, la condition de Kutta Joukowski est réalisée grâce aux solutions circulatoires associées. Des résultats pratiques sont présentés pour valider la méthode. Ils sont comparés à des résultats expérimentaux et à des résultats fournis par d'autres méthodes numériques.

1.- INTRODUCTION -

Les méthodes numériques occupent une place de plus en plus importante dans l'analyse des formes aérodynamiques complexes en régime transsonique. La méthode des différences finies est la plus utilisée : dans ses versions récentes, elle est rapide (méthodes semi-directes ou méthodes de factorisation) et elle permet de "capturer" les chocs éventuels (méthodes de viscosité artificielle ou méthodes de densité retardée). Cependant, elle semble limitée dans l'immédiat à des formes simples (voilure + fuselage simplifié).

La méthode des éléments finis, par contre, est plus indiquée pour des formes complexes (possibilité de maillage quelconque et traitement exact des conditions aux limites), mais son utilisation en régime transsonique est encore du domaine de la recherche. On peut signaler deux difficultés :

- 1) - il faut savoir éliminer les chocs de détente qui ne sont pas physiquement acceptables, mais sont contenus dans l'équation du potentiel,
- 2) - les principes variationnels classiques ne s'appliquent plus, car les fonctionnelles considérées perdent leurs propriétés de convexité lorsque le nombre de Mach local dépasse l'unité.

L'objet de ce rapport est de présenter une méthode d'éléments finis basée sur une approche variationnelle et valable en régime transsonique. Cette méthode a été conçue pour accepter des maillages quelconques et permettre ainsi le calcul d'avions complets. Dans les paragraphes qui suivent on trouvera un résumé de la formulation théorique ainsi que des résultats préliminaires pour des voilures et un ensemble voilure-fuselage.

* Ingénieur Aérospatiale - Aérodynamique théorique

** Ingénieur CERT (ONERA) - Groupe Analyse Numérique

2.- DEVELOPPEMENT THEORIQUE -

2.1 - Equations -

Dans la présente analyse, l'écoulement aérodynamique est décrit par l'équation générale du potentiel, sous forme conservative

$$\operatorname{div}(\rho \vec{\operatorname{grad}} \varphi) = 0 \quad (1)$$

dans le domaine de calcul Ω (voir figure 1) où

$$\rho = \rho(\varphi) \quad (2)$$

désigne la densité au point courant. Les conditions aux limites associées à cette équation sont des conditions de Neuman :

a) - flux de masse nul à la paroi et sur le plan de symétrie

$$\vec{\operatorname{grad}} \varphi \cdot \vec{N}_0 = 0 \quad \text{sur } \Gamma_0 \quad (3)$$

b) - flux de masse imposé sur la frontière à l'infini

$$(\rho \vec{\operatorname{grad}} \varphi - \rho_\infty \vec{V}_\infty) \cdot \vec{N}_\infty = 0 \quad \text{sur } \Gamma_\infty \quad (4)$$

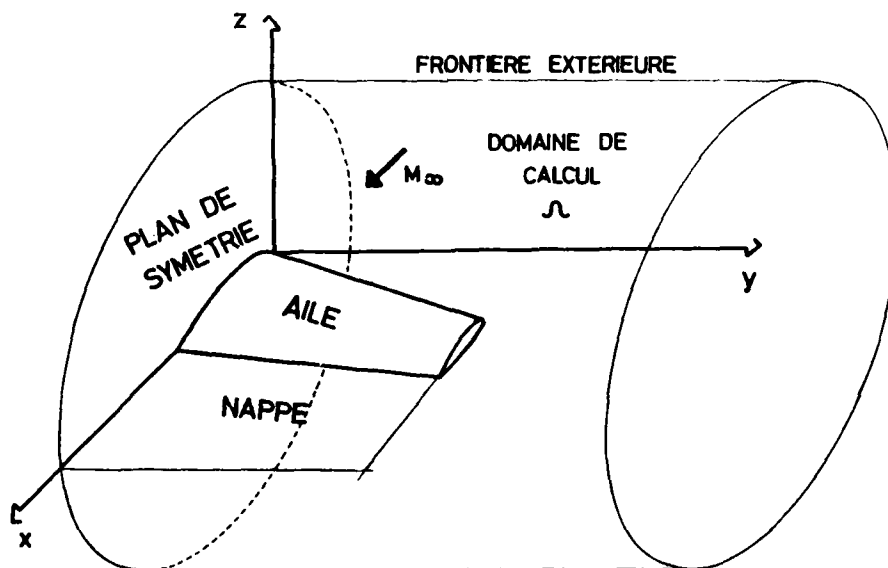


FIG: 1

Ces équations sont déduites des équations d'Euler stationnaires en faisant l'hypothèse d'irrotationalité. Puisqu'un écoulement irrotationnel est isentropique, l'introduction d'un potentiel impose le remplacement des ondes de choc par des discontinuités au travers desquelles l'entropie est conservée. On se limitera donc aux écoulements transsoniques stationnaires où les ondes de choc sont suffisamment faibles pour justifier cette hypothèse. Par ailleurs, les effets visqueux ne sont pas pris en compte et ils devront être introduits ultérieurement au moyen d'un couplage avec un calcul de couche limite.

2.2 - Méthode -

La méthode de résolution est basée sur une extension du principe variationnel de BATEMAN. Ce principe donne la solution des problèmes subcritiques comme étant le potentiel φ qui minimise la fonctionnelle $J(\varphi)$, intégrale de la pression $p(\varphi)$ sur le domaine de calcul Ω (voir fig.1):

$$J(\varphi) = - \int_{\Omega} p(\varphi) d\tau - \int_{\Gamma_{\infty}} (\rho_{\infty} \vec{V}_{\infty} \cdot \vec{N}_{\infty}) \varphi d\sigma \quad (5)$$

Malheureusement, dès qu'apparaissent des zones supersoniques dans l'écoulement, cette fonctionnelle n'est plus concave partout et l'extremum cherché ne peut plus être obtenu par une méthode de descente.

On considère alors la fonctionnelle de pression modifiée $\tilde{J}(\varphi)$:

$$\tilde{J}(\varphi) = - \int_{\Omega} [c p(\varphi) - (1-c) d \frac{|\vec{\text{grad}} \varphi|^2}{2}] d\tau - \int_{\Gamma_{\infty}} (\rho_{\infty} \vec{V}_{\infty} \cdot \vec{N}_{\infty}) \varphi d\sigma \quad (6)$$

où c et d sont des fonctions ponctuelles à définir (pour $c \equiv 1$ on retrouve la fonctionnelle de pression de BATEMAN). On peut montrer :

- a) - que $\tilde{J}(\varphi)$ est strictement concave dans l'espace des fonctions à dérivées de carré sommable $H^1(\Omega)$ si :

$$\begin{cases} c \leq 1 & \text{lorsque le mach local } M(\varphi) < 1 \\ \text{et} & \\ c < \frac{1}{1 + [M(\varphi) - 1] \frac{p(\varphi)}{d}} & \text{lorsque } M(\varphi) > 1 \end{cases} \quad (7)$$

- b) - que la stationnarité de $\tilde{J}(\varphi)$ par rapport à φ dans $H^1(\Omega)$ implique :

$$\text{div} \{ [c p(\varphi) + (1-c) d] \vec{\text{grad}} \varphi \} = 0 \quad (8)$$

$$\text{et} \quad \{ [c p(\varphi) + (1-c) d] \vec{\text{grad}} \varphi - \rho_{\infty} \vec{V}_{\infty} \} \cdot \vec{N}_{\infty} = 0 \quad (9)$$

Ces deux résultats constituent la base de la méthode itérative proposée. On définit une suite d'intégrales de pression $\{\tilde{J}_n(\varphi)\}$, modifiées de façon à assurer leur concavité partout grâce au choix de c vérifiant les conditions (7). Chacune de ces intégrales a donc pour minimum une fonction potentiel unique φ_n . Si à chaque itération n on prend pour fonction $d = p(\varphi_{n-1})$, la solution φ du problème transsonique peut être obtenue en tant que limite de la suite $\{\varphi_n\}$. En effet, à convergence, cette limite vérifie l'équation générale du potentiel (1) ainsi que les conditions aux limites (3 - 4).

Il faut remarquer que le choix $c \equiv 0$ qui satisfait aussi les conditions de concavité (7) correspond à la linéarisation habituelle de l'équation au potentiel, c'est à dire :

$$\text{div} \{ p(\varphi_{n-1}) \vec{\text{grad}} \varphi_n \} = 0 \quad (10)$$

Cependant les fonctions C données par les formules (7) permettent une approximation non linéaire plus riche de l'intégrale de pression (5). La méthode proposée laisse donc espérer une réduction substantielle du nombre des itérations n .

Il reste à assurer la convergence de la suite $\{\varphi_n\}$ vers la solution physique du problème transsonique et l'élimination des chocs de détente. Ceci est réalisé en introduisant de la viscosité artificielle dans les équations, au moyen de la méthode de la "densité retardée" préconisée par HAFEZ, SOUTH & MURMAN¹.

Celle-ci consiste à remplacer, dans les zones supersoniques, la densité ρ au point courant par la densité $\tilde{\rho}$ en un point situé légèrement en amont, suivant la formule :

$$\tilde{\rho} = \rho - \nu (\rho - \rho_A) \quad (11)$$

où

$$\nu = \text{MAX} \left[0; 1 - e^{-\varepsilon (M^2 - 1)} \right] \quad \varepsilon \approx 1. \quad (12)$$

et ρ_A représente la densité sur l'élément situé immédiatement en amont du point courant. On montre qu'il y a équivalence entre la méthode de la densité retardée et les méthodes de décentrage de JAMESON² et MURMAN ET COLE³, qui sont utilisées en différences finies. Cependant, l'approche densité retardée se prête mieux à la discrétisation par éléments finis⁴.

2.3 - Discrétisation -

Le domaine de calcul Ω est représenté par une partition d'éléments qui sont des hexaèdres dont les faces sont des quadrilatères gauches. Sur cette partition, le potentiel φ est approché par une approximation isoparamétrique trilineaire qui ne dépend que des valeurs du potentiel aux noeuds du maillage. Ainsi chaque problème continu de détermination du potentiel φ_n , minimum de l'intégrale \tilde{J}_n , est remplacé par un problème discret aux N inconnues $\varphi_{n,i}$ pour $i = 1, \dots, N$. Pour cela, l'intégrale \tilde{J}_n n'est pas calculée exactement, mais de façon approchée par une formule de quadrature sur chaque élément. Une formule de GAUSS à huit points d'intégration est utilisée à proximité du corps et une formule à un point d'intégration pour le reste du domaine. La détermination des $\varphi_{n,i}$ est un problème de minimisation sans contrainte d'une fonction concave. La solution est unique et elle est obtenue par l'algorithme des gradients conjugués. Cet algorithme permet une faible occupation de la mémoire de l'ordinateur, puisqu'il nécessite seulement le stockage de trois vecteurs de dimension N .

2.4 - Condition de KUTTA - JOUKOVSKI -

Dans le cas d'un écoulement autour d'un corps portant, la condition de KUTTA - JOUKOVSKI (égalité de pression à l'intrados et à l'extrados du bord de fuite) conduit à une fonction potentiel φ qui présente une discontinuité. Cette surface de discontinuité symbolise un sillage issu de la ligne du bord de fuite du corps portant et on supposera qu'elle a une forme déterminée a priori. Le potentiel solution du problème portant est recherché sous la forme d'une combinaison linéaire du potentiel solution du problème continu associé, et de potentiels circulatoires, qui sont des fonctions harmoniques présentant une discontinuité étalon au bord de fuite. Les coefficients de la combinaison linéaire sont obtenus à partir de la condition de KUTTA-JOUKOVSKI, écrite en des points de contrôle le long du bord de fuite sous la forme :

$$\|\vec{V}_{\text{intrados}}\| = \|\vec{V}_{\text{extrados}}\| \quad (13)$$

Ces équations non linéaires sont résolues par un processus itératif de NEWTON qui est mené parallèlement aux itérations n du problème transsonique.

Une telle formulation permet d'assurer l'égalité des pressions ainsi qu'une allure convenable du potentiel au bord de fuite du corps portant.

3.- RÉSULTATS PRELIMINAIRES -

La méthode présentée ci-dessus a été conçue pour simuler l'écoulement transsonique autour d'avions complets. En effet, le développement théorique a montré que l'approche éléments finis n'est pas restreinte à des maillages de type "cartésien déformé", comme ceux utilisés en différences finies. Cette liberté dans le choix du maillage permet le traitement de conditions aux limites compliquées. La mise en oeuvre informatique a été faite de façon à conserver cette propriété et accepter des maillages quelconques. Le but de ce rapport n'est pas de décrire une procédure pour générer de tels maillages. On présentera plutôt des résultats destinés à valider la méthode et obtenus avec des maillages plus classiques sur des géométries représentatives : voilures et combinaison aile-fuselage.

3.1 - Résultats pour ailes à la paroi -

Trois types de voilures ont été analysées et les résultats comparés à des résultats antérieurs et à des données expérimentales. La première voilure, désignée SUTO est une voilure droite à profil NACA 0012, d'allongement 6. La seconde, désignée M6, a été étudiée expérimentalement à l'ONERA⁵. La troisième est une voilure supercritique conçue à l'Aérospatiale sous le nom de 10AG5 ; sa forme en plan est représentée sur la figure 2.

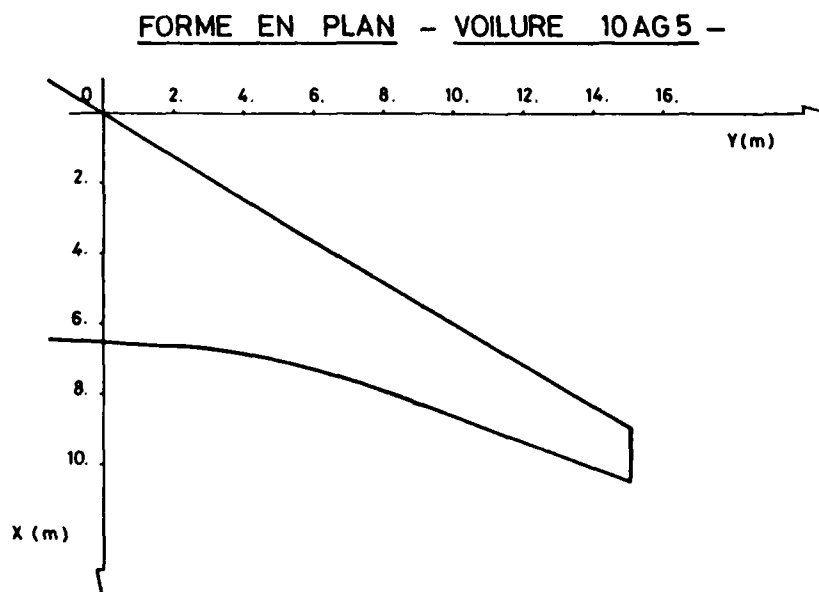
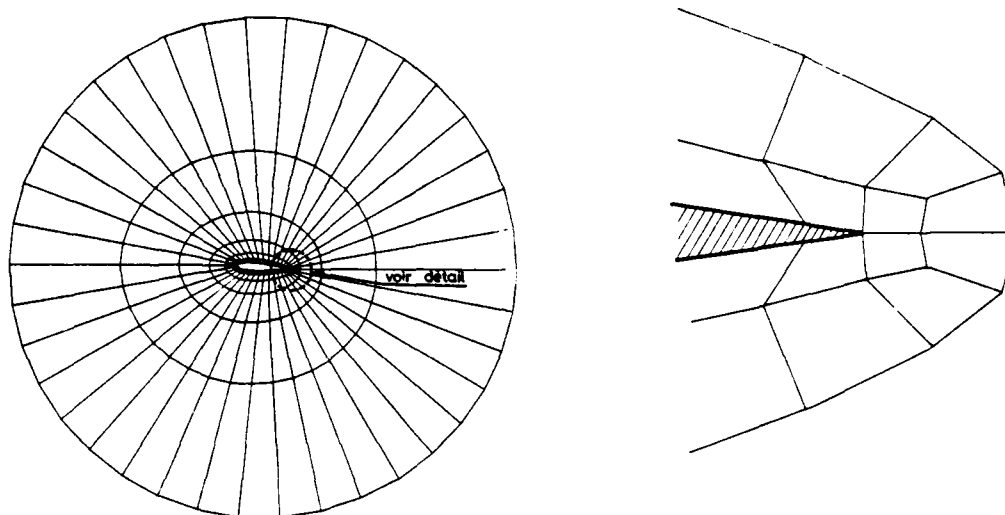


FIG: 2

Le maillage utilisé pour chaque voilure comprend 5468 éléments et il est réalisé par tranches bidimensionnelles juxtaposées. La figure 3 donne un exemple de maillage dans une tranche ; la disposition des mailles au bord de fuite (détail de la figure 3) n'est possible que dans une approche éléments finis.



Y=Cte COUPE DU MAILLAGE

FIG: 3

DETAIL FIG:3 - MAILLAGE AU BORD DE FUITE

Le tableau suivant résume les cas de calcul présentés dans les figures 4 à 22 :

CAS N°	VOILURE	MACH M	INCIDENCE
1	SUTO	0.001	2°
2	SUTO	0.8	0°
3	SUTO	0.75	1,5°
4	M6	0.84	0°
5	M6	0.92	0°
6	10AG5	0.8	- 0,255°

Pour la vérification des résultats, on dispose :

- a) - dans le cas incompressible, d'une méthode de singularités développée à l'Aérospatiale (solution quasi-exacte),
- b) - d'une méthode de différences finies non conservative développée par A. JAMESON et D.A. CAUGHEY sous le nom de FLO-22⁶,
- c) - pour l'aile M6, des résultats expérimentaux de l'ONERA,
- d) - pour l'aile 10AG5, des résultats expérimentaux obtenus par l'Aérospatiale.

Le cas de calcul incompressible permet de tester la précision de la méthode et sa capacité à traiter les problèmes portants. Les résultats sont excellents, tant pour les courbes de coefficients de pression que pour la répartition de portance locale en envergure. Au bord de fuite, ils présentent même un traitement de la singularité meilleur que ceux des différences finies.

Les comparaisons sont plus approximatives pour les calculs transsoniques. A cela, il existe trois raisons principales :

- a) - la méthode des éléments finis est conservative alors que celle des différences finies ne l'est pas,
- b) - la méthode des éléments finis ne tient pas compte pour l'instant des effets visqueux qui sont présents dans les essais,
- c) - enfin le maillage d'éléments finis est trop grossier, surtout dans la direction longitudinale (il n'y a que 25 points sur l'extrados d'un profil)

La figure 10 permet d'ailleurs de voir l'influence du maillage pour un cas transsonique bidimensionnel. On note que la méthode des éléments finis génère un choc très raide, pratiquement réparti sur une maille.

Les résultats présentés ci-dessus ont été obtenus dans leur majorité sur un ordinateur CDC CYBER-174. Dans le cas de calcul n° 2, on a utilisé :

200 minutes de temps CP
58240₁₀ mots de mémoire centrale
252830₁₀ mots de mémoire ECS

Pour ce même cas, la formulation variationnelle généralisée nécessite 8 fois moins d'itérations n que la formulation linéarisée (10) qui est employée habituellement.

3.2 - Résultats pour combinaison aile-fuselage -

Afin de montrer la capacité de la méthode à traiter des configurations réalistes, une combinaison aile-fuselage a aussi été étudiée. La figure 23 donne un plan 3 vues de cet ensemble. Il s'agit d'un cas non portant et on considère seulement le quart du domaine entourant l'obstacle. On pourra compléter par symétries. S'agissant de résultats préliminaires un maillage grossier de 3000 éléments (dont 48 sur un côté de la voilure) est utilisé. Les figures 24 et 25 montrent les isobares à la surface du corps en régime incompressible et en régime transsonique ($M_{\infty} = 0.8$).

4.- CONCLUSION -

Le résumé d'une méthode de calcul originale des écoulements transsoniques tridimensionnels stationnaires vient d'être présenté, ainsi que quelques résultats préliminaires. Ces résultats permettent de valider l'approche éléments finis et ils donnent une idée de sa généralité. Le travail futur va porter sur deux points principaux :

- a) - brancher le programme de calcul sur un générateur automatique de maillages quelconques, qui permettent d'utiliser pleinement les possibilités de la méthode,
- b) - améliorer les performances de la méthode, en y incorporant notamment la technique des maillages imbriqués.

On peut penser qu'alors cette méthode constituera un véritable outil aérodynamique pour les écoulements transsoniques.

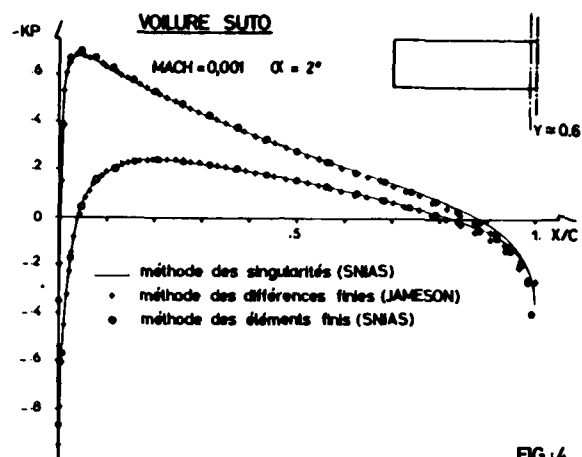


FIG. 4

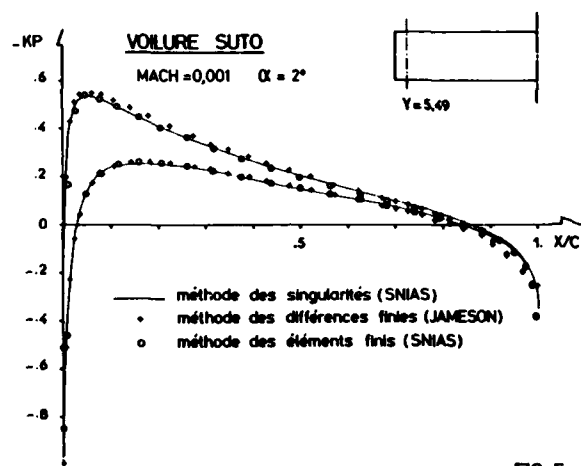


FIG. 5

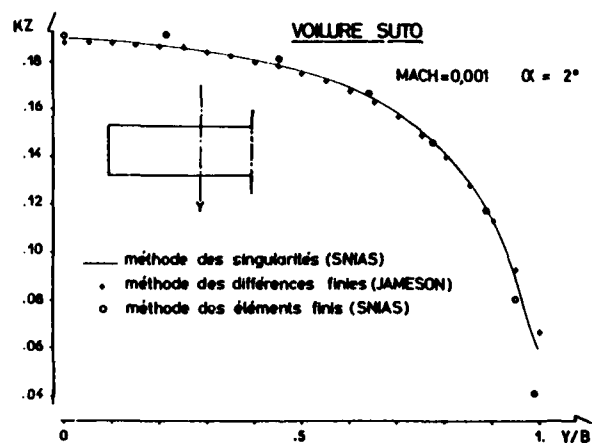
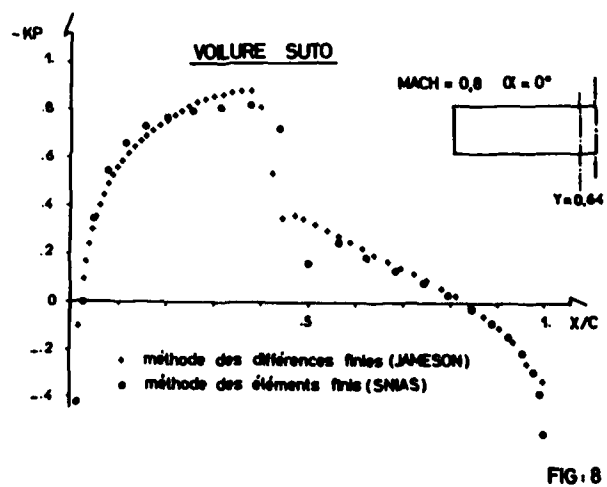
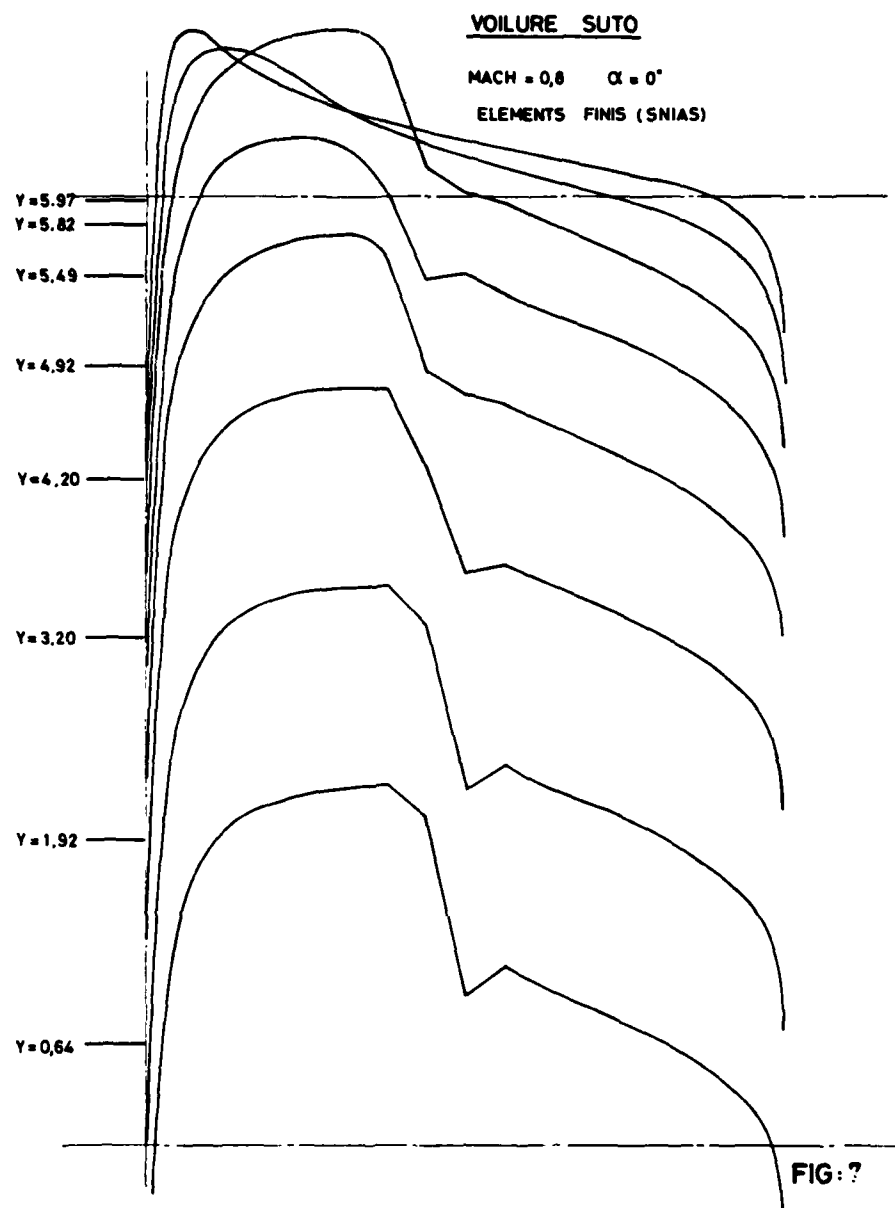


FIG. 6



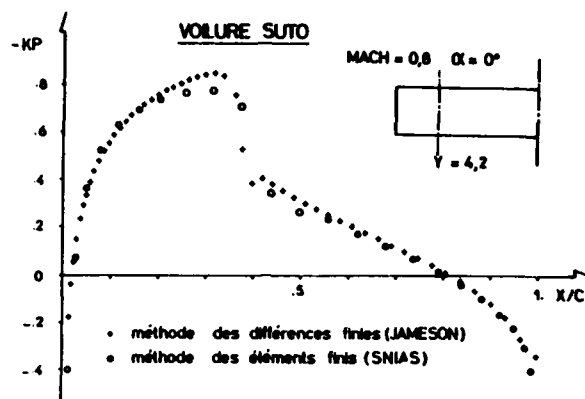


FIG:9

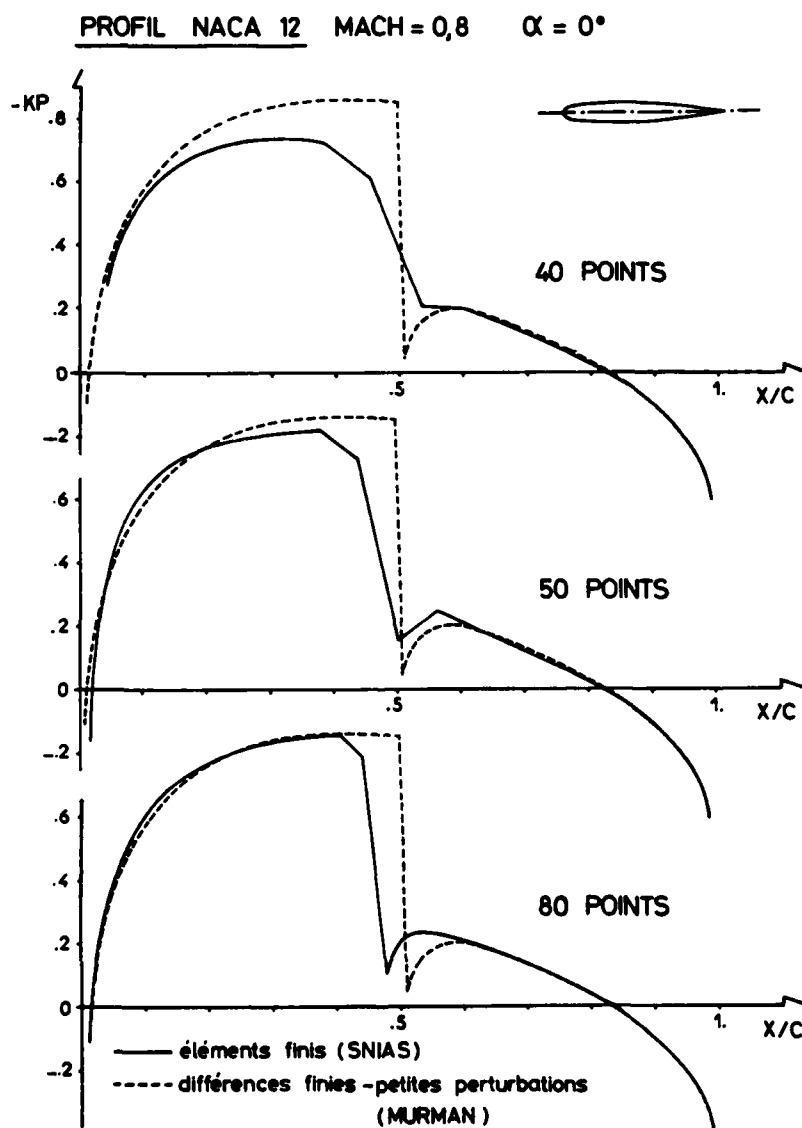


FIG:10

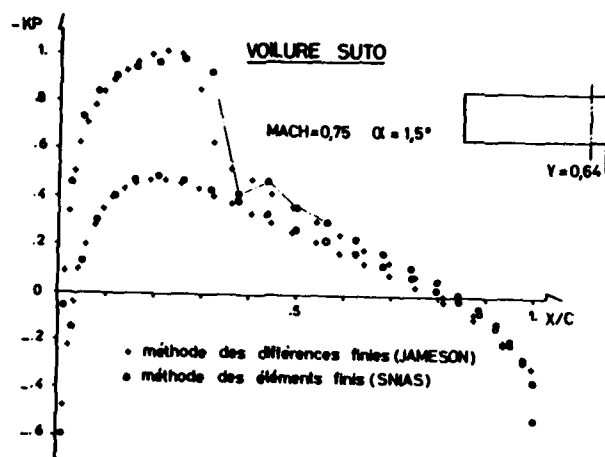


FIG. 11

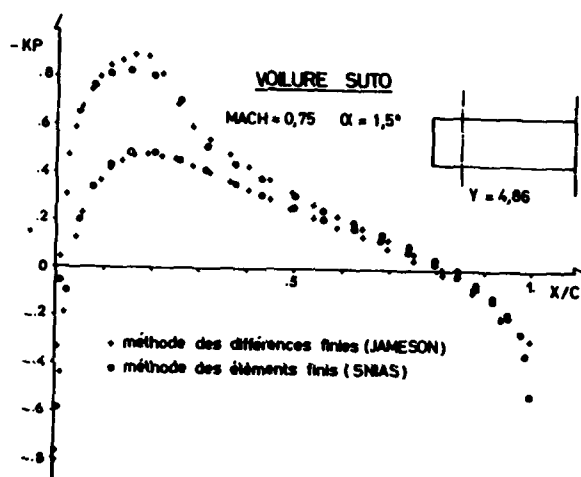


FIG. 12

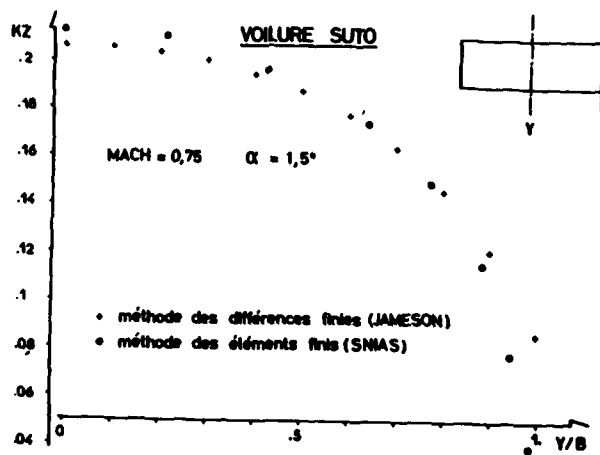


FIG. 13

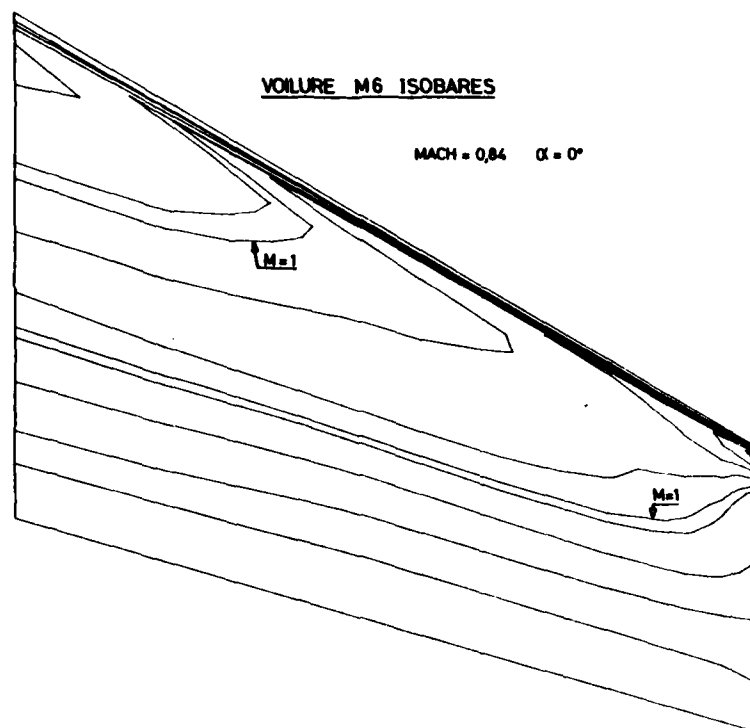


FIG. 14

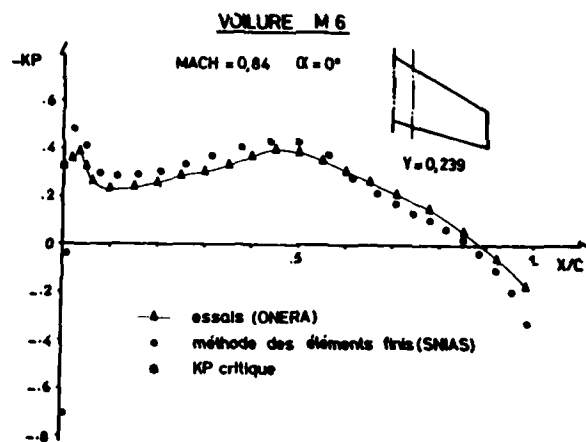


FIG. 15

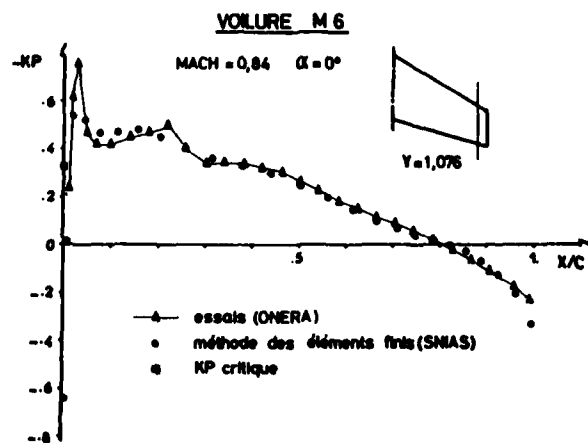


FIG. 16

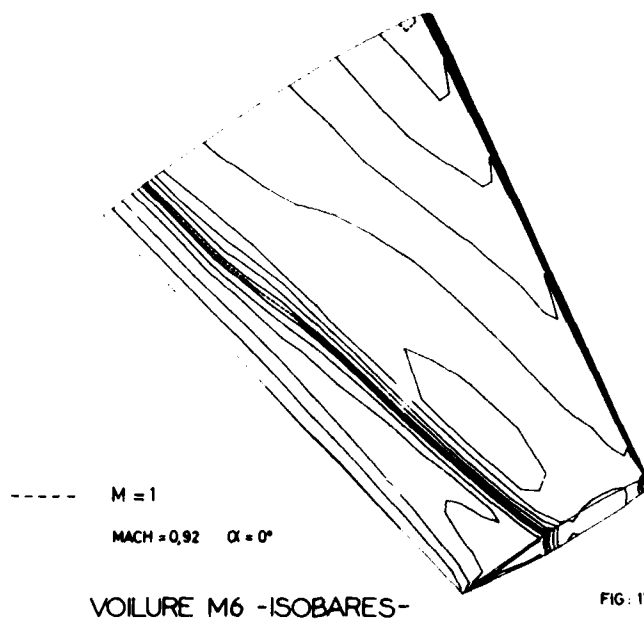


FIG: 17

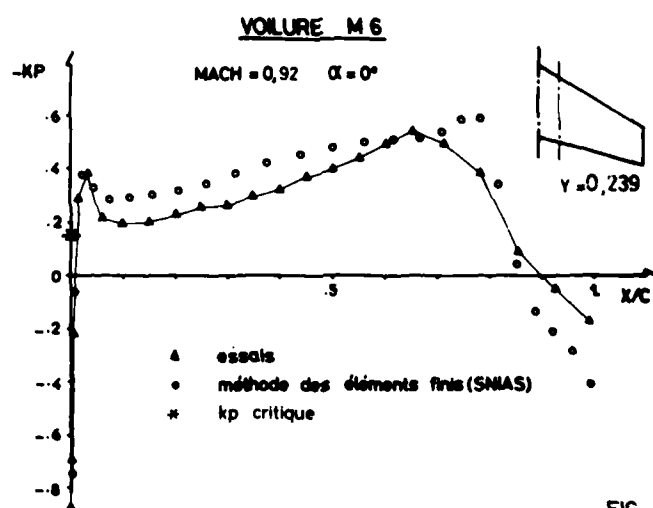


FIG: 18

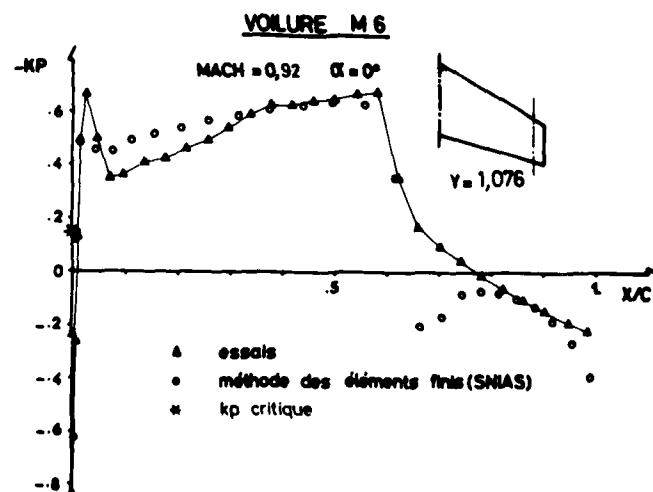


FIG: 19

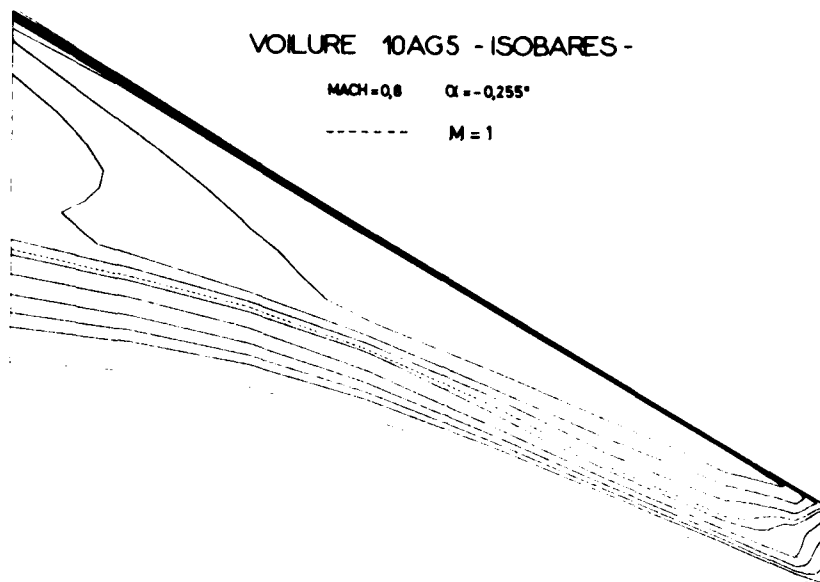


FIG : 20

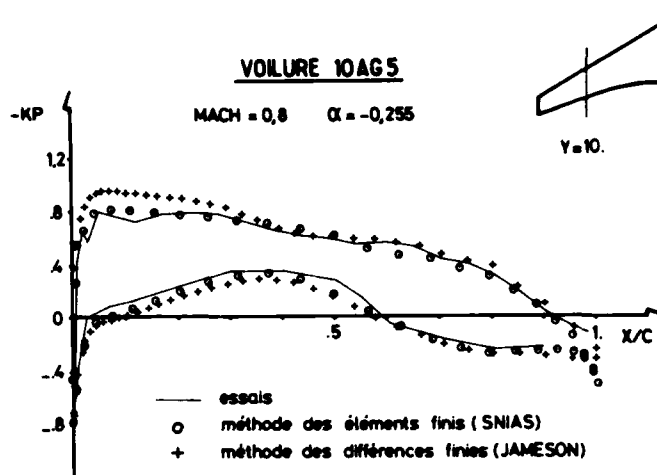


FIG : 21

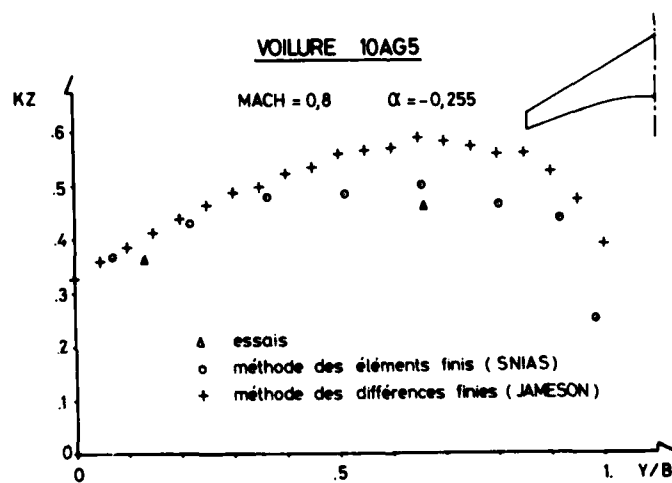


FIG : 22

GEOMETRIE VOILURE FUSELAGE

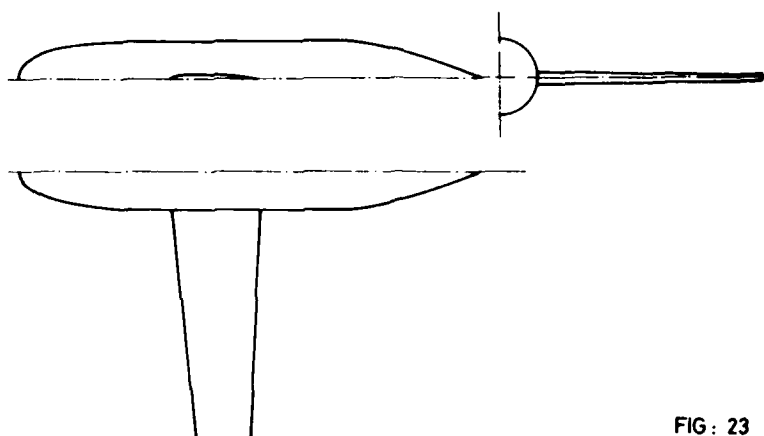


FIG. 23

VOILURE + FUSELAGE - ISOBARES -

MACH = 0 $\alpha = 0^\circ$

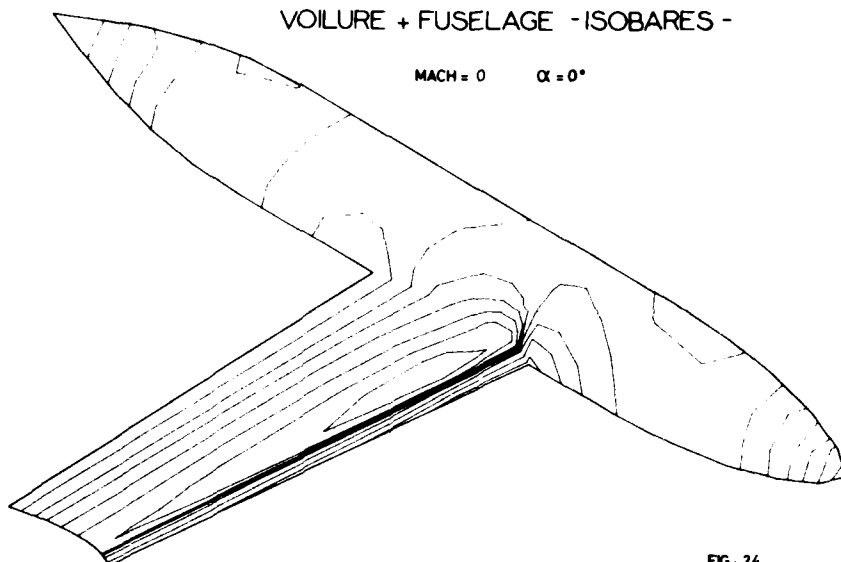


FIG. 24

VOILURE + FUSELAGE - ISOBARES -

MACH = 0,8 $\alpha = 0^\circ$

----- M = 1

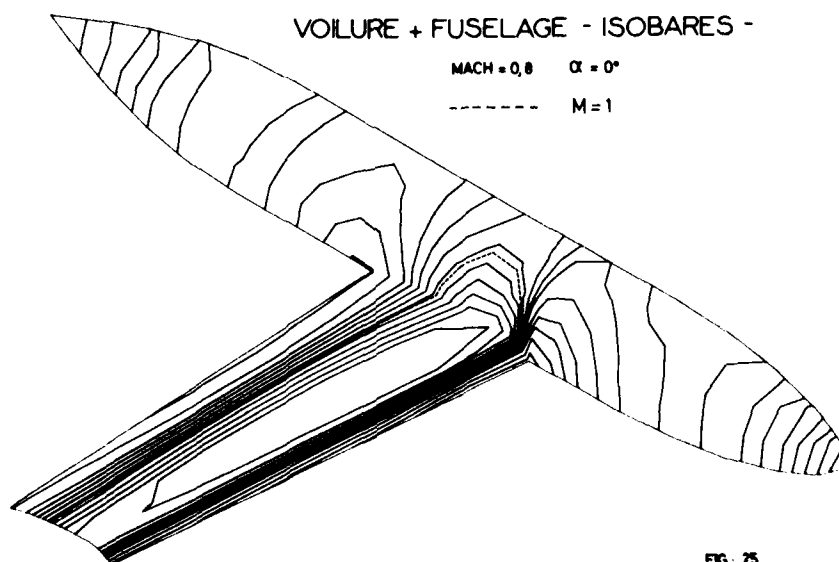


FIG. 25

REFERENCES

- 1 - M.M. HAFEZ, J. SOUTH, E.M. MURMAN : "Artificial Compresibility Methods For Numerical Solution Of Transonic Full Potential Equation", AIAA Paper 78-1148 (1978).
- 2 - A. JAMESON : "Transonic Flow Calculations", V.K.I Lecture Series - Computational Fluid Dynamics, Rhode-St-Genèse, Belgium, March 15-19, 1976.
- 3 - E.M. MURMAN, J.D. COLE : "Calculation Of Plane Steady Transonic Flows", AIAA Journal 9 (1971) pp. 114/121.
- 4 - A. EBERLE : "Transonic Potential Flow Computations By Finite Elements : Airfoil And Wing Analysis, Airfoil Optimization", DGLR/CARTEur 6 Symposium, Transonic Configurations, Bad Harzburg, June 13-15, 1978.
- 5 - V. SCHMITT, F. CHARPIN : "Pressure Distributions On The ONERA-M6-Wing At Transonic Mach Numbers", AGARD - Advisory Report N° 138.
- 6 - A. JAMESON, D.A. CAUGHEY : "Numerical Calculation Of The Transonic Flow Past A Swept Wing", Courant Institute Of Mathematical Sciences, ERDA Mathematics and Computing Laboratory, C00-3077, 1977.

REMERCIEMENTS

Les auteurs souhaitent exprimer leurs remerciements à MM. COUOT, KALFON et MAZET, du Groupe Analyse Numérique au C.E.R.T, pour leur contribution à cette étude ; à Mr. MIRAT pour le développement des programmes de tracé, à Mme. H. DANDINE pour la frappe du manuscrit et à Mr. LASSERRE pour le tracé et l'édition des figures.

Ce travail a été partiellement financé par la DIRECTION DES RECHERCHES ETUDES ET TECHNIQUES (contrats 79/1031 et 80/090).

ETUDE PAR LA METHODE DES ELEMENTS FINIS DES
INTERACTIONS VOILURE-FUSELAGE-NACELLE D'UN AVION
DU TYPE FALCON A MACH = 0,79

par Gilbert HECKMANN

Département des Etudes Théoriques Aérodynamiques
 Division des Etudes Avancées
 AVIONS MARCEL DASSAULT BREQUET AVIATION
 78, Quai CARNOT 92214 St-CLOUD (FRANCE)

0 - INTRODUCTION

- 0.1 - L'adaptation du moteur GARRETT ATF3-6, sur le biréacteur d'affaires FALCON 20 équipé en série d'un General Electric CF 700, mit en évidence un accroissement de traînée en écoulement transsonique important et imprévu, bien que l'ensemble fuselage-nacelle ait été étudié préalablement par des méthodes traditionnelles.

L'étude en soufflerie de la configuration nouvelle montra des chocs sur l'avant de la nacelle moteur et sur l'arrière de la voilure à l'extrados près de l'emplanture à Mach = 0,79 : l'écoulement de l'air entre voilure et nacelle était localement supersonique. Il fut donc décidé de modifier la forme et la position de la nacelle et du mât.

La configuration complexe fuselage-voilure - mât-nacelle devait être étudiée en écoulement supercritique en tenant compte du débit du moteur. Une technique s'imposa : celle des ELEMENTS FINIS qui permet le calcul aérodynamique en écoulement tridimensionnel et transsonique avec chocs dans un domaine géométriquement quelconque avec des conditions aux limites requises.

A l'époque, la méthode des éléments finis n'était pas suffisamment performante, à cause entre autres des problèmes de maillage dans les cas complexes et de ceux de la convergence du calcul avec chocs importants.

- 0.2 - Nous nous proposons de montrer ici, que la maîtrise d'une méthode de calcul transsonique permet de résoudre des problèmes aérodynamiques, non détectables quelques années auparavant autrement que par des essais en vol ou en soufflerie.

Après avoir étudié brièvement le problème en soufflerie, et présenté les outils mathématiques et informatiques indispensables, nous présenterons les méthodes d'exploitation et les résultats de calcul sur deux configurations :

- avec nacelle d'origine dite N1 et mât 1
- avec nacelle définitive dite N5 (position et forme modifiées) et mât 8.

1 - CARACTERISATION DES PROBLEMES TRANSSONIQUES

- 1.1 - Le dépouillement des premiers vols du FALCON 20 G montra une augmentation de traînée importante par rapport au FALCON 20 F. Cependant les deux avions ne différaient que par leurs moteurs : le FALCON 20 F est équipé de deux General Electric CF 700 de 2040 kg de poussée au point fixe pour un débit de 59 kg/s et une dilution de 2 ; le FALCON 20 G utilise deux GARRETT ATF3-6 de 2470 kg de poussée grâce à un débit de 74 kg/s et une dilution de 2,8 environ.

Le moteur ATF3 a donc besoin d'une entrée d'air nettement plus grande que celle du CF 700. La figure 1 montre la proximité de la voilure et de la nacelle dans les deux cas : une variation de volume de celle-ci entraîne une variation importante du couloir entre nacelle, fuselage et voilure.

Les deux avions ayant le même fuselage et la même voilure, le supplément de traînée ne pouvait résider que sur la partie arrière. L'avion des essais en vol fut équipé de fils de laine sur la nacelle, le mât, le fuselage arrière. L'examen en vol montra un décollement important sur l'intrados du mât, sur la partie inférieure de la nacelle avoisinante et sur le fuselage situé en arrière. Des mesures de pression prouvèrent l'existence de zones où le nombre de Mach dépassait 1,4 : raison amplement suffisante pour entraîner des décollements et par conséquent l'accroissement de traînée (figure 2).

- 1.2 - Des essais aérodynamiques furent effectués dans la soufflerie transsonique $\Sigma 4$ de Saint-Cyr l'Ecole. Les deux premières maquettes utilisées (le FALCON 20 F à moteur CF 700 et le FALCON 20 G à moteur ATF3 dans la nacelle N1) mirent en évidence le problème détecté en vol par l'obtention de l'écart de traînée entre les deux avions et la mesure de pressions statiques sur le mât ~~et sur le fuselage~~ ^{et sur le fuselage} du moteur. L'écart de traînée, inexistant en dessous de Mach 0,7, dépassait 12 % à Mach 0,83 (figure 3).

L'existence de chocs importants sur le mât, le fuseau et même la voilure (figure 4a et 4b) fut mise en évidence par des visualisations pariétales de l'écoulement. Les décollements détectés en vol n'étaient pas nettement visibles sur l'arrière du fuselage.

La mesure des pressions sur l'intrados du mât recoupa parfaitement le vol (figure 2). L'effet du nombre de Reynolds n'était pas visible sur la pression pariétale, donc le phénomène transsonique de vol était bien représenté par la soufflerie.

- 1.3 - Des calculs théoriques par singularités et par éléments finis, associés à la soufflerie, permirent des modifications de la forme du mât, de la forme de la nacelle et de la position de ceux-ci sur le fuselage (voir paragraphe 2.4).

La configuration obtenue permit de diminuer le nombre de Mach local sur le mât et sur la nacelle N5 et par suite, de réduire voire supprimer la zone transsonique de l'écoulement dans le couloir entre voilure et nacelle : si une recompression existait encore dans cette zone, elle ne devait pas être importante car non détectée par les visualisations pariétales. La traînée de l'avion devenait égale à celle de son prédécesseur le FALCON 20 F (figure 3).

2 - CONTRAINTES DE FABRICATION ET CALCULS THEORIQUES

- 2.1 - Pourquoi après avoir défini avec succès la forme arrière du fuselage du triréacteur FALCON 50, l'aérodynamique théorique avait-elle été incapable d'obtenir un résultat correct dans le cas du FALCON 20 G ?

La réponse est simple : les contraintes sur les formes extérieures n'étaient pas du tout les mêmes. Dans le cas du FALCON 50, le Bureau d'Etudes, les calculs de résistance des matériaux ou les coûts de fabrication imposaient des exigences faciles à satisfaire sur une forme extérieure d'un avion qui restait à définir : la forme du profil d'implanture de la voilure ou la "taille de guêpe" du fuselage arrière furent déterminées en tenant compte de la présence des fuseaux moteur.

- 2.2 - Le problème du FALCON 20 G était beaucoup plus contraignant : le fuselage et la voilure, dont les outillages avaient été fabriqués pour le FALCON 20 F, ne pouvaient en aucun cas être modifiés. L'opération de changement de moteur devait être exécutée le plus rapidement possible. Le mât du réacteur, plus gros que l'ancien, devait s'accrocher aux mêmes points sur le fuselage.

Les modifications autorisées ne permettaient pas de réduire notablement les zones supersoniques et le nombre de Mach local ; le problème était sans conteste celui d'un écoulement supercritique tridimensionnel avec des nombres de Mach importants et des chocs dont la modélisation était indispensable.

- 2.3 - Lors de la première définition, les calculs avaient été effectués par méthode de singularité tridimensionnelle. Le second membre de l'équation de Poisson $\Delta \varphi = -M^2 \frac{\partial V}{\partial s}$ représenté par des sources réparties dans l'espace ne permettait pas de dépasser un nombre de Mach local de 1. environ : le problème transsonique ne pouvait être traité ni même détecté.

- 2.4 - Lors de la détection en vol des problèmes évoqués ci-dessus, nous possédions un nouvel outil de calcul : la méthode des éléments finis. Mais à ses débuts, seules des configurations simples (une nacelle seule par exemple : figure 5) pouvaient être calculées dans un écoulement avec ondes de choc faibles ; l'outil théorique était toujours insuffisant pour retrouver dans notre cas les résultats de vol ou de soufflerie (chocs forts, influence de la voilure).

Tout au plus avait-on pu modifier légèrement le mât (figure 6), l'extérieur de la nacelle et indiquer la position optimale de celle-ci dans l'espace en tenant compte du champ aérodynamique de la voilure et du fuselage (figure 7). Mais il était impossible par calcul théorique de savoir si les améliorations apportées étaient ou non suffisantes en remplaçant la nacelle N1 par N5 calculée différemment.

Aujourd'hui il en est tout autrement. La méthode des éléments finis a fait des progrès considérables. Nous avons développé des maillages automatiques de l'espace rendant calculable toute configuration. Nous nous proposons donc ici d'illustrer, sur un exemple, certaines des possibilités de ces programmes récemment mis au point.

3 - RAPPELS SUR LA METHODE DES ELEMENTS FINIS

- 3.1 - La modélisation des écoulements tridimensionnels à potentiel transsonique, autour d'un obstacle partant, d'un fluide parfait compressible conduit à la résolution du problème non linéaire aux limites mixtes dans un domaine (Ω) limité par (Γ) .

- | | | |
|-----|---|---|
| (1) | $\vec{\nabla} \cdot \rho \vec{\nabla} \varphi = 0$ | φ potentiel de vitesse discontinu dans Ω |
| (2) | $\rho = (1 - k \vec{\nabla} \varphi ^2)^\alpha$ | densité du fluide dans Ω |
| (3) | $(\rho \vec{\nabla} \varphi \cdot \vec{n})^+ = (\rho \vec{\nabla} \varphi \cdot \vec{n})^-$ | Rankine - Hugoniot ($\vec{\nabla} \varphi$ discontinu) |
| (4) | $\Delta \varphi < k$ | condition d'entropie |
| (5) | $\varphi^+ = \varphi^- + l$ | sur la nappe de discontinuité (l = circulation) |
| (6) | $ \vec{\nabla} \varphi ^+ = \vec{\nabla} \varphi ^-$ | sur le bord de fuite (JOUKOVSKI) |
| (7) | $\frac{\partial \varphi}{\partial n} = g$ | Neuman homogène ou non |
| (8) | $\varphi = 0$ | pour fixer le niveau du potentiel |

avec $\alpha = \frac{1}{\gamma - 1}$ $k = \frac{\gamma - 1}{\gamma + 1} \frac{1}{C^*{}^2}$

C^* vitesse critique

γ rapport de chaleurs spécifiques

La condition de Neuman est soit homogène dans le cas de glissement sur l'obstacle ($g = 0$), soit non homogène ($g = \vec{V}_\infty \cdot \vec{n}$) à la limite de l'écoulement non perturbé ou dans le plan d'entrée du moteur ($g = \vec{V}_M \cdot \vec{n}$).

Une particularité des écoulements transsoniques à potentiel réside dans l'existence de chocs de faible intensité (Mach amont au choc inférieur à 1,5), imposés par la condition d'irrotationnalité, dus au caractère mixte elliptique (subsonique), hyperbolique (supersonique) des équations (1) et (2). A travers un choc l'écoulement doit satisfaire les conditions de Rankine - Hugoniot (3) (où \vec{n} est la direction normale à l'écoulement). Les chocs inclus dans les solutions de (1) et (2) sont des chocs de compression ou de détente. Afin d'éviter ces derniers une condition d'entropie est modélisée sous la forme (4).

Le domaine de calcul relatif au FALCON 20 G est représenté sur la figure 8 avec les équations à résoudre et les conditions aux limites.

3.2 - Le problème (1) (2) (8) consiste à trouver φ solution de

$$(9) \quad T(\varphi) = 0 \quad \varphi \in V$$

T opérateur non linéaire (transsonique)

V espace fonctionnel incluant les conditions aux limites, les contraintes de portance et d'entropie. La méthodologie utilisée est la technique des moindres carrés fonctionnels. Elle consiste à remplacer (9) par un problème de minimisation dans une norme fonctionnelle appropriée à l'espace dans lequel on cherche φ : en l'occurrence H^{-1} dual de l'espace de Sobolev H^1_0 . (GLOWINSKI, PIRONNEAU (IRIA-FRANCE), PERIAUX, POIRIER (AMD-BA) : références de 1 à 4).

L'algorithme général consiste en deux boucles de calcul :

- l'une externe sur la circulation fixant la portance via la condition de JOUKOVSKI
- l'autre interne sur la compressibilité via un problème de contrôle optimal résolu par gradient conjugué.

3.3 - La mise en oeuvre informatique des algorithmes de moindre carré fonctionnels couplés à des méthodes d'éléments finis sur des configurations industrielles complexes (avion complet) soulève plusieurs difficultés liées aux grandes dimensions. La tétraédrisation de l'espace conduit à des dizaines de milliers d'éléments et à des matrices à centaines de milliers d'éléments non nuls. La répétition des calculs (itérations) nous a fait choisir une résolution directe du type Cholevski - profil où l'opérateur de Dirichlet est factorisé sous la forme $A = LL^T$

(L^T matrice triangulaire inférieure)

Malheureusement le nombre d'éléments non nuls de L est bien supérieur à celui de A (quelques millions). L'industrialisation de ces méthodes nous force à utiliser des processus nouveaux (méthodes de factorisation incomplètes, opérateurs auxiliaires de conditionnement...) et l'utilisation intensive donc optimale de mémoire auxiliaire (disques ou bandes magnétiques) s'avère indispensable avec des méthodes de transfert des données appropriées.

4 - PROBLEMES DE MAILLAGE TRIDIMENSIONNELS

4.1 - Jusqu'à présent les problèmes qui se posaient pouvaient être résolus soit par intervention manuelle (mailles sur la surface extérieure de l'avion en singularités) soit par des maillages bidimensionnels répétitifs (fig. 9) pour des traitements par différences finies avec prise en compte correcte des conditions limites (domaines complexes impossibles), soit par découpage direct de l'espace réel non supporté par un calcul transsonique.

4.2 - La méthode des éléments finis à base de tétraèdres permet de traiter un maillage vraiment tridimensionnel autour de corps de forme quelconque. Dans un premier temps les discrétisations étaient de type bidimensionnel (voilure, voilure + fuselage obtenus par déformation du plan de symétrie, entrées d'air avec topologie de révolution) en utilisant des hexaèdres comme mailles intermédiaires. Deux problèmes sont apparus.

La taille des ordinateurs limitait le nombre d'éléments de discrétisation. De plus le développement des zones supersoniques impose une limite extérieure notablement plus éloignée de l'avion que pour un calcul entièrement subsonique. De toute façon, il était aussi indispensable que logique d'utiliser à fond les possibilités : éléments petits dans les zones à fort gradient de vitesse, éléments très gros dans les zones peu perturbées, éléments allongés dans la direction normale au gradient local. Ceci est obtenu par condensation d'un maillage plus régulier tout en gardant sur les noeuds conservés des informations topologiques de création.

Une zone complexe tridimensionnelle devait être décomposée en sous ensembles disjoints traités par les méthodes précédentes. Puis les interstices sont remplis par une méthode absolument générale mais coûteuse : il aurait été inconcevable, notamment pour des raisons de temps de calcul, d'utiliser cette méthode générale dans le domaine complet. Elle consiste à remplir de tétraèdres joints un volume limité par une surface fermée constituée de triangles.

- 4.3 - Des vérifications sont opérées à tous les niveaux soit automatiquement soit en mode conversationnel à l'aide de visualisations sur écran. Par exemple tous les tétraèdres doivent avoir un volume positif : les faces dites limites donc communes à un seul élément doivent se trouver sur une limite du domaine de calcul. Des informations topologiques par noeuds ou éléments sont indispensables pour le calcul (types de conditions aux limites) ou pour l'exploitation des résultats (repérage de la surface de l'avion, limitation spatiale d'une zone).

Les figures 10 et 11 donnent l'allure d'une coupe plane du maillage, l'une normale au plan de symétrie juste en avant du bord d'attaque de la nacelle, l'autre parallèle à ce même plan et passant par le centre de la nacelle (avant remplissage de l'espace autour de la nacelle). La figure 12 montre le maillage sur la peau externe de l'avion.

5 - RESULTATS ET COMPARAISON AVEC LES ESSAIS EN SOUFFLERIE

- 5.1 - Nacelle 1 : Le calcul par éléments finis à $Mach = 0,79$ et $CZ = 0,30$ conduit sur la voilure au système d'ondes de choc habituel : un choc faible sur la voilure à mi-profil dans le sens de l'envergure C1 et un choc issu du bord d'attaque du profil d'emplanture C2 qui rencontre le premier. Ce résultat aurait pu être obtenu par un calcul schématisant simplement la voilure et le fuselage. Mais ce qui est plus intéressant c'est l'apparition d'une zone supersonique qui se termine par une recompression C3 entre la nacelle et l'extrados voilure. Il est difficile, par manque de mesures en soufflerie ou en vol, de savoir si les pressions sont exactes mais le gradient de recompression très important est suffisant pour créer un décollement de la couche limite (voir 5.2) ce qui explique les visualisations pariétales (figure 16). Le champ de vitesse est représenté dans l'espace sur la figure 13 dans une coupe verticale.

La zone supersonique qui était de faible importance lors du calcul avec une nacelle isolée s'est donc étendue jusqu'à la voilure à cause de l'effet de "couloir" (figure 15) tout en accroissant le nombre de Mach maximum sur la nacelle.

Nous pouvons vérifier, par analogie, l'existence de chocs sur la nacelle (figure 18). Le seul résultat qualitatif, outre la position des chocs, est la mesure de pressions sur le mât. Le calcul recoupe correctement celle-ci dans la partie supersonique (figure 17). Le choc s'est bien développé correctement ainsi que la zone supersonique mais néanmoins le résultat est totalement différent du résultat bidimensionnel (figure 6). La répartition des nombres de Mach dans une coupe de l'espace passant entre la nacelle et le fuselage est représentée figure 14. On y remarque deux zones supersoniques : l'une à nombre de Mach peu élevé sur l'avant de la voilure, l'autre entre le mât et la voilure. Le nombre de Mach dépasse à peine 1 sur l'arrière du profil de la voilure (résultat analogue figure 14), mais il atteint 1,4 comme en soufflerie, sous l'intrados du mât près du bord d'attaque. La valeur de pression calculée est représentée figure 15.

5.2 - Extension à un fluide visqueux

Le champ de pression ou de vitesse dans l'espace étant connu, il est facile d'évaluer les gradients de pression en suivant les lignes de courant du fluide. Le calcul de couche limite (épaisseur, épaisseur de déplacement, cisaillement, etc...) s'opère en tenant compte des courbures longitudinales et transversales de la surface avec des conditions initiales et aux limites qui sont celles du vol ou de la soufflerie.

Sur un avion civil en croisière et correctement mis au point, les ondes de chocs si elles existent sont faibles sinon elles entraîneraient une traînée d'onde et une traînée due au décollement des couches limites qui nuiraient aux performances. Néanmoins il existe, lors des itérations, des ondes de chocs fortes qui obligent à tenir compte dans le calcul de la variation d'entropie du fluide.

- 5.3 - Influence du débit du moteur : les résultats précédents (5.1) ont été obtenus en imposant dans le calcul un débit d'air dans la nacelle correspondant à celui du moteur en vol. Il est à noter que les essais en soufflerie tenaient compte correctement de cette contrainte. Mais le débit du moteur a une très grande influence sur la zone supersonique dont une des raisons d'exister est le contournement des lèvres de nacelles. La forme de celles-ci doit en effet être un compromis entre les cas de vol en croisière et le décollage par fort vent de travers.

Cependant il faut noter que les problèmes transsoniques apparaissent ici au-delà de $Mach 0,75$ (figure 3). Le nombre de Mach à l'entrée du compresseur varie peu lors d'un vol en croisière. S'il est indispensable d'imposer le bon débit du moteur pour faire un calcul réaliste, la configuration obtenue ne devrait pas poser de problèmes aérodynamiques majeurs lors des vols dans des conditions normales.

- 5.4 - Nacelle 5 : L'étude de la configuration modifiée montre la disparition totale de zone supersonique sur l'extrados voilure vers le bord de fuite près de la nacelle moteur (figures 16 et 17), comme en soufflerie et en vol. Il reste bien entendu des poches supersoniques sur le mât et sur la nacelle (figure 19) mais le nombre de Mach maximum atteint a diminué notablement et les gradients de recompression, quand ils existent, ne font plus décoller la couche limite. En conséquence, les phénomènes de buffeting et d'accroissement de traînée (figure 3) par rapport au FALCON 20 F ont disparu.

6 - CONCLUSION

6.1 - Avant l'utilisation de méthode d'éléments finis, les calculs d'écoulements non visqueux étaient limités soit par le nombre de Mach local (compressible subcritique traité par singularités) soit par la complexité de l'espace (transsonique et méthodes de différences finies).

6.2 - Pour démontrer la puissance des méthodes par éléments finis, il fallait :

- a - un exemple complexe analysé physiquement par la soufflerie ou les essais en vol
- b - une solution mathématique aux équations transsoniques à potentiel discontinu (JOUKOVSKI) et à vitesse discontinue (chocs)
- c - une mise en oeuvre informatique pour un problème à un très grand nombre d'éléments de discrétisation
- d - une construction géométrique de l'espace discrétisé dans un cas tridimensionnel quelconque

Les recoupements avec les essais en soufflerie et en vol du FALCON 20 G ont permis de valider l'ensemble cohérent de programmes répondant aux impératifs b, c et d.

REFERENCES

- 1 - J. PERIAUX et G. POIRIER -
Méthodologie pour résoudre les équations transsoniques tridimensionnelles d'un fluide parfait compressible - Note interne AMD-BA -
- 2 - M.O. BRISTEAU, R. GLOWINSKI, J. PERIAUX, P. PERRIER, O. PIRONNEAU, G. POIRIER -
Application of optimal control and finite element methods to the calculation of transonic flow and incompressible viscous flows (Laboria Report 294) -
- 3 - J. PERIAUX -
Resolution de quelques problèmes non linéaires en aérodynamique par des méthodes d'éléments finis et de moindres carrés fonctionnels (Thèse de 3e cycle Université Pierre et Marie Curie 1979) -
- 4 - R. GLOWINSKI, B. MANTEL, J. PERIAUX, O. PIRONNEAU, G. POIRIER -
An efficient preconditioned conjugate gradient method applied to non linear problems in fluid dynamics (Versailles 1979) -
- 5 - P. PERRIER -
Utilisation de l'ordinateur pour le dessin de configurations aérodynamiques -
- 6 - P. PERRIER et W. VITTE -
Eléments de calcul d'aérodynamique tridimensionnelle en fluide parfait - Colloque aérodynamique appliquée AFITAE - Nov. 70 -
- 7 - J. PERIAUX et P. PERRIER -
Utilisation de la méthode des E.F. en aérodynamique non linéaire-VKI computational fluid dynamic 1976 -
- 8 - P. PERRIER -
Problèmes de calculs en transsonique - Symposium Transsonic Configurations DGFLR - June 78 -
- 9 - G. HECKMANN -
Ecoulement à potentiel tridimensionnel portant - Colloque aérodynamique appliquée AFITAE - Nov. 71 -
- 10 - A. JAMESON -
Transonic flow calculations - VKI lecture series 87 - Computational fluid dynamics 1976 -
- 11 - Philippe PERRIER -
Calculs de configurations aile-fuselage en transsonique - Rapport DEA int. 1977 -
- 12 - J. PERIAUX -
Calcul tridimensionnel de fluide compressible par la méthode des éléments finis - Colloque aérodynamique appliquée Nov. 73 -
- 13 - J. PERIAUX -
Three-dimensional analysis of compressible potential flows with the finite element method - International Journal for Num. méth. in eng. - Vol. 9 - 1975 -
- 14 - J. NAVES -
Calcul d'ensembles aile-fuselage en régime transsonique - Problèmes posés par la mise en exploitation des méthodes d'éléments finis - Colloque aérodynamique appliquée A.A.A.F. - Nov. 75 -
- 15 - J. PERIAUX et al -
Use of optimal control theory for the numerical solution of transonic flows - International Symposium on F.E.M. - SWANSEA 1974 - S.M. LIGURE 1976 -

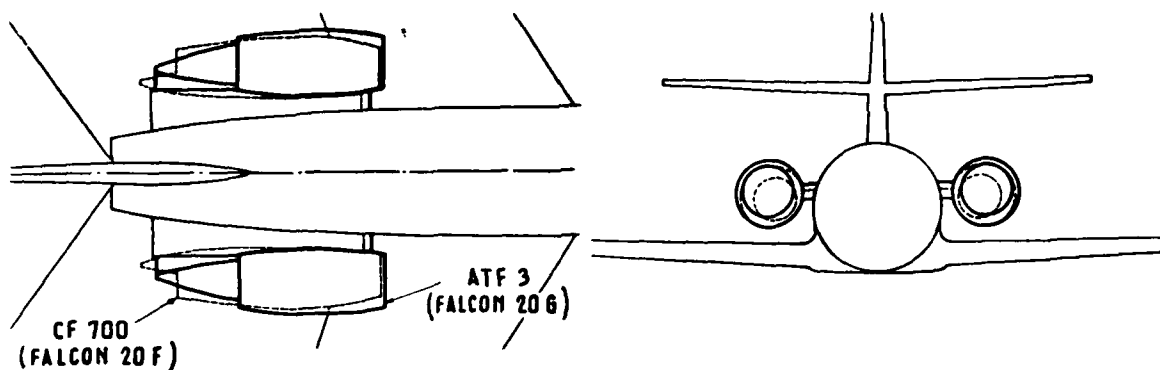


Fig. 1 - FALCON 20F / FALCON 20G : comparaison de l'encombrement des moteurs.

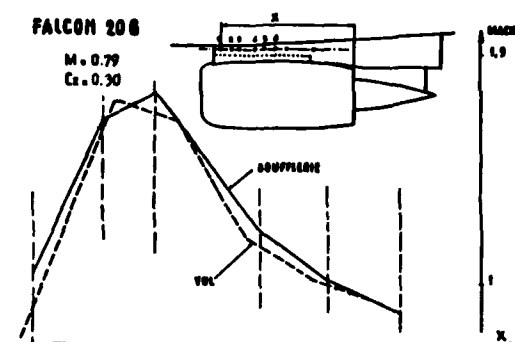


Fig. 2 - FALCON 20G : comparaison des Nbre de Mach en vol et en soufflerie (Nacelle 1, mât 1)

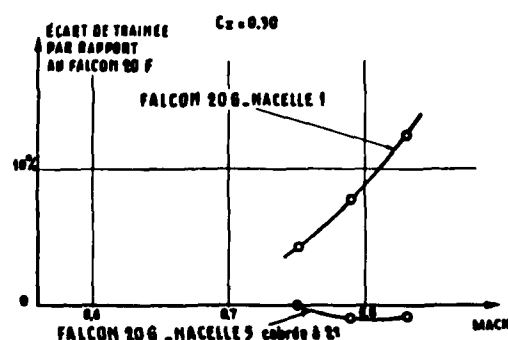


Fig. 3 - Comparaison de la traînée du FALCON 20F avec celle du FALCON 20G (avant et après modification).

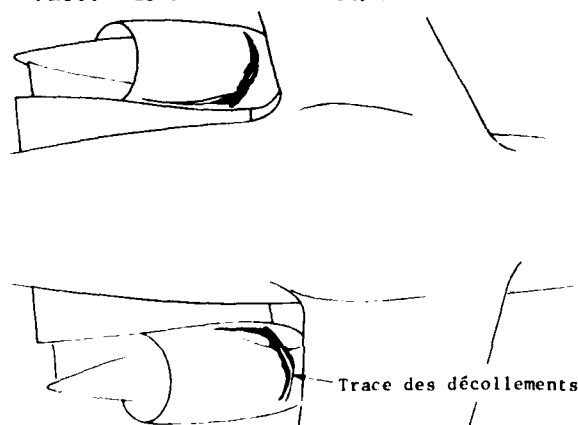


Fig. 4a - Mise en évidence, en soufflerie des décollements sur la nacelle 1

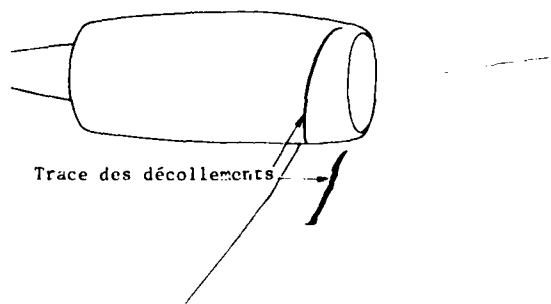
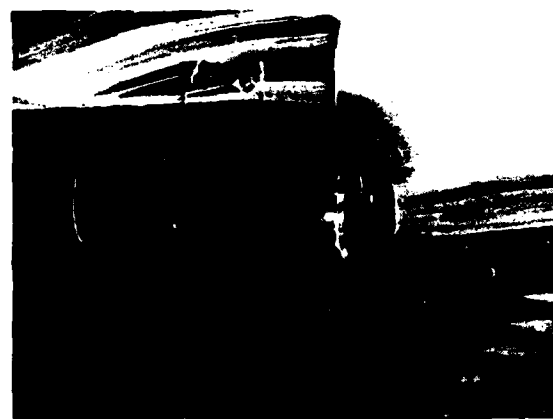


Fig. 4b - Mise en évidence, en soufflerie des décollements sur la voilure

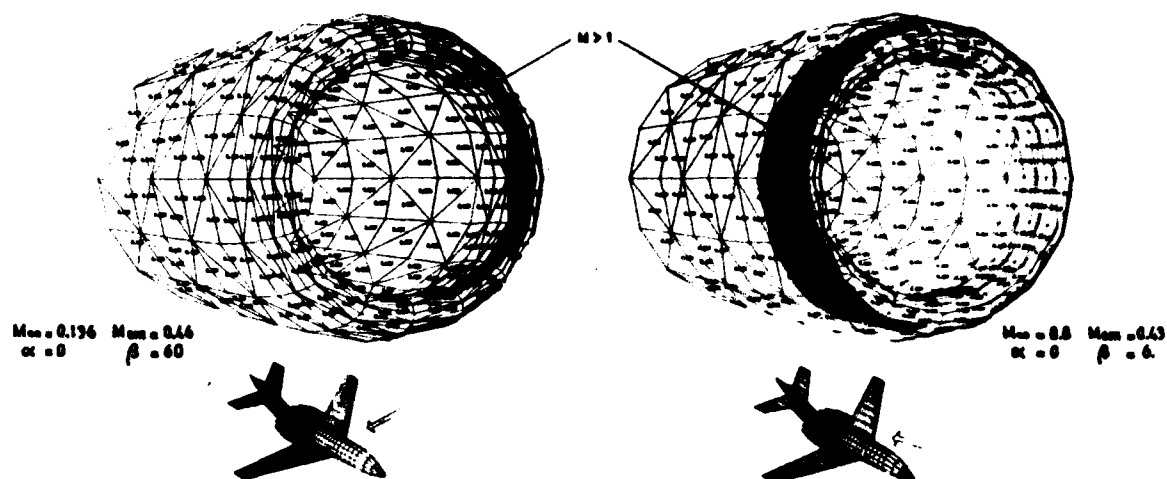
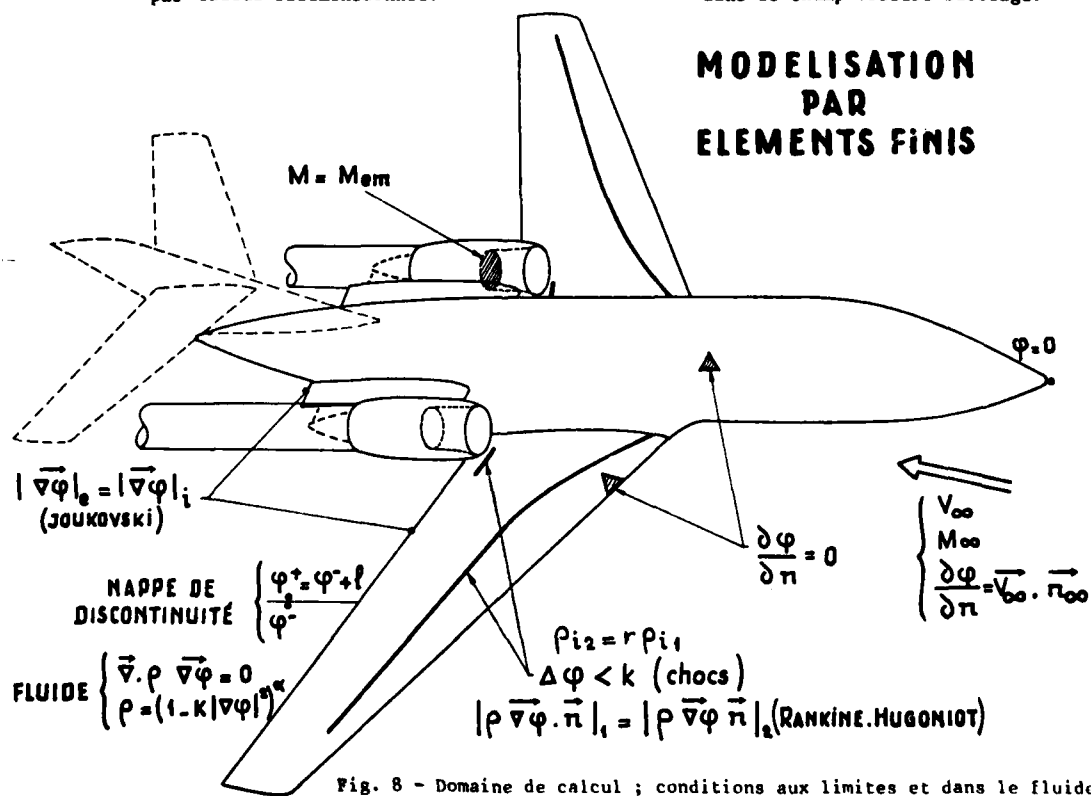
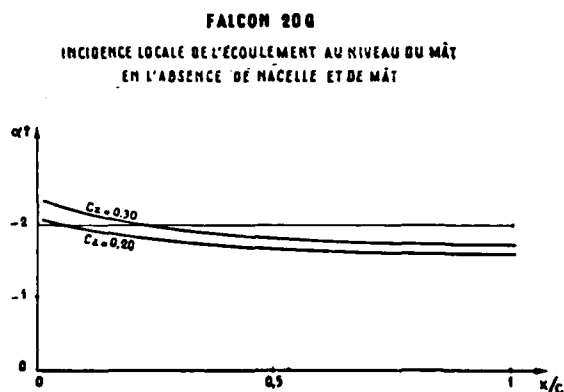
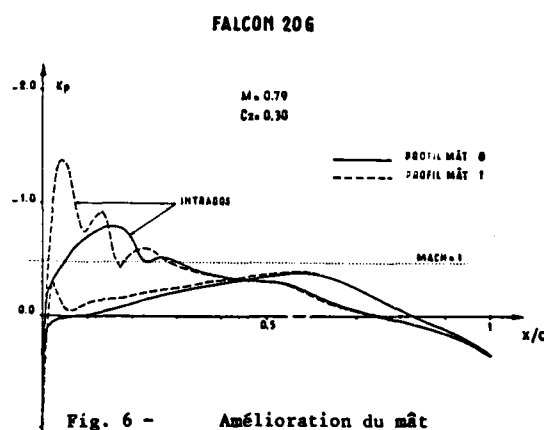
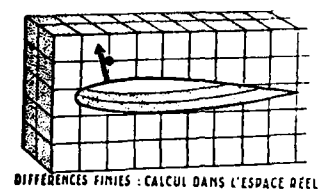
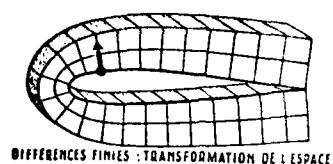


Fig. 5 - Configuration d'une nacelle isolée : décollage et croisière.





ÉLÉMENTS FINIS : MAILLAGE DE TYPE BIDIMENSIONNEL

Fig. 9 - Maillage topologiquement bidimensionnel.

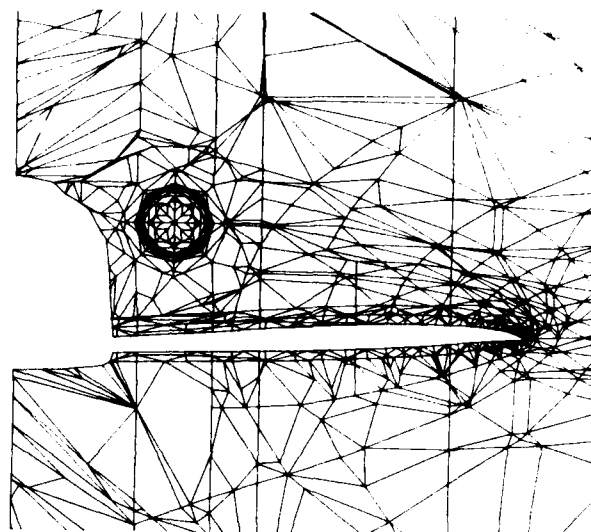


Fig. 10 - Coupe du maillage 3D FALCON 20G (normalement au plan de symétrie).

COUPES
D'UN TETRAEDRE
PAR UN PLAN
QUELCONQUE

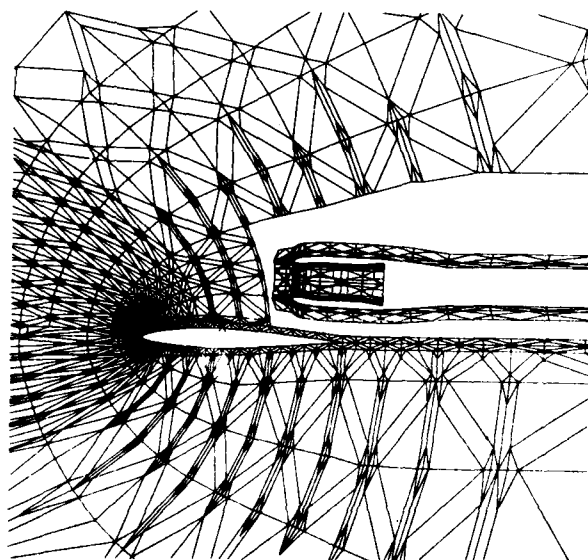
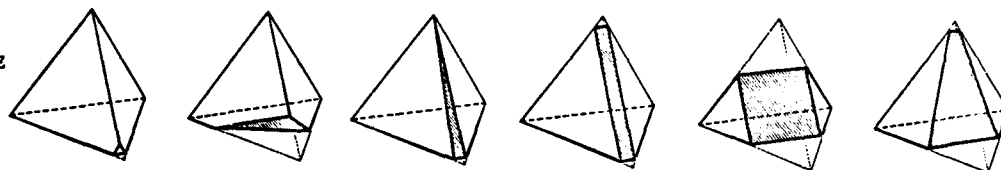


Fig. 11 - Coupe verticale du maillage 3D FALCON 20G passant par l'axe du moteur (avant remplissage).

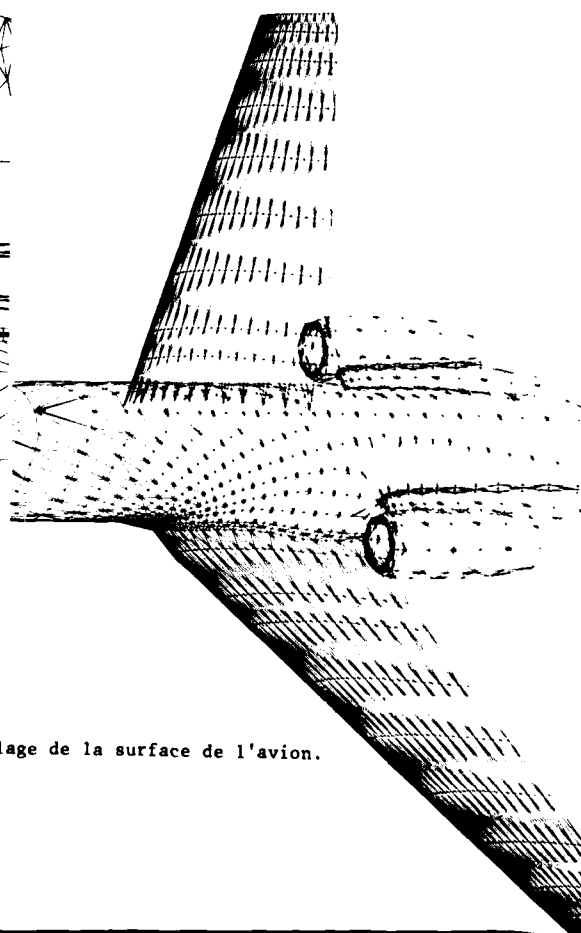
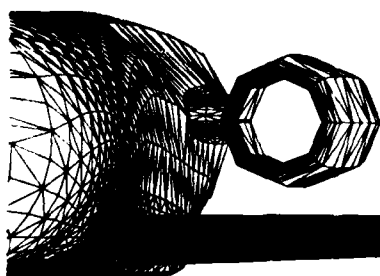


Fig 12 Maillage de la surface de l'avion.



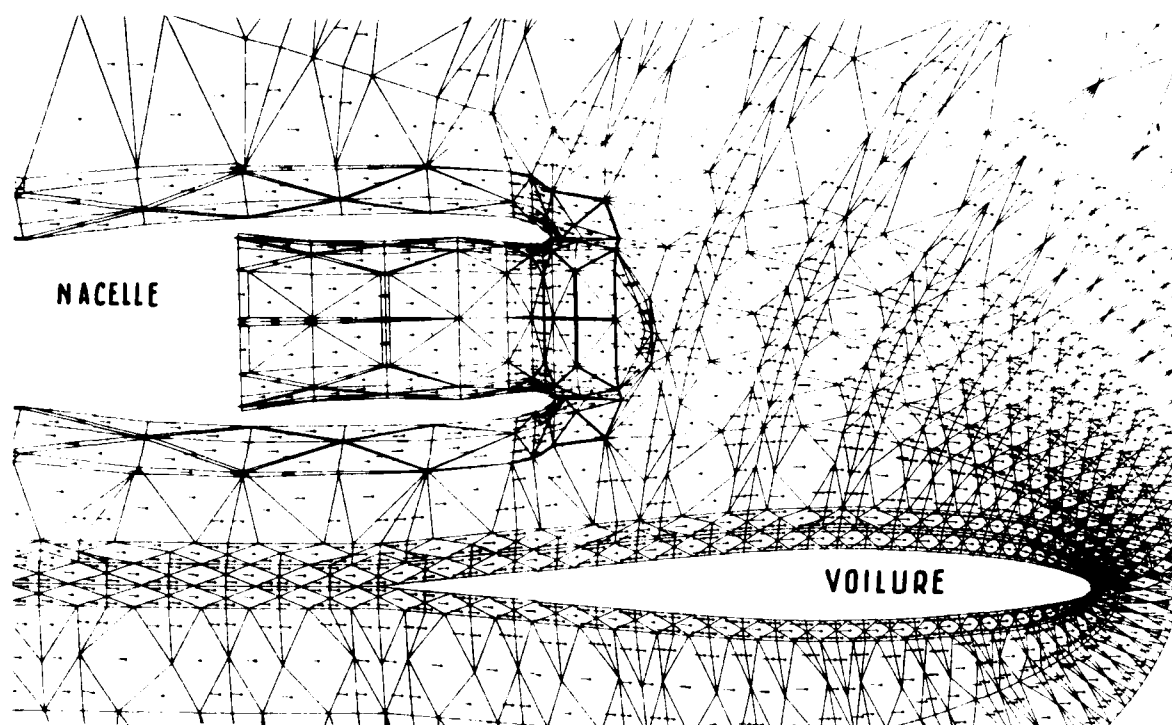


Fig. 13 - Champ des vitesses (Coupe parallèle au plan de symétrie avion).

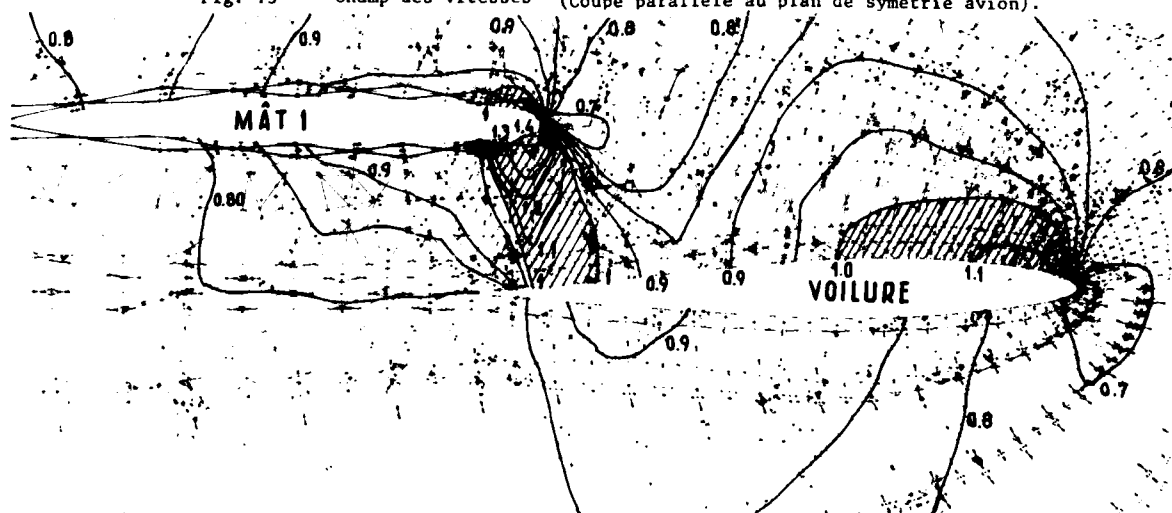


Fig. 14 - Répartition du nombre de Mach entre Mât 1 et voilure. (en présence de la nacelle).

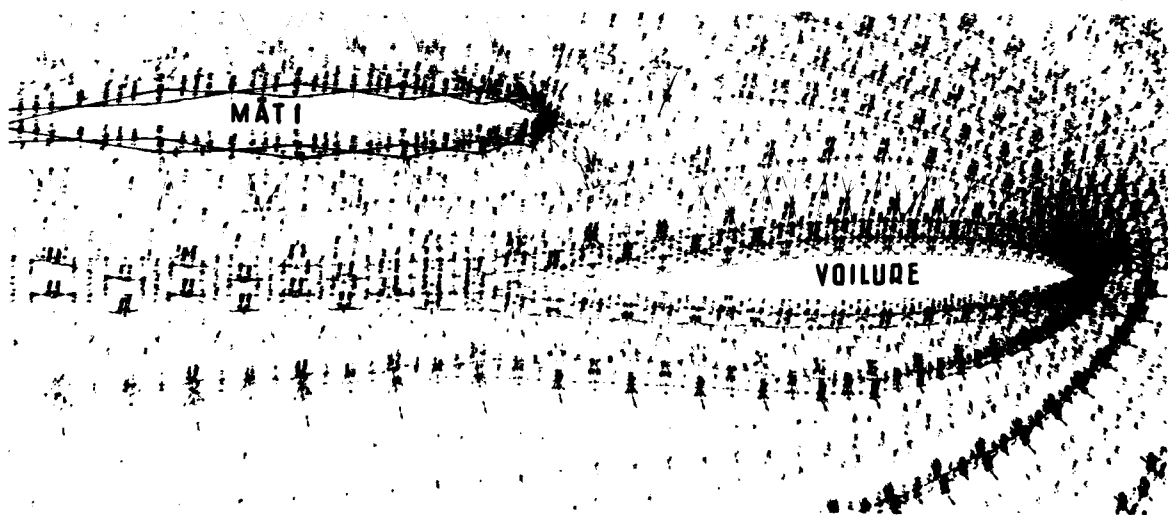
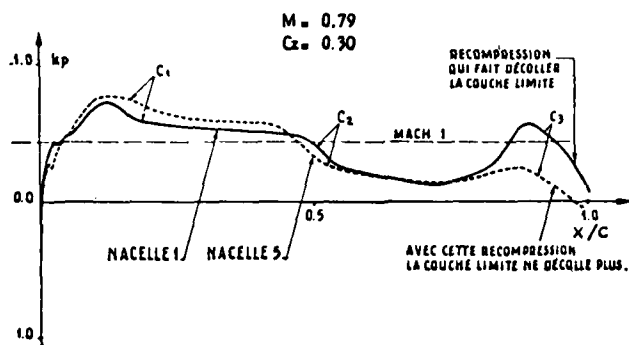
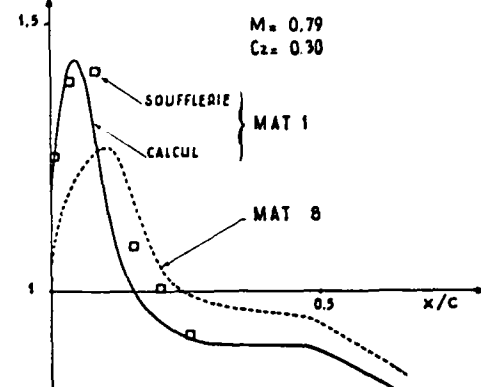


Fig. 15 - Répartition des pressions (K_p) entre mât 1 et voilure.

FALCON 20 G - NACELLE 1 / NACELLE 5

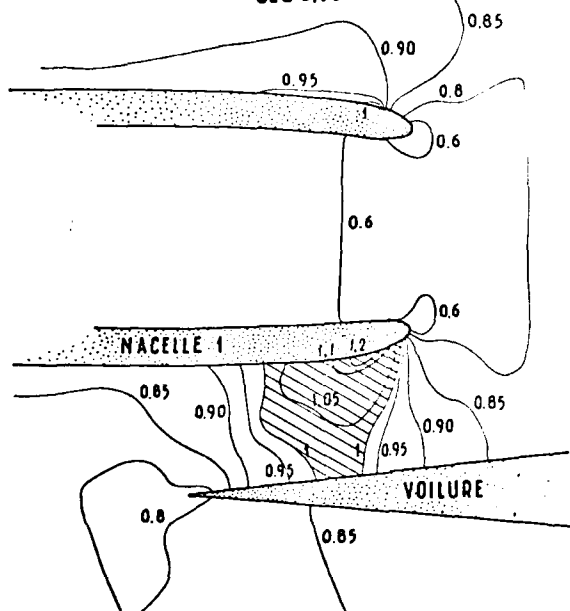


FALCON 20 G - NACELLE 1 / NACELLE 5



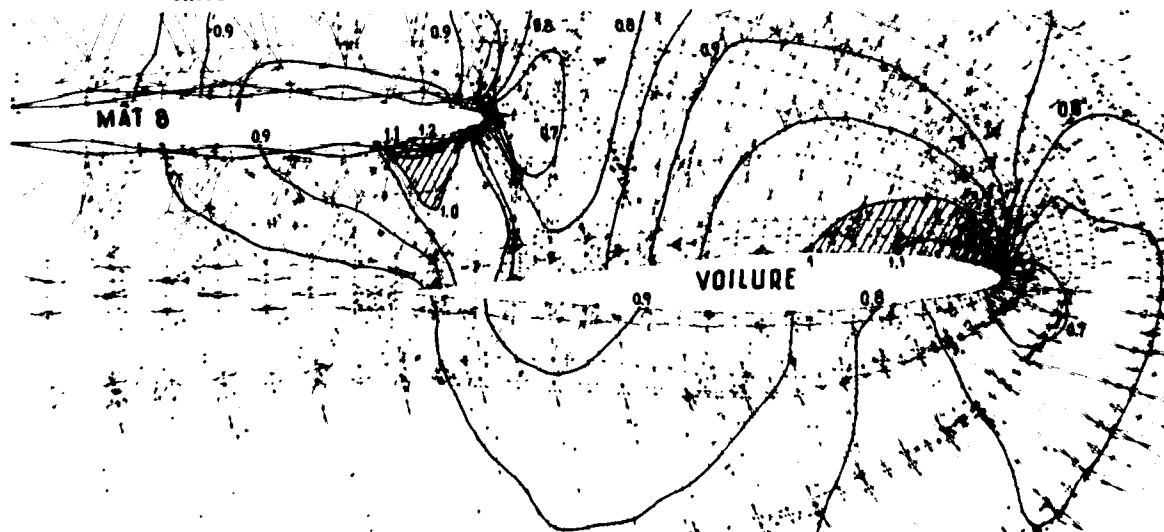
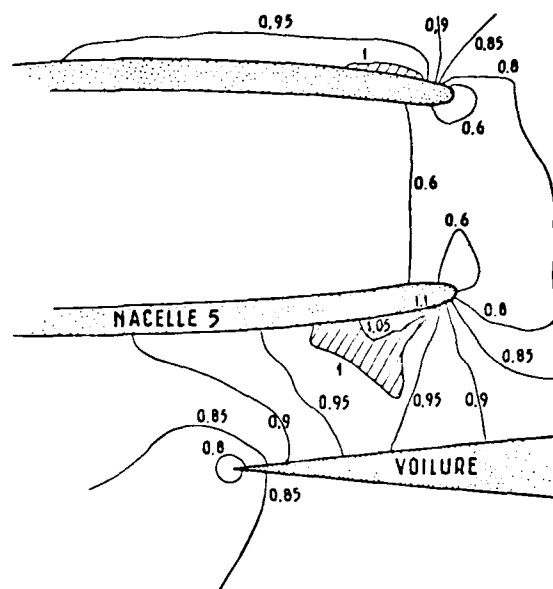
FALCON 20 G

$M = 0.79$
 $C_z = 0.30$



FALCON 20 G

$M = 0.79$
 $C_z = 0.30$



INCREASING THE VALUE OF AIRFORCES BY IMPROVING EXTERNAL STORE CONFIGURATION

Clifford L. Bore

British Aerospace Aircraft Group
Kingston-Brough Division
Kingston
Surrey

SUMMARY

This paper surveys the value of improvements to the external stores configuration, such as reduced drag (with consequent improvements of performance), and reduced release disturbances to the trajectory. It is shown that the effectiveness/cost ratio of a fighter C.A. airforce could be improved greatly - perhaps better than doubled - by refining the aerodynamics of external store carriage, and that the payoff in value should be over 100 times the cost of re-equipment.

INTRODUCTION

Some 15 years ago, aircraft designers were becoming concerned that the drag of external stores (including carriers) was excessive. Could it be right that we take such care with the smoothness of the aircraft, but tolerate such crude excrescences on the stores (Figure 1)?

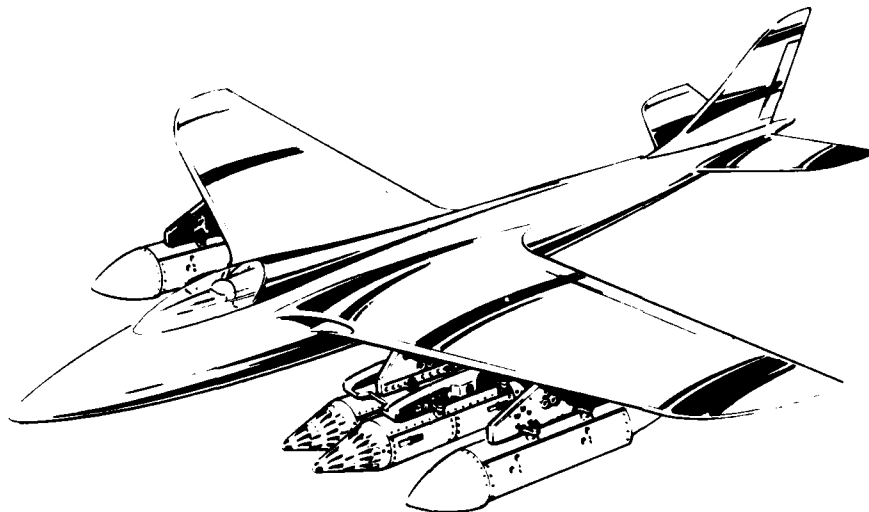


Figure 1 WHY SHOULD AERODYNAMIC CLEANLINESS STOP AT THE PYLON?

In the U.K. research was started into drag reduction, which soon showed major improvements. Eventually it was realised that action to incorporate many of these improvements would need NATO-wide co-operation and in 1974 the U.K. suggested a NATO Working Group. The Working Group was set up by the AGARD Fluid Dynamics Panel (under my chairmanship) with members from the Flight Mechanics Panel and the Structures and Materials Panel.

We considered that the aerodynamic effects of stores (including pylons and carrier in the term "stores") were far wider than drag alone, so the Working Group studied not only drag and its immediate consequences (such as degraded performance and manoeuvrability) but also aspects such as release trajectory, flutter, loads and stability.

However, we were determined that our report (1) should lead to action, so we tried to answer in advance the sort of questions that budget-bosses might raise while deferring a decision. Obviously they would be entitled to say something like this:

"O.K., you believe you can reduce drag, and release disturbances and so on by redesigning stores. You may well be right, but do you realise how much it will cost to change them? Those stores COST A LOT OF MONEY, and we will not spend much more without very good reason! How much are those improvements worth - in MONEY?"

My paper today concentrates largely on answering those questions a little less vaguely than in the report, but it is important to emphasise that this was only a small part of our report (1). The main drive of that was to understand and improve the aerodynamic effects of stores. One important section was the chapter on drag, reviewed meticulously by Barry Haines, who will discuss that topic in the next paper.

I do not claim that my evaluation of improvements is accurate or particularly novel, or that it is elegant enough to become fashionable for academics, but I do believe it is important. It is important because it concentrates our attention on the things that matter most, and helps us all to get the most defence for our taxes, but most of all it is important that we learn to translate from aerodynamicists' language to budget-boss' language and thus get action on our recommendations.

ASSESSING THE VALUE OF AN AIRFORCE

Value is related to the amount one would be prepared to pay for the usefulness supplied, in the circumstances. Thus the value may vary greatly with the circumstances: for example the value of a parachute would differ according to whether one was falling out of an aeroplane, or drowning. Richard III must have appreciated this distinction, when he assessed the loan of a horse as equivalent to his kingdom.

Since value can vary greatly from one scenario to another, and there is uncertainty about future scenarios, we have to envisage a probable mixture of scenarios. For illustration we will consider Close Air Support (CAS) operations in a "European" scenario, which implies sophisticated opposition in a short, sharp war - at the end of which most of our aircraft have been put out of action.

Factors of Effectiveness Value

The effectiveness of an airforce is proportional to the number of targets it can destroy before it is put out of action. Clearly this effectiveness is proportional to a number of factors, such as the rate the aircraft can transport warload (W), the average availability of the aircraft in wartime (A), and the target killing effectiveness (K). Let us examine these more closely.

Factors of Effectiveness Value (V)

Value \propto Effectiveness

Effectiveness \propto (Warload rate, unimpeded)X
(Availability in wartime)X
(Kill effectiveness)

whence:-

$$V = WACK \dots\dots\dots(1)$$

where C is the constant of proportionality.

Warload Transport Rate (W)

W = Mass of ordnancetransportable when unimpeded, relative to datum aircraft.

$$= (\text{Load of ordnance, per sortie})_R \times (\text{Number of sorties, per day})_R$$

Here the sortie rate (N) depends on

$$\left. \begin{array}{l} * \text{ turn-round time } (r) \\ * \text{ block speed } (v) \\ * \text{ distance from base to battle area } (d) \end{array} \right\} N = \frac{1}{\frac{r+2d}{v}}$$

thus:-

$$W = \left(\frac{L}{\frac{r+2d}{v}} \right)_R \dots\dots\dots(2)$$

Where the suffix R indicates that the parameter is to be made "relative" by dividing by the comparable parameter for the datum aircraft.

Availability in Wartime (A)

Availability = average fraction of aircraft days usable during war.

This depends on factors:-

$$\begin{array}{ll} t = \text{fraction of total time usable} & \left\{ \begin{array}{l} \text{bad weather capability} \\ \text{night time capability} \\ \text{target availability} \end{array} \right. \\ a = \text{fraction of aircraft usable} & \left\{ \begin{array}{l} \text{survivability} \\ \text{repairability} \\ \text{maintainability} \end{array} \right. \\ b = \text{fraction of bases usable} & \left\{ \begin{array}{l} \text{runway length requirement} \\ \text{ground hardness requirement} \\ \text{base survivability (including detectability)} \end{array} \right. \\ s = \text{availability of stores} & \left\{ \begin{array}{l} \text{logistics} \\ \text{interchangeability} \end{array} \right. \end{array}$$

Thus:

$$A = (tabs)_R \dots\dots\dots(3)$$

Target Killing Effectiveness (K)

K = specific rate of destroying targets (per unit of ordnance released) relative to datum aircraft and stores.

This depends on various aspects, but not generally in a simple law of proportionality:-

- * power of weaponry
- * active guidance of weaponry
- * aiming accuracy of aircraft
 - { aircraft controllability.
 - { sighting system.
 - { pilot's workload and fatigue.
- * accuracy of stores trajectory
 - { ejector/carrier dynamics.
 - { aerodynamic release disturbance.

The Constant of Proportionality

If we arrange that all the factors of Value are made non-dimensional by making them ratios, relative to the factors appropriate to a known datum aircraft, then the constant C amounts to the value of an airforce comprising a given number of the datum aircraft. Now that value is not set by engineers or by accountants: it is a political judgement.

I suggest we assume that the government, in its collective wisdom, has decided that the value of the datum airforce is not less than its current lifetime cost. Then it follows that the value C is at least the lifetime cost of the datum airforce.

For most comparisons the value C is not needed accurately, but it seems that typically it is around 5 times the cost of buying the aircraft (Figure 2).

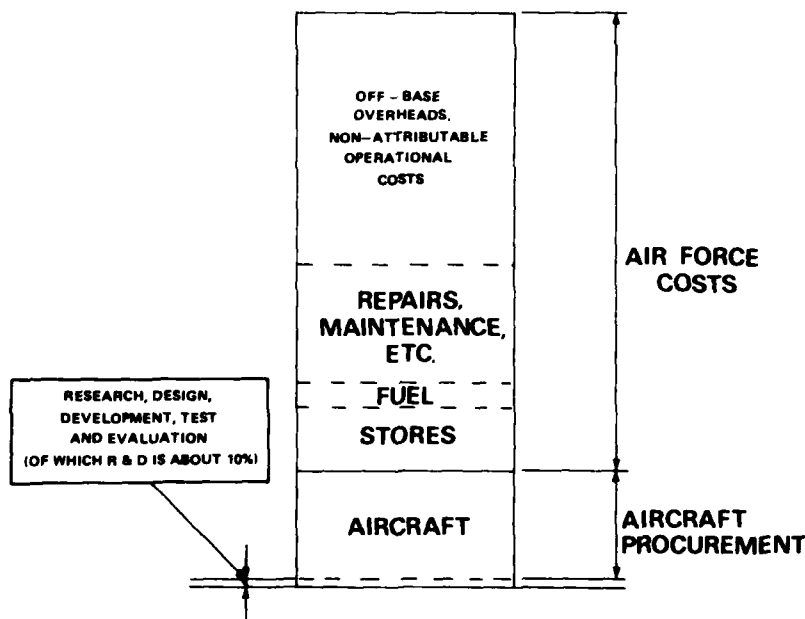


Figure 2 APPROXIMATE LIFE-CYCLE COSTS OF C.A.S. AIRFORCE

For the order of magnitude, the constant C is around \$5 billion for an airforce of (say) 120 CAS aircraft. So if we double the effectiveness of that airforce, we add \$5 billions worth of value - and even a mere 1% increase in effectiveness is worth \$50M.

Overall Value

Substituting from (2) and (3) into (1) we get

$$V = C \left(\frac{L}{r+2d} \right)_R (\text{tabs})_R K_R \dots\dots\dots (4)$$

EFFECTS OF STORES

For some of the terms in the value equation, it is difficult to work out how they depend on normal performance data. Our present aim is not to go deeply into that, simply to illustrate the sort of sensitivity involved in a typical example. For our example we will take the calculations performed by Professor Dr. J. Barche for chapter 7 of Reference 1, for a hypothetical Close Air Support (CAS) aircraft.

Generally there are two possible ways of reaping the benefit of aerodynamic improvements. First, for existing aircraft we can make use of the improved performance capabilities. Second, for new aircraft on the drawing board, the aircraft can be shrunk to smaller size and cost for the given capabilities. We will look at both ways, in turn.

1) Example of Existing CAS Aircraft

For the first example the datum aircraft will be taken as the nominal CAS aircraft when fitted with stores and carriers of current aerodynamic crudity. The improved aircraft is the same machine but fitted with aerodynamically smoother stores and carriers.

With current knowledge the installed drag of service bombs and their carriers can be reduced by around 50%, and missiles could be improved by about 25% of current drags. So it should be feasible to reduce store drag overall by about 30% (which is comparable with the entire drag of the wing - see Figure 3).

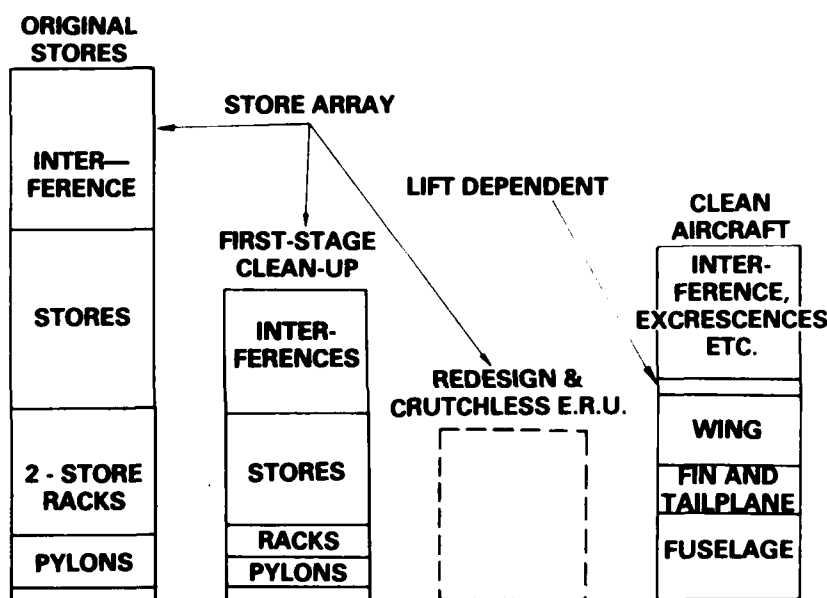


Figure 3 DRAW OF STORE ARRAY, AND CLEAN AIRCRAFT

Such a reduction of drag would allow the aircraft to penetrate to target faster with a given warload ($M = 0.81$ instead of $M = 0.74$ in this example) or to range further at given speed.

The effect on the warload transport term (W) is not large, giving an increase of perhaps 4% to the term in square brackets, in (4).

In the availability term (a) we note that the only terms affected by the drag are the aircraft availability term (a) - by virtue of improved survivability in the face of defences, and perhaps the "time available" term (t) - by virtue of greater range permitting more target availability.

Aircraft survivability varies greatly with the nature of the defences, but for low-altitude intrusion against most defences, the survivability increases sensitively with increased speed of penetration, but decreases with height (which has to increase with speed over bumpy terrain). For the speed change and low height concerned here the factor (a) relevant to ground-to-air defences probably ranges from about 1.15 to 2.70.

In the face of enemy fighters, the first factor of concern is the probability of not being seen and attacked - a factor which increases with increasing penetration speed with stores on). Once the enemy fighter has started turning to attack, our CAS aircraft should jettison its bombs, so its manoeuvrability is now affected by the drag of the installed air/air missiles and the empty bomb carriers. Drag reductions on the missiles and carriers may be worth about 3% of the drag of the clean aircraft, and on the bare pylons about 5% of the clean aircraft drag; a total reduction of over 5% of the drag of the datum aircraft with bombs gone. Typically, this may increase the specific excess power by some 6 m/sec, and the manoeuvrability with it. Assessment of the effects of these improvements cannot be accurate, but

the combined effects of higher penetration speed (with bombs on) and higher agility (with bombs gone) suggests a factor on survivability in the face of enemy fighters of about 1.25. In addition, the extra agility should enable our CAS to shoot down perhaps 17% more of the enemy fighters than before: a factor that will enter into the target-killing effectiveness term, K.

Taking a mixture of ground defences and fighter defences, it seems that the improved survivability due to drag reductions could plausibly be represented by $A \approx 1.25$.

If the option were taken to use the reduced drag to range further over enemy territory (at the original penetration speed) the situation would be quite different. Area coverage over enemy territory goes up sensitively and with it the availability of targets: if the aircraft were based at half its datum radius of action from the battle edge, the area coverage would be increased about 70%. However, block time and particularly the exposure to enemy defences (all at original speed, remember) go up. The latter effect may worsen survivability by about 1.8 at maximum range. When the bombs are gone, the aircraft benefits from its extra agility and speed on the way home. The increased target availability and the worsened aircraft survivability at the maximum increased range seem to balance out and leave the airforce about as effective as the datum airforce. However, at lesser ranges (still above the maximum for the datum aircraft) there remains an option to penetrate faster as well as cover more targets, so the average availability term a is above unity.

Availability of stores (as denoted by s) is not, of course, dependent on the aerodynamics, but it is relevant to introduce the term here. It has been stated by senior officers that NATO forces lose 30% to 50% of potential effectiveness through lack of interchangeability, and bomb racks were singled out for comment. Furthermore, many existing racks are very old, and suffering from corrosion and fatigue. It will also be argued that the qualities shared by most current racks are excessive drag and inaccurate release trajectory. It follows that if the NATO airforces were re-equipped with racks that would admit interchangeability of stores, the benefit would correspond with a factor (s) between 1.4 and 2.0.

The target-killing effectiveness (K) is affected by store aerodynamics on two main counts: the aiming accuracy of the aircraft, and the disturbances to the release trajectory.

The aiming accuracy of the aircraft can be affected by buffet (perhaps due to local underwing separations, or perhaps a change in the stalling pattern on the upper surface), or by changes of stability and controllability (mostly due to changes in downwash pattern at the tail) or more generally by the excessive drag (which may make the pilot think: "with that load aboard, the aircraft manoeuvres with the agility of an old cow"). There is, indeed, a famous supersonic aircraft (when clean) that has been described thus when carrying a big load of external bombs!

Even if the aircraft can be pointed in time in the right direction, there are often severe disturbances to the release trajectory due to the complicated and sensitive variations of airflow around the carriers (particularly triple and multiple carriers). Bombs may go on wildly different trajectories (sometimes damaging the aircraft) according to which station they were carried on, the speed and incidence, and the setting of the ejector release unit. Furthermore the effective stiffness and inertia characteristics at a carrier may vary wildly according to the number of bombs still carried. So after all the trouble and expense involved in getting the aircraft to the target area, the bombs may scatter widely, and even "shoot" down the parent aircraft!

The number of variables involved can be large, and flight testing is extremely expensive, so important areas of techniques have been under development both in wind tunnels and computational fluid dynamics. An important group comprises various two-sting rig techniques (where the store is moved on a separate sting through the aircraft flow field).

Probably the newest wind-tunnel technique is that known as the Accelerated-Model Rig (AMR), which is now in regular use in the pressurised wind-tunnel of British Aerospace at Brough (Fig. 4). In this, the main error of "light model" jettisons is corrected by accelerating the aircraft model upwards away from the store, so that the store experiences the aircraft flow field for the right time and distance. This technique thus combines accuracy with quickness, for little more cost than light-model jettisons.

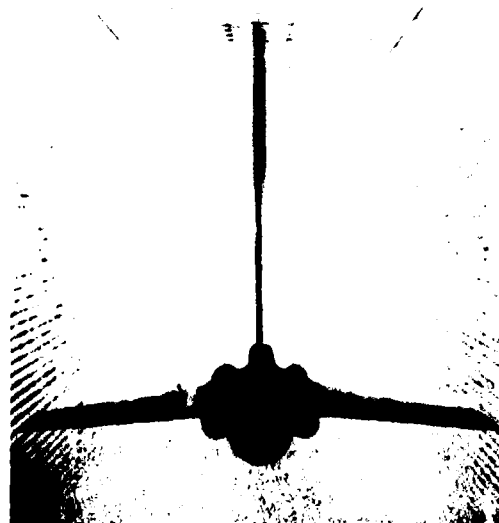


Figure 4 ACCELERATED-MODEL RIG
IN THE PRESSURISED
WIND TUNNEL AT BROUGH

Developing and applying the various techniques for store jettison predictions has absorbed a significant fraction of the thin slice of money allocated to R & D, but they save far more money from the flight test programmes. For example, two-sting rig techniques saved \$16M on the A-7D programme.

At a more fundamental level, it is known that wing-mounted multiple-store carriers introduce many variables and penalties not found with conformal carriage under the fuselage. Unfortunately, it is not always possible to carry stores conformally. In general, it is clear that store release aerodynamics gives scope for many different advances in value.

Targets, weapons and aircraft vary so much that it is hardly possible to typify the effects. As an arbitrary illustration, consider a small target that needs a direct hit, being attacked with iron bombs. If redesigned carriers reduced the length and width of the mean scatter pattern by 14%, the probability of a direct hit would be increased by a factor of 1.3 and (at least for such targets) the effectiveness value would be multiplied by that factor. It seems likely that the scatter pattern could be improved more than this. Release disturbances may also affect guided weapons, for loss of "lock-on" has sometimes occurred under severe disturbances. For lack of a statistically weighted assessment, I will take the arbitrary factor $K=1.3$ as a guide to the value of improvements to release trajectories.

Now we can summarize the overall effects of the various factors discussed above. We have assessed them as follows:-

Warload transport rate	$W \approx 1.04$	(factor sortie rate)
Aircraft availability	$a \approx 1.25$	(improved survivability)
Stores availability	$s \approx 1.4$ to 2.0	(interchangeability etc.)
Kill efficiency	$K \approx 1.3$	(trajectory accuracy)

While all other factors remain unaffected, at about unity.

The product of the aerodynamic terms alone (i.e. excluding S) comes to about 1.7, and the stores availability term brings the overall factor on value to between 2.36 and 3.38. Thus, if the datum value (C) of the airforce were taken as \$5B, the aerodynamic improvements alone would be worth an additional \$3.45B - which is perhaps 6 times the total purchase cost of all the stores. When the benefits of store interchangeability and improved rack logistics are included, the total improvement of value ranges from around \$7B to \$12B, for the small airforce considered. These are useful contributions, and I would happily accept a commission of 0.1% on them! So much for the benefits that would arise on an existing aircraft.

2) Example of new aircraft, on the drawing board

If we have a project on the drawing board, and we are presented with improved stores, we can choose various ways to adapt the design to take advantage of the reduced drag and other benefits.

One way would be to shrink both the airframe and the engine to maintain the datum performance and agility, and cheapen the aircraft by making it smaller. Then we finish with our "shrunk" aircraft having equal "old-cow-like" agility to the original, but with slightly less cost - but we would still have the improved weapon delivery accuracy and stores availability. Probably we may finish with aircraft 4% or 5% lighter than datum, costing perhaps 1½% less to buy, and using about 10% less fuel. Overall, we would have saved about 2% of the cost of the datum airforce, while relinquishing the 30% improvement in value that would have stemmed from extra agility and survivability. So this is not the best way to go.

The better way (and usually the more practical choice) is to leave the engine alone, and take advantage of the store-drag reduction to shrink the airframe. This way, we further improve the agility and consequently the survivability - as well as saving a trifle on the costs.

Some rough figuring suggests that the combat mass would be reduced about 0.8% from that of the original aircraft when carrying the low-drag store array, and the specific excess power would be improved as much. The penetration speed hardly increases, but the survivability in air combat improves perceptibly (partly on account of the smaller aircraft size being harder to detect). The effect on value is small - probably raising a to about 1.26. The reduction in cost also is small: about 0.25% off the cost of the aircraft and spares, or 0.08% off the life-cycle cost of the airforce - a saving of around \$4M.

CONCLUSIONS

By examining the value of aerodynamic improvements to stores, we have seen that there are two areas where extremely large improvements can be made:

1) low drag can lead to greatly increased survivability, and 2) more predictable store trajectory can greatly improve the target-killing effectiveness, and also save substantial costs from flight test programmes.

A programme of fitting better stores and carriers could greatly increase the availability of stores in action, - the value exceeding the cost by perhaps two orders of magnitude.

The benefits obtained by reducing airforce costs tend to be small compared with those due to increased effectiveness value.

It is worth remarking that we have not considered store mass here, but there are benefits to come from reduced total mass.

Reference

1. C.L. Bore (Ed.) Unpublished AGARD report (1977)
et al

PROSPECTS FOR EXPLOITING FAVOURABLE AND MINIMISING ADVERSE
AERODYNAMIC INTERFERENCE IN EXTERNAL STORE INSTALLATIONS

A B Haines
Assistant Chief Executive
Aircraft Research Association Ltd
Manton Lane, Bedford
England

SUMMARY

External store installations are frequently a source of considerable adverse aerodynamic interference giving large increases in drag, reductions in usable lift and poor store release characteristics. Research has however shown how this adverse interference can be greatly alleviated or even transformed into favourable interference. This paper reviews some of the available evidence for a wide variety of arrangements. The nature of the interference, both adverse and favourable, is described, particular emphasis being placed on the major adverse interference in standard multiple carriers and in some underwing installations. The possible benefits of wing tip carriage and carefully arranged underfuselage arrays are noted. Throughout, stress is laid on the fact that dramatic improvements might be possible by adopting a radical approach to store carriage.

1. INTRODUCTION

This conference is concerned with aerodynamic interference. A leading question is: how can we design to minimise adverse aerodynamic interference and to exploit favourable interference? Nowhere is this more important than when we are considering external store installations on military combat aircraft. This is self-evident: one only has to look at any photograph, eg Fig 1a, of a combat aircraft on show at a flight display. It is surrounded by a vast number of different stores which typically have to be carried in many alternative arrangements below the wing, above the wing, at the wing tips or below the fuselage. As Pugh has observed in a recent lecture, (1), they are the 'raison d'être' for the aircraft. Pugh also noted that even a photograph does not tell the full story. Fig 1b contrasts the true geometric view of a hypothetical aircraft with a heavy load of guided weapons and an 'aerodynamic view' in which the frontal area of each item has been scaled up in proportion to its contribution to the total drag. The message is clear and Fig 1c which compares the drag increment due to two standard triple carriers loaded with Mk 10 454 kg bombs and mounted underwing with the drag of the parent clean aircraft (2), is typical of many others that could be quoted. This figure also illustrates that it is not simply a question of there being a large number of stores: the drag increment of the two fully loaded carriers is far greater than 6 times the free air drag of a single Mk 10 bomb/pylon tested in isolation. Clearly, the interference within the carrier, and between the store installation and the aircraft wing has greatly increased the drag increment by a factor which increases progressively with Mach number. Above $M = 0.75$, the drag increment - just to carry 6 stores - is greater than the drag of the clean aircraft: a poor result when one considers that the clean aircraft has been designed to achieve a drag-rise Mach number of more than $M = 0.85$. Fig 1d presents another example frequently quoted in the literature (2,3); it is based on model test data for the F-4 in the AEDC 4ft tunnel and shows that the F-4 is only estimated to achieve $M = 1.3$ when carrying 12 x Mk 82 bombs on a multiple carrier (MER) underfuselage and 2 triple carriers (TER) underwing as compared with $M = 2.1$ at a higher altitude for the datum aircraft.

Standard external store installations are therefore fertile ground for serious aerodynamic interference. In late 1974, the AGARD FD Panel set up a Working Party to consider 'Drag and Other Aerodynamic Effects of External Stores'. The group reported (4) in late 1977 and much of the material in the present paper is taken from the chapter on 'Drag' in the Group Report. Wherever possible, however, the evidence has been updated and extended. In particular, the scope of the paper has been widened to cover more than drag because high drag is only one possible manifestation of aerodynamic interference. Reference will be made to the effects of the stores on the flow field, aircraft stability, usable lift and buffet boundaries and the store load and release characteristics. One aim of the paper will be to demonstrate that by alleviating adverse interference and by reducing the viscous effects and improving the quality of the flow, one should be able not merely to decrease the drag but to reduce other loads or at least make the characteristics more predictable and repeatable - a very important aim when considering store release.

2. EXAMPLES OF ADVERSE AND FAVOURABLE INTERFERENCE

Let us start by tabling some typical examples of the interference drag that can arise with standard equipment and standard store arrangements. First, Fig 2a gives an idea of the extra drag due to interference within a triple carrier. Tests were made in the ARA 9ft x 8ft transonic tunnel on 1/4 scale models of a standard triple carrier loaded with Mk 10 454 kg bombs and mounted on two different pylon/adaptor arrangements (2,4,5). It will be seen that the drag increment due to adding a single bomb increases progressively with the number of bombs that are already present. If one defines a low speed assembly drag factor as the ratio of the measured drag at $M = 0.4$ to the sum of the measured drags of the components in isolation, one obtains values ranging from 1.19 for the carrier with a single bomb up to 1.75 for the fully loaded carrier with pylon/adaptor A. At high Mach numbers, eg $M = 0.9$, the analysis of the data for A suggested that the interference drag due to adding a shoulder bomb expressed as a percentage of the drag of a single pylon-mounted bomb increases from about 60% when it is the first bomb to about 300% for the second and to about 400% when it is the last bomb to be added to the carrier. The figure also demonstrates that the results depend considerably on the details of the pylon/adaptor design. At first sight, it may seem strange that apparently, the changes in pylon/adaptor have most effect on the drag increment due to adding the bottom bomb to the carrier but the explanation of this apparent anomaly lies in the fact that the pylon/adaptor evidently has more effect on the complex, highly viscous flow situation when 3 bombs are present.

For a twin arrangement, one would predict that in inviscid flow, there would be high suction on the side of the bombs and hence, an attractive force between the stores, modified in the real flow by compressibility and viscous effects. With the triple, the viscous effects are more dominant and tests (and in particular, store release tests) have shown that there is often a repelling or explosive force between the stores. The complex flow over the stores in the fully loaded triple carrier is illustrated by the photographs in Fig 2a. These show the flow with pylon/adaptor A at $M = 0.75$; the photographs were taken after the tunnel run and for the two lower pictures, the bottom bomb was removed to show the oil flow patterns in the channel formed by the 3 bombs and carrier body. For a bomb in isolation, one would predict two peak suction near the shoulder between forebody and centre parallel section, and near the start of the afterbody. Adverse pressure gradients and reduced surface shear stress would be expected on the centre-body and this is supported by the appearance of the oil flow pattern on the outer side of the shoulder bomb. It is of course the flow in the channel and its consequences over the rear of the bombs that is of most interest. The flow diverts away from the small passage between the bombs and the CBTE body and it will be seen that near the nose/parallel centre-body junction, the combination of high sideflow angles and high local velocities result in a local shock-induced separation. The effects of these separations convect downstream in the channel to produce very extensive separations and/or rolled up vortex flows over the rear of the bombs. The presence of the ERU forward crutching arms does not help: they are clearly in an ideal location to induce a large area of separated flow over the top and inside surfaces of the shoulder bomb afterbodies. The top and inner fins of the shoulder bomb and the top fins of the bottom bomb are apparently immersed in a highly confused wake. Standard multiple carriers are therefore a potent source of adverse aerodynamic interference likely to give major increases in drag as shown in Fig 2a and poor release characteristics. Fortunately, these ill effects can be greatly reduced by improving the aerodynamic cleanliness of the carrier body and mounting assembly and by repositioning the stores - I will return to this theme later in the paper.

Turning to the interference between store installations and the parent aircraft, Fig 2b illustrates the interference that can arise with underwing pylon-mounted stores (one store per pylon, no multiple carriers). It should be noted that in Fig 2b, the ordinate is the drag per store, ie for the case where there were 3 stores per wing on separate pylons, the graph shows $1/6 \times$ the total drag increment for the stores/pylon combinations. The results are for $C_L = 0$ and refer to Mk 10 454 kg bombs mounted on wing A (see §3). Admittedly, results for $C_L > 0$ would be less dramatic but on the other hand, results for other wings, eg wing B: see Fig 5, could be more serious: hence, it is fair to suggest that Fig 2b is a typical picture. Once again, serious adverse interference is evident, particularly at high subsonic speeds. If expressed as installation drag factors, the values reach about 5 at $M = 0.9$. It will be seen later in the paper that rather than quoting installation factors, it is probably more sensible to relate such results to the drag characteristics of the clean aircraft. A single pylon-mounted store per wing degrades the drag-rise Mach number of the combination; a multiple arrangement with say, 3 pylon-mounted stores completely modifies the nature of the flow over the wing lower surface and introduces a significant drag creep ahead of the steep drag rise.

Mounting stores below a wing designed without regard to the consequences of store carriage can therefore lead to serious adverse interference. Mounting the stores in arrays under the fuselage can however lead to favourable interference as illustrated in Fig 2c. The upper picture has been used in several earlier papers (4,5). It shows the results of tests in the ARA transonic tunnel in which 4 rows of 5 small stores with flat bases were mounted on a pallet below a flat-bottomed fuselage. Above about $M = 0.92$, the total drag increment for the 20 stores is smaller than the increment for a single row of 5 stores: to reiterate, the total drag increment and not just the drag per store! It is clear that favourable tandem effects are sufficient to offset the adverse effects due to the side-by-side carriage. However, it may be argued that this very favourable result is simply due to the fact that they are small stores mounted tangentially and mostly immersed in the boundary layer. However, it is certainly fair to compare the lower picture in Fig 2c with Fig 2b. This lower picture was based on more recent evidence from tests in the RAE 8ft x 6ft tunnel on an array of 6 large boattailed stores, again mounted tangentially on a pallet below an aircraft fuselage. Even in this case where the stores are much larger in relation to the size of the aircraft, the drag increment for the array consisting of 3 rows of 2 stores is generally, particularly at high Mach number, less than the sum of the free air drag of the stores in isolation. Favourable interference is thus a genuine possibility and in the AGARD Working Party report (4), other examples are to be found, often interpreted in terms of the stores having produced a better longitudinal distribution of cross-sectional area for the complete configuration.

Having now set the scene, let us look in more detail at the sources of interference and the possibilities for improving the store layouts.

3. UNDERWING FUEL TANKS AT LOW C_L

It seems appropriate to start the detailed discussion by considering the interference effects due to the carriage of external fuel tanks. A fuel tank is the simplest and probably the cleanest type of store. Fuel tanks are generally carried on pylons below the wing or fuselage. It is far more efficient to carry them under the fuselage. For example, in model tests (6) at AEDC for the F-4C, it was found that carrying fuel in a 2264 litre (600 gal) tank under the fuselage was more than 4 times as efficient at $M = 0.7$ and almost 3 times as efficient at $M = 0.9$ as carrying fuel in 1396 litre (370 gal) tanks under the wing, efficiency being defined as the ratio of fuel capacity divided by the installed drag. Nevertheless, on many aircraft there are practical reasons why the fuel tanks have to be carried underwing and Fig 3a presents results for 15 different aircraft/fuel tank combinations. In all cases the tanks were pylon-mounted under the wing near mid-semi-span; except for the curves marked A and B, this figure was included in the Working Party report (4). The graph shows the variation with Mach number at $C_L = 0$ of a 'figure-of-merit' or inverse efficiency,

$$\lambda_I = \frac{\text{Measured installed drag increment (or drag in isolation)}}{\text{Estimated profile drag for tank/pylon at low Mach number}}$$

ie assuming the estimate in the denominator is correct, $\lambda_I = 1.0$ implies zero net drag contributions from flow separations, base drag, bluntness drag, excrescence drag, wave drag and interference within the assembly and between the assembly and the aircraft.

The results for a typical fuel tank in isolation are included for comparison. The figure clearly illustrates that most of the drag increment is related to the installation interference effects. For the tank in isolation, λ_I is less than 1.1 up to $M = 0.94$ but for the installed tank assemblies, values of λ_I ranging from 1.2 to 3.5 are obtained even at $M = 0.6$; rapid increases in λ_I with Mach number are already occurring at $M = 0.6$ in the worst case but not to beyond $M = 0.86$ in the best case. At first sight, it may appear an impossible task to predict or interpret this figure but certain trends can be deduced. First and foremost, as shown in Fig 3b, there is a trend for both λ_I at $M = 0.6$ and M_{Dg} , the Mach number for the start of the rapid increase in λ_I , to improve in sympathy with the drag-rise Mach number M_D of the clean wing. This is only to be expected: an increase in M_D will generally imply a reduction in wing thickness/chord ratio and/or an increase in wing sweepback and thus, a reduction in the suction below the wing lower surface and a later appearance of a shock wave in the channel between the wing and tank. Research has shown that the appearance of this shock wave generally collates with M_{Dg} . With tanks of a standard shape, therefore, it may be difficult to obtain notably better results than those implied by the dashed lines in Fig 3b but the significant point is that there are a fair number of installations where the interference is such that the results do not approach this norm.

Let us consider two of these examples. First, Fig 3c compares configurations 6 and 11. This is discussed in detail in Ref 5. For both cases, the installed drag values for $C_L = 0$ lie above the norm, Figs 3a,b, but the excess is far greater for case 6; even at $C_L = 0.4$ where one would expect some improvement, the results are still poor. Looking at the geometry, it will be seen that in case 6, the tank is larger relative to the aircraft. Partly because the pylon is relatively thin (7% thick compared with 13% thick for case 11), the crutch arms are exposed and unfaired. A simple estimate suggests that the drag of these crutch arms treated as isolated excrescences would be about the same as the extra drag of the thicker pylon in case 11 but it has generally been found that such excrescences can induce serious interference if the flow downstream of the excrescences encounters a region of high adverse pressure gradient. This would be true in the present case. The major weakness however with configuration 6, is the rapidly diverging channel at the rear. All three surfaces, ie wing, pylon and tank contribute to this divergence. One could say that the installation could not have been tailored better to produce a shock across the channel at a relatively low Mach number, or to produce a flow separation on one or all of the rear surfaces! Extra viscous drag and early wave drag are therefore only to be expected. Fig 3c shows a revised configuration for which the interference would be expected to be less; the λ_I curve for this revised configuration is a speculative estimate: no tests have been made on this layout.

Second, Fig 3d presents a comparison between cases A and B. These results are for the same tank mounted on the same pylon at the same spanwise position on two wings A and B of the same planform but which differ in section shape. The section of wing B is thicker and is designed to give more rear loading. Strictly, the results for A and B are not comparable with the other cases in Fig 3a because two additional bare pylons were present on the inner and outer wing and thus it is probable that the values of λ_I have been increased by the aerodynamic interference between the tank/pylon and these other pylons. However, it is still fair to compare A and B and Figs 3a,b show that the values of λ_I and M_{Dg} are much poorer for wing B. These differences can be explained qualitatively in terms of the measured pressure distributions over the wing lower surface. These are shown in Fig 3d for $M = 0.80$ for a station at $0.4 \times$ semi-span, ie inboard of the tank. These distributions can be described as follows:

	A	B
Clean wing	Subcritical	Subcritical
Wing with 3 pylons	Subcritical	Strong shock, no separation
Wing with 3 pylons and tank	Strong shock, no separation	Shock-induced separation*

* Indicated by the lower pressures downstream of the shock relative to the other cases and by the partial collapse of the supersonic region ahead of the shock.

One can therefore forecast from the pressure distributions that both the wave drag and the viscous drag will be higher with the tank mounted on wing B. The greater interference for a given Mach number and C_L is a consequence of the different pressure distributions over the clean wings. The significant features are that near 0.35c the suction is about 70% higher on wing B than on wing A and that the subsequent adverse pressure gradient is about twice as great.

It would be wrong to conclude however that the greater interference with wing B is an inevitable consequence of attempting to carry the tank on a more advanced, thicker wing. For example, as with configuration 6 in Fig 3c, one could either

- (i) move the tank forward or aft in an attempt to separate longitudinally the peak suction on the wing and the tank,
- or (ii) change the shape of the tank to one with a parallel centre section opposite the peak suction on the wing,
- or (iii) reshape the rear of the tank with either a longer, less tapered boattail or a raised upper line, ie a banana-shape tank,
- or (iv) modify the pylon design,
- or (v) change the wing camber-line to produce a more suitable shape of lower surface pressure distribution.

It is worth noting that concept (ii) was introduced more than 30 years ago on an early jet fighter to eliminate flow separation and buffeting problems that had resulted from the underwing carriage of a tank having a continuous longitudinal variation in cross-sectional area. The problem was solved by changing the tank shape to one with a forward, parallel mid and tapered aft section mounted in such a position that the peak suction at the junctions between the three sections were displaced fore and aft of the peak suction in the clean wing flow field. Now, when the need for care in eliminating adverse interference is even greater with modern wing designs, the concept is rarely used. This is not true of configuration 6 discussed above but in this case, for practical reasons, the concept was misapplied as will be realised from the sketch in Fig 3c. Logistically, it may be unattractive to think in terms of a different tank shape for different aircraft and to some extent, one could argue that (i-iv) should be regarded as palliatives for a

situation that should not have arisen. The real lesson - and this will become even clearer in §5 below - is that wings should be designed with store carriage in mind from the outset. At the very least, one should design a wing/pylon combination rather than a clean wing.

4. UNDERWING STORES: FACTORS AFFECTING INTERFERENCE DRAG AT LOW C_L

4.1. Store Shape

It should be apparent from the discussion of the fuel tank examples in Fig 3 that the aerodynamic interference with underwing mounted stores is likely to be proportionately more serious for clean streamlined stores than for parallel or dirty stores. Even relatively small changes to the shape of the store can have a significant effect on the interference. This is shown by the comparison in Fig 4a. Two alternative stores X and Y were mounted (8) on wing A, Fig 3d, on the same underwing pylon at 0.55 x semi-span. The two stores have about the same overall dimensions but a somewhat different shape, store Y having a bluffer nose, a longer parallel centre section and a shorter boattail. The free air drag and indeed, the installed drag increment was much greater for store Y but as shown in Fig 4a, the interference contribution ΔC_{Di} to the drag increment,

$$\text{ie } \Delta C_{Di} = C_{Di\text{installed}} - C_{Di\text{isolated}}$$

is generally somewhat less for store Y, particularly in the range $M = 0.80 - 0.85$. There are two possible qualitative interpretations of this result. Either it is an example of a general trend that when the store shape is such that there is poor flow over the store afterbody even under free-air conditions, there is less chance that the interference with the wing flow field will further degrade the flow over the afterbody. Or the shape and position of store X are such that the interference increases the wing wave and/or viscous drag. Oil flow patterns for $M = 0.85$, $C_L = 0$ suggested that the second interpretation is more likely in this case. The main features of these flow patterns are reproduced in the sketch in Fig 4a:

- (i) with store Y, the shock is further aft - consistent with the position of the start of the afterbody,
- (ii) with store X, the sweepback of the shock both outboard and inboard of the store is somewhat less than with store Y,
- and (iii) with store X, the change in flow direction through the shock is notably more acute, thus implying a stronger shock.

It is thought that (iii) is the dominant factor.

This comparison has been included to act as a warning against naive use of interference drag factors and to encourage the hope that by attention to detail and with the benefit of the theoretical calculations that will be possible in the future, adverse interference can be alleviated.

4.2. Store Depth below the Wing

Various investigations, eg Refs 5,9,10,11 have specifically considered the effects of the vertical position of a store below the wing. All have confirmed that this can be an important parameter but it is difficult to draw simple generalised conclusions. When the flow is entirely subcritical, an increase in the length and hence, surface area of the pylon will increase the pylon profile drag but will generally tend to reduce the interference drag. There is however a fair amount of evidence indicating that when the flow is supercritical the adverse interference first increases with store depth before it starts to decrease. Oil flow tests and pressure plotting measurements have shown that with a longer pylon, the flow separations in the wing-eylon junctions can be less severe. The channel between wing and pylon is therefore less constricted and the flow can expand to a higher local Mach number. The shock as well as being longer in extent, is stronger and there are therefore two reasons why the wave drag is increased.

An example of the effect of store depth is shown by the drag results in Fig 4b. A missile-type store was mounted at two vertical positions below the wing of a 25° sweptback wing research model in the ARA transonic tunnel (11). At low Mach number, at both $C_L = 0$ and 0.3, the drag increment was higher with $H/D = 0.88$ than with $H/D = 1.23$, thus showing that in this particular case, the reduction in interference as the store and wing were moved apart more than offset the extra pylon profile drag. Above $M = 0.75$, however, the drag increment increased with Mach number more rapidly with $H/D = 1.25$, thus supporting the hypothesis of extra wave drag when the wing and store are further apart.

Quantitatively, the results could well be different with other stores on other wings and the correct choice of pylon length will depend on the aircraft requirements. It seems possible that in many cases, a compromise will have to be made between a short pylon to improve the dash capability with bare pylons and a long pylon to minimise the drag and usable lift penalties at high C_L (a point not illustrated in this paper).

4.3. Spacing of Pylons across the Span

In §§3, 4.1, 4.2 we have been concerned with the carriage of a single store per wing panel. In practice, however, it is likely that current and future aircraft will be designed to carry a heavy store load requiring 2, 3 or even as many as 5 pylons per side. Tests have been made (8) to show whether the drag increments for a 3-pylon load of 3 stores on wing A of the previous example are sensitive to the spanwise spacing of the pylons. Three alternative spacings were compared, the widest and narrowest spacings being indicated by the photographs of Fig 4c. The graph shows the variation with Mach number of $\Delta(\Delta C_{Di})$ where

$$\Delta(\Delta C_{Di}) = (\Delta C_{Di})_{\text{narrow}} - (\Delta C_{Di})_{\text{wide}}$$

and

$$\Delta C_{Di} \text{ is defined as in the example in §4.1.}$$

The figure shows that as might have been expected, bringing the stores closer together increases the interference drag at low and moderate Mach numbers, the maximum changes being as much as $\Delta(\Delta C_{Di}) = 0.0030$ or perhaps 15% of the drag of the clean aircraft. At high subsonic speeds, the trend begins to reverse

until ultimately, the drag increment is less with the narrow spacing. The Mach number for the crossover increases with C_L .

The oil flow patterns in Fig 4c offer a partial explanation for the change in sign of $\Delta(C_D)$ between low and high Mach number, eg between $M = 0.75$ and 0.80 at $C_L = 0$. Irrespective of the spacing, the main feature of these flow patterns is the near-unswept shock below the wing between the pylons. With the narrow spacing, this quasi-one-dimensional flow is already established at $M = 0.75$ with the terminal shock and flow separations behind the shock extending from one pylon to the next. With the wide spacing, this type of pattern does not become fully established until $M = 0.80$ but then, the shock waves in the wider gullies between the stores appear to be stronger. The pictures therefore help to explain why $\Delta(C_D)$ increases more rapidly above $M = 0.75$ with the wide spacing, the increase being sufficient to give higher $\Delta(C_D)$ than with the narrow spacing above $M = 0.80$. There is an obvious similarity between these effects of spacing and the effects of store depth as already described.

For configurations of the type discussed here, store spacing is clearly a significant parameter; the optimum value would depend on the aircraft operating requirements. It is possible however to envisage how the adverse interference, ie the values of $\Delta(C_D)$ might be reduced by either changes in pylon design or store relative longitudinal position, ie store stagger. In the present case, the pylons were of simple design with symmetrical slab-sided sections; the shocks between the pylons tended to be unswept because they extended from the peak suction on the outboard side of the inner pylon (aft of its maximum thickness) to the peak suction on the inboard side of the outer pylon (ahead of its maximum thickness); change in design might improve the shock sweep. The store longitudinal positions were chosen with the aim of minimising the c.g. shifts for partial and full store loads; these considerations may be less vital in the future with the advent of active controls and acceptance of relaxed stability.

4.4. Effect of Wing Design: Multiple Carriage on Separate Pylons

The influence of wing design has already been discussed in §3 with reference to the drag increments for an underwing tank installation on wings A and B (same planform, different sections). Comparative tests were also made (7) on these wings with three stores of shape Y mounted on three separate pylons. Results and oil flow patterns from these tests are presented in Fig 5. The upper graphs compare the $C_D - M$ variation for $C_L = 0.2$ for (a) the clean wings, (b) the wings with 3 bare pylons per wing and (c) the fully loaded configurations. It should be noted that the false zeros on the ordinate scales have been staggered by amounts corresponding to the estimated low speed profile drag of respectively, the pylons and the pylons plus stores: in other words, if there were no interference drag, the three pairs of curves would start at low Mach number at the same levels.

The addition of the pylons and then the stores reduces the drag-rise Mach number and by implication, the penetration speed by significant amounts, at least 0.1 in Mach number. This is only to be expected and to some extent at least, is an inevitable consequence of carrying a heavy store load underwing in what has generally been accepted as a 'standard' arrangement. In passing, it should be noted that in this and succeeding sections up to §5.2, we are only concerned with the multiple carriage of stores on separate pylons at different stations across the span. 'Standard' underwing carriage of a multiple store load can in practice imply the use of a triple carrier, eg as on the F-4 Phantom, or a twin carrier as on the Harrier but these cases are not considered here because of the difficulty of separating the store-wing interference from the interference within the multiple carrier.

It is clear that the relative assessment of wings A and B depends on whether the pylons/stores are fitted or not. Clean, the reduction in the Mach number for the steep drag-rise for wing B relative to wing A is about $\Delta M = 0.035$ but with pylons, it is as much as $\Delta M = 0.06$ and with pylons/stores, about $\Delta M = 0.055$. The unexpected feature of these results is the striking effect of the bare pylons. This is a significant conclusion because the aircraft will still be carrying its pylons on the return from the target and hence this is a configuration that should if possible be optimised. Also, the shape of a pylon is probably less sacrosanct - or less constrained by other factors - than the shape of most stores.

Fig 5 also shows the wing lower surface pressure distributions for stations at 0.60 and $0.72 \times$ semi-span on wing A and at 0.64 and $0.74 \times$ semi-span on wing B, for $C_L = 0.2$, $M = M_X$. The stations are between the middle and outer pylons, the outer stations being very close to the outer pylons. For the clean wings, the flow is subcritical in both cases although it is significant that the values of $(-C_p)$ near $0.3c$ are almost twice as great for wing B as for wing A. Adding the pylons on wing A leads to a local supersonic region inboard of the outer pylon while on wing B, this region appears to extend across the whole panel to the middle pylon. Adding the stores produces a strong shock wave in the gully between the stores as already seen in Fig 4c with poor flow behind the shock particularly on wing B. Near the outer pylon on wing B, the separation is already sufficient to degrade the supersonic region; this is hardly surprising bearing in mind that $M = M_X$, $C_L = 0.2$ is far up the drag-rise for this configuration.

These pressure distributions do not however tell the full story. Fig 5 also contains photographs of oil flow patterns for $M = M_X$, $C_L = 0.2$ for wings A and B with three bare pylons. Weak shocks and fairly narrow pylon wakes are evident in the picture for wing A but generally, the flow is relatively well behaved compared with wing B where there are substantial flow separations both inboard of the outer pylon and downstream and outboard of the inner and middle pylons. These pictures suggest that the drag creep in the results for wing B with bare pylons must be largely associated not with premature wave drag but with gross viscous effects particularly downstream of the pylons.

The full assessments of wings A and B including factors not discussed here could still favour wing B. It is a more advanced wing with notable advantages in usable lift and fuel volume. In designing wing B, it was accepted that there would be some loss in drag-rise Mach number at low C_L : a reduction of 0.03 was deemed acceptable. It must be emphasised strongly that the fact that the reduction is about 0.06 with the pylons fitted does not destroy the concept of the advanced wing design. It merely shows that one should design the wing-eylon and if possible, the wing-pylons-stores as an entity. The simple pylons that were adequate on wing A are no longer acceptable on wing B. Aerodynamically, as isolated pylons, they were respectable designs: 6.5% thick, symmetrical, slab-sided, elliptic nose, tapered aft section. Looking at

the oil flow picture, however, it seems inconceivable that one would not be able to modify the pylon design to reduce the viscous interference effects on the wing.

5. UNDERWING STORES: OTHER ASPECTS OF INTERFERENCE

5.1. Aircraft Stability and Usable Lift

If it is of course self-evident that underwing stores will interfere with the flow over the wing lower surface. Until recently, however, it has not been fully realised that the stores can modify the flow over the wing upper surface and that this can have serious consequences, particularly when the flow is supercritical. To start with a simple example, Fig 6 presents results from tests at $M = 0.85$ on a model of an aircraft with a wing of moderate sweepback and moderate aspect ratio tested with and without two underwing stores per wing. Fig 6a shows the wing upper surface pressure distribution for a station near mid-semi-span and it will be seen that the addition of the stores increases the suction in the supersonic region and hence, the shock strength. Two factors can contribute to this interference: an increase in upwash and an increase in local velocity. The shock strength is increased - but by varying amounts - across the complete span and thus, the shock-induced separation leading to a forward movement of the shock occurs at a lower incidence. This is shown in Figs 6b,c for stations at mid-semi-span and $0.85 \times$ semi-span. However, the important point is that these effects were not quite the same at all spanwise stations. The differences appeared trivial at first sight but they were sufficient to modify the C_m - a variation as shown in Fig 6d. The results for the clean wing were marginally acceptable; with stores, however, there was an unacceptable pitch up. This is an aspect of store interference which is clearly very configuration-dependent but it cannot be ignored when seeking to optimise the configuration.

The interference with the upper surface flow has more dramatic consequences at high C_L near the usable lift boundary. Two examples drawn from the results of the experiments (7) on wings A and B are presented in Fig 7. First, at the top of the page, data from incidence traverses at a relatively high subsonic Mach number, $M = M_x + 0.07$, indicate serious adverse interference, eg on the lift break, by about $\Delta C_L = -0.05$ for the bare pylons or $\Delta C_L = -0.25$ for the fully loaded case. Measured pressures are shown for 3 stations at 2 incidences. With and without pylon cases are compared at the same incidence. The distributions show that as might be expected, some of the loss in break C_L is due to the interference with the lower surface flow which is still substantial even at this incidence, particularly near the outer pylon. The significant point however is that the flow breakdown on the upper surface appears to occur at a lower incidence: the deterioration between $\alpha = 4.9^\circ$ and 6.7° at 0.64 and $0.73 \times$ semi-span is certainly much more rapid when the pylons are fitted. Once again, relatively small increases in shock strength have been sufficient to provoke these differences. It is possible that these effects could have been averted or at least postponed to a higher Mach number by moving the pylon-wing intersection further aft. The more dramatic effect from fitting the stores is of somewhat academic interest because it is unlikely that the fully loaded aircraft would have sufficient thrust to reach these conditions.

The results in the lower half of Fig 7 have been included to illustrate that the interference effects of underwing pylons/stores on usable lift are not necessarily adverse. These results for $M = M_x$ again show a reduction in break C_L from both the pylons and the stores but the subsequent reduction in lift-curve slope is less and the development of the stall is then more progressive. Indeed, the very fact that data can be presented for the cases with pylons and with pylons/stores up to a high incidence is itself significant because with the clean wing, the test could not be continued beyond the abrupt lift break because of severe model bounce. Pressure distributions, with and without stores are compared for two stations (between the middle and outer stores as in Fig 5) at three incidences, the lowest being near separation-onset. It will be seen that stores off, there is a lift contribution from the forward supersonic region at both stations at $\alpha = 8^\circ$ and 9.5° followed by a collapse at both stations at 11° whereas stores on, the supersonic region has already completely collapsed at one but only one station at $\alpha = 9.5^\circ$: in other words, an earlier but more progressive stall, stores on. This implies earlier buffet onset but better buffet penetration. The presence of the pylons and the stores is tending to dictate the manner in which the areas of separated flow extend with increasing incidence and as a result, the stall development is likely to be less sensitive to other variables: for example, there is evidence from tests on other wing designs that the presence of underwing stores can alleviate any tendency to lateral problems such as wing drop and wing rock. This statement would not however be true of every wing design: examples could be quoted where the exact opposite would apply.

Speculatively and arguably, a wing design philosophy can be suggested that would exploit this possible favourable interference of the pylons/stores on the stall development. One should design the clean wing to carry as much lift as possible at buffet-onset; there is then the risk that the flow will tend to break down all across the span at almost the same incidence; however, the addition of underwing pylons (and stores) could then slightly degrade the stall onset but give the progressive breakdown that is required for satisfactory flying qualities. This design philosophy has been set out in broad terms: to follow it literally may not be possible with a given design at all Mach numbers. The interference from the pylons/stores is probably due to their effect on the spanwise upwash distribution ahead of the swept leading edge of the wing; the detailed effects could be modified by small changes in the geometry of the wing-eylon leading edge junction.

5.2. Buffet at low C_L

As a final contribution from the results of the tests (7) on wings A and B, Fig 8 presents $C_B - C_L$ curves* for $M = M_x$ and $M = M_x + 0.07$ for wing B with and without pylons/stores. It will be seen that even at $M = M_x$, the stores are tending to provoke a buffet response at low positive C_L while at $M = M_x + 0.07$, with stores, there is no C_L -range that can be described as being free from buffet and even the bare pylons give significant buffet at low C_L . Most modifications introduced to reduce the drag increments should also tend to alleviate the buffet.

* $C_B = \frac{\text{tuned rms wing root strain}}{\text{dynamic pressure}}$

5.3. Flow Fields: Store Loads and Release

Various references, eg Ref 12, have concluded that for underwing stores, the flow field about the aircraft with stores may be the most important parameter affecting the store trajectory. Mathews in Chapter 5 of Ref 4 notes that the flowfield is likely to vary with aircraft, store, store position, adjacent stores, flight conditions, and aircraft attitude. As an illustration, Fig 9 shows the velocity components measured (13) in two lateral planes near the front and rear of 3 M-117 bombs on a TER on the inboard wing station of an F-4 at $M = 0.85$. The flow survey was made with the stores present. There is much downwash near the nose of the weapon on the bottom station and much upwash near the tail. This typical flowfield produces an extremely large nose down aerodynamic pitching moment on large diameter stores, particularly at higher Mach numbers and again to quote Mathews, 'has been found to result in unsatisfactory release trajectories for many weapons.'

This example has introduced the confusion that was avoided when discussing the performance data, ie some of the interference is between the store installation and the wing and some would be present in the flowfield around the TER in isolation. It will be suggested later that the latter could be alleviated by repositioning the stores on the carrier but also, it is plausible to suggest that the changes in flow direction in pitch would have been less if the stores had been mounted either further aft or further forward: changes that would also probably have reduced the drag increments. Indeed, the important general point is that any modification that reduces drag by eliminating or reducing the tendency for a strong shock wave or major flow separation is also likely to reduce the sensitivity of the store loads to C_L , Mach number and minor differences in geometry and fitting of individual stores. This should serve to make the trajectories more predictable and repeatable: a worthwhile aim in itself.

6. WING TIP-MOUNTED STORES

Wing tip carriage is increasingly becoming a favoured option for carriage of slender missiles. There may be practical reasons for this, eg a missile mounted well forward at the tip will have a good unobstructed field of view and it may be the best position to avoid ground clearance problems. However, on many wings, it is also an attractive proposal aerodynamically and it certainly should be discussed in this paper because it provides a prime example of favourable aerodynamic interference.

The AGARD FDP Working Party Report (4) included two examples (14,15) showing that wing-tip carriage of external stores can reduce the lift-dependent drag. Fig 10 presents some results from a recent series of tests which are of considerable interest because surface pressure measurements are available to help in the interpretation of the favourable interference. Tests were made on a sweptback wing research model fitted alternatively with a curved wing tip and with a cropped square-cut tip on which was mounted a model of a missile and its launcher. The tests covered a wide range of Mach number but the results for $M = 0.7$ presented in Fig 10 are typical of those obtained at Mach numbers up to at least $M = 0.9$. They are non-dimensionalised using the geometry of the wing with the square-cut tip. The drag increment at a given C_L from adding the missile and its launcher decreases with C_L becoming negative above about $C_L = 0.3$. A prediction based on treating the missile and launcher as an effective extension of the span gives very good agreement with the measured results up to quite high values of C_L . This may suggest a very simple analogy but a detailed study of the pressure distributions measured in these tests shows that this analogy does not entirely represent the physics underlying the favourable interference.

Fig 10 shows that the reduction in the lift-dependent drag collates with an increase in lift at a given incidence; some of this extra lift is generated on the missile itself but mostly, it is produced on the outer wing as shown by the local C_N values for the station at $0.95 \times$ semi-span. Indeed, the local lift at this station is almost as great as for the wing with curved tip and is greater than would be predicted on the effective span analogy. Further, the changes in chordwise loading at this station due to the addition of the missile cannot be explained simply by a change in induced incidence. Comparison of the results from the tests with and without the missile tail fins shows that some of the extra lift even at this station some distance away from the fins is due to local interference between the fins and the rear wing (increased suctions on the upper surface, increased pressures on the lower surface).

The results in Fig 10 and in the earlier comparisons (14,15) are for conventional tip-mounted installations. It does not need much imagination to suggest that it might be possible to exploit the favourable interference further by repositioning the missile. Winglet research is obviously relevant. Not all the interference can be described as favourable: the increased adverse pressure gradients near the leading edge on the upper surface near the wing tip-launcher junction at low Mach numbers and a further forward shock position near the tip at higher Mach numbers could have adverse consequences particularly for wings designed to stall progressively inwards from the extreme tip. However, with care, it should be possible to avoid these local problems and thus reap the benefits of the favourable interference.

7. BASIC CONCEPTS FOR FAVOURABLE INTERFERENCE (OR MINIMISING ADVERSE INTERFERENCE)

The discussion in §§3-6 has concerned wing-store interference. Let us now consider store-store interference and the implications for carrier design and for multiple store arrangements, eg below the fuselage. Three basic concepts (16) are available to reduce adverse or to produce favourable interference viz

- (i) increased lateral spacing of the stores,
- (ii) longitudinal stagger between adjacent stores,
- and (iii) tandem carriage of the stores.

Fig 11 presents results from tests in the 2ft x 1½ft tunnel at RAE Farnborough in which drag measurements were made (17) on various arrays of stores mounted on 45° sweptback struts from the roof of the tunnel. The pylon extended one store diameter from the roof and so the stores were positioned just clear of the roof boundary layer; in effect, the stores were being tested close to a reflection plane simulating the surface of a wing with zero thickness. Results are shown in Fig 11 for 2 types of store, one with a pointed nose and the other with a hemispherical bluff nose. The results have been collapsed in the form of three interference drag factors, viz

$$K_y = \frac{\text{Drag of row of 2 stores}}{2 \times \text{drag of individual store}}$$

for a row of 2 stores at different lateral spacings, y ,

$$K_{st} = \frac{\text{Drag of staggered row of 2 stores}}{2 \times \text{drag of individual store}}$$

for a row of 2 stores at a given lateral spacing (0.25 calibres) but different longitudinal stagger, X_{st} ,

(ie with zero stagger, $K_{st} = K_y$)

$$K_T = \frac{\text{Drag of column of 2 stores}}{2 \times \text{drag of individual store}}$$

for a column of 2 stores at different axial separation, X_T .

The graphs in Fig 11 give an idea of what might be achieved ideally with these 3 basic concepts. It should be noted that the actual values of K_y , K_{st} , K_T and their variation with Mach number depend considerably on the shape of the store. Some of the main features of the results are described below.

7.1. Lateral Spacing

2 stores side-by-side at the close spacing ($y = 0.015$ calibres) typical of store carriage on standard twin carriers clearly gives appreciable adverse interference: the values of K_y increase from about 1.5 at low Mach number to maxima of 1.65 - 1.75 before decreasing to 1.3 - 1.4 at transonic speeds. The maxima in these curves occur at a Mach number close to the drag-rise Mach number M_{Dg} of the individual store if tested in isolation. Increased lateral spacing rapidly reduces the adverse interference at Mach numbers below M_{Dg} , the decrease with y at low speeds being predicted reasonably by the equation

$$K_y = 1 + \frac{0.42}{\exp(y'/0.42d)}$$

where d = store diameter

and y' = minimum distance between the two stores

Above $M = M_{Dg}$, the benefits of increased lateral spacing become less pronounced, the variation with y tending to disappear first at low values of y . Near and above $M = 1$, the changes in K_y with y only amount to about 0.1.

When applying this concept to an actual twin or triple carrier, other factors intrude, eg an increase in y will tend to give more surface area on the carrier body and will modify the interference between the stores and this body. On a practical installation, the variation of D/q with y can therefore be non-monotonic particularly at high subsonic speeds. This is yet another example of a phenomenon already noted in other areas, viz if one widens a channel between two surfaces, one can reduce low speed viscous interference but allow the supercritical flow to expand to a higher local Mach number, thus increasing the wave drag. In general, however, for aircraft with a heavy store load, it is probably the results at Mach numbers up to M_{Dg} that are important and thus, increased lateral spacing should be helpful. In addition to the reduction in drag, the increased lateral spacing should improve the release characteristics - less tendency for a collision during release and more opportunity to use an optimum ejection angle. The possible benefits on maximum store release speeds are shown in Fig 13 to be discussed in §7.3 below.

7.2. Store Stagger

A relatively small amount of stagger, eg $X_{st} = 1$ calibre is sufficient to displace the peak suction regions near the shoulders of the store and Fig 11 shows that this can reduce the drag significantly, particularly at Mach numbers near M_{Dg} . The values of K_{st} for $y = 0.25$ calibres are then about 1.2 as compared with maxima in the range 1.4 ~ 1.6 for stores with zero stagger. Having displaced the peak suction regions, there is then little further change in drag until the forward shoulder of the rear store has moved aft of the rear shoulder of the forward store. There is then a further reduction in K_{st} , eg for $X_{st} = 4$ and 6 calibres for the pointed nose store and $X_{st} = 6$ calibres for the bluff nose store. Values of K_{st} near 0.8 are then obtained at transonic speeds. The most sensible way of describing this result is to say that the favourable interference to be expected (see below) from carrying stores in tandem can still be achieved to some extent with store centres displaced laterally by 1.25 calibres.

Longitudinal stagger of the stores as a means of reducing the drag of loaded multiple carriers at high subsonic and transonic speeds was being suggested (18) as early as 1966 and again at an AGARD FDP conference (19) in 1973. Tests (4,5) on a 1/4 scale model of a standard triple carrier on the ARA isolated store drag rig showed that staggering the bombs on the shoulder stations by 0.92 calibres forward and aft of the bottom bomb reduced the drag by more than 20% at $M = 0.9$. These and other results have confirmed that stagger can reduce the adverse interference in a practical installation. The benefits affect more than just drag: forces and moments on both installed and released stores can be reduced, as illustrated in Fig 12.

These results in Fig 12 are taken from tests (20) in which the close interference forces and moments between two Mk 10 bombs mounted underwing on a standard twin carrier have been measured during simulated release of the inboard 'free bomb'. Tests were made with the bombs mounted side-by-side and staggered fore-and-aft, by ± 1 calibre, the positive sign denoting that the inboard 'free bomb' is staggered aft. Load measurements were made on the sting-mounted 'free bomb' and the carrier-mounted 'captive bomb' and also pressures were measured on the lower surface of the carrier both along the carrier centre line and above the 'free bomb' centre line. Results for $M = 0.80$ are presented in Fig 12. The pressure distributions appearing above/below the bomb pictures were taken with the captive bomb respectively present and absent; the free bomb was slightly below its installed position. The bottom graphs show the effect of stagger on the variation of store pitching moment and yawing moment with vertical displacement of the free bomb with and without the captive bomb present.

The pressure measurements on the carrier clearly show that store stagger is effective in reducing the store-store and store-carrier interference. The shock strengths are reduced with both positive and negative stagger, the highest peak local Mach numbers being $M_1 = 1.41$ (1.41) for side-by-side carriage,

$M_1 = 1.30$ (1.22) for positive stagger and $M_1 = 1.26$ (1.09) for negative stagger, the values in brackets referring to the single bomb case.

Poor release characteristics are often diagnosed as being due to the magnitude of the aerodynamic yawing moments and nose down pitching moments on the released stores and the results in the lower graphs indicate that positive stagger should be very helpful in both respects. Note: with positive stagger, moments for first bomb to be released are given by $X_{st} = 1$, captive bomb present and for the second bomb by $X_{st} = 0$, no captive bomb.

Mathews in Ref 4 also quotes an example where staggering the stores on an MER was found to reduce the installed pitching moments. He draws the conclusion that 'store staggering appears to offer considerable potential for both drag reductions and store separation improvements and that additional research in this area is highly recommended.'

7.3. Tandem Carriage

Returning to Fig 11, the bottom pair of graphs illustrate that carrying stores in tandem is a powerful method of obtaining favourable interference, particularly with bluff-nose stores. If the stores are virtually nose-to-tail, ie $X_T = 0.005$ calibres, the reduction in overall drag for a column of 2 stores amounts to about 30% near $M = 1.0$ for the bluff nose and 20% for pointed nose stores; even at a separation of 3 calibres, these figures are 20% and 15%. In inviscid subcritical flow, one would predict compensating buoyancy effects decreasing the drag of the front store and increasing the drag of the aft store. The actual measurements showed that with the stores close together, these opposing trends were present at $M < M_D$ but the increase in drag of the rear store was not sufficient to offset the reduction in drag of the forward store. At high Mach number near $M = 1.0$, the drag of even the rear store could be less than the drag of the store in isolation. Five mechanisms for drag reduction in a tandem arrangement were listed in Ref 4, viz

- (i) the rear store is in a stream of reduced mean dynamic pressure,
 - (ii) at very small spacings, the nose of the rear store is in an essentially dead-air region behind the base of the forward store (this applies to stores with large effective base area),
 - (iii) the wake of the forward store can modify the flow separation characteristics from the nose of a relatively bluff rear store,
 - (iv) the rear store is in a stream of reduced Mach number and thus, the onset of wave drag from the rear store is delayed and also, the shock wave on the forward store is probably moved forward thus reducing the wave drag of this store,
- and (v) the longitudinal cross-sectional area distribution of the combination is better than for the forward or rear stores in isolation and thus, the wave drag at transonic speeds will be less.

Once again, the concept of tandem carriage is not new. Ref 4 quotes results obtained (18) in 1966 at CAL showing that the drag increments due to adding 3 stores to the rear station of an MER was appreciably less than that from adding the first 3 stores to the empty carrier - by 15% at $M = 0.8$ or more than 40% at $M = 1.2$. Drag results for tandem carriers (5) and for tandem arrangements (21) of stores under a fuselage are also quoted in Ref 4: all show large drag reductions broadly consistent with Fig 11, the improvements being frequently about 40% at transonic speeds and particularly noticeable for stores with a completely bluff nose. Methods for the quantitative prediction of these effects are being developed.

In addition to the drag improvements, tandem carriage can also lead to better release speeds. Tests on a model of the Phantom showed that the store installed loads for tandem carriers were of the same order as for a standard twin carrier; the moments were in fact somewhat smaller. Even with the same loads, release from a tandem carrier could be preferable because sideways movement during release does not have to be limited because of the proximity of an adjacent store as with a twin carrier.

A Schoch/Couvert analysis (22) was used (23) to forecast maximum safe release speeds on the basis of the store loads measured for stores mounted on various different carriers on Phantom. It is believed (23) that this simplified analysis yields a reasonable idea of the speed at which the release trajectories begin to depart significantly from those observed at low speeds and that relatively at least, the estimates should be reliable. The results are shown in bar chart form in Fig 13. It will be seen that compared with a standard twin carrier, use of an improved twin carrier employing wider lateral spacing and some stagger gave a 40% improvement in predicted release speed but the best results were obtained with a tandem carrier where the increase was nearly 100%. In practice, of course, an increase of 100% would not be possible because the aircraft fully loaded would not be capable of flying at these speeds. In other words, therefore, the results indicate that with tandem carriers, the release characteristics do not impose any limitation on the safe release speeds.

The case for tandem carriage on grounds of drag and store release is therefore very strong and the concept should be exploited whenever possible. It is appreciated that carrier flexibility, CG/stability considerations can raise problems but it is hoped that the latter will be less serious on future aircraft equipped with active control technology.

8. FEASIBLE DRAG IMPROVEMENTS FOR PRACTICAL STORE ARRANGEMENTS

Research in the UK over the past 8 years has shown that large improvements in the drag of multiple external store arrangements are feasible. The improvements are achieved by judicious application of the concepts discussed in §7 and by refining the general aerodynamic cleanliness of the assemblies, eg by fairing of external away braces. The reductions in drag imply less adverse interference, better flow, weaker shocks, less extensive separations and so in many cases, the reductions in drag should be accompanied by smaller installed loads and better and more predictable release characteristics. Figs 14a-c,e,f illustrate the reductions in drag thought to be feasible; in all cases, present in-service equipment is taken as the datum for comparison. In most cases the 'feasible improvements' are based on

actual test data and are for arrangements that could be engineered in practice, eg the carriers were designed to allow space for the ejector release units and are not idealised configurations.

8.1. Carriers

The scales of all the graphs are the same, the stores in all cases are Mk 10, 454 kg bombs. To this extent, the results are specific but the gains are so large that hopefully, this is of little consequence. Summarising the results for say, $M = 0.85$:

- (i) the drag of the fully loaded triple carrier, Fig 14a, can be reduced to only about 33% of the fully loaded standard CBTE. As a measure of the achievement, the drag of the feasible triple carrier at this Mach number is only about 20% greater than the simple sum of the isolated drags of three separate bombs and the empty carrier. Three bombs can be carried for less drag than a single bomb on the present in-service triple carrier or two bombs on the present in-service twin carrier,
- (ii) the drag of the empty triple carrier, Fig 14b, can be reduced to less than 25% of the drag of the empty standard triple carrier and in isolation, the drag-rise can be postponed to about $M = 0.98$,
- (iii) the drag of the loaded twin carrier, Fig 14c, can be reduced to less than 60% of that of the standard twin carrier of the type shown. Relative to the practice adopted on some aircraft of carrying two stores on a standard triple carrier, the figure is less than 30%.

These figures are for carriers in isolation. The improvements may be even larger if the carrier is mounted underwing but might not be as great if a number of carriers are installed close together underfuselage (unless the whole array was then designed as a unit).

Many factors enter into the design of a good twin carrier. These include the lateral spacing of the stores, the store ejection angle, the longitudinal stagger of the stores, the surface area, fineness ratio and shape of the carrier itself. The standard twin carrier has a body in the form of a thick faired plate of low aspect ratio but various other possible types of twin carrier can be envisaged as shown in Fig 14d. Oil flow patterns (4) from 1/4 scale model tests at ARA have shown that with poor twin carrier designs

- (a) there can be considerable outflow over the bomb nose, rolling up to form a vortex over the top of the bomb with a clearly defined secondary separation line,
- (b) the flow diverts downwards and accelerates over the bomb nose leading to a shock in the entry to the bomb-carrier passage, this shock being strong enough to induce a local flow separation,
- (c) air is sucked through the gaps between the bombs and carrier body near and between the fixation bolts, thus adding to the confused flow situation further aft.

With a good twin carrier design, however, these features are much less pronounced and indeed, the flow over the bombs can appear to be relatively innocuous (4).

8.2. Underwing Stores

Fig 14e presents a similar in-service standard versus feasible comparison for the carriage of 3 store under a wing panel, ie 6 stores per aircraft. For the 'standard' arrangement, the stores are carried on a standard triple carrier as on Phantom; an intermediate curve shows what might be achieved for the same 3 stores mounted on 3 separate pylons as in the arrangements discussed earlier in §§4,5. Fig 14e suggests that at $M = 0.85$, for example, it would be feasible to reduce the drag to less than 65% of the value for the simple arrangement on 3 separate pylons and less than 40% of that of the in-service arrangement using a standard triple carrier.

The Mach number scale of this figure clearly depends on the model selected for the comparison. It may be helpful to note that in the particular case shown in Fig 14e, M_D for the clean wing was about $M = 0.82$.

8.3. Underfuselage Stores

Fig 14f presents a comparison for the multiple carriage of bombs underfuselage. In the standard installation, the bombs are mounted on standard multiple carriers. The graph suggests that relative to this datum, it should be possible to reduce the drag by about 40% and to achieve a drag increment at $M = 1.1$ that is no greater than that for the standard arrangement at $M = 0.9$. At high subsonic and transonic speeds, the forecast 'feasible' drag increment was less than the free air drag of the bomb in isolation, ie it is possible to mount the stores in a closely packed array and obtain some overall favourable interference. These are measured results; almost certainly, they could be improved further in a truly conformal arrangement, (see §9 below).

It should be noted that the model chosen for this comparison is not the same as for the underwing store comparison and to that extent, it may be misleading to present the two figures side-by-side. Nevertheless, the implication that it is preferable to carry a heavy store load in arrays under the fuselage rather than underwing can be accepted as a valid conclusion. Other examples supporting this conclusion and drawn from US research (21,25) are to be found in Ref 4. Ideally, the stores should be mounted tangentially* (or semi-submerged if the penalties of empty cavities after the stores have been dropped (25) can be minimised), in tandem with close longitudinal spacing, with due regard to the longitudinal distribution of cross-sectional area for the complete configuration and with the ejector units hidden within the fuselage or behind a specially devised pallet. We have therefore arrived at the theme of conformal carriage which is clearly the prime approach for mounting stores in a way that will exploit favourable aerodynamic interference.

* not necessarily under the fuselage; Ref 24 argues the case for a radical overfuselage installation.

9. CONFORMAL CARRIAGE

The aim with conformal carriage is to carry the external stores as closely as possible to the external surface of the aircraft. The best way of accomplishing this is to either extend the surface of the aircraft to meet the stores or to enclose the mounting racks within the aircraft so that the stores meet the surface. The primary emphasis to date has been on fuselage mounted arrangements, the advantages of which have been demonstrated in flight on at least the F-4 and F-15 aircraft in the United States. It seems probable that wing-mounted conformal arrangements could also be developed. To date, slipper tanks have been the only common example of this approach.

It should be remembered that the conformal carriage concept has other major advantages apart from drag reductions, eg it allows the use of bluff stores which would give unacceptable performance penalties if mounted on external carriers but which one may wish to use for the sake of their desirable release and trajectory characteristics and second, it allows the use of locations which may have a notable benefit on the aircraft stability, control and handling qualities. Concentrating the loadings closer to the aircraft rotational (stability) axes can improve the inertial qualities to the extent that an aircraft loaded with stores behaves comparably with an unloaded aircraft, the major difference in 'feel' to the pilot being merely that due to the greater vehicle weight. Various practical problems may however make conformal carriage difficult to engineer on some aircraft; these problems are however outside the scope of the present paper. The aim here is to highlight the performance benefits which show that conformal carriage can 'exploit favourable aerodynamic interference' to an outstanding extent.

9.1. F-4 Conformal Carriage Flight Demonstration (26)

Fig 15a shows the conformal carriage adaptor which was designed and fitted to the F-4 for the flight test programme (27). 49 positions were available for mounting ejector racks including 3 rows of 4 racks side-by-side for any given store loading. The fairing over these racks provided a clean, smooth installation on the undersurface of the fuselage. Tests were made with and without the forward fairing. Both flight and tunnel tests showed that the subsonic drag of the F-4 with the conformal adaptor was less than the drag of the clean aircraft. A similar result was obtained with the conformal fuel tank installation (28), 'Fast Pack', on the F-15, which is described in §9.2 below and shown in Fig 16. It would be easy to dismiss these as particular, coincidental results but in fact, it could be claimed that they show the usefulness of the conformal arrangements in improving the aerodynamic cleanliness of the overall configuration.

Some selected results from the flight test programme are shown in Figs 15b-e. For example, Figs 15b,c give an idea of the likely performance benefits of conformal carriage for 12 x Mk 82 bombs, ie a typical representative store load on the F-4 Phantom. It will be seen that at high altitude and Mach numbers in the range 0.7 - 0.8, the reduction in specific range for this store load is only about 6% with conformal carriage as compared with 20% with conventional carriage on a conventional TER/MER/TER arrangement. This also implies a major fuel saving for a given mission. Even without the stores, ie on the return flight, no extra fuel is needed to carry the empty conformal carrier as compared with 12% for carrying the empty standard carriers. The figures for the low altitude condition are also impressive: the reduction in specific range is 5% rather than 27% for the standard carriers and indeed, conformal carriage of the 12 Mk 82 stores can be accomplished at nearly the same cost as operating the F-4 with conventional carriers and no stores. Flying with the empty conformal adaptor at this altitude required 7% less fuel as compared with the clean F-4 (no pylon or carriers)! The conventional arrangement could not be flown for the acceleration flights but an estimated curve is shown for a conventional Mk 82 payload arrangement showing that the maximum performance would then be barely supersonic whereas the conformal carriage arrangement allowed operation at supersonic speeds over a wide range of altitude. Fig 15d shows the large expansion of the flight envelope.

Fig 15e shows the performance achieved with conformal carriage of 2 types of bluff stores: full details of the stores are given in Ref 4 but it is sufficient in the present paper merely to comment that this is another potential advantage of conformal carriage: it enables one to carry compact arrays of bluff stores which are likely to have superior store separation, trajectory and impact characteristics. To carry these stores in any other fashion would produce very large incremental drags. The tests with the arrays of bluff stores included an additional fairing installed on the forward ramp (Fig 15a) and store on, this improved the performance. In operational practice, however, it would be necessary to either retract, deflate or jettison the fairing after store release to avoid a significant drag penalty. Amongst the many conclusions that could be made from the results, one striking comparison worth quoting is that flying with a compact array of 9N bluff stores (ordnance almost 40% greater than 12 Mk 82) gives a specific range at low altitude greater than the clean F-4 up to a Mach number of 0.85.

The main conclusion (26) from the F-4 programme is that the performance advantages of conformal carriage were convincingly demonstrated in both flight tests and in supporting wind tunnel tests. Obviously, the precise quantitative results are a function of the aircraft design and it would not be possible on all aircraft to devise retrospectively arrangements that would give such large performance advantages. However, the results should provide the spur to design new aircraft with conformal carriage in mind from the outset.

9.2. F-15 Conformal Fast Pack Pallets

As a second example of conformal carriage, reference can be made to the prototype flight test programme (28) undertaken by McDonnell Douglas Corp, which showed that two fuel pallets mounted in the wing-fuselage junction of the F-15 as shown in Fig 16a could provide an additional 5808 litres fuel capacity without undue compromise to the air superiority capability of the basic aircraft. Each pallet, or tank, had a streamline shape designed with regard to the longitudinal cross-sectional area distribution of the complete aircraft-tank combination. Fig 16a also illustrates that the conformal pallet could be used not only for fuel storage but also to carry electronics, weapons or guns. Additional payload could be tangentially attached externally: Fig 16b shows that the addition of the pallets reduced the subsonic drag level and delayed the drag-rise; at supersonic speeds, it allowed the carriage of 5808 litres of fuel for a drag increment that was only about 40% and 65% respectively of the drag increments for 4828 litres carried

conventionally underwing or 6791 litres carried partly underwing and partly underfuselage: a major achievement fully justifying the suggestion that on new aircraft in the future, the aim should be to design with these radical ideas for store carriage in mind from the outset.

10. CONCLUDING REMARKS

The two main aims of this paper have been first to describe the nature of the major adverse and favourable aerodynamic interference encountered with external store installations and second, to present some examples of the improvements that should be feasible. The main conclusions are as follows:

1. With existing external store arrangements, the drag increments can be very large and the release characteristics can pose serious problems.
2. Research has already shown how major improvements could be achieved. Many of the proposals should be feasible even on existing aircraft. Larger improvements should be possible on new aircraft types provided the external store requirements are specified and borne in mind in the early phases of the design.
3. To obtain the full benefit from advanced wing design, the wings should be designed with due regard to store carriage. In particular, the wing/underwing pylons should be considered together. If this is done, it should be possible to alleviate adverse interference at low C_L and to achieve some favourable interference on the flow breakdown at high C_L at moderate and high subsonic speeds.
4. Research should be undertaken to exploit further the favourable interference possibilities of wing tip carriage of slender missiles.
5. New multiple carriers and underfuselage arrays of stores should aim to exploit the concepts of tandem carriage and store stagger and should avoid very close lateral spacing of the stores.
6. For new aircraft, the complete configuration should be designed as an entity with due regard to its longitudinal cross-sectional area distribution and with the stores mounted either in conformal packages or from conformal pallets.

Research to date notably in the UK on multiple carriers and in the US on conformal carriage has pointed the way. The theoretical methods now being developed and which form the subject of other papers at this conference will provide the means. It is hoped that this paper will have helped to stiffen the resolve to develop new radical approaches to store carriage.

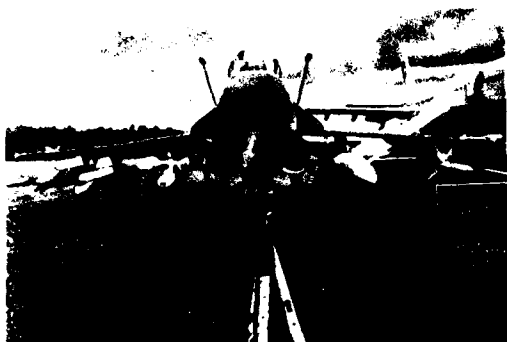
11. ACKNOWLEDGEMENTS

The author wishes to thank MOD(PE) and RAE for permission to use some of the material contained in this paper. Most of the results of tests in the ARA transonic tunnel quoted in the paper were obtained in research funded under MOD(PE) research contracts. Further, the author acknowledges the help of various colleagues at RAE and ARA while preparing this paper, in particular, Mr D H Peckham and Mr D E Treadgold of RAE and Mr J B Berry, Mr P G Hutton and Mrs I Capps of ARA. Finally, parts of the paper are based directly on Chapter 2 of the AGARD FDP Working Party Report on 'Drag and Other Aerodynamic Effects of External Stores', for which Mr J H Nichols Jr of DTNSRDC and the present author were joint editors.

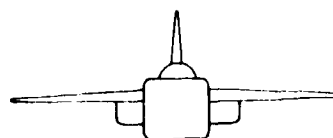
REFERENCES

1. Pugh P G. Store carriage and release - the raison d'être of the military aircraft: a personal view. 1979. Lecture given at RAeS. To be published in Journal RAeS.
2. Haines A B. The reduction of the installed drag of multiple store carriers. 1975. Paper no 7, JTCC Aircraft/Stores Compatibility Symposium Proceedings, Arlington.
3. Evaluation of the conformal carriage concept on the performance and basic static longitudinal stability of the F-4E aircraft. 1971. AFATL-TR-71-76.
4. Drag and other aerodynamic effects of external stores. 1977. AGARD-AR-107.
5. Haines A B. Drag of external stores: present standards and possibilities for reduction. 1975. ARA Report 40.
6. Whorric J M. Effect of various external stores on the static longitudinal stability, longitudinal control, and drag characteristics of the model F-4C airplane. 1973. AEDC-TR-73-186.
7. Berry J B, Stanniland D R, Haines A B. The implications of wing/store interference on wing design. Unpublished ARA communication.
8. Day J, Berry J B. Measurements of the incremental drag due to various combinations of Mk 10 1000 lb bombs installed on the Z.29/2 combat aircraft wing research model. Unpublished ARA communication.
9. Berry J B, Hutton P G, Haines A B. The drag of external stores. An analysis of some experimental data and a proposed framework for the prediction of installed drag increments. 1969. ARA Report 11.
10. Ottensooser J. Some effects of longitudinal and vertical store position variation on a 0.10 scale F-8 aircraft model. 1968. NSRDC Test Report AL-46.
11. Berry J B. Pressure plotting and drag measurements on store-pylon installations on a swept wing half model. 1978. ARA Report 47.
12. Marshall J C, Summers W E. An analysis of the relative importance of parameters required for the simulation of store separation trajectories. 1971. Aircraft/Stores Compatibility Symposium Proceedings, Vol 2, Dayton, Ohio.
13. Davis R E. Flow field characteristics beneath the F-4C aircraft at Mach numbers 0.5 and 0.85. 1970. AEDC-TR-70-8.
14. Silvers H N, King T J Jr. Investigation at high subsonic speeds of bodies mounted from the wing of an unswept-wing-fuselage model. 1952. NASA RM L52J08.
15. Bucciantini G. Private communication. 1975.
16. Hoerner J F. Fluid-Dynamic drag. New York. Published by the author. 1965.
17. Lee P. Drag measurements at transonic speeds of individual stores within multiple store arrangements. Unpublished RAE Memo.

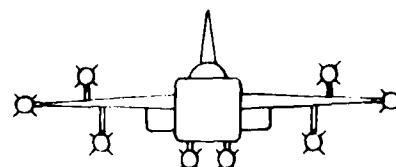
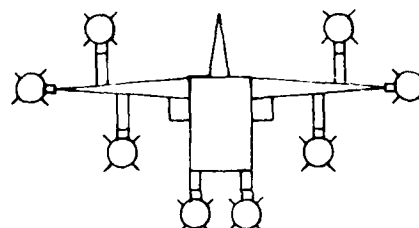
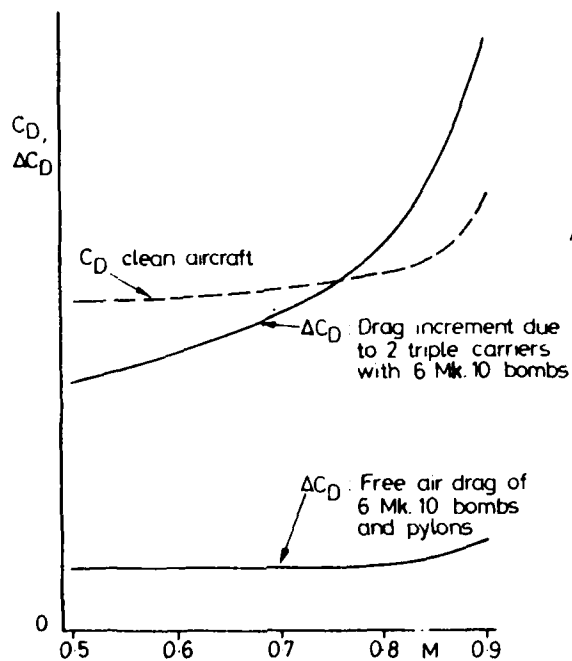
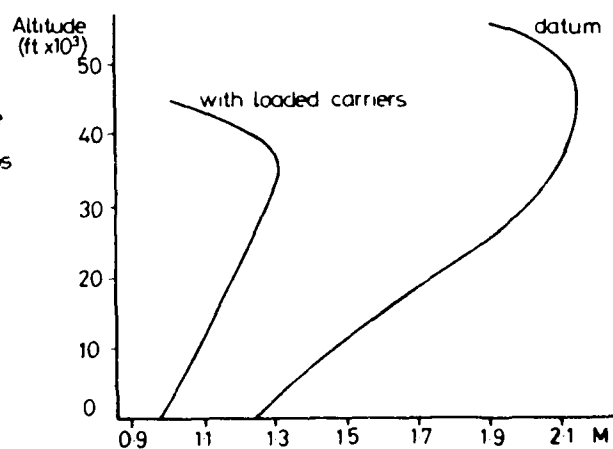
18. Analysis of high speed wind tunnel tests on single and multiple carriage bomb racks. 1966. Douglas Aircraft Co Inc Report No LB-32647.
19. Pugh P G, Hutton P G. Aerodynamic drag. 1973. AGARD CP 124. Paper no 19.
20. Jordan R. Measurement of close interference forces between bombs on a twin carrier during simulated release. Effects of stagger and bomb incidence. Vol 1: Free and captive bomb loads. Vol 2: Pressure distributions on twin carrier. Unpublished ARA note.
21. Ottersosser J. Drag effects of various methods of carrying fuselage mounted stores. 1968. NSRDC Aero Report 1150.
22. Schindel O H. Store Separation. 1975. AGARDograph 202.
23. Pugh P G. Private communication.
24. Gough M N, Carlson D R. Advanced weapons carriage concepts through integrated design. 1979. AIAA paper 79-0092.
25. Furey R J, Martin C J. A study of captive flight drag and separation characteristics of lifting body (half-bomb and half-pod) store configurations. 1970. AGARD CP 71.
26. Nichols J H Jr, Martin C J. Conformal weapons carriage - joint service development program. 1971. DTNSRDC Rpt 4027 AL-1188.
27. Nichols J H Jr. The conformal carriage joint service development program. 1973. JTCG Aircraft/Stores Compatibility Symposium, Sacramento.
28. F-15 weapon/fuel carriage improvements with Fast Pack conformal pallets. 1975. McDonnell Douglas Report MDC A 3507.

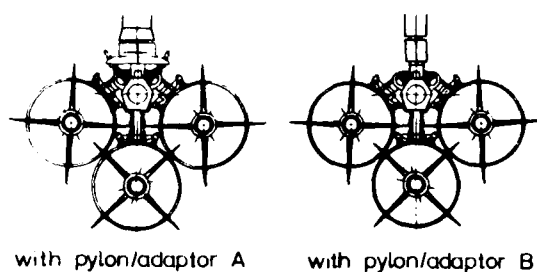
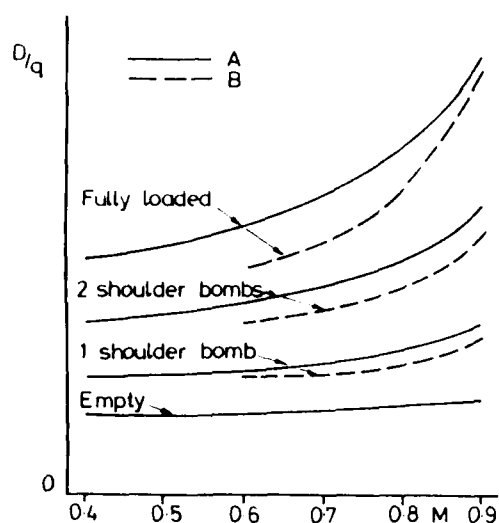


a. MULTIPLE STORE LOADS



clean aircraft

with weapons
geometric viewwith weapons
aerodynamic drag viewb. THREE VIEWS OF AN AIRCRAFT
(From Pugh)c. ΔC_D FOR MULTIPLE UNDERWING
INSTALLATIONS
(From ARA complete model tests)d. EFFECT OF LOADED MULTIPLE CARRIERS
ON PERFORMANCE ENVELOPE OF F-4E
(based on AEDC 1/20 scale model tests)FIG. 1 MULTIPLE CARRIAGE OF EXTERNAL STORES
FERTILE GROUND FOR MAJOR AERODYNAMIC INTERFERENCE



a. INTERFERENCE WITHIN STANDARD TRIPLE CARRIER.
(Mk 10 1000lb bombs)



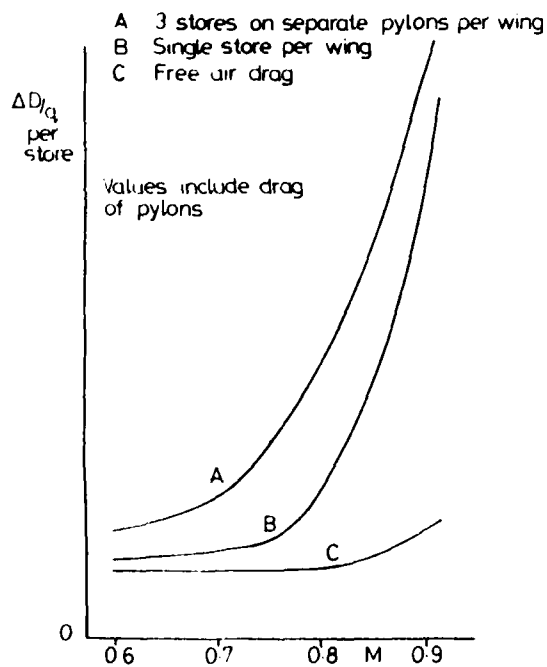
SIDE VIEW



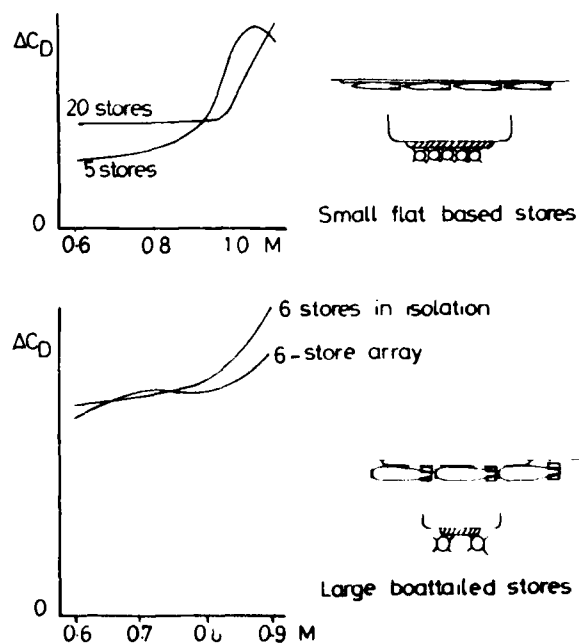
VIEW WITH BOTTOM BOMB REMOVED



OIL FLOW AT M=0.75 WITH A



b. ADVERSE INTERFERENCE UNDERWING



c. FAVOURABLE INTERFERENCE UNDERFUSELAGE

FIG. 2 EXAMPLES OF FAVOURABLE AND ADVERSE INTERFERENCE

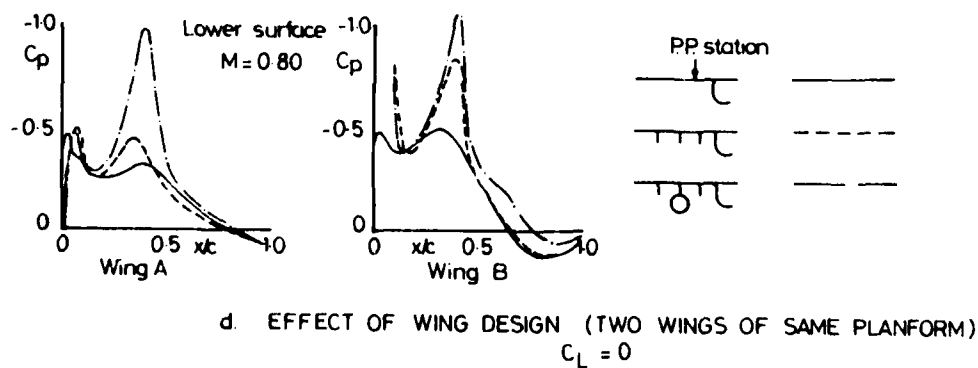
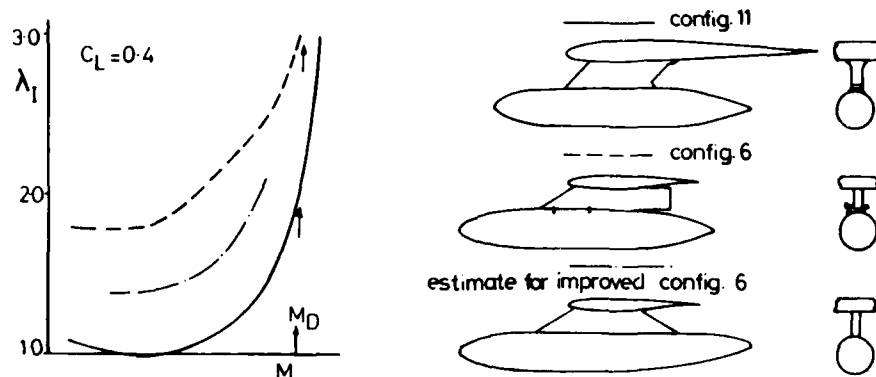
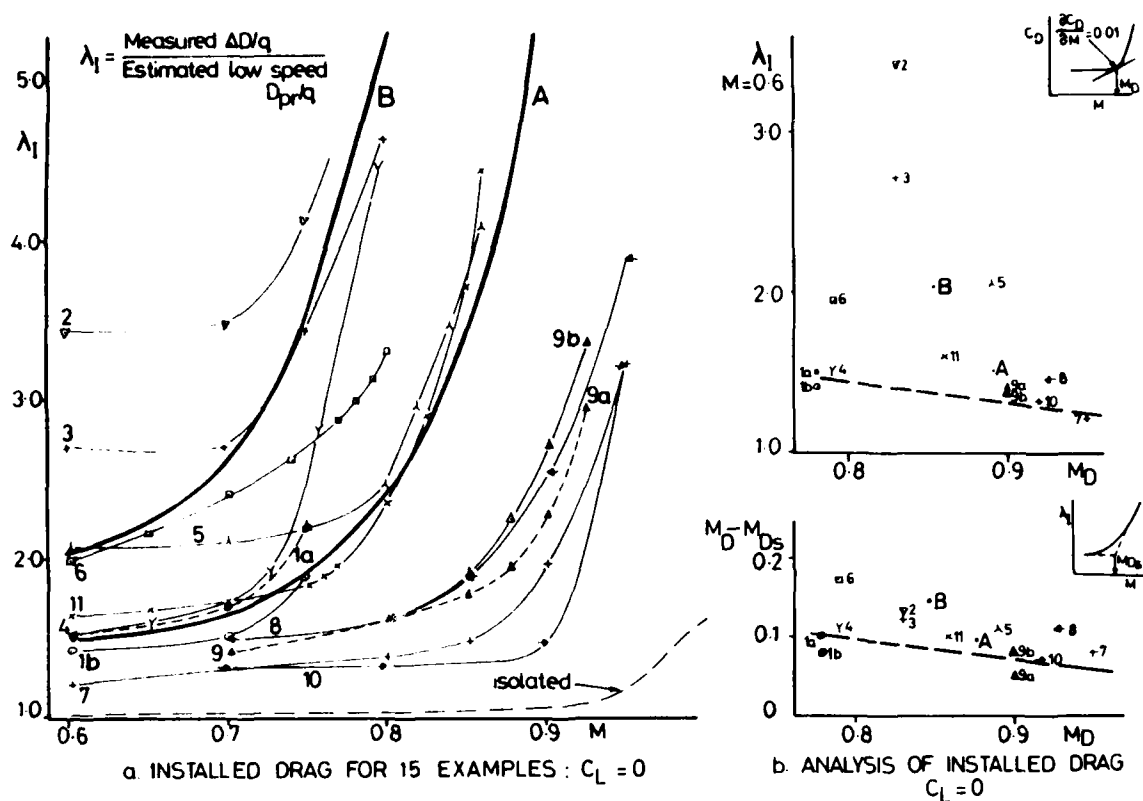
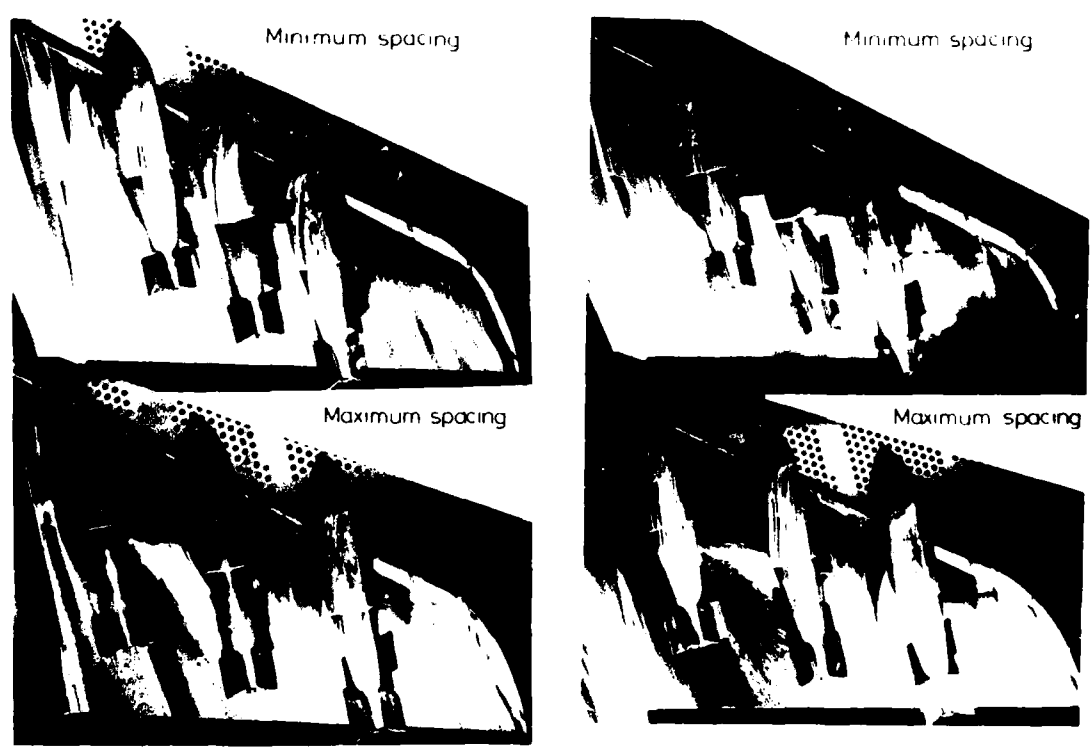
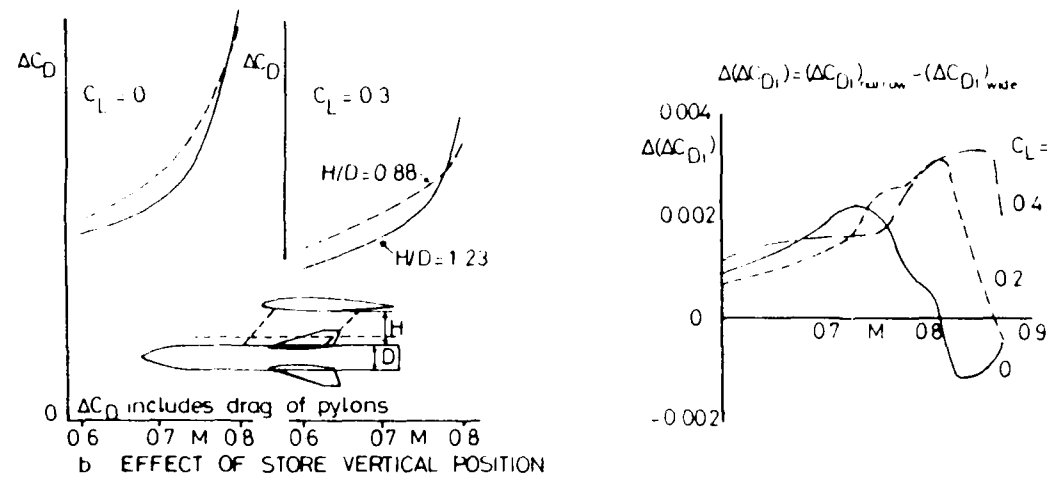
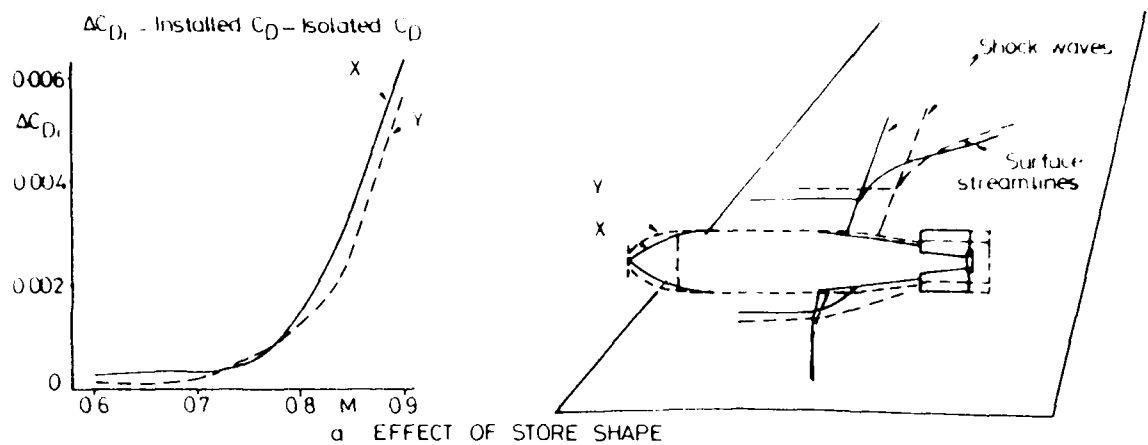


FIG. 3 EFFECT OF UNDERWING TANKS



c EFFECT OF LATERAL SPACING (3 STORES ON SEPARATE PYLONS)

FIG 4 EFFECT OF UNDERWING STORES AT LOW C_L

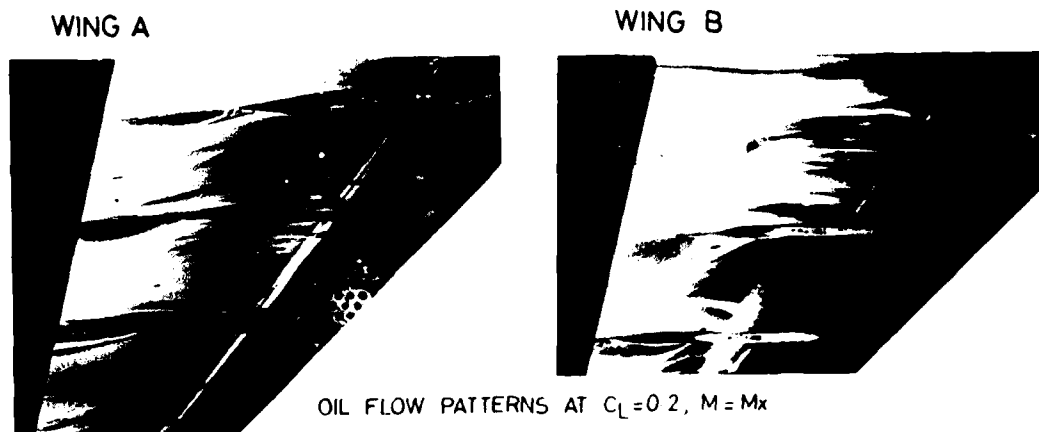
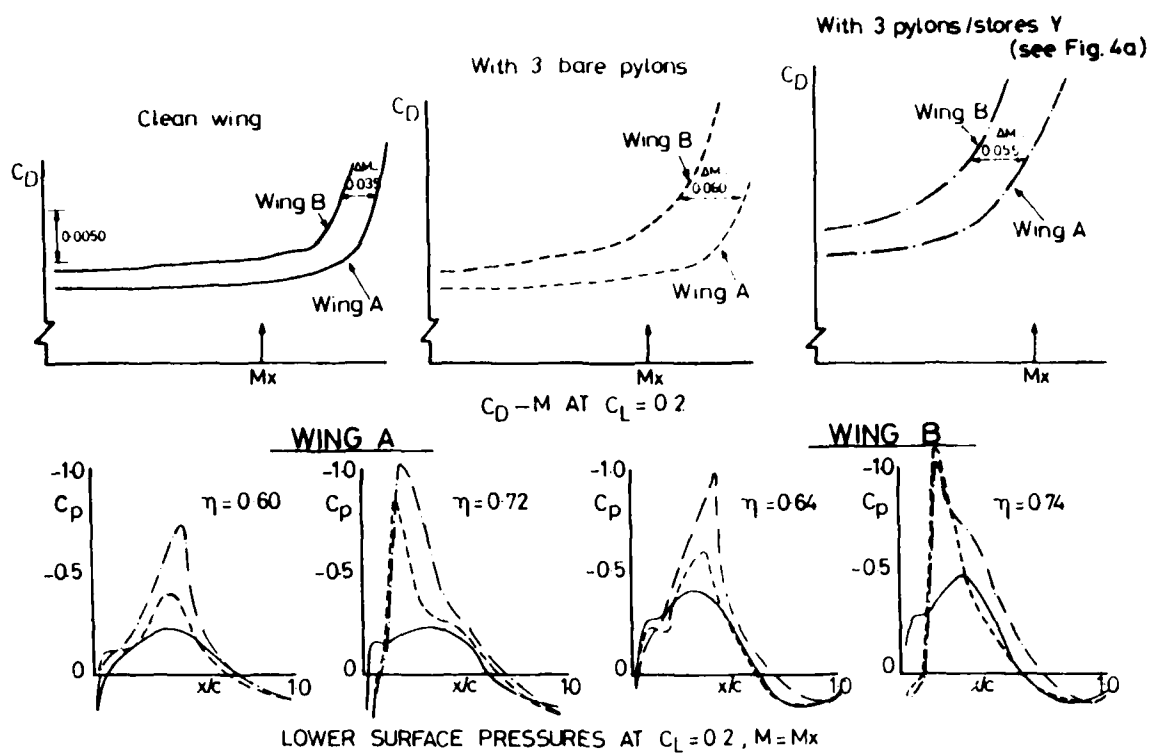
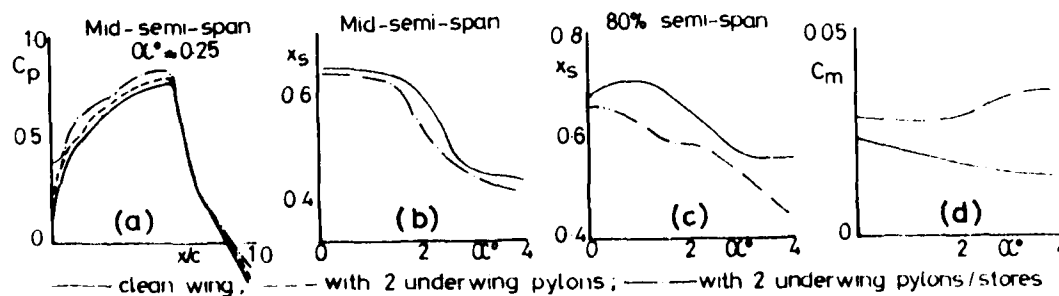
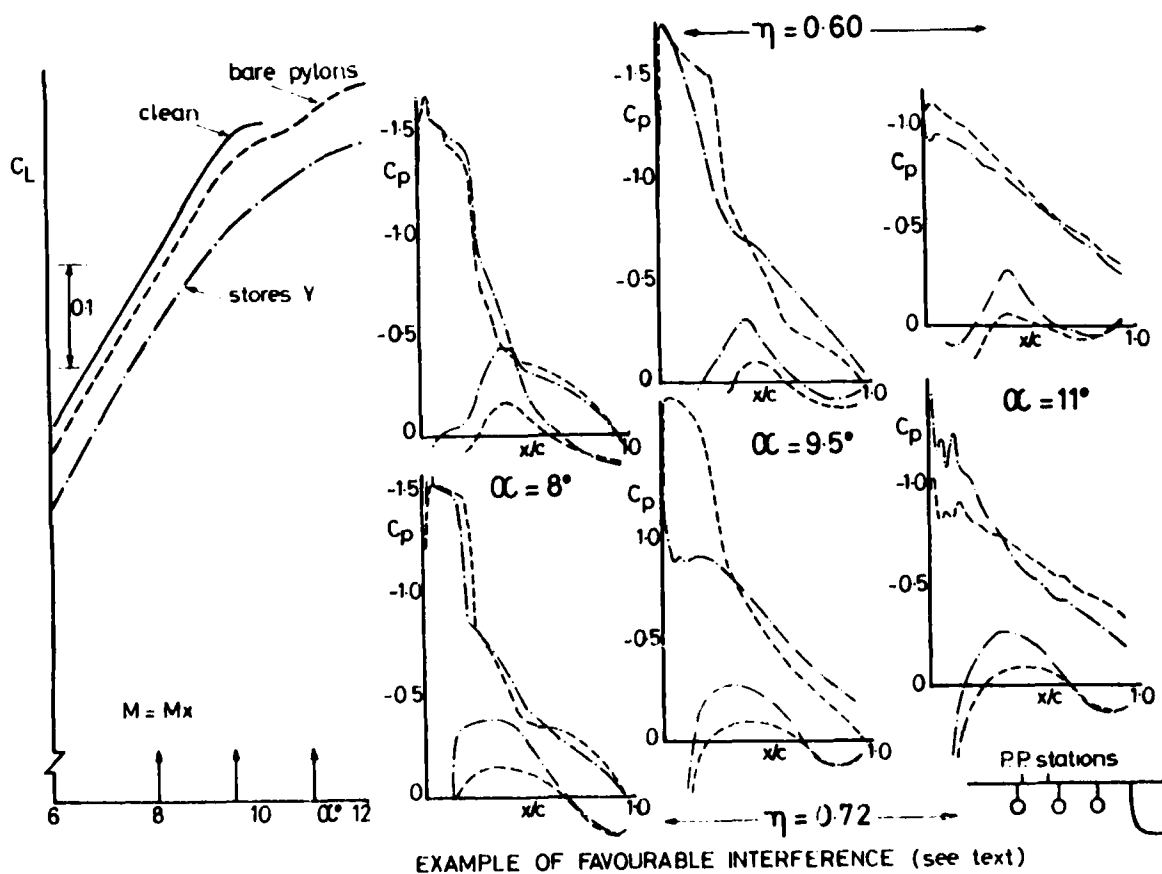
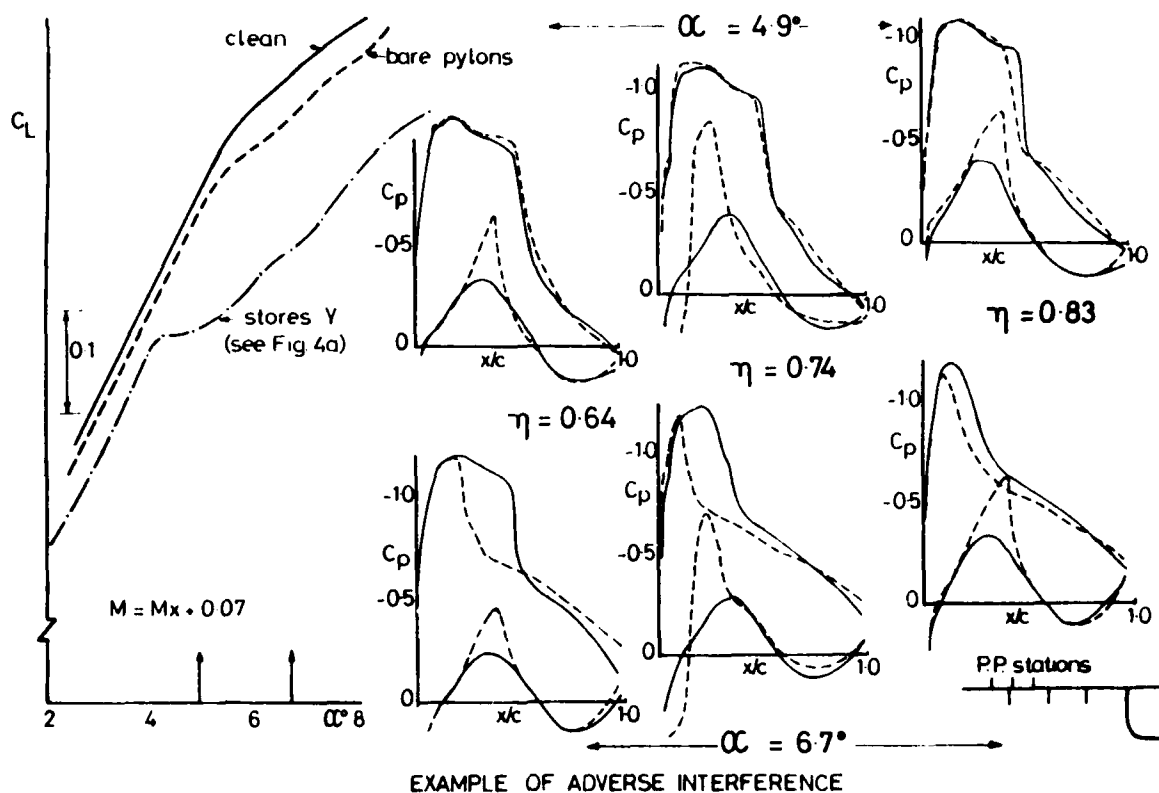
FIG.5 INFLUENCES OF WING DESIGN ON UNDERWING STORES/PYLONS AT LOW C_L 

FIG.6 EFFECT OF UNDERWING STORES ON UPPER SURFACE FLOW

FIG. 7 EFFECT OF UNDERWING STORES AT HIGH C_L

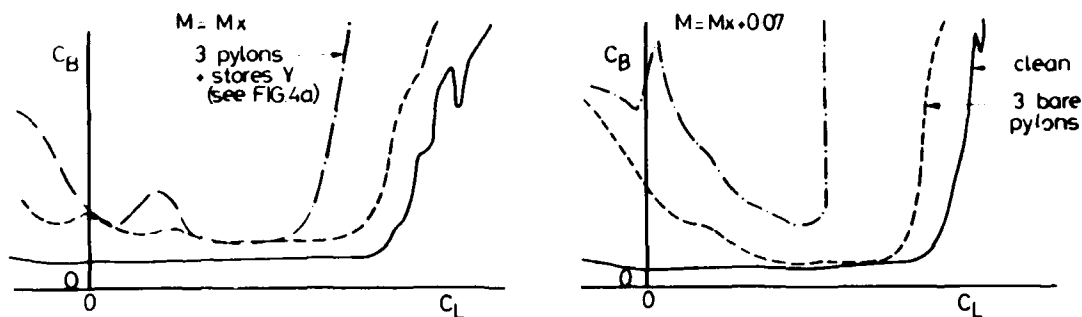


FIG. 8 EFFECT OF UNDERWING STORES ON BUFFET

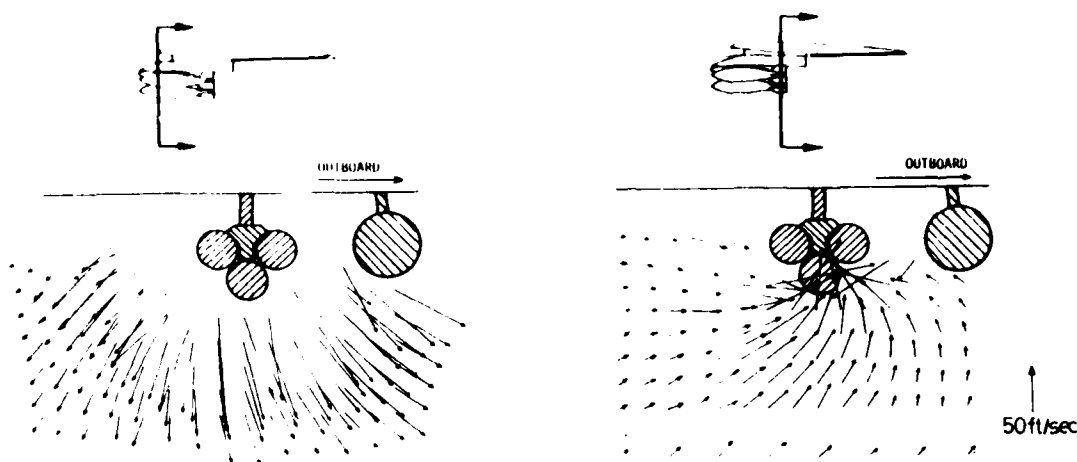
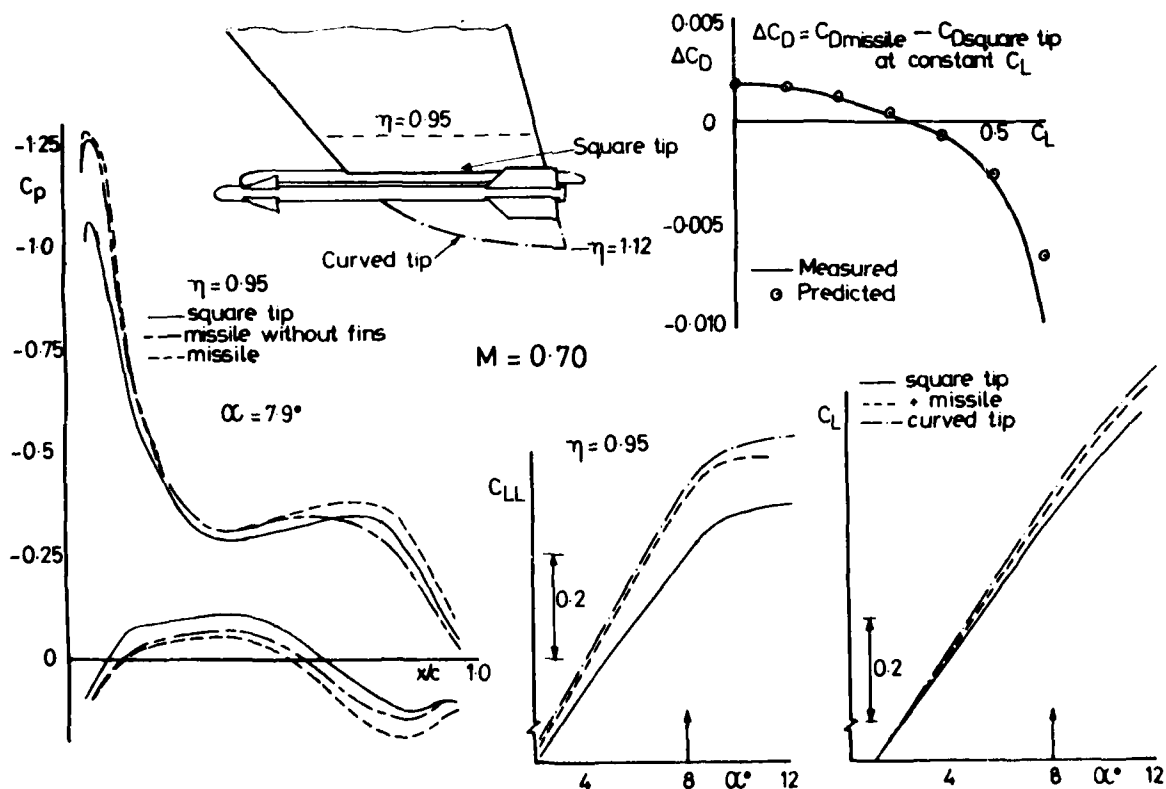
FIG. 9 EFFECT OF UNDERWING STORES ON FLOW FIELD: F-4 AT $M=0.85$ 

FIG. 10 EFFECT OF WING TIP-MOUNTED STORES

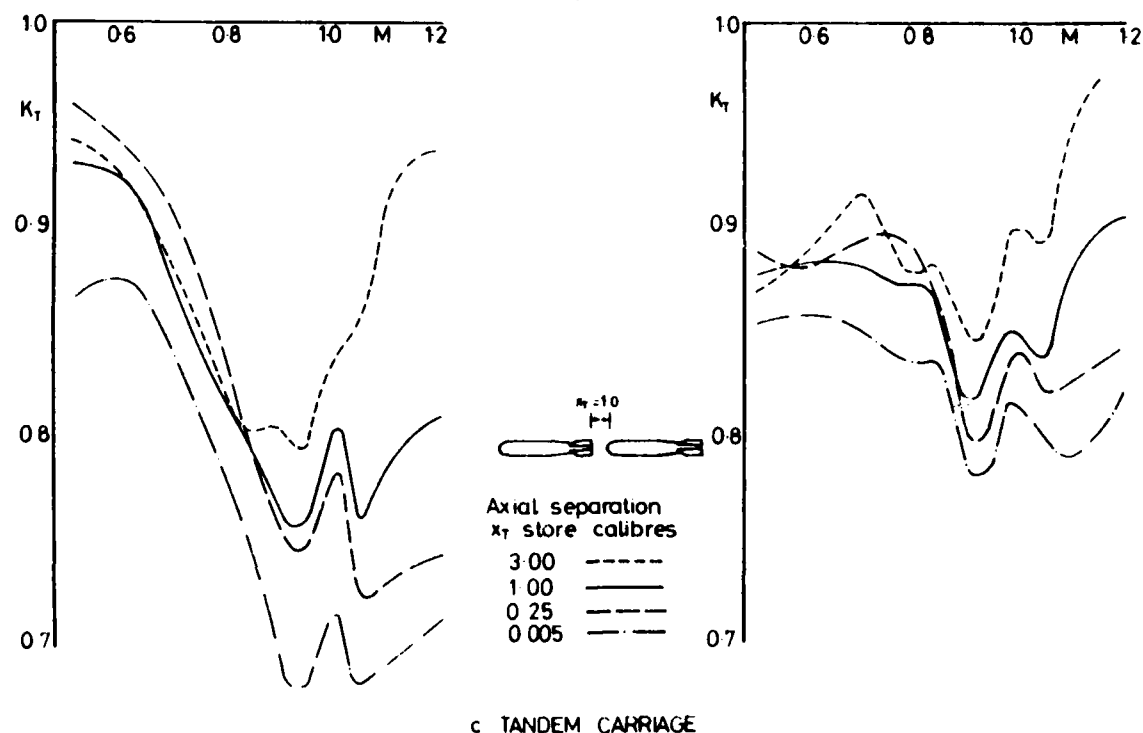
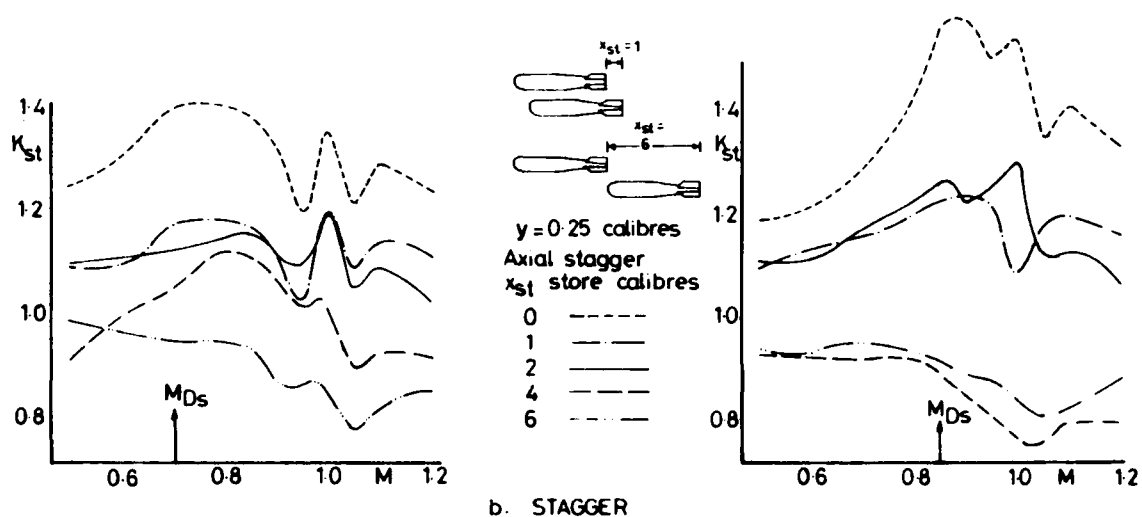
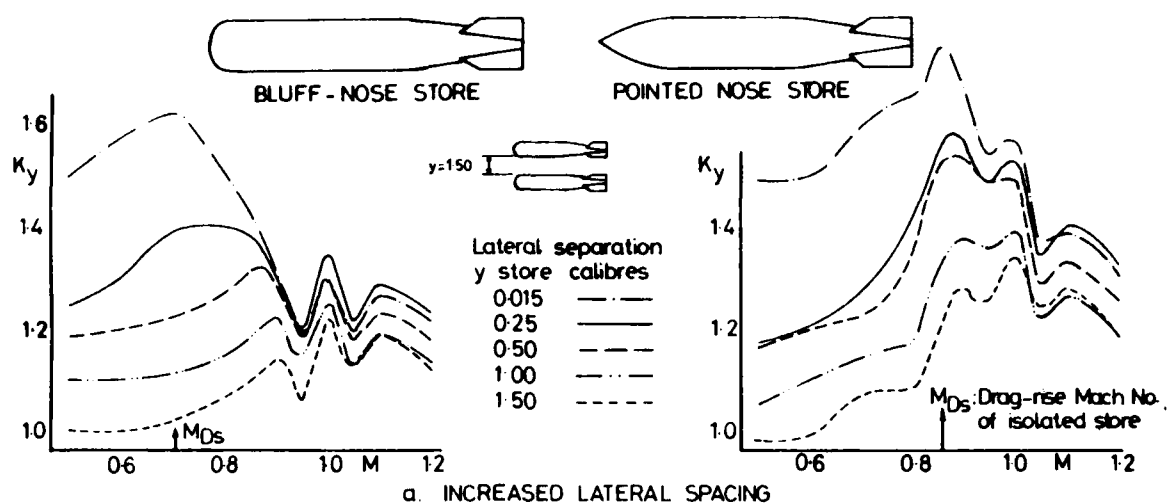


FIG. 11 FAVOURABLE INTERFERENCE CONCEPTS

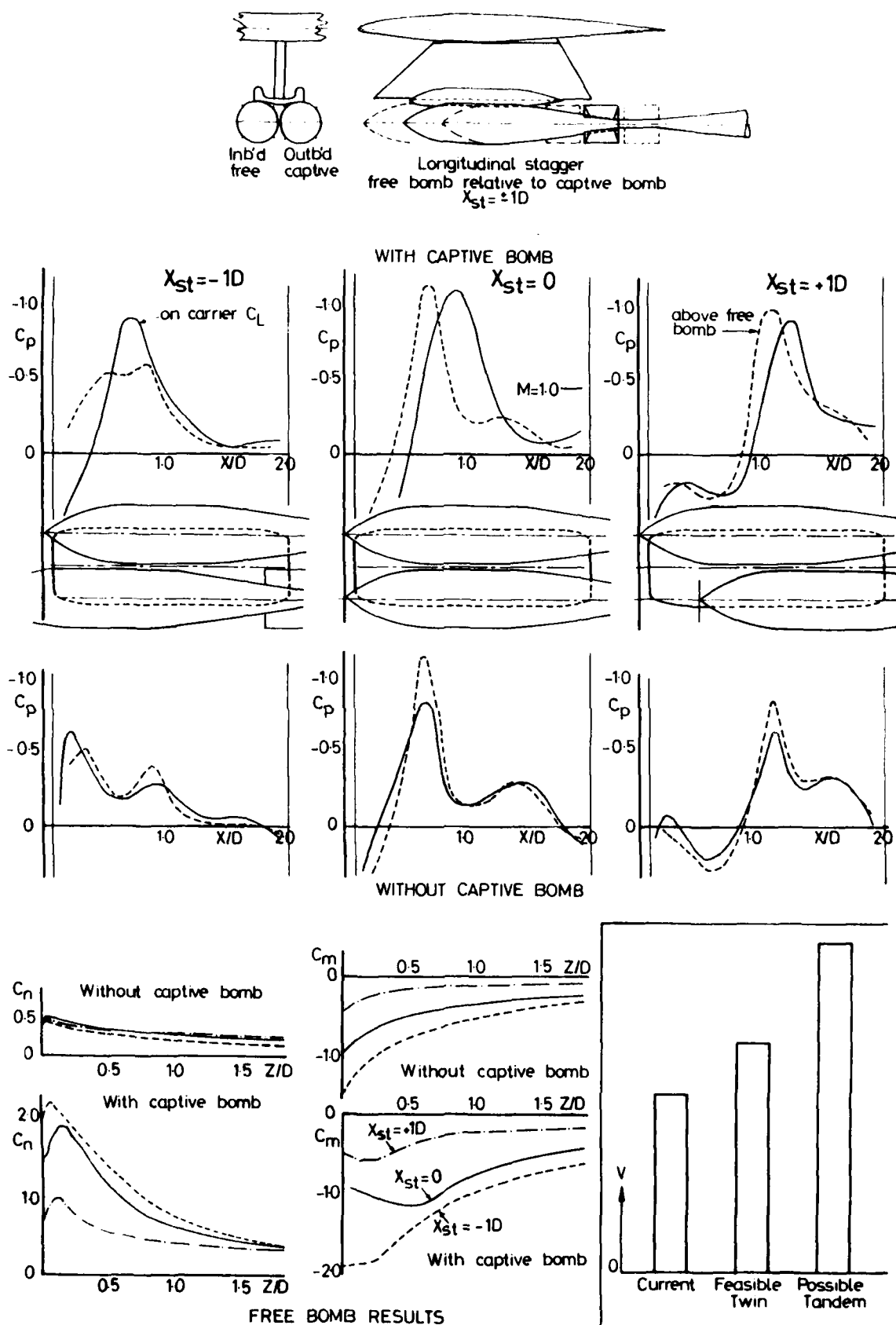


FIG. 12 EFFECT OF STAGGER ON STORE RELEASE LOADS FROM TWIN CARRIER : $M=0.80$

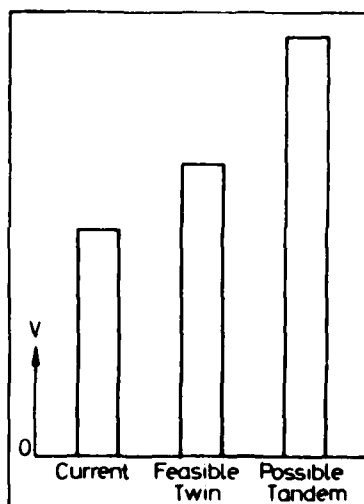


FIG. 13 RELEASE SPEEDS : F-4

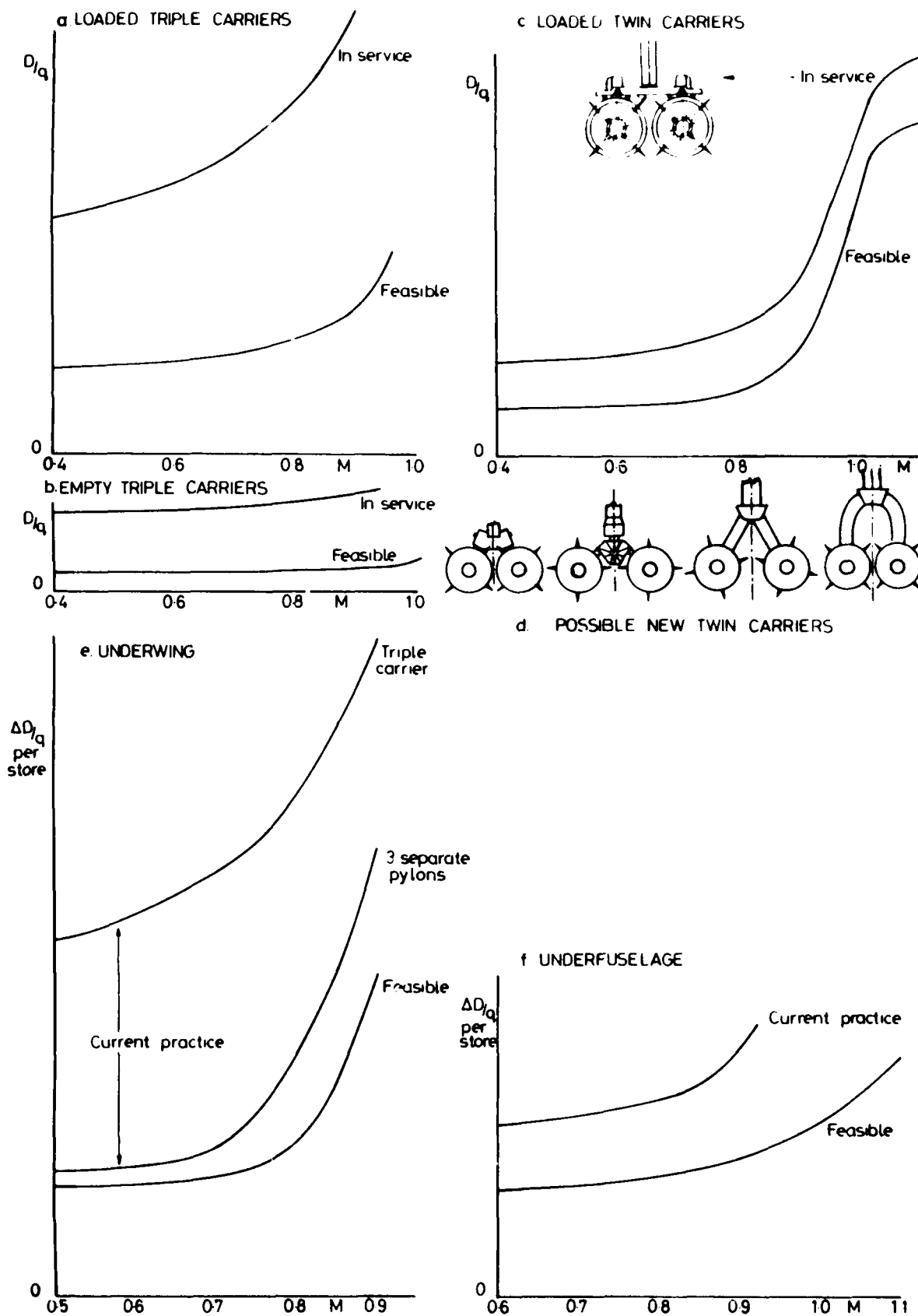
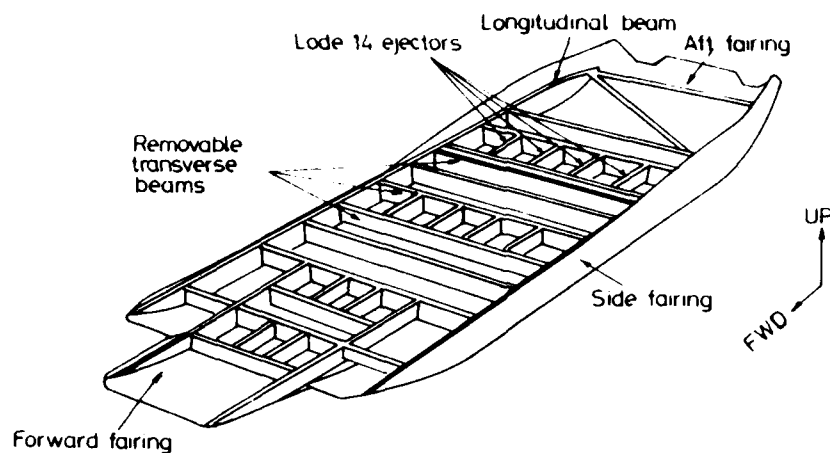
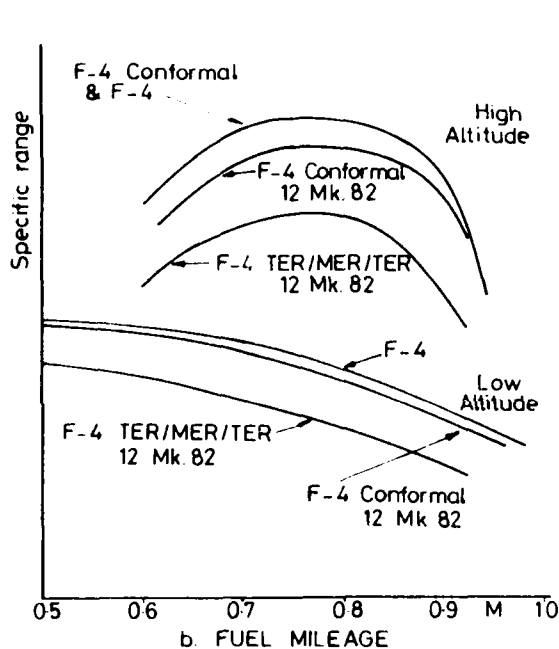


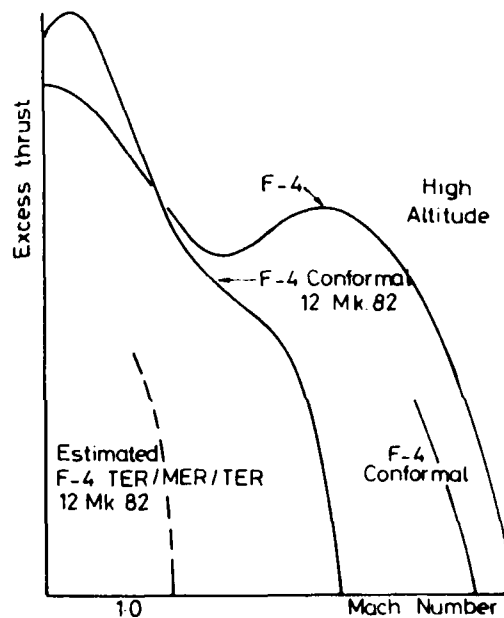
FIG. 14 FEASIBLE DRAG IMPROVEMENT: U.K. RESEARCH



a F-4 CONFORMAL CARRIAGE ADAPTOR

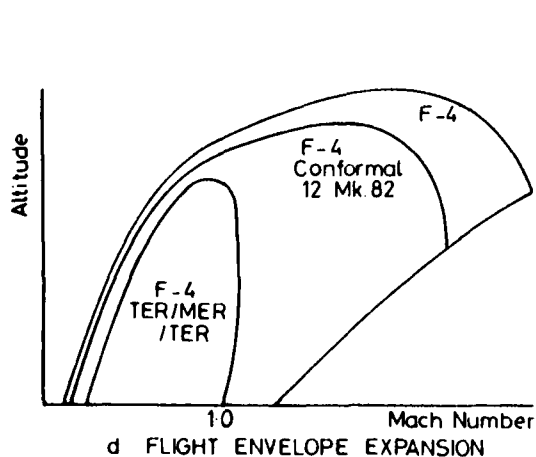


b. FUEL MILEAGE

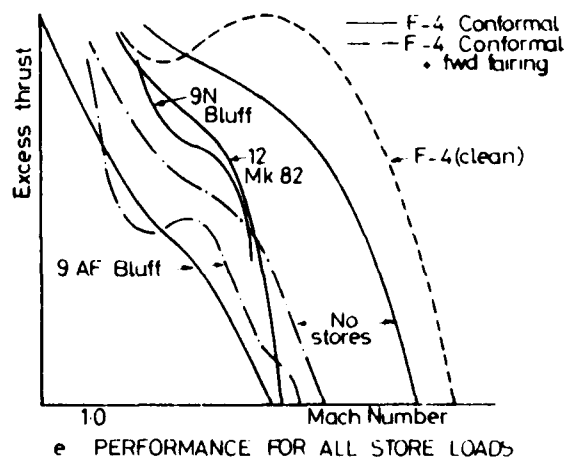


c ACCELERATION

CARRIAGE OF 12 MK. 82 STORES

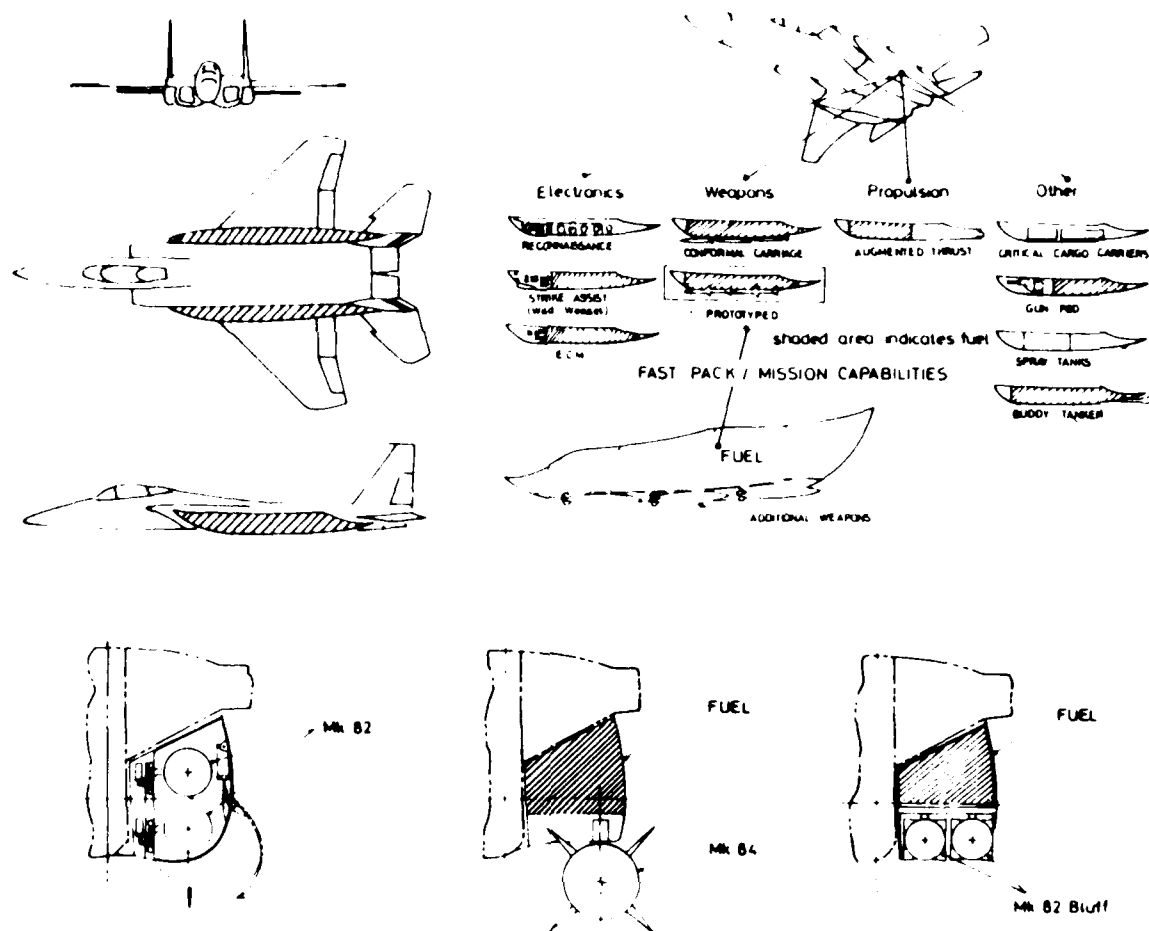


d FLIGHT ENVELOPE EXPANSION

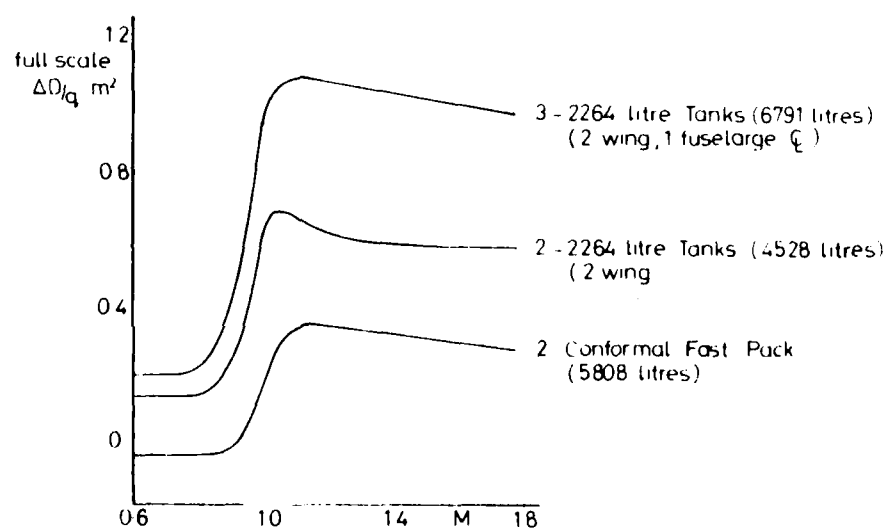


e PERFORMANCE FOR ALL STORE LOADS

FIG 15 F-4 CONFORMAL CARRIAGE



a POSSIBLE FUEL/STORE ARRANGEMENTS



b TYPICAL REDUCTIONS IN DRAG INCREMENT

FIG.16 F15 - CONFORMAL CARRIAGE STUDY

EVALUATION OF AIRCRAFT INTERFERENCE EFFECTS ON EXTERNAL STORES AT SUBSONIC AND TRANSONIC SPEEDS

by

RONALD DESLANDES
MBB Unternehmensbereich Flugzeuge
8000 München 80 - Germany

SUMMARY

To analyse the separation behaviour of external stores from a combat aircraft, the store loads must be evaluated at all times after release. The resulting forces and moments are highly unsteady and depend upon:

- the non-uniform flowfield around the aircraft
- the store motion itself.

The exact evaluation of unsteady aerodynamics of such complicated configurations is nearly impossible, due to the required

- computer capacity
- cost effectiveness

Simplifying assumptions lead to the quasilinearization of the time dependence to omit unsteady calculations and to the use of the flow angularity technique to minimize computational time.

The MBB-Store Separation Programme System *) will be presented as a possible solution. The mixed experimental analytical approach realized here is not restricted by compressibility effects, but will be mainly described at subsonic flows. However the transonic and supersonic extensions will be mentioned, as well as the application of the programme system to realistic combat aircraft missions under realistic conditions, such as

- jettison at high q manoeuvre
- multiple jettison
- rail- and drop-launch of missiles

NOTATION

ALFAF ($^{\circ}$)	aircraft angle of attack
AC	Subscript for: aircraft
BETA ($^{\circ}$)	Sideslip angle
C_N	Store normal force coefficient
C_x, C_y, C_z	Store force coefficients
C_l, C_m, C_n	Store moment coefficients
CPU	Central-processor-unit (Times on IBM 370/3033)
CTS	Captive Trajectory System
EDP	Electronic Data Processing
q (m/s^2)	acceleration of gravity
l (m)	Store length
M, Ma	Mach number
n_z	Load factor w.r.t. the z-direction
S	Subscript for: store
S_1, \dots, S_n	Store sections
t (sec)	time
Δt (sec)	time-step or interval
U (m/s)	free stream velocity
$U_{flow, local}$ (m/s)	local velocity vector in a flowfield
U_{store} (m/s)	velocity of the store
$U_{store, local}$ (m/s)	resultant velocity of a store section
X, Y, Z	cartesian coordinates
α ($^{\circ}$)	angle of attack
β ($^{\circ}$)	angle of sideslip
η_T ($^{\circ}$)	Tailplane setting
ω_y (1/s)	rotation velocity w.r.t. to the y-axis

*) The MBB-SSP-System has been sponsored by the FRG Ministry of Defense, Department RüFo 4.

1. INTRODUCTION

The missions of the today's fighter aircraft generation are inconceivable without an external store equipment.

Such a configuration is shown in Fig. 1, pointing out two major areas of the external-store-aerodynamics:

- the carriage flight configuration,
- store separation from the aircraft.

Range of Tasks of Store Configurations



Store carriage

- drag and stability of the complete configuration
- stress due to the steady installed loads

Store release

- unsteady loads (including steady loads) at any time during the trajectory

Fig. 1

The topics of investigation of weapon carriage are the determination of overall drag- and stability changes of the complete configuration, so that the real flight performances can be assessed. Great importance also lays in recording the steady loads on the installed stores to ensure optimal design of the local airframe strength.

The second area deals exclusively with the overall store aerodynamics in the vicinity of the aircraft. In this case store loads have to be accurately evaluated, including all unsteady effects occurring between the installed and free falling store positions.

Since all problems of the evaluation of loads on external stores appear here, the following will primarily deal with the release situation.

Fig. 2 therefore gives an overview of all possible release conditions for several stores under different aspects of manoeuvring flight. In addition to the simple case of steady interference between the aircraft and the store, other coupling effects must be taken into account, such as:

Release Conditions

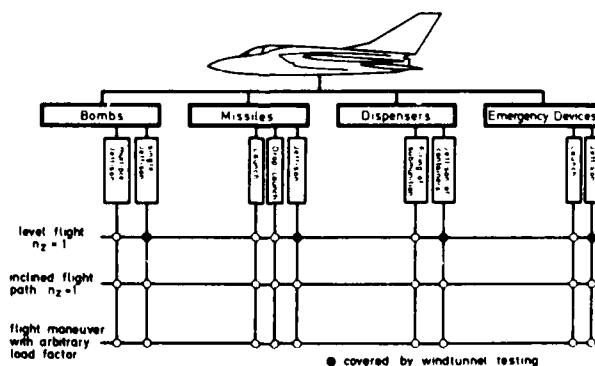
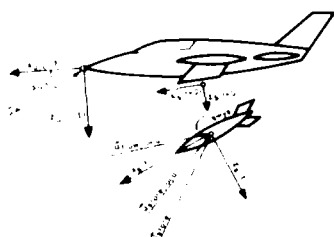


Fig. 2

- unsteady interference between several stores in the case of a multiple jettison
- dynamic interferences due to the relative motion between store and aircraft at flight manoeuvres.

Aerodynamic Task to Evaluate the Loads on a Released Store



Description of

- 1st Order Effects due to A/C interference
- 2nd Order Effects due to store release and A/C maneuver motions
- 3rd Order Effects due to store-store interference (1st + 2nd order of adjacent stores during multiple jettison)
- Higher Order Effects due to store-A/C interference

Fig. 3

Looking at wind tunnel drop tests, it is obvious that only straight and level flight parameters can be realized, because there is only one available flow direction. This fact justifies the development even of complicated theoretical procedures to match all the remaining release conditions.

So the evaluation of loads on the external store can be formulated as the aerodynamic coupling of four main effects, shown on fig. 3 and consisting in:

- first order effects: standing for the steady interference of the aircraft on the air flow around the store
- second order effects: due to store motion and aircraft motion effects on the store effective angles of attack and sideslip, including store and aircraft rotations during release and maneuvering with arbitrary load-factors.
- third order effects: occurring only during multiple jettison and consisting in first and second order effects of adjacent stores in motion.
- finally higher order effects: or the disturbance on the store caused by aircraft components close to this store and induced by the reciprocal interference of the store on these components.

2. EVALUATION OF INTERFERENCE EFFECTS ON A RELEASED STORE

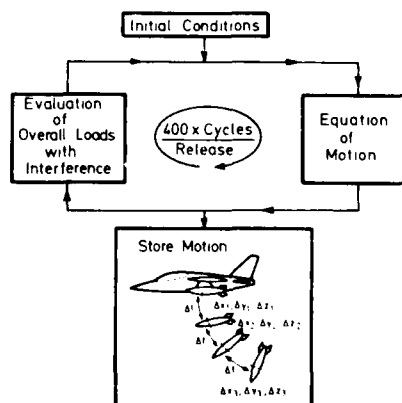
A typical design concept used to evaluate these interference effects is shown in fig. 4.

It generally consists in a large do-loop which combines two main partial tasks:

- the interference evaluation by fluid dynamics and aerodynamics
- and the resulting store motion by flight mechanics.

During one release calculation about 400 do-loop runs must be performed, whereby interference is calculated in 400 different quasi-steady positions of the aircraft and the external store.

Typical Programme Design Concept



Time-Dependant-Quasilinearisation-Boundary

$$\Delta t_{\max} (\text{cycle}) \leq \frac{\text{store length}}{|\text{store velocity}|} (\text{sec})$$

Fig. 4

2.1 Quasi-linearisation of time

This quasi-steady approach is only valid if the load alternation on the external store, during release, occurs slowly enough to be neglected. In this case it is reliable to operate with variable time steps which are calculated by deviding the store length by its velocity. These intervals can be interpreted as the time taken by an air particle to pass the external store. If those steps are too long, store motion and consequently also interference evaluation will be completely misrepresented.

This effect is shown in fig. 5, where the store inclination has been plotted versus flight time. The dashed line indicates the range in which the time intervals were set too large, the solid lines those where Δt is small enough for the quasi-linearisation. Curve (1) shows, in the dashed part, much higher inclinations as curve (2). Thus the store, due to high drag at high incidences, is considerably decelerated along this dashed part of (1). At about 2.5 sec the velocity has decreased enough to match the quasi-linear condition with the initial value of Δt . Now the high pitch amplitude rapidly decreases to normal values and the store motion becomes stable. Interference evaluation, flying time and ground-impact-point differ completely from the results plotted for curve (2). In that case Δt was correctly chosen to match the quasi-linear-condition at any time of trajectory. With shorter time steps the results remain stable.

It is obvious that the use of variable time steps has one further advantage. This method of quasilinearization, always operates with an optimum time interval, and thus saves CPU time by reducing the do-loop-runs during the release calculations.

Effect of Time-Step
on the Interference Loads

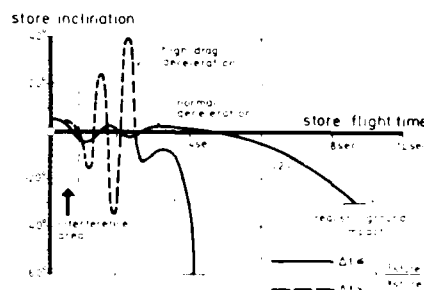


Fig. 5

2.2 Interference Concepts

Ideal Interference Evaluation Concept



Description
of: all interference effects

Basic Assumptions:
quasi-steady motions during
a time-step of
 $\Delta t = \frac{L_{store}}{V_{store}}$

optimistic estimated
CPU-time 2 min per cycle
(on IBM 370/3033) 800 min per release

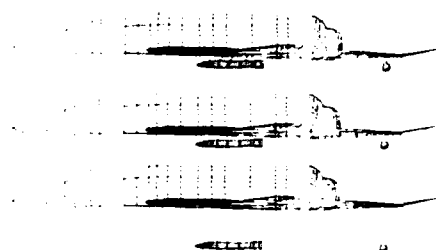
Fig. 6

As seen before, each loop-cycle during a trajectory computation implicates an absolutely new interference situation between the aircraft and the released store. Assuming a quasi-steady motion of aircraft and store, an idealised concept to evaluate interference is presented in fig. 6.

It should work on the basis on the potential theory, taking into account all compressibility effects. Estimating a high optimistic value of 2 min CPU for each complete solution, one release calculation would take a total of 800 min. CPU. Even the use of much faster computers would make no difference to the fact, that such solutions in closed form are absurd and must give way to simplified methods.

Such a concept is shown in fig. 7. The basic simplification consists in assuming that second and third order interference effects can be neglected, and that the total interference (first + higher order) is only a local function, which decreases with growing of the relative distance between store and aircraft. Interference is once calculated at four different positions of the aircraft and the store, using potential panel methods, e.g. Ref. (1), Ref (2) or Ref. (3). The resulting store-coefficients are fed to the programme as initial conditions, providing a linear decrease between two different store positions. Since only a single flow direction can be simulated, all effects of second and third order have to be neglected. This means that trajectories generated with this concept, are only acceptable as long as the ejector accelerations during release were low and the store subsequently moved slowly and with smooth or nearly no rotation. This method, used at MBB in 1974, displayed one great advantage: low CPU-time to compute a trajectory.

Basic Interference-Concept



DESCRIPTION OF:

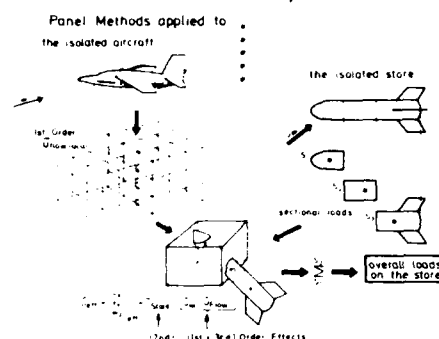
- first order effects due to A/C-interference
- higher order effects due to store-A/C-interference

BASIC ASSUMPTIONS

- interference is a local function and decreases linearly
- motion-effects can be neglected

Fig. 7

Current Interference Concept (MBB-SSP)



Basic Assumptions

- higher order effects can be neglected
- quasi-steady motions of stores and aircraft for $\Delta t = \frac{L_{store}}{V_{store}}$

Fig. 8

The current interference concept is based on the flow angularity technique, quite familiar to those methods described by Korn (Ref. 4), Grosse/Bristow (Ref. 5) and Fernandes (Ref. 6). The so-called MBB Store Separation Programme System (MBB-SSP) specially utilizes data derived from modern potential theory.

First of all, two preliminary computations are separately performed, in order to evaluate the external flowfield around the aircraft and to predict the isolated external store aerodynamics.

Aircraft Flowfield:

In the first run the surface of the aircraft is subdivided into several two-dimensional elements, having each a constant singularity distribution. The disturbance potential of the aircraft is then evaluated to fulfill the kinematic flow condition (no flow through the surface) on each of these so-called panels. The disturbance potential and the potential of the undisturbed flow are summed up to the total potential of the aircraft. From this, the velocity components of the entire flowfield can now be computed. In practice this computation is confined to a corridor in which the trajectory of the external store is expected. These flow-grids are generated only once around the proper aircraft and are then stored on EDP-disks, ready to be called up for all further computations.

Isolated Store Aerodynamics:

The pressure distribution of the isolated store is determined by the same method. Only here, the velocity components are computed directly on the store surface, permitting thus the determination of the panel pressure coefficients. In a further step the distribution so found is partially summed up to the characteristic sectional-loads of the external store.

Interference

The required interference evaluation is then performed during the trajectory calculation in the previously mentioned do-loop. There the disturbed flowfield components together with the proper velocities of store and aircraft are converted into effective flow angularities on each section of the store. Interference forces and moments are found by partially superposing the store sectional derivatives with the local flow angularities, and then by summing up these partial loads to total store loads.

This approximation covers the subsonic Mach number range, but still yields reasonable results in the transonic range, when measured grids are used.

The basic assumption of this interference concept consists in considering any higher order interference effect of the external store to be negligibly small.

2.3 Used Panel Model

Aircraft (2000 Surface Elements)
Used in Flowfield Calculations



Store (400 Panels) to Evaluate
the Isolated Store Aerodynamics



Fig. 9 shows two of the used panel models. A comparatively large number of panels is required to evaluate the disturbance flow field. High amounts of CPU-Time (about 20 min) for solving these systems of equations, however, occur only during the primary computations.

A smaller number of panels (400 or less) is sufficient, when determining the isolated store aerodynamics. (CPU-Time amount: 4. min or less).

Fig. 9

2.4 Results of Flow-Field Calculations

On Fig. 10 four streamlines are plotted around the aircraft shape to describe the disturbed flow at typical carriage stations. The flight situation corresponds to 8° angle of attack at $M = 0.6$. Near the fuselage centerline the flow is well ducted and follows the underfuselage surface. At the lower fuselage corner the streamlines are displaced sidewardly and maintain nearly the freestream inclination. The inboard wing streamline first follows the lower wing surface in an upward-outboard directed motion, and then is deflected by the wing downwash field. Due to high local sidewash effects the outboard wing streamline is ducted to the tip where it interacts with the tip-vortices. There it changes from the lower wing surface to the upper one and moves inwards.

Underfuselage and Underwing
Streamlines
 $M=0.6 \quad \alpha=8^\circ \quad \beta=0^\circ$

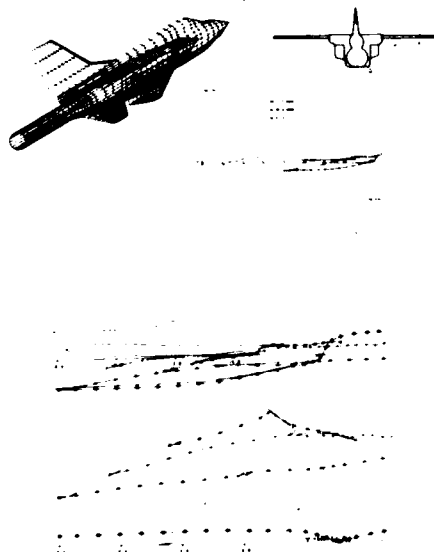


Fig. 10

Streamlines in Regions with
Heavy Disturbances

$M=0.9 \quad \alpha=8^\circ \quad \beta=5^\circ \quad \eta_{tail}=10^\circ$ (nose up)
(potential theory of Ref [3])

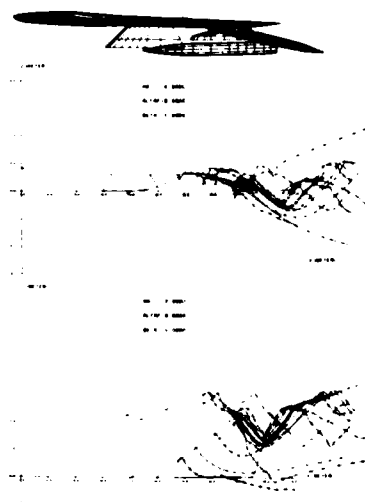


Fig. 11

The situation shown in Fig. 11 is much more complicated. Flight conditions are here $M = 0.9$ at 8° angle of attack and $+5^\circ$ sideslip. In addition, a store is mounted on the outboard wing pylon in front of the 10° nose-up inclined taileron. High interference regions are demonstrated here by vortex roll-up, strong sidewash and downwash effects. Finally Fig. 12 shows a comparison between theoretical and experimental flow-field data at the lower fuselage centerline and near the wingbody intersection area. Angle of attack of the freestream is set at 8° , with $M = 0.7$ (fuselage) and $M = 0.6$ (underwing). In spite of light overpredicted interferences near the canopy and wingbody-intake sections, the theory is in excellent agreement with the experimental data. This can also be stated for the sidewash component β shown on Fig. 12 (results taken from Ref. (7)).

Comparison Between Measured and Predicted Flowfield

$M=0.7 \quad \alpha=8^\circ \quad \beta=0^\circ$

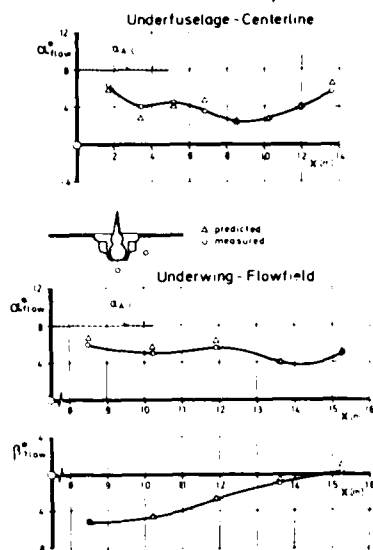


Fig. 12

First order interference is here defined as the difference between the freestream and the local flow angularities.

2.5. Loads on the external stores

The maximum interference due to store installation is shown on Fig. 13.

There, the store normal force coefficient is plotted versus the angle of attack for the isolated and the installed store. Maximum interference is the difference between both curves.

In both cases nonlinearities occur at higher angles of attack.

Static Interference (1st Order)

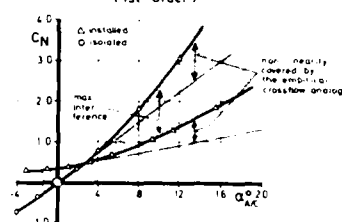


Fig. 13

It is obvious that the linear potential theory does not reproduce the strong nonlinear effects of vortex shedding on the store. Therefore the empirical crossflow analogy described in Ref. (8) and Ref. (9) is used to cover those effects.

Load-Coefficient on a Wing Pylon Mounted Store

$M = 0.6$

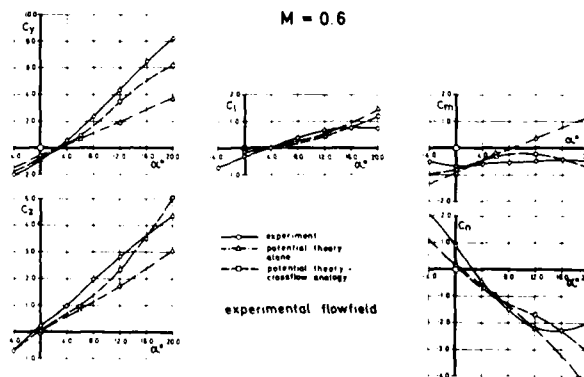


Fig. 14

On Fig. 14 carriage loads of a wing-pylon mounted store are plotted against some experimental results up to 20° of aircraft incidence. This evaluation includes only first order effects, because the relative velocity between store and aircraft motion is zero. Measured data are marked by circles, linear potential results by triangles and total loading including non-linearities by squares.

Underfuselage installation loads are shown for the same store on fig. 15. The parallel shifting of the moment-characteristics is due to a slightly differing centers of pressure between theoretical model and analyzed store, which was equipped with 4 wings plus 4 fins and a missile-launcher on its top. (see also fig. 9)

As mentioned before, second and third interference effects tend to change the effective angle of attack of the jettisoned store. Therefore these effects were evaluated for an underfuselage jettison case at $M = 0.9$ and $\alpha_{AC} = 11.5^\circ$. The resulting angles have been plotted versus the vertical displacement of the store relative to the aircraft in Fig. 16.

Load-Coefficient on a Fuselage-Pylon
Mounted Store
 $M = 0.6$

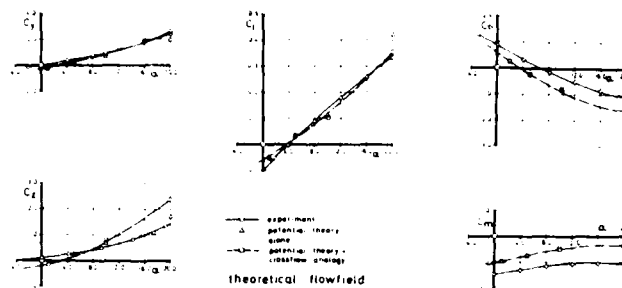


Fig. 15

Analysis of Interference Effects
on the Store Angles of Attack
(pitching up store)

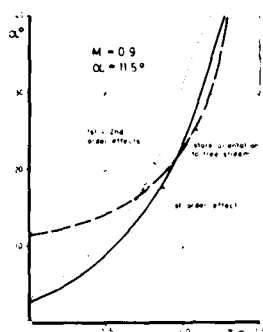


Fig. 16

Effective Angles at Body-Nose
and Body-Tail due to 1st + 2nd
Order Interference Effects

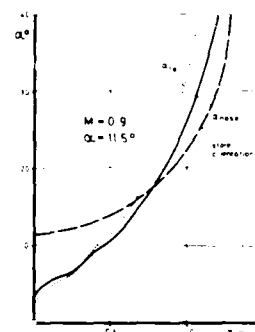


Fig. 17

The broken line represents the orientation of the store respective to the aircraft free stream direction during release. It starts at 11.5° and increases with a rapidly changing curvature. The solid line includes only the first order interference effects. It starts with the local flow inclination of 2.5° in the vicinity of the underfuselage and smoothly increases with vertical displacement due to decreasing interference. The dotted line demonstrates first and second order effects on the effective angle of attack. A break of its slope occurs at about $z = 0.10$ due to the end of the ejection acceleration (end of piston stroke). It then continues with a slightly higher gradient than the solid curve. First order interference is the difference between store inclination and the solid line. So first plus second order effects on the store effective angles of attack also appear as the difference between the dotted line and the inclination. Third order effects are zero, for it is a single jettison case.

Fig. 17 then shows the situation of body-nose and tail sections. Here the solid line gives the values of effective angles at the nose and the dotted one at the tail of the body. The orientation is identical as in the previous case (broken line).

Effect of Pitch-Control on
Interference

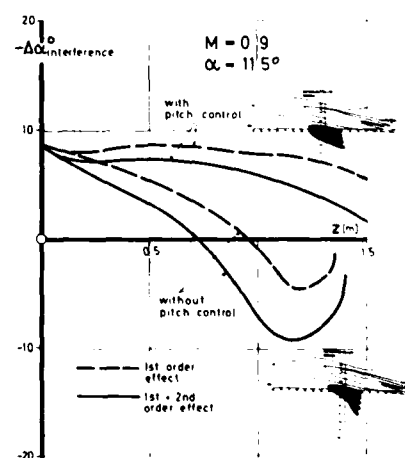


Fig. 18

Effects of slight changes of the initial condition on the interference evaluation is shown on fig. 18. The lower lines have been calculated by subtracting the store orientation and effective angle of attack of Fig. 16. The broken line stands for first order effects, the solid one for the first and second order effects. Applying now pitch control on the store with an ejection release unit, the store motion changes completely and thus also the interference calculation results. Positive $-\Delta\alpha$ indicate a high interference region with low local inclinations and strong velocity changes in the flow field. A negative $-\Delta\alpha$ indicates a pitch up of the released store, when it occurs in the vicinity of the aircraft.

Thus it is clear that the solid lines always give a pessimistic view of the separation behaviour compared with the broken lines. This is a typical dynamic response effect, and cannot be reproduced by steady grid measurements as done with a CTS-System, and where the interference effects on dynamic derivatives are not taken into account. This fact however is of great importance, for theoretical results should have always a sufficient security margin when predicting safe separation limits.

Trajectory-loads are shown on fig. 19. The normal force and the pitching moment of the jettison without pitch control have been plotted versus the vertical displacement. Due to the lack of suitable tests, comparison is made for theoretical first and first + second order effects with free flight measured store aerodynamics, marked by the broken lines. Actual load measurements from CTS-Rigs are only valid to describe first order effects. To measure realistic trajectory-loads it would be necessary to jettison a store with a flight data recording equipment.

2.6 Effect of varying sectional loads

Trajectory computations with different partitioning of the store geometry have shown an important effect on the separation behaviour. Fig. 20 therefore shows

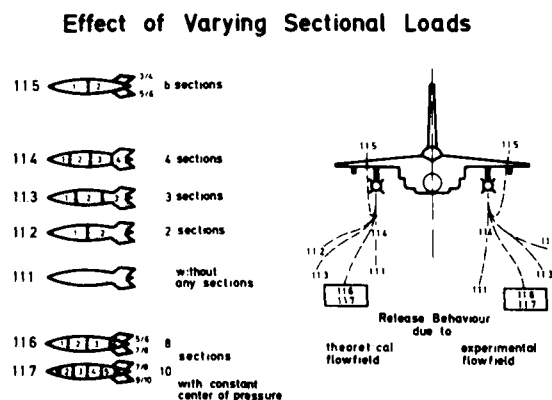


Fig. 20

the calculated tendencies for different sectional models of one store. Nearly any separation type can be reproduced. Trajectories 1.1.1 to 1.1.4 accentuate the effective angles of attack on the body axis. Number 1.1.5 takes the fin's angles into account, but with a rough approximation of the load-distribution on the body. Finally 1.1.6 and 1.1.7 indicate a stable tendency. Using additional sections no further changes occur. Analyzing these results, it was found that the trajectory becomes stable when using sections of the store with a constant center of pressure. Cases with fewer sections alternate the load distribution on the store surface, and thus lead to wrong moment curves and wrong trajectories.

3. COMPUTATION OF SEPARATION, COMPARISON WITH EXPERIMENTAL RESULTS

The usefulness of the MBB-SSP System has been proved in many recent store separation projects. Two of these typical results are plotted against flight test data on fig. 21; on the left side an emergency jettison and on the right side a firing case at $M = 0.8$ with $\alpha_{AC} = 4.5^\circ$.

Trajectory Loads with 1st Order only, and 1st + 2nd Order Interference Effects

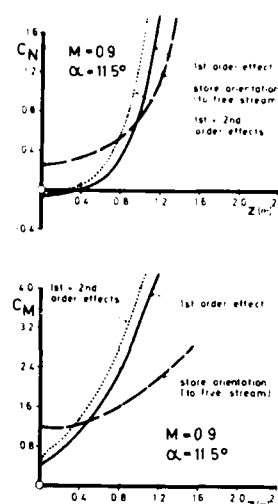


Fig. 19

Comparison with Flight Test Data

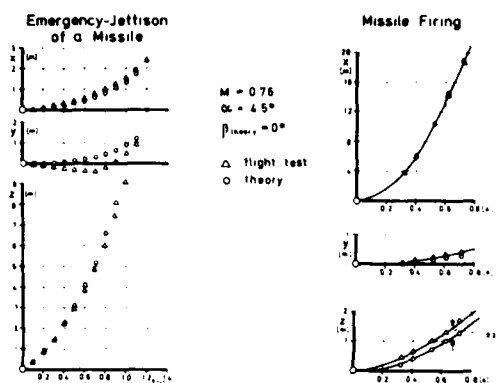


Fig. 21

Longitudinal, vertical and lateral displacements are plotted versus time. Triangles indicate test data, circles the theoretical prediction. Differences in lateral displacement shown here are due to sideslip during flight test. All other displacements are matching well.

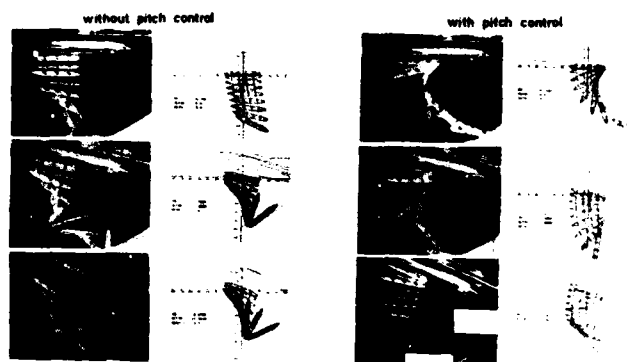
Comparison with Windtunnel Drop Tests
(FROUDE-Scaling)M=0.5 $\alpha = 0^\circ, 14^\circ, 23^\circ$ 

Fig. 22

Comparison with wind tunnel data is presented on fig. 22. It includes an α -variation with and without pitch control up to 23° with different stores. Finally some more complicated cases are demonstrated on fig. 23, such as:

- missile launch
- missile drop launch
- multiple jettison
- firing of submunition from carried dispensers
- range-analysis of submunition.

COMPLICATED RELEASE

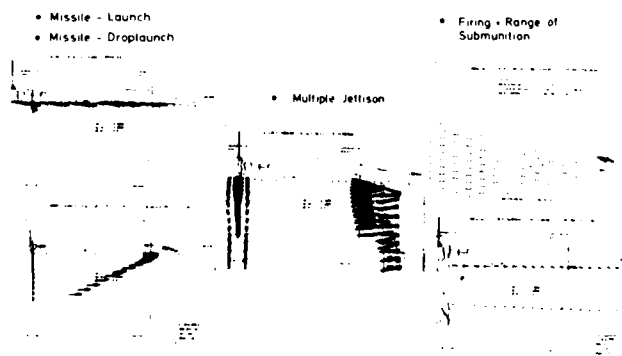


Fig. 23

4. CONCLUDING REMARKS

The combination of the flow angularity technique with modern potential theory is a powerful tool to evaluate interference effects during store separation. Theoretical and experimental data can be optionally used, without any difficulty. The greatest advantage is the CPU-reduction achieved using this concept with sufficient accuracy. Thus, one timestep of the do-loop affording 0.019 sec of CPU, the complete trajectory is calculated with only 7.6 sec. CPU.

A further advantage is the application to complicated and realistic manoeuvres with any load factor as well as in cases of multiple jettison where several flowfields must be superposed within an iteration after each time step.

The only inaccuracy is given by the fact that any reciprocal interference on the store due to its own disturbance must be neglected during the first few steps of the trajectory.

Finally, the actual lack of theoretical methods to evaluate the disturbances of arbitrary transonic 3D-configurations restricts this concept to the use of expensive experimental transonic flowfields.

5. REFERENCES

1. KRAUS W.
SACHER P. Das MBB-Unterschall-Panelverfahren 3-dim. Potentialtheorie bei beliebig vorgegebener Mehrkörperanordnung (Vortrag), MBB UFE 672-70, 1970.
2. WOODWARD F.A. An Improved Method for the Aerodynamic Analysis of wing-body tail configurations in subsonic and supersonic flow, NASA CR 2228, 1973.
3. KRAUS W. Ein allgemeines Panelverfahren zur Berechnung der dreidimensionalen Potentialströmung um beliebige Flügel-Rumpf-Leitwerkskombinationen in Unter- und Überschall, MBB-UFE 1136, 1974.
4. KORN S.C. Use of the flow angularity technique for predicting store separation trajectories, USAF/AFAL Eglin AFB, 1971.
5. GROSE G.
BRISTOW D. Load on External Stores, AGARD CP 71, 1971.
6. FERNANDES F.D. A method for predicting interference forces and moments on aircraft stores at subsonic speeds AGARD Washington CP 71, 1970.
7. TOMASHZEWSKI K. Ermittlung des Einflusses einiger potentialtheoretischer Kompressibilitätsmodelle auf die Außenströmung um eine Flügel-Rumpf-Leitwerk-Kombination im Unterschall, MBB/FE122/S/PUB/3, 1979.
8. JORGENSEN L.H. A method for estimating static aerodynamic characteristic for slender bodies of circular and noncircular cross section alone and with lifting surfaces at angles of attack from 0° to 90°, NASA-TN-D-7228, 1973.
9. WARDLAW A.B. Jr. Prediction of Normal Force, Pitching Moment and Yaw Force on Bodies of Revolution at Angles of Attack Up to 50° Using Concentrated Vortex Flow Field Model, Navel Ordnance Lab. NOLTR 73-209, 1973.
10. SANDAHL C.A.
FAGET A. Similitude Relations for Free-Model Wind Tunnel Studies of Store-Dropping Problems, NACA-TN-3907, 1957.
11. DESLANDES R. Theoretische Bestimmung der Trajektorien abgehender Flugkörper von Kampfflugzeugen, MBB UFE 1361-78, 1978.

STUDY OF TRANSONIC FLOW FIELDS ABOUT AIRCRAFT:
APPLICATION TO EXTERNAL STORES

Stephen S. Stahara
Nielsen Engineering & Research, Inc.
510 Clyde Avenue, Mountain View, CA 94040

SUMMARY

A review is presented of an extensive experimental/theoretical program which is directed toward establishing a predictive method for determining firstly, three-dimensional transonic flow fields about parent aircraft and secondly, loading distributions on external stores located in these nonuniform flow fields. The work represents several stages in the systematic development of a theoretical capability for enabling aircraft/store compatibility studies at transonic speeds with applications to aircraft store design optimization and store certification programs.

The primary emphasis of the work has been on the development and verification of a theoretical method for the rapid computation of nonlinear three-dimensional transonic flow fields due to modern fighter-bomber configurations, accounting for effects of the fuselage/wing/pylon components. The objectives of the paper are two-fold: (1) to describe the extensive companion experimental program and present highlights of those results, which include detailed measurements of both flow fields and surface pressures (parent and external store), taken in a systematic component buildup; and (2) to discuss the development of the associated theoretical method, describe its application to a class of idealized fighter-bomber configurations, and display comparisons with data from the parallel experimental program, including both flow field and store loading distribution results.

1. INTRODUCTION

The safe and controllable separation of external stores, either powered or unpowered, from modern fighter-bomber aircraft remains a current problem of significant military importance. Operational limitations due to dangerous store release characteristics can reduce aircraft mission effectiveness and survivability. Consequently, development of accurate engineering predictive methods for determining clear separation as well as optimizing store design and placement fills a critical dual role. Use of such methods not only enhances the performance and safety of weapon delivery, but also provides a means for reducing the time required for both wind-tunnel and full-scale flight tests relating to store certification programs.

Development of such methods for purely subsonic and purely supersonic flows has been successfully underway for some time^{1,2}. Favorable applications of these procedures³⁻⁵ have demonstrated their effectiveness for establishing weapon system design criteria. For transonic speeds, the application of such techniques becomes significantly more complicated. A more intense development of the basic theoretical solution procedure is required due to the essential nonlinear character of the flow. The linear methods previously developed for the subsonic and supersonic regimes do not apply and finite-difference solutions are necessary. However, for the complex geometries typical of realistic external store/fighter-bomber configurations, together with the large number of individual cases usually required for design or parametric analysis, exclusive use of three-dimensional finite-difference methods is not practical. These limitations identify the primary constraints on any prediction method for determining external store transonic aerodynamic behavior in the near vicinity of a parent aircraft. That is, the method must be capable of predicting with sufficient accuracy the essential nonlinearities of the nonuniform parent-generated three-dimensional transonic flow field surrounding the store, while maintaining a minimum of computational requirements so as not to limit severely its use as a design tool. Additionally, the method must be capable of treating complex geometries involving nonaxisymmetric fuselages/inlets/multiple pylon-store combinations characteristic of modern fighter-bombers.

In order to accomplish such a theoretical development in a rational systematic fashion, a specifically-designed wind-tunnel test program was simultaneously carried out to establish the essential data base to check and verify the predictive method at crucial stages. The experimental results obtained from this series of three tunnel entries are not only important to the present effort, but are of significant general value to 3-D transonic modeling efforts in that they comprise a generic data base of detailed three-dimensional transonic flow field measurements about a simplified wing/body combination which has not been previously available.

In the following section we describe the extensive companion experimental program and present highlights of those results, which include detailed measurements of flow fields (pressures and three velocity components), surface pressures (wing/body fuselage and external store), and wing/body forces and moments, taken in a systematic component buildup--wing/body/alone, wing/body/pylons, wing/body/pylons/attached-store, wing/body/pylons/separated-store, and store-alone.

The emphasis of the theoretical work has been on the development and verification of a predictive method for the rapid computation of nonlinear three-dimensional transonic

flow fields about idealized fighter-bomber configurations, accounting for effects of the fuselage/wing/pylon components. In the third section, we discuss the development of the associated theoretical method, describe its application to a class of wing/body configurations, and display comparisons with data from the parallel experimental program.

2. EXPERIMENTAL PROGRAM

2.1 Overview and Rationale

The basic rationale underlying the experimental program was to select realistic model geometries and flow conditions so as to provide data for the parallel theoretical program representative of modern fighter-bomber configurations operating at transonic cruise conditions; while at the same time maintaining as much geometric simplicity as possible so as to be able to separate out individual effects of different components. Test conditions had to ensure topological coverage of all important transonic flow conditions - from mildly supercritical, to strongly supercritical to mildly supersonic. The primary data would consist of (1) detailed flow field surveys in the near vicinity of the parent, in particular in locations typical of attached and initially-separated stores, and (2) detailed external store surface pressure measurements for store locations throughout the flow field survey grid. To achieve the desired coverage of various transonic conditions, testing near Mach number one was initially anticipated (and later confirmed) to be inevitable. Consequently, a means for both assessing and, if necessary, accounting for tunnel wall effects was considered essential. In order to achieve this, limited corroborative testing in a much larger tunnel was planned for assessment purposes; and in the tunnel where the primary testing would be done, supplementary outer flow field surveys would be taken to provide measured boundary conditions for input into the theoretical predictive method to account for tunnel interference. Parent model surface pressures and force and moment measurements were planned to provide additional inner flow field information as well as to assist in evaluation of tunnel interference and viscous effects. Finally, minimization of tunnel interference effects insofar as possible by (1) appropriate model sizing, (2) aerodynamically-clean configuration design, and (3) test condition selection at low to moderate lift would be undertaken.

2.2 Model Design

The design of the test model was constrained by the dual objectives of (1) testing a simplified but geometrically-related configuration characteristic of modern fighter-bombers, and (2) obtaining as wide a range as possible of transonic flow conditions. The model size was established by the conflicting requirements of minimizing wind-tunnel interference and maximizing pressure probe accuracy measurements. To provide a critical evaluation of the flow field predictive method, two different sets of wings having identical planforms are needed.

The model chosen is illustrated in Figure 1 and is an idealized 22.5:1 scale model of the F-16. The fuselage is circular with a three-caliber parabolic-arc nose profile followed by a straight cylinder. The two sets of identical planform wings are mid-mounted, cropped delta wings having thickness only (zero camber and twist) profiles whose coordinates are based on (1) a scaled F-16 wing (4% thick), and (2) a NACA 65A006 airfoil. A force balance is included in the model, and 25 surface pressure taps are provided on the fuselage surface.

2.3 Test Program Description

Three separate tunnel tests, as summarized below,

- 4T-wing-body alone
 - * flow field pressures, velocities
 - * fuselage surface pressures, forces/moments
- 16T-wing-body alone
 - * selected flow field pressures, velocities
 - * limited fuselage surface pressures, forces/moments
- 4T-wing-body/pylon/stores combination
 - * flow field pressures, velocities
 - * external store surface pressures
 - * fuselage surface pressures, forces/moments

were performed at the Arnold Engineering Development Center (AEDC) using the 4T and 16T Propulsion Wind Tunnel test facilities; and are reported in detail in references 6 and 7. The initial entry was in the AEDC 4T Transonic Tunnel where the primary diagnostic flow field data for the wing-body alone were obtained. The second entry was in the AEDC 16T Transonic Tunnel and was made to obtain a limited amount of selected repeat data for assessing both wind-tunnel interference as well as tunnel flow quality effects. The final entry was in the AEDC 4T tunnel where both detailed flow field data as well as detailed external store surface pressures were obtained for the original wing-body augmented by various wing and fuselage pylon/store combinations.

In the initial 4T entry, in order to obtain all of the important flow conditions of interest in transonic flight - from subcritical to slightly supercritical, to strongly

supercritical, to mildly supersonic - testing was carried out at three Mach numbers ($M_\infty = 0.925, 0.975, 1.025$) and three angles of attack ($\alpha = 0^\circ, 2^\circ, 5^\circ$). The principal flow field data were taken using the Captive Trajectory System (CTS) at typical store locations on the pressure side of the wing. Secondary data were taken on the suction side of the wing in order to obtain additional diagnostic information for evaluating the flow field prediction model. Figure 2 provides a photograph of the wing-body model and sting mount in the 4T tunnel, together with the conical flow-field survey probe on the CTS. In order to provide an idea of the flow field detail obtained, we have prepared Figure 3 which displays the grid survey locations for the inner flow field. Symmetric side-by-side surveys were made to assess flow quality and repeatability. Figure 4 displays the outer flow field surveys which were taken on a cylindrical surface as far from the model centerline as the CTS would allow ($R = 14.14$ inches) to provide measured outer boundary conditions as input to the theoretical model to evaluate wind-tunnel wall interference. Model fuselage pressures and forces and moments were obtained at all test conditions.

For the 16T entry, to obtain the corroborative flow field data, selected survey locations were used from the flow field grid as denoted in Figure 3 in the y-z crossflow plane view by the symbol \oplus , while the corresponding outer grid is denoted in Figure 4. The test conditions included the three Mach numbers ($M_\infty = 0.925, 0.975, 1.025$) of the 4T tests, but only the angles of attack $\alpha = 0^\circ, 5^\circ$. Fuselage surface pressures and forces and moments were also obtained at each test condition.

In the final 4T entry, the experimental procedure consisted of two separate systematic model-buildup sequences involving various pylon/store combinations added to the basic wing-body. For the first sequence, flow field velocities and pressures were obtained for each configuration in those regions normally occupied by an attached or initially-separated store. The various wing-body/pylon/store configurations tested together with their flow field grids are illustrated in Figure 5. The wing pylons employed had 30° swept leading edge and a straight trailing edge with a biconvex 4% thickness profile, while the fuselage pylon had both straight leading and trailing edge also with a biconvex 4% thickness profile. The dummy stores mounted on these pylons were axisymmetric ogive/cylinders having a 2-caliber nose and 8.5 caliber length and a $3/4$ inch diameter. Geometric details of the pylons and stores are provided in reference 7. As before, force/moment and surface pressure measurements were taken on the wing-body model, together with outer flow field measurements. Figure 6 provides a photograph of the test model with the wing-mounted pylon and stores and the CTS-mounted flow survey probe. The second model-buildup sequence involved a special pressure-instrumented store of identical geometry as the dummy stores involved in the first sequence, but mounted on the CTS and positioned in normal store-attached and various store-separated positions. The configurations tested in this sequence involved configuration 24 and 25 of Figure 5 with the dummy store replaced by the metrically-identical instrumented one. At each flow condition in this sequence, detailed surface pressure distributions on the instrumented store were obtained from a single longitudinal row of surface pressure taps by rolling the store through 360° at 10° roll-angle increments.

2.4 Test Results

A thorough survey of the experimental results from the initial 4T entry (wing-body alone) has verified that the test parameters were exceptionally well selected for providing as wide a range of transonic phenomena as possible. The data display flow conditions from subcritical to slightly supercritical, to strongly supercritical, to mildly supersonic, as were desired. For the two subsonic free-stream Mach numbers, Figure 7 illustrates this fact and displays the growth of the supersonic pockets on the pressure and suction sides of the wing. The results are for a (x,z) plane located at the spanwise location $y = 2$ inches (25% semispan) and are for the model with the scaled F-16 wing. The figure on the top indicates the extent of the supersonic zone at $M_\infty = 0.925$ for the three angles of attack, while corresponding results for $M_\infty = 0.975$ are shown in the bottom plot. The symbol M_L denotes the local Mach number. Since the vertical limits of the inner flow surveys were $1 \leq |z| \leq 5$ inches, the maximum lateral locations of the larger supersonic pockets on the suction side were beyond the last inner survey location at $z = 5$ inches. However, only for the $M_\infty = 0.975, \alpha = 5^\circ$ case did the pocket extend out to the outer flow survey location at $z = 14$ inches. These results indicate the extreme sensitivity of the flow at supercritical conditions. Analogous results for $M_\infty = 1.025$ are shown in Figure 8 which displays the variation and growth of the embedded subsonic pocket. Of particular note in both Figures 7 and 8 is that, at modest angles of attack, flow conditions on the pressure side of the wing remain primarily subsonic for a wide range of conditions.

An indication of the quality of the data obtained in the 4T tunnel is indicated in Figure 9 which displays side-to-side symmetry comparisons for flow surveys of sidewash and upwash at $M_\infty = 0.975$ and $\alpha = 0^\circ$ at a vertical location just under the wing ($z = 1$ inch) and at the location $y = 14$ inches which is at 50% semispan. In these surveys, the x location of the local leading and trailing edges of the wing are denoted by LE and TE. The comparisons indicate extremely good flow field symmetry and are typical of the 4T data. A close examination of all the data has indicated that at extreme spanwise locations near the wing tips, discrepancies of one-quarter of a degree are observed which can actually be traced to tunnel flow quality, but this is already at the limits of the accuracy attainable (Ref. 6) for these tests.

In order to achieve the range of flow conditions desired for the aerodynamically clean model configurations tested, the necessity of selecting two of the test Mach numbers so close to one ($M_\infty = 0.975, 1.025$) was unavoidable. Consequently, the question of whether

significant wall interference effects were present in the data is quite pertinent. In addition, since subsequent tunnel entries are planned, establishment of the band of free-stream Mach numbers about $M_\infty = 1$ outside of which tunnel effects are small is essential.

An indication of the presence of wind-tunnel effects in the 4T data is provided by Figure 10 which displays the comparison of body surface pressures obtained on the scaled F-16 wing/body combination from tests in the AEDC 4T and 16T tunnels. Indicated in the upper plot are the nonlifting results for $M_\infty = 0.925$, $\alpha = 0^\circ$, while corresponding lifting, pressure side results for $M_\infty = 0.975$, $\alpha = 5^\circ$ and $M_\infty = 1.025$, $\alpha = 5^\circ$ are displayed in the two lower plots. The results shown for the nonlifting $M_\infty = 0.925$ flow exhibit essentially no interference effects and are typical at this Mach number for lifting conditions as well. Those shown in the middle plot for the pressure side for $M_\infty = 0.975$, $\alpha = 5^\circ$ indicate good agreement at axial locations ahead of, behind, and over the major portion of the wing root chord axial position, with some slight discrepancies near the root chord leading edge and trailing edge, while similar pressure side results for $M_\infty = 1.025$, $\alpha = 5^\circ$ indicate somewhat larger discrepancies in those regions. As a direct indication of tunnel interference effects, however, these discrepancies are clouded by two additional factors present in the 16T data. These are (1) the model/sting support strut from the tunnel floor, and (2) flow quality effects. The 16T model support strut is known to be capable of causing a Mach number decrement of up to $M_\infty = 0.01$ in the test section (Ref. 6). Compensation for that decrement has been attempted in the comparisons for the $M_\infty = 1.025$ results shown in the bottom figure. Here the 4T tunnel results for $M_\infty = 1.025$, shown as the circular symbol (\odot), have been extended to $M_\infty = 1.015$ (---) to compare with the 16T data by interpolating between the 4T results for $M_\infty = 0.975$ and 1.025 . Some improvement is indicated but the discrepancies are not eliminated.

Our conclusions from the comparative wing-body alone tunnel tests are that (1) essentially no interference exists at $M_\infty = 0.925$, (2) at $M_\infty = 0.975$ and 1.025 minor interference exists on the pressure side of the wing/body, and (3) the outer flow field measurements obtained will afford a means, if necessary, of accounting for tunnel effects in the theoretical predictions.

With regard to the final 4T entry, on the basis of the tunnel interference results from the initial 4T and 16T tests for the wing-body alone, test Mach numbers were selected at $M_\infty = \{0.925, 0.950, 1.05, 1.10\}$ and angles of attack $\alpha = \{0^\circ, 2^\circ, 5^\circ\}$ in order to avoid as much as possible even the slight interference observed at $M_\infty = 0.925$ and 1.025 , while still covering the spectrum of flow conditions characteristic of transonic flight. A thorough survey of the experimental results for the various wing-body/pylon/store configurations has indicated that the test conditions were again well selected. The data typically display conditions from mildly supercritical to strongly supercritical, to mildly supersonic for the various combinations tested. For the two subsonic free-stream Mach numbers, Figure 11 illustrates the variation with angle of attack of the size of the embedded supersonic pockets for the wing-body configuration with wing-pylon/stores. The results are for a (x,z) plane located exactly at the wing-pylon span location ($y = 3.5$ inches). The figure at the top displays results for the extent of the supersonic zone at $M_\infty = 0.925$ for the angles of attack $\alpha = 0^\circ, 2^\circ, 5^\circ$, while corresponding results for $M_\infty = 0.950$ are provided in the bottom plot. In this (x,z) plane, the vertical limit of the survey locations was $1.98 \leq z \leq 2.73$ inches. The results indicate two separate supersonic pockets; one on the ogive nose of the store and terminating at or near the shoulder, and another located rearward of the first extending over the cylindrical portion of the store. At $M_\infty = 0.925$, the results in the upper plot indicate substantial supersonic pockets at $\alpha = 0^\circ$, which notably contract at $\alpha = 2^\circ$, and which at $\alpha = 5^\circ$ disappears altogether on the nose but remains over a small axial interval on the cylindrical portion of the store. These results are in distinct contrast to those for the wing-body alone (see Fig. 7), which displayed only a very small supersonic pocket at $\alpha = 0^\circ$, which disappeared altogether at $\alpha = 2^\circ$, and indicate a substantial effect of the pylon and store on the flow field. The corresponding results at $M_\infty = 0.950$ in the lower plot display a similar trend, but maintain a notably larger supersonic pocket on the cylindrical portion of the store even at $\alpha = 5^\circ$. These latter flows provide typical strongly supercritical results, while the former provide corresponding mildly supercritical results.

3. THEORETICAL PROGRAM

3.1 Summary of Flow Field Method Development

The development of the theoretical method for predicting the parent-generated three-dimensional transonic flow field has proceeded through a series of increasingly more accurate, but computationally more expensive methods as were indicated as being required from comparisons with data from the companion experimental program. Starting with the simplest, as summarized below, these were methods based on

- Classical transonic equivalence rule
- Extended transonic equivalence rule
- Nonlinear 3-D correction procedure

In the following sections, we will briefly describe each method, discuss their respective strengths and weaknesses, and display typical comparisons of results predicted by each with data.

3.2 Classical Transonic Equivalence Rule

The transonic equivalence rule (TER) was developed initially in the form, now known as the classical or thickness-dominated limit, by Oswatitsch (Ref. 8) for nonlifting wings, and extended later to moderately lifting wings (Ref. 9) and slender configurations of arbitrary cross section (Ref. 10). Subsequent extension of the rule (Ref. 11) to include situations where the lift is significant both revealed its dependence on lift as well as clarified the classical limit and range of validity. In essence, the rule provides the basis for greatly simplifying the calculation of transonic flows past special but aerodynamically-important classes of three-dimensional configurations. It accomplishes this by recognizing that the structure of transonic flows past slender shapes in the vicinity of $M_\infty = 1$ consists of two distinct but coupled domains whose governing equations and boundary conditions are significantly easier to solve than the full 3-D transonic potential equations. The fundamental structure of the equivalence rule is found to be governed principally by a similarity parameter δ^* (Ref. 11) involving a combination of the configuration thickness ratio, lift force, and leading-edge sweep, and represents essentially the ratio of lift/thickness effects. Depending on the magnitude of δ^* , the nonlinear outer problem classifies into one of three domains: (1) $\delta^* \ll 1$, thickness-dominated, (2) $\delta^* = O(1)$, intermediate, and (3) $\delta^* \gg 1$, lift-dominated. For the modern fighter-bomber configurations and operating conditions of interest in this study, the similarity parameter δ^* is small (Ref. 12) and the subsequent flows lie within the classical or thickness-dominated limit. In this limit, the solution domains consist of an inner region governed by a linear equation, the same as in slender-body theory, and an outer nonlinear region consisting of the axisymmetric flow about an "equivalent" nonlifting body of revolution having the same longitudinal distribution of cross-sectional area.

The theoretical essentials of the classical TER are illustrated in Figure 12, which displays the decomposition of the flow into its first-order inner and outer components and the resulting uniformly-valid composite solution; that is

$$\phi = \phi_{2,i} + \phi_{2,t} - \phi_{2,B} + \phi_B \quad (1)$$

Here, each component has the meaning indicated in Figure 12. The first-order lift ($\phi_{2,i}$) and thickness ($\phi_{2,t}$) inner solutions describe, respectively, the translating and expanding cross section in the y,z plane, and satisfy the two-dimensional Laplace equation in the crossflow plane together with the no-flow boundary condition at the body surface. The first-order outer solution ϕ_B satisfies the axisymmetric transonic small-disturbance equation indicated in the figure subject to an inner boundary condition determined by the "equivalent" body singularity source distribution, and an outer boundary condition related to flow conditions far from the configuration. These would correspond, for example, to free-air conditions or to those appropriate to a tunnel environment.

Previous applications (Ref. 13) of the classical TER to various nonaxisymmetric slender bodies and a thin triangular wing of unit order aspect ratio displayed very good agreement with data, and provided a basis for application to the configurations of interest in this study. The TER procedure was applied to the idealized F-16 wing-body model shown in Figure 1. A description of the appropriate inner and outer solution procedures developed is provided in reference 12. Figure 13 provides typical results of the TER theory with 47 data for the wing-body model with the scaled (4% thick) F-16 thickness-only wing (see Fig. 1). In that figure, we have displayed theoretical and experimental comparisons at $M_\infty = 0.975$ of the local upwash α_u and sidewash α_s angles, in degrees, for a longitudinal survey at the crossflow location $(y,z) = (4,-1)$ inches, which is at the 50% semispan location and as close vertically to the wing as surveys were taken. The plots in the left of the figure provide results for $\alpha = 0^\circ$, while those on the right are for $\alpha = 5^\circ$. In general, the comparisons are quite good, capturing both the level and the trend of the data in all locations except near the trailing edge. In that region, the results become spurious. These results are essentially unchanged at the lower subsonic ($M_\infty = 0.925$) and supersonic ($M_\infty = 1.025$) Mach numbers tested. Initially, it was believed that this behavior was due to discontinuities in the axial area distribution derivatives due to breaks in the wing planform. Various smoothings of those derivatives, however, ameliorated the problem slightly (Ref. 14). A close examination of the flow structure in the vicinity of the wing tip and the trailing edge revealed that those changes in planform for the aspect ratio of the model tested ($R = 2.98$) induce three-dimensional spanwise variations which are beyond the capability of slender-body theory which underlies the basis of the classical equivalence rule. Consequently, the deficiency is one in terms of aspect ratio. For applications to the configurations of interest in this study, an extension or modification of the classical TER is necessary to overcome this limitation.

3.3 Extended Transonic Equivalence Rule

In an attempt to alleviate the aspect ratio shortcomings of the classical TER, we have examined an extended equivalence rule in which the two-dimensional inner solutions in the original TER are replaced by three-dimensional solutions obtained from paneling methods. The corresponding composite solution is then given by

$$\phi = \phi_{3,t+\alpha} - \phi_{3,B} + \phi_B$$

Here $\phi_{3,t+\alpha}$ is the solution to the three-dimensional Laplace equation for an arbitrary angle of attack α ; $\phi_{3,B}$ is the linearized axisymmetric flow about an

AD-A094 086 ADVISORY GROUP FOR AEROSPACE RESEARCH AND DEVELOPMENT--ETC F/G 20/4
SUBSONIC/TRANSONIC CONFIGURATION AERODYNAMICS.(U)
SEP 80

UNCLASSIFIED AGARD-CP-285

NL

2 OF 1
20/4-1

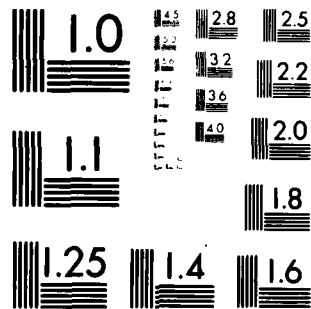


1



1

1



MICROCOPY RESOLUTION TEST CHART
NATIONAL BUREAU OF STANDARDS 1963-A

flow past the equivalent body, and ϕ_B is the usual nonlinear axisymmetric solution to the transonic small-disturbance equation for nonlifting flow past the equivalent body.

In this form, it was anticipated that the appropriate three-dimensional spanwise variations of the flow, which could not be represented accurately by the two-dimensional inner solutions, would be obtained; while the nonlinear transonic effects would hopefully be captured sufficiently accurately from the axisymmetric equivalent body solutions. Additionally, paneling method solutions for $\phi_{3,t+\alpha}$ for both the subsonic and supersonic cases already exist (Refs. 1 and 2). In Figures 14 and 15, we display results for the extended equivalence rule corresponding to those provided in Figure 13 for the classical TER. Figure 14 provides a comparison of theoretical predictions and data at $M_\infty = 0.975$ and $\alpha = 0^\circ$ for the axial velocity ratio as well as the local upwash and sidewash angles along the survey location at $(y,z) = (4,-1)$ inches, while Figure 15 provides corresponding comparisons for $\alpha = 5^\circ$. The results of the extended equivalence rule are indicated by the flagged solid circles (\bullet), while the three-dimensional paneling method results ($\phi_{3,t+\alpha}$) are shown as solid circles (\bullet), and data as open circles (\circ). At points ahead of the trailing edge, the extended equivalence rule and the linear theory are essentially identical, indicating no correction from the axisymmetric equivalent body calculations. However, near the trailing edge, the extended equivalence rule results, although providing significantly improved results from the classical TER, display a serious discrepancy in both axial velocity and sidewash. The upwash component would not be expected to display much of an equivalent body correction at this location due to the restraining influence of the wing in the vertical direction.

One of the notable features of the above results, as well as a significant result of this study as determined from a large number of similar comparisons at a variety of flow conditions throughout the transonic range, is the reasonably good predictions of the lateral velocity components (upwash and sidewash) as predicted by the three-dimensional paneling methods for this configuration even at free-stream Mach numbers quite close to one. The axial velocity component, as would be expected and as shown in Figures 14 and 15, consistently displays a large discrepancy between the linear solution and data in the trailing edge region where shock waves are present. For that velocity component, a three-dimensional nonlinear solution is necessary to account for the 3-D character of the shock in that region. However, as discussed in the store loading calculation section below, external store loads in the presence of parent-aircraft, depend primarily on the lateral velocity components, and secondarily on the axial velocity component, with the exception being regions where parent-generated shock waves impinge on the store. Consequently, we conclude that three-dimensional paneling methods can be used to predict the parent-generated lateral velocity components, while a 3-D nonlinear procedure is necessary to account for transonic effects on the axial velocity component. This has formed the basis of the method described in the next section.

3.4 Nonlinear 3-D Correction Method

Based on the observation that paneling method solutions are capable of providing good predictions of lateral (but not axial) velocity components for certain fighter-bomber like configurations; and the hypothesis that the addition of geometric complexities to a basic configuration can be treated with differences between appropriate paneling method solutions, and that the primary transonic effects generated by these configurations are due to the wing, the following nonlinear correction procedure is suggested for solution decomposition to account for various geometry modifications of a basic configuration. For pylon addition to a basic wing-body, we have

$$\phi = \left(\phi_{3,WBP} \right)_{Lin} - \left(\phi_{3,WB} \right)_{Lin} + \left(\phi_{3,WB} \right)_{NL} \quad (3)$$

where $(\phi_{3,WBP})_{Lin}$ and $(\phi_{3,WB})_{Lin}$ denote paneling method solutions for the wing-body/pylon and wing-body alone configurations, and $(\phi_{3,WB})_{NL}$ denotes a nonlinear 3-D transonic finite-difference solution for the wing-body alone.

A similar decomposition has been employed with success in reference 15 to model geometrically-complex fuselage effects on wing pressures at transonic speeds. The primary point is that as long as detailed transonic effects are not required on the modeled component, then such a procedure is capable of providing good representations of the primary lift and volume effects of the modeled component upon the remainder of the flow.

For the pylon addition to the wing-body, we have tested this decomposition experimentally by comparing the difference in results for flow quantities for the wing-body/pylon and wing-body alone as measured and as predicted by the paneling method solutions. In Figure 16, we provide such a comparison for the differences in the three velocity components for a wing pylon addition at a flow survey directly under the pylon $(y,z) = (3.5, -1.23)$ inches for $M_\infty = 0.950$ and $\alpha = 0^\circ$. The axial locations of the wing and pylon leading and trailing edge are denoted by LE, TE and PLE, PTE, respectively. We note that, as in the case of the wing-body alone, the paneling solutions provide good predictions of the upwash and sidewash components, but display a familiar discrepancy in the axial velocity component in location and magnitude of the compression in this case near the shock by the pylon trailing edge. A similar but somewhat milder discrepancy is illustrated in Figure 17 which displays the corresponding comparisons for the wing-body with fuselage pylon.

In order to examine the magnitude of the nonlinear correction $(\phi_{3,WB})_{NL}$ to the composite solution, we have determined a number of nonlinear 3-D transonic small-disturbance solutions for the wing-body alone both to provide some benchmark solutions to compare

against the other theoretical solutions, as well as to input into the composite solutions given by Eq. (3) to determine wing-body/pylon solutions. For these solutions, we employed the 3-D transonic small disturbance (TSD) procedure of reference 16 which is based on the procedure originally developed by Bailey and Ballhaus (Ref. 17). Figure 18 provides a comparison of theoretical results and data for the three velocity components at $(y,z) = (4,-1)$ inches for $M_\infty = 0.950$ and $\alpha = 5^\circ$. The agreement for all three velocity components is quite good, capturing the transonic effect on the axial velocity component and also providing an additional indication that tunnel interference effects at this Mach number are minimal, as the theoretical results are for a free-air boundary condition.

The effect of the 3-D nonlinear correction for this flow field is provided in Figure 19 which displays a comparison of theoretical and experimental results for local upwash and sidewash for the wing-body with wing pylon at a flow survey location directly under the wing pylon $(y,z) = (3.5,-1.98)$ inches. The theoretical result with the nonlinear correction is indicated as the solid curve, while the corresponding paneling method result is shown as the dashed curve. Both predictions compare quite well with data, with the nonlinear results somewhat superior. The importance of these differences in the theoretical lateral velocity predictions to the store loading determination are discussed in the following section.

3.5 Store Loading Method

The current procedure employed for determining store loading distributions is described in detail in reference 1. The method proceeds by first determining the non-uniform flow field due to the parent but with the store absent. The loading distribution on the store is then determined by locally employing apparent mass concepts together with the nonuniform crossflow velocity components at the locus of points corresponding to the position that the longitudinal axis of the store would occupy in the flow. The procedure accounts for buoyancy due to streamline curvature as well as local slender-body loading, and a viscous crossflow correction to account for vortex separation can be included. Such a loading determination procedure avoids the time-consuming integration of surface pressures, and has proven to be quite accurate for the many subsonic applications carried out to date (Refs. 1, 3-5).

Application of this procedure employing the ogive/cylinder store model and the theoretically-generated flow fields illustrated in Figure 19 provides the normal dC_N/dx_s and sidewash dC_W/dx_s loading distributions shown in Figure 20 for a store location directly under the wing pylon at $M_\infty = 0.950$ and $\alpha = 5^\circ$. The results indicate little difference in loading when employing the 3-D nonlinear corrected flow field or the linear paneling method flow field, presumably since the loading method only makes use of the lateral velocity gradients for which Figure 19 indicated no substantial differences. Comparison of the theoretical results with data indicates generally good agreement except in the vicinity of the large gradient near the pylon trailing edge. That deficiency in a high-gradient region is demonstrated more clearly in Figure 21 which provides a comparison of measured and theoretical normal force loading distributions for simulation of a store separated from a wing pylon at $M_\infty = 0.950$, $\alpha = 0^\circ$, and $(y,z) = (3.5,-1.45)$ inches. At $\alpha = 0^\circ$, discrepancies are present in the regions near both the pylon leading and trailing edge, while at $\alpha = 5^\circ$ the deceleration of the flow has eliminated the discrepancy at the pylon leading edge and reduced but not eliminated that near the pylon trailing edge.

These comparisons serve to identify two deficiencies of the present loading calculation procedure as applied to transonic flows; i.e., (1) the procedure cannot handle steep gradients in the parent-generated flow field accurately, and (2) the method does not account for store-induced transonic effects.

The importance of the latter effect is shown in Figures 22 and 23. Figure 22 displays data-only results for measured local upwash at $M_\infty = 0.925$, 0.950 , and 1.050 for a flow survey location directly under the wing pylon at $\alpha = 0^\circ$ and 5° . These results illustrate strong transonic effects near the pylon trailing edge which are greatest for $M_\infty = 1.050$ and more pronounced at $\alpha = 0^\circ$ than at $\alpha = 5^\circ$, as would be expected due to the slowing of the flow. Figure 23 displays the measured loading distribution when the store is placed in the flow in such a manner that the store longitudinal axis corresponds to the flow survey location of Figure 22. Note that the transonic effects are strongest near the pylon trailing edge and for $\alpha = 0^\circ$ as would be anticipated from Figure 22. However, the measured normal-force gradient is strongest for $M_\infty = 0.950$ rather than 1.050 where the measured flow field gradient is largest. This is assuredly due to the local transonic effects on the relatively large store employed - which would be greatest at a strong supercritical oncoming Mach number, but would disappear at lower or higher Mach numbers. This is verified by the fact that the phenomenon has almost disappeared when the angle of attack is changed from 0° to 5° , which acts to slow the flow significantly on the pressure side of the wing and substantially reduce the local transonic effects induced by the store itself.

We have recently developed a modification to the loading calculation procedure to account for store-generated transonic effects by applying the transonic equivalence rule to the store alone and accounting for store-induced transonic effects on the crossflow velocity components in the loading calculations. This result will be reported in detail in a future publication.

An indication of the magnitude of this improvement is provided in Figure 24 which displays a comparison of the difference in the pitching moment coefficient C_{m_q} variation throughout the transonic regime when including and not including store-generated transonic

effects. The results indicated in the bottom plot are for an ogive/cylinder store similar to that considered in the wing-body tests, but of 5 caliber rather than 8.5 caliber length. These results were carried out for uniform free-air flow past the store-alone, for which the previous method without parent-generated flow field curvature reduces to the slender-body result. The effect of this modification to the loading calculation has an even more dramatic effect when boattailing (and/or fins) are employed on the rear of the store. That change in pitching moment for a boattail addition is also indicated in Figure 24 for a 1/2 caliber conical boattail.

3.6 Ancillary Theoretical Developments

Two important ancillary theoretical developments, which were partially-developed under the present effort and which, although important in their own right, will have a significant effect on the future development of theoretical external store predictive methods. The first is a rapid perturbation method for predicting nonlinear transonic flows and impacts on the 3-D nonlinear correction method discussed in section 3.4 in that it would minimize the number of computationally-expensive 3-D nonlinear finite-difference solutions that would be required for a particular parametric or design study.

The procedure employs two "expensive" nonlinear solutions separated by some reasonable change in an arbitrary geometric or flow parameter to predict a range of neighboring nonlinear solutions at trivial computational cost. The method uses coordinate straining to account for displacement of discontinuities or rapid but continuous high-gradient maxima. It has been applied to a variety of 2- and 3-D problems (Refs. 18 and 19) to predict surface properties. Reference 19 provides a summary of a wide variety of nonlinear subsonic and transonic flow applications. In particular, a number of transonic examples with large surface shock movement over the parametric range considered are provided. The results display a remarkable accuracy.

Figure 25 displays an application of that method to the prediction of the 3-D transonic flow fields about the wing/pylon combination for which results were previously provided in Figure 19 employing the nonlinear 3-D correction method. In Figure 25, we have used the composite 3-D nonlinear correction solutions (see Eq. (3)) for the local upwash α_L at $M_\infty = 0.950$ and $\alpha = 0^\circ$ and 5° , given by the dashed (---) and dash-dot (-.-.) curves, respectively, to predict the corresponding result at $\alpha = 2^\circ$, indicated by the solid (—) curve. That theoretical result is meant to be compared with the data points indicated by the crosses (x). Agreement is excellent.

The other development relates to a transonic wind-tunnel interference assessment procedure which can provide the means for evaluating the effect of tunnel walls on data taken about parent/external stores configurations. An effective means of accounting for wind tunnel effects can be particularly important to store certification programs which rely heavily on tunnel programs to provide information for flight tests.

The concept is to obtain experimental pressure measurements during a tunnel test program on a convenient control surface located somewhat inward from the actual tunnel walls so as to be removed from local wall disturbances. These conditions are then employed in a computational procedure to determine the potential flow about the model interior to the control surface. Results for two-dimensional (Ref. 20) and axisymmetric (Ref. 21) flows have demonstrated the effectiveness of the procedure for accounting for tunnel interference effects. Although we have not yet carried out the full 3-D tunnel interference calculation for the wing/body model tested, we have performed a series of calculations in which we approximately assessed tunnel interference present in the initial 4T wing-body alone test (Ref. 6).

For those calculations, we replaced the 3-D wing/body by its equivalent body of revolution determined from the actual wing/body axial area distribution. Measured pressure distributions obtained along a cylindrical control surface located 14.1 inches from the tunnel centerline (max. distance for the CTS) at several Mach numbers and for $\alpha = 0^\circ$ were employed as an outer boundary condition in a nonlinear axisymmetric TSD calculation for the interior potential flow. Results are shown in Figure 26 for the surface pressure coefficient along a portion of the equivalent body corresponding to the location of the leading and trailing edge of the wing root chord for flow at $M_\infty = 1.025$. The closed circles indicate the results employing the measured outer boundary condition, while the x's represent the corresponding results using a free-air outer boundary condition. The difference between the two provides an indication of the level and location of the interference present.

The comparisons shown in Figure 26 indicate that for $M_\infty = 1.025$ essentially no interference exists over most of the axial locations corresponding to the wing root chord, denoted by LE and TE, with the exception of the vicinity near the trailing edge. Analogous comparisons at $M_\infty = 0.975$ displayed similar results with even less discrepancy near the wing trailing edge, while that at $M_\infty = 0.925$ showed no discrepancy at all between the free-air results and that employing the measured pressure-distribution outer boundary condition. This is in exact correspondence with the experimental results obtained from the 4T and 16T tests as indicated in Figure 10. Consequently, even this rather approximate use of a measured outer boundary condition for assessing wind tunnel interference about a 3-D configuration can provide important information regarding the location and magnitude of wall effects.

4. CONCLUDING REMARKS

A review has been presented of a combined experimental/theoretical investigation of transonic flow fields about aircraft with application to external stores. The objective of the work has been firstly on the development and verification of a theoretical method for the computationally-efficient determination of nonlinear three-dimensional transonic flow fields due to modern fighter-bomber like configurations, accounting for fuselage/wing/pylon components; and secondly, on the accurate determination of loading distributions on external stores. An extensive companion experimental wind-tunnel test program based on an idealized F-16 model was carried out in order to provide the essential data base to verify the theoretical method. The data obtained from that program include detailed pressure and velocity component measurements of the flow fields, surface pressures on the wing-body fuselage and external store, and wing-body forces and moments. These have been taken in a systematic component buildup from wing-body alone, wing-body plus wing or fuselage pylons, wing-body/pylons plus attached stores, wing-body/pylons plus separated store, and store alone; and represent a generic data base of detailed three-dimensional transonic flow measurements about a simplified wing-body combination which has not been previously available. Consequently, they are of significant general value to 3-D transonic modeling efforts.

Development of the theoretical flow field predictive method has proceeded through a series of three successively more accurate, but computationally more expensive models, beginning with procedures based on the classical transonic equivalence rule, then to an extended transonic equivalence rule in which the linear 2-D crossflow solutions were replaced by linear 3-D solutions obtained by paneling methods, and ultimately to the nonlinear 3-D correction procedure currently being employed. In the latter procedure, the full geometry effects of the wing-body/pylon configuration are accounted for by employing linear 3-D paneling method solutions, while the essential 3-D nonlinear effects, which are primarily due to the wing, are accounted for through a nonlinear correction using a 3-D finite-difference solution of the nonlinear transonic small-disturbance equation for the wing-body alone. Extensive comparisons of predictions from each of these theoretical methods with data from the companion experimental program have been made (Ref. 7) and typical examples of those comparisons have been presented here. One of the notable results of these comparisons determined from a large number of comparisons at a variety of flow conditions throughout the transonic range, is the reasonably good predictions of the lateral velocity components (sidewash and upwash) as predicted by the 3-D linear paneling methods for the wing-body and wing-body/pylon configurations considered. Similar comparisons for the longitudinal velocity component, however, consistently show a large discrepancy between the 3-D linear solution and data in the regions near shock waves, as might be expected. For that velocity component, the nonlinear correction is significant and must be included.

Extensive comparisons of theoretical results and data for loading distributions on the external stores immersed in the nonuniform wing-body/pylon flow fields have also been made at a variety of flow conditions throughout the transonic range (Ref. 22) and typical results of those comparisons have been presented. While in good overall agreement, these comparisons have served to point out deficiencies in the current loading determination method when applied to transonic flows. These relate to the inability of the method to account accurately for (1) high-gradient regions - either transonic or otherwise; and (2) store-generated transonic effects. Preliminary results of an effective method for successfully treating the latter are presented.

Finally, two ancillary theoretical developments; (1) a rapid perturbation method for predicting nonlinear transonic flows, and (2) a wind tunnel interference assessment procedure, that were partially developed under this effort, were described insofar as they relate to the present external store problems. Preliminary applications of these methods indicate that (1) the perturbation method can provide an effective means for obtaining related nonlinear 3-D flow fields, thereby substantially reducing the computational requirements for a design or parametric analysis, and (2) a wind tunnel interference assessment procedure based upon employing measured pressures on an outer control surface can successfully indicate both level and location of tunnel wall effects.

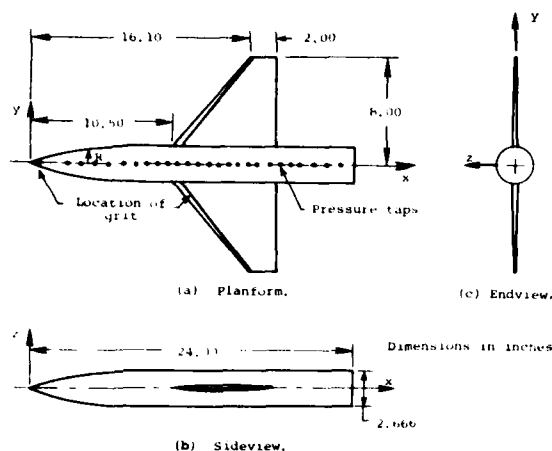
5. REFERENCES

1. Dillenius, M.F.E., Goodwin, F.K., and Nielsen, J.N.: Extension of the Method of Predicting Six-Degree-of-Freedom Store Separation Trajectories at Speeds Up to the Critical Speed to Include a Fuselage with Noncircular Cross Section. Vol. I - Theoretical Method and Comparisons with Experiment. AFFDL-TR-74-130, Mar. 1974.
2. Dillenius, M.F.E., Goodwin, F.K., and Nielsen, J.N.: Prediction of Supersonic Store Separation Characteristics. Vol. I - Theoretical Methods and Comparisons with Experiment. Technical Report AFFDL-TR-76-41, Vol. I, May 1976.
3. Spahr, H.R.: Theoretical Store Separation Analyses of a Prototype Store. J. of Aircraft, Vol. 12, No. 10, Oct. 1975, pp. 807-811.
4. Spahr, H.R.: Theoretical Store Separation Analyses of a Prototype Store and Comparison with a Flight Drop Test. AIAA Paper No. 74-776, presented at AIAA Mechanics and Control of Flight Conf., Anaheim, CA, Aug. 5-9, 1974.

5. Spahr, H.R., Everett, R.N., and Kryvoruka, J.K.: A Multifaceted Store Separation Analysis. Proc. of the AIAA 9th Aerodynamic Testing Conf., Arlington, TX, June 7-9, 1976, pp. 292-300.
6. Perkins, S.C., Jr., Stahara, S.S., and Hemsch, M.J.: Data Report for a Test Program to Study Transonic Flow Fields About Aircraft with Application to External Stores. Vols. I-VI. AFOSR-TR-78-1485 to 1490, July 1977.
7. Stahara, S.S. and Crisalli, A.J.: Data Report for a Test Program to Study Transonic Flow Fields About Wing-Body/Pylon/Store Combinations. Vols. I-III, AFOSR-TR-79-1070 to 1072, Jan. 1978.
8. Oswatitsch, K.: Die theoretischen Arbeiten über schallnahe Strömungen am Flugtechnischen Institut der Kungl. Teckniska Högskolan, Stockholm, Eight International Congress on Theoretical and Applied Mechanics, Istanbul, 1952, pp. 261-262.
9. Spreiter, J.R.: Theoretical and Experimental Analysis of Transonic Flow Fields. NACA-University Conf. on Aerodynamics, Construction, and Propulsion II, "Aerodynamics", 1954, pp. 18-1, 18-17.
10. Heaslet, M.A. and Spreiter, J.R.: Three-Dimensional Transonic Flow Theory Applied to Slender Wings and Bodies. NACA Rept. 1318, 1957.
11. Cheng, H.K. and Hafez, M.M.: Transonic Equivalence Rule: A Nonlinear Problem Involving Lift. J. of Fluid Mech., Vol. 72, 1975, pp. 161-188.
12. Stahara, S.S., Hemsch, M.J., Perkins, S.C., Jr., and Spreiter, J.R.: A Rapid Predictive Method for Three-Dimensional Transonic Flow Fields About Parent Aircraft with Application to External Stores. Paper presented at Fourth JTCG Aircraft/Stores Compatibility Symposium, Eglin Air Force Base, FL, Oct. 1977.
13. Stahara, S.S. and Spreiter, J.R.: Transonic Flow Past Nonaxisymmetric Slender Shapes - Classical Equivalence Rule Analysis. AIAA Journal, Vol. 17, No. 3, Mar. 1979, pp. 245-252.
14. Crisalli, A.J., Stahara, S.S., Nielsen, J.N., and Spreiter, J.R.: The Development of Rapid Predictive Methods for Three-Dimensional Transonic Flow Fields About Fighter Bomber Aircraft. NEAR TR 198, July 1978.
15. Chen, A., Tinoco, E., and Yoshihara, H.: Transonic Computational Design Modifications of the F-111 TACT. AIAA Paper No. 78-106, Jan. 1978.
16. Mason, W.H., Mackenzie, D., Stern, M., Ballhaus, W.F., and Frick, J.: An Automated Procedure for Computing the Three-Dimensional Transonic Flow Over Wing-Body Combinations, Including Viscous Effects; Volume I - Description of Analysis Methods and Applications. AFFDL-TR-77-122, Oct. 1977.
17. Ballhaus, W., Bailey, R., and Frick, J.: Improved Computational Treatment of Transonic Flow About Swept Wings. NACA SP-2001, 1976.
18. Nixon, D.: Perturbation in Two- and Three-Dimensional Transonic Flows. AIAA Journal, Vol. 16, No. 7, July 1978.
19. Stahara, S.S., Crisalli, A.J., and Spreiter, J.R.: Evaluation of a Strained Coordinate Perturbation Procedure: Nonlinear Subsonic and Transonic Flows. AIAA Paper No. 80-0339, Jan. 1980.
20. Kemp, W.B., Jr.: Transonic Assessment of Two-Dimensional Wind Tunnel Wall Interference Using Measured Wall Pressures. NASA Conf. on Advanced Technology Airfoil Research, Langley, VA, Mar. 1978.
21. Stahara, S.S. and Spreiter, J.R.: A Transonic Wind Tunnel Interference Assessment - Axisymmetric Flows. AIAA Paper No. 79-0203, Jan. 1979.
22. Crisalli, A.J., Stahara, S.S., and Hemsch, M.J.: The Rapid Prediction of Aircraft Store Loading Distributions at Transonic Speeds. NEAR TR-204, Oct. 1979.

6. ACKNOWLEDGMENTS

Support for the research reported in this investigation was provided by the Air Force Office of Scientific Research under Contract No. F44620-75-C-0047 with Lt. Col. Robert C. Smith and Dr. James D. Wilson as Technical Monitors. Support for the wind-tunnel test program was provided by the Air Force Flight Dynamics Laboratory with Mr. Calvin L. Dyer as Technical Monitor.



Wing Coordinates	4 percent Airfoil	8 percent Airfoil	Surface Pressure Locations
$x, in.$	$y, in.$	Percent Chord	Drift, $\theta, in.$
0.0	0.0	0.0	0.0
0.5	0.10	2.5	0.050
1.0	0.11	5.0	0.090
1.5	0.453	7.5	0.172
2.0	0.583	10.0	0.250
2.5	0.703	15.0	0.350
3.0	0.813	20.0	0.450
3.5	0.912	30.0	0.617
4.0	1.000	40.0	0.842
4.5	1.078	50.0	1.090
5.0	1.146	60.0	1.310
5.5	1.203	65.0	1.500
6.0	1.250	70.0	1.654
6.5	1.287	80.0	2.012
7.0	1.313	85.0	2.170
7.5	1.328	90.0	2.478
8.0	1.333	100.0	2.790
			3.000

Fig. 1.- Geometric details of idealized F-16 wing-body model.

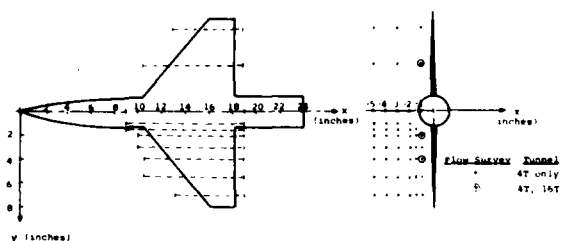


Fig. 3.- Inner flow field survey locations for wing-body model tests in AEDC 4T and 16T tunnels.

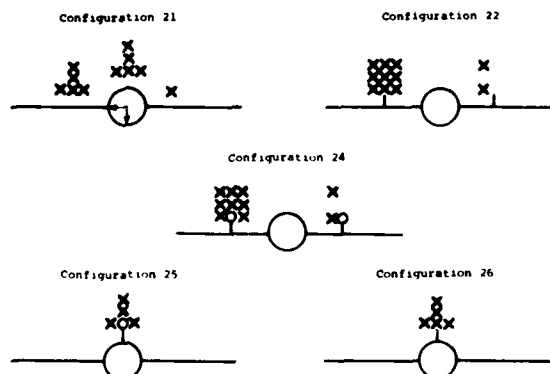


Fig. 5.- Cross-sectional illustration of various wing-body/pylon/store configurations and flow field survey grids employed in AEDC 4T test, viewed from rear of model.



Fig. 2.- Wing-body model and CTS-mounted flow survey probe in AEDC 4T tunnel.

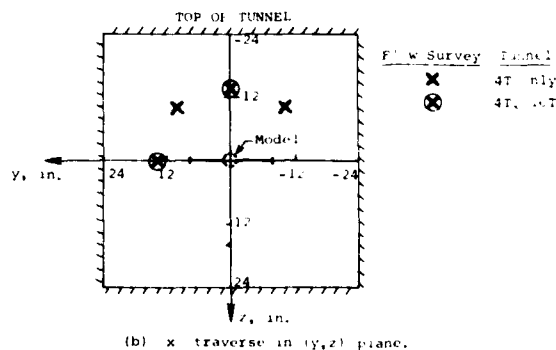
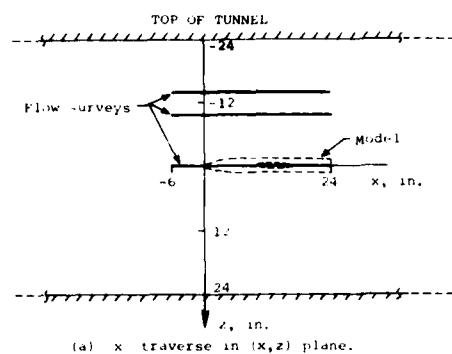


Fig. 4.- Outer flow field survey locations for wing-body model tests in AEDC 4T and 16T tunnels.



Fig. 6.- Wing-body model with wing-mounted pylon and stores and flow survey probe in AEDC 4T tunnel.

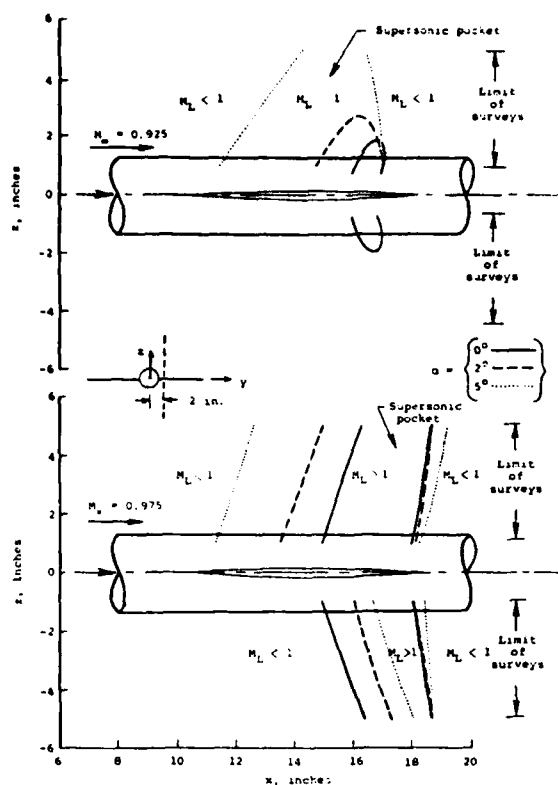


Fig. 7.- Embedded supersonic pockets on pressure and suction side of wing-body model at quarter-span location at the tested angles of attack for $M_\infty = 0.925$ and 0.975 .

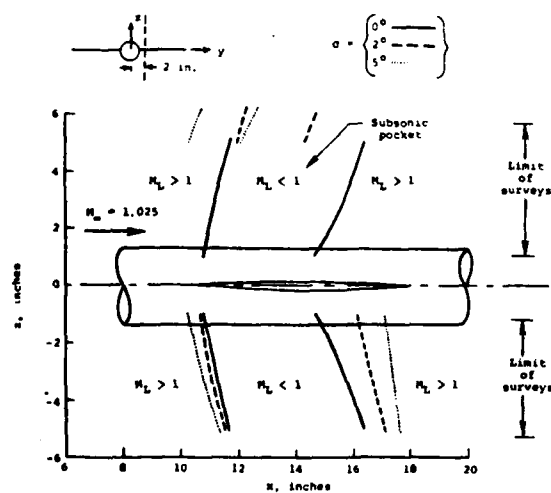


Fig. 8.- Embedded subsonic pockets on pressure and suction side of wing-body model at quarter-span location at the tested angles of attack for $M_\infty = 1.025$.

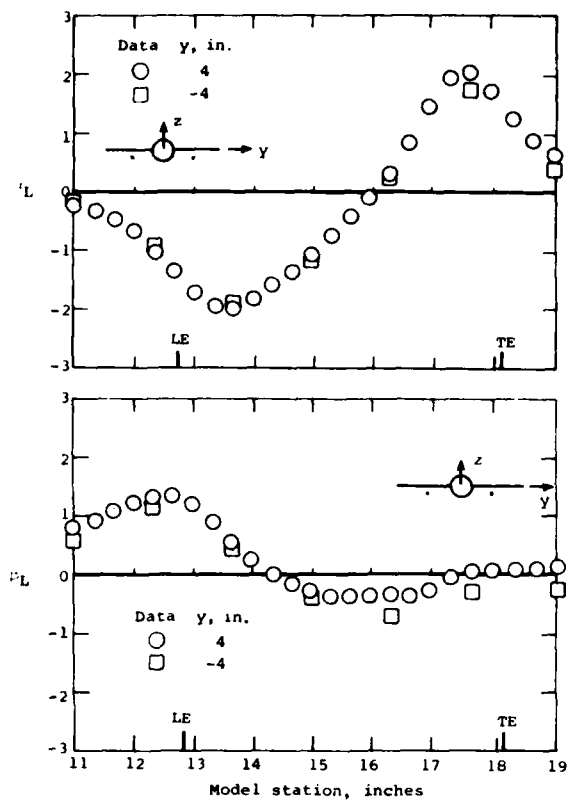


Fig. 9.- Side-to-side symmetry comparisons of local upwash and sidewash of the 4T data for the wing-body model at $z = -1.0$ in., $\alpha = 0^\circ$, $M_\infty = 0.975$.

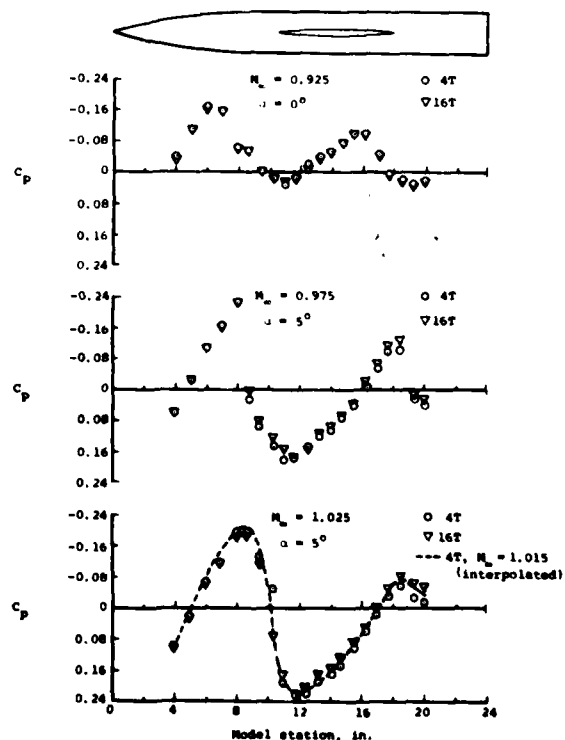


Fig. 10.- Comparison of fuselage surface pressure coefficients from AEDC 4T and 16T tests for the wing-body model.

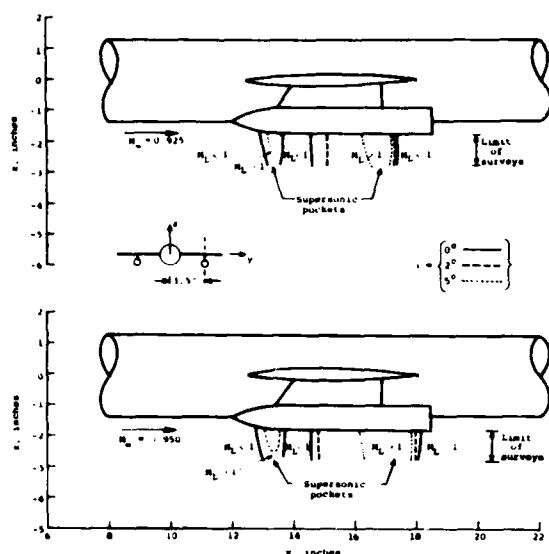


Fig. 11.- Embedded supersonic pockets directly under store for wing-body model with wing-pylon/stores at various angles of attack for $M_\infty = 0.925$ and 0.950 .

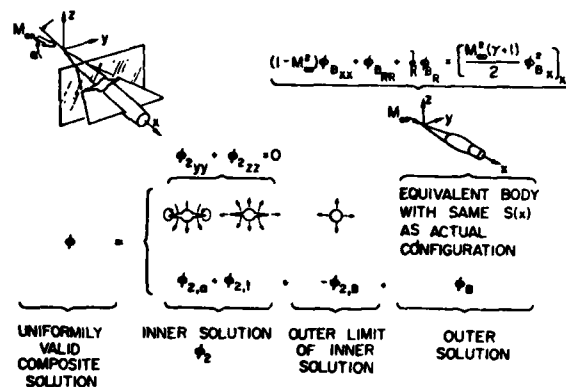


Fig. 12.- Classical transonic equivalence rule for thickness-dominated transonic flows past slender configurations.

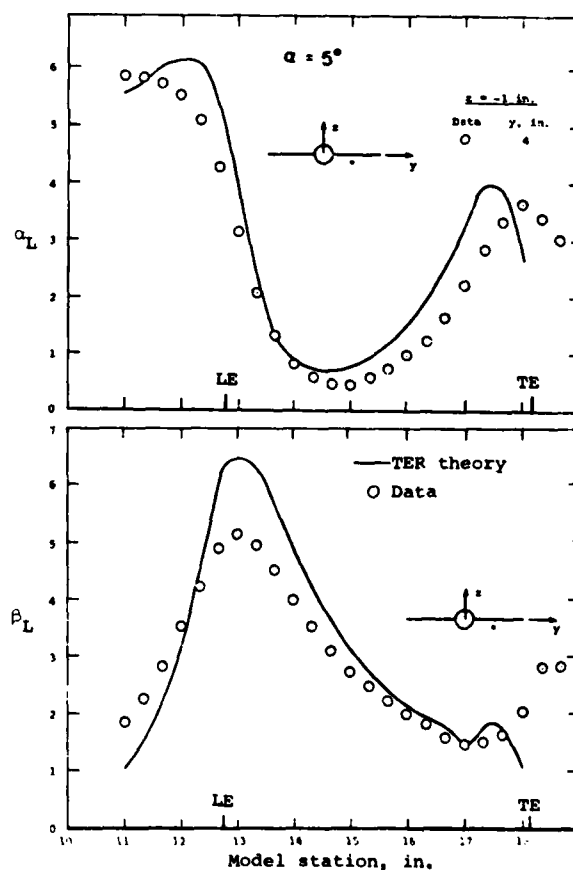
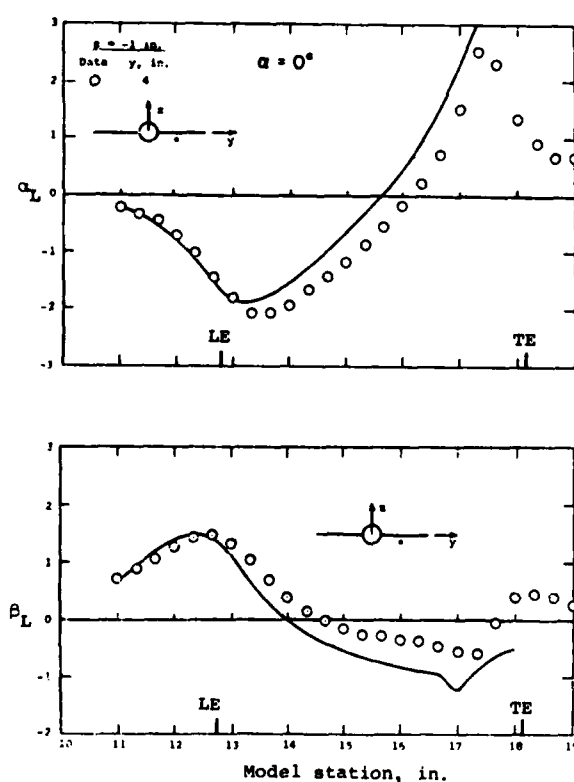


Fig. 13.- Comparisons of classical transonic equivalence rule theoretical results and data for local upwash and sidewash angles for flow past the wing-body model at $M_\infty = 0.975$ and $\alpha = 0^\circ, 5^\circ$.

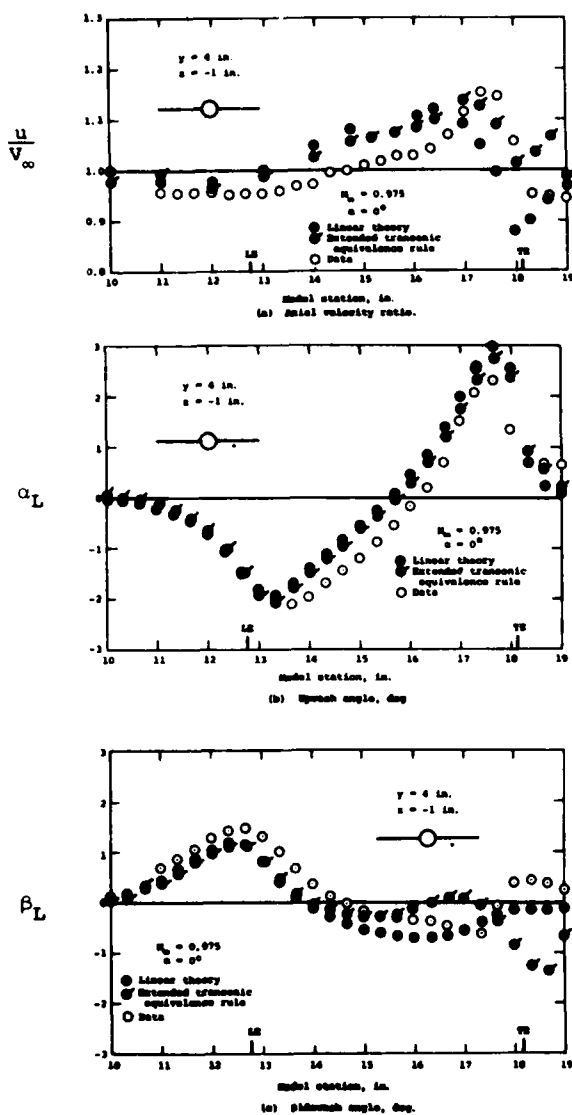


Fig. 14.- Comparison of extended equivalence rule theoretical results and data at $M_\infty = 0.975$ and $\alpha = 0^\circ$.

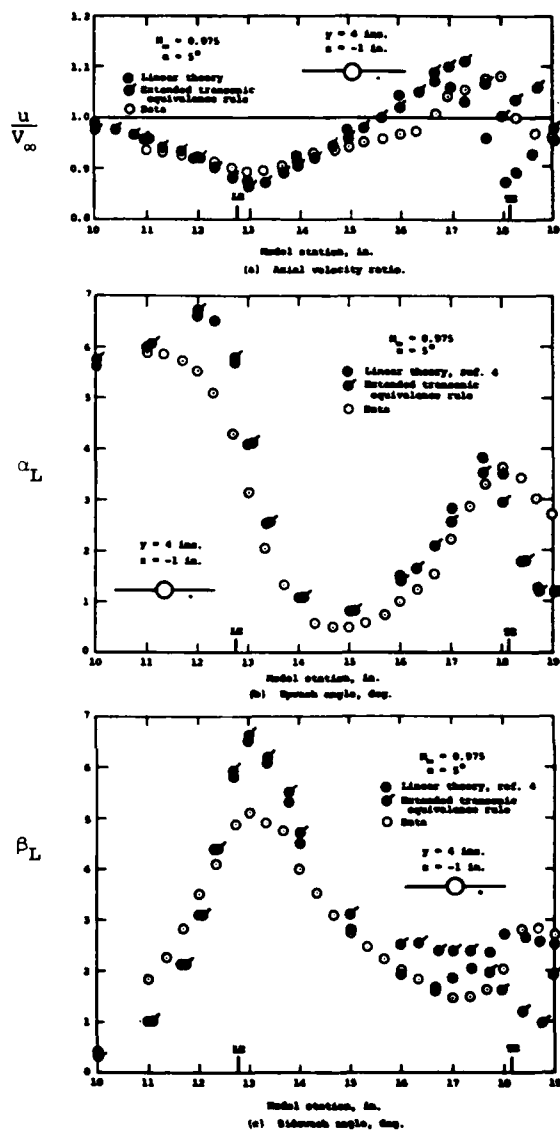


Fig. 15.- Comparison of extended equivalence rule theoretical results and data at $M_\infty = 0.975$ and $\alpha = 5^\circ$.

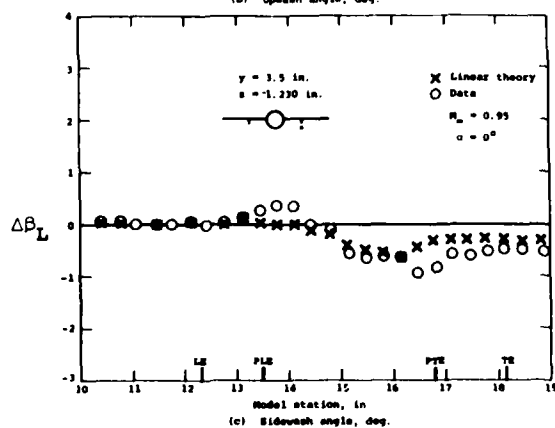
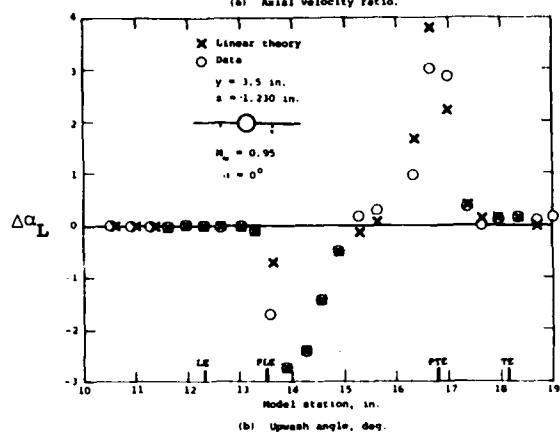
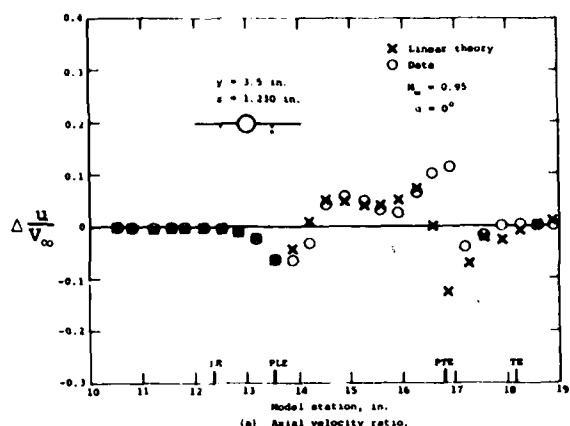


Fig. 16.- Comparison of measured and paneling method theoretical differences between wing-body/pylon and wing-body alone flow field quantities directly under wing pylon at $M_\infty = 0.950$ and $\alpha = 0^\circ$.

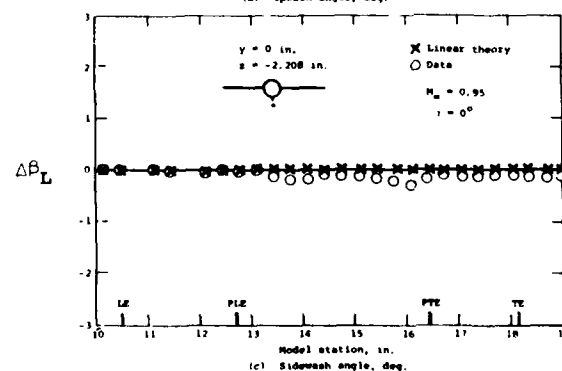
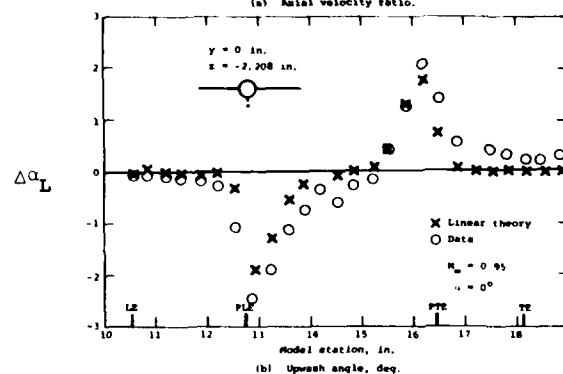
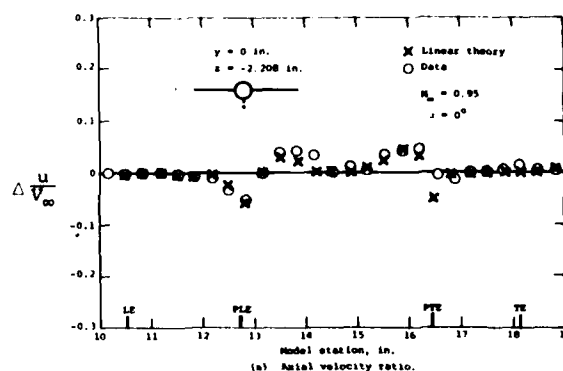


Fig. 17.- Comparison of measured and paneling method theoretical differences between wing-body/pylon and wing-body alone flow field quantities directly under fuselage pylon at $M_\infty = 0.950$ and $\alpha = 0^\circ$.

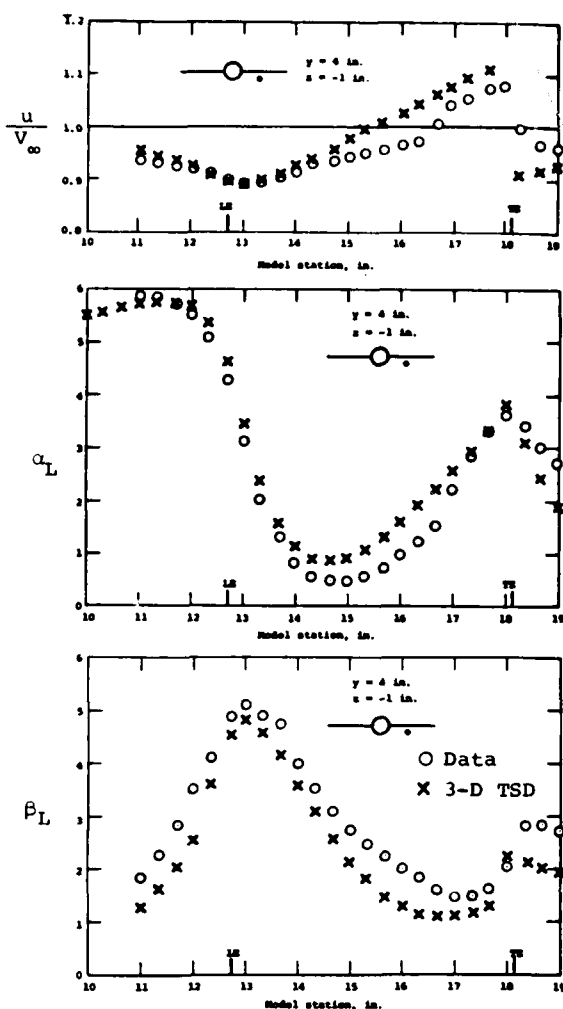


Fig. 18.- Comparison of three-dimensional TSD finite-difference results and data at $M_\infty = 0.950$ and $\alpha = 5^\circ$.

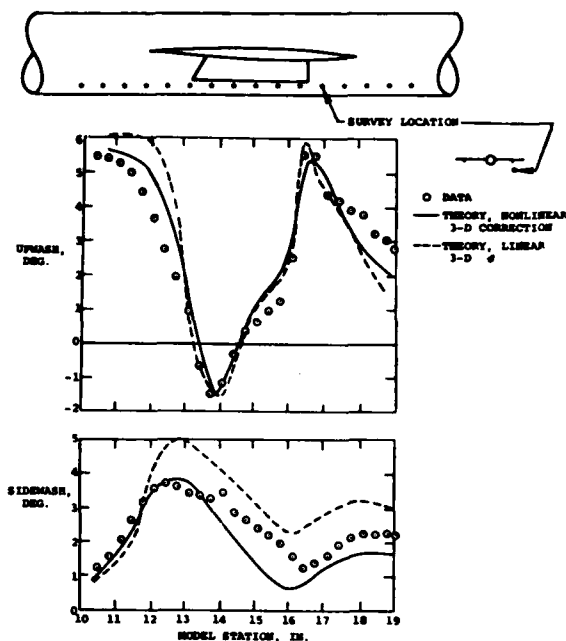


Fig. 19.- Comparison of theoretical and experimental results for local upwash and sidewash angles for the wing-body/pylon model directly under the wing pylon at $M_\infty = 0.950$ and $\alpha = 5^\circ$.

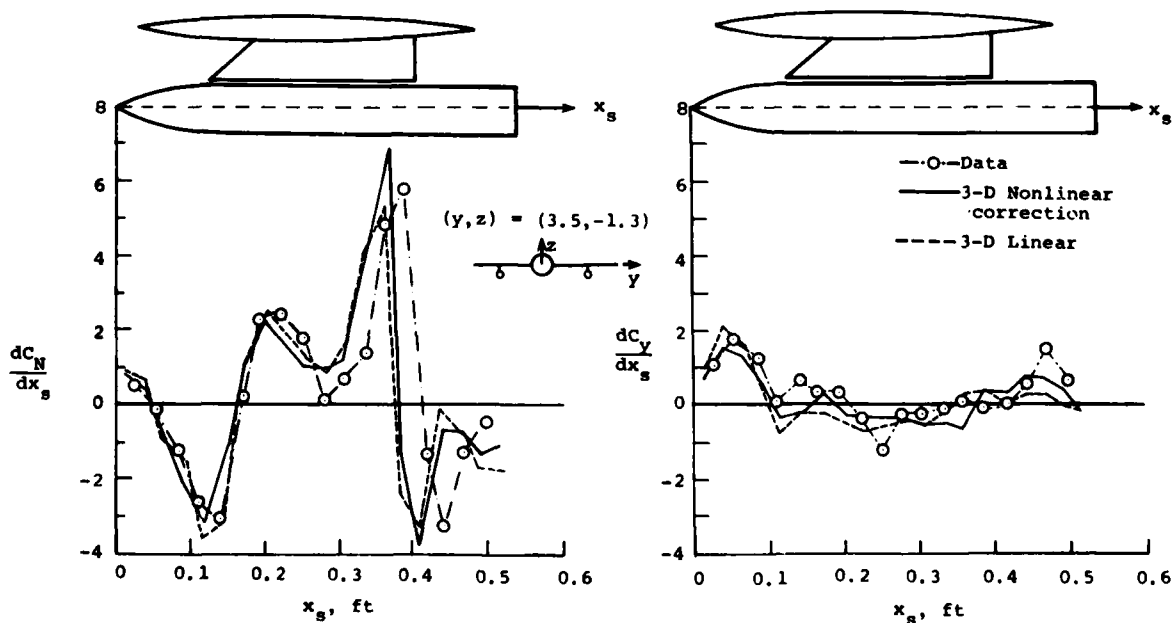


Fig. 20.- Comparison of theoretical and experimental external store loadings for a store location directly under wing pylon at $M_\infty = 0.950$ and $\alpha = 5^\circ$.

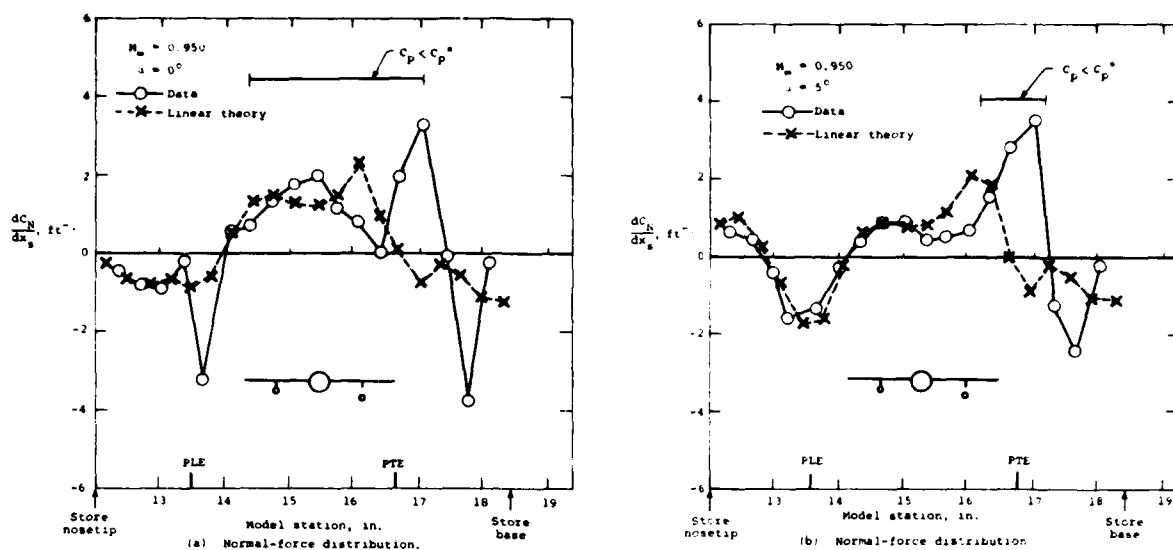


Fig. 21.- Comparison of measured and theoretical normal-force loading distributions based on paneling method flow field for store separated from wing pylon simulation at $M_\infty = 0.950$ and $\alpha = 0^\circ, 5^\circ$.

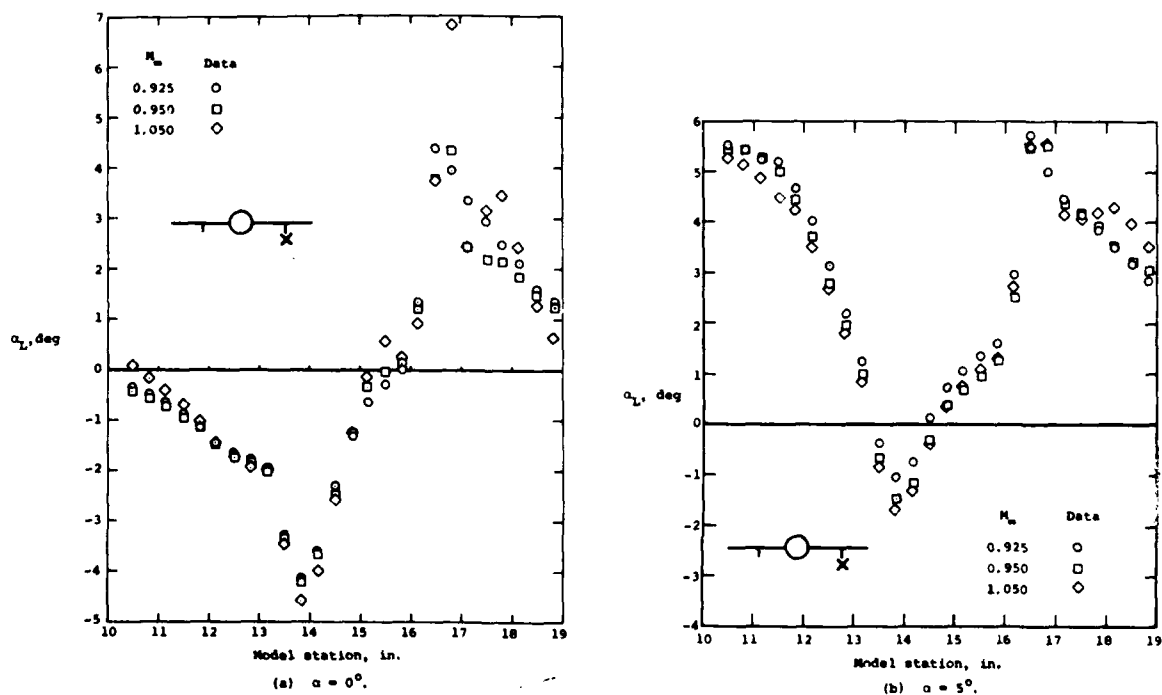


Fig. 22.- Measured upwash for wing-body/pylon model for flow survey location directly under wing pylon at the test Mach numbers and $\alpha = 0^\circ, 5^\circ$.

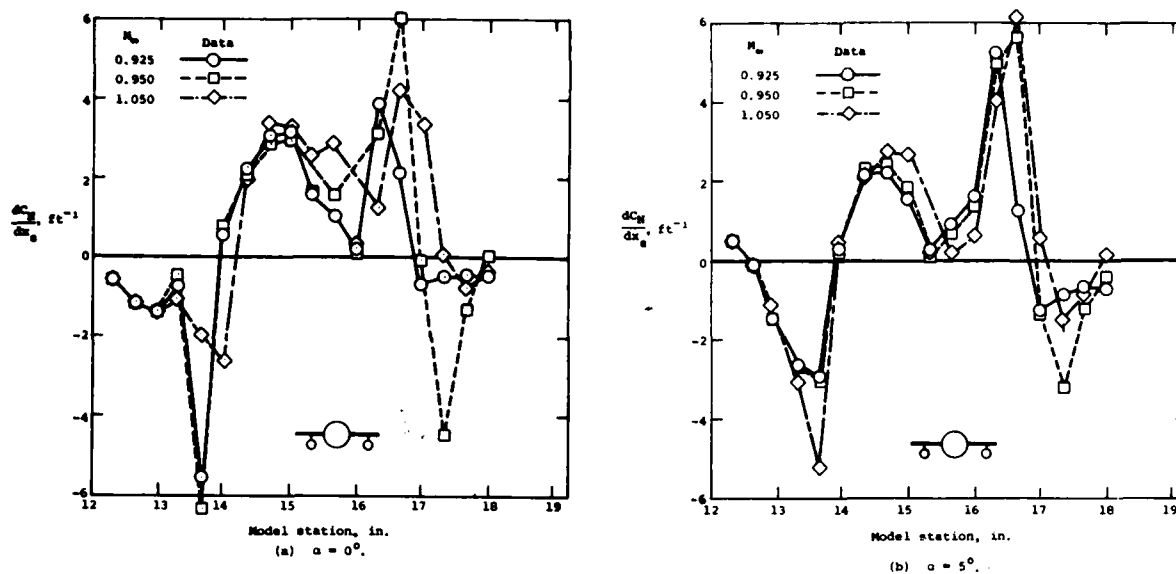


Fig. 23.- Measured normal-force loading distributions for external store attached to wing pylon on wing-body/wing-pylon/store model at the test Mach numbers and $\alpha = 0^\circ, 5^\circ$.

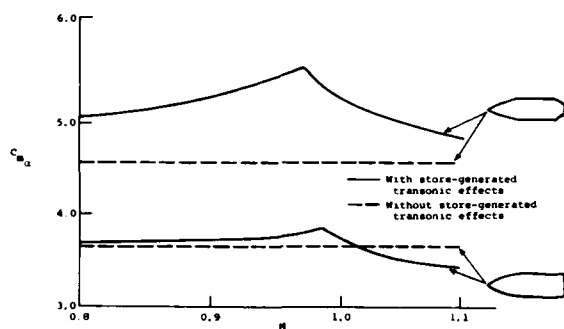


Fig. 24.- Comparison of external store theoretical pitching moment variation through transonic regime with and without store-generated transonic effects for an ogive/cylinder and an ogive/cylinder/conical boattail store.

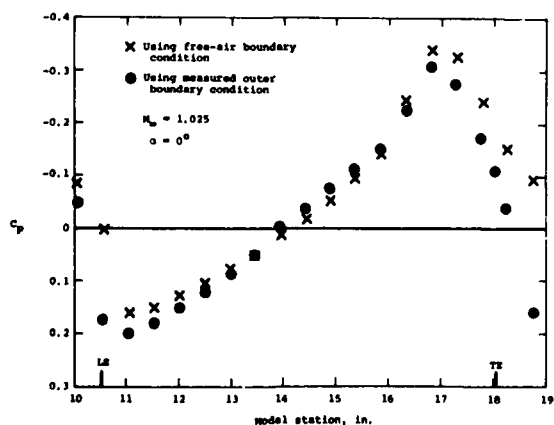


Fig. 26.- Comparison of theoretical surface pressure coefficients on the equivalent body of the idealized F-16 wing-body model using free-air and measured pressure outer boundary conditions.

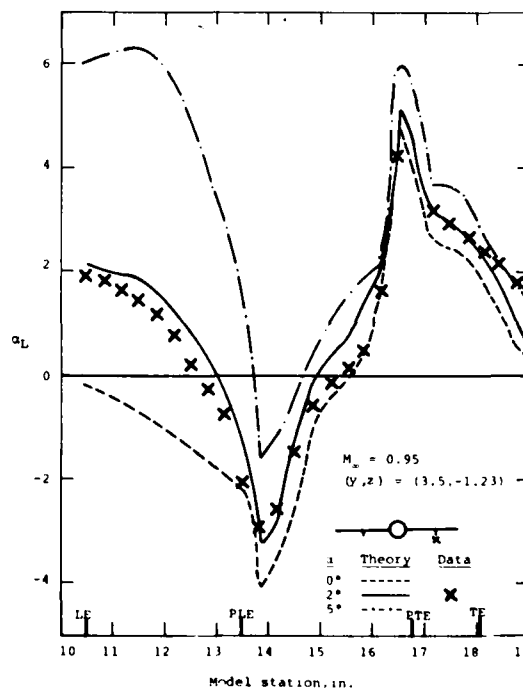


Fig. 25.- Comparison of perturbation-predicted nonlinear results and data for local upwash directly under wing pylon for wing-body/pylon model at $M_\infty = 0.950$ and $\alpha = 2^\circ$.

AERODYNAMIC SUBSONIC/TRANSONIC AIRCRAFT DESIGN STUDIES BY NUMERICAL METHODS

Wolfgang Schmidt

Dornier GmbH, Theoretical Aerodynamics Dep.
D-7990 Friedrichshafen, Germany

SUMMARY

The need and use of computational aerodynamics in the design of aircraft and missile configurations in steady flow conditions is explored through several examples. These include aircraft and missile synthesis programs for predesign and evaluation work of aircraft and missile weapon systems, subsonic and transonic airfoil and high lift design, subsonic and transonic inviscid and viscous wing and aircraft design including leading edge vortex flows, aircraft-engine integration and threedimensional flows with separation.

Use of these numerical and semi-empirical methods can substantially increase airplane performance capabilities while reducing risk, flow time, and testing requirements and thus total cost. The capabilities of current aerodynamic methods are demonstrated by comparison with windtunnel-results and by case studies.

INTRODUCTION

Aircraft development costs have escalated exceedingly within the last four years. Greater emphasis must be placed on exploring analytically and experimentally new configuration concepts aimed at substantially expanding airplane performance capabilities. The present state of the art in aerodynamic analysis and design requires extensive configuration iterations through repeated wind tunnel testing that is costly, time consuming, and relies heavily on inhouse experiences and expertise. Significant advances have been achieved recently in aerodynamic computational methods which allow the numerical computation of flows around three dimensional configurations and provide valuable guides to those seeking understanding of specific problems or those pushing innovative design concepts.

At Dornier a selection of numerical and semi-empirical methods in fluid mechanics has been established which have application to the analysis and design of general aviation and transport aircraft as well as fighter type configurations and missile weapon systems in the subsonic and transonic speed regime. A great amount of effort and emphasis has been placed on the validation of these methods and on establishing limits in applicability. Results to date have been encouraging and the use of those methods can provide a substantial reduction in time as well as cost to achieve a good design.

This paper addresses to the validity and application of current aerodynamic sizing programs, subsonic high lift airfoil and wing analysis methods, transonic inviscid and viscous airfoil and maneuver slat/flap codes, program systems for subsonic and transonic viscous threedimensional flows, engine inlet/airframe integration, buffet onset prediction, and delta wing and strake flow analysis by nonlinear potential flow models.

DESCRIPTION OF COMPUTATIONAL AERODYNAMIC METHODS

A large selection of computational methods are available that have broad application to the analysis and design of general aviation, transport, and fighter aircraft as well as missiles flying in the subsonic and transonic speed regimes. A thorough review of these methods will not be given here since the background literature is easily accessible. On the other hand, their main feature pertinent to the work presented herein are briefly discussed.

Aircraft Synthesis Systems

Three different packages are available at Dornier to design and size aircraft systems, see Ref. 1, 2, 3. The block diagram of method [3] given in Figure 1 is more or less representative for aircraft design procedures. Based on a minimum set of information about mission requirements and aircraft size as well as basic aircraft geometry configuration studies, trade-offs and optimizations can be performed. The aerodynamic characteristics within this program are determined by a semi-empirically based computer program, Ref. 4, which is an improved and extended version of Ref. 5. This method evaluates rapidly and accurately the aerodynamic longitudinal characteristics of general aviation, large, and fighter aircraft from takeoff through landing and through the subsonic, transonic, and supersonic speed regimes. It calculates lift, moment and drag characteristics at both low- and high-lift conditions, including the effects of ground proximity during landing and takeoff, as well as buffet onset boundaries.

As input only the configuration geometry and the flight condition are needed, however, user supplied data can be used internally. The program includes the capability of analyzing both fixed-wing and variable sweep-wing configurations as well as strake-wing and supercritical wing designs.

Missile Synthesis System

A similar computer package is used for missile design, Ref. 6. A variety of different missile configurations can be handled by the program whose block diagram is depicted on Fig. 2. The aerodynamic characteristics within this package are again determined by a semi-empirically based computer program, Ref. 7, which is specially tailored for slender missile configurations. This method evaluates very rapidly the aerodynamic longitudinal characteristics of missiles from 0 to 90 degrees angle of attack and roll through the subsonic, transonic, and supersonic speed regimes. For hypersonic speed the angle of attack range is restricted to attached flow. As input only the configuration geometry and the flight condition, are needed. The program includes the capability of analyzing wings and tails in +, X, as well as interdigitated positions. Bodies can consist of different axisymmetric sections and for wings also flaps are permitted.

Subsonic Airfoil and High Lift Systems Design

Several two-dimensional subsonic methods have been developed, by various organisations, which are able to analyse viscous single and multiple element airfoil flow up to maximum lift, e.g. Ref. 8, 9, 10. All three methods are in use at Dornier since the physical models used are quite different.

The method of Grashof [8] at present is restricted to the analysis of twodimensional airfoils in viscous incompressible steady flow with or without separation. For this theory two properties of such flows with dead air regions are of basic importance:

- in the separated flow a pressure distribution appears which is typical for dead air flows, e.g. $C_p = \text{const}$
- between the dead air region and the distant wake a relatively narrow region exists, where the velocities vanish in time average (free stagnation point)

The physical flow is modelled by three zones, Fig. 3

- the inviscid and an irrotational external flow
- the boundary layer flow
- the dead air flow

These three zones interact mutually. The events within the dead-air region are not studied in detail, but only their integral reaction upon the external flow is considered. The influences of the boundary layer and of the dead air upon the external flow are simulated by a fictitious body. Within the attached flow region the physical body is thickened by the displacement thickness of the laminar or turbulent boundary layer. Downstream of the separation point a fictitious contour has to be constructed such that the potential flow over this body is just causing that pressure distribution which is typical for dead air flows.

Therefore in potential flow a mixed boundary value problem has to be solved. The rear stagnation point in this idealised flow corresponds to the free stagnation point in the real flow and coincides with the trailing edge of the fictitious body extension.

The method of Jacob [9] can be applied to simulate the viscous flow over systems of up to five airfoils in almost incompressible ($M_\infty < 0.20$) flow including multiple separation on the upper surface. The method verifies a three part flow model

- attached flow or flow with short separation bubbles
- "open separation" regions
- "closed separation" zone

The attached flow is computed as the converged solution of the potential flow and the laminar or turbulent boundary layer including transition and short separation bubble treatment. The "open"-type separation is simulated by typical source distributions (from numerical experiments) which simulate a dead air region with nearly constant pressure. Only past the last airfoil section in streamwise direction a closed separation zone is constructed by sinks and sources. The potential flow models are solved by a superposition of basic solutions. The boundary layers are computed by integral methods. No special attention is given to confluent layers.

The method of Leicher [10] is the most general one, as far as the range of airfoil systems and the types of separation are concerned. In contrast to the preceding ones, this method does not model the separated region as a dead air region by a potential flow model, but computes the displacement thickness of the separated boundary layer. A subsonic compressible twodimensional panel method and a set of boundary layer programs are connected with each other by the surface transpiration or equivalent source concept. By successive application of both programs finally a converged viscous flow analysis is available. Drag is estimated on the basis of the Squire and Young formula correlating the momentum losses to drag.

All boundary layer methods used are of integral type. The laminar code is a twodimensional version of Stock's general compressible laminar boundary layer integral method [11]. Transition can either be specified by input or is estimated by a modified empirical Michel correlation. Laminar stall as well as short laminar separation bubbles are included. For attached turbulent boundary layers Nash's method is used. Turbulent separation is modeled within the turbulent boundary layer method by semi-empirical assumptions as well as reattachment. Confluent boundary layers are treated identically as in Goradia's program, Ref. 12.

Three-Dimensional Subsonic Potential Flow-Methods for Arbitrary Configurations

A computational method has been developed in Ref. 13 that can treat arbitrary subsonic three-dimensional potential flows including inlet flow fields. This is a linear method solving Laplace's equation satisfying exact boundary conditions based on Ref. 14 and 15. In this approach the velocity potential at any point in a flow field is expressed in terms of the induced effects of source and doublet (or vortex) sheet distributed on the boundary surfaces. The configuration surfaces are divided into panels, and hence, this approach is known as a panel method. Essentially, this is a general three-dimensional boundary value problem solver that is capable of being applied to most problems that can be modeled within the limitations of potential flow. Compressibility effects are approximated by the Goethert rule, and thus analysis of transonic flow is not possible with this method. Viscous effects can be represented by the surface displacement or transpiration concept. An improved higher order method [16] is available as a pilot code. These methods are ideally suited for analyzing complex aircraft configurations in subsonic flow.

Three-Dimensional Vortex Lattice Method for Arbitrary Configurations Including Vortex Lift

A method based on vortex lattice theory has been developed at Dornier that can be applied to the combined analysis, induced drag optimization, nonlinear vortex lift (based on Polhamus Analogy) computation, and jet simulation of three-dimensional configurations of arbitrary shape [17], [18]. This is a linear method solving Laplace's equation satisfying thin wing boundary conditions on the camber surface and optionally curved wake influence. The optimization process utilizes the method of Lagrange multipliers. Compressibility effects are approximated by the mass flux rule. Its ease of use, high computational speed, and design capability make it particularly valuable in evaluating design variations, arriving at optimized configurations, and designing new wing camberline shapes.

Three-Dimensional AIC Methods for Wings with Leading Edge Vortex Separation

The flow at the leading edge and tip edges of a swept wing with sharp edges separates at moderate to high angles of attack, the separation producing vortex sheets that roll up into strong vortices above the upper surface of the wing. The formation of these vortices is responsible for the well known nonlinear aerodynamic characteristics exhibited over the angle-of-attack range. Several theoretical methods are in use to predict these characteristics. While the leading-edge-suction analogy as used in Ref. 18 and already described in the preceding chapter is well suited for total force and moment prediction, more sophisticated methods are necessary to predict detailed pressure distributions and flow fields above swept wings with leading-edge vortex separation. The use of vortex lattice concepts with free vortices in Ref. 19, 20, 21 led to methods which reasonably well predict the vortex cone location, but still do not produce good detailed flow fields. Only the application of a new, general, potential flow computation technique as described in Ref. 22, 23 led to reasonable solutions. Based on this fundamental work efforts are going on at Dornier, Ref. 24 to establish an accurate and reliable method for flow field prediction with free vortex flow. The essential elements of these flow models are depicted on Fig. 4. On all surfaces the flow must be parallel to the configuration. The trailing edge sheet (wake) is either frozen or aligned with the local flow, the free sheets emerging from the wing leading edge and tip are force free, the fed sheet is an extension of the free sheet, and feeds vorticity to the vortex core. Kutta conditions are imposed along the appropriate leading, side, and trailing edges of the wing in the presence of free sheets emanating from these edges. Bi-quadratic doublet distributions are used as singularity-types.

Wing Characteristics with and without Flaps in Viscous Subsonic Flow Including Separated Regions

In the past extensive evaluation of experimental data has been performed to establish the semi-empirical method in Ref. 25 for the estimation of lift distribution, total lift, moment and drag coefficients for moderate to high aspect ratio wings with and without flaps up to maximum lift.

Starting from either experimental or theoretical airfoil section characteristics beyond maximum lift the semi-empirical correlations are used to construct wing section characteristics which include planform, flap and other three-dimensional geometrical effects. In the next step a lifting line method is used iteratively to correlate the spanwise effective angle of attack and the local lift coefficient in agreement with the wing section characteristics. Body effects are included through its influence on lift distribution. Finally, the local lift coefficients are used to compute from the corresponding wing section characteristics moment and drag coefficients. The method has to be applied very carefully, especially if planform shapes are used which exceed the configurations being used for establishing the empirical correlation airfoil-wing section characteristics.

Three-Dimensional Viscous Body Flow Field Analysis

A general three-dimensional boundary layer method has been developed at Dornier that can analyse either laminar or turbulent compressible flows on arbitrarily shaped wings and bodies in curvilinear nonorthogonal coordinates Ref. 27, 28, 29.

The laminar method is not restricted to small crossflow. For the evaluation of the integral thicknesses one parameter velocity profiles for the main stream direction and two parameter velocity profiles for the cross-flow direction are used. The one parameter profile family is based on the similar solutions of the boundary layer equations, the two parameter profile family results from a polynomial expression, where no boundary conditions of the Pohlhausen type (direct relation to gradients of flow properties at the outer edge of the boundary layer (compatibility condition)) are applied. The x- and y-momentum and the x- and y-moment of momentum integral equations are used for the solution. Only for the case of orthogonal coordinates 1st order moment of momentum equations are introduced. They result from the x- and y-momentum equations, which are multiplied by the velocity components u and v, respectively before the integration. For non-orthogonal coordinates 1st order moment of momentum equations do not produce solutions even when multiplying the momentum equations by linear combinations of the velocity components u and v. For curvilinear, non orthogonal coordinates 2nd order moment of momentum equations are developed, where the multiplication is done by the square of the resultant velocity \bar{U} . Since these equations are much more complicated, the 1st order equations, which concern only the orthogonal case, are used for these problems.

The turbulent integral method has been developed at Dornier following ideas of Myring and Smith. The streamwise profiles are represented by Coles profiles, the cross-flow profiles by Mager or Johnston profiles. Skin friction is computed directly from the velocity profiles. The influence of compressibility is accounted for by applying Eckert's reference temperature concept. The equations finally solved are the x- and y-momentum equation and the entrainment equation (equilibrium entrainment). To provide for non-equilibrium entrainment lag entrainment has been included. Both methods have been tested extensively against finite difference methods, other integral methods and experimental results and have proven to be very reliable and fast tools.

To provide the inviscid outer flow field as output to the boundary layer program, interface programs are used to transfer the corresponding data from the inviscid method to the boundary layer program and vice versa. The inclusion of boundary layer technique into the analysis of transport and fighter aircraft design provides for a better representation of the real flow field for determining wing pressure, but also enables more accurate drag estimates to be made as well as estimates of maneuver-boundaries.

More recently there is increasingly interest in numerical solutions of the Navier Stokes equations to simulate flowfields with separation. In Ref. 26 a three-dimensional steady Navier-Stokes solver is presented which applies to the vorticity formulation. The higher order finite difference approximation is characterised by a free parameter derived from an exact solution of the linear form of the Burgers equation. This parameter balances the convective part of the difference equation thus causing an upwind (convective) scheme for large and a centered (diffusive) scheme for small cell Reynolds numbers. At present the application of this method is restricted by its extensive CPU-time for three-dimensional cases.

Safe Release and Flight Path of External Stores

Present day fighters have to perform missions carrying quite different external stores under wing and fuselage. Those external stores not only influence the aerodynamics of the carrier, but also cause problems during release. A set of computer programs has been developed at Dornier [31] which reasonably well predicts as well safe release under disturbances and carrier dynamics as delivery characteristics. The carrier interference effects on the store load are computed by a modified semiempirically corrected singularity method, while the store aerodynamics are taken either from experiments or the missile aerodynamics program of Ref. 7. Carrier and store dynamics are simulated by a 6 DOF-program. Main purpose of this prediction method is to reduce the total amount of wind tunnel testing and flight test to validate the flight envelope permitted under carriage.

Two-Dimensional Methods for Transonic Airfoil and Cascade Analysis/Design

Several two-dimensional transonic methods have been developed or evaluated at Dornier, which are able to analyse airfoils or cascades [32], [33], [34], [35], [36]. The TSP-methods are highly improved by the mass-flux formulation [34] even for thick airfoils and have demonstrated its usefulness in as much as analysis and mixed analysis/design problems can be solved including viscous effects based on the displacement thickness as well as unsteady transonic flow for flutter prediction [35]. Flow time as well as computer costs are fairly small. The full potential methods are superior at high angle of attack and for analysis/design in the leading edge region. Jameson's FL06 [16] has proven to be very accurate and fast due to his fast solver but is lacking flexibility due to the circle plane mapping involved. There is some indication that the finite volume techniques like the flux finite element method [37] for the full potential equation or the quasi-time dependent method [38] for the Euler eq. are the more interesting ones as far as the engineering environment to support and guide a design process is concerned. An advantage of the finite volume Euler method is the accuracy over the whole speed regime from subsonic to supersonic free stream Mach numbers even for flow with strong shocks.

A finite volume method for the solution of the two-dimensional time - averaged Navier Stokes equations is under development at Dornier [39] but more work has to be done to make it useful for practical design.

Two-Dimensional Methods for Transonic Multielement Airfoil Analysis/Design

As a joint venture between Saab and Dornier a numerical method has been developed for the analysis and mixed analysis/design mode of two-dimensional transonic flow around twoelement airfoil systems [40]. [41] Arbitrarily shaped airfoil sections can be treated through the use of a series of conformal mappings. The physical domain outside the two sections is mapped into the ring domain between two concentric circles, the interior of the outer circle being the exterior of the main airfoil and the exterior of the inner circle being the exterior of the secondary airfoil. Within this ring domain the flow field is computed solving the nonconservative full potential equation by means of Jamesons rotated difference scheme and SLOR in combination with nonlinear extrapolation and multigrid technique. Viscous flow is simulated by coupling the inviscid code to a set of boundary layer methods [38].

Two-Dimensional/Axisymmetric Methods for Transonic Inlet Flow Fields

Two different methods are being used at Dornier, one developed at Saab [43] to compute the transonic flow around axisymmetric inlets for a prescribed mass flow ratio. The inlet consists of an initial part of arbitrary geometry which is continued to downstream infinity as a straight circular tube. With a sequence of conformal mappings and a final coordinate stretching the whole exterior and interior flow field is mapped to a rectangular domain in which the full potential equation is solved using type-dependent line relaxation. The second one is the Dornier-developed finite volume method for calculating axisymmetric and plane pitot-type inlet flow fields at supersonic as well as subsonic free stream Mach numbers [44]. This second order accurate time dependent method solves the Euler equations in integral conservation-law form. The equations are written with respect to a cartesian coordinate system in which at supersonic speed a body and bow shock fitted mesh adjusts in time to the motion of the bow shock that is automatically captured as part of the weak solution. At the compressor entrance plane inside the cowl static pressure is prescribed as subsonic boundary condition. The method can treat arbitrary lip shapes and is presently being extended to a three-dimensional version. The integration of the pressure distribution from the inlet throat to the crest will provide valuable data for the drag estimation as long as no large viscous effects are apparent.

Three-Dimensional Transonic Potential Flow Methods

Several three-dimensional transonic potential flow methods have been developed, by various organizations, which are able to analyse either isolated wing or wing-body combinations [45], [46], [47], [48], [49], [51] Evaluation of the methods developed at Dornier [46], [50], the methods developed as a joint venture with FFA, Ref. 48, 51, and a Dornier version of FLO22 indicate that the three-dimensional Dornier TSP-MF method based on the mass flux concept is a useful design tool, in as much as arbitrary fuselage shapes can be modeled, analysis as well as mixed analysis/design problems can be solved, shock strength as well as positions are well predicted, and the low computer cost in combination with the highly automated input provide the basis for a method to be used in the engineering environment. On the other hand the lack of dense mesh spacing in the nose region imply use of grid embedding as described in Ref. 51. FLO22 quite often is giving fairly good agreement with experimental results, but it should be kept in mind that this method is not conservative and neither does give correct drag data nor correct viscous results if a boundary layer method is coupled. The detailed two-dimensional studies indicated that the approach of using finite volume techniques to solve either the full potential equation or the Euler equations are the most promising ones for complex three-dimensional flow computations. A pilot code on Euler has been completed [52], on the full potential equation is nearly completed [53].

Buffet Onset Prediction for Wings

Some years ago a light buffet prediction method has been developed at Dornier as outlined in Ref. 54. A buffeting coefficient is defined which is directly related to the rms value of the wing root bending moment. Assuming that local lift oscillations are caused by flow separation and are proportional to the length of the separated flow at a spanwise station, this buffeting coefficient is set equal to the integral evaluated along the wing span of the product of local separation length and the distance from the wing roots. Based on empirical correlations it was found that light buffet is reached if this buffet coefficient is equal to 0.1. Separation length versus span can either be estimated by stripwise application of two-dimensional transonic and boundary layer methods or fully three-dimensional viscous flow simulation like in Ref. 50.

The limit of this method is reached if no longer the relationship between separation length and the rms value is valid. To avoid this problem in Ref. 50 a semiempirical approach is included based on working plots established by evaluating experimental data. These plots include the influence of geometrical and aerodynamic parameters on the buffeting behaviour of wings.

APPLICATION OF METHODS

Aerodynamic Sizing Program for Aircraft

Aerodynamic sizing programs are highly important tools in the initial phase of configurations studies. Their low cost, input simplicity and reliability in use prove them very useful for project engineers. However, aerodynamicists carefully have to survey the application since the integrated program system is based on semi/empirical methods for the components, which implies a limitation in the configuration space. To improve accuracy input of specific aerodynamic characteristics is allowed as soon as data are available either from experiments or more accurate methods. On Fig. 5 a redesign of the F4 Phantom is shown, only based on a three-side view and an adjustment in $C_{L\ max}$ based on experience with an other fighter. The agreement looks fair.

Aerodynamic Sizing Program for Missiles

Although missile configurations look much simpler in geometry than aircraft, their aerodynamics are highly nonlinear and very hard to predict. However, the present semiempirical prediction code proves to be very general in application and fairly accurate. This method not only is used for performance prediction but also for store separation. Moment characteristics imply the limitations of this method, especially in the range of $20 < \alpha < 70$ degrees. But even other much more sophisticated methods suffer from inaccuracy in this angle of attack range.

Due to its generality and input simplicity as well as very low cost this method is used widely. Again, the final accuracy can be improved by input of component characteristics if available. On Fig. 6 a typical example for a canard controlled configuration is portrayed. While lift and drag look very good, the moment curve has some deviation in magnitude. No fitting has been applied to this case.

Subsonic High Lift Section Analysis

The performance of subsonic mechanical high-lift devices is of high importance for the overall economy and operational efficiency of present day general aviation and transport aircraft. Although a lot of experimental data is available, and thus sizing can be applied by modifying existing configurations, theoretical tools are important and needed. However, due to the complexity of the flowfield with a variety of separated regions all component methods are suffering from modelling. Therefore different methods with different models are used at Dornier to get different results from different points of view.

Grashof's method is presently restricted to single element airfoils, but the flow model used seems to be reliable and accurate. A comparison with experiments is depicted on Fig. 7. Although pressure constancy in the separated region is not prescribed explicitly, the agreement is good.

For Jacob's method different comparisons are known from his publications, even with ground effects. In the present paper only a comparison of results for a three- and four element configuration is shown to indicate the value of such a method for understanding slat efficiency. The four element is the same as the three element one, but with slat. The decrease in the pressure peak on the main airfoil and the first flap is nicely shown. Almost no influence is indicated on the second flap.

For Leicher's method various comparisons are found in Ref. 10, but the separation modelling has been improved recently to provide better results for flows with large separated regions.

Subsonic Panel Methods

Panel aerodynamic methods have been used at Dornier since 1971. During this time period, the panel method has been validated as a very reliable tool in predicting the aerodynamic characteristics of airplanes operating at subcritical Mach numbers. More recently the handling of such programs has been highly improved by semi-automatically generated paneling using CADAM-software as depicted on Fig. One interesting example of its use has been on the initial design phase of the Alpha Jet [13]. A typical example showing isobars is depicted in Fig. 1. In this example, main emphasis has been given to the design of the channel between the wing lower surface, the body side and the engine inlet.

The panel methods can also be used to study the mutual interference between different components including the engine inlet for different engine conditions. Panel arrangement and results in comparison with wind tunnel experiments are portrayed in Fig. 2.

Such results provide very accurate information for local design modifications, while only final selected ones are tested in the wind tunnel to verify predictions.

Vortex Lattice Methods

Vortex lattice methods are very easy to handle and fast tools for design studies, not only for simple wing shapes but also for winglets, high lift devices, wind tunnel wall interference, shrouded propellers, jet effects and wing-wing interference problems. They provide not only accurate lift and moment curves, but also very good induced drag results. This method has been used extensively at Dornier for linear flow problems, while the use in nonlinear aerodynamics is fairly new. As shown in Fig. 3, the vortex-lattice method in combination with Polhamus-Analogy is a very reliable tool to predict the nonlinear flow behaviour caused by leading edge separation [18]. The deviations in the moment curve for small, resp. negative lift is due to deficiencies in the body description. Even configurations with leading and/or trailing edge flaps are simulated nicely. For modern fighter design with wings of large sweep this method plays an important role in wing as well as maneuver flap design.

Leading Edge Vortex Flow Fields

In the present form, the program is a research tool for numerical experimentation; the major emphasis is to incorporate different models and to study basic modelling as well as flow field effects.

Delta wings provide many inside for understanding leading edge vortex flow. In addition, they represent a simple geometry which is ideal for numerical experimentation. Fig. 13 shows the free vortex sheet development over the wing and a comparison of the pressure distribution. The agreement with the Boeing method is very good, but the experimental pressures still are different. Nicely the decrease in pressure due to the trailing edge Kutta condition can be seen. On Fig. 14 the importance of a proper wake modelling can be seen since the wake can not be treated as frozen at all to reproduce the correct physics shown by the Hummel-experiment. Continuing work is going on to simulate the flowfield over strake-type wings and bodies with free vortices by coupling with boundary layer programs.

Subsonic High Lift Wing Analysis

This very useful tool for high lift design of general aviation-, transport- and at least moderate aspect ratio fighter configurations meets the engineering requirements since it is a fast tool for the estimation of maximum lift as well as stall characteristics in the pre-phase studies of aircraft, when no windtunnel results are available. The use of this method needs an experienced aerodynamicist for complex configurations with part span flaps or boundary layer fences are involved. The upper part of Fig. 15 shows the comparison in lift, moment and drag versus experimental results for an unswept AR-9 wing. The lower part portrays the lift distribution versus span for three angles of attack in comparison with experimental results from oil flow pictures. The configuration now is an AR-6 wing with part span flaps. Both comparison clearly indicate the usefulness of such a method.

If further experiments are available the range of applicability can be increased or updated by establishing new working plots.

Three-Dimensional Viscous Body Flow Field Analysis

The three-dimensional boundary layer development greatly influences the performance of subsonic and transonic aircraft. While the use of boundary layer method to study wing characteristics has become quite popular, e.g. [27], [55], [56], only a few items are known for three-dimensional body analysis. Through its validation the Dornier method [28], [29] has been extensively tested for flows over ellipsoids at angle of attack. Fig. 16 portrays some of the results for an axis-ratio 8 ellipsoid.

Separation line pattern over the whole range of incidence agree well with those predicted by the finite difference method of Geissler and even the shear stress at the wall compares very well with that measured by DFVLR or computed by Cebeci's FD method. More recent studies [29] on the symmetry lines nicely reproduce the switching characteristics of the separation point versus α [Fig. 17].

However, more work has to be done to combine this method with inviscid programs in order to study separation and vortex shedding from bodies.

On Fig. 18 first results of Stock's inverse integral method [30] are shown for an infinite swept wing. This code will provide the basic capability to compute through separation.

Although it is presently far beyond the engineering application, some results of Haase's three-dimensional steady Navier Stokes Solver [26] are portrayed on Fig. 19 for the ellipsoid mentioned before. Even in research computations the applications are limited due to the total amount of grid points either in Re-number (scaling of the thin layers) or in complexity. Future computers and accelerated schemes, however, will provide the basis for such computations.

Safe Release of External Stores

Aircraft store compatibility is one of the major problems for present day fighters. One indication might be the devotion of a whole session of the present AGARD Conference to this subject. The problem can be seen at least three-part: Carrier-disturbances by store carriage and release, free store release, and accurate weapons delivery. The present examples only address to safe release, although methods are frequently in use to study the other effects. The attempt of Fig. 20 is to show by simulations with the computer code of Ref. 31 the influences of carrier interference and dynamic store derivatives on the release of two different store. The final simulation agrees well with the experimental data. But I would like heavily stress the importance of the inclusion of dynamic derivatives in store release simulation since they seem to play an important role.

The present method is extensively used in release studies for new configurations or for standard carrier with new stores. In a more recent version even the release of target-type stores fixed to a cable can be simulated.

Transonic Airfoil/Cascade Analysis/Design

The validation of two-dimensional transonic potential flow methods is almost established by numerous supercritical airfoil designs based on CFD methods. Fig. 21 shows computed versus measured pressure distributions for the Dornier A-1 12 % thick airfoil, viscous as well as wall effects in the computations included [32]. The result clearly indicates the importance of boundary layer effects even in the design region. Although design as well as analysis of this section have been done using TSP, we are aware of the limitations of TSP-methods. However, the type of numerical method, especially conservation of mass, can have stronger influence on the results than the TSP-assumptions. Therefore, more recent studies led to the development of a two-dimensional flux-finite element method for the full potential equation which at present only has been verified for the analysis/design of cascades [37], see Fig. 22, and to a finite volume method to solve the quasi time-dependent Euler equations around airfoils [38] as shown in Fig. 23. For comparison, also the TSP-MF results are included, while there is almost no difference in the non-lifting case, a large effect is apparent for lift. Careful studies of shock and Kutta-condition will clarify this difference.

Both flux methods are very general in their application to arbitrary configuration shapes and nonorthogonal mesh systems. While the FFEM-method is very fast (0.15 ms per iteration and mesh point IBM 370/158), the finite volume method (0.8 ms) is best suited to produce datum solutions and accurate results for strong shocks which lie beyond the isentropic assumptions.

Since transonic flow phenomena do not only play an important role in aerodynamic design but also in flutter analysis, the Dornier-TSP method has been extended to treat harmonically oscillating airfoils [35]. The comparison in Fig. 24 indicates fair agreement with other transonic methods as well as experimental data. However, more work has to be done here to include viscous effects and nonlinear effects which imply the use of more complete unsteady equations.

Transonic Two-Element Airfoil Analysis/Design

The performance of mechanical high-lift devices is of increasing importance for the overall economy and operational efficiency of all types of aircraft. The use of such devices for combat aircraft at transonic speed offers the chance of greatly enhancing maneuvering capabilities without affecting cruise performance. Climb and turn rates of existing modern fighters at transonic speed are remarkably improved by the use of slats and flaps, although these configurations have not been optimized as such devices.

At low speed such devices can be efficiently designed by means of numerical methods and a lot of available experimental data. At transonic speed, however, we are lacking experimental data for airfoils with slats and flaps to establish a data base. Extensive wind tunnel testing on such airfoil systems is highly costly due to the large number of parameters and at transonic speed no simple interpolation in a data base is possible. Only since recently transonic viscous analysis/design methods are in use for configuration studies and improvements. In Fig. 25 results are depicted for an airfoil/slat configuration with upper slat surface and main airfoil shape plus lower surface slat pressure distribution as input. The results for this mixed analyses/design mode run agree very well with the experimental data and indicate clearly the large separated region on the lower slat surfaces. This mode can be used not only to understand the flow field characteristics of existing slats or flaps, but also to efficiently redesign configurations to avoid separation. Fig. 26 indicates a redesign process for the slat lower surface to a NACA 64A010 airfoil section.

For analysis problems viscous effects have to be included not only by means of laminar and turbulent boundary layers, but also short and long separation bubbles, confluent boundary layers and trailing edge separation. The present system of codes for viscous transonic two-element airfoil analysis has been successfully applied to simulate the flow field around the Do-A4 airfoil with a slat or flap. In Fig. 27 and 28 results are compared with the experimental data. The computed pressures agree fairly well with the experimental ones, even for cases with large separated regions where viscous effects completely dominate. Since such numerical simulations are rather fast and inexpensive, it is obvious that such computational methods are useful tools for designers looking for efficient high lift and maneuver devices. The design time as well as cost can be much reduced by using such numerical results.

Transonic Inlet Analysis

The efficiency of modern transonic and supersonic aircraft to quite a large extent depends on the recompression characteristics and the avoidance of separation causing distortion. Experience has proven pitot-type inlets to be well suited to design criterion at supersonic as well as subsonic and transonic speed. For the investigation of such types of flow fields with subsonic free stream Mach numbers, Dornier has adapted Arlinger's method for axisymmetric inlets [43]. A typical result with good agreement is shown in Fig. 29. Although this method gives very accurate results, it lacks the generality for extensions to three-dimensional configurations. Since the study of pitot-inlets at supersonic and large subsonic free stream raises some questions about the disregard of total pressure losses due to shock in methods using the potential equation, Dornier decided to develop its own method based on the numerical solution of the full Euler equations. First results of the plane and axisymmetric version of this finite volume method [44] are portrayed in Fig. 30. Fair agreement is reached for the fairly low supersonic Mach number with Arlinger's supersonic version as well as experimental data. Unfortunately we are lacking experimental data for a detailed evaluation at higher Mach numbers. For application in realistic aerodynamic design studies for fighters a three-dimensional version of the finite volume method is nearly completed. For final flow simulations the corresponding viscous codes will be coupled.

Transonic Wing/Wing-Body Analysis

The validation of three-dimensional transonic potential flow methods has been reported recently in several papers, e.g. see References 48, 50, 56 and 57, to name a few. During the application of the TSP-MF method for analysis as well as design case studies, it was found that the method is well suited to meet the requirements of engineering in as much as the code is fast (0.14 ms per iteration and grid point), designed for interactive treatment and very general in its use as depicted in Fig. 31.

For final results the full potential loop can be used to ensure no major errors due to TSP-assumptions. However, this code is suffering from its orthogonal grid system in as much as the leading edge representation for swept wings is poor as long as no extremely fine grid systems are used. The Figures 32-39 show some of the results for validation of the method for a wide range of configurations. Relatively thick large aspect ratio wings as well as moderate aspect ratio fighter wings with complex fuselage shape have been designed or analyzed before the wind tunnel test became available.

For fighter configurations with complex bodies the deviations at higher Mach numbers don't seem to be to TSP assumptions rather than inadequate fuselage modelling. Full potential FL022 computations for the wing alone did not improve the agreement.

For transport type configurations in analysis (Fig. 34) as well as mixed analysis/design mode (Fig. 37) the method proved to be very reliable, but is suffering from the poor leading edge description. However, the basic character of the pressure distribution and the shock position and strength is fairly well predicted. The recently included grid unbedding technique in the TSP-MF method [51] highly improves the leading edge and shock resolution as shown on Fig. 39.

The PT-7 configuration shown on Figure 36 has been a design case study [48] testing extensively the mixed mode capabilities of the TSP-method as a joint venture between Dornier and FFA.

First results of the three-dimensional finite volume Euler code [52], [59] are portrayed on Fig. 38.

Since two-dimensional experience has indicated the large influence of the viscous effects, also in three-dimensional flows, the viscous displacement thickness effect of the three-dimensional boundary layer over the wing has to be taken into account in order to produce accurate performance characteristics. The coupling of the three-dimensional boundary layer integral methods [27], [28] with inviscid potential flow programs provides the capability for better wing design, for diagnosis of specific wing design problems, and for evaluating the wing performance beyond the Reynolds number range of present wind tunnels. Since the boundary layer program allows for arbitrary, even nonorthogonal coordinate systems, no special interface programs are needed to convert grid systems. Only corresponding data handling in the inviscid method coordinate system is needed. Thereby it is possible to cycle several times between viscous and inviscid programs. In Fig. 36 the changes in pressure distribution corresponding to the number of iteration cycles is portrayed. It has been found that a number of cycles between the transonic potential flow program and the boundary layer code is necessary to achieve a satisfactory converged solution, i.e., until the pressure distribution and the boundary layer displacement thickness δ^* do not change significantly between cycles. The general trends of the measured pressure distributions are matched by the theory. However, a finer mesh would improve the agreement in the nose as well as shock region. In Fig. 36 also the corresponding changes in displacement thickness for section 2 and the variation of the computed separation line are shown. It is clearly indicated that a boundary layer method within this cycle has to be able to treat separated regions since the fully inviscid initial solution might exhibit relatively large partial separation although the final converged viscous solutions is almost free of separated regions. For completeness, the spanwise lift distribution and the computed dragrise curve are also included. Measured and calculated dragrise compare reasonably well. The capability of estimating the spanwise variation of wing drag components, lift distribution and separation, identifies the critical wing design regions and allows for proper wing modification with reasonable assurance of success.

Light Buffeting Prediction

Although buffet is only one and possibly even a very weak limitation in maneuver for fighter configurations, it can be thought as a first indication for other more severe evidents. The Dornier method for light buffet prediction [54] presently is restricted to sweep angles $0 < \gamma_{25} < 50^\circ$, thicknesses $0.04 < f/c < 12$, aspect ratios $2 < AR < 7.5$ and moderate camber $0.035 < f/c < 0$. This limitation results from the configurations used to establish the working plots. Extensions are possible by establishing new plots. The comparisons on Fig. 40 with experiments clearly validate the method as an engineering tool.

Recently this method has been included in the aircraft aerodynamics prediction code [4] to provide buffet information even in configuration studies.

CONCLUDING REMARKS

The significant advances that have been made in computational fluid mechanics are having considerable impact on the aerodynamic design process. Subsonic panel and vortex lattice methods, when used within their limits of application, provide valuable insight into complex flow fields, guidance for achieving integrated designs, and ability to explore innovative configuration designs. The use of these methods can substantially increase airplane performance capabilities. The integrated computer program system to analyse subsonic and transonic, viscous flow over airfoils, multi-element airfoil systems and wings and wing-body combinations for transport as well as fighter aircraft have emerged as a very important tool to support the wing design process, and to support diagnostic investigation of the aircraft performance.

Rewarding as the accomplishments in computational aerodynamic design have been, much work remains yet to be done. The three-dimensional transonic inviscid flow methods need to be generalized to include the complete configuration and to greatly simplify the user's input and output data manipulation and reduce computer as well as man costs. The three-dimensional boundary layer method needs to be enhanced to include the fuselage, to handle surface intersection problems, and to analyse separated flows. Most work has been towards better numerical methods at design conditions of modern aircraft. However, off-design is limiting the capabilities or real configurations. A lot of work in CFD and experiments has to be done to understand those phenomena causing maneuver boundaries. This will imply more work on unsteady time-accurate flow simulations.

However, all integrated systems of computer programs are only operational as design tools within the project engineering area, if the easy preparation of input data, the visibility of output, the flow time required to get final results, and the computer costs or running these methods are highly improved. If these enhancements are not included, we may never experience the use of numerical simulation and reduced reliance on the wind tunnel in airplane design as many computer experts suggest and the basic capabilities of modern methods promise.

ACKNOWLEDGEMENT

The author wishes to acknowledge the contributions of his colleagues at Dornier, FFA and SAAB who conducted many of the analyses reviewed in this paper. Appreciation is extended to Mr. Lynch at Douglas Aircraft Corporation, for his contribution to the Douglas-Wing comparisons, and to Dr. Jacob, DFVLR, for providing his code, as well as to different agencies at the German BMVg and BMFT who supported method development and application.

REFERENCES

1. Oman, B.H., Pederson, S.K., Karl, N.P., and Reed, T.F.: Computer Program to Perform Aircraft Design Synthesis. AFFDL-TR-74-35, April 1974
2. Newman, L., et al: D-SYN, a Computer Program to Size Aircraft, Nothrop Program C025, 1979
3. Ebeling, P., et al: Ein Digitalrechenprogramm für parametrischen Entwurf und Leistungsrechnungen von Flugzeugen (APFEL). IABG-Report B-WT 1205/01, 1975
4. Fritz, W.: Aerodynamikbaustein für ein Programmsystem zur parametrischen Entwurfs- und Leistungsrechnung von Flugzeugen. Dornier FB 79/46 B, 1979
5. Schemensky, R.T.: Development of an Empirically Based Computer Program to Predict the Aerodynamic Characteristics of Aircraft. AFFDL-TR-73-144, 1973
6. Ebeling, P., Pfisterer, E., et al: Ein Digitalrechenprogramm zu Entwurf und Optimierung von Flugkörpern. IABG-Report B-WT 1207/01, 1975
7. Mathauer, H.: Erweiterung des Rechenprogramms LARV zur Bestimmung der aerodynamischen Beiwerte von Flugkörpern. Dornier FB 79/44B, 1979

8. Grashof, J.: Berechnung der Druckverteilung auf Körpern mit Totwasser. ZAMM 55, T130, 1975
9. Jacob, K.: Berechnung von Profilsystemen bei Unterschallströmung mit mehrfacher Ablösung. DFVLR-IB 252-79 A05, 1979
10. Leicher, S.: Berechnung von Profilen und Hochauftriebs-Profilsystemen im Unterschall mit Simulation von Ablösung. Dornier BF30-/80, 1980
11. Stock, H.W.: Integralverfahren zur Berechnung dreidimensionaler, laminarer und turbulenter Grenzschichten. Dornier FB 77/51B, 1977
12. Stevens, W.A., Goradia, S.H., and Braden, I.A.: Mathematical Model for Two-Dimensional Multi-Component Airfoils in Viscous Flow. NASA-CR-1943, 1971
13. Zimmer, H.: Berechnung der Druckverteilung an dreidimensionalen Unterschall-Triebwerkseinläufen mit dem Panelverfahren. Paper given at the Meeting of the DGLR Fachausschuss für luftatmende Triebwerke, Dec. 1972, Friedrichshafen
14. Rubbert, P.E. et al: A General Method for Determining the Aerodynamic Characteristics of Fan-in-Wing Configurations. TR67-61A, USAAVLABS, 1967
15. Kraus, W. and Sacher, P.: Das Panelverfahren zur Berechnung der Druckverteilung von Flugkörpern im Unterschallbereich. ZfW, Heft 8, Sept. 1973, S. 301-311
16. Lucchi, C.W.: Ein Panelverfahren höherer Ordnung für kompressible Unterschallströmungen. Dornier FB 78/13B, 1978
17. Lucchi, C.W. and Schmidt, W.: Vortex Lattice Approach for Computing Overall Forces on V/STOL Configuration. ACARD CP 204, p. 19-1-19-8, 1976
18. Wedekind, G.: Verbesserung der Berechnung der Widerstandspolaren von gewölbten Konfigurationen mit größerer Vorderkantenpeilung unter Verwendung der Saugkraftanalogie. Dornier-BF10-1666/80, 1980.
19. Rehbach, C.: Calcul d'écoulements autour d'ailes sans épaisseur avec nappes tourbillonnaires évolutives. Rech. Aérosp. no. 1973-2, S. 53-61
20. Schroeder, W.: Berechnung der nichtlinearen Beiwerte von Flügeln mit kleinem und mittlerem Seitenverhältnis nach dem Wirbelleitverfahren in inkompressibler Strömung. DFVLR-Inst. A IB 151-76/18, 1976
21. Jepps, S.A.: The computation of vortex flows by panel methods. VKI Lecture Series 1978-4
22. Brune, G.W., Weber, J.A., Johnson, F.T., Lu, P., and Rubbert, P.: A three-dimensional solution of flows over wings with leading-edge vortex separation, Part I: engineering document. NASA CR-132709, 1975
23. Johnson, F.T., Tinoco, E.N., Lu, P., and Epton, M.A.: Recent advances in the solution of three-dimensional flows over wings with leading edge vortex separation. AIAA-paper 79-0282, 1979
24. Wagner, B.: Berechnung der dreidimensionalen Strömung mit Vorderkantenablösung. Dornier BF30-1700/80, 1980
25. Proksch, H.J.: Berechnung von Flügelauftrieb, -momenten und -widerstand ohne und mit Klappen in reibungsbehafteter Unterschallströmung einschließlich abgelöster Strömung. Dornier FB 76/41B, 1976
26. Haase, W.: Separation and Vortex Pattern on a Spheroid at Incidence. US-German DEA Meeting 1980, Annapolis.
27. Stock, H.W.: Three-Dimensional Boundary Layers on Wings and Bodies of Revolution. US-German DEA-Meeting 1979, TR AFFDL-TR-78-111, p. 32-56, 1978
28. Stock, H.W., and Horton, H.P.: Ein Integralverfahren zur Berechnung dreidimensionaler, laminarer, kompressibler, adiabater Grenzschichten. Dornier FB79-22B, 1979
29. Stock, H.W.: Laminar Boundary Layers on Inclined Ellipsoids. US-German DEA Meeting, April 1980, Annapolis
30. Stock, H.W.: Inverse Computations of Turbulent Boundary Layers on Infinite Swept Wings Including Separated Regions. US-German DEA Meeting, April 1980, Annapolis
31. Benner, W., Fritz, W.: Theoretische Untersuchungen zum Abgang und zur Flugbahn von Außenlasten. DGLR-Symposium Bad Godesberg, 1979
32. Kühl, P., and Zimmer, H.: Die Entwicklung von Tragflügelprofilen für Verkehrsflugzeuge mit verbesserten Schnellflugeigenschaften. Dornier FB74/16, 1974
33. Sator, F.G.: Determination de Profiles de Grilles d'Aubes Pour Compresseurs Axiaux Transsonique. These No. 254 (1976), EPFL Lausanne

34. Schmidt, W.: A Self-Consistent Formulation of the Transonic Small-Disturbance Theory. In: Recent Developments in Theoretical and Experimental Fluid Mechanics, p. 48-57, Springer Verlag, 1979
35. Fritz, W.: Transsonische Strömung um harmonisch schwingende Profile. Dornier FB78/168, 1978
36. Jameson, A.: Accelerated Iteration Schemes for Transonic Flow Calculations Using Fast Poisson Solvers. New York Univ. ERDA Report C00-3077-82, 1975
37. Lucchi, C.W., and Schmidt W.: Nachrechnung transsonischer Gitter, Dornier FB79/25B, 1979
38. Rizzi, A.W., and Schmidt, W.: Finite Volume Method for Rotational Transonic Flow Problems. Proc. 2nd GAMM-Conf. on Num. Methods in Fluid Mech. Köln 1977, p. 152-161
39. Sator, F.G., and Schmidt, W.: Solution of the Navier-Stokes Equation for Turbulent Transonic Flow in Two-Dimensional Turbomachinery Cascades. 4th Int. Conf. on Num. Methods in Fluid Mech., 1978, Tiflis
40. Arlinger, B.: Analysis of Two-Element high Lift Systems in Transonic Flow. ICAS Paper 76-13, 1976
41. Arlinger, B. and Schmidt, W.: Design and Analysis of Slat Systems in Transonic Flow. 11th ICAS Congress, Lisbon, 1978
42. Leicher, S.: A Method for the Calculation of Viscous Flow over Airfoils with Slats or Flaps at Transonic Speed. US-German DEA-Meeting, April 1979, Meersburg.
43. Arlinger, B.: Calculation of Transonic Flow Around Axisymmetric Inlets. AIAA-Paper 75-80, 1975
44. Rizzi, A.W. and Schmidt, W.: Study of Pitot-Type Supersonic Inlet-Flowfields Using the Finite-Volume Approach. AIAA-Paper 78-1115, 1978
45. Lomax, H., Bailey, F.R., and Ballhaus, W.F.: On the Numerical Simulation of Three-Dimensional Transonic Flow with Application to the C141 Wing. NASA-TN-D 6933, 1973
46. Schmidt, W., Rohlf, S., and Vanino, R.: Some Results Using Relaxation Methods for Two- and Three-dimensional Transonic Flows. Proc. of the 4th Int. Conf. on Num. Methods in Fluid Dyn., Boulder 1974, Springer Verlag, New York, 1975, p. 364-372
47. Jameson, A., and Caughey, D.A.: Numerical Calculation of the Transonic Flow Past a Swept Wing. New York Univ. ERDA Report C00 3077-140, 1977
48. Schmidt, W., and Hedman, S.: Recent Explorations in Relaxation Methods for Three-Dimensional Transonic Potential Flow. ICAS-Paper 76-22, 1976
49. Jameson, A., and Caughey, D.A.: A Finite Volume Method for Transonic Potential Flow Calculations. AIAA Paper 77-635, 1977
50. Fritz, W., Leicher, S., Schmidt, W., and Stock, H.W.: Fortsetzung der Untersuchungen zur Auslegung überkritischer Tragflügel für Verkehrsflugzeuge. Teil II: Theoretische Arbeiten. BMFT-FB W79-07, 1979
51. Hedman, S.: An Application of the Embedded Grid Technique to Calculation of Transonic Flow Over Wings FFA-AU-1600, 1980
52. Schmidt, W., and Rizzi, A.W.: Finite Volumen-Verfahren zur Lösung der Euler-Gleichungen für dreidimensionale transsonische Strömungen. Dornier FB79/28B, 1979
53. Leicher, S.: Ein finites Volumen-Verfahren zur Lösung der vollen Potentialgleichung in dreidimensionaler transsonischer Strömung. Erscheint als Dornier FB, 1980
54. Proksch, H.J.: Ermittlung der Buffeting-Grenzen von Kampfflugzeugen. Dornier Rep. EA-101/2916, 1973
55. Lynch, F.T.: Recent Applications of Advanced Computational Methods in the Aerodynamic Design of Transport Aircraft Configurations. 11th ICAS Congress, 1978
56. Da Costa, A. Larry: Application of Computational Aerodynamics Methods to the Design and Analysis of Transport Aircraft. 11th ICAS Congress, 1978
57. Lynch, F.T., and Schmidt, W.: Viscid Three-Dimensional Flow Simulation on Transonic Wings. US-German DEA-Meeting, April 1979, Meersburg
58. Drougge, G., Agrell, N., Hedmann, S., Torngren, L.: Evaluation and Analysis of Computations and Experiments for Transonic Wing Body Configurations. XI ICAS Proceedings p. 325-332, 1978
59. Drougge, G.: An Investigation of a Swept Wing-Body Configuration with Drooped Leading Edge at Low and Transonic Speeds. AGARD-FDP-Symposium May 1980, München

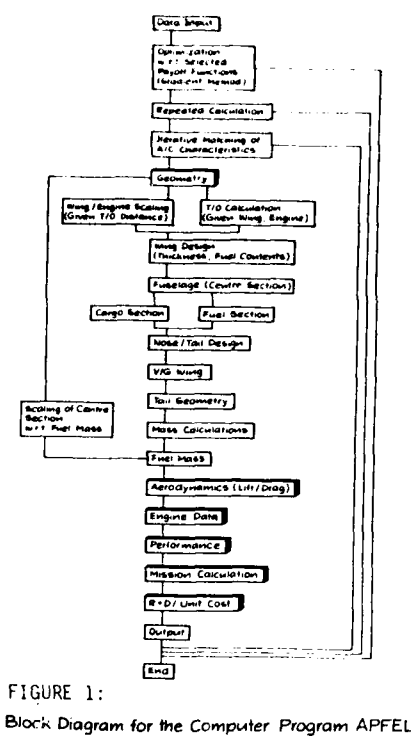


FIGURE 1:

Block Diagram for the Computer Program APFEL

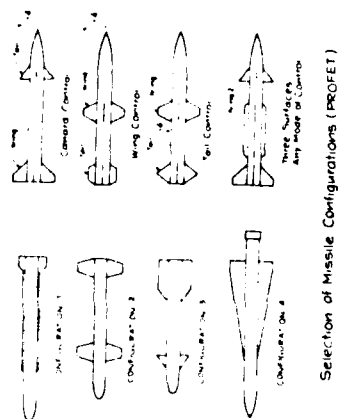
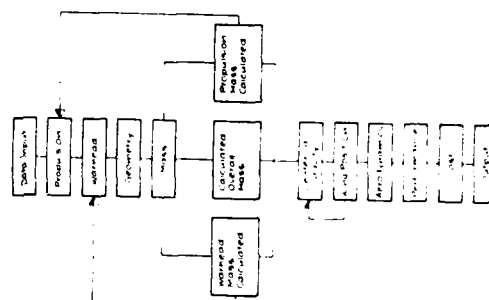


FIGURE 2:



Block Diagram for the Computer Program PROFET

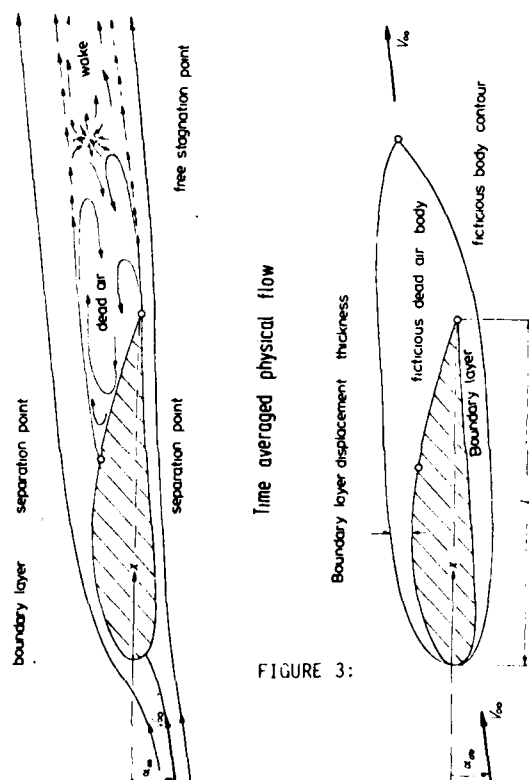


FIGURE 3:

Flow model in Grashof method

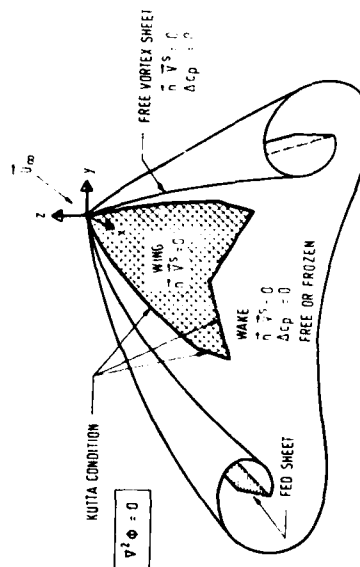
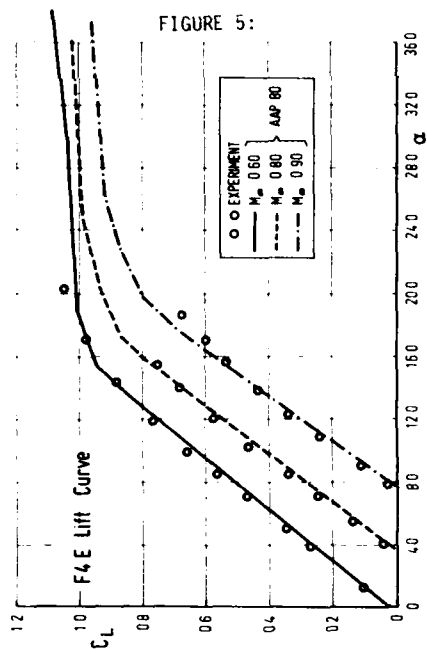
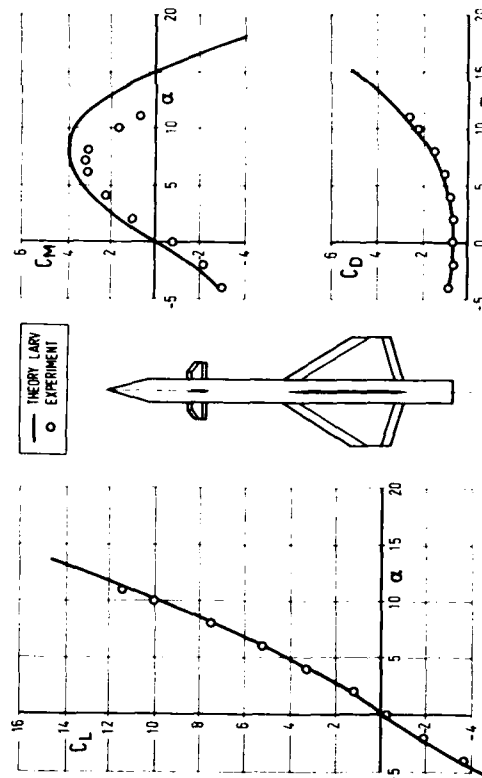


FIGURE 4:

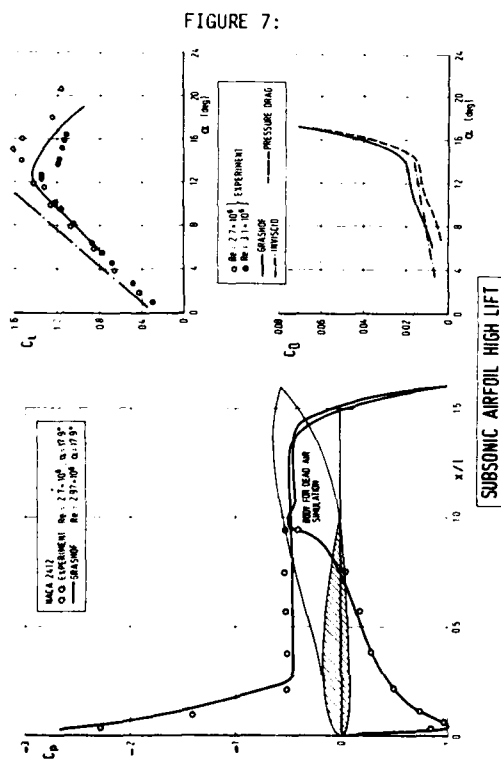
LEADING EDGE VORTEX FLOW MODEL



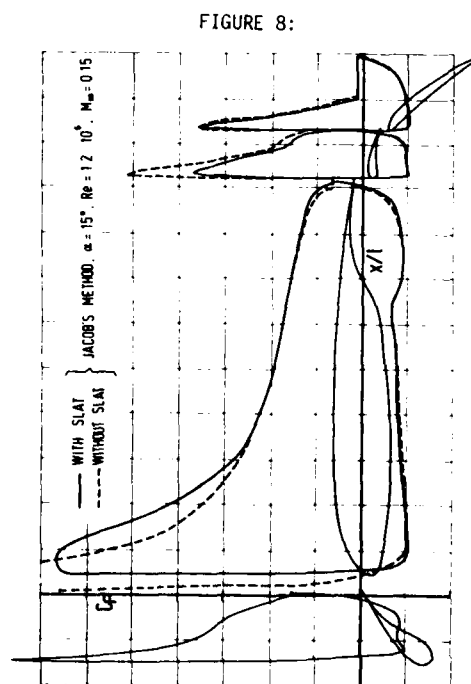
AIRCRAFT AERODYNAMICS PREDICTION CODE



MISSILE AERODYNAMICS PREDICTION CODE



SUBSONIC AIRFOIL HIGH LIFT



HIGH LIFT AIRFOIL SYSTEM

FIGURE 9: ALPHA-JET-ISOBARS

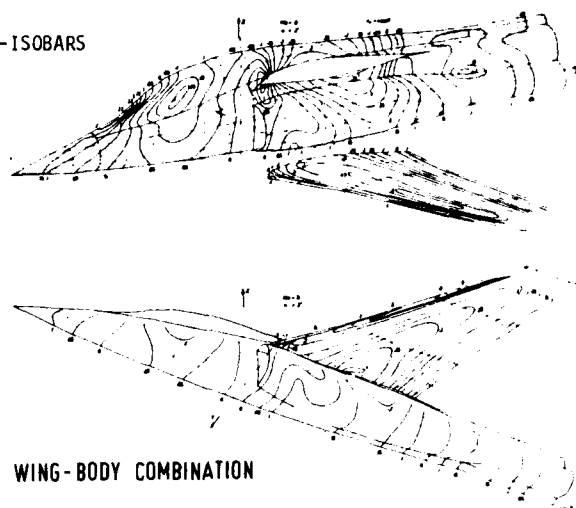


FIGURE 10: ENGINE INLET

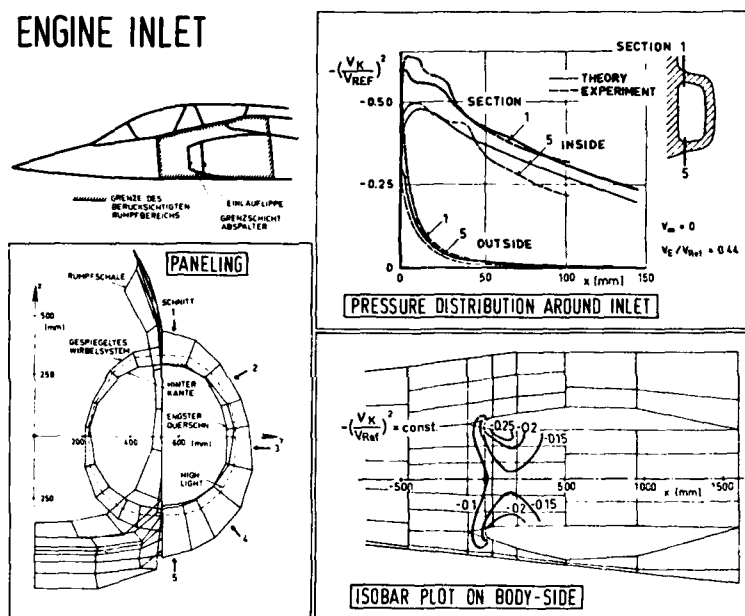
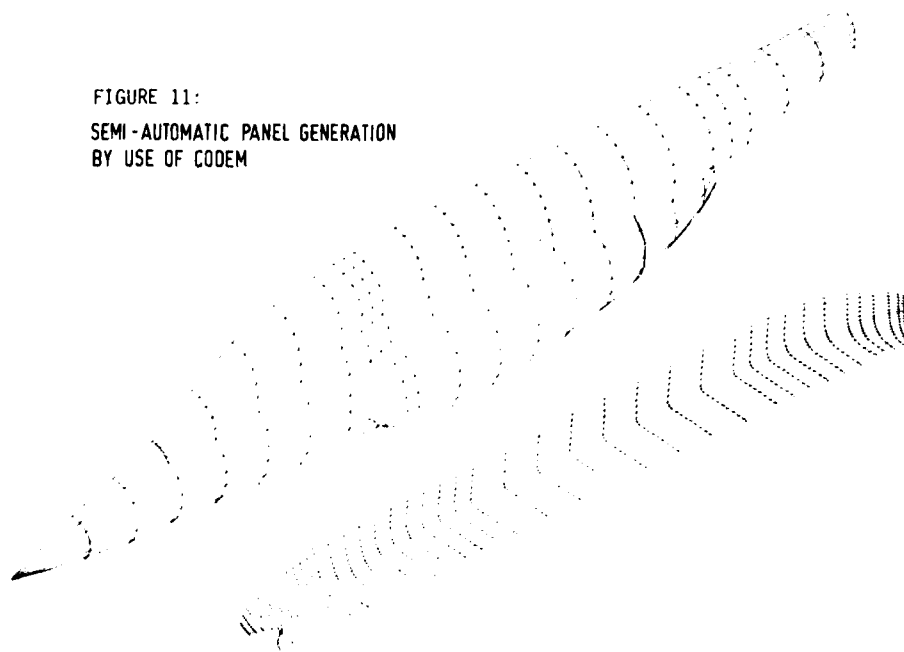
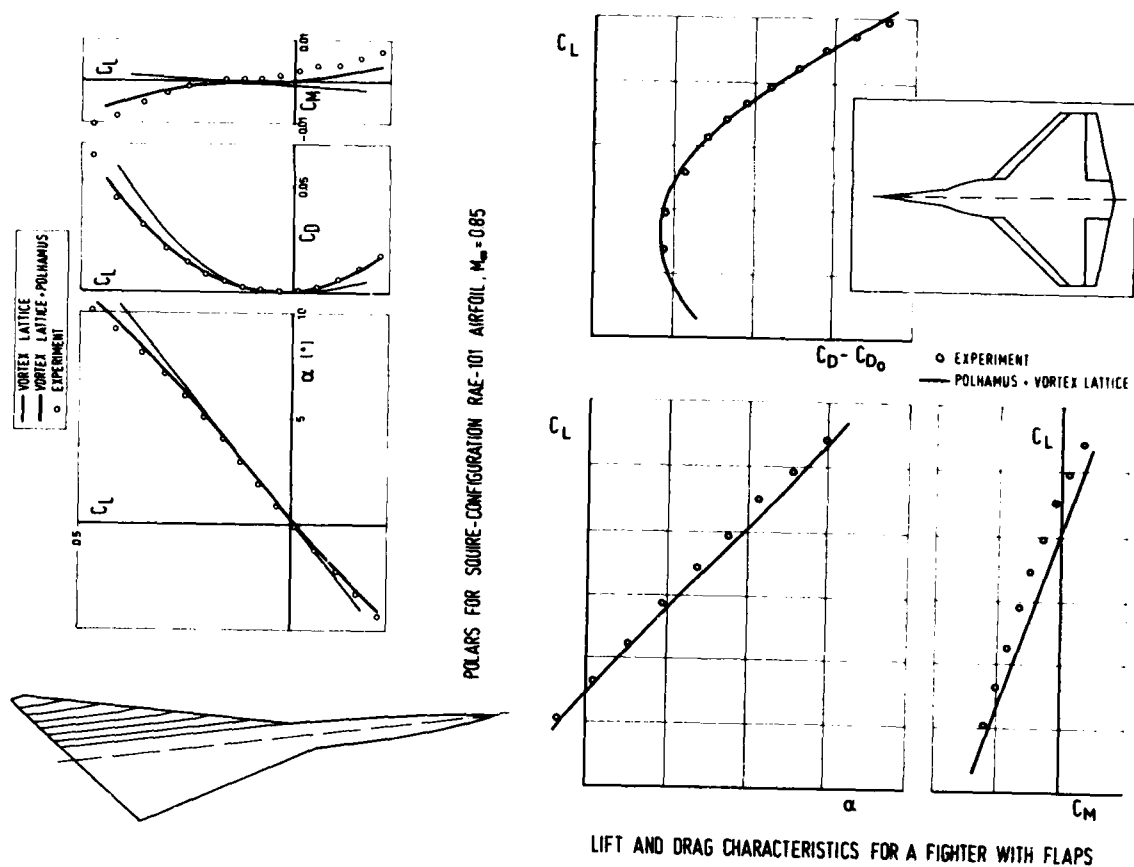
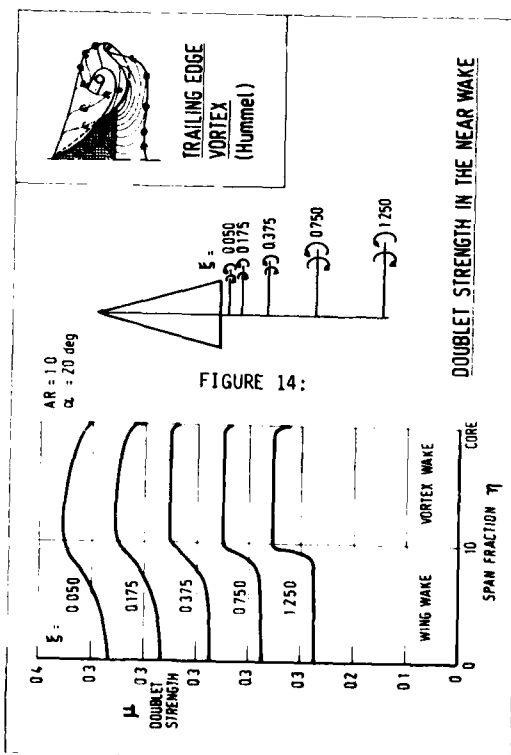
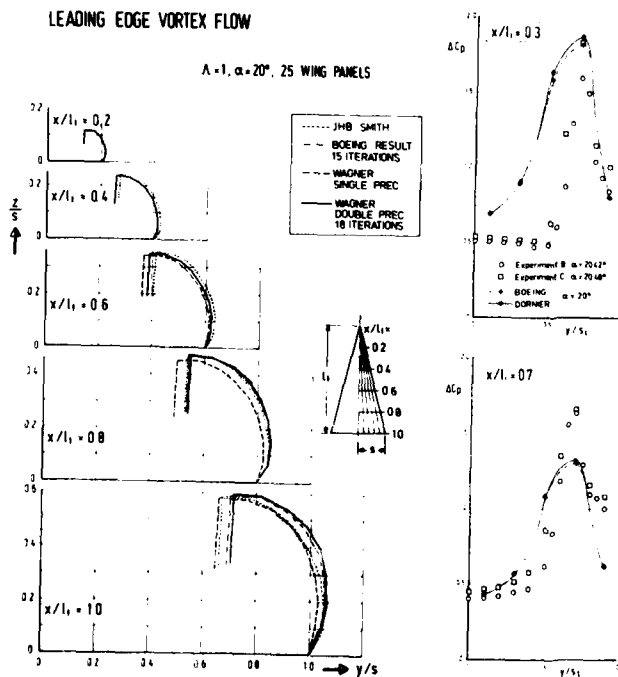
FIGURE 11:
SEMI-AUTOMATIC PANEL GENERATION
BY USE OF CODEM

FIGURE 12: NONLINEAR VORTEX LATTICE METHOD

FIGURE 13:
LEADING EDGE VORTEX FLOW

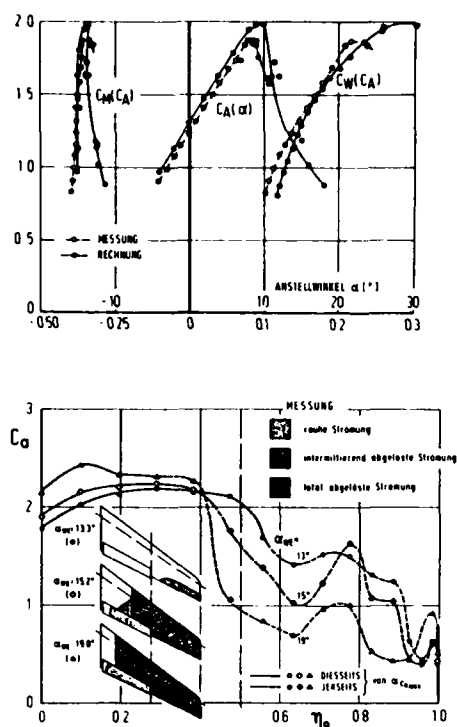


FIGURE 15:
WING HIGH LIFT CHARACTERISTICS PREDICTION

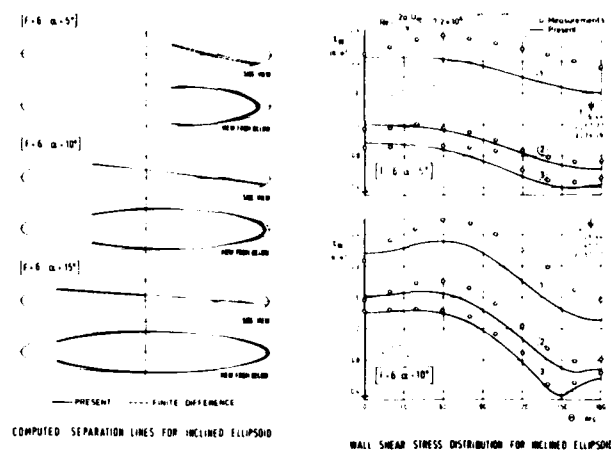


FIGURE 16: BOUNDARY LAYER DEVELOPMENT ON
AN ELLIPSOID

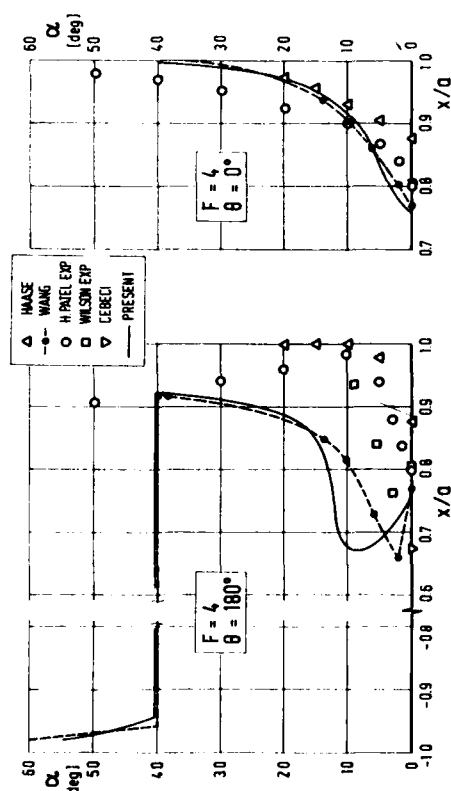


FIGURE 17: SYMMETRIC-LINE SOLUTIONS FOR
AN ELLIPSOID

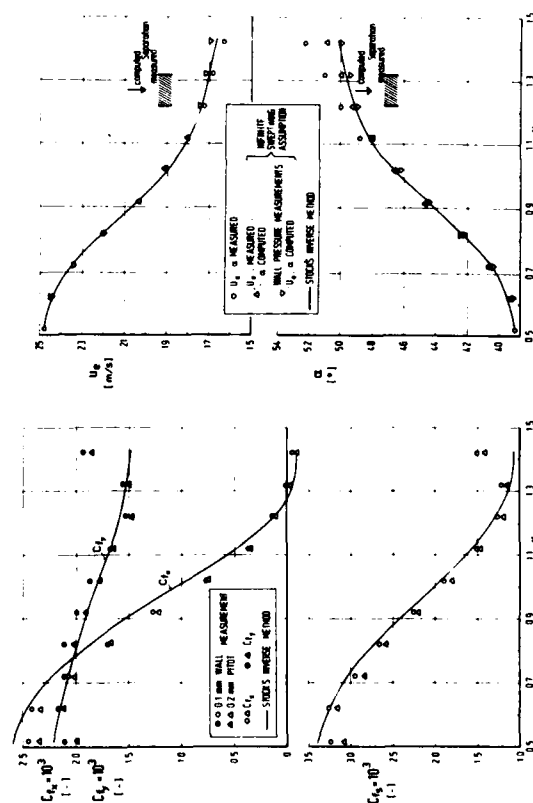


FIGURE 18: INVERS BOUNDARY LAYER METHOD

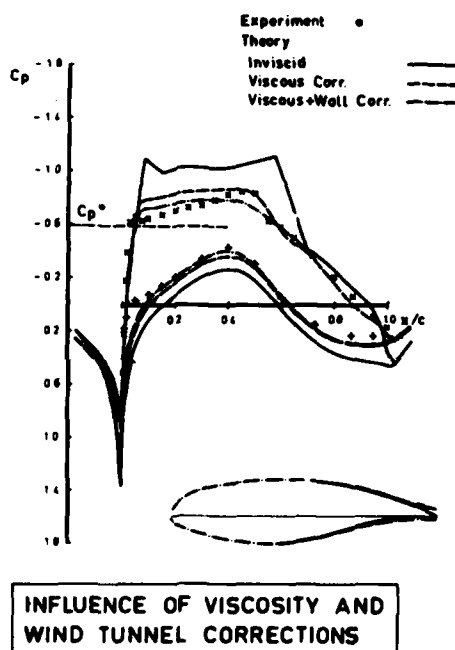
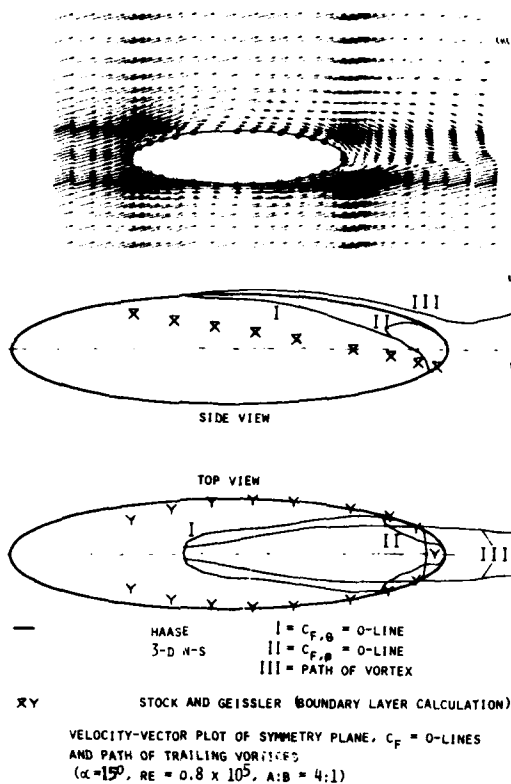
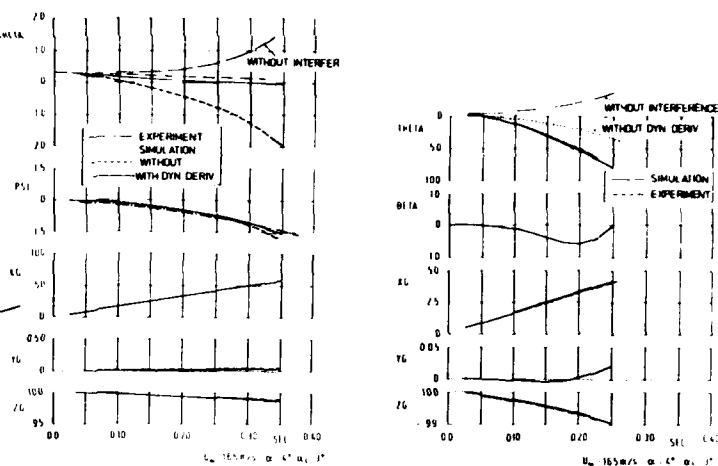


FIGURE 21:



RELEASE M 116 A2 FROM ALPHA-JET

RELEASE LAU 51 FROM ALPHA-JET

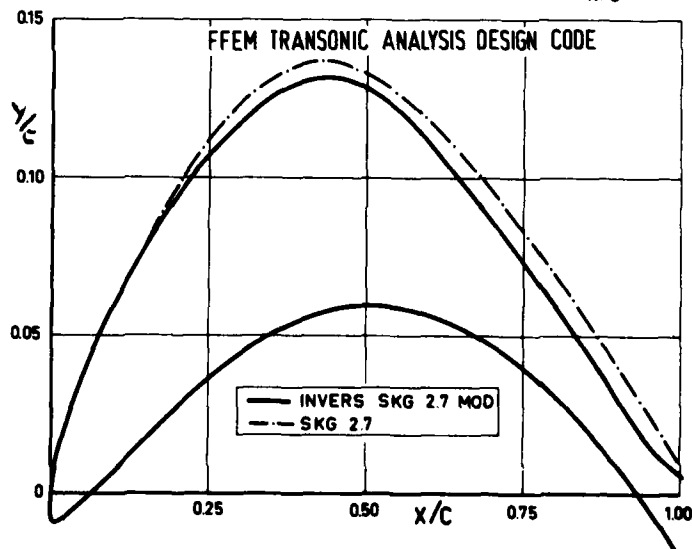
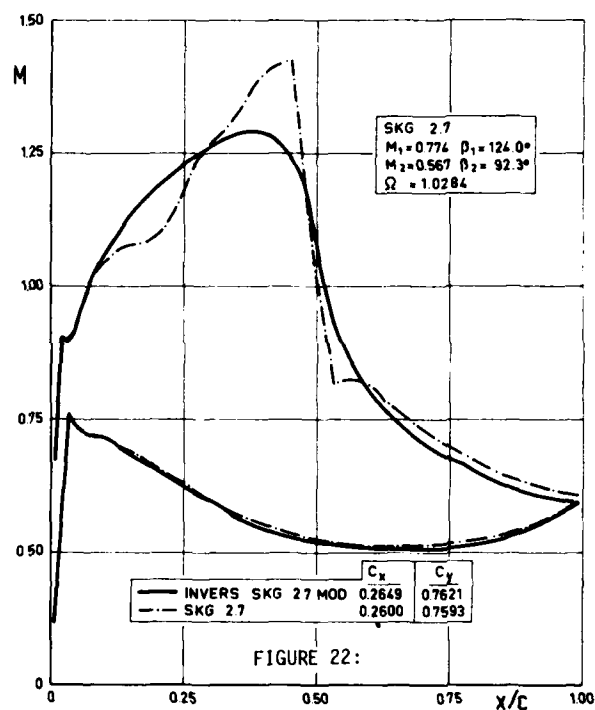


FIGURE 23:

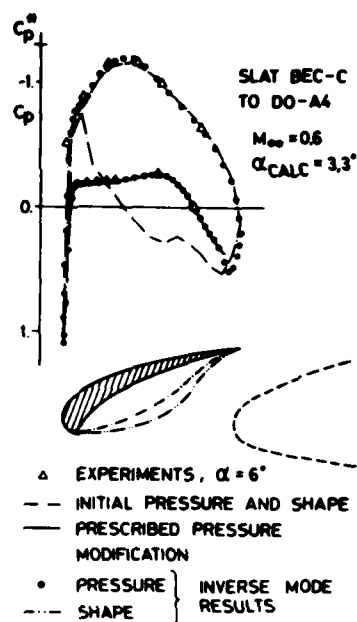
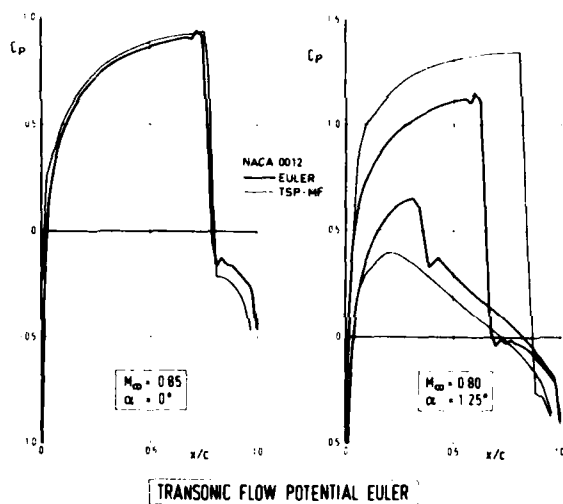


FIGURE 25:

SLAT SEPARATION DETERMINED
BY MIXED ANALYSIS - DESIGN
MODE RUNS

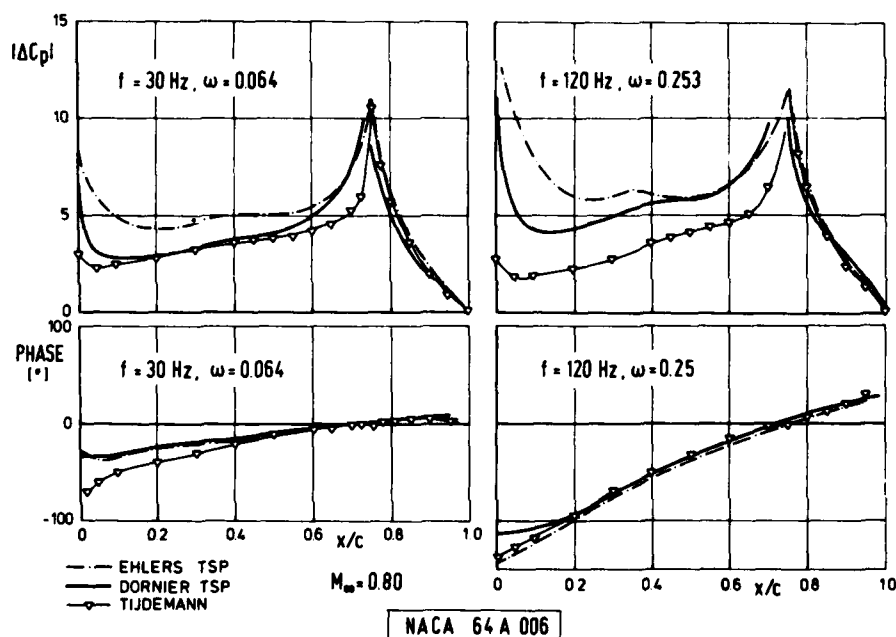


FIGURE 24: UNSTEADY TRANSONIC FLOW

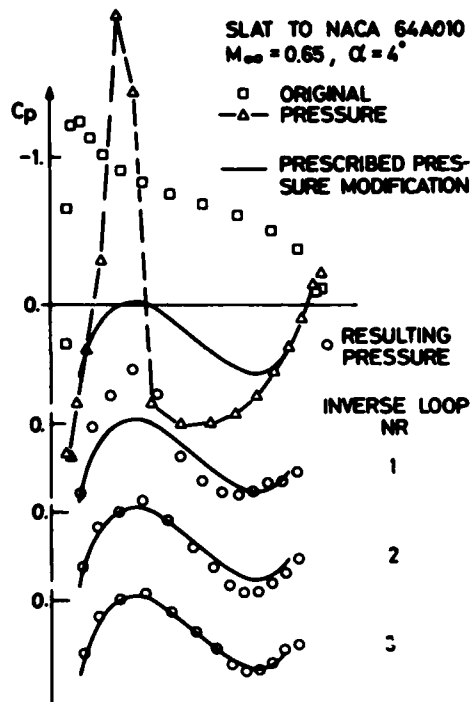
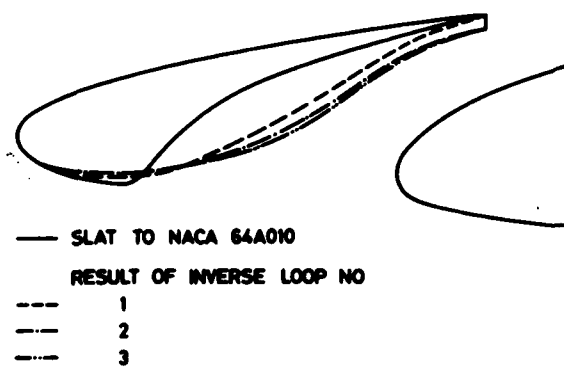
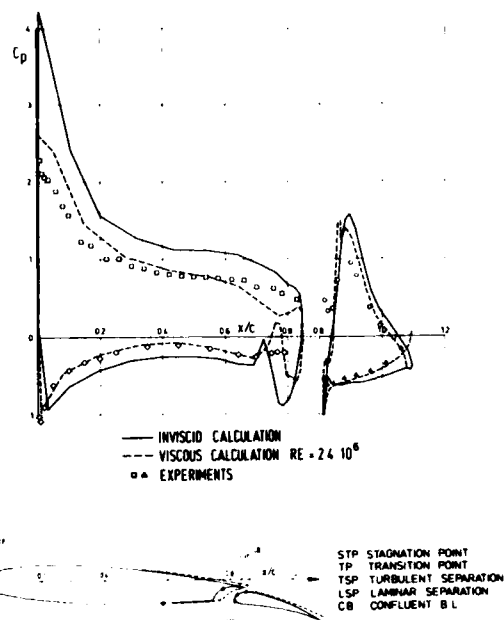
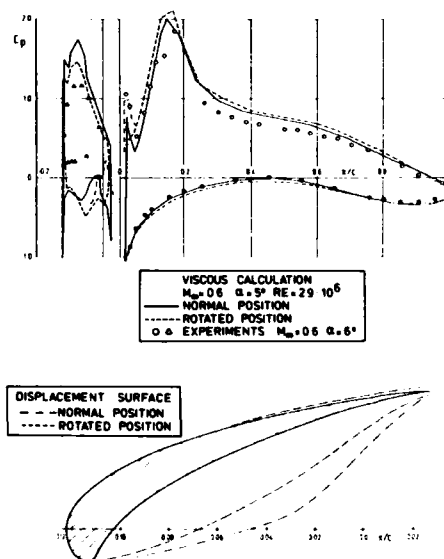


FIGURE 26:

SUCCESSIVE SLAT SHAPES IN
REDESIGN PROCESSFIGURE 28:
DO-A4 WITH FLAP POS.1
 $M_{\infty} = 0.5$, $\alpha = 4^\circ$ 

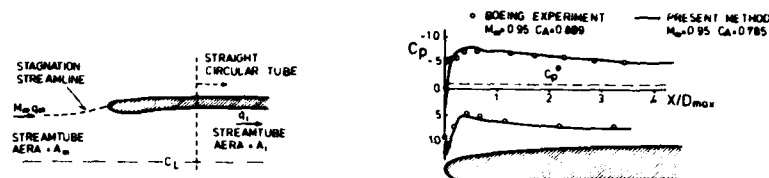


FIGURE 29:

ARLINGER METHOD FOR TRANSONIC AXISYMMETRIC INLETS

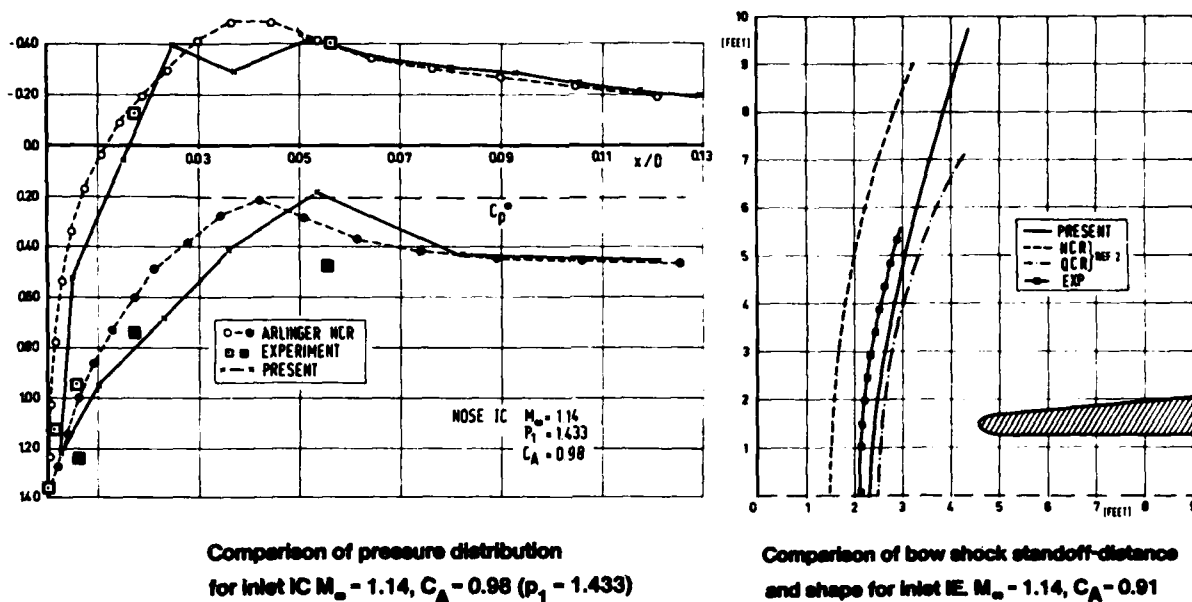


FIGURE 30:

FIGURE 31:

ANALYSIS AND DESIGN OPTIONS

- 1 ANALYSIS NORMAL VELOCITY COMPONENT SPECIFIED, PRESSURE CALCULATED
 - OPTIONALLY CAMBER OR THICKNESS CAN BE CHANGED ON PORTIONS
- 2 DESIGN TANGENTIAL VELOCITY COMPONENT SPECIFIED, NORMAL COMPONENT COMPUTED → SHAPE
 - ARBITRARY PORTIONS ON UPPER AND/OR LOWER SURFACE CAN BE CHANGED
- 3 MIXED PROBLEMS ON SOME PORTIONS TANGENTIAL, ON OTHERS NORMAL VELOCITY COMPONENTS SPECIFIED FINAL SHAPE AND PRESSURE COMPUTED
 - OVER SOME CHORDRANGE PRESSURE IS PRESCRIBED ON UPPER AND/OR LOWER SURFACE SPAN-SECTIONS WHILE FOR THE REST SHAPE IS GIVEN
 - SHAPE ON SOME STATIONS IS CHANGED
 - PRESSURE ON UPPER OR LOWER SURFACE IS CHANGED WITH THICKNESS OR CAMBER CONSTRAINT

FLOW CHART OF ANALYSIS / DESIGN SYSTEM

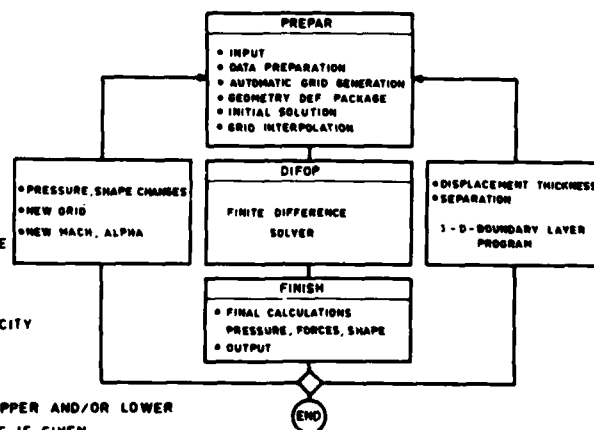


FIGURE 32: ALPHA-JET WITH TRANSONIC WING

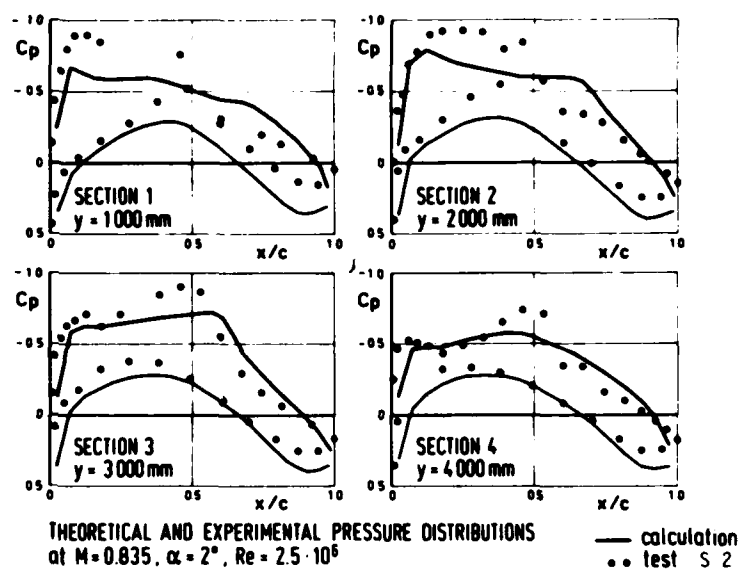
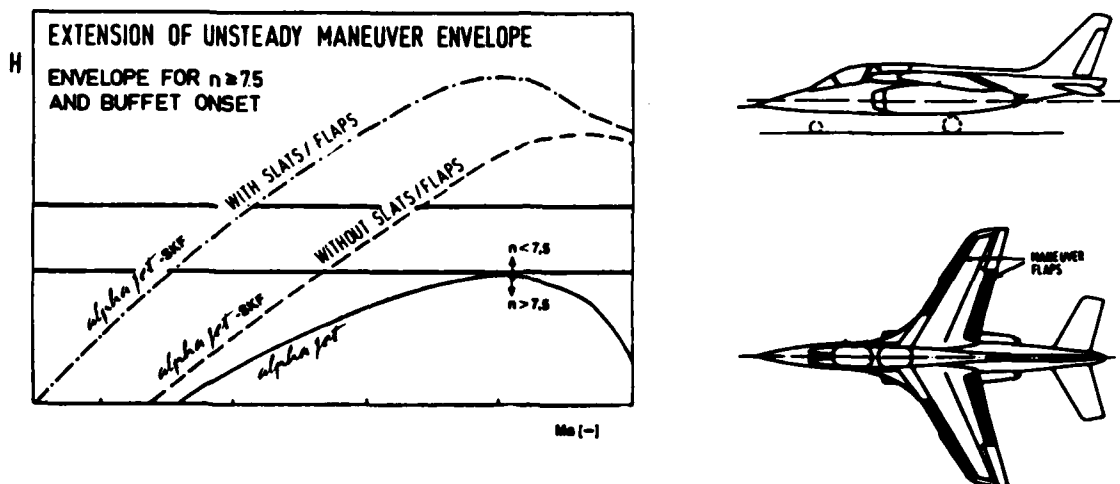
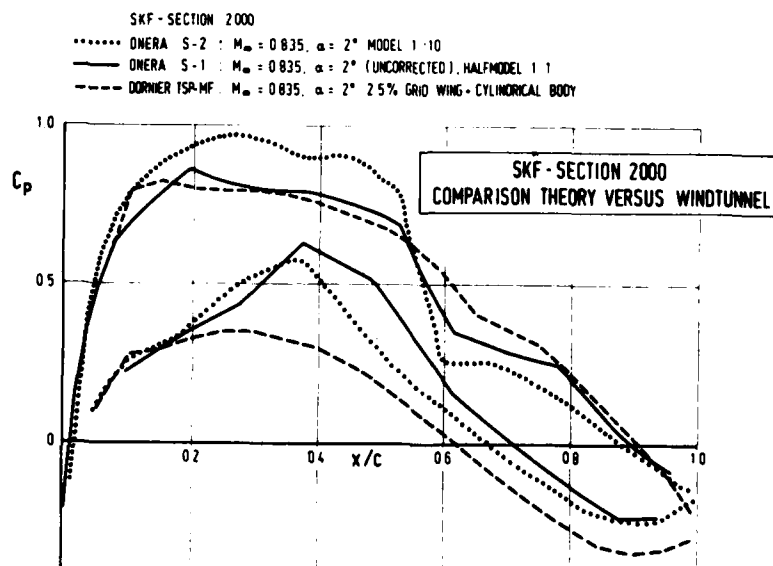
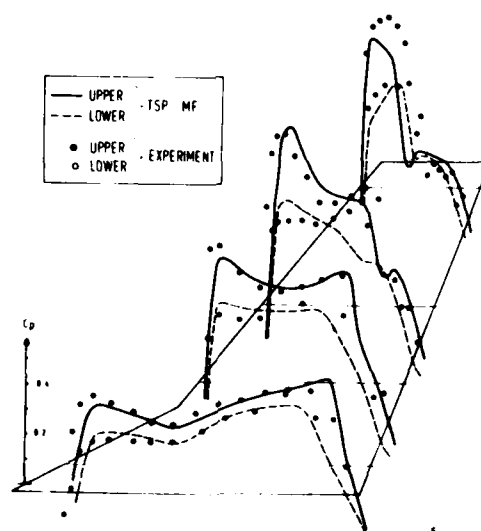
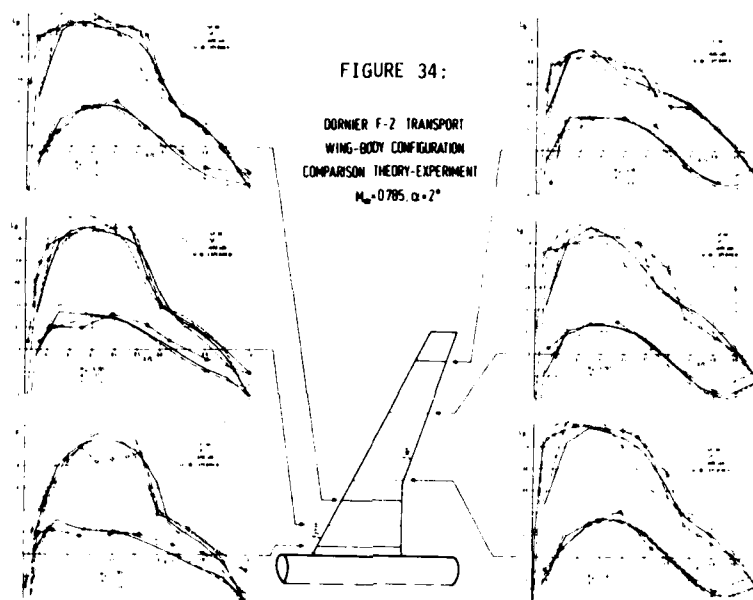


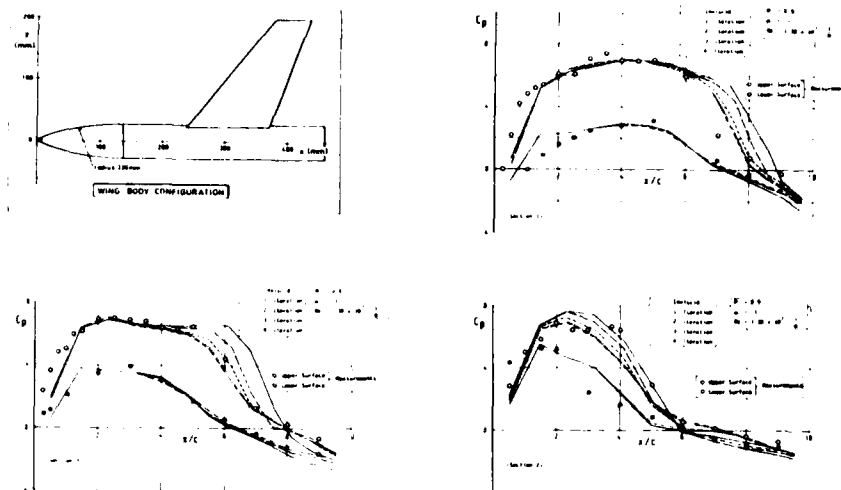
FIGURE 33:



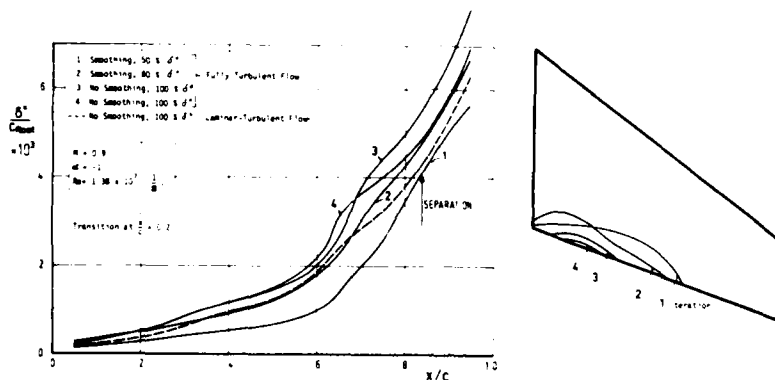


$M_\infty = 0.925$, $\alpha = 10^\circ$ FFA-SAAB PT 8

FIGURE 35:

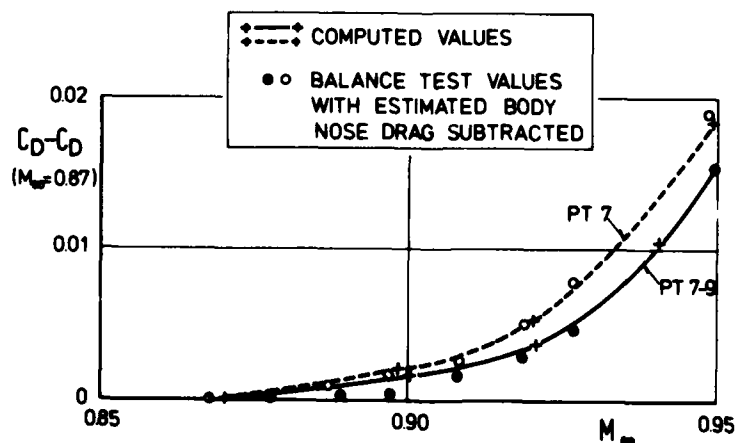


PRESSURE DISTRIBUTION FOR PT7 WING-BODY COMBINATION
VARIATION WITH VISCOUS ITERATIONS



DISPLACEMENT THICKNESS DISTRIBUTION ON THE PT7 WING (SECTION 2)
ON THE UPPER SURFACE DURING THE ITERATION PROCEDURE

CALCULATED SEPARATION LINES DURING
ITERATION PROCEDURE ON THE PT7 WING



COMPARISON OF WING DRAG INCREMENTS
FOR PT7 AND PT7-9 AT $C = 0.15$

FIGURE 36:

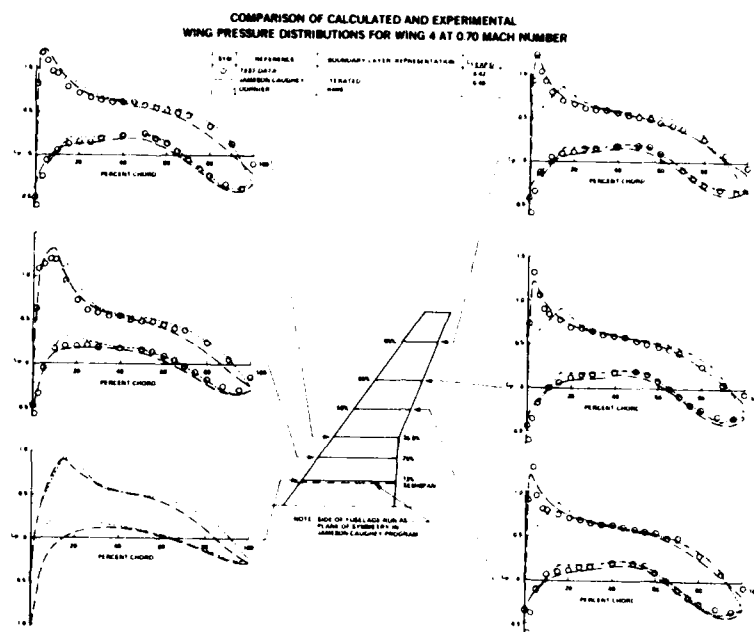
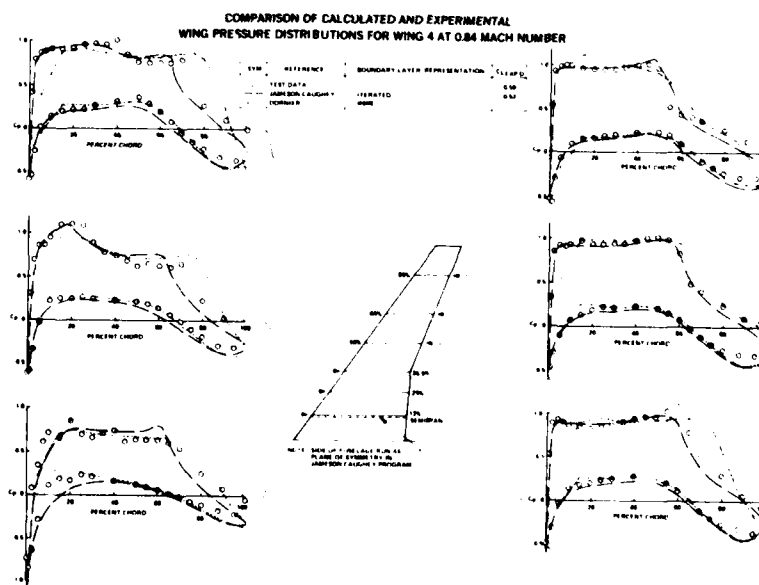


FIGURE 37:



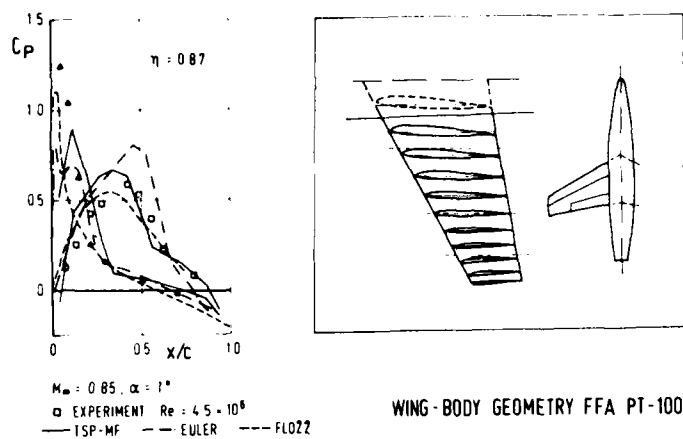


FIGURE 38: COMPARISON OF EULER VERSUS POTENTIAL FLOW

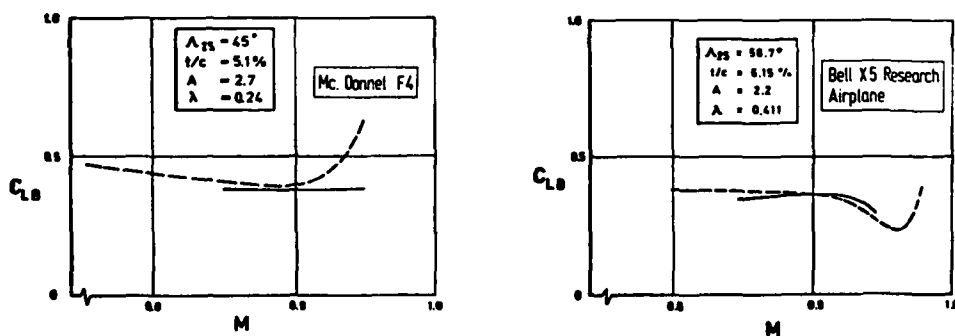
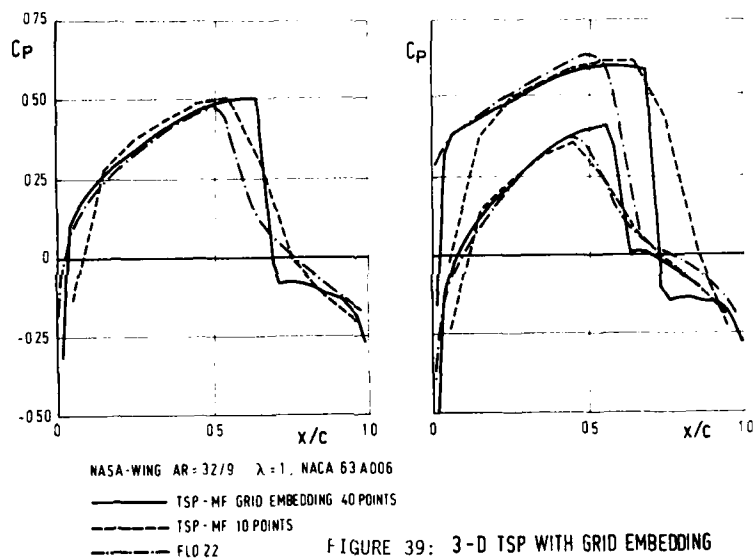


FIGURE 40: Comparison of the Boundary for Light Buffeting

DESIGN OF ADVANCED TECHNOLOGY TRANSONIC AIRFOILS AND WINGS

by

H. Sobieczky *

Institut für Theoretische Strömungsmechanik

Göttingen, Germany

SUMMARY

Recently a new method for the design of shock-free configurations in the supercritical regime has been presented. It is based on the use of fictitious gas flow in the supersonic domain in order to provide an elliptic continuation of the basic equations. Solutions of the latter ensure suitable sonic surfaces, which are used subsequently as initial condition for conventional shock-free supersonic field computation and configuration shape modification.

New concepts in wing design to meet the requirements of higher efficiency of future aircraft include airfoil shape modifications such as for the Laminar Flow Control (LFC) wing, or for the Circulation Control Wing (CCW). Results of shock-free flows past such airfoils are presented.

The new design method can also be used for three-dimensional flow. The redesign of a simple test wing is illustrated in detail, the structure of shock-free local supersonic regions on aft and forward swept wings is studied.

INTRODUCTION

The requirements of fuel efficient flight have forced the operating conditions of modern transport aircraft into the high speed regime. This fact brought a large number of challenging theoretical questions to be answered for the development of computational procedures for analysis and design of aircraft components, but also many problems had and still have to be solved if experimental investigation in high speed wind tunnels should reliably predict aerodynamic performance. The design goals for a new generation of efficient aircraft to be reached by theoretical and experimental work are dominated by the need to increase flight speed but to suppress the accompanying negative effects resulting from recompression shock waves and viscous interaction.

The knowledge of analytical solutions for inviscid transonic flows without shocks given by Ringleb [1] did not consequently yield theoretical results for shock free flows past wings or airfoils first, before experimental verification could affirm theoretically born concepts. Mathematical questions about existence and stability left doubts about the practical value of such flows; also the transonic regime was considered more a transition phase to supersonic operating conditions, necessarily passed only in acceleration and deceleration phases of the flight. This situation changed when supersonic transport was postponed in the United States. Consequently the design conditions were moved into the high subsonic regime with many transonic flow phenomena occurring and thus actualizing many unsolved problems. Whitcomb's [2] and Pearcey's [3] experimental work brought first results of practically shock-free airfoil flows in transonic speeds. Also first analytical shock-free flow results were given by Nieuwland [4], computational design methods were developed by Garabedian and Korn [5], and by Boerstol [6]. Another, more recent and urgent call for design techniques for efficient aircraft resulted from sharply rising fuel costs. Systematical methods for aircraft design are needed now more than ever and the supercritical (nearly shock-free) wing seems to be one of the most promising components among the many innovations currently studied, tested and already used in new aircraft.

The mentioned design methods for airfoils work in the hodograph plane, where the basic equations are linear in contrast to nonlinearity observed in 2D or 3D physical space. A number of airfoils was obtained and many were tested experimentally. This was a good start toward the goal of systematic computerized design but hodograph methods are not applicable to three-dimensional flow past wings and other realistic components of aircraft. For 2D and 3D flow analysis numerical procedures were developed [7,8,9,10] to predict flow past given configurations. These methods allow the determination of shock waves in the flow with reasonable accuracy. Also viscous interaction effects, mostly important at the trailing edge of wings by affecting the circulation, are already included into transonic analysis codes for airfoil flows [11]. This situation, namely the lack of systematic design tools for the development of new configurations, but availability of reliable analysis methods led to development of a theoretical optimization procedure requiring large numbers of analysis runs for parametric variations of given configurations to find optimal shapes [12].

In this paper the availability of analysis methods is used for design in a different way. A new idea to obtain shock-free 2D airfoils and 3D wings rests on previous work in the hodograph for airfoils, where the rheoelectric analogy was used to obtain shock-free flows [13]. While being much less economical than the computerized hodograph method [5] quoted earlier, application of the analogy led to a very simple new transonic boundary value problem, which is not restricted to the hodograph approach and not restricted to 2D flows. Mathematically a method of analytic continuation it may be interpreted physically as a gas flow with certain fictitious properties. Existing

* Research Scientist

numerical analysis codes are converted and extended to design tools, first examples for inviscid shock-free configurations obtained from conventional input shapes were presented [14]. The evolution of the method from rheoelectric hodograph experiments to numerical design programs in physical space is described elsewhere [15]. Airfoil design by these indirect and direct approaches is reviewed [16].

The purpose of this paper is an illustration of the method applied to some recently presented new aerodynamic concepts [17,18]. New ways to control boundary layer and circulation lead to new airfoil shapes and variable wing geometry requires investigation of numerous new planforms. The chosen design examples are intended to encourage the design engineer to use the outlined methods for practical problems which involve transonic flow presently, as well as for configuration studies which might find a realization in the future.

ELLIPTIC CONTINUATION AND FICTITIOUS GAS

A detailed description of the design method applied in this paper is given elsewhere [14,15,16]. Here a short explanation is given for the method termed "Elliptic Continuation Method" or, with respect to physical illustration a "Fictitious Gas" design procedure. For a given configuration to be systematically altered in order to be in shock-free transonic flow at certain operating conditions (defined by M_∞ the Mach number and α the angle of attack) the process is described shortly.

For an existing reliable analysis algorithm in conservation form for isentropic irrotational gas flow we alter the density - velocity relation $\rho(q)$ in such a way that the resulting basic partial differential equation to be solved becomes elliptic in the entire velocity range. The isentropic flow relation

$$\frac{\rho}{\rho^*} \text{ isentr.} = \left[\frac{\gamma+1}{2} - \frac{\gamma-1}{2} \left(\frac{q}{a^*} \right)^2 \right]^{1/(\gamma-1)} \quad (1)$$

with critical conditions denoted by superscript *, ensures an elliptic type equation only up to the critical speed, $q < a^*$, while for $q > a^*$ the equation becomes hyperbolic. Consequently we leave (1) unchanged up to $q = a^*$ but introduce an artificial relation $\rho = F(q)$ which replaces (1) in the domain $q > a^*$. We choose, illustrate and use in the following examples the function

$$\frac{\rho}{\rho^*} \text{ fictit.} = \left(\frac{q}{a^*} \right)^{-P} \quad (2)$$

and realize that $P = 1$ means $(\rho/q) = \text{const.}$ which leads to parabolic type while $P > 1$ still gives hyperbolic type equations. For elliptic type our fictitious relation (2) therefore is restricted to $P < 1$. Relations (1) and (2) are drawn in Figure 1, with different exponents P . We observe that only the parabolic limit $P = 1$ ensures the same gradient of relations (1) and (2) at the contacting sonic point $q = a^*$. One might expect discontinuous slope of a combined relation (1)/(2) in the subsonic/supersonic domain to result in discontinuous behavior of solutions of the equations at the sonic surface, but numerical experiments showed that none of such difficulties occurred in both finite element [18] and finite difference [19] evaluation of the all elliptic partial differential equations. Different values of P were studied; our experience resulting from these calculations is that

$$0.5 < P < 0.9 \quad (3)$$

seems to give optimal resulting sonic surfaces, "optimal" in view of the subsequent calculation of the real local supersonic region to be outlined in the following chapter.

We introduce (2) now into the analysis algorithm and switch from the use of (1) in locally computed subsonic flow to (2) if the flow is supersonic. Also, we suppress the switch to upwind differencing and the use of numerical viscosity in the analysis code, because these tools are introduced for effective calculation of hyperbolic type flow including shock waves which do not occur in our

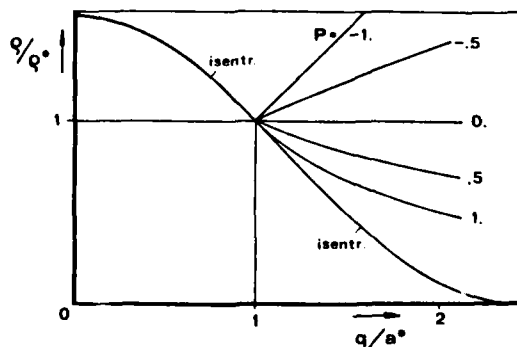


Figure 1. Isentropic and fictitious density - velocity relations.

all elliptic problem. When calculating an example now we see that convergence of the numerical relaxation procedure is reached much faster than in a mixed type flow analysis because we have, numerically, essentially a subsonic flow problem to solve.

The result of this calculation is a correct one where subsonic flow is found. It also gives sonic surfaces which are found by interpolation in the field. Inside a sonic surface we have solved a fictitious supersonic flow problem (or a flow problem with fictitious gas behavior if the speed of sound is exceeded) which ensures conservation of mass and momentum globally, which is important for the subsequent calculation of the real supersonic domain. For this we need to know the flow vector \vec{v} distribution on the sonic surface where $|\vec{v}| = a^*$. A smooth distribution of the velocity components u, v, w along the sonic surface is the initial condition for the calculation of a local supersonic flow domain with a marching procedure as will be described next.

ONION PEEL COMPUTATION OF LOCAL SUPERSONIC FIELDS

Fictitious gas computation provided a sonic surface which has to be used subsequently to find the supersonic part of the flow and a new body surface compatible with the entire resulting shock-free flow. For plane airfoil flow the method of characteristics is used in the same way as in the hodograph methods [5,13] to find the solution which is defined beyond the resulting airfoil contour f , see Figure 2a. Two characteristics ξ, η and the sonic line h enclose the computed flow field. In 3D flow characteristics are replaced by Mach conoid envelopes ξ, η originating from the intersection of sonic surface h and stream surface f , Fig. 2b. Characteristics and Mach conoids in 3D flow allow an extension of some knowledge about 2D transonic flow phenomena but an effective 3D method of characteristics for local domains has not yet been developed. The 2D method of characteristics may give results with limit lines with locally infinite velocity gradients and multi-valued solutions. The resulting flow is not smooth and shock-free if the limit line occurs in physical flow between sonic line and stream line. Similar problems may occur in a 3D evaluation method, limit surfaces may show and announce that no shock-free solution is possible for the previously computed subsonic outer flow and operating conditions. These limitations should not be confused with possible numerical problems of a 3D marching procedure described next.

In 2D and 3D flow the local supersonic domain has to be computed starting at the sonic surface which means starting with Cauchy initial data and proceed into a direction falling outside of the Mach conoids. This is of no consequence in 2D flows but in 3D flow it results in a numerical instability requiring a careful filtering of possibly growing high frequency perturbations in the marching procedure, [21].

For large wing sweep or low aspect ratio lifting wings the sonic surface may wrap around the leading edge so that establishment of a marching direction from the sonic surface toward the initial configuration boundary may not be suitable simply normal to the wing planform (Figure 3a) but along curved lines, e.g. defined by parabolic coordinates around the section nose focal point (Fig. 3b). The initial configuration surface within the sonic surface may be used for a 3D grid definition, like onion peels, Fig. 3c.

The numerical marching procedure consists of establishing partial derivatives of the velocity components (u, v, w) into the marching direction which is performed by use of the partial derivatives of the (u, v, w) - distribution along a given surface (starting with the sonic surface) and solving the system of continuity and irrotationality equations. Velocity gradients are obtained explicitly this way and used to extrapolate to a neighboring surface of the "onion peel" grid between sonic and initial surface. The step from one to the next surface is performed iteratively with averaged gradient ensuring second order accuracy. Partial derivatives of (u, v, w) - data along a surface are obtained by spline differentiation, which ensures, together with a suitable grid spacing, the aforementioned filtering of high frequency perturbations.

Arriving at the initial surface will define new flow directions which are used to integrate the new body stream wetted by supersonic flow, [22]. Closure errors of the deformed surface indicate conservation errors in the first step elliptic computation and/or in the second step onion peel marching procedure.

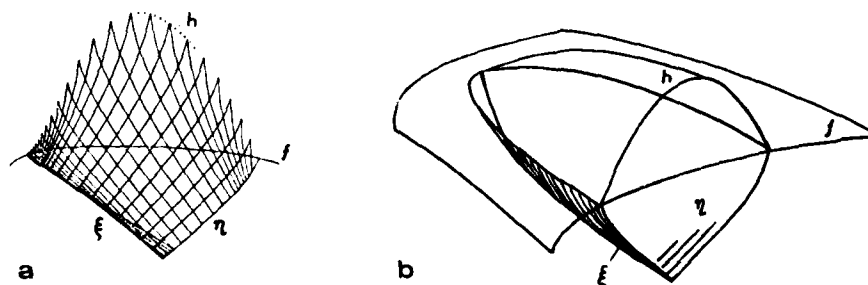


Figure 2. Local supersonic shock-free flow field in 2D (a) and 3D (b).

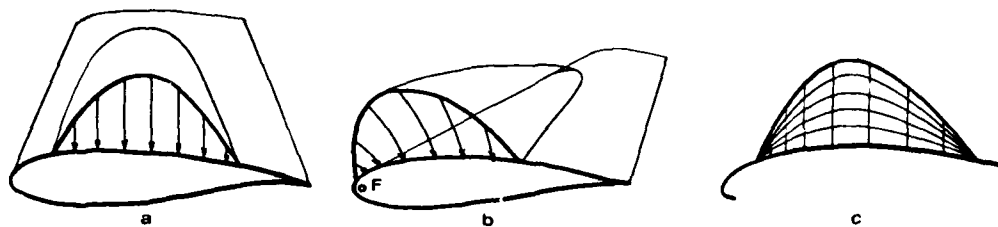


Figure 3. Onion peel computation of local supersonic field. Marching normal to planform (a), marching along parabolic coordinates (b), Onion Peel grid using initial configuration (c).

INITIAL CONFIGURATION FOR SHOCK-FREE REDESIGN

The two-step design procedure for supercritical flow makes use of the fact that a shock-free local supersonic region influences the surrounding subsonic flow qualitatively like additional body displacement. Outer flow therefore cannot distinguish between a body in isentropic flow with density (1) and a body somewhat thicker within the supersonic region in a flow with higher fictitious density (2): a thicker body shape is compensated by narrower adjoining stream tubes. We conclude that initial configurations for the design method will be flattened by the process. The type of desired pressure distribution may be influenced to some extent by the choice of fictitious gas properties but more effectively also by addition of thickness bumps on the body. This is especially necessary if an existing supercritical configuration should be optimized for some new operating conditions: The flat upper airfoil or wing surface in combination with the higher density fictitious gas results in supersonic domains forming patches of a complicated structure on the wing, see Fig. 11 in [21]. It was shown [16] that existing supercritical airfoils which were found with a hodograph method can also be verified by the present method: an added surface bump was adjusted iteratively to the subsequently subtracted amount of thickness. So a "supercritical" configuration has to be made "conventional subsonic" before it is suitable for supercritical redesign. It is concluded that subsonic configurations like NACA - airfoil series are well suited input for transonic redesign which seems reasonable because a large complex of experience with low speed airfoils and wings exists and much of it may easily be extended into the supercritical regime by this approach.

DESIGN OF SHOCK-FREE AIRFOILS

For illustration of the airfoil design process we choose a reliable transonic analysis method. Jameson's finite difference relaxation algorithm is used for inviscid flow computation; the airfoil is mapped conformally into a circle [8]. Different concepts exist for an effective treatment of viscous interaction between boundary layer and potential outer flow: one way is the addition of boundary layer displacement thickness to the airfoil and compute inviscid flow past this new effective shape (displacement concept). With boundary layer thickness growth depending on the outer flow pressure distribution this requires an iterative process with each step performing conformal mapping of a new effective shape to a circle. The viscous wake is represented by an open trailing edge and an inviscid wake model with constant thickness downstream to infinity. Disadvantages of this method are the time-consuming mappings and poor representation of viscous effects near the trailing edge and from the wake. A different approach overcomes the problem of repeated mappings by establishing a surface velocity distribution defined by boundary layer displacement growth, (transpiration concept). Viscous interaction of boundary layer and wake at the trailing edge is treated with Melnik's theory [11], airfoil design using this approach is described elsewhere [23].

Results from a design method including viscous effects based on the displacement concept are given in this paper. Starting with an initial guess displacement thickness is modeled by a function

$$\delta^*/c = \sum_{k=1}^{ke} CBL_k \cdot (x/c)^{EBL_k} \quad (4)$$

Suitable choice of the exponents EBL allows good representation of boundary layer computation results, obtained here with Rotta's integral method [24]. On the upper surface close to the trailing edge results of the boundary layer computation are unreliable and displacement is modeled by an ad-hoc technique based on wind tunnel boundary layer and wake measurements [25] and comparisons with results of the interaction theory [11]. Results are illustrated here for shock-free redesign of a given initial configuration 14,6 % thick rear loaded airfoil. The design goal for lift coefficient is $c_L = 0.6$ at a Mach number $M_\infty = 0.73$ and a Reynolds number $Re = 7 \cdot 10^6$. At first, analysis computation of the given airfoil at design conditions, ($c_L = 0.6$ is obtained with an angle of attack $\alpha = 1.4^\circ$), shows that the flow is not shock-free, see Figure 4. The analysis version of the code includes treatment of shock-boundary layer interaction which provides a corrected wall pressure distribution at the shock foot point based on Inger's theory [26], description of an incorporation of this theory into the inviscid flow and boundary layer computation is given elsewhere [27]. Next we switch the program to the design version using the fictitious gas concept with $P = 0.9$ and the

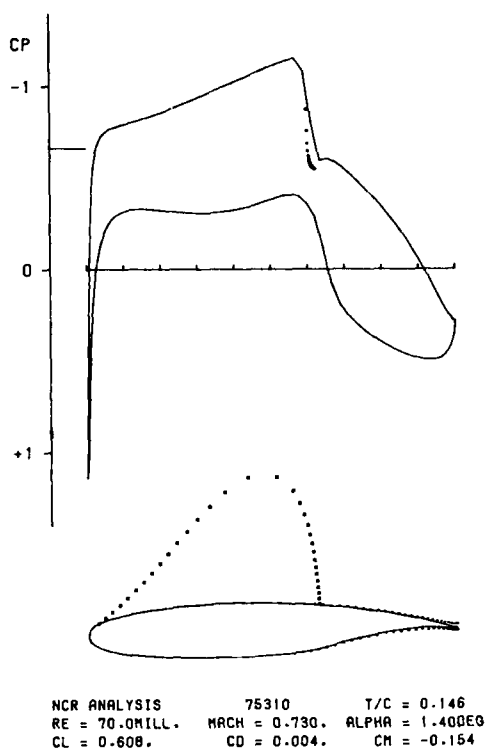


Figure 4.
Analysis of initial configuration airfoil
at specified operating conditions.

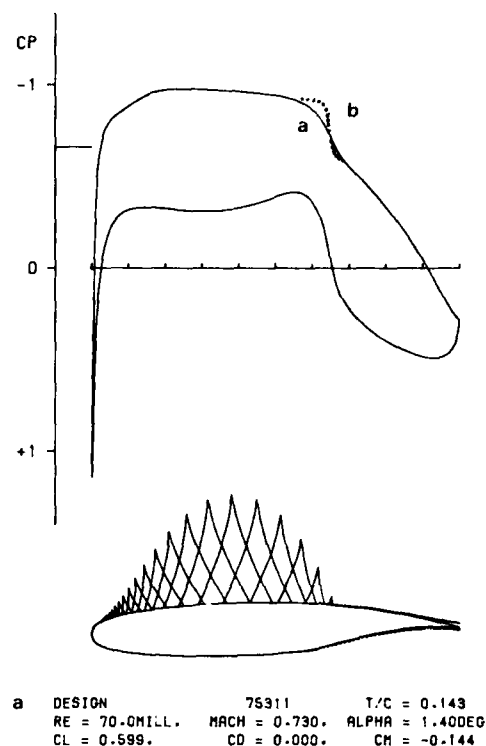


Figure 5.
Shock free redesign of airfoil Fig. 4 (a) and
subsequent analysis verification (b).

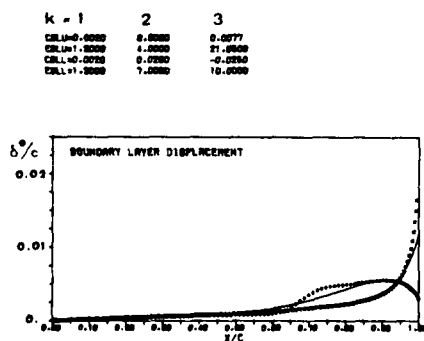


Figure 7.
Boundary layer displacement thickness
modeled (lines) and verified (symbols).

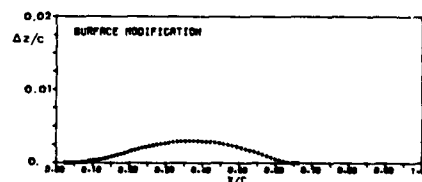


Figure 6.
Surface modification of airfoil Fig. 4 to be
shock-free at specified operating conditions
Fig. 5.

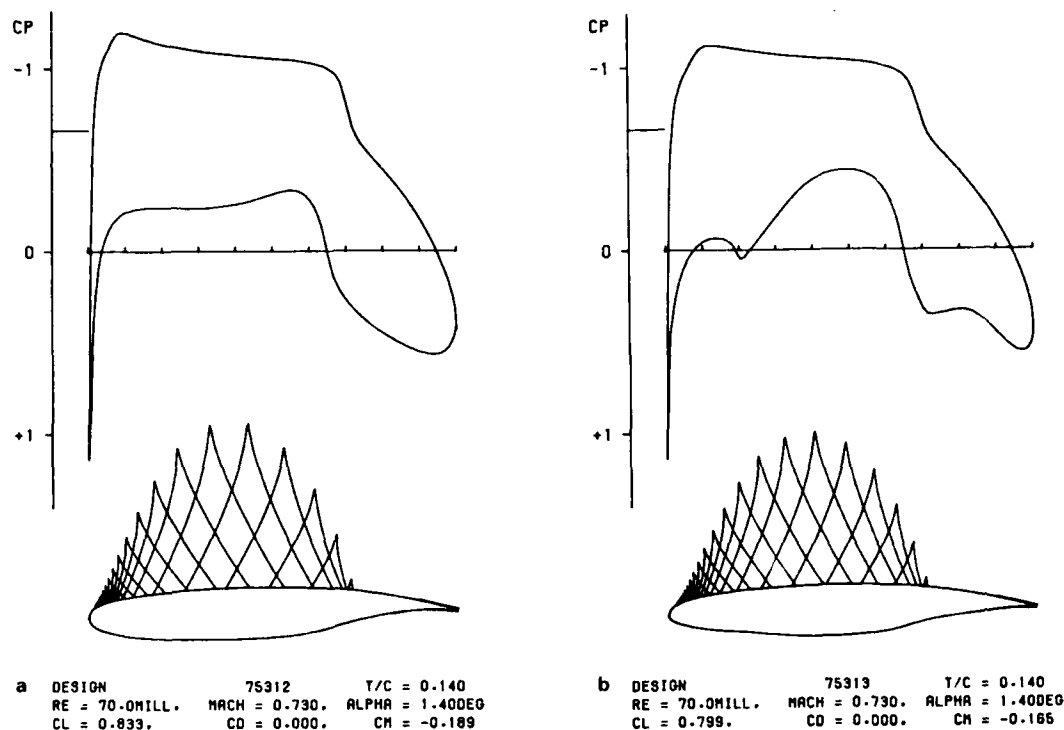


Figure 8. Redesign of the airfoil Fig. 4 with laminar flow control (a), lower surface modification for LFC applications (b).

method of characteristics. The result is a shock-free airfoil with a rooftop - type pressure distribution, see Figure 5. A subsequent analysis control of the new airfoil shows practically shock-free flow, too, as illustrated in Fig. 5. Present results were obtained on an IBM 370/158 machine with single precision.

The redesigned airfoil differs from the initial configuration only along the arc wetted by supersonic flow. Figure 6 shows the amount of surface modification smoothly distributed between 2 and 67 percent chord on the upper surface. The maximal local thickness reduction is situated at 38 percent chord, airfoil thickness is reduced from 14.6 to 14.3 percent. Figure 7 shows boundary layer displacement computation results (symbols) and analytical modeling including trailing edge correction (lines). Only three components ($k_e = 3$ in (4)) were used for simplicity for upper and lower side displacement thickness which seems generally sufficient for satisfactory modeling, except perhaps here on the rear loaded part of the lower side. The design example presented in Fig. 5 has been obtained for a high Reynolds number with an almost fully turbulent boundary layer. With respect to the concept of maintaining laminar flow over a large portion of a wing, different design computations were carried out for prescribed transition stations. Viscous displacement growth is reduced this way and the effective Kutta condition allows for higher circulation.

Figure 8a shows a design with assumed transition at 60 percent chord, lift coefficient has increased remarkably. In Fig. 8b another design is illustrated, here the initial configuration has been changed on the lower surface prior to the shock-free design process in order to guarantee the desired subsonic pressure distribution for a Laminar Flow Control (LFC) wing section. The concept is studied for application in long range transport aircraft [29].

While boundary layer control is regaining some portion of ideal inviscid performance, the concept of Circulation Control (CC) offers similar advantages for different applications. A well-known phenomenon called the Coanda effect is used to obtain high circulation around airfoils with round trailing edge, see Figure 9a. Tangential blowing from a slot maintains attached flow around a large part of the rounded trailing edge. Circulation is controlled this way and allows for extremely high lift. The concept has been investigated experimentally [30] and applications for helicopter rotors are studied.

An idealized treatment of circulatory flow past round trailing edge airfoils may be carried into the transonic regime using our shock-free airfoil design code. As a simple initial configuration we choose a 20 % thick ellipse and fix the trailing stagnation point on some prescribed position on the round trailing edge, thus modeling the main influence of a Coanda jet on potential outer flow, Figure 9b. Circulatory flow around the ellipse results in large local supersonic regions, we ask for design limits in Mach number and lift coefficient defined by the occurrence of limit lines showing from inside of the airfoil contour. Figure 10 shows some results, two of them are extreme cases where surface deformation brings almost corners to the contour. These design limits are shown in a $c_L - M_\infty$ diagram Figure 11.

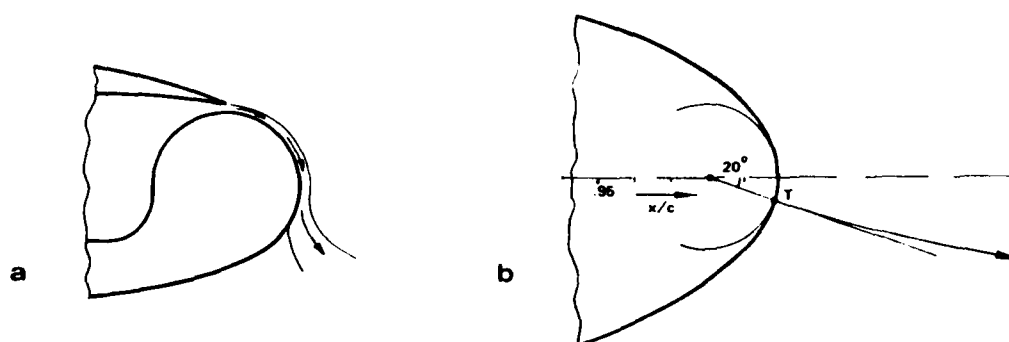


Figure 9. Circulation control with a Coanda jet (a), inviscid outer flow model with fixed trailing edge stagnation point (b).

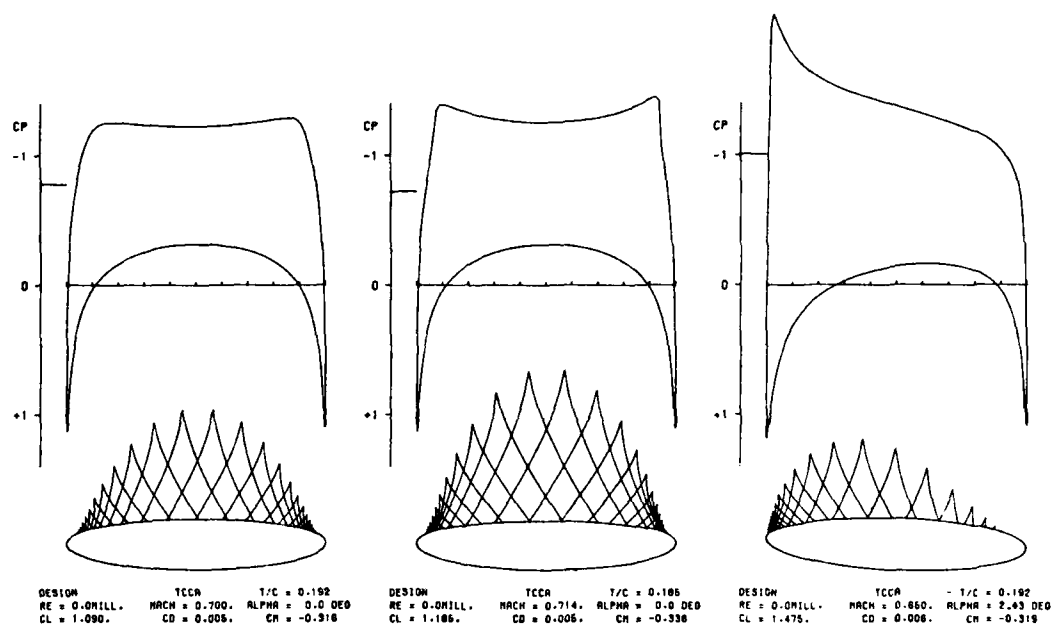
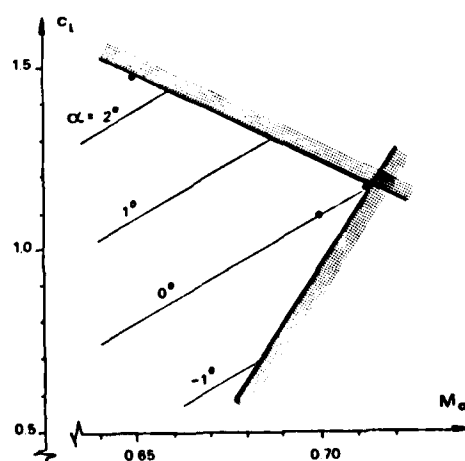


Figure 10. Shock-free transonic flows past redesigned 20 % thick ellipse.

Figure 11.
Design limits for shock-free inviscid
redesign of a 20 % thick ellipse.



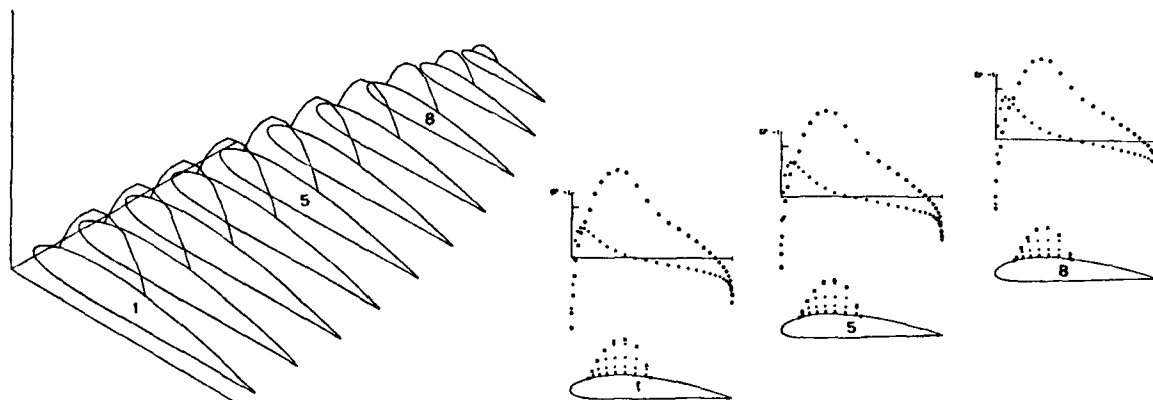


Figure 12. Fictitious gas analysis: sonic surface and pressure distribution on an elliptic test wing with NACA 4415 sections. ($M_\infty = 0.7$, $\alpha = 0^\circ$, $c_L = 0.58$)

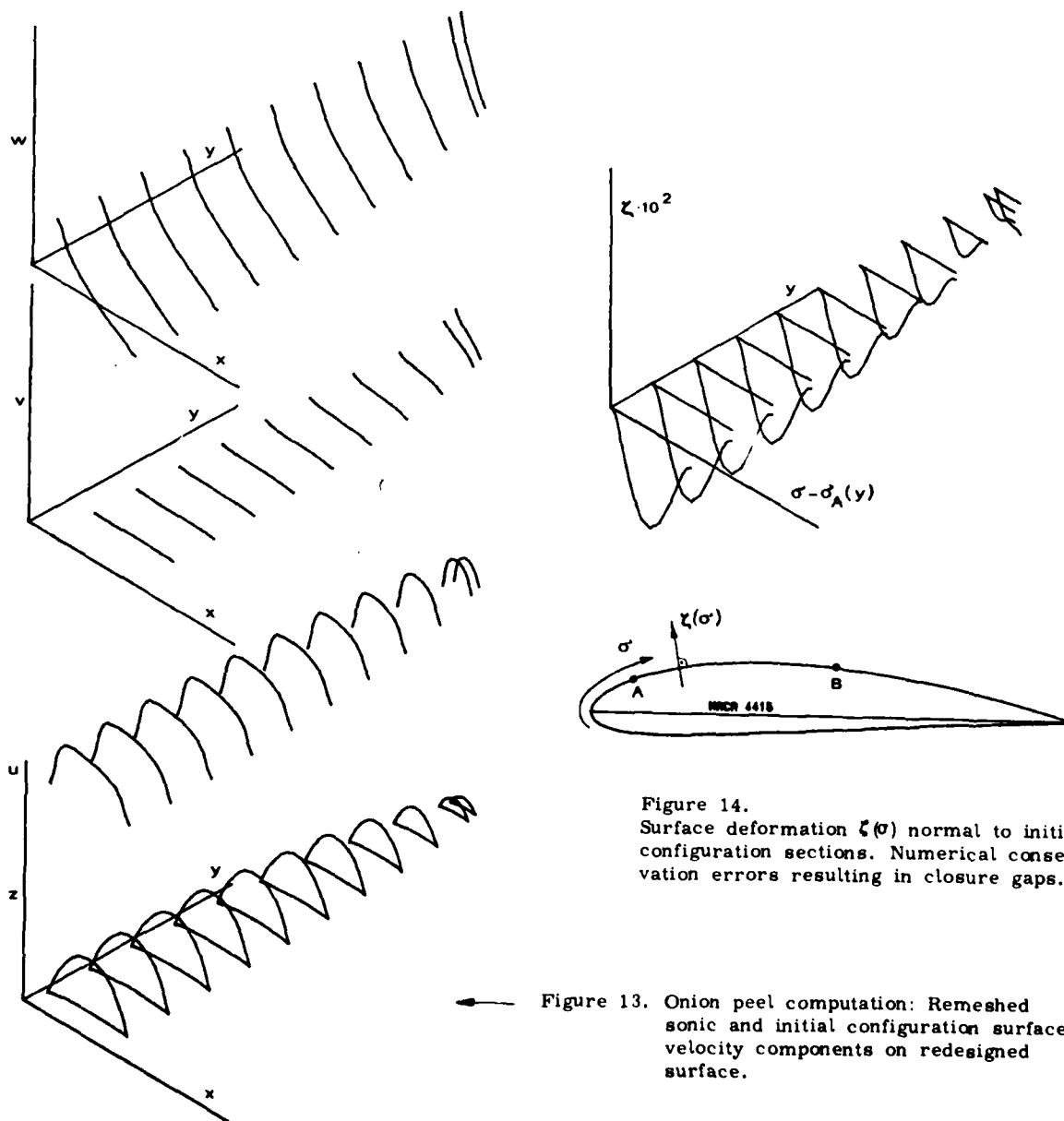


Figure 14. Surface deformation $\zeta(\sigma)$ normal to initial configuration sections. Numerical conservation errors resulting in closure gaps.

Figure 13. Onion peel computation: Remeshed sonic and initial configuration surface; velocity components on redesigned surface.

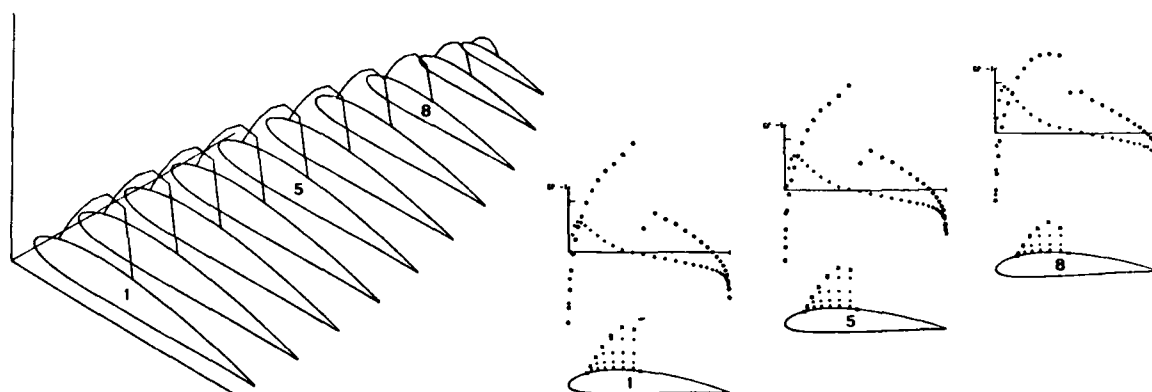


Figure 15. Analysis of initial configuration elliptic test wing ($M_\infty = 0.7$, $\alpha = 0^\circ$, $c_L = 0.58$).

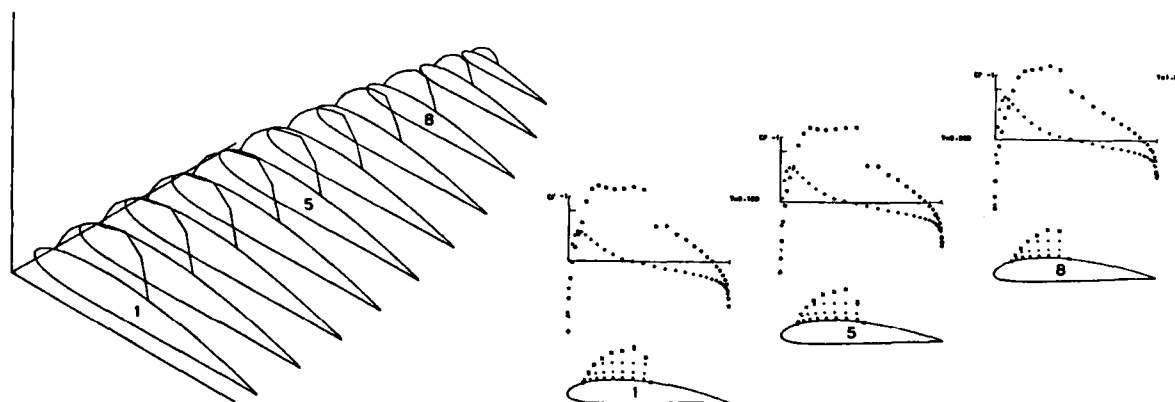


Figure 16. Analysis of redesigned configuration elliptic test wing ($M_\infty = 0.7$, $\alpha = 0^\circ$, $c_L = 0.58$).

DESIGN OF 3D SHOCK-FREE FLOWS: A TEST WING EXAMPLE

So far this paper illustrated some airfoil design results including viscous effects or at least inviscid idealizations supporting new concepts to control viscous effects. The design of shock-free airfoils has proved to be an important first step of practical supercritical wing design but nevertheless any systematic extension of computational techniques from 2D into 3D space is welcome to the design engineer.

For 3D wing design the "Onion Peel" marching procedure is used but present experience with practical cases is less extensive than with airfoil design. Also 3D boundary layer computation is less advanced. Illustration given for shock-free wing design in this paper is restricted to inviscid flow. In the following results for a simple unswept test wing are given, see Figures 12 - 16. An elliptic planform with aspect ratio $AR = 16/\pi = 5.1$ and a straight quarter chord line is chosen. With a center chord length $c = 1$ the rounded wing tip is located at $x = 0.25$ and semispan $y = 2$. One single airfoil, the NACA 4415 is used to define all wing sections. Wing twist is prescribed by the relation

$$\epsilon^0 = 2.5(1 - 0.25 y^2).$$

For inviscid isentropic and fictitious gas analysis a simple finite element method based on a variational principle was developed and provided by A. Eberle [31]. For our redesign concept the code was extended by a careful interpolation of the sonic surface results, this is illustrated in Figure 12: the isometric view shows the test wing and a sonic surface obtained by fictitious gas analysis ($P = 0.9$) at a Mach number $M_\infty = 0.7$. Computational grid points are marked within the fictitious supersonic region on some representative sections. We observe that the size of the supersonic region relative to the local chord length is rather constant. Pressure distribution within the subsonic field outside the sonic bubble is already the resulting design pressure. Lift and drag coefficients are also already design results, they will not be altered by the subsequent computation

of local supersonic flow. Interpolated values of the velocity distribution are found on each section, here on some 8 - 10 points along the sonic lines, depending on the number of grid intersections.

Next the sonic surface values (geometry and velocity components) are redistributed by a spline fit on a new grid with more points (here: 20) on the sonic lines. From experience with the method of characteristics in 2D it follows easily that sonic surface grid points should be distributed with a density proportional to streamline curvature, which follows from the velocity gradients along the sonic surface. Also, a spanwise redistribution of sections may be useful, here only the outermost section distance was reduced due to the large gradients of geometry and velocity near the rounded elliptic tip. For definition of an Onion Peel grid we also remesh the initial configuration surface within the sonic bubble, in the present case 5 Onion Peels were used to march from sonic to initial surface as illustrated in Fig. 3c. Geometry and resulting velocity components on the new wing surface are illustrated in Figure 13. The smooth distribution indicates a successful suppression of any numerical instabilities. Velocity defines a new shock-free distribution of the pressure coefficient replacing the fictitious supersonic part of the results in Fig. 12. The new surface is found by iterative integration of the differences between directions of resulting velocity (u, v, w) and the initial configuration using the stream surface condition

$$(z_x)_y = c_x = (w - v \cdot z_{oy}) / (u - v \cdot x_{oy})$$

where $x_o(y)$, $z_o(y)$ define a line along the wing stream surface. Numerical conservation errors result in closure gaps of the integrated surface. In Figure 14 the resulting surface deformation without correction is drawn: a closure gap approximately 10 percent of the maximum surface deformation is observed which seems satisfactory with respect of the chosen crude tolerance requirements in the analysis method. After a closure correction the present result is used now to define an analytical bump $\zeta(\sigma)$ to be subtracted from the initial configuration sections. In the present case this requires modifications of the NACA 4415 sections between sonic expansion (A) and recompression (B) points, Fig. 14. The maximum value of surface deformation is

$$\zeta_{\max}/c = 0.0043$$

and occurs on the center section.

The modeled analytical surface deformation $\zeta(\sigma)$ is introduced now into the wing geometry generator code, a flattened test wing is created. An over-all control of the design was carried out next by using the original wing analysis code. For comparison also the initial configuration was analyzed with the same operating conditions (as illustrated earlier in Figures 4 and 5 for airfoil design). Figure 15 shows the initial configuration in isentropic flow exhibiting a local supersonic region terminated by a strong shock. Analysis results for the redesigned wing are shown in Figure 16. A very weak shock - compared to the other case - is still observed but shape and extent of the sonic surface come close to the design result in Fig. 12.

The present test wing example will be investigated also by other analysis and design methods and subsequently viscous displacement will be modeled from a suitable 3D boundary layer computation. Such a result may serve also as an experimental test case in a transonic wind tunnel. However until then, parallel to the necessary improvements of the method, studies of inviscid outer flows seem useful to extend knowledge about the structure of local supersonic fields embedded in flows past different types of configurations.

STRUCTURE OF LOCAL SUPERSONIC FLOW PAST AFT AND FORWARD SWEPT WINGS

Another test of the shock-free redesign procedure is an investigation of forward swept wings in transonic flow and a comparison with equivalent wings with aft sweep. Simple configurations with aspect ratio 5 and NACA 4-digit sections were used to study the influence of sweep on the structure of possible shock-free flow. Two wings with equal aft and forward sweep, respectively, of the quarter-chord line were redesigned to be shock-free at a Mach number $M_\infty = 0.74$. The wings have the same spanwise section and twist distribution. Angle of attack was adjusted for both cases so that equal $c_L = 0.45$ was obtained. Wing planforms with the resulting area of supersonic flow for equal (M_∞, c_L) operating conditions are drawn in Figure 17. We observe that the local supersonic field on the aft swept wing extends from the center to the tips with approximately equal size, while the field on the forward swept wing does not extend to the tips but is stronger in the center region. We conclude that wing tip effects on aft swept wings might pose more practical problems than on equivalent forward swept wings. A breakdown of shock-free flow at the tip of aft swept wings due to interaction with the tip vortex seems almost inevitable if tip vortex and sonic bubble are not separated by a winglet. Our shock-free redesign procedure is perturbed if the sonic bubble is "open" toward the tip. A proper formulation of the Cauchy initial value problem needs data on a closed bubble in order to keep the resulting stream surface completely within the domain of dependence defined by the Mach conoid envelopes Fig. 2b. The error of "open" sonic bubbles is reflected in intolerable surface deformation closure gaps in the tip region (see Fig. 14 for the elliptic test wing) or even a breakdown of the marching procedure due to uncontrollable numerical instabilities proceeding from the tip toward the center. Our present experience to handle such effects is still very limited but the favorable effect of "closing" an open sonic bubble by a winglet seems manifest.

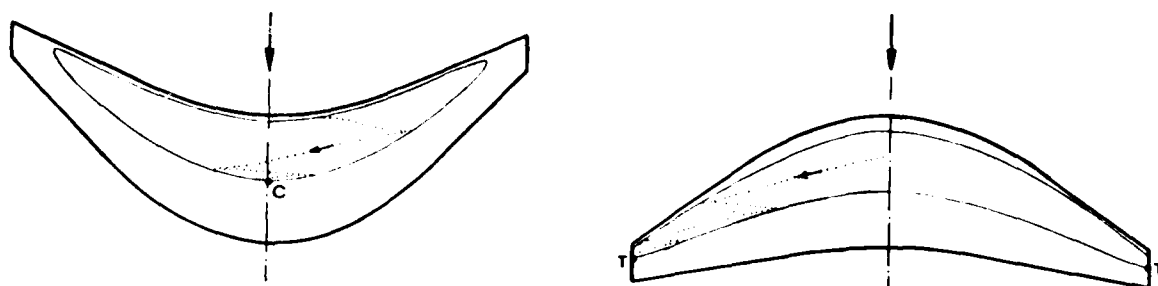


Figure 17. Aft and forward swept wing planforms. Surface area wetted by supersonic flow at equal M_∞ and c_{L1} . Characteristics on wing surface.

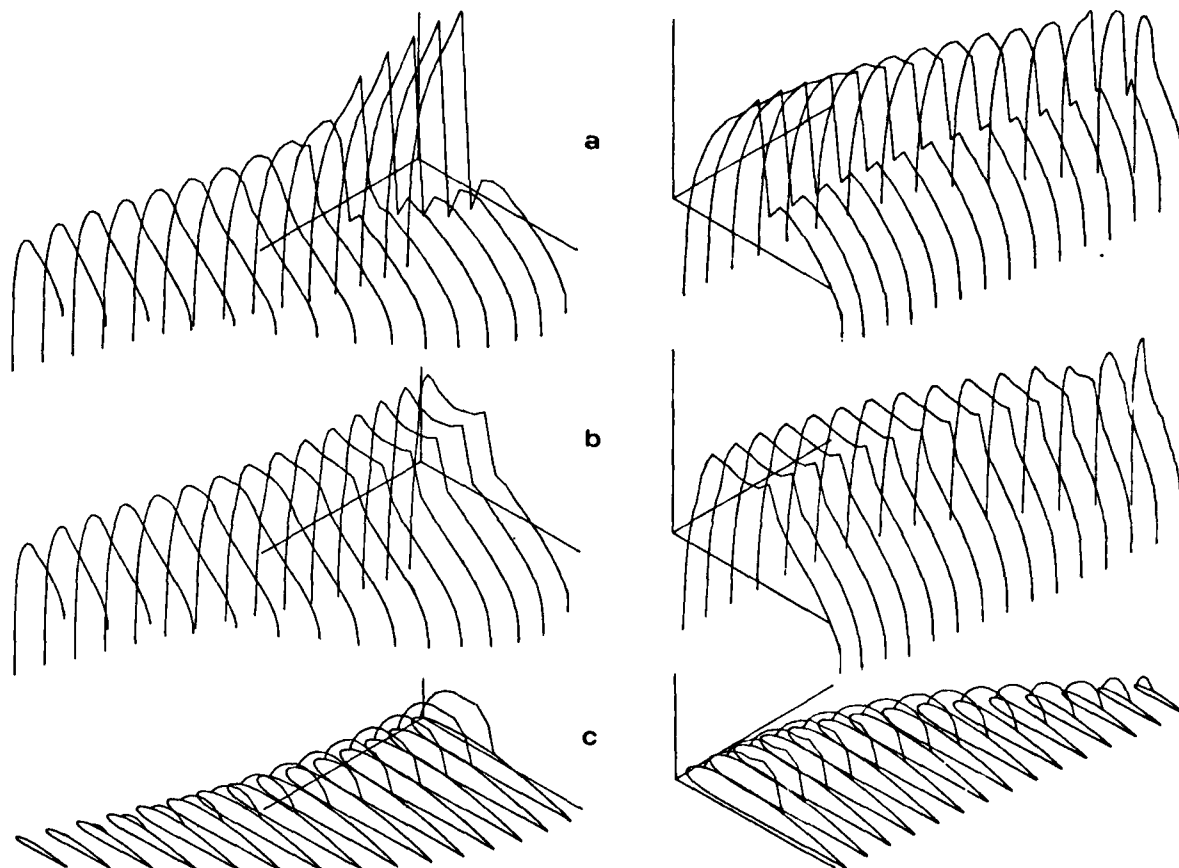


Figure 18. Analysis of aft and forward swept wings: upper surface pressure distribution of initial (a) and redesigned (b) wings, sonic surface on redesigned wings (c).

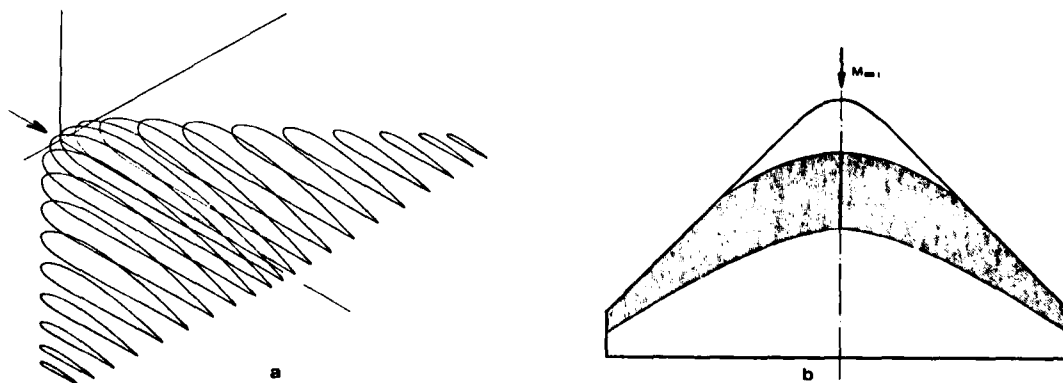


Figure 19. Thick delta wing with adaptive shape for shock-free flight at variable operating conditions.

Forward swept wings, on the other hand, need special care at the center region. Following the characteristics on the surface on both swept wings, Fig. 17, we end at the tips T on the aft swept wing, but on the sonic recompression point C of the center section on the forward swept wing. We conclude that any perturbation of the shock-free field is washed into points T and C, respectively. Forward sweep has a contracting effect on the flow past the upper surface. A wing body configuration with a forward swept wing therefore should be more sensitive to area ruling of the body than the aft swept wing. Analysis of the present redesigned swept wings show good agreement with the design prediction, see Figure 18.

ADAPTIVE CONFIGURATIONS

The chosen examples of swept wings Fig. 17 are investigated at relatively low transonic Mach numbers so that the suitable marching direction of the Onion Peel procedure is normal to the plan-form (Fig. 3a). For higher Mach numbers and larger sweep, parabolic coordinates (Fig. 3b) need to be introduced. Such a case is studied as another test example, Figure 19a. A very thick low aspect ratio delta wing serves to study surface modifications for varying Mach numbers. The local supersonic field extends to the leading edge (Fig. 19b) along a large portion of span.

For design Mach numbers lower than $M_{\infty 1}$ the resulting supersonic field is reduced in size and extent on the wing surface, it vanishes at the critical Mach number $M_{\infty cr}$ where the flow is completely subsonic. Our design method allows shock-free redesign for supercritical conditions $M_{\infty cr} < M_{\infty} < M_{\infty 1}$ with a constraint, say prescribed $c_L(M_{\infty})$, which is met by variation of the design-angle of attack.

We may think of a possible realization of the different shock-free shapes for different Mach numbers by adaptive section geometry of the wing provided by mechanical devices like elastic or pneumatic deformation, suction and blowing or a combination of these means [32]. An application of adaptive section geometry to a thick span loader flying wing might be a suitable 3D experimental test case for the concept because of available space within the wing to house the mechanism for shape variation.

CONCLUSION

A systematical method to design supercritical shock-free 2D and 3D configurations is illustrated. Simplified examples are chosen from airfoils and wings which are used in advanced technology aerodynamic concepts. With the outlined methods theoretical tools are presented to extend essentially subsonic design aerodynamics into the transonic regime.

REFERENCES

- [1] Ringleb, F., "Exakte Lösungen der Differentialgleichung einer adiabatischen Gasströmung. Z. angew. Math. Mech. 20, (1940) p. 185.
- [2] Whitcomb, R.T., and Clark, L.R., "An airfoil shape for efficient flight at supercritical Mach numbers," NASA TM X-1109 (Confidential Report), (1965).
- [3] Pearcey, H.H., "The Aerodynamic Design of Section Shapes for Swept Wings," Advances in Aeronautical Sciences, Vol. 3, (1962), pp. 277-322.
- [4] Nieuwland, G.Y., "Transonic Potential Flow Around a Family of Quasi-Elliptical Airfoil Sections," National Lucht en Ruimtevaart Laboratorium Rept. TR-T 172, Amsterdam, The Netherlands, (1967).
- [5] Garabedian, P.R. and Korn, D.G., "Numerical Design of Transonic Airfoils," Numerical Solution to Partial Differential Equations, Vol. II, Academic Press, New York, (1978), pp. 253-271.
- [6] Boerstol, J.W., Design and analysis of a hodograph method for the calculation of supercritical shock-free airfoils, NLR TR 77046 U (1977).
- [7] Murman, E.M., and Cole, J.D., "Calculation of Plane Steady Transonic Flows," A.I.A.A.J., vol. 9 (1971), pp. 114-121.
- [8] Jameson, A., "Iterative solution of transonic flows over airfoils and wings, including flows at Mach 1." Comm. Pure Appl. Math. 27 (1974).
- [9] Ballhaus, W.F., Bailey, F.R., and Frick, I., "Improved Computational Treatment of Transonic Flow about Swept Wings." NASA CP 2001, (1976).
- [10] Jameson, A., Caughey, D.A., "Numerical Calculations of the Transonic Flow past a Swept Wing." NASA CR - 153297, (1977).
- [11] Melnik, R.E., and Chow, R., "Asymptotic Theory of Two-dimensional Trailing Edge Flows," NASA Conference on Aerodynamic Analysis Requiring Advanced Computers, NASA SP 347, (1975).
- [12] Hicks, R., and P.A. Henne, "Wing Design by Numerical Optimization," AIAA Paper 77-1247, Seattle, Wash., (1977).

- [13] Sobieczky, H., "Entwurf überkritischer Profile mit Hilfe der rheoelektrischen Analogie", Deutsche Luft- und Raumfahrt DLR-FB 75-43 (1975).
- [14] Sobieczky, H., N.J. Yu, K.-Y. Fung, A.R. Seebass, "New Method für Designing Shock-free Transonic Configurations," AIAA Journal Vol. 17, No. 7 (1979).
- [15] Sobieczky, H., "Rheograph Transformation and Continuation Methods," Von Karman Institute for Fluid Dynamics, Lecture Series 1980 - 4, "Mathematical Methods in Fluid Mechanics", (1980).
- [16] Sobieczky, H., "Related Analytical, Analog and Numerical Methods in Transonic Airfoil Design," AIAA paper 79-1556 (1979).
- [17] CTOL Transport Technology - 1978, NASA Conference publication 2036, (1978).
- [18] Advanced Technology Airfoil Research Conference, NASA Conference publication 2045, (1978).
- [19] Eberle, A., "Profiloptimierung für transsonische Strömung mittels der Methode der finiten Elemente und Charakteristiken," MBB Report UFE 1362 (Ö) (1977).
- [20] Yu, N.J., P.E. Rubbert, "Transonic wing redesign using a generalized fictitious gas method," Boeing Document D-180-25309-1 (1979).
- [21] Fung, K-Y., H. Sobieczky, A.R. Seebass, "Numerical Aspects of the Design of Shock-free Wings and Wing-Body Combinations," AIAA paper 79-1557 (1979).
- [22] Yu, N.J., "An Efficient Transonic Shock-free Wing Redesign Procedure using a fictitious gas method," AIAA paper 79-0075 (1979).
- [23] Nebeck, H.E., H. Sobieczky, R. Seebass, "Boundary - layer displacement and wake - curvature effects on the design of a family of shock-free supercritical airfoils," Paper presented at the AGARD FDP Symposium on computation of viscous/inviscid interaction (1980).
- [24] J.C. Rotta, "FORTRAN IV-Rechenprogramm für Grenzschichten bei kompressiblen ebenen und achsensymmetrischen Strömungen," Deutsche Luft- und Raumfahrt, Forschungsbericht 71-51 (1971).
- [25] E. Stanewsky, P. Thiede, "Boundary layer and wake measurements in the trailing edge region of a rear-loaded transonic airfoil", DEA-Meeting "Viscous and Interacting Flow Field Effects", Meersburg/Bodensee, (1979).
- [26] Inger, G.R., Analytical Theory of Transonic Shock-Turbulent Boundary-Layer Interaction" AIAA Journal, 14, 9, pp. 1266-1272, (1976).
- [27] Nandanan, M., E. Stanewsky, G.R. Inger, "A computational procedure for transonic airfoil flow including a special solution for shock-boundary layer interaction", AIAA paper 80-1389 (1980).
- [28] Kacprzynski, J.J., Ohman, L.H., Garabedian, P.R., and Korn, D.G., "Analysis of the flow past a shockless lifting airfoil in design and off-design conditions," N.R.C. of Canada Aeronautical Report LR 554, Ottawa (1971).
- [29] Allison, D.O., I.R. Dagenhart, "Design of a laminar - flow - control supercritical airfoil for a swept wing", CTOL Transport Technology 1978 NASA CP 2036, Part 1 (1978) p. 395.
- [30] Englar, R.J., "Circulation Control for High Lift and Drag Generation on STOL Aircraft," AIAA Journal of Aircraft, Vol. 12, No. 5, (1975), pp. 457-463.
- [31] Eberle, A., "Eine Methode der finiten Volumen zur Berechnung der transsonischen Potentialströmung um Flügel aus dem Druckminimumintegral", MBB Report UFE 1407(Ö) (1978).
- [32] Sobieczky, H., A.R. Seebass, "Adaptive Airfoils and Wings for Shock-free Supercritical Flight," Invention Disclosure, The University of Arizona, Tucson, AZ, Engineering Experiment Station Report TFD 78-02 (1978).

INTERFERENCE ASPECTS OF THE A310 HIGH SPEED WING CONFIGURATION

by

J.A. Jupp
Head of Fluid Dynamics,
Aerodynamics Department
BRITISH AEROSPACE (Aircraft Group)
Hatfield-Chester Division
Hatfield, Hertfordshire

SUMMARY

The development of the A310 wing represents a major milestone in the history of European transonic wing design for large transport aircraft. Since the completion of the wing for the A300, the revolution in computational methods for predicting pressure distributions has enabled the A310 design to be carried out almost wholly theoretically, allowing more time and effort in the wind tunnel programme to be directed towards important interference effects between the wing and other components of the aircraft.

Following an overview of the impact of the advances in computational methods, these "interference" aspects of the A310 wing design will be presented in this paper. Topics from the theoretical design programme include the effect of the fuselage representation on the inboard wing transonic design and the influence of the tailplane in the optimisation of the wing twist for minimum drag etc. Highlights from the experimental wind tunnel programme include the development of the wing root leading edge fillet to improve wing/fuselage viscous interference, and the optimisation of the flap support fairings for the minimum high speed interference. Attention is drawn to the importance of these aspects in developing a successful integrated aerodynamic design for a transport aircraft.

INTRODUCTION

The A310 is the latest addition to the Airbus Industrie family of transport aircraft, using a shortened version of the A300 fuselage to give a capacity of about 210 passengers (compared with 260). Initial project studies explored options including the use of the A300 wing with and without modifications, but several factors, with the greatly increased price of fuel in the fore-front, resulted in a decision to design a completely new wing of reduced size for the A310. Although the configuration of the wing is superficially very similar to the A300 (Figure 1), it does in fact represent a major milestone in the history of European wing design for large transport aircraft cruising at high subsonic speeds.

The wing for the currently very successful A300, now in service with airlines worldwide, was designed using approximate subsonic theoretical methods and relied heavily on wind tunnel testing and the experience of the Hatfield design team to obtain good supercritical flow development at the design cruise conditions. Between the completion of the basic A300 wing design in 1969 and the start of the A310 design in December 1976, there has been a revolution in theoretical pressure distribution computation methods led by our friends in the United States.

For the first time it became possible to compute the transonic flow field around a three-dimensional wing with embedded regions of supersonic flow terminated by shock waves. Apart from advancing the aerodynamic standards achievable, this new theoretical capability had a significant effect on the timescales of the wing design process, and released time and effort in the experimental wind tunnel programme to investigate the "interference" problems involved in integrating the wing with the other components of the aircraft. Indeed, with the advanced aerodynamic standards that were being sought on the A310, it was realised right at the start of this new project that this integration of the wing was potentially going to be more difficult than on the A300.

A complete description of the aerodynamic wing design for the A310 would be quite outside the scope of this paper, as well as being outside the terms of reference of this Symposium. Therefore, following a short description of the impact of the new computational methods on the aerodynamic standards achieved and on the organisation of the wind tunnel programme, I will be concentrating in this paper on just those aspects of the high speed wing design concerned with the interactions with the rest of the aircraft.

IMPACT OF THE ADVANCE IN COMPUTATIONAL METHODS

Before passing on to the main objective of this paper, it is relevant to say something on the broad impact that the new computational methods have had on the wing design process. The A310 wing was designed using computer programs developed by the Royal Aircraft Establishment, the Aircraft Research Association and 'in house' at B.Ae. Hatfield. The use of these programs was responsible for a major advance in aerodynamic standards which would have been very difficult and time consuming to achieve with the

mix of experimental and approximate subsonic computational methods available at the time of the A300 design. The advance achieved is indicated in Figure 2 where the spanwise distribution of wing thickness-chord ratios, and the compressibility drag rise boundaries from High Reynolds Number tests on the clean wings (mounted on identical fuselages), are compared for the A300 and A310. It may be seen that the A310 wing is substantially thicker, especially at the inner end where it has most effect on wing weight and fuel volume etc., and carries considerably more lift at the expense of a slight loss in Mach Number capability at lower lift coefficients. In fact, as it turned out, the wind tunnel programme had very little impact on the wing design process in achieving this advance. This was a very different situation to that on the A300, as may be seen by reference to the paper by McRae (Reference 1) given to the Royal Aeronautical Society in 1973.

In this context it is interesting to compare the list of high speed wind tunnel models and overall timescales relevant to the basic wing design for the A300 and A310. In Figure 3 abridged versions of Tables 3 and 5 from Reference 1 are compared with the equivalent data for the A310. Also given are the dates for the start of the theoretical wing design and for the wing geometry definition of the respective aircraft. In fact, the difference in model testing is even more appreciable than it appears at first sight, as the two dimensional wing section testing for the A310 was at no time significantly in advance of the three dimensional testing. These two dimensional sections were included only as an 'insurance' for comparison with the complete models to assist in diagnosing any major problems if they occurred, and to provide vehicles for rapidly checking minor modifications for the outboard wing sections if necessary. The first A310 three dimensional model (Wing 4 in Figure 3) incorporated a very preliminary inner wing design, and was committed for testing to get an early check on the buffet boundary and general characteristics of the new advanced outboard wing sections for the A310, as well as to provide a model on which to start investigating the various interference problems that will be discussed later in this paper. Wing 5 was a very minor modification to Wing 4 to increase the thickness in the region of 90% chord without (as it turned out) affecting the aerodynamics of the wing.

Wing 6 had an identical outboard wing to Wing 5, and incorporated the definitive inboard wing design from the theoretical design programme. As expected, this wing showed similar buffet characteristics to Wing 5, but a much improved drag rise boundary.

At this stage, the theoretical predictions of the buffet limited altitude capability of the aircraft were being borne out by the two and three dimensional test results. Following further project optimisation studies by Airbus Industrie, the decision was taken to increase the wing area to improve the altitude capability, mainly by increasing the chord at constant wing thickness (giving a pro-rata reduction in wing/thickness chord ratio). This was done in principle by redesigning the lower surface of the wing sections and maintaining the same upper surface aerodynamic features on the new Wing 18 as on the previous Wing 6, thus involving very little aerodynamic redesign.

Wing 18 was successfully first tested at ARA Bedford in August 1978, leading to the choice of this wing for the A310 in the Autumn of 1978. Because of the particular circumstances at the time each aircraft was going through its project phase, it is very difficult to give comparative milestones for the A300 and A310, but the start and completion dates given in Figure 3 are as closely equivalent as it is possible to be.

Summarising then, the modern computational methods have led to a significant improvement of aerodynamic standard in reduced timescales and with less tunnel testing than was the case for the A300. On the other side of the equation it must be said that this does not necessarily mean that the A310 wing design in total was carried out any more cheaply than the A300. Computing costs balanced the reduction in experimental costs, but nonetheless the timescales that might have been involved in seeking the same advance in performance with the older theoretical/experimental methods could easily have been more than twice as long as the present achievement of less than two years, if successful at all!

FACTORS IN THE A310 HIGH SPEED WING DESIGN

The factors involved right from the start of the A310 wing design process are shown in Figure 4. Looking through these items in turn, the investigations fell into three main areas; the theoretical wing design already referred to, the wind tunnel test programme and a combined programme including flight testing on the A300 aimed at cleaning up the gaps, steps, etc., due to manufacturing tolerances and control surfaces, and at checking their effects on the characteristics of the new advanced wing design. Having referred to the impact of the new computational methods and shown the general advance achieved relative to the A300, a full description of the basic high speed wing design (items 1 and 2 in Figure 4) is outside the scope of this present paper as mentioned earlier. However, some aspects of the theoretical design are relevant under the heading of "interference" (items 2 and 3) and these will be discussed along with items 4, 5 and 6 in Figure 4 which were investigated mainly experimentally. For the most part, items 7, 8 and 9 were concerned with the practical aspects of incorporating gap sealing and revised control surface configurations (as demonstrated in flight on the A300) to improve the cruise drag standard of the wing, and with checking that the

characteristics of the high speed control surfaces could be read across from the A300 to the new advanced wing design. Again, a part of this investigation was relevant to interference problems (item 9).

Thus it will be seen that a major proportion of the effort that went into the design of the A310 was directed towards solving problems concerned with integrating the wing into the aircraft as a whole, and in the remainder of this paper something will be said about these factors in turn.

INNER WING DESIGN

The theoretical transonic design of the inboard wing was of course dominated by interference problems, fundamentally due to the presence of the fuselage complicated by the need to make the inboard wing as thick as possible to improve weight and fuel volume, and to stow the undercarriage behind the basic structural wing box. Up to a year or so before the start of the A310 programme, the theoretical methods at our disposal could only cope with the wing root by treating it as the centre section of an isolated swept wing. The only further allowance made for the fuselage was in recognising that it had a pressure field as an isolated body which effectively increased the flow velocities over the wing. This was incorporated in the wing design process as a requirement for a higher design Mach Number than directly implied by the aircraft cruise conditions.

Approximating the wing root section at the fuselage side by the centre section of an isolated swept wing was known to be inadequate even at the time of the A300 design, and the situation was worse when the newer methods offered the possibility of designing for shock-free supersonic flow over the wing surface. This is shown in Figure 5, where an acceptable near shock-free theoretical pressure distribution for the centre section of an isolated swept wing is compared with the predicted pressure distribution for the wing/fuselage combination, with the same geometry at the same conditions. It may be seen that a stronger shock is present on the wing upper surface with the fuselage present, but on the other hand, the velocities on the wing lower surface are less than predicted in the "wing alone" case. These effects were indeed demonstrated on a research wing designed by the wing-alone transonic theory in the period before the start of the work for the A310. Of course, the A310 was designed (by an iterative procedure) to achieve the original near shock-free type of pressure distribution in the presence of the fuselage, and full use was made of the effect of the fuselage on the wing lower surface to design for the maximum root thickness consistent with the desired lift distribution across the span and the practical restraints on the depth of the wing centre section within the fuselage.

It should be noted that the wing/fuselage transonic flow calculation method available to us for routine use at the time of the A310 wing design represented the fuselage as an infinitely long body of constant cross-sectional shape. At least for the A310 application, and perhaps generally for transport aircraft where the wing is mounted on the parallel sided centre section of the fuselage, this assumption had been shown to be quite adequate as long as the fuselage "supercriticality" effect mentioned earlier is taken into account. The effect of the finite length of the fuselage on the increase in the flow velocities past the wing was an important consideration for the A310, which being a reduced capacity derivative of the A300 has a fuselage with a relatively high diameter to length ratio. Simple isolated body calculations showed that the effective average increase in flow Mach Number past the wing due to the shortening of the fuselage relative to the A300 was of the order $\Delta M = 0.0045$. Thus at constant flight Mach Number, a reduction in the drag rise Mach Number of the wing by the same amount was predicted, and was incorporated in the wing design process. Although close to the accuracy achievable in the wind tunnel tests, the equivalent small but not negligible effect on cruise drag was indeed found in experiment (Figure 6).

The wing planform for the A310 is very heavily cranked at the trailing edge (Figure 1). Similar to the A300, this resulted from a requirement to maintain the trailing edge sweep of the outboard wing whilst giving (a) sufficient space and depth in the inner wing to stow the undercarriage behind the main load carrying structural wing box and (b) more scope for increasing the overall depth of the inner wing for lighter weight and increased fuel tank volume. There has been some discussion about the problems that such a pronounced trailing edge crank might cause in a modern wing design, but with the design philosophy we followed for the A310, the planform crank just did not give any significant trouble. Certainly, the three dimensional calculation methods available at the time were believed to be misleading in the region of the planform crank. However, here the experience of the design team helped, and we followed the same basic concept as on the A300 in designing for isobars (lines of constant pressure) in the forward supercritical flow region which lay along constant percentage chord lines of the basic "trapezium" wing planform (Figure 2). This was backed up by arranging the generators actually defining the doubly curved surface of the wing along the same lines, and defining the curvature of the inboard trailing edge so that the wing section incidence was held low just inboard of the crank.

One example of the success achieved is given in Figure 7, where wind tunnel test wing upper surface isobars for the supersonic zone are shown at a condition where a substantial shock wave has formed above the cruise lift coefficient range and close to the buffet boundary at the long range cruise Mach Number. A near constant shock sweep

has been maintained (indicated by the region where the isobars bunch together at the rear of the supersonic zone) with some weakening of the main shock on the inner wing with a hint of the formation of the traditional forward "lambda" double shock system near the root.

EFFECT OF THE TAILPLANE ON WING TWIST OPTIMISATION

In searching for an improvement in aerodynamic standards it is very rarely, if ever, that an advance is obtained completely free from attendant problems which must be allowed for in the total optimisation of the project. Thus in obtaining the improved clean wing standards indicated in Figure 2, it was inevitable that the increased load carrying capability of the wing sections was accompanied by higher sectional nose down pitching moments. This in turn implied higher tailplane down-loads to trim the aircraft about its centre of gravity, to some extent reducing the load carrying improvement from the wing and also increasing the importance of considering the wing plus tailplane drag in the trimmed condition, when optimising such parameters as wing twist and load distribution across the span. Particularly on a highly loaded, high aspect ratio swept wing, there are very powerful reasons for wishing to increase the load carried inboard relative to outboard, either by tapering the planform or by reducing the incidence of the outboard wing sections. Not the least of these is the consideration of wing weight and indeed the A310 wing is more highly tapered than that of the A300. This further leads to a requirement to add more "wash out" to the wing (i.e. reduce the local wing section incidence outboard) to reduce the maximum local lift coefficients which tend to occur well outboard due to the basic effects of sweep and taper. The limit on what can be done in this respect is the vortex drag penalty incurred, due to the spanwise loading moving further and further away from the optimum elliptic loading for minimum vortex drag.

However, concentrating the load inboard on the three dimensional swept wing gives a nose-up pitching moment, which helps to compensate the increase in nose down sectional pitching moment referred to earlier. This effect then tends to reduce the tail down-load, which has two important effects on drag: (a) for a given trimmed lift coefficient the wing lift coefficient is reduced, reducing the wing vortex drag and, particularly at important cruise conditions, the wing compressibility drag, and (b) the drag of the tailplane itself is similarly reduced. Hence, an early parametric study was carried out which showed that at the long range cruise conditions of lift and Mach No. the wing vortex drag penalty relative to the elliptically loaded "optimum" could be allowed to rise significantly to obtain the optimum overall drag.

WING ROOT FILLET OPTIMISATION

We now turn to some of the interference aspects investigated in the experimental programme. In general, it has been found that these items (summarised in Figure 4) have not in the end had a very large effect on the aerodynamic design of the wing itself, rather that the increase in wing thickness allowed by the advance in standards made it that much more difficult to maintain or improve upon the current standards of low interference drag due to the wing/fuselage junction etc., achieved on the A300. Looking at the wing root first, the traditional development area is at the rear of the wing chord where without suitable filleting of the junction a region of separated flow is likely to result. The very large increase in thickness/chord ratio of the root section on the A310 led to the expected worsening of the separation problem relative to the A300, with the result that the wing root trailing edge fillet has been increased in size giving the saving in cruise drag as shown in Figure 8. It should, of course, be remembered that the cruise drag improvements quoted in Figure 8 are indeed relative to A300 type fillets, but as applied to the A310 and are not improvements which could be achieved anyway on the A300. It is perhaps less widely realised but nonetheless well documented (for example references 2 and 3) that there is also a flow separation problem at the leading edge of the wing. Without special filleting, the fuselage boundary layer approaching the wing cannot traverse the adverse pressure gradient close to the leading edge stagnation zone, and it separates from the fuselage side, rolling up into a "stand-off vortex" which is shed above and below the wing/fuselage junction. The energy going into the vortex - and hence drag - can be expected to be a function of the boundary layer thickness approaching the wing and the width of boundary layer flow affected, which must clearly in turn be a function of the wing root depth close to the leading edge.

The significance of the wing root "stand-off vortex" was appreciated by the Hatfield design team more than fifteen years ago in work on a quite different project, and indeed a fillet aimed at suppressing this vortex was included on the A300. However, because of the relatively smaller wing root leading edge radius of the A300, the potential gain for suppressing the vortex completely was fairly modest - of the order 1% of cruise drag - and so only a small partially effective leading edge fillet was incorporated which would not interfere with the chosen geometry of the leading edge high lift devices. On the other hand, with the A310 wing root design, which was much thicker than the A300 especially near the leading edge, tunnel tests soon showed that the potential improvement in cruise drag for suppressing the stand-off vortex was significantly higher - of order 11%. With this higher potential gain and the increased emphasis on fuel economy at the time of the A310 design, it was decided to incorporate a larger wing root leading edge fillet to suppress the vortex fully and this time design the high lift device around the fillet.

The development of this leading edge fillet for the A310 was a classic example of the use of traditional "try it and see" experimental methods. It was feasible to envisage using theoretical methods to assist in designing the fillet, but it was clear that in this case it was far more economical in time and effort to do the job in the wind tunnel. The problem was one which could be attacked in the initial stages in an unpressurised low speed wind tunnel, where several configurations could be studied quickly and cheaply. Even in these sophisticated days, there are still some circumstances left where there is no substitute for a human operator with an eye for a smooth line and with an experienced thumb to mould the plasticene! Following initial development, a more restricted set of fillet shapes was checked at higher Reynolds Number and at cruise Mach Numbers. A photograph of the flow streamlines over the surface of the chosen fillet at a typical cruise condition is shown in Figure 9, where it may be seen that the vortex has been completely suppressed with the flow dividing smoothly along the leading edge of the fillet. The cruise drag saving relative to the A300 size fillet was of order 1 1/3% as indicated in Figure 8.

FLAP SUPPORT FAIRINGS

Naturally, most of the important aerodynamic aspects in optimising the flaps themselves, and their support and drive systems, were concerned with the flap effectiveness in improving take-off climb performance and reducing take-off and landing distances. Aerodynamic efficiency then had to be balanced against weight, and structural and mechanical simplicity. However, the fairings necessary to enclose the flap supports and drive system have a significant effect on cruise drag, both from the straightforward increase in skin-friction drag from the extra surface area, and from interference with the drag rise characteristic etc. of the wing at cruise Mach Numbers.

It was recognised from tests done at the time of the A300 development that the underwing fairings designed for that aircraft (see Figure 1) had a beneficial effect on the wing drag rise lift coefficient/Mach Number boundary, which under some conditions more than offset a small low Mach Number basic adverse interference drag increment due to adding the fairings below the wing. An example of this from A300 wind tunnel tests is shown in Figure 10(a), where the interference drag (that is, the drag over and above a simple skin friction plus form drag estimate) due to adding the fairings to the wing is plotted against lift coefficient at a typical cruise Mach Number. Although a small reduction in drag with increasing lift coefficient might be expected as the general flow velocities reduce on the wing lower surface, it may be seen that the trend is not progressive, the interference drag reducing slowly to a lift coefficient of about 0.4 followed by a much more rapid fall-off until the interference has become favourable above a lift coefficient of about 0.43. It was also noted that the A300 fairings had the effect of increasing the wing lift at a constant incidence and this appeared to be the key to the changes in interference drag, as became clearer in the work for the A310.

The alternative flap systems that were considered for the A310 required the investigation of the high speed interference effects of the three types of fairings shown in the sketch in Figure 10. Fairing (1) was similar to the A300 type (see also Figure 1) except that it was suitable for a flap with less rearward translation when deployed for take-off and landing. This implied that for minimum additional surface area the parallel sided centre section of the fairing finished well before the wing trailing edge, and the fairing was closed with only a small length extending aft of the wing. Fairing (2) was designed for approximately the same flap area extension as was Fairing (1), but for a completely different support system. This fairing was much narrower in front view than (1), which meant that the fairing could be closed completely in front of the wing trailing edge, but on the other hand it extended to a greater depth below the wing. Fairing (3) was very similar to the A300 design. It was suitable for two alternative support and drive systems which were being investigated for flaps giving rather more area extension than those for which Fairings (1) and (2) were designed.

The effect that these fairings had at a typical cruise Mach Number can be seen by referring to Figure 10(b). The Mach Number is the same as for the A300 in Figure 10(a), and again the interference drag is presented, that is with the estimated isolated skin friction and form drag subtracted from the experimental drag increment due to adding the fairings to the wing. Also shown, in Figure 10(c), is the effect that all the fairings had on lift at constant incidence, and these increments were found to reflect directly into the lift coefficient for the onset of buffeting - that is into the maximum altitude capability of the aircraft. All fairings were found to have an adverse interference drag at low lift coefficients relative to the simple estimate. However, as may be seen from Figure 10, they had a remarkably different effect as lift coefficient increased, which appears to correlate directly with their effect on lift coefficient at constant incidence. Fairing (3) shows a similar behaviour to the A300, as was expected from the similarity in geometry. Lift is increased at constant incidence and at high lift coefficient the interference on drag is favourable. Fairing (1) had a neutral effect on both lift and drag, and Fairing (2) reduced lift at constant incidence and showed an increased adverse effect on drag at high lift coefficient. Flow visualisation carried out during the high speed tests showed that this different behaviour could not be explained by the presence of local shock waves around the fairings, by flow separation in the wing/fairing junctions, nor by any fundamental changes in the wing upper surface supercritical flow development or shock pattern.

When these different interference characteristics were first noted (between the behaviour of the A300 fairings and Fairings (1) and (2)), a low speed test was quickly set up to see whether, just as for the wing root fillet investigation, the cheaper low speed facility could be used to develop improved geometries. It was found that at low speed the lift effects were still present but that the differences in drag interference had disappeared. This appeared to confirm the suspicion that we already had that the basic effect of the different fairings was the change in lift, which was presumably coming from a change in the pressure distribution on the wing lower surface due to the presence of the fairings. Thus, at low speed one might expect only minor differences in drag interference, but at a constant lift coefficient at cruise Mach Number the wing upper surface would be operating at differing levels of shock wave drag depending on which fairings are present. It was quickly shown in the low speed tests that rearward extension of the parallel part of Fairings(2) (i.e. as Fairings(3)), thus making them more alike those of the A300, recouped the lift increase at constant incidence. High speed tests on Fairings (3) then confirmed that the favourable drag interference characteristics had also been obtained.

Further evidence of the reason for the drag interference behaviour is given in Figure 10, where the lift coefficient for the onset of wing (upper surface) compressibility drag is given, and can be seen to be closely associated with the point at which the rapid change in interference drag level starts on the A300 fairings and A310 Fairings (2) and (3). The reason for the basic effect of the fairings on lift has not yet been fully explored, but clearly it is critically dependent on the extent and shape of the fairings near the wing trailing edge. The principles of Fairing (3) were then used in the design of the final fairings for the A310, which were similar to those on the wind tunnel model shown in Figure 13.

NACELLE/PYLON/WING INTERFERENCE

The general problems of installing the powerplant below the wing are well known and have indeed been the subject of several papers given to AGARD conferences in the past (for example Reference 4). On large transport aircraft with wing mounted by-pass fan-jet engines, the forward slung pylon mounted installation is almost universal and the A300 and A310 are no exception. The main problem at cruise Mach Numbers of course is to ensure that premature shock wave drag is not encountered due to the very high flow velocities which can exist in the "channel" presented to the airstream between the wing lower surface, the pylon side and the nacelle upper surface. The interaction with the engine exhaust flow, particularly the fan stream, exacerbates the problem, and it is indeed possible for the presence of the wing to induce a shock pattern and attendant interference drag within the fan exhaust flow itself. As always, the situation is one of compromise between the optimum aerodynamics and a practical engineering installation. Even on the aerodynamic side in deciding the pylon geometry for instance, there is a possible conflict between what is required to delay shock wave onset, and to give the optimum effect on other parameters such as the wing span loading and induced drag.

Traditionally, and this was the case for the A300, the wing itself has been designed in the absence of the interference effects due to the engine installation, and then the nacelle position and support pylon geometry have been designed to minimise any adverse interactions. With the experience gained on the A300, the overall effects from the engine installation were borne in mind in the A310 wing design process, but having said that, this did not have a very big impact. A complete description of the aerodynamic work entailed in the A310 engine installation is not possible in this paper if for no other reason than that the work is still continuing. The current investigation is aimed at settling the last details of the pylon fairing shapes behind the main structural cantilever member which supports the engine, and in the junctions between the wing and pylon and nacelle. However, this work is all mainly concerned with optimising the pylon geometry and in this present paper on the A310 wing configuration we must return to the effects on the wing design itself.

There were three basic effects of the presence of the engine nacelle and pylon which were considered in the high speed wing design. The first was the effect already referred to of significantly increased flow velocities over the forward part of the aerofoil chord, and this had an input into the choice of the aerofoil lower surface pressure distribution as shown in Figure 11. Although the flatter "rooftop" type of pressure distribution did have some advantages, for instance the reduced level of maximum velocity, it was rejected among other reasons (a) for the higher velocities forward on the chord where the superimposed effect from the engine is worst, and (b) coming back to the trim drag problem it would have further increased the nose down pitching moments of the wing sections. The second effect that was recognised in the wing design was that, although there is very little influence on the form of the wing upper surface pressure distributions, the presence of the nacelle does have an effect on the incidence of the "onset" flow seen by the wing sections. The effective wing section incidence is reduced near the nacelle and theoretically this can be recouped by re-twisting the wing. Although it would not be possible, or even desirable, to offset this local effect completely, because of the implications on the structural complexity, etc., a certain amount of extra incidence was built into the wing around the planform crank area. Model tests showed that indeed the presence of the nacelle and pylon appeared to have had little detrimental effect on the supercritical flow development of the wing upper surface.

The third and last effect on the wing design was mainly a geometric one. Installing the modern large fan jet engine below the wing puts space at a premium in the vertical direction with the requirements to provide adequate clearance between the wing, the engine and the ground, and on the other hand to reduce the main landing gear leg length to a minimum dictated by other parameters to save weight and cost. Thus, in setting up the spanwise wing dihedral it was necessary to get as much height as possible at the engine station relative to the main landing gear hinge position, although this was not allowed to compromise the overriding consideration of not interfering with the aerodynamics of the wing upper surface. This led to the very pronounced "gull wing" effect shown in Figure 12, but where it may be seen that the junction of the wing upper surface and the fuselage has not been allowed to go much below 90° and the spanwise curvature anywhere on the forward part of the wing upper surface has been held to very low values.

Sufficient wind tunnel testing was done before the wing geometry was frozen to demonstrate that the nacelle installation effects could be held at least to the same levels as on the A300. As already mentioned, a comprehensive optimisation programme for the powerplant installation was then mounted, and is still proceeding, making full use of the latest techniques for simulating the engine airflows. One of the series of models tested, or soon to be tested, in England and France is shown in Figure 13, this model being the first A310 half model using a Turbine Powered Simulator engine, which was tested last year in the 9ft. x 8ft. (2.7m x 2.4m) transonic tunnel at the Aircraft Research Association, Bedford.

THE "CLEAN UP" PROGRAMME

Items 7 and 8 of Figure 4 will not be discussed fully in this paper as they are part of the routine product development programme for any family of civil airliners, particularly with the current emphasis on reducing drag to the absolute minimum for improved fuel economy. Item 9 however was of particular importance for the A310. It was an essential part of the overall economics of the new wing that many of the same manufacturing techniques and timescales for building the main structural wing box could be applied as for the A300. It was therefore important that such imperfections as steps at the joints between wing skins, and the minimum practical tolerances on the accuracy with which the wing profile could be maintained across the chord, should not interfere with the advanced aerodynamic performance being sought and being demonstrated on the high speed wind tunnel models (which of course had been built to the theoretical geometry). Somewhat to our surprise, our theoretical work and a check wind tunnel test showed that the required tolerance on steps at joints was not likely to lead to any significant new problems on the A310 wing design. However, a cautionary note was sounded on the effect of inaccurate profiles. Again, the advent of the new era of transonic computational methods enabled us to superimpose a surface "Wave" on the nominal profile and quickly investigate the effect on the supercritical flow development of varying its position, magnitude and wavelength. Indeed, this would have been very difficult to check by wind tunnel testing because of the time and expense of the number of models involved, even if these were only simple two-dimensional wing sections.

The results of the theoretical investigation into the effects of profile errors proved very valuable, and showed that the "waviness" criterion that had been used for the A300 (a maximum permitted ratio of wave amplitude to wave length) was not appropriate, as at certain critical conditions long wavelengths could lead to even worse interference with the supersonic flow development than short wavelengths, for a given wave amplitude. The criterion for the A310 was therefore recast in terms of maximum permitted wave amplitudes alone and checks were carried out on existing wings built for the A300 to see if this new criterion was being met (and therefore was likely to be met on the A310). These checks were in the main very satisfactory, and confirmed that the basic manufacturing procedures could be carried forward to the A310.

CONCLUDING REMARKS

In the preceding sections of this paper I hope that I have been able to demonstrate that the high speed design of a wing for a modern transport aircraft involves the consideration of the aircraft as a complete entity. Also that this formed a very large part of the aerodynamic design programme for the A310, to ensure that the basic advances offered by the new transonic computational methods were not thrown away by interference penalties. All through the A310 programme the close family relationship with the A300 enabled the already good standards set by that aircraft to be used as a yardstick in assessing the new design. The situation is summarised in the last figure, Figure 14, in terms of one of the parameters which go towards building up the total drag of the aircraft. This is the same parameter as used in Figure 2 to demonstrate the advance achieved with the A310 clean wing relative to the A300, that is the "compressibility drag rise boundary" or alternatively the lift coefficient boundary at which the aircraft drag increases by approximately 10% above the datum value at low Mach Number.

The drag rise boundary is particularly important for a transport aircraft as it virtually defines the limit of operating conditions - beyond this limit the drag rises so rapidly that operations will be uneconomic for a civil transport or there will usually be an unacceptable reduction in range, perhaps the more important effect for military transports. The data in Figure 2 was obtained from wind tunnel tests of the

two clean wings on the same fuselage to demonstrate the basic improvement obtained from the new wing. The starting point for summarising the interference effects in Figures 14 (a) and (b) are these same drag rise boundaries effectively converted to a "wing alone" standard such that the fuselage super-velocity effect discussed earlier is zero. Figure 14 (a) then demonstrates for the A310 wing the reduction in Mach No. due to (1) mounting the wing on a finite length fuselage (of the A310 geometry), (2) adding engine nacelles, pylons and flap track fairings to the wing and (3) trimming the aircraft about the centre of gravity. It may be seen that the first and largest difference, approximately 0.015 of Mach Number, is a direct result of the supervelocity effect due to the closure of the forward and rear ends of the fuselage. The next difference is due to the nacelles and pylons, which being mounted underwing have their worst effects at low lift coefficient when the wing lower surface velocities are highest. The slight improvement in the drag rise boundary at high lift coefficient is due to the beneficial effect of the flap track fairings as previously discussed. The final difference, due to trimming, is mainly caused by the additional lift carried by the wing to maintain constant overall lift on the aircraft, counteracting the download on the tailplane required to balance the wing pitching moments again as previously discussed. Thus, at typical cruise lift coefficients these interference effects have reduced the Mach Number capability of the wing by about $\Delta M = 0.025$, although about two-thirds of this was a basic effect of the fuselage which was allowed for in choosing the wing design point.

Figure 14 (b) summarises the influence on the A310 drag rise boundary compared with the equivalent effects on the A300 wing. It may be seen that at typical cruise lift coefficients (rather lower on the A300 than on the A310) the "complete aircraft" boundary for the A300 is just less than $\Delta M = 0.02$ slower than the idealised wing boundary, compared with the 0.025 for the A310. Nonetheless, it was only by paying a great deal of attention to the problem of integrating the wing into the overall concept of the new project that the residual additional loss on the A310 was kept so small, to a level in fact which was quite fundamental having chosen the derivative fuselage and in seeking the improved lift performance from the wing as discussed in detail in the preceding sections of this paper. The "complete aircraft" boundary for the A310 of course still shows a significant improvement over that of the A300 at the higher lift coefficients that will be used by the new aircraft, and when put together with the increase in wing thickness shown in Figure 2, still represents a very significant advance over the A300 which is already as good as, or better, than any comparable aircraft flying today.

At the time of this conference, the main aerodynamic development of the A310 wing is completed and we are now looking towards the future, the first flight in 1982 and the subsequent flight test programme. As I hope I have shown, the work concentrated as much on the interactions between the wing and the other components of the aircraft as on the wing itself, laying a firm foundation for the success of this project. We look forward to the A310 taking its proper place alongside the A300 in the expanding Airbus Industrie family of civil transports that will be available for the 1980's and beyond.

REFERENCES

1. D.M.McRae: 'The Aerodynamic Development of the Wing of the A300B' Aeronautical Journal, July 1973.
2. D.Thwaites (Editor). 'Incompressible Aerodynamics' Oxford University Press, 1960. Figure XII.34 (Also Frontispiece)
3. G.M.Bowes: 'Aircraft Lift and Drag Prediction and Measurement' AGARD Lecture Series No.67, May 1974, Pages 4-36,37.
4. 'Airframe/Propulsion Interference' AGARD Conference Proceedings No.150, 1975.

ACKNOWLEDGEMENTS

The author wishes to thank Airbus Industrie and British Aerospace for permission to publish this paper, British Aerospace for the facilities for its preparation, and colleagues in the fluid dynamics section for their invaluable assistance.

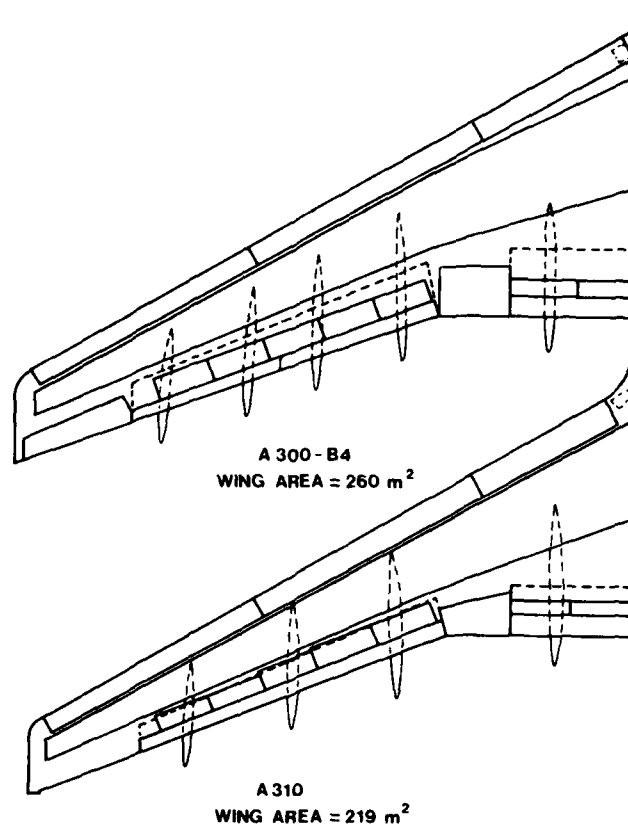


Figure 1. Wing Planform comparison

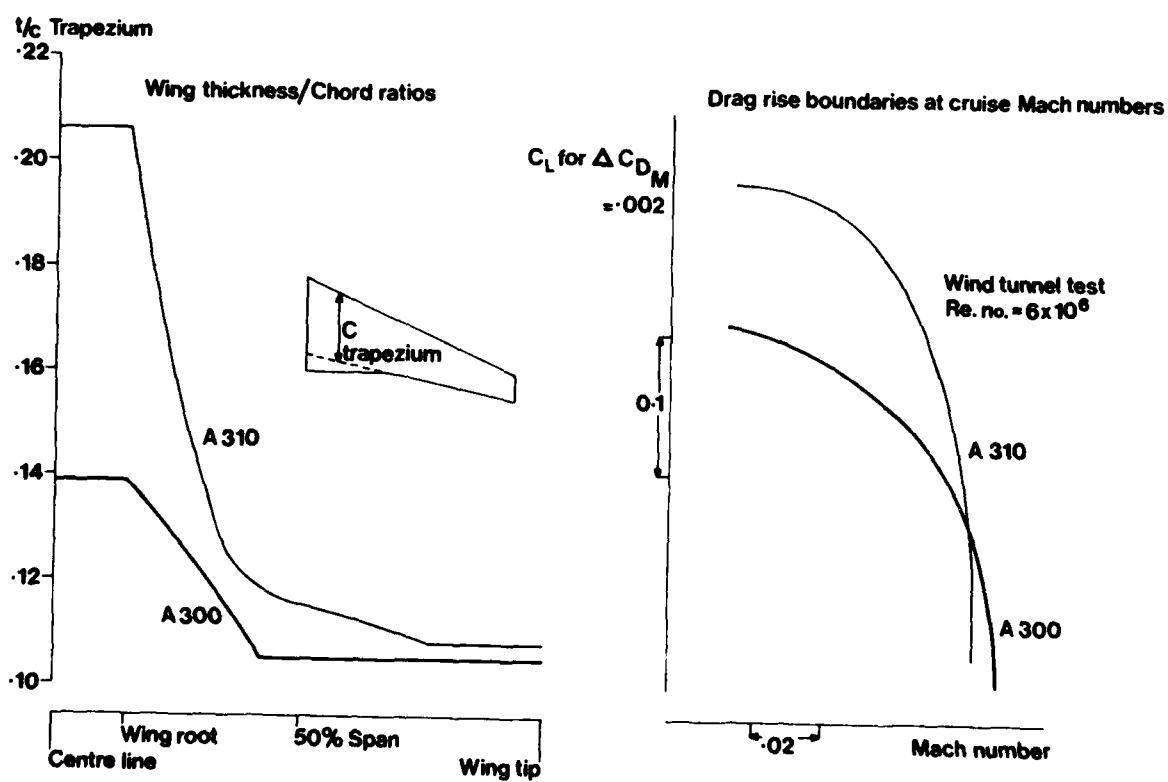


Figure 2. A310/A300 Technology comparison

(a) Two Dimensional Wing Section Tests

A300*			A310		
Model No.	Date		Model No.	Date	Description
5/1	Jul 67		35/1	Jul 77	Section for 209 m ² wing planform crank
5/2	Jul 67		35/2	Jul 77	Section for 209 m ² wing - 75% semi-span
5/2	Jul 67		35/3	Aug 77	Minor modification to 35/1
5/2	Aug 67		35/5	Aug 78	Section for 219 m ² wing planform crank
7/2	Dec 67				
7/3	Feb 68				
7/14	Mar 68				
12/6	May 68				
12/6	Jun 68				
7/16	Jul 68				
12/16	Aug 68				
7/3	Feb 69				
7/16	Feb 69				

(b) Three Dimensional Wing Tests

A300*				A310				
Air-craft	Wing No.	Initial** Tests		Air-craft	Wing No.	Initial Tests	Tunnel	Remarks
A300 (original project)	6	Feb 68		A310 ₂ 209m ² Wing	4	Aug. 77	9x8 ARA	Preliminary inboard wing "Final" outboard wing
	7	Feb 68						
	8	Feb 68			5	Aug. 77	9x8 ARA 8x8 RAE	Minor modification to Wing 4
	9	May 68			6	Apr 78	9x8 ARA	Same outboard wing as 5. "Final" inboard wing
	12	May 68						
	17	Jul 68						
	19	Aug 68		A310 ₂ 219m ² Wing	18	Aug 78	9x8 ARA 8x8 RAE	New Planform Same design principles as Wing 6
A300B (final Aircraft)	21	Jun 69						
	23	Apr 69						
	25	Apr 69						
	27	Nov 69						

NOTES: *Abridged data from Tables 3 & 5 of Reference 1

**Only initial tests are relevant to wing design of both A300 and A310 by definition as a modification results in new wing number.

(c) Overall Wing Design Timescales

	A300	A310
Effective Start of Theoretical Wing Design -	August 1966	December 1976
Geometry Freeze for Wing Structure -	August 1969	November 1978

Figure 3. Comparative wind tunnel testing relevant to the wing design of the A300 and A310.

Theoretical wing design

Wind tunnel investigation

(1) Basic outboard advanced transonic section design.

(2) Three dimensional transonic design of inner wing including fuselage interference.

(3) Wing twist optimised for best trimmed drag and altitude capability.

(4) Wing/fuselage viscous interference

(6) Nacelle/Pylon/Wing interference.

(5) Flap support fairing/wing interference.

Combined tunnel/flight/theoretical investigation

(7) Effects of revised control surface configuration

(8) Clean up of gaps, steps etc.

(9) Effect of manufacturing tolerances etc. on advanced aerodynamic design.

Figure 4. Factors in the high speed wing design for the A310.

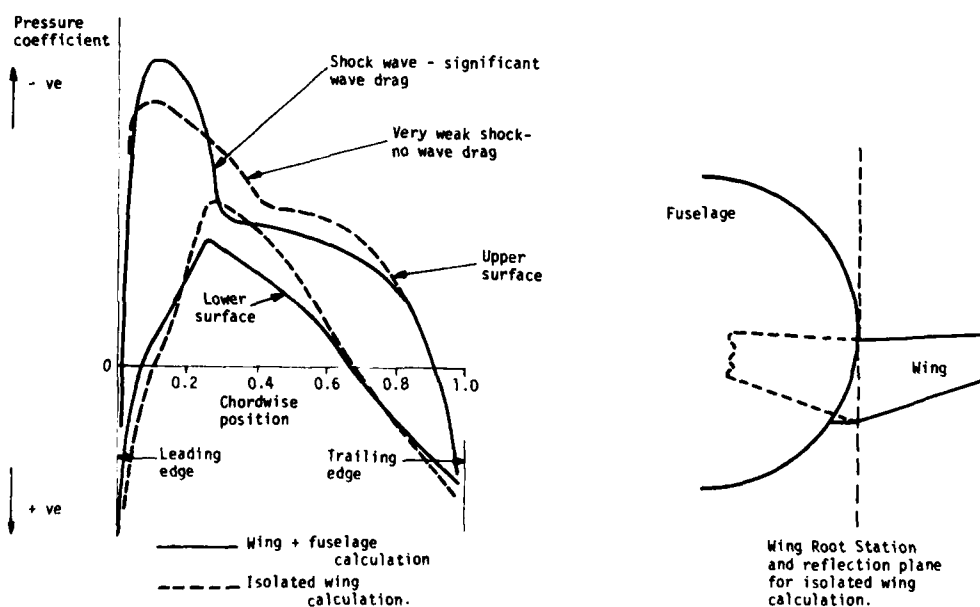


Figure 5. Effect of fuselage representation on wing root calculated transonic pressure distribution

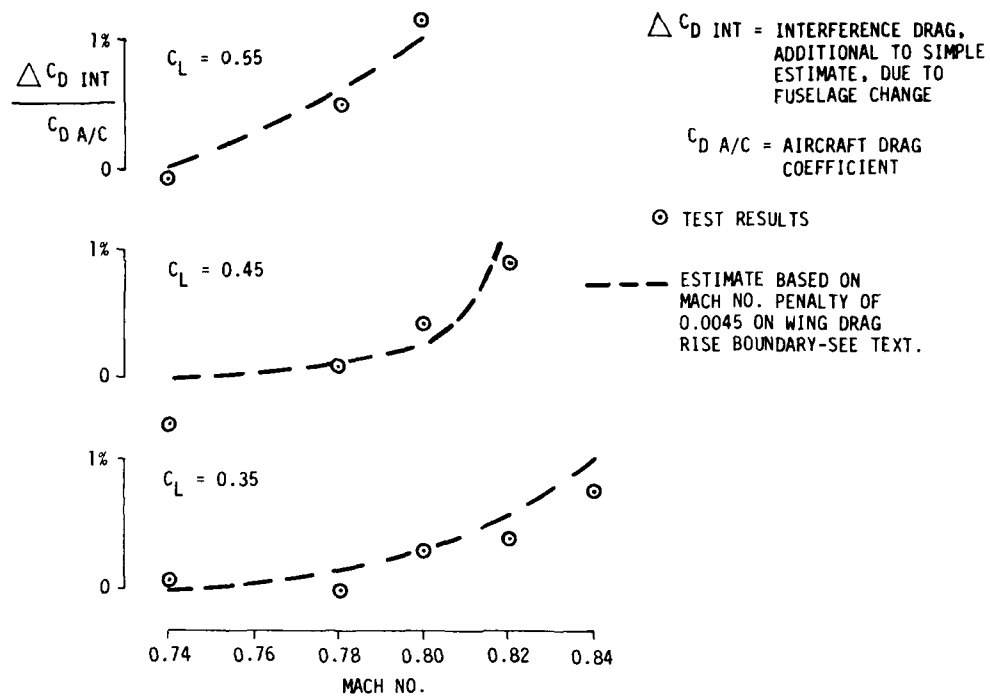


Figure 6. Effect of change of fuselage fineness ratio on compressibility drag.

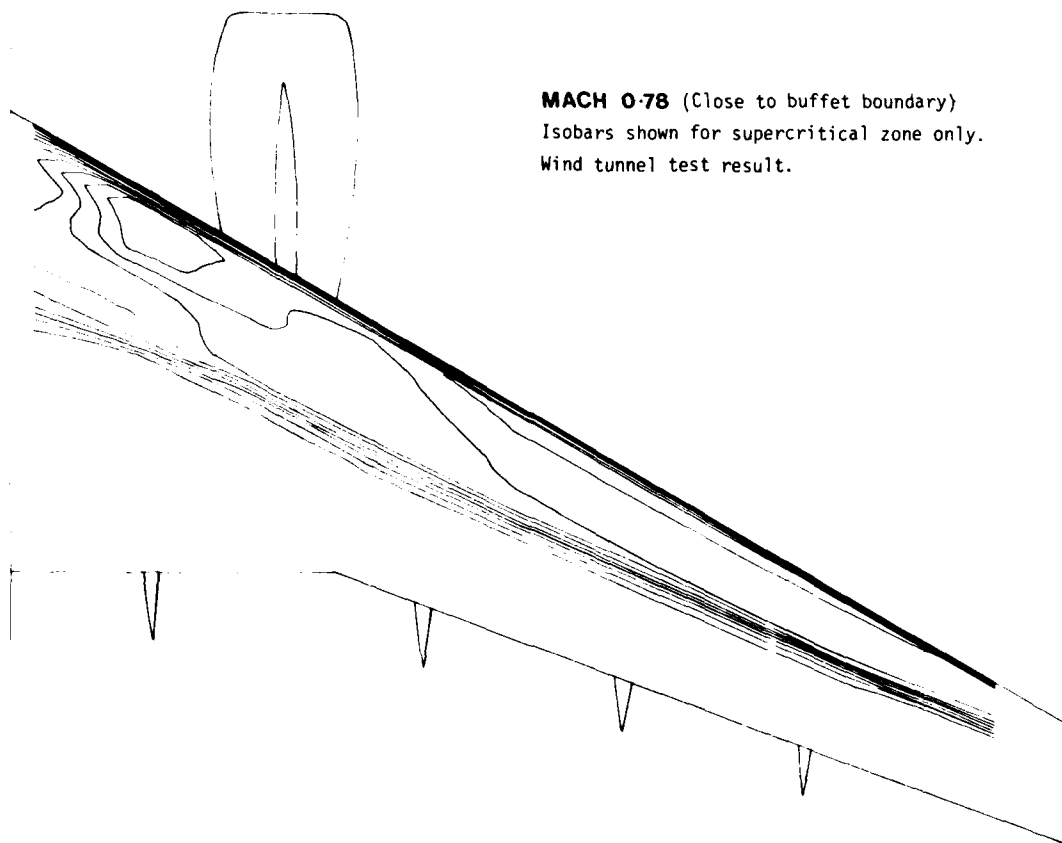


Figure 7. Wing upper surface isobars demonstrating uniform shock sweep

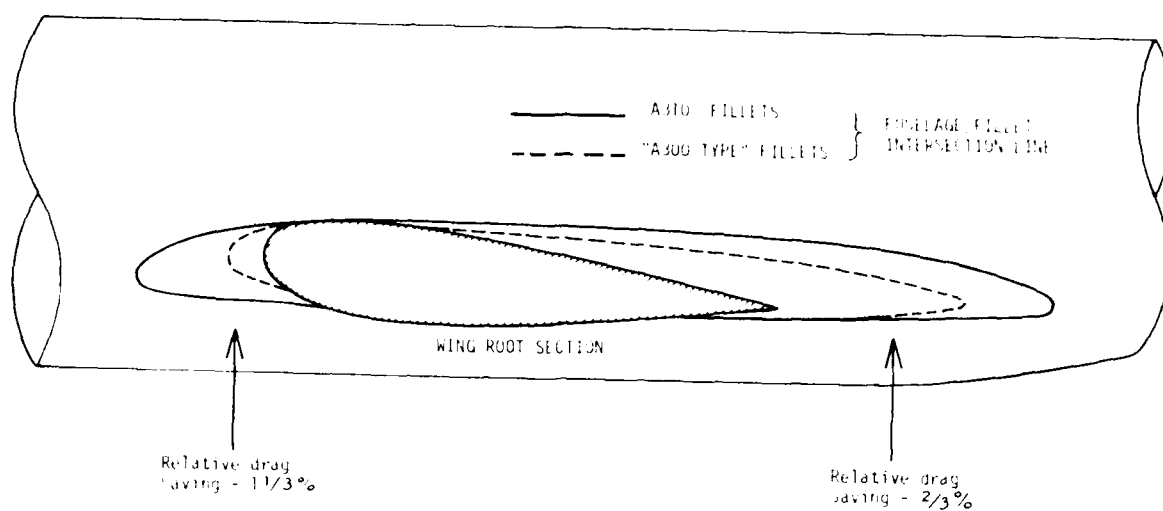


Figure 8. Optimisation of A310 Wing Root Fillets - Drag improvements relative to "A300 type".

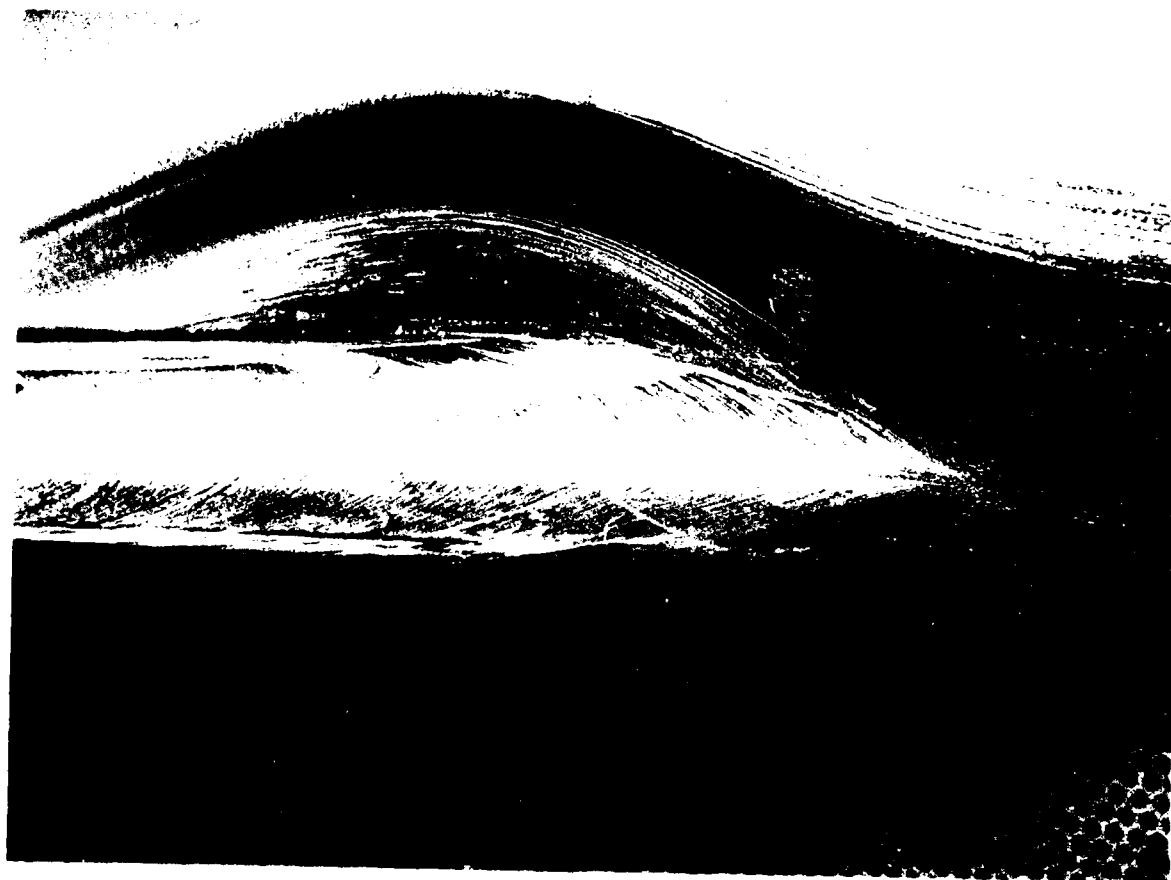


Figure 9. Surface flow streamlines over the A310 wing root leading edge fillet.

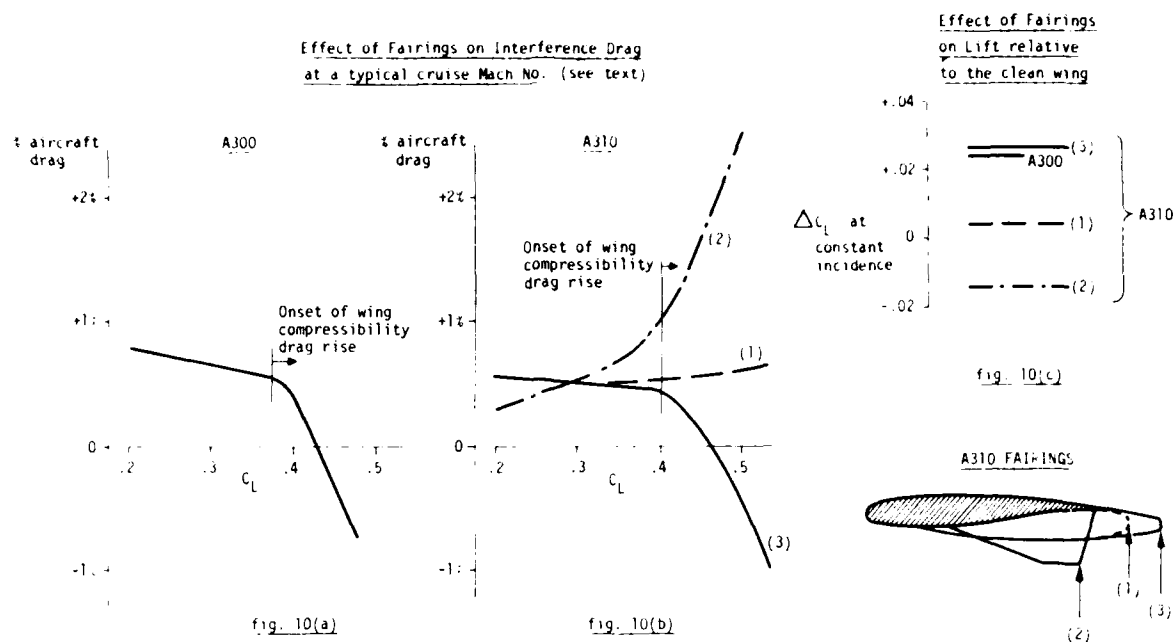


Figure 10. Interference effects of flap support fairings

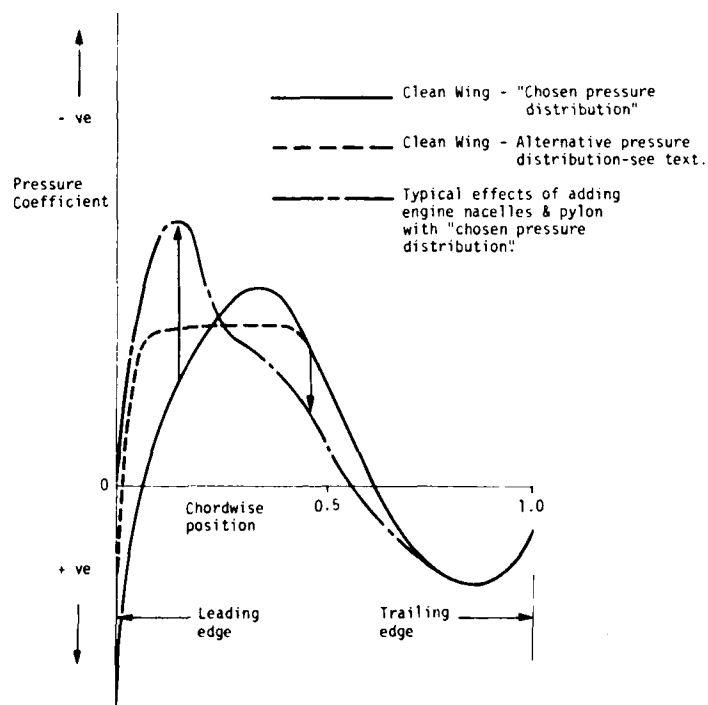


Figure 11. Design wing lower surface pressure distributions and typical effect of engine installation.

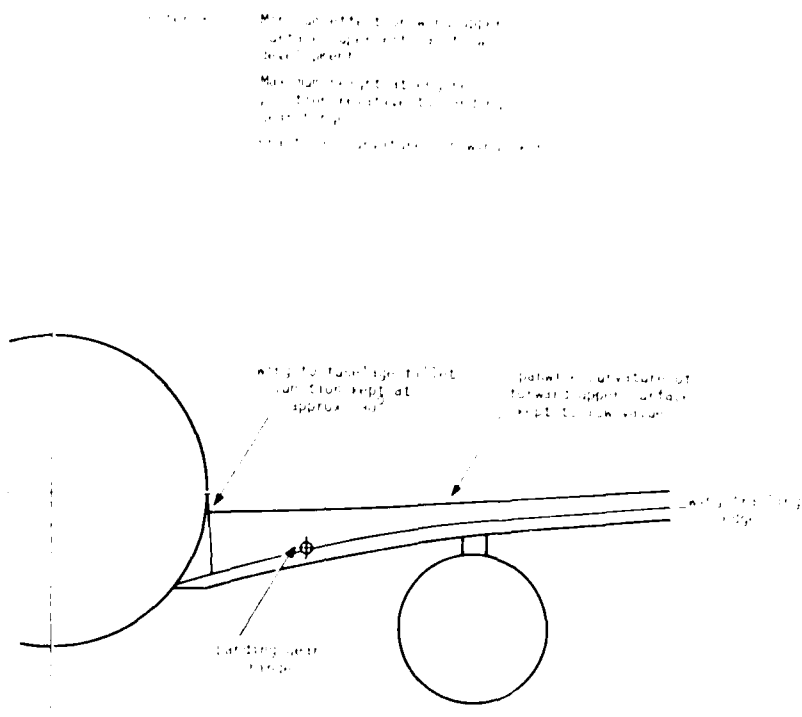


Figure 12. Wing spanwise dihedral distribution.



Figure 13. First A310 turbine powered simulator model mounted in the Aircraft Research Association 9ft x 8ft (2.7 x 2.4 m) transonic wind tunnel, Bedford.

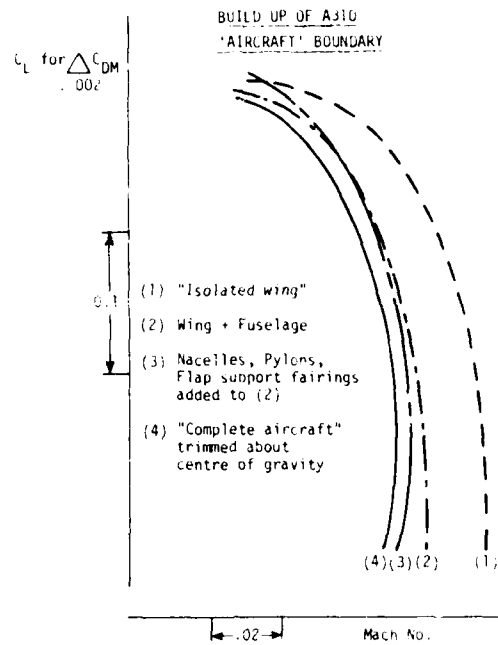


FIG. 14a

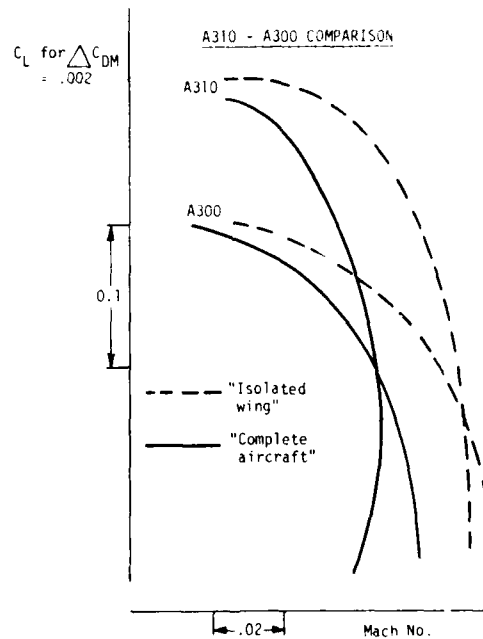


FIG. 14b

Figure 14. Summary of interference effects on the wing drag rise boundary.

TRANSONIC WING TECHNOLOGY FOR TRANSPORT AIRCRAFT

G. Krenz and B. Ewald

Vereinigte Flugtechnische Werke GmbH
D 2800 Bremen, Hünefeldstraße 1-5, FRG

SUMMARY

Transport aircraft currently under development and production are designed on the basis of improved supercritical aerofoils which allow the use of higher aspect ratio wings with increased thickness. Extensive research and design efforts have been undertaken in the USA and Europe to improve transonic wing technology, work in Germany was concentrated in a cooperative programme between the aircraft companies the DFVLR and the ONERA in France. - Basic results from this programme are given in the paper which describe the present standard of transonic wing aerodynamics taking into account impacts on structure and aeroelastics.

The current research programme in USA, the Aircraft Energy Efficiency Programme (ACEE) and corresponding programmes in Europe aim at improved economics. The main objectives in the transonic flight regime are:

- o High Aspect Ratio Wing
- o Wing-Engine-Integration
- o Active Control with movable wing parts.

This requires further progress in basic research in some traditional fields of fluid dynamics such as boundary layer flow and unsteady aerodynamics for practical application to transport aircraft design. - The paper deals with the current work in Germany on these subjects and shows the application of results produced so far for improved aircraft design.

Most work in the field of modern transports concentrates on civil aircraft of low-wing design. VFW has conducted initial investigations of how to use this design concept as a hybrid wing in the upper fuselage position for military aircraft in order to save production and development costs. The paper contains first results on this subject.

NOTATION

AR	aspect ratio	R_N	Reynolds number
c	aerofoil / wing chord	t/c	aerofoil / wing thickness ratio
C_D	drag coefficient	u	velocity component
C_L	lift coefficient	x	streamwise coordinate
C_p	pressure coefficient	y	spanwise coordinate
C_p^*	critical pressure coefficient	α	angle of attack
C_Q	suction coefficient	Λ_{25}	quarter chord wing sweep
K	grain size	η	spanwise coordinate in fractions of half wing span
M	Mach number		

1. INTRODUCTION

Early in 1975 most of the research work in Germany, which was directly applicable to civil transport aircraft development, was combined into a joint programme of the German Aircraft Industry with the DFVLR, the so called "Civil Component Programme" (Ziviles Komponenten-Programm "ZKP"). The programme was organized and funded by the German Ministry of Research and Technology.

The first phase of this programme ZKP I, covered four years terminating in 1979. A second phase, ZKP II, has been defined and initiated. The total expenditure for all ZKP tasks at present is about 20 millions DM per year.

The aerodynamics of modern transport airplanes was covered by the ZKP I programme with the participation of VFW, MBB and the DFVLR; Dornier had an associate status with a smaller amount of theoretical and experimental work. This paper deals with some results of the programme showing the direct impact on modern transport development.

The main parts of the ZKP I aerodynamic tasks were:

- o Two dimensional transonic wing section development.
- o Three dimensional wing development of high loaded civil transport wings.
- o Study of wing-engine and wing-fuselage interference.
- o Improvement of transonic wind tunnel measurement with regard to transition fixing for drag and buffet onset testing.
- o Development of large scale/high Reynolds number transonic wind tunnel testing including special tests for surface irregularities, engine simulation and unsteady aerodynamics.
- o Theoretical work on the development and improvement of 2-D and 3-D transonic methods.

FIG. 1 gives an outline of work done in the aerodynamic section of the ZKP I (1975 - 1979). A more detailed presentation of the large scale half model work is given at the end of this meeting in the paper of Mr. Anders, Mr. Gravelle and Mr. Giacchetto.

The aerodynamic work in the ZKP was and is closely related to the aircraft development tasks at VFW. FIG. 2 gives an impression of the relationship to aircraft project and development work.

For future versions of the A 300 family the aerodynamic research and development is extended in the ZKP II (1979 - 1982) with the main objectives as shown in FIG. 3 being:

- o High aspect ratio wing
- o Propulsion - airframe integration
- o High lift devices
- o Manoeuvre load control
- o Relaxed static stability.

This task is in good agreement with NASA's Aircraft Energy Efficiency Programme (ACEE), showing similar views on future research in the field of new technology transports.

The following chapters describe some main aerodynamic results from the Civil Component Programme, starting with the ZKP I which was completed in 1979.

2. RESEARCH PROGRAMME IN TRANSONIC AERODYNAMICS

The programme aimed to update the work in the German aerospace companies and DFVLR with emphasis on the transonic flight regime of civil transport aircraft and to prepare a technical basis for wing design of A 300 derivatives. At the climax of the programme it was mainly A 310 wing technology that was covered.

The whole programme was subdivided into two parts, one covering basic research work, the field of theoretical and experimental transonic aerodynamic methods and the other aimed at development of actual aerofoil and wing designs, under comparable design objectives by each partner, and, to be measured under the same test conditions in the DFVLR-Göttingen (airfoil tests) and the NLR-Amsterdam (wing tests) wind tunnels. The best wing judged by cruise performance i.e. buffet boundary and L/D , resulting from the NLR tests was chosen for the manufacture of a large half model 1 : 5.4 scale A 310, to be tested in the S1 Modane of ONERA, France.

2.1 2-D-SECTION WORK

2.1.1 Aerofoil Design and Wind Tunnel Tests

The VFW aerofoil Va 2 can be taken as representative for outlining the 2-D results achieved in the programme. A comparison of geometry and results with the other ZKP aerofoils is given in [1].

Main design objectives, besides requirements such as delayed buffet onset and drag rise, were to establish continuous flow development with increasing incidence and Mach number, i.e.:

- o Shock free pressure distribution at the design
- o Avoidance of double shock below the design to prevent drag creep
- o Stable shock position beyond the design with separation beginning at the aerofoil trailing edge.

The A 300 section was taken for reference tests and judgement of the new section design. The 2-D-tests were performed in the DFVLR-Göttingen wind tunnel using different strip positions. FIG. 4 shows the development of pressure distribution at the design Mach number $M = 0.75$. The 13% thick aerofoil is shock free at $C_L \approx 0.6$

when using transition at 30 % chord upper and 25 % chord lower side. Under off-design conditions, the shock position remains rather stable up to the buffet onset, which occurs at $C_L \approx 0.95$. The buffet onset as well as the drag rise boundary can be taken from FIG. 5.

To obtain the profile characteristics at higher Reynolds number, 2-D measurements were done in the DFVLR tunnel in Braunschweig. The quality of this tunnel was checked by comparative testing of profiles already measured in the ARA tunnel. FIG. 6 shows the influence of Reynolds number on maximum lift at two Mach numbers. The region of transition at higher Mach numbers from laminar boundary layer-shock to turbulent boundary layer-shock interaction may occur between Reynolds numbers of approximately $5 \cdot 10^6$ and $10 \cdot 10^6$. At $R_N = 13 \cdot 10^6$ there is no influence of the transition strip.

2.1.2 2-D-Transonic Flow Calculation Methods

The experimental work in the ZKP was accompanied by large efforts in theoretical methods for aerofoil design and transonic flow calculation. For 2-D potential flow the method of Bauer, Garabedian and Korn was found most reliable, however, a new difference method [2] was established, which can be used for calculation of more complex transonic flow fields, such as around arbitrary multi-element configurations. A further method for 2-D potential flow calculation which was established by using finite elements is described in [3], and a third new method applicable for design of shock free configurations in transonic flow has been developed and is described in [7]. All three new methods form the basis for 3-D Transonic Methods which are referred to in chapter 2.2.2.

2.2 3-D-WORK IN TRANSONIC FLOW

2.2.1 Wing Design and Wind Tunnel Tests

Using the aerofoil research as basis, the ZKP partner firms tested their developed wings in the NLR and DFVLR wind tunnels. The results of the wings F1 (VFW), F2 (Domier), F3 (MBB) and F4 (DFVLR) were compiled in [1]. This paper deals mainly with the results of the ZKP programme on the basis of VFW research and development work.

The aerofoil Va 2 (described in 2.1) formed the basis for the wing design. Besides the usual design performance criterion, at the design point ($M = 0.78$, $C_L = 0.45$) and at off-design, linear wing lofting was of primal importance for the following reasons:

- o Linear lofting enables the uncomplicated study of the main aerodynamic features in the primary design stages.
- o The wing rear loading sections, which are disadvantageous for the flaps, should not be further complicated by non-linear lofting.

For these reasons a linear lofting between three stations (root, kink, tip) along percent lines of wing chord was chosen for the design.

Furthermore the following boundary conditions had to be observed:

- o A rear spar as high as possible was required to reduce structural weight and increase storage capacity.
- o A large as possible profile thickness at "root" and at "kink" was aimed at because of the strong influence of the inner wing on wing weight and torsion stiffness.
- o Strong reduction of profile thickness in the wing outer sections had to be avoided to control aeroelastic effects by outboard ailerons usage.

FIG. 7 shows the designed wing F1 planform and thickness distribution. Sections used for pressure measurements are additionally marked.

The wind tunnel tests were performed at the NLR-Amsterdam, FIG. 8 contains a typical plot of spanwise pressure distribution at the design Mach number. This figure demonstrates that we succeeded to build-in the favourable Va 2 aerofoil characteristics into the 3-D wing design, however, the adequate wing cruise L/D and buffet onset performance during the A 310 design work, was considerably improved by mainly changing the flow characteristics of the inboard wing. FIG. 9 shows the improvement of buffet onset and drag rise boundary of wing B10.3V, which was one of the first A 310 designs, from the ZKP wing F1. Both wings have the same planform and thickness distribution with linear lofting between three stations (root, kink, tip) along percent lines of wing chord.

The wing F1 was selected after the NLR high speed tests for the manufacture of the large ZKP task, 1:5.4 scale half model for testing in the ONERA S1 MA. At that time, however, as the wing B10.3V was already designed, it was chosen because of its better performance.

A detailed description of the wind tunnel programme, test technique and results of the ONERA measurements is given in paper 29 of this AGARD meeting by G. Anders (VFW) and A. Gravelle (ONERA).

Main objectives of the test were:

- o Check of high Reynolds number influence on wing flow development by pressure plotting tests, buffet onset determination and flow visualization.
- o Measurement of specific big model tasks such as surface irregularities, fillets, fairings etc.
- o Measurement of engine-wing-interaction with wing mounted and tunnel floor mounted through flow nacelles.
- o Unsteady pressure plotting tasks on the wing and aileron by unsteady aileron movements.

In FIG. 10 the test comparison between NLR-HST at $R_N = 2.5 \cdot 10^6$ and ONERA S1 MA at $R_N \approx 12 \cdot 10^6$ is shown. The effects of R_N on $C_{L_{max}}$ and flow separation are evident. For example at Mach number $M = 0.78$ or $M = 0.8$, the begin of the lift curve non-linearity, which is a criterion for buffet onset, is increased by $\Delta C_L \approx 0.05$.

Regarding FIG. 6 and taking into consideration that there is good agreement between $C_{L_{max}}$ and 8.0 slope of the wing basic aerofoil versus Reynolds number a similar increase of $\Delta C_L \approx 0.05$ is obtained by extrapolating the curve at $R_N = 2.5 \cdot 10^6$.

FIG. 11 shows the change in lift and drag caused by a step at the slat trailing edge. For this simulation test, the inner slat of 1/3 wing span, extends 10 mm (at full scale A 310 wing), at its trailing edge above the wing contour. This increases the drag at a usual C_L by about 5 %.

The large model with 4 m half span could be used for extensive studies of the transonic flow development by visualization tests. One such result, presented in FIG. 12, shows the laminar-turbulent boundary layer transition, which confirms 2-D-test results (FIG. 6), wherein the transition from laminar to turbulent boundary layer-shock interaction seems to occur between Reynolds numbers of $5 \cdot 10^6$ and $10 \cdot 10^6$, taking into account that the shock is positioned between 30 % and 40 % chord at the outboard wing.

2.2.2 3-D-Transonic Flow Calculation Methods

A considerable part - approximately 35 % of the ZKP Research - was channeled for the development and application of theoretical methods for the calculation of transonic flows. The aircraft companies and DFVLR used different approaches.

a) Method of Analogue Wing Sections

The first transonic wing design necessitated a rapid clear calculation method which was as outlined in [4], and tested on a proven configuration - the A 300. It consists essentially of the calculation of the 3-D effects with the aid of an established subsonic panel method, and the transonic calculation of singular wing sections using analogue profiles with the application of a reliable 2-D transonic method. This method takes into consideration the strong interference caused by fuselage or engines and offers the advantage of wing section analysis and improvement for the wing design. It was successfully practiced on earlier wing designs in ZKP and A 310 programmes by VFW.

The disadvantage lies in the non-adequate estimation of 3-D transonic effects, which can be considerable.

b) Improvement of Existing 3-D-Transonic Methods

The "Theory of Small Perturbation" TSP, was the most advanced at the beginning of ZKP I. Restrictions for its practical usage arose from the inaccurate estimation of leading edge flows. Dornier [5] successfully improved on this method by accurately estimating the boundary conditions and including terms of higher order in the potential equation. The coupling of this method with their own boundary layer computation based on an Integral Method [6], was also achieved by Dornier, resulting in a complete method for the calculation of transonic wings.

The currently best known method in Europa and USA, and next to TSP most widely used is from Jameson. Dornier and DFVLR in ZKP have made efforts for the application of this method.

c) Development of New 3-D-Transonic Methods

A new design method for shock free configurations in transonic flow has been developed by the DFVLR [7]. It is based on the use of fictitious gas flow in the supersonic regime in order to provide an elliptic continuation of the basic equations. Solutions of the latter ensure suitable sonic surfaces, which are used subsequently as initial condition for conventional shock-free supersonic field computation.

Another new approach was developed by MBB [8] using finite elements. In contrast to finite difference procedures used mostly for transonic potential flow computation, finite element schemes do not need the construction of a strictly orthogonal mesh grid for the discretization of the spacial potential distribution. This makes the finite element approach attractive for the calculation of flow fields with complex solid boundary geometries.

A third new method using finite differences has been developed at VFW [9] to calculate the transonic flow using the full transonic potential equation. Streamline coordinates are calculated by singularity methods (panel methods) which enable the treatment of arbitrary body shapes and interference problems.

Considerable reduction of computing time is achieved by calculating the greater part of the flow field, i.e. the pure subsonic flow region, by means of panel method using streamline analogy and applying the finite difference method only to a small perimeter around the supercritical region of the flow field. For the sake of further computing time reduction and simplification of handling the method a 2-D computing grid is used sectionwise. This grid is similar to the 3-D net, but it is calculated by a 2-D panel method. Then a consequent simplification has been made. Instead of treating the supercritical flow field by a 3-D finite difference method, a 2-D finite difference method is applied sectionwise to the 3-D potential equation. In this case not only the necessary boundary conditions but also all derivatives in spanwise direction are calculated by means of a 3-D panel method.

The method has three main advantages:

- o Calculation of strong transonic interferences such as between wing and engine is possible.
- o Design of the wing can be treated sectionwise.
- o The computing time is small with about 2 min CPU-time on IBM 3033 for 400 iterations for one section.

FIG. 13 shows results of this method compared with wind tunnel test results on the ONERA M6 wing.

3. FUTURE RESEARCH IN TRANSONIC AERODYNAMICS

Work on the Transport Aircraft sector is considered mainly as a continuation of the Civil Component Programme in ZKP II and is executed with the aim to develop the Airbus family concept. Fundamental research in the Boundary Layer field is done together with DFVLR in the RuFo Programme, sponsored by the German Ministry of Defence. FIG. 14 outlines the mainpoints of the research in the Transport Wing Aerodynamics.

One objective is the improvement of the 2-D section performance. Besides a stepwise aerofoil improvement, and considering high and low speed requirements, great improvements were achieved by boundary layer suction at the shock [10], [11]. FIG. 15 shows the single slot-suction concept, which after theoretical investigations at VFW, was tested in cooperation with the DFVLR in Göttingen wind tunnel. FIG. 16 contains the lift curve and the drag polar with and without suction at $M = 0.76$, which is above the design Mach number for the profile Va 2 as shown in FIG. 4. Maximum lift is increased from $C_L = 0.86$ to $C_L = 0.99$ using a suction coefficient of 0.0006. The results show only small improvements above $C_Q = 0.0004$, which is also demonstrated by FIG. 17, containing the pressure distribution with and without suction operating. The suction influence on the boundary layer profile is shown in FIG. 18. In this case separation occurs without suction at $X/C = 0.9$, showing a thick boundary layer already developing far upstream.

The condition is changed with suction. One observes a thin boundary layer before the shock, a small separation bubble behind the suction slot at $X/C = 0.65$ and reattached flow down to the trailing edge.

Contrary to the distributed suction with minislots or miniholes needed for flow laminarisation, this slot suction concept seems to be practicable without too much structural complication. Low suction quantities are sufficient to achieve good improvements in maximum lift and buffet boundary, so that useful application to production aircraft seems possible.

Another objective in FIG. 14 is the wing design near the fuselage. The root section is of high importance for wing aerodynamics, wing structure and storage capacity. Profiles of different design concepts having the same maximum thickness, see FIG. 19, fulfill the non-aerodynamic requirements dissimilarly. It is evident that aerofoil B has a greater fuel volume and provides more undercarriage space behind the rear spar for the same nominal thickness ratio as aerofoil A. Furthermore, the greater height of the rear spar of section B reduces structural weight of the wing.

The shape of the leading edge effects the flow around the aerofoil nose. A blunt leading edge has increased suction compared to an aerofoil with a smaller leading edge radius, FIG. 19. A wing root fillet is usually fitted to prevent fuselage boundary layer separation near the wing leading edge, however, the size and shape of the fillet, optimized for low cruise drag, depends on the pressure distribution of the basic root section, and is normally increased for blunt leading edges. As the fillet effects the leading edge flap design at the fuselage, the design of the fillet must be such to match the low and high speed regimes.

A further task in transonic aerodynamics is the wing-engine interaction, as indicated in FIG. 14. The change of wing pressure distribution on both sides of the engine, represented by a through-flow double-body nacelle, taken from NLR-HST tests, is given in FIG. 20. The lower wing surface inboard of the engine is considerably effected whilst outboard the engine, the influence is on both wing surfaces. To separate the combined pylon-nacelle effects, tests were run with the large ZKP-model at ONERA S1 MA, where the nacelle was fixed at a sting mounted on the tunnel floor. The results in FIG. 21 show, that the pod alone has the main influence on the upper wing pressure distribution. Therefore the change of pod position relative to the wing can be taken as measure for the change of pressure distribution on the upper wing surface, which is important for the wing design. FIG. 22 shows the corresponding picture for a more rearward and slightly lower nacelle position. The effect is quite similar though slightly smaller. Starting from this position the nacelle was moved closer to the wing in three steps with the results, presented in FIG. 23. The Δc_p is recorded as difference of the pressure at the new positions ②, ⑦, ⑥ against the pressure at position ⑧ over the wing chord up to the shock. At the shock, as Δc_p increases considerably for any small change of the shock position, it is therefore not representative for nacelle-wing interference.

Aft of the shock region, the change of the wing pressure distribution caused by the nacelle is small and is therefore omitted in FIG. 23. A comparison with FIG. 22 shows, that the main effect at the forward wing, is to increase the upper surface c_p by the same order of magnitude (10 %), as produced by the pod in its lowest position. The maximum shift in nacelle position from (8) to (6) is in the order of wing thickness at the pod station. For this magnitude of shift we can conclude, that local modifications of the upper forward wing surface are sufficient to compensate for the adverse nacelle effects.

For better engine representation, the jet simulation has to be included. The TPS technique is provided for future ZKP tests. For the conventional engine location, the jet is expected to enforce the through-flow nacelle effects.

4. DESIGN CONSIDERATION FOR HYBRID WINGS

The low wing concept, the commonest civil aircraft configuration, is the basis of most of the studies in the transport-aerodynamic field: High wing aircraft are usually preferred as military transports because of better loading capabilities. The question arises of the choice of the high or low wing concept. Besides the diverse requirements of a civil and military aircraft, the fuselage effects on the two wing arrangements are very dissimilar. A design study on the above was conducted and first results are discussed below.

A low wing configuration with a pre-development A 310 wing and a A 300-type fuselage were tested in NLR-HST. The wing, described in 2.2.1, had 3 lofting sections, at fuselage, kink and tip. The simple geometry for the suitable wing, enabled the investigation to be concentrated on the root section. After varying the root section and keeping the kink section unchanged, the uncomplicated linear lofting on the percent chord lines rendered the complete wing to be quickly defined.

FIG. 24 and FIG. 25 show the low and high wing concept, respectively, and FIG. 26 shows the comparison between theoretical and test values of the pressure distribution at the root of the low-wing. The NLR-HST tests were completed at Reynolds number $Re = 2.5 \cdot 10^6$, the computations done by the "Method of Analogue Wing Sections". The agreement was satisfactory enough to enable a theoretical comparison between a low and high wing configuration. FIG. 27 shows the calculation at the root for the two wing positions. The deviation in the pressure distribution is considerable.

The geometry alteration necessary for the high wing root section to have the same low wing pressure distribution in FIG. 27, was investigated. FIG. 28 shows the results. The deviation is considerable, especially in the wing box region. This could be partly explained as a positive additional camber arising to compensate for the absent upper surface fuselage displacement.

There is a possibility to compensate this camber increment by cambering the profil after the wing-box, however the profil deviation at the rear spar indicates that the thickness distribution has also changed.

Consequently, this shows that an optimal low-wing cannot achieve the same aerodynamic performance in the high-wing position without altering the wing box.

Following further theoretical work with the high-wing, comparative tests are planned aiming to achieve the best possible performance for the high wing without changing the wing-box of the low-wing.

REFERENCES

- [1] G. Krenz
(VFW) Transonisch profilierte Tragflügel für Verkehrsflugzeuge.
Forschungsbericht BMFT-FB 79-11
- [2] K.D. Klevenhusen
(VFW) A Calculation Method for Multielement Aerofoils in Subsonic and Transonic
Potential Flow.
AIAA-80-0340
- [3] A. Eberle
(MBB) Eine Methode finiter Elemente zur Berechnung der transsonischen Potential-
strömung um Profile.
LFK 7512 Ergebnisbericht Nr. 31
- [4] G. Krenz, R. Hilbig
(VFW) Transonic Wing Design for Transport Aircraft.
DGLR/GARTEur 6 Symposium "Transonic Configurations", Bad Harzburg, FRG,
June 13-15, 1978
- [5] W. Fritz, S. Leicker,
W. Schmidt,
H.W. Stock
(Dornier) Fortsetzung der Untersuchung zur Auslegung überkritischer Tragflügel für
Verkehrsflugzeuge.
Teil II: Theoretische Arbeiten,
LFF 7604, Bericht Nr. Do. 78/11

- [6] H.W.Stock
(Dornier) Integralverfahren zur Berechnung dreidimensionaler Grenzschichten.
Jahrestagung 1977 der DGLR, Berlin, Vortrag Nr. 77-015
- [7] H. Sobieczky
(DFVLR) Design of Advanced Technology Transonic Airfoils and Wings.
AGARD-Symposium "Subsonic/Transonic Configuration Aerodynamics".
May 5-7, 1980
- [8] A. Eberle
(MBB) Transonic Potential Flow Computations by Finite Elements: Airfoil and
Wing Analysis, Airfoil Optimization.
DGLR/GARTEur 6 Symposium "Transonic Configurations", Bad Harzburg, FRG
June 13-15, 1978
- [9] K.D. Klevenhusen,
H.Struck, H.Jacob
(VFW) Neue Rechenverfahren zur sub- und transonischen Interferenzströmung im
ebenen und räumlichen Fall.
LFK 7511, Ergebnisbericht Nr. 44
- [10] P. Thiede, G.Dargel
(VFW) Extension of the Off Design Region of Supercritical Airfoils by Local
Boundary Layer Suction.
RuFo 4, Auftrags-Nr. T/RF 41 / 70021 / 71420, 1980
- [11] P. Thiede
(VFW) Supercritical Airfoil Flow Control by Slot Suction in the Shock Region.
Bericht VFW Ef 908, 1980.
DEA-Symposium, Annapolis, USA, May 15-17, 1980

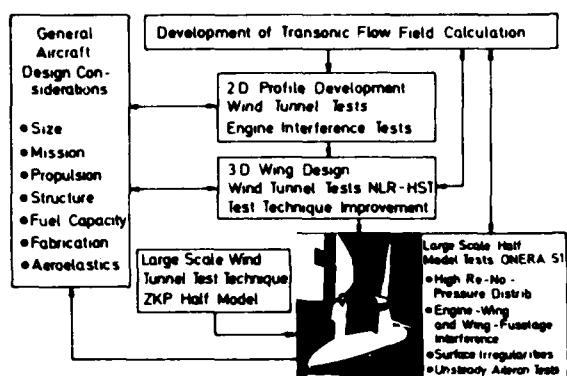


FIG. 1 Programme Objectives
ZKPI, Aerodynamic Tasks

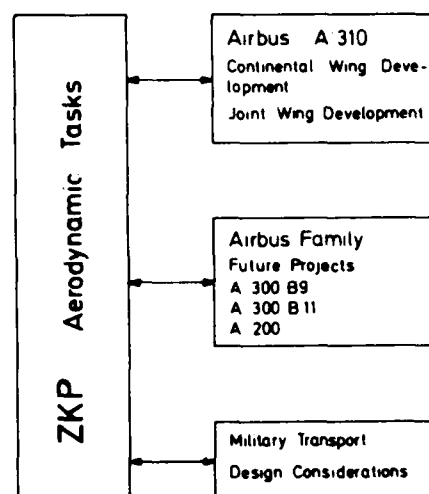


FIG. 2 Relationship between ZKP
and Aircraft Development

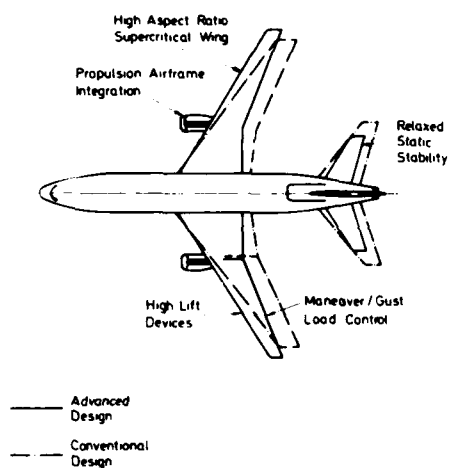


FIG. 3 Civil Component Programme
ZKP II Objectives

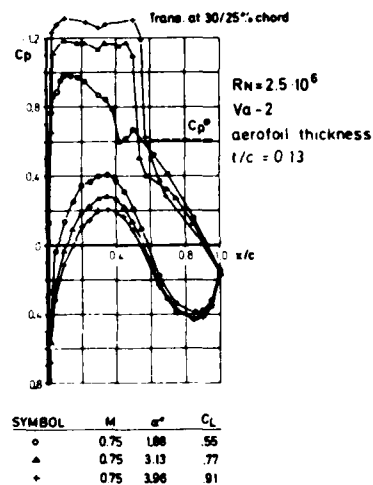


FIG. 4 2D-Section Tests at DFVLR-Göttingen

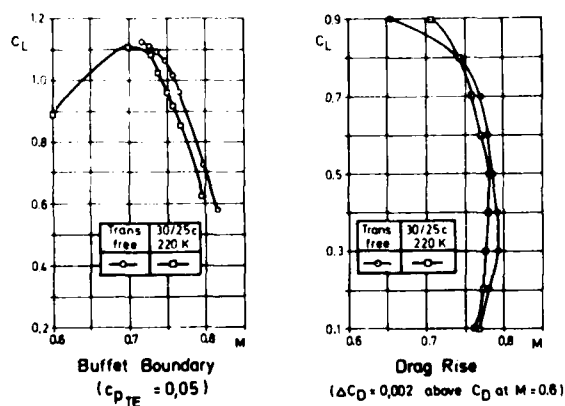


FIG. 5 2D Section Tests DFVLR Göttingen

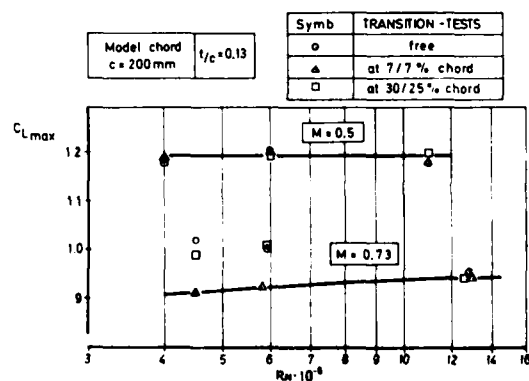


FIG. 6 Section Tests in the Windtunnel
DFVLR - Braunschweig

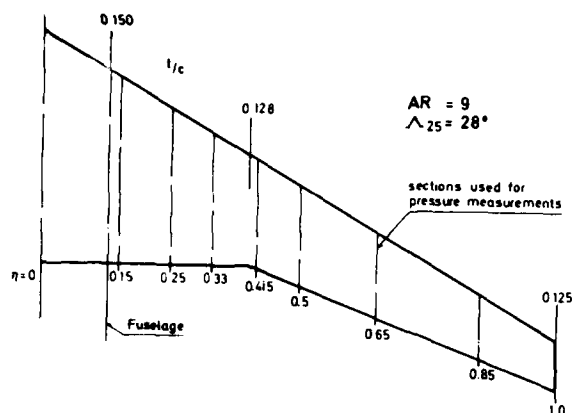


FIG. 7 Basic Geometry of Wing F1

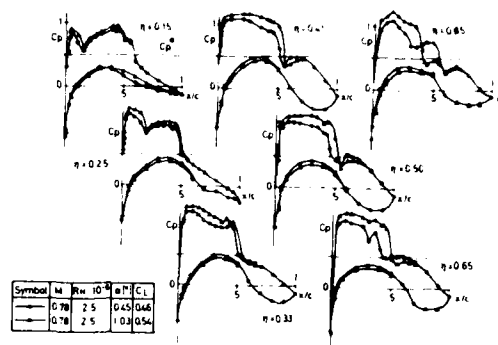


FIG. 8 Wing F1 Tested at NLR-HST

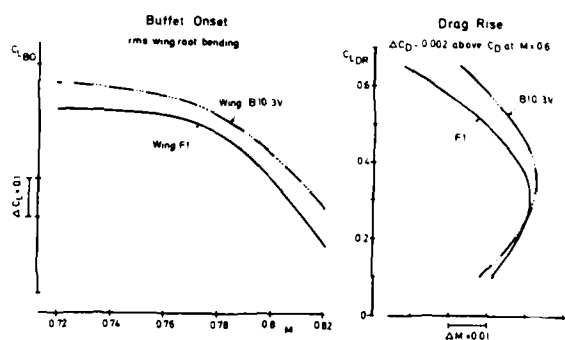
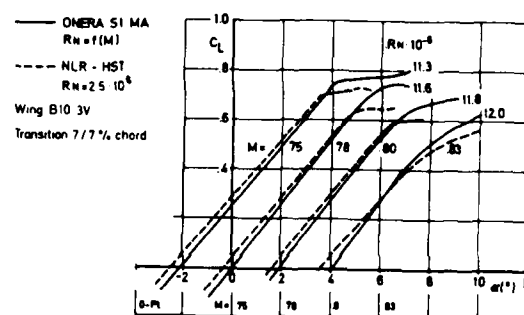
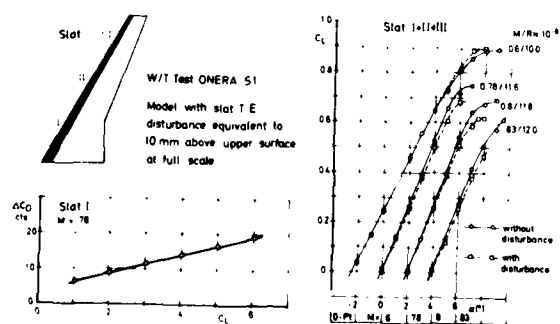
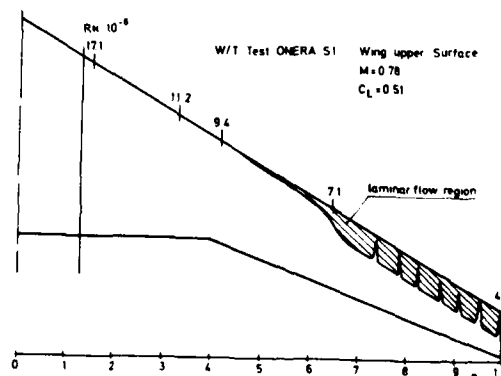
FIG. 9 Windtunnel Tests NLR-HST Amsterdam
 $R_N = 2.5 \cdot 10^6$ 

FIG. 10 Influence of Reynolds-Number on Lift

FIG. 11 Change in Drag and Lift due to
Surface IrregularitiesFIG. 12 Boundary Layer Transition
from Acenaphthene Tests without Trans. Fixing

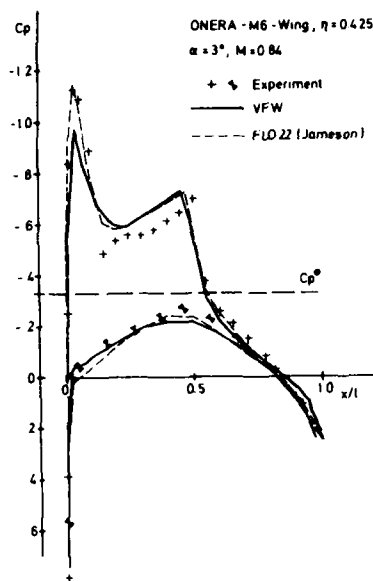


FIG. 13 Comparison Experiment/Calculation

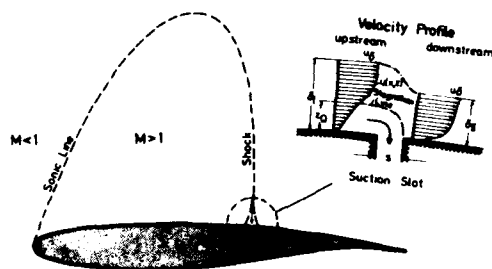


FIG. 15 Supercritical Aerofoil Single Slot Suction Concept

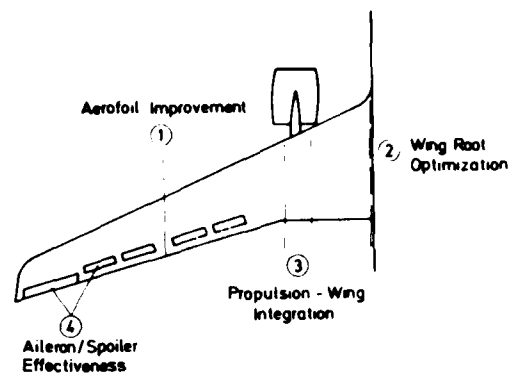


FIG. 14 Future Research in Transonic Aerodynamics

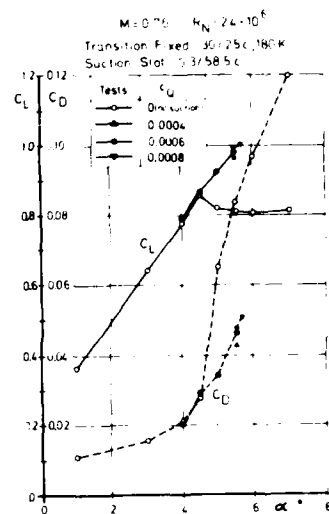


FIG. 16 Va-2 Section Lift Curve and Drag Polar with and without Slot Suction

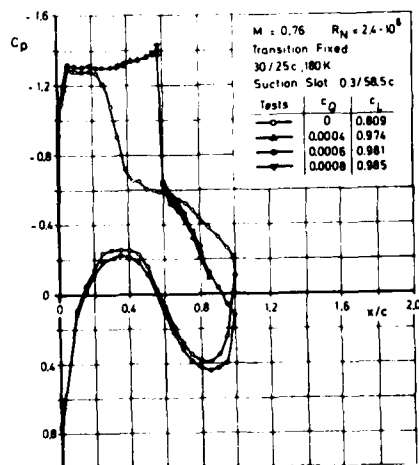


FIG. 17 Va-2 Aerofoil Pressure Distribution with and without Slot Suction

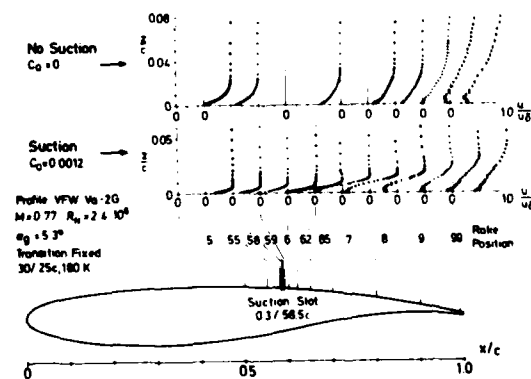


FIG. 18 Suction Influence on Boundary Layer Profile

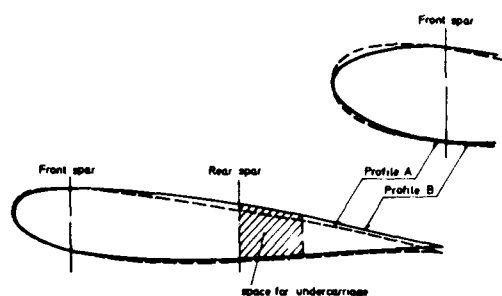


FIG. 19 Root Section Comparison

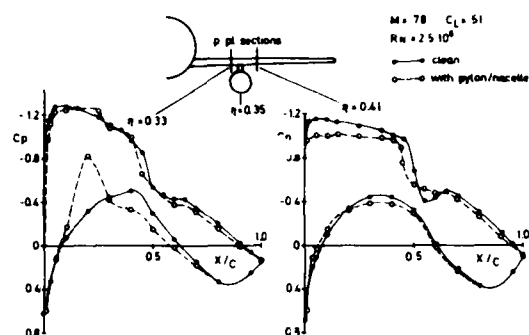


FIG. 20 Windtunnel Tests at NLR - HST, Wing B10.3V

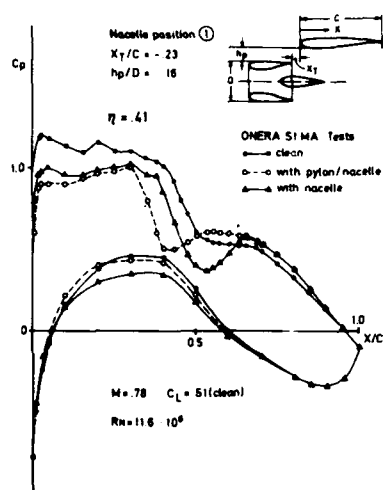


FIG. 21 Pylon/Nacelle Influence on Wing B10.3V Pressure Distribution

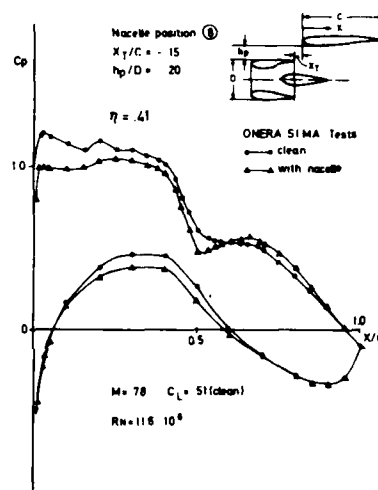


FIG. 22 Pylon/Nacelle Influence on Wing B10.3V Pressure Distribution

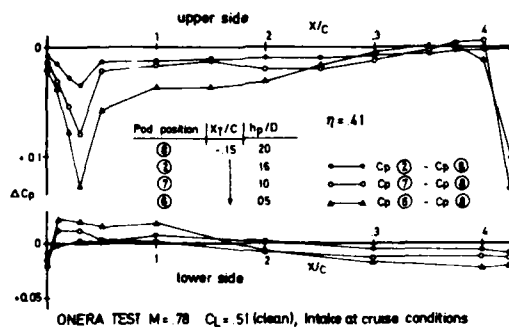


FIG. 23 Change of Wing Pressure Distribution due to decreasing Nacelle Distance from Wing

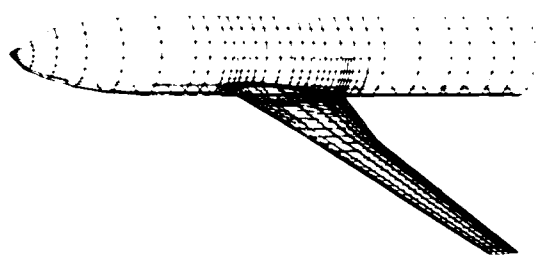


FIG. 24 Low-Wing-Panel Model for Flow Calculation



FIG. 25 High-Wing Panel Model for Flow Calculation

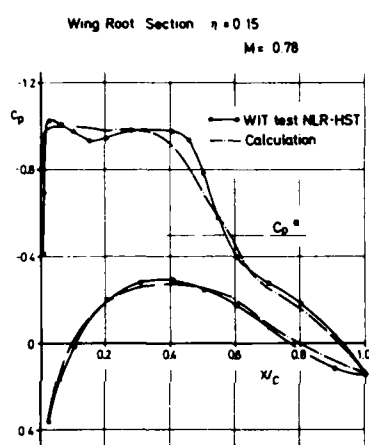


FIG. 26 Comparison Calculation Experiment

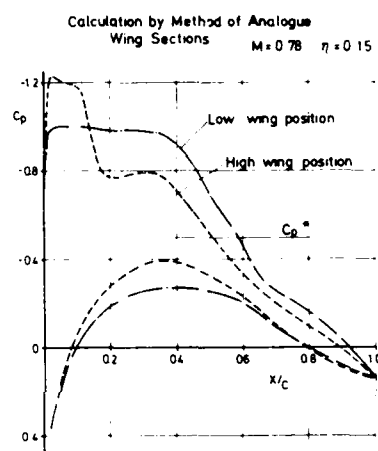


FIG. 27 Wing Root Pressure Distribution

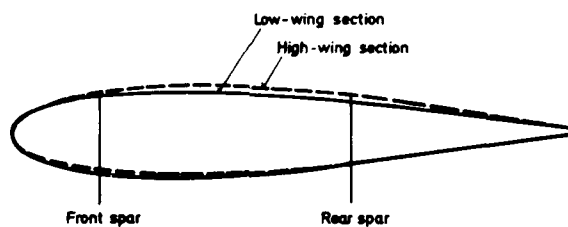


FIG. 28 Wing Root Sections producing the same Pressure Distribution

DESIGN AND EXPERIMENTAL VERIFICATION OF A TRANSONIC WING FOR A TRANSPORT AIRCRAFT

by

G. Redeker N. Schmidt R. Müller

Institut für Entwurfsaerodynamik
Deutsche Forschungs- und Versuchsanstalt für Luft- und Raumfahrt e.V. (DFVLR)
Flughafen, 3300 Braunschweig, FRG

SUMMARY

Due to drastic increase in fuel costs a new generation of transport aircraft is projected worldwide in all aeronautical institutions. One means at short sight to reduce the amount of fuel burned considerably is the application of transonic wing technology.

This paper describes a study of a wing design for a transport aircraft like the AIRBUS A310 including the effects of fuselage by using a transonic wing.

Starting from the requirements of the aircraft and having in mind that a conventional wing planform should be used due to communality reasons, a basic airfoil for the sheared part of the wing has been designed and tested in the DFVLR Transonic Windtunnel Braunschweig (TWB).

On the basis of this airfoil a wing design has been made trying

- to realize minimum induced drag and
- to transfer the good aerodynamic characteristics of the airfoil on the wing.

Force, moment and wing surface pressure measurements on a halfmodel of a wing-fuselage combination have been performed in the 1m x 1m Transonic Windtunnel of DFVLR-Göttingen.

The results of these investigations indicate the good aerodynamic efficiency of the wing.

NOTATION

x, y, z	coordinate system	Re	Reynolds number based on airfoil chord or on aerodynamic wing chord
s	semispan of wing	α	angle of attack
$n = y/s$	coordinate in spanwise direction	c_p	static pressure coefficient
c	local wing chord, airfoil chord	c_p^*	static pressure coefficient at local Mach number $Ma = 1.0$
c_R	wing root chord	c_n	normal force coefficient of wing section
A	aspect ratio	c_l	lift coefficient of airfoil
λ	taper ratio	c_d	drag coefficient of airfoil
Λ_L	leading edge sweep	c_m	pitching moment coefficient of airfoil, referred to quarter chord point
Λ_{25}	sweep of quarter chord line	c_L	lift coefficient of wing
t/c	local wing thickness, airfoil thickness	c_D	drag coefficient of wing
Y_R	fuselage diameter	c_M	pitching moment coefficient of wing referred to N_{25}
Y_K	trailing edge kink location	N_{25}	geometric wing center
ϵ_F	twist angle of wing		
Ma	Mach number		

1. INTRODUCTION

Due to drastic increase in fuel costs a new generation of transport aircraft is projected worldwide in all aeronautical institutions [1, 2, 3]. The reduction in fuel consumption by applying new technologies in aerodynamics, structures, propulsion, flight guidances and control reaches from 5% to 10% at short sight and from 20% to 40% in the future.

For the next generation of transport aircraft which will go into service in 1982/83 (e.g. AIRBUS A310 and BOEING 767) the transonic wing technology is the most promising means in aerodynamics for higher economy and fuel consumption reduction. The benefits of this technology can be exploited in a variety of ways:

- A thicker wing in comparison with a conventional one can be used to achieve a required performance, resulting in reduced structural wing weight and increased volume for the fuel. This may also lead to wing designs with higher aspect ratio which is consequently connected by a reduction of lift-dependent drag being one of the prerequisites for saving fuel.
- The cruising speed can be increased due to the shift of the dragrise Mach number to higher values when using the same wing thickness as for the conventional wing. This way nowadays seems to be not reasonable due to the increasing fraction of fuel costs of the direct operating costs (DOC). The trend in the future will tend to a reduced cruising speed.
- The angle of leading edge sweep can be reduced resulting again in a reduced structural weight, if the span remains constant, connected with some improvements in maximum lift at low speeds.
- The capability of higher lift coefficients of transonic airfoils enables the design engineer to increase the wing loading and decreasing the wing area. Thus a considerable reduction in drag and also in weight and production costs is achieved, although a higher induced drag is produced. The application of this way demands a still better performance of high lift systems for take-off and landing.

Which of these various possibilities given here is realized in an aircraft project depends on the missions and on the other requirements.

In order to guarantee and to develop further the transonic wing technology and in order to reduce the risk of development by applying this new technique on civil aircraft projects an extensive research programme was started in 1975 in Germany sponsored by the Ministry of Research and Technology. In this programme - known as Civiles Komponenten Programm (CKP) - German aerospace industry and the research establishment DLR worked together.

The present paper gives a short description of the part of work being done in the framework of CKP in the Institute for Design Aerodynamics of DLR concerning transonic airfoil and wing design.

2. DESIGN REQUIREMENTS

The basic aim of this study was the design of the highspeed wing in combination with a fuselage for a transport aircraft with passenger capacity of A310 (Fig. 1). The idea in using transonic wing technology was to restrict this potential to the section shape only, that means the wing planform should be the same as for conventional wings. Investigations about minimization of fuel consumption, direct operating costs, wing box weight, and flight range lead to the wing planform which is shown in Fig. 2. The planform is a swept tapered wing with a kink in the trailing edge for carrying the landing gear as it is used for most of the known subsonic transport aircraft.

The main parameters are:

aspect ratio	$A = 9.5$
taper ratio	$\lambda = 0.5$
leading edge sweep	$\Lambda_1 = 27.1^\circ$
sweep of quarter chord line of outer wing	$\Lambda_{25} = 25^\circ$
trailing edge kink at 0.4 of semispan	
fuselage radius	0.126 of semispan.

The wing should fulfil the following design requirements:

- $Ma = 0.785$ cruise Mach number
 $c_L = 0.5$ lift coefficient
 for optimum lift/drag ratio and long range flight
- $Ma = 0.82$ cruise Mach number
 $c_L = 0.4$ lift coefficient
 for highspeed cruise.

By using the benefits of transonic wing technology wing thickness should be increased to approximately 15% at the wing root and to 12% to 13% at the outer part of the wing. These values represent a considerable augmentation of wing thickness compared with the existing A300B wing having a constant thickness of 10.5% from root to tip although the leading edge sweep of A300B is still 3° higher.

As at this time no reasonable method for designing three-dimensional transonic wings is available the usual procedure is to develop or optimize a wing section which is built in a wing planform and then to optimize the wing itself. Procedures as described here are presented in [4, 5]. Redesign procedure starting from given wing geometries trying to improve the wing characteristics are given in [6, 7, 8]. But with these methods only simple configurations have been treated.

As the aspect ratio of transport aircraft wings is in the order $A \approx 10$ the pressure distributions on the

wing surface mainly depend on the wing sections. Only near the tip and in the wing root region considerable three-dimensional effects are expected. For this reason the proceeding stated above by carefully designing the wing section seems to be the best way to come to a good wing design.

3. AIRFOIL DESIGN AND EXPERIMENTAL RESULTS

The design values of lift coefficient and Mach number for the airfoil have been derived from the wing requirements given in chapter 2 using simple sweep theory:

$$\begin{aligned} Ma_{2D} &= Ma_{3D} \cdot \cos \Lambda_{25} \\ c_n &= \frac{c_L}{\cos^2 \Lambda_{25}} \cdot 1.2 \end{aligned}$$

The factor of 1.2 in the equation for the normal force coefficient c_n of the airfoil takes into account the lift losses of the finite wing at the root and at the tip. With the values of $Ma_{3D} = 0.8$ and $c_L = 0.45$ (average values of the two design requirements) the following data come out:

- Mach number $Ma_{2D} = 0.73$
- Normal force coefficient $c_n = 0.65$.

The design aims of the airfoil were: shockfree isentropic recompression near the design condition and a satisfactory off-design behaviour. Former investigations on upper surface pressure types 9 indicated that a sloping rooftop pressure distribution will have these features. Starting point for the airfoil design was a known shockfree airfoil DFVLR 48080 designed by Sobieczky's hodograph-method [10] for a lower normal force coefficient in the beginning of the ZKP (Fig. 3). The shockfree pressure distribution for this 13.5% thick airfoil is shown as case (A) in Fig. 3. The normal force coefficient at $Ma = 0.73$ is $c_n = 0.5$ which as wing requirements changed was too small. Therefore the airfoil contour had to be modified in the direction of getting more lift. This has been done by changing the airfoil contour of the lower side in the rear part near the trailing edge, thus introducing rear-loading step by step.

The calculated pressure distributions of two of the modifications, shown as case (B) and (C) in Fig. 3, provided normal force coefficients of $c_n = 0.6$ respectively $c_n = 0.65$. This could be achieved without having remarkable negative effects on the airfoil characteristics. It is shown that the supersonic region is slightly increased combined with a lot of rear-loading. The pressure distribution of the upper surface seems to remain shockfree in the course of the modification process. The calculated drag coefficients indicated no severe increase due to increased lift. The calculations have been done with the well-known Bauer/Garabedian/Korn/Jameson method for two-dimensional transonic viscous flow [11].

Calculations for off-design conditions to a great extent showed that the airfoil case (C), hereafter denoted as DFVLR-R4, proved to satisfy the design requirements. The design process is described in more details in [12]. Some of the calculated results will be discussed with corresponding measurements.

Experiments with the airfoil DFVLR-R4 have been done in the DFVLR Transonic Windtunnel Braunschweig (TWB) [13] at Reynolds numbers from $Re = 3 \cdot 10^6$ to $9 \cdot 10^6$ without and with transition strip. The experimental results at free transition have been analysed in details in [14] and have been partly discussed at the GARTEUR/DGLR meeting [15]. Thus this paper discusses to a certain extent the influence of Reynolds number and transition strip on aerodynamic coefficients and pressure distribution.

Fig. 4 presents a comparison between predicted pressure distributions and measured ones for two normal force coefficients at a Mach number of $Ma = 0.73$. The agreement is excellent not only for the case near design at $c_n = 0.6$ but also for a higher value of $c_n = 0.77$, which is near dragrise. The drag level is also well predicted by the calculations after the BGKJ-method.

In order to improve the knowledge about this airfoil with respect to higher Reynolds number additional tests varying Reynolds number and tests without and with transition strip have been carried out. Fig. 5 presents results of force and moment coefficients indicating the influence of transition strip and Reynolds number. The left part shows the aerodynamic coefficients of normal force c_n , drag c_d and pitching moment c_m versus angle of attack at $Ma = 0.73$ and $Re = 6 \cdot 10^6$. The open symbols denote values without transition strip while fixed transition results are indicated by full symbols. The strip with a width of 1% of chord was made from carborundum of grain size 220 and was located at 7% chord length on upper surface and at 30% chord length at lower surface. In the figures it is denoted as 220K 7/30L. These positions have proved to be reasonable from boundary layer calculations at high Reynolds numbers. It is shown that for the transition fixed results the nonlinear behaviour of c_n versus α at high values of c_n is reduced leading to a smaller normal force. The drag coefficient is increased about 10% in the region of unseparated flow but the rapid dragrise is not affected. The nose down pitching moment is also reduced about 10%.

The development of these differences due to transition strip with Reynolds number is shown in the right figure at a constant angle of attack $\alpha = 10^\circ$. The biggest differences occur at the lowest measured Reynolds number at all coefficients.

The c_n -value at fixed transition is continuously increased with increasing Re , while at transition free c_n is decreasing from $Re = 3 \cdot 10^6$ to $5 \cdot 10^6$ and then is also increasing. The tendency of the two curves indicates that they will run together at higher Reynolds numbers. The c_d -values at fixed transition drop with increasing Re , while at transition free the drag values remain nearly constant. This is due to the interaction of laminar and turbulent boundary layer with moving transition location. At the highest Reynolds number the curves indicate a remarkable difference although the tendency is the same for the normal force coefficients. It seems that c_d for fixed transition is too high due to an

The c_m -values at transition fixed show an increase in nose down pitching moment, while at transition free a decrease followed by a slight increase is indicated. This behaviour could be explained by looking at the corresponding pressure distributions in Fig. 6. For a constant Mach number $Ma = 0.73$ and a constant angle of attack $\alpha = 10^\circ$ the pressure distributions are plotted. The two left figures indicate the influence of transition strip at two Re-numbers $Re = 3 \cdot 10^6$ and $Re = 6 \cdot 10^6$. A big difference can be stated at $Re = 3 \cdot 10^6$ indicating a remarkable loss in rear-loading and a forward shift of the shock location due to the transition strip. At $Re = 6 \cdot 10^6$ these differences decrease considerably, thus the pressure distributions for this case look very similar each other. From these results and from the force and moment coefficients of the previous figure it can be stated that measurements at low Reynolds number $Re < 5 \cdot 10^6$ with fixed transition give no reasonable results, because the type of pressure distribution is completely changed.

The right figure indicates the influence of Reynolds number at transition free. It is shown that the pressure at the lower side is nearly unaffected, only some small differences occur at the trailing edge and at the location of maximum thickness. On the upper surface the shock location is influenced in that way that at the lowest Re-number the shock is located the farthest to the trailing edge. With increasing Re it slightly moves forward and then at $Re = 9 \cdot 10^6$ tends to move backwards again. This behaviour is responsible for the development of the aerodynamic coefficients discussed in Fig. 5. But it can be stated that for this airfoil the pressure distributions at all measured Re-numbers with transition free are of that type or are very similar to those, which were measured with transition fixed at $Re > 5 \cdot 10^6$. That means for this airfoil it seems to be better to measure without transition strip if one is forced to test at Reynolds numbers $Re < 5 \cdot 10^6$.

The aerodynamic efficiency of the airfoil DFVLR-R4 is shown in Fig. 7 in a c_l -Ma-diagram, where lines of constant $(c_l/c_d) \cdot Ma$ are plotted for $Re = 6 \cdot 10^6$ for the two cases transition fixed and transition free. It is indicated that the values of the results for transition fixed are about 10% lower than those with free transition. But what comes out here is that the location of the maximum value of this expression is not affected by the transition strip. For both cases it lies in the region of Mach number and c_l where the design condition is located. In the left figure the curves for dragrise and buffet onset are marked and one sees that the dragrise curve is tangential to the lines of constant aerodynamic efficiency in the region of design condition.

Extensive experimental results have shown that the DFVLR-R4 airfoil fulfils the requirements and therefore it was chosen as basic wing section.

4. WING DESIGN AND EXPERIMENTAL RESULTS

Wing design has been carried out under the following aspects:

- minimum induced drag by elliptic lift distribution along wing span,
- shockfree or nearly shockfree recompression of upper surface pressure,
- straight isobars on wing surface.

For high aspect ratio wings the pressure distribution mainly depends on the characteristics of the wing section. Therefore the basic airfoil DFVLR-R4 has been developed for the sheared part of the wing. Aspiring to straight isobars along lines of constant percentage on most of the wing area it is supposed that the good characteristics of the airfoil will determine the behaviour of the whole wing.

With an inverse vortex-lattice method [16] for wing-body combinations with infinite long cylindrical bodies the wing twist along wing span has been evaluated in the first design step. This was achieved by assuming a load distribution - obtained for the airfoil DFVLR-R4 at the design point - along wing span according to the prescribed elliptic lift distribution. The calculated twist was then approximated by straight lines along span using four defining wing stations to build up the wing contour. In Fig. 8 the defining wing stations are marked by indicating wing thickness and twist angle.

The four stations are:

I	wing root at	$n = 0.126$;	$\epsilon_F = 4.5^\circ$
II	trailing edge kink at	$n = 0.409$;	$\epsilon_F = 1.8^\circ$
III		$n = 0.7$;	$\epsilon_F = 0.9^\circ$
IV	wing tip at	$n = 1.0$;	$\epsilon_F = -0.5^\circ$.

In the outer part of the wing from the station II to station IV the airfoil DFVLR-R4 was used to build up the wing. For this reason the airfoil was converted to streamwise direction by the cosine of sweep angle Λ_{25} and then rotated due to the calculated twist angle. In order to get a simple surface the wing contour was generated by a linear lofting procedure between the defining stations.

The wing root section has to be modified in order to take into account

- the influence of the presence of the fuselage,
- the effect of decreasing sweep of the isobars in the central part of a swept wing, and
- a higher wing thickness for the undercarriage.

The design process of the wing root region has been done with the aid of a finite difference method for three-dimensional transonic flow around wing-body combinations based on the transonic small perturbation potential equation (TSP). The computer programme used has been established by DORNIER [17]. In the calculations only the direct version of this computer code was used, thus the wing contour was evaluated by iteratively calculating the pressure distribution and improving the wing shape. This led to a wing contour in the wing root having a section thickness of 15% and providing a pressure distribution with moderate suction peaks and no shift of minimum pressure towards the trailing edge as it is usual in the central part of a swept wing. This wing is denoted as DFVLR-F4. Extensive calculations using a 5% grid (50 000 grid points) varying Mach number and angle of attack have been done to check the off-design behaviour of the wing. Fig. 9 shows the predicted pressure distribution for the long range cruise case ($Ma = 0.785$, $c_L = 0.5$). Surface pressure distributions indicate that over the whole wing span lift by supersonic shock-free flow is produced in combination with considerable rear-loading. In the outer part of the wing the pressure distributions are very similar each other and look like those of the basic airfoil DFVLR-R4. In the inner part it is seen that the wing loading is decreased due to the prescribed elliptic lift distribution.

A windtunnel halfmodel was constructed and built for force and surface pressure measurements. Fig. 10 gives an overview of this model with the main dimensions. The semispan of the wing is about 600 mm, while the fuselage diameter is about 148 mm with a length of nearly 1.2 m. The wing was equipped with five pressure measuring stations with a total number of 180 pressure holes. This halfmodel was tested in the Transonic Windtunnel of DFVLR Göttingen [18] at a maximum Reynolds number of $Re = 2 \cdot 10^6$ based on the aerodynamic chord of the wing. The test arrangement in this tunnel can be seen from Fig. 11. The halfmodel is mounted on a plate which has a distance of 21 mm from the tunnel wall taking into account the effect of tunnel wall boundary layer. In order to measure the model forces only, a 0.5 mm slot between model and plate has been realized. The results of these tests have been discussed partly in [19, 20] and in more details in [21]. Some of these results will be discussed here with respect to effects of fixed transition.

Fig. 12 presents results of pressure distributions at five spanwise stations at the design Mach number $Ma = 0.785$ for three lift coefficients. Reynolds number is $Re = 1.9 \cdot 10^6$ and transition is not fixed.

It can be seen that over the whole span supersonic flow is achieved. In the outer part of the wing nearly shockfree or pressure distributions with weak shocks occur. Shock location is about 60% of local chord. Near the kink a slight breakdown in the supersonic region is visible at the two lower lift coefficients, which vanishes when lift is further increased. This seems to be a kink effect and has to be investigated further. In the wing root region the pressure develops with a very weak oblique shock wave. In contrast to the calculated results more nose lift is generated. This is due to the crude representation of the wing nose in the calculation grid.

The normal force distributions along wing span indicate a decreasing wing loading in the inner part of the wing resulting from the elliptic lift distribution.

The influence of a transition strip on the pressure distribution is shown in Fig. 13. For $Ma = 0.785$ and $\alpha = 0^\circ$ at $Re = 1.9 \cdot 10^6$ pressure distributions with and without fixed transition are compared. The location of the transition strip is indicated in the upper right part of Fig. 14. It has been made from carborundum of grain size 100 and is denoted as 100K in the figures.

The effect of this strip is similar to that applied to the airfoil discussed in Fig. 6. In the outer wing part the shock location is shifted forward in direction to the leading edge and the rear-loading is reduced considerably. These effects increase when sweeping from kink to tip. The lift loss is about 10% at the same angle of attack, while the drag coefficient is increased about the same amount.

A plain view on the location of weak shocks and isobar patterns in the wing planform at design lift coefficient $c_L = 0.5$ and $Ma = 0.785$ is given in Fig. 14 for both cases with and without transition strip. The left half of this figure describes the transition free case. It can be seen that a weak shock is located at 60% on the outer wing. In the kink region it splits up in a double shock system, while on the inner wing part the rear shock vanishes. At the trailing edge kink there is a little zone of rear separation coming from the double-shock system. The isobar pattern makes clear these facts but it can be stated that a satisfactory pattern is achieved in the outer part of the wing.

The right half of Fig. 14 gives the situation for the transition fixed results. Only one curved pattern of a weak shock can be seen and its location is about 50% of local chord on the outer wing portion. No rear separation is indicated. The isobar pattern for this case is satisfactory, too.

The aerodynamic efficiency of the wing for the transition free results is given in Fig. 15. It can be seen that the highest values of $(c_L/c_D) \cdot Ma$ are achieved in the region where the design requirement for the long range cruise is located. The values themselves seem to be a little bit small. This is due to measured drag coefficients originating from halfmodel tests. Extensive data evaluation and comparisons between halfmodel and fullmodel tests [22] showed that the measured drag coefficients from the halfmodel tests give the correct tendency with angle of attack and Mach number, but the value is too high because of a nearly constant increment in drag.

The marked dragrise boundary, derived from $\Delta c_D = 0.002$ above c_D at $Ma = 0.6$, shows that both design points lie within the economic flight region. This figure clearly indicates that the wing DFVLR-F4 fulfils the design requirements.

5. CONCLUSIONS

In this paper a wing design for a transonic transport aircraft has been described using transonic wing technology. Compared to the standard of AIRBUS A300 the potential of this technology has been used to

- increase average wing thickness from 10.5% to 12.5%,
- reduce leading edge sweep angle from 30° to 27° , and
- increase cruising lift coefficient to $c_L = 0.5$.

Starting point for the wing design is a carefully developed airfoil DFVLR-R4 which has been tested extensively in the windtunnel. For high aspect ratio wings it is shown that good airfoil characteristics are the basis for a successful wing design. Windtunnel tests of a halfmodel of the wing DFVLR-F4 indicate the high standard of the advanced design. In order to get rid of the shortcomings of halfmodel tests, further windtunnel tests on a fullmodel will be prepared. This will be done within the framework of the European cooperation in GARTEUR (Group for Aeronautical Research and Technology in Europe) for which this model was chosen to be tested in the major transonic windtunnels of the aeronautical research establishments in Europe and to serve as the basic geometry for calculation purposes.

6. REFERENCES

- [1] CTOL Transport Technology - 1978. NASA CP 2036, Part I, II (1978).
- [2] POISSON-QUINTON, PH. Energy Conservation Aircraft Design and Operational Procedures. AGARD-LS-96 (1978), p. 9-1 to 9-47.
- [3] POPE, G.G. Prospects for Reducing the Fuel Consumption of Civil Aircraft. Aeron. Journ. 83, 1979, p. 287-295.
- [4] HANEY, H.P. JOHNSON, R.R. Computational Optimization and Windtunnel Test of Transonic Wing Designs. AIAA Paper No. 79-0080 (1979).
- [5] LORES, M.E. SMITH, P.R. Supercritical Wing Design Using Numerical Optimization and Comparison with Experiments. AIAA-Paper No. 79-0065 (1979).
- [6] SOBIECZKY, H. YU, N.J. FUNG, K.Y. SEEBASS, A.R. A New Method for Designing Shock-Free Transonic Configurations. AIAA-Paper No. 78-1114 (1978).
- [7] YU, N.J. An Efficient Transonic Shock-Free Wing Redesign Procedure Using a Fictitious Gas Method. AIAA-Paper No. 79-0075 (1979).
- [8] SHANKAR, V. MALMUTH, N.D. COLE, J.D. Computational Transonic Design Procedure for Three-Dimensional Wings and Wing-Body Combinations. AIAA-Paper No. 79-0344 (1979).
- [9] KÖRNER, H. Entwurf und Windkanalerprobung überkritischer Profile im Rahmen der ZKP-Aufgabe "Flügelsektion". DFVLR - IB 151-76/20 (1976).
- [10] SOBIECZKY, H. Transonic Design in 2 and 3 Dimensions. GARTEUR/DGLR-Symp. "Transonic Configurations", Bad Harzburg, FRG, June 1978, DGLR No. 78-066.
- [11] BAUER, F. GARABEDIAN, P. KORN, D. JAMESON, A. Supercritical Wing Sections II. Springer Verlag, New York (1975).
- [12] REDEKER, G. SCHMIDT, N. HANSEN, H. Entwurf eines Tragflügels für den transsonischen Geschwindigkeitsbereich im Rahmen der ZKP-Aufgabe "Flügelsektion". DFVLR - IB 151-77/20 (1977).
- [13] STANEWSKY, E. PUFFERT, W. MÜLLER, R. Der Transsonische Windkanal des Instituts für Aerodynamik der DFVLR: Eichung der modifizierten Meßstrecke und Vergleichsmessungen am Profil CAST 7/DO A1. DFVLR - IB 151-77/10 (1978).
- [14] REDEKER, G. MÜLLER, R. Messungen am Profil DFVLR-R4 im Transsonischen Windkanal Braunschweig. DFVLR - IB 151-78/3 (1978).
- [15] REDEKER, G. MÜLLER, R. Design and Experimental Verification of Two Supercritical Airfoils. GARTEUR/DGLR-Symp. "Transonic Configurations", Bad Harzburg, FRG, June 1978, DGLR No. 78-075.
- [16] KÖRNER, H. Ein Verfahren zur Berechnung der Verwindung und Verwölbung des Flügels bei vorgegebener Lastverteilung unter Berücksichtigung des Rumpfes. DLR-FB 75-12 (1975).
- [17] SCHMIDT, W. HEIDMAN, S. Recent Explorations in Relaxation Methods for Three-Dimensional Transonic Potential Flow. ICAS-Paper No. 76-22 (1976).
- [18] HOTTNER, TH. LORENZ-MEYER, W. Der Transsonische Windkanal der Aerodynamischen Versuchsanstalt Göttingen (zweite Ausbaustufe). Jahrbuch der DGLR 1968 (1969), S. 235-244.
- [19] REDEKER, G. SCHMIDT, N. Design and Experimental Investigations of a Wing for a Transonic Transport Aircraft. GARTEUR/DGLR-Symp. "Transonic Configurations", Bad Harzburg, FRG, June 1978, DGLR No. 78-085.

- [20] REDEKER, G. Transsonischer Tragflügel DFVLR-F4 als europäisches Testmodell. DFVLR-Nach-
SCHMIDT, N. richten, Heft 27 (1979), S. 36-39.
- [21] REDEKER, G. Ergebnisse der Messungen am Flügel DFVLR-F4 im Transsonischen Windkanal
Göttingen. DFVLR - IB 151-79/12 (1979).
- [22] SCHMIDT, N. Ergebnisse der Halbmodellmessungen am VFW-Flügelentwurf B1X/1-1 im Trans-
sonischen Windkanal Göttingen. DFVLR - IB 151-79/7 (1979).

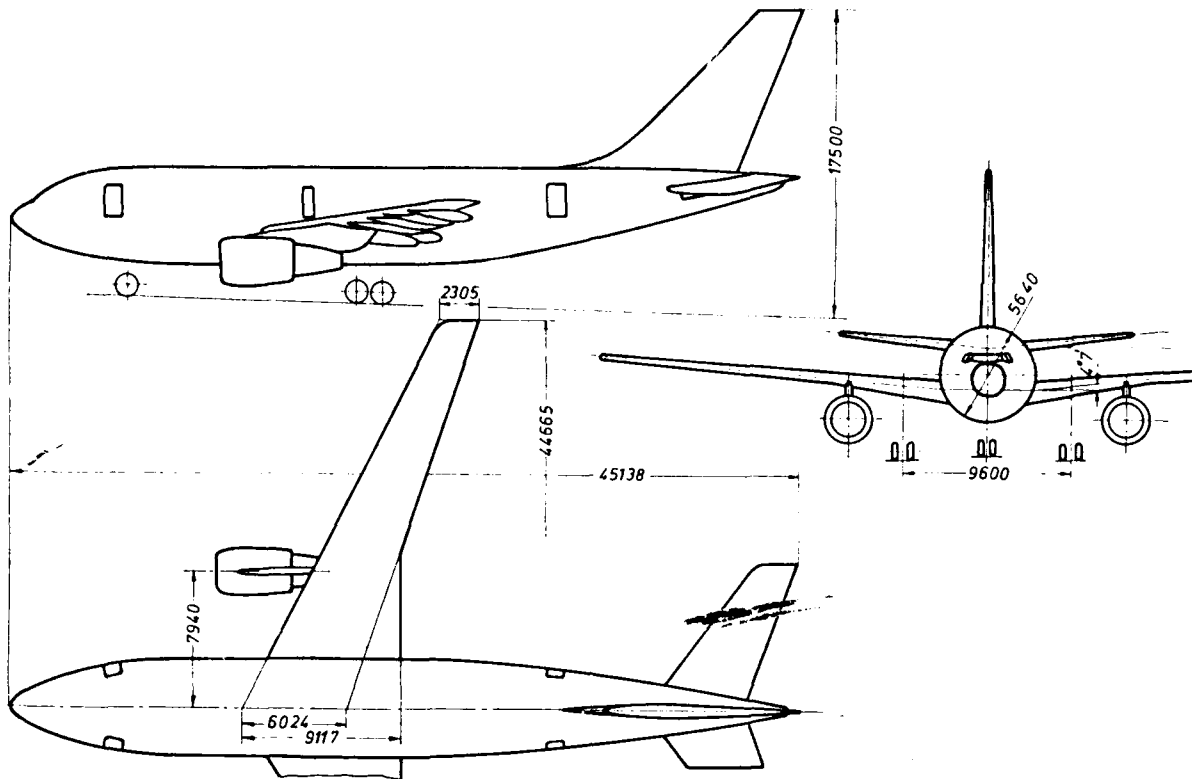


Fig. 1: View of Design Example for AIRBUS A310 (dimensions in mm)

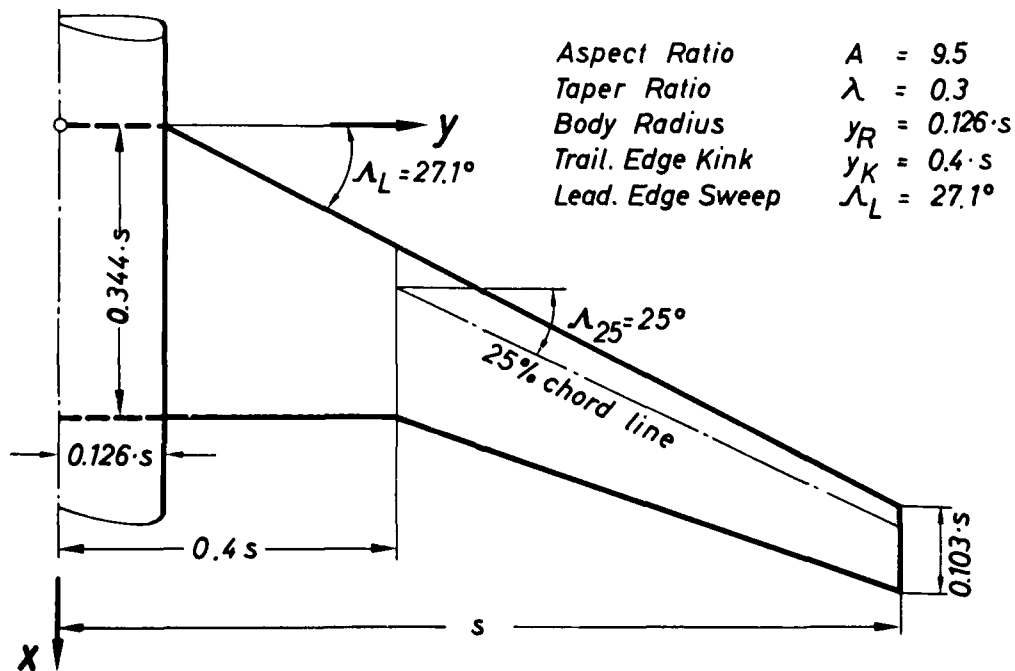


Fig. 2: Geometry of Wing Planform DFVLR-F4

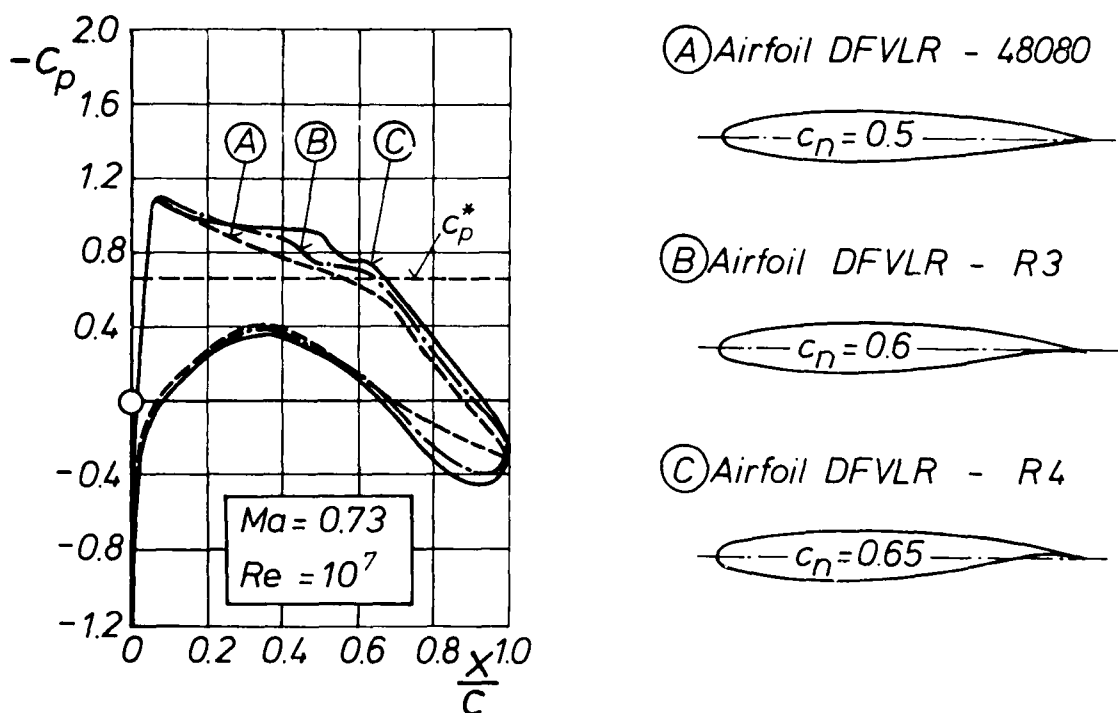


Fig. 3: Transonic Airfoils, Design and Modification

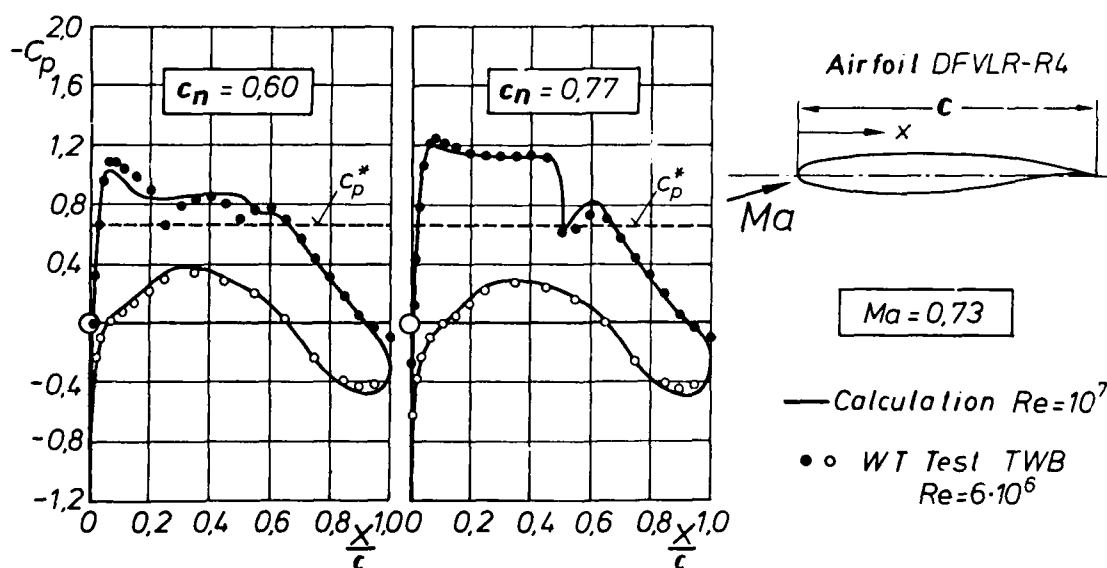


Fig. 4: Comparison of Predicted and Measured Results for Airfoil DFVLR-R4

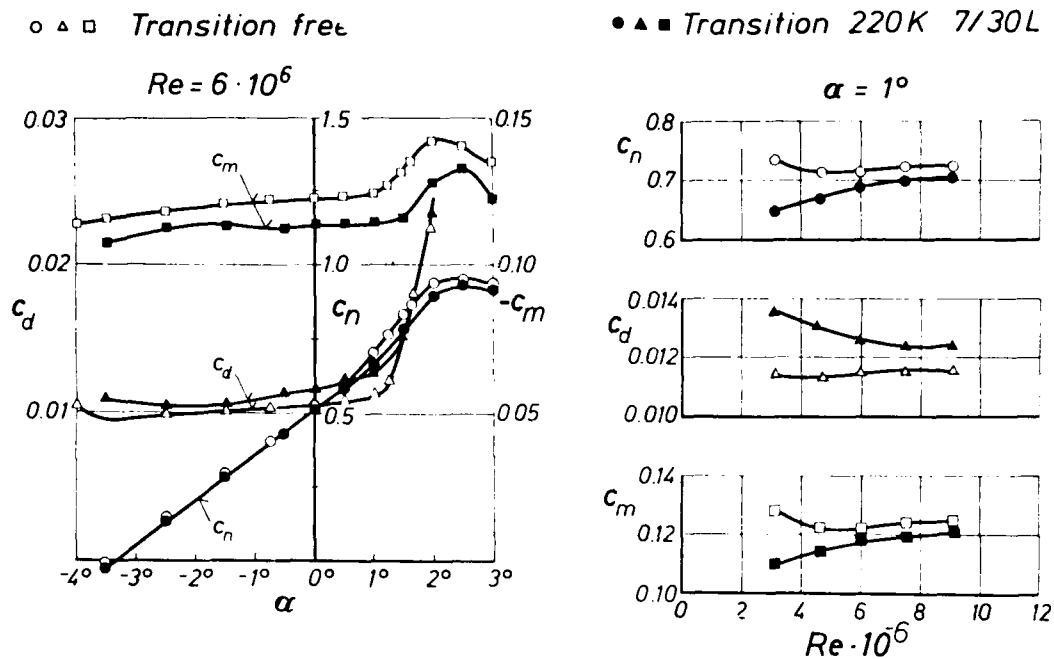


Fig. 5: Influence of Transition Strip and Reynolds Number on the Aerodynamic Characteristics of DFVLR-R4 at $Ma = 0.73$

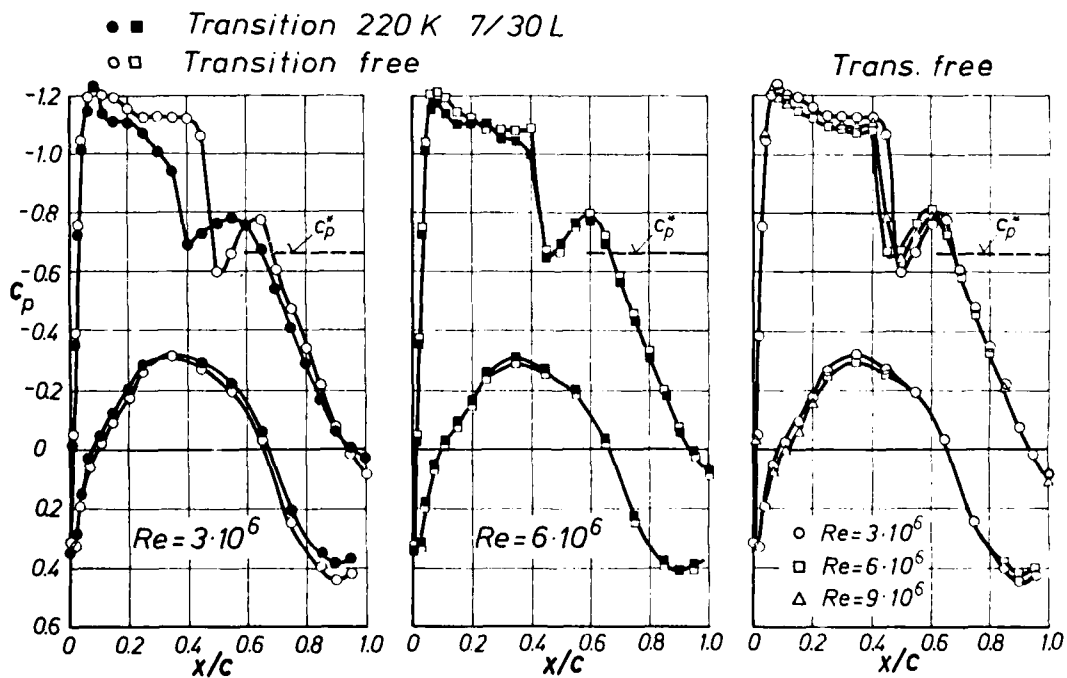


Fig. 6: Influence of Transition Strip and Reynolds Number on Pressure Distributions of DFVLR-R4 at $Ma = 0.73$ and $\alpha = 1^\circ$

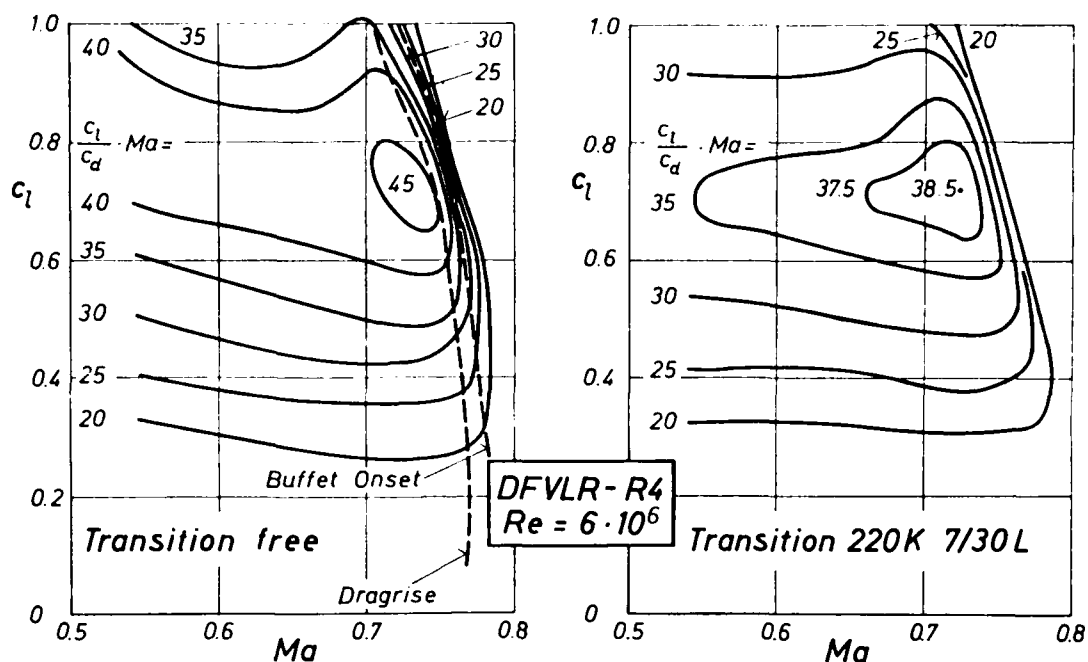


Fig. 7: Influence of Transition Strip on the Aerodynamic Efficiency of the Airfoil DFVLR-R4

Design

$$Ma = 0.785$$

$$c_L = 0.5$$

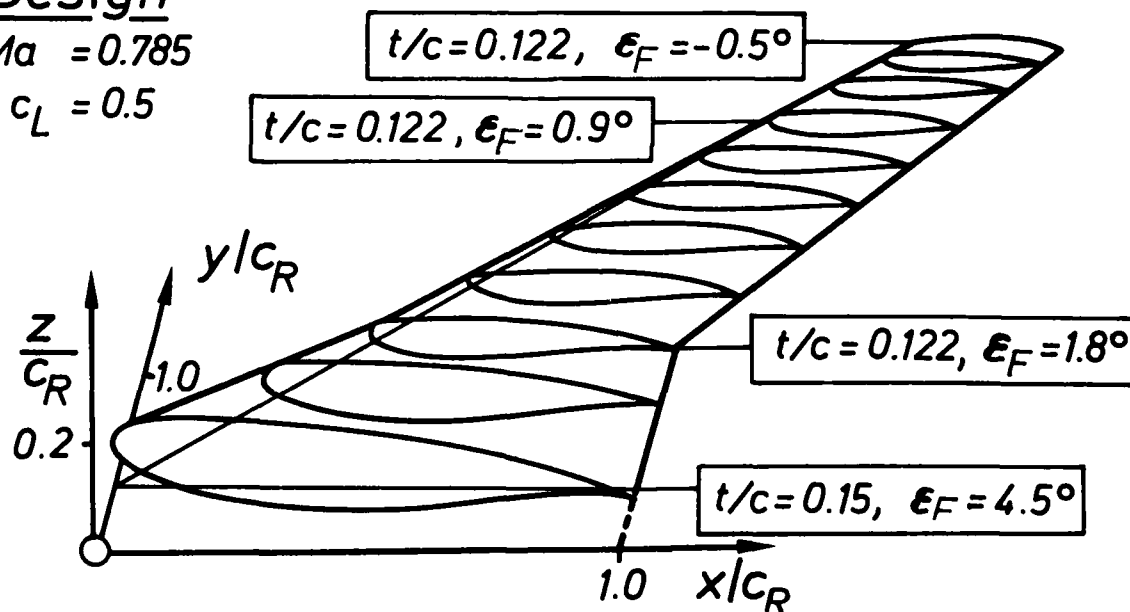


Fig. 8: View of Wing DFVLR-F4

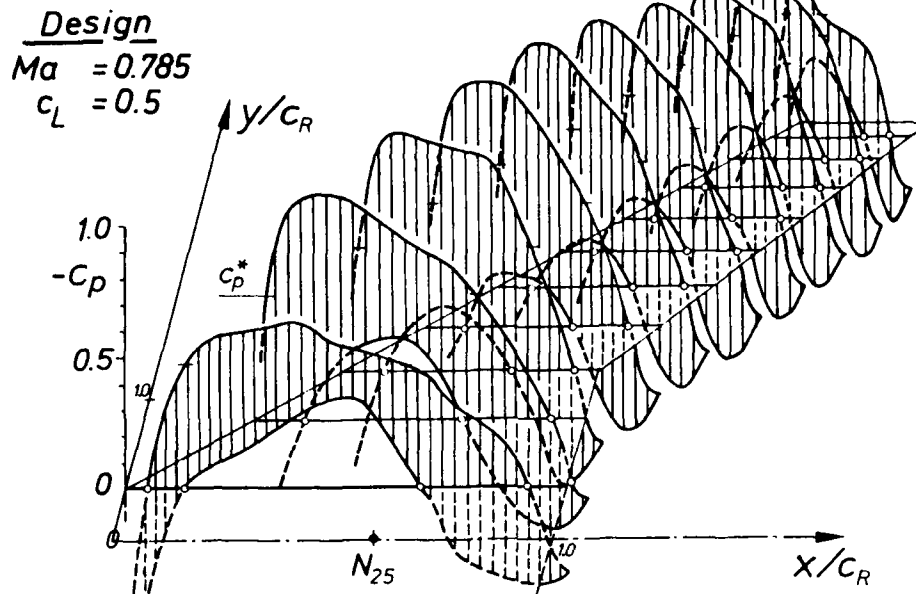


Fig. 9: Calculated Pressure Distribution at Design Condition for Wing DFVLR-F4

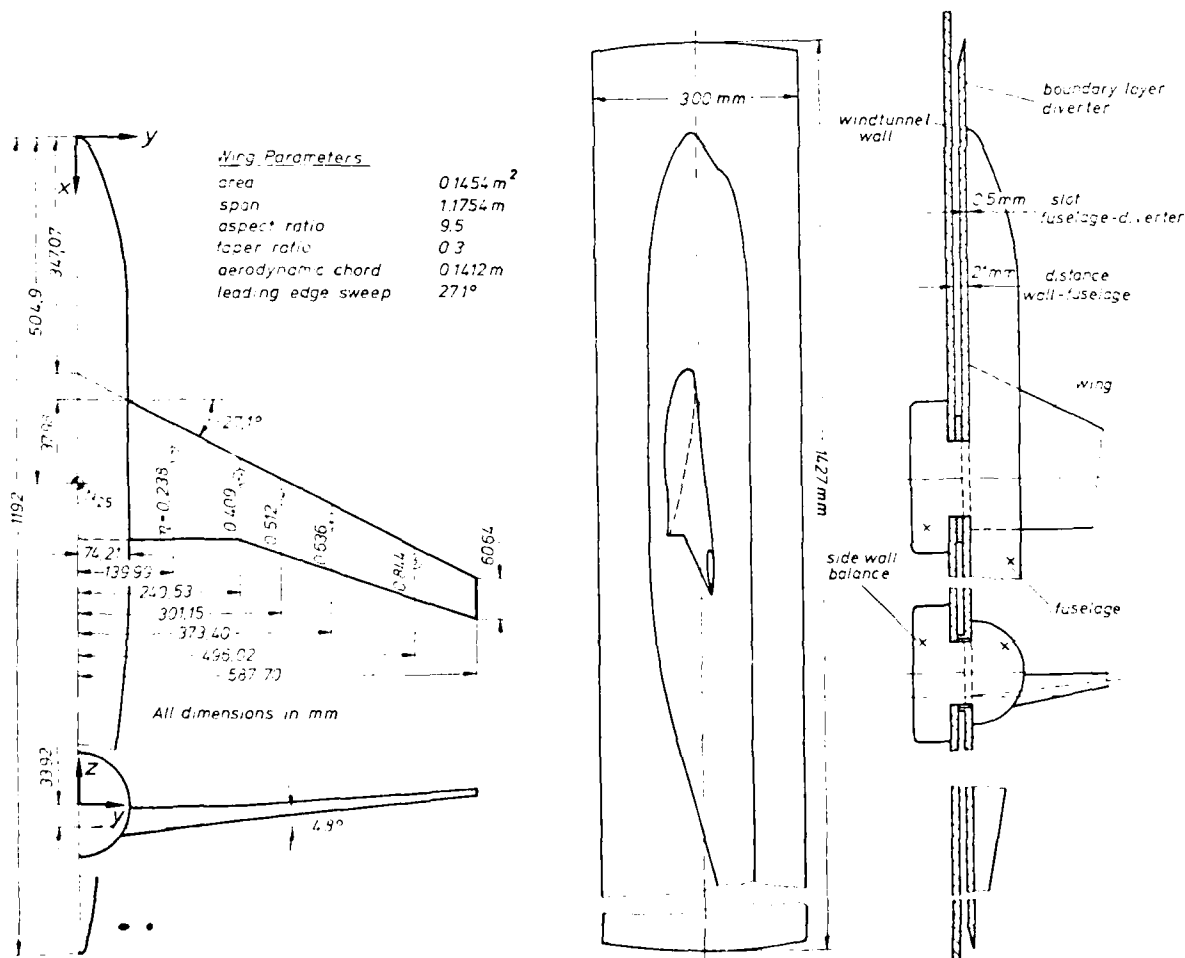


Fig. 10: Windtunnel Halfmodel of Wing-Body-Combination with Wing DFVLR-F4

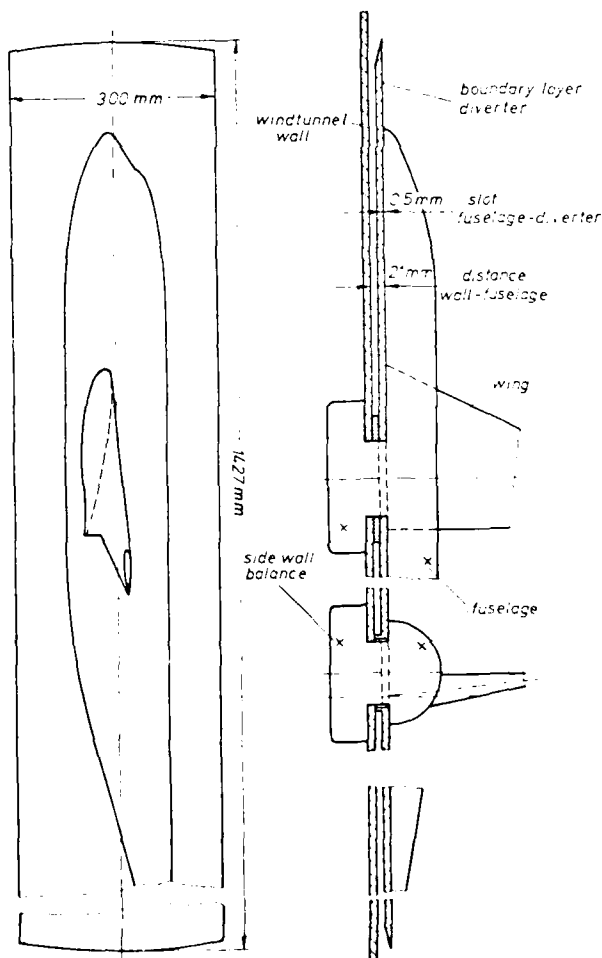


Fig. 11: Test Arrangement in the Transonic Windtunnel of DFVLR-Göttingen

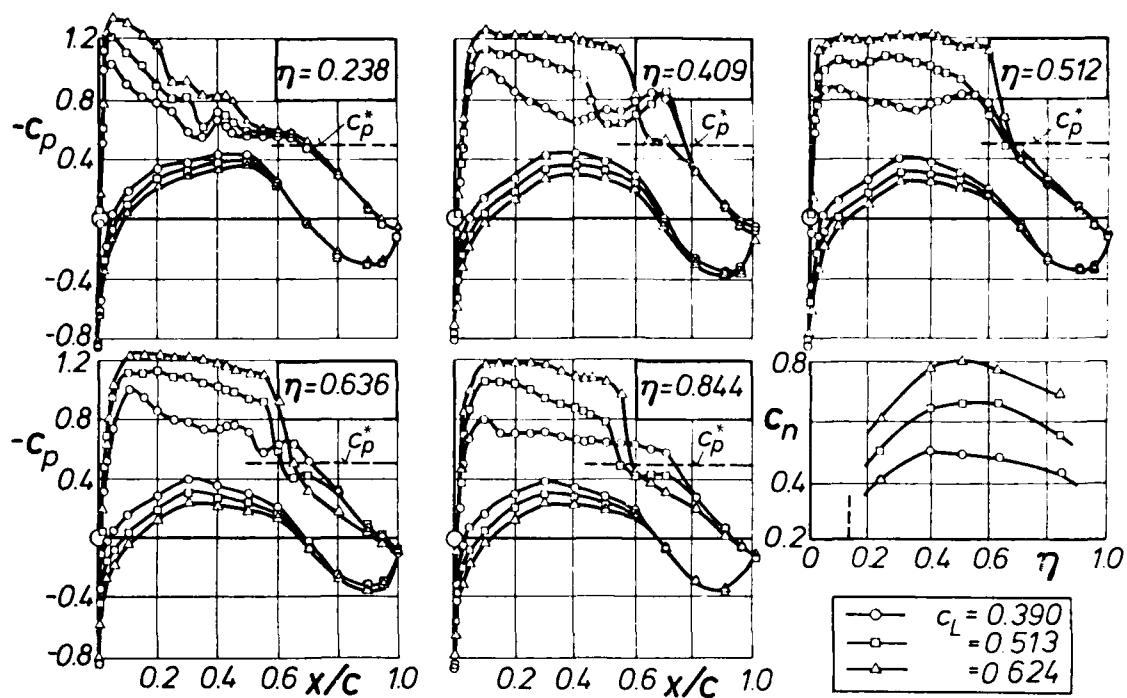


Fig. 12: Pressure Distribution of Wing DFVLR-F4 at $Ma = 0.785$ and $Re = 1.9 \cdot 10^6$ (Transition free)

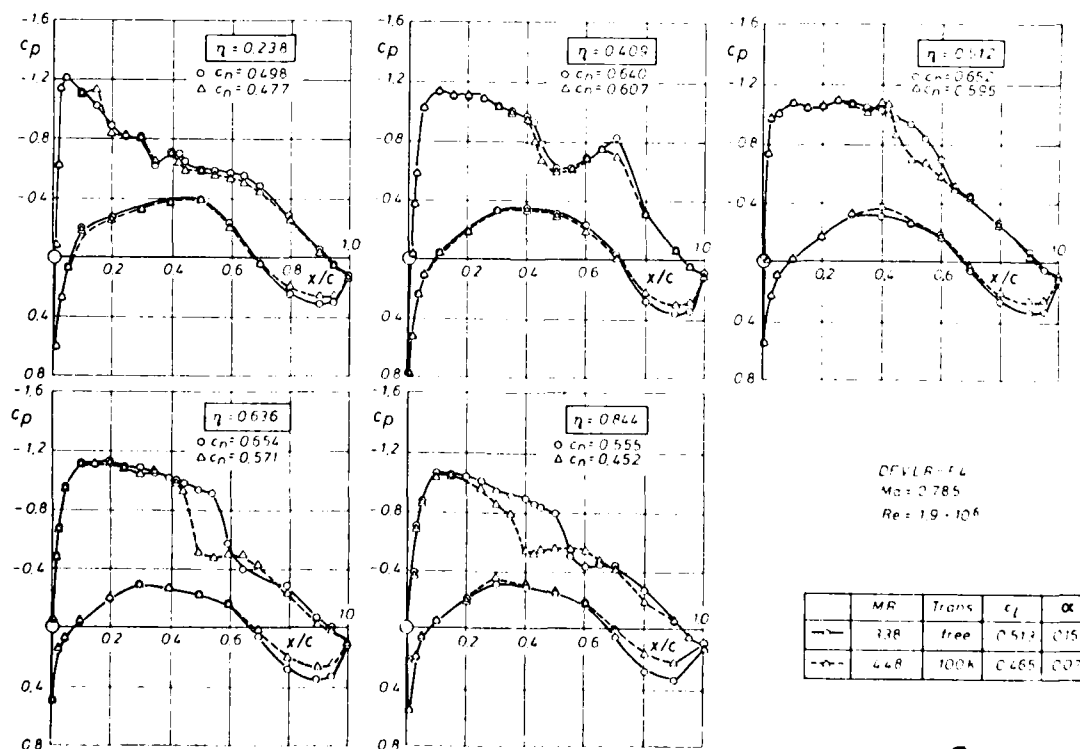


Fig. 13: Influence of Transition Strip on Pressure Distribution at $Re = 1.9 \cdot 10^6$ and $\alpha = 0^\circ$

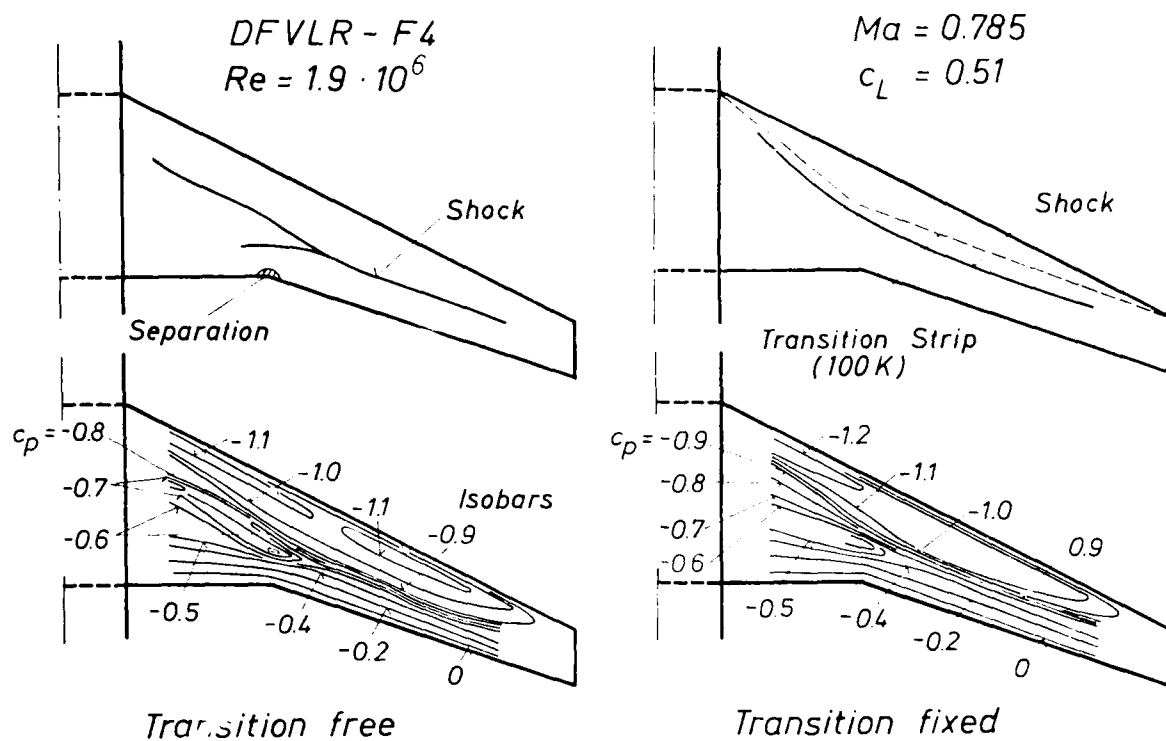


Fig. 14: Influence of Transition Strip on Shock Location and Isobar Pattern at Design Condition

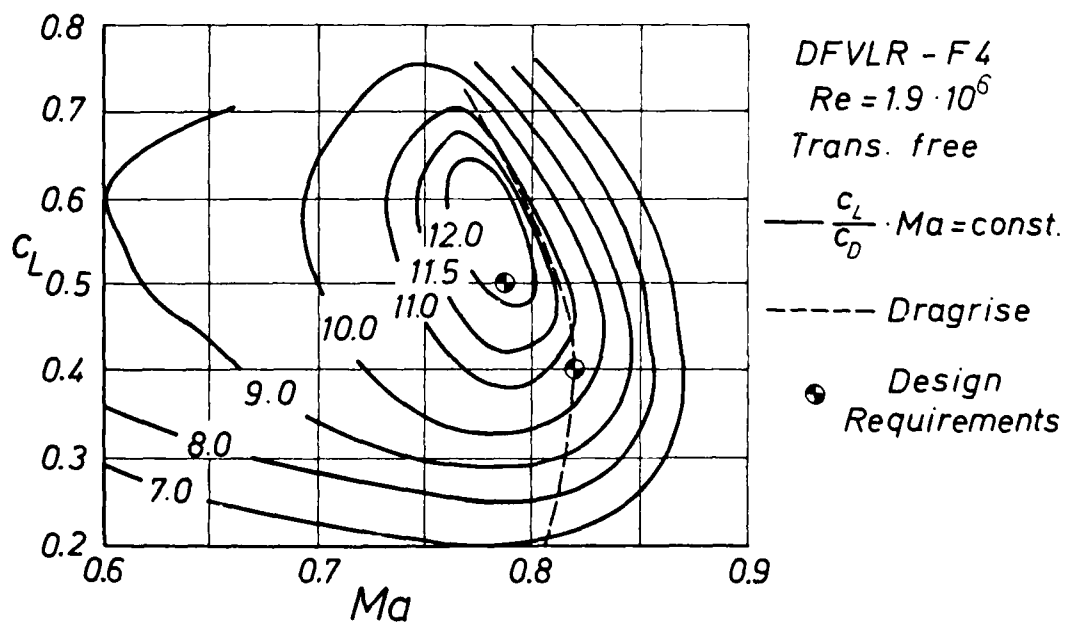


Fig. 15: Measured Aerodynamic Efficiency $(c_L/c_D) \cdot Ma = \text{const.}$

THE TALE OF TWO WINGS

by

E. ATRAGHJI, NRC/NAE*
 L. THORNQVIST, SAAB-SCANIA
 L. TORNGREN, FFA*

*The Aeronautical Research Institute of Sweden
 *National Research Council, National Aeronautical Establishment
 OTTAWA, ONTARIO, CANADA, K1A 0R6
 Tel. (613) 998-3263

SUMMARY

The present paper focuses on an experimental investigation to determine the relative merit of two design philosophies for a wing destined for a trainer-attack aircraft operating at high subsonic speeds.

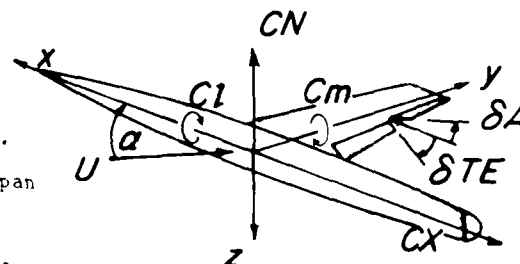
One wing, designed by SAAB-SCANIA, has a variable leading edge deflection capability intended to cope favourably with landing and manoeuvre cases without causing a drag penalty in the cruise regime.

The other wing, designed by FFA, has a leading edge profile which is permanently set as a compromise for all flight conditions. This leads to a possible higher drag during the cruise and reduced manoeuvre capability but with the definite advantage of mechanical simplicity and weight saving.

The experimental investigation, conducted at the NAE in the range $0.5 < M < 0.99$ and, thus, precludes the take-off and landing phases, shows that a carefully tailored wing using FFA's design concept need not suffer from either increased drag during the cruise or reduced manoeuvre capability although it may experience a slightly reduced drag divergence Mach number.

LIST OF SYMBOLS

α	angle of attack - deg.
α_g	local geometric incidence - deg.
$b=1.75265m$	reference span - $b/2 = s$ semi span
c	local chord
$c=0.24117m$	reference aerodynamic mean chord
C_N, C_X	aerodynamic normal and axial force coefficients $N/q.S, X/q.S$, respectively
C_m, C_l	aerodynamic pitching and rolling moment coefficients $m/q.S.c, l/q.S.b$, respectively
C_L, C_D	aerodynamic lift and drag coefficients $L/q.S, D/q.S$, respectively
CL_α, Cm_α	lift and pitching moment curve slopes, respectively - per radian at $\alpha=0^\circ$ (obtained from third order curves fitted to the data in the range $-5^\circ < \alpha < 5^\circ$)
C_{pb}	base pressure coefficient = $(P_{base} - P)/q$
G	accelerometer output - gs
M	free stream Mach number
M_{dd}	drag divergence Mach number ($\partial C_D / \partial M = 0.1$)
N_1	output of balance forward normal force gauge
P, q	free stream static and dynamic pressures, respectively
Re	Reynolds number based upon c and free stream properties
$S=0.11964m^2$	reference area for half model
$S_b=0.00570m^2$	base area for half model
t/c	thickness to chord ratio
U	free stream velocity



x, y, z right hand orthogonal system of body axes
See sketch, above, for positive directions of forces, moments and angles.

INTRODUCTION

In recent years development work has been going on in Sweden on a light trainer-attack aircraft to operate at high subsonic speeds. This project was recently cancelled. Some of our findings are worth reporting and, herein, we recall the tale of two wings proposed for this aircraft.

In broad terms, the desirable features affecting the wing design of this aircraft were:-

- i) good handling qualities > attached flow/controlled separation throughout flight envelope including transonic dives
- ii) good cruise performance > low drag at cruise lift and high drag divergence Mach number
- iii) good manoeuvre capability > high useful lift before 'severe' buffet
- iv) simplicity of design > usability in service
- v) light structural weight > higher payload/greater economy

One approach to attain the first three objectives has been to use variable geometry. The type considered in this instance is a full length leading edge section which can be deflected to maintain attached flow over the wing surface at high angles of attack, for landing and manoeuvre, and retracted during the cruise to reduce the drag and increase the drag divergence Mach number.

While variable geometry is undoubtedly beneficial, in creating the ideal profile under a variety of flow conditions, it conflicts with the other two equally desirable features- a simple and light weight wing. To ease the task of choosing between various alternatives in arriving at a final compromise solution, the ideal wing concept is first contemplated without consideration (within reason) of simplicity of design or eventual weight penalty. Against this wing as a varistick the aerodynamic performance of simpler, fixed geometry, wings may be judged. The tale we tell is one about a 'perfect' wing and another which approaches it in aerodynamic performance but has the advantage of simplicity.

Details of the wing designs are given in References 1 and 2. Previous experimental investigations conducted at lower Reynolds number are reported in References 3 and 4. Here, we discuss only the results of the final round from an experimental investigation, conducted at high speed, undertaken co-operatively by SAAF-SCANIA, FFA and NAB. See also References 5 and 6.

The investigation was carried out in the 1.5 m x 1.5 m transonic test section of the NAB's transonic blowdown wind tunnel (See Reference 7). A half model configuration was employed to attain a Reynolds number (based on aerodynamic mean chord) of 15 million with occasional runs performed at Reynolds number 18 million.

The 1/2-sec. model is shown in Figure 1. It consists of a fuselage with jet intake, a swept wing equipped with two pylons, wing tip launcher and missile, and a horizontal stabilizer. The wings have a taper ratio $TR=0.4$, aspect ratio $AR=4.0$, a 1/4-c line sweep angle $\Lambda=27^\circ$, a trailing edge flap and an aileron. In each case the maximum thickness to chord ratio at the wing-fuselage junction was kept approximately the same, $t/c=10\%$.

The variable geometry wing has a variable leading edge droop capability. The leading 24mm of the airfoil section along the full length of the span may be deflected, enabling a choice of 0° , 10° or 20° droop angle to be selected. In addition, it has a boundary layer fence located on the upper surface at about 90% of the wing semispan. Such devices are employed to improve the stall characteristics of the wing. They do not always succeed but they always cause additional drag.

The condensed information regarding the geometry of the two wings is shown in Figure 2. Comparisons between the profiles of the two wings at three critical stations are shown in Figure 3. In the following, we adopt the designation V-xx-vy when referring to the wing with variable leading edge deflection and F6-yy when referring to the wing with fixed leading edge geometry where xx and yy in the above designations refer to the leading edge deflection angle and trailing edge flap angle in degrees, respectively. The simplified form V and F6 will be used when the flaps are undeflected.

For this model the blockage area ratio was 0.84% and the ratio of the wing area to the tunnel cross-sectional area was 0.05375.

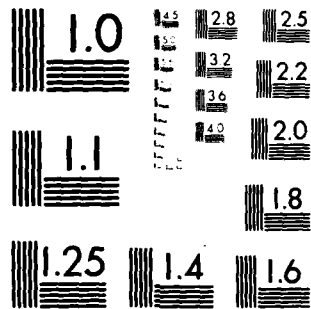
AD-A094 086 ADVISORY GROUP FOR AEROSPACE RESEARCH AND DEVELOPMENT--ETC F/G 20/4
SUBSONIC/TRANSONIC CONFIGURATION AERODYNAMICS.(U)
SEP 80

UNCLASSIFIED AGARD-CP-285

NL

3 of 7
AGARD-CP-285





MICROCOPY RESOLUTION TEST CHART
NATIONAL BUREAU OF STANDARDS 1963-A

The scope of the investigation is summarized in the Table.

Overall forces and moments were measured with an externally located 5-component balance. The base pressure was also measured but was not used to correct for base drag. It should be noted, however, that, due to the through flow, permitted by the open intake, the base pressure was invariably close to free stream static pressure, resulting in a maximum pressure coefficient $-0.05 < C_{pb} < 0.07$. And, since the ratio of the base area to the wing reference area is $S_b/S = 0.04768$, the contribution of the base pressure to the total drag is quite small. Measurement of buffet onset and magnitude was attempted using an accelerometer mounted near the wing tip in the case of Wing V. In the case of Wing F6 there was no provision for an accelerometer. Instead, the root mean square (rms) of the ac-components of the output from the balance gauges were measured following previous success at such measurement as indicated in Reference 8.

2.0 DISCUSSION

We shall first discuss the cruise case. Cruise is herein defined as flight at $M > 0.5$ in the range $0 < C_N$ or $CL < 0.2$. The drag coefficient C_D at three constant values of CL is plotted against Mach number and compared for the two wings in Figure 4. The drag divergence Mach number, M_{dd} , is higher for Wing V by a $\Delta M = 0.013$. Below M_{dd} , the drag coefficient of Wing F6 is actually lower for CL values > 0.1 . For Mach numbers above M_{dd} and values of $CL < 0.1$ Wing V retains its superior performance. We would like to note in passing that the observed drag creep is partly due to the sensitivity of the balance to ambient static pressure and temperature drift. Although no correction for these effects has been made to the data, the comparison of the results of the two wings is still valid since the two wings were tested under identical conditions.

The static longitudinal stability characteristics of the two wings are compared in Figure 5 where C_m is plotted against C_N . The stability characteristics are seen to be similar for the two wings in the Mach number range $0.5 < M < 0.921$. For the higher Mach numbers, $0.921 < M < 0.963$, Wing F6 remains stable while Wing V shows signs of becoming unstable near C_N values close to zero.

Experience with swept wings indicates that if a reduction of the longitudinal static stability should occur with increasing Mach number it usually heralds problems with aileron effectiveness in that range of Mach number. For this reason, we investigated the aileron effectiveness in the Mach number range of decreased longitudinal static stability- $0.92 < M < 0.98$. We attempted this by measuring the change in the rolling moment coefficient, ΔC_l , obtained from two runs conducted at identical conditions, where the aileron was set to 5° in one run and to -5° in the other. Although, strictly speaking, this procedure is not accurate for determining aileron effectiveness, since the final centre of pressure location for a full model may be different compared to that of two 'halves' of the model, the procedure is considered useful in providing qualitatively valuable information. A comparison of ΔC_l for the two wings generated by a 5° aileron deflection is shown in Figure 6. We note that Wing F6 has the higher aileron effectiveness but shows signs of a decreasing trend with increasing Mach number even though the static stability characteristics would suggest otherwise. Wing V shows signs of a reversal of its aileron effectiveness in the Mach number range $0.945 < M < 0.965$.

We conjectured that loss of aileron effectiveness is the result of shock stall causing flow separation over the aileron. This led us to explore the effect of using a symmetric deflection of the ailerons to improve the longitudinal static stability of Wing V. The result is shown in Figure 7. Clearly, a worthwhile improvement of the static margin has been realized. It is interesting to note that either a positive or a negative deflection give similar improved static stability.

At this juncture we would like to direct our attention to the effects of Reynolds number. We have chosen critical Mach number cases to illustrate these effects.

The effects of increasing the Reynolds number on the static longitudinal stability of Wing V are shown in Figure 8. A small improvement is noted. The effects of increasing the Reynolds number on aileron effectiveness are shown in Figure 9. It is seen that this effect is not consistent. An increase in Reynolds number may yield a substantial improvement in aileron effectiveness at one Mach number but it could also result in a decreased effectiveness at another Mach number. We re-emphasize, therefore, the need for testing at full scale Reynolds number conditions.

Manoeuvre

We shall limit our discussion to two typical manoeuvre cases at Mach 0.5 and 0.7. In this context we are primarily interested in achieving high useful CL_{max} (i.e. pre-buffet onset) without incurring the penalty of increased drag due to flow separation. A comparison of CL versus α for the two wings, with and without flap deflections, is presented in Figure 10. Clearly, without flap deflection, Wing F6 is superior. In practice, when manoeuvres are performed at high angles of attack, the leading edge of Wing V is deployed automatically to either 20° or 10° depending on the Mach number. Both wings employ a 10° trailing edge flap deflection for lift augmentation. Under these circumstances, both wings provide sufficient range of linear lift increase with α (up to $CL = 1.0$ at $M = 0.5$ and $CL = 0.7$ at $M = 0.7$) as shown in Figure 10. However, to illustrate the true relative merit of the two wings we consider the comparison shown in Figure 11 where

the lift/drag ratio is plotted against CL . Clearly, Wing P6 is superior at both Mach numbers with and without flap deflections except in a small range of $CL > 1.1$ at Mach 0.5. We would like to note, however, that Wing V employs, in this instance, a 20° leading edge flap deflection which is suitable for high CL values. At lower CL a smaller leading edge deflection would likely be more suitable.

Although a high CL_{max} is a desirable goal to achieve in order to extend the manoeuvre capability of the aircraft, one must ensure that such high CL_{max} values are attained outside the buffet boundary. A method for predicting buffet onset has been to locate the point of inflection in the CX versus α curve. In Figure 12 we present plots of CX versus α for the two conditions discussed above at $M=0.5$ and $M=0.7$. The task of determining buffet onset by this method is difficult, as the location of the point of inflection is somewhat elusive. We, therefore, employed an accelerometer mounted near the wing tip of wing V for a better assessment of buffet onset and severity. We also measured the rms of the ac-component of the output from the balance gauges in the hope of using this measurement as a basis for comparing buffet onset boundaries for the two wings. This latter technique was employed since Wing P6 was not equipped with an accelerometer. The results are presented in Figure 13. Using the first technique, i.e. locating the point of inflection in the CX versus α curves, we can say that, in a qualitative sense, buffet onset occurs at a higher angle of attack on Wing V at Mach 0.5 and at a lower angle at Mach 0.7 as compared with Wing P6. This finding is substantiated by the comparisons of $rms(N1)$ shown in Figure 13. By comparing $rms(N1)$ - measured in lbs - for Wing V with the accelerometer output $rms(G)$ - measured in gs -, we note that it is indeed justifiable to use the $rms(N1)$ signal to predict buffet onset, even though, $rms(G)$ is a slightly more sensitive indicator of buffet onset than $rms(N1)$. This being so, then by comparing $rms(N1)$ for the two wings we can further deduce that buffeting occurs gradually on Wing V while it has a tendency to occur sharply on Wing P6 at least at Mach 0.5. We also note that at $M=0.5$ the amplitude of the $rms(N1)$ signal is higher for Wing P6 suggesting that buffet severity could be higher on the latter wing. At Mach 0.7 we note a reversal of the above phenomena on the two wings.

Effect of Stores

In the preceding discussion the wings were equipped with stores (two pylons, tip missile and launcher). To study the effect of stores we chose to investigate configuration P6 without stores and to compare the two results. In Figure 14 we show the effect of stores on the lift and pitching moment curve slopes at $\alpha=0^\circ$. It is seen that the addition of the stores results in a favourable effect (CL_α is increased and Cm_α is decreased) at Mach numbers below M_{dd} . The Mach numbers at which the first maximum value of the lift and pitching moment curve slopes occur remain unchanged by the addition of the stores. It is also noted that the stores cause a drastic change in the Cm_α versus M curve in a narrow Mach number band.

The drag increases, as would be expected, see Figure 15, except at $M=0.5$ and values of $CL > 0.45$ where the addition of the stores generates beneficial interference and results in a higher lift/drag ratio. A plausible explanation is that the presence of the missile and launcher at the tip influences the trailing vorticity, in much the same manner as a wing tip fence would, resulting in a lower induced drag.

Wind Tunnel Interference

Preliminary analysis of results obtained from an investigation conducted on a 1/13-scale half model tested in the same tunnel indicates that the 1/9.5-scale model discussed above may be too large for this tunnel at the higher transonic Mach numbers investigated. However, we have no reason to believe that the comparisons and ideas discussed above would be substantially altered by the presence of wall interference effects.

3.0 CONCLUSIONS

Two design philosophies for a wing destined for an attack aircraft were investigated experimentally. In the first case, the wing is equipped with a leading edge that can be deflected mechanically to cope favourably with landing and manoeuvre cases without suffering a drag penalty in the cruise regime. In the second case, the wing leading edge profile is permanently set as a compromise for all flight conditions. The results indicate that, using the second concept, a carefully tailored wing can be generated which need not suffer from either a drag penalty or reduced manoeuvre capability. And, although the latter wing has a lower CL_{max} and a lower buffet onset boundary at $M=0.5$, and, suffers from a slightly lower drag divergence Mach number, such a wing may have the overall advantage of simplicity and lighter weight.

The effect of Reynolds number was studied on Wing V in the range $12 < Re \times 10^{-6} < 18$ in a few critical Mach number instances. It was found that increasing the Reynolds number resulted in improved longitudinal static stability but did not consistently improve aileron effectiveness.

The presence of stores, studied on Wing P6 only, results in a higher lift and pitching moment curve slopes, and, as expected, a higher drag. However, at the lowest Mach number investigated, $M=0.5$, there is evidence indicating that the presence of stores

results in a reduction of the induced drag.

4.0 REFERENCES

1- NOT AVAILABLE

2- Drougge, G., "An Investigation of a Swept Wing-Body Configuration with Drooped Leading Edge at Low and Transonic Speeds", Paper #22 presented at the AGARD FDP Symposium on Subsonic/Transonic Configuration Aerodynamics, held in Munich, Germany, May, 1980.

3- Nordvik, R., "An Investigation of the High Lift Capabilities of the 25° Swept Transonic Wing PT10 with and without Drooped Leading Edges", FFA TN AU1520, 1979.

4- Torngren, L., "An Experimental Investigation at Transonic Speeds of some Swept Wings (PT100 - PT103) at Reynolds number 1.0×10^6 - 1.4×10^6 ", FFA TN AU1476, to be published.

5- Atraghji, E., "Experimental Investigation Conducted on the SAAB-SCANIA T-m12 and S15-m6 Models", NAE LTR Report 5X5/0125, to be published.

6- Atraghji, E., "Experimental Investigation Conducted on the FFA PT10-m5 Model", NAE LTR Report 5X5/0126, to be published.

7- Brown, D. (Ed.), "Information for users of the National Research Council's 5-Ft X 5-Ft Blowdown Wind Tunnel at the National Aeronautical Establishment", NRC-NAE LTR-NA-6, September, 1977.

8- Yoshihara, H. and Fatta, J., Anderson, A. and Pick, G., "The Aerodynamic Design and Test of an Attack Type Configuration at Supercritical Flow Conditions", Department of the Navy, Air Systems Command Report published under contract No N00019-71-C-0387, September, 1972.

SUMMARY OF WIND TUNNEL INVESTIGATION

Wing	Nominal M range	Re $\times 10^{-6}$	Stores	δLE	δTE	δA	Reference
V	0.500-0.990	12	x	0	0	0	5
	0.965-0.975	18	x	0	0	0	
	0.935-0.990	12	x	0	0	5	
	0.95	5	x	0	0	5	
	0.965-0.975	18	x	0	0	5	
	0.5	12	x	20	10	0	
	0.5	12	x	20	15	0	
	0.7	12	x	10	10	0	
	0.7	12	x	7.5	10	0	
P6	0.500-0.975	12	-	-	0	0	6
	0.875-0.925	18	-	-	0	0	
	0.500-0.700	12	-	-	0	0	
	0.500-0.975	12	x	-	0	0	
	0.925-0.975	12	x	-	0	5	
	0.500-0.700	12	x	-	10	0	

δLE leading edge deflection angle - deg.

δTE trailing edge flap angle - deg.

δA aileron angle - deg.



Fig.1 Wind tunnel model

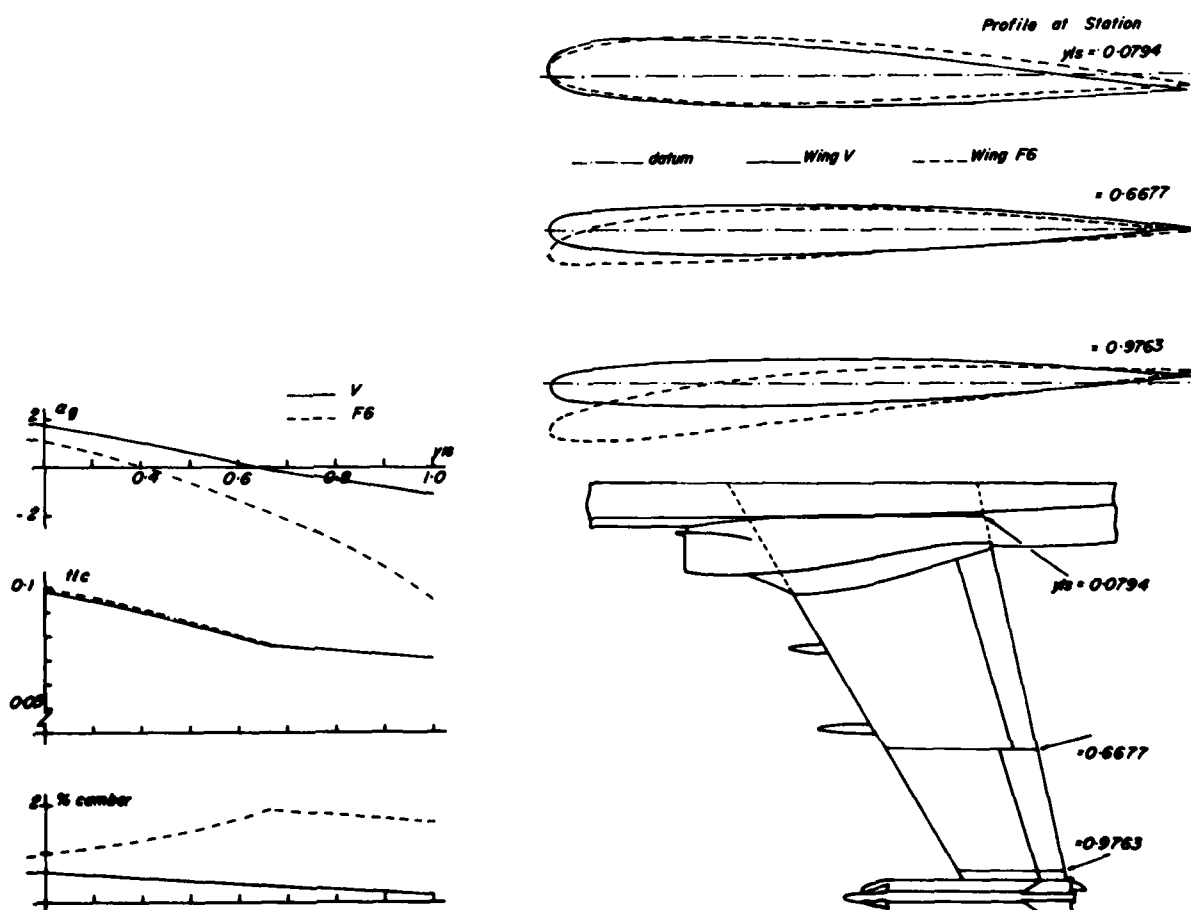


Fig.2 Geometries of wings V and F6

Fig.3 Profile shapes of wings V and F6

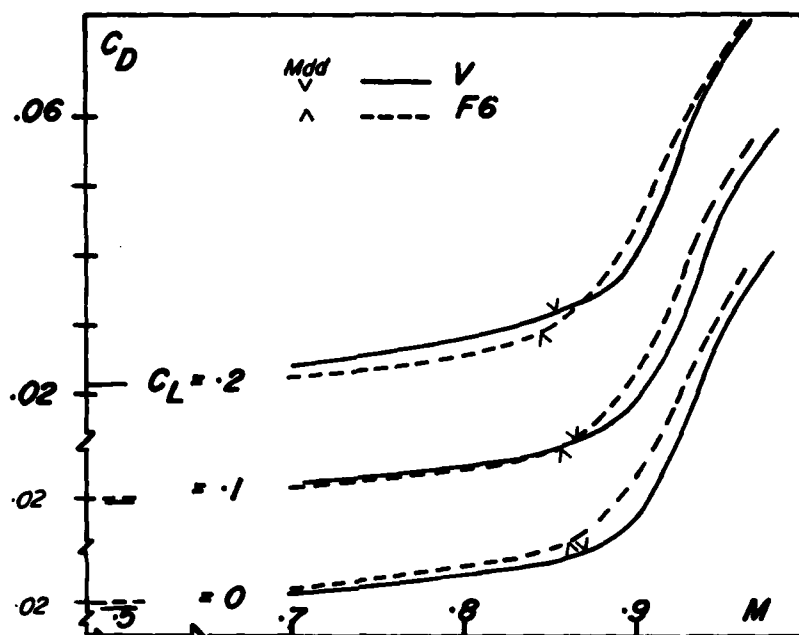


Fig.4 Comparisons of C_D versus Mach number at various C_L

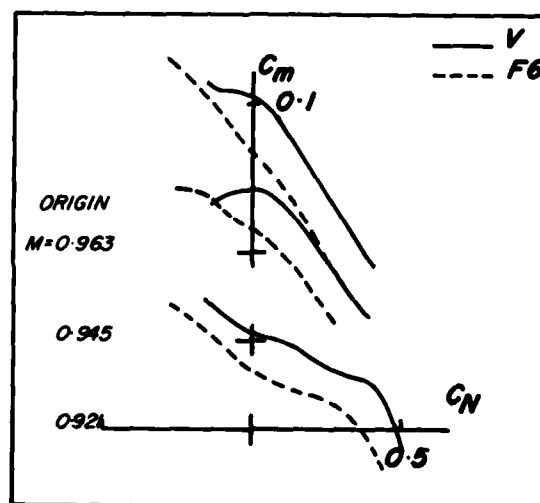
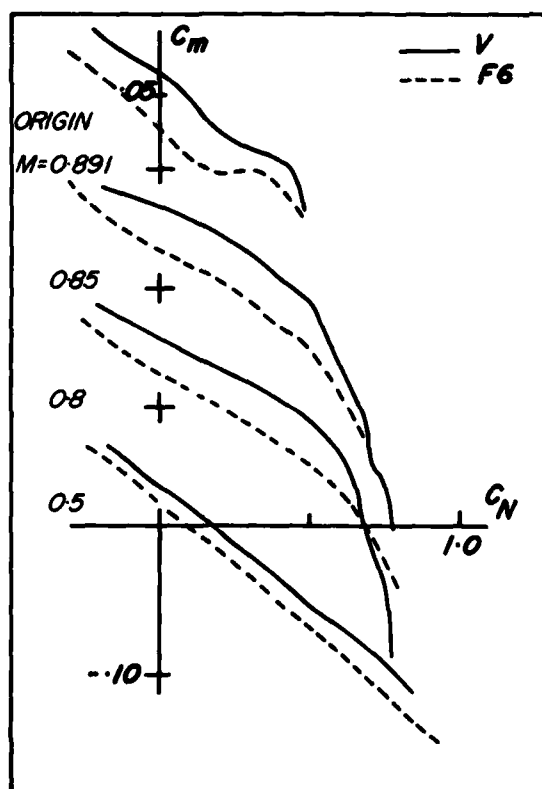


Fig.5 Comparisons of C_m versus C_N at various Mach numbers

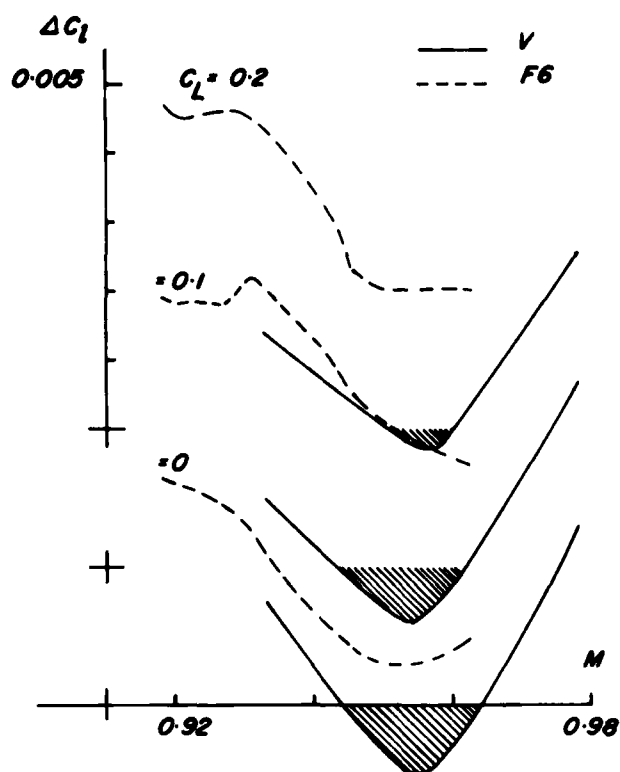


Fig.6 Comparisons of ΔC_l versus Mach number

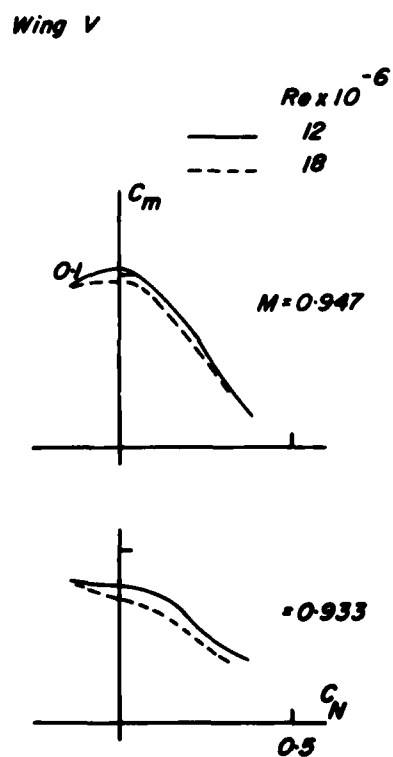


Fig.8 Effect of Reynolds number on C_m versus C_N

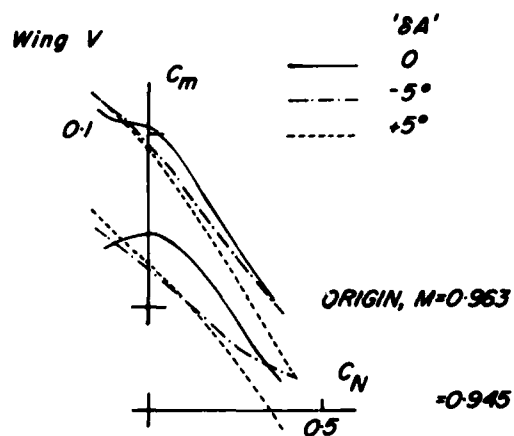


Fig.7 Effects of 0° , -5° and $+5^\circ$ ' δA ' deflection on C_m versus C_N

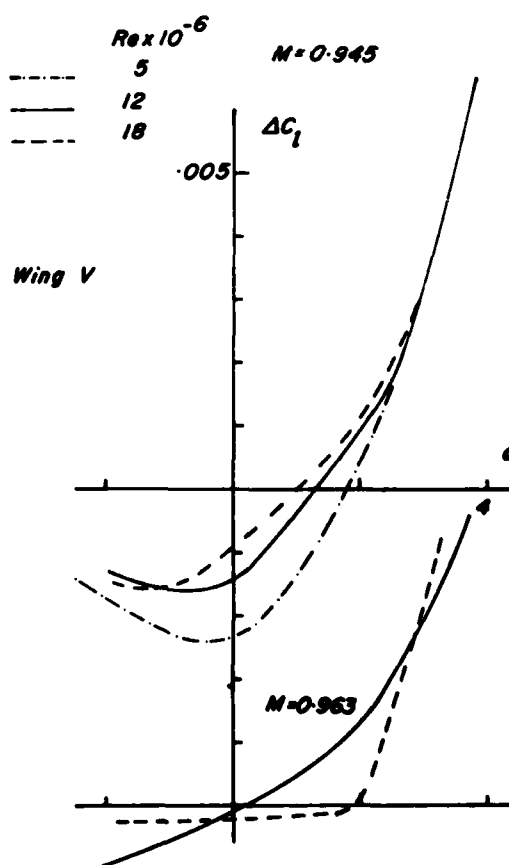


Fig.9 Effect of Reynolds number on aileron effectiveness

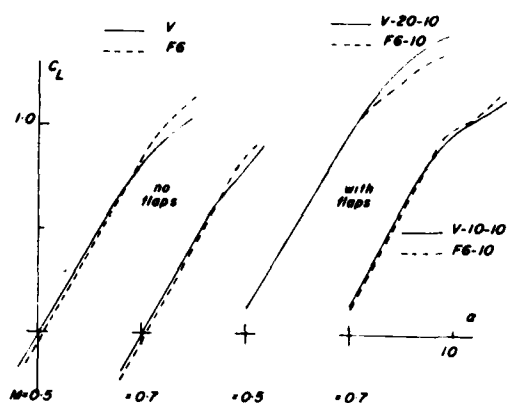
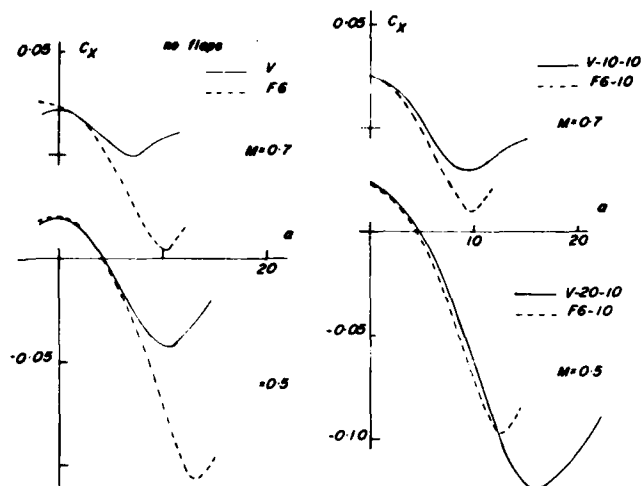
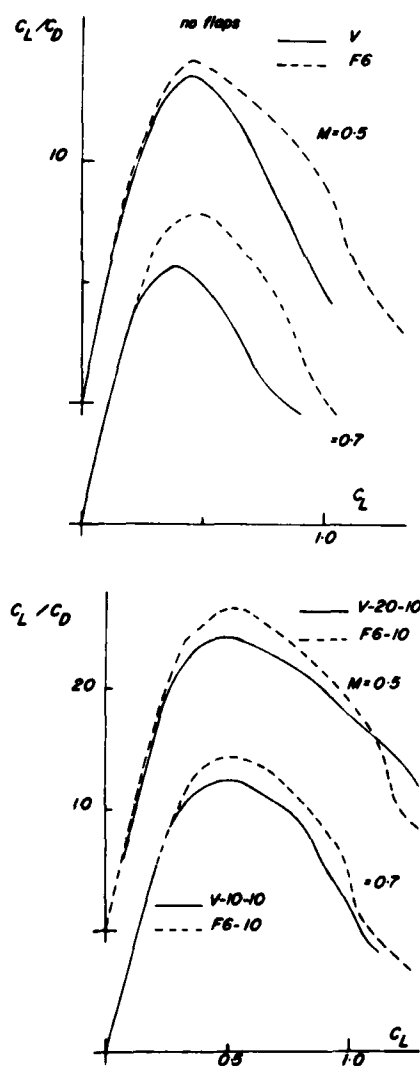
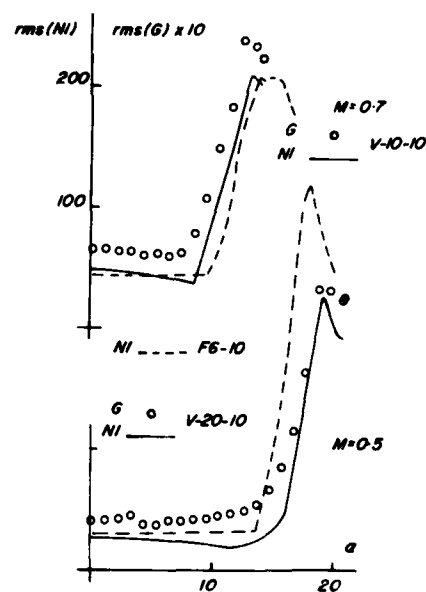
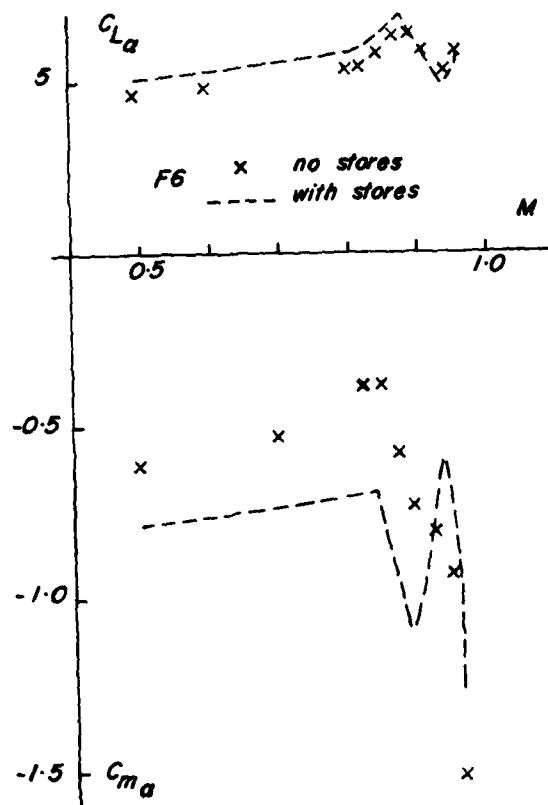
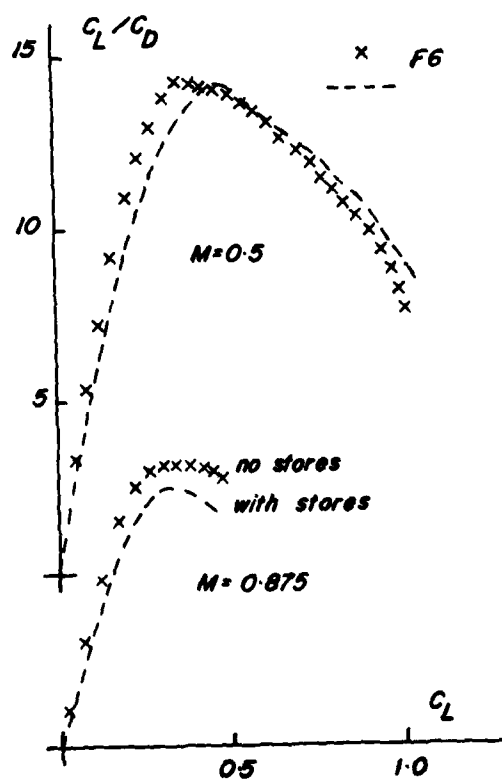
Fig. 10 Comparisons of C_L versus α Fig. 12 Comparison of C_X versus α Fig. 11 Comparisons of C_L/C_D versus C_L 

Fig. 13 Comparison of buffet onset and buffet characteristics

Fig. 14 Effect of stores on $C_{L\alpha}$ and $C_{m\alpha}$ Fig. 15 Effect of stores on C_L/C_D versus C_L

SOME PARTICULAR CONFIGURATION EFFECTS
ON A THIN SUPERCRITICAL VARIABLE CAMBER WING
by

D. R. Holt
British Aerospace-Aircraft Group
Principal Aerodynamicist
Kingston-Brough Division
Brough
North Humberside
HU15 1EQ
U.K.

B. Probert
British Aerospace-Aircraft Group
Senior Aerodynamicist
Warton Division
Warton
Preston
Lancs
PR4 1AX

SUMMARY

The first part of the paper concentrates on three aspects of the design of the wing for a supersonic single-engined combat aircraft. To provide the necessary transonic manoeuvre capability, the wing has considerable leading-edge droop and rear loading: at low "g", variable camber devices are used to remove these effects to enhance the performance. These devices are also used to optimise the performance throughout the flight envelope.

The thin wing is subjected to considerable aeroelastic distortion. The effects of this distortion on wing twist are shown to be large and beneficial and are quantified theoretically via wing pressure distributions and experimentally via drag and drag-rise Mach number comparisons.

In the absence of methods for designing the wing/strike combination in a vortex dominated flow, two "non-interfering" strikes were designed to follow the wing streamlines at two different incidences. Results show that these strikes produced negligible drag increments at low and moderate incidences, though at elevated incidences they were less powerful than more conventional designs.

The final part of the paper deals with the productionisation of the wing. Using simple expressions for aeroelastic effects two jig shapes are defined using straight line generators. The first is based on three control stations and the second on only two. Theoretical and experimental results are used to show that such practical constraints on wing design do not impair the performance drastically.

1. INTRODUCTION

Attempts, using sub-critical design methods, to produce a wing with good transonic characteristics have always hit upon the great difficulty of accommodating both efficient high lift performance (for sustained manoeuvre) and a high drag-rise Mach Number at low lift (for sea level dash). The former will normally require considerable amounts of camber and twist (wash-out) which, at low lift, lead to excessive suction near the lower surface leading-edge over the outer wing. This then leads to the premature appearance of shock waves and hence a low drag-rise Mach Number. When, as in the present exercise, the need for a significant supersonic capability limits the allowable wing thickness, to say, 5% chord, this problem is greatly exacerbated.

With the advent of transonic calculation methods which can handle shock waves, it is possible to design wings at very much higher values of lift coefficient (C_L) than the sub-critical method allowed. Once again, with fixed geometry, this only adds to the difficulty of providing an adequate Mach Number capability for the sea level dash. Of course, this can be overcome by relaxing the surface curvature in the affected region thus leading directly to a wing whose thickness: chord ratio increases from root to tip (though the thickness itself, naturally, decreases). It had been supposed¹ that this situation could be alleviated by the use of a leading-edge flap (deflected down for high-lift and up for low-lift). The same notion could be applied to the trailing-edge where the rear loading, necessary for the high lift case, could be removed by upward deflection of a control. For this latter case, in particular, a flap is a more efficient means of modifying the lift - whilst remaining free of wave drag - than is incidence. As is shown in the next Section, once variable camber devices are included in the design from the outset, they become much more powerful than is the case if they are added to an existing fixed geometry design.

The use of a thin wing covering both high lift ($C_L > 0.7$) and low lift ($C_L \approx 0.05$) conditions directs attention towards "static" (as opposed to dynamic) aeroelastic distortion. The high lift condition may well be associated with a normal acceleration in excess of 8g, whereas the latter condition is appropriate to straight and level, or 1g, flight. Between these two conditions, the aeroelastic distortion is considerable - and generally favourable. For the present research exercise it was decided to include the effects on twist, due to both bending and torsion, but to ignore the effects on both camber and anhedral. The effect on camber is in fact quite small, but the effects on anhedral are important from the stability and control viewpoint. These aeroelastic effects are the subject of Section 3 below.

At the time that this present exercise started there appeared to be no readily available method for designing strikes. One could neither design the wing, at moderate incidence, in the presence of the strike, nor design the strike, at high incidence, in the presence of the wing. At the same time, some experiments had shown that whilst strikes can extend the wing performance to very high incidences, they can - in some instances - generate relatively large drag increments at moderate incidences. It was decided to test the notion of designing the strike so as not to interfere with the wing flow at moderate incidence. The purpose of this exercise was two-fold, firstly to discover whether this approach was possible within the restrictions of wing and fuselage geometries and secondly to discover how such a strike would perform at high incidence. Since the difficulties of designing such a strike are particular to the incidence used, two separate strikes (for two incidences) were chosen in the hope that the results would be more generally applicable.

The design of these two strakes is discussed in section 4 below; section 5 presents an assortment of experimental results on the above topic.

As already implied the wing definition obtained is representative of an in flight shape, with approximate aeroelastic effects included through the medium of incremental wing twist. The shape derived consisted of a large number (7) of control stations along the span and implies that the surface geometry is of a fairly complex shape. If applied to an aircraft project this might lead to manufacturing difficulties and weight penalties, at least for conventional alloy structures. Difficulties would be compounded if spars were twisted, with non straight hinge lines for high lift device actuation, power hinges etc. The final part of the paper deals with such practicalities which has been termed - productionisation.

2. THE VARIABLE CAMBER DEVICES

The calculation methods available for the design of the wing included Albane's² three-dimensional transonic small perturbation method together with an inverse (or design) version thereof. For subsonic conditions, a panel method was used together with some calculations using a three-dimensional turbulent boundary layer method. This latter method is an integral one which treats both the streamwise and crossflow velocity distributions as, essentially, two-parameter profiles by using the law of the wall and wake.

Clearly the most difficult area of the design is the transonic one. At the time that the present work was envisaged, there was very little, if any, verification of the validity of the T.S.P. method for thin wings.

Thus it was decided to perform a limited design and test exercise in two dimensions as a prelude to, and proof-of-concept of, the three-dimensional work. For this two-dimensional work the camber changing devices were much simpler than those adopted for the three dimensional wing, the mode of operation was, however, identical and is described below.

2.1 Two dimensional design

Only two design points were considered for this exercise, being the two-dimensional equivalents of a high Mach Number sustained manoeuvre and the sea level dash though a third flap configuration, essentially mid-way between these two extremes, was tested. The camber changing devices were plain flaps, hinged on the chord line of the aerofoil at $x/c = 0.1$ and 0.75 . Figure 1 shows the combination of C_N and Mach Number for which conditions free of drag-rise were sought and the associated flap angles (a negative deflection is leading-edge or trailing-edge "up"). Also shown are the corresponding pressure distributions obtained during the design process using the viscous version of the RAE T.S.P. method³. Use of the T.S.P. rather than a more exact method, enabled some confidence to be generated for the ensuing three-dimensional phase where only the T.S.P. method was then available.

The aerofoil thickness chord ratio was 5.8% and the top-most pressure distribution shows a considerable degree of rear-loading and a far-aft rooftop. This latter was attributable, at least partly, to the decision to employ a thick trailing-edge and the end of the rooftop is, very conveniently, close to the trailing-edge flap hinge-line.

Reducing the incidence of this section would have very little effect on the amount of rear loading; thus low values of C_L could only be obtained by partly balancing the positive lift at the rear by nearly equal negative lift over the front which would necessitate a very large suction peak towards the leading-edge on the lower surface. Thus the bottom pressure distribution shows the situation (at the slightly higher Mach Number of 0.81) when both flaps are deflected upwards by an equal amount. At this Mach Number, sonic conditions are equivalent to $C_p = 0.41$, so that both compression corners on the upper surface are in subsonic flow though small patches of supercritical flow are predicted on the lower surface.

For the intermediate flap setting ($0^\circ/-3.5^\circ$) the good upper surface flow of the datum aerofoil is retained with, of course, much reduced rear loading - sonic conditions here are equivalent to $C_p = -0.46$ so most of the flow is subcritical.

Though experimental results will, in the main, be confined to Section 5 of this paper, it is convenient to complete the discussion of the two-dimensional exercise with some appropriate results (Figure 2). Clearly, as far as drag-rise Mach Number is concerned, the datum section is deficient by 0.01 in Mach Number. However, the curves for the remaining two flap angles indicate that a smooth envelope can be drawn (with varying flap angles) which would encompass this design point. Elsewhere the drag-rise boundaries are considerably better than the targets. The boundaries of pressure divergence and lift break follow the same pattern for all three flap settings, though for the datum aerofoil ($0^\circ/0^\circ$) the margin between the two is always small and disappears for Mach Numbers below 0.7. It is interesting to note that if one were to increase C_L progressively at, say, $M = 0.78$, seeking first to minimise drag and then to provide the maximum lift capability then the sequence, or schedule, would be $-3.5^\circ/-3.5^\circ + 0^\circ/3.5^\circ + 0^\circ/0^\circ + 0^\circ/-3.5^\circ + -3.5^\circ/-3.5^\circ$. At the lower Mach Numbers, this reversal of the schedule does not occur and positive (downward) settings would improve the high lift performance.

2.2 Three-dimensional design

Having established the value of camber changing devices in the above exercise, the three-dimensional exercise could start. From the outset it had been decided that this would employ some form of flexible skin devices - of modest chordwise extent - to mollify the curvature changes in the flap knuckle regions. A very brief review of the properties of these flexible skins is given below together with the influence of the leading-edge flap on the wing section geometry. This is followed by a description of the resulting aerodynamic design.

2.2.1 Geometrical Considerations

The geometrical definition of the flexible skin variable camber devices was based upon a conservative

interpretation of engineering schemes which were available at the start of the work. When deflected, the flexible skin will adopt a shape dependent on the elastic properties of the material, the external load distribution (a point load would give a parabola) and the type of support. Simple exercises indicated that, for aerodynamic purposes, a bi-quadratic curve (matching x , z and $\frac{dz}{dx}$ at either end of the flexible skin) was neither too optimistic or too pessimistic. On this basis various lengths of flexible skin are compared in Figure 3 in terms of distributions of slope and radius of curvature for a leading-edge device deflected through 5 degrees. For a fixed-hinge flap, i.e. no flexible skin, the radius of curvature would be 0.042C; the longest flexible skin shown (0.073C) increases this value by a factor of about 12.

Variable camber devices also give relief from the limit to the allowable thickness: chord ratio. Figure 4 shows a notional outer-wing section, where the upper surface has been designed for the transonic manoeuvre condition and the lower surface for the low level dash. Assuming mutual independence of the two surfaces (which appears to hold to a remarkable degree even in transonic flow) these surfaces can be joined together (as shown) along leading and trailing edges to provide a suitable wing section. In this particular example, the resulting thickness: chord ratio is 0.075 and this could only be reduced, for a fixed camber wing, by compromising either the high lift performance or the sea level dash capability, or both. Using variable camber, the desired lower surface shape can be reproduced, when required, with a much thinner section. In fact, the thickness: chord ratio and the leading-edge flap chord tend to be directly related. It will be noted that for the two flap configurations illustrated, concave "corners" are present for one surface or the other; in transonic flight, these are always associated with locally - subcritical flow conditions.

These considerations led to the manoeuvre devices outlined in planform on Figure 5. It will be noted that, whereas the trailing-edge device is a constant percentage of the wing chord, the leading-edge device increases in relative size from root to tip.

2.2.2 Aerodynamic Design

Figure 6 shows typical flight conditions for a combat aircraft which were identified as being of possible significance from the wing design viewpoint. The manoeuvre points are all at altitude, save for the one centred near $M = 0.65$ which is at low-level. For the present research exercise, this point had little impact on the design. The 1 "g" conditions include (in ascending order of Mach Number) loiter, cruise at sea level and at altitude, penetration, escape and maximum speeds at low level and at altitude. As has been stated, the latter influenced the design in a simple, but overriding, manner via the maximum allowable thickness: chord ratio.

It was already clear that two primary design points were, sustained manoeuvre at $M \approx 0.9$ and sea level dash at $M = 0.9+$. The choice of the third primary design point was based on considerations sketched in Figure 7. Figure 7(a) illustrates the possibility that the drag-rise boundaries for the two wing/flap configurations might be such as to cast doubt on the performance at intermediate flap settings. Thus the third design point could be used to guard against this possibility. Alternatively (Fig. 7(b)) it may be the high-lift performance at lower Mach Numbers which is in doubt. The first possibility was discounted on the basis of the two-dimensional results (Fig. 2) and the three primary design points were taken as:-

1. Sustained manoeuvre, $M = 0.9$ (high "g")
 2. Sea-level dash, $M = 0.9+$ (low "g")
 3. Sustained manoeuvre, $M = 0.8$ (high "g")
- Secondary design points then include
4. Sustained manoeuvre, $M = 1.2$ (moderate to high "g")
 5. Sustained manoeuvre, $M = 0.6$ (high "g")

Figure 8 shows calculated pressure distributions (in potential flow) for condition 1 above together with typical leading- and trailing-edge contours (to distorted x - z scales). Although the lower surface "corners" appear to indicate deflected flaps, this is the datum (i.e. zero deflection) configuration since, on the upper surface, the second derivative of z is continuous throughout. The pressure maxima, resulting from these corners, are clearly evident at approximately $x/c = 0.1$ and 0.75 . For design point 3 above, the leading-edge flap is deflected down through 5 degrees and the trailing-edge similarly through 2 degrees. Once again (Fig. 9) the Mach Numbers normal to the shocks do not imply any likelihood of shock induced separation.

Discussion of the remaining primary design point, the sea level dash, necessitates some consideration of aeroelastic distortion which is the subject of the next Section.

3. AEROELASTIC EFFECTS

From the wing design viewpoint, the primary effects of aeroelastic distortion are the change introduced into the wing twist distribution. Changes in anhedral are of secondary importance and have been discounted for the present exercise. In order to evaluate the twist effect, some structure must be assumed, or designed, at least for the wing box. A conventional multi-spar thick skinned box was assumed whose distortion under load was in no way constrained by the variable-camber devices. Some typical twist distributions are illustrated in Figure 10; the curve labelled HIGH "g" FLIGHT represents the aerodynamic requirement derived to meet design points 1 and 3 as described above and represents some 9.2 degrees washout from centre-line to tip. The curve marked "ORIGINAL LOW "g" FLIGHT" is the twist used in the present exercise to represent low "g" flight conditions. The two dashed curves represent jig and low g flight shapes according to a more recent evaluation, the difference being the result of a more detailed structural analysis and up-dated aerodynamic loading data. Thus it would appear that the results for the present low g wing (to be presented later) will be optimistic particularly as regards drag. However, it is clear that a less conventional approach to the wing structural design could provide adequate torsional stiffness (for flutter, divergence etc.) whilst giving increased bending flexibility and so increase the favourable influence of aeroelastic distortion via the twist distribution.

The aerodynamic benefits resulting from the reduction in twist at low "g" are illustrated in Figure 11. Here the flaps have been deflected upwards through 5 degrees at the leading-edge and 4 degrees at the trailing-edge from the datum position. Pressure distributions are shown for the wing with both the high and low "g" twist distributions. Over the outer wing, the latter twist distribution produces a dramatic reduction in the peak suction on the lower surface leading to the prediction of an improvement in drag-rise Mach Number. For both twist distributions, the effect of the trailing-edge deflection is to reduce the rear-loading over the outer wing and to reverse it over the inboard wing.

The remaining subsonic/transonic design point is the manoeuvre at approximately 0.6 Mach Number. If this were at sea level then the twist should be slightly less than that of the datum high g case, whereas if it represented a manoeuvre at 10,000 ft then the twist should be about 1 degree more. For the present exercise, the datum twist was assumed with flap deflections of 10 and 4 degrees at leading- and trailing-edges respectively. Of course this configuration is of interest for post drag-rise (or even post-separation onset) performance at higher Mach Numbers.

4. NON-INTERFERING STRAKES

The philosophy adopted for the wing/fuselage junction was to maximise the lift-drag efficiency. Thus gross wing streamlines (above and below the wing) were traced downstream starting from a ring ahead of the wing which gave the necessary fuselage volume in the relevant region. Of course, as the lower streamlines pass the wing, they tend to swing outwards continuously and this is not compatible with a finite body. Bearing in mind such "practicalities", the resultant fuselage shape gives low drag and high lift carryover; put in simple terms this can be viewed as making the fuselage behave like a wing rather than converting part of the wing into an extension of the fuselage.

A natural extension of this philosophy was to see if the strakes could be designed in like manner. Though the resultant tests would need to check for any accompanying deterioration in the high incidence performance. Two strakes, of the same planform, were to be designed for the high "g" wing at particular incidence. The first incidence chosen was that of the primary design point 1. The geometrical difficulty of following these streamlines within the constraints of the wing and fuselage lines led to the second incidence being taken as half this value. The two strakes are shown in Figure 12 where at station F-F (the strake/wing junction) both strakes have the same cross-section. As might be expected the main difference between the strakes is in spanwise camber.

5. RESULTS

In describing the performance of the wing, the effects of the variable camber devices and the aeroelastic distortion are inextricably bound together so these will be discussed jointly in the first sub-section below. The second sub-section deals with the non-interfering strakes.

5.1 The Clean Wing

We first compare pressure distributions for the high "g" (datum) wing in Figure 13. The theoretical results (the solid line) represent a viscous wing-alone calculation by the transonic small perturbation method² at almost the same lift coefficient as the experimental wing/body results. At $\alpha = 0.5$ the essential features of the pressure distributions are very similar; the experimental data show a greater leading-edge suction emanating from the intersection between the wing leading-edge and the fuselage. The leading-edge shock is more abrupt and the final shock is some 5% chord further forward than in the wing-alone calculation. Further outboard, at $\alpha = 0.68$, experiment shows that forward and rear shocks have merged whereas theory shows them still to be distinct. The position of this merging is important since this is where separation would be first expected; in fact much of the design effort for the manoeuvre case was expected in forcing this point as far outboard as possible. Further outboard still, in the single shock region, experiment consistently yields a shock which is further aft than theory. That these effects are mainly attributable to the omission of the body from the calculations is demonstrated by the isobars of Figure 14. Here an inviscid wing/body calculation (dashed lines) is compared with experiment (solid lines) at closely similar incidences and lift coefficient. This similarity results from a near-balance between the body nose lift and wing viscous effects which were both omitted in the calculation. The resulting isobars are, however, extremely close particularly as regards the shock intersection point. To the designer this level of agreement is very satisfying and gives every confidence in the use of such calculation methods for wing design purposes.

Turning now to the measured forces and moments, Figure 15 shows the effect of the variable camber devices on the drag-rise boundary of the wing. For all the results in this section, the model was fitted with a representative fin but no tailplane. Although not strictly relevant to the high "g" wing shape, the improvement provided by upward flap deflection at low values of C_L is clear.

The low "g" wing shows further substantial gains at moderate values of C_L but, apparently, little improvement at the very lowest values. To complete the story, of course, one must look at the actual drag values and some indication of these is given by $C_{D_{MIN}}$ - the minimum drag coefficient as incidence varies. The value of C_L at which this minimum occurs, varies with flap angle but was nearly zero for both high and low "g" wings with $-5/-4$ flap angles. Thus the low "g" wing gives substantial drag benefits throughout the Mach Number range. At low C_L the drag-rise boundaries for flap angles of $5/2$ and $10/4$ are always inferior to that of the datum wing, though their high lift and post-drag rise performance is often superior.

Figure 16 illustrates the comparative lift and drag performance at low Mach Number. It is noticeable that the low "g" wing with upward flap deflection gives more lift, at low incidence, than the datum high "g" wing. The reduced twist of the former has outweighed the effect of the changes in camber. The L/D polars indicate that, at this Mach Number, the particular combination of 5 degrees leading-edge flap deflection and 2 degrees at the rear offers no advantage over the other combinations (at no value of C_L is it superior). Also shown is a curve labelled $C_D = C_{D_0} + \frac{C_L^2}{\pi A}$, C_{D_0} here has been taken to be the value given by the low "g" wing. This, and similar curves on Figure 17¹⁸ and 18, is included to give some yardstick against which to judge the high lift performance (bearing in mind that the real values of C_{D_0} for the flapped high "g" wings are much higher than for the low "g" wing).

Figure 17 presents similar information at a Mach Number of 0.8; it is noticeable that the largest flap deflection appears to change the character of the initial lift break. The L/D curves for the high "g" wing now show a clearer family relationship from which it is possible to evaluate an envelope curve and hence an optimum flap schedule. The curves shown, now fall short of the dashed curve and we shall see that this short-fall increases with Mach Number.

At a Mach Number of 0.88 (Figure 18), it is apparent that some boundary layer control devices are necessary to cope with the lift break for the high "g" wing. This Mach Number is beyond the drag-rise for the 10/4 configuration at all incidences, but this configuration is still useful from the L/D viewpoint at the higher values of lift coefficient. It is much more difficult to establish an optimum flap schedule in this situation, since such a schedule must first seek to delay drag-rise but must eventually pass through it.

5.2 The wing with strakes

Figure 19 compares the isobars on the wing with and without the second strake at $\alpha = 3.3$ degrees (i.e. 0.3 degrees above the non-interfering design condition). The modifications produced by the addition of the strake are entirely confined to a small area near the strake/wing intersection. Pressure data was only obtained with this strake design but forces data can be used to indicate that the first strake was more successful than the second.

Figure 20 gives a similar comparison of isobars at the higher incidence of 8.8 degrees at a Mach Number of 0.88. Once again this second design of strake only introduces modest changes suggesting that this strake will not control the outer wing as has been observed with conventional strakes in the past. In other words, this strake will not put right any basic wing faults in this area.

The performance of the two strakes is compared with that of the datum high "g" wing at $M = 0.65$ in Figure 21. The second strake clearly has the greater lift capability but the first strake has zero drag penalty over a wide range of lift coefficient. The increment produced by the second strake is, however, not large, the change in the maximum value of (L/D) being equivalent to a drag increase of 7 drag counts.

At a Mach Number of 0.88 (Fig. 22), a similar situation arises except that here both strakes have a small adverse effect on the lift at low incidences, still accompanied by zero drag penalty for strake 1 and a small drag penalty for strake 2. Thus for this wing, the general conclusion can be drawn that the lower the incidence at which the strake is designed then the greater will be both the lift capability and the drag penalty at moderate incidences. The aircraft designer can then select the right strake for a particular application or, bearing in mind weight and cost, articulate the strake.

6. PRODUCTIONISATION

The final part of the paper deals with the subject of productionisation. The wing shape already derived consisted of seven control stations and if applied to an aircraft project could lead to manufacturing problems or at least some weight penalties. Though such difficulties could be overcome the opportunity was taken to assess the sensitivity of the pressure distributions and wing performance to geometry changes aimed at simplifying the wing lines. From the manufacturing point of view the ideal wing would have a constant wing section along the span, with zero twist, at least for conventional alloy structures. Such a drastic simplification is clearly out of the question here as severe aerodynamic penalties would be incurred. Nevertheless, two phases of work were initiated. The first was aimed at finding an equivalent wing shape which consisted of only three control stations. The second phase went further and attempted to find a compromise with only two control sections. Once again, for consistency, the main theoretical tool used was the Albane² three-dimensional transonic small perturbation method in wing-body inviscid mode.

6.1 Three control station representation

The method adopted is illustrated in Figure 23 and basically consists of making an approximate assumption for aeroelastic effects (based on bending beam theory with empirical corrections near the wing tip), subtracting these to obtain a '0' g or jig shape, productionising this, re-introducing the aeroelastics (as incremental twist and camber) and re-calculating the wing loads and pressures. This is an iterative procedure and eventually it was found that a reasonable representation of the wing geometry could be obtained with only three control stations along the span, with straight line generations between each station. This is illustrated in Figure 24A where pre-and-post productionised wing surface generators are shown. The main difficulty arises over the inner wing region, where in order to reduce shock strengths the section is thinned over the rear of the wing, giving effectively a discontinuity in spanwise slope distribution. The twist distribution was also modified slightly in order to increase the loading over the wing root and was of linear lofted form to ensure straight line wing leading and trailing edges. The resulting '0' g and high 'g' pre-and-post productionised wing twists are shown in Figure 24B and it should be noted that aeroelastic effects are significant (amounting to almost 6° twist at the tip).

The level of agreement between the pre-and-post productionised wing pressures and loadings is shown in Figure 25. The distributions are very similar though shock waves are slightly stronger on the productionised shape. Off design cases at other (M , Cl) conditions were checked, with manoeuvre devices and aeroelastic effects applied as appropriate, and were found to be satisfactory.

6.2 Two control station representation

However, the productionisation process was taken further in an attempt to obtain a simple two control station representation. The sensitivity of the pressure distributions to such a drastic simplification is shown in Figure 26 where an early attempt involved extrapolating the inner wing generators outwards to the tip. This produced excessive camber in the outer wing region and the TSP calculations on pressures reflect this through the large suction and strong shocks over the rear of the wing. Thus care was needed if a suitable approximation was to be found.

Eventually, an averaging technique was employed as shown in Figure 27 and the resulting pressure distributions indicated that shock waves were further back on the chord, but of similar strength. Outer wing suction levels were similar to the previous 3 control station representation. Thus it appeared that for this particular configuration, a simplified geometry could be obtained without any obvious aerodynamic penalties. Thus two wings were made, one representative of the three control station case at a high 'g' condition, the other of the two control station wing, with detachable leading and trailing edges for high lift checks. Unfortunately, use had to be made of an existing model fuselage, which was oversized for the wing area/loads which could be taken on the balance. Thus the body/wing span is greater by 5% than that on the model with the unproductionised wing described earlier.

6.3 Results

Results for the three control station wing are quoted here in fig. 28 as $(L/D).v.C_L$ curves for $M = 0.88$ and $M = 0.55$. In both cases there is a small shortfall in $(L/D)_{max}$ which amount to 3%. For the higher Mach Number, at high C_L , the short fall is more pronounced though at these conditions the wing is operating above its design condition and the varicamber devices would be deployed to greater deflections, hence improving (L/D) as shown earlier. It is felt that the larger body is a contributor to this drag increase particularly at the higher subsonic Mach Numbers.

Overall, even though this investigation is somewhat inconclusive it was quite encouraging that such considerable simplification to the wing geometry can be made without incurring severe aerodynamic penalties with respect to the idealised shape. However, more work is obviously needed before this can be claimed as a general conclusion.

7. FINAL REMARKS

Variable camber devices have been shown to represent a powerful means of matching a variety of disparate transonic points for a thin wing if designed into the wing from the outset. In particular, trailing-edge devices allow the designer to provide good high-lift performance without degrading the sea level dash capability. Leading-edge devices can be used to combine both high and low-lift transonic performance whilst retaining a supersonic capability. The design of a variable camber wing must take account of many structural and engineering constraints and these will vary from situation to situation. Since most wings require variable camber devices for field performance, their use in this wider context should not present any insuperable problems with regard to the overall systems required.

The distortion of thin sweptback wing under load has been shown to have a powerful and beneficial influence on the design, particularly in matching the wing twist for the various "g" conditions. The wing design exercise then becomes a process of matching the properties of the wing structural distortion and of the variable camber devices to the required performance.

In addition it has been shown that it is possible to design strakes with only a small drag penalty by matching the strake to the wing streamlines at particular incidences. In the present exercise, increasing this "non-interfering" incidence reduced the drag penalty to zero, but did detract a little from the lift capability at high incidences.

Finally it has been shown that when practical constraints are considered it is possible, in this particular instance, to obtain a simpler wing definition with three control stations without incurring severe aerodynamic penalties. Theoretical calculations imply that further simplification to a two control station wing should be possible.

References

1. D. R. Stanniland The effects of deflecting flaps on strike/fighter aircraft.
R.Ae.S. Journal, 1974.
2. C. M. Albone Numerical solutions for flow past wing body combinations.
IUTAN Symposium Transsonicum II
Ed. K. Oswatitsch and D. Rues. Springer-Verlag, 1976.
3. M. G. Hall Recent developments in methods for calculating transonic flow over
M. C. P. Firmin wings. I.C.A.S. Paper 74-18, 1974.

Acknowledgement

This work has been carried out with the support of the Procurement Executive, Ministry of Defence.

THEORETICAL PRESSURE DISTRIBUTIONS

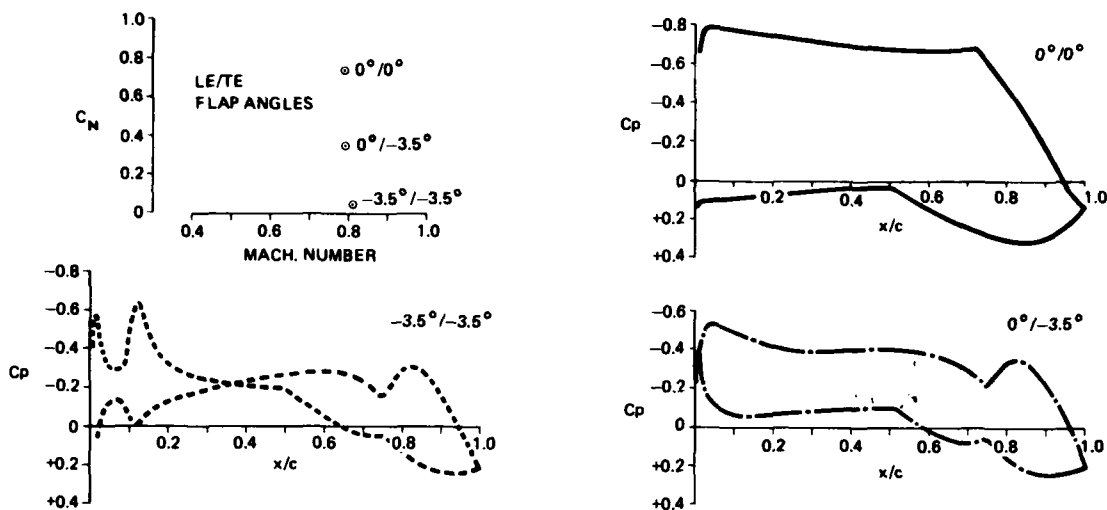


Fig.1 Two dimensional design conditions

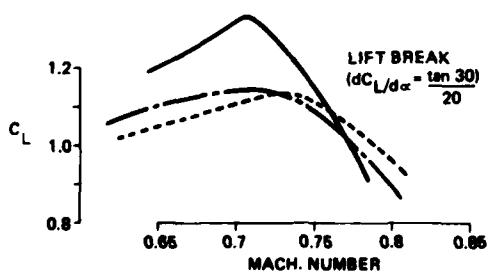
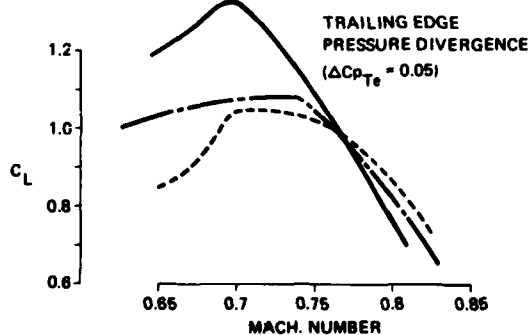
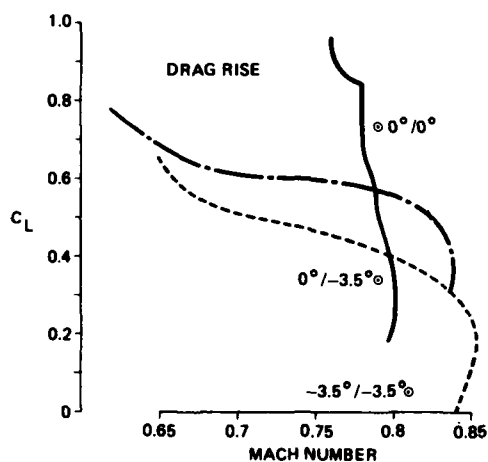


Fig.2 Two dimensional experimental results

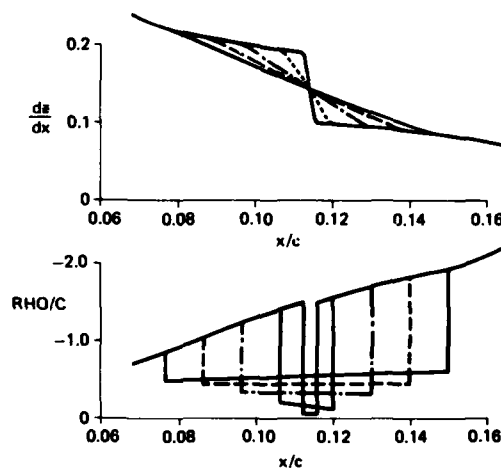


Fig.3 Effect of flexible skin on leading edge flap knuckle

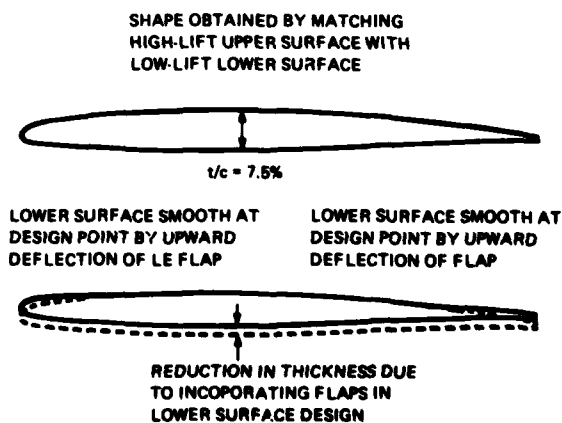


Fig.4 Effect of variable counter device on section thickness

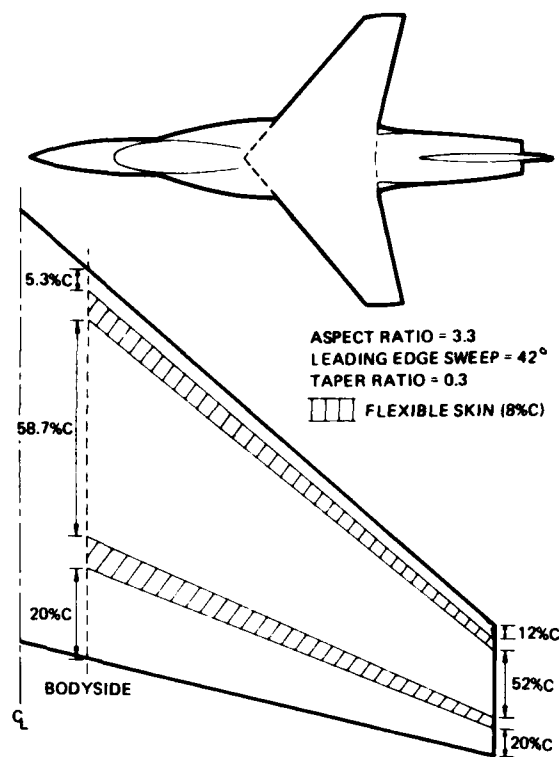
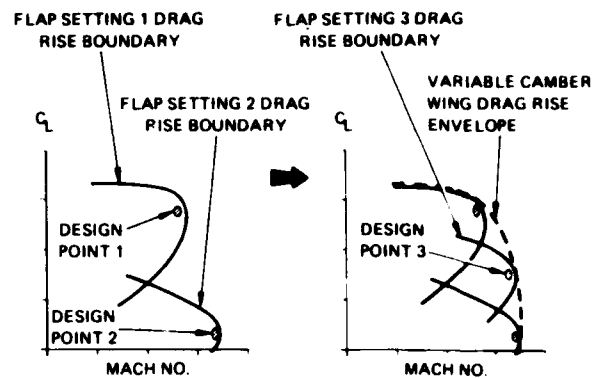
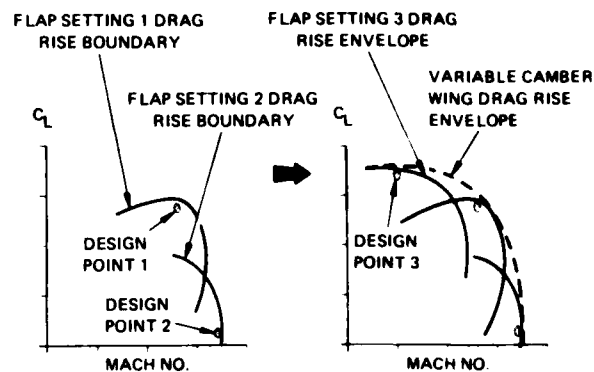


Fig. 5 Model geometry



First possibility



Second possibility

Fig. 7 Choice of the third design point

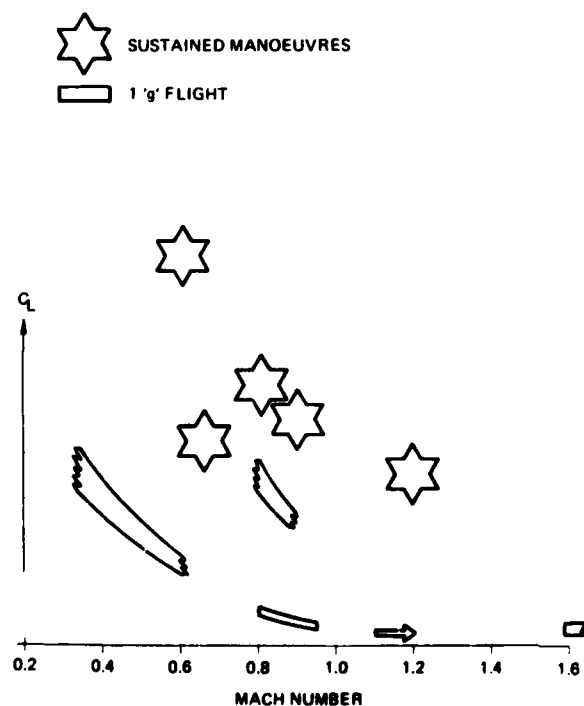


Fig. 6 Identified flight conditions

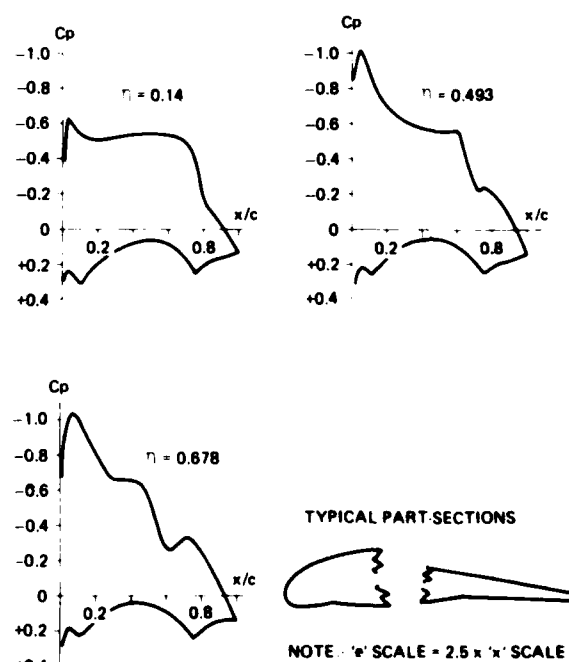


Fig. 8 Pressure distribution and typical part-section for transonic manoeuvre (Design point 1)

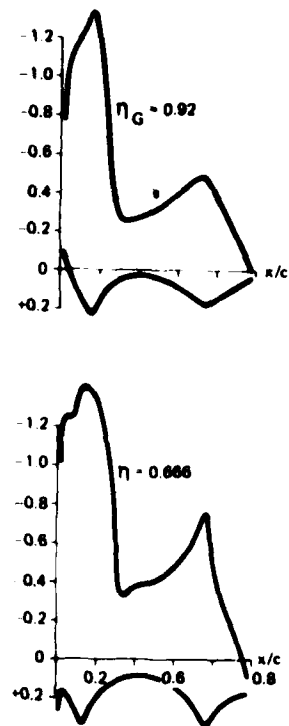


Fig.9 Pressure distribution for Design Point 3

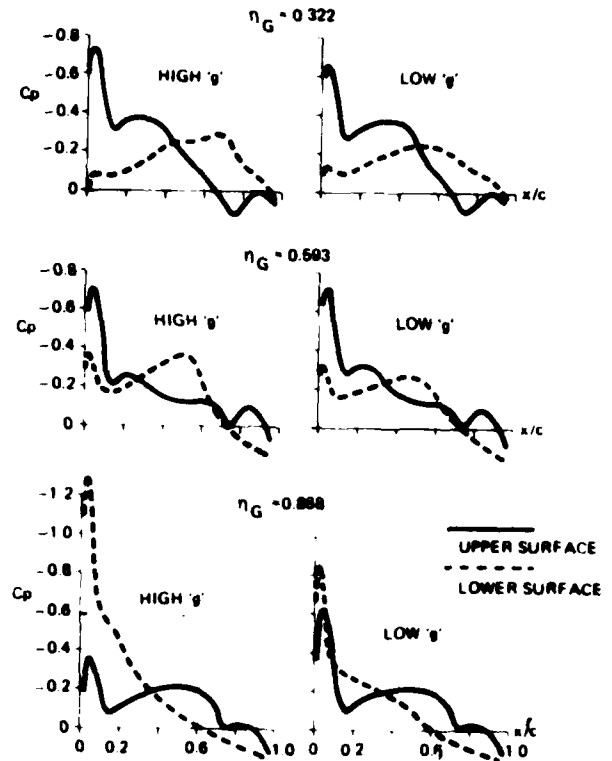


Fig.11 Pressure distribution for flap deflections -5 to -4

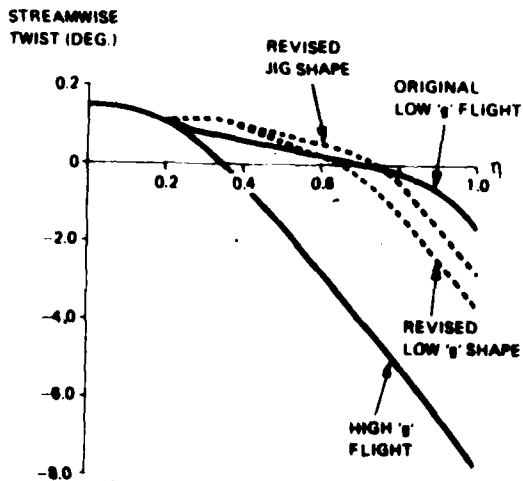


Fig.10 Aeroelastic effects on wing twist

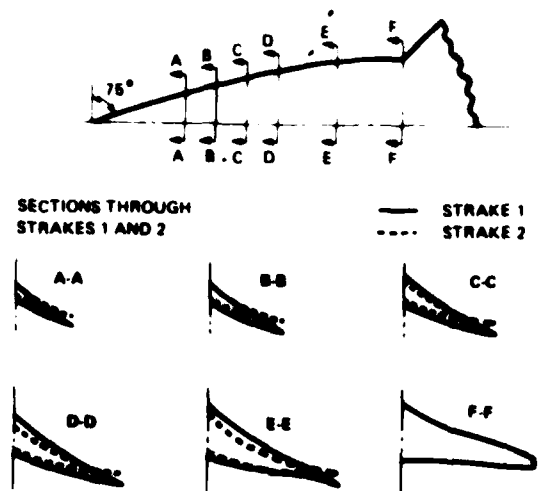


Fig.12 Non-interfering strake geometries

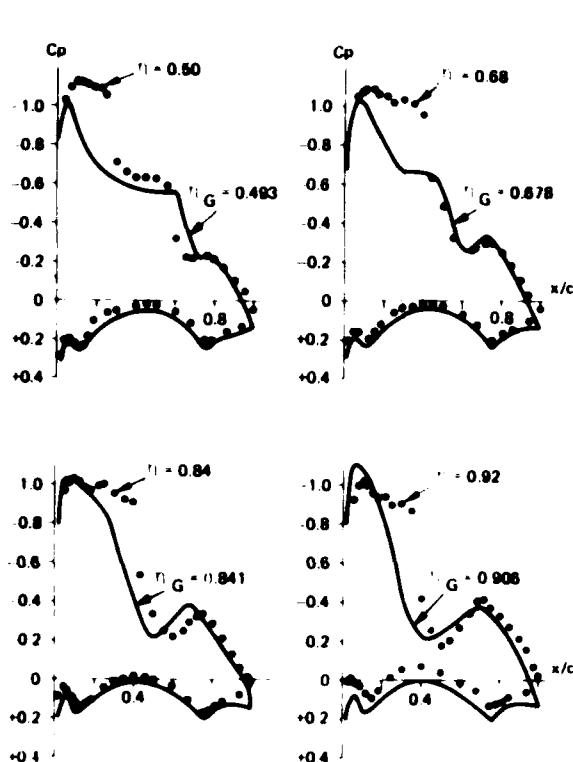
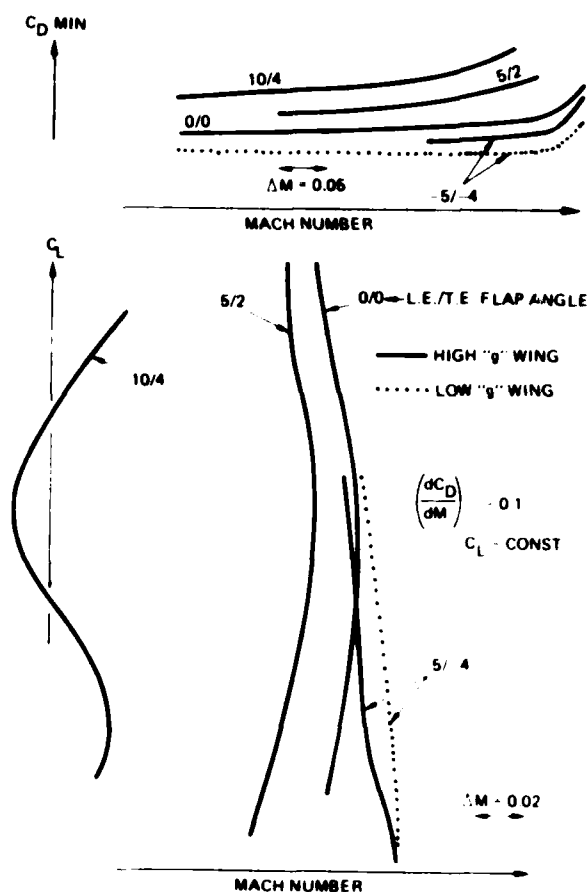
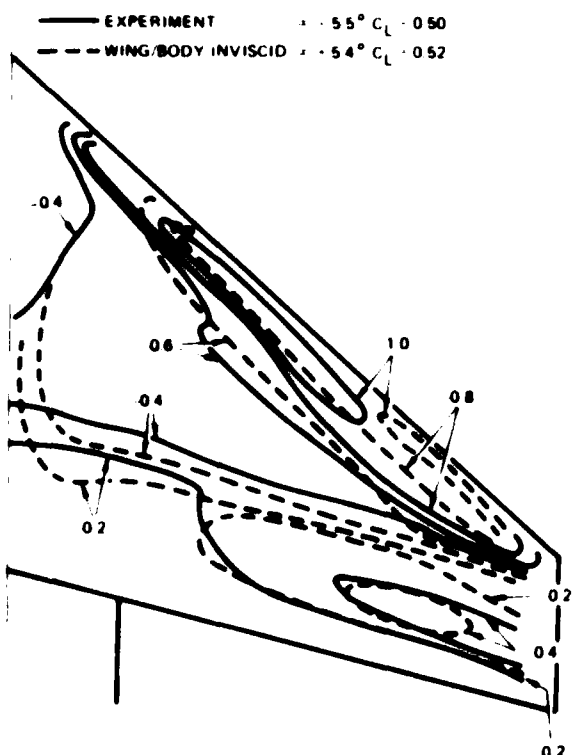
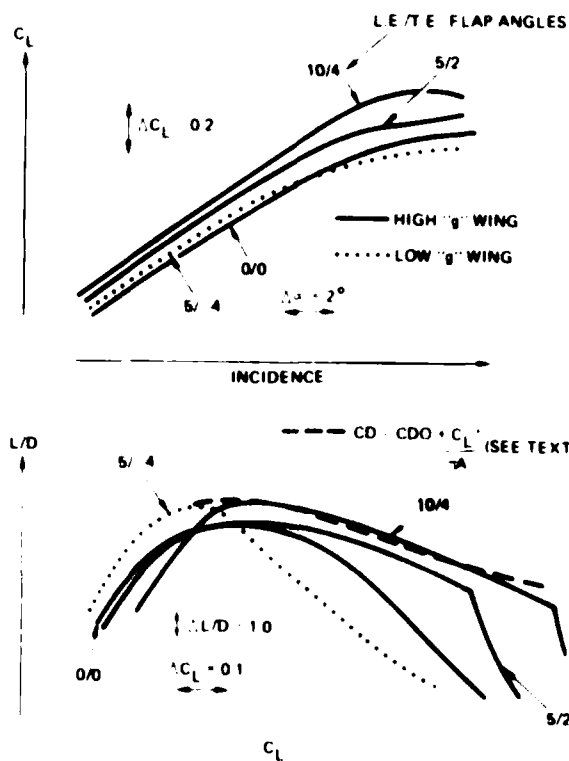
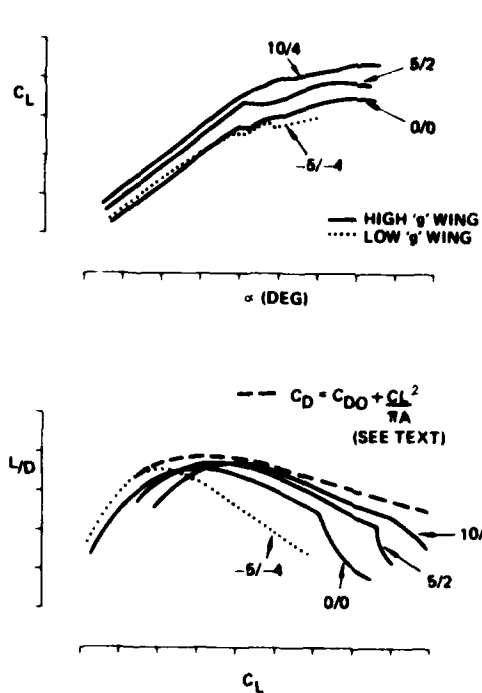
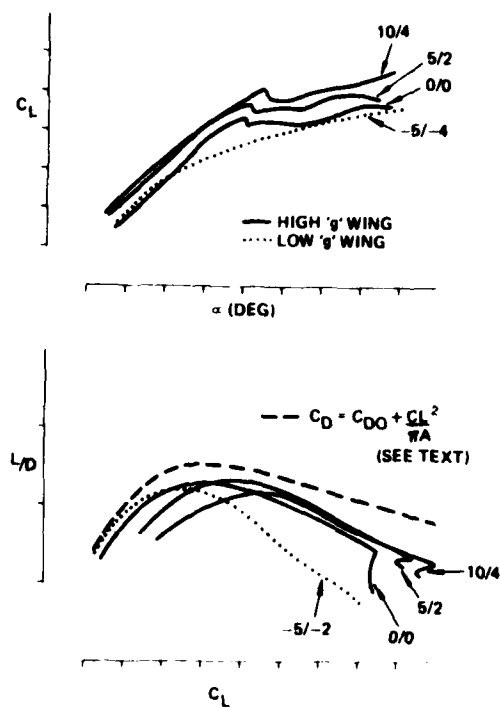
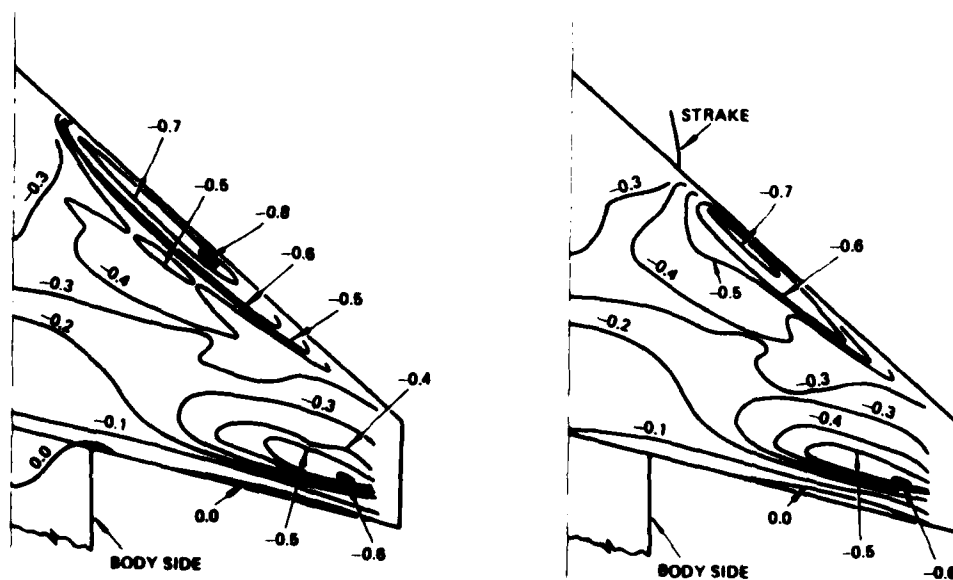
Fig. 13 Pressure distributions at $M=0.88$ 

Fig. 15 Drag - rise mach numbers

Fig. 14 Isobars at $M=0.88$ Fig. 16 Lift and drag at $M=0.65$

Fig.17 Lift and Drag at $M = 0.8$ Fig.18 Lift and Drag at $M = 0.88$ Fig.19 Isobars, Strake on and off, $M = 0.88$, $\alpha = 3.3^\circ$

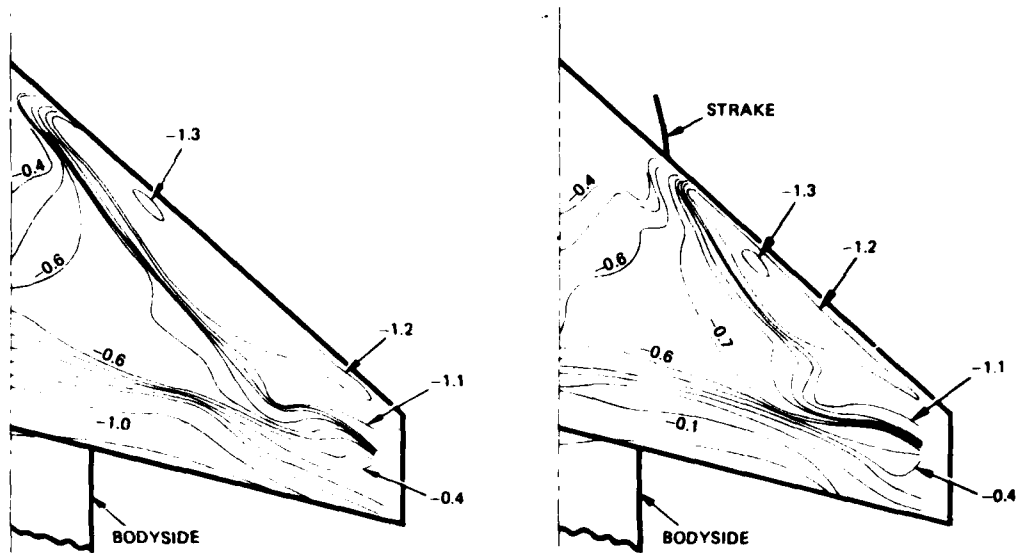


Fig.20 Isobars, strake on and off, $M = 0.88$ $\alpha = 8.8^\circ$

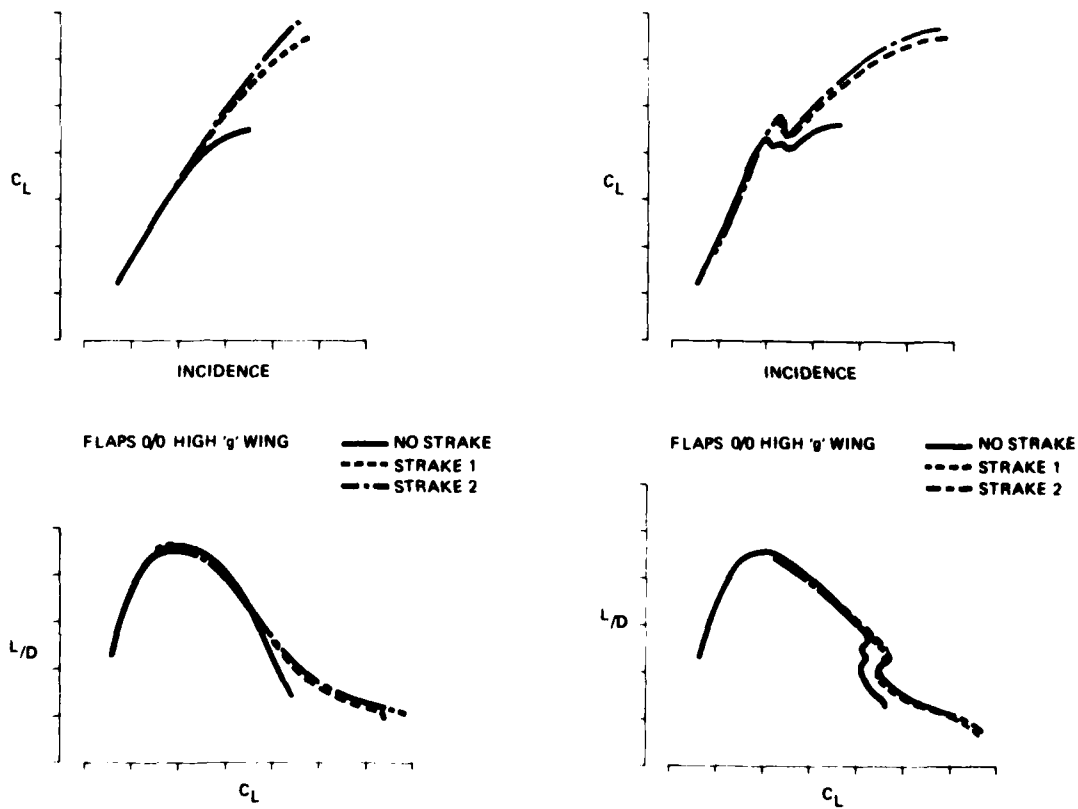
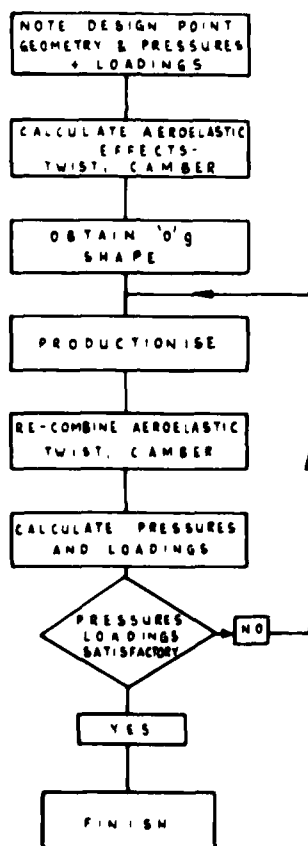


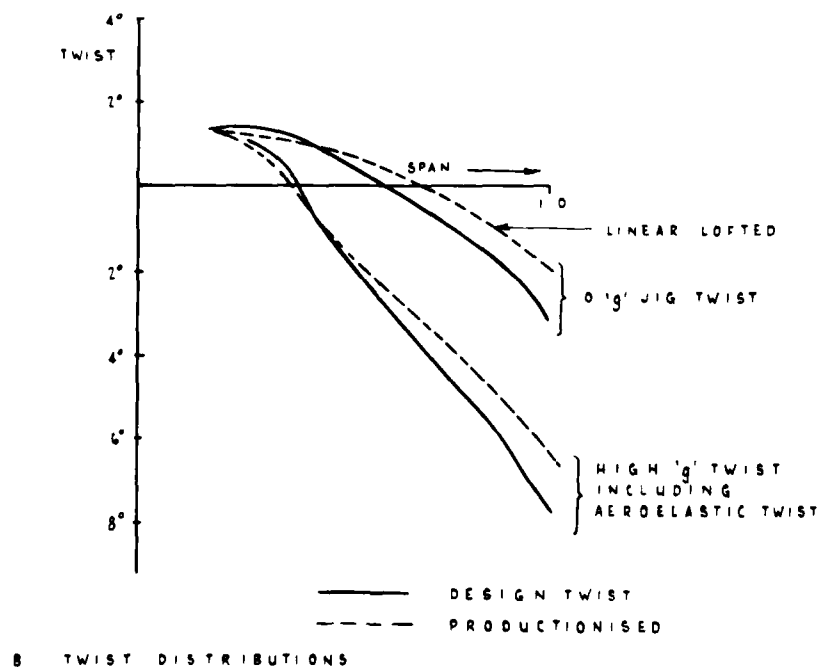
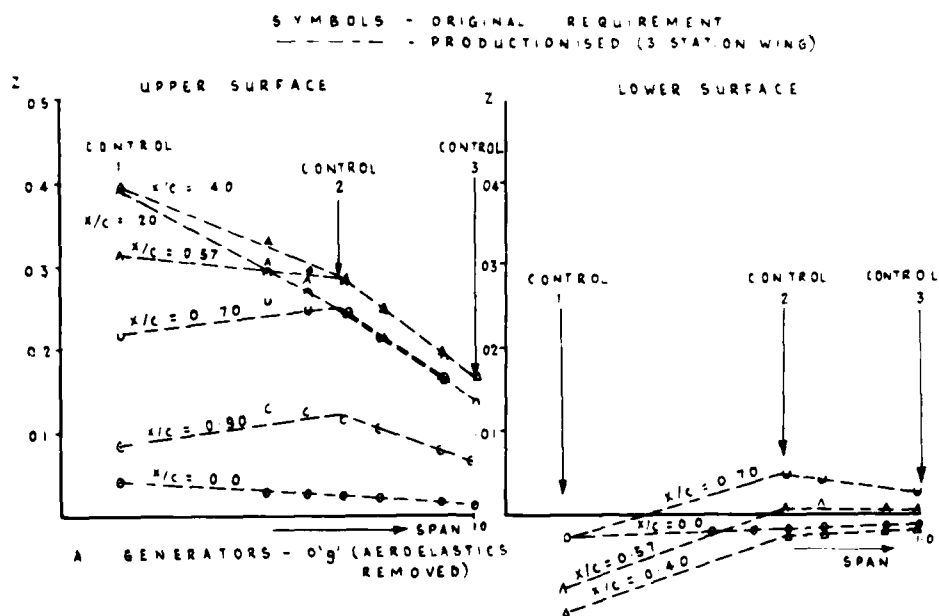
Fig.21 Effect of strakes at $M = 0.65$

Fig.22 Effect of strakes at $M = 0.88$



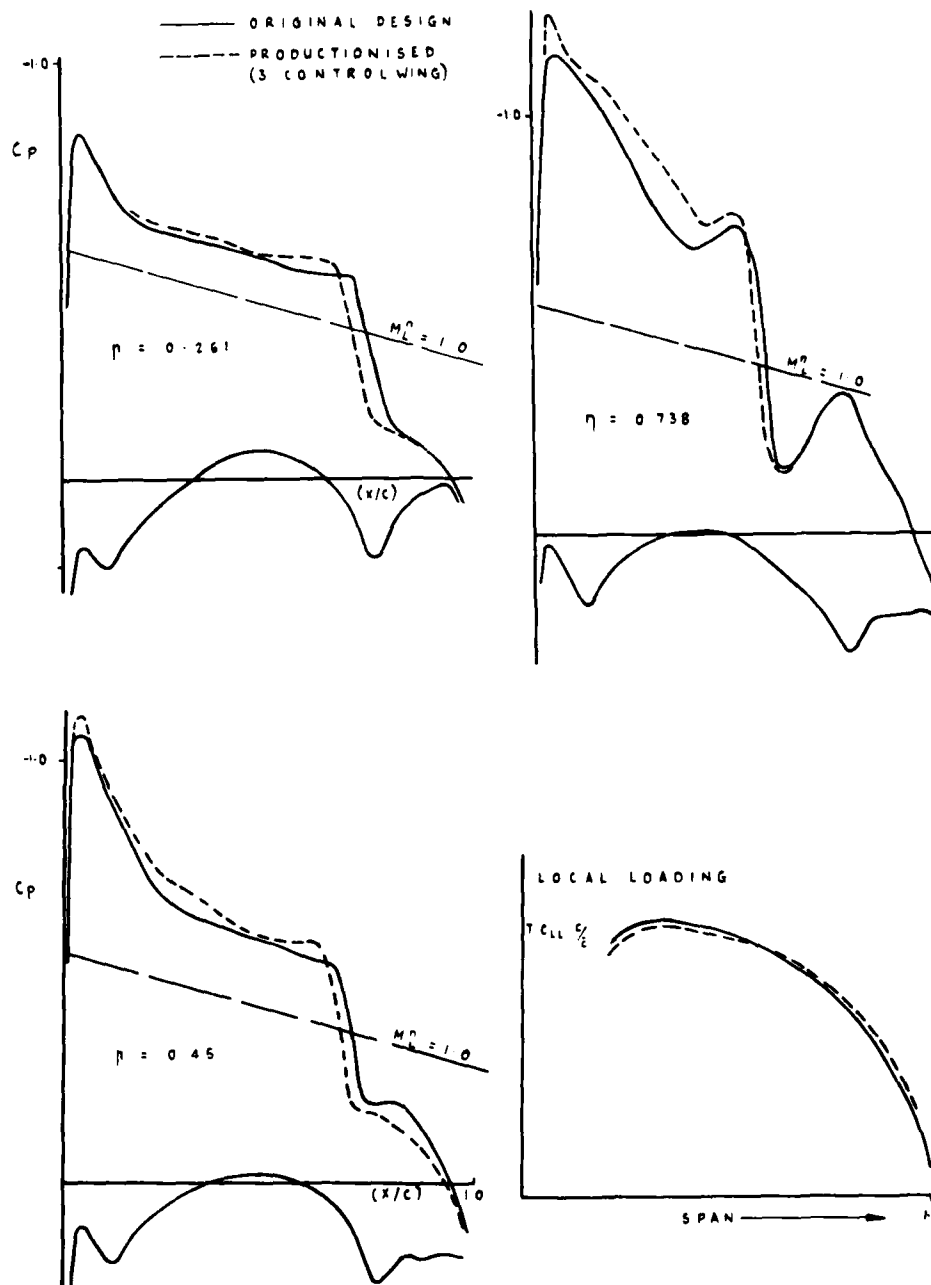
PRODUCTIONISATION PROCEDURE

FIG 23



COMPARISON OF 3-CONTROL STATION WING
WITH ORIGINAL LINES

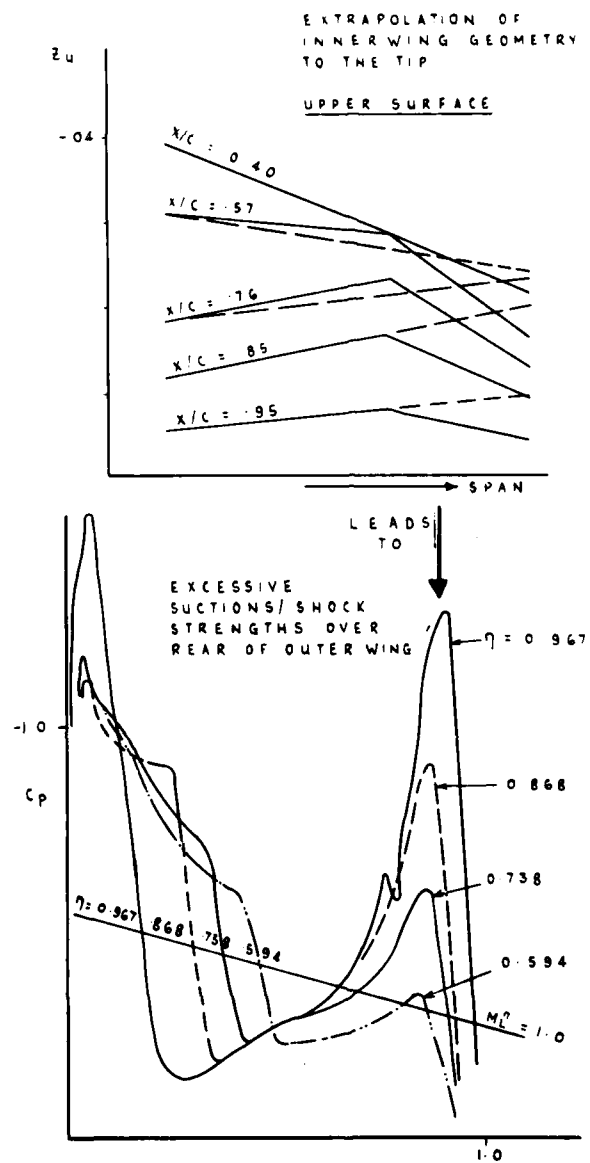
FIG. 24



COMPARISON OF PRESSURE DISTRIBUTIONS
AT DESIGN POINT

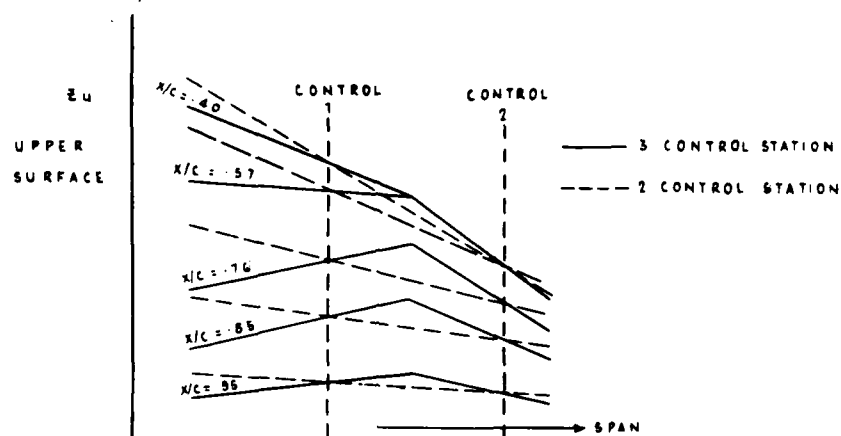
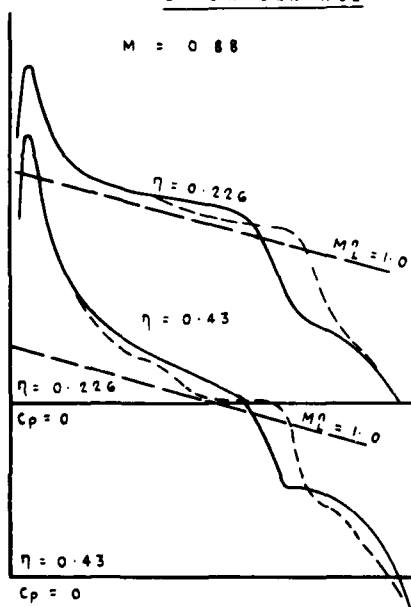
$M = 0.88$
TSP WING + BODY INVISCID THEORY

FIG 25



EFFECT OF EXTREME GEOMETRY SIMPLIFICATION ON PRESSURES

FIG. 26

a) GEOMETRYPRESSURES ON
UPPER SURFACE $M = 0.88$ 

— 3 CONTROL
STATION WING
- - - 2 CONTROL
STATION WING

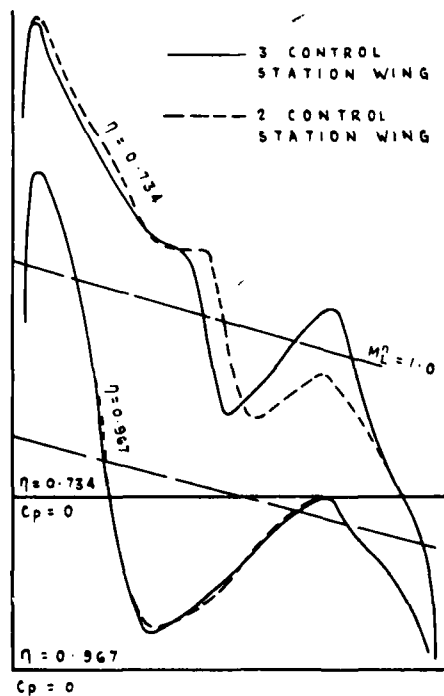
TWO CONTROL STATION APPROXIMATION

FIG 27

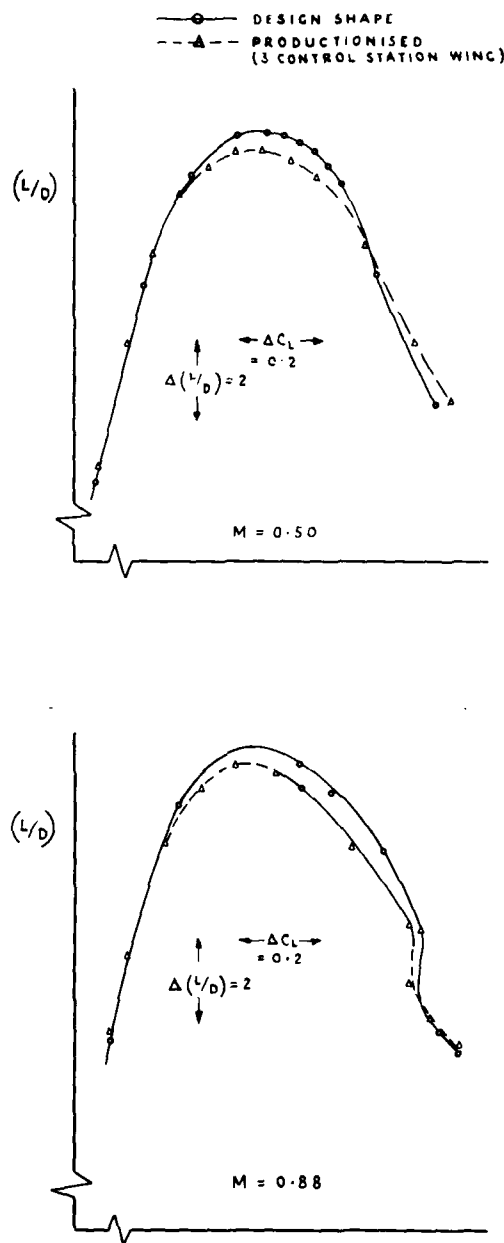
EXPERIMENTAL RESULTS

FIG 28

A CONSTRAINED INVERSE METHOD FOR THE AERODYNAMIC DESIGN
OF THICK WINGS WITH GIVEN PRESSURE DISTRIBUTION
IN SUBSONIC FLOW †

* by
J.M.J. Fray and J.W. Slooff**
NATIONAL AEROSPACE LABORATORY (NLR)
Anthony Fokkerweg 2
1059 CN AMSTERDAM
The Netherlands

SUMMARY

A computational method is presented for the design of "thick" wings with given pressure distribution in subsonic flow, in the presence of a body and/or other airplane components of fixed geometry. The method combines well-established linear techniques for the analysis of thick-wing configurations, and for the design of asymptotically thin wings. These techniques are used in an iterative way.

The design codes have been constructed in such a way that constraints on the spanwise distributions of thickness, twist, leading-edge radius and trailing-edge angle can be taken into account. In this way the designer may execute control over the geometry at the cost of a penalty in the pressure distribution.

Examples of application to a swept wing and a wing-body configuration are given.

CONTENTS

- 1 INTRODUCTION
- 2 GENERAL OUTLINE OF THE PROBLEM AND SOLUTION METHOD
- 3 THE INVERSE METHOD
 - 3.1 Leading edge correction
 - 3.2 The basic linear inverse method
 - 3.3 Geometry update and geometry constraints
- 4 TYPICAL COMPUTATION TIMES
- 5 APPLICATIONS
 - 5.1 Wing alone
 - 5.2 Wing-body configuration
- 6 CONCLUSIONS
- 7 REFERENCES
- 8 figures

LIST OF SYMBOLS

B	body area
C_L	configuration lift coefficient
C_p	pressure coefficient
C_p^*	critical pressure coefficient (local Mach number 1)
K	kernal function
S	wing area
S_w	area of trailing vortex sheet
u	chordwise perturbation velocity component
x, y, z	cartesian co-ordinates
ξ, η, ζ	
γ	vorticity
δ	indicates defect
Δ	indicates difference (between upper and lower surface)
σ	source strength
μ	doublet strength

Subscripts

b	refers to body
c	refers to camber
low	refers to lower surface
t	refers to thickness
up	refers to upper surface
w	refers to wing

1 INTRODUCTION

One of the most important and challenging problems in aircraft configuration optimization is the design of the section shapes of wings which, in (close) proximity with bodies of fixed geometry perform aerodynamically according to given requirements.

At present two different approaches to this problem can be distinguished in the literature on the subject. The most recent, most expensive, and possibly the most promising one in the long run, is called direct optimization. In this approach an aerodynamic object function, such as drag, is minimized computationally by varying the parameters that describe the geometry of the wing. While doing so the solution may

* Senior Research Engineer
** Head, Theoretical Aerodynamics Dept.

† The underlying research was carried out partly under contract for the Netherlands Agency for Aerospace Programs (NIVR).

be subject to geometric and/or aerodynamic constraints¹.

The second and more classical approach, involving the use of so-called inverse methods, is an order of magnitude cheaper in use and not necessarily less useful to the aerodynamic designs in the next few decades to come. By means of inverse methods the wing section shapes can be found that will generate a given pressure distribution at a given freestream Mach number. The task of the aerodynamicist is to specify the pressure distribution such that the wing geometry to be found will perform aerodynamically as required (Fig. 1).

One of the problems that may be encountered when using inverse methods is that an aerodynamically attractive pressure distribution may require a physically unrealistic geometry (such as locally negative thickness) or, in general, a geometry that is unattractive from the structural engineer's point of view. In the inverse methods that can be found in the literature (see e.g. Refs. 2-5) the problem is not recognized or dealt with adequately. In the present authors' opinion this significantly limits the usefulness of these methods.

The present paper describes an inverse method for thick wings in subsonic flow, based on 1st generation panel method technology, which allows constraints on the geometry to be specified. The method has been formulated such that the pressure distribution on both upper and lower surface and geometrical characteristics like thickness, angle of twist, trailing-edge angle and leading-edge radius may be prescribed. The resulting over-determined problem is solved in a weighted least-squares' sense.

Although the method is strictly only valid for subsonic flow conditions, it has been applied satisfactorily in the design of supercritical wings (see Ref. 6 and paper 25 of this colloquium).

2 GENERAL OUTLINE OF THE PROBLEM AND SOLUTION METHOD

The problem of finding the section shapes of a wing with a given planform that will generate a given pressure distribution is non linear in the boundary conditions. Hence the solution must be found by iteration.

The iterative scheme chosen here is basically as presented in figure 2. Starting from some given geometry a standard analysis calculation program (the non-planar NLR Panel Method⁷) is applied to obtain the associated pressure distribution. If this pressure distribution is not close enough to the target, the inverse loop is entered, through which, by means of the linear inverse thin wing theory, an approximation is obtained of the necessary changes of the geometry. With the analysis of the updated geometry the loop is closed. This process is repeated until the calculated pressure distribution is sufficiently close to the specified target.

In general mathematical terms the problem and solution method can be formulated as follows.

We want to solve for the geometry Z from the non-linear equation

$$NZ = F \quad (2.1)$$

In eq. (2.1) N is a non-linear operator, relating a given geometry to a pressure distribution. F represents the target pressure distribution.

Suppose a linear operator L , approximating N in some sense, is known. Then, by rewriting eq. (2.1) into

$$NZ - LZ + LZ = F$$

$$\text{or} \quad LZ = F - (NZ - LZ)$$

an iteration process can be defined by

$$LZ^{(n+1)} = F - (NZ^{(n)} - LZ^{(n)}) \quad (2.2)$$

or in correction/residual formulation:

$$L \delta Z^{(n+1)} = -R^{(n)} \quad (2.3)$$

$$\text{with} \quad \delta Z^{(n+1)} = Z^{(n+1)} - Z^{(n)}$$

$$\text{and} \quad R^{(n)} = NZ^{(n)} - F$$

In the present approach N is the operator implied in the NLR Panel Method, and L is the operator of the linear thin-wing theory.

The convergence properties of the iteration process can be analyzed by rewriting eq. (2.2) into

$$Z^{(n+1)} = L^{-1} F - AZ^{(n)} \quad (2.4)$$

$$\text{with} \quad A = L^{-1} (N - L) \quad (2.5)$$

An alternative formulation of eq. (2.1) is

$$Z = L^{-1} F - AZ \quad (2.6)$$

Subtracting eq. (2.6) from eq. (2.4) gives

$$Z^{(n+1)} - Z = - (AZ^{(n)} - AZ) \quad (2.7)$$

The process (2.7) is convergent if, mathematically spoken, operator A is a contraction, which means that A must have the property

$$\|AZ^{(n)} - AZ\| \leq \lambda \|Z^{(n)} - Z\| \quad (2.8)$$

$$\text{with} \quad 0 < \lambda < 1 \quad (2.9)$$

This is easily verified by combining (2.7) and (2.8) from which it follows that

$$\|Z^{(n+1)} - Z\| \leq \lambda \|Z^{(n)} - Z\| \quad (2.10)$$

implying convergence under condition (2.9).

The condition (2.9) can be shown to be fulfilled, if we confine ourselves to the set of geometries, having a thickness $O(\epsilon)$ ($\epsilon < 1$). Because L is the operator of the thin-wing theory, the following relation between N and L holds:

$$NZ = LZ + \epsilon L_1 Z \quad (2.11)$$

$$\text{or } N - L = \epsilon L_1 \quad (2.12)$$

with L_1 bounded for $\epsilon \rightarrow 0$.

Suppose the distance between $Z^{(n)}$ and Z is (some small value) μ , i.e.:

$$\|Z^{(n)} - Z\| = \mu \quad (2.13)$$

Because of continuity properties of L , it is reasonable to assume that then also:

$$\|L_1 Z^{(n)} - L_1 Z\| = O(\mu) \quad (2.14)$$

According to (2.5) and (2.12) it follows that

$$AZ^{(n)} - AZ = L^{-1} [\epsilon L_1 Z^{(n)} - \epsilon L_1 Z] \quad (2.15)$$

and therefore

$$\|AZ^{(n)} - AZ\| \leq \epsilon \|L^{-1}\| \|L_1 Z^{(n)} - L_1 Z\| \quad (2.16)$$

Substitution of (2.14) in (2.16) yields

$$\|AZ^{(n)} - AZ\| \leq \epsilon \|L^{-1}\| O(\mu) \quad (2.17)$$

Finally, introduction of (2.13) implies

$$\|AZ^{(n)} - AZ\| \leq \lambda \|Z^{(n)} - Z\| \quad (2.18)$$

with $\lambda = O(\mu)$.

Hence condition (2.9) is satisfied for ϵ small enough.

It may be emphasized that the solution of (2.1) certainly not depends on thin wing theory. The operator L is only used in defining the iteration process. Therefore the accuracy of the approximating theory is only important as far as the convergence characteristics are concerned. This is expressed by the statement $\lambda = O(\epsilon)$. It might be expected that the requirement $\lambda < 1$ (eq. (2.9)) is not a stringent one on the value of ϵ . As a matter of fact, calculations (see section 5) confirm, that rather thick wings can be determined.

3 THE INVERSE METHOD

A further break-down of the block "INVERSE METHOD" in figure 2 is presented in figure 3. It features a number of sub-blocks, the main contents of which is described in the following paragraphs.

3.1 Leading edge correction

It is well known that linear thin-wing theory exhibits a singular behaviour at the leading edge. For wings with round-nosed sections this is not the case with the non-planar panel method of reference 6.

In section 2 it is stated that, for reasons of convergence, the planar theory has to approximate the non-planar theory (see for instance eq. (2.12)). Hence, we must expect the condition for convergence to be violated locally at the leading edge.

The remedy is found by applying to both the calculated and the target surface velocity distribution an inverse form of the Riegels'-type leading-edge correction that is contained in the compressibility correction of the NLR Panel Method 7. In the block "LEADING-EDGE CORRECTION" the target and the calculated pressure (velocity) distributions are, in the same way, linearized into chordwise perturbation velocity components. From the latter the defect linearized perturbation velocities δu_{up} and δu_{low} on the wing upper and lower surface, respectively, are calculated.

As usual in the thin-wing theory these perturbation velocities are combined to yield a symmetrical part $\delta \bar{u}$ due to thickness, and an anti-symmetrical part $\delta(\Delta u)$ due to lift:

$$\left. \begin{aligned} \delta \bar{u} &= \frac{1}{2} (\delta u_{up} + \delta u_{low}) \\ \delta \Delta u &= \frac{1}{2} (\delta u_{up} - \delta u_{low}) \end{aligned} \right\} \quad (3.1)$$

3.2 The basic linear inverse method

According to linear, thin wing theory, the effects of changes in thickness and lift can be represented by distributions in the wing mean plane of resp. sources and vortices:

$$\delta \bar{u}(x, y) = \iint_S \sigma(\xi, \eta) K_S(x, y; \xi, \eta) d\xi d\eta \quad (3.2)$$

$$\delta \Delta u(x, y) = \frac{1}{2} \gamma(x, y) \quad (3.3)$$

The source strength σ is related to the change δz_t in wing thickness by

$$\sigma = 2 \frac{\partial}{\partial x} (\delta z_t) \quad (3.4)$$

whereas the spanwise component γ of the vorticity vector is related to the change δz_c of camber and twist

$$\frac{\partial}{\partial x} (\delta z_c) = \iint_{S+S_v} \gamma(\xi, \eta) K_v(x, y; \xi, \eta) d\xi d\eta \quad (3.5)$$

(In this notation the Kernel function K_v includes the effect of the trailing vorticity, satisfying Helmholtz law).

From (3.3) and (3.5) it follows that the correction to the chord wise slope of the wing camberline can be determined from the integral expression

$$\frac{\partial}{\partial x} (\delta z_c) = 2 \iint_{S+S_w} \delta(\Delta u)(x, y) K_v(x, y; \xi, \eta) d\xi d\eta \quad (3.5)$$

The correction to chordwise slope of the thickness distribution can be determined from the integral equation

$$2 \iint_S \frac{\partial(\delta z_t)}{\partial \xi} (\xi, \eta) K_s(x, y; \xi, \eta) d\xi d\eta = \delta \bar{u}(x, y) \quad (3.6)$$

This equation, which is of the same type as that of the lifting surface theory, is of singular nature and does not have a unique solution. In lifting surface theory the additional condition rendering a unique solution is the Kutta condition. In the inverse thickness problem the corresponding additional condition is that of trailing closure, i.e.

$$\int_{le}^{te} \frac{\partial}{\partial x} (\delta z_t) dx = 0 \quad (3.7)$$

In the present method the additional condition (3.8) is conveniently satisfied by introducing a new dependent variable μ defined by

$$\sigma = \frac{\partial \mu}{\partial x} \quad (3.8)$$

Substitution in (3.7) gives

$$\iint_S \frac{\partial \mu}{\partial \xi} K_s d\xi d\eta = \delta \bar{u} \quad (3.9)$$

Integration by parts with respect to ξ gives

$$\int_{le}^{te} d\eta \int_{le}^{te} \frac{\partial \mu}{\partial \xi} K_s d\xi = \int_{le}^{te} d\eta \left[\mu K_s \int_{le}^{te} - \int_{le}^{te} \mu \frac{\partial K_s}{\partial \xi} d\xi \right] \quad (3.10)$$

From equation (3.9) it follows that

$$\mu = \int \sigma dx = 2 \int \frac{\partial}{\partial x} (\delta z_t) dx = 2 \delta z_t \quad (3.11)$$

and thus, because of the closure condition

$$\mu_{le} = \mu_{te} = 0 \quad (3.12)$$

Substituting (3.13) into (3.11) and defining

$$K_d = - \frac{\partial K_s}{\partial \xi} \quad (3.13)$$

eq. (3.7) can be rewritten as

$$2 \iint_S \delta z_t (\xi, \eta) K_d(x, y; \xi, \eta) d\xi d\eta = \delta \bar{u}(x, y) \quad (3.14)$$

Note that this is the analytical formulation of the representation of the thickness by a distribution of doublets in the wing mean plane, with their axis in chord wise direction. Note also that in (3.15) the closure condition is satisfied implicitly.

The equations derived thusfar, refer to the case of a wing alone. When a body is present the vortices and doublets in the wing mean plane will induce normal velocities on the body.

To neutralize these effects the body is covered with sources, which on their turn will contribute to the normal and tangential velocities on the wing. When these effects are taken into account, the final system of integral equations to be solved can be written as:

$$\left. \begin{aligned} \iint_S \mu (\xi, \eta) K_d(x, y, \xi, \eta) d\xi d\eta + \iint_B \sigma (\xi, \eta, \zeta) K_{T_w}(x, y; \xi, \eta, \zeta) dB &= \delta \bar{u}(x, y) \\ \gamma(x, y) &= 2 \delta \Delta u(x, y) \\ \iint_S \mu (\xi, \eta) K_d(x, y, z; \xi, \eta) d\xi d\eta + \iint_{S+S_w} \gamma (\xi, \eta) K_v(x, y, z; \xi, \eta) d\xi d\eta \\ &+ \iint_B \sigma (\xi, \eta, \zeta) K_{N_B}(x, y, z, \xi, \eta, \zeta) dB = 0 \end{aligned} \right\} \quad (3.15)$$

When μ , γ and σ are known, δz_t and δz_c can be determined from eq. (3.12) and the integral relation

$$\frac{\partial}{\partial x} (\delta z_c) = \iint_{S+S_w} \gamma (\xi, \eta) K_v(x, y; \xi, \eta) d\xi d\eta - \iint_B \sigma (\xi, \eta, \zeta) K_{N_w}(x, y; \xi, \eta, \zeta) dB \quad (3.16)$$

respectively.

To discretize the integral equations the wing mean plane and the body surface are divided into panels (plane quadri-laterals). The vorticity and x-doublet distributions on the wing and the source distribution on the body are approximated by piecewise constant distributions on a panel.

It can be shown that a constant x-doublet distribution on a panel is equivalent to the combination of a line source at the leading edge of the panel and a line sink of equal strength at the trailing edge.

By this nature the method for solving the thickness problem may be called a "source lattice method", analogous to the vortex lattice method in the lifting surface theory.

Evaluation of the integrals at the midpoints of the panels leads to a system of linear equations which may be written as

$$\left. \begin{aligned} \sum_{k=1}^N \sum_{l=1}^N \mu_{k,l} K_{d,i,j,k,l} + \sum_m \sigma_m K_{T,i,j,m} &= \delta u_{i,j} \\ \gamma_{i,j} &= -\delta A u_{i,j} \\ \sum_{k=1}^N \sum_{l=1}^N \mu_{k,l} K_{d,i,k,l} + \sum_{k=1}^N \sum_{l=1}^N \gamma_{k,l} K_{v,i,k,l} + \sum_m \sigma_m K_{N,i,m} &= 0 \end{aligned} \right\}$$

Similarly the integral expression (3.17) becomes

$$\frac{\partial}{\partial x} (\delta z_c)_{i,j} = \sum_{k=1}^N \sum_{l=1}^N \gamma_{k,l} K_{v,i,j,k,l} - \sum_m \sigma_m K_{N,i,j,m}$$

In (3.18) and (3.19) i,k and j,l are integers identifying chordwise and spanwise positions of wing panels respectively; m identifies body panels. K_d , K_T , etc. are the so-called aerodynamic influence coefficients.

3.3 Geometry update and geometry constraints

The values of $\delta z_c (=z_1)$ and $\frac{\partial}{\partial x} (\delta z_c)$ are evaluated at the midpoints of the panels. The changes of the thickness distribution and the camberlines at the panel corner points may be derived from

$$\left. \begin{aligned} \delta z_{t,i,j} &= \frac{1}{8} (\mu_{i-1,j-1} + \mu_{i,j-1} + \mu_{i-1,j} + \mu_{i,j}) \\ \delta z_{c,i+1,j} &= \delta z_{c,i,j} + \frac{1}{2} \left\{ \frac{\partial}{\partial x} (\delta z_c)_{i,j-1} + \frac{\partial}{\partial x} (\delta z_c)_{i,j} \right\} * (x_{i+1,j} - x_{i,j}) \end{aligned} \right\}$$

With the formulation given above, the formulation of equations that will take care of constraints on the geometry is only a small step.

The wing thickness, leading edge radius and trailing edge angle can be controlled by equations of the type

$$\frac{1}{8} (\mu_{i-1,j-1} + \mu_{i,j-1} + \mu_{i-1,j} + \mu_{i,j}) = DZT_{i,j}$$

where i,j and $DZT_{i,j}$ may be specified.

The constraints on the wing twist can be formulated by

$$\frac{1}{2} \sum_{i=1}^{i2-1} \left\{ \frac{\partial}{\partial x} (\delta z_c)_{i,j-1} + \frac{\partial}{\partial x} (\delta z_c)_{i,j} \right\} * (x_{i+1,j} - x_{i,j}) = DZC_{i2,j} - DZC_{i1,j}$$

Where $i1$, $i2$, j and $DZC_{i2,j} - DZC_{i1,j}$ may be specified. By means of equation (3.14) the terms $\frac{\partial}{\partial x} (\delta z_c)$ can be expressed in the variables γ and σ :

$$\begin{aligned} &\frac{1}{2} \sum_{k=1}^N \sum_{l=1}^N \gamma_{k,l} \sum_{i=1}^{i2-1} \left\{ K_{v,i,j-1,k,l} + K_{v,i,j,k,l} \right\} (x_{i+1,j} - x_{i,j}) \\ &- \frac{1}{2} \sum_m \sigma_m \sum_{i=1}^{i2-1} \left\{ K_{N,i,j-1,m} + K_{N,i,j,m} \right\} (x_{i+1,j} - x_{i,j}) = DZC_{i2,j} - DZC_{i1,j} \end{aligned}$$

By adding the equations (3.21) and (3.23) to the system (3.18) an overdetermined system of linear equations is obtained for the unknowns μ , γ and σ . This system is solved in a weighted least squares' sense. By varying the weight factors on the equations representing the constraints, the designer may guide the iterative process to a solution that is a suitable compromise between the geometrical constraints and the aerodynamic requirements as specified by the target pressure distribution.

4 TYPICAL COMPUTATION TIMES

To give some idea of the computation times involved, four major subprograms may be distinguished. For a wing-body configuration with 440 body panels and (2*) 300 wing panels the required CPU times on a CDC Cyber 12 are

- determination of the influence coefficients for the inverse method (only once) 100 sec
- determination of the coefficient matrices after specification of the weight factors (only after a change of factors) 100 sec
- solution of the linear inverse problem 200 sec per iteration
- NLR Panel Method 2000 sec

5 APPLICATIONS

The capabilities of the method are illustrated for a wing alone of simple planform, and for a wing-body configuration with the same wing planform at a free-stream Mach number of 0.7.

The parameters defining the wing planform are:

- aspect ratio $A^* = 1$
- taper ratio $\lambda = 0.3$
- quarter-chord sweep angle $\Lambda_{c/4} = 15^\circ$.

- The characteristics chosen for the pressure distribution are:
- an elliptic load distribution in spanwise direction,
 - a flat, no-lift upper surface distribution, up to 90% of the chord,
 - an overall lift coefficient of 0.7.

5. Wing alone

A front view of the panel arrangement is shown in figure 4. The initial wing section geometry was defined by the NACA 0012 airfoil at design incidence and zero twist.

The first series of iterations was made with:

- a high weight on the trailing edge radius (target value 1.0)
- a low weight on the leading edge radius (target value 0.1) of the local chord,
- zero weight on thickness and twist.

The pressure distribution obtained after four iterations is reported in figure 5a where it is compared with the starting and target distribution. Further iterations did not produce any noticeable effect, except near the leading edge where a small local instability has developed. The experience is, that such instabilities, when they occur, are of neutral rather than catastrophic nature. If required they can be easily removed by intermediate smoothing.

A front view of the generated wing is shown in figure 6a. The figure clearly illustrates the fact that an aerodynamically appealing pressure distribution may require an unattractive geometry. The spanwise gradients in thickness and twist that are evident from figure 6a would probably be unacceptable from the point of view of wing structure and production.

To demonstrate the usefulness of the geometrical constraints a further series of calculations was made in which regular spanwise distributions of thickness and twist were specified with high weight factors attached to them. After three more iterations the results shown in figure 7 and 8 were obtained. Figure 8 illustrates that the geometrical goals with respect to thickness and twist have been realized. The associated penalty in pressure distribution is small, as shown in figure 7.

6. Wing-body configuration

The wing-body configuration considered is shown in figure 9. It consists of a fuselage with a cylindrical cross-section, except in the wing-body junction area, and a high-positioned wing with the same overall dimensions as the wing alone in the preceding paragraph. The target pressure distribution selected was also identical to that of the isolated wing.

Figure 9a shows the results of design calculations with a strong constraint on the trailing-edge angle. The wing chosen for the starting configuration was that of figure 6b. Note that because of the presence of the fuselage, the pressure distribution near the root has changed considerably. The final result was obtained after three iterations.

A front view of this wing is presented in figure 9a. As might have been expected it suffers from similarly large spanwise gradients in thickness and twist as the isolated wing of figure 5a. Here also the wing may be "straightened" by applying high weights on thickness and twist (Fig. 9b) at the cost of a penalty in pressure distribution (Fig. 9b).

7. CONCLUDING

A panel-type method has been described for the design of wings with given pressure distribution in subsonic flow, in the presence of bodies of fixed geometry. The method has been formulated such that requirements with respect to the section geometry in terms of twist, thickness, leading-edge radius and trailing-edge angle can be taken into account. In this way the designer may execute control over the geometry at the cost of a minimum penalty in pressure distribution.

This last feature is considered to be of eminent importance in practical wing design. Its usefulness has been illustrated by examples.

8. REFERENCES

1. Hicks, R.M. and Henne, P.A. Wing design by numerical optimization. AIAA Paper No. 77-1247 (1977).
2. Woodward, P.A. Analysis and design of wing-body combinations at subsonic and supersonic speeds. J. Aircraft, Vol. 5, no. 6 (1968).
3. Rubbert, P.E. and Saaris, G.R. Review and evaluation of three-dimensional lifting potential flow analysis method for arbitrary configurations. AIAA Paper no. 72-188 (1972).
4. Lock, R.C. Research in the U.K. on finite difference methods for computing steady transonic flows. IUTAM Symposium Transonicum II, Göttingen (1975).
5. Henne, P.A. An inverse transonic wing design method. AIAA Paper 80-0330 (1980).
6. Slooff, J.W. and Voogt, N. Aerodynamic design of thick supercritical wings through the concept of equivalent subsonic pressure distribution. Paper presented at DGLR/GARTEUR symposium on transonic configurations, Bad Harzburg, June 1978.
7. Labrujère, Th.E., Looze, W. and Slooff, J.W. An approximate method for the calculation of the pressure distribution on wing-body combinations at subcritical speeds. AGARD CP. no. 71, paper 11 (1970).

ACKNOWLEDGEMENT: The authors are indebted to Mr Piers of NLR for his advice on various mathematical aspects of the method.

* It is emphasized that the configurations and target pressure distributions chosen should not be considered to be representative for a realistic aircraft configuration; they merely serve the purpose of demonstrating the capabilities of the present design method.

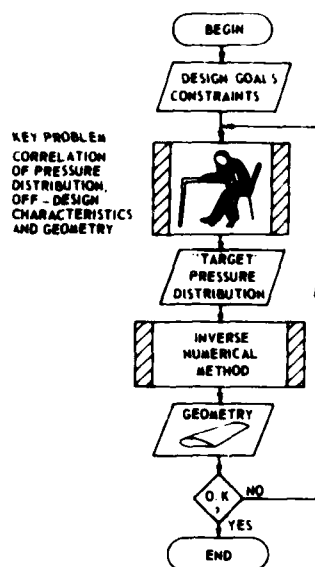


Fig. 1 Interactive design procedure

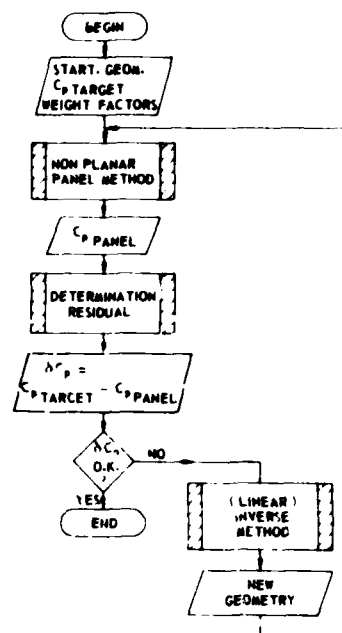


Fig. 2 Flow diagram of iteration process

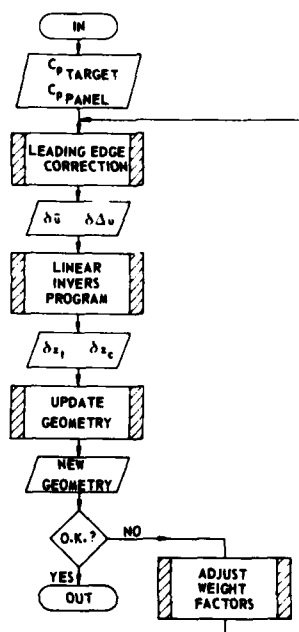


Fig. 3 Flow diagram of inverse method



Fig. 4 Top view and panel arrangement of example wing

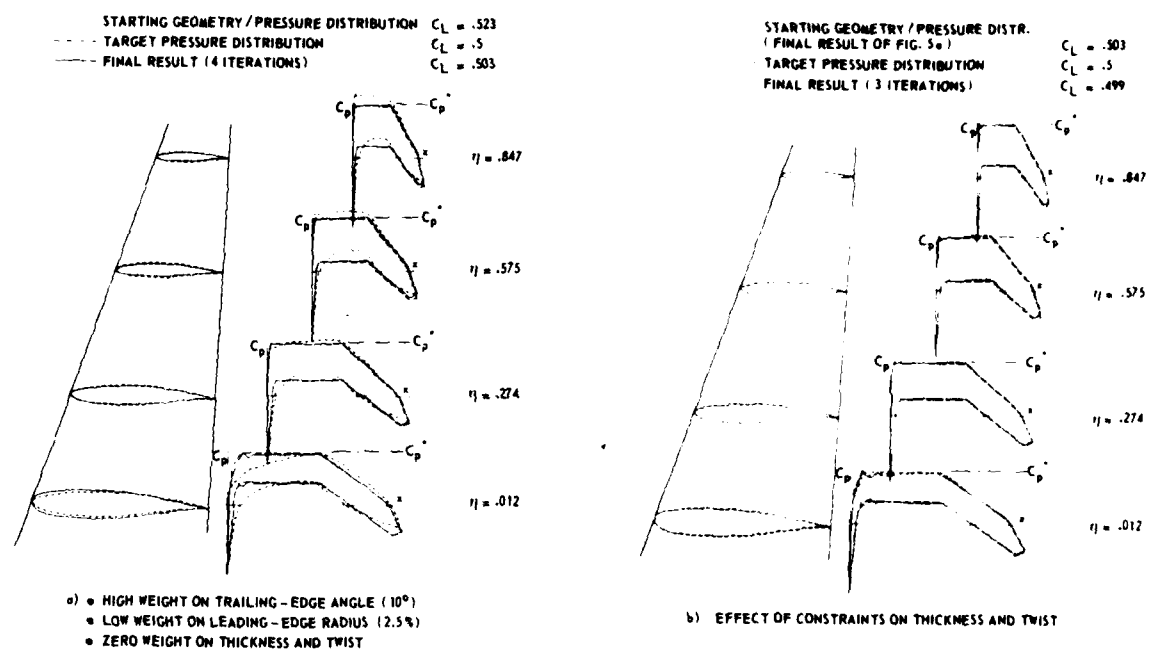
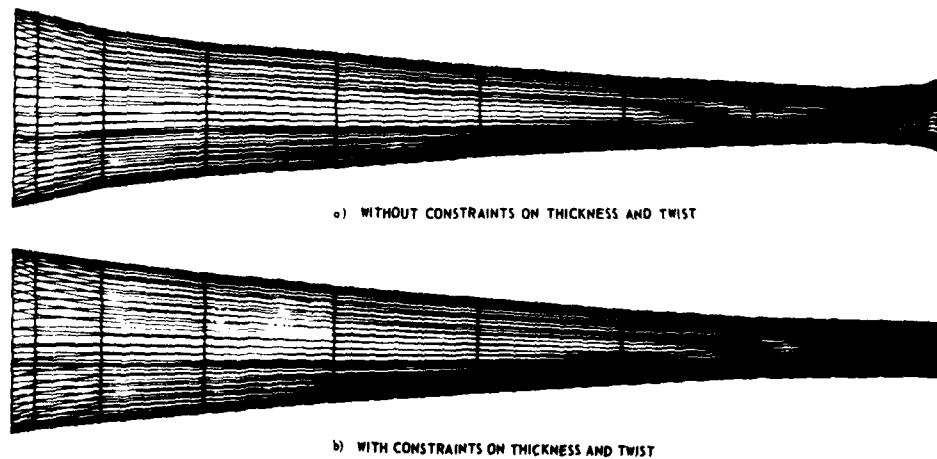
Fig. 5 Results for wing alone ($M_\infty \approx 0.7$)

Fig. 6 Front view of wing configurations of fig. 5 (z-scale enlarged 5x)

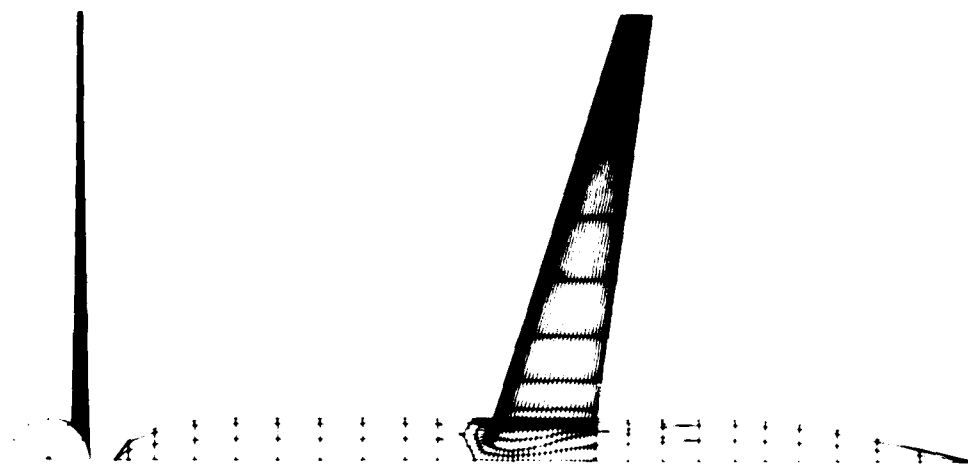


Fig. 7 Top and front view and panel arrangement of wing-body configuration (body at zero angle of attack)

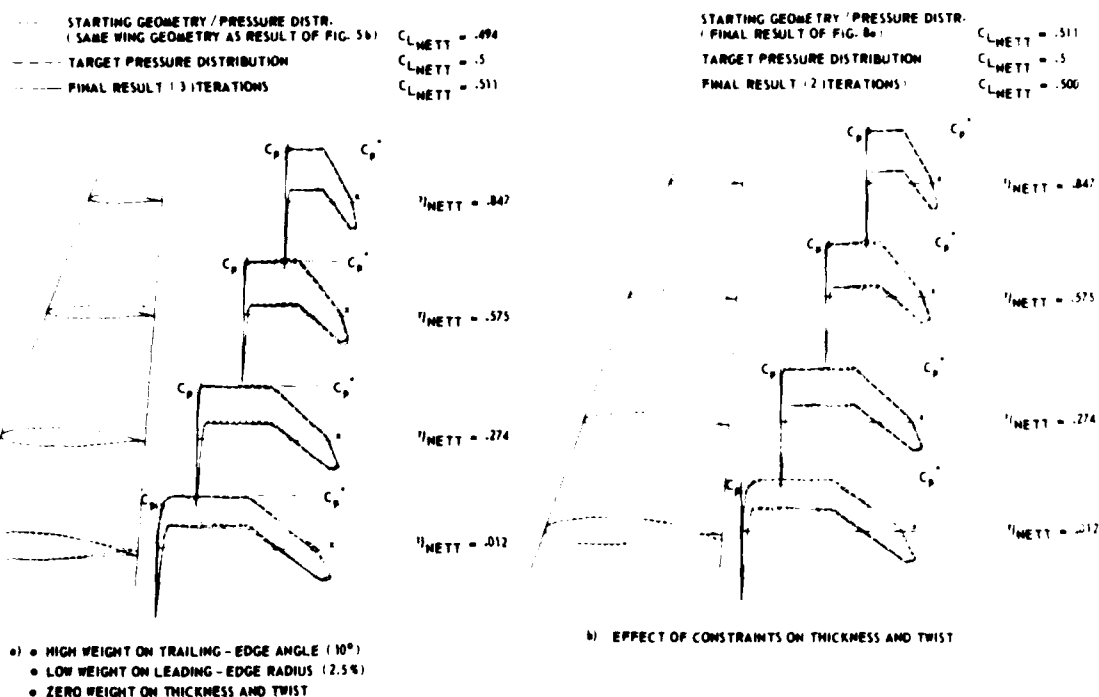


Fig. 8 Results for wing-body configuration ($M_\infty = 0.7$)

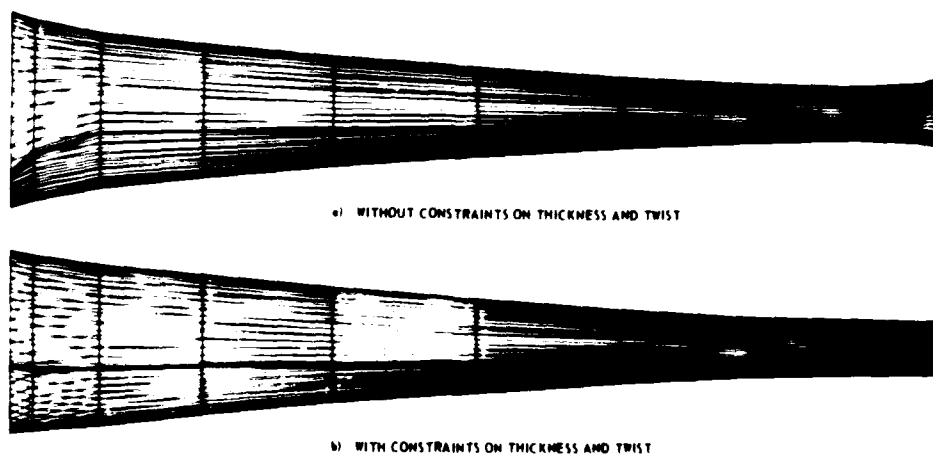


Fig. 9 Front view of wings of wing-body configurations of fig. 8 (z scale enlarged 5x)

JET-WING INTERACTION TO GIVE IMPROVED COMBAT PERFORMANCE

by

A. Vint

BRITISH AEROSPACE, WARTON, ENGLAND PR4 1AX

SUMMARY

U.S. model test results for aircraft configurations having propulsive jets emerging close to the wing trailing edge have shown significant beneficial effects on lift and drag. The effects could be turned to advantage for combat aircraft if a configuration were chosen having this feature.

Examination of jet flap theory has led to the development of a modified theory capable of giving rapid estimation of the jet-wing interaction on aircraft lift, drag and pitching moment. Recently published experimental data together with recent experimental results obtained at BAe have been used to substantiate the estimation method.

Study of the consequences on aircraft performance has shown that substantial benefits may be obtained in low speed, low altitude combat situations but that there is little if any influence for cruising flight.

Many aspects of jet-wing interaction remain uninvestigated; the most important are briefly described and a short examination made of the probable impact on the conclusions of the basic study.

NOTATION

A	Gross wing aspect ratio
\bar{c}	Gross wing mean aerodynamic chord
C_D	Drag coefficient based on S
C_L	Lift coefficient based on S
$C_{L\ J/OFF}$	Jet off C_L
C_m	Pitching moment coefficient based on S and \bar{c}
C_T	Thrust coefficient based on S ($= T/qS$)
$C_{T'}$	Local thrust coefficient based on S' ($= T/qS'$)
C_μ	Jet momentum coefficient ($= \dot{m}v_j/qS$)
$C_{\mu'}$	Local jet momentum coefficient ($= \dot{m}v_j/qS'$)
F	Factor used in calculating $\Delta C_{L\ AERO}$
G	Corrected gain factor ($\equiv \Delta C_{L\ AERO}/C_\mu \sin(\theta + \alpha)$)
\dot{m}	Jet mass flow rate
q	Free stream dynamic pressure
S	Gross wing area)
S'	Local wing area) FIG 3
t/c	Wing thickness to chord ratio
T	Nozzle gross thrust
v_j	Jet exit velocity
x_{JET}	Longitudinal position of jet exit
x_{REF}	Longitudinal position of moment reference centre
α	Wing incidence
$\Delta C_{D\ AERO}$	Jet induced drag coefficient
$\Delta C_{L\ AERO}$	Jet induced lift coefficient
$\Delta C_{m\ AERO}$	Jet induced pitching moment coefficient
ΔC_m	Total incremental pitching moment due to jet
λ	S'/S
ν	Factor used in calculating $\Delta C_{L\ AERO}$
θ	Angle of jet relative to wing reference plane
σ	Factor used in calculating $\Delta C_{L\ AERO}$

1. INTRODUCTION

As a part of the studies on combat aircraft performance at B.Ae Warton an investigation into the effects of jet-wing interaction has been carried out. Recent U.S. model test data has indicated that significantly beneficial effects on airframe performance may be achieved by taking advantage of the phenomenon and it was one of the aims of the study to identify if the benefits were large enough to justify a full study of all the repercussions on a combat aircraft design.

The beneficial effects of jet-wing interaction have, of course, been known about for many years and there are several aircraft to which they have been applied. Up to the present time, however, the effects have, in general, been obtained through the use of full span blown flaps and have been aimed at improving the aircraft take-off and landing characteristics e.g. Buccaneer. The benefits and the method of obtaining them are illustrated in fig 1 based on data from ref 1. Here a highly deflected flap has a thin jet of low momentum coefficient blown at its leading edge and the improvement which occurs is caused primarily by a boundary layer control effect i.e. the momentum from the jet re-energising the boundary layer on the flap upper surface, avoiding separation and hence giving a very large increase in lift. However, it is also shown that once full attachment of the flow on the flap is achieved further increase in the jet momentum leads to further increased lift though at a lower rate. This is the jet flap effect coming into play: the jet wake acts in a similar manner to an extended flap, giving increased lift through increased circulation induced over the wing; this effect being generally referred to as "super-circulation lift".

One of the problems of full span blown flaps, however, is that the mechanism required is complex, requiring ducting of hot, high pressure air from the engine through the wing to the wing trailing edge and this has probably been the main reason that the blown flap has not seen much wider application. The recent U.S. model test data however (ref 2-7) suggests that the complexity of the blown flap may in fact not be necessary and that at least some of the benefits of jet-wing interaction may be obtained simply by locating the main propulsive jets at the wing trailing edge (fig 2). Here the boundary layer control aspect is omitted, apart from that due to jet entrainment, but the full super-circulation effects are retained. Though fig 1 suggests that these may be small it is to be noted that the momentum of the main propulsive jet is an order of magnitude higher than that generally employed with the blown flap. Also if flap deflections are restricted to relatively low values such as might be used in combat rather than during landing, the boundary layer control aspects become much less important as flap separation is then either non-existent or very small.

A study was therefore put in hand to identify if wing trailing edge location of the main propulsion jets were likely to give significant benefits to aircraft combat performance, to gain some insight into the problems associated with obtaining this improved performance and to attempt to identify aspects of jet-wing interaction which have not been well-covered upto the present time. This paper briefly describes the study and the conclusions drawn from it.

2. DEVELOPMENT OF A PREDICTION METHOD

Initial investigation into ways of correctly estimating the effects of jet-wing interaction on lift, drag and pitching moment, which are the essential prerequisites of a sensible analysis of performance effects, revealed that there was no generally applicable, easy to use theory fully documented in one source. Similarly, examination of available experimental data indicated that it was also not generally applicable and that attempts to correlate the data e.g. via a corrected gain factor (G) had not met with very much success (ref 2). Only the method given in ref 8 was readily available but, on examination, was deemed much too complex a calculation for this type of study.

The starting point of the study was therefore to derive a rapid estimation method, based on theory but with any necessary empiricism, to obtain reasonable predictions of existing experimental data. After suitable investigation it was decided that a good theoretical method was required to obtain sensible estimates of the increments in lift and that drag and pitching moment effects could be evaluated from this calculated lift with relative ease based on empiricism. The theory of Maskell and Spence (ref 9) modified (via ref 10) for part span effects, fig 3, was therefore chosen for the evaluation of lift increments; drag increments were evaluated by the equation in ref 3; and pitching moment changes were evaluated from consideration of plain flap pitch effects.

2.1 Estimation Method for ΔC_L AERO

From ref (10) we have for a high aspect ratio jet flapped wing with zero flap chord:

$$C_L = F \left[(1 + (t/c)) \left(\lambda \theta \left(\frac{dC_L}{d\theta} \right) + \nu \alpha \left(\frac{dC}{d\alpha} \right) \right) \right] - t/c C_{\mu'} (\theta + \alpha) \quad (1)$$

$$\text{where } F = \left(A + \frac{C_{\mu'}}{\pi} \right) / \left(A + \frac{2}{\pi} \left(\frac{dC_L}{d\alpha} \right)_{\infty} - 2(1 + \sigma) \right) \quad (2)$$

$$\left(\frac{\partial C_L}{\partial \alpha} \right)_{\infty} = 2\pi (1 + 0.151 \sqrt{C_{\mu'}} + 0.219 C_{\mu'}) \quad (3)$$

$$\left(\frac{dC_L}{d\theta} \right) = \sqrt{(4\pi C_{\mu'} (1 + 0.151 \sqrt{C_{\mu'}} + 0.139 C_{\mu'}))} \quad (4)$$

$$\nu = \left[S' \left(\frac{dC_L}{d\alpha} \right)_{\infty} + (S - S') \left(\frac{dC_L}{d\alpha} \right)_{C_{\mu} = 0} \right] / S \left(\frac{dC_L}{d\alpha} \right)_{\infty} \quad (5)$$

S' and S are the relevant wing areas as shown in fig 3. Examining the above equations indicates that several simplifications are possible:

1. For a convergent nozzle at low pressure ratio $C_{\mu}' \approx C_T'$
2. For thin wings $t/c \approx 0$
3. To give $\Delta C_{L \text{ AERO}}$, $\nu \alpha \left(\frac{dC_L}{d\alpha} \right)_{\infty}$ is replaced by $\alpha \left(\nu \left(\frac{dC_L}{d\alpha} \right)_{\infty} - 2\pi \right)$ in equation (1)
4. $\left(\frac{dC_L}{d\alpha} \right)_{C_{\mu} = 0} = 2\pi$ so that equation (5) reduces to $\nu = \left(S' \left(\frac{dC_L}{d\alpha} \right)_{\infty} + (S - S') 2\pi \right) / S \left(\frac{dC_L}{d\alpha} \right)_{\infty}$

$$\text{and hence the simplification 3 reduces to } \alpha \left(\nu \left(\frac{dC_L}{d\alpha} \right)_{\infty} - 2\pi \right) = \alpha \frac{S'}{S} \left(\left(\frac{dC_L}{d\alpha} \right)_{\infty} - 2\pi \right)$$

5. Subtract $C_T \sin(\theta + \alpha)$ from equation 1 to give $\Delta C_{L \text{ AERO}}$

6. $\sigma \approx 0$

Hence equations 1 to 5 reduce to:

$$\Delta C_{L \text{ AERO}} \approx F \left(\lambda \theta \left(\frac{dC_L}{d\theta} \right) + \alpha \frac{S'}{S} \left(\left(\frac{dC_L}{d\alpha} \right)_{\infty} - 2\pi \right) \right) - C_T \sin(\theta + \alpha) \quad (6)$$

$$\text{where } F = \left(A + \frac{2C_T'}{\pi} \right) / \left(A + 2\pi \left(\frac{dC_L}{d\alpha} \right)_{\infty} - 2 \right) \quad (7)$$

$$\left(\frac{dC_L}{d\theta} \right) = \sqrt{4\pi C_T' (1 + 0.151\sqrt{C_T'} + 0.139 C_T')} \quad (8)$$

$$\left(\frac{dC_L}{d\alpha} \right)_{\infty} = 2\pi (1 + 0.151\sqrt{C_T'} + 0.219 C_T') \quad (9)$$

2.2 Estimation Method for $\Delta C_{D \text{ AERO}}$

Reference 3 suggested that $\Delta C_{D \text{ AERO}}$ can be calculated from

$$\Delta C_{D \text{ AERO}} = \frac{(C_{L \text{ JET OFF}} + \Delta C_{L \text{ AERO}})^2 - C_{L \text{ JET OFF}}^2}{0.75 \pi A} \quad (10)$$

and this equation was adopted unmodified.

2.3 Estimation Method for ΔC_m

Assuming that a jet emerging from a wing trailing edge is acting in a manner similar to a mechanical flap then, using data sheets, it can be shown that the increment in lift acts at approximately the 50% chord position of the wing area S' i.e.

$$\Delta C_{m \text{ AERO}} = - \left(\frac{x_{50\%S'} - x_{\text{ref}}}{\bar{c}} \right) \cdot \Delta C_{L \text{ AERO}}$$

In order to allow for the direct effect of the jet for trimming purposes a further term can be added to give

$$\Delta C_m = - \left(\frac{x_{50\%S'} - x_{\text{ref}}}{\bar{c}} \right) \cdot \Delta C_{L \text{ AERO}} - C_T \sin \theta \left(\frac{x_{\text{jet}} - x_{\text{ref}}}{\bar{c}} \right) \quad (11)$$

3. EFFECT OF REDUCED SPAN JET ON JET-INDUCED LIFT

In order to determine whether the study was worth proceeding with it was deemed necessary to check the primary effect of using the main propulsive jet i.e. of much lower than full span, on the predicted incremental lift. In fig 4 the variation of lift with jet affected wing area (S'/S) is shown as a

percentage of the lift obtainable with a full span jet. Typically, for a reheated combat aircraft engine mounted at the wing trailing edge, S'/S would lie between 0.15 and 0.3. From fig 4 it can be seen that between 25% and 45% of the effect of a full-span jet would be obtained. This result, plus the previously mentioned fact that the momentum of the propulsive jet is an order of magnitude greater than that generally used with full span blown flaps, led to the conclusion that location of the propulsive jet at the wing trailing edge was likely to give very useful improvements in lift.

4. COMPARISON OF EXPERIMENTAL RESULTS WITH PREDICTION

There is a large amount of jet wing interaction data now available and it is not possible to present comparisons for all of this. The following therefore deals with two examples chosen as being most representative of the type of configuration most likely to be used in conjunction with jet wing interaction.

4.1 Lift and Drag Increments

In reference 6 results are presented for the effects of jet-wing interaction over a range of incidence angles likely to be met during combat and with jet deflection effects included. The increments in lift obtained are reproduced in fig 5 along with the predicted values. As can be seen good agreement is achieved which is very encouraging when one considers all the variables which influence the magnitude of the induced lift in a real situation. It is also notable that without jet deflection the effects are very small. Similarly, using the method to predict the effect on the drag polar of the jet wing interaction shows (fig 6) that sensible values are obtained and leads to the conclusion that J.W.I. effects can be predicted with reasonable confidence. Note that direct thrust effects have been removed.

Fig 6 also illustrates the main effects of J.W.I.:

- . little change in the drag polar below the drag break
- . significant increase in the lift coefficient at which the drag break occurs.
- . increased maximum lift coefficient
- . large reductions in induced drag at lift coefficients above that corresponding to the zero jet effects drag break e.g. at a C_L of 2 a 26% reduction is achieved experimentally, with 21% being predicted.

These results were obtained at a comparatively low jet momentum coefficient (0.2). Further results have been obtained recently at BAe Warton for much higher momentum coefficients (~ 3.5) with jet deflection, and examples of the increases in lift achieved are given in fig 7 at low incidence and fig 8 at high incidence compared with the predicted values.

The increments in fig 7 show good agreement with the predicted values up to a momentum coefficient of approximately 2 with the measured values increasing significantly above prediction at higher momentum. The reason for this increase is not known at present but is most likely due to a boundary layer control effect coming into play as the jet entrainment is increased. At 40° incidence (fig 8) the prediction and measurement show reasonable agreement up to a jet momentum of 0.5 to 0.6; in this case the measured values are much lower than the prediction at greater jet momentums. Again the reason for the difference between measurement and experiment is not known but it is possible that it is due to a breakdown of the wing flow.

The effect of the jet on the drag polar for the cases given in figs 7 and 8 are shown for a jet momentum of 0.5 in fig 9. Here agreement between prediction and experiment is excellent though it should be noted that this is for a jet momentum value where the lift increment is also well predicted.

It is to be noted that the effect on the drag polar of the jet wing interaction is very similar in both figs 6 and 9 i.e. the most significant effect is an increase in the lift coefficient at which the drag break occurs, giving a large reduction in induced drag at high lift.

4.2 Pitching Moment

The comparison of predicted and measured pitching moment for the case of figs 5 and 6 is given in fig 10. Agreement here is very good, indicating that the approximation obtained from simple consideration of mechanical flaps is justified providing extreme accuracy is not required.

4.3 Overall

Other test data was examined and compared with prediction. In general it was found that the method gave reasonable prediction of lift, drag and pitching moment changes, and hence a suitable aircraft configuration was chosen to identify as far as possible the overall effects on aircraft performance. It was notable however, that one of the configurations against which the method was checked (fig 2 configuration 4 + ref 2) consistently gave induced jet effects well below prediction. At present, although reasons for this loss of jet induced effects can be suggested, no solution can be offered - it can only be recommended that if full jet wing interaction is found to be a desirable feature then this type of configuration is to be avoided.

5. APPLICATION OF PREDICTION METHOD TO A COMBAT AIRCRAFT CONFIGURATION

5.1 Configuration

The results from the predictions for a wing-body indicated that the jet wing interaction gave, especially when combined with the direct forces of a deflected jet, significant nose down pitching moment (fig 10). This obviously has to be trimmed out for a full aircraft configuration and it can be seen that with a conventional aft-tailed aircraft very large penalties are likely to be incurred due partly to the loss in total lift and partly to the increase in trim drag (fig 11). If a foreplane is used, however,

simple consideration of the balancing of the aircraft suggests that the nose down pitching moment may be turned to advantage as it gives increased foreplane lift leading, at higher incidences, to a significant increase in total lift.

A canard configuration was therefore chosen as the most suitable vehicle for evaluation of jet-wing interaction effects on performance and a schematic of the aircraft planform is given in fig 12.

5.2 Effect of J.W.I. on the trimmed drag polar

Two cases were considered:

1. Aircraft balanced to give minimum trim drag at low lift i.e. neutrally stable foreplane off, with nozzle deflection being used at the higher lift coefficients.
2. The same aircraft as in 1 but balanced to give maximum lift at high incidence i.e. with a forward position of the c.r. and having no jet wing interaction or jet deflection capability.

The resulting trimmed drag polars for these two cases are shown in figs 13 and 14 for $M = 0.4$ and $M = 0.2$ respectively and several interesting effects are apparent: For $M = 0.4$ (fig 13)

- . at low lift coefficients, i.e. during cruise, the aircraft balanced for minimum trim drag (case 1) has an induced drag that is 20% below its high-lift trimmed companion (case 2).

- . Case 2 would have a maximum lift 13% greater than case 1 if the benefits of J.W.I. on case 1 were not present

- . For case 1 the effect of 30° jet deflection is to give an increase in maximum lift of approximately 40% relative to the same case without jet deflection or J.W.I.

- . The benefits of J.W.I. are very small without a deflecting nozzle capability.

For $M = 0.2$ (fig 14) it was found that jet deflection must be limited due to a lack of foreplane trim power. However, as the jet momentum coefficient was approximately 4 times that of the $M = 0.4$ value the jet induced effects are much greater for a given jet deflection. Fig 14 shows in fact that these two effects cancelled out so that the overall effects at $M = 0.2$ and $M = 0.4$ are very similar. It should be noted that foreplane trim power could be increased by, for example, a larger foreplane if it were thought necessary to have greater lift at the lower Mach numbers. For this study however the foreplane size was kept at the original value chosen.

In view of the poor relative induced drag at low lift for case 2 i.e. the aircraft balanced to give maximum lift at high incidence, this case was dropped from the study as it was not felt to be a satisfactory alternative to the aircraft in case 1. The study was therefore restricted to a comparison between the aircraft of case 1 with jet deflection and J.W.I. and the same aircraft but with no jet deflection or jet wing interaction.

5.3 Effect of Jet Wing interaction on Airframe efficiency

Airframe efficiency, measured by total (i.e. thrust included) lift-drag ratio, as a function of total lift is given in fig 15. This figure shows quite clearly that the main benefit is obtained at high lift coefficient i.e. $Cl_{TOT} > 1.9$ and that if 30° jet deflection is retained at lift coefficients below this value significant penalties result, primarily due to the lack of a beneficial jet induced effect coupled with the loss in axial thrust of the deflected jet. This penalty is quite simply removed, of course, by reducing the jet deflection at lower lift coefficients and hence is not significant.

Fig 15 also clearly shows the improvement in maximum lift obtainable with J.W.I. and jet deflection and it is interesting to examine the breakdown of this lift increase. In fig 16 it is seen that the J.W.I. component of lift whilst being significant is in fact only 35% of the total improvement obtained. The remainder of the improvement is due to the increase in trim lift and in direct jet lift.

6. EFFECT OF JET-WING INTERACTION ON COMBAT AIRCRAFT OPERATIONAL PERFORMANCE

6.1 Sustained and attained turn rate

It has been shown that although there may be some effect on drag at low lift it is small. The largest effects are clearly at the high lift end of the drag polar and hence appear as changes in sustained turn rate, where thrust and drag are equal, and in attained turn rate where lift is at its maximum value.

At low altitude, however, as Mach number is increased the attained turn rate is determined by structural limitations and also the sustainable lift coefficient reduces rapidly as the thrust coefficient reduces with increasing Mach number. In fact for this configuration above approximately $M = 0.4$ the maximum sustainable lift coefficient is below that corresponding to the break in the drag polar above which jet induced effects give a benefit. At Mach numbers below 0.4 the sustainable lift increases rapidly until at a Mach number slightly below 0.2 the sustainable and attainable lift coefficient are equal. Note that the precise Mach numbers are very dependent on configuration and would change for different engine/airframe combinations. These effects are summarised in fig 17 at low altitude to indicate that jet wing interaction plus jet induced effects give an improvement on sustained turn rate below approx $M = 0.4$, whilst the improvement in attained turn rate is effective below approximately $M = 0.55$.

At high altitude the situation is similar (fig 18) but the 'g' limit is above that corresponding to the maximum attainable turn rate, even with jet induced effects included, up to at least $M = 0.9$ - but it should be noted that this figure does not allow for any Mach number effects on the jet induced lift prediction.

6.2 Combat Performance

Studies at BAe Warton using the one on one combat simulator, wherein pilots are able to fly against a computer driven model, have shown that three performance parameters stand out as having major significance in air combat. Specific excess power $((T - D) V/W)$ at high speed, low level, which is a measure of the aircraft's ability to accelerate, was found to be important especially in the initial stages of the combat.

During the combat the aircraft tended to be used in the region between max sustainable and max attainable turn rate in an attempt to turn inside an opponent. This pointed to peak attainable turn rate as the important parameter. As the combat continued towards its final stages and as a result of flying in the region between max sustainable and peak attainable i.e. where drag is greater than thrust, the encounter gradually loses height until, as the lower altitudes are reached, speed rather than altitude is sacrificed. Hence the final stage of the combat is at low speed low altitude where the ability to turn more quickly than an opponent without losing speed i.e. a better sustained turn rate, becomes of major importance.

On the basis of this type of reasoning and with the supporting evidence of the combat simulation results a combat correlation parameter (C.C.P.) was derived which showed that shots ratio i.e. the difference in the number of firing chances for each aircraft divided by total number of firing chances was a function of S.E.P. at $M = 0.9$, S.L., Peak attained turn rate at S.L. optimum Mach number and attained turn rate at $M = 0.7$ sea level, the parameters covering acquisition, combat, and final stage of combat respectively. i.e. $\text{SHOTS RATIO} = \text{S.E.P.}^a M = 0.9 \text{ S.L.} \times \text{A.T.R.}^b \text{PEAK S.L.} \times \text{S.T.R.}^c M = 0.75 \text{ S.L.}$

As far as jet wing interaction effects are concerned it can be seen that, though there is no effect on high speed S.E.P., the effects on the other two parameters are very significant. Application of the combat correlation parameter to the S.T.R./TR relationship given in fig 17 and using the zero jet deflection, zero jet effects aircraft as baseline produces the effect shown in fig 19. This figure shows that an aircraft with jet deflection capability and jet-wing interaction has a C.C.P. approximately 80% greater than that of the same aircraft without these benefits. This leads to a shots ratio advantage of the J.W.I. aircraft of 0.45 - a very large advantage.

However, the deflecting nozzles required introduce a fairly significant weight penalty, and this must be allowed for. Fig 19 shows that the advantage in shots ratio is still very large however, approximately 0.3, and would suggest that an aircraft equipped with a deflecting nozzle and taking advantage of beneficial jet wing interaction would, in close combat, be in a good firing position twice as often as that of the same aircraft not so equipped.

7. OTHER FACTORS AFFECTING JET-WING INTERACTION

An overall summary of the findings of the report is given in fig 20 but it should be realised that these findings are based on the overall assumption that the jet wing interaction effects have been adequately predicted and will be achieved on a real aircraft in flight. Although attempts have been made to account for the prime factors which significantly affect the magnitude of J.W.I. many have not been allowed for, mainly because no adequate theoretical method appears to exist but also because of the lack of directly applicable experimental data.

A number of possible factors are shown in fig 21, with an indication of the probable effect on the findings of the study. Taking one of these, it is suggested that effects at high Mach number i.e. close to $M = 1.0$ may be favourable. Some evidence in support of this is available in reference 11 reproduced here as fig 22. The data indicates that at $M = 0.9$ a deflected jet from the wing trailing edge affects the upper surface shock in a favourable manner, moving it aft and decreasing its strength. It would seem likely, therefore, that the presence of a trailing edge jet will make design of a good transonic wing somewhat simpler and could allow slightly higher Mach numbers to be reached before significant drag rise occurs.

8. CONCLUSIONS

An investigation into the effect of jet-wing interaction on combat aircraft performance has led to the development of a prediction technique which appears to give reasonable estimates of the more significant changes which occur. Use of the prediction technique has shown that a conventional propulsive jet at the wing trailing edge gives a significant improvement in the high lift characteristics of the wing providing jet deflections of up to 30° can be provided.

Application of the predicted effects to a projected aircraft showed that the best configuration would be the canard, to provide beneficial trim effects of the deflected thrust, and that large improvements in sustained turn rate at low speed and in peak attained turn rate at low level would be obtained. The nett result of the improved turn rates is a very large increase in combat effectiveness, assessed by means of a combat correlation parameter, even when the weight penalty associated with the required deflecting nozzles is included.

9. FURTHER WORK

The study has revealed the major effects of jet-wing interaction on combat performance via a theoretically based prediction technique adequate for this purpose. However many factors exist which are not properly accounted and which may influence the overall aircraft performance to a significant extent. The first priority for further work must therefore be to extend the scope of the theoretical method to accurately account for as many of the other factors as possible.

In support of this development, experimental measurements will be required, firstly to provide data for comparison purposes and secondly to allow for factors which may not be adequately accounted for theoretically e.g. effect of jet vertical location. In view of the fact that current data appears to be specific to a particular configuration with, in general, only small variations of geometry, parametric

investigations would appear to be the order of the day so that the effect of gross variations may be examined. Experiments of this nature would have the twin advantages of relative simplicity and wide application and would form, when coupled with a developed theoretical method, a powerful tool at the aircraft designers disposal, enabling a good assessment of the overall benefits of jet wing interaction effects to be carried out.

10. REFERENCES

1. MALAVARD L,
POISSON-QUINTON, PR.,
JOUSSERANDOT, P.

C.N.E.R.A. TN37
1956

Recherches theoriques et experimentales sur le controle
de circulation per soufflage appliques aux ailes d'avions
2. CAPONE F. J.
NASA TND8039
DECEMBER 1975

The effects on propulsion induced aerodynamic forces of
vectoring a partial span rectangular jet at Mach numbers
from 1.2 to 2.0
3. SEDGEWICK T. A.
AIAA 75-1319
OCTOBER 1975

Investigations of non-symmetric two dimensional nozzles
installed in twin engined tactical aircraft.
4. BOWER, D. L.,
BUCHAN, F.
AIAA 78-1082
JULY 1978

An investigation of the induced aerodynamic effects of a
vectored non-axisymmetric exhaust nozzle.
5. BRADLEY R. G.,
JEFFRIES R. R.,
CAPONE F. J.
AIAA 76-917
SEPTEMBER 1976

A vectored engine over the wing propulsive lift concept
6. THOMAS, J. L.,
PAULSON, J. W.,
YIP, L. P.,
JOURNAL OF AIRCRAFT
MAY 1978

Deflected thrust effects on a close-coupled canard
configuration
7. CORSON, B. W.,
PUTNAM, L. E.,
NASA TMX-2309
AUGUST 1971

Lift induced on a swept wing by a two-dimensional partial
span deflected jet at Mach numbers from 0.2 to 1.3
8. DATCOM
SECTION 6
JANUARY 1974

Symmetrically deflected flaps and control devices on
wing - body - tail configurations
9. MASKELL E. C.
SPENCE D. A.
PROC. of ROYAL SOCIETY
SERIES A 1959

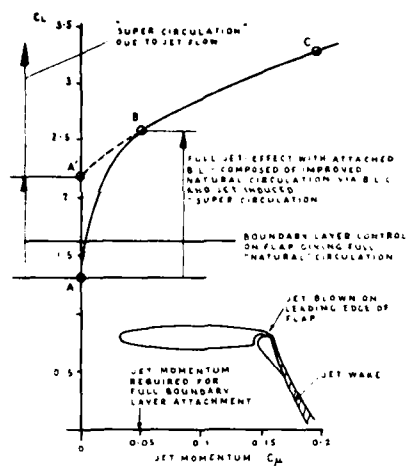
A theory of the jet flap in three dimensions
10. WILLIAMS, J.,
BUTLER, S. F. J.,
WOOD M. N.
R.A.E. AERO 2646
JANUARY 1961

The aerodynamics of jet flaps
11. GRAHAME, W. E.,
HEADLEY, J. W.,
ROGERS, L. W.,
AGARD CP83-71
PAPER 6

Recent experience in the transonic testing of two-dimensional
swept and straight wings with high lift devices.

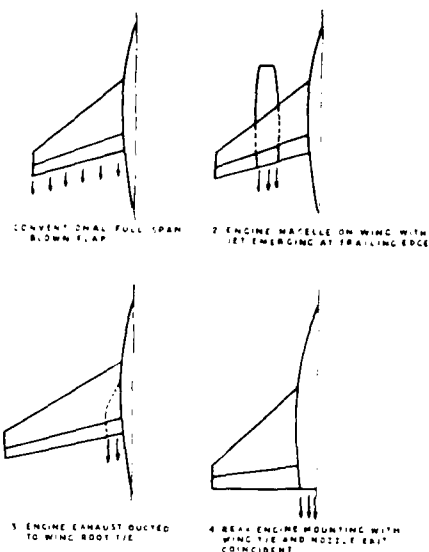
11. ACKNOWLEDGEMENTS

Grateful thanks are extended to my colleagues at British Aerospace for their assistance during the preparation of the various phases of the report. I would also like to thank the Grumman Aerospace Corporation, Bethpage, New York for allowing the use of a powered wind tunnel model from which some of the results presented were obtained.



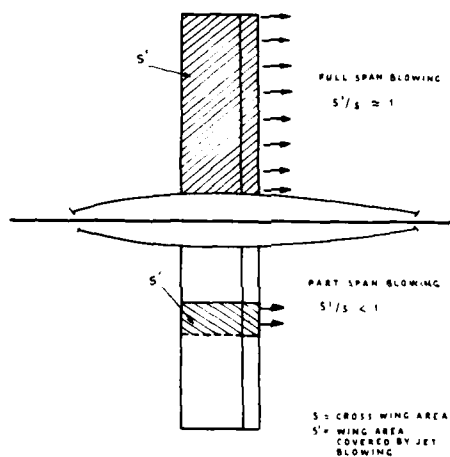
JET FLAP EFFECT ON LIFT

FIG 1

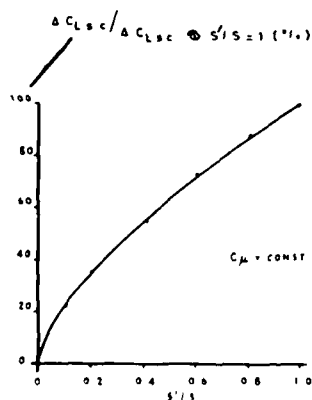


POSSIBLE CONFIGURATIONS TO TAKE BENEFIT OF BENEFICIAL JET-WING INTERACTION

FIG 2

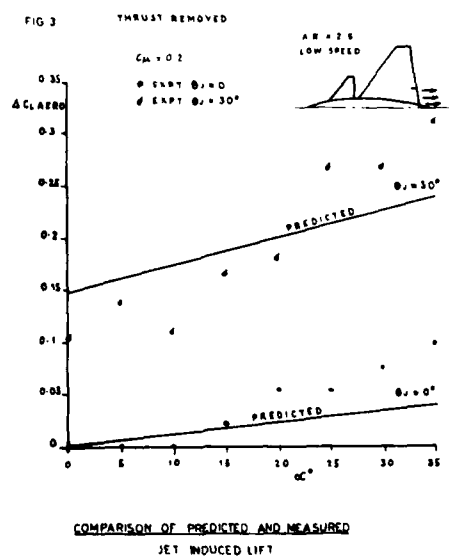


CONCEPT OF PART-SPAN JET BLOWING



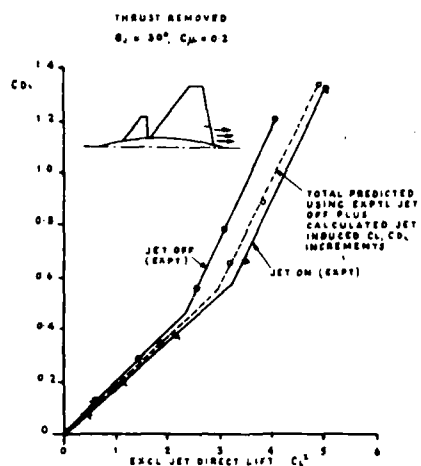
EFFECT OF PART-SPAN BLOWING ON SUPER CIRCULATION EFFECT

FIG 4



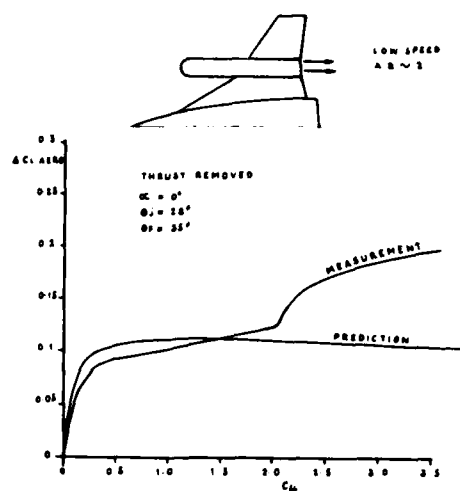
COMPARISON OF PREDICTED AND MEASURED JET INDUCED LIFT

FIG 5



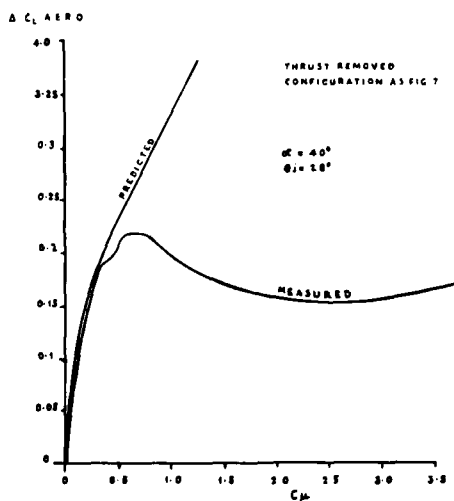
COMPARISON OF PREDICTED AND MEASURED JET-
INDUCED EFFECTS ON INDUCED DRAG POLAR

FIG 6



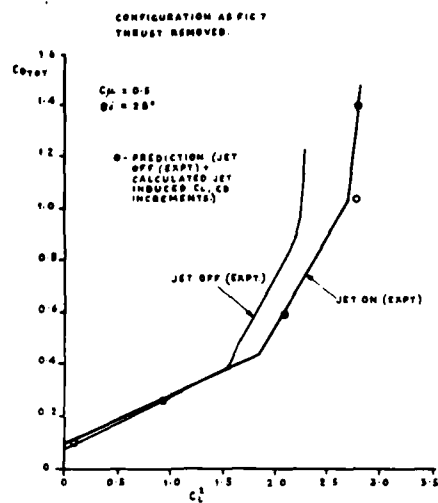
COMPARISON OF PREDICTED AND MEASURED
JET INDUCED LIFT

FIG 7



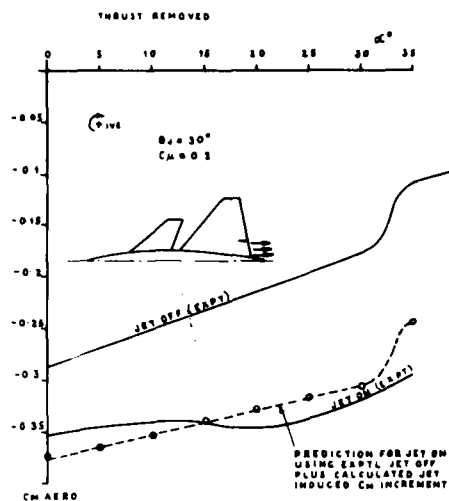
COMPARISON OF PREDICTED AND MEASURED
JET INDUCED LIFT

FIG 8



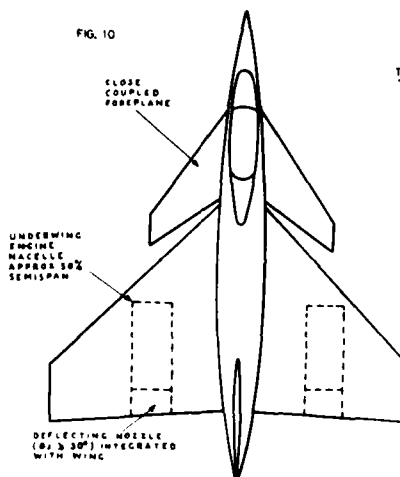
COMPARISON OF PREDICTED AND MEASURED JET INDUCED
EFFECTS ON INDUCED DRAG POLAR

FIG 9



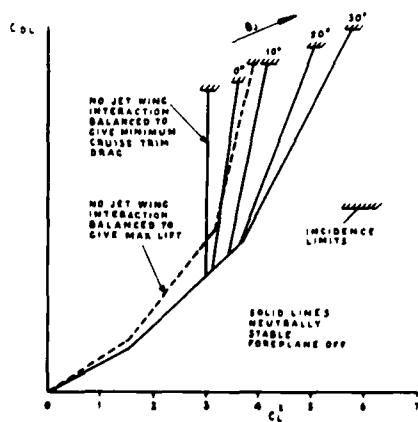
COMPARISON OF PREDICTED AND MEASURED
JET INDUCED PITCHING MOMENT

FIG. 10



CANARD CONFIGURATION FOR JET WING
INTERACTION STUDIES

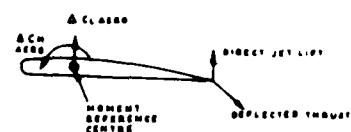
M=0.4
THRUST REMOVED



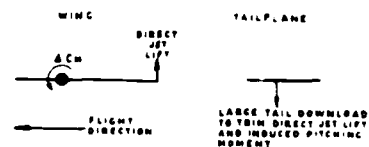
PREDICTED TRIMMED INDUCED DRAG POLAR
FOR CANARD CONFIGURATION
WITH JET ENHANCEMENT

FIG. 13

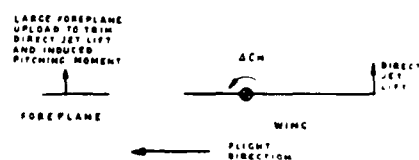
1 INCREMENTAL INDUCED EFFECTS ON WING



2 CONVENTIONAL AIRCRAFT REQUIREMENTS TO TRIM JET INDUCED EFFECTS



3 CANARD AIRCRAFT REQUIREMENTS TO TRIM JET INDUCED EFFECTS

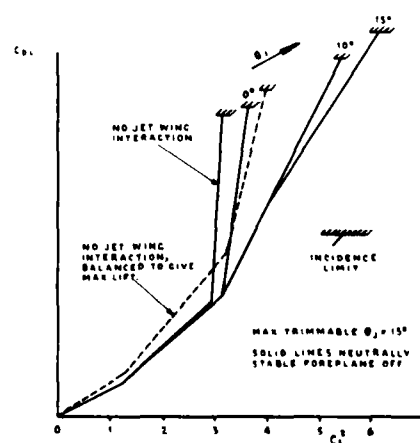


TRIM CONSIDERATIONS WITH JET INDUCED EFFECTS

FIG. 11

FIG. 12

M=0.2
THRUST REMOVED



PREDICTED TRIMMED INDUCED DRAG POLAR
FOR CANARD CONFIGURATION
WITH JET ENHANCEMENT

FIG. 14

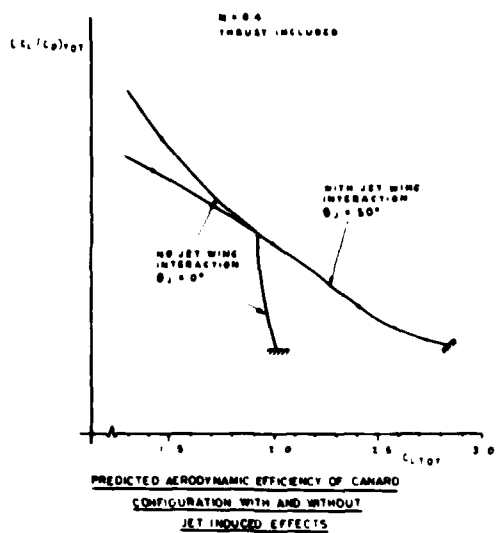


FIG 15

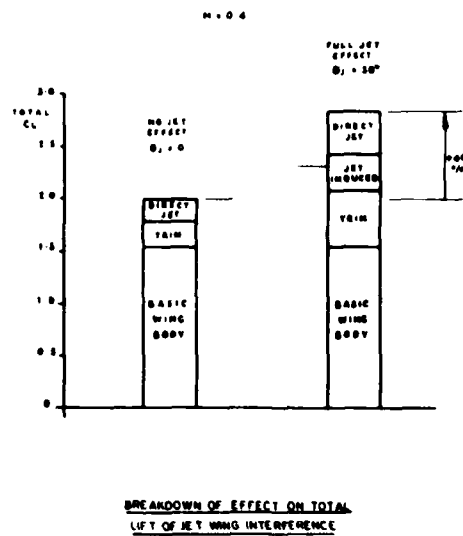


FIG 16

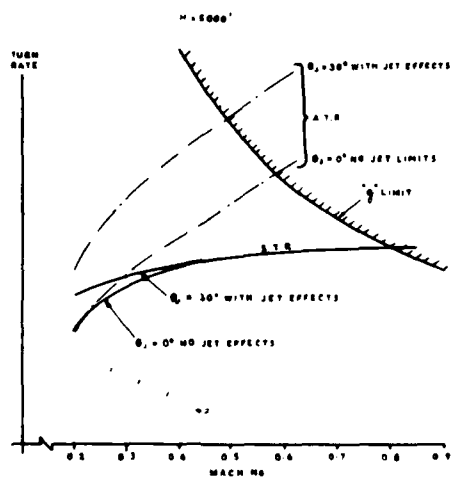


FIG 17

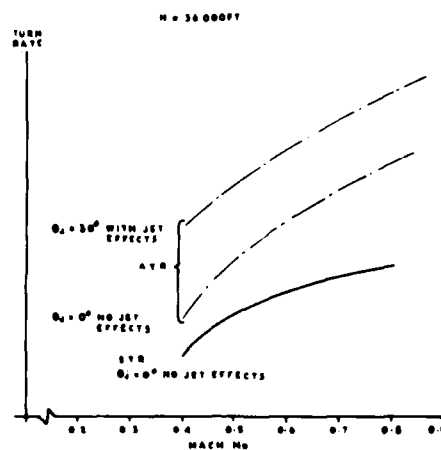
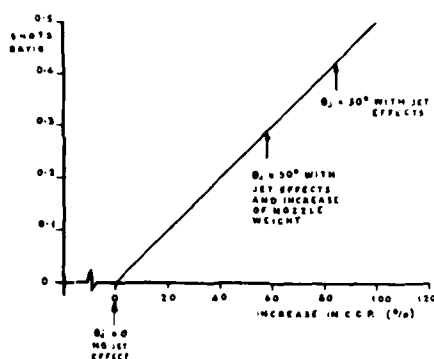


FIG 18

$$CCP = SEPL \times STRJ \times ATW^2$$



PREDICTED EFFECT OF JET
ENHANCEMENT ON COMBAT CORRELATION PARAMETER

FIG 19

CURRENT THEORY GIVES REASONABLE AGREEMENT
WITH EXPERIMENT

LARGE GAINS ACHIEVABLE USING CONVENTIONAL
MAIN ENGINE NOZZLE INTEGRATED WITH WING
RATHER THAN FULL SPAN THIN JET

EFFECTS ARE SIGNIFICANTLY INCREASED
WITH A DEFLECTED JET

BEST CONFIGURATION IS THE CANARD

LIFT IMPROVEMENT THROUGH JET WING
INTERACTION, FOREPLANE LIFT TO TRIM AND
DIRECT JET LIFT

MAJOR EFFECT ON AIRCRAFT IS LARGE
GAIN IN COMBAT EFFECTIVENESS AT LOW
SPEED LOW LEVEL

LITTLE OR NO EFFECT FOR CRUISING FLIGHT

SUMMARY OF EFFECTS OF JET WING INTERACTION

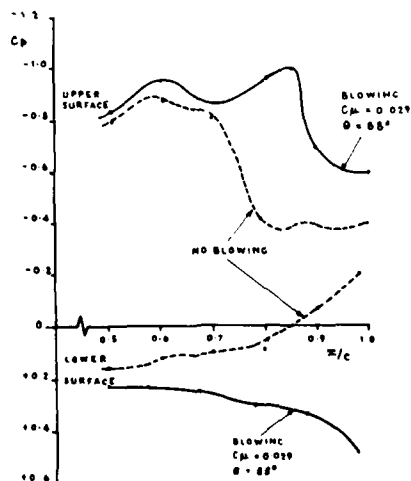
FIG 20

ITEM NO	CONFIGURATION CHANGE/ OPERATING REGIME	PROBABLE EFFECT
1	NOZZLE SHAPE: CIRCULAR OR RECTANGULAR	FAVOURABLE TO RECTANGULAR
2	IMPROVED HIGH LIFT DEVICES	FAVOURABLE
3	SPANWISE JET LOCATION	FAVOURABLE TO INBOARD POSITION
4	INDUCED DRAG AT LOW LIFT COEFFICIENTS	?
5	THICK JET	UNFAVOURABLE
6	VERTICAL SEPARATION BETWEEN JET AND WING TRAILING EDGE	UNFAVOURABLE
7	LONGITUDINAL SEPARATION BETWEEN JET AND WING TRAILING EDGE	UNFAVOURABLE
8	PROXIMITY OF CONTROL SURFACES	?
9	HIGH MACH NO	FAVOURABLE
10	EFFECT OF REYNOLDS NO	?

CONFIGURATIONAL AND OPERATIONAL
DETAILS REQUIRING FURTHER INVESTIGATION

FIG 21

SOURCE: AGARD CP83-11 PARA 7 FIG 15
M=0.9, $\alpha=6^\circ$



EFFECT OF WING TRAILING EDGE
JET ON HIGH SUBSONIC PRESSURE DISTRIBUTION

FIG 22

JET/WING INTERFERENCE FOR AN OVERWING ENGINE CONFIGURATION

Dr. R.A. Sawyer
 University of Salford, Salford M5 4WT, U.K.
 and
 M.P. Metcalfe
 British Aerospace, Manchester, U.K.

SUMMARY.

Low speed wind tunnel tests on the interference between a powered jet and a two-dimensional wing have been carried out. Detailed pressure distributions over the wing are presented for jet to free stream velocity ratios of 2:1, 3:1 and 5:1, over a range of incidences. The configuration of the jet nozzle, wing section and the relative positions of the engine and the wing, correspond to a moderate by-pass ratio engine mounted over the wing of a low-wing feeder liner aircraft.

Large increments in upper surface pressure coefficient (ΔC_p up to -0.9) due to the jet are found, and in all cases these result in positive increments to wing lift with some increase in wing drag. Changes in the relative incidence and in the stream-wise displacement of engine to wing do not give extra beneficial effects.

Entrainment rates into the jet and the path of the jet relative to the wing have been established by measurement and by flow visualisation.

Theoretical considerations show that it is the bound vorticity associated with jet curvature which produces the pressure increments on the wing surface, and that trailing vortex and jet entrainment effects are for the most part negligible.

INTRODUCTION.

This investigation was prompted by the proposal to replace the turbo-prop engines on the BAe. 748 by jet engines. These would have to be mounted above and ahead of the wings so that there will be a considerable interference effect between the jet efflux and the upper surface of the wing. Computer programmes to calculate wing/nacelle/pylon interference have been relatively unsophisticated in the modelling of the jet efflux (see Hardy (1), for example) and often treat the jet as a straight, round, constant velocity body of fluid with little attempt to represent entrainment into the jet or distortion of the jet cross-section. It is known from experimental and theoretical work on jets blowing across a stream, that the pressures on adjacent wing surfaces may be predicted by modelling the jet path, the jet blockage and entrainment, and the jet trailing vortices (as shown by Tipping (2) and other workers). Although in this present application the distortion of the jet may be very much smaller, a similar treatment of the jet development could be necessary. The overwing location of engines has positive benefits as regards reduction in jet noise at the ground, as well as favourable aerodynamic interaction with the wing, and it is therefore necessary to establish the magnitude of the interference effects and to improve computer programmes so that these effects may be predicted with greater accuracy. This present investigation concentrates on the wing upper surface pressure distribution, the changes produced by the relative velocity of the jet efflux to the free stream and the effects of changes in overall incidence of the wing and engine.

DESCRIPTION OF APPARATUS.

All the experiments were performed in the 3' x 4' Low Speed Wind Tunnel at the University of Salford, with the model inverted to allow the wing to be mounted on the tunnel's external mechanical balance, and the engine nacelle supporting brackets to be attached to the bottom turntable. The datum position of the nacelle and wing (shown in figure 1) corresponded to a projected overwing mounting of a turbofan of moderate bypass ratio on a low wing feedliner.

The wing as designed had a constant cross-section identical in shape to that at the engine location on the full scale aircraft to aid possible computer simulation and to eliminate any effects that taper might have on the pressure distribution. A 1/10 scale was chosen to allow sufficient detail to be simulated, whilst staying within the constraints of the tunnel cross-section, which gave an 0.28 m chord and 1.12m span wing. The aerofoil has a maximum thickness/chord ratio (t/c) of 0.17 and

has an incidence of 2.6° to the aircraft zero incidence setting. The wing had a series of brass tubes laid into it, running spanwise, at $x/c = 0.1$ and every $0.1c$ to $x/c = .9$ on the upper surface and from $x/c = 0.1$ to $x/c = 0.8$ with a similar spacing on the lower surface. Pressure tapings were drilled into each of these at 9 stations on the lower surface (4 each side of the engine nacelle centre line) at intervals of 0.2 in y/c , and at 11 stations on the upper surface, at $y/c = 0.1, 0.2, 0.3, 0.5$ and 0.8 either side of the nacelle centre-line. To take the chordwise pressure distribution at any particular span position therefore required covering the pressure tapings with adhesive tape.

The engine efflux was simulated by feeding compressed air (from a centrifugal blower) through the support strut to the nozzle. As only cases of the engine forward of the wing were considered, it was only necessary to simulate the jet exit flow (according to Hardy (1)), a long cylindrical forebody being quite a good approximate representation of the intake airflow streamline. To be representative of a modern turbofan of moderate by pass ratio, it was decided to simulate both the fan and jet exhaust velocities, and to include an exhaust diffuser. The size of the exhaust diffuser was obtained by scaling a suitable full-size drawing. A typical turbofan for installation to a low-wing feederliner had jet/fan velocity ratios of between 1.33 and 1.57 through its flight regime. This was simulated, using standard diameter pipes, by the design shown in figure 2., and a comparison of compression areas and exit areas gives a theoretical jet/fan velocity ratio of 1.38 .

The wing was mounted inverted in the tunnel by means of pivots at the $\frac{1}{4}$ chord position and a tail arm to the pitching moment strut. The simulated engine nacelle was held in a collar which in turn could be moved along a circular arc mounting bracket beneath the tunnel floor. By making the centre of the arc lie on the wing pivot line, this enabled both wing and engine to be rotated relative to the tunnel flow whilst keeping the same relative incidence and displacement if required. The whole jet nozzle was sleeved onto the cylindrical forebody to allow alterations in the streamwise displacement of nozzle and wing.

EVALUATION OF JET ENTRAINMENT VELOCITY.

(i) Theoretical Analysis

A free jet occurs when a fluid is discharged from a nozzle or orifice into an unbounded volume of otherwise undisturbed fluid. Disregarding very small velocities of flow, the jet becomes completely turbulent at a short distance from the point of discharge, and because of the turbulence the emerging jet becomes partly mixed with the surrounding fluid at rest. Particles of fluid from the surroundings are then carried away by the jet so that the mass flow increases in a downstream direction. The velocity of these particles of fluid can be resolved into 2 components, one parallel to the recognised jet boundary, which becomes the streamwise jet velocity, and one normal to the boundary, the jet entrainment velocity.

If a smooth and sufficiently large nozzle is used, however, the initial flow immediately in front of the aperture will be a uniform laminar jet of the same diameter as the aperture separated from the surrounding undisturbed fluid by a very thin boundary layer. The boundary layer becomes thicker, with increasing downstream distance, due to the action of molecular viscosity, and the thickness of the region of appreciable mean velocity gradient becomes so large that the motion is unstable to small disturbances and the flow becomes turbulent. Eventually the turbulent mixing region interacts with all the constant velocity core and fully developed turbulent flow is then established.

Analysis of such a flow by Schlichting (3) shows that, in the fully developed turbulent flow, the jet radius r_j , is proportional to x (axial distance), and maximum axial velocity U is proportional to $1/x$. Townsend (4) computed the distribution of the radial mean velocity in a circular jet for different radial distances r , and plotted it non-dimensionally against r/r_j . Close to the axis v/U was positive, i.e. the mean velocity normal to the flow axis was towards the jet boundary, but as u/U decreased v/U became negative, reaching a value of $v/U_m = -0.024$ at the jet boundary.

This is very close to the values of v/U quoted by Krenz (5) who obtained the following formulae by considering mass flow rates at different positions along the jet and calculating the necessary increase in flow per unit area of jet boundary:-

Mass flow rate through the nozzle or orifice (d is orifice diameter).

$$\dot{m}_j = \rho U_j \pi \left(\frac{d}{2}\right)^2$$

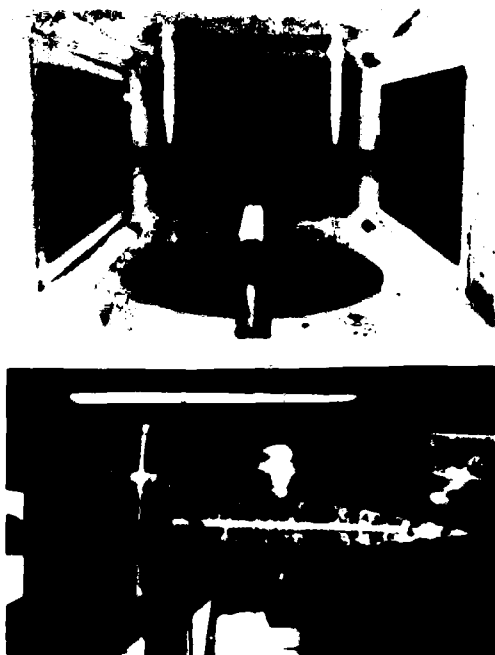
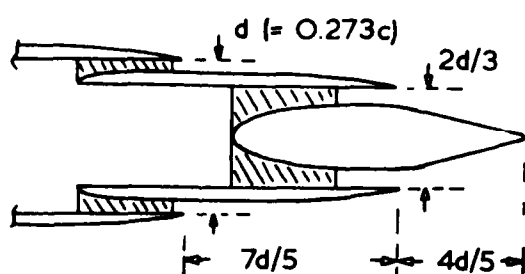
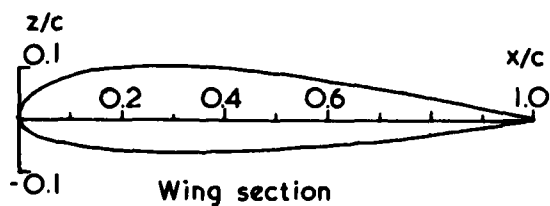


Figure 1 General arrangement



Nozzle construction



Wing section

Figure 2

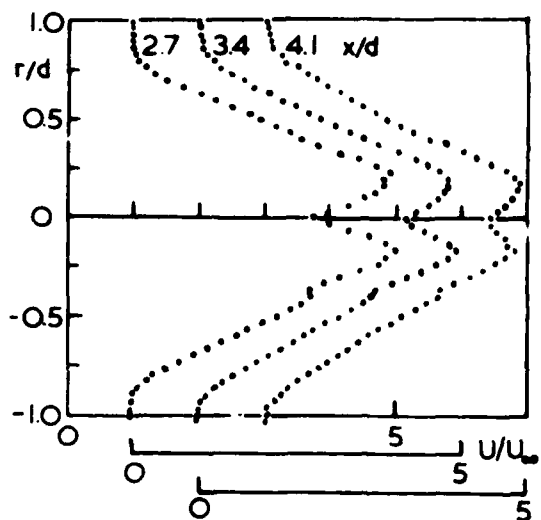
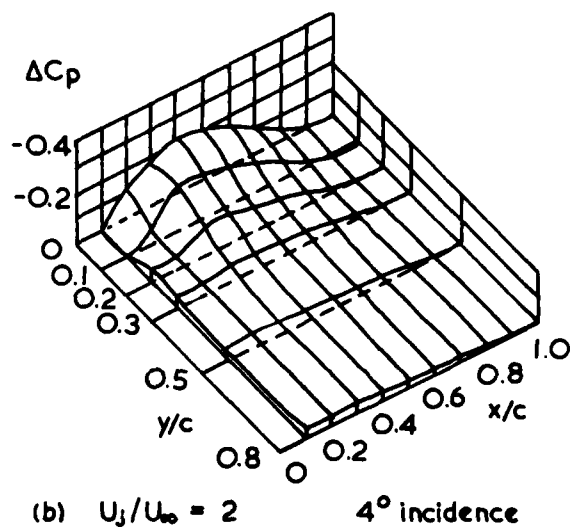
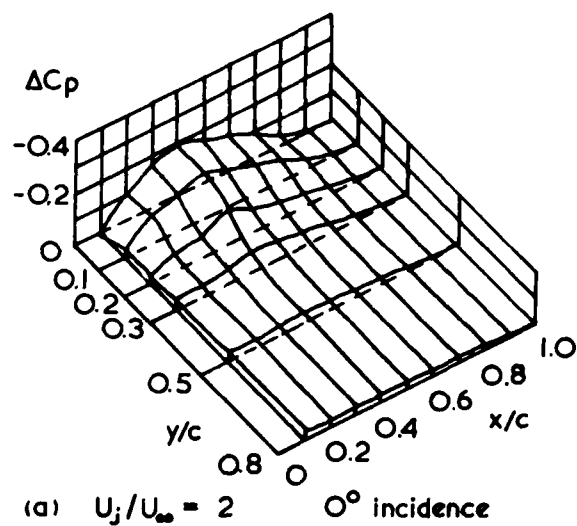


Figure 3 Jet velocity profiles

Figure 4 Upper surface ΔC_p distributions

Mass flow rate the jet at a position x along the axis

$$\dot{m}(x) = 2\pi\rho \int_0^R U r dr.$$

v_n , the entrainment velocity normal to the jet boundary is then given as

$$\frac{v_n}{U_j} \approx -\frac{1}{2} \frac{d}{r_j} \frac{d(m(x)/m_j)}{d(x/d)}.$$

The solution of this equation is dependent on the velocity profile, and so there will be two distinct solutions, one for entrainment in the initial mixing layer region and one for the main turbulent jet region. The solutions given are:-

For entrainment into the mixing layer

$$\frac{v_n}{U_j} \approx 0.027 - 0.0043 \frac{r_c}{r_j} \quad (\text{where } r_c \text{ is the radius of the central core}).$$

And for entrainment into the main jet flow

$$\frac{v_n}{U_j} \approx 0.038 \frac{d}{r_j}.$$

Due to the proximity of the wing to the engine in terms of x/d , only the first result is considered during this investigation giving values of v_n/U_j of between -0.023 and -0.027 up to at least 6 diameters downstream.

Such an analysis can now be developed to include a circular jet in a co-flowing stream. From Schlichting's consideration of the smoothing out of a velocity discontinuity it can be seen that the free jet boundary is just a particular case of the interaction of two parallel flows with different velocities. The effect of the surroundings being a co-flowing stream (say of velocity U_∞) is to modify equation above to

$$\frac{v_n}{U_j - U_\infty} \approx 0.027 - 0.0043 \frac{r_c}{r_j}.$$

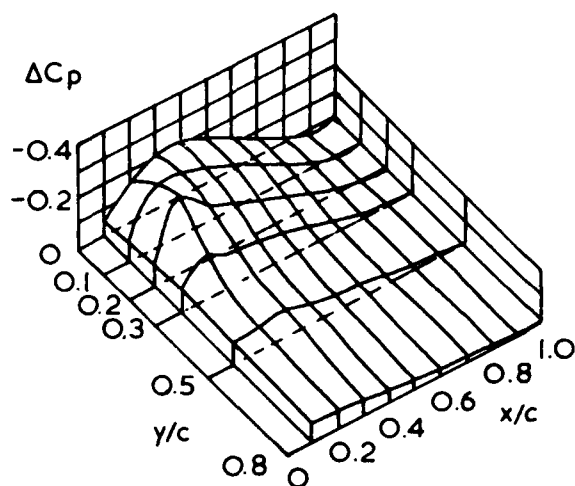
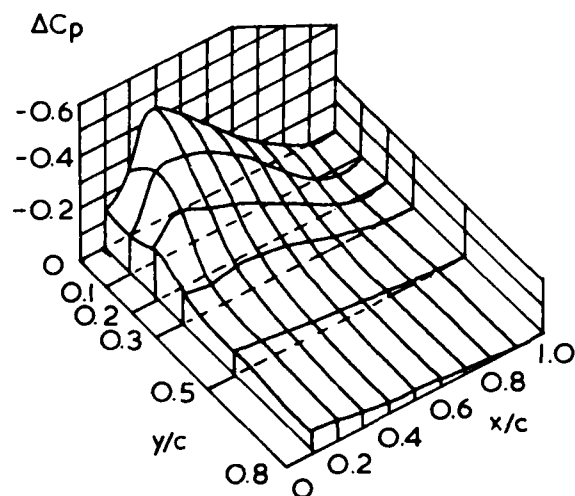
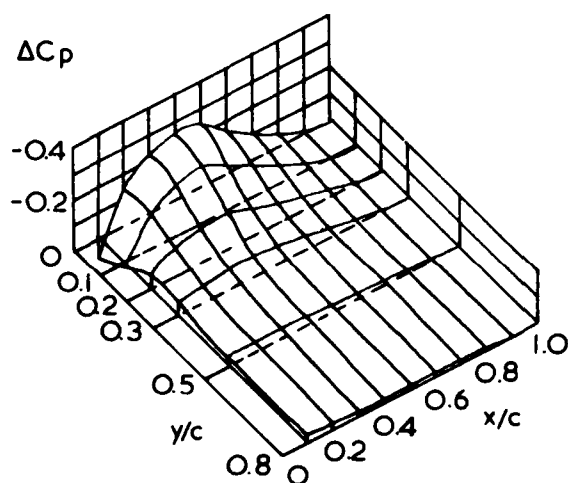
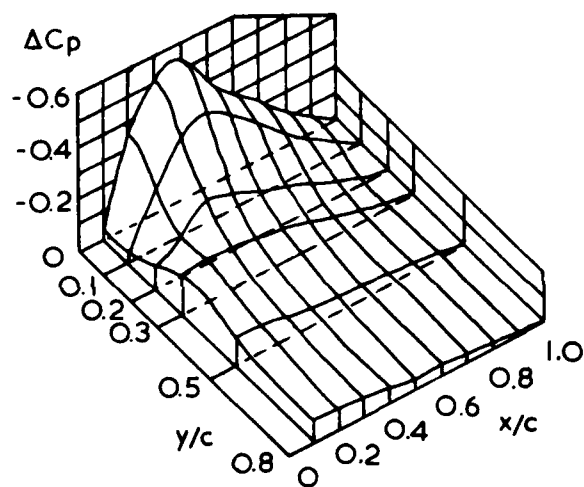
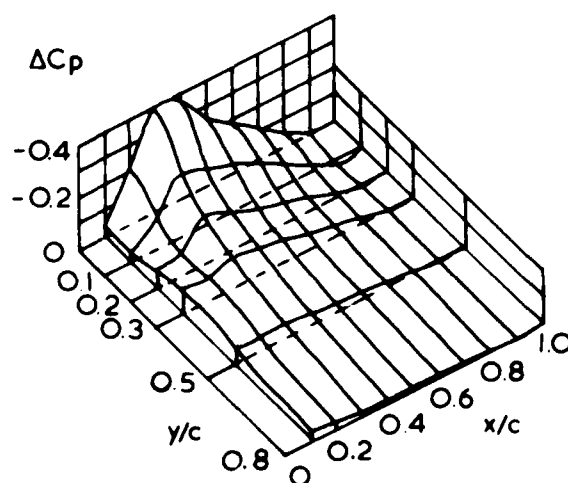
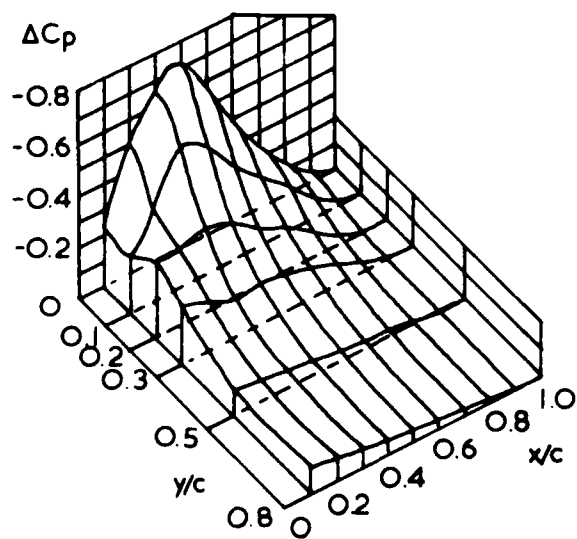
Although the nozzle used simulates both fan and core flows and the effect of the exhaust diffuser, the above analysis is used as a basis for comparison since until the velocity discontinuity between the fan and core flow smooths out, entrainment occurs mainly between the freestream and the fan flow.

(ii) Measurement of jet velocity profile and comparison of entrainment values

The jet entrainment velocity for the engine simulation was established by a series of measurements taken with the engine parallel to the freestream without the presence of the wing. Detailed total and static pressure profiles were made at $x/d = 2.7, 3.4$ and 4.1 downstream of the fan exit, where d is the diameter of the fan exit nozzle, and the velocity profiles shown in figure 3 were calculated from these. The average jet entrainment velocity was then found by considering the change in volumetric flow rate with x/d and gave an average value of $v_n/(U_j - U_\infty) = 0.0101$, where U_j is taken as the jet maximum exit velocity and $U_j/U_\infty = 1.5$.

This experimentally derived value of v_n is lower than predicted, because in the theoretical calculation no allowance was made for the exhaust diffuser and jet core cowl causing the efflux to converge in on the nozzle axis. This reduces the rate of growth of the efflux, as growth becomes relative to the centre of the fan jet which is itself becoming closer to the nozzle axis. Consequently the outer mixing layer velocities are smaller. The entrainment rate is slower as the turbulent mixing velocities are lower than would be expected for a non-conveying jet having velocity difference $U_j - U_\infty$.

The tests on the engine do show, however, the existence and relative magnitude of the entrainment velocities for a velocity profile closer to that of an actual turbofan than the theoretical analysis considers.

(c) $U_j/U_\infty = 2$ 8° Incidence(f) $U_j/U_\infty = 3$ 8° incidence(d) $U_j/U_\infty = 3$ 0° incidence(g) $U_j/U_\infty = 5$ 0° incidence(e) $U_j/U_\infty = 3$ 4° incidence(h) $U_j/U_\infty = 5$ 4° Incidence

JET EFFLUX INTERFERENCE WITH ADJACENT WING.

A theoretical flow model of jet efflux interference with adjacent wing can be established by representing the jet efflux by a line of sources along the jet flow axis, and modelling wing thickness by a surface of sources and wing loading by a vortex lattice. This is essentially the method used by Hardy (1) and very similar to that used by Krenz (5) in his theoretical derivation of results. Both their programs do, however, include nacelle/wing interference by representing the nacelle by a source distribution on the body surface. The effect of the nacelle can be eliminated, though, by only calculating the change in pressures and velocities due to the jet efflux, if the nacelle is further upstream than the wing leading edge. Such a model can be further refined by representing jet entrainment by ring sinks, of appropriate strength, along the jet efflux.

To establish and verify such a model does require, however, a set of experimental results for comparative purposes. An investigation was therefore undertaken that would produce the changes in the coefficient of pressure distribution on the wing surface due to the jet efflux.

A series of wind tunnel tests were performed, for a variety of angles of incidence and efflux/freestream velocity ratios, in which both the spanwise and chordwise pressure distributions were established with both the jet running and not running. The difference between the two C_p 's is then due to the jet efflux. (This is as opposed to Krenz (5) who considered the effect of the nacelle and jet efflux together by taking readings with just the wing in the tunnel, and with the wing and engine simulation in with the jet running).

During these tests the wing was set at an initial incidence of $\alpha = 2.6^\circ$ relative to free-stream, and the engine at $\alpha = 6^\circ$, to represent a feasible installation position on an existing low-wing feedliner. Horizontal and vertical separations of $0.0135 \times$ wing chord and $0.105 \times$ fan diameter between the centre of the core exit and the wing leading edge were used (as can be seen in figures 1 and 2). The results of these tests are shown in figures 4(a) to (i), where ΔC_p , the difference between the C_p 's with the jet-on and jet-off, has been mapped over the wing surface.

Two further tests were performed, to investigate the effects of changing the relative engine/wing incidence and horizontal positions and the results at a span position of $0.2c$ show that there are no significant extra beneficial effects to be gained,

Figure 5 has been included to show the relative magnitude of ΔC_p to C_p beneath the efflux centre line, for a series of incidences.

Finally, a set of flow visualisation photographs were obtained (by feeding smoke through the centrifugal blower) to enable the jet curvature over the wing to be measured. These were taken at incidences of 4° and 8° at 4 velocity ratios, and are included as figures 6(a) to (h).

ESTIMATION OF JET CURVATURE AND ENTRAINMENT EFFECTS ON PRESSURE DISTRIBUTIONS

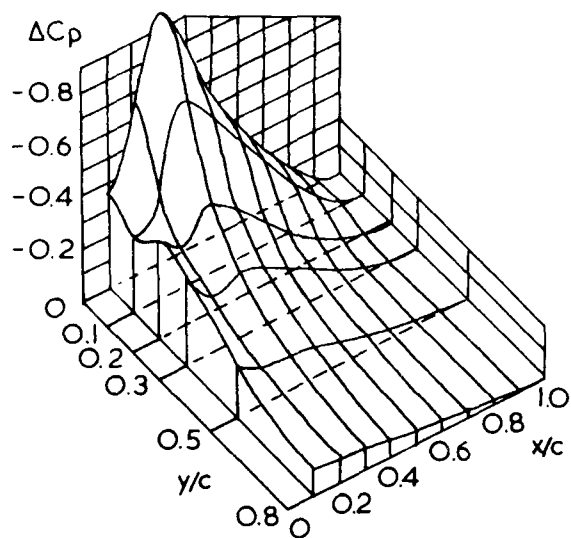
The effects of jet curvature on the wing pressure distribution may be calculated by replacing the jet by a continuous distribution of horse-shoe vortices along the axis of the jet. The bound vortex elements will be of span d , the jet diameter, and of strength k per unit distance along the axis, where k is determined from the condition that the lift per unit length on the jet will be equal to the jet momentum divided by the local radius of curvature R of the jet path. Thus

$$\rho U_\infty d k = \frac{\pi}{4} d^2 \rho U_j^2 / R$$

The trailing vortices in the jet produce only spanwise interference velocities at the wing surface, but the bound vorticity along the jet axis produces streamwise velocity increments. These changes in streamwise surface velocity result in the major effects on the wing pressure distribution found in the experiments. The streamwise velocity increment du from a bound vortex element of span d and strength $k dx$ at a distance z above a plane surface is given by

$$du = \frac{1}{2\pi} d k z dx / (x^2 + y^2 + z^2)^{3/2}$$

approximately, including the effect of the image vortex in the plane. Here x and y are streamwise and spanwise displacements of the field point P from the element. The total velocity increment at P is given by



(i) $U_j/U_\infty = 5$ 8° incidence

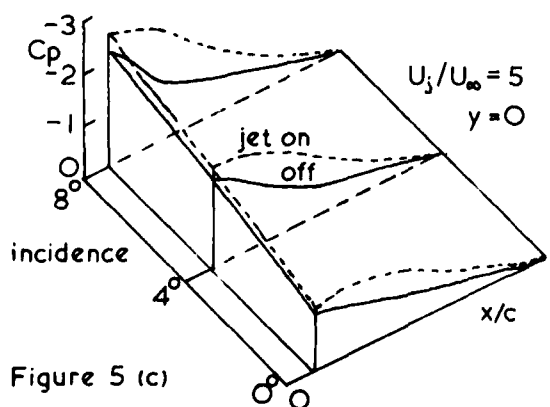
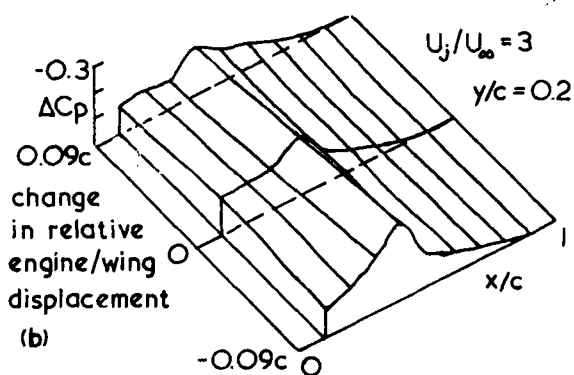
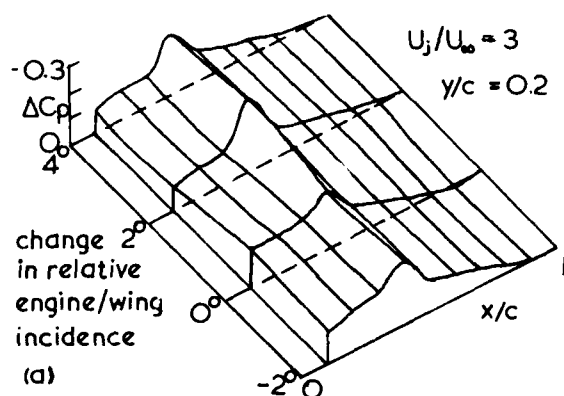


Figure 5 (c)

Figure 6 Smoke photographs of jet path

(a) to (d) 4° , (e) to (h) 8° incidence



(a) $U_j/U_\infty = 1$



(b) 2



(c) 3



(d) 5

$$\frac{U}{U_\infty} = \frac{1}{3} \left(\frac{U_j}{U_\infty} \right)^2 \frac{d^2}{c R_{\max}} \int_0^1 \frac{S d\xi_1}{\tilde{R} \{ (\xi - \xi_1)^2 + \eta^2 + \zeta^2 \}^{3/2}}$$

where $\xi = x/c$, $\eta = y/c$, $\zeta = z/c$, $\tilde{R} = R/R_{\max}$.

The integral has been evaluated making the following simplifying assumptions: (i) the wing surface is replaced by a flat plane $\zeta = 0$, (ii) the height of the jet above the surface ξ is constant, and (iii) the distribution of curvature follows the form shown in figure 7, where the maximum curvature of the jet is determined from the smoke photographs. Thus

$$\frac{1}{\tilde{R}} = \begin{cases} 5 (\xi_1 - 0.1), & \text{for } 0.1 \leq \xi_1 \leq 0.3 \\ \frac{5}{3} (0.9 - \xi_1), & \text{for } 0.3 \leq \xi_1 \leq 0.9 \\ 0, & \text{otherwise.} \end{cases}$$

The shape of the jet path for the case $U_j/U_\infty = 5$ with model incidence 8° with this distribution is shown on figure 7. Although the cross-section of the jet is severely distorted for smaller values of U_j/U_∞ , the photographs clearly show the path of the main body of the jet fluid, which contains nearly all the jet momentum.

In order to compare the results of the above analysis with the measured values of ΔC_p , changes in the streamwise velocity increment Δu from that which exists when $U_j = U_\infty$ have been calculated. Thus

$$\frac{\Delta u}{U_\infty} = \Delta \left\{ \frac{1}{8} \left(\frac{U_j}{U_\infty} \right)^2 \frac{d^2}{c R_{\max}} \right\} \int_0^1 \frac{S d\xi_1}{\tilde{R} \{ (\xi - \xi_1)^2 + \eta^2 + \zeta^2 \}^{3/2}}$$

The corresponding theoretical increments in pressure coefficients ΔC_p at the wing surface for $U_j/U_\infty = 2, 3$ and 5 for the model incidence of 8° , taking $d/c = 0.2$, $\xi = 0.2$ and $\eta = 0$, are shown in figure 8 with the experimental values for comparison. Figure 9 shows the calculated ΔC_p distributions for $U_j/U_\infty = 5$, model incidence of 8° , and $\eta = 0, 0.1, 0.2, 0.3, 0.5$ and 0.8 . Figure 10 shows the calculated ΔC_p for $U_j/U_\infty = 5$, $\eta = 0$ and model incidences of 0° and 4° .

The agreement between theory and experiment is satisfactory, and this shows that it is the bound vorticity associated with jet curvature which is chiefly responsible for the interference pressures. The trailing vortex strength may be found by integrating the bound vorticity distribution along the jet axis. At the trailing edge, the trailing vortex strength is $\frac{\pi}{10} \frac{U_j^2}{U_\infty} \frac{cd}{R_{\max}}$, which has the value $\pi U_\infty d$ for the case $U_j/U_\infty = 5$

with the model at 8° incidence. The spanwise surface velocities induced by the trailing vortex pair and their images produce a maximum surface streamline inclination of the order of 14° to the stream direction. This is in agreement with surface oil flow patterns which show appreciable spanwise flow of this magnitude in a limited region below the jet near the trailing edge. The effect of these spanwise velocities is to give pressure increments of at most $\Delta C_p = -0.03$ over this limited area of the wing.

Entrainment effects may be assessed by placing a distribution of sinks along the jet axis whose strength is sufficient to produce the entrainment rates found for a free jet in a co-flowing stream. The resulting spanwise velocities at the wing surface produce streamline inclinations of at most 1° . Even if the entrainment rates into the curved jet are several times larger than for an undistorted jet, the effect on the pressure distribution will still be negligible.

Thus it appears that a full solution to the interference problem is possible provided the jet path can be accurately predicted.

CONCLUSIONS.

The measured increments in wing pressure distribution due to the velocity of the jet show considerable lift effects (ΔC_p up to -0.9) over the upper surface for the higher jet velocity ratios. There will be some increase in wing drag associated with the ΔC_p distributions. Changes in the relative incidence and chordwise displacement of the jet to the wing over a limited range shows that the datum arrangement is near to an optimum configuration.

Flow visualisation shows that the jet path has significant curvature in the stream direction. Theoretical considerations show that the ΔC_p distributions may be calculated with reasonable accuracy assuming that the major effect is one of bound vorticity in the jet necessary to account for the observed curvature of the jet path. Entrainment and trailing vorticity effects are in general negligible.

(e) $U_j/U_\infty = 1$ 

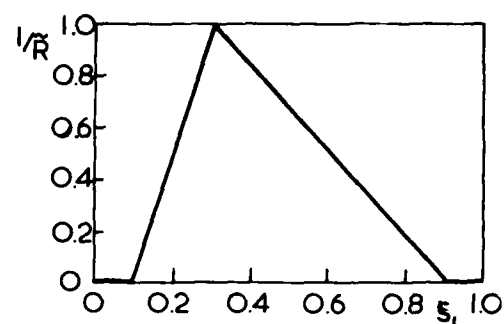
(f) 2



(g) 3



(h) 5



Assumed curvature distribution

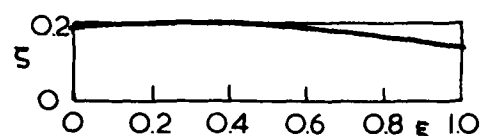
Jet path; $U_j/U_\infty = 5$, 8° incidence

Figure 7

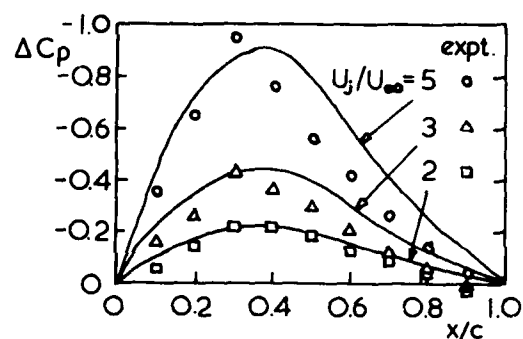
Theory. ΔC_p at $y=0$, 8° incidence

Figure 8

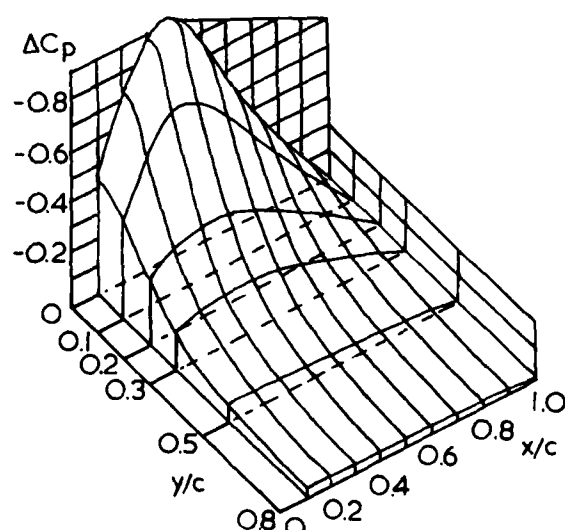
Theory. $U_j/U_\infty = 5$, 8° incidence

Figure 9

REFERENCES.

1. B.C. Hardy. A computer program to estimate the interference on a wing due to a nacelle at subsonic speeds. RAE 75075 (1975).
2. J.C. Tipping. The induced flow effects of a round turbulent jet issuing normally from a flat plate into a mainstream parallel to the plate. Ph.D. Thesis. University of Bristol. (1975).
3. H. Schlichting. Boundary Layer theory. Pergamon Press, London. (1955).
4. A.A. Townsend. The structure of turbulent shear flow. C.U.P. (1956).
5. G. Krenz. Airframe-engine interaction for engine configurations mounted above the wing: part 1, interference between wing and intake/jet. AGARD-CP-150. (1975).

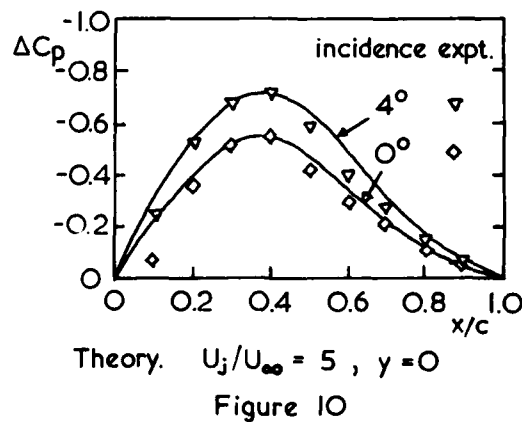


Figure 10

INTERFERENCE EFFECTS OF CONCENTRATED BLOWING AND VORTICES ON A TYPICAL FIGHTER CONFIGURATION*

by

W. STAUDACHER

MESSERSCHMITT-BÖLKOW-BLOHM GmbH
Unternehmensbereich Flugzeuge
Postfach 80 11 60
8000 München-Ottobrunn, West Germany

SUMMARY

An experimental investigation was carried out to demonstrate the effects of separated stable vortex flows on lifting surfaces.

Generation and/or stabilization and control of these vortex systems was obtained by means of

- planform variation (such as strakes, short coupled canards)
- modifications of wing section (shape and camber of L.E., L.E. flaps)
- concentrated spanwise blowing for arbitrary planforms
 - blowing from the wing root (body side)
 - blowing from 41 outboard stations, systematically varied

Specific and combined results of these modifications are shown, optimum jet positions, in respect of various criteria applied, were derived. Some typical results are presented, demonstrating the effects of strakes and/or spanwise blowing on

- performances
- stability and control
- dynamic characteristics
- flow fields

1. SCOPE OF INVESTIGATION

The investigation reported herein is embedded in a program for development of "Wings with Controlled Separation", conducted by a working group of same name (members: DFVLR, MBB, VFW) and sponsored by the German Ministry of Defence (RüFo 4 and ZTL-Program).

The experimental approach taken by MBB, heading this working group, is depicted in Fig. 1.

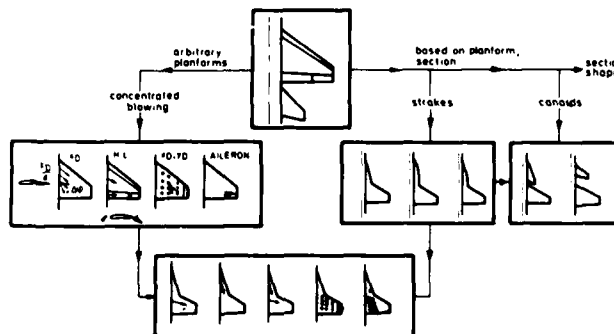


FIG. 1 EXPERIMENTAL APPROACH

The basic idea is to use different ways in creating controlled separation:

- Early attempts (starting in 1969) are based on planform variations such as leading-edge-extensions or strakes, short coupled canards etc. Combinations with modified section shapes i.e. L.E.-radii, -camber and -flaps are warping of the hybrid wings were investigated (fig. 1 only shows one of the three basic planforms). Results of this program are reported in References [1 - 15].

* this work was sponsored by the German Ministry of Defence (RüFo 4 and ZTL-Program)

- Another way of generating controlled separation independent of wing geometry is presented by the technique of concentrated spanwise blowing (see References [16 - 25]).

Starting in 1975 and still going on, the effect of concentrated blowing is investigated on arbitrary planforms, partially non exhibiting a "natural" tendency of rolled-up, stable vortex systems.

- In a first step blowing from the wing root, the nozzles being housed in the body side-walls, was tested for basic and strake wing. Optimum jet positions were derived by variation of chordwise nozzle locations, nozzle-height and -sweep on the respective planforms, demonstrating the relative merits of the different techniques (blowing over wing, strake, flaps and combined blowing).
- In a second step it was decided to investigate the effect of spanwise/chordwise positions of the nozzle on both planforms, as it was felt that there was a lack of systematic data in this field. So a grid of 41 outboard jet locations was introduced.

Experimental data derived in this way finally allowed to establish a total optimum nozzle location for the addressed configurations (including aerodynamic and structural/configurational aspects).

Nevertheless it should be kept in mind that this "total optimum" again is a compromise of integrating different systems and techniques and so will vary with progress or importance of any disciplines involved.

2. DESCRIPTION OF MODELS AND APPARATUS

Pilot model geometry is shown in Fig. 2. Model structure and scale was varied to derive the different data

- 6-component force (low speed/high speed models)
- pressure distributions (low speed/high speed models)
- flow fields (low speed model)
- sectional load data (low speed model)
- dynamic derivatives ("strapped" down high speed model)

Mach number regime investigated is $0.15 \leq M \leq 2.0$, spanwise blowing was examined in low speed tests only.

The basic wing is defined by $AR = 3.2$ / $\Lambda_{LE} = 32^\circ$ / $\lambda = 0.3$.

The wing is cambered and twisted, the basic section is NACA 64A006, varied over the span.

Additional modifications consist of a maneuver-flap system (full span L.E. slats, single slotted fowler flaps on the T.E. over 2/3 of the exposed span) and detachable strakes of different shape but constant area ratio (11% reference area).

Roll control is provided by a conventional tip aileron and the allmoving horizontal tail.

For spanwise blowing from the wing root the model-body incorporates an internal, sting mounted blowing system with different faired jet exits (at 10% / 25% / 40% of wing root, over the T.E. flap and at 10% strake-wing root chord).

For blowing from outboard wing positions an external sting fixed nozzle was used. By that way for all blowing cases mere aerodynamic interference effects were measured and no effects of jet reaction forces could get on the internal balances.

The systematic variation of outboard jet locations comprised 41 nozzle positions over the wings:

- 10/25/40/70% wing chord
- 10/25/40/60/80% exposed semispan
- 4 positions over the aileron
- 17 positions in the strake region

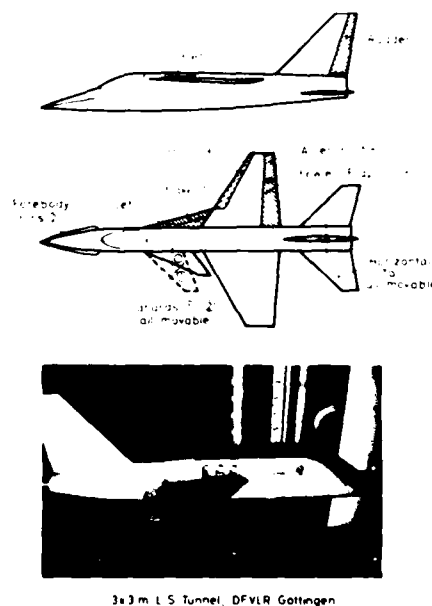


FIG. 2 PILOT MODEL

The simple convergent nozzles (7.5 or 15 mm ϕ) were usually driven supercritically.

In the course of the investigation the following test facilities were used for the purposes denoted:

- 3 x 3 m Low speed tunnel of DFVLR Göttingen
 - 6-comp. force tests
 - pressure distribution and flow fields
 - sectional loads
- 1 x 1 m Transonic tunnel of DFVLR Göttingen
 - 6-comp. force tests
 - pressure distribution
- 8 m ϕ Transonic tunnel S1 Modane, ONERA
 - 6-comp. force, $0 \leq \alpha \leq 90^\circ$
- 1.8 x 1.8 m High speed tunnel S2 Modane, ONERA
 - dynamic derivatives, $M \leq 0.8$
- 4.5 x 3.5 m F1 Le Fauga, Toulouse, ONERA
 - low speed dynamic derivatives $0 \leq \alpha \leq 50^\circ$

3. INTRODUCTORY REMARKS

3.1 Choice of Basic Wing Planform

At the early beginning of the program we did not know too much about the quantitative effects of the strakes. But from preceeding flow visualization tests in the water tunnel some qualitative guesses, say speculations, were possible. So the selection of the basic wing planform was decisively influenced by the good experiences (from flight and wind tunnel testing) with a moderately swept trapezoidal wing of medium aspect ratio (VJ 101, F104). The reasons why finally this planform was taken are listed in Fig. 3.

- a. from pitching moment considerations at high a.o.a. (in fear of the yet unknown amount of strake-induced pitch-up tendencies) stable (pitch-down) characteristics of the basic wing were assumed to be highly desirable (as symbolized in fig. 3 by the inserted SHORTAL/MAGGIN pitch-up boundary)

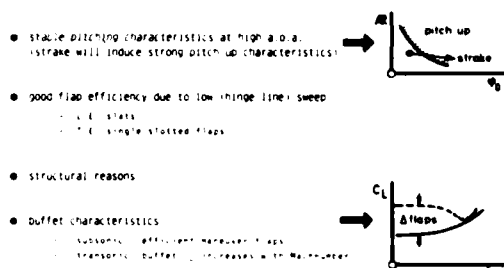


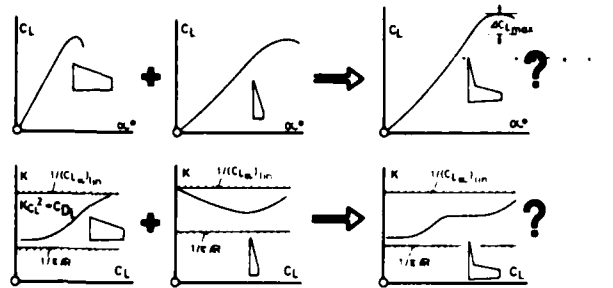
FIG. 3 REASON FOR CHOICE OF BASIC WING- PLANFORM

- b. The round nosed wing should incorporate an effective high-lift and maneuver flap system. The low sweep of this planform would additionally be in favour of the effectivity of the
 - L.E. slats
 - T.E. single-slotted fowler flaps
 selected for this wing.
- c. Structural reasons such as considerations for
 - weight
 - stiffness
 - flutter characteristics
 were taken in consideration from the beginning.
- d. Maneuver boundaries of the basic wing such as buffet should have a tendency to rise in lift with increasing Mach number (see fig. 3), thus giving the possibility to adequately add the superior efficiency of the maneuver flap system at lower speeds.

This early reflections still hold, now knowing the possibility to relax the conditions a., as the pitching characteristics of the complete configuration are extremely depending on the position and shape of horizontal tail.

3.2 Strake-Wing

From water tunnel test we early knew that the (effective) L.E. sweep of a strake should be at least 75° . For our planform it was found sufficient to use an area ratio $S_{\text{strake}}/S_{\text{ref}}$ of about 10% (11% was chosen). To go back to the origins, Fig. 4 is demonstrating the initial, naive but basic question, which has led to the development of the strake wing (at least from our side) and which is based again on a widely used principle: superposition.



How aerodynamically useful is a combined strake-wing planform with a moderate sweep? The answer is: it is useful for the respective mission of these wings for the respective conditions.

FIG. 4 QUESTION (simplified, but basic)

4. RESULTS

4.1 Effect of Strakes

4.1.1 Overall performances

The overall effects of strakes on maneuver performances and flying qualities - many of them of favourable, some few of detrimental influence to aerodynamic characteristics - are well known and (less well) understood meanwhile.

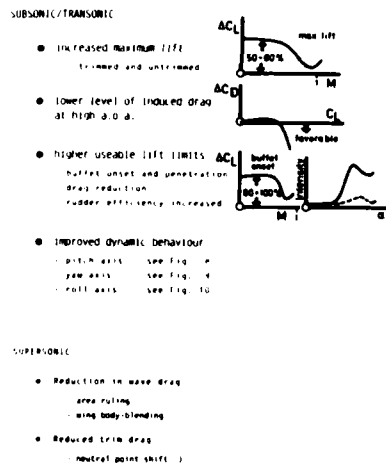


FIG. 5 SUMMARY OF ADVANTAGES DUE TO STRAKES

4.1.2 Flow fields

A comparison of the flow fields behind the basic and the strake wing at an a.o.a. $\alpha = 15^\circ$ is given in Figures 6 and 7, representing a vertical cut on the longitudinal position of the (detached) horizontal tail. Top of fig. 6 presents the local velocity ratios v_1/v , the lower part of the graph is showing the velocity vectors directly, as derived by a multihole-probe.

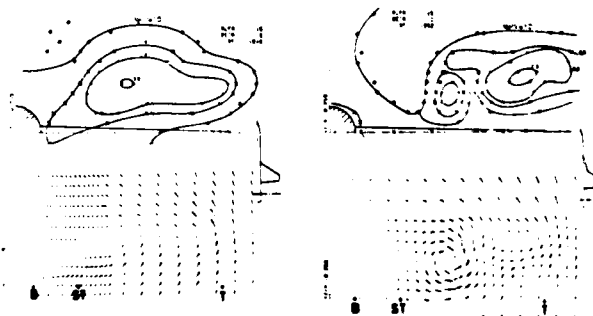


FIG. 6 FLOWFIELDS BEHIND WINGS $\alpha = 15^\circ$
top: local velocity ratios
bottom: vector of velocity

The flow field behind the basic wing is diffuse and is dominated by extended regions of low energy due to the beginning stall of the wing, whilst behind the strake wing the flow is controlled by the existence of a strong strake vortex just starting to unite with the higher located weaker outboard vortex. At 20° a.o.a. the strake vortex system is completely filling the otherwise totally stalled region. There is no evidence of an expected second vortex system then. For clarity, spanwise stations for body side (B), strake-kink (St) and wing tip (T) are drawn in.

In Fig. 7 an analogous comparison is presented for the two wings giving now the local a.o.a. distributions for different heights above the wing plane ($ZF < 0$). There is a weak indication for the existence of a rather diffuse tip vortex behind the basic wing (top of fig. 7). The bottom of fig. 7 is drastically demonstrating that one should avoid positioning the horizontal tail above the wing plane because there exist, apart of the pitch-up danger, rapid jumps in the distribution of incidences near the strake vortex system. The worst case in vicinity of the path of the vortex would give a change in local a.o.a. of $|\Delta\alpha| = 60^\circ$ for a 10% spanwise movement.

The fat line drawn in fig. 7, bottom, is representing the selected position of the horizontal tail, well situated below the wing plane.

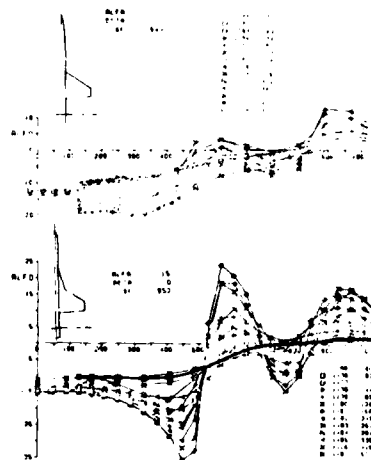


FIG. 7 LOCAL AOA DISTRIBUTIONS
BEHIND WINGS
 $\alpha = 15^\circ$

4.1.3 Dynamic derivatives

Some of the features a strake is imposing on the dynamic characteristics were already published in Ref. [22], the results now being completed up to extreme a.o.a. (this part of the experimental program was also carried out in a scientific cooperation ONERA/MBB, using their test facilities S2, Modane and - here - F1 Le Fauga, Toulouse). Results of the forced oscillation tests are given in Figures 8, 9 and 10 for the characteristics of damping-in-pitch, yaw and roll respectively, always comparing data of basic wing and strake-wing-configuration (tail on).

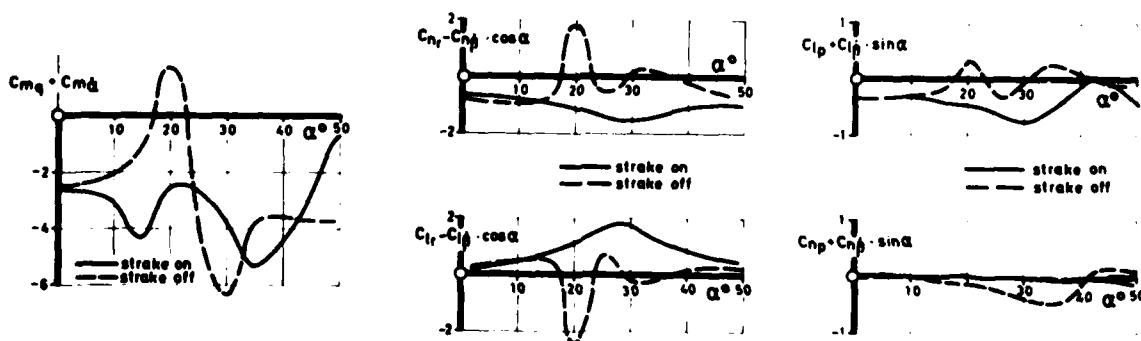


FIG. 8 EFFECT OF STRAKE
ON PITCH DAMPING

FIG. 9

EFFECT OF STRAKE
IN YAW-MOTION

FIG. 10

EFFECT OF STRAKE
IN ROLL-MOTION

The basic configuration without strake is diverging in damping in pitch, yaw and roll near maximum lift ($\alpha \approx 20^\circ$) of the trapezoidal wing, accompanied by a simultaneous rapid divergence in the cross coupled derivative ($C_{l_r} - C_{l_r}^0 \cdot \cos\alpha$) and (not shown here) in the respective side force derivative ($C_{y_r} - C_{y_r}^0 \cdot \cos\alpha$) at the same a.o.a. The strake wing configuration never showed an excited motion, there was only an indication of mild divergence in damping in roll near $\alpha = 42^\circ$ (fig. 10). Improvements in damping in roll and pitch so far are attributed to the restoring effects of the strake vortex system on

the wing itself, hence may be denoted as "direct" effects. The more astonishing thing is found, comparing the characteristics of damping in yaw and analysing the strake effect there. No divergence is found on the strake wing for damping in yaw, the cross derivative shows the same tendency. But there is a change in sign of the sideforce derivative ($C_{Y\dot{\alpha}} - C_{Y\dot{\beta}} \cdot \cos \alpha$) near $\alpha = 35^\circ$ for the strake configuration, too. This means that the positive effect of the strake can be split in two contributions:

- for $15 \leq \alpha \leq 35^\circ$ the strake is improving the flow conditions on the vertical tail relative to the basic wing flow field;
- for $\alpha > 35^\circ$, in the post-stall a.o.a.-regime of the strake wing, the body vortex system (effect of the strake on the pair of vortices, spreading from the body nose) is favourably influenced by the presence of the strake, thus the forebody contribution is preserving damping in yaw.

This combined effect for damping in yaw is the "indirect" effect of the strake on dynamic characteristics.

4.1.4 Leading edge devices for vortex control

Leading edge flaps are well known as a means of increasing maximum angle-of-attack and restoring L.E. suction (lift/drag tailoring) in classic aerodynamics. In References [9] and [12] they are used to control the vorticity shed from the strake - L.E. by using positive and negative deflections of a nose flap and by introducing "inverted" Krüger flaps.

The attempt to use inverted nose flaps to decouple the effective a.o.a. from the geometric one on a highly swept wing is shown in Figures 11 to 13. For the configuration with and without T.E. flap deflection ($\delta_f = 30^\circ$) the effect of deflecting the nose flap up ($\delta_n = 10^\circ$ streamwise) is demonstrated for lift, drag and pitching moment.

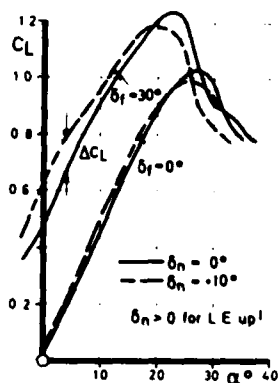


FIG. 11
EFFECT OF INVERSED
L.E. FLAP DEFLECTION
ON LIFT OF A
HIGHLY SWEPT WING

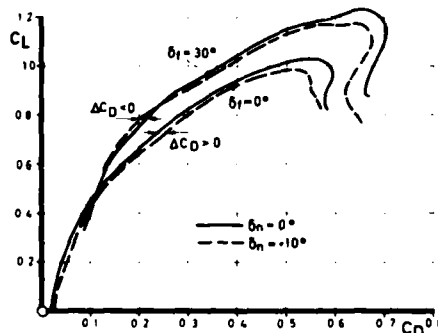


FIG. 12 EFFECT OF INVERSED L.E.
FLAP ON DRAG OF A
HIGHLY SWEPT WING

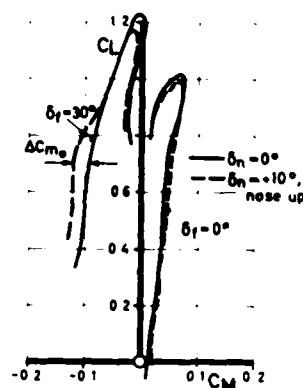


FIG. 13
EFFECT OF INVERSED
L.E. FLAP DEFLECTION
ON PITCHING MOMENT
OF A HIGHLY SWEPT WING

Configurations with L.E. up are developing for $\alpha \leq 20^\circ$ more lift than for the "nose clean" case.

Lift and pitching moment show characteristics for $\delta_f = 0^\circ$ as expected: a small increase in lift with angle of attack (fig. 11) and a nearly unchanged pitching moment with a slight tendency for a forward shift of neutral point and aerodynamic center.

For the case of deflected trailing edge flaps and positive (nose up) L.E. flaps deflection and unexpected strong effect of the latter device is found for lift and pitching moment at low angles of attack. There is even found a slight drag reduction (fig. 12). The increase in lift cannot be attributed to the additional vortex lift solely, as can be seen by comparison to the case $\delta_f = 0^\circ$. So the reason has to be a change in the effectiveness of the deflected T.E. flap.

Evidently there is a strong positive interaction between the L.E. vortex system, amplified by the upward deflected L.E. flaps, triggering attached flow on the trailing edge flap as evidenced by the now negative increment in zero-lift-moment (fig. 13). This reduction in drag and increase in lift for constant α is an additional favorable contribution of controlled vortex system giving improvements in take-off performances, e.g.

Another example, how the shed L.E. vorticity can be manipulated is given in Fig. 14.

A kind of L.E. spoiler was used to find out if there is a possibility to decrease the inevitable loss in L.E. suction (and hence increase in lift dependent drag) on wings exhibiting this type of separation.

The "spoiled" configuration gave more - at least not less-lift and indeed showed a 10% reduction in lift-dependent drag. Of course, zero lift drag of the spoilers is shifting the respective total polar to the right but nevertheless there is a cross over of the two polars at medium a.o.a. then. Watch, that again effectiveness of a rather simple approach and device was confirmed by experiment, which is something out of the common in the field of aerodynamics.

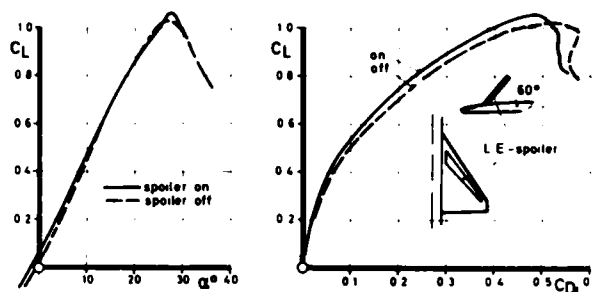


FIG. 14 EFFECT OF L.E.-SPOILER

4.2 Spanwise Blowing

Concentrated spanwise blowing is regarded to be a technique to generate controlled separations independent of wing geometry on planforms, that do not exhibit a natural tendency to develop stable vortex systems. It can be used in the same way to stabilize existing L.E. vortex systems on delta and strake wings, e.g. thus improving in general high-lift and maneuver-characteristics at low speeds (see References [16 - 25], [32 - 44]). There are some possible applications for transonic maneuvering as shown in Ref. [45] or for departure prevention and spin recovery by blowing from the body nose, Ref. [46]. This paper will concentrate on effects, found by blowing over the wing and is confined to low speed application of spanwise blowing. The reasons for it are discussed in depth in Ref. [23].

4.2.1 Blowing over the basic wing

The nozzle positions were optimized for the different wings in two test phases (References [19], [25]), the first of which only dealt with nozzle locations in the body side walls; longitudinal position, sweep and deflection angle and height of the nozzles were systematically varied (see fig. 1 and Ref. [23]) to give an optimum nozzle position.

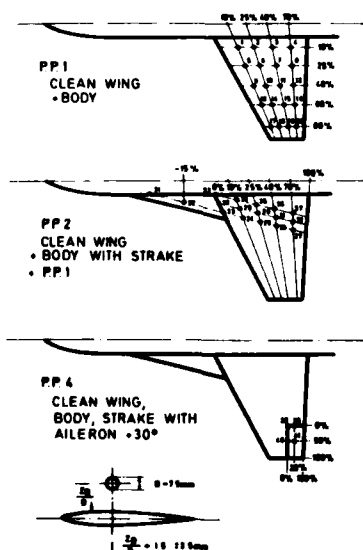


FIG. 15 TESTED NOZZLE POSITIONS

Returning to the first test phase, Fig. 16 is demonstrating part of the optimization process. Criterion used is the maximum jet induced lift increment ΔCL_{max} (due to a constant blowing intensity $c_\mu = 0.1$) plotted versus chordwise position and jet sweep angle.

In the second test phase the same models were used and a systematic variation of outboard jet locations was carried through according to Fig. 15.

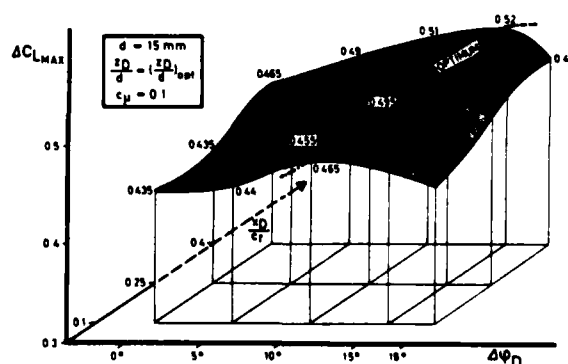


FIG. 16 OPTIMIZATION OF JET POSITION AND DIRECTION (blowing from the wing root)

Optimum position is defined by

- chordwise position at 40% root chord
- nozzle height 1.5 ϕ
- blowing direction $\psi_D = \Lambda_{LE}$ according to $\Delta\psi_D = 15^\circ$.

Nozzle height was found to be the most insensitive parameter in this range ($Z_D/D = 1.0$ to 2.0), so it was decided to keep nozzle height constant for the outboard wing blowing.

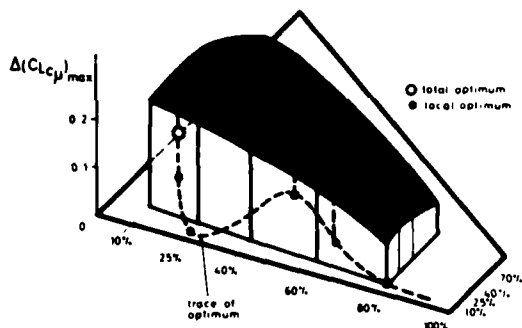


FIG. 17 EFFECT OF NOZZLE POSITION ON OUTBOARD WING

Fig. 17 is an equivalent to fig. 16, now showing the effect of outboard nozzle locations for the same criterion. Note, that for this investigation only one wing half had an external blowing nozzle, hence the lift increment induced is only about half compared to fig. 16.

The trace of the local optimum (constant spanwise cuts) is drawn in the wing plane, demonstrating that the total optimum is shifted to the earlier established optimum for blowing from the wing root. Hence the most simple system (in terms of weight, structure, mechanics supply, complexity etc) is the aerodynamic most efficient here, which indeed is a non-typical example in aeronautical engineering.

The general effects of spanwise blowing are well known. They are similar to those of strakes for drag and lift characteristics, but give more linearity in pitching characteristics. For detailed information see Ref. [16ff], we shall deal with the effects of concentrated blowing for roll control here.

Asymmetric blowing can be used as roll control with or without simultaneously deflecting ailerons. Fig. 18 is comparing these cases including the efficiency of the aileron alone (curve ②). Curve ① is giving the effect of asymmetric blowing alone ($c_{\mu} = 0.05$) from a station at 60% span and 25% chord, curve ④ is the combined effectivity of blowing a deflected aileron. Curve ③ was derived by adding the values of curves ① + ②. Hence the difference between ④ and ③ is the positive interference of spanwise blowing with the deflected aileron.

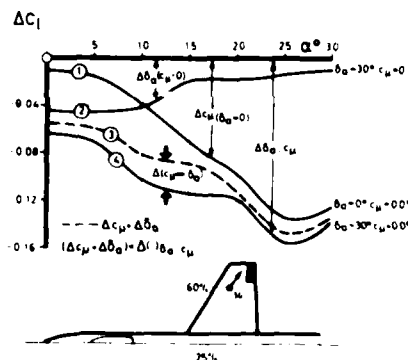


FIG. 18 ROLL POWER DUE TO AILERON AND/OR SPANWISE BLOWING

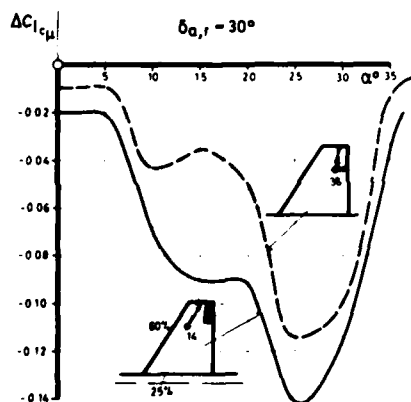


FIG. 19 EFFECT OF JET POSITION ON AILERON POWER

In Fig. 19 the effects are compared of blowing over the wing and blowing over the deflected aileron (blowing over the aileron hinge-line). Evidently there is more effectivity in curing the flow "in front" of the deflected aileron than on the stalled aileron itself, so that profit can be drawn from the forward induction effect of the deflected aileron.

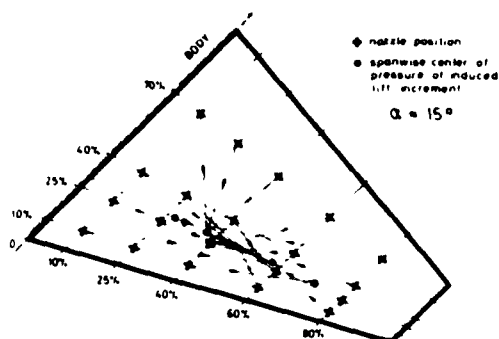


FIG. 20 NOZZLE POSITION AND CENTER OF INDUCED LIFT INCREMENT AS DERIVED BY ASYMMETRIC BLOWING

The local optimum positions, when applying different criteria, are shown in Fig. 21. The criteria used are

- maximum induced lift increment ΔC_{Lmax}
- increase of lift/drag - ratio at C_{Lmax} , $\alpha_{max} = 15^\circ$
- optimum lift/drag ratio $(L/D)_{opt}$
- lift increment at α_{max} , $\Delta C_{L\alpha_{max}}$

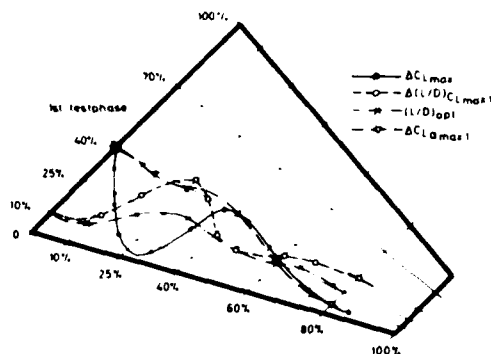


FIG. 21 LOCAL OPTIMUM POSITIONS FOR DIFFERENT CRITERIA

All optima are found near or forward of 40% chord. As the spanwise gradients are small for locations inboard of 40% span, the total optimum for all criteria is the wing-body intersection. Hence the formerly found optimum from testphase 1 is confirmed again.

4.2.2 Blowing over the strake wing

In general spanwise blowing is less effective on the strake wing, because this wing already incorporates a certain amount of non-linear lift production (the strake wing without blowing equals the blown $c_u = 0.1$ basic wing, see Ref. [23], in lift and consequently drag production). Hence the spanwise blowing is losing the triggering effect on the strake wing, has to start from a higher level of vortex lift and is less effective.

It can be shown that there is an effect of saturation in non-linear lift production (Ref. [25]), similar to the well known characteristics when passing from BLC to super-circulation.

Keeping that in mind the reduced production of rolling moment by blowing on the strake relative to blowing over the aileron is easily explained, see Fig. 22 and the same is true for the comparison of identical blowing on the two wings, given in Fig. 23.

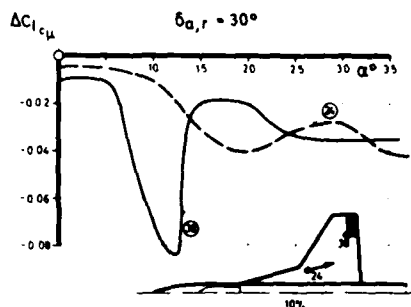


FIG. 22 EFFECT OF CONCENTRATED BLOWING ON AILERON POWER (STRAKE WING)

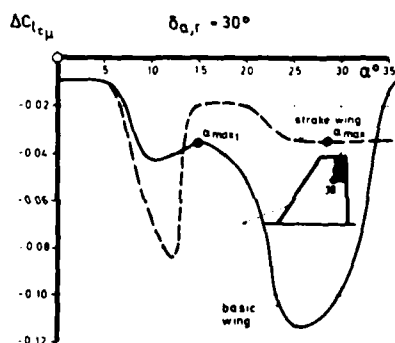


FIG. 23 BLOWING OVER THE AILERON EFFECT OF WING PLANFORM

Nevertheless blowing on the strake wing with jet directions approximately equal to the L.E. sweep of the strake is attractive if one takes into account the system integrated effects (thrust and lift component of the jet), for more details, see Ref. [23].

4.3 Summary

Concentrated blowing is offering a high versatility for improving the high-lift and maneuver performances directly. In a less direct manner possibilities arise to retain stability and control to higher angles of attack. Some of the unique features of this technique were addressed, when blowing over lifting surfaces. Fig. 24 gives an overview of additional advantages obtainable by use of concentrated blowing for different purposes blowing from other parts of the configuration.

BLOWING OVER LIFTING SURFACES

- increased maximum lift
- reduced drag level at high angle of attack
- improved roll control
 - aileron efficiency
 - asymmetric blowing
- higher maneuver limits
 - buffet
 - stability (reduction of α -shifts)
 - reduction of spin susceptibility (fig. improved)

BLOWING OVER CONTROLS

- increased efficiency
- spin prevention or recovery (aileron, rudder, vertical tail)

BLOWING OVER THE FOREBODY

- control of vortex shedding
- departure prevention

FIG. 24 EFFECTS OF SPANWISE
BLOWING IN THE SUBSONIC
(TRANSONIC) FLIGHT REGIME

5. REFERENCES (direct)

- [1] STAUDACHER W.
Verbesserung der Manöverleistungen im hohen Unterschall
MBB-UFE 896-72 (DGLR-72-126) 1972
- [2] STAUDACHER W. / ZECH A.
Transsonische Profil- und Flügelformen (Hochauftriebsmittel für den
Luftkampf, $Ma = 0.5 + 0.9$)
MBB-UFE 908-72 ZTL 1972
- [3] ZECH A. / STAUDACHER W. / BRETTAUER N.
Untersuchungen im Unterschall an Flügeln mit Strakes für Kampfflugzeuge
MBB-UFE 1019-73 RÜFo 1973
- [4] STAUDACHER W.
Zum Einfluß von Flügelgrundriß-Modifikationen auf die aerodynamischen
Leistungen von Kampfflugzeugen
MBB-UFE 1033-73 (DGLR 73-71) 1973
- [5] STAUDACHER W.
Flügel mit Strakes (Transsonik, experimentell)
MBB-UFE 1059-73 ZTL 1973
- [6] KRAHL H.
Untersuchung der Interferenz und der Lastverteilung bei Kampfflugzeug-
Konfigurationen mit Strakes
VFW-F 4.01/74 ZTL 1974
- [7] BAUMERT W.
Messungen am Prinzipmodell Flügel mit Strakes bei symmetrischer An-
blasung
DFVLR IB 157-75A13 ZTL 1974
- [8] SCHRÖDER W.
Untersuchungen über die Umströmung von Tragflügeln mit geknickten Vor-
derkanten und gepfeilten Außenflügeln bei mäßiger Unterschallgeschwin-
digkeit
DFVLR IB 151-74/71 ZTL 1974
- [9] STAUDACHER W.
Flügel mit Strakes (experimentell)
MBB-UFE 1154 ZTL 1974

- [10] BÖDDENER W.
Kraftmessungen an einem Flugzeugmodell mit Strakes, Bestimmung der
Ruderwirksamkeiten sowie Einfluß von Spoilern und Bremsklappen
DFVLR IB 157-75C12 ZTL 1975
- [11] BAUMERT W.
Druckverteilungsmessungen am Prinzipmodell Flügel mit Strakes bei
unsymmetrischer Anblasung
DFVLR IB 157-75A17 ZTL 1975
- [12] STAUDACHER W.
Flügel mit Strakes (experimentell)
MBB-UFE 1223 ZTL 1975
- [13] KRAHL H. / STEUER R.
Klärung realisierbarer Möglichkeiten des Hochauftriebs
(Flügel mit Strakes)
VFW 4.01-75 ZTL 1975
- [14] EBERLE A. / STAUDACHER W. / ZECH A.
Advanced Aerodynamics for Transonic Flight
ICAS Paper No. 76-12 1976
- [15] STAUDACHER W. / HÜNECKE K.
Flügel mit und ohne Strakes im Post-Stall-Bereich
Gemeinschaftsarbeit MBB-UFE 1300 / VF Ef-652 ZTL 1976
- [16] HÜNECKE K. / KRAHL H.
Grundsatzuntersuchungen über spannweitiges Ausblasen
VFW-F KB Ef-626 1976
- [17] STAUDACHER W.
The Effects of Jets, Wakes and Vortices on Lifting Surfaces
AGARD FDP RTD / MBB-UFE122-AERO-MT-263 1976
- [18] LEDY J.P. / TURBIL R.
Essai d'une maquette complète d'un avion de combat MBB, à l'échelle
1/5.5, avec jets transversaux, dans la veine d'expérience no 1 de la
soufflerie S1MA
Procès-verbal no 2/3302 SNG 1977
- [19] STAUDACHER W. / BÖDDENER W. / WULF R.
Grundsätzliche Untersuchungen über spannweitiges Ausblasen und stabili-
sierten Wirbelauftrieb
Gemeinschaftsbericht MBB-UFE 1320 / DFVLR IB 157-77 A25 RüFo 1977
- [20] STAUDACHER W.
Flügel mit kontrollierter Ablösung
MBB-UFE 1343 (8) / DGLR Nr. 77-028 1977
- [21] POISSON-QUINTON Ph.
Slender Wings for Civil and Military Aircraft
8th Theodore v. Karman Lecture 1978
- [22] STAUDACHER W./LASCHKA B./SCHULZE B./POISSON-QUINTON Ph./CANU M.
Some Factors Affecting the Dynamic Stability Derivatives of a Fighter-
Type Model
AGARD FDP Athens, May 1978, Paper 11 1978
- [23] STAUDACHER W./LASCHKA B./POISSON-QUINTON Ph./LEDY J.P.
Effect of Spanwise Blowing in the Angle-of-Attack Regime $\alpha = 0 \div 90^\circ$
ICAS A1-02, Lisboa
- [24] STAUDACHER W./LASCHKA B./POISSON-QUINTON Ph./LEDY J.P.
Aerodynamic Characteristics of a Fighter-Type Configuration During
and Beyond Stall
AGARD CP 247, Paper 8 1978
- [25] STAUDACHER W. / STIEB R. / BÖDDENER W.
Verbesserung der aerodynamischen Leistungen durch konzentriertes
Ausblasen
MBB S/R/1499 RüFo 1980

REFERENCES (related)

- [26] LUDWIG H.
Zur Erklärung der Instabilität der über angestellten Deltaflügeln
auftretenden freien Wirbelkerne
AVA-Bericht 1961
- [27] HUMMEL D.
Untersuchungen des Strömungsfeldes, insbesondere des Aufplatzens der
Wirbelkerne, an einem schlanken Deltaflügel
DFL-Bericht Nr. 0196 1963
- [28] HUMMEL D.
Untersuchungen über das Aufplatzen der Wirbel an schlanken Deltaflügeln
Z. Flugwissenschaften 1965
- [29] POLHAMUS E.C.
A Concept of the Vortex Lift of Sharp-Edge Delta Wings Based on a
Leading-Edge-Suction Analogy
NASA TN D-3767 1966
- [30] SACHER P. / PFANZEDER D.
Nichtlineare Theorie für Flügel kleiner Streckung: Voruntersuchung im
Wasserkanal
EWR Nr. 454-69 1969
- [31] WENTZ W.H. Jr.
Vortex Breakdown on Slender Sharp-Edged Wings
J.A. Vol. 8 No. 3 1969
- [32] DIXON C.J.
Lift Augmentation by Lateral Blowing over a Lifting Surface
AIAA No. 69-193 1969
- [33] CORNISH J.J. III
High Lift Application of Spanwise Blowing
ICAS Paper No. 70-09 1970
- [34] DIXON C.J.
Lift and Control Augmentation by Spanwise Blowing Over Trailing Edge
Flaps and Control Surfaces
AIAA Paper No. 72-781 1972
- [35] BRADLEY, R.G. / SMITH C.W. / BHATELEY I.C.
Vortex-Lift Prediction for Complex Wing Planforms
J. Aircraft Vol. 10 No. 6 1973
- [36] BRADLEY R.G. / WRAY W.O.
A Conceptual Study of Leading-Edge Vortex Enhancement by Blowing
AIAA-Paper No. 73-656 1973
- [37] BRADLEY R.G. / SMITH C.W. / WRAY W.O.
An Experimental Investigation of Leading-Edge Vortex Augmentation by
Blowing
NASA CR-132515 1974
- [38] CAMPBELL J.F.
Effects of Spanwise Blowing on the Pressure Field and Vortex-Lift
Characteristics of a 44° Swept Trapezoidal Wing
NASA TN-D 7907 1975
- [39] BRADLEY R.G. / WHITTEN P.D. / WRAY W.O.
Leading-Edge Vortex Augmentation in Compressible Flow
AIAA Paper No. 75-124 1975
- [40] KNORR G.
Experimenteller Vergleich zweier Ausblaskonzepte am Modell eines
leichten STOL-Flugzeuges
TU Braunschweig, Studienarbeit 1975
- [41] JENKINS M.W.M. / MEY R.T.
A Large-Scale Low-Speed Tunnel Test of a Canard Configuration with
Spanwise Blowing
AIAA Paper No. 75-994 1975

- [42] CAMPBELL J.F.
Augmentation of Vortex Lift by Spanwise Blowing
AIAA Paper No. 75-993 1975
- [43] NUGMANOV H.Kh.
Experimental Study of Spanwise Airjet Influence on Wing Aerodynamic
Characteristics
Izvestiya VUZ. Aviatsionnaya Tekhnika 1976
- [44] KRUPPA E.W.
A Wind Tunnel Investigation of the KASPER Vortex Concept
AIAA Paper No. 77-310 1977
- [45] DIXON C.J. / DANSBY T. / POISSON-QUINTON Ph.
Benefits of Spanwise Blowing of Transonic Speeds
ICAS Paper No. A1-01, Lisboa 1978
- [46] CORNISH J.J. / JENKINS M.W.M.
The Application of Spanwise Blowing for High Angle of Attack Spin
Recovery
AGARD CP 247, Paper 9 1978

ETUDE EXPERIMENTALE DE L'INTERACTION ENTRE UNE VOILURE D'AVION SUBSONIQUE RAPIDE
ET UNE NACELLE DE MOTEUR A HAUT TAUX DE DILUTION
par P. LEVART

Office National d'Etudes et de Recherches Aérospatiales
29, avenue de la Division Leclerc
92320 CHATILLON - FRANCE

RESUME

L'apparition de configurations nouvelles d'avions subsoniques civils (voilure supercritique et moteur à haut taux de dilution) a conduit à une étude expérimentale de l'interaction nacelle-jet-voilure-pylône en transsonique. A cet effet un dispositif d'essai a été développé dans la soufflerie S3Ch de l'ONERA.

Les maquettes de nacelles simulent au moyen de deux jets d'air comprimé un moteur double flux, à l'échelle 1/18,5. Elles sont fixées à l'extrémité d'une balance de dynalpie mesurant la poussée d'arrière-corps et le coefficient de débit.

La maquette de l'aile est placée entre les parois latérales de la veine. Les pressions sont mesurées par 456 prises réparties en 8 sections. Le C_x de l'aile est obtenu par sondage de sillage.

Il est possible de faire varier les paramètres suivants :

- position relative aile/nacelle ;
- nombre de Mach amont (de 0,3 à 0,8) ;
- taux de détente du jet ;
- présence du pylône ;
- type de nacelle.

L'interaction nacelle-voilure peut ainsi être étudiée au moyen du bilan global poussée-traînée, en fonction des divers paramètres.

Le dispositif d'essai est décrit en détail, et un exemple des résultats illustrant les possibilités de ce montage est présenté.

SUMMARY

The oncoming of a new generation of subsonic transport aircraft (with supercritical wing and high by-pass ratio turbofans) has led to an experimental study of wing-nacelle-jet-pylon interference in transonic flow. To this end, a test set-up has been developed at the ONERA S3Ch wind-tunnel.

The nacelle models represent a turbofan by means of two compressed air jets. The scale is 1/18,5. The nacelles are fixed on a thrust balance measuring afterbody thrust and discharge coefficients.

The wing is located between the sidewalls of the test section. Pressures are measured through 456 holes located on 8 airfoils. Drag coefficient of the wing is obtained by wake survey.

The following parameters can vary :

- wing/nacelle position ;
- upstream Mach number (from 0.3 to 0.8) ;
- jet pressure ratio ;
- with/without pylon ;
- type of nacelle.

Wing nacelle interference can thus be studied by means of total thrust-drag analysis, as a function of the various parameters.

The test set-up is described, and examples of results are presented illustrating the possibilities of this set-up.

1 - INTRODUCTION -

Le problème de l'interaction nacelle-voilure sur les avions civils a été abordé dans les années passées par de nombreux auteurs [1 à 13]. Cependant, peu d'études portent sur le cas des voilures supercritiques, qui peuvent être plus sensibles aux interactions que les voilures classiques, ou le cas des nacelles de moteurs à haut taux de dilution, comportant une soufflante de grande dimension qui nécessite de rapprocher au maximum la nacelle de l'aile.

Une étude assez générale de l'interaction nacelle-jet-voilure a donc été entreprise en soufflerie afin de disposer des éléments de base nécessaires au choix de la position relative nacelle-voilure, pour ce genre de configuration.

2 - METHODE ET MOYENS D'ESSAIS -

Les essais se sont déroulés dans la soufflerie S3 de Chalais-Meudon à l'ONERA.

2.1 - Soufflerie S3 de Chalais-Meudon -

C'est une soufflerie subsonique/transsonique, continue, à retour. La section est quasi-octogonale. Les dimensions de la veine d'expérience sont : hauteur = 0,8 m ; largeur = 0,9 m ; diamètre du cercle circonscrit = 1 m (section = 0,66 m²). La longueur totale de la veine est 1,75 m et la longueur utile correspond aux dimensions des hublots : 0,60 m. La pression génératrice est voisine de la pression atmosphérique. La température génératrice est croissante en fonction du nombre de Mach, depuis la température ambiante jusqu'à 340 K environ pour $M = 0,9$.

Les parois latérales sont pleines et parallèles (ce sont les hublots).

Pour cette étude, les parois haute et basse sont pleines, de façon que l'incidence induite par effets de parois soit faible. Des essais probatoires en veine vide effectués pour des nombres de Mach compris entre 0,3 et 0,9 ont donné des résultats satisfaisants. Toutefois, lors des essais détaillés ici, le nombre de Mach amont n'a pas dépassé 0,80.

2.2 - Balance de pesée d'arrière-corps -

La plupart des études expérimentales de l'interaction nacelle-voilure effectuées à ce jour se sont surtout attachées à évaluer l'influence de la présence de la nacelle propulsive (plus ou moins bien simulée) sur les caractéristiques de l'aile. Une des originalités de la présente étude est que, de plus, on mesure l'influence de la présence de la voilure sur les performances du moteur, en fonction des divers paramètres. A cet effet la nacelle propulsive est placée sur une balance de pesée d'arrière-corps particulièrement adaptée à l'étude des arrière-corps de moteurs à haut taux de dilution.

Le schéma du montage est représenté figure 1.

Le principe est celui du dard amont où la maquette à étudier est fixée à l'aval d'une canne axiale qui sert à amener les flux d'air comprimé et les tubes de mesure des pressions. La balance utilisée est une balance à une composante (poussée axiale) et comporte un barreau dynamométrique équipé de jauges de contrainte.

La maquette de la nacelle est composée d'une partie non pesée (carène d'entrée d'air jusqu'au maître-couple) et d'une partie pesée (arrière-corps proprement dit).

Dans une première version, la liaison entre la partie pesée et la partie non pesée était assurée par un dynamomètre annulaire situé dans la partie amont de la nacelle. Or, les premiers essais ont fait apparaître des difficultés liées à cette disposition : la place allouée au dynamomètre étant exiguë, celui-ci se trouvait ancré sur trop peu de matière. En essai, il subissait des contraintes thermiques et mécaniques telles que la mesure précise de la poussée devenait impossible.

Depuis, le dynamomètre a été reporté à l'amont de la canne et la suspension entre partie pesée et partie non pesée est assurée par un roulement annulaire.

Le contrôle de la couche limite sur le dard en amont de la nacelle est réalisé par deux dispositifs successifs fonctionnant simultanément : un dispositif de soufflage tangentiel et un dispositif d'aspiration au droit de la carène d'entrée. Ces deux dispositifs permettent de réduire l'épaisseur de la couche limite sur l'arrière-corps et de reproduire un écoulement externe réaliste.

2.3 - Maquettes en essai -

2.3.1 - Voilure -

La maquette de l'aile est présentée figure 2. C'est une aile de 220 mm de corde et de 12,5 % d'épaisseur relative. Elle est placée avec un angle de flèche de 28° entre les parois latérales de la soufflerie. Le profil est un profil SNIAS de type supercritique. L'aile est vrillée linéairement de 3° sur la largeur de la veine. La maquette est équipée de 456 prises de pression pariétale réparties en huit tranches avec, sur chaque tranche, 30 prises à l'extrados et 27 à l'intrados.

De plus, la traînée de l'aile peut être déterminée au moyen de sondages de sillage. Des explorations en pression d'arrêt sont effectuées pour six positions en envergure correspondant à des tranches de l'aile garnies de prises de pression pariétale.

Les acquisitions des pressions de sillage et des pressions pariétales ne sont pas simultanées, mais le peigne reste monté en veine (en position rétractée) pendant toute la durée des essais. Il importait donc de vérifier que la présence du peigne n'influence pas sensiblement les pressions relevées sur l'aile. La figure 3 montre une répartition de pression relevée sur l'aile, avec et sans peigne à l'aval.

Les essais ont été réalisés en déclenchant artificiellement la transition de la couche limite par des grains de carborundum collés près du bord d'attaque de l'aile, à l'extrados et à l'intrados. La bande de transition, de 3 mm de large, est placée à 13,6 mm du bord d'attaque.

L'aile est fixée entre les parois de la veine mais il est possible de faire varier son incidence, son altitude et sa position longitudinale.

2.3.2 - Nacelles -

Les maquettes de nacelles ont été fournies par la SNECMA. Elles représentent fidèlement, à l'échelle 1/18,5, des solutions envisagées pour l'arrière-corps du moteur à haut taux de dilution CFM 56.

La poussée est obtenue au moyen de deux jets d'air comprimé simulant les flux du moteur.

Trois maquettes de nacelles ont été essayées. Elles sont représentées figure 4. Deux nacelles sont à flux confluents, l'une courte (FCC) et l'autre longue (FCL). La troisième est du type court, à flux séparés (FSC).

Elles sont équipées de prises de pression sur la méridienne supérieure du carénage externe.

2.3.3 - Pylônes -

Le mât qui lie la nacelle propulsive à l'aile joue un rôle prédominant dans l'interaction voilure-nacelle. Il est donc important, dans une étude expérimentale, de représenter ces mâts de façon réaliste. Le mât a été représenté pour quatre configurations dont deux avec nacelle FCL, une avec nacelle FCC et une avec nacelle FSC.

Les mâts sont solidaires de l'aile. Comme les nacelles sont pesées, il ne doit exister aucun contact mécanique entre le mât et la nacelle. Ceci explique le fait qu'un espace existe entre la nacelle et le mât.

Le montage complet de l'étude d'interaction nacelle-voilure est représenté figure 5.

2.4 - Configurations essayées -

Les essais se sont déroulés en trois parties :

- a) Après détermination de l'incidence à adopter, étude des caractéristiques de l'aile seule dans la veine, à différents nombres de Mach.
- b) Etude de la poussée et des répartitions de pression externe des 3 nacelles, essayées seules en veine.
- c) Etude de l'interaction nacelle-jet-voilure-pylône par essai simultané de l'aile et du fuseau.

Cette dernière partie comporte plusieurs chapitres :

- influence du taux de détente du jet moteur sur les caractéristiques de l'aile ;
- influence du nombre de Mach amont ;
- influence de la position relative aile/nacelle ;
- influence du type de nacelle ;
- influence de la présence du pylône.

L'influence du taux de détente a été étudiée pour des valeurs allant du débit naturel (c'est-à-dire simulant le jet sortant d'une nacelle creuse) à la croisière.

Le nombre de Mach amont a varié entre 0,3 et 0,8.

Pour chacune des nacelles FSC et FCC, plusieurs positions relatives ont été étudiées. Elles définissent un T avec trois positions sur une horizontale et deux ou trois sur une verticale. Ces positions sont définies sur les figures 6 et 7. La nacelle FCL a été essayée à deux positions relatives, toutes deux en présence d'un mât. Ces positions sont définies sur la figure 8.

L'étude de l'influence de la présence du pylône a été effectuée sur une position relative avec nacelle FSC (n° 21') et sur une autre avec nacelle FCC (n° 18').

3 - EXEMPLE DE RESULTATS -

Le présent montage d'essais permet donc d'acquérir un grand nombre de renseignements sur l'interaction nacelle-voilure : répartition de pression sur l'aile et sur les nacelles, mesure de la poussée et du coefficient de débit des moteurs. Pour chaque configuration il est donc possible de déterminer un bilan poussée-traînée global. Les résultats qui suivent donnent une idée des possibilités du montage.

Pour l'analyse, les résultats ont été corrigés des effets de paroi selon la théorie exposée dans [14] en leur affectant une incidence et un nombre de Mach "corrigés" constants dans la veine d'essai.

Sur chaque section, les coefficients aérodynamiques ont été obtenus par intégration des mesures de pression. Les C_x^* et C_x globaux de l'aile ont été obtenus par intégration des C_x et C_x locaux en fonction de l'envergure. Il en résulte que les coefficients globaux ne concernent que la partie de l'aile comprise entre les deux rangées extrêmes de prises de pression.

3.1 - Influence du jet -

Une manière simple couramment utilisée pour représenter les configurations complètes d'ailes équipées de nacelles consiste à utiliser une nacelle creuse, à travers laquelle circule un débit naturel d'air. Il est intéressant de vérifier si cette représentation n'est pas trop simpliste, en essayant l'ensemble aile + nacelle pour différents débits d'air allant du débit naturel au débit représentant la poussée en croisière, et en comparant les coefficients aérodynamiques locaux et globaux. La figure 9 montre qu'une variation notable du taux de détente du jet entraîne une variation qui est très faible en C_x , et modérée en C_x ;

Ces résultats confirment ceux obtenus par El-Ramly et Rainbird [15] sur une configuration semblable.

Ces essais montrent donc l'intérêt de la procédure consistant à utiliser des nacelles perméables lorsqu'on ne s'intéresse qu'aux caractéristiques de l'aile.

Par contre, les poussées obtenues en débit naturel et en débit croisière sont très différentes, ainsi que les répartitions de pression sur la carène de la nacelle, surtout sur le capot primaire moteur, qui est directement soumis à l'influence du jet secondaire. La figure 10 montre l'influence du jet sur la portance et la traînée des diverses tranches en envergure, pour différents nombres de Mach.

De plus, les figures 11 et 12 montrent l'influence du taux de détente des jets sur les répartitions de pression sur l'aile, à deux positions en envergure, l'une (figure 11) étant très proche de l'axe du jet et la seconde étant la plus éloignée (figure 12). Dans ce dernier cas l'influence du taux de détente du jet est tout à fait négligeable.

3.2 - Interaction nacelle-voilure sur les répartitions de pression -

La figure 13 montre l'effet de la présence de l'aile sur les répartitions de pression sur la carène de la nacelle FSC, pour deux nombres de Mach. L'influence est sensible, surtout à $Mo = 0,794$.

Les figures 14 et 15 montrent l'influence de la présence de la nacelle FSC sur les répartitions de pression sur l'aile, en deux envergures. L'effet est marqué sur la section centrale (figure 14) ce qui n'est pas surprenant, mais aussi sur la tranche la plus éloignée (figure 15). L'effet se traduit surtout à cette envergure par la remontée vers l'amont du choc à l'extrados de l'aile.

3.3 - Influence de la position relative aile-nacelle -

3.3.1 - Influence de la position horizontale -

La figure 16 montre la variation du C_x de l'aile et du coefficient de poussée de la nacelle provoquée par un déplacement horizontal relatif aile/nacelle.

On note que la traînée de l'aile et la poussée de la nacelle sont des fonctions croissantes de la distance relative. Le bilan global d'interaction représenté aussi figure 16 est toujours favorable et fait apparaître que la meilleure position est la position 21' qui est celle où l'aile et la nacelle sont le plus proche l'une de l'autre.

3.3.2 - Influence de la position verticale -

La figure 17 montre que, quand l'aile s'éloigne verticalement de la nacelle, la traînée de l'aile et la poussée de la nacelle diminuent faiblement. Le bilan global d'interaction, qui est toujours favorable, indique la position la plus éloignée comme étant la meilleure, mais l'écart avec les autres positions est faible.

Les résultats des deux paragraphes ci-dessus confirment ceux de [16].

3.3.3 - Etude des répartitions de pression sur la nacelle -

La figure 18 montre l'évolution des pressions sur la nacelle, pour les diverses positions relatives étudiées en débit de croisière. Le niveau de pression sur la carène secondaire augmente quand on rapproche l'aile de la nacelle horizontalement ou verticalement, sauf pour la dernière prise, à la position 21'.

3.4 - Influence du type de nacelle -

Les deux types de nacelle FSC et FCC ont été comparés en présence de l'aile en position analogue, c'est-à-dire pour des distances du bord d'attaque du profil central de l'aile au plan de référence des maquettes de nacelles identiques.

* Les sondages de sillages ont été effectués lors d'une seconde campagne d'essai. Au moment de la rédaction du présent document les résultats des C_x de sillage n'étant pas encore disponibles, l'évaluation des C_x a été effectuée à partir de l'intégration des pressions sur l'aile.

Comparée à la nacelle FSC en position 10, la nacelle FCC engendre sur l'aile une forte diminution de traînée alors que la présence de l'aile a le même effet sur la poussée des deux nacelles, ce qui donne un bilan global poussée-traînée plus favorable pour la nacelle FCC (voir figure 19).

3.5 - Influence de la présence du pylône -

Deux configurations, ne différant que par la présence ou l'absence de pylône ont été comparées. Le type de nacelle est le même (FSC), de même que la position relative aile-nacelle (21'), l'incidence, le nombre de Mach amont (0,794) et le taux de détente des jets.

La figure 20 montre la différence entre la répartition de pression sur l'aile pour $\eta = 0,456$. On constate que localement à l'intrados, la présence du pylône provoque une accélération sensible de l'écoulement.

Toutefois, lorsqu'on s'éloigne en envergure, à $\eta = 0$ (figure 21) l'influence de la présence du pylône sur la répartition de pression est négligeable.

4 - DISCUSSION DES RESULTATS -

Les résultats présentés ici font appel à des C_x locaux et globaux obtenus par intégration des pressions sur l'aile. Ils devront être confirmés par la détermination des C_x obtenus par sondage des sillages de l'aile ; les essais ont eu lieu lors d'une seconde campagne, dont les résultats ne sont pas encore exploités.

D'autre part, l'étude de la position relative aile-nacelle a été effectuée sans pylône. L'importance de ce dernier, soulignée en 3.5 nécessiterait une étude en présence du pylône. Malheureusement, le type de montage utilisé ici est peu pratique pour une telle étude (il faut réaliser une forme de pylône pour chaque position de nacelle).

En ce qui concerne la mesure de poussée d'arrière-corps, le dispositif a été calibré au moyen d'une tuyère étalon de type ASME qui est présentée figure 22. Les essais ont été effectués pour des nombres de Mach externes et des taux de détente variables et comparés à ceux obtenus avec une tuyère analogue du banc de dynalpie BD2 de l'ONERA à Modane, ainsi qu'à une formule proposée par l'ASME. La figure 23 résume ces comparaisons et montre que l'accord est bon, tant pour le coefficient de poussée isentropique η_u que sur le coefficient de débit C_D , ce qui valide les résultats relatifs à la poussée.

5 - CONCLUSION -

Un montage d'essais d'interaction nacelle-voilure a été développé à la soufflerie S3Ch de l'ONERA pour des configurations d'essais subsoniques à venir, c'est-à-dire à voilure supercritique et nacelles de moteurs double flux à haut taux de dilution. Les caractéristiques de l'aile sont déterminées par relevé des répartitions de pression pariétale en 8 sections, et sondage du sillage à l'aval de ces sections. Les nacelles sont placées à l'aval d'un dard amont amenant les flux d'air comprimé. La poussée d'arrière-corps et le coefficient de débit de tuyère sont mesurés. L'étude de l'effet de nombreux paramètres peut ainsi être effectuée :

- taux de détente du jet moteur ;
- nombre de Mach amont ;
- position relative aile-nacelle ;
- type de nacelle ;
- présence du pylône.

Les résultats présentés illustrent les multiples possibilités de ce montage qui est appelé à l'avenir :

- d'une part à faciliter la compréhension des phénomènes d'interaction ;
- d'autre part, à valider les méthodes de prévision théorique correspondantes.

NOTATIONS

B	1/2 envergure de l'aile	P_i	pression d'arrêt locale
C	corde de l'aile	P_{i0}	pression génératrice de référence
C_D	coefficient de débit de tuyère	P_{i1}	pression d'arrêt du jet secondaire
C_x	coefficient de traînée	Q_0	pression dynamique de référence $Q_0 = 0,7 \rho_0 M_0^2$
C_{xp}	coefficient de traînée de pression de la portion d'aile garnie de prises de pression	R_N	nombre de Reynolds mesuré au col de la tuyère étalon
C_z	coefficient de portance de la portion d'aile garnie de prises de pression	S	surface de référence de l'aile
D	diamètre de la nacelle dans le plan d'éjection secondaire	x	abscisse comptée sur une méridienne de la nacelle (origine plan de référence nacelle)
F/A_S	coefficient de poussée de la nacelle	X	abscisse du plan d'éjection secondaire (origine B.A. de la corde centrale de l'aile)
K_p	coefficient de pression $K_p = \frac{P - P_0}{Q_0}$	y	distance en envergure (origine : section n° 8 de l'aile)
K_x	coefficient de traînée locale d'une tranche d'aile	Z	distance verticale (origine : axe veine)
K_z	coefficient de portance locale d'une tranche d'aile	α	incidence de l'aile
M_0	nombre de Mach amont	$\eta = \frac{Y}{B}$	envergure réduite
p	pression statique locale	η_0	coefficient de poussée isentropique
p_0	pression statique de référence		

ABREVIATIONS -

FCC nacelle à flux confluents courts
 FSC nacelle à flux séparés courts

FCL nacelle à flux confluents longs

REFERENCES

- 1 KHO Y.G.
Wind-tunnel measurements on the interference between a jet and a wing, located outside the jet. Part I.
NLR TR 77009 U
- 2 ZANDBERGEN
Experimental investigation of the aerodynamic characteristics of a wing in propulsive jets
NLR TR 77081
- 3 M. WITTMANN and W. FISCHER
Institut für Luft- und Raumfahrt, TH Aachen
Investigation of the interaction between Engine Nacelle and Wing
DLR FB 74-32, 1974
- 4 SWAN-SIGALLA
The problem of installing a modern high bypass engine on a twinjet transport aircraft.
AGARD CP-124
- 5 KUTNEY
Airframe/Propulsion system Integration Analysis Using the Propulsion Simulator Technique.
AGARD CP-71-71
- 6 SAIZ
Interaction des jets des réacteurs GE CF6 50 sur la cellule de l'Airbus en croisière
Simulation en soufflerie (Bordeaux)
AAAF 1974
- 7 PATTERSON J.
A wind tunnel investigation of jet wake effect of a high-bypass engine on wing nacelle interference
drag of a subsonic transport
NASA TND 4693
- 8 MUNNIKSM - JAARSMA
Jet Interference of a podded Engine Installation at Cruise conditions.
AGARD CP 150
- 9 G. KRENZ
Airframe engine interaction for engine configurations mounted above the wing.
Part I : interference between wing and Intake/Jet
AGARD CP 150
- 10 B. EWALD
Part II : engine jet simulation problems in wind-tunnel tests.
AGARD CP 150
- 11 RANEY D.J. - KURN A.G.
Wind-tunnel investigation of jet interference for underwing installation of high bypass ratio engine
RAE TR 68049 1968
- 12 PAULEY G.
Interim note on tests with a wing mounted fan nacelle with the fan jet simulated by cold air blowing
and alternatively by a gas generator shroud
ARCCP 1111
- 13 PATERSON FLECHNER
Jet wake of a high bypass engine on wing nacelle interference drag of a subsonic transport airplane
NASA TN D 6067 (1970)
- 14 PINOZOLA M., LO C.F.
Boundary interference at subsonic speeds in wind tunnels with ventilated walls.
AEDC TR 69.47 - Mai 1969
- 15 Z. EL RAMLY, V.J. RAINBIRD
Effect of simulated jet engines on the flowfield behind a swept back wing.
Journal of Aircraft Vol 14 n° 4, avril 1977, p. 343-349.
- 16 S.E. ALDRIDGE, J.L. NYE
Experimental results of high bypass ratio turbofan and wing aerodynamic interference
AGARD CP 71

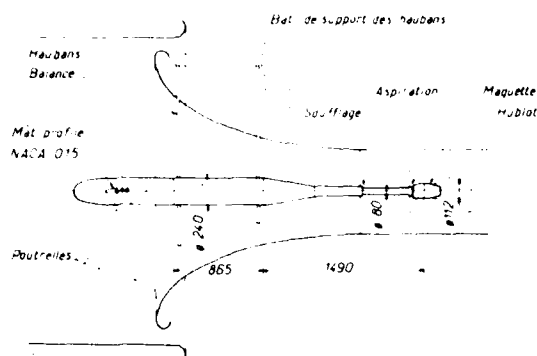


Fig. 1 - Schéma du montage D4.

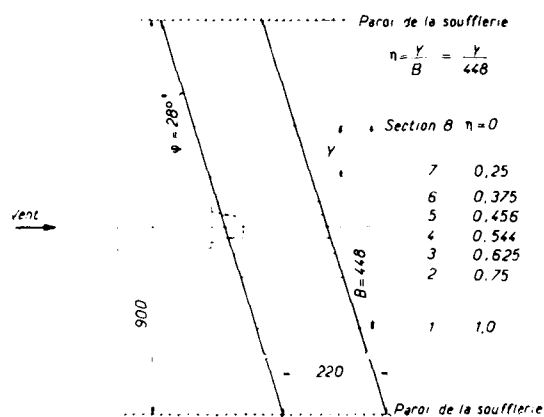


Fig. 2 - Maquette AS401 - Positions des sections de mesures de pression.

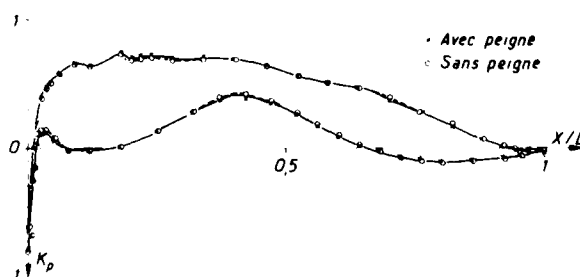
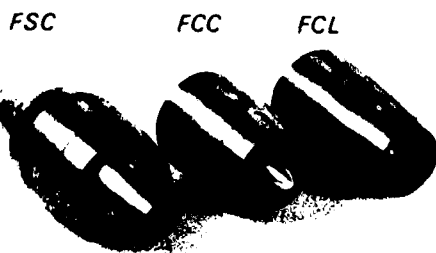
Fig. 3 - Influence de la présence du peigne de sondage de sillage sur la répartition de pression sur l'aile. $M_0 = 0,794$; $\alpha = 1^\circ$; $\eta = 0,544$. Position 25 sans pylone. Nacelle FSC croisière.

Fig. 4 - Maquettes d'arrière-corps CFM 56.

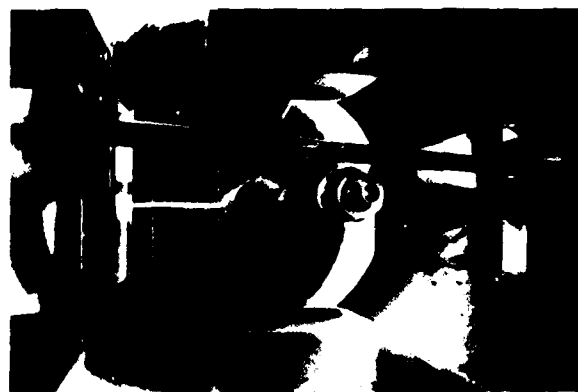


Fig. 5 - Montage d'essai d'interaction nacelle-voilure à la soufflerie S3Ch de l'ONERA.

	X	X/C	Z	Z/D
10	26,5	0,12	21,5	0,18
11	26,5	0,12	29,85	0,25
13	26,5	0,12	44,28	0,37
14'	50,73	0,23	21,5	0,18
21'	0,21	0,001	21,5	0,18
25	24,78	0,11	21,5	0,18

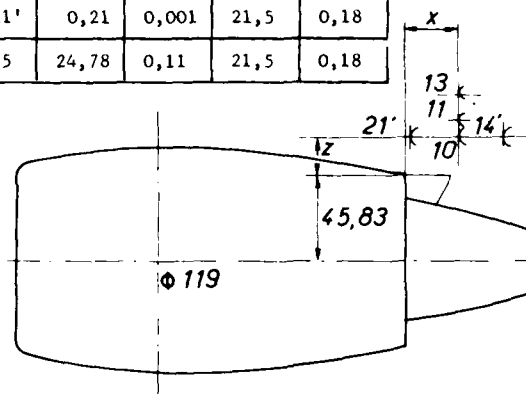


Fig. 6 - Positions relatives étudiées. Nacelle FSC.

	X	X/C	Z	Z/D
15	- 50,94	- 0,23	29,5	0,39
16'	- 65,21	- 0,30	29,5	0,39
17	- 50,94	- 0,23	39,75	0,52
18'	- 21,15	- 0,10	29,5	0,39

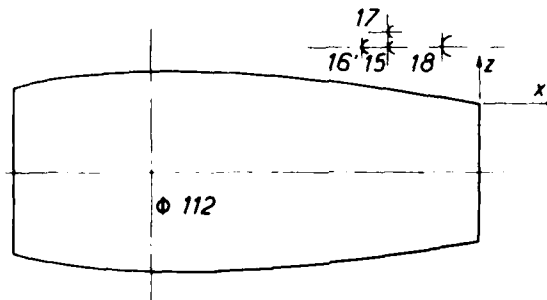


Fig. 7 - Positions relatives étudiées. Nacelle FCC.

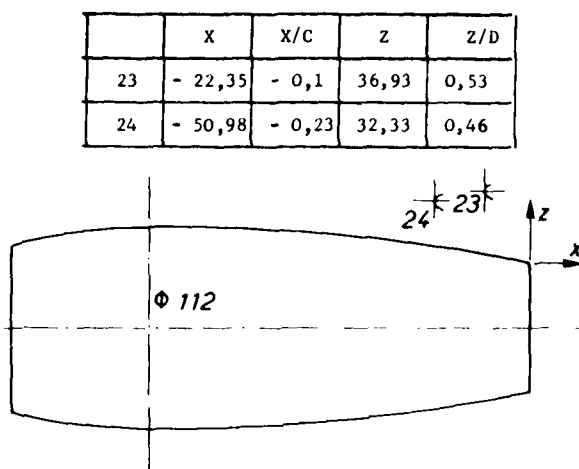
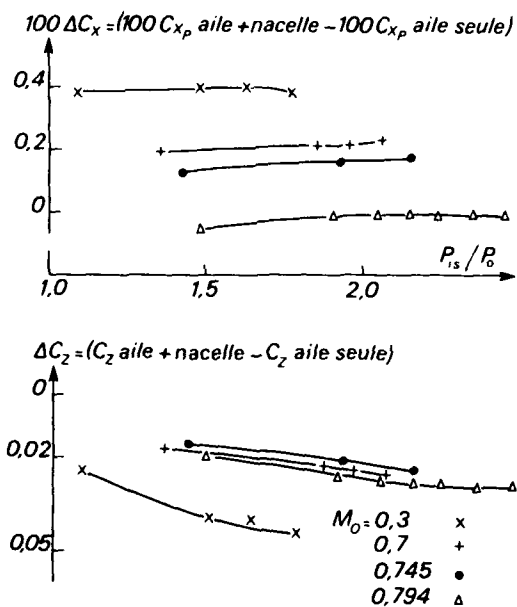
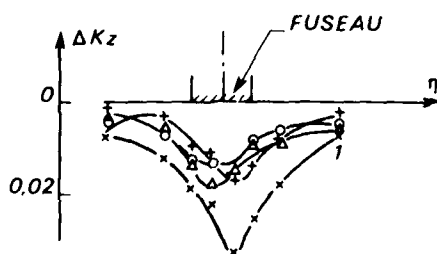


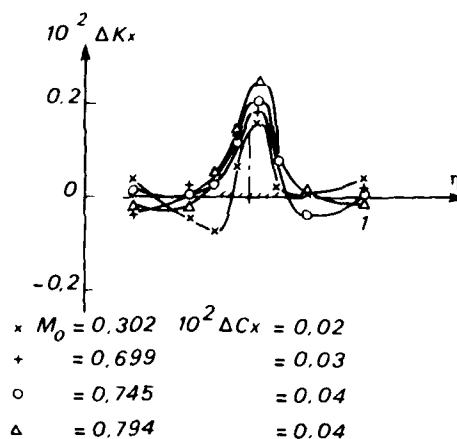
Fig. 8 - Positions relatives étudiées. Nacelle FCL.

Fig. 9 - Influence du taux de détente du jet. Position 10. Nacelle FSC. $\alpha = 1^\circ$.

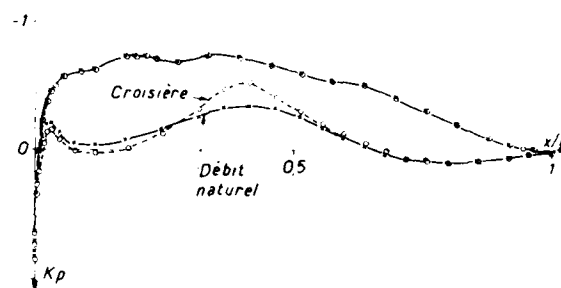
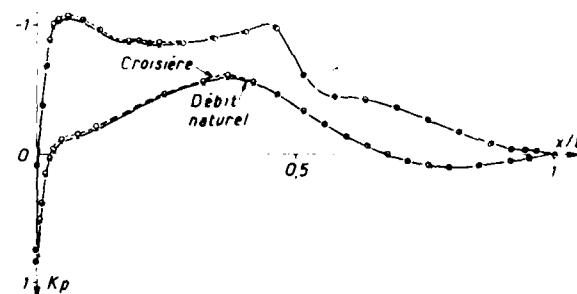
x	$M_0 = 0,302$	$\Delta C_z = -0,016$
$+$	$= 0,699$	$= -0,008$
o	$= 0,745$	$= -0,008$
Δ	$= 0,794$	$= -0,009$



a



b

Fig. 10 - Influence du nombre de Mach sur les répartitions de C_x et C_z de l'aile en fonction de l'envergure. Nacelle FSC. Position 10. $\alpha = 1^\circ$.Fig. 11 - Influence du taux de détente du jet sur les répartitions de pression sur l'aile. $M_0 = 0,794$; $\alpha = 1^\circ$; $\eta = 0,544$.Fig. 12 - Influence du taux de détente du jet sur les répartitions de pression sur l'aile. $M_0 = 0,794$; $\alpha = 1^\circ$; $\eta = 0$. Nacelle FSC en position 10.

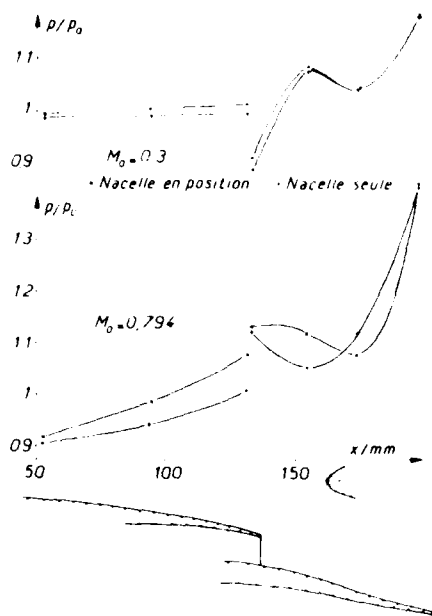


Fig. 13 - Influence de la présence de l'aile sur les répartitions de pression sur la nacelle FSC en croisière.

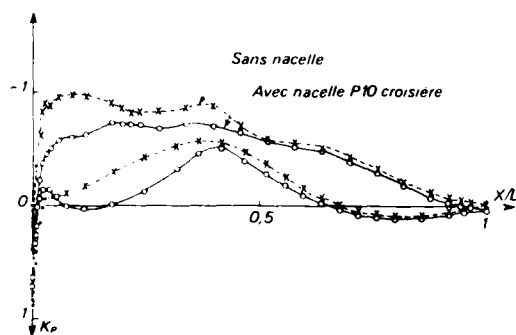


Fig. 14 - Influence de la présence de la nacelle sur la répartition de pression sur l'aile. $M_0 = 0,794$; $\alpha = 1^\circ$; $\eta = 0,544$.

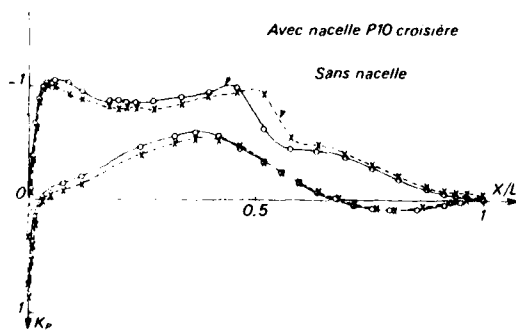


Fig. 15 - Influence de la présence de la nacelle sur la répartition de pression sur l'aile. $M_0 = 0,794$; $\alpha = 1^\circ$; $\eta = 0$.

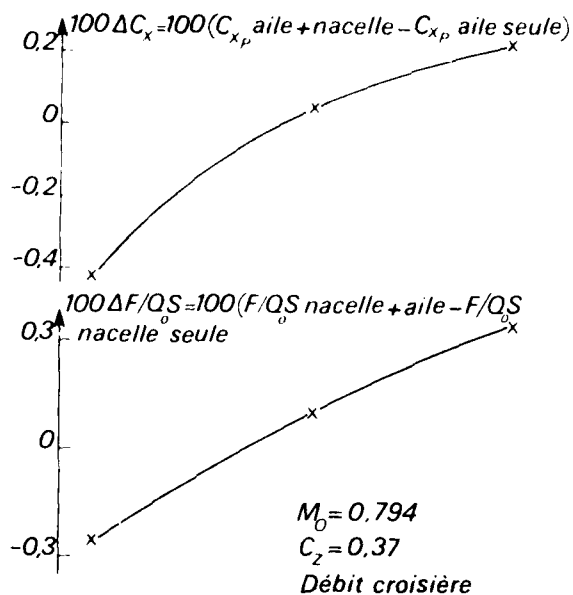


Fig. 16 - Influence de la position relative horizontale.

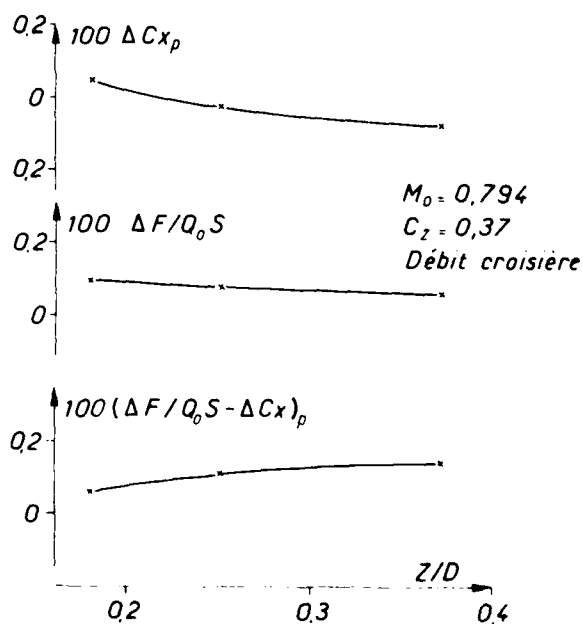


Fig. 17 - Influence de la position relative verticale.

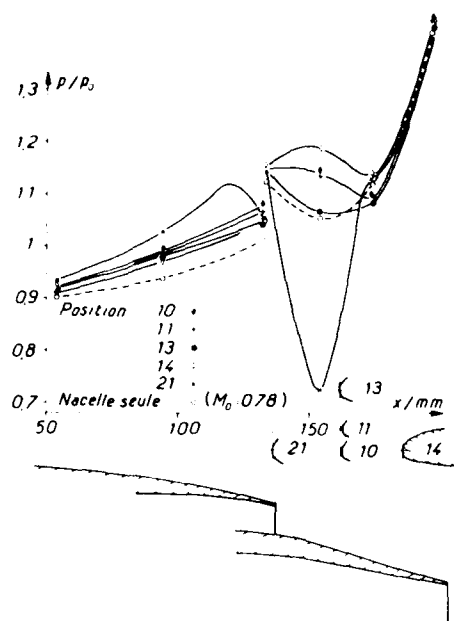


Fig. 18 - Influence de la position relative aile/nacelle sur les répartitions de pression sur la nacelle FSC. $M_0 = 0,794$; $\alpha = 1^\circ$. Croisière.

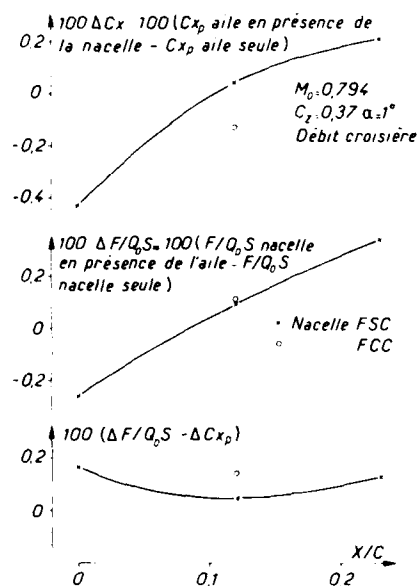


Fig. 19 - Influence du type de nacelle.

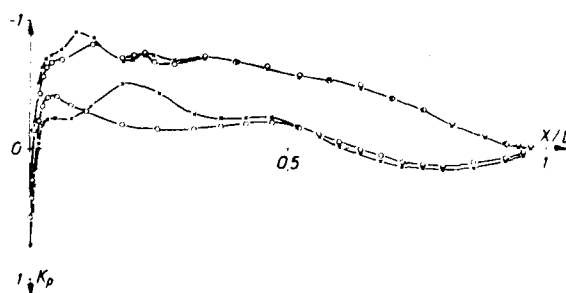


Fig. 20 - Influence de la présence du pylône sur la répartition de pression sur l'aile. $M_0 = 0,794$; $\alpha = 1^\circ$; $\eta = 0,456$. Nacelle position 21. Débit croisière.

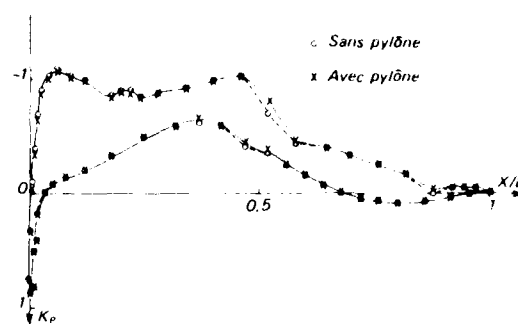


Fig. 21 - Influence de la présence du pylône sur la répartition de pression sur l'aile. $M_0 = 0,794$; $\alpha = 1^\circ$; $\eta = 0$. Nacelle FSC position 21. Débit croisière.

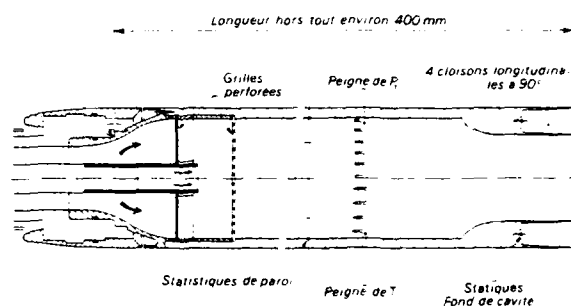


Fig. 22 - Montage tuyère de référence S3 Chalais.

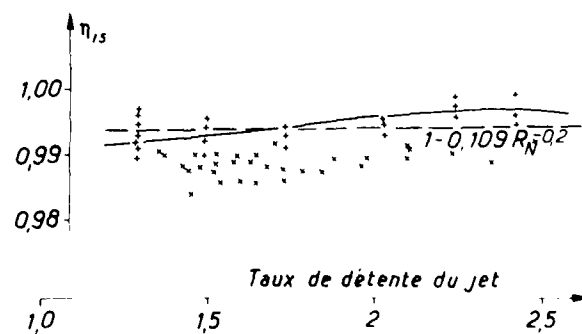
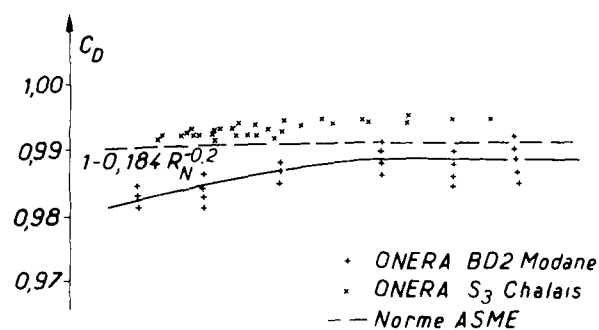


Fig. 23 - Comparaison des essais d'une tuyère de référence ASME.

A WIND TUNNEL INVESTIGATION OF THE AERODYNAMIC CHARACTERISTICS OF FORWARD SWEEP WINGS

by

Dr. T. M. Weeks

Lt. G. C. Uhuad

Capt. R. Large

Air Force Wright Aeronautical Laboratories

Flight Dynamics Laboratory

Wright-Patterson AFB

Ohio, 45433

SUMMARY

An experimental investigation of a forward swept wing and a state-of-the art "equivalent" aft swept wing was conducted to compare the relative performance of both wings at identical transonic maneuver design conditions ($C_L = 0.9$ and $M = 0.9$) and to determine any associated drag penalty of the forward swept wing for a high supersonic cruise condition ($C_L = 0.075$, $M = 2.0$). At the transonic maneuver design condition, the results indicate a significant reduction in the profile drag of the forward swept wing relative to the aft swept wing. The forward swept wing drag exhibited extreme sensitivity to wing root height and incidence variations. Guided by computation employing modified small disturbance theory a relocation of the FSW root from a mid to high body position and an increase in incidence of 0.8 degrees was accomplished. This resulted in a two hundred count drag reduction at $C_L = 0.9$. A drag penalty was recorded at $M = 2.0$ for the forward swept "cruise wing." The cruise wing had the same sweep and "box geometry" as the transonic maneuver wing but with reduced camber and twist accomplished by flap deflection. The drag penalty decreased at lower supersonic Mach numbers. The results of this test indicate that aft swept wing transonic aerodynamic design methods can be used to design and analyze forward swept wings with only minor modifications.

LIST OF SYMBOLS

ASW	Aft Swept Wing
AR	Aspect Ratio
b	Span ~ ft
BL	Butt Line ~ ft
c	Section Chord ~ ft
C_{avg}	Average Geometrical Wing Chord
C_D	Drag Coefficient ~ $\frac{D}{qs}$
$(C_{D_L})_{profile}$	Profile Drag Coefficient Due to Lift
C_{D_i}	Induced Drag Coefficient
$C_{D_{min}}$	Minimum Drag Coefficient
C_L	Lift Coefficient ~ $\frac{L}{qs}$
C_{ℓ}	Section Lift Coefficient
Q_L	Fuselage Centerline
C_p	Pressure Coefficient ~ $\frac{p-p}{q}$
CP	Center of Pressure
e	Span Efficiency Factor
FSW	Forward Swept Wing
L/D	Lift to Drag Ratio
M	Mach Number
MAC or \bar{c}	Mean Aerodynamic Chord
q	Dynamic Pressure
RN	Reynolds Number
S_w	Wing Reference Area - Ft^2
S_c	Canard Reference Area - Ft^2
t/c	Thickness Ratio
s/c	Percent Chord
y/b or η	Spanwise Station
Alpha or α	Angle of Attack ~ degrees
Beta or β	Sideslip Angle ~ degrees
τ	Taper Ratio
ΔLE	Leading Edge Sweep Angle ~ degrees
$\Delta Shock$	Shock Sweep ~ degrees

INTRODUCTION

An investigation of a forward swept wing (FSW) versus a state-of-the-art aft swept wing (ASW) was conducted to compare the relative performance of both wings at a transonic maneuver condition ($C_L = 0.9$, $M = 0.9$) and to determine the associated drag penalty of the

FSW for a high supersonic cruise condition ($C_L = 0.075$, $M = 2.0$). The results indicate a significant reduction in profile drag for the FSW relative to its ASW counterpart. A small penalty was recorded for the forward swept supersonic cruise wing. This latter wing was designed to represent the same sweep and box geometry as the transonic maneuver wing but was uncambered and had its twist reduced through variable camber flaps. This study was conducted under a joint effort by the USAF AFWAL/Flight Dynamics Laboratory and Grumman Aerospace Corporation.

DISCUSSION

The concept of forward swept wings is not entirely new. In the investigation of the different methods of delaying the onset of the drag rise for flight in the vicinity of the speed of sound, it was found that sweeping the wings provided the most effective technique of increasing the drag divergence Mach number. Aerodynamically the same effect can be obtained regardless of the direction of sweep. However, current aircraft designs favor the use of aft sweeping in order to avoid the phenomenon of structural divergence inherent on forward swept wings operating at a high dynamic pressure condition which cannot be solved through conventional (metallic) structures without paying an excessive wing weight penalty. Recent advances in composite materials technology is now providing a promise of eliminating this problem of structural divergence with little or no wing weight penalty.

With composite materials, the wing skin laminates can be tailored to provide favorable wing panel deflections at Mach numbers considerably higher than previously attained with conventional structure swept forward wings. Until the advent of composite materials, very few forward swept wing aircraft were designed and only a very limited number were actually built and flown. Some notable examples include the HANSA HFB 320 and the JUNKERS JU-287. The former is currently operational as a business jet and the latter flew over a dozen times before being damaged by allied bombers during World War II. Renewed interest in forward swept wing investigations, stimulated by the advances in composite materials, have provided several new design additions.

Some of the aerodynamic benefits of forward swept wings include spin resistance, extended high angle of attack lateral control and lower transonic maneuvering drag. The forward swept wing separation pattern generally starts from the root and gradually propagates outboard. This allows attached flow to be maintained over the outboard wing panels, retaining aileron effectiveness at high angles of attack where aft swept wings may exhibit degradations in lateral control.

The theoretical transonic maneuver drag advantage of FSW over an equivalent ASW are due to the two lift dependent components of drag (Fig 1), induced drag and profile drag due to lift, which can be shown to be less than that of an aft swept wing when both wings are designed under identical transonic design conditions.

a) Profile Drag Due to Lift: During the Grumman HIMAT program, experimental investigations of a series of supercritical wings have shown a direct relation between leading edge sweep and profile drag at the maneuver lift conditions. Analysis of the data showed that while maintaining shock location and utilizing the Grumman supercritical "K" airfoil, the profile drag decreases with leading edge sweep in a manner shown in Fig 2. In comparing forward and aft swept wings, if the condition of identical shock sweep, shock location, aspect ratio and taper ratio are applied, the resulting leading edge sweep of a forward swept wing is less than that of the aft swept wing (Fig 3). Hence, from Figure 2, utilizing the same HIMAT wing design method and the Grumman supercritical "K" airfoil, the FSW indicates a reduction in profile drag by a value proportional to the difference in sweep of both wings.

b) Induced Drag: The other reason for a FSW drag advantage can be explained as follows: Under a condition of equal lift and identical spanload, the center of pressure of the FSW is more inboard along the swept structural span than the ASW (Fig 4). Consequently, the bending moment about a pivot point can be considerably less. If the span of the FSW is then allowed to increase, while maintaining wing area, until the pivot bending moments are equal, the accompanying increase in aspect ratio decreases the induced drag. In order to validate this FSW drag advantage (Fig 5) a series of wind tunnel investigations were conducted by Flight Dynamics Laboratory, in cooperation with Grumman on forward and aft swept wing models of identical aerodynamic designs.

Model and Test Description: Three wind tunnel entries were made in 1978, 1979. Figures 6 and 7 show the general arrangement of the model. The model was area ruled separately for the forward and aft swept wings, (Fig 8). In all three entries, the wing aspect ratio, taper ratio, reference area, planform and airfoil section ("K") were identical for both FSW and ASW.

a) First Entry: Tested both forward and aft swept maneuver condition wings ($C_L = 0.9$, $M = 0.9$). The FSW required twist distribution is essentially opposite but also reduced to that of the corresponding ASW (Fig 9). The calculated shock sweep angles were $+40^\circ$ for the aft and forward swept wings respectively. In this case, the ASW had a 48.7° leading edge sweep whereas the FSW has a -28.7° leading edge sweep. The FSW twist for this condition was about 10° with -5.8° wing root incidence. The ASW total twist was $+9^\circ$ with $+9^\circ$ wing root incidence. Both wings were designed to satisfy a high body lift condition. Transitioning the paper design to the practical model posed difficulties that were impossible to satisfy this high body design condition simultaneously for both wings. This difficulty stems out of the opposite twist requirements of the initial wing location criteria that was then selected was to make the quarter chord points of the mean geometric chords of both wings identical.

b) Second Entry: Tested both FSW and ASW in their supersonic cruise configuration. Wing planform and height were derived from the first entry. Twist and camber were reduced on both wings. The aft swept wing total twist was 12° with a root incidence of 11° . The FSW total twist was 6.8° with a -5.8° root incidence (Fig 10). The "box" geometry from 15% to 60% chord were made identical to the first entry wings.

c) Third Entry: The initial wing location criteria used during the first entry had resulted in the FSW being mislocated such that the wing root was operating in a region of excessive fuselage upwash. The final entry tested only the FSW maneuver case. Wing height was changed such that the crest point of the centerline airfoil coincided with the top of the fuselage as in the ASW case. Sweep was increased to -30° and wing root (Fig 11) incidence was modified to increase the leading edge height from the fuselage centerline. Other components of the model were identical for all testing. The model consisted of a hardback with external body pieces. A set of canards was fabricated to provide limited assessment of canard effects. The configuration incorporated a centerline vertical tail. Two tails were fabricated with one having rudder deflection capability. Tests were conducted in the 4 foot transonic tunnel of the Propulsion Wind Tunnel Facility of the Arnold Engineering and Development Center. Tests were conducted over a Mach range from 0.6 to 1.3 and at 2.0. Reynolds number was fixed at 3.5×10^6 per foot. Six component force and moment data were taken along with model pressure data during the first and second entry. No pressure data were obtained during the third entry. Oil flow data were also obtained for all flow conditions (Fig 12).

TEST RESULTS

Transonic Maneuver Condition: The wing location criteria used for the first wind tunnel entry resulted in the fabrication of the forward swept wing such that the wing root leading edge height was only 0.1875 inch above the fuselage reference line. The aft swept wing root leading edge height was 1.0625 inches. A comparison of chordwise pressure (Fig 13) distributions at two spanwise station farthest from the wing-body junction ($\text{ETA} = 0.625$ and 0.85) shows that the FSW lower surface pressure is higher than the ASW. This is the mechanism that allows a forward swept wing to have a lower profile drag, provided that the condition of equal shock sweeps are satisfied throughout the full wing span (Fig 3). Although this desired pressure trend exists in some regions of the FSW during the test, a comparison of drag at the maneuver condition shows that the FSW was considerably higher than the ASW for a wing-body configuration (Fig 14). An examination of the first set of pressure and oil flow data (Ref 6) shows that loss of lift (Fig 15) and separation is occurring in the vicinity of the wing-body junction. The effects of the addition of canards are to improve the FSW drag (e.g. 200 counts for a 5° deflection at $C_L = 0.9$) and provide a marked straightening of the oil flow patterns on the inboard areas affected by canard downwash. The same canards provided no appreciable effects on the ASW. These findings indicate that the FSW was mislocated so that the inboard wing area was operating in a region of excessive fuselage upwash thereby causing premature separation and shock unsweeping. This made the first FSW vs ASW comparisons unsatisfactory since the condition of near identical flow (i.e. equal shock sweeps) were not satisfied.

In an unpublished study conducted by the External Aerodynamics Group, using a transonic small disturbance code on the FSW, it was found that improvements in chordwise pressure and spanwise load (Figure 16A and 16B) can be obtained by varying the wing height from $WL = 0.2$ to $WL = 0.8$. The shock location shows a rearward movement and the spanload increases near the fuselage centerline. Guided by these calculations, the FSW was modified in order to make the crest point of the centerline airfoil coincident with the top of the fuselage. This modification raised the root leading edge to 0.625 inch above the fuselage reference line. Matching the ASW and FSW root leading edge heights was desired but the geometric constraint imposed by the FSW fuselage diameter and the reverse root incidence limited this wing relocation. Figure 17 shows a comparison of the modified FSW (third entry) to the first entry ASW at the maneuver design condition. The FSW exhibits 40 counts lower drag than the ASW and a 235 count improvement from the first FSW entry.

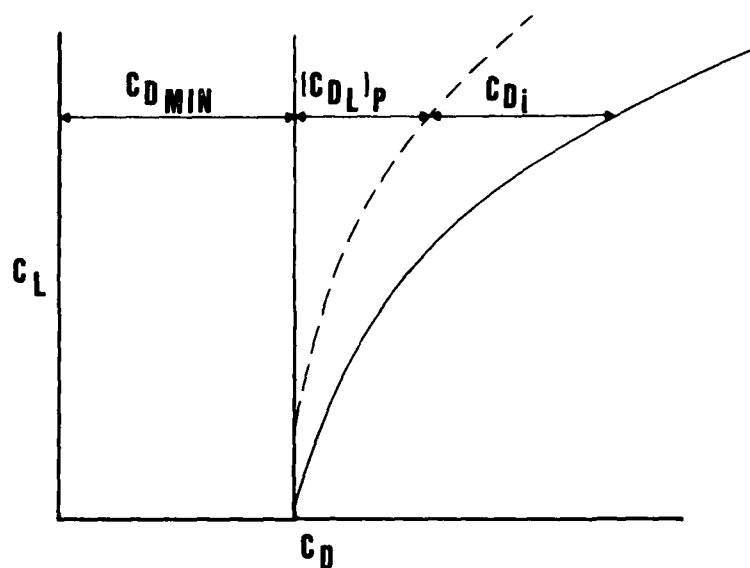
Since the aspect ratios of both wings were constrained, only the profile drag reduction was directly verified. However an indication of the potential induced drag advantage can be seen by comparing pivot bending moment data. A comparison of the ASW integrated moment of area of the spanload (Fig 18) about an axis at $y = 2.007$ " where the equivalent FSW bending gage is located, to the direct FSW gage readings (Fig 19) showed that the FSW bending moment was 20 in-lb less than the ASW moment.

Supersonic Cruise: A drag penalty was recorded for the FSW cruise wing at a high supersonic Mach number (2.0). For this test, only the wing camber and twist were modified. Sweeps were retained from the maneuver wing designs, consequently, the FSW leading edge becomes supersonic at a lower Mach number than the ASW. The same geometric reason that provides an advantage for FSW transonically, may become a disadvantage if the wing sweep is fixed. A better comparison for a high Mach number condition can be made by using the condition of equal leading edge sweeps. Figure 20 shows that at lower supersonic Mach numbers, the difference in drag decreases.

CONCLUDING REMARKS

Some of the results of a wind tunnel investigation of the aerodynamic characteristics of forward swept wings have been discussed. It was shown that under identical transonic aerodynamic design conditions, a forward swept wing can be designed to provide lesser profile drag than an equivalent aft swept wing. A potential for further drag reduction was shown by comparing the wing bending moments and showing that the FSW bending moment is

lower thereby allowing possible growth in FSW aspect ratio and reducing induced drag. The achievement of comparable point design transonic maneuvering drag performance indicates that current aft swept wing aerodynamic design methods can be used to design forward swept wings with little or no modifications. Additionally, FSW drag and wing inboard pressures exhibit extreme sensitivity to wing root height and incidence variations as a result of a strong and synergistic effect of the fuselage and wing upwash on the inboard wing flow. This area requires careful consideration during the wing design and fabrication process.



$$C_D = C_{D \text{ MIN}} + C_{D_L}$$

$$C_{D_L} = (C_{D_L})_P + C_{D_i} \quad \leftarrow \text{LIFT DEPENDENT DRAG}$$

WHERE: C_{D_i} - INDUCED DRAG

$(C_{D_L})_P$ - VISCIOUS (PROFILE) DRAG DUE TO LIFT

FIGURE 1. DRAG BREAKDOWN

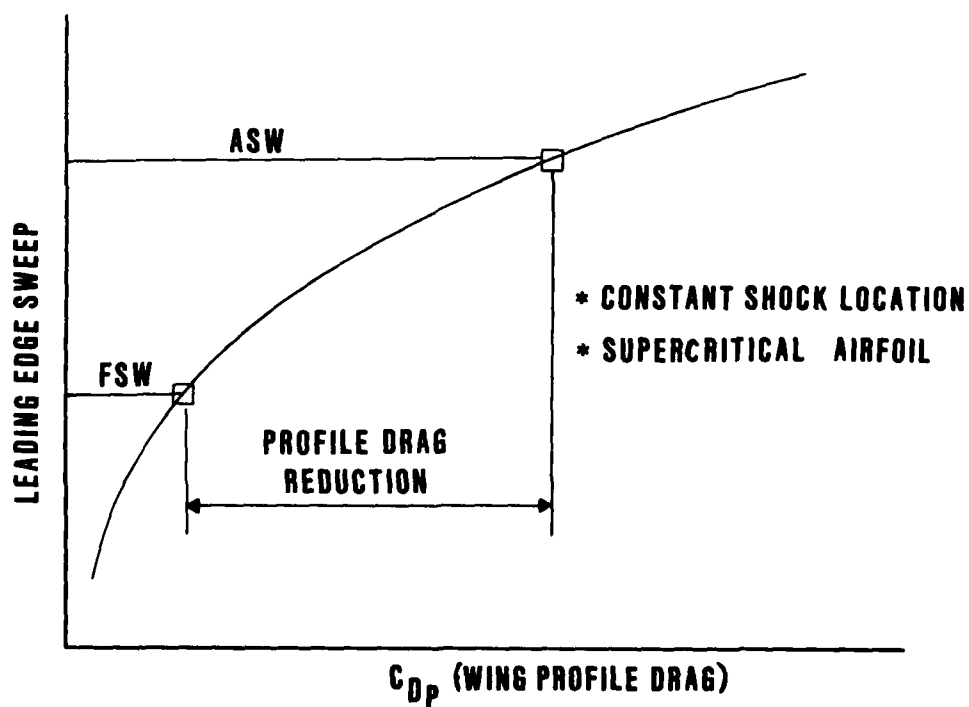


FIGURE 2. PROFILE DRAG

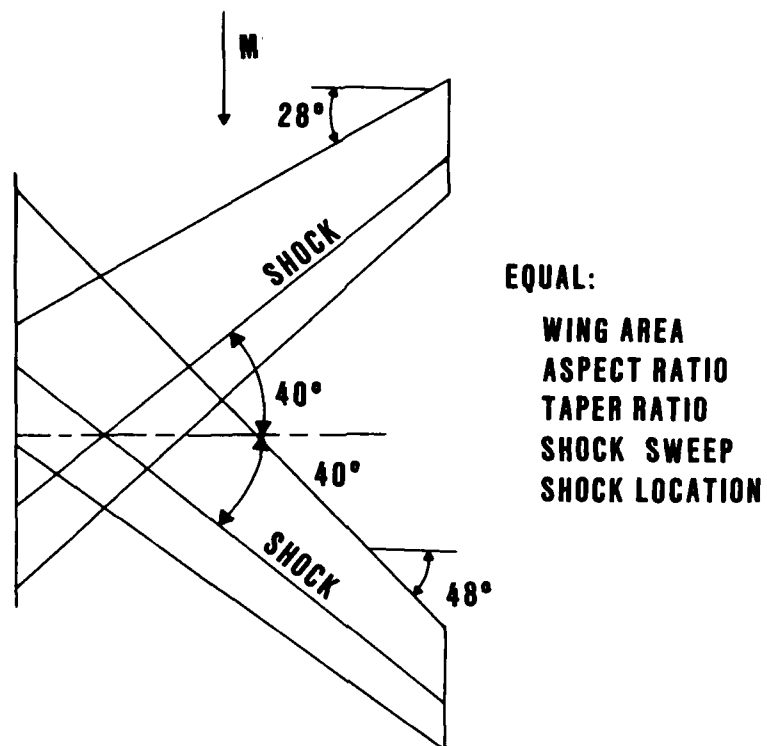


FIGURE 3. **LEADING EDGE SWEEP COMPARISON**

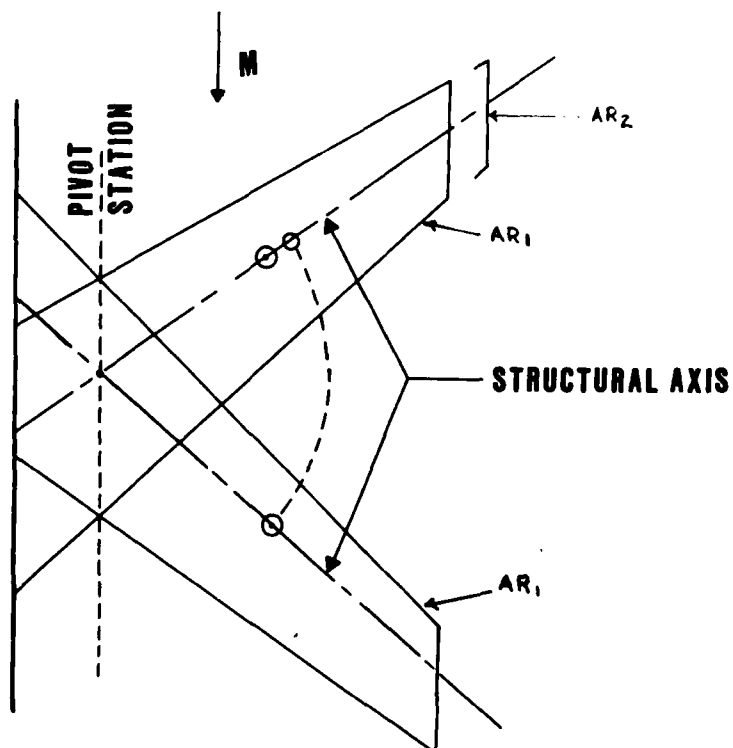


FIGURE 4. **CENTER OF PRESSURE**

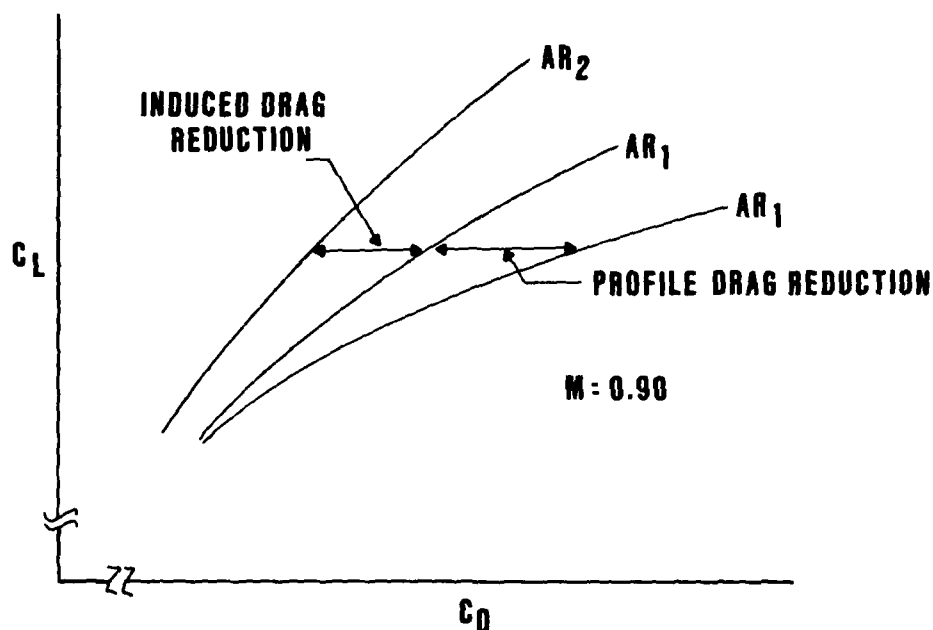


FIGURE 5. FORWARD SWEPT WING DRAG ADVANTAGE

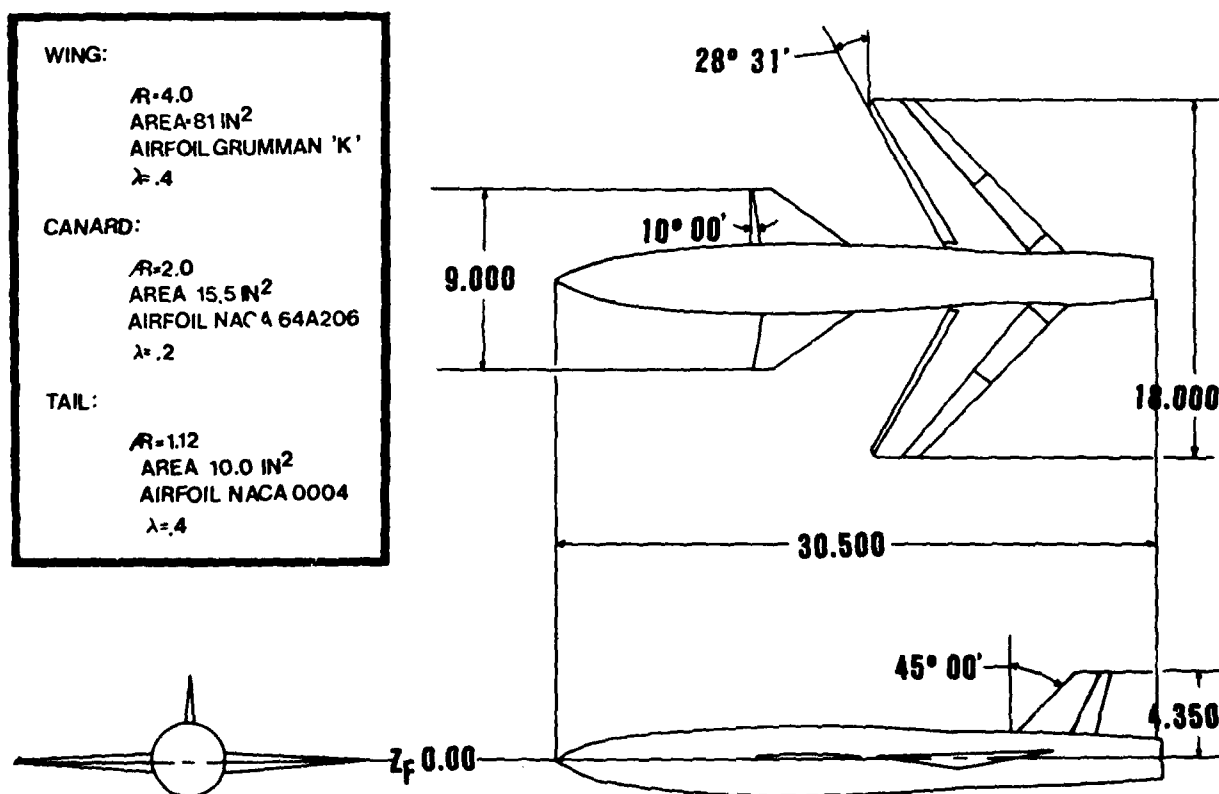


FIGURE 6. GENERAL ARRANGEMENT FORWARD SWEPT WING

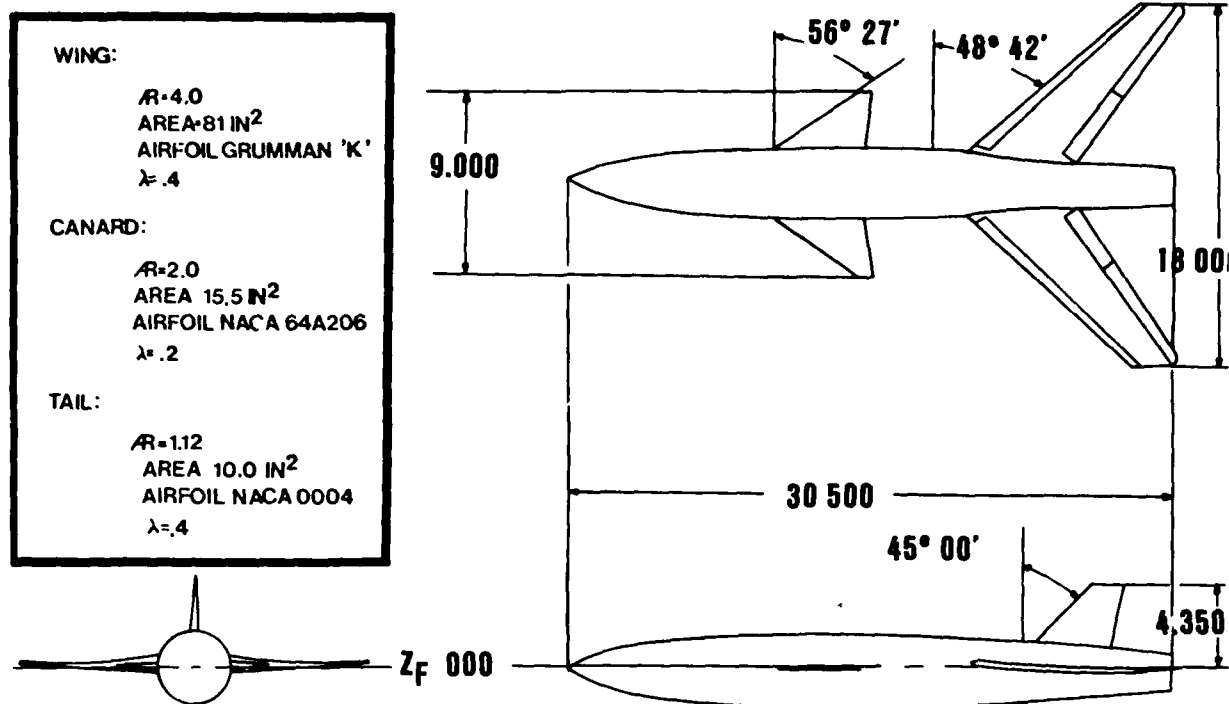


FIGURE 7. GENERAL ARRANGEMENT AFT SWEPT WING

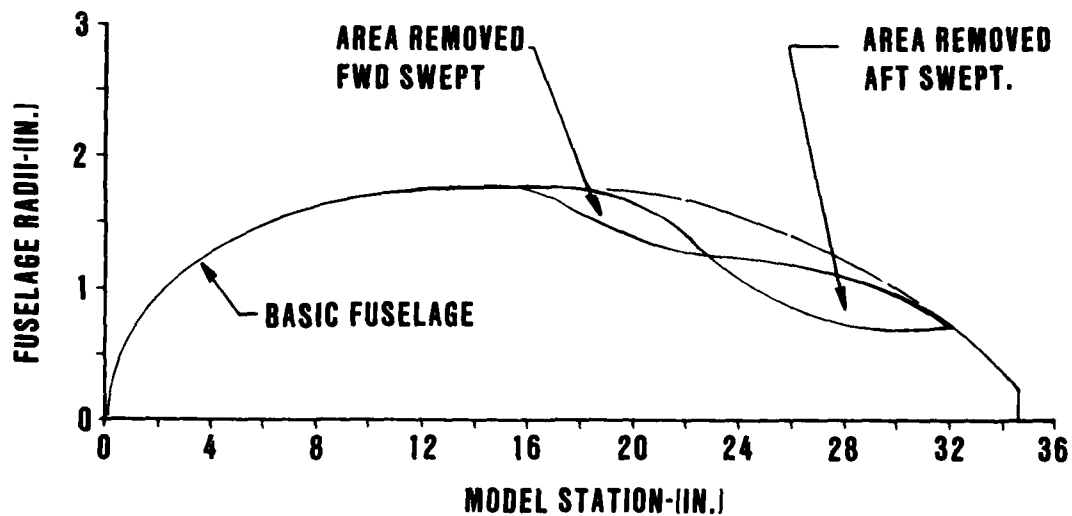
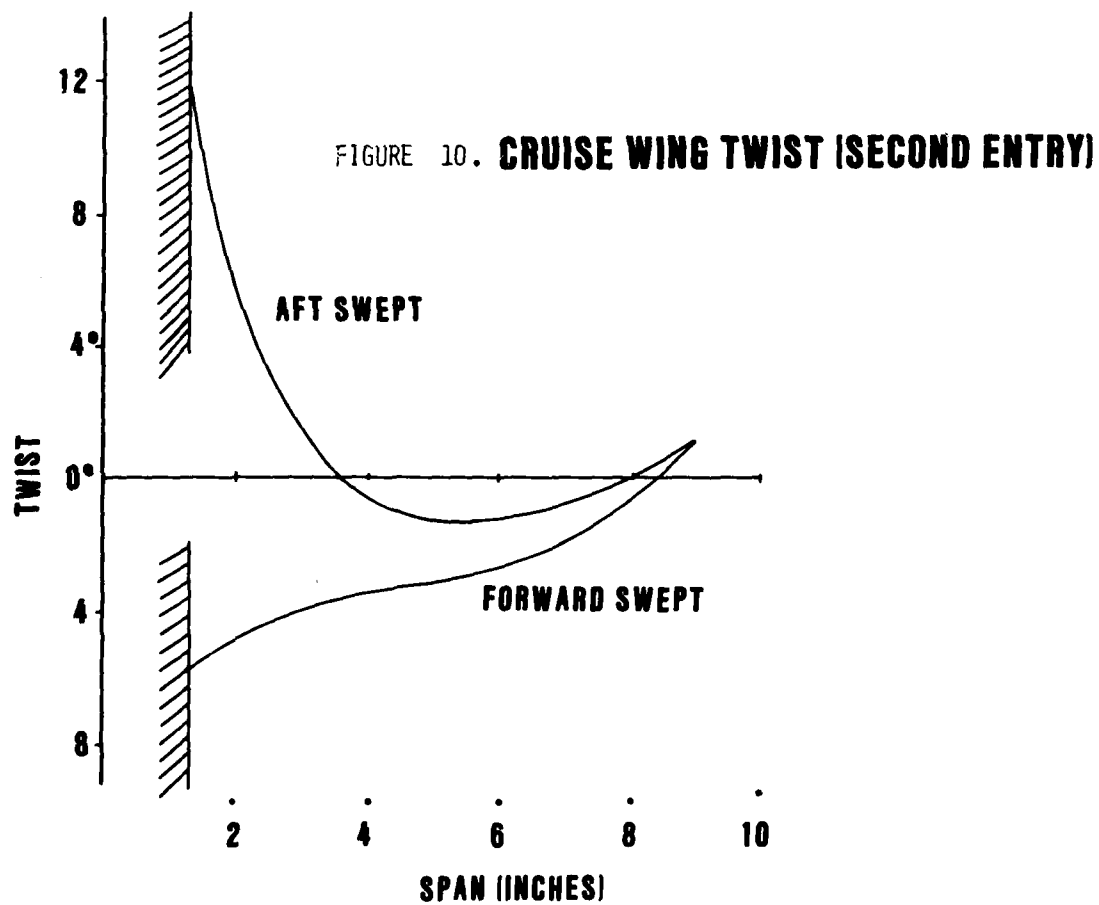
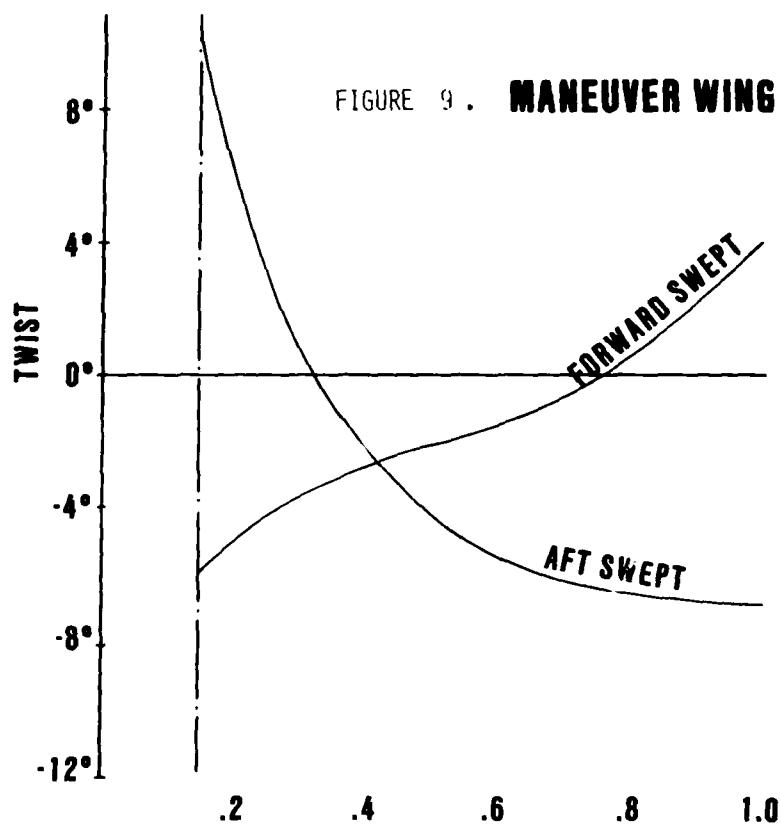


FIGURE 8. MODEL AREA RULING



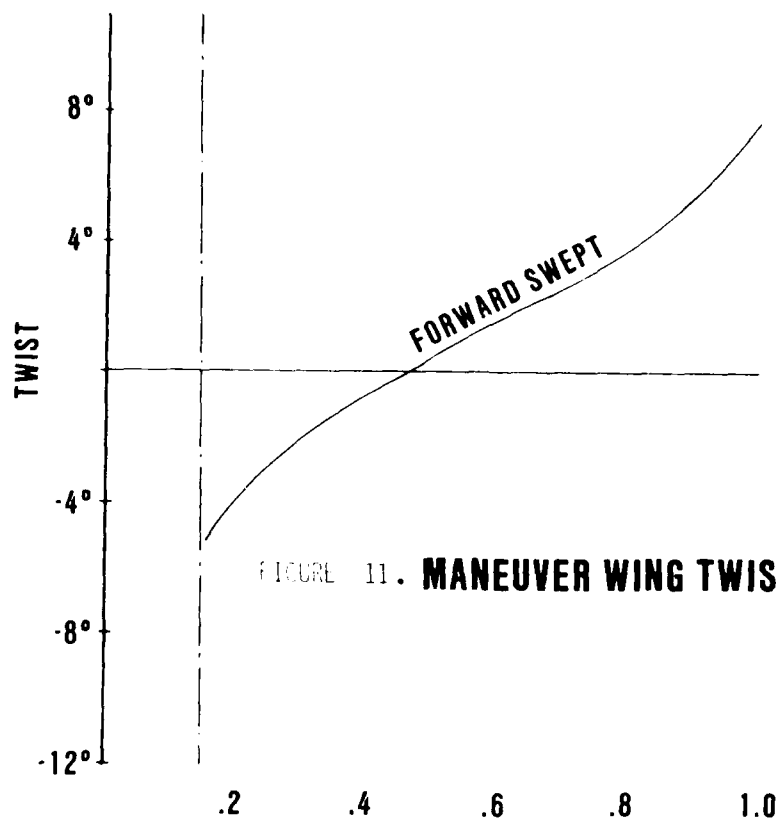


FIGURE 11. MANEUVER WING TWIST (THIRD ENTRY)

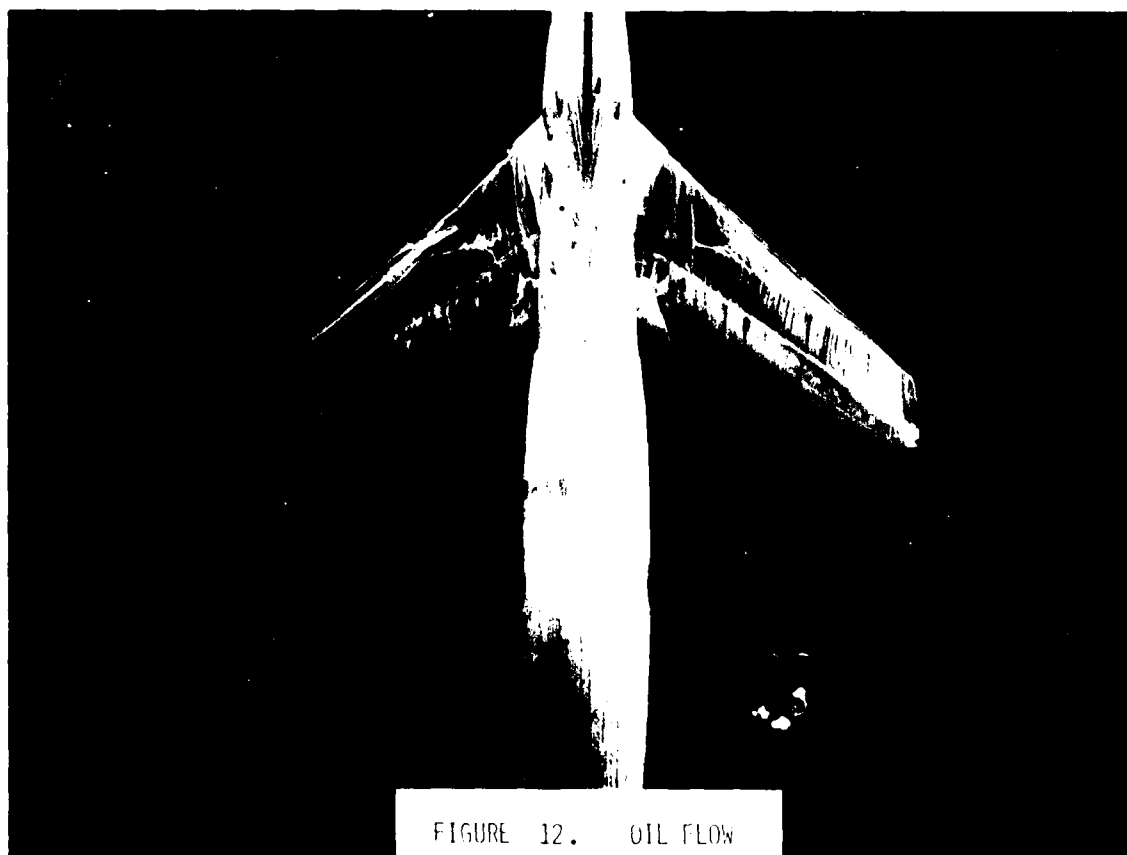
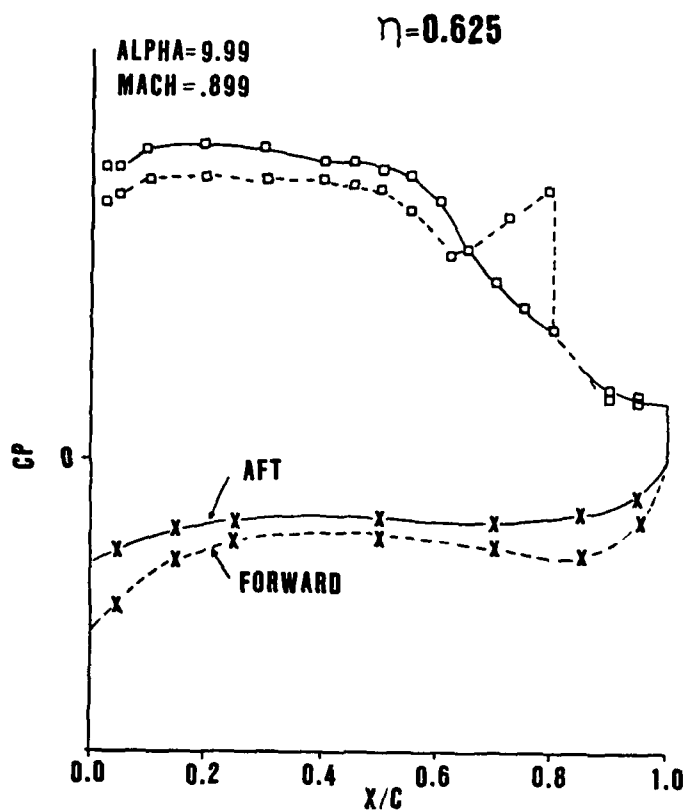
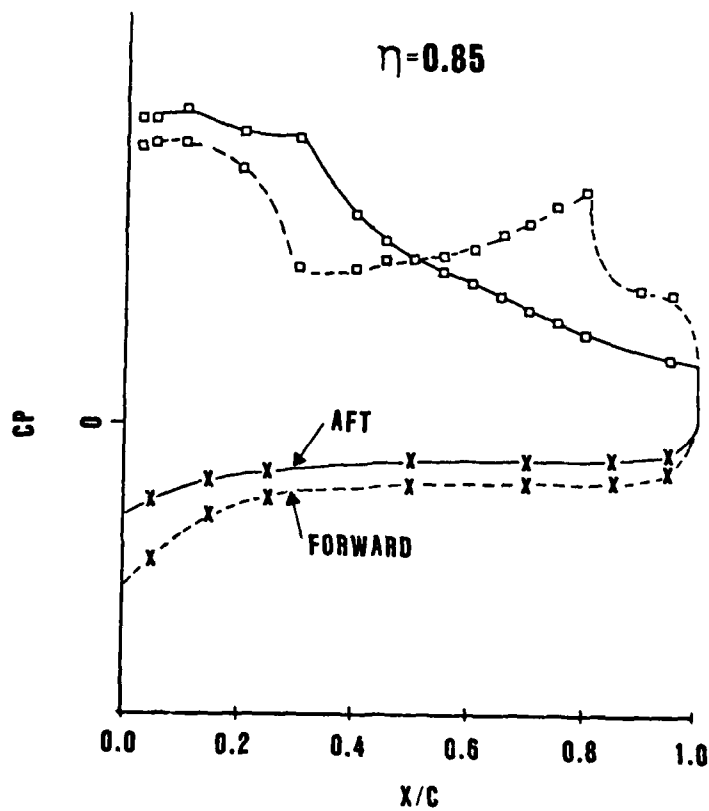


FIGURE 12. OIL FLOW

FIGURE 13A. **PRESSURE DISTRIBUTION (FIRST ENTRY)**FIGURE 13B. **CONCLUDED**

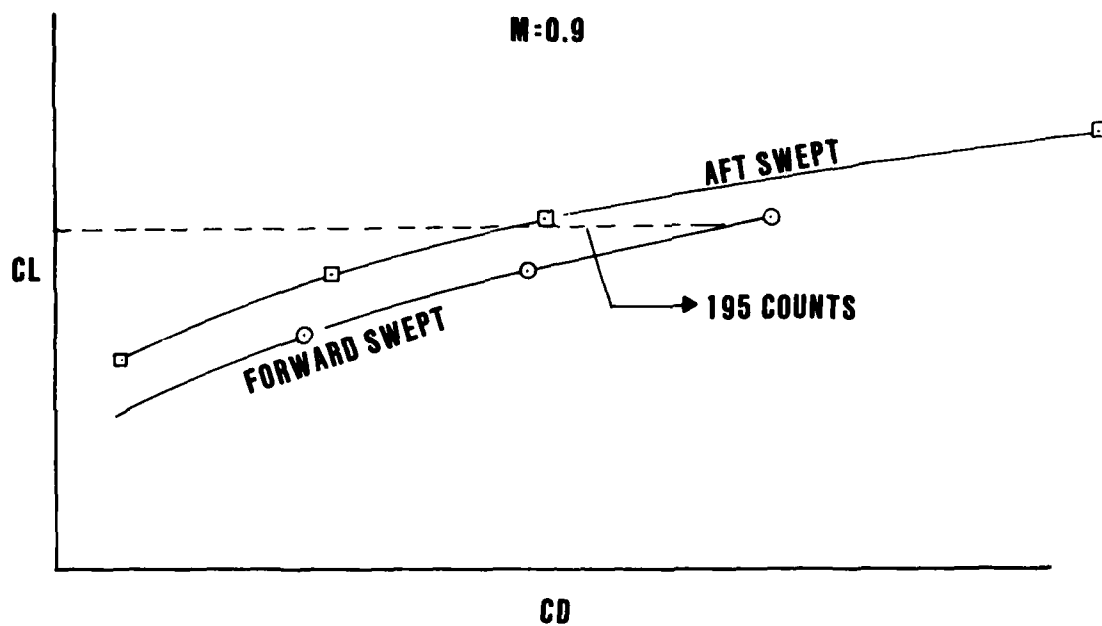


FIGURE 14. **MANEUVER WING DRAG COMPARISON (FIRST ENTRY)**

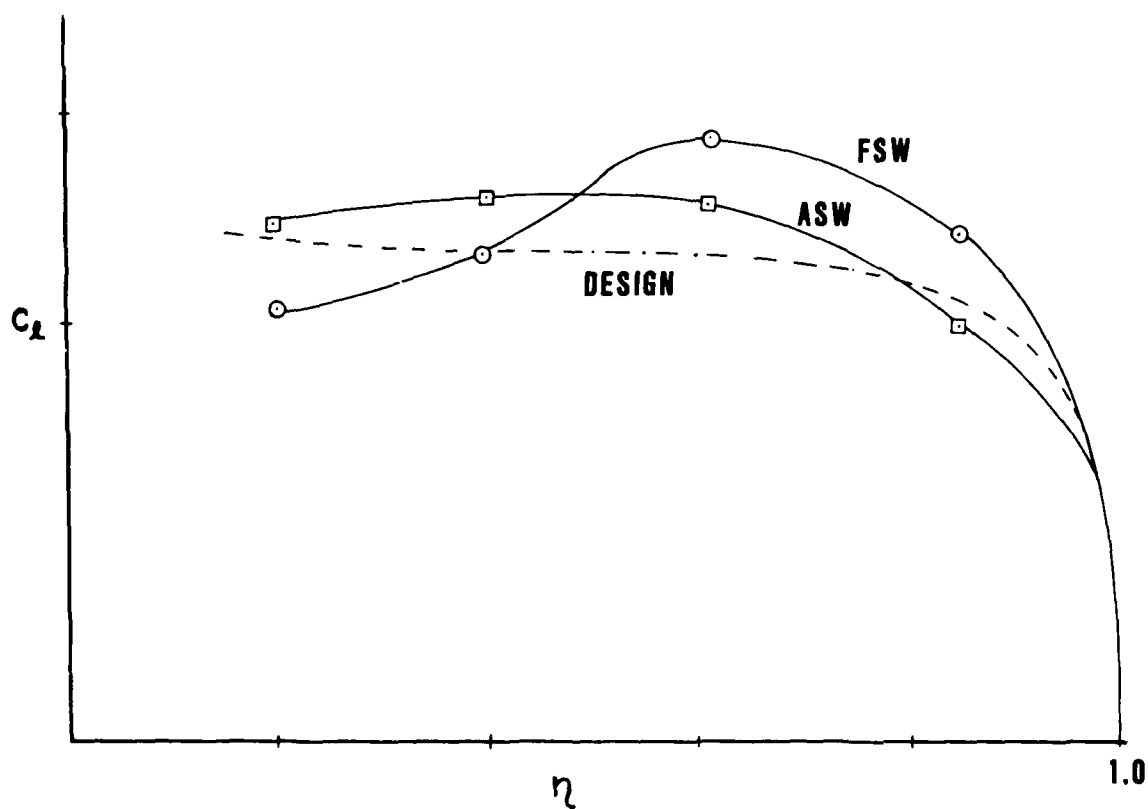


FIGURE 15. **MANEUVER WING SPANWISE LOAD (FIRST ENTRY)**

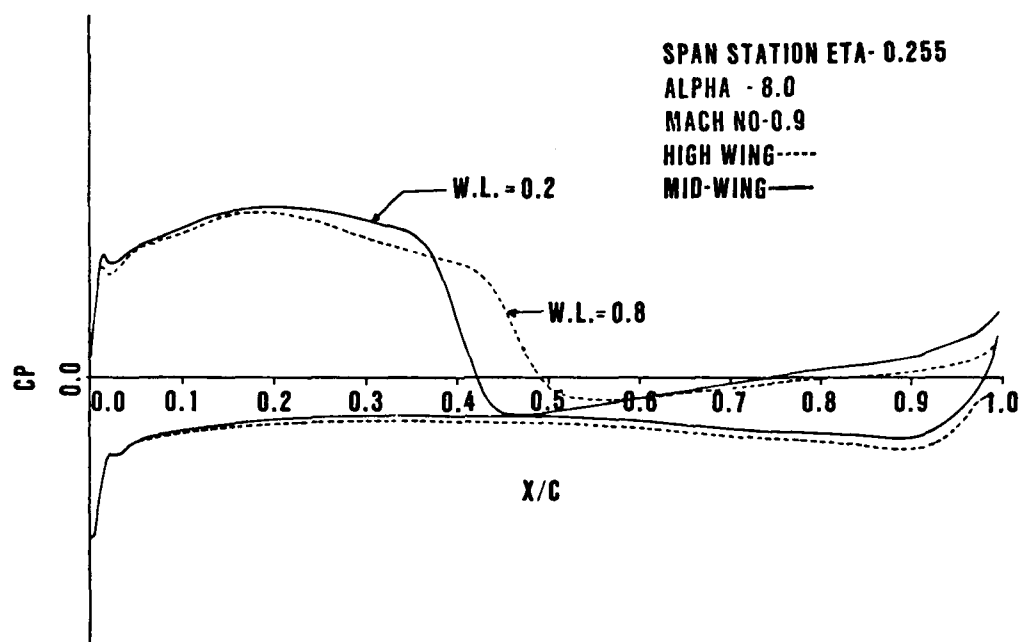


FIGURE 16A. EFFECT OF WING HEIGHT ON CHORDWISE PRESSURE DISTRIBUTION

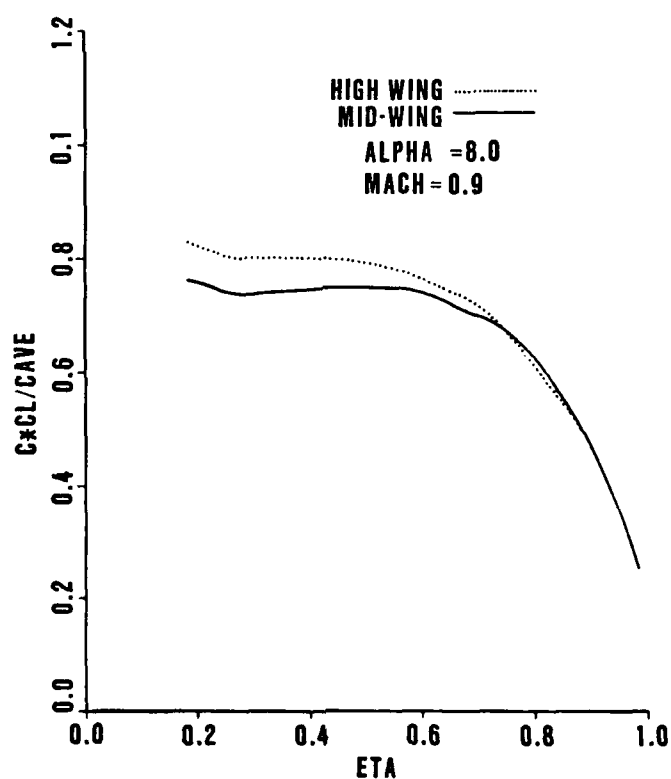


FIGURE 16B. EFFECT OF WING HEIGHT ON SPANWISE LOAD DISTRIBUTION.

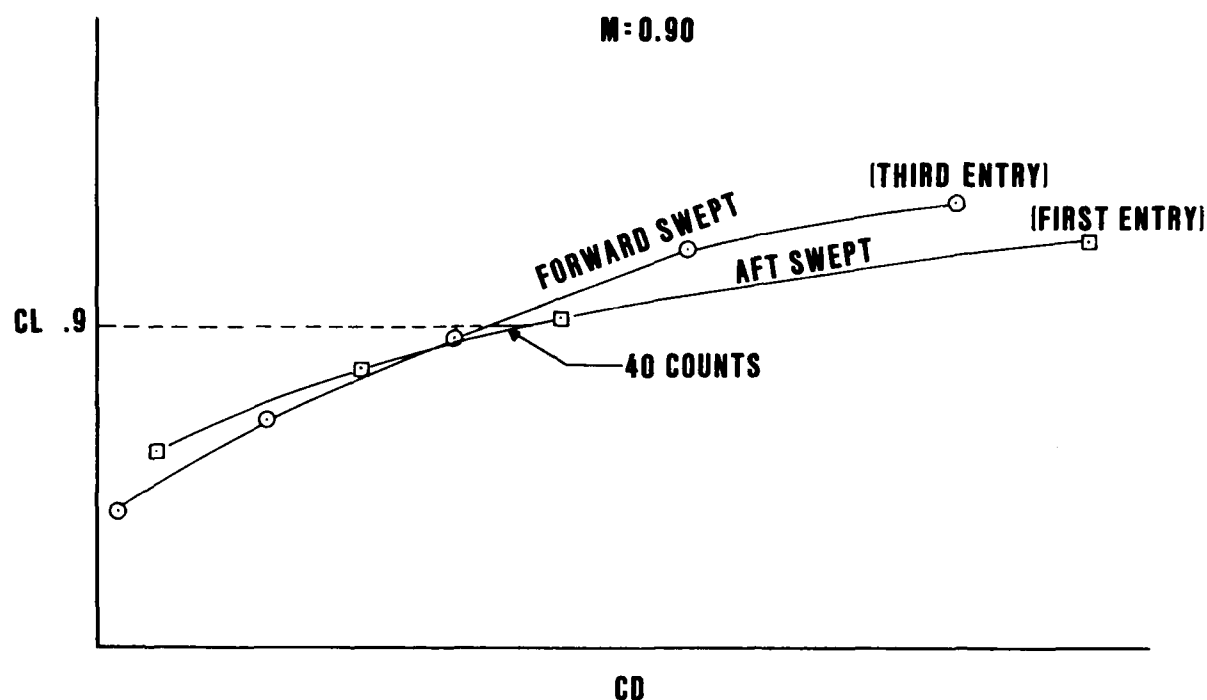


FIGURE 17. MANEUVER WING DRAG

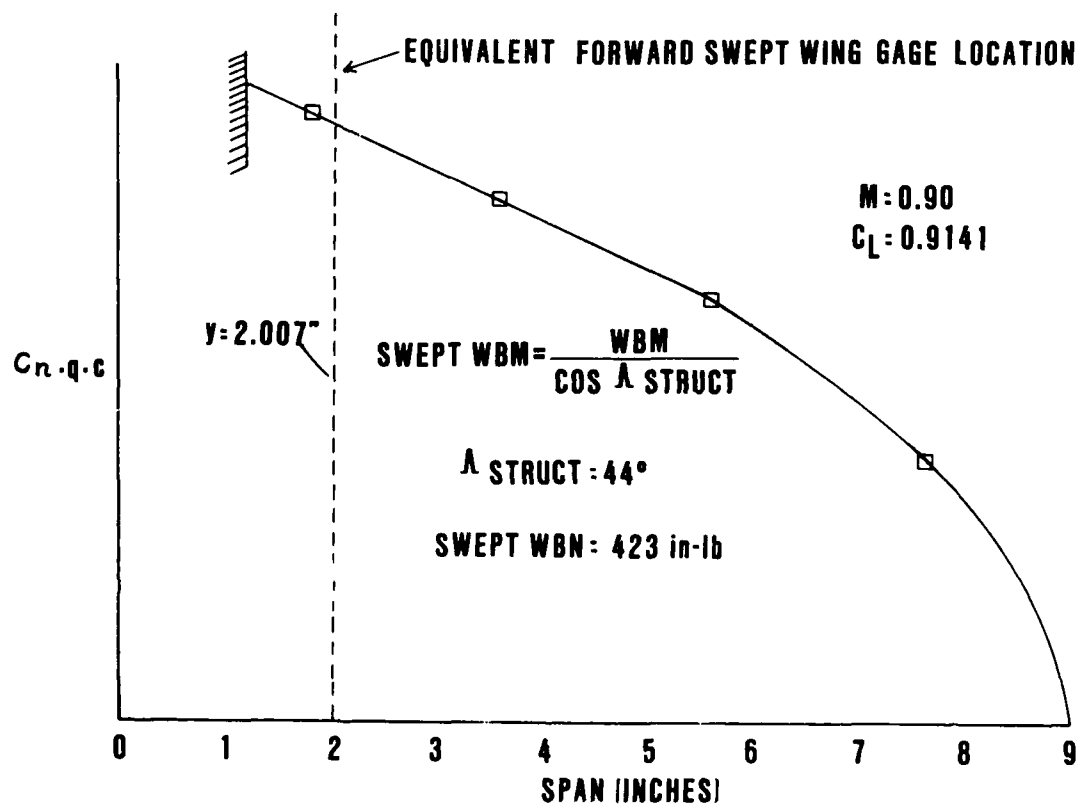


FIGURE 18. MANEUVER AFT SWEPT WING BENDING MOMENT

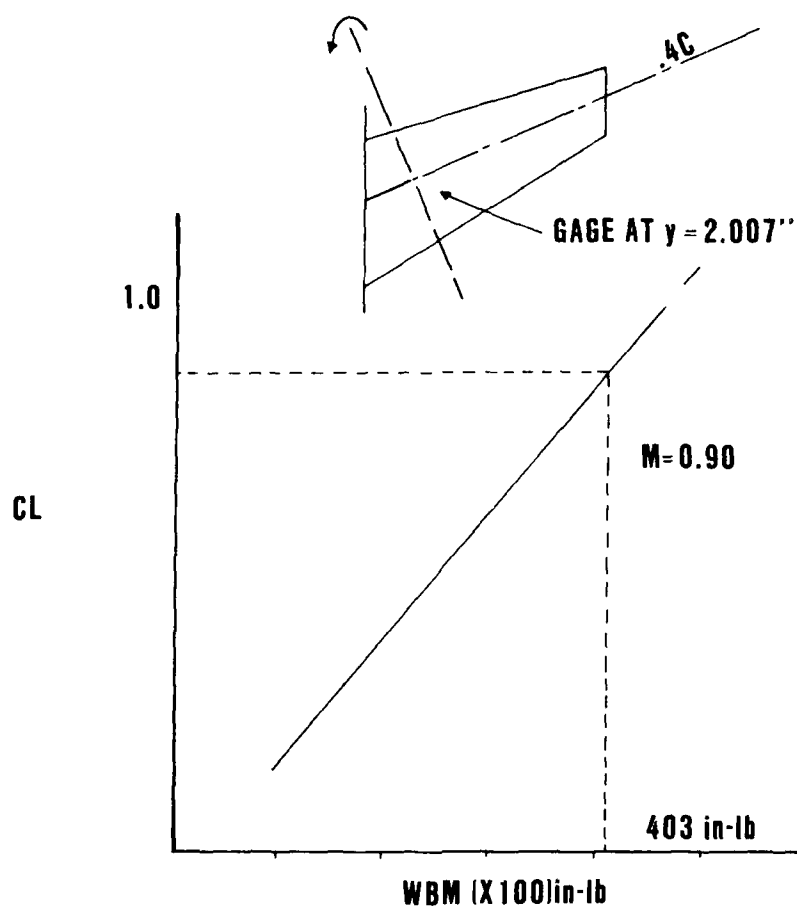


FIGURE 19. FORWARD SWEPT WING BENDING MOMENT.

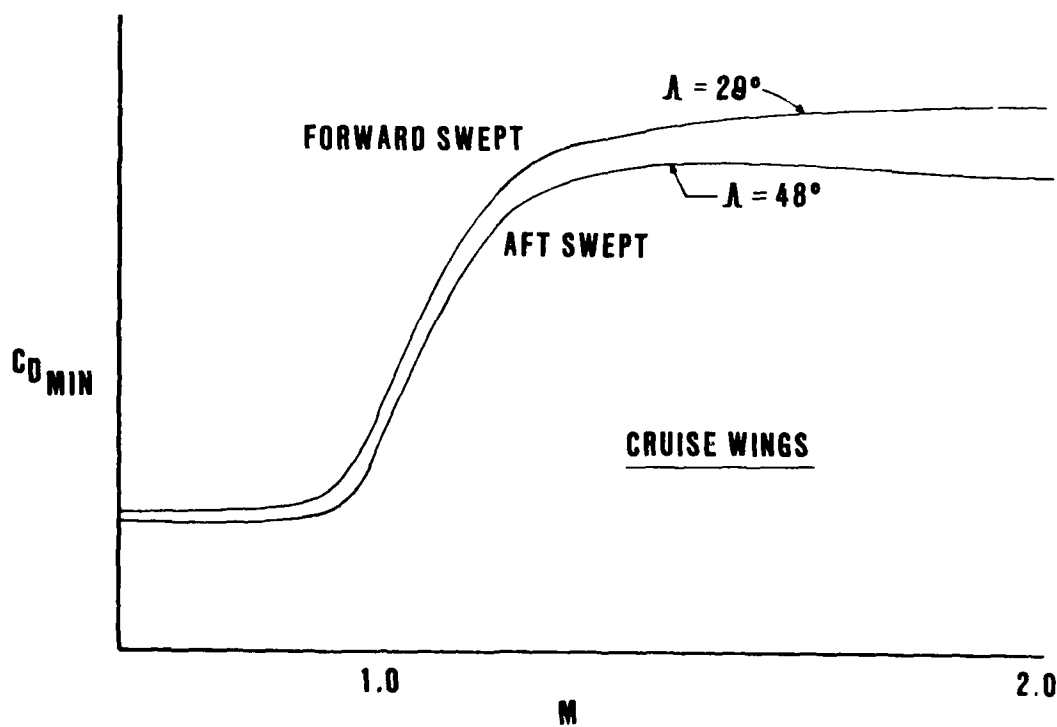


FIGURE 20. CRUISE WING DRAG

AD-A094 086 ADVISORY GROUP FOR AEROSPACE RESEARCH AND DEVELOPMENT--ETC F/G 20/4
SUBSONIC/TRANSONIC CONFIGURATION AERODYNAMICS.(U)

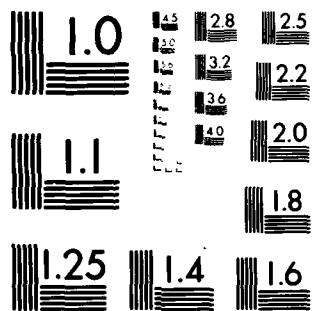
SEP 80

UNCLASSIFIED AGARD-CP-285

NL

4
10
10





MICROCOPY RESOLUTION TEST CHART
NATIONAL BUREAU OF STANDARDS-1963-A

AN INVESTIGATION OF A SWEEP WING-BODY CONFIGURATION WITH DROOPED LEADING EDGE AT LOW AND TRANSONIC SPEEDS

Georg Drougge*

The Aeronautical Research Inst. of Sweden

FFA-Box 11021

S-16111 Bromma

Sweden

Summary

This investigation of a swept wing design with a slight leading edge droop was aimed at giving the highest possible $C_{L_{max}}$ at low speed and manoeuvre without drag penalty at transonic cruise speed.

The basic, non-drooped wing was designed (using an inverse transonic small disturbance method) to have a critical Mach Number of around $M = 0.85$ at $C_L = 0.2$. The sweep angle is 25° , the aspect ratio 4 and the taper ratio 0.4. Several drooped leading edges, about 15% of the local chord and also including spanwise variation, were designed and tested.

Numerical calculations were done for the low speed-high lift case using a vortex-lattice panel method and for the transonic speed case, first using a small disturbance method, later a full potential equation method (Jameson's FLO22) and finally also a full Euler equations method (Rizzi).***

The experimental investigations were performed at low speeds at FFA ($Re \sim 3 \cdot 10^6$), at transonic speeds at FFA ($Re \sim 1.5 - 4 \cdot 10^6$) and at NAE, Canada ($Re \sim 12 - 18 \cdot 10^6$). These are mainly balance measurements but also some pressure distribution measurements have been obtained.

The results indicate that it is possible to design a wing which has no transonic cruise drag penalty but which has a higher $C_{L_{max}}$ and also better manoeuvre performance than the wing without droop.

INTRODUCTION

This paper reviews a numerical and experimental study of the design of a swept wing for a subsonic-transonic combat aircraft. The study has been going on, with greater or lesser intensity, since 1977 and has recently been completed.** The aircraft project was cancelled during the spring 1979. The investigations were then completed as a wing research study. The aim was to find a wing design which by using a slight droop of the leading edge would give as good $C_{L_{max}}$ characteristics as possible at low speed and in manoeuvre

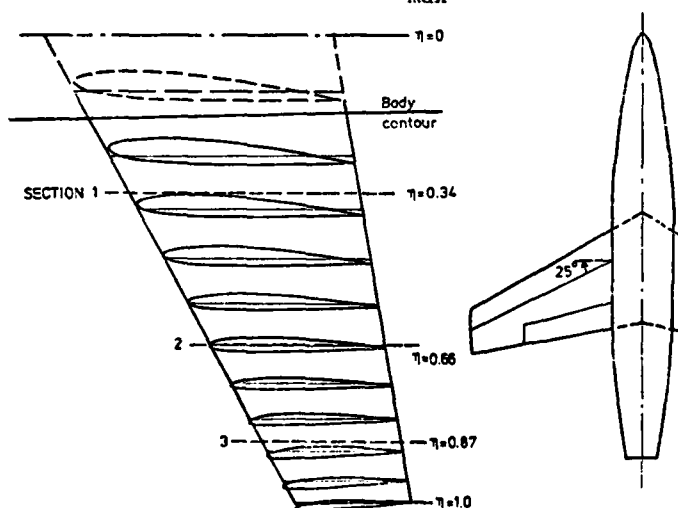


FIGURE 1. Wing-body design and geometry for PT-100. Sections 1, 2 and 3 are pressure tapped

but with no or very small drag penalty at transonic cruise speed. For civil transport aircraft studies regarding the effect of wing leading edge droop have been performed for instance for Airbus as is reported in a paper by D.M. Mc Rae (Ref.1).

1. WING-BODY DESIGN AND GEOMETRY

The basic non-drooped wing, PT-100, was designed using an inverse method, based on the FFA-Dornier transonic small perturbation (TSP) theory as described in Ref.2. The method was further applied, Ref.3, and it was concluded that it could be used as a design tool for wing-body configurations. When analysing the results more closely it was also tentatively found that a slight nose-droop might not result in any too severe transonic cruise drag penalty. The geometry of the non-drooped PT-100 is shown in Figure 1. The design aimed at a wing-body configuration with a critical Mach number

*Head of Aerodynamics Department

**In the investigation the following groups of people have taken part: From the subsonics section: M. Ingelman-Sundberg, R. Nordvik and S. Stridsberg. From the transonics-supersonics section: S.-E. Gudmundson and L. Torngren. From the numerical fluid dynamics section: S. Hedman, N. Agrell, L.-E. Eriksson and A. Rizzi. The FLO22 computations were carried out by Ingemar Lind, ANASYN, INC. as a consultant. For the transonic tests at NAE, Canada, which were performed as a joint NAE-FFA research project, E. Atraghji, NAE and L. Torngren, FFA, were responsible.

The investigation has been sponsored by The Swedish Defence Materiel Administration, Air Materiel Department.

***We are grateful to W. Schmidt, Dornier, for his cooperation on the development of this computer program.

of about $M = 0.85$ at $C_L = 0.2$. This was achieved by having the maximum local Mach number equal to 1.2 on the upper surface for $M = 0.85$. The pressure plateau was then terminated at a chordwise position which made the pressure gradient over the rear part of the wing mild enough to avoid boundary layer separation. The lower surface was then chosen to give an overall C_L of about 0.2. This resulted in a wing design with a rather large twist. The spanwise twist and thickness distribution is shown in Figure 2. The planform and thickness distribution were identical with that of the now cancelled Swedish combat aircraft project - see also paper 14 of this Symposium, (Ref.4).

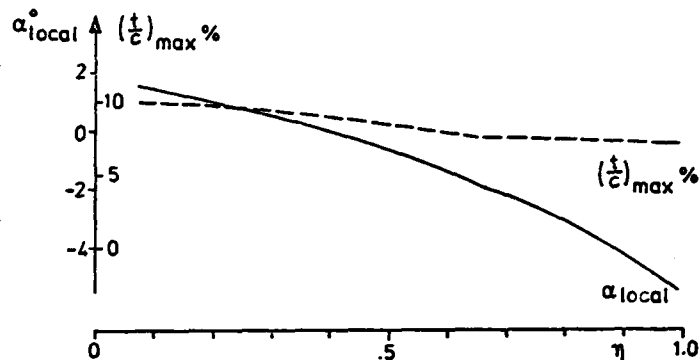


FIGURE 2. The twist angle α_{local} and the rel. thickness t/c distribution along the span

The inverse wing design method results in a wing geometry which is formed from an upper and lower surface and is not generated from a profile. For construction and manufacturing purpose the wing PT-100 finally was generated using straight spanwise generators between the root-section ($\eta = 0$) and a section at $\eta = 0.66$ (Section 2 in Figure 1) and then from this last section to the tip section, $\eta = 1.0$. It was then recomputed, using direct TSP computations, to determine whether the modification altered the original pressure distributions to any great extent. This was the case and in Figure 3 the distributions are given for three sections. It may

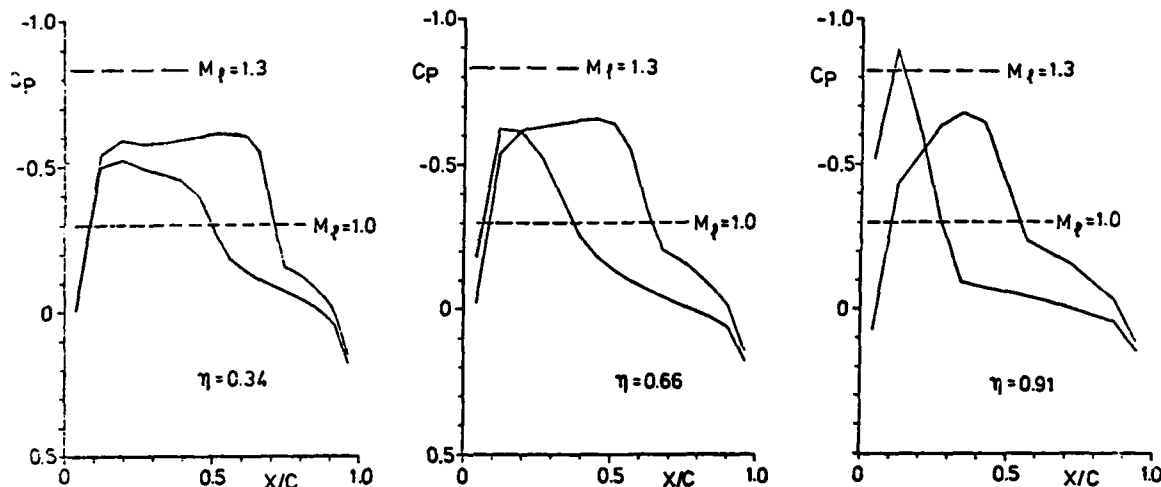


FIGURE 3. Chordwise pressure distributions at $M = 0.85$ and $\alpha = 1$ computed by the TSP-method for three spanwise sections for PT-100

be pointed out here that there is a suction peak on the lower side of the leading edge and also that there is no rear loading on the wing. Rear loading could probably be achieved by changing the rear lower surface of the wing, thereby obtaining higher C_L and lower C_D for the basic wing. This was not done, since the main objective was to compare the effect of different leading edge drooping for a given wing.

The TSP method used could not cope with the leading edge region and the wing nose was designed in the following way. The nose radius at the root section was chosen to be 1% and to be 2% at the tip section; in both cases with the local chord as unit. From there on curves were fitted to the main wing at around 15% of the local chords in a way to give as good C_L -max values as possible. How this was achieved will be discussed in more detail in a forthcoming ICAS paper (Ref.5), where also will be described how the two drooped leading edge modifications PT-101 and PT-102 were designed. The geometries for these leading edges are shown in Figure 4.

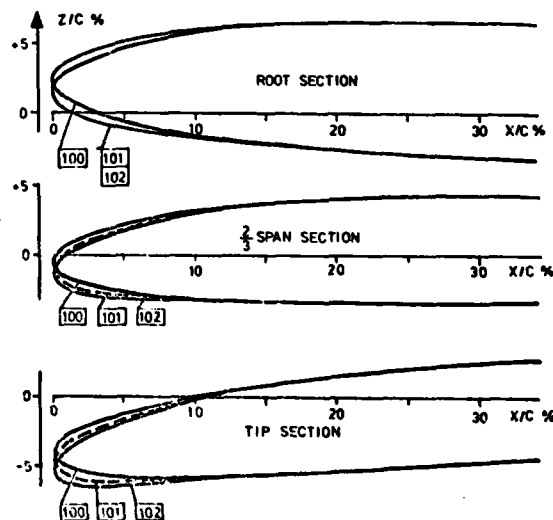


FIGURE 4. The leading edge geometries for PT-100, PT-101 and PT-102

2. THE FIRST PHASE OF THE INVESTIGATION

2.1 The transonic wind tunnel tests at low Re for PT-100, PT-101 and PT-102

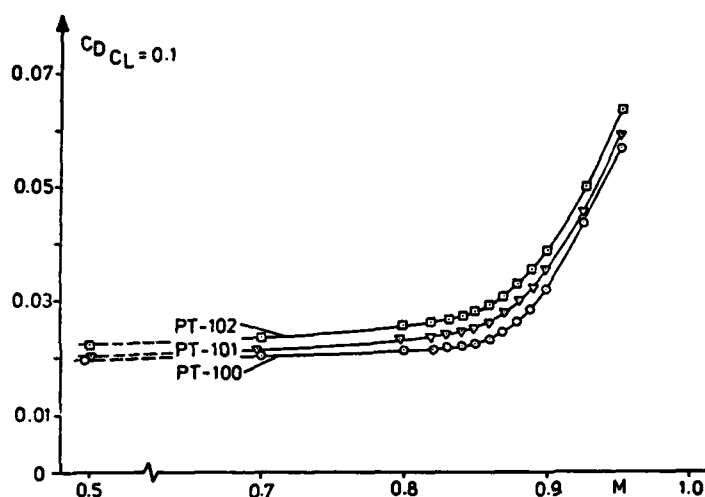


FIGURE 5. The experimental drag coefficients for $C_L = 0.1$. $Re = 1.2 - 1.8 \cdot 10^6$

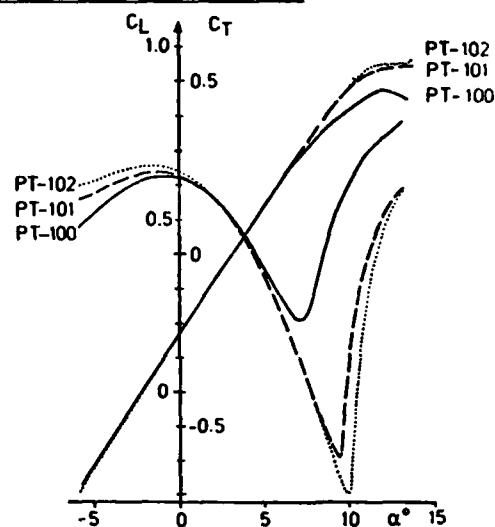


FIGURE 6. C_L and C_T as a function of α for PT-100, PT-101 and PT-102 for $M = 0.5$

The first experiments in the first phase were transonic and were performed in the FFA 1×1 m wind tunnel (S4). This tunnel is of vacuum type with atmospheric stagnation pressure which gives Reynold's numbers of about $1.2 - 1.8 \cdot 10^6$, based on the aerodynamic mean chord. The model was sting-mounted. Some of the results are summarized in Figures 5 and 6. (A more complete data report is found in Ref.6.) It is seen at once that the transonic drag characteristics for a reasonable cruise C_L , say 0.1, are not acceptable for the drooped wings, not even for PT-101 with the more moderate drooping of the leading edge. However, it is furthermore evident that the C_L -curve at a manoeuvre Mach number of, say 0.5, is a lot more satisfactory for PT-101 than for PT-100 but also that PT-102 gives only marginal improvement. From the behaviour of the tangential force C_T in Figure 6 it may be concluded that the increase of buffet onset is at least 0.2 between PT-100 and PT-101. The configuration PT-102 as a transonic wing should be forgotten hereafter. It is however included in the results from the low speed tests, which are described below.

2.2 Some preliminary low speed tests of the leading edges of PT-100, PT-101 and PT-102

In order to get quick information about the $C_{L_{max}}$ characteristics at take-off and landing speeds for the three leading edges an available so called research wing with constant chord was used. Different leading edges could be fitted to this wing and the three leading edges of PT-100, PT-101 and PT-102 were tested in this way. The leading edge profiles had to be constant along the span and the section at $\eta = 0.95$ was chosen for comparison. The results are reported in full in Ref.7 and also in Ref.5. From Figure 7 the effect of

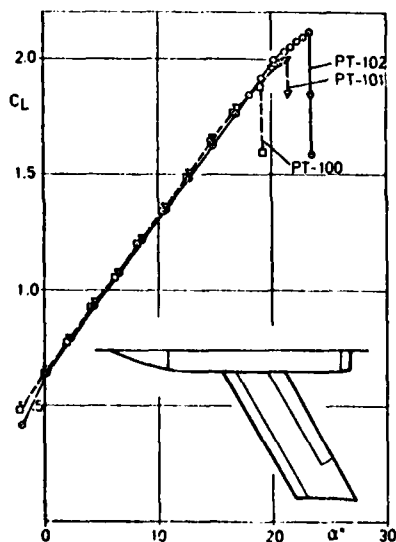


FIGURE 7. The low speed $C_{L_{max}}$ results for the constant chord research wing fitted with the leading edges at $\eta = 0.95$ for PT-100, PT-101 and PT-102

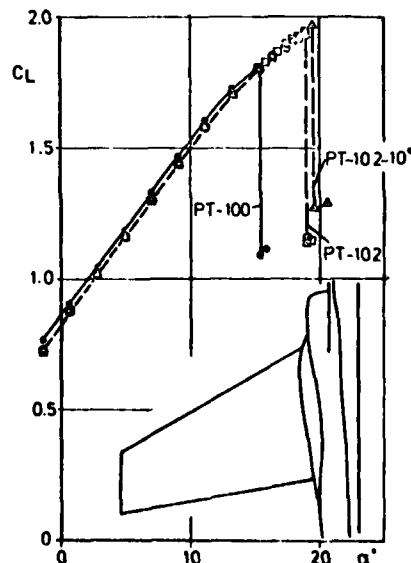


FIGURE 8. The low speed $C_{L_{max}}$ results for PT-100 and PT-102

drooping the leading edges can be seen on $C_{L_{max}}$, noting of course that the results apply only to this wing with constant chord and constant profile. It was then decided to proceed with some tests with the correct planform.

2.3 $C_{L_{max}}$ for PT-100 and PT-102

Figure 8 summarizes the results with the correct planform. More details and analyses can again be found in Ref.5 and Ref.8, where also for instance the sensitivity to disturbances at the leading edge and also the stalling characteristics are discussed.

One test series was also run for wing PT-102 with the drooped leading edge deflected 10°. Not much further increase in $C_{L_{max}}$ was obtained by this, which is an interesting feature.

These low speed tests conclude the first phase of the investigation.

2.4 Conclusions from the first phase of the investigation

The leading edges tested, where the droop increased monotonously from root to tip, gave not acceptable transonic drag characteristics, not even for the moderate droop in PT-101. The improvements in $C_{L_{max}}$ for start and landing were however not without interest and the increase in usable C_L at manoeuvre speeds were rather good. It was therefore decided to enter into a second phase and see if it was possible to find a design that gave better compromise between drag at transonic speeds and maximum lift at low and moderate subsonic speeds.

3. THE SECOND PHASE OF THE INVESTIGATION

In order to obtain a better foundation for what was intended to be a more advanced design it was first necessary to get a better and more detailed picture of the flow field around the wings. The theoretical tools to obtain this had now also been made available, which was not the case when the first phase of the study started.

Transonic calculations using the full potential equations were done with the FLO22 program, Refs.9 and 10. Very recently also some computations were performed for PT-100 at $M = 0.85$ with the Euler equations, Ref.12. The incompressible calculations for high angles of attack concerned the pressure distribution on the leading edge and were made with a 3-D vortex lattice method combined with a 2-D vortex panel method. These methods are described in Ref.11. In contrast to the FFA-Dornier TSP method the effect of the body cannot be included in any of the other transonic methods. More detailed experimental information was obtained from pressure distribution measurements on PT-100 at transonic speeds on a half model in the FFA TVM wind tunnel, which gives a Reynolds number of about $4.5 \cdot 10^6$.

It was also finally decided to check the transonic results at fairly high Reynolds numbers. This was done as a joint NAE-FFA research project in the 5 foot wind tunnel at NAE, Canada.

3.1 The transonic case calculations

Figure 9 gives the result for PT-100 and PT-101 at $M = 0.85$ and an angle of attack* which gave a C_L of about 0.2. The C_p curves are plotted against the chordwise coordinate x/c as well as the vertical thickness coordinate z/c where c is the local chord. Three spanwise stations are chosen and from the $C_p - x/c$ curves it is now clearly seen how the suction peak on the lower side of the leading edge develops along the span and gives very high local Mach numbers resulting in both wave drag and especially at low Reynolds numbers separation. The separation bubbles were clearly seen from oil flow tests made during the first phase transonic wind tunnel investigation. As could be expected the separation was located at the outer part of the wing.

From the $C_p - z/c$ curves the local drag coefficients can directly be estimated and the effect of the drooping on the drag is immediately seen. For $\eta = 0.3$ the local drag is practically independent of the drooping but for $\eta = 0.6$ the leading edge thrust does not quite counterbalance the increase in wave drag. For $\eta = 0.9$ the leading edge thrust is obviously negative due to the fact that the suction peak is located on the wrong part of the leading edge.

The effect of the drooping applied in PT-101 on the local drag as a function of the span η is still more obvious from Figure 10, where it can be concluded that the main difference in transonic drag between PT-100 and PT-101 is on, say, the outer third of the wing.

*The nominal angle of attack was changed about 2 degrees (due to a change in the wing reference plane relative to the body axis) at some time during the study. To avoid confusion the lift is always quoted instead.

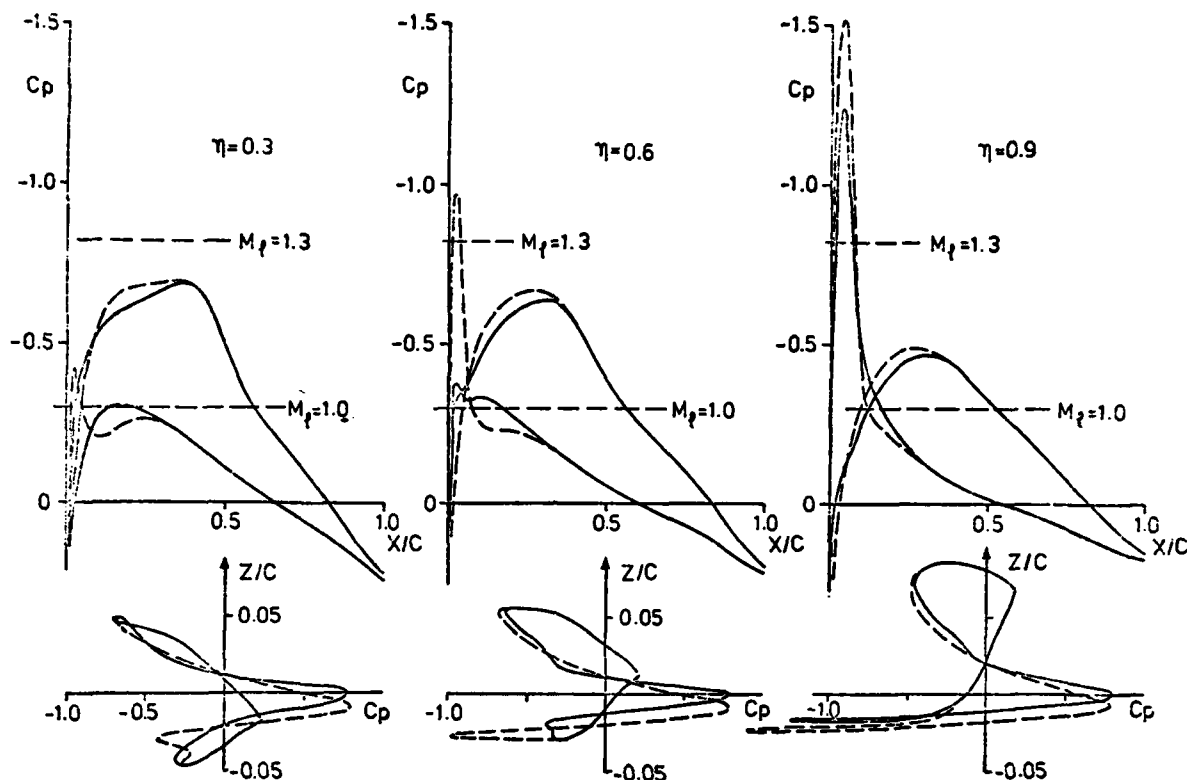


FIGURE 9. The FLO22 C_p distribution versus x and z for the wings PT-100 (solid line) and PT-101 (dotted line) at $M = 0.85$ and $C_L \approx 0.2$

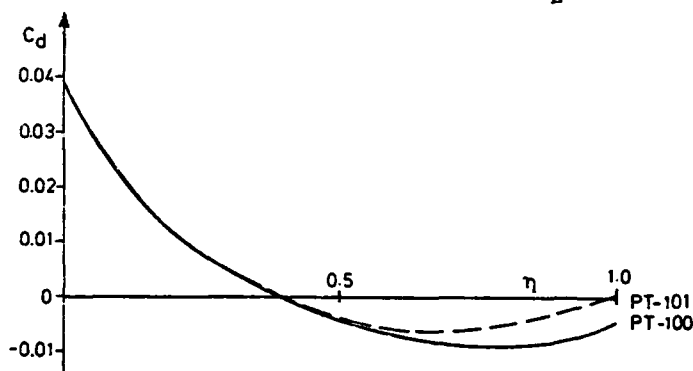


FIGURE 10. The local drag coefficient C_d as a function of the span η for PT-100 and PT-101

3.2 The incompressible calculations for high angles of attack

The 3-D vortex lattice method combined with a 2-D vortex panel method mentioned earlier and described in Ref. 10 was applied to PT-100 to find the spanwise load distribution on the leading edge (10% of the local chord was chosen). In Figure 11 an example is shown and it is seen that the highest load (which is a measure of the suction peak and consequently of how steep the recompression afterwards is) is located around 60% of the span. It is interesting to note that this is the case also when the trailing-edge flap is deflected 25° . More results and analysis can be found in Ref. 5 and Ref. 11. The results imply that the drooping of the leading edge could probably be relaxed on the outer third of wing, which - see Figure 10 - should have a beneficial effect on the transonic drag characteristics.

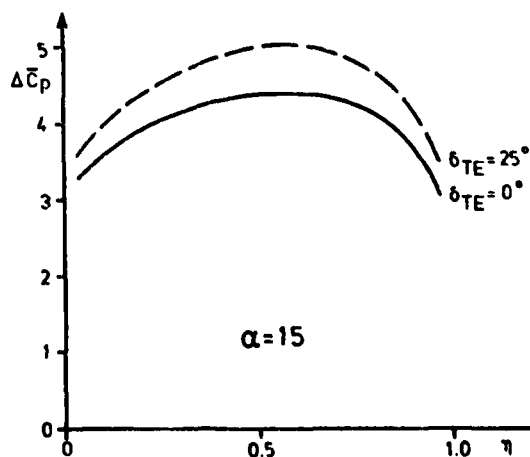


FIGURE 11. $\Delta C_p = [C_{p\text{lower}} - C_{p\text{upper}}]$ mean value for $0 \leq x/c \leq 0.10$ for $\alpha = 15^\circ$

Before we turn to the design of such a wing we will first see how the experimental pressure distributions at transonic speeds compare with the calculations.

3.3 Experimental pressure distributions for PT-100 at $M=0.85$ and comparison with calculations

A half model of a PT-100 wing-body configuration was used and the pressures were measured in three spanwise sections, see Figure 1. The wind tunnel was the FFA TVM-500 pressurized transonic wind tunnel, which gave a Reynolds number of about $4.5 \cdot 10^6$ at a Mach number of 0.85. Only the results for the spanwise section $\eta = 0.87$ are given in Figure 12 since this section is situated in the most critical part for the transonic drag. The FLO22 numerical results (Refs. 9 and 10) are given together with the Euler equation computations (Ref. 12), both with the influence of the body. The TSP-results from the original design computations are also shown, where the influence of the body is included. The agreement between the different numerical calculations and also between these and the experiments is not good. Without further extensive analysis it is difficult to say whether the disagreement is due to discretization problems or to the rather strong local shocks in the non-conservative full potential solution or in the conservative but small disturbance method.

From many other calculations with the FLO22 program within the present study we have found that the results agree quite well (with experiments) around the leading edge, where also the mesh is very fine. This seems to be the case even when the local Mach number (on the profile) is very high, say 1.5-2.0, and consequently resulting in shock waves with non-isentropic flow behind. In any case the FLO22 calculations seem to be able to predict drag differences when reasonably small geometrical modifications are applied to the leading edge. In this way it has been possible to guide the developments of the consecutive steps in this wind design study.

3.4 The design of PT-105 and PT-106

As mentioned earlier the facts that the drag increase due to drooping the leading edges is mainly on the outer third of the span and also that the critical (most loaded) section for CL_{max} lies somewhere around 60% of the span both imply that the drooping should be relaxed outside that section. This should give a better compromise between transonic cruise drag characteristics and CL_{max} both for low speed and at manoeuvre.

PT-100 was again used as the basic wing. In Figure 13 are shown the locus of the vertices of the leading edges Z_{LE} for PT-100, PT-101 and the two new designs, PT-105 and PT-106. For PT-100 the line Z_{LE} is only the measure of the amount of twist but for the other three wings Z_{LE} gives the drooping characteristics. The geometry of the PT-105 leading edge was then chosen, after many trials, to give the best pressure distribution after the pressure minimum. This was done by looking at the canonical distribution as suggested by AMO Smith, Ref. 13. The detailed design was worked out by L-E Eriksson and the details are found in Ref. 11 and Ref. 5.

Wing 106 had the drooped leading edge (still about 15% of the local chord) even more turned upwards towards the tip of the span. This wing nose design was worked out by Ingemar Lind and its details can be found in Ref. 10. A negative camber was added to the first 25% of the chord and along the outer third of the span, starting now from PT-105. The suction peak at the lower side of the nose close to the tip was of course reduced in this way, but there was also the risk that the critical section, which deter-

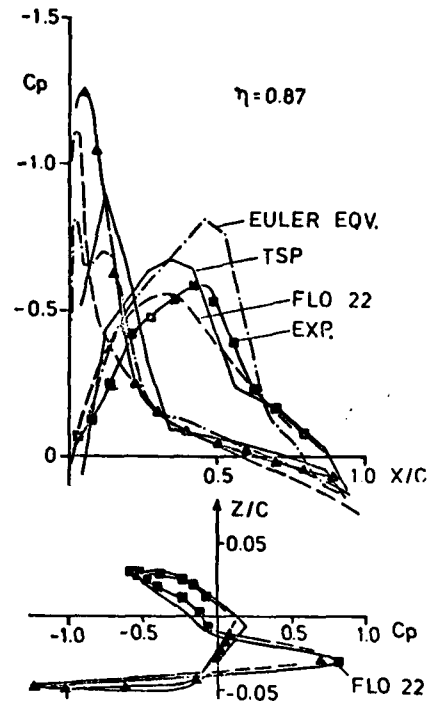


FIGURE 12. Experimental pressure distributions for PT-100 at $\eta = 0.87$ and $M = 0.85$ and $Re = 4.5 \cdot 10^6$. Included are also the results from the different calculation methods

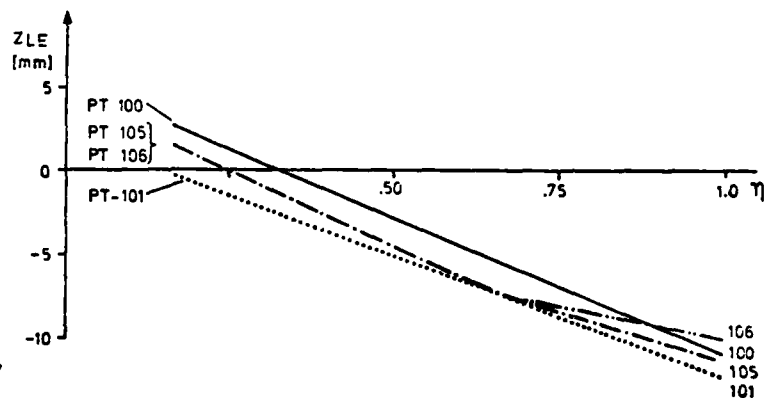


FIGURE 13. The locus Z_{LE} of the vertices of the leading edges over η for the wings

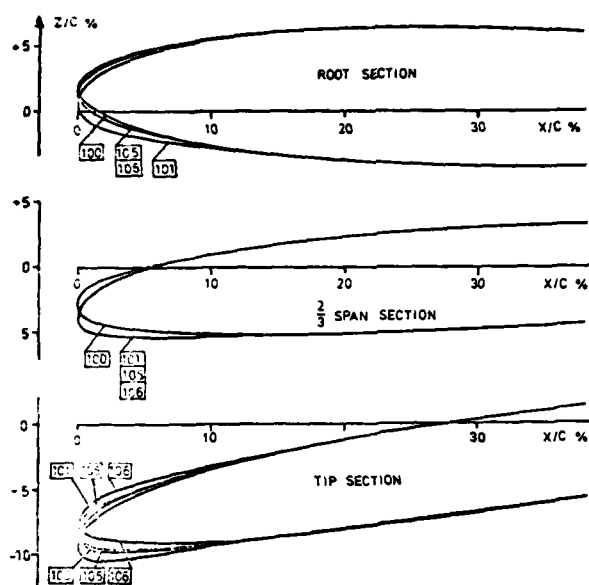


FIGURE 14. The leading edge geometries for the wings

mined low speed CL_{max} had moved out towards the tip and worsened the CL_{max} characteristics.

The leading edges for the two new designs PT-105 and PT-106 are shown in Figure 14 together with PT-100 and PT-101 for comparison.

Again FLO22 computations were made for the two new wings and the results are given in Figure 15, now only for $\eta = 0.9$ where the largest effects were to be expected. The earlier results for PT-100 and PT-101 are also included. Figure 16 shows the local drag coefficients C_d over the span for the four wings. It is seen that the effect of relaxing the droop on the outer third of the wing is beneficial - if the FLO22 computations are reliable and if boundary layer separation effects are small at very high Reynolds numbers.

The final check can thus only be found from high Reynolds number tests, but before we manufactured the rather expensive models for the NAE transonic high Re testing the low speed CL_{max} characteristics for PT-105 and PT-106 were investigated.

3.5 Results from the PT-105 and PT-106 low speed CL_{max} tests

The complete test results can be found in Ref.5 or Ref.14. The investigation was carried out in the FFA low speed wind tunnel and from the results is the C_L - α curve for the three wings PT-100, PT-105 and PT-106 taken, Figure 17. The trailing edge flap has again a deflection angle of about 35° . It was found that practically no increase in CL_{max} occurred when Re was increased from 3.1 to $3.6 \cdot 10^6$. (The effect of increasing Re from 1 to 2 to 3 million was, however, very pronounced.) The increase in CL_{max} is not very spectacular but since the transonic drag increase was expected (from the computations) to be negligible or even negative and since also the manoeuvre characteristics would probably be quite good it was decided to perform the final transonic tests at NAE.

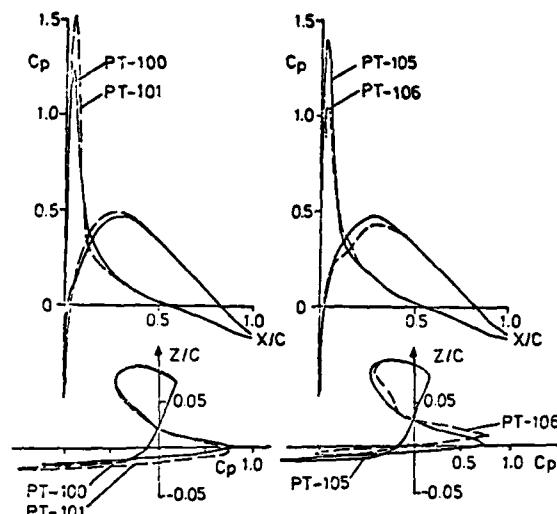


FIGURE 15. The FLO22 C_p distribution over x and z for $\eta = 0.9$ for PT-100, PT-101, PT-105 and PT-106. $M = 0.85$ and $CL \approx 0.2$

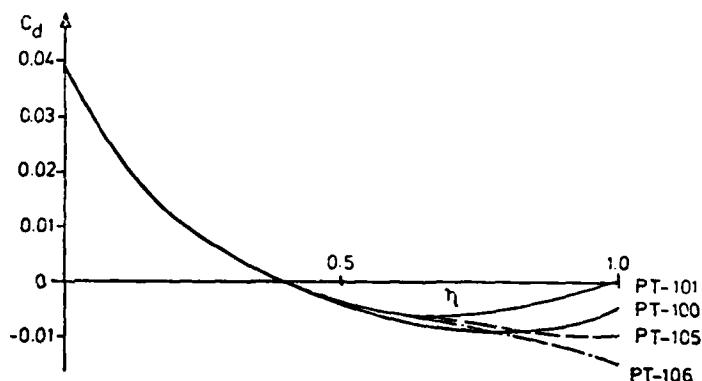


FIGURE 16. The local drag coefficient C_d as a function of the span η for the wings. $M = 0.85$ and $CL \approx 0.2$

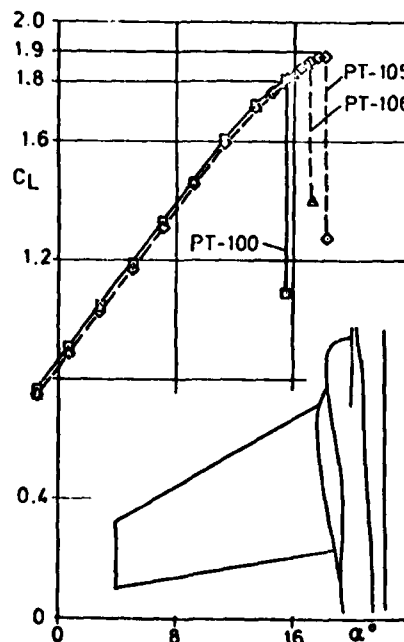


FIGURE 17. Low speed CL curves for $\delta_{TE} = 35^\circ$ and $Re = 3.1 \cdot 10^6$

3.6 The transonic high Re tests for PT-100, PT-105 and PT-106

These results were obtained during two different test periods in the NAE transonic wind tunnel where Re up to $18 \cdot 10^6$ could be reached. The wind tunnel, models and testing technique are described in another paper (Ref.4) so it will suffice to give some of the final results.

In Figure 18 the transonic drag characteristics for $C_L = 0.1$ and $C_L = 0.2$ are shown for PT-100, 105 and 106. From the early FFA low Re test an estimate of the corresponding values for PT-101 are also included for comparison.

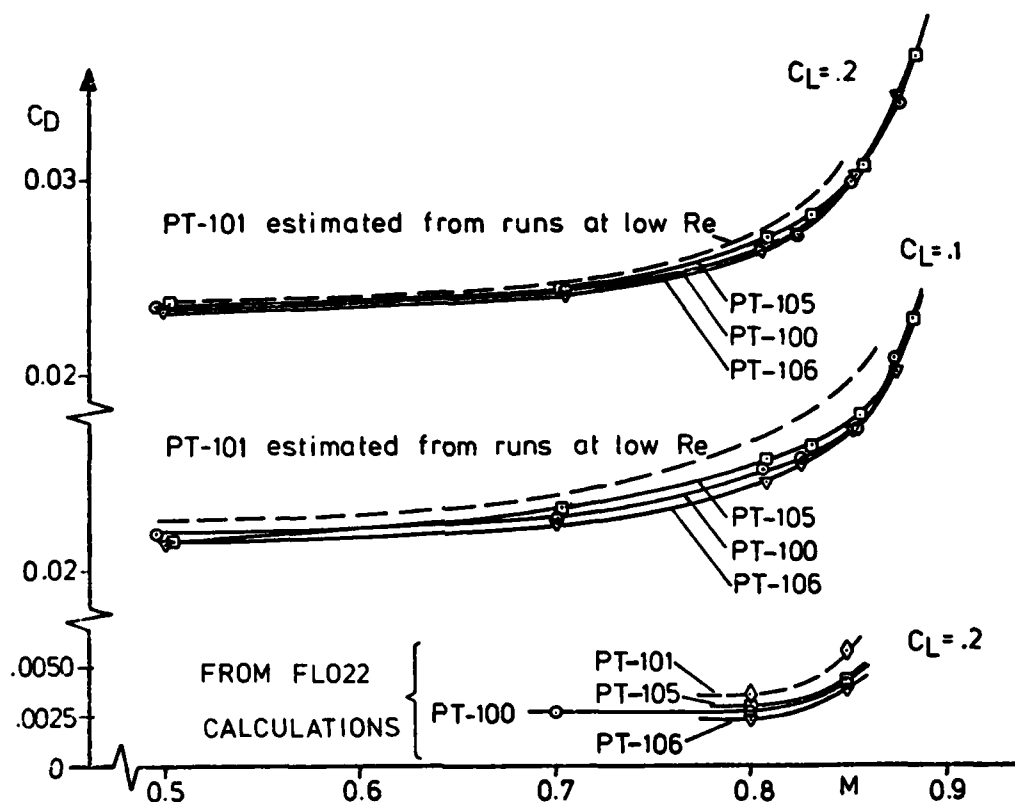


FIGURE 18. The drag coefficient C_D for $C_L = 0.1$ and 0.2 from the NAE tests at $Re = 12 \cdot 10^6$. Included are also the calculated drag values for $C_L = 0.2$

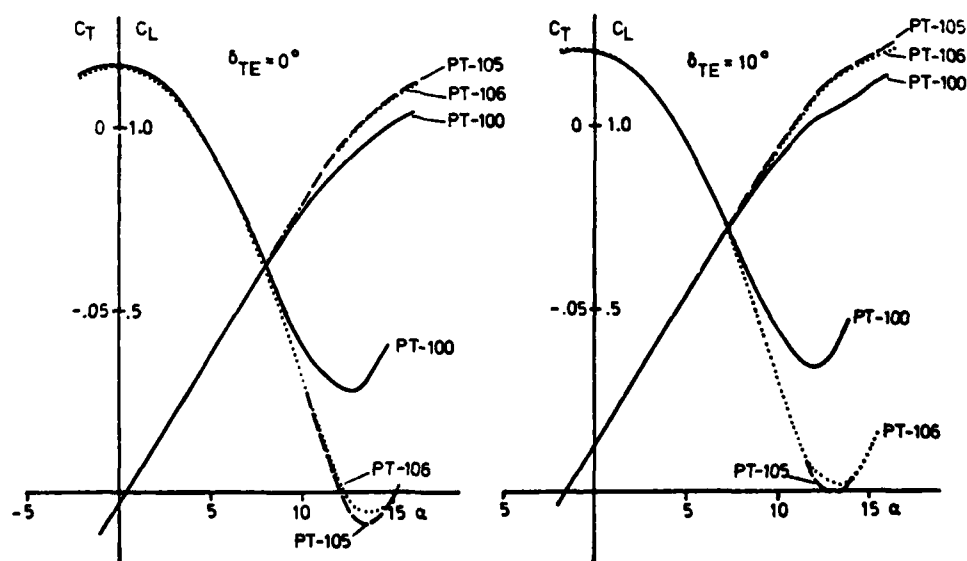


FIGURE 19. C_T and C_L as a function of α for $\delta_{TE} = 0^\circ$ and $\delta_{TE} = 10^\circ$ for PT-100, PT-105 and PT-106 at $M = 0.5$

Also included are the results from the FLO22 evaluation of the total drag C_D for $C_L \approx 0.2$. The agreement as regards the Δ -effects on drag for the four wings is surprisingly good and the experiments, at these high Reynolds numbers, confirm that PT-105 has a slightly higher and PT-106 a slightly lower drag than the basic wing PT-100. They are also both much better than PT-101 in this respect, again in agreement with the calculations. In Figure 19 the C_T and C_L values at $M = 0.5$ are given for manoeuvre considerations.

4. CONCLUSIONS AND POSSIBLE FURTHER DEVELOPMENTS

The benefits from drooping the leading edge with a compromise between low speed C_{Lmax} , manoeuvre C_{Lmax} and transonic drag characteristics are certainly not spectacular but it is obviously possible to get these benefits without any transonic cruise drag penalties at all. It should also be possible to trade a slight drag penalty (for military aircrafts) against improvements in manoeuvre characteristics and/or better start- and landing C_{Lmax} . If the improvements could be made large enough, the complication and weight penalty of a nose flap for a low cost attack aircraft might be avoided and at the same time a less vulnerable mechanical design is obtained. Also for the case when a nose flap is unavoidable the conditions for the aerodynamic design of a flap should be more favorable by starting from a slightly drooped leading edge.

It is quite certain that the compromise suggested in this study, i.e. PT-105 or PT-106 is not the best solution for the wing. The basic wing PT-100 can probably be made a better starting point by decreasing its present wing twist somewhat. At transonic cruise this should give higher local Mach number on the upper surface on the outer part of the wing and decrease the local Mach number at the critical lower side close to the leading edge. PT-100 and its derivatives have very likely not found the balance in this respect.

A few recent numerical experiments on PT-105 have shown, as an example, that a decrease of the twist angle by a few degrees for the outer third of the wing improved the transonic drag characteristics another 10 to 15 counts. However, it is not investigated how much of the C_{Lmax} values have to be given up for this low drag. Some of the C_{Lmax} loss - at manoeuvre - may perhaps be recovered through aeroelastic tailoring.

REFERENCES

1. Mc Rae, D.M.: The aerodynamic development of the wing of the A 300 B. Aeronautical Journal, July 1973
2. Schmidt, W. and Hedman, S.: Recent Explorations in Relaxation Methods for Three-Dimensional Transonic Potential Flow. ICAS Paper 76-22, Ottawa, 1976
3. Agrell, N., Drougge, G., Hedman, S. and Torngren, L.: Evaluation and Analysis of Computations and Experiments for Transonic Wing-Body Configurations. ICAS Paper 78- , Lisbon 1978.
4. Atraghji, E., NAE, Canada, Thörnqvist, L., SAAB-SCANIA, Sweden and Torngren, L., FFA, Sweden: The Tale of Two Wings. AGARD FDP Symposium on Subsonic/Transonic Configuration Aerodynamics, Paper no. 14. Munich, May 5-7, 1980
5. Ingelman-Sundberg, M. and Eriksson, L.-E.: Optimizing the fixed leading edge shape of a transonic wing to suit the landing high lift requirements. Paper to be published at the 12th ICAS Congress, Munich, October 12-17, 1980
6. Torngren, L.: An experimental investigation at transonic speeds on some swept wings (PT-100 - PT-103) at Reynolds numbers $1.0 - 1.4 \cdot 10^6$. FFA Technical Note AU-1476 (to be published)
7. Stridsberg, S.: An investigation, using a constant chord swept wing, of possible gains in C_{Lmax} with different leading edge droops designed considering transonic drag. FFA Technical Note AU-1489 (to be published)
8. Nordvik, R.: An investigation of the high lift capabilities of the 25° swept transonic wing PT-10 with and without drooped leading edges. Configurations 100 and 102. FFA Technical Note AU-1520, Part 1, 1979
9. Jameson, A. and Caughey, D.A.: Numerical calculation of the transonic flow past a swept wing. New York University, Mathematics and Computers, C00-3077-140, June 1977
10. Lind, I.: Transonic flow calculations and aerodynamic optimization of wings PT-100 - PT-106 and PT-1 using computer codes FLO22 of Jameson and CONMIN of Vanderplaats. ANASYN Report 800116 (to be published)
11. Eriksson, L.-E.: Calculation of leading edge load and pressure distribution for swept tapered wings with deflected trailing edge flaps at low speed by a combined 3-D vortex lattice method and 2-D vortex panel method. FFA Technical Note AU-1441:2 (to be published)
12. Rizzi, A. and Eriksson, L.-E.: Computational Method to Solve the Euler Equations for Transonic Flow over Wings. FFA Technical Report AU-1441:2, Part 1 (to be published)

22-10

13. Smith, A.M.O.: High-Lift Aerodynamics. Journal of Aircraft, June 1975
14. Nordvik, R.: An investigation of the high lift capabilities of the 25° swept transonic wing PT-10 with and without drooped leading edges. Configurations 104, 105 and 106. FFA Technical Note AU-1520, Part 2, 1979

INTERACTION AÉRODYNAMIQUE ENTRE UN CANARD PROCHE ET UNE AILE EN FLECHE EN ÉCOULEMENT TRANSSONIQUE

par Yves BROCARD et Volker SCHMITT

*Office National d'Etudes et de Recherches Aérospatiales (ONERA)
92320 Châtillon (France)*

RESUME

Dans le but de décrire aussi finement que possible l'effet d'un canard proche sur l'écoulement autour d'une voilure en flèche, des essais sur une aile en présence ou non de canards ont été effectués en écoulement transsonique dans la soufflerie S2MA. Les conditions d'essais ont couvert, pour quatre configurations, le domaine $0,3 < Mo < 1,2$ pour des incidences allant de 0° à 32° . Les résultats les plus significatifs sont présentés sous forme, d'une part, d'efforts globaux et de répartitions de pressions sur l'aile principale et, d'autre part, de visualisations pariétales.

L'analyse de l'influence de la compressibilité sur les performances de l'aile seule montre un effet important du nombre de Mach sur le gradient de portance à l'origine et sur l'incidence d'apparition du régime tourbillonnaire. Par ailleurs, on observe sur les courbes de portance et de moment de tangage des changements de pente brusques attribués à l'arrivée de l'éclatement du tourbillon au-dessus de l'aile, beaucoup plus marqués en subsonique élevé. A $Mo = 1,20$ apparaît, dans l'écoulement de retour du tourbillon, une onde de choc au pied de laquelle un décollement secondaire se fixe lorsque l'incidence augmente.

La présence du canard modifie l'écoulement sur l'aile d'une manière assez comparable en transsonique à ce qui est observé en subsonique : diminution de la pente à l'origine et retard dans le développement du tourbillon. Toutefois la dégradation de la portance tourbillonnaire est aussi retardée ce qui fait que les portances au décrochage de l'aile sont pratiquement égales avec ou sans canard. La présence du canard atténue la discontinuité due à la migration de l'éclatement du tourbillon mais amplifie deux autres discontinuités qui se produisent à des incidences plus élevées et qui sont liées à l'apparition et la dégradation d'un tourbillon secondaire assez intense.

AERODYNAMIC INTERACTION BETWEEN A CLOSE-COUPLED CANARD AND A SWEPTBACK WING IN TRANSONIC FLOW

ABSTRACT

A swept wing model was tested with and without a canard in the transonic wind tunnel S2MA with a view towards a detailed description of the effects of a close-coupled canard on the flow around the main wing. Test conditions ranged, for four configurations from a Mach number of .3 to 1.20 and up to 32° angle of attack. The most significant results in terms of force and pressure measurements on the main wing and wall flow visualizations are presented.

The compressibility effect analysis for the wing alone configuration shows that the Mach number has a marked effect on the lift gradient at low incidence and on the vortex onset angle of attack. Besides, an abrupt change in the lift and the pitching moment curves gradients, more visible for the high subsonic Mach numbers, is related to the vortex breakdown arrival on the wing. At $Mo = 1.20$ a shock wave appears within the reverse flow of the vortex and fixes a secondary separation when the angle of attack increases.

In transonic flow the canard changes the flowfield on the wing in a similar way as it does in incompressible flow : a decrease in the lift gradient and a delay in the vortex development. But the vortex lift decay is delayed so that the maximum lift is about the same with or without canard. The canard attenuates the discontinuity due to the vortex breakdown migration but increases two other discontinuities which occur at higher angles of attack and which are connected with the formation and the bursting of a quite strong secondary vortex.

NOTATIONS

b	: envergure de l'aile
b_0	: longueur de référence (fig. 1)
b_c	: envergure du canard
c	: corde de l'aile mesurée normalement au bord d'attaque
c_c	: corde du canard mesurée normalement au bord d'attaque
C_m	: coefficient de moment de tangage
C_N	: coefficient de force normale
C_{Nl}	: coefficient de force normale locale dans une section
C_{Nt}	: coefficient de force normale tourbillonnaire
C_z	: coefficient de portance
$C_{z_{max}}$: portance au décrochage
K_p	: coefficient de pression
$K_{p_{B.F.}}$: coefficient de pression mesuré à l'extrados près du bord de fuite ($x/c = 0,98$)
$K_{p_{min}}$: valeur minimale de K_p au droit de l'axe du tourbillon
l	: corde à l'emplanture de l'aile
M_0	: nombre de Mach à l'infini amont
M_l	: nombre de Mach local calculé à partir de p/p_0
p	: pression pariétale
p_0	: pression génératrice
Re_l	: nombre de Reynolds = $\frac{\rho_0 l}{\mu_0}$
S	: surface de référence de l'aile
S_c	: surface de référence des canards
X, Y, Z	: trièdre de référence (fig. 2)
X_1, Y_1	: axes de référence pour les sections de prises de pression.
α	: incidence
α_d	: incidence d'apparition du tourbillon
α_c	: incidence de discontinuité à cabrer
$\alpha_{c_{2max}}$: incidence de portance maximale
α_e	: incidence d'apparition de l'éclatement du tourbillon au-dessus du plan de l'aile
α_p	: incidence de discontinuité à piquer
λ	: allongement
ν_0	: viscosité cinématique
φ	: flèche de l'aile
φ_c	: flèche du canard

1 - INTRODUCTION -

La recherche d'une meilleure manœuvrabilité en vol transsonique pour les avions de combat a conduit les aérodynamiciens à étudier les possibilités offertes par les configurations de type canard proche. On sait en effet qu'un canard proche peut créer, sur une aile en flèche, une interaction tourbillonnaire favorable dont on peut tirer profit à grande incidence.

Le mécanisme de cette interaction étant très complexe, des recherches approfondies assez nombreuses sont actuellement en cours sur ce sujet dans différents laboratoires [1, 2 et 3]. De son côté, l'ONERA a entrepris des études à caractère fondamental à la fois sur le plan expérimental et sur le plan de la mise au point des moyens de prévision. Ces études ont pour objet la description fine de l'écoulement, peu de résultats détaillés étant disponibles actuellement.

Lors de la réunion AGARD de Mai 1979 à Naples ont été présentés [4] les premiers résultats obtenus sur une configuration très simple dans le cas d'écoulements à basse vitesse ($M_0 = 0,3$). Cette communication a pour but de présenter les résultats expérimentaux les plus significatifs dans le domaine transsonique en dégageant d'abord l'effet de la compressibilité sur les caractéristiques de l'écoulement autour de l'aile seule puis en étudiant les modifications apportées lorsque un plan canard est installé en amont de la voilure.

2 - CONDITIONS EXPERIMENTALES -

La maquette et le montage ont été décrits en détail en [4] et seules leurs caractéristiques principales seront rappelées ici. L'aile principale est une demi-maquette d'aile rectangulaire, cylindrique montée à la paroi (fig. 1). Le dispositif de fixation de l'aile permet d'en faire varier la flèche mais pour ces essais, une flèche constante et égale à 60° a été choisie. Cette aile présente, normalement au bord d'attaque un profil symétrique ONERA D ($\alpha_c = 0,105$) à caractère "peaky" [5].

Les plans canards sont montés sur la plaque de garde dont l'objet est de soustraire l'ensemble de la maquette aux effets de la couche limite se développant sur la paroi de la soufflerie. Ils ont une forme géométrique semblable à celle de l'aile mais leur envergure et leur flèche sont variables. Trois formes en plan de canards : C1, C4 et C6, placés dans la position PO3 (voir tableau 1 et fig. 1), ont fait l'objet d'essais en écoulement transsonique.

L'aile principale est pesée au moyen d'une balance à six composantes et des répartitions de pression sont mesurées dans six sections normales au bord d'attaque (fig. 1). En revanche, les canards ne disposent d'aucun équipement spécifique mis à part des orifices pour l'émission de fluides colorés.

Les essais dont les résultats sont présentés ici ont eu lieu, pour la plupart, dans la veine transsonique de la soufflerie pressurisée S2MA du centre ONERA de Modane (fig. 2) pour des nombres de Mach allant de 0,275 à 1,20 et des incidences de 0° à 32° . Ils ont en général été effectués à un nombre de Reynolds Re_l constant et égal à $2,32 \cdot 10^6$ pour limiter les déformations structurales tant du point de vue du vrillage que du passa-

ge au travers de la plaque de garde. Cependant quelques essais à faible nombre de Mach ou pour des incidences modérées ont pu être faits à $R_{e,l} = 5 \times 10^6$. Dans tous les cas la transition était naturelle sur les canards et sur l'aile.

Quelques résultats d'essais dans la soufflerie basse vitesse F1 sont aussi présentés pour des conditions d'essais précisées en [4] ($M_o = 0,27$, $R_{e,l} = 5 \cdot 10^6$).

3 - COMPORTEMENT AERODYNAMIQUE DE L'AILE SEULE -

Afin de pouvoir juger de l'effet sur l'écoulement autour de l'aile principale de l'interaction entre celle-ci et un canard proche, il est nécessaire de décrire tout d'abord le comportement aérodynamique de l'aile seule. En particulier les effets de la compressibilité sur les écoulements tels qu'ils ont pu être décrits à faible vitesse en [4] et [6] seront exposés dans ce chapitre.

3.1 - Description générale -

Le comportement aérodynamique de l'aile AFV D placée à 60° de flèche est conforme à celui des ailes en flèche à bord d'attaque arrondi. Quelle que soit la vitesse on observe schématiquement selon l'incidence trois régimes d'écoulement que l'on distingue aisément sur une courbe de portance (fig. 3) :

- aux faibles incidences l'écoulement est non décollé sauf au bord d'attaque où apparaît un bulbe de décollement laminaire mais dont l'étendue est très limitée. La courbe de portance quasi-linéaire est typique d'un tel écoulement (I) ;

- vers 4° d'incidence dans notre exemple ($M_o = 0,92$, $R_{e,l} = 2,3 \cdot 10^6$) on observe la formation au bord d'attaque d'un tourbillon en cornet dont l'effet principal est de créer un supplément de portance. La courbe de portance s'écarte alors de la droite précédente (II) ;

- aux fortes incidences on montre que l'axe du tourbillon en pivotant lentement vers l'emplanture s'écarte de plus en plus du plan de l'aile. Le tourbillon se désorganise progressivement, l'écoulement ne recolle plus sur toute l'envergure à l'aval du tourbillon et la portance tourbillonnaire diminue fortement. On assiste à une décroissance du gradient de portance (III) puis au décrochage.

On observe en outre sur la figure 3 une discontinuité à $\alpha_c = 11,5^\circ$ qui se retrouve sur la courbe du moment de tangage. On verra plus loin qu'elle est liée à l'arrivée du point d'éclatement du tourbillon au-dessus de l'aile.

3.2 - Écoulements aux faibles incidences et apparition du tourbillon -

Le premier effet de la compressibilité qui peut être observé est l'évolution du gradient de portance à l'origine en fonction du nombre de Mach (fig. 4). Compte tenu de la géométrie de l'aile (flèche, allongement) l'allure de cette courbe est celle que l'on pouvait attendre (règle de Prandtl Glauert [6]) et elle ne présente pas de particularités.

Figure 5 sont présentées à titre d'exemple les répartitions de pression exprimées en nombre de Mach local, dans la section 3, pour différents nombres de Mach. A $M_o = 0,70$, la présence du bulbe de décollement laminaire se traduit par un petit plateau de pression qui donne une allure particulière à la recompression après le pic de survitesse. Comme pour le profil ONERA D

[7] le bulbe grossit lorsque le nombre de Mach de l'écoulement croît. Puis à partir d'un nombre de Mach voisin de 0,7 pour le profil et de 1,15 pour l'aile en flèche, un plateau de survitesse se développe au bord d'attaque en aval duquel la recompression se fait au travers d'un choc (figure 5, $M_o = 1,20$, $x/c = 0,10$).

Si le nombre de Mach de l'écoulement est encore augmenté le niveau des survitesses au bord d'attaque reste constant, mais le plateau s'allonge et le choc se produit alors de plus en plus loin du bord d'attaque.

Etant donné la limitation à $M_o = 1,20$ pour les essais sur l'aile en flèche, la zone supersonique avec recompression par choc n'est jamais très étendue. Son existence est toutefois confirmée dès $M_o = 1,15$ à 8° d'incidence par l'évolution du nombre de Mach local, portée figure 6, pour la prise de pression située à $x/c = 0,01$ en fonction du nombre de Mach de l'écoulement et pour chaque section de mesure. Bien que, à cette incidence, on soit pratiquement dans tous les cas en présence du régime tourbillonnaire le phénomène reste le même et on remarque sur la figure 6 la limitation du niveau de survitesse ("pressure freeze" [8]) à partir de $M_o = 1,15$.

L'observation des répartitions de pression à 4° ou 6° d'incidence a mis en outre en évidence, pour les nombres de Mach supérieurs à $M_o = 1,05$, l'existence sur tout ou partie de l'aile de plusieurs petits tourbillons qui cheminent dans le lit du vent. Ainsi on peut repérer sur les répartitions de nombre de Mach local à 4° d'incidence et à $M_o = 1,2$ présentées figure 7 les traces de ces tourbillons sous forme de légères dépressions dans les sections externes 4, 5 et 6 et indiquées par une flèche. Le report de la position de ces dépressions sur une forme en plan de l'aile permet de reconstituer le cheminement de ces tourbillons. Ce phénomène avait déjà été observé par Squire et al [9] lors de visualisations par enduit visqueux d'écoulements autour d'ailes en delta à des nombres de Mach élevés ($M_o = 1,51$) et pour des incidences voisines de 4° . L'origine de ces "streamwise vortices" a été attribuée au développement d'une couche limite tridimensionnelle avec fort écoulement transversal et donc cisaillement notamment lors du contournement du bord d'attaque ou au travers d'une onde de choc. En effet, dans les deux cas les lignes de courant de l'écoulement extérieur peuvent former des angles importants avec les lignes de courant pariétales. Une instabilité dans la couche limite peut alors déclencher des tourbillons de faibles dimensions et dont l'espacement régulier en envergure est lié à l'épaisseur de la couche limite à l'endroit de leur apparition.

L'analyse faite par Squire et al a montré que ces tourbillons, pour les ailes en flèche, avaient un sens de rotation identique à celui du tourbillon en cornet qui se développe lorsque l'incidence est plus élevée.

Ces tourbillons avaient en général été mis en évidence au moyen de visualisations par enduit visqueux qui donnent une définition très fine de l'écoulement pariétal sans que la répercussion sur les répartitions de pressions ou les efforts globaux ait été relevée. Pour nos essais, cette technique de visualisation n'a pas été utilisée. Les visualisations par fluides colorés ne donnent pas une définition assez fine mais le film qui a été pris lors d'une variation continue de l'incidence montre toutefois, aux incidences voisines de 4° , quelques échappements de tourbillons. En revanche, la disposition particulière des

sections de prises de pression sur notre aile, normalement au bord d'attaque, permet de couper le trajet de cas tourbillons et ainsi de mesurer les dépressions qu'ils engendrent.

La figure 7 permet en outre de voir, dans les sections internes 2 et 3, des recompressions proches du bord de fuite en aval d'un plateau à M_1 constant et voisin de 1,45. Cette recompression est l'ébauche de ce qui, à nombre de Mach plus élevé ou à des flèches plus faibles (30° ou 40°) [10], forme une onde de choc arrière (rear shock) qui vient couper l'onde de choc avant (forward shock) proche et parallèle au bord d'attaque pour former un système de chocs dont la trace sur le plan de l'aile prend une forme de λ [8, 11].

Les répartitions en envergure de la force normale, telle qu'elle peut être calculée par intégration des profils de pression dans les sections de mesure (la valeur portée pour la section 1 a été pondérée de façon à tenir compte de la troncature de cette section par l'emplanture) évaluées à différents nombres de Mach mettent en évidence (fig. 8) les particularités des écoulements aux nombres de Mach supersoniques.

Pour $Mo \leq 0,92$, la répartition est d'allure quasi elliptique contrairement à ce qu'on observe lorsque $Mo \gg 1,10$. A grand nombre de Mach la répartition obtenue entre les sections 1 et 4 est due à l'évolution du plateau de pression présent entre le choc et la recompression arrière. L'augmentation de la force normale au bout d'aile entre les sections 4 et 6 est créée par la multiplication du nombre des tourbillons longitudinaux passant dans chaque section lorsqu'on se rapproche de l'extrémité (voir fig. 7). Aux nombres de Mach intermédiaires $0,92 < M_1 < 1,10$, les répartitions en envergure sont déformées par l'apparition en extrémité de voilure du tourbillon principal qui pour ces valeurs du nombre de Mach apparaît avant 4° d'incidence (voir fig. 9).

Vers 4° d'incidence on a vu (fig. 3) que le gradient de portance augmentait dénotant l'apparition du tourbillon en cornet. La valeur de cette incidence est variable selon le nombre de Mach de l'écoulement mais encore plus avec le nombre de Reynolds. Figure 9 est portée l'incidence d'apparition du tourbillon α_c en fonction du nombre de Mach pour deux valeurs du nombre de Reynolds. Cette incidence est celle à partir de laquelle la courbe de portance s'écarte de la partie linéaire.

L'évolution avec le nombre de Mach est conforme avec ce qu'ont trouvé Rogers et al [8]. L'augmentation de l'incidence α_c après le minimum vers $Mo = 1$, est selon [8] liée au fait que le décollement qui engendre le tourbillon a lieu au pied du choc avant et non plus lors de la recompression qui suit directement le bord d'attaque dans les cas subsoniques.

On observe en outre que la variation avec le nombre de Reynolds, très importante à faible vitesse tend à s'atténuer en transsonique. On a pu montrer [6] que, à faible vitesse, la variation brutale de l'incidence d'apparition du tourbillon de 5° à 12° lorsque le nombre de Reynolds atteint une valeur de l'ordre de 3×10^6 (fig. 10) pouvait être reliée au comportement du bulbe de décollement laminaire qui est présent, sur cette aile dès 1° d'incidence. Ce bulbe est de type long ou court selon que le nombre de Reynolds est modéré ou élevé et son évolution lorsque l'incidence augmente est très différente dans les deux cas. Ceci conduit, dans le cas du profil à un décrochage respecti-

vement précoce ou tardif, l'incidence d'apparition du régime tourbillonnaire présente la même évolution brutale pour un nombre de Reynolds voisin.

Pour les écoulements transsoniques le nombre de Reynolds de transition est plus faible et l'apparition du tourbillon se fait en présence d'un bulbe court d'abord en extrémité d'aile puis, lorsque l'incidence augmente, le point de naissance se rapproche de l'apex.

3.3 - Développement et désorganisation du tourbillon -

L'apparition du tourbillon de bord d'attaque a pour conséquence d'augmenter le gradient de portance. Cet effet est dû à la dépression qu'induit le tourbillon lors de son passage au-dessus de l'aile et qui donne aux répartitions de pression une forme en cloche caractéristique. Une telle répartition a été représentée schématiquement figure 11 dans le cas de notre aile. L'aspect de l'écoulement pariétal ainsi que celui des pseudo-lignes de courant dans une coupe normale au bord d'attaque sont aussi représentés et permettent de définir certaines notions utilisées dans la suite du texte.

La comparaison des champs de pression mesurés à 12° d'incidence pour différents nombres de Mach (fig. 12) montre combien la position de la trace du tourbillon et le niveau des dépressions sont influencés par le nombre de Mach. Les courbes de force normale tourbillonnaire (fig. 13) mettent aussi en évidence un effet important du nombre de Mach sur le supplément de force normale apporté par le tourbillon. La force normale tourbillonnaire est obtenue en retranchant de la force normale mesurée, la force normale qui serait obtenue en l'absence de décollement tourbillonnaire et qui peut être évaluée à partir du gradient de portance à l'origine :

$$C_N = \left(\frac{dC_z}{d\alpha} \right)_{\alpha=0} \sin \alpha \approx \alpha$$

ou grâce à des méthodes de calcul déjà décrites [4, 6].

On remarque ainsi que, aux incidences modérées (entre 5° et 10°) le démarrage plus précoce du tourbillon en subsonique élevé rend la force normale tourbillonnaire plus élevée pour ces nombres de Mach alors que pour les incidences plus élevées l'augmentation du nombre de Mach fait diminuer la force normale maximale produite par le tourbillon.

On distingue aussi sur ces courbes une très nette discontinuité se produisant entre 11° et 16° d'incidence et qui provoque sur les courbes de moment de tangage un brutal autocabrage (fig. 3). L'intensité de la discontinuité et l'incidence α_c à laquelle elle se produit évoluent avec le nombre de Mach de l'écoulement. Cette incidence est reportée figure 14 avec la courbe de l'incidence de décrochage ($\alpha_{Cz \max}$).

Cette discontinuité qui a déjà été observée dans le passé [12, 13] est liée à la migration du point d'éclatement du tourbillon dont le passage dans chaque section de l'aile peut être repéré par la diminution rapide de $K_{p \min}$ en fonction de l'incidence (fig. 15). On peut aussi suivre le cheminement vers l'apex de l'éclatement avec l'incidence (fig. 16). On remarque ainsi que, si à $Mo = 0,275$ la migration est progressive, en revanche à $Mo = 0,92$ l'éclatement lorsqu'il arrive au-dessus de l'aile vers 12° se déplace brusquement jusqu'à la section 4. La dégradation de la portance provoquée par l'éclatement est particulièrement bien

mise en évidence sur les courbes de force normale locale obtenues par intégration des répartitions de pression dans chaque section (fig. 17).

Un aperçu plus complet des modifications de l'écoulement d'extrados provoquant la perte de portance peut être donné par le tracé des lignes isobares.

Celles-ci sont déterminées à partir des champs de pression mesurés pour les incidences entourant le phénomène. Pour le cas déjà mentionné, à $Mo = 0,92$ un exemple en est donné par les figures 18 a et b représentant respectivement les cartes isobares à 11° et 12° d'incidence. Dans le premier cas (fig. 18a) on décèle un écoulement tourbillonnaire très régulier. La ligne de recollement du tourbillon principal est orientée suivant le réseau des lignes isobares très rapprochées qui aboutissent à proximité du bord de fuite de l'aile à son extrémité libre. Sur le tracé suivant (fig. 18 b) on ne remarque des modifications notables que dans la partie externe de l'aile. Dans cette partie l'intensité de la dépression a diminué considérablement. De même, on observe un élargissement du tourbillon qui ne recolle plus sur l'aile.

Ce dernier point peut être mis en évidence par la mesure de la pression dans une prise très proche du bord de fuite ($X/C = 0,98$) lors d'une variation continue de l'incidence (fig. 19 a). Ainsi à $Mo = 0,92$ le non recollement se manifeste par une divergence brutale de la pression simultanément dans les sections 5 et 6 vers $11,5^\circ$ d'incidence. Les courbes relatives aux sections 4 et 3 présentent une divergence moins abrupte pour des incidences plus élevées ce qui correspondrait à la migration, vers l'apex du point d'écèlement. Ces courbes mettent aussi en évidence d'autres modifications importantes de l'écoulement. A partir de 6° la diminution des $-K_p$ dans les sections 6, 5 et 4 est due au développement du tourbillon. En effet, en l'absence de tourbillon (avant 6°), la couche limite issue de la pseudo ligne d'arrêt est épaisse lorsqu'elle arrive au bord de fuite. Son épaisseur augmente avec l'incidence et par effet de déplacement la pression diminue. Par contre en présence du tourbillon la couche limite est issue de la ligne de recollement qui, lorsque l'incidence augmente se rapproche du bord de fuite. On est alors en présence d'une couche limite peu épaisse et dont l'épaisseur tend même à diminuer d'où l'augmentation de la pression avec l'incidence après 6° .

Vers $18,5^\circ$ la diminution des $-K_p$ dans les sections 4 et 3 détaillée plus loin au chapitre 4.2, est créée par la réorganisation de l'écoulement sous forme d'un tourbillon secondaire et qui est à l'origine d'un moment piqueur à peine perceptible dans le cas de l'aile seule.

L'étude des écoulements à $Mo = 1,20$ révèle des différences importantes avec ce qui vient d'être décrit pour les nombres de Mach subsoniques. Un premier exemple est donné par l'évolution des pressions au bord de fuite (fig. 19 b) qui révèle d'une façon similaire (diminution des $-K_p$ en sections 6 et 5) l'apparition du régime tourbillonnaire vers 9° d'incidence, mais en revanche, diverge pour une incidence de 11° , qui ne coïncide plus avec celle de l'autocabrage ($\alpha_c = 15,8^\circ$). A cette incidence, on ne constate qu'une augmentation brusque des pentes dans les sections 6 et 5.

Une autre différence réside dans l'apparition, vers l'extrémité de l'aile, d'une recompression au sein de l'écoulement de retour du tourbillon proche de la surface de l'aile et dont les caractéristiques sont celles d'une recompression par choc. Les visualisations à 12° , 14° et 16° (fig. 20) montrent que cette onde de choc ne produit à 12° qu'une déviation dans l'écoulement puis qu'à 14° une sorte de bulbe de pied de choc se forme et qu'enfin à 16° le décollement se déplace brutalement pour avoir lieu au droit de l'onde de choc. De plus, si à l'incidence la plus faible l'onde de choc est limitée en envergure aux sections 5 et 6, elle s'étend vers l'apex lorsque l'incidence croît. Les répartitions de nombre de Mach local, pour 12° d'incidence (fig. 21a) mettent bien en évidence l'apparition d'une recompression brutale en section 6 entre $X/C = 0,72$ et $0,65$ qui à 16° (fig. 21b) s'étend en envergure jusqu'à la section 4.

4 - EFFET D'UN CANARD PROCHE SUR LE COMPORTEMENT AERODYNAMIQUE DE L'AILE -

4.1 - Ecoulement à faible incidence et apparition du tourbillon -

L'étude de l'interaction entre le canard et la voilure en écoulement incompressible [4] a mis en évidence une diminution sensible du gradient de portance de l'aile à faible incidence en présence du canard par rapport au cas de l'aile seule. La figure 22, où est présentée l'évolution du gradient de portance avec le nombre de Mach de l'écoulement pour différents cas de canards comparée à celle de l'aile seule montre que cette tendance observée en écoulement incompressible ($Mo = 0,275$) se conserve quel que soit le nombre de Mach jusqu'à $Mo = 1,20$.

Cette diminution du gradient est due à la déflexion de l'écoulement créée par le canard. Les calculs effectués au moyen d'une méthode de singularités traitant les nappes tourbillonnaires en écoulement incompressible [14] ont montré [4] que la déflexion créée par le canard n'intéressait pratiquement que la région interne de la voilure située directement en dessous de la nappe issue du bord de fuite du canard. Ceci est aussi visible sur les distributions de force normale en envergure obtenues par intégration des répartitions de pression dans chaque section (fig. 23*) où le déficit de portance en présence du canard est limité à la partie interne de l'aile. Cet effet explique une diminution de gradient d'autant plus importante que l'envergure du canard est plus grande comme le montre la figure 24 où l'évolution du gradient de portance est portée en fonction de l'envergure du canard (rapportée à celle de l'aile). Cette figure montre de plus que les canards à 60° de flèche dont l'extrémité se trouve plus proche de l'aile ont, à envergure égale, un effet plus marqué que les canards à 40° de flèche, et que le rapprochement en X des canards vers l'aile de la position P03 à la position P12 a aussi tendance à accentuer la diminution du gradient de portance.

* Ces courbes sont tracées avec le nombre de Mach local M_l en ordonnée. Celui-ci est calculé à partir de P/P_∞ et ne représente pas le vrai nombre de Mach local car dans un tourbillon la pression d'arrêt n'est pas partout égale à la pression génératrice et la pression statique est fortement évolutive.

** Les valeurs pour la section 1 sont pondérées pour tenir compte de la troncature de cette section avec l'emplanture.

La présence du canard modifie peu l'incidence d'apparition du tourbillon de bord d'attaque de l'aile excepté pour le canard C4. La figure 25 permet de comparer les courbes d'apparition du tourbillon en fonction du nombre de Mach pour différents canards à la courbe obtenue pour l'aile seule. Une différence notable n'est décelable que dans le cas du canard C4 pour lequel on observe un net retard à l'apparition du tourbillon à faible vitesse et un effet de la compressibilité plus marqué que pour l'aile seule. La diminution de l'incidence d'apparition avec le nombre de Mach est importante pour cette configuration et l'incidence minimale obtenue ($2,5^\circ$ vers $Mo = 0,96$) est inférieure à celle observée pour l'aile seule ($3,5^\circ$). Par contre pour les autres cas de canards, la tendance est d'atténuer les effets de la compressibilité. Notons toutefois que ces incidences sont déterminées à partir du changement de pente des courbes de portance, changement dont la détermination est assez imprécise malgré le nombre élevé des points de mesure (3 points par degré).

4.2 - Effet de la présence du canard sur le développement du tourbillon de l'aile -

La comparaison des courbes de force normale tourbillonnaire en présence ou non d'un canard (fig. 26) met en évidence une différence notable quant à l'évolution de l'apport en portance dû au tourbillon.

Jusqu'à 11° d'incidence on observe un retard au développement du tourbillon dans les cas avec canard. A $11,5^\circ$ l'arrivée de l'éclatement provoque la dégradation de la force normale due au tourbillon tandis que dans les cas des canards à grande envergure (C1 et C4) il faut attendre jusqu'à 20° pour observer une telle dégradation.

Le maximum de force normale tourbillonnaire ainsi atteint est alors bien supérieur avec que sans canard.

La figure 27 présente à $Mo = 0,275$ l'évolution avec l'incidence de la position du point d'éclatement sur l'aile, position déterminée à partir des répartitions de pression (chap. 3.3), elle montre que le canard provoque un retard à la migration du point d'éclatement vers l'apex, ce qui est à l'origine du supplément de force normale tourbillonnaire observé.

A l'extrémité de l'aile, c'est-à-dire loin de la zone d'influence du canard, le retard dû au canard est nul mais il apparaît progressivement lorsque le point d'éclatement se rapproche de l'apex.

Aux nombres de Mach plus élevés l'approche de l'éclatement au-dessus de l'aile induit une discontinuité sur les courbes de portance et plus encore sur les courbes de moment de tangage. La présence du canard modifie considérablement l'importance de cette discontinuité et l'évolution ultérieure de l'écoulement. C'est ce que met en évidence la figure 28 où sont comparées les courbes de moment de tangage en fonction de l'incidence pour différents cas de canards. Ainsi, on observe que l'autocabrage lié à la migration du point d'éclatement qui se produisait à $11,5^\circ$ dans le cas de l'aile seule tend à être retardé en incidence lorsque l'envergure du canard s'accroît mais surtout diminue en intensité jusqu'à disparaître dans le cas du canard C4P03. Par contre on remarque que, à des incidences plus élevées, apparaissent d'une façon plus marquée d'autres discontinuités, la première étant à piquer α_p

(pitch down) la seconde à cabrer α_c (pitch up) qui ne sont pratiquement pas perceptibles dans le cas de l'aile seule.

Pour comprendre l'origine de ces discontinuités il faut remarquer tout d'abord que l'action principale d'un canard sur le tourbillon de l'aile est, à incidence donnée, de rapprocher du bord d'attaque le tourbillon, ce qui a pour effet de diminuer son étendue dans une section et d'augmenter l'intensité des dépressions qu'il engendre sur l'aile. Ceci a été constaté [4, 6] en écoulement incompressible pour lequel les essais au tunnel hydrodynamique ont montré par ailleurs que l'axe du tourbillon était plus proche de la surface de l'aile en présence d'un canard. En écoulement transsonique on observe le même phénomène. A titre d'exemple figure 29 sont comparées les répartitions de nombre de Mach local dans la section 5 à $Mo = 0,84$ et 8° d'incidence et pour différents cas de canards, ce qui illustre ce qui vient d'être dit plus haut.

L'arrivée de l'éclatement au-dessus de l'aile a pour effet, dans une configuration avec canard de modifier les répartitions de pression en créant une recompression brutale au sein de l'écoulement de retour du tourbillon. Elle est visible sur la figure 30, où sont présentées les répartitions du nombre de Mach local à 8° , 12° et 16° dans la section 5 pour la configuration C1P03 (pour laquelle l'autocabrage se produit vers $15,5^\circ$ - fig. 28) sur la courbe correspondant à 16° entre $x/c = 0,55$ et $x/c = 0,50$. Sur les visualisations par fluides colorés, elle se traduit par une ligne de décollement franche sur laquelle les lignes de courant pariétales de l'écoulement de retour aboutissent avec un angle important (fig. 31) contrastant avec le schéma b plus classique où ces lignes de courant prennent une inflexion en avant de la ligne de décollement pour y aboutir d'une façon presque tangente.

Notons que ce schéma (a) n'est pas fondamentalement différent de ce qui a pu être observé pour la configuration aile seule à $Mo = 1,20$ lorsqu'un choc apparaît dans le tourbillon en extrémité d'aile (chapitre 3-3). Et il n'est pas exclu, mais les informations disponibles ne permettent pas d'être plus affirmatif, que en présence d'un canard l'éclatement qui accompagne l'augmentation des dimensions du noyau crée les conditions nécessaires pour que la recompression se fasse au travers d'un choc qui engendre le décollement secondaire.

Notons enfin que, si ce schéma a pu être observé sur les visualisations pour la configuration aile seule à $Mo = 0,92$ il était dans tous les cas limité à une région très réduite de l'aile (entre les sections 3 et 4) et n'était pratiquement pas perceptible sur les répartitions de pression.

Ce qui est remarquable dans le type d'écoulement qui existe donc en configuration avec canard et au droit de l'éclatement du tourbillon principal est que ce décollement va engendrer, pour des incidences légèrement plus élevées, un tourbillon secondaire contrarotatif dont le développement rapide est à l'origine de la discontinuité à piquer observée sur la figure 28, en particulier à $18,5^\circ$ pour la configuration C4P03. Les répartitions de nombre de Mach local dans la section 5 pour cette configuration à 8° , 12° , 16° et 20° (fig. 32 a) montrent successivement la recompression brutale à 12° liée à l'arrivée de l'éclatement, puis à 16° l'apparition (autour de $x/c = 0,25$) d'un tourbillon secondaire, visible sur les visualisations par fluides colorés, dont l'effet de succion devient très important

à 20°. Les répartitions dans la section 2 pour les mêmes conditions (fig. 32 b) montrent aussi un changement important entre 16° et 20° où la poche de dépression, au lieu d'avoir un développement complet vers le bord d'attaque, est limitée par une petite recompression. Malgré les similitudes avec ce qui a été vu plus haut, y compris d'ailleurs sur les visualisations où cette recompression correspond à la ligne de décollement secondaire qui recule donc brutalement entre 16° et 20° de $x/c = 0,18$ à 0,325, ce comportement ne semble pas devoir être associé à l'arrivée dans cette section de l'éclatement.

Il en résulte une diminution du gradient de portance dans la région de l'emplanture de l'aile qui s'accompagne en extrémité d'une augmentation de la portance due au développement du tourbillon secondaire et l'ensemble conduit à la discontinuité à piquer observée. La troisième et dernière discontinuité du moment de tangage qui, de nouveau, est à cabrer est quant à elle créée par la désorganisation complète du tourbillon principal et du tourbillon secondaire qui rend les répartitions de pression complètement plates (fig. 33). Cette désorganisation, lorsqu'il y a le canard C4P03 remonte brutalement vers 22° jusqu'à la section 3 puis chemine lentement vers l'apex. Ce changement est très visible sur les visualisations par fluide coloré où la ligne de décollement secondaire remonte subitement vers le bord d'attaque pour laisser place à des lignes de courant pariétales très organisées et ressemblant fort aux effets d'un tourbillon "classique" mais ne présentant, au niveau de la surface de l'aile, aucun gradient de vitesse (voir schéma fig. 34).

Toutes ces variations dans les schémas d'écoulement, ainsi que leur migration, peuvent être mises en évidence par les courbes de $K_{p\min}$ où, pour chaque section de mesure, la valeur minimale du coefficient de pression K_p est portée en fonction de l'incidence (fig. 35). Ainsi l'arrivée de l'éclatement se traduit par une diminution des $K_{p\min}$ dans les sections 6, 5 et 4. Le développement du tourbillon secondaire entre 16° et 22° fait augmenter les $K_{p\min}$ tandis que, à 18,5°, la transformation de l'écoulement dans les sections 1 et 2 provoque le moment à piquer. Enfin, la désorganisation complète des tourbillons est responsable de la chute brutale, vers 22°, des $K_{p\min}$ dans les sections extrêmes qui se propage ensuite vers l'apex.

La figure 36 montre, pour le cas C4P03, l'évolution des incidences auxquelles se produisent les deux discontinuités du moment de tangage en fonction du nombre de Mach. Ces courbes sont typiques en allure et en valeur de ce que l'on observe pour les autres cas de canards.

Pour les nombres de Mach supersoniques, les écoulements rencontrés sur l'aile en présence d'un canard sont très proches de ceux décrits dans le cas de l'aile seule si ce n'est qu'on constate un décalage en incidence.

Pour ce qui est de la portance au décrochage, en dépit du retard important à la désorganisation du tourbillon créé par le canard et à cause de la forte déportance due à la déflexion générale de l'écoulement, il n'a pas été observé

de gain important en présence d'un canard par rapport au cas de l'aile seule (fig. 37) la forme en plan de l'aile étant moins propice à ce point de vue que, par exemple, les ailes en delta [15].

5 - CONCLUSION -

Les résultats d'une étude visant à la description des écoulements sur une aile à 60° de flèche en écoulement sub ou transsonique ($0,275 \leq M_\infty \leq 1,20$) dans une large gamme d'incidences ($0^\circ \leq \alpha \leq 32^\circ$) ont été présentés dans une première partie.

Mise à part l'évolution avec le nombre de Mach de grandeurs telles que le gradient de portance à l'origine, l'incidence d'apparition du tourbillon et la portance au décrochage typiques de ce type de voilure, des phénomènes particuliers au régime transsonique ont pu être mis en évidence. Ainsi, l'arrivée de l'éclatement du tourbillon au-dessus de la voilure induit un moment piqueur très prononcé en écoulement transsonique.

Par ailleurs, pour les nombres de Mach supersoniques, il se forme, à des incidences modérées (4° à 8°) et avant que le tourbillon principal n'apparaisse, des tourbillons longitudinaux dans la partie externe de la voilure qui modifient considérablement les répartitions de charge en envergure. Aux incidences plus élevées, on peut supposer qu'apparaît, au sein du tourbillon et vers l'extrémité de l'aile, une onde de choc au pied de laquelle se forme, lorsque l'incidence augmente, un bulbe puis un décollement qui devient le décollement secondaire du tourbillon.

Dans une deuxième partie les modifications apportées par la présence d'un canard proche aux écoulements sur l'aile ont été analysées. Dans toute la gamme des nombres de Mach, le gradient de portance à l'origine est diminué et ce d'autant plus que l'envergure du canard est plus grande. Par contre l'incidence d'apparition du tourbillon est peu modifiée par rapport au cas de l'aile seule mais le supplément de force normale dû au tourbillon est, aux fortes incidences, plus important.

L'arrivée de l'éclatement au-dessus de l'aile induit une recompression brutale et prématurée au sein du tourbillon qui elle-même entraîne le décollement secondaire puis la formation d'un tourbillon secondaire. Le développement de ce dernier puis la désorganisation complète du système à deux tourbillons induisent sur les courbes de moment de tangage deux nouvelles discontinuités qui étaient à peine perceptibles dans le cas de l'aile seule.

REFERENCES -

- [1] LACEY D.W.
Aerodynamic characteristics of the close-coupled canard as applied to low to moderate swept wings.
Volume 1 : general trends
DTNSRDC - 79/001 - Jan. 1979
- [2] LAMAR J.E., LUCKRING J.M.
Recent theoretical developments and experimental studies pertinent to vortex flow aerodynamics with a view towards design.
AGARD CP 247 - Oct. 1978
- [3] SONNLEITNER W.
Wind tunnel investigation of controls for DFC on a fighter-type configuration of higher angles of attack.
AGARD CP 262 - Mai 1979

- [4] BROCARD Y., SCHMITT V.
Interaction aérodynamique entre un canard
proche et une voilure.
AGARD CP 262 - Mai 1979 - ONERA TP 1979-95
- [5] VINCENT DE PAUL M.
Recherches expérimentales sur des profils
d'ailes supercritiques.
AGARD CP 35 - ONERA TP 632 (1968)
- [6] BROCARD Y., MANIE F.
Etude des caractéristiques de l'écoulement
tourbillonnaire sur une aile en flèche.
Colloque AAAF - Lille 1979 - ONERA TP
1979-147
- [7] VINCENT DE PAUL M., DYMENT A.
Recherches sur les profils d'ailes en
écoulement subsonique élevé.
L'Aéronautique et l'Astronautique n° 19
(1970-3) - ONERA TP n° 815 (1970)
- [8] ROGERS E.W.E., HALL I.M.
An introduction to the flow about plane
swept-back wings at transonic speeds.
The Journal of the Royal Aeronautical
Society - Vol. 64, n° 596, 1960
- [9] SQUIRE L.C., JONES J.C., STANBROOK A.
An experimental investigation of the
characteristics of some plane and
cambered 65° delta wings at Mach numbers
from 0.7 to 2.0.
RAE Report n° Aero 2655 (1961)
- [10] SCHMITT V., MANIE F.
Écoulements subsoniques et transsoniques
sur une aile à flèche variable.
La Recherche Aérospatiale - n° 1979-4 -
ONERA TP 1979-102
- [11] MONNERIE B., CHARPIN F.
Essais de tremblement ("Buffeting")
d'une aile en flèche en transsonique.
Aéronautique et Astronautique n° 50
(1975-1) - ONERA TP. 1975-11
- [12] HUMMEL D., SRINIVASAN P.S.
Vortex breakdown effects on the low speed
aerodynamic characteristics of slender
delta wings in symmetrical flow.
J. of the Royal Aeronautical Society,
Vol. 71 - April 1967
- [13] ELLE B.J.
On the breakdown at high incidences of
the leading edge vortices on delta wings.
Journal of the Royal Aeronautical Society
vol. 64 - August 1960
- [14] REHBACH C.
Calcul instationnaire de nappes tourbil-
lonnaires émises par des surfaces por-
tantes fortement inclinées.
AGARD CP 247, Paper n° 14 - 1978
- [15] HALE R.W. - ORDWAY D.E.
Prediction of aerodynamic loads on close
coupled canard configurations. Theory and
experiment.
AGARD CP 204 - Paper n° 8 - 1976

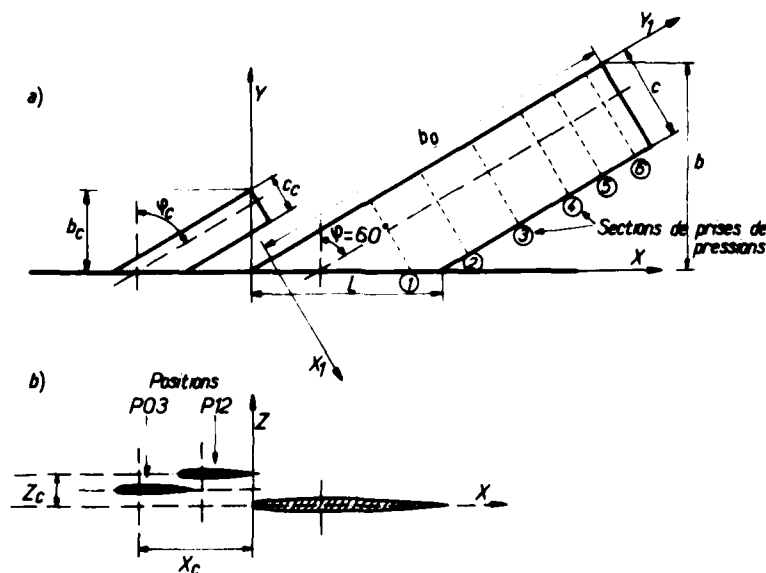


Fig. 1 - Schéma du montage d'essais

a) vue en plan

b) section à l'emplanture

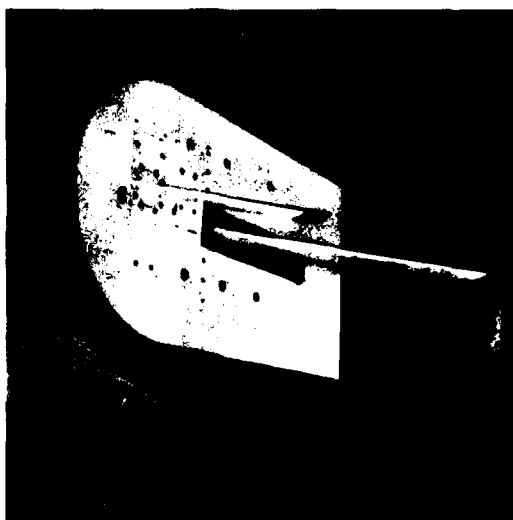


Fig. 2 - Vue du montage sur la paroi verticale de la veine transsonique de la soufflerie S2MA.

Fig. 3 - Courbes de portance et de moment de tangage.

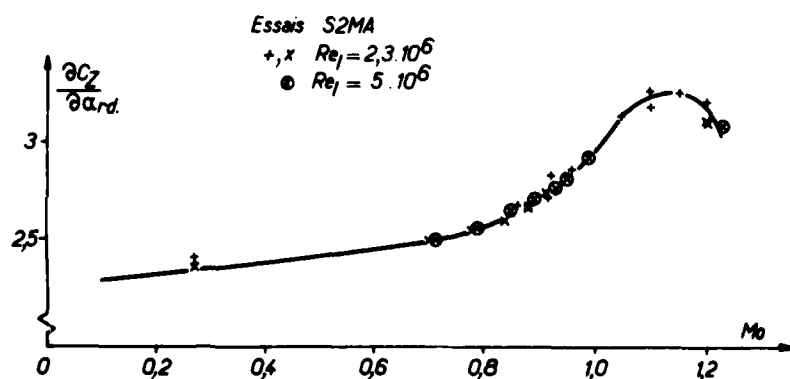
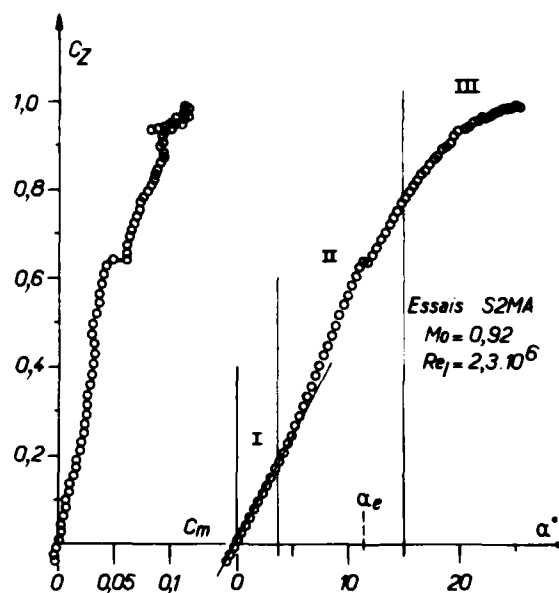


Fig. 4 - Evolution du gradient de portance en fonction du nombre de Mach.

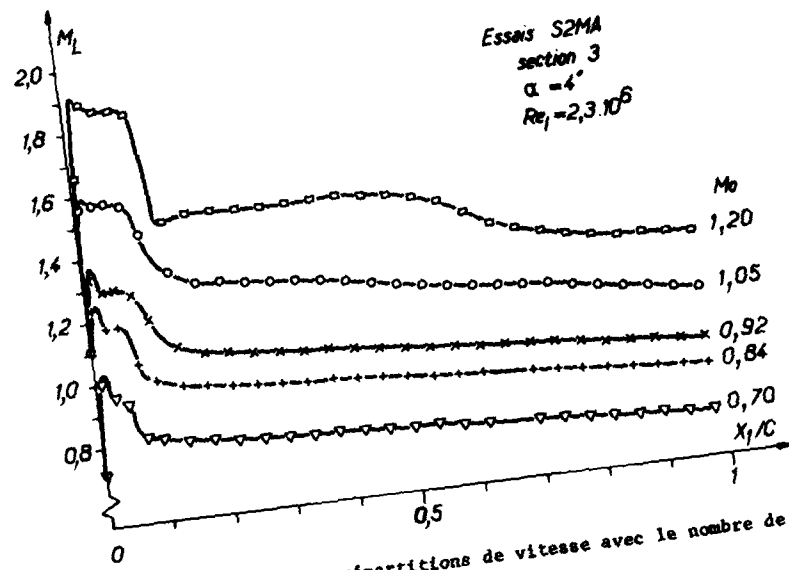


Fig. 5 - Evolution des répartitions de vitesse avec le nombre de Mach de l'écoulement.

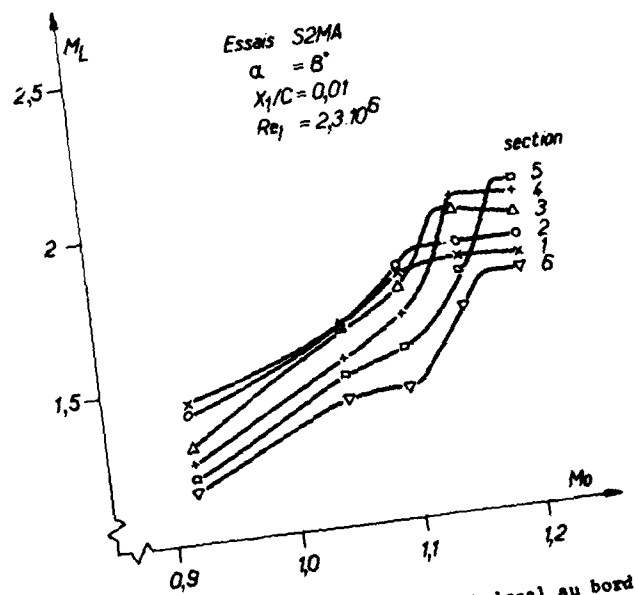


Fig. 6 - Evolution du nombre de Mach local au bord d'attaque.

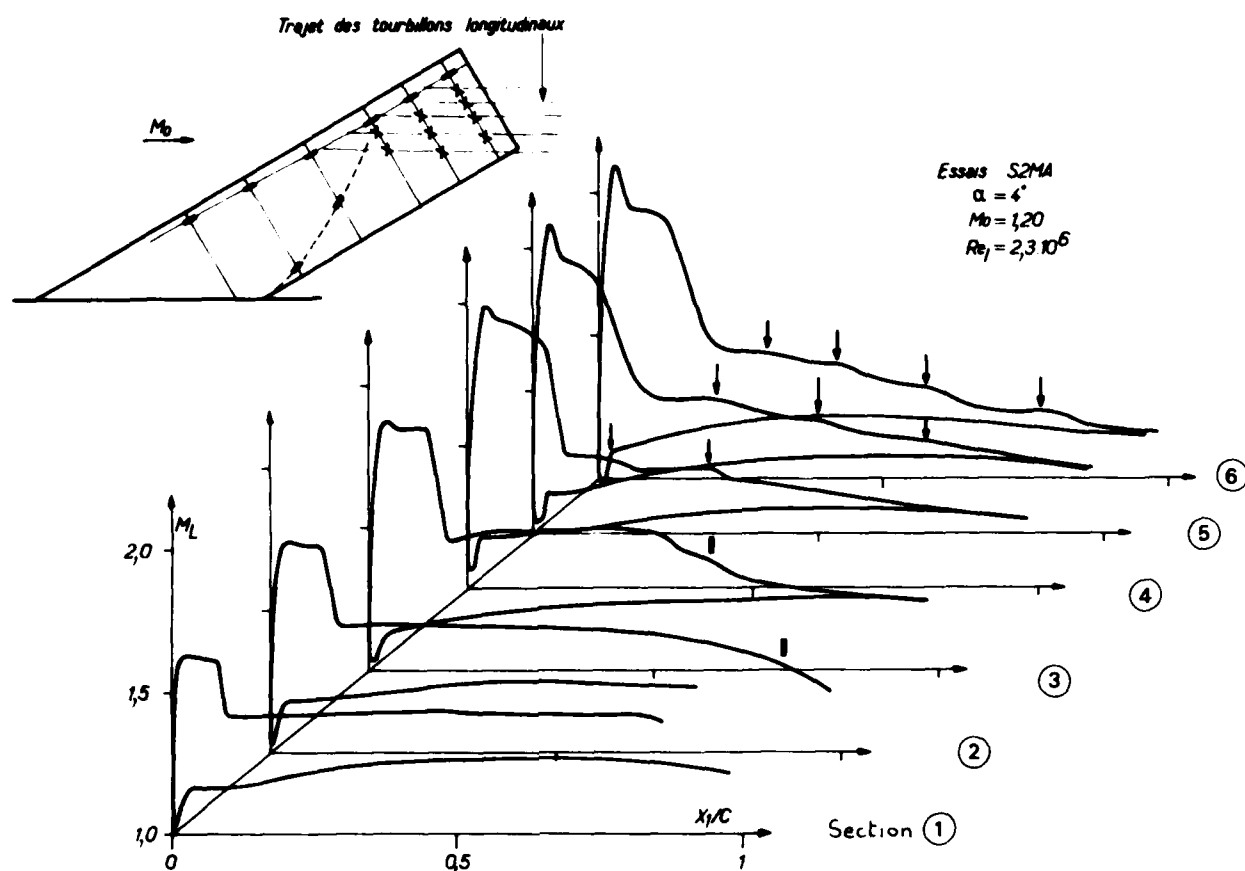


Fig. 7 - Mise en évidence des tourbillons longitudinaux.

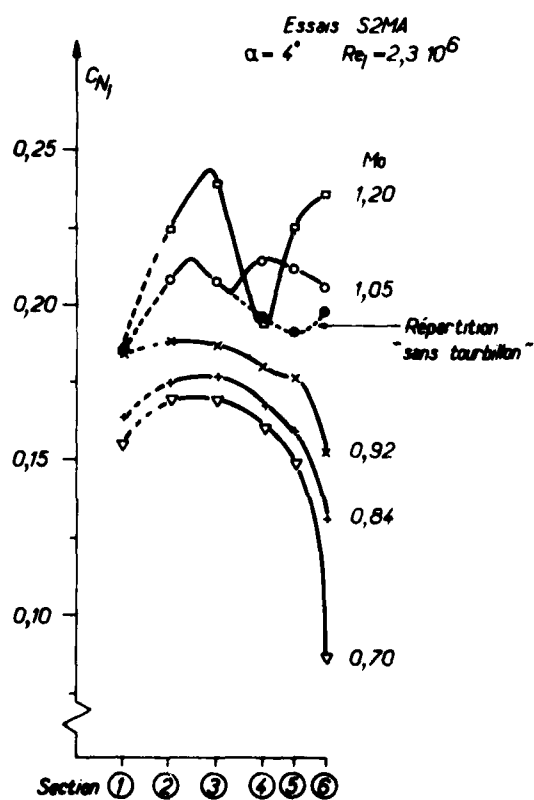


Fig. 8 - Répartition de force normale en envergure.

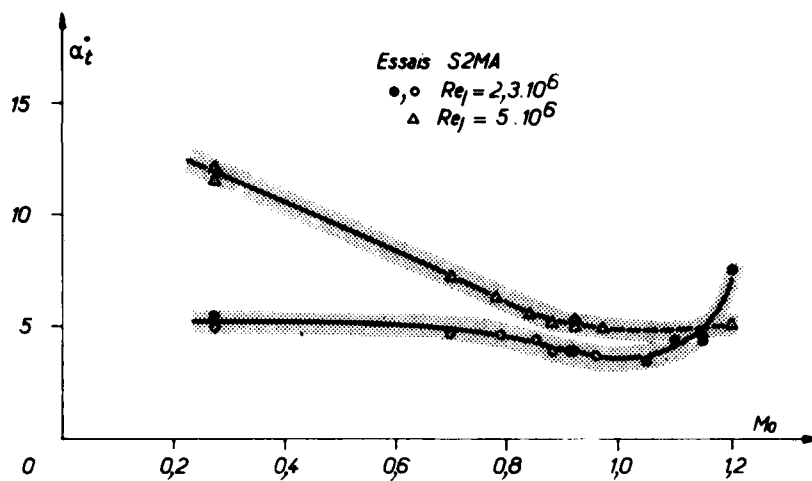


Fig. 9 - Incidence d'apparition du régime tourbillonnaire.

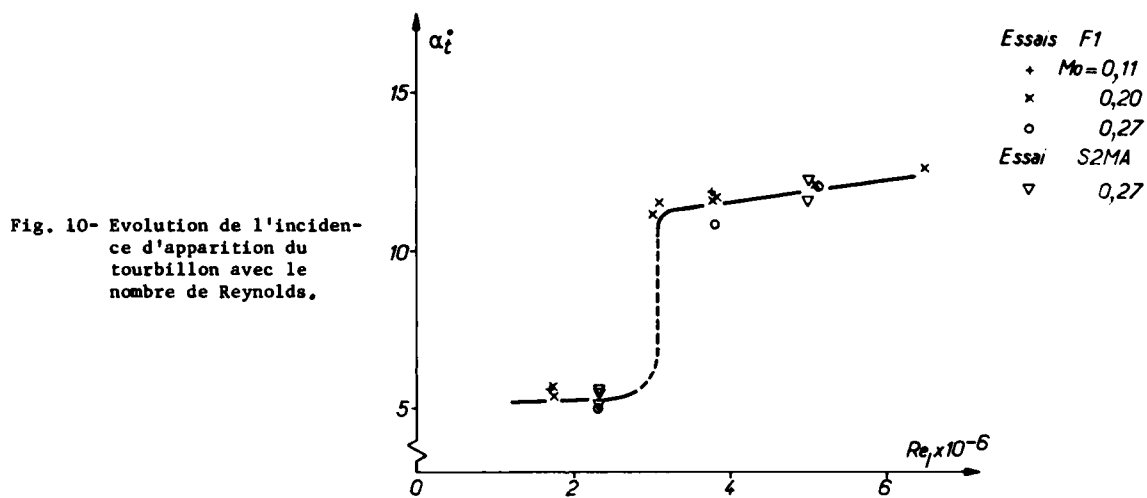


Fig. 10 - Evolution de l'incidence d'apparition du tourbillon avec le nombre de Reynolds.

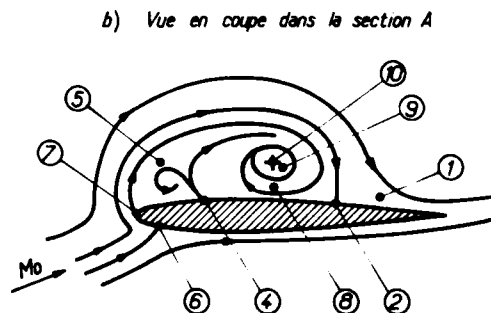
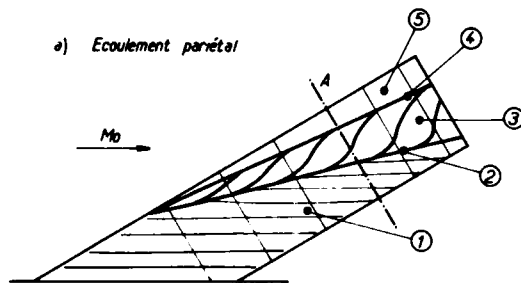
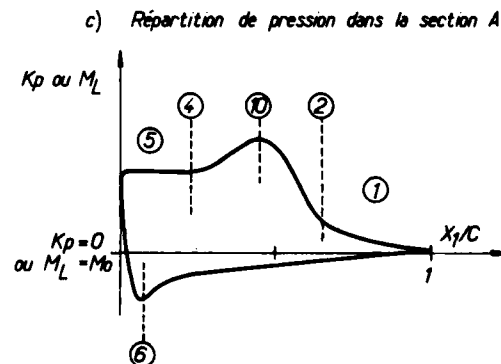


Fig. 11 - Description de l'écoulement avec formation du tourbillon en "cornet".

- ① Ecoulement non décollé ou recollé
- ② Ligne de recollement
- ③ Trace de l'écoulement de retour du tourbillon
- ④ Ligne de décollement secondaire
- ⑤ Région "d'eau morte" avec formation éventuelle de tourbillons secondaires
- ⑥ Pseudo ligne d'arrêt
- ⑦ Ligne de décollement primaire
- ⑧ Ecoulement de retour
- ⑨ Noyau du tourbillon
- ⑩ Axe du tourbillon



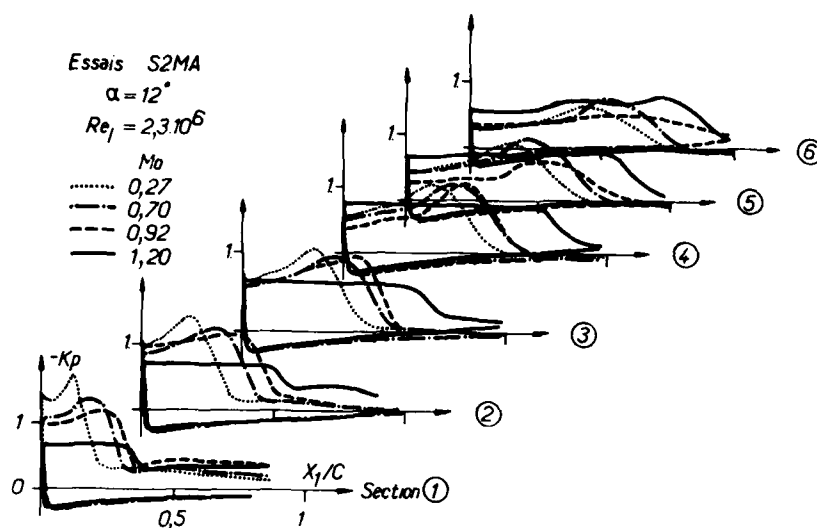


Fig. 12- Effet du nombre de Mach sur le champ de pression.

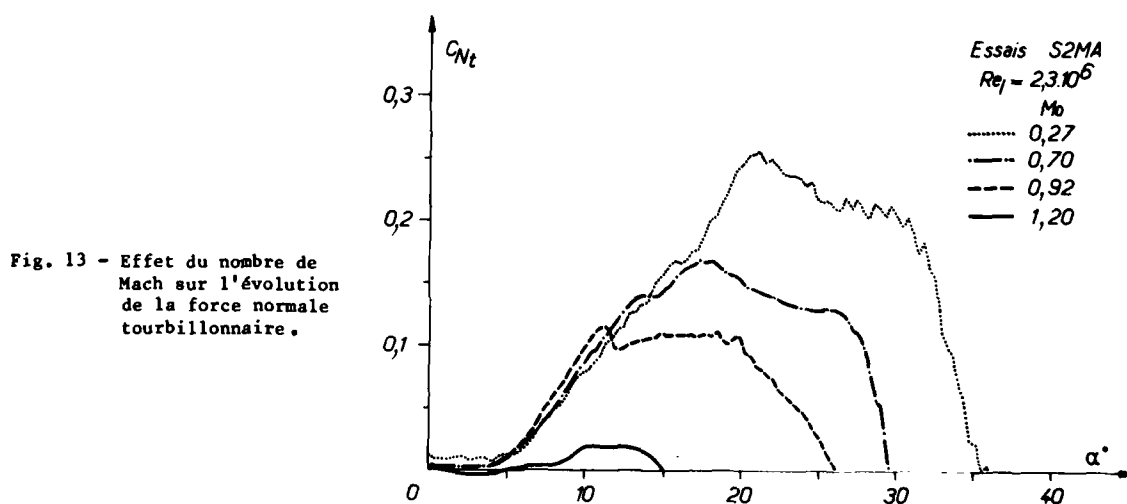


Fig. 13 - Effet du nombre de Mach sur l'évolution de la force normale tourbillonnaire.

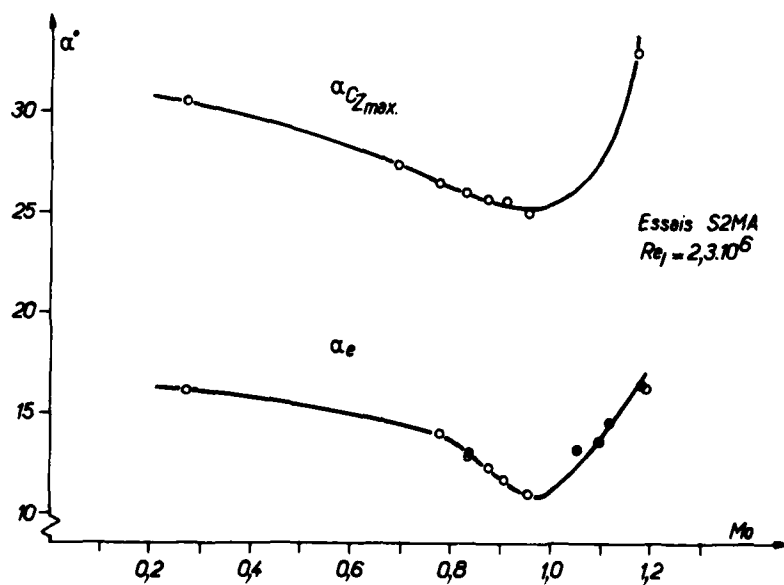


Fig. 14- Incidences α_e d'arrivée de l'éclatement et α_{C2max} de décrochage.

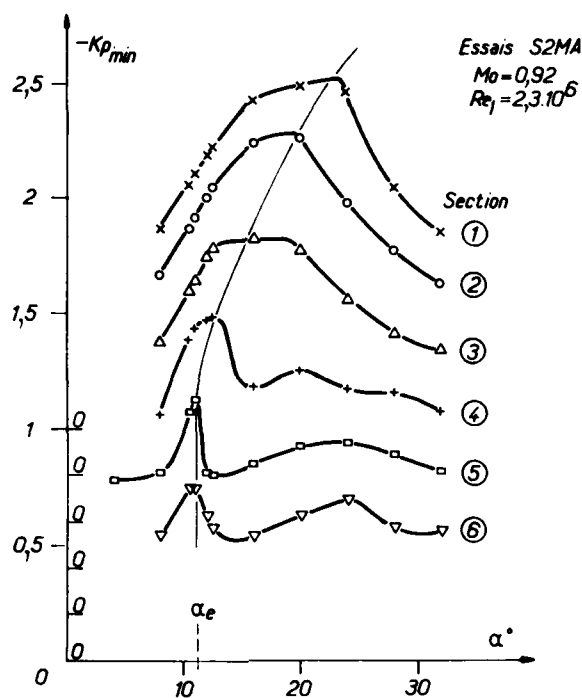
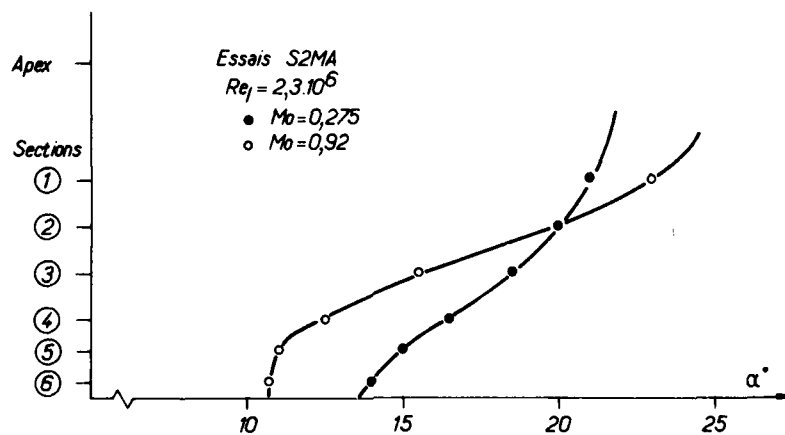
Fig. 15 - Evolution du Kp_{min} avec l'incidence.

Fig. 16 - Evolution avec l'incidence de la position de l'éclatement du tourbillon - Effet du nombre de Mach.

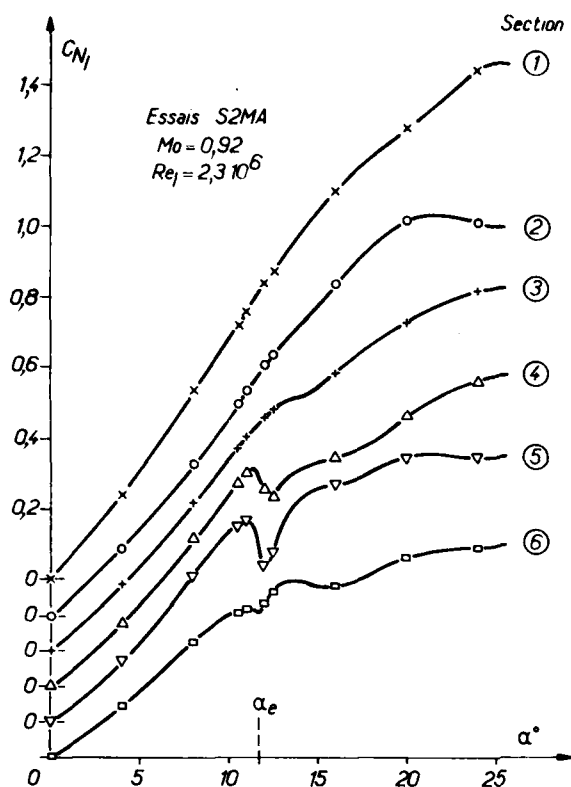


Fig. 17- Evolution de la force normale locale dans chaque section.

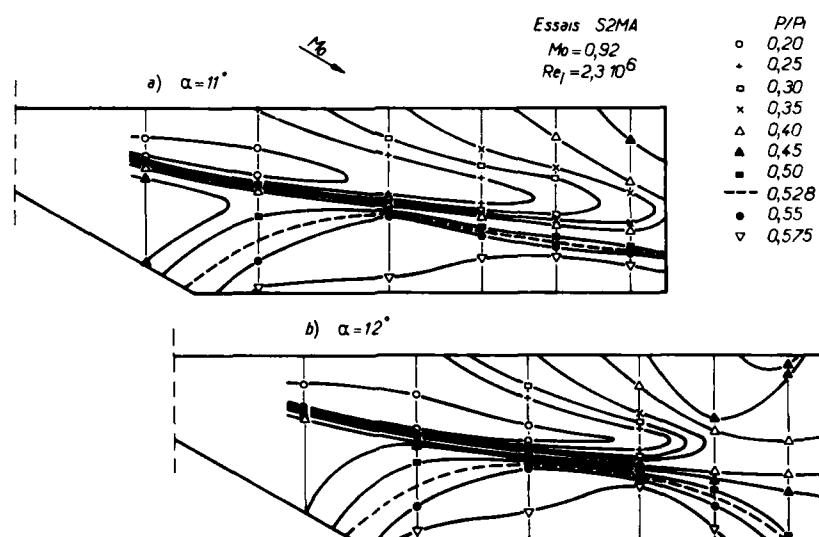


Fig. 18 - Lignes isobares avant et après l'arrivée de l'éclatement.

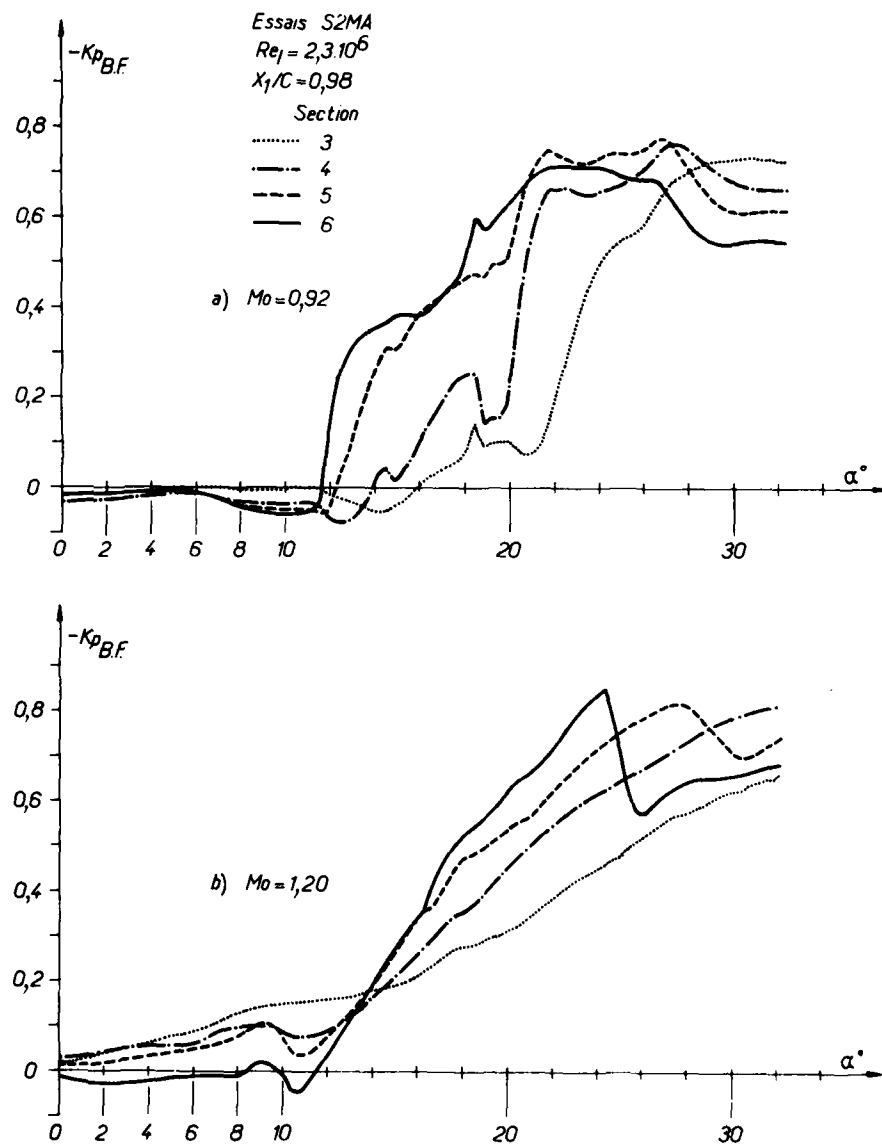


Fig. 19 - Evolution de la pression mesurée au bord de fuite avec l'incidence.

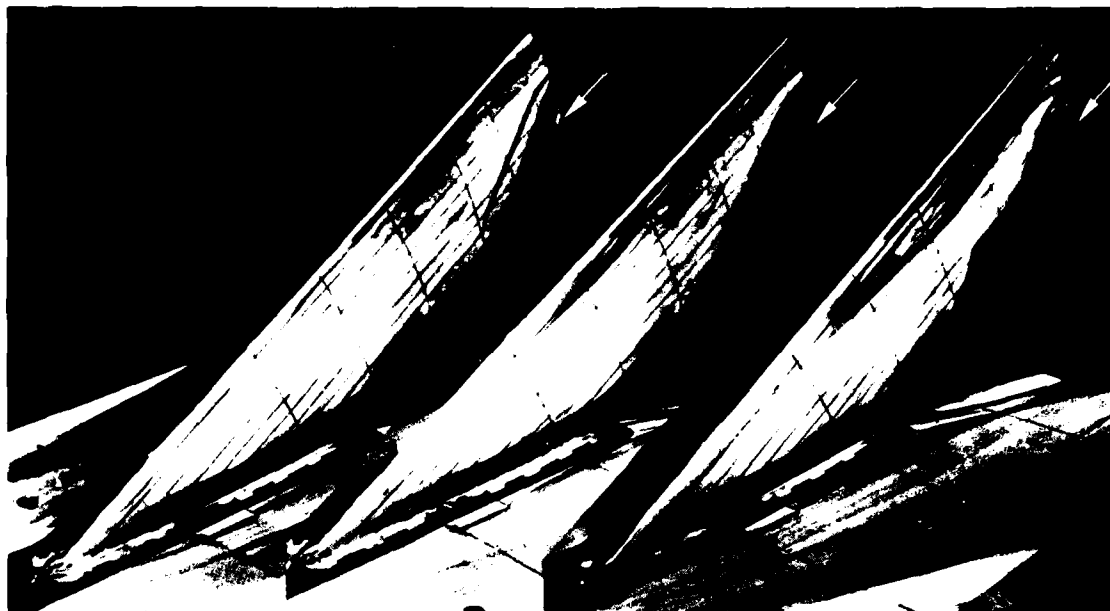


Fig. 20 - Visualisations par fluides colorés à $Mo = 1,20$.
 $\alpha = 12^\circ$ $\alpha = 14^\circ$ $\alpha = 16^\circ$

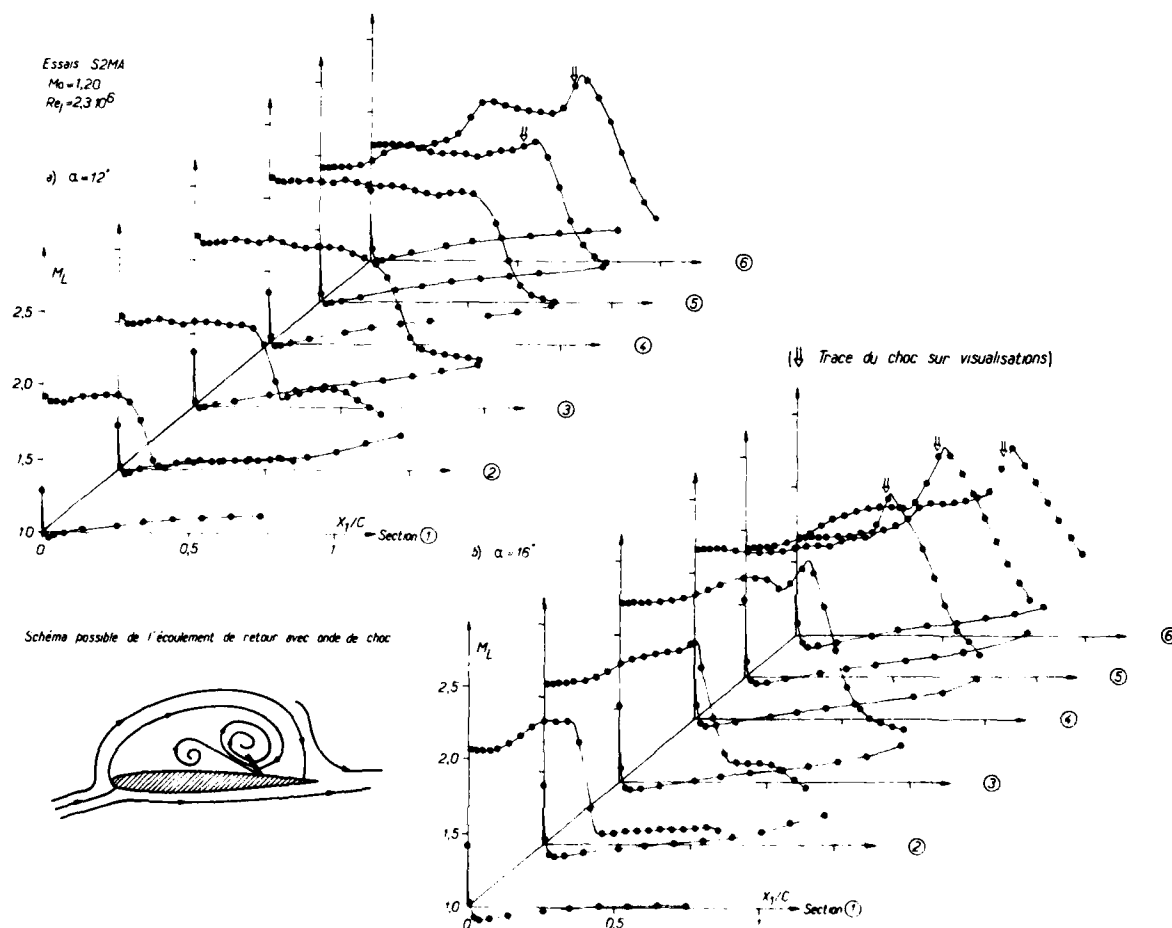


Fig. 21- Répartitions de nombre de Mach local à $Mo = 1,20$
 a - $\alpha = 12^\circ$ b - $\alpha = 16^\circ$

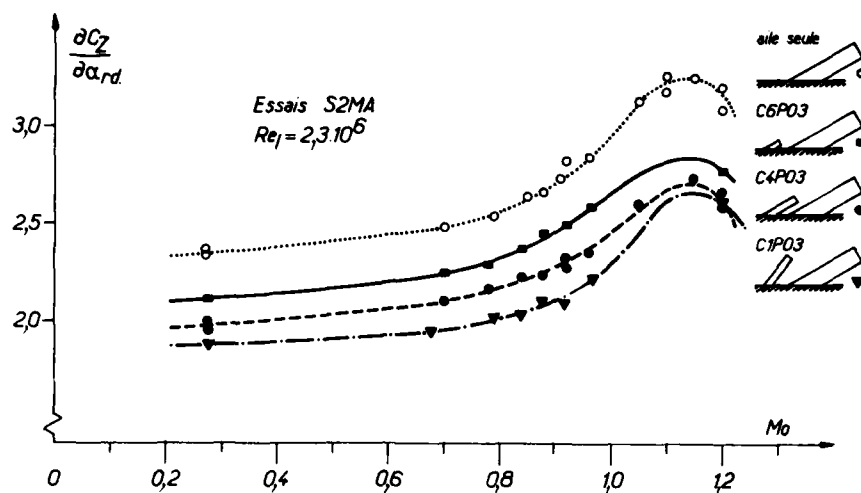


Fig. 22- Gradient de portance à l'origine - Effet des canards.

Fig. 23 - Comparaison des répartitions de charge en envergure à faible incidence.

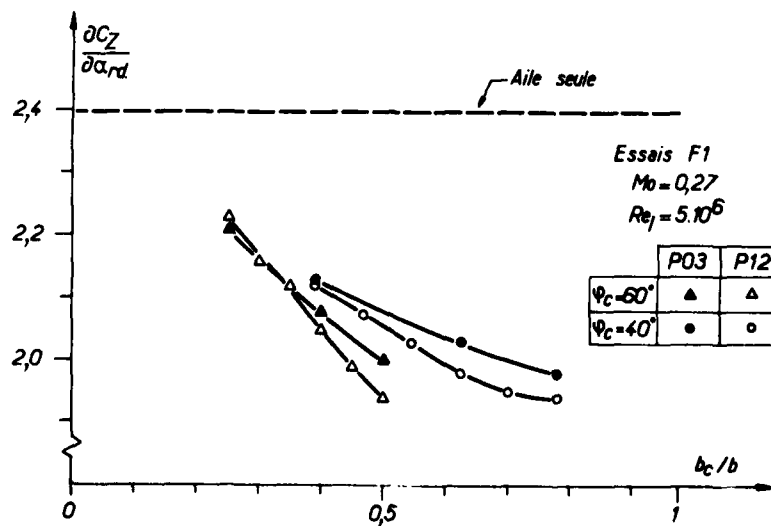
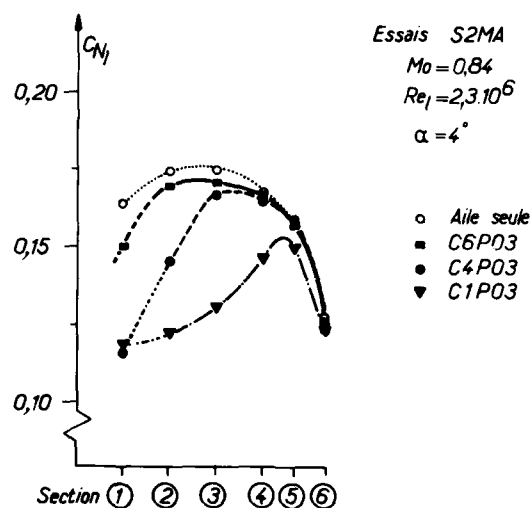


Fig. 24- Evolution du gradient de portance avec l'envergure des canards.

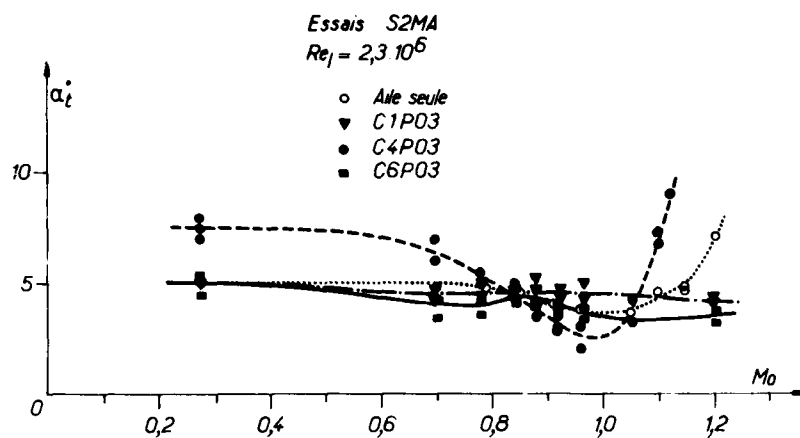


Fig. 25- Incidence d'apparition du tourbillon.

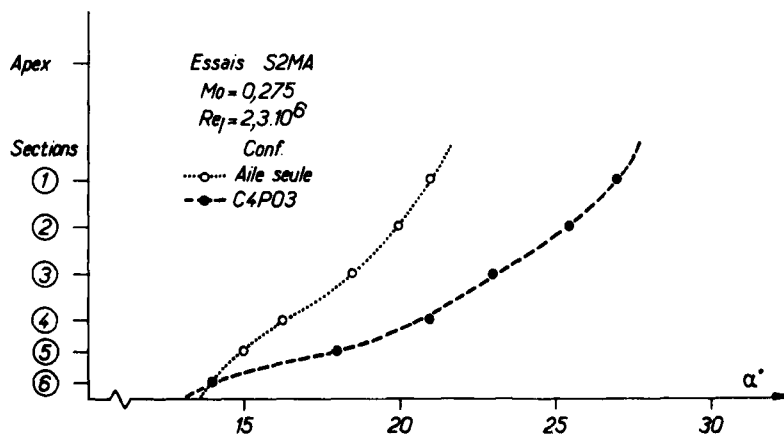
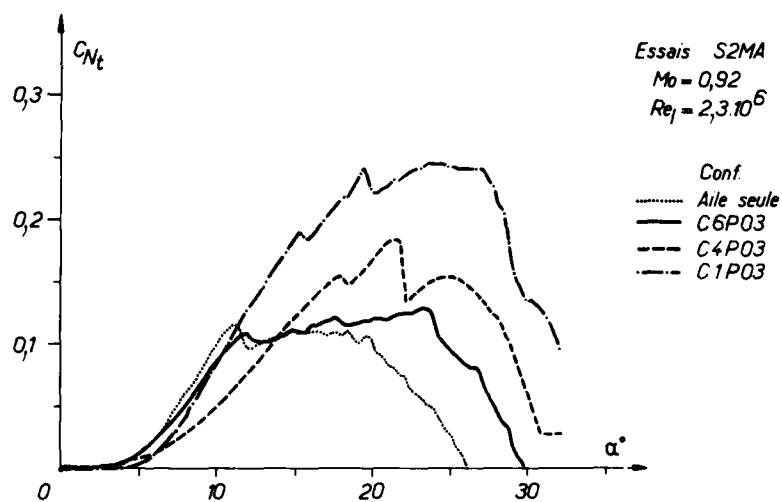
Fig. 26- Coefficient de force normale tourbillonnaire
Influence de la présence d'un canard.

Fig. 27- Evolution avec l'incidence de la position de l'éclatement relevée à partir des répartitions de pression.

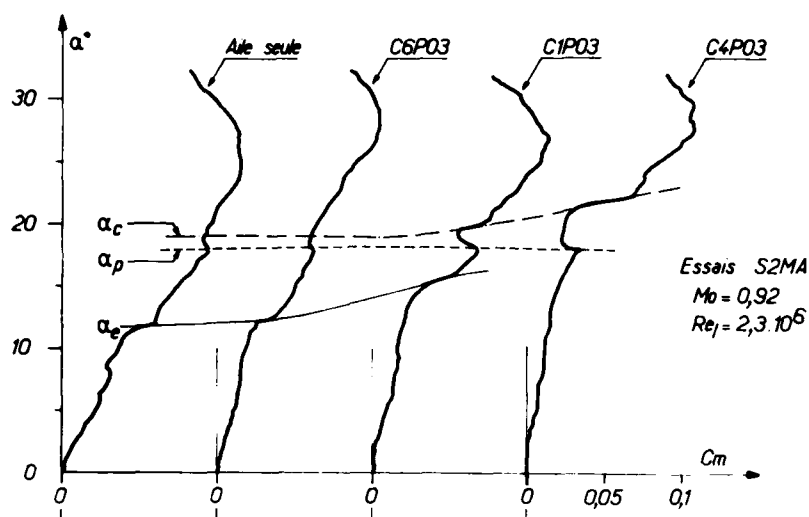


Fig. 28- Comparaison des courbes de moment de tangage.

Fig. 29- Effet des canards sur les répartitions de nombre de Mach local.

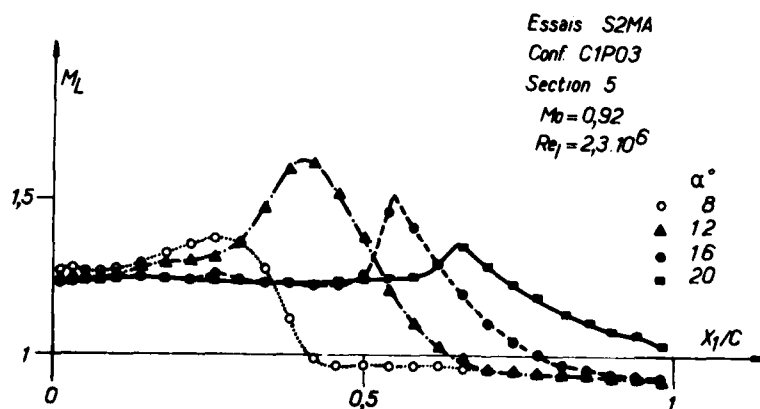
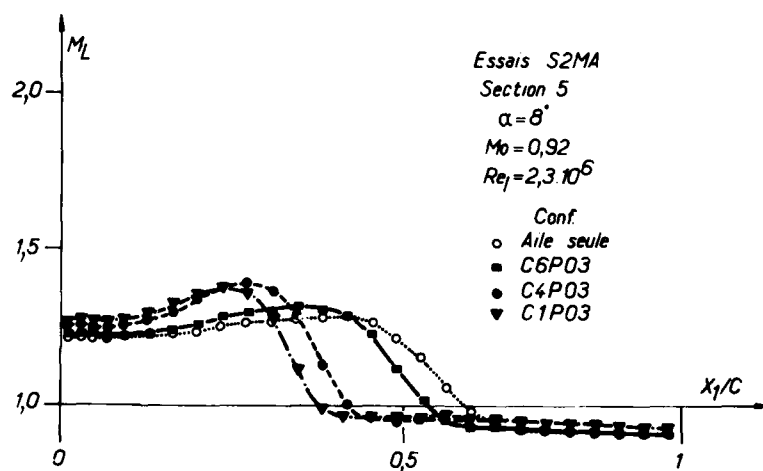
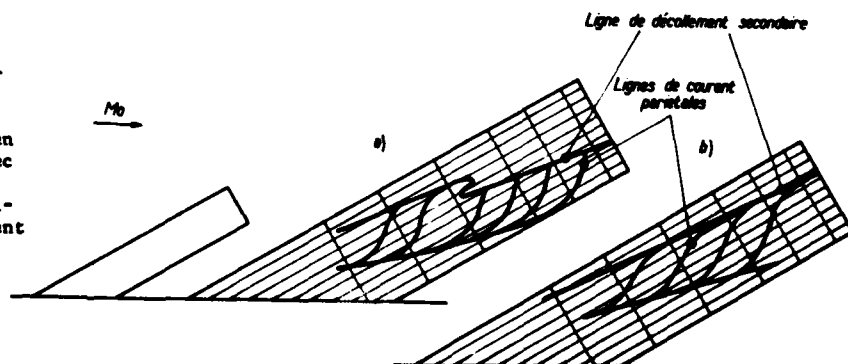


Fig. 30- Effet de l'arrivée de l'éclatement en présence d'un canard.

Fig. 31- Schémas d'écoulement pariétal visualisé par fluides colorés en configuration avec canard - a après et b avant l'arrivée de l'éclatement sur l'aile.



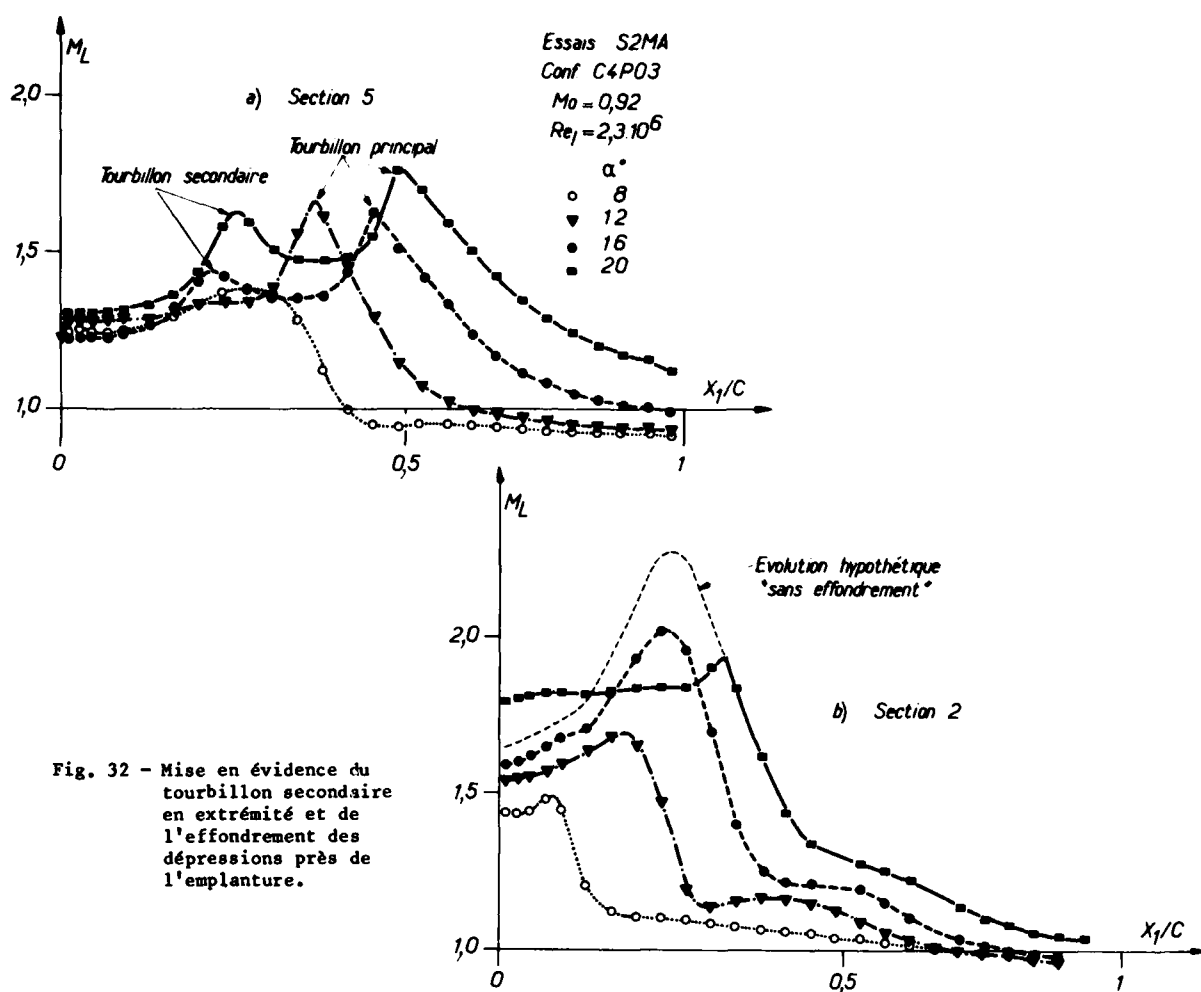


Fig. 32 - Mise en évidence du tourbillon secondaire en extrémité et de l'effondrement des dépressions près de l'emplanture.

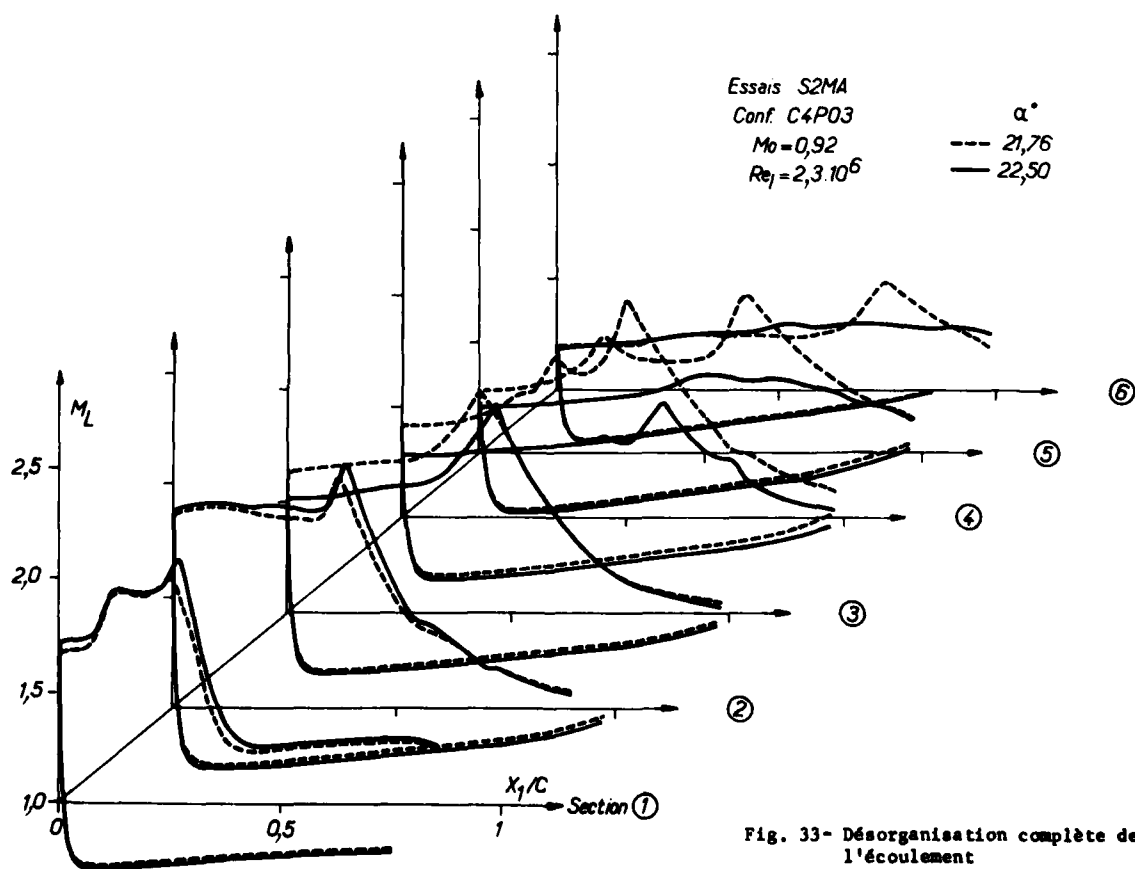


Fig. 33- Désorganisation complète de l'écoulement

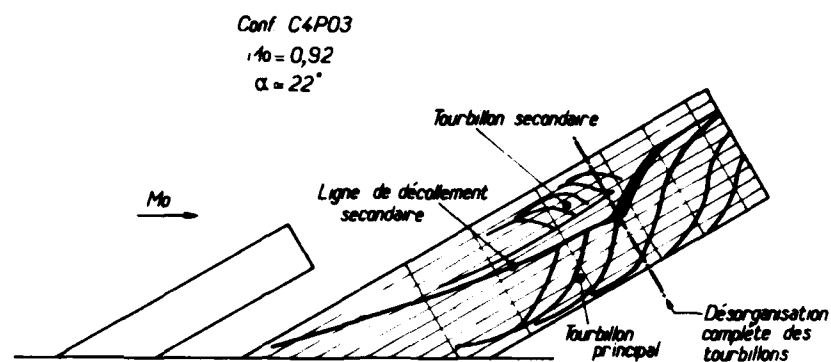
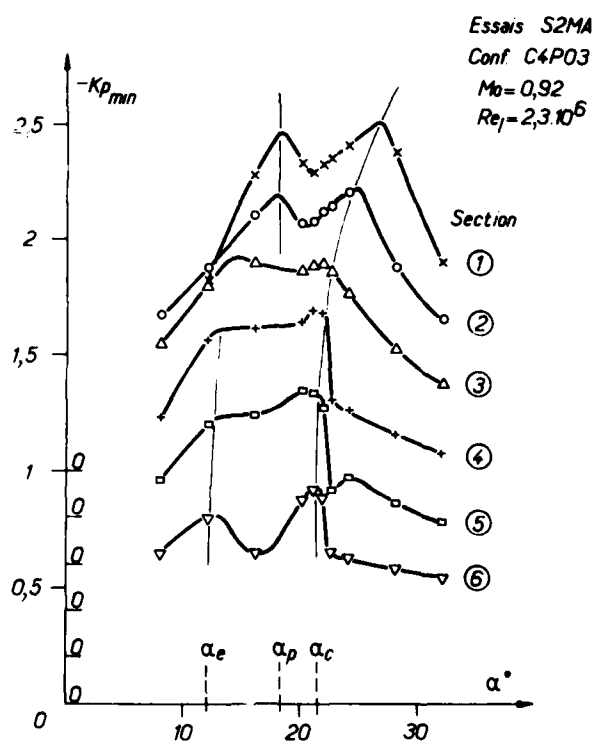


Fig. 34 - Schéma des lignes de courant pariétales.

Fig. 35 - Evolution des Kp_{min} avec l'incidence.

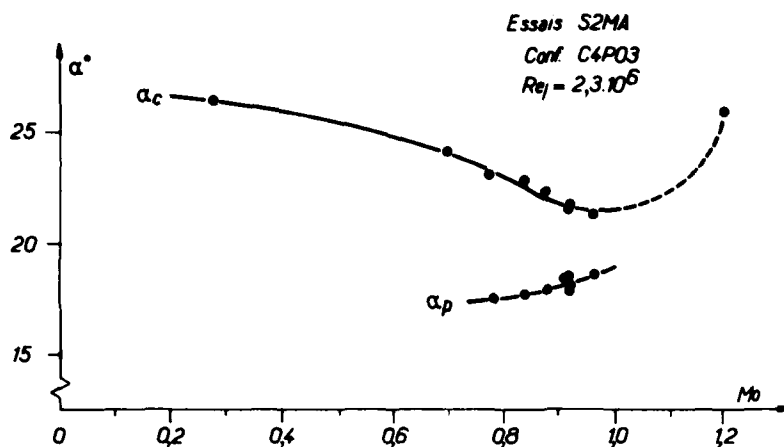


Fig. 36- Evolution des incidences de discontinuités de moment de tangage avec le nombre de Mach.

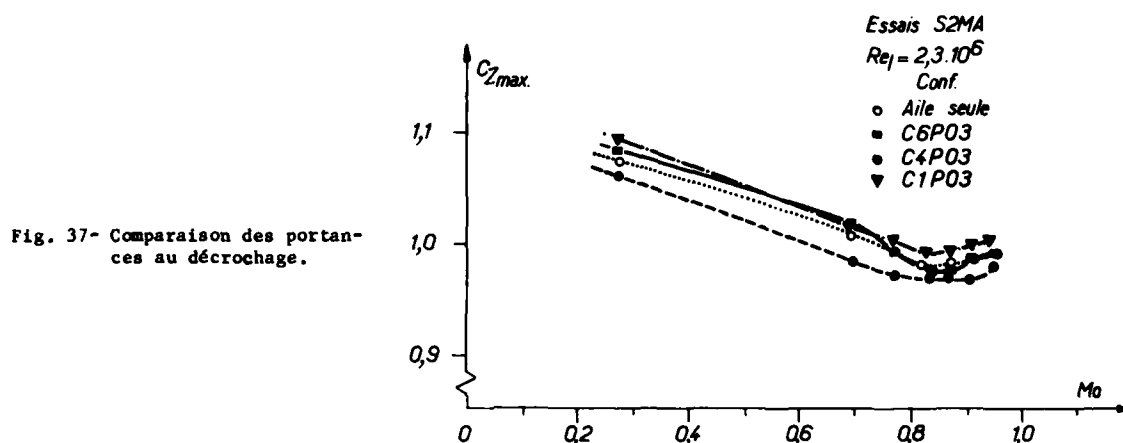


Fig. 37- Comparaison des portances au décrochage.

Caractéristiques géométriques du montage d'essai

- a) aile ($l=0,400m$)
b) plans canard
c) positions des plans canard
d) sections de prises de pression sur l'aile ($b_0=0,800m$)

a	$\Psi(^{\circ})$	λ	$b(m)$	$c(m)$	$S(m^2)$
AFV-D	60	2,69	0,430	0,20	0,1373

b	Conf.	Ψ_c	λ	b_c/b	c_c/c	S_c/S
	C1	40	6,94	0,778	0,40	0,235
	C4	60	3,20	0,500		0,210
	C6		1,98	0,250		0,085

c	Conf.	x_c/l	z_c/l
	P03	-0,60	0,08
	P12	-0,25	0,16

d	Section	1	2	3	4	5	6
	γ_1/b_0	0,30	0,45	0,60	0,75	0,85	0,95

Tableau 1 - CARACTERISTIQUES GEOMETRIQUES DU MONTAGE D'ESSAI.

a) aile principale ($l = 0,400 m$)

b) plans canards

c) positions des plans canards

d) sections de prises de pression sur l'aile ($b_0 = 0,800 m$)

SOME AERODYNAMIC INTERFERENCE EFFECTS THAT INFLUENCE THE TRANSONIC PERFORMANCE OF COMBAT AIRCRAFT

by

D Treadgold

K H Wilson

Royal Aircraft Establishment
Farnborough Hants UK

SUMMARY

The magnitude of the effects of viscous interactions, aeroelasticity and the aerodynamic interaction between the wing and fuselage are discussed in the context of a swept wing planform typical of some designs of combat aircraft. Illustrations drawn from experimental measurements and theoretical calculations show the significant influence of these factors on the form of the supercritical flow development at high subsonic speeds. An example is given of some experimental measurements indicating how small changes to the contour of the fuselage can produce significant changes in the drag measured at high subsonic speeds. The example shows that fuselage shaping can contribute to the development of a desirable form of supercritical flow on the wing with consequential benefit in drag levels at these speeds.

NOMENCLATURE

α	angle of incidence	C_p	pressure coefficient
η	$= \frac{y}{s}$ spanwise location	$C_{p_{TE}}$	pressure coefficient at the wing trailing edge
η_N	$= \frac{y - R}{s - R}$ spanwise location for 'net' wing	C_p^*	Value of the pressure coefficient for sonic velocity normal to lines $\frac{z}{c} = \text{constant}$
λ	taper ratio	M	Mach number
Λ	sweepback angle	M_S	Mach number ahead of shock-wave
Λ_{LE}	sweepback angle of leading edge	R	radius of body cross section
Λ_{TE}	sweepback angle of trailing edge	R_e	Reynolds number
A	aspect ratio	c	wing chord
C_d	local sectional drag coefficient	\bar{c}	mean chord
C_D	drag coefficient	s	semi span of wing
C_{D_0}	(drag coefficient - nominal induced drag), $C_{D_0} = C_D - C_L^2 / \pi A$	t	wing thickness
C_L	lift coefficient	x	distance downstream from the wing leading edge
C_m	pitching moment coefficient	x_T	x at transition
		y	spanwise distance

1 INTRODUCTION

The variety of different roles, the wide range of operating conditions and other requirements, make the aerodynamic characteristics of a modern combat or strike aircraft host to many, and difficult, interference or interaction problems. Notionally, some of these can have a profound influence on the performance of the aircraft, especially in the highly sensitive transonic speed range. Manoeuvre performance, for example, may be influenced by any impact they may have on the buffet-free lift boundaries, or the stability and control characteristics; whilst the sustained turn and cruise performance may be influenced by any impact they may have on the drag.

In this paper we will merely examine, for the transonic range, three such interference or interaction effects in relation to the aerodynamic behaviour of swept wings of planform appropriate to combat aircraft. These are:

- The influence of viscous effects, representing an interaction between the development of the boundary-layer and the form of the inviscid external flow development.
- The interaction between the aerodynamic characteristics and the elastic deformation of the wing under steady aerodynamic loading.
- The interaction between the flow over the wing and the shape of the fuselage.

Wind tunnel experiments, especially those providing pressure distributions, are helpful in identifying the nature and magnitude of some interference effects, but the theoretical methods now under development will, when proven, offer the potential for a more fundamental understanding of the effects and will lead, hopefully, to ways of favourably manipulating the interactions. Various methods for

computing three-dimensional transonic flows now exist, or are in various stages of development, in many countries of the West. These methods cover a wide spectrum of attempted accuracy in mathematical modelling the flows. They vary in the exactness of the flow equation used, the numerical techniques adopted and the degree of generality of the boundary shapes to which they can readily be applied. For the interaction problems considered here, it is the latter aspect which is of particular concern.

The theoretical results presented in this paper are derived from calculations made using the RAE Mk IV Transonic Small Perturbation (TSP) computer program. The program is based substantially on the method described by Albane et al in reference 1, but with additional procedures that offer the option of treating more general fuselage shapes, albeit in an approximate fashion. The approximation involves relating boundary conditions on the actual body to adjacent grid points on a chosen prismatic surface generated by selected grid lines of the computing network parallel to the fuselage axis.

Options are provided in the program that permit the calculation of viscous interactions and aero-elastic interactions. This is done economically by periodically interrupting the flow field calculation loop to inject updated boundary conditions suggested by boundary-layer calculations, and/or structural deformations, based on the current pressure and loading information from the flow field calculation. Boundary-layers are represented by their displacement effect. This is calculated in the laminar region using a yawed wing assumption, and downstream of a chosen transition location, a three-dimensional integral method based on the work of Smith² and Green et al³ for the turbulent region. Aero-elastic deformations are calculated using a matrix of structural influence coefficients specified in the input data to the program.

Other more accurate computer programs are under development in the UK, but at present these are not assembled into a computer package that offers the generality of application provided by the Mk IV TSP program.

2 VISCOUS EFFECTS

Only brief mention is made here of the significant effect that the development of the boundary-layer can have on the transonic aerodynamic characteristics, since it will be covered more fully in a forthcoming AGARD symposium. The objective here is merely to permit an appreciation of the magnitude and nature of the effect in the context of the type of swept wing combat configurations which are our present concern.

Figure 1 gives an illustration, for the case of an isolated wing, of the predicted changes in the pressure distribution that are brought about by the displacement effect of the boundary-layer. In this instance the Reynolds number used in the calculations is fairly typical of wind tunnel model testing. Dramatic reductions in lift at a fixed angle of incidence are apparent. In this case a 23% reduction in the lift is incurred at an incidence of 6°. This is associated with reductions in the suction peaks and forward movements of the shock-waves. It is seen that the effects increase in magnitude progressively towards the wing tip. Much of the change is a direct result of reduction in the effective incidence at positive lift conditions, that simply arises from the relatively larger displacement thickness of the boundary-layer on the upper surface of the wing, compared with that on the lower surface, near the trailing edge. A closer resemblance between the distributions is seen by comparing the calculations for the viscous flow with those for the inviscid flow at 5°, when the lift coefficients are more closely matched. Even so, whilst the peak suctions are more closely matched, some significant differences remain in positions and strengths of the shock-waves. In the two dimensional case it is often possible to obtain a tolerably good comparison in this way. In the three-dimensional case, however, it is largely the spanwise variation that occurs in the change of effective incidence which complicates the issue. The situation may be expected to be further complicated for configurations having interfering components, perturbing further this spanwise variation. The mechanism of this may be either through their influence on the pressure distribution on the wing, or directly through entrainment, of the boundary-layer flow the adjacent components, or the converse.

In its present form, the computer program takes account only of the influence of the boundary-layer developing on the wing surface and no account is taken of the entrainment of the boundary-layer from the fuselage, for example. It is conjectured that this omission may be of significance to the shortfall observed later, in the adequate prediction of the effects of changes in body contours in the wing root junction.

3 AEROELASTIC EFFECTS

The wide range of conditions, both of speed and altitude, embraced by the operating envelope demanded of a present-day combat aircraft implies, in general, that significant elastic structural deformation must be entertained. It is, therefore, increasingly necessary to give due consideration to the possible impact of this on the aerodynamic behaviour of the wing and tail unit. This is especially necessary for wings of high sweepback angle operating at transonic speeds.

The point is illustrated by the example given in Figures 2(a) and 2(b). Here wind tunnel measurements of the lift and pitching characteristics are shown for a variable sweep aircraft design with wing sweepback angles of 27° and 42°, at which the corresponding wing aspect ratios are 7 and 5.5 respectively. The measurements were made with wings of a composite construction that simulate, under the wind tunnel loading, elastic deformations appropriate to an aircraft manoeuvring at standard sea-level conditions at corresponding Mach numbers. The simulation is not, of course, precise, since in this static simulation, the inertia terms arising from the mass of the wing structure are not represented. Thus the deflections would be somewhat less than those simulated, if the scaled elastic properties were precisely matched and so some allowance has to be made for this. Included in the figure for comparison, are measurements made with rigid models, one representing the geometry in a 5 g manoeuvre and the other representing its geometry in an unloaded equivalent form. The reduction in the slope of the lift curve

and destabilising effect due to the elastic deformation, are clearly evident. This is particularly so for the wing at the higher angle of sweep, when it is seen that $dC_L/d\alpha$ is reduced by as much as 20% and the aerodynamic centre is moved forward by about 10% of the mean chord. These aerodynamic changes are largely due to the change of the local effective incidence across the span, which is brought about by the bending of the wing and which is offset only partially by the torsional deformation. There are, as a consequence, significant changes in the spanwise loading as a result of the increased 'wash out' produced by the deformation of the wing. Attendant changes in the downwash at the tail can be expected as a result of this, with a further consequential effect on the longitudinal stability characteristics.

Because of the relatively high aspect ratio of the wing, it might be considered as a rather extreme example, so a further illustration is given, again for a wing with a leading edge sweep of 42° , but this time with an aspect ratio of 3.3 and a wing thickness more appropriate to a fixed wing combat aircraft with supersonic operational requirements. Calculated spanwise loading distributions are shown in Figure 3 for a Mach number of 0.8. Again for comparison, calculations are shown for a rigid and an elastic wing. In this instance the rigid wing shape used for reference is that of the unloaded elastic wing which has a designated shape giving a lift coefficient of 0.8 at a sea level Mach number of 0.8. Figure 4 shows the magnitude of the changes in effective incidence produced by the elastic deformation. For the sea level condition quoted, this amounts to a change of more than 7° at the wing tip. Significant changes to the supercritical flow development can therefore be expected.

These changes are illustrated by the comparison of the calculated chordwise pressure distribution, shown in Figure 5, for the rigid and elastic wings at approximately the same overall lift coefficient. At the condition shown, for a Mach number of 0.8, the difference in the supercritical regions is evident. The supercritical region at the tip of the rigid wing is far more extensive and its terminal shock-wave is much stronger, whilst inboard, the pressure coefficients fall well below C_p^* . For the aeroelastic wing, the spanwise development of the supercritical region is more uniform and thus we can expect rather different high speed stalling characteristics from those of its rigid equivalent.

The implication of the difference in stalling behaviour and different drag characteristics, caused by aeroelastic effects, should be carefully examined in the optimisation of combat aircraft configurations, both from the aerodynamic and structural viewpoints. A suitable computer program can assist in the process, since the supercritical flow development at various points in the flight envelope may be readily studied with different options for the elastic properties of the wing.

4 WING-FUSELAGE INTERACTION

Using an earlier, but basically similar, version of the RAE Mk IV TSP program without the inclusion of viscous effects, Albone¹ was able to demonstrate good agreement between the predicted and measured pressure distributions for a simple wing and fuselage combination. One of the illustrations from Reference 1, showing this, is reproduced in Figure 6. This Figure also shows for comparison, the pressures calculated for a 'net' wing, in isolation, formed by joining the exposed wing panels together. This comparison gives a notional indication of the nature of the interference effects and the extent of the wing affected. Significant changes in the form of the supercritical region are apparent, which are, of course, far more marked over the inboard part of the wing. It would appear that the good agreement with predictions, without allowance for the boundary-layer, was possible because its effects are not large; the pressure gradients are favourable ahead of the shock-waves and the adverse pressure gradients over the rear of the section are mild, for the simple RAE 101 section involved.

The more extensive supercritical regions and far more severe adverse pressure gradients, commonplace with the advanced sections now in use, pose a greater challenge. Results, more typical of this situation, are given in the comparison of predicted and measured pressure distributions shown in Figure 7. The theoretical predictions appear to give a fair representation of the form of the development of the supercritical region, in both the chordwise and spanwise direction. The degree of agreement is not as good as one is accustomed to with similar comparisons in two-dimensional flow⁴. Nevertheless, the theory is able to give some valuable guidance in the design of wings, by indicating how the supercritical regions may be engineered to give good lifting potential and the desired form of high speed stall development. On the other hand, the methods may not be sufficient to give adequate guidance for the optimisation of three-dimensional configurations, from drag considerations at high subsonic speed conditions. This appears to demand a far higher degree of precision in defining the positions and strengths of the shock waves, than displayed here.

Just how dominating the influence of the fuselage can be in affecting the supercritical flow development on the wing, can be judged from experimental measurements of the chordwise pressure distributions shown in Figure 8. This is an example where the same wing has been mounted in fuselages of different shape, but with roughly the same width at the wing position. A sketch of the two configurations is given in Figure 9. One fuselage has a roughly square cross section, whilst the other, which is shorter, has an elliptic cross section with fairings in the wing root intended to suppress some of the undesirable flow features in the wing-body junction. In both cases the wing is mounted above the fuselage axis.

The experimental measurements shown in Figure 8, are for a Mach number of 0.87. For the square section body, the results are given for an angle of incidence of 4.1° which gave a lift coefficient of 0.45. For the elliptic body, experimental data was not available at precisely matching conditions of incidence angle or lift coefficient, but these can be inferred from the two test conditions shown.

For the same incidence one can infer that the change in fuselage has produced significant changes in the pressure distribution and shock-wave system that extend out to 75% of the semi-span at least. The suction peaks are far higher for the elliptic fuselage, particularly at the inboard stations, and the forward shock is well in evidence at the 24% station. The rear shock-wave is also affected and is

generally further aft for the elliptic body. Some of the behaviour can probably be attributed to the higher super-velocities generated by the higher streamwise curvature of the elliptic body.

If the comparison is made at the same lift coefficient, then the shock-wave is located at more nearly the same chordwise position at 83% semispan, although again the suction peak is still greater for the elliptic body. Inboard we again find the forward shock-wave more in evidence, higher super-critical velocities and a rear shock-wave that is further aft with the elliptic body. For the square section body the rear shock-wave is far weaker and the forward shock-wave is not apparent at 24% semispan, although at that station the experimental measurements show a secondary expansion starting at about 30% chord which may be terminated by a weak shock-wave. This latter feature, if genuine, is difficult to explain, unless it is the result of a local disturbance produced by a vortex from the wing-body junction.

Changes in the supercritical flow development of this magnitude can clearly be expected to influence the buffet-free lifting characteristics and obviously the fuselage effects cannot be ignored in the wing design process. The example just given is one involving a gross change in fuselage shape, but we will in our next example consider the sensitivity of the wing characteristics to more modest geometric changes confined to the area of the wing-body junction.

Body shaping has long been recognised as a means of reducing drag at supersonic speeds, as was demonstrated in the early fifties by the pioneering work of Whitcomb and Kuchemann⁶, for example. There have been numerous experimental demonstrations of the effectiveness of the method applied in various ways. Notable among these is the experimental work of McDevitt⁷. The theoretical flow field methods now available enable us to obtain a better understanding of the mechanism of this highly effective means of drag reduction in the high subsonic and transonic speed range. Hopefully this will lead to the development of effective techniques, applicable under lifting conditions, that can be applied to the type of combat aircraft configurations considered here.

Caughey and Jamerson⁸ have applied their full-potential method to the configurations tested by McDevitt⁷ that had axisymmetric waisting applied to basic Sears-Haase body in combination with a wing aspect ratio of 4 and a symmetrical NACA 64 A015 section. The comparisons of the pressure distributions with those calculated for zero lift conditions look encouraging, although the locations and strengths of the shock-waves are not all that well predicted. What is more encouraging, if not a little surprising, is that the drag reduction derived from the body waisting appears to be fairly well predicted by the calculations. This was found in spite of the need to make simplifications in the modelling of the fuselage in the calculations, involving the assumption of cylindrical extensions of the body to infinity upstream and downstream of the wing. In this example, the drag reduction was very large and of the order of 70 drag counts at a Mach number of 0.8 and 100 counts at a Mach number of 1.0. (One drag count = $\Delta C_D = 0.0001$).

Results published by Newman and Klunker⁹ also give a useful insight into the distribution of the drag reductions at transonic speeds from transverse area changes of wing-body combination. Using small disturbance theory with a conformal mapping technique, they calculated the transonic flow over a wing mounted on an axisymmetric body with and without the waisting suggested by simple transverse area distribution considerations. They were able to give an interesting demonstration of how the overall drag reduction from the waisting was derived. The drag increment from the body was positive, but this was more than cancelled by the reduction in drag of the wing. This drag reduction was a result of reduced shock wave strengths over most of the wing span at a Mach number of 0.8.

The fact that minor geometric changes can result in sizeable drag changes is also apparent in measurements made, a few years ago in the ARA 6 ft x 8 ft tunnel, on a combat wing research model to which alternative body fairings were fitted. The basic fuselage of this model was the elliptic section already described and which is shown in Figure 4. The wing concerned in this experiment had a similar planform but different section from that of the experimental study previously mentioned. The alternative fairings on the body above the wing are shown in Figure 11. The experiment predated the present computer programs for calculating transonic flows over wing-body combinations. It represented an investigation of two intuitive designs of the fairing providing roughly similar cross sectional area distributions. Neither fairing has any serious pretension to being an optimum shape from drag point of view.

The first fairing which we will refer to as fairing A, was designed to conform for the most part, to a stream surface of the gross wing flow - of the wing formed by extending the leading and trailing edges of the wing to the fuselage centre-line. This seemed a logical option since the wing had been originally designed for a condition at a Mach number of 0.87, assuming that planform and using the version of small perturbation flow field method for the isolated wing which was all that was available at that time. This same method was used to determine a suitable stream surface for a fairing that could be blended with the existing fuselage sections maintaining a smooth cross sectional area distribution.

The second option, leading to fairing B, was more vaguely defined, but it attempted to preserve a contour at its intersection with the wing, that resembled the form of the streamlines of the wing at 50% semi-span at the design condition for 0.87 Mach number. Notionally this was intended to derive some benefit from constraining the flow to behave more nearly like a sheared wing flow and to maintain the sweep of the isobars at the wing root. The remaining lines of the fairing were simply a result of maintaining a smooth area distribution, matching that of fairing A as closely as possible, and blending into the existing fuselage shape.

It is evident from the sketch given in Figure 12 that fairing B has a slightly greater cross sectional area just ahead of the wing than fairing A. This was a concession, necessary because of a practical constraint imposed by the construction of the model, which otherwise would have involved an unacceptable departure from the intended streamline shape in the junction. Estimates suggest that even at sonic speeds, the drag penalty that would be incurred by the combination with fairing B, due to this additional area, would only be of the order of 3 drag counts.

The wind tunnel tests made covered only the rather limited range from a Mach number of 0.825 to 0.925. Over this range there was very little difference in the buffet-free lift boundary produced by different fairings. This was probably to be expected, since the breakdown of the attached flow was determined on this wing by flow conditions well outboard. The difference in the drag characteristics produced by the two fairings is of more interest. The measured drag coefficients, with a nominal induced drag component, $C_{L^2}/\pi A$ subtracted are shown plotted against the lift coefficient in Figure 11 for Mach numbers of 0.87 and 0.925.

Figure 11 clearly shows the beneficial effect of fairing A. At 0.87 Mach number the drag is about 14 counts less at a lift coefficient of 0.35. At 0.925 Mach number the benefit is greater. At both Mach numbers the benefits diminish at high and very low lift coefficients. This behaviour appears consistent with the difference in the strength of the rear shock-wave, as can be inferred from estimated Mach numbers ahead of this shock-wave, shown in the figure.

At a Mach number of 0.87, there is little difference in the behaviour of the trailing edge pressure for the two fairings, excepting for a slightly earlier rise apparent at 72% span with fairing A. There is certainly no indication in the trailing edge pressures of adverse effects of either fairing at moderate lift coefficients. The rear shock-wave is far weaker for fairing A for the most part, and certainly over the inboard part of the wing. Figure 12 shows even more clearly the better supercritical flow development obtained with fairing A at 24% semi-span for lift coefficients between 0.2 and 0.4, where the drag benefits are greatest. The loss in lift incurred with fairing A, arising from the lower suction ahead of the shock-wave and its further forward location, is well compensated for by the effect of the increased suction maintained around 20% chord. The isobars shown in Figure 13 show how this gradual recompression seen at 24% semi-span with fairing A is maintained to some extent further outboard. With fairing B the shock-wave is well defined and is swept roughly parallel to the trailing edge out to 70% semi-span.

Returning to Figure 11(b), we see at a Mach number of 0.925 a similar correspondence between the different shock-wave strengths and the differing drag characteristics of the two fairings. In this case, however, the situation is complicated by the impact the fairing change has had on the trailing edge pressure rise. This is not, of course, unrelated to the differences in the shock-wave strengths, but it is apparent that, with fairing A, the initial rise in the suction occurs at a higher lift coefficient for all the spanwise stations, thus adding to the benefits of this fairing.

Superficially we see that fairing A appears to produce a more attractive flow over the wing; it is, however, of interest to investigate to what extent the changes on the wing contribute to the drag differences measured on the wing-fuselage combinations. An attempt has therefore been made to take the analysis a little further by integrating the surface pressures measured to obtain the drag component. Attempting to find absolute values for the pressure drag in this way is not normally a very rewarding process. It is renowned for its potential inaccuracy, particularly if there is limited coverage of the pressure measurements in critical regions of the aerofoil near stagnation points and near suction peaks, for example. In the present case, the process is slightly more legitimate, since we need concern ourselves only with integrating the differences in pressure at the same model attitude with the different fairings fitted. Fortunately, the changes to the suction peaks are not apparently very great. The more serious errors probably arise from the difficulty in precisely locating the shock-waves, but it is thought that, in this case, it will cause the drag difference to be underestimated. Inaccurate as the process undoubtedly is, the results show a remarkable degree of self-consistency and, moreover, show a remarkably close correlation in the trends, with Mach number and angle of incidence, apparent in the balance measurements of the overall drag of the wing-fuselage combination. This can be seen from the comparisons given in Figure 14 for the model at angles of incidence of 3.1° and 5.2° .

The analysis thus lends support to the view that it is the changes produced on the wing that are dominant in causing the drag changes, rather than pressure changes on the fairings themselves. It is also worth noting the considerable extent of the wing affected by the change, as is shown in Figures 14(a) and (b). There is an interesting parallel with the theoretical findings of Newman and Klunker⁹ mentioned earlier.

Figure 15 shows the calculated chordwise pressure distributions for various spanwise stations compared with the pressures measured at a Mach number of 0.87 for an angle of incidence of 5.2° . The general level of agreement achieved is similar to that seen earlier in Figure 7 for the simpler fuselage shape. It can be seen, by comparing Figures 15(c) and 15(d), that the more major changes indicated in the experimental measurements that contributed to the beneficial drag behaviour with fairing A, are not greatly in evidence. There is a slight hint in the theory of the changes in the pressures over the forward part of the chord near the wing root for the different fairings, but there is no evidence of the gradual recompression and weaker shock-wave for fairing A which produced most benefit to the drag. It seems difficult to fault the experimental data, especially in view of the apparent mutual consistency of the pressure and balance measurements which we have been able to demonstrate. We have yet to diagnose the real cause of the apparent failure of the predictions to give a correct indication of the changes produced by the fairings. It might be argued that to resolve such subtle geometric changes asks too much of the theories at their present state of development.

Some of the blame for the present discrepancy may be attached to the limited accuracy in modelling the body with the procedures used in the Mk IV TSP program, since these precluded any streamwise variation of the grid locations at which equivalent body boundary conditions had to be applied. The limitations of the small perturbation method cannot be ignored. A further uncertainty remains concerning the magnitude of the viscous interaction in the region of the junction. In the computer program used, only the boundary-layer development on the wing has been included, and it may prove to be necessary to model more correctly the displacement surface to include the boundary-layer on the fuselage and its interaction with that on the wing.

If we compare the two oil flow photographs given in Figure 15, which show the flow for the two fairings at similar conditions at a Mach number of 0.87, it is clear that major differences are apparent in surface streamlines. The outward flow from the fairing on to the wing is very evident in the junction

in the case of fairing B. Perhaps it is the failure to model such features arising from the viscous interaction that contributes to the shortfall of the present prediction. Paradoxically, however, the greater variation between the measurements and the predictions occurs with fairing A which has the more orderly flow in the wing-fuselage junction and which is perhaps slightly better modelled in the theory.

5 CONCLUDING REMARKS

Viscous interactions, aeroelastic effects and the aerodynamic interaction between the wing and fuselage all have an impact on the development of the supercritical flow regions on the sort of swept wing configurations typical of some combat aircraft designs. Computer programs used to optimise the aerodynamic performance of such wings need therefore to model these features correctly.

The task of provision of adequate guidance from theoretical transonic methods for achieving drag reductions is challenging - a challenge that must be met if drag penalties at high subsonic speeds are to be eliminated at an early design stage by such methods.

The example given suggests that it is possible to obtain by a suitable shaping of the fuselage an improved form of supercritical flow development with consequent benefits in drag reduction at high subsonic speeds.

Some refinement of transonic calculation methods is necessary if the design is to be done effectively. Such refinements may, in general, need to include a better mathematical modelling of the viscous interaction in the region of the junction of the wing and fuselage.

REFERENCES

- 1 C M Albone Numerical solutions for transonic flows past wing-body combinations.
M G Hall Symposium Transsonicum 11, Springer-Verlag, New York pp541-548 (1976)
G Joyce
- 2 P D Smith An integral prediction method for three dimensional compressible turbulent boundary-layers.
ARC R&M 3739 (1974)
- 3 J E Green Prediction of turbulent boundary-layers and wakes in compressible flows by
D G Weeks a lag-entrainment method.
J W F Brooman ARC R&M 3791 (1973)
- 4 M R Collyer Improvements to the viscous Garabedian and Korn (VGK) method for calculating
R C Lock transonic flows past an aerofoil.
RAE TR 78039 (1978)
- 5 R T Whitcomb A study of zero-lift drag-rise characteristics of wing-body combinations near the speed of sound.
NACA RM L52H08 (1952)
- 6 D Kuchemann Design of wing junction, fuselage and nacelles to obtain the full benefit of sweptback wings at high Mach number.
RAE Report No Aero 2219 (1947)
- 7 J B McDevitt An experimental investigation of two methods for reducing transonic drag of swept-wing body combinations.
NACA RM A55B21 (1955)
- 8 D A Caughey Numerical calculation of transonic potential flow about wing-body combinations.
AIAA Journal Vol 17 No 2 (1979)
A Jameson
- 9 P A Newman Numerical modelling of tunnel-wall and body-shape effects on transonic flow over finite lifting wings.
E B Klunker NASA SP-347 Part II pp1189-1212 (1975)

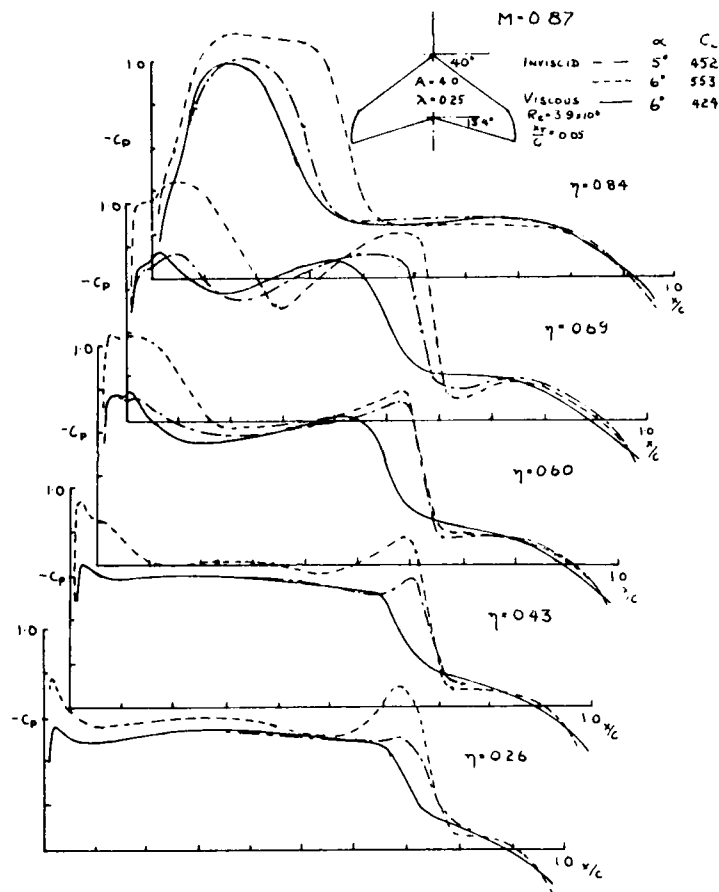


Fig 1 Comparison of the pressure distribution calculated for an isolated wing with and without viscous effects included

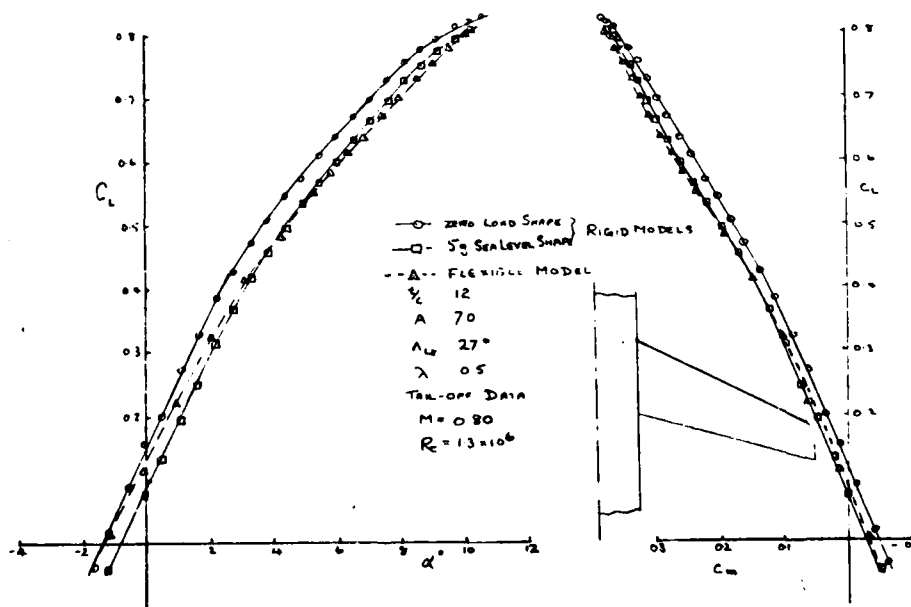


Fig 2a Experimental demonstration of the effects of aeroelasticity on lift and pitching moment characteristics - $\Lambda_{LE} = 27^\circ$

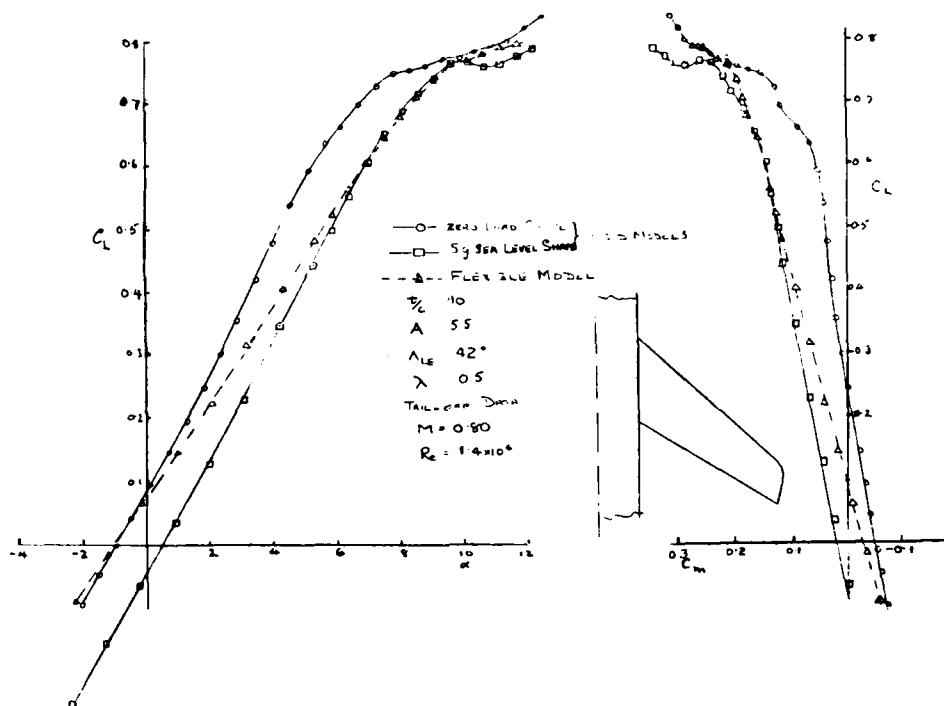


Fig 2b Experimental demonstration of the effects of aeroelasticity on lift and pitching moment characteristics - $A_{LE} = 42^\circ$

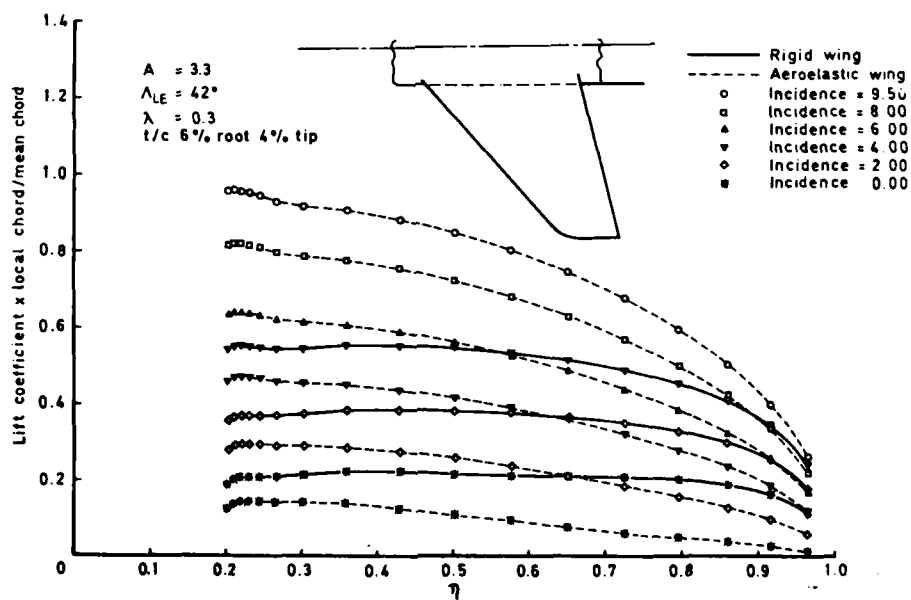


Fig 3 Calculated effect of aeroelasticity on the spanwise loading distribution - $M = 0.80$ sea level

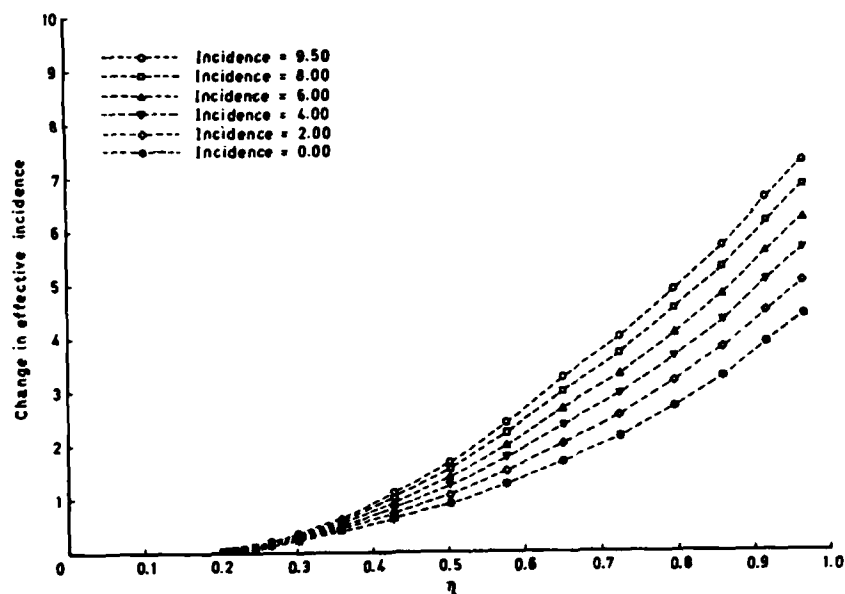


Fig 4 Calculated changes in effective incidence due to aeroelasticity - $M = 0.8$ sea level

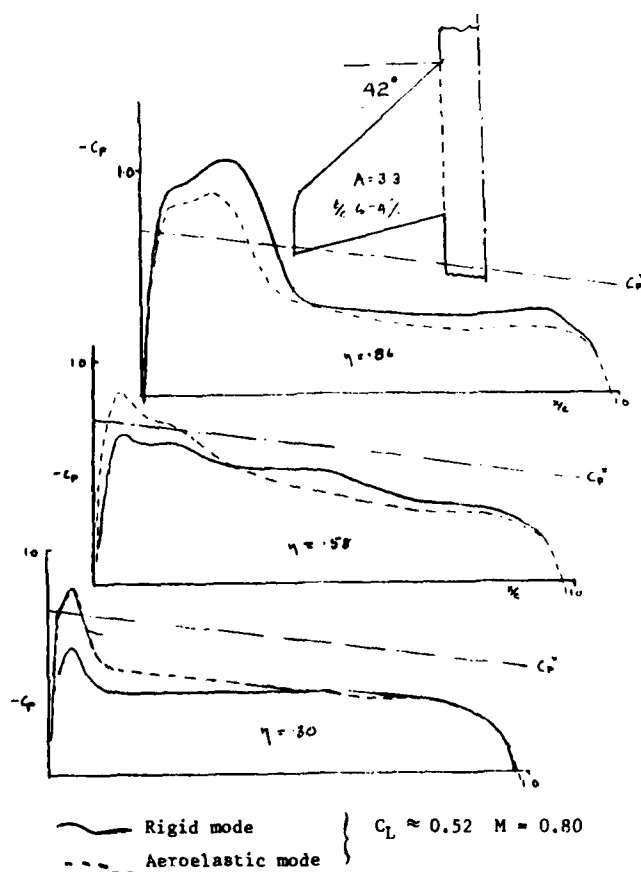


Fig 5 Calculated changes in chordwise pressure distribution due to aeroelastic effects

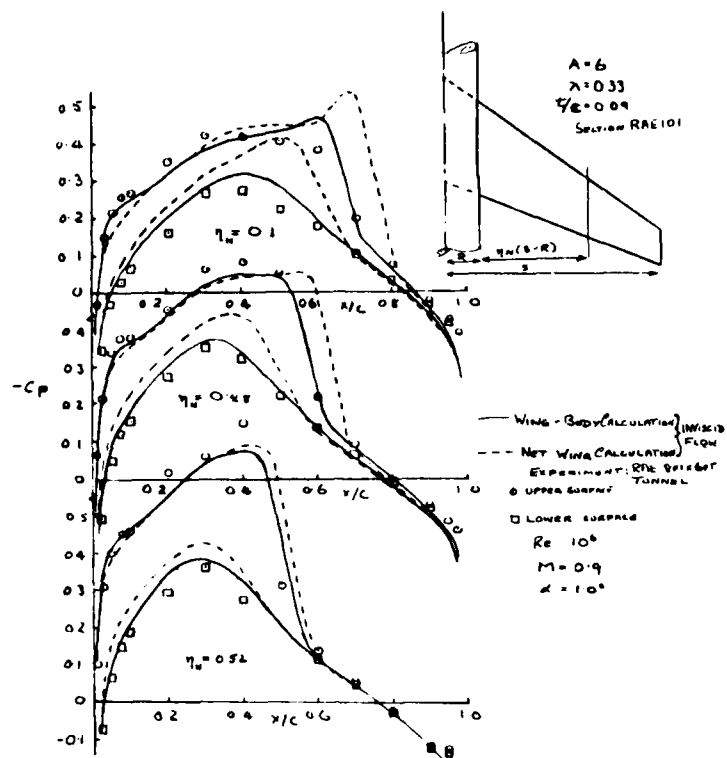


Fig 6 Calculated and measured pressure distribution for an isolated wing and a simple wing-body combination (from Ref 1)

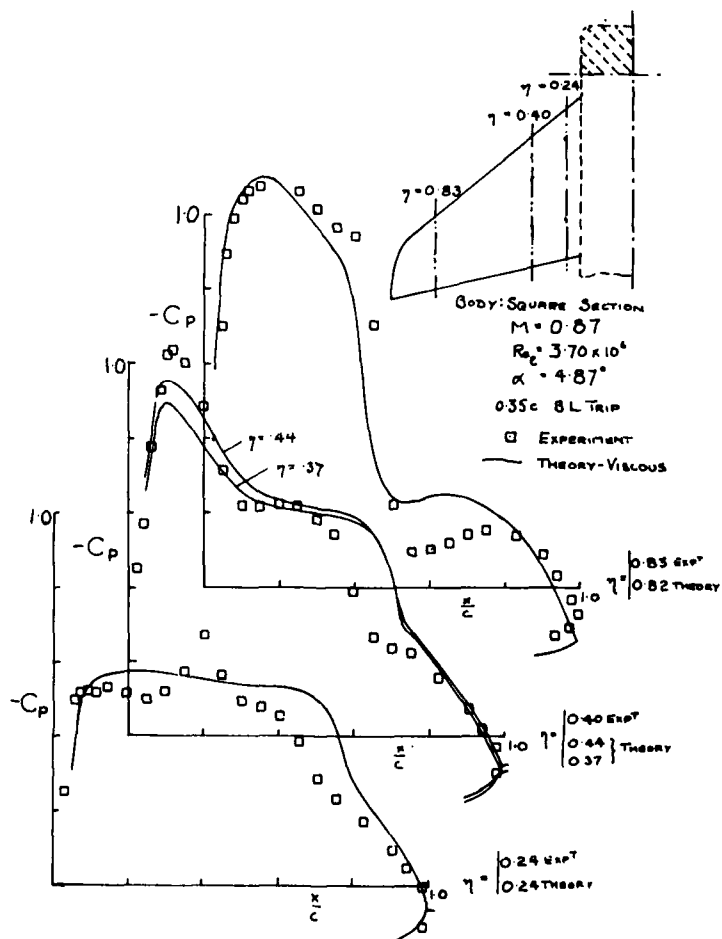


Fig 7 Calculated and measured pressure distributions for a wing-body combination allowing for viscous effects

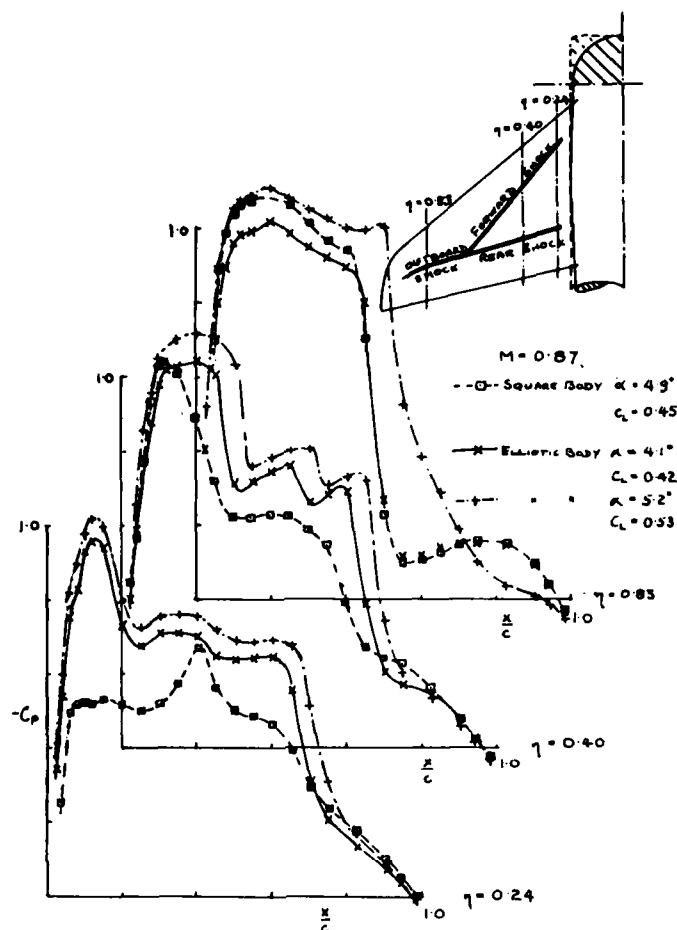


Fig 8 Comparison of measured chordwise pressure distributions for two alternative body shapes

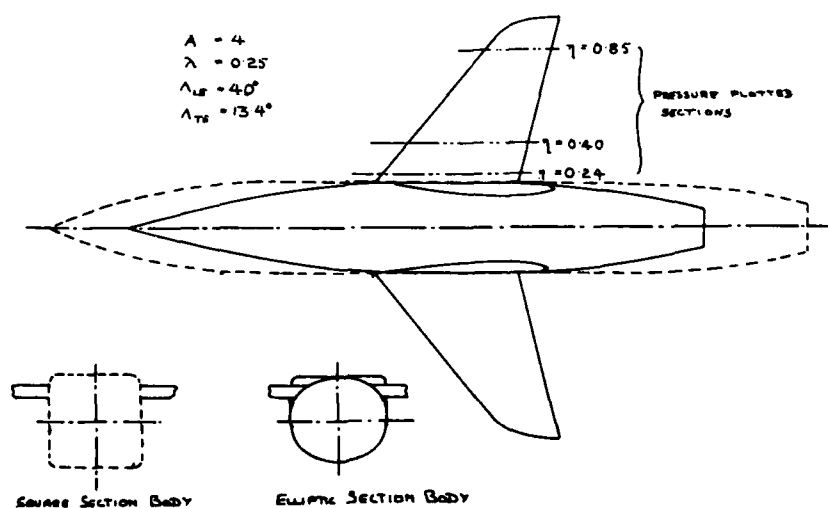


Fig 9 Sketch of research combat wing mounted on different fuselages

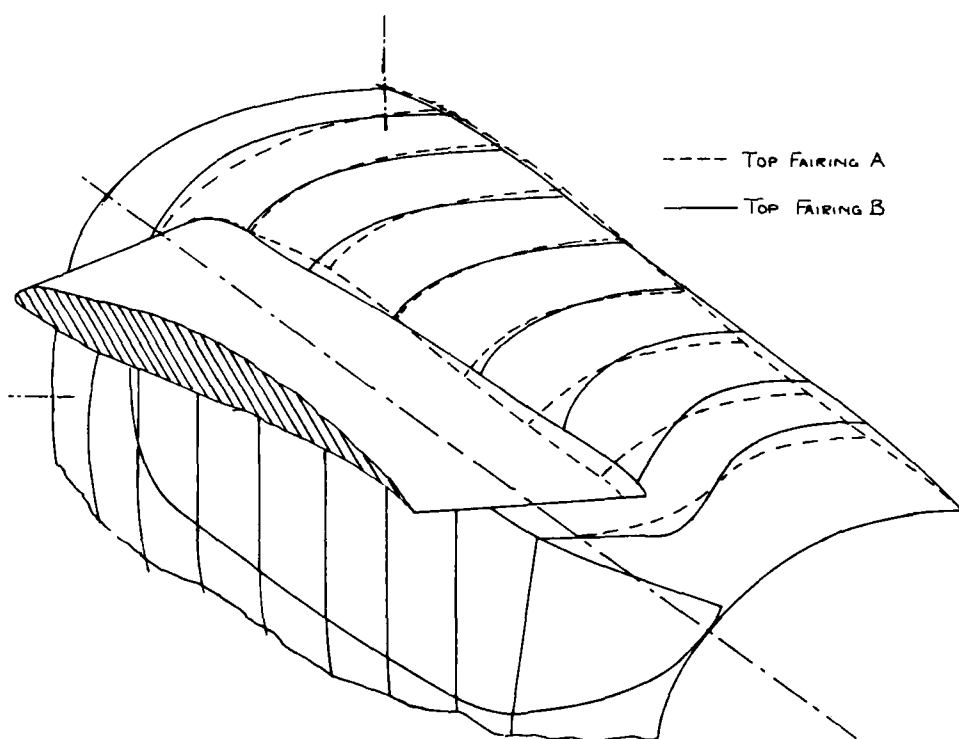


Fig 10 Sketch of fairings A and B tested with elliptic body-wing combination

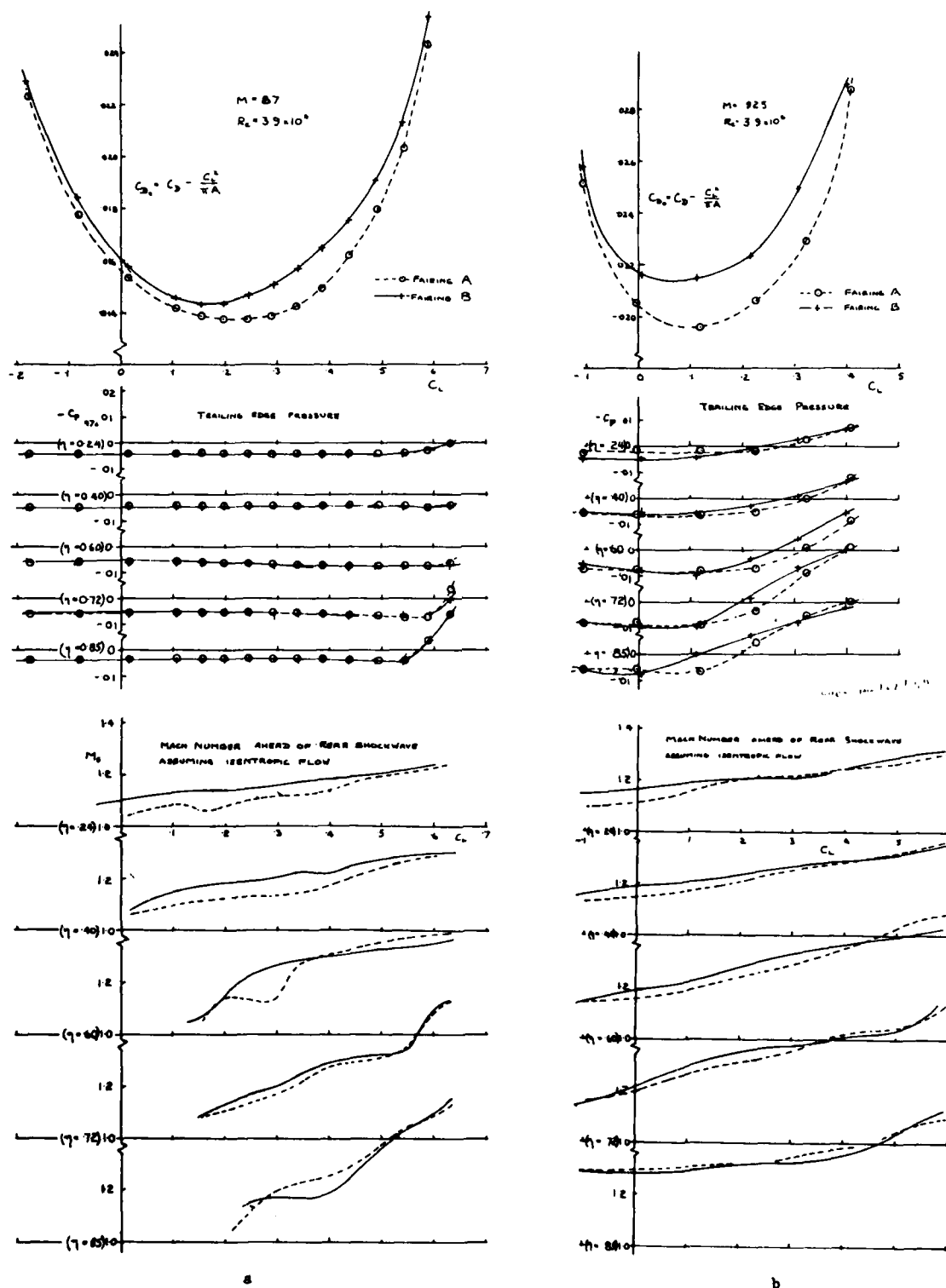


Fig 11a&b Measured drag characteristics with fairings A and B fitted

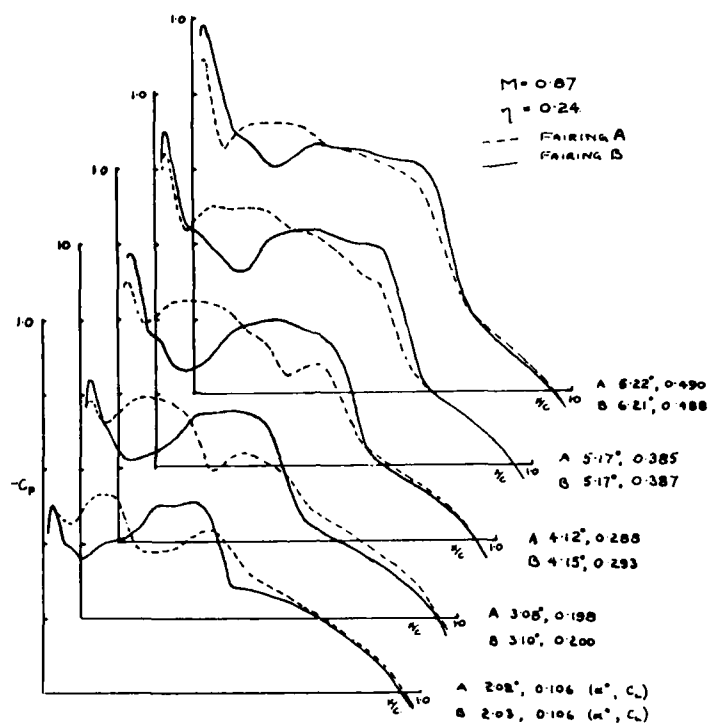


Fig 12 Variation of the upper surface pressure distribution with lift coefficient for $\eta = 0.24$, $M = 0.87$

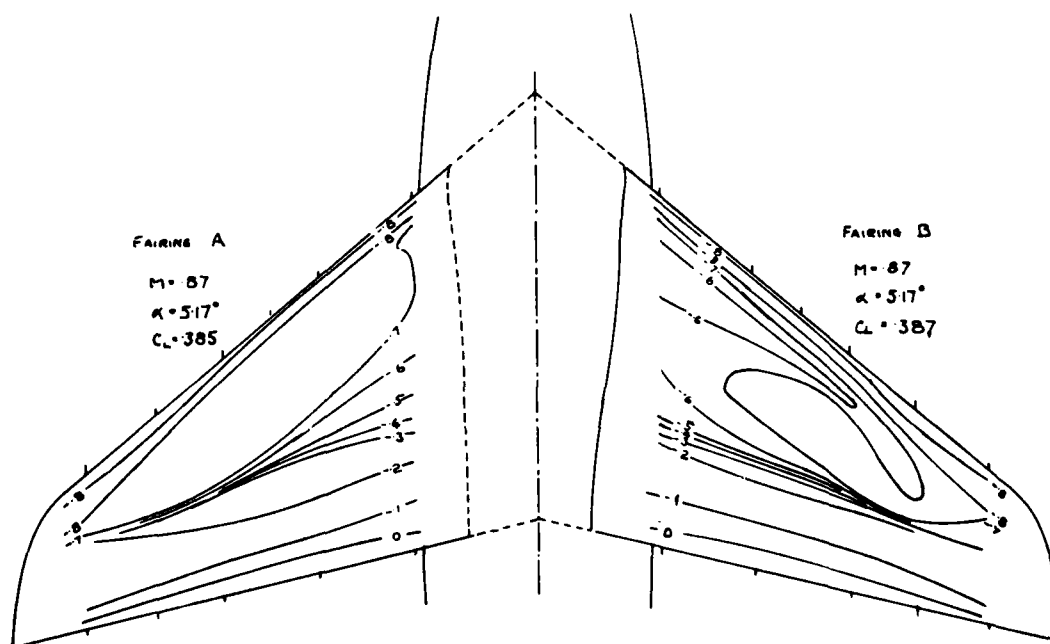


Fig 13 Comparison of the upper surface isobars for fairings A and B - $M = 0.87$

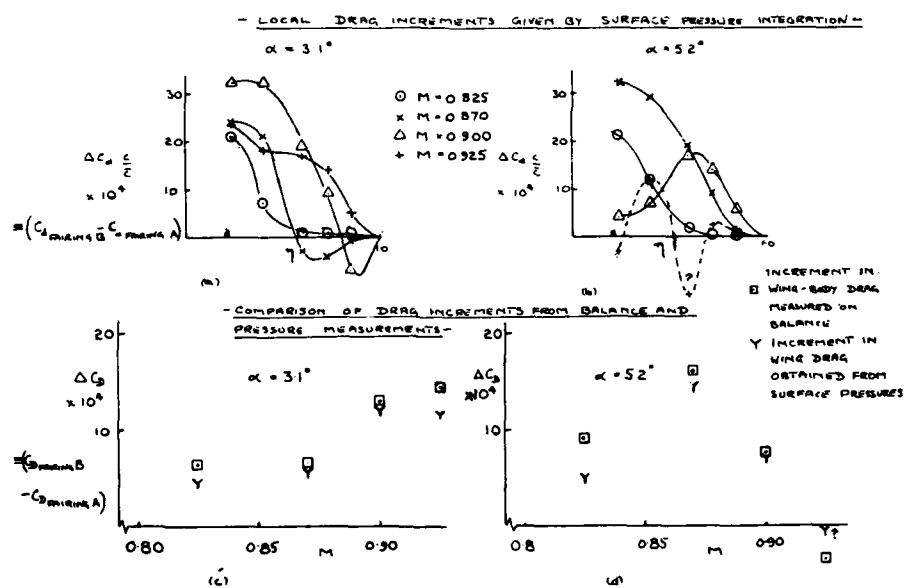


Fig 14 Comparison of differences in drag with fairings A and B obtained from pressure and balance measurements

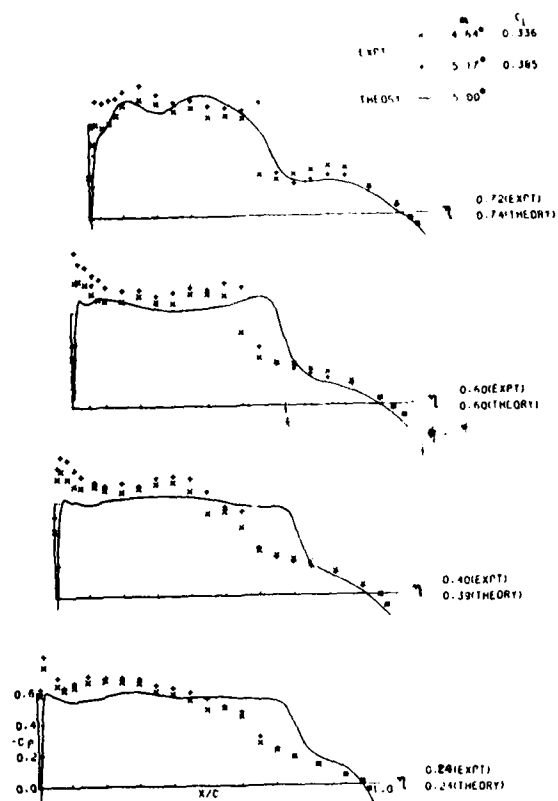


Fig 15a Comparison of measured and calculated chordwise pressure distributions for fairing A, $M = 0.87$

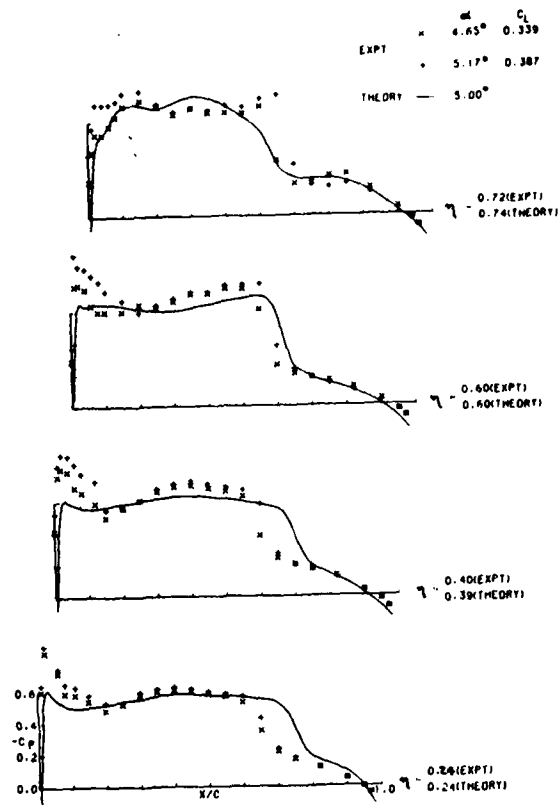


Fig 15b Comparison of measured and calculated chordwise pressure distributions for fairing B, $M = 0.87$

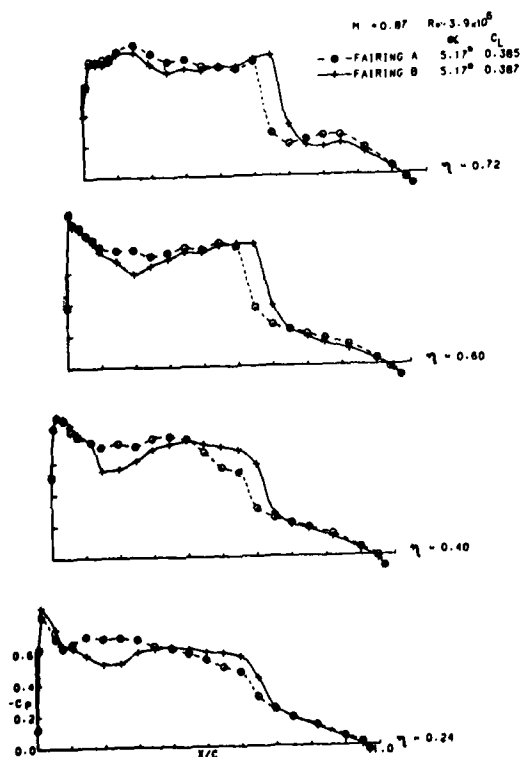


Fig 15c Comparison of the measured chordwise pressure distributions for fairings A and B

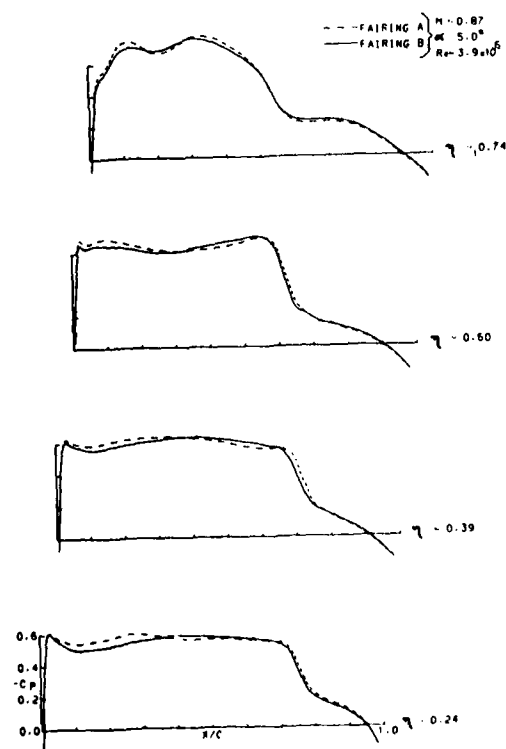
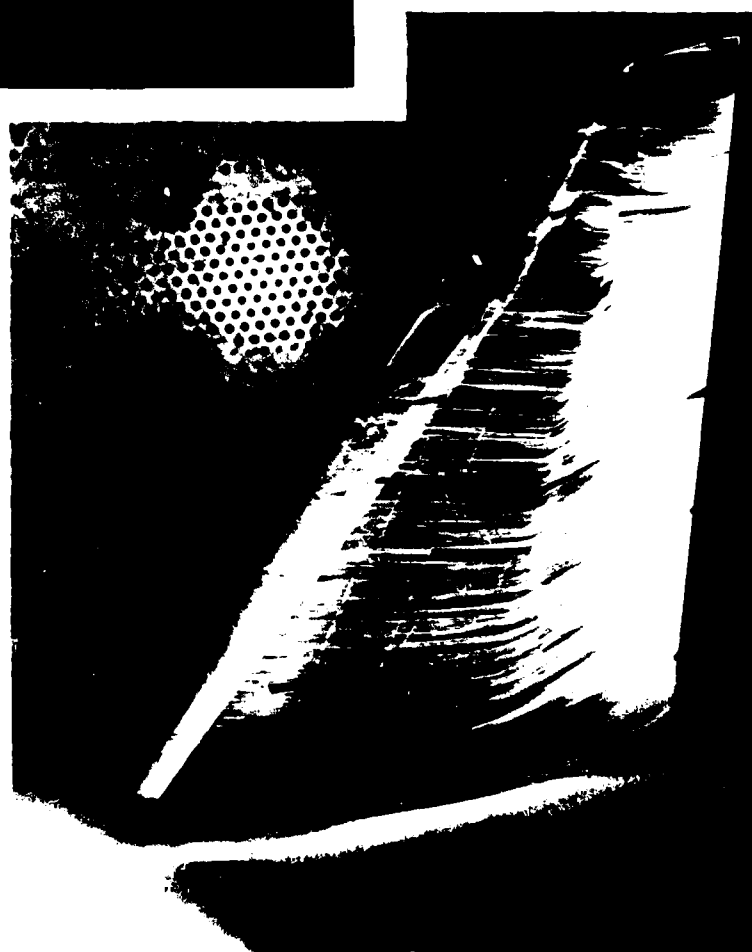


Fig 15d Comparison of predicted chordwise pressure distributions for fairings A and B



$\alpha = 5.7^\circ$ $C_L = 0.437$

Fig 16a Oil flow photograph -
fairing A, $M = 0.87$



$\alpha = 5.7^\circ$ $C_L = 0.433$

Fig 16b Oil flow photograph -
fairing B, $M = 0.87$

281

DESIGN STUDY FOR THE INNER WING OF A
TRANSONIC WING-BODY COMBINATION OF ASPECT RATIO 8

by

N. Voogt
J.Th. v.d. Kolk
Aerodynamics Department
Fokker Netherlands Aircraft Industry
Postbus 7600
Schiphol Oost
The Netherlands

SUMMARY

An application is presented of a transonic design procedure for wing-body combinations. The procedure which combines direct and inverse panel-type computations is based on the relationship between the exact transonic solution and an equivalent subsonic pressure distribution. The latter can be obtained by applying the subsonic panel method at the design condition for a shock-free airfoil designed by hodograph theory.

The paper will concentrate on the design of the inner wing where several problems arise due to the three-dimensional character of the flow, which prevents a unique determination of the equivalent subsonic pressure distribution.

Two essentially different approaches were followed by prescribing either a subcritical or a supercritical flow condition at the wing root. It will be shown that the subcritical flow condition at the wing root can be achieved for a range of wing geometries with leading edge extensions on the inner wing or alternatively, by applying extensive body-contouring to a wing originally designed to have supercritical flow at the root.

For the nominally shock-free flow condition the results of windtunnel tests on the wing-body combinations presented have confirmed the adequacy of the design process to generate constrained inner wing geometries with specified aerodynamic characteristics.

1. INTRODUCTION

In 1973 a research program for the development of advanced wing technology was initiated in the Netherlands. The program which is conducted in close cooperation between the Netherlands Agency for Aerospace Programs (NIVR), NLR and Fokker, was preceded in the late sixties at NLR by the work of Nieuwland and Spee (1). They demonstrated in 1969 that a local supersonic shock-free flow field can be obtained as an exact solution of the transonic equations by using hodograph theory. This flow-field showed to be stable in real flow.

The work was extended by Boerstael (2) who developed a transonic design method based again on hodograph theory. In combination with other potential flow and boundary layer analysis codes, this method can be applied to generate profile sections for optimized target pressure distributions.

At the time, 1973, there were no exact computational design methods for transonic wing-body combinations. Reliable transonic analysis and design codes based on full potential equations have only recently been introduced for the wing alone case (3), (4). Therefore the approach adopted was to develop a design procedure for transonic configurations on the basis of existing direct and inverse subsonic singularity methods (5).

In the course of the program several research wings were designed and tested to investigate the usefulness of the design procedure. Basis for the wing design are transonic 2-D target pressure distributions, which determine design as well as off-design wing characteristics. One of the important design problems is to ensure that 3-D effects do not disturb the reproduction of the basic airfoil section-characteristics in the three-dimensional wing.

This paper describes an early design study aimed, in particular, at shaping the wing geometry near the wing root to obtain a practical wing shape and to minimize unwanted 3-D effects.

The design process is described in the next section and considerations for the selection of target pressure distributions are presented in section 3. Applications of the method for the design of an inner wing for a wing-body research model are discussed in section 4. Finally a comparison with experiments is described in section 5.

2. THE DESIGN PROCESS

The aerodynamic design problem is to find the wing geometry which produces at a given combination of design lift coefficient C_L and free stream Mach number M_∞ an upper surface flow with an extensive region of supercritical flow and with minimal losses due to shock formation. The calculation of such a complicated flow field presents difficulties, especially in the presence of a body. The available numerical tools in 1973 were for the 2-D case:

- * Boerstool hodograph method for transonic shock-free airfoil design (2)
- * BGKJ finite-difference method for subsonic and transonic off-design calculations (6)
- * NLR panel method for subsonic flow calculations (7)
- * Boundary layer methods.

The situation for the 3-D case is more complicated due to the lack of adequate transonic methods for wing-body combinations in 1973. The at the time available methods were:

- * NLR panel method for non-planar wings
- * Inverse singularity method for a planar wing in the presence of a body
- * Boundary layer method

Because the available 3-D methods could only handle subsonic flow problems, the transonic design problem was transformed into an equivalent subsonic one and then solved by means of the existing 3-D subsonic methods. The procedure is shown schematically in fig.1.

Starting point is the selection of a 2-D transonic target pressure distribution which can be expected to yield a nearly shock-free design condition with attached flow as well as acceptable off-design characteristics. The exact inverse hodograph method is used for the airfoil design. For this airfoil the 2-D panel method - applied at the theoretical design Mach number and angle of attack - provides the equivalent subsonic pressure distribution. The difference between this pressure distribution and the transonic one is called the transonic correction and represents the error introduced by using a subsonic method for supercritical flow. For shock-free flow the transonic correction is a smooth chord wise function. Its precise form depends on the particular airfoil selected. It is only applied on the upper surface, unless supercritical velocities are allowed on the lower surface.

The basic assumption behind the design procedure is that the transonic correction is convertible to 3-D conditions by applying simple sweep theory to both transonic and equivalent subsonic pressure distributions. As explained in the next section this can only be justified in the quasi-2-D flow region.

The wing geometry which has to generate the target pressure distribution at the design condition, is obtained through an iterative process using both direct and inverse panel methods. As a starting point for the 3-D computations the pressure distribution is calculated for a wing-body combination with airfoil sections derived from the 2-D basic shock-free airfoils. The differences between the calculated and target pressures have to be eliminated by thickness- and camber modifications computed by the inverse method. This method takes body influence into account and geometric constraints can be applied to avoid unrealistic geometric characteristics. The method is presented in detail in ref.(8).

3. CONSIDERATIONS FOR TARGET PRESSURE DISTRIBUTIONS

On the part of the wing where the flow can be considered as quasi-2-D the transonic target pressure distribution is derived by transforming the basic 2-D pressure distributions - of which several are specified along the wing span - through the equivalence rule for tapered wings (9). This rule ensures that the streamwise Mach number distribution on the wing is similar to the shock-free Mach number distribution on the 2-D airfoil section.

On the inner wing upper surface the transonic target pressure distribution can be selected on the basis of physical and empirical considerations. There has to be a smooth transition from the quasi-2-D flow on the outer wing to the flow condition at the wing root, for which several options exist.

Figure 2 shows three typical transonic target isobar patterns investigated during the design study. Two of these (a) and (b) represent subcritical flow at the wing root while the third one, (c), allows a small region of supercritical flow at the root. In both cases (a) and (b) the supercritical isobars are forced to form closed loops in approaching the wing root. In case (b) the leading edge isobars are swept forward to decrease the normal component of the local Mach number. This target isobar pattern requires a curved leading edge. For case (c) the mid-chord suction level was forced to decrease rapidly towards the root in order to suppress rear shock development at or prior to the design condition.

Figure 2(d) illustrates the various amounts of supercritical flow on the inner wing upper surface. For the kink section at 40% semi-span the target pressures are derived from a basic shock-free airfoil section.

For the definition of the 3-D equivalent subsonic target pressure distribution the relevant 2-D distributions on the outer wing are transformed in a similar way as the basic transonic 2-D pressure distributions. On the inner wing outside the quasi-2-D flow region the specification of the equivalent subsonic target pressure distribution is no longer a straight forward process. Therefore engineering experience must be applied in extrapolating the equivalent subsonic target pressure distribution further inboard. Due to the incorporation of semi-empirical compressibility terms the NLR panel method is capable of reproducing pressure distributions for flows with small supercritical regions with fair accuracy. Therefore the difference between transonic and equivalent subsonic target pressures can be assumed to be zero at the wing root, even for case (c).

For the lower surface the required spanwise lift distribution determines the level of the subcritical target pressure distribution. The freedom in the choice of the lower surface chordwise pressure distribution is utilized by applying geometric constraints such as prescribed trailing edge angles, torsion box thickness, etc.

4. APPLICATIONS FOR INNER WING DESIGN

Based on the three types of target isobar pattern described in section 3 several inner wing design approaches were studied for a wing-body research model of aspect ratio 8 and 20° sweep of the quarter chord line. The required design condition was a lift coefficient of .45 at a free stream Mach number of .75. Accounting for viscous effects the potential flow design Mach number and lift coefficient were .74 and .52 respectively. At the kink section the target pressure distribution was based on airfoil NLR 7301.

4.1 Straight leading edge and subcritical root(a)

To obtain a starting geometry the 16% thick kink section based on NLR 7301 was extrapolated inboard and the pressure distribution was computed for $M = .74$ and zero degrees angle of attack. The results in fig.3 clearly show the high suction levels on the upper and lower surfaces close to the fuselage and a distortion of the pressure distribution due to 3-D effects.

After 3 iterations the pressure distribution on the outer part of the inner wing is more or less converged. Near the root it has adopted the proper chordwise shape, but the level has not improved. Simultaneously the thickness distribution has changed dramatically and ranges from 4% near the root to 18% in the mid-inner wing region. In these iterations no geometric constraints were applied and as a consequence the thin root section has obtained a negative trailing edge angle.

It can be concluded that for this case studied the required combination of planform, target pressure distribution and body shape is physically unrealistic. However, it will be shown later that a realistic solution can be obtained by manipulating the shape of the body in the interference region.

4.2 Curved leading edge and subcritical root(b)

When the inner wing planform is modified in the sense that the local leading edge sweep angle is introduced as a new parameter, the situation is entirely different. Fig.4 shows that this parameter can have significant consequences. A number of design iterations were performed for a planform with two slightly different leading edge extensions and similar target pressure distributions. It appears that while the pressure distribution is converging for both cases, the sectional geometries in the two cases have diverged completely. Again the largest geometric gradients are found close to the wing root.

The strong three-dimensional flow for this type of inner wing, apparently permits a large degree of freedom in shaping the inner wing geometry. In order to avoid unrealistic shapes like the one in fig.5 the design process may be guided by applying geometric constraints to the inverse program.

The influence of variations of the leading edge sweep angle was investigated for a number of inner wing configurations with different planforms. An empirical correlation could be made between spanwise variation of leading edge sweep and thickness distribution for this type of target pressure distribution.

On the basis of this correlation an inner wing was designed with a thickness ratio variation ranging from 16% at the kink to 18% at the wing root.

4.3 Straight leading edge and supercritical root(c)

For this case an initial geometry was defined by interpolating between the 16% thick kink section and a root section which was modified to counteract body influence. Fig.6 shows that at the mid-inner wing station the computed pressure distribution is already close to the target, but at the root station the suction level is far too high on a large part of the upper surface. This is in accordance with the result of fig.3 for the same planform, although due to the modification of the section shape the type of pressure distribution is quite different.

Again the leading edge sweep angle has a strong influence on the pressure distribution as shown by the result of the second direct computation for a configuration with the same section shapes but with 10° more leading edge sweep. For the entire inner wing the suction level has decreased considerably such that for the mid-innerwing station the difference between calculated and target pressure levels is now unacceptably large.

Therefore for further design iterations an intermediate planform was selected with 5° more sweep on the leading edge relative to the outer wing leading edge. The result of a few iterations with geometric constraints on thickness, twist and trailing edge angles is shown in fig.7. For this regular geometry - the thickness ratio varies between 16% at the kink and 17% at the root - the calculated pressure distribution has converged appreciably, except near the body where especially the mid-chord suction level remains too high.

Two possibilities for further convergence were considered. In the first place by section modification calculated by means of the inverse method with relieved geometric constraints. The modification requires decreased curvature over most of the upper surface and an increased twist angle. This leads to unacceptable spanwise geometric gradients.

The other possibility considered was to leave the wing sections unchanged but to modify the wing-body fairing such that the velocity level is decreased over the mid-chord region on the wing adjacent to the body. The modification of the wing-body fairing selected is shown in fig.8. On the front part the curvature is increased to speed up the flow and thereby to increase the suction peak and over the rear part the streamwise curvature is modified to decelerate the flow. As a result of the modification a pressure distribution could be obtained which was sufficiently close to the target.

4.4 Design of a fairing for subcritical flow at the root

The effect of the fairing modification on the pressure distribution raised the question whether the pressure distribution at the wing root could be further influenced by more extensive modifications of the wing-body fairing. With the objective to bring down the wing root velocities to a subcritical level a number of successive changes and computations were made to the wing-body fairing. To be able to represent curvature variations accurately the panel density was increased and the front part was extended to half a chord length ahead of the wing.

The final result in fig.9 shows that the front and rear parts of the fairing are convex surfaces while the area in between is concave to decelerate the flow over the wing. The transition from convex to concave takes place near the leading edge i.e. in front of the suction peak on the wing.

The effect on the inner wing pressure distribution is shown in fig.10. The wing root has become subcritical and the change of the pressure distribution further outboard illustrates the spanwise influence of the modification. The loss of wing lift associated with the reduction of the upper surface suction level was partly recovered by additional contouring of the fairing lower surface.

5. COMPARISON WITH EXPERIMENTS

In combination with the same outer wing three inner wing configurations, each representing one of the possible target isobar patterns, discussed in section 3, were tested in the NLR high speed tunnel. The first case is an inner wing with a curved leading edge and thickness ratios between 16% at the kink station and 18% at the wing root (section 4.2). The second is the inner wing with straight leading edge and supercritical flow at the root (section 4.3) and thickness ratios between 16% at the kink station and 17% at the root. For the third configuration the extended fairing (section 4.4) was added as a glove on the previous model.

Results of windtunnel tests for the first two cases have been presented in some detail in Ref.5. Figure 11 which is reproduced from this reference compares measured pressure distributions at the design condition with expected transonic pressure distributions. The latter are obtained from the result of panel method computations at the potential flow design condition after conversion by removing the transonic correction. The weak shock wave which at the design condition originated from the mid-inner wing region did not contribute to any significant 3-D transonic wave drag.

The theoretical and experimental upper surface pressure distributions for all three configurations are compared in fig.12 for a pressure station near the wing root. The mutual differences between the computed pressure distributions are reproduced in the experiment apart from a local disturbance near the leading edge for the configuration with the extended fairing. The spanwise effect of the fairing appeared to be insufficient to influence the inner wing shock wave.

6. CONCLUDING REMARKS

A design procedure for transonic wing-body combinations has been applied to explore its usefulness for the inner wing design of advanced civil transport wings. The procedure which incorporates a transonic 2-D design method and direct and inverse 3-D subsonic singularity methods, is based on the concept of equivalent subsonic pressure distribution.

The inner wing design problem was approached from different view points by considering a transition from quasi-2-D "shock-free" supercritical flow on the outboard part to either a subcritical or a supercritical flow condition at the wing root.

The results of the design study aiming at wing designs for cruise flight at $M=0.75$ can be summarized as follows:

- * a subcritical flow condition at the wing root can not be achieved for a simple inner wing geometry but requires either a planform with a curved leading edge or extensive contouring of the wing-body fairing for a regular inner wing geometry
- * a supercritical flow condition at the wing root can be combined with a regular inner wing geometry by applying modest contouring of the wing-body fairing

- * experimental verification at the design condition confirmed the adequacy of the design procedure for both the subcritical- and supercritical approaches at the wing root
- * the combination of inverse computations with constrained section modifications and direct computations manipulating the wing-body fairing provides an effective approach to advanced aerodynamic wing design.

REFERENCES

1. Nieuwland, G.Y., Spee, B.M.
"Transonic Airfoils: Recent Developments in Theory, Experiment and Design".
Annual Reviews of Fluid Mechanics, vol.5, 1973, pp.119-150
2. Boerstoeel, J.W.
"Design and Analysis of a Hodograph Method for the Calculation of Supercritical Shock-free Airfoils".
NLR-TR-77046 U. Ph.D.thesis, 1977.
3. Jameson, A., Caughey, D.A.
"Numerical Calculation of the Transonic Flow past a Swept Wing".
New York University, ERDA Report COO-3077-140, 1977.
4. Henne, P.A.
"An Inverse Transonic Wing Design Method".
AIAA paper-80-0330, 1980.
5. Slooff, J.W., Voogt, N.
"Aerodynamic Design of Thick, Supercritical Wings, through the Concept of Equivalent Subsonic Pressure Distribution".
NLR-MP-78011 U, 1978.
6. Bauer, F., Garabedian, P., Korn, D., Jameson, A.
"Supercritical Wing Sections", part I (1973), part II (1975)
Springer Verlag.
7. Labrujere, Th.E., Loeve, W., Slooff, J.W.
"An Approximate Method for the Calculation of the Pressure Distribution on Wing-body Combinations at Subcritical Speeds".
AGARD CP.No.71, paper 11, 1970.
8. Fray, J.M., Slooff, J.W.
"A Constrained Inverse Method for the Aerodynamic Design of Thick Wings with given Pressure Distribution in Subsonic Flow".
Paper to be presented at AGARD symposium: Subsonic and Transonic Configuration Aerodynamics, München, 1980.
9. Lock, R.C.
"An Equivalence Law relating Three and Two Dimensional Pressure Distributions.
ARC, R&M 3346, 1962".

Acknowledgements

The authors wish to thank Prof. Blom of Fokker and Mr. Slooff of NLR for their many helpful suggestions on this subject.

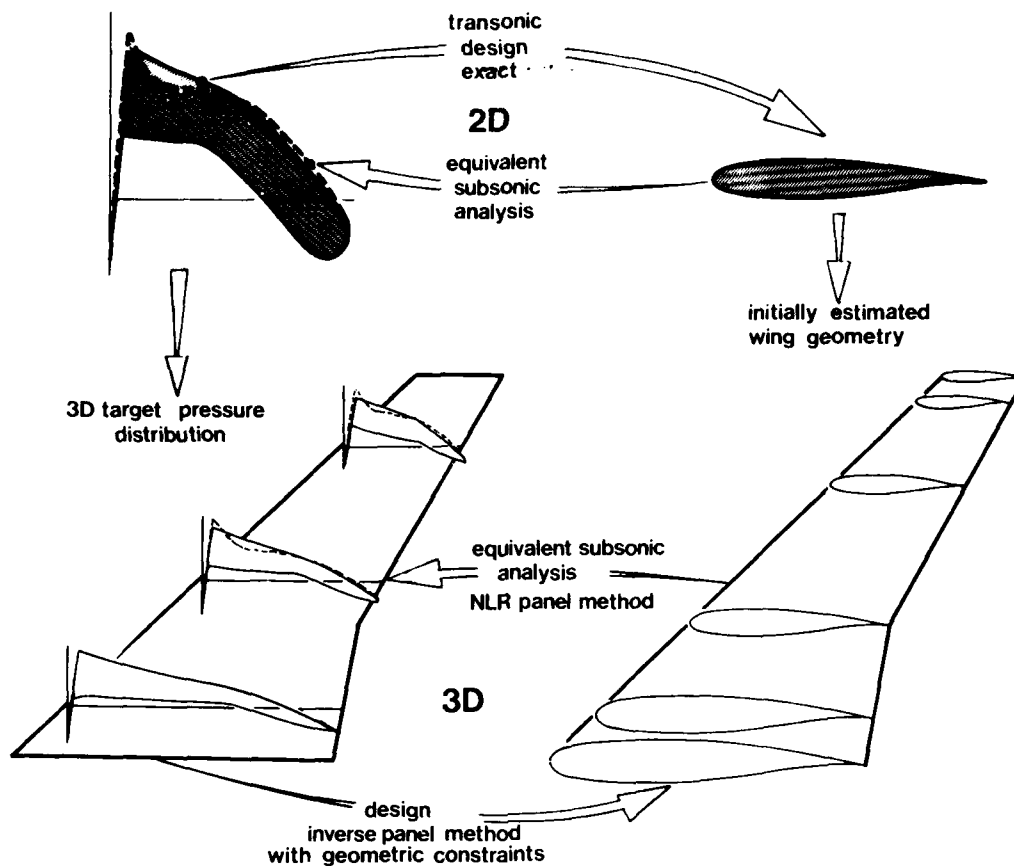


FIG.1 INTERACTION OF COMPUTATIONAL METHODS FOR THE DESIGN PROCEDURE

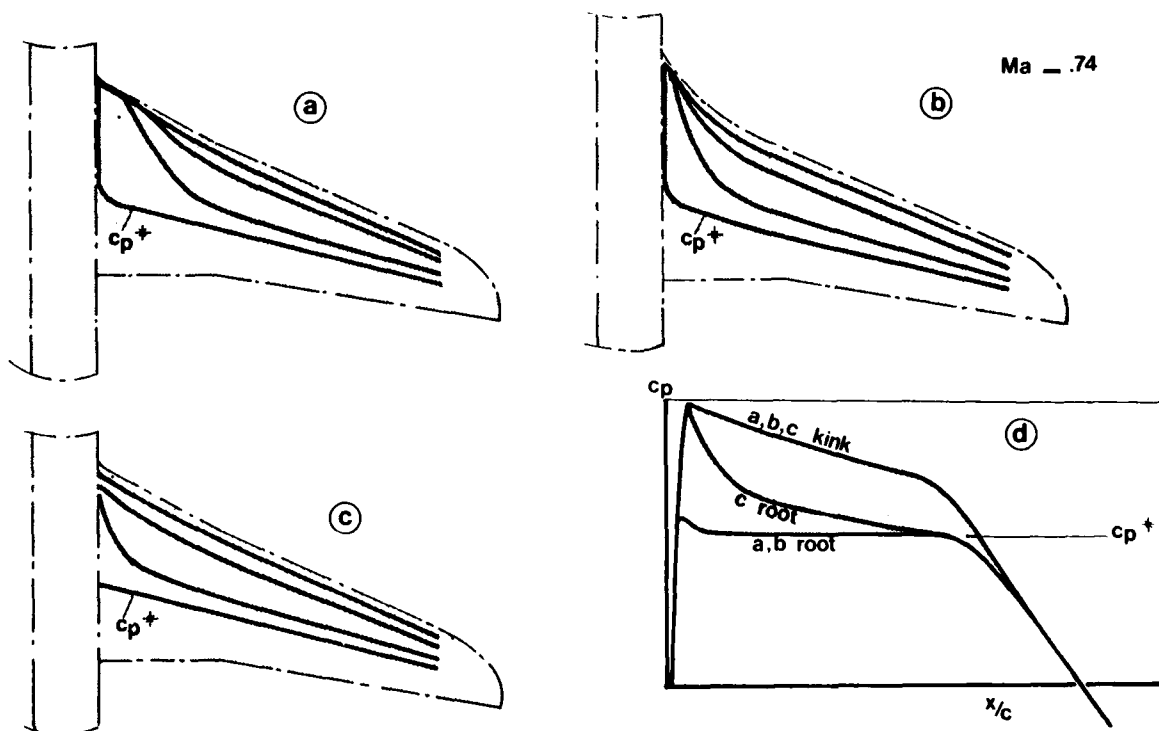


FIG.2 UPPER SURFACE TRANSONIC TARGET PRESSURE DISTRIBUTIONS

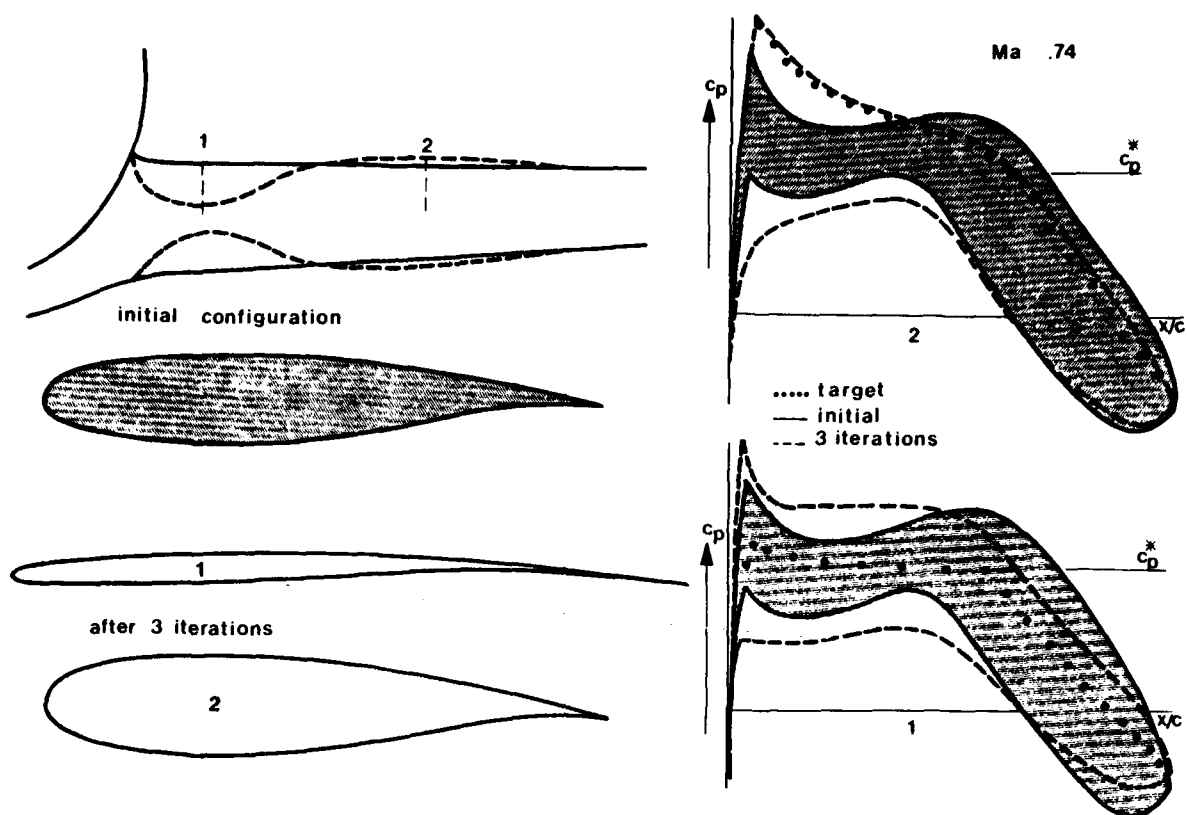


FIG. 3 RESULTS OF ITERATION PROCESS FOR CASE (a) WITH STRAIGHT LEADING EDGE

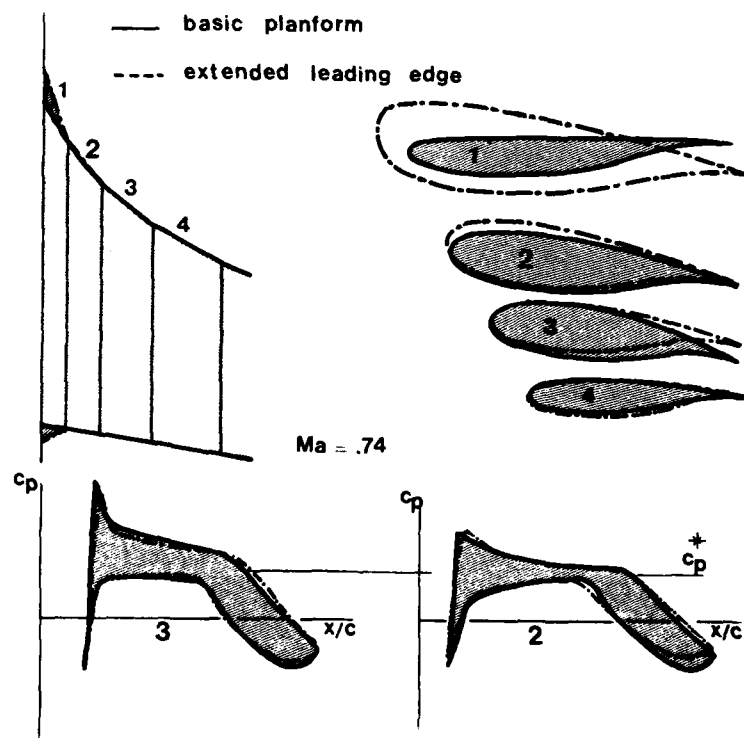


FIG. 4 CONVERGENCE PROBLEM FOR CASE (b)



FIG.5 UNCONSTRAINED GEOMETRY NEAR WING ROOT FOR CASE (b)

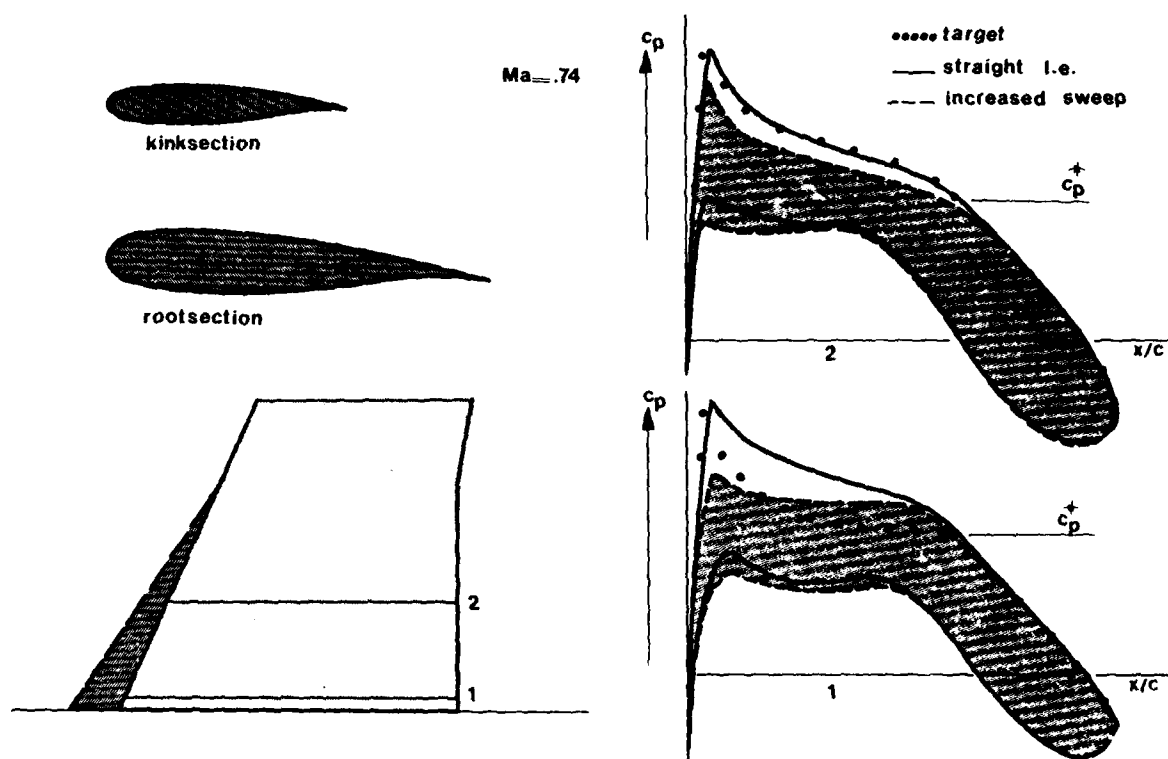


FIG.6 RESULTS FOR CASE (c) WITH DIFFERENT LEADING EDGE SWEEP ANGLES

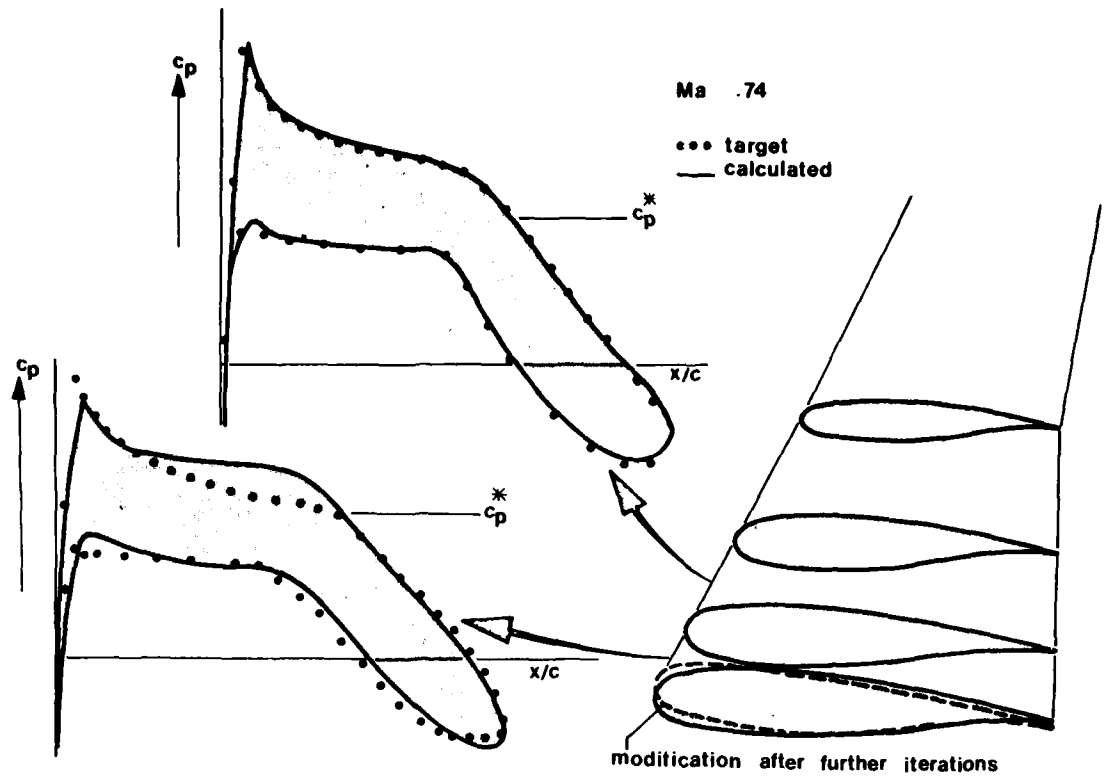


FIG. 7 NEARLY CONVERGED SOLUTION FOR CASE (c)

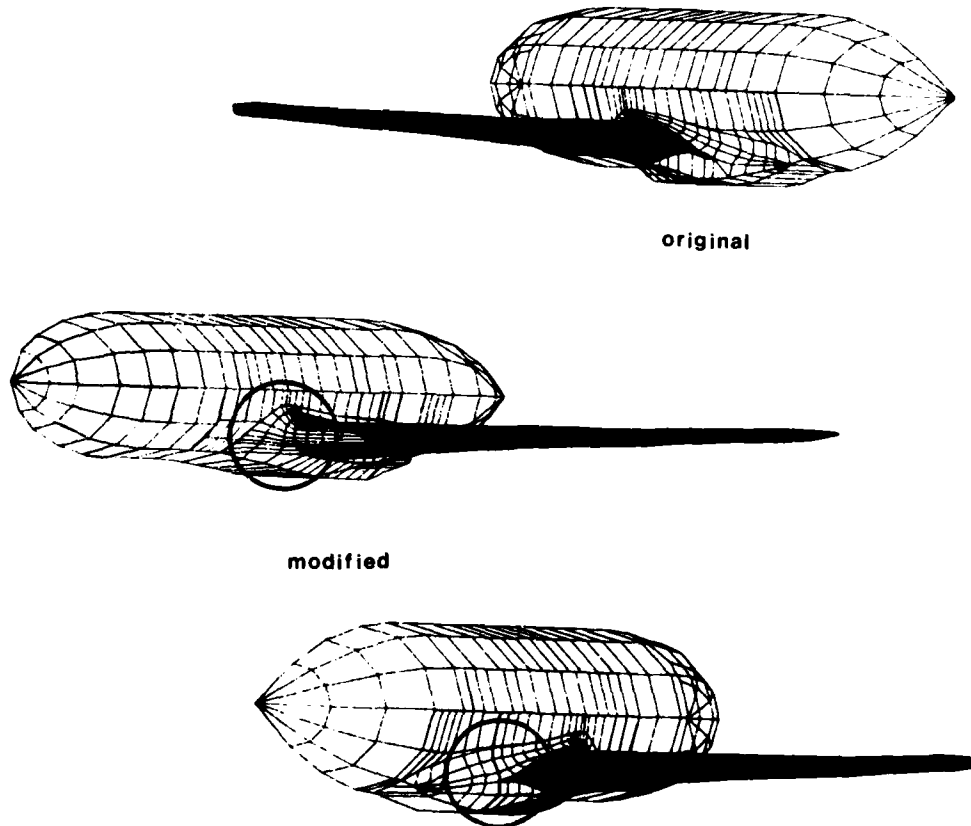


FIG. 8 MODIFICATION OF WING-BODY FAIRING FOR CASE (c)

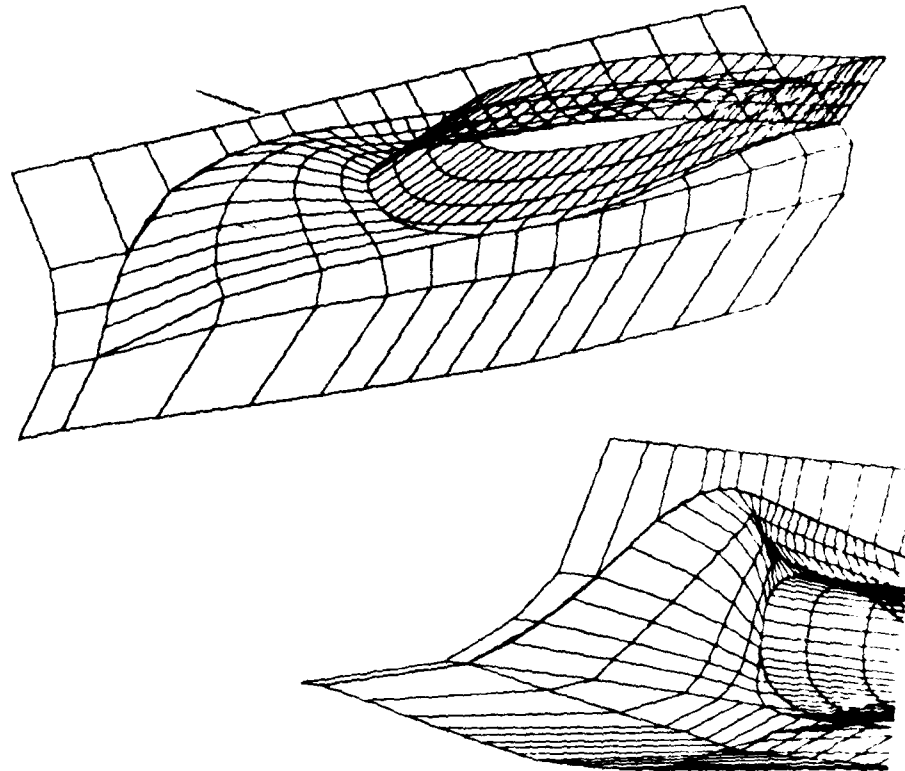


FIG.9 GEOMETRY OF EXTENDED WING-BODY FAIRING

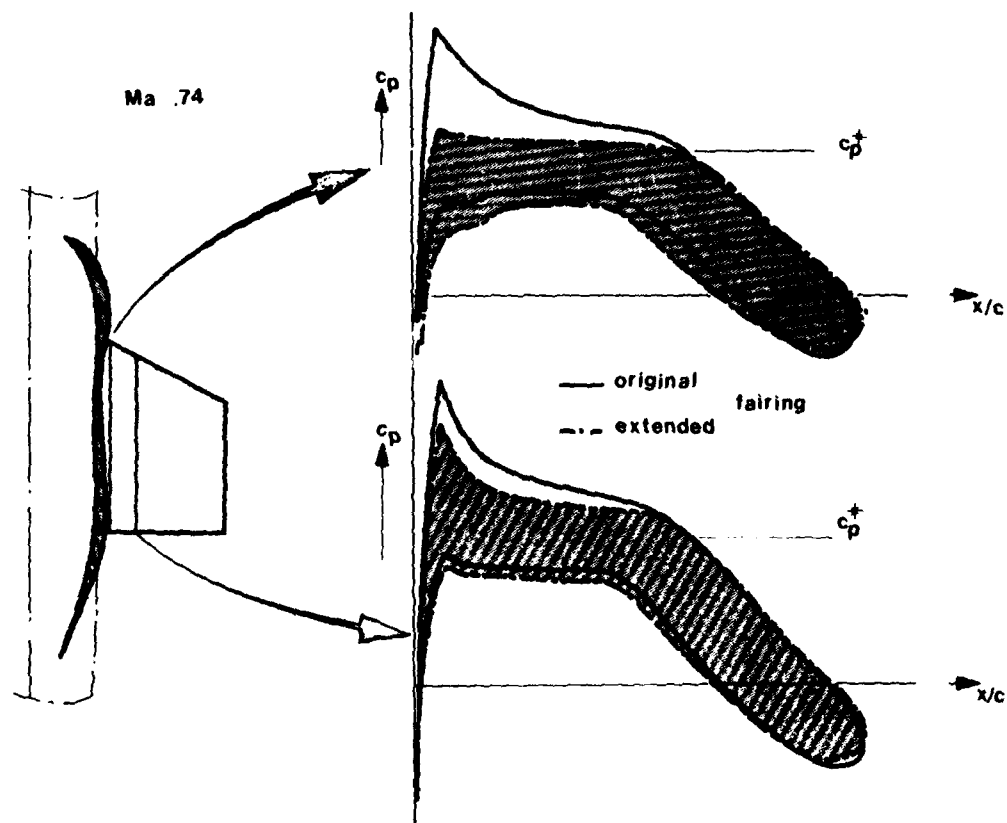


FIG.10 EFFECT OF EXTENDED FAIRING ON INNER WING PRESSURE DISTRIBUTION

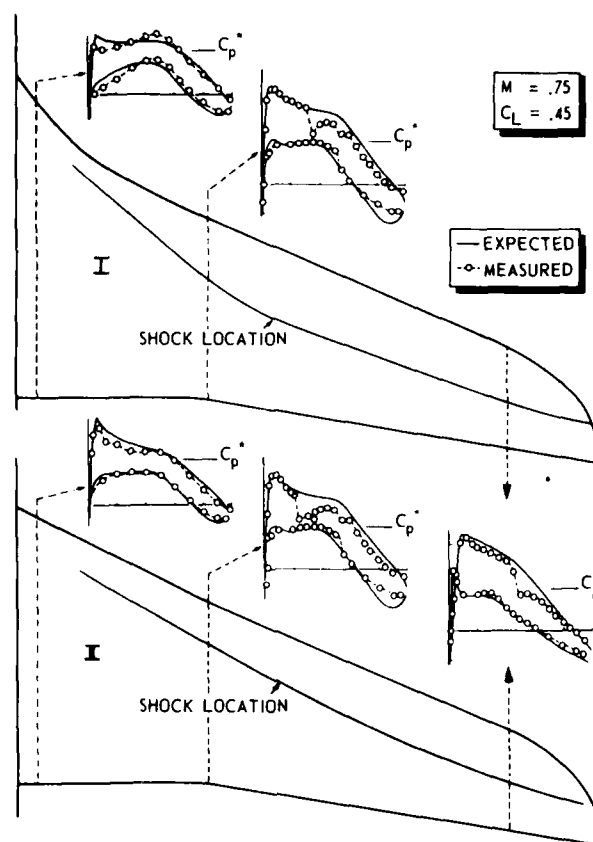


FIG. 11 COMPARISON OF EXPERIMENTAL AND EXPECTED TRANSONIC PRESSURE DISTRIBUTIONS FOR WINGS I AND II.

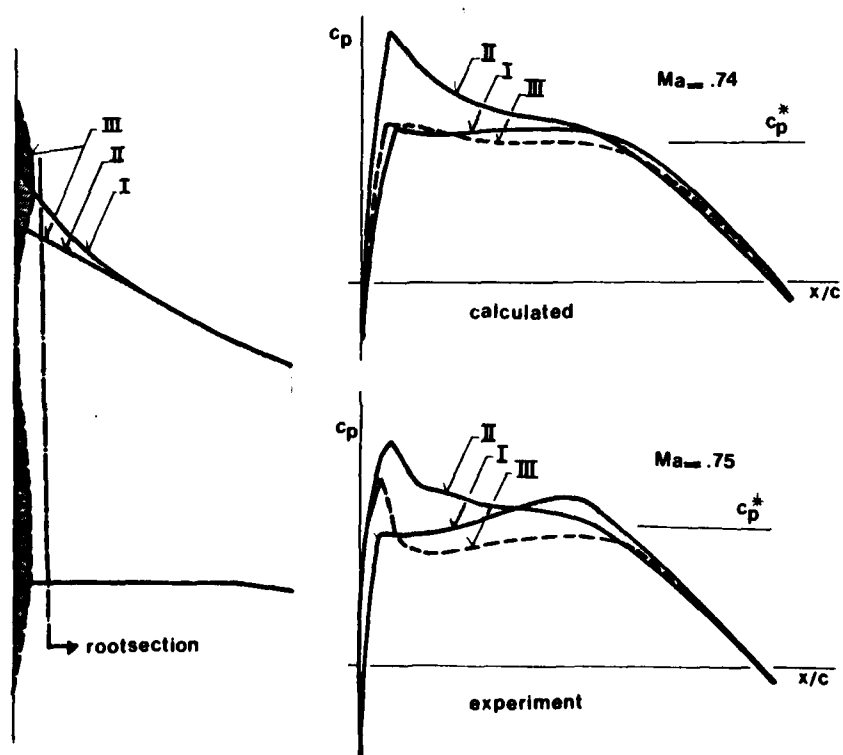


FIG. 12 COMPARISON OF CALCULATED AND EXPERIMENTAL PRESSURE DISTRIBUTIONS AT THE WING ROOT FOR THE THREE CONFIGURATIONS.

COMPLEX CONFIGURATION ANALYSIS AT TRANSONIC SPEEDS*

C. W. Boppe
and
P. V. Aidala
Grumman Aerospace Corporation
Bethpage, N.Y. 11714

SUMMARY

Advanced performance requirements of new combat and transport aircraft together with design time constraints intensify the development and application of three-dimensional computational analyses. This paper describes a computational method which has been developed for the specific purpose of providing an engineering analysis of complex aircraft configurations at transonic speeds. While a complete description of the methodology is included, particular attention is given to the recently incorporated wing viscous interaction and canard capabilities. The treatment of fuselage fairings, nacelles, and pylons is reviewed. The means for keeping computing resources at reasonable levels are identified. Three configurations have been selected for correlations with experimental data. Taken together, the comparisons illustrate the full extent of current analysis capabilities. The configurations include 1) a wing-fuselage-canard fighter, 2) a transport with fuselage fairings, four nacelles, four pylons, and 3) a space vehicle which includes an external fuel tank and rocket boosters (transonic launch configuration).

INTRODUCTION

The cost of wind tunnel and flight test experimentation is increasing along with the requirements for advanced transonic cruise and maneuvering performance levels. The number of design variables that must be investigated has increased with the addition of new propulsive and structural constraints. To compound problems, the lead times required for model manufacturing and checkout have not been reduced significantly. Clearly, advanced computational methods are required to insure that future aircraft designs will exhibit true aerodynamic performance gains over existing technology designs.

Fortunately, the field of transonic computational aerodynamics has experienced considerable growth during the past decade. Aerodynamic performance gains in the transonic flight regime are of particular interest because most transports cruise at transonic speeds and many combat aircraft missions require a sustained transonic maneuvering capability. The inherent physical complexity of transonic flows coupled with new design requirements insures future growth in transonic design and analysis methodology. We can expect that time and cost constraints will limit future experimentation to numerical design verification and "fine tuning."

Until recently, transonic computational analyses have been restricted to simple shapes such as airfoils, axisymmetric bodies, isolated wings, and simple wing-body configurations. These simple shapes, however, rarely present severe problems to the aircraft designer or the engineering analyst. On the other hand, complex configurations are particularly vulnerable to unexpected component interference effects at transonic speeds, and a considerable amount of experimentation is now required to resolve this type of problem. The multiple nested grid approach¹⁻³ has made it possible and practical to analyze complex configurations at transonic speeds. This type of analysis provides both grid resolution for detailed component analysis and grid versatility for the study of various aerodynamic interference effects. Waggoner⁴ recently reported on the ability of a wing-body pilot code to predict subtle force and moment increments that result from wing section and planform modifications. This study indicates that the computer tool can be used to effectively control total design space. Many design variables can be reduced long before the first wind tunnel test.

This paper describes an approach that has evolved over the past four years. The resulting computational method has been developed for the specific purpose of providing an aerodynamic engineering analysis for complex configurations at transonic speeds. Unlike a basic research-oriented code, many approximations and compromises have been made to enhance computational flexibility and reliability. Thus, in addition to illustrating the details of configuration interference-related pressure fields, this paper will describe the means by which they are simulated. The accompanying sample cases illustrate transonic aerodynamic interference effects caused by pylons, canards, nacelles, pods, fuselage fairings, and wing viscous effects.

COMPUTATIONAL GRID AND FLOW EQUATION

A three-dimensional computational method must overcome both grid versatility and grid resolution problems in order to be effective. Most finite-difference relaxation schemes for three-dimensional flows employ coordinate systems which simplify the application of boundary conditions. This approach evolves naturally from techniques developed for two-dimensional and axisymmetric flows. As three-dimensional geometries become more complex, the form-fitting grid approach becomes harder to implement. Applications to realistic aircraft configurations are compromised in one way or another.

Mesh point density must be sufficient to resolve aerodynamic details of small aircraft components and their overall effect on the complete configuration. This puts a severe strain on the conventional single grid approach. A single coordinate system which is constructed for the analysis of a wing-fuselage configuration will be totally inadequate for studying the effects of a small pod or pylon surface mounted below the wing. The problem is due to the large disparity in size of the various components of the configuration. Current restrictions on computing resources make it impractical to do a detailed analysis throughout the flow field.

The present method uses a nested or embedded grid scheme (Figure 1). Independent grid systems are constructed for each of the configuration wing and body components. High mesh point resolution is obtained close to the air-

*This work was supported by NASA-LRC under Contract NAS1-14732 and by the U.S. Air Force under Contract AFFDL F-33615-78-C-3014.

craft surface where flow gradients are high and details are important. This high-density pattern is not carried into the far field where gradients are mild. Note that nacelles, canards, and other components can be added or removed (along with their grid systems) without changing the basic structure of the analysis. Configuration boundary points will vary between 5000 and 7000 depending on the configuration complexity.

Figure 2 illustrates a typical boundary surface along with the surrounding crude and fine grid point arrays. The boundary represents either a wing or body surface. Interaction between the two coordinate systems is achieved by means of an overlap region. Flow field potentials at the global crude grid points are interpolated to provide outer boundary conditions for the fine grid system. The flow field is relaxed providing a detailed flow solution between the boundary surface and the fine grid outer boundary. Fine grid potential values are then used to update crude grid points on the inside boundary of the overlap region. The outer flow field is then relaxed. This cycle is repeated until both grid systems are satisfactorily converged.

The flow field is solved iteratively by using successive-line-over-relaxation procedures. The flow governing equation in terms of the disturbance velocity potential is

$$\left[1 - M_\infty^2 - (\gamma + 1) M_\infty^2 \phi_x^2 - \left(\frac{\gamma + 1}{2}\right) M_\infty^2 \phi_x^2\right] \phi_{xx} - 2M_\infty^2 \phi_y \phi_{xy} + \left[1 - (\gamma - 1) M_\infty^2 \phi_x^2\right] \phi_{yy} + \phi_{zz} = 0 \quad (1)$$

This modified small disturbance equation is consistent with planar boundary conditions. As a result, simple rectangular coordinate arrays can be used extensively. This facilitates the implementation of the grid embedding technique. Care has been taken, however, to insure that the flow equation is suitable for modeling swept shock waves which typically are encountered in applications.

FUSELAGE, POD, AND NACELLE SIMULATION

Body-type surfaces which include fuselage, pods, and nacelles are simulated by computing appropriate values of the flow field potential at points in the grid system which lie close to the true body surface. These boundary points are computed before the relaxation sweep and are fixed. Unlike wing and pylon boundary conditions, the body-type boundary condition is approximate in the sense that the flow equation is not solved at the body boundary points.

Figure 3 illustrates a typical body surface along with the grid field points that enter into the computation of the body boundary point potential value. For body side points, three point extrapolated difference operators provide the V and W velocity components required. Pod and nacelle surfaces differ from those of the fuselage in that component yaw angle is included in the boundary condition along with the surface normal and component incidence angle. Initial computations for under- and over-wing nacelles indicated that a conventional streamtube simulation that does not account for contouring and deflections would not be satisfactory. For this reason, nacelle streamtube surfaces are not modeled. Instead, flow field potentials are computed on the inlet and exhaust surfaces based on the mass flow ratio and the exhaust pressure ratio, respectively. A three point extrapolated difference operator provides the axial (U) velocity component.

Surface normal vectors which enter into fuselage boundary conditions are provided by a mathematical geometry modeling system developed by Vachris and Yaeger⁵. The surface geometry is modeled by specifying key cross-section lines and body lines. These lines may be likened to the ribs and stringers used in fuselage manufacturing processes. Figure 4 illustrates a typical array of line models which have been augmented for interrogation by a fine grid system. Note that the actual grid point representation of the fuselage shape is approximate with large surface discrepancies near the nose region. The surface boundary slopes that are enforced at the grid points are exact. Slender body theory provides a correction for the surface displacement effect which is suitable when cross-sections are nearly circular in character. Additional details of the fuselage boundary simulation can be found in Reference 2 while nacelle and pod boundary conditions are provided in Reference 3.

WING AND PYLON BOUNDARY CONDITIONS

The wing and wing wake surfaces are modeled in a plane which lies along rectangular coordinate lines. Wing boundary conditions are enforced in an evenly spaced embedded grid system (Figure 5). The wing and wake points that lie on this surface are double valued. Extrapolations to the surface are not required. Wing chord leading and trailing edges are positioned midway between two grid points. A shearing transformation provides uniform grid resolution between the wing root and tip. Circulation jump conditions are enforced between the wing trailing edge and the back plane which represents downstream infinity.

Pylon surfaces are not aligned with the wings sheared coordinate system. Boundary point instabilities will result if special provisions are not made. These instabilities become increasingly severe with higher wing sweeps, higher grid densities, and larger volumes of supersonic flow. An image or dummy grid point concept is used to enforce pylon boundary conditions. The grid points that are used to compute the axial and cross-flow velocity components must be carefully chosen to insure that the system diagonal dominance is enhanced³. This scheme is identical in character to that employed at fuselage sides and symmetry planes¹ which are similar to pylon surfaces because they are not aligned with the wing grid system.

CANARD SURFACES

Canard surface boundary conditions are imposed in the same manner as wing surface boundary conditions. However, the treatment of two lifting surfaces which may have an arbitrary distance between them presents problems which the basic grid embedding scheme can only partially solve. If computing resources were unrestricted, these problems would not be severe.

The aforementioned solution process involves both a global crude and embedded fine grid systems. The crude mesh system is made up of cells which are evenly spaced between the wing root leading edge and the wing tip trailing edge. Beyond these limits, the cells are gradually stretched so that the first and last points represent infinity. About 38 of the 50 cells fall on the wing planform. The resulting mesh points that fall along the wing spanwise cuts must be sufficient for interactions with the embedded fine grid arrays. If the existing crude grid arrangement is used to repre-

sent two separated planforms, resolution on the small wing and canard tip chords would be compromised. Crude/fine grid interaction may be impaired. Crude grid cells could be increased, but this would increase computing time and storage requirements. In addition, the total number of required cells would then be a function of the planform separation.

In order to maintain canard-wing-body computer resource requirements at levels comparable to wing-body levels, a special streamwise grid transformation is used. The following transformation relates the computational variable ξ to the physical variable X .

$$X = a_1 + a_3 \xi + a_5 \xi^3 + a_7 \xi^5 + a_8 \left(\frac{\xi}{1 - \xi^2} \right) \quad \text{For } -1 < \xi < 1 \quad (2)$$

$$-\infty < x < \infty$$

The characteristic length (CL) is taken to be the total streamwise length of the two planforms. Note that the existing 50 streamwise cells are evenly spaced in the computational domain. The a_8 coefficient which controls the grid stretching to infinity is set equal to one-third the CL. Note that the transformation is symmetric about the $\xi = 0$ axis for $a_1 = 0$. The coefficients are computed by using the following constraints. First, sixty percent of the computational grid lines are required to lie in a region of length 0.9 CL. Second, the highest grid density region has no less than four grid lines along the planforms minimum chord (typically, the canard tip chord). As a final constraint, the transformation function must have a local maximum at $\xi = 0$. The last variable, a_1 , is adjusted to position the systems two high-density regions about the critical reduced tip chord areas. A typical wing-body-canard configuration along with the streamwise grid arrangement superimposed can be seen in Figure 6. Note that the grid point distribution must satisfy two basic requirements: First, the points must be optimized for resolution given arbitrary two planform arrangements, and second, the stretching to infinity must be consistent with the decay of the disturbance potential. The transformation just described is the result of considerable experimentation. It should prove to be satisfactory for a wide range of two-wing configurations.

A separate embedded fine grid system is constructed for each planform. Each system employs a shearing transformation which is used to align the grid with the planform leading and trailing edges (Figure 7). Fortunately, these grid systems are independent, and it is not necessary to develop a single grid transformation which is suitable for the planforms together. Interference between the canard and wing surface is transmitted by the all encompassing global crude grid structure.

The canard and wing surfaces may be separated by a vertical distance. The lifting surface wakes are constrained to lie in a plane. This is an approximation of the physical flow in which the wake surface is deflected by the lifting surface downwash field (Figure 8). The undeflected wake assumption is widely used in computational methods. Apparently, only subtle errors are introduced when a single wing is analyzed. For wing-canard solutions, however, the canard wake may be very close to the wing surface. Wake displacement effects may be significant. These effects have yet to be investigated.

LIFTING SURFACE VISCOUS ANALYSIS

Wing viscous effects are computed by coupling a modified Bradshaw⁶ boundary layer computation with the basic finite-difference potential flow scheme. The modification extends the two-dimensional technique to incorporate first order sweep effects. The boundary layer method provides details of the thin viscous layer which is close to the wing surface. The global inviscid calculation provides the wing pressure distributions required by the boundary layer analysis. The physical quantities that are of primary concern are the skin friction drag component, C_{Df} and the boundary layer displacement thickness, δ^* . This approach has been chosen primarily because it is relatively inexpensive. Although it is approximate in the three-dimensional sense, computations indicate that it is probably consistent with other compromises which have been made.

Examples of viscous flow phenomena occurring on wing sections have been sketched in Figure 9. Note that a supercritical type shape has been illustrated, but similar flow characteristics would be observed on conventional section shapes with control surface deflections. Details of the shock wave-boundary layer interaction are not computed because the Bradshaw scheme operates with a relatively crude 40-point chordwise grid pattern. This effect includes both a local thickening of the boundary layer and a weakening of the shock wave strength. Instead, non-conservative finite-difference operators are employed to approximate the flow equation. These operators do not conserve mass across shock wave surfaces. This fortuitously approximates the shock weakening phenomena. Global boundary layer displacement thickness effects are predicted by the present method. For aft-loaded wings or wings with control surface deflections, this effect can have a dramatic effect on wing loading and shock wave positions.

The modified chord technique of Nash and Tseng⁷ has been implemented by Mason⁸. This scheme permits a two-dimensional boundary layer method to be extended to the three-dimensional case provided that the flow does not deviate far from the infinite sheared wing type. The effective wing sweep angle is taken to be that of the mid-chord span line which varies between the wing root and tip (Figure 10). In addition, an effective Reynolds number is required. This is obtained by requiring that the shear component in the normal direction bear the same relationship to an effective Reynolds number that the actual shear stress has to the specified Reynolds number. This is accomplished by using the Reynolds number based on the momentum thickness at transition in the Karman-Schoenherr formula. Bradshaw's turbulent boundary layer method provides the foundation for this scheme. The initial laminar boundary layer is predicted by Thwaites method modified for compressible flow.

The coupled viscous/inviscid interaction solution requires that the boundary layer computation be performed during flow field development. The computed boundary layer displacement thickness slopes are added to the wing geometric surface slopes to provide an equivalent inviscid wing shape for the inviscid scheme. In the present small-disturbance method, only the boundary condition slopes are modified. The planar wing boundary surface does not change. The viscous computation will stop when flow separation is predicted. At this point, the slope of the displacement thickness boundary is extrapolated to the trailing edge. This will permit the calculation to proceed. However, if separation points are in front of the 94-97% chord region, computed and experimental flow fields may be significantly different.

Many wings that are of practical interest have section shapes with cove regions. The existence of this type of geometry coupled with extreme flow conditions can become a problem during the solution process if cove-type separations are encountered. The conventional slope extrapolation process will not produce the proper δ^* character. To

overcome this problem, an empirical relation developed by Bavitz⁹ for two-dimensional flows has been extended to permit its application to three-dimensional flows. This temporary "fix" allows the solution to proceed. When the more realistic attached cove flow fields are computed, the relation is not required.

Viscous corrections to the wing surface boundary condition are refined on every 20th relaxation cycle using an under-relaxation factor of 0.6. For a typical wing-fuselage configuration, there are 15 spanwise stations along the wing between the root and tip. The viscous computation is performed twice at each wing station, once for the upper surface, and once for the lower surface. Figure 11 illustrates the dramatic variation in viscous effects that might be encountered in practical applications. Each example has been taken from the mid-wing region of the sample configurations which will be described in a subsequent section. The first application shows the surface slope modification to a thin high lift fighter wing section. The second application is representative of a thick transport wing. The final example illustrates the low aspect ratio delta wing section found on the Space Shuttle Orbiter.

CONSERVATION OF COMPUTING RESOURCES

An inexperienced analyst applying some of the more sophisticated computational aerodynamic methods of today may use more resources to perform an investigation than an experimentalist. This, in part, defeats the purpose of the computer tool. Care must be taken to insure that computing time and core storage requirements are kept to as low a level as possible. The present method requires 50 minutes of CPU time on the IBM 370 system. IBM 3030 CPU time is approximately 25 minutes while the CDC 7600 times are approximately 10 to 12 minutes. To some, this resource level may seem excessive. The potential user, however, should be aware of what can be determined or evaluated for this investment. This section will describe some of the techniques that are used to keep computing resource requirements at "reasonable levels." The next section will provide a foundation of past experience which illustrates computational capabilities.

The multiple embedded grid approach enhances configuration boundary point efficiency. Conventional methods with a single grid place 2% of the total field points on the configuration as boundary points. The present nested grid scheme enriches this level to 4%. This increase in boundary point efficiency can be used in different ways. The total number of field points can be halved and resolution will be equal to a conventional scheme. This would result in reduced computer running times, or, the total number of field points could be comparable to a conventional scheme. This would increase boundary surface resolution by a factor of two. While some investigators have used the embedded grid system to reduce computing cost¹⁰, the present method is primarily concerned with enhanced boundary resolution. It can be seen that if a conventional method is used to obtain 7000 surface boundary points, a total of 350,000 field points would be required. The resources required for a solution would render the code impractical for engineering applications.

The computed results presented in this paper were obtained by fixing the number of relaxation cycles rather than by specifying a convergence criteria. One-hundred crude grid iterations were followed by 80 crude/fine cycles. Experience indicates that wing lift effects propagate very slowly for high aspect ratio wings as the flow field evolves. By taking the solution at a fixed number of cycles, a portion of the configuration lift may be lost. To compensate for this lift loss, high aspect ratio configurations are typically analyzed at a higher incidence than that given by the experiment. Typically, a 1/2 degree angle-of-attack increment is required. This artifice may be used in lieu of doubling or tripling the iteration cycle count to obtain an absolute lift level.

Computations indicate that nacelles and pylons have a relatively small effect on the global flow field when compared to the disturbances caused by the main wing and the fuselage. This difference is partially due to the size of these components and the fact that loadings are usually low. To take advantage of this effect, nacelle and pylon boundary conditions are enforced only during the last half of the solution process. This reduces the number of operations required for complex configuration simulation and saves computer input/output which is needed for boundary surface potential computations.

Note that a simple two-dimensional finite-difference method has been selected for computing viscous effects in a strip type mode. This approach increases computer resource requirements by 30% when compared to an inviscid analysis. Incorporation of a three-dimensional integral method would probably result in a comparable increment. If, however, a three-dimensional finite-difference scheme were incorporated, costing increments would be in the 400% to 500% range. The user must evaluate the predictive capability of each scheme and judge what value each scheme has. Considering most practical engineering applications, the capability/cost relation provided by the two-dimensional approach is very attractive.

The computational method requires a single global crude grid system and multiple embedded fine grid arrays. The computer code, however, need be dimensioned for only a single crude grid and a single fine grid system because grid interactions involve only two systems. Additional fine grid systems are stored on disk units to be called upon when needed. As a result, the codes basic core storage requirement does not increase as configuration complexity increases.

COMPARISONS WITH EXPERIMENT

Correlations with experimental force and pressure data have been made for a large number of aircraft configurations. Three of these cases have been selected because they illustrate variety in geometry and large variations in flow field severity. In addition, if the separate cases are combined, many features of the code are demonstrated. It should be noted that slender shapes and mild flow conditions that cater to small disturbance assumptions are not included. In particular, the fighter configuration maneuvering flow condition is extreme and the space shuttle orbiter geometry is quite blunt. The transport configuration shock waves are comparable to those typically encountered at cruise conditions.

Figure 12 illustrates an advanced wing-fuselage-canard fighter configuration which has been designed for a fighter-penetrator mission. Correlations with experimental wing and canard pressures¹¹ have been superimposed on the configuration sketch to show the three-dimensional character of the resulting flow field. Comparisons are somewhat impaired by wing tip lower surface flow separation and a canard leading edge flow phenomena which is not well understood. But, the global flow character of this high lift ($C_L \sim 0.67$ $M = 0.9$) transonic maneuvering wing is predicted. Note that canard upwash/downwash interference effects can be identified along the main wing leading edge between the root and tip.

Three wings were designed for this wind tunnel model. Transonic maneuver wing comparisons were plotted in

Figure 12. Force comparisons for this wing, the transonic cruise wing and supersonic cruise wing can be seen in Figure 13. The character of the different drag polar shapes is predicted. This configuration is now undergoing refinements which are generated by combining the computational method with the optimization techniques of Vanderplaats¹².

The Lockheed C-141 transport configuration can be seen in Figure 14. Data from both wind tunnel and flight tests are available. This case is interesting because it illustrates interference effects caused by nacelles, pylons, fuselage fairings, and viscous effects. The fuselage geometry model, made up of body and cross-section lines, can be seen in Figure 15. Wing-body juncture and landing gear fairings can be identified.

Figure 16 (A-D) compares wind tunnel pressure data¹³ taken at four wing stations. The flow condition is $M = 0.77$, $\alpha = 1.5^\circ$, and $R_e = 2 \times 10^6$. Note that the analysis method angle-of-attack is $1/2$ -degree higher than that of the experiment. The experimental variations in flow field character which result from the addition of the nacelle/pylon combinations are accurately predicted. The inboard station has been selected to demonstrate the effect of the wing boundary layer. Figure 17 shows the computed result that would be obtained if an inviscid analysis were performed. Although the wing section is conventional in character, the viscous effects are significant.

Flight test data for the C-141 at the flow condition $M = 0.82$, $\alpha = -0.3^\circ$, $R_e = 36 \times 10^6$ is contained in Reference 14. This reference also provides inviscid isolated wing computational code correlations. These code results were compromised by many geometric modeling restrictions. In addition, they were produced seven years ago. It is interesting to note that if the present method is used in an isolated wing mode, the comparison with flight test data is not significantly different than that given by Reference 14 (Figure 18). Correlation is only fair on the wing upper surface, and it is very poor on the lower surface at this inboard station. The lower surface discrepancy is caused by a combination of nacelle/pylon and fuselage interference effects. The dominant effect, however, is a flow acceleration caused by the fuselage landing gear fairing. The computed wing-fuselage-nacelles-pylons result can be seen in Figure 19. The superimposed computed pressures for this case can be seen in Figure 20. The lower surface flow acceleration and shock wave is predicted. Comparisons at two outboard stations can be seen in Figure 21.

The Space Shuttle launch configuration can be seen in Figure 22. Reference 15 provides pressure data for all of the components throughout the transonic launch range. Figure 23 shows the details of the orbiter, external tank, and solid rocket booster line models. This diagram also illustrates the axial resolution that is available when embedded fine grid arrays are employed. Figure 24 provides a more accurate representation of the actual geometry details that are resolved depending on whether the flow about the external tank is of primary interest (Figure 24A) or that of the orbiter (Figure 24B).

Pressure distribution comparisons for the top and bottom external tank centerline can be seen in Figure 25 at the flow condition $M = 0.9$, $\alpha = 0^\circ$. Disturbances caused by the orbiter nose shape are apparent. The orbiter's wing flow is severely separated inboard and this affects the entire wing. However, a typical wing outboard pressure comparison has been included in Figure 26.

Data/analysis comparisons for the non-symmetric orbiter fuselage are interesting because they show body fairing disturbances. In addition, the flow character varies depending on whether the transonic Mach number is slightly less than or greater than 1.0. Mach 0.9 and Mach 1.1 correlations can be seen in Figure 27 (A-D). The change in flow character observed aft of the canopy at $M = 1.1$ is probably caused by expansion waves reflecting off bow and windshield shock waves. Note that the bottom centerline pressures are in part influenced by struts and connectors which cannot be adequately modeled.

CONCLUDING REMARKS

A transonic computational method which may be applied in the analysis of complex aircraft configurations has been described. Throughout the text, the simplicity of the method has been stressed. Coordinate systems are essentially rectangular in character, boundary conditions are planar, linear interpolations are used for multiple grid interactions, a simple two-dimensional strip boundary layer analysis provides viscous effects, and finally, a fast, easy to use fuselage modeling system yields arbitrary body surface normals. When compared to other computational methodology, this approach lacks sophistication. However, this simplicity plays an important role in providing the flexibility required to treat complex configurations.

During the past four-year period, several papers have been written to describe the evolution of this computational method¹⁻³. These papers illustrate computed results for isolated bodies, isolated wings, and wing-body configurations. This paper includes computed results for aircraft configurations with canards, nacelles, pylons, fuselage fairings, and severe wing viscous effects. It is interesting to note that a single method can be used to analyze all of these configurations, from the simplest isolated body to the most complex wing-fuselage geometry. While no basic research purpose is served, the engineering analyst can put this capability to use in studying component interference effects. In effect, the computer analysis can be used in the same manner as a wind tunnel.

REFERENCES

1. Boppe, C. W., "Calculation of Transonic Wing Flows By Grid Embedding," AIAA Paper 77-207, January 1977.
2. Boppe, C. W., "Computational Transonic Flow About Realistic Aircraft Configurations," AIAA Paper 78-104, January 1978.
3. Boppe, C. W. and Stern, M. A., "Simulated Transonic Flows for Aircraft with Nacelles, Pylons and Winglets," AIAA Paper 80-130, January 1980.
4. Waggoner, E. G., "Computational Transonic Analysis for a Supercritical Transport Wing-Body Configuration," AIAA Paper 80-129, January 1980.
5. Vachris, A. F. and Yaeger, L. S., "Quick-Geometry - A Rapid Response Method for Mathematically Modeling Configuration Geometry," NASA SP-390, October 1975, pp. 49-73.
6. Bradshaw, P. and Ferriss, D. H., "Calculation of Boundary Layer Development Using the Turbulent Energy Equation," J. Fluid Mech., Vol. 46, 1971.

7. Nash, J. F. and Tseng, R. R., "The Three-Dimensional Turbulent Boundary Layer on an Infinite Yawed Wing," *The Aeronautical Quarterly*, November 1971, pp. 346-362.
8. Mason, W. H. et al., "An Automated Procedure for Computing the Three-Dimensional Transonic Flow Over Wing-Body Combinations, Including Viscous Effects," Air Force Flight Dynamics Laboratory Report, AFFDL-TR-77-122, Vol. I, October 1977.
9. Bavitz, P. C., "An Analysis Method for Two-Dimensional Transonic Viscous Flow," NASA TN D-7718, January 1975.
10. Henne, P. A., "An Inverse Transonic Wing Design Method," AIAA Paper 80-330, January 1980.
11. Spurlin, C. J., "Wind Tunnel Test of a 1/15 Scale CDAF Model at Mach Numbers from 0.6 to 1.5," AEDC Report AEDC-TSR 79-P28, May 1979.
12. Vanderplaats, G. N., "CONMIN - A Fortran Program for Constrained Function Minimization," NASA TM X-62282, August 1973.
13. Lores, M., Lockheed Wind Tunnel Data.
14. Lomax, H., Bailey, F. R., and Ballhaus, W. F., "On the Numerical Simulation of Three-Dimensional Transonic Flow with Application to the C-141 Wing," NASA TN D-6933, August 1973.
15. Chee, H., "Results of a Pressure Loads Investigation on a 0.03 Scale Model (47-OTS) of the Integrated Space Shuttle Vehicle Configuration 5 in the NASA Ames Research Center 11 X 11 Foot Leg of the Unitary Plan Wind Tunnel (IA81A)," NASA CR-141,836 thru CR-141,842, November 1975.

ACKNOWLEDGEMENT

The authors wish to note that Drs. Mark A. Stern and Warren H. Davis, Jr. of the Aerodynamics Section were responsible for nacelle simulation development.

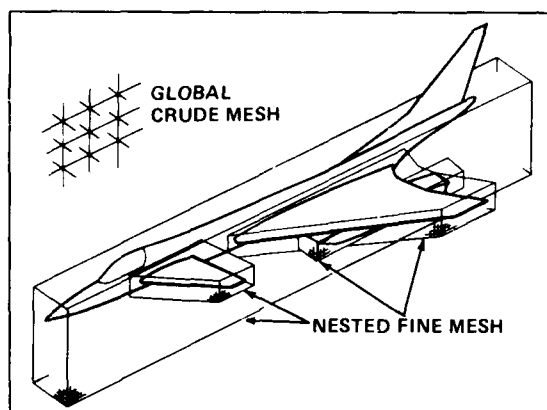


Figure 1 Complex Aircraft Multiple Mesh Arrangement

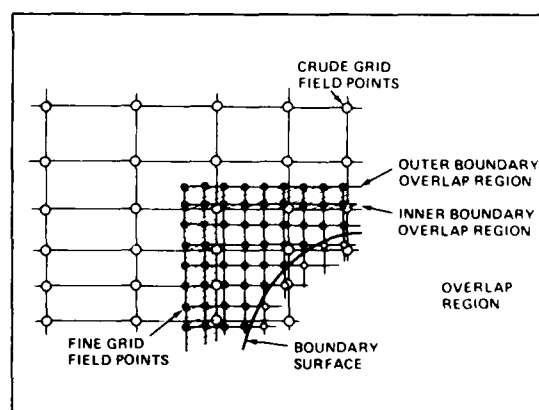


Figure 2 Crude/Fine Grid Interface

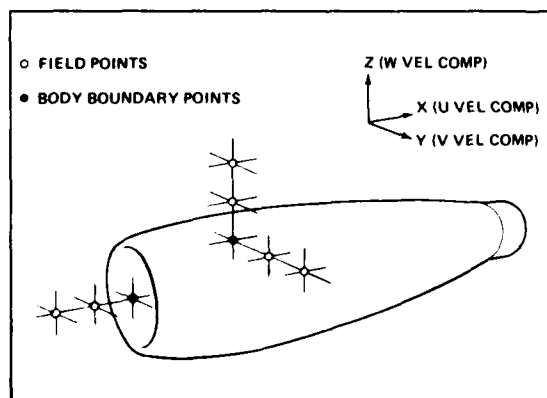


Figure 3 Body Boundary Surface Points

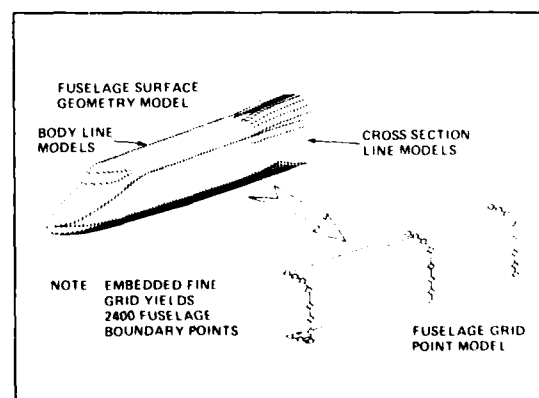


Figure 4 Fuselage Surface Geometry & Grid Point Models

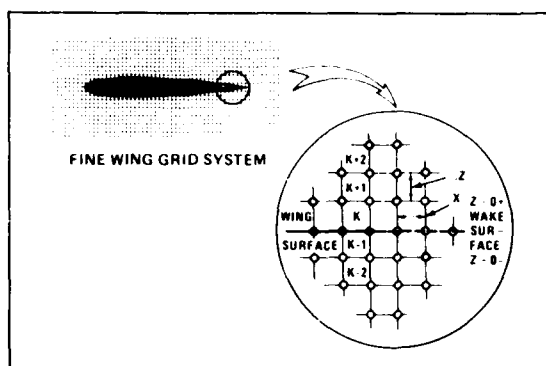


Figure 5 Wing/Wake Surface Boundary Points

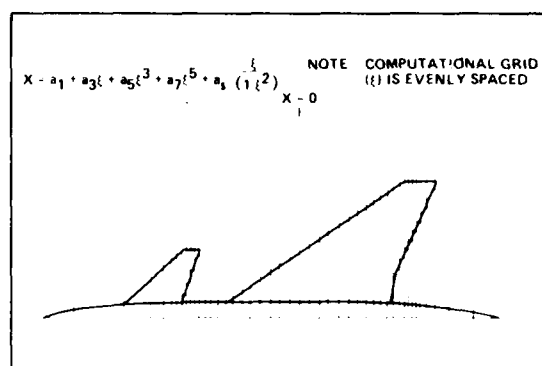


Figure 6 Wing-Body-Canard Configuration with Crude Streamwise Grid Arrangement

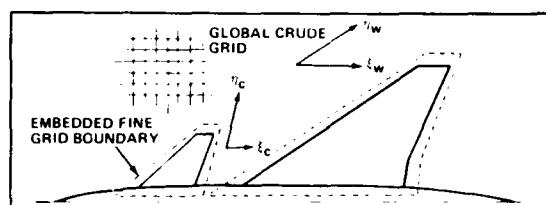


Figure 7 Independent Skewed Grid for Canard & Wing Surfaces

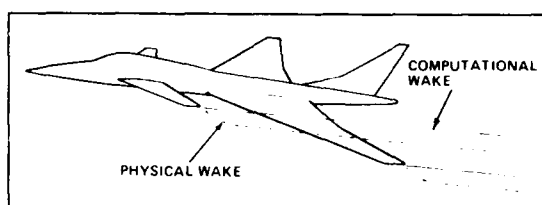


Figure 8 Computational & Physical Wake Surfaces

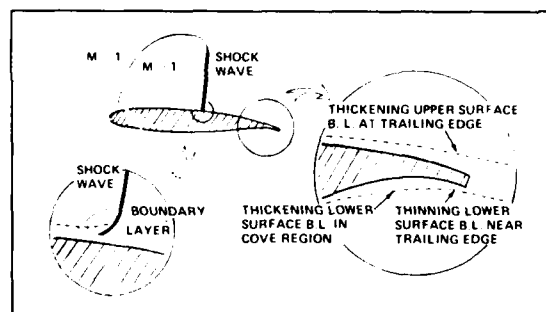


Figure 9 Wing Section Viscous Flow Phenomena

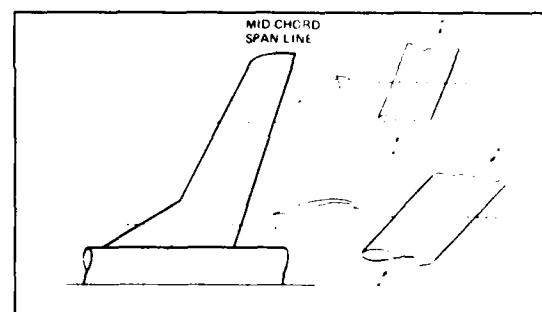


Figure 10 Wing Sweep Angle for Boundary Layer Computation

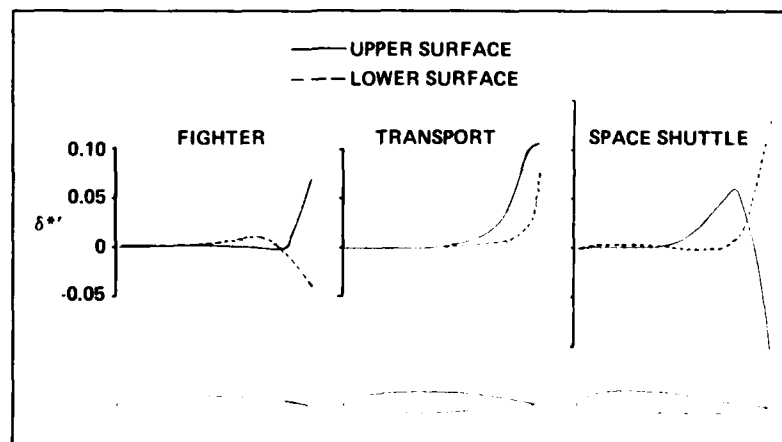


Figure 11 Wing Section Boundary Layer Characteristics

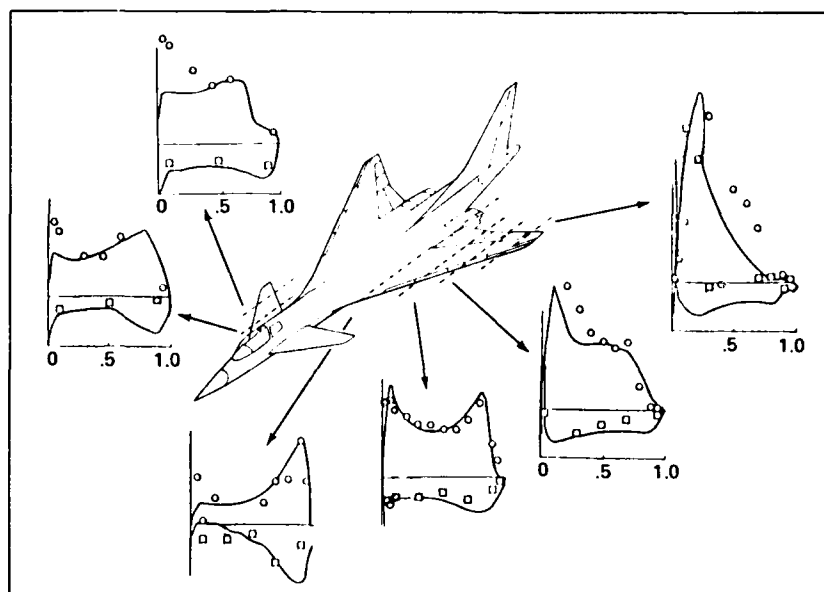


Figure 12 Wing-Body-Canard Pressure Distribution
Correlation ($M = 0.90$, $C_L \sim 0.67$)

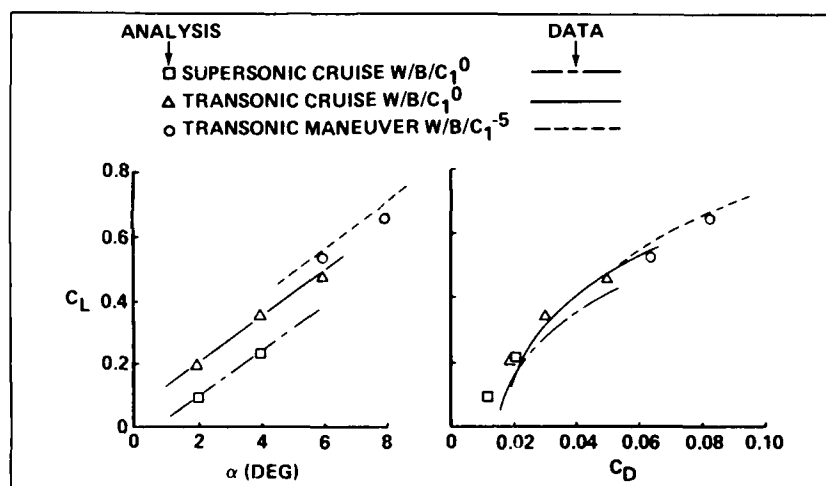


Figure 13 Wing-Body-Canard Force Correlation ($M = 0.90$)

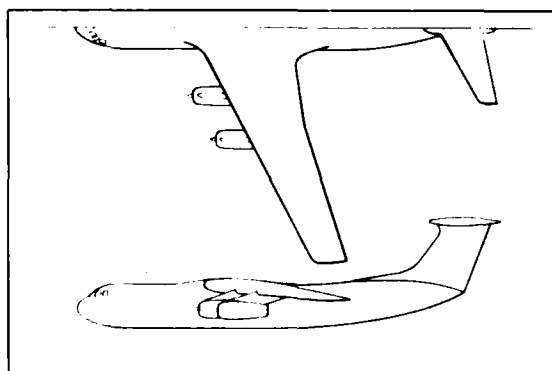


Figure 14 Lockheed C-141 Configuration

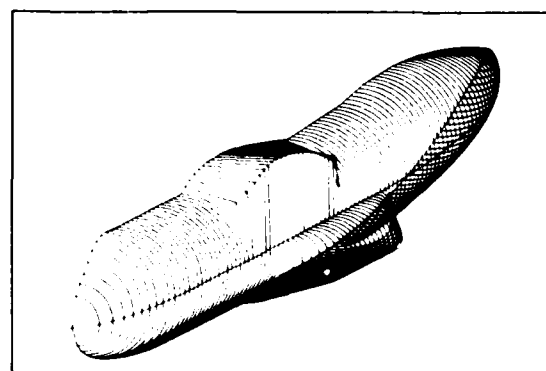


Figure 15 C-141 Fuselage Geometry Model

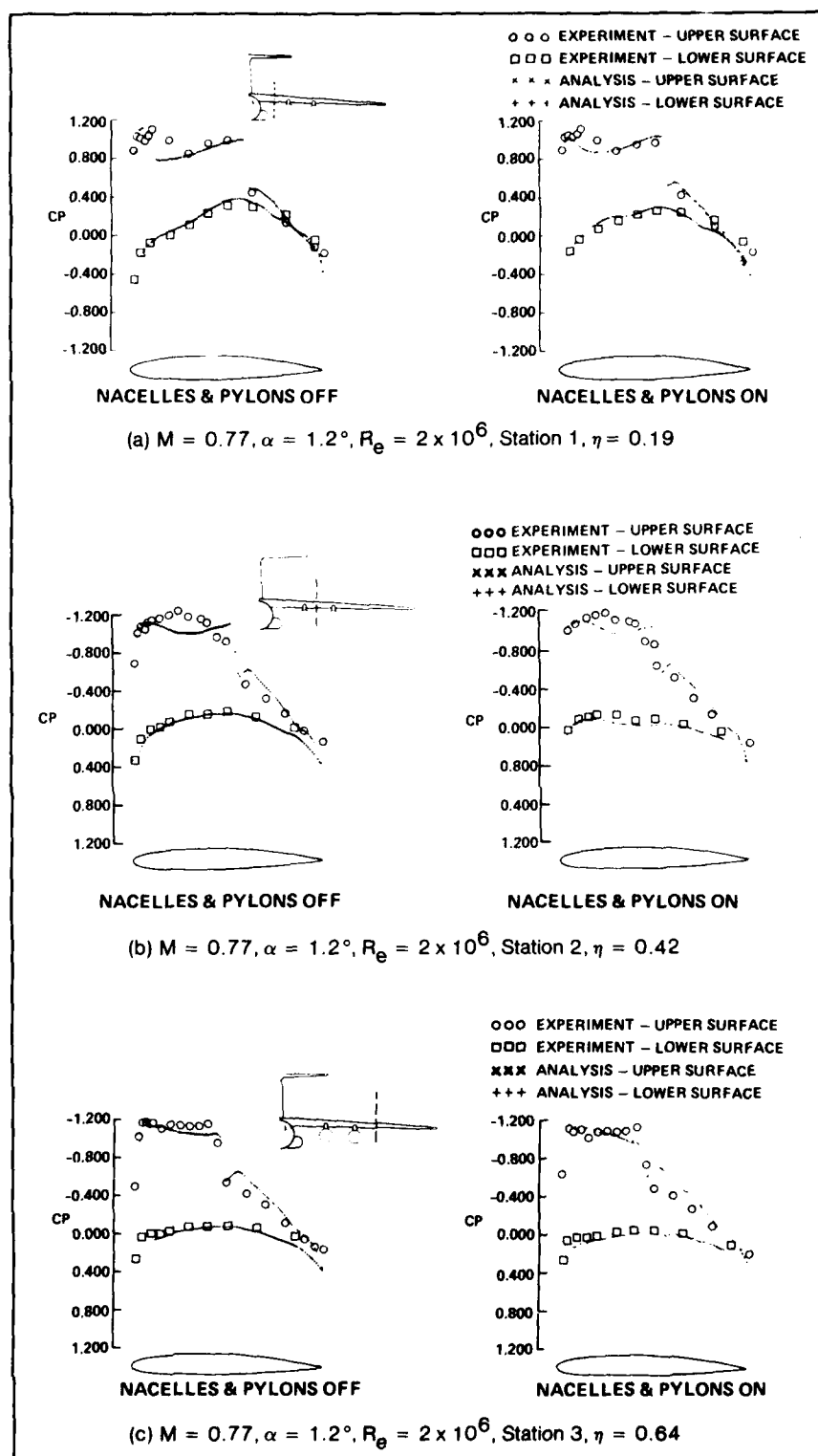


Figure 18 C-141 Wing Pressure Distribution Correlation

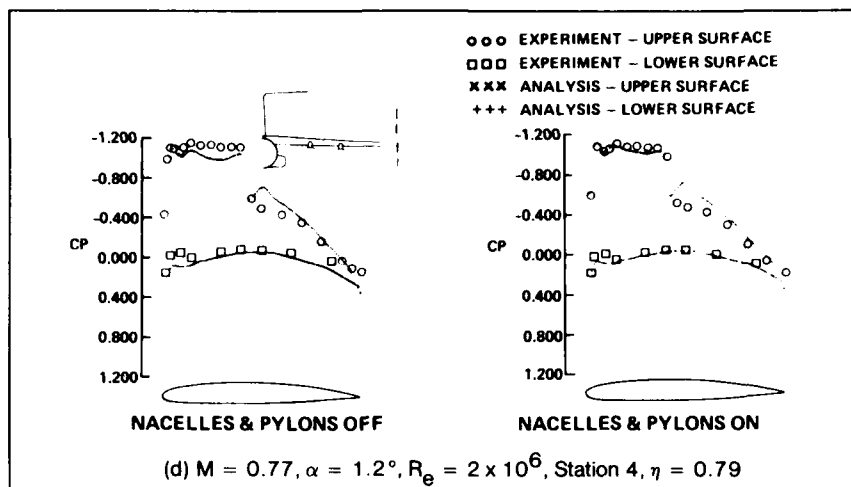


Figure 16 C-141 Wing Pressure Distribution Correlation

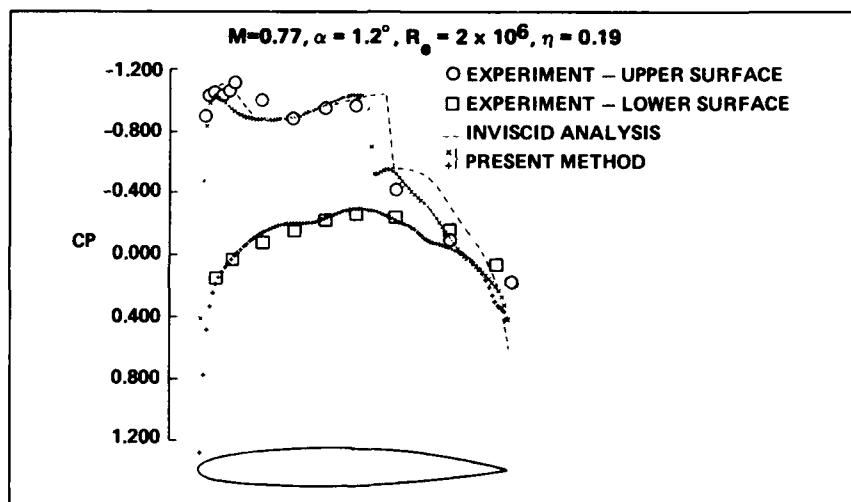


Figure 17 Effect of Boundary Layer on Computed Wing Pressures at C-141 Wing-Body Junction

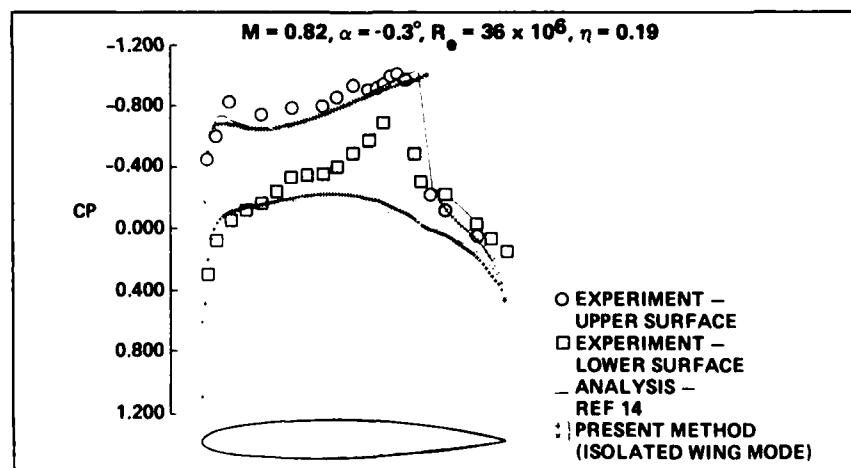


Figure 18 Isolated Wing Simulation of C-141 Wing-Body Junction Flow Field

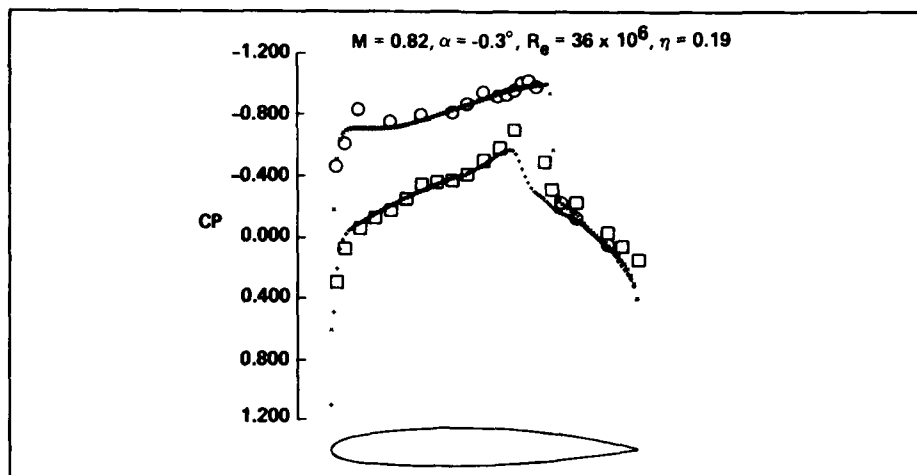


Figure 19 C-141 Wing-Body Juncture Pressure Distribution Correlation

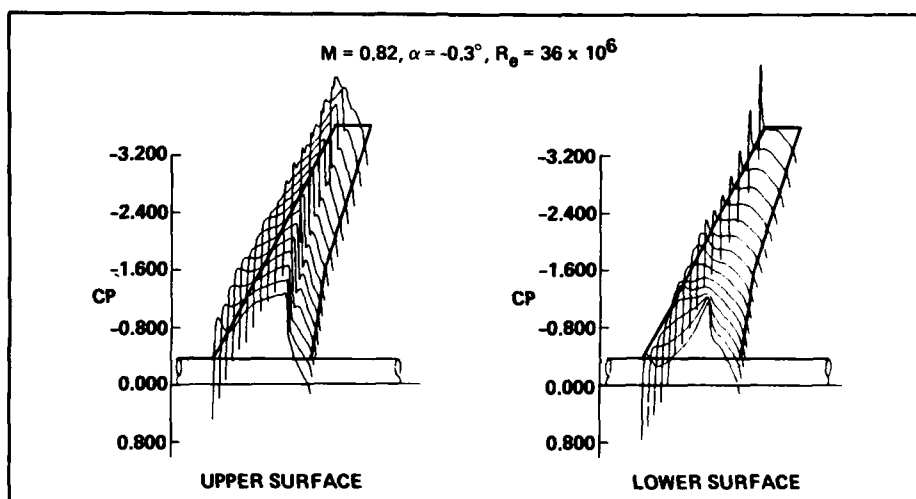


Figure 20 C-141 Superimposed Computed Pressure Distributions

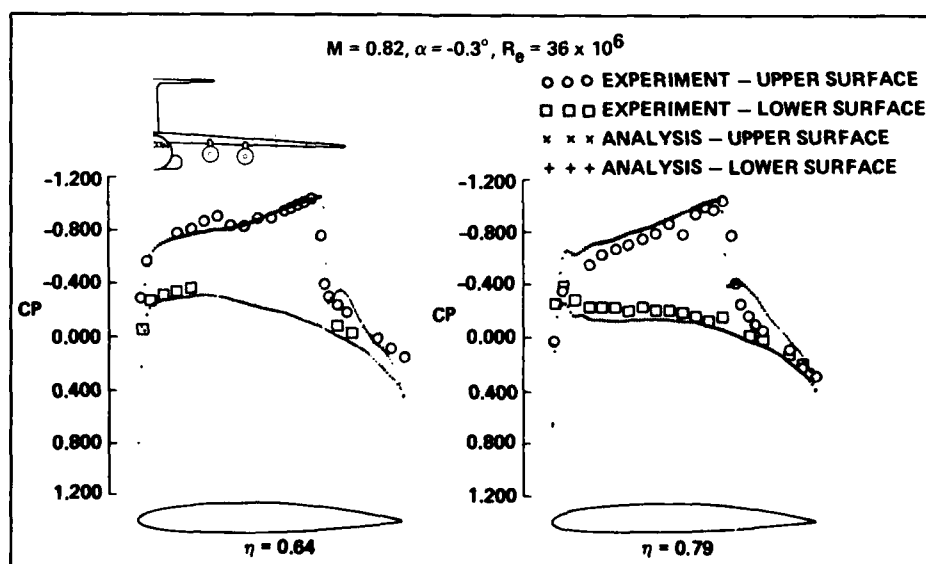


Figure 21 C-141 Wing Pressure Distribution Correlation

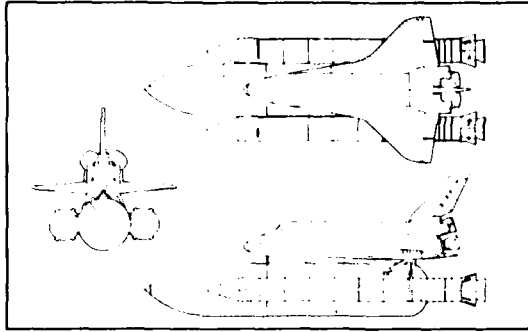


Figure 22 Space Shuttle Launch Configuration

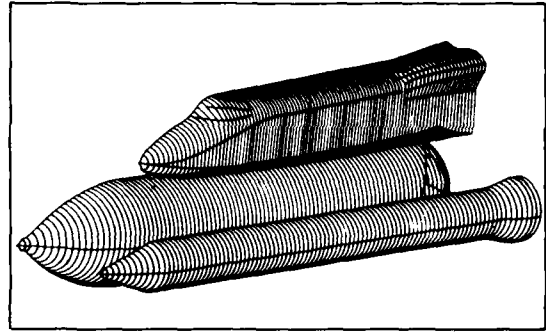


Figure 23 Shuttle Orbiter, External Tank & Solid Rocket Booster Geometry Model

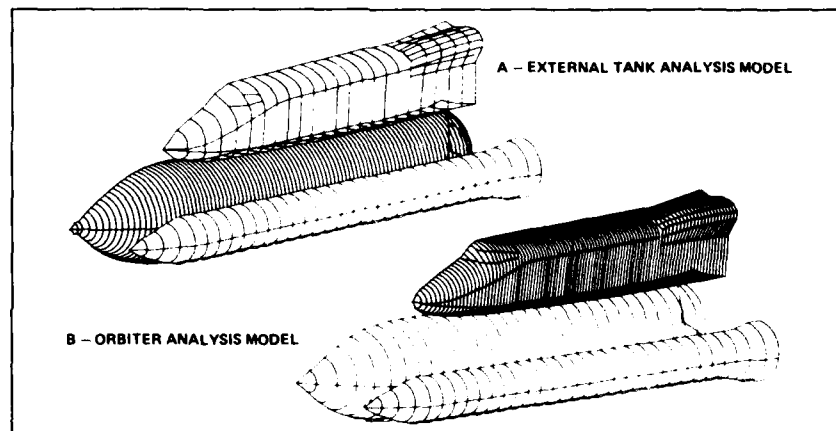


Figure 24 Resolution of Geometry for External Tank & Orbiter Analysis

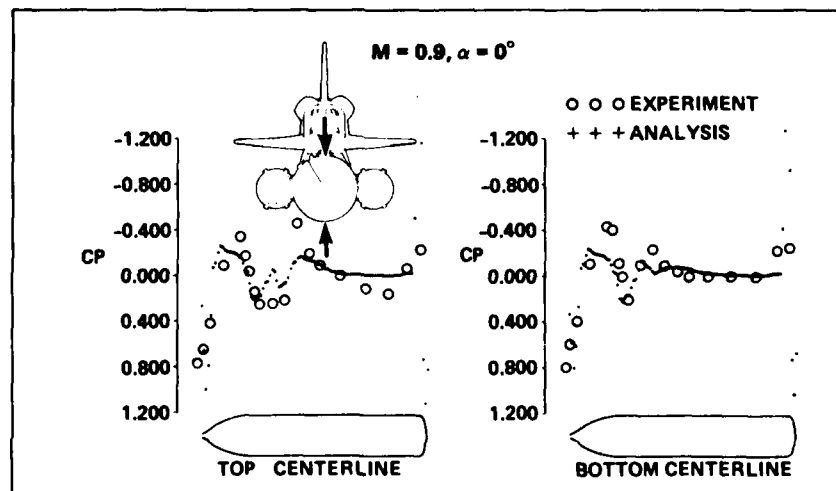


Figure 25 Space Shuttle External Tank Pressure Distribution Correlation

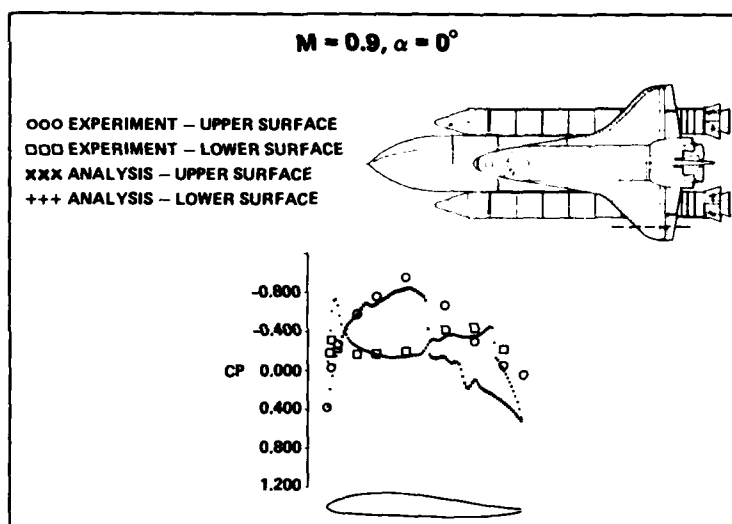


Figure 26 Space Shuttle Wing Pressure Distribution Correlation

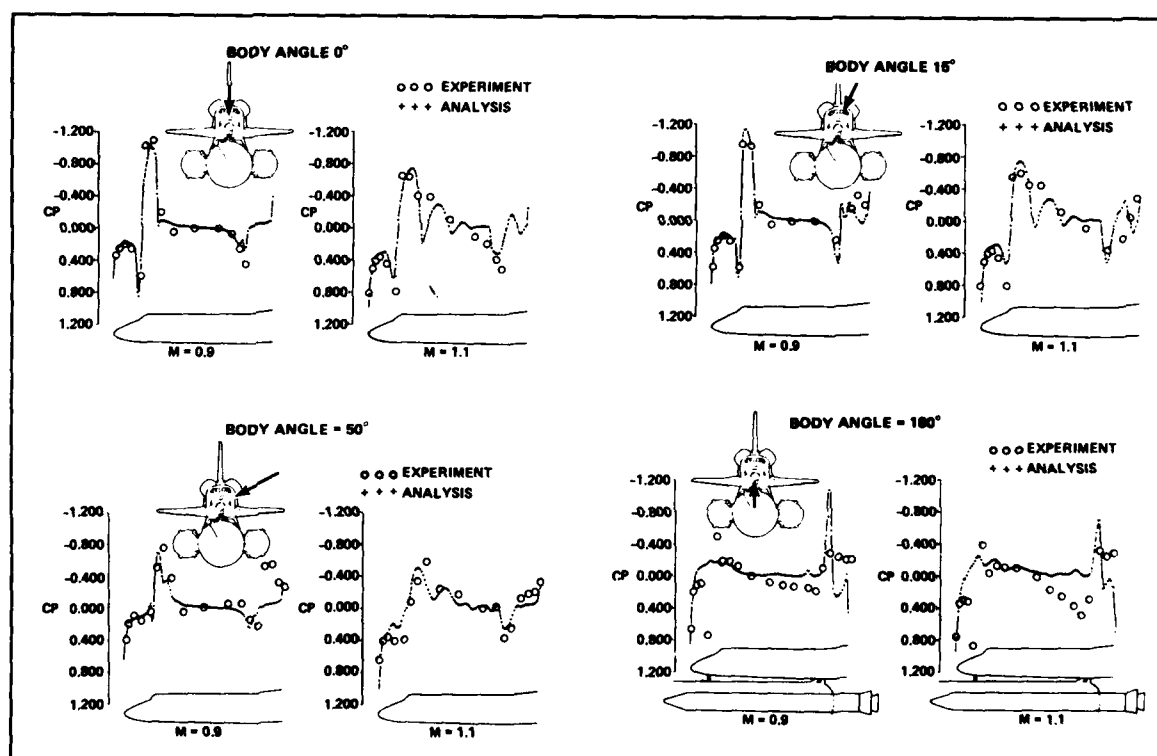


Figure 27 Space Shuttle Orbiter Pressure Distribution Correlation

THEORETICAL AND EXPERIMENTAL STUDIES OF AERODYNAMIC INTERFERENCE EFFECTS

by
I. H. Rettie
Chief Engineer
Aerodynamics Technology Staff

Advanced Airplane Branch
Boeing Military Airplane Company
Seattle, Washington 98124
U.S.A.

1. SUMMARY

Continued refinement of air vehicle configurations has led to a number of specific studies where the mutual interaction of components has been carefully analyzed to understand the nature of the interference effects and to exploit those which were found to be favorable.

The techniques involved are explained by describing specific studies undertaken by The Boeing Company under contract to NASA and USAF. These are in the areas of winglets and wing-mounted engine nacelle installations.

Theoretical studies of aerodynamic forces on winglets have shed considerable light on the mechanism by which these devices can reduce drag at constant total lift and on the necessity for proper alignment and cambering to achieve optimum favorable interference. Results of engineering studies, wind tunnel tests and performance predictions are reviewed for installations proposed for the AMST YC-14 and the KC-135 airplanes.

The other major area of aerodynamic interference discussed is that of engine nacelle installations. Slipper and overwing nacelles have received much attention in recent years because of their potential for noise reduction, propulsive lift and improved ground clearance. A major challenge has been the integration of such nacelles with the supercritical flow on the upper surface of a swept wing in cruise at high subsonic speeds.

2. INTRODUCTION

Aerodynamic forces on a body are indicated and can be measured by disturbances in the flow downstream. Such disturbances include flow patterns resulting from trailing vortex systems, Mach wave propagation, momentum deficits in wakes and regions of turbulence caused by separations of the flow around the body. It is clear that if disturbances which are opposite in nature can be superimposed by careful juxtaposition of the components of an airplane the net force (e.g., drag) can be reduced. This is the basis of the so-called Area Rule. In more detail, if a disturbance caused by a severe adverse pressure gradient or a region of greatly accelerated flow can be mitigated by superposition of a favorable gradient or a region of decelerated flow the resulting air vehicle design will show a significant improvement in efficiency.

Air vehicle contours have achieved a high degree of refinement over the past quarter century resulting from the greater attention paid to interference problems and from the formidable progress made in theoretical design techniques. Modern high speed computers have enabled computational fluid dynamics to advance to the point where confident predictions of flow characteristics can be made for arbitrary streamlined bodies at subsonic, transonic and moderate supersonic Mach numbers.

In this paper are discussed two different types of interference problem where theoretical design tools were used to determine optimum contouring and where experimental data are available to verify the results. The first of these is the close integration of an engine nacelle and a swept wing at high transonic Mach number. The second is the addition of winglets to the tips of a swept wing in order to reduce induced drag at a given value of lift. All the work described here was done by The Boeing Company under contracts to NASA and USAF.

3. WING AND NACELLE INTEGRATION

The nacelle houses an engine and exhibits faired lines forward and aft to accommodate inlet and exhaust areas. Drag increments above skin friction levels can arise from high supersonic velocities near the inlet lip and from adverse pressure gradients in the boat-tailed area. If the nacelle is mounted adjacent to a swept wing the mounting structure can interrupt the isobar pattern of the wing flow and cause severe strengthening of the shock pattern on the upper surface in high speed flight.

Figure 1 shows the type of installation to be discussed here. A forward location of the nacelle places the boat-tailing so that its effect can be offset by the acceleration of flow around the leading edge of the wing. Thus the peak suction on the wing can be locally reduced. However, the plan view shows the problem of flow constriction which occurs in the inboard junction. This must be relieved by adjusting the inboard nacelle lines in the region of the wing leading edge so as to regain a streamline flow similar to that of the wing alone. The principles involved are explained in Figure 2. Typical wing upper surface pressure gradients are shown to deflect an approaching streamline in a manner different to that of the lower surface pressure gradients. Figure 2(b) illustrates the effect on the flow field of adding an infinite vertical plate aligned with the freestream approaching an infinite swept wing. Before the plate is added, two undisturbed streamlines approach the wing and

follow the paths indicated over the upper and lower wing surfaces. If the plate is then added midway between these two approaching streamlines, the wing span load distribution is perturbed as shown in the lower half of the figure. The portion of the plate over the wing upper surface is at an angle of attack to the flow of the undisturbed streamlines. Negative pressures develop on the left side of the plate and positive pressures on the right side. On the wing lower surface, the effect of the plate is not as pronounced, since its angle of attack to the undisturbed lower surface streamlines is much smaller. Therefore, the wing loading is increased to the left of the plate and decreased to the right. From consideration of the plate as one side of a fuselage or of a nacelle, it is apparent that failure to streamline-contour such a surface would result in undesirable changes in the chordwise and spanwise pressure distributions. The deterioration would include isobar and shock unsweeping and more adverse pressure levels, pressure gradients, and load distribution.

The objective at a given high speed cruise condition should be to achieve local Mach numbers no higher than those of the wing alone in the inboard junction and lower than those of the wing alone in the outboard junction. Care must be taken to minimize any lift loss by mounting the pod as low in relation to the wing as is practicable. Then the final result should demonstrate a degree of favorable interference similar to that obtained in an early Boeing test and shown in Figure 3.

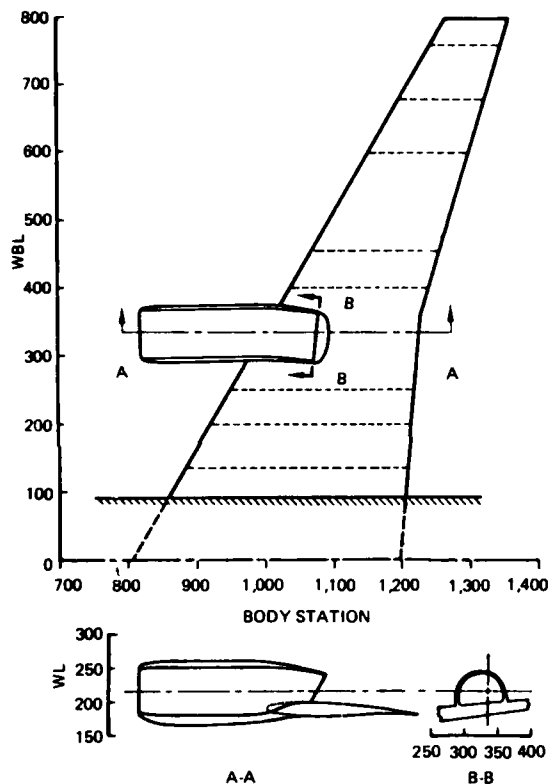


Figure 1. Configuration Geometry

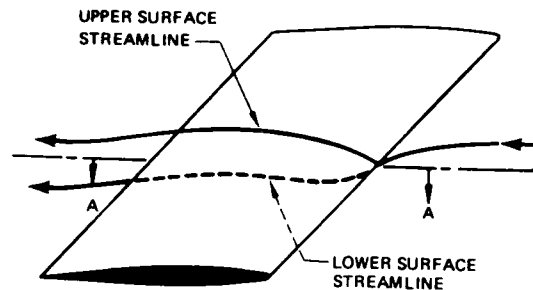


Figure 2(a). Streamline on a Swept Wing

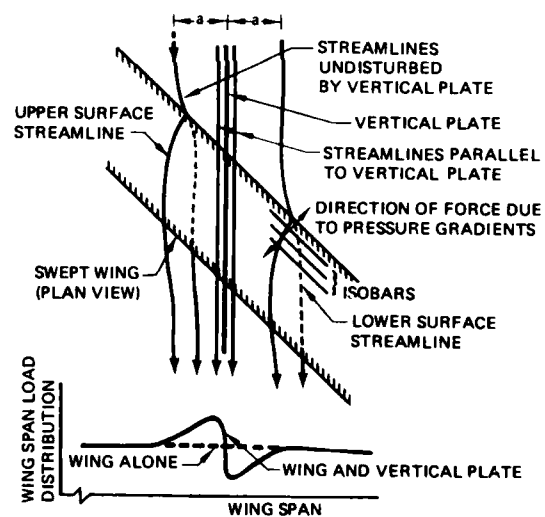


Figure 2(b). Effect of a Vertical Plate on the Flow Field of a Swept Wing

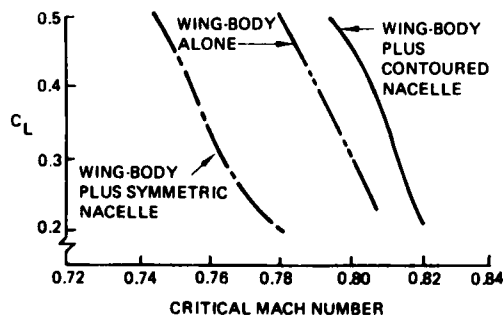


Figure 3. Drag Effect of Contouring Overwing Nacelles

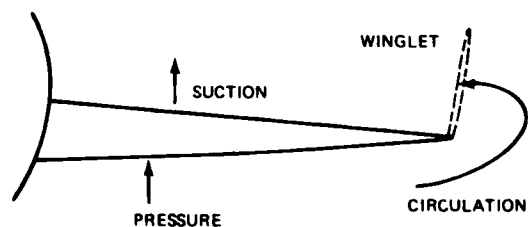


Figure 4. Winglet Flow Environment

4. WINGLETS

The winglet interference problem exhibits similar and some different characteristics. Referring to Figure 4, it can be seen that the basic effect of the winglet must be to inhibit flow around the wing tip thus increasing the lift carried by the wing near the tip and reducing induced drag at a given value of lift. A close examination of the winglet environment shows (Figure 4) that it is immersed in a cross flow. If the winglet is loaded in the same sense as the wing the vertical sheet of trailing vortices causes a cross flow in the opposite direction thus creating opportunities for favorable interference. Expressing this in another way the cross flow induced by the wing rotates the vector of force on the winglet forward thus reducing the net drag increment.

In this way a well designed winglet will be significantly more successful than would be indicated by the "endplate effect" alone. A secondary interference problem exists in the junction between wing and winglet. Care must be taken to avoid excessive adverse pressure gradients which might arise from the superposition of the two thickness forms. In this regard note that a winglet mounted downwards might be easier to design and offers the same opportunities for reduction of drag. Also, the existence of a dihedral angle on the wing or an outward cant of the winglet will be beneficial.

Comparisons between winglets and wing tip extensions involve the complete aerodynamic and structural design of the wing. On the basis of purely aerodynamic considerations the increase in span will probably always be superior. Wing bending moments may, however, be greater for a given performance improvement. Note that the bending moment induced by the lateral force on the winglet is relatively small, particularly over the inboard part of the wing. This possibility has led to consideration of winglets canted in front elevation in order to determine the best compromise between the penalty in wing bending moment and the improvement in induced drag.

The application of winglets to existing airplanes as product improvement items is obviously very important since in such cases the tolerable increases in wing bending moments are strictly limited. Careful design may therefore maximize the performance benefits available within a given wing strength.

5. FLOW COMPUTATION AND AERODYNAMIC DESIGN

All the theoretical studies associated with the nacelle and winglet work described in this paper were accomplished using the subsonic paneling computer program developed at Boeing known as A-230. This code is based upon a three-dimensional potential flow solution to the inviscid flow equations. The basic incompressible solution is modified to account for subsonic compressibility effects by means of the Gothert rule.

The program (see References 1, 2 and 3) is basically a computational routine which calculates the strength of source and doublet sheets distributed over arbitrary surfaces so as to satisfy a given set of boundary conditions on those surfaces. Flow quantities on the surface and in the space around are then calculated and can be integrated to provide forces and moments. Usage of the program is quite general with no distinction between applications to, say, a wing body problem or a nacelle problem. It is applicable equally to external airplane flows and to internal flows in inlets, ducts or wind tunnels.

Green's theorem establishes that the velocity potential at any point in a flow field can be expressed in terms of the induced effects of source and doublet (or vortex) sheets distributed on the boundary surfaces. Existence and uniqueness theorems enable the formulation of properly posed boundary value problems for modeling of a real physical flow field. In order to set up a computational method suitable for high speed digital computers, the boundary surfaces are divided into small panels which are arranged in networks. Source and doublet strengths are assigned to each panel and are determined by the solution of a set of linear algebraic equations relating the singularity strengths to the boundary conditions. The code is currently operational on the CDC 6600 computer. Recent developments incorporating curved panels with varying source and doublet strengths across their surfaces are being incorporated in the PANAIR computational system and are described in Reference 4. These sophistications were not employed in the work to be described here.

Source Panels: These are four-sided and defined by the spatial coordinates of the corners. The panel is coplanar with the midpoints of the lines connecting adjacent corner points. One boundary condition per panel is used. This is a statement specifying the spatial coordinates of the boundary point, the direction corners of a unit vector and the desired velocity component along that unit vector. For an impermeable surface, then, the boundary conditions are specified as in Figure 5(a). The boundary point is positioned at the panel centroid, the unit vector is normal to the plane of the panel and the specified velocity is zero.

Doublet Panels: These are defined by the four corner points as above. Since a constant strength doublet sheet induces the same velocity field as a line vortex lying along its perimeter, a doublet panel (Figure 5(b)) may also be viewed as a quadrilateral ring vortex. Thus a network of doublet panels (Figure 5(c)) provides the same flow as a lattice of ring vortices. The boundary condition is stated in exactly the same way as for the source panels. Doublet panels are particularly suited for the representation of highly curved surfaces such as ducts. This is because the numerical errors due to surface curvature are of second order in the angle subtended by the panel. Doublet panels are also used within a boundary surface such as an airfoil in order to provide net circulation. In this case they do not directly control the external flow which is determined by the panels on the surface.

The doublet panel network provides a complex panel building block which can be used to simulate a nearly continuous general distribution of vorticity by a method of superposition of panels. This is explained in Figure 6. Note how the single doublet panel columns are superimposed to provide a two-dimensional vortex surface. The extension to a three-dimensional surface with doublet panel networks allows construction, for example, of trailing vortex sheets composed of closely spaced, nearly continuous vortex elements.

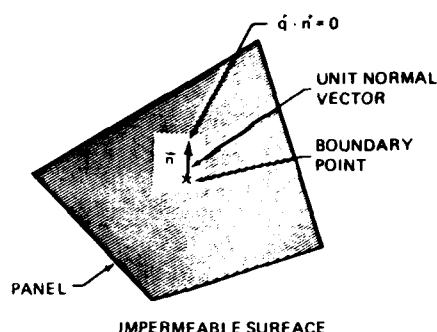


Figure 5(a). Boundary Conditions for an Impermeable Surface

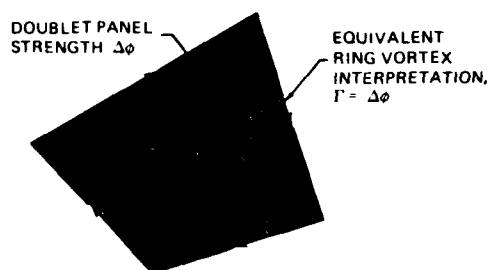


Figure 5(b). Constant-Strength Doublet Panel

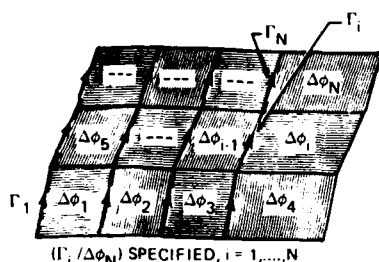


Figure 5(c). Doublet Network Panel

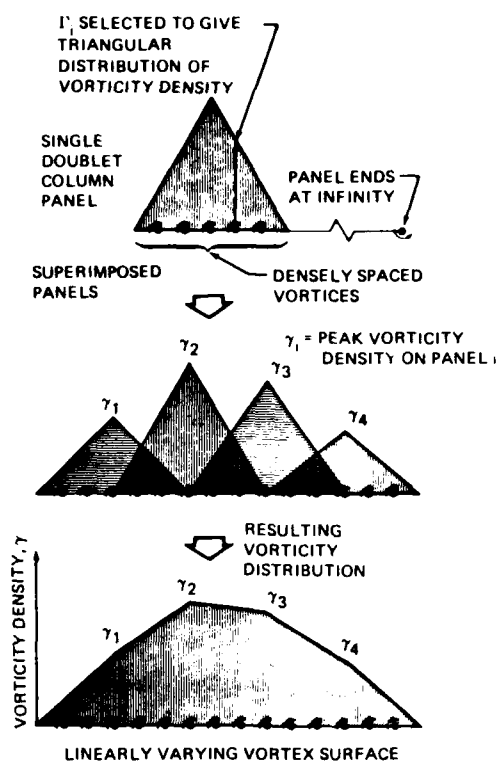


Figure 6. Construction of Two-Dimensional Linearly Varying Vortex Surface by Superposition of Doublet Column Panels

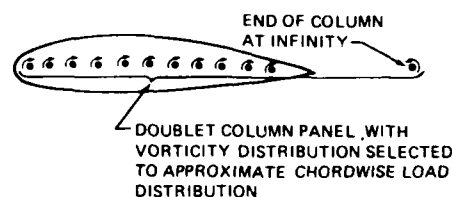


Figure 7. Internal Doublet Column Representation Suitable for Moderately Thick Airfoil

Wing Modeling - For a thin wing where the normal velocity component is continuous across the surface, doublet networks are used. A thick wing is represented by surface source networks with doublet panel columns internally as shown on Figure 7. The internal flow will then be approximately parallel with the internal camber line and the surface source strengths will approximate to the rate of change of airfoil thickness. For highly cambered airfoils or for high angles of attack this single internal weighting may not suffice. Then two internal doublet networks are used simulating the loadings due to angle of attack and camber respectively. In this case an additional boundary condition is required and a convenient requirement is that of flow parallel to the camber line at mid chord.

Nacelle Modeling - Where the objective is to investigate interference flows on a wing surface, this is done most economically with a doublet lattice shell on the exterior surface of the nacelle. Kutta conditions are applied around the exit and the trailing vorticity is simulated. If surface pressures on the nacelle are required, source panels are provided on the interior and exterior nacelle surfaces and interior doublet panels are used to provide the Kutta condition and the trailing vorticity. The effect of the jet can be simulated by identifying a jet boundary shape and panels simulating the distribution of entrainment are then positioned on the jet boundary.

Typical Results - A large number of examples have been published of paneled designs and comparisons of theoretically computed pressures with test data. A relatively simple one is given here primarily to illustrate the method. Figure 8 shows the surface panel representation of the Boeing 737 airplane and the doublet network used to model the wing mounted engine. Comparisons with theory and experiment are shown with nacelles both on and off. A design capability is provided in the code so that the inverse problem can be solved to determine an aerodynamic shape which will produce a given pressure distribution.

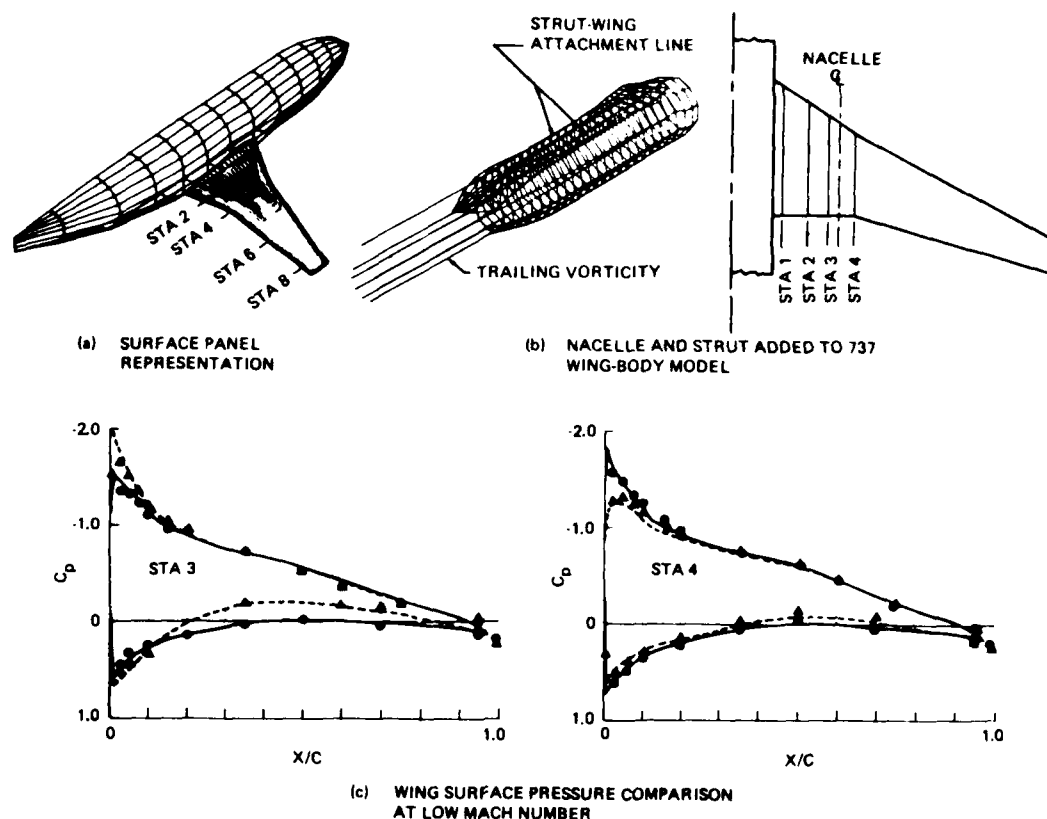


Figure 8. Test and Theory Comparison Showing Influence of Close-Coupled Nacelle Installation on Wing Surface Pressures, Boeing 737

UPPER SURFACE BLOWING NACELLES

A good example of application of this potential flow design process to an aerodynamic interference problem is that of nacelles mounted on the upper surface of a swept wing. The purpose of this configuration is to obtain powered lift at low speeds by blowing engine exhaust air over the upper surface of the wing and a deflected flap. The work was done by Boeing under contract to NASA and is reported in References 5 and 6. The design condition for the study was chosen to be at a Mach number of 0.8 and a lift coefficient of 0.2. The wing was swept at 30° (quarter chord). An engine bypass ratio of 10 was selected in order to meet a noise goal of 55 EPNdB at 153m (500 ft) sideline distance at takeoff and landing.

Both two- and four-engine designs were studied using an existing wing and body design. Preliminary designs were created using approximate wing and body streamlines for the inboard contours of each nacelle and allowing the outboard contours to develop as required to provide the required nacelle internal volume. The spanwise location of these nacelles was selected to provide optimum coverage of the trailing edge flap by the exhaust flow. That part of the aerodynamic design does not concern us here, but was dictated by the requirement for the aeroplane to operate to and from a 610m (2000 ft) field. A D-shaped exit nozzle was chosen together with a flap system which would produce a smooth, radiused upper surface when extended at low speeds for efficient vectoring of the exhaust flow.

The modeling of nacelles for upper surface blowing must be accomplished so as to represent the internal flow of the nacelle and to expose the problems of interference with the wing flow at high speeds. Figure 9 shows the paneling used to model the surface and the lifting system. The Gothert rule was applied for compressibility effects. In fact, the calculations were carried out at a freestream Mach number of 0.7 in order to reduce the extent of supercritical flow. As the Mach number is increased to 0.8, the wing streamlines will remain essentially unchanged in the plan view. They will, of course, change shape considerably in the side view as expansion to high transonic Mach numbers occurs, but the critical contours of the nacelle are in the plan view, not in the side view. Therefore, the use of plan view wing streamlines generated analytically at 0.7M was judged to be valid for the purpose of providing suitable aerodynamic contours at 0.8M.

Preliminary computations provided an approximate lift curve for the configuration and from this a design incidence of zero degrees was chosen. Pressure data was computed initially along the nacelle crown and keel lines and also along lines at approximately the inboard and outboard extremes of the nacelle (3 o'clock and 9 o'clock positions in front view). As an example of this cycle 1 data, see the pressure distributions along the inboard side of the nacelle, Figure 10. It is clear that the variation of pressure along the nacelle implies a boat-tail angle whereas the design was supposed to follow a streamline. This and other modifications were exercised in a second cycle and the isobar patterns shown in Figure 11 were achieved.

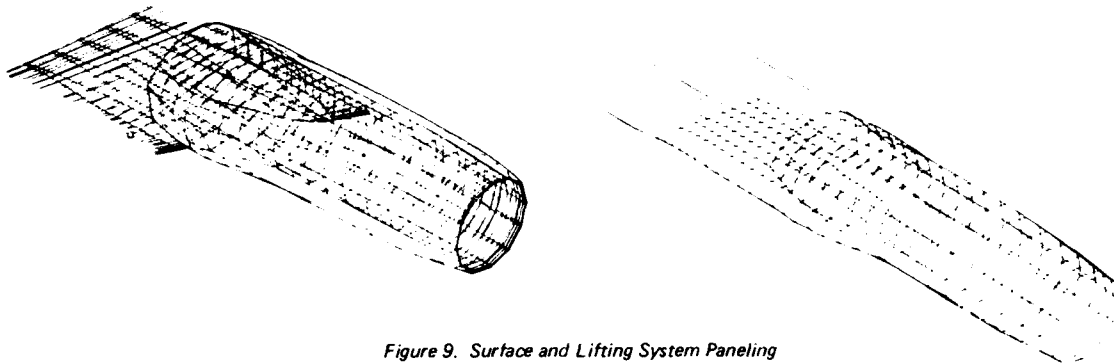


Figure 9. Surface and Lifting System Paneling

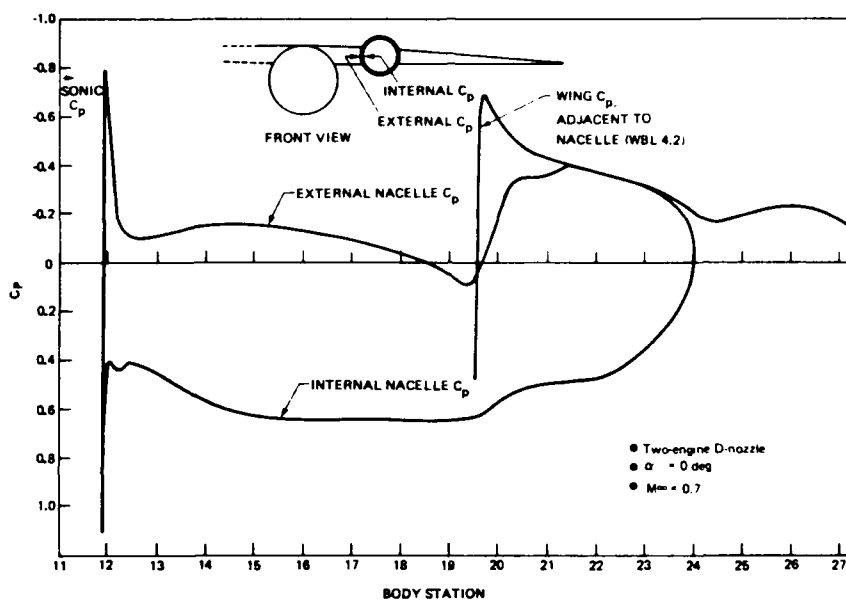


Figure 10. Pressure Distribution Along Inboard Side of Nacelle, Internal and External

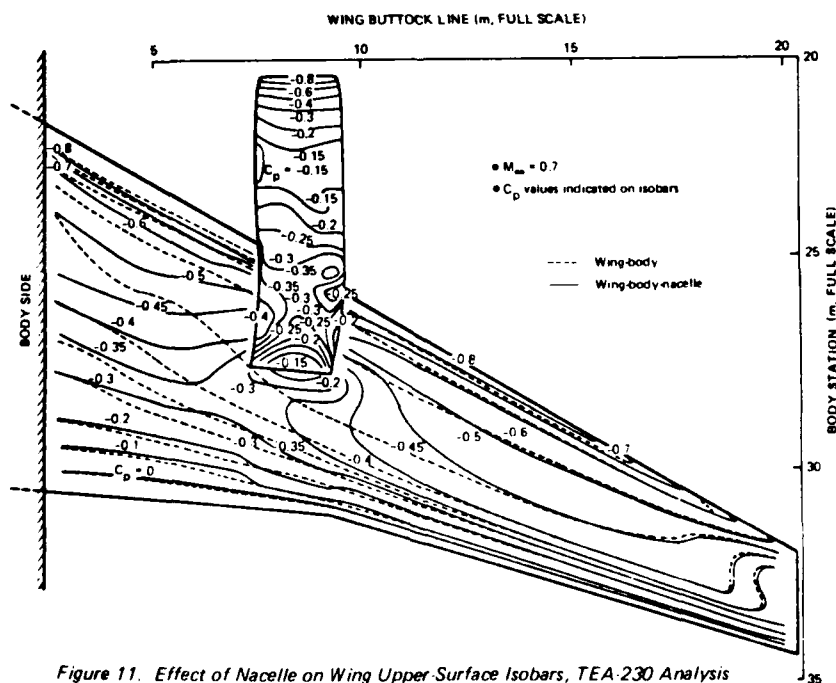


Figure 11. Effect of Nacelle on Wing Upper-Surface Isobars, TEA-230 Analysis

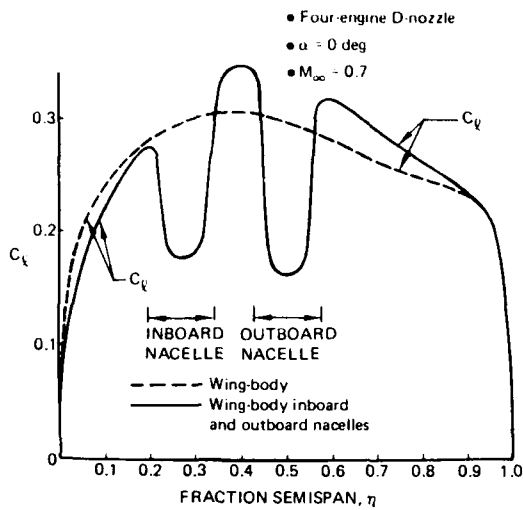


Figure 12. Effect of Nacelles on Sectional Lift Distribution

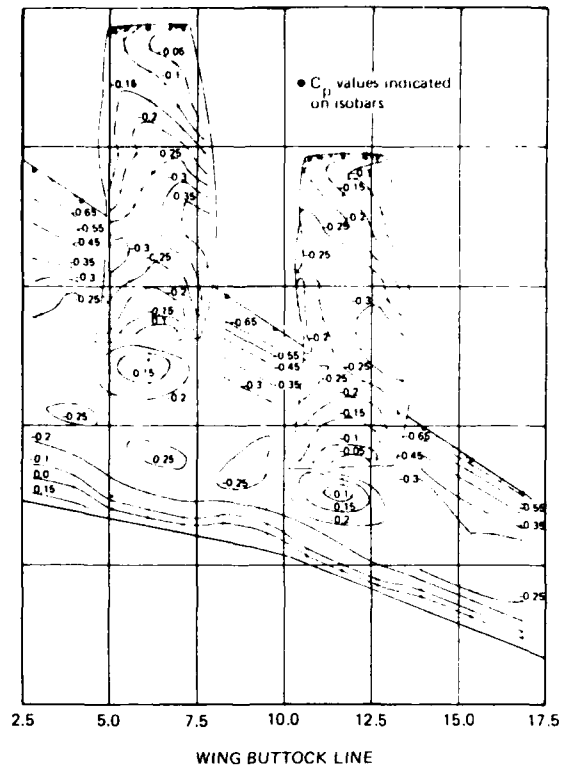


Figure 13. Upper-Surface Isobars,
Four-Engine D-Nozzle Case, $M_\infty = 0.7$, $\alpha = 0$ deg

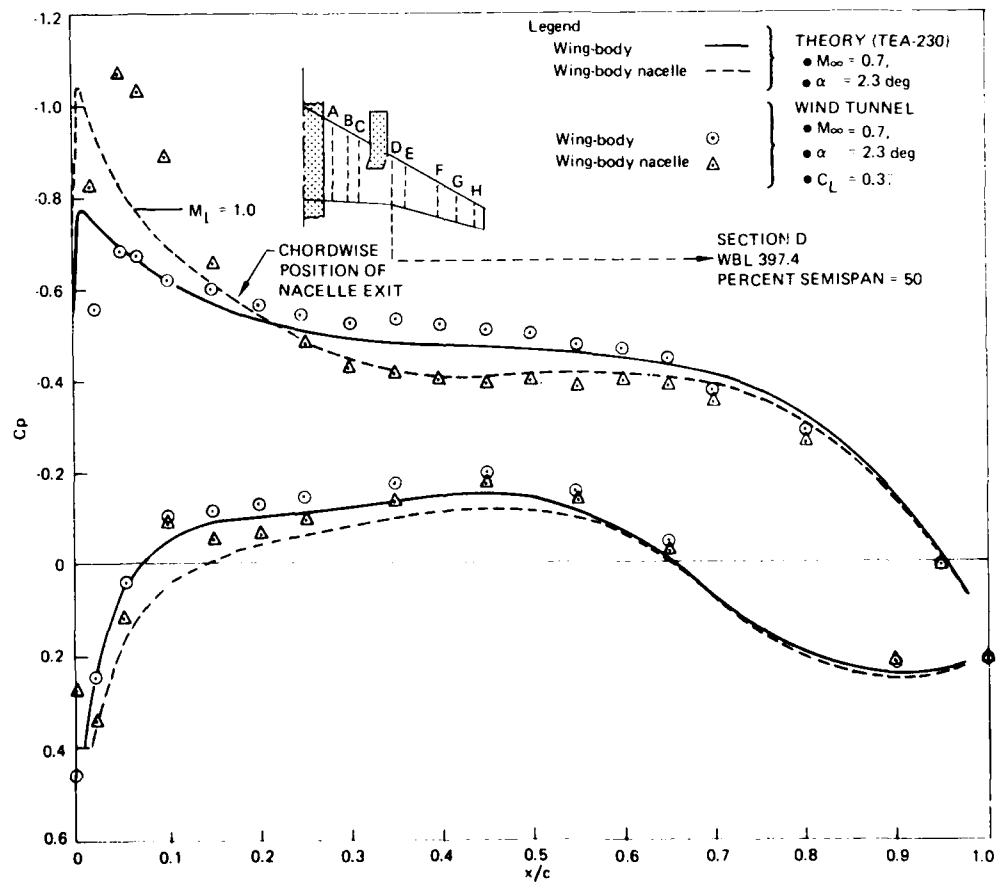


Figure 14. Comparison of Wing Pressure Distribution From TEA-230 Analysis With Wind Tunnel Data—Wing-Body-Nacelle Configuration

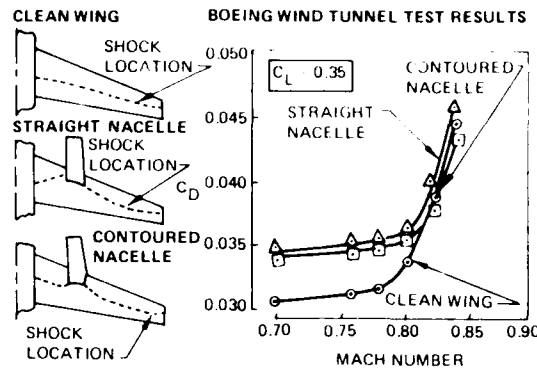


Figure 15. Installation of Overwing Engine on High-Speed Wing

The four-engine design was evolved similarly through two cycles. The major problem in the four-engine design is illustrated by the span loading of Figure 12. The high level of lift between the nacelles makes the presence of a shock in that channel almost unavoidable. The design process is to offload that part of the wing as much as possible so that the shock is not too strong and to contour the nacelles so that the shock will be swept to about the same degree as the wing. In achieving this latter objective it is the contouring of the inboard side of the outboard nacelle which is crucial.

Figure 13 illustrates the isobar pattern on the upper surface of the wing and nacelles. The isobars on the outboard part of the wing were not determined all the way to the tip, but are expected to be relatively undisturbed. The pressure distribution over the two nacelles is well behaved and similar in nature to that of the two-engine D-nozzle nacelle. On the forward part of the wing, the isobar sweep outboard of the nacelles is continued inboard between the nacelles and on the wing inboard of the nacelles. In the channel between the nacelles, this favorable sweep is an encouraging aspect of the design, although the isobars are expected to become distorted and unswept at higher Mach numbers in the wind tunnel. The sweep of the inboard forward isobars has unexpectedly deteriorated slightly as compared to the two-engine D-nozzle case. The isobars between the nacelles suggest that a wing shock could emanate from both corners of the exit. The crucial aspect of this design is whether the two parts of this shock can be made to merge into a single, swept shock in which energy losses would be small.

Following this theoretical work, test hardware was built by NASA to the lines determined as above for the two-engine design and test data is expected to be available this year. A concurrent in-house study at Boeing led to a similar two-engine over-wing design for which test-theory comparisons between test data and theory are available, as shown in Figure 14. The wing had a sweep angle of 27° but was otherwise similar. Discrepancies between test and theory are seen to be small except where supercritical flow is present. Here presumably the Gothert compressibility correction breaks down. Figure 15 shows the force measurements taken in the Boeing wind tunnel test indicating the improvement obtained by contouring. Note the effect on the shock pattern. With contouring, the sweep of the shock is reasonably well maintained across the wing span so that the associated losses in energy return to about the level for the wing alone.

DESIGN OF WINGLETS FOR THE YC-14 AMST AIRPLANE

This study was conducted under contract (F33615-76-C-0740) with the USAF Flight Dynamics Laboratory at the Wright-Patterson Base in Ohio and is reported in Reference 7. Included were parametric investigations of winglet area, aspect ratio and cant angle. Variations of structure weight due to changes in wing bending moment were included. Thus the overall variation in airplane performance was estimated by the formula shown in Figure 16. The change in induced drag was estimated by means of a vortex lattice computer program. The parasite drag includes skin friction, profile and interference drag estimated by semi-empirical methods.

The winglet design process started with determination of a span loading for minimum induced drag. Camber and twist distributions were selected from vortex lattice computations and a supercritical airfoil section was chosen. Finally, the geometry was paneled for the 3D potential flow analysis program and final tailoring accomplished on that basis. Since the YC-14 (see photograph, Figure 17) is a high wing aeroplane, advantage was taken of the lower velocities underneath the wing to concentrate most of the effort on downward winglets. Figure 18 shows the scope of the parametric study and Figure 19 shows the typical effect of a well designed winglet on the span loading of the wing. The primary outputs of the parametric study are summarized in Figure 20 where typical changes in induced drag, wing root bending moment and weight are shown.

Finally, the performance effects of the winglets considered can be summarized as in Figure 21. At this stage it is apparent that there is a favorable variation of cant angle towards the limit where the winglet becomes a span extension. It is interesting to note that for upward winglets aspect ratio is a fairly powerful parameter, whereas for downward winglets it appears to have little effect. Operating weight considerations biased the choice of winglet towards small area ratios. Operational limitations also favored a minimum increase in span. For these reasons, an aspect ratio of 2.0, area ratio of .0319 and cant angle of 160° were chosen. Sweep and taper ratio variations affected the performance benefit to a small degree only and values of 30° and 0.4 respectively were chosen in order to minimize possible effects on flutter margins. Thus an overall performance improvement of 4.6% was indicated. This figure includes 5.6% aerodynamic drag reduction and about 1% equivalent increase due to structure weight.

$$\Delta C_{D_{NET}} = \Delta C_{D_{winglets}} + C_{D_{parasite\ winglets}} + \Delta C_{D_{profile\ airplane}} + \Delta C_{D_{trim}} + \Delta W_{t\ winglets} \Delta C_D / \Delta W_t$$

where

- $\Delta C_{D_{NET}}$ = total drag change due to winglets, including weight penalty
- $\Delta C_{D_{winglets}}$ = change in wing induced drag due to the addition of winglets
- $C_{D_{parasite\ winglets}}$ = winglet parasite drag (skin friction, form drag, and interference drag)
- $\Delta C_{D_{profile\ airplane}}$ = the change in airplane drag (less the airplane induced drag) due to a change in airplane angle of attack
- $\Delta C_{D_{trim}}$ = change in trim drag due to the addition of winglets
- $\Delta W_{t\ winglets}$ = total winglet plus wing installation weight penalty
- $\Delta C_D / \Delta W_t$ = drag weight trade factor for equal fuel burned

Figure 16. Breakdown of Performance Effects of Winglets



Figure 17.

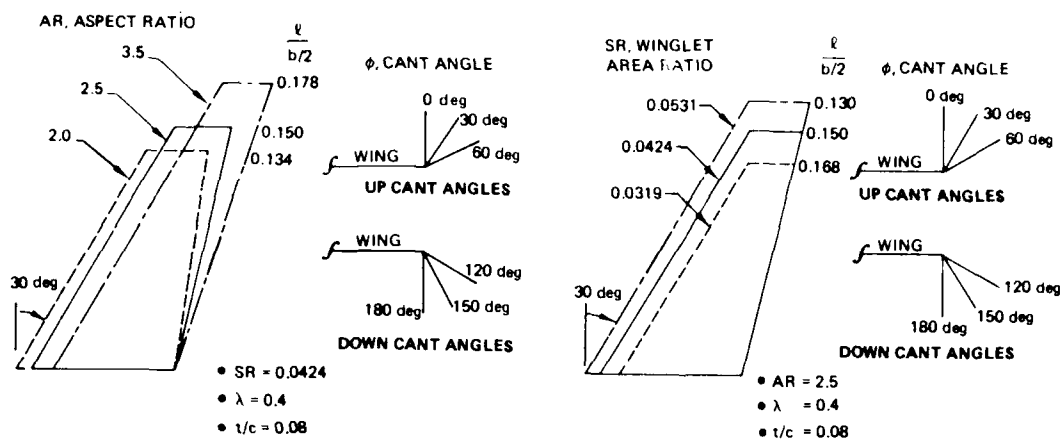


Figure 18. Winglet Parametric Study

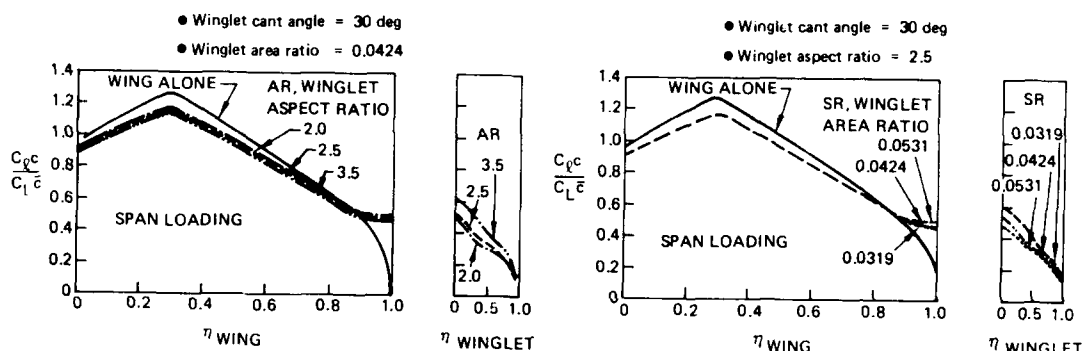


Figure 19. Effect of Winglet on Wing Span Loading

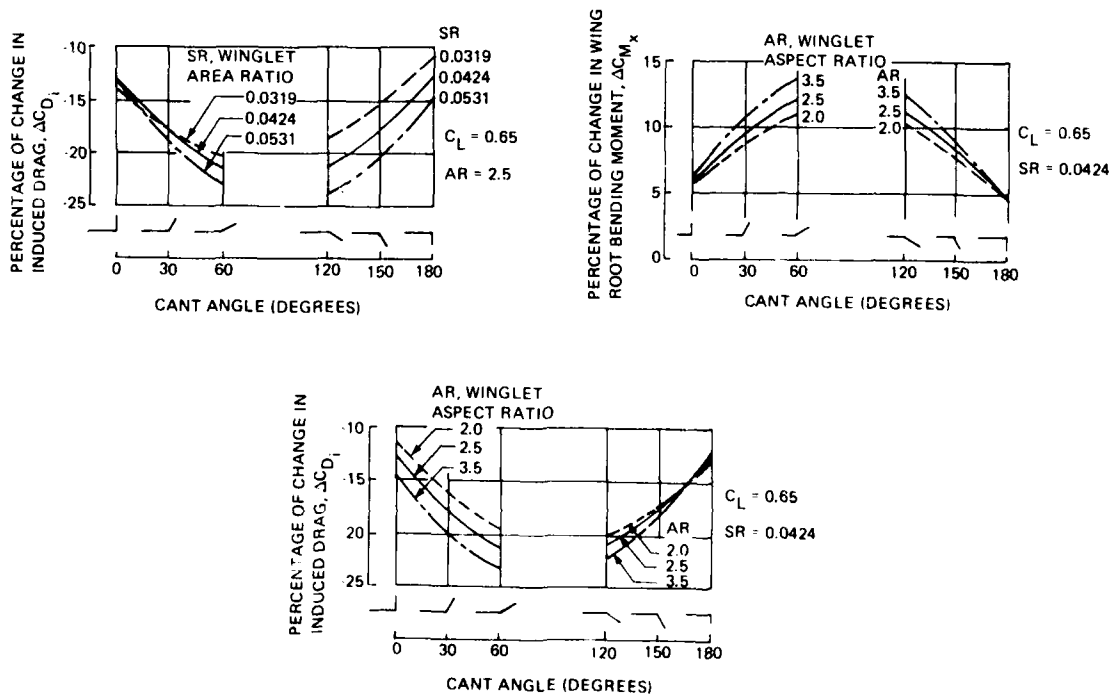


Figure 20. Parametric Winglet Effects

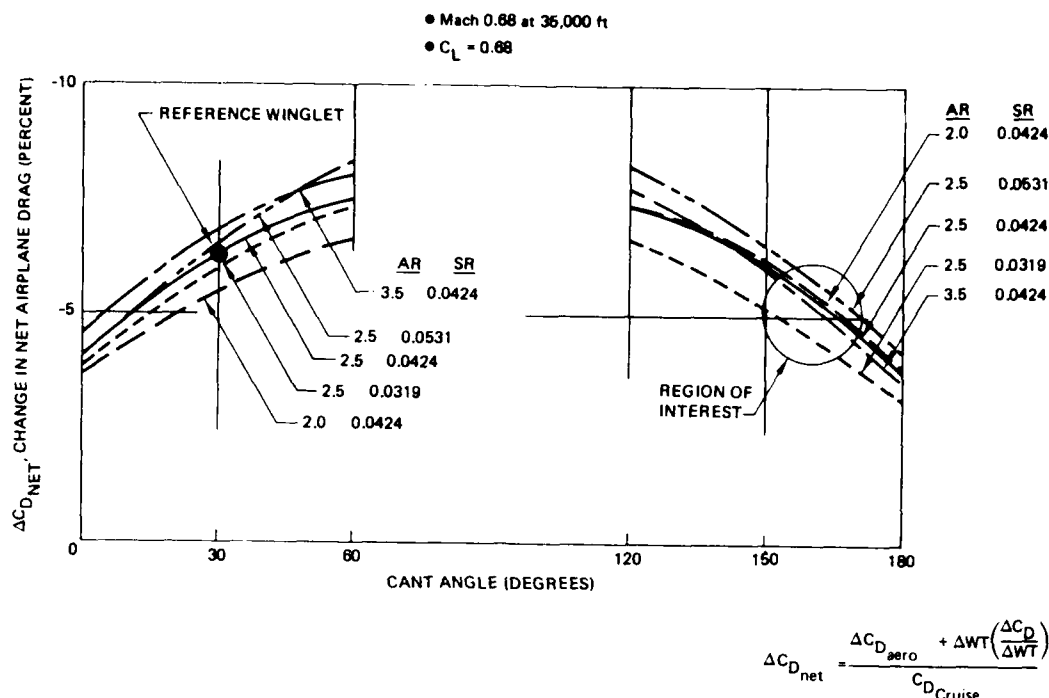


Figure 21. Net Airplane Drag Reduction Used in Winglet Selection

Tailoring of the winglet airfoil section was conducted by means of the 3D potential flow program and test-theory comparison for the initial winglet design F1 are shown in Figure 22. Computed pressure distributions on the wing near the tip and on the winglet are shown in Figure 23. These explain the nature of the favorable interference which has been achieved. The suction on the upper surface of the wing is increased slightly as a result of the reduced downwash. This is because a large part of the trailing vorticity which was previously shed from near the wing tip is now shed over the span of the winglet. The pressure on the lower surface of the wing is increased significantly as a result both of the reduced downwash and of the reduced outward flow on the wing surface. The winglet carries a side force which is vectored slightly forwards as a result of the sidewash induced locally by the wing. These effects provide a significant improvement in drag without a large increase in wing root bending moment since the proportion of the wing span which is affected is small, as is the arm of the sideforce on the winglet. It is important that the load at the base of the winglet should match that on the adjacent part of the wing so that no vorticity is shed at the junction. An important corollary of these arguments is that the benefits of a winglet in terms of reduced induced drag will be greater if the original wing is more highly loaded near the tip.

The winglets were tested in the Boeing Transonic Tunnel at Mach numbers from 0.50 to 0.74. Nominal Reynolds numbers ranged from 3 to 4 million per foot. The 3D potential flow studies indicated some improvements which were incorporated in a second winglet design denoted F2. The differences in twist and camber are shown in Figure 24. The revised winglet design was indeed the better of the two (Figure 25). Figure 26 shows, in tabular form, the predicted and measured drag increments. These are in good agreement so that the prediction methods can be considered to be reliable.

Lift and pitching moment data showed relatively minor effects due to incidence. In addition, lift and pitching moment increments due to winglets did not vary significantly with Mach number in the range of the test. At a constant lift coefficient, the winglets generate a more negative pitching moment and allow the airplane to fly at a lower angle of attack.

In summary, parametric studies provided data for predictions of performance improvements from a wide range of optimized winglet geometries. In the selected case a detailed tailoring of the winglet lines was accomplished and the predicted performance was slightly exceeded in the wind tunnel. Further studies of winglet applications to the YC-14 could therefore be made on the basis of the analytical data. As an example, see the predictions of Figure 27 where a winglet of slightly larger aspect ratio and area will produce a net improvement of 6.2% in range.

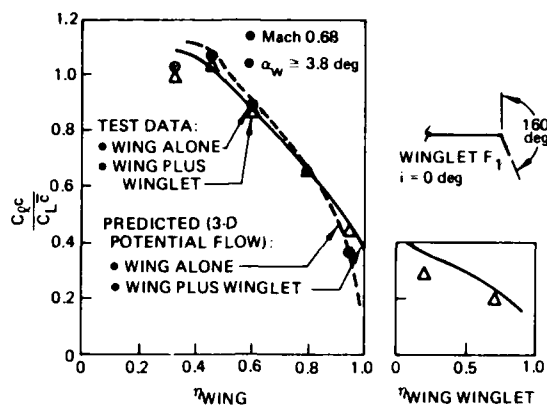


Figure 22. Wing Plus Winglet Span Load Distributions, Test and Theory Comparison

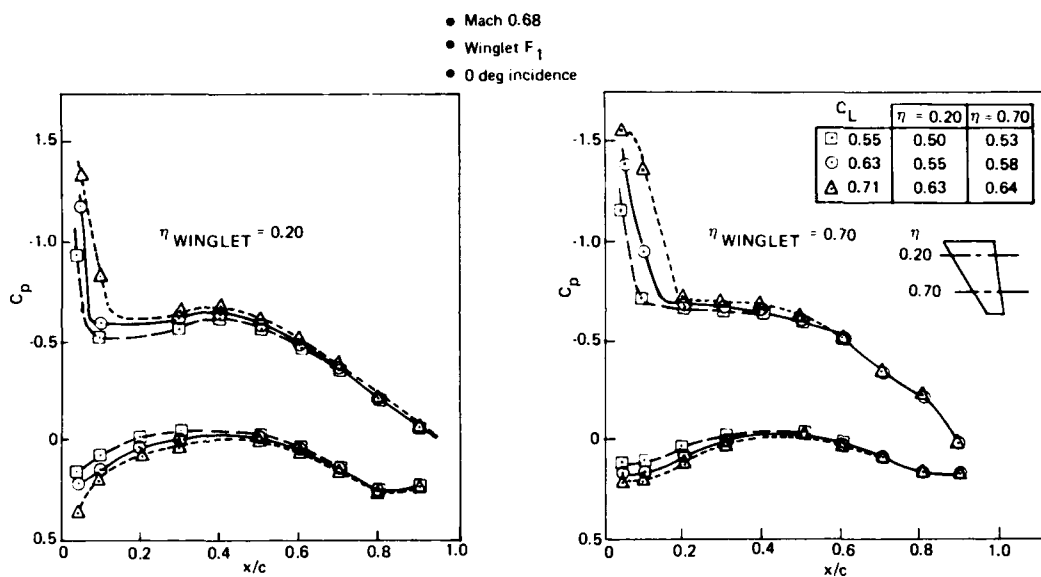


Figure 23. Winglet Pressure at Mach 0.68

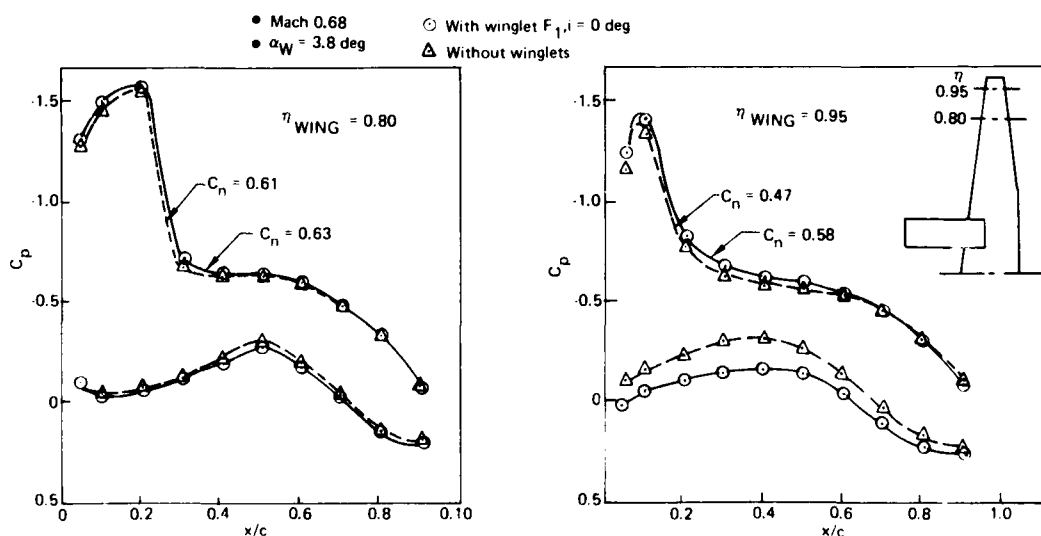


Figure 23. Effect of Winglet on Outboard Wing Pressures, Mach 0.68

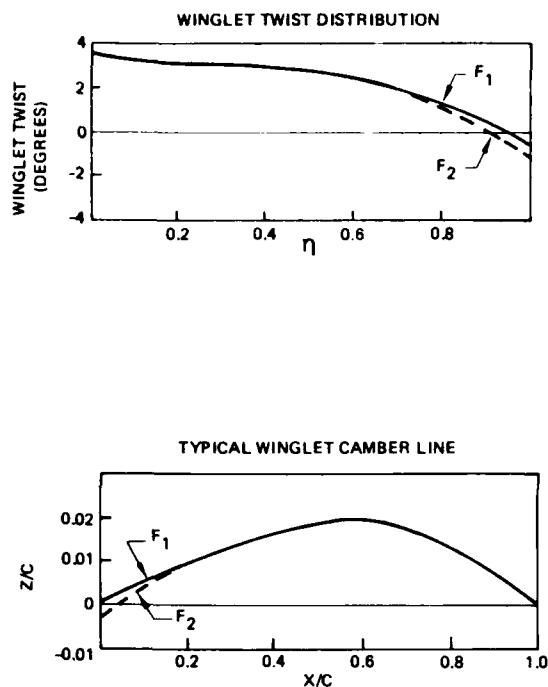


Figure 24. Revised Winglet Twist and Camber

Mach 0.68, $C_L = 0.65$		
Increment	Predicted	Actual
ΔC_D	-0.0023	-0.0025
ΔC_M	-0.007	-0.014
$\Delta \alpha$ (deg)	-0.20	-0.20
ΔAC (%)	1.62	1.8
ΔC_{L_α} (1/deg)	+0.0036	+0.003

Notes:

- Δ = winglet on-winglet off at constant C_L
- Predicted values based on 3-D potential flow computer program, A230
- Actual values from wind tunnel test data with winglet F_2 at $i = 0$ deg

Figure 26. Winglet Test-Theory Increment Comparison

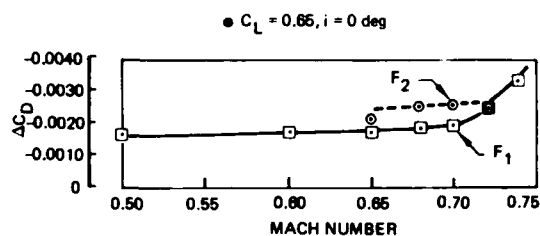


Figure 25. Effect of Mach Number on Winglet Drag Reduction

Mach 0.68, 35,000 ft $C_L = 0.68$	
Component	Percent of cruise drag
ΔC_{D_i}	-5.7
$\Delta C_{D_{parasite}}$ winglets	+0.8
$\Delta C_{D_{profile}}$ airplane	-2.8
$\Delta C_{D_{trim}}$	0.0
$\Delta C_{D_{aero}}$	-7.7
$\Delta C_{D_{weight}}$	+1.5
$\Delta C_{D_{net}}$	-8.2

$\Lambda = 2.5$ $\Lambda = 30$ deg
 $\theta = 30$ deg $\lambda = 0.4$
 $SR = 0.0424$ $t/c = 0.8$

Figure 27. Drag Summary for Parametric Reference Winglet

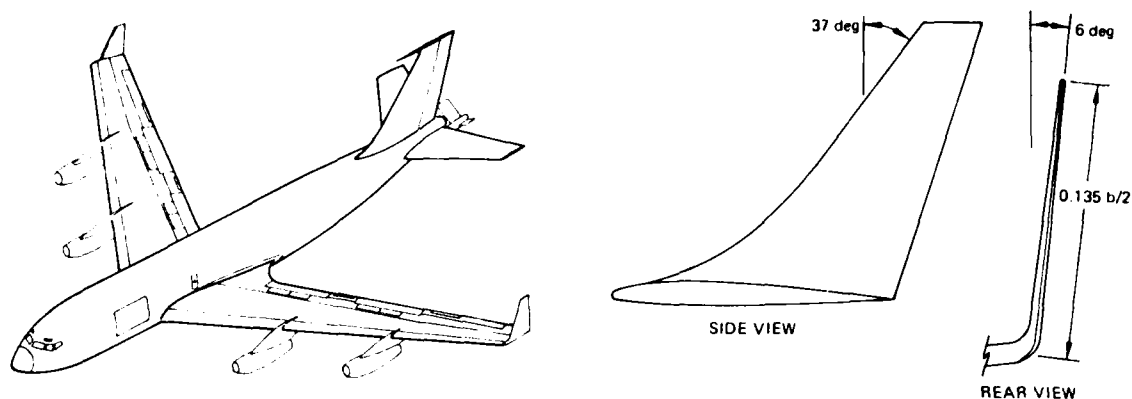


Figure 28. Typical Winglet Application to KC-135

DESIGN OF WINGLETS FOR THE KC-135 AIRCRAFT

There is little doubt that one of the principal virtues of winglets is that they afford a significant performance improvement as a retrofitable modification which has minimal impact on the structure or operation of the aircraft. Increments in wing bending moments are small and there need be no increase in wing span. The USAF decided, therefore, to study the possibility of demonstrating winglet effects in flight on an existing military aircraft. Both the KC-135 and the C-141 were evaluated. The KC-135 was chosen partly because its wing has an appreciable dihedral which would be favorable to the installation of an upward winglet. Figure 28 shows the installation which was envisaged.

The design was based upon a study conducted previously for the B747 airplane and the work was carried out by Boeing under contract to the USAF. It is reported in References 8 and 9. An alternative type of winglet (Figure 29) was analyzed during the early part of the study. This had an upward winglet mounted in an aft location with a smaller downward winglet forward of it. The effects of upward winglet cant and of the addition of the downward winglet are shown in Figure 30. With the upward winglet at 0° cant and no downward winglet there is a noticeable valley in the wing pressure distribution at 30% chord. The flow accelerates over the winglet, causing an aft peak to develop on the wing. This type of pressure distribution is undesirable because of the possibility of shock development and separation problems. When the winglet is canted 20° outward, there is some improvement in the pressure distribution. The valley is filled in slightly, and the aft peak drops and moves forward. Lower surface pressures show some increase. The addition of the downward winglet has similar beneficial effects. The valley is filled in considerably more than with cant, but the aft peak does not drop quite as much. The noticeable increase in pressure on the lower surface brings to light an important use of the downward winglet. Suppose that the outboard wing section cannot carry the desired increase in loading through reduction of upper surface pressures. A downward winglet could be added so that part of this load is carried by increasing the lower surface pressures. This might improve the upper surface flow enough so that the section would work properly. The analysis of the addition of a downward winglet indicated a 2% reduction in induced drag. The downward winglet also reduced the upward winglet leading-edge pressure peaks to provide pressure gradients which are more favorable to the boundary layer. This configuration would therefore be suitable for the low speed, high lift conditions that produce locally high sidewash at the wing tip.

As long as an adequate solution could be found, it was decided to retain a simple upward winglet. As in the YC-14 study discussed above, an extensive parametric study was conducted of winglet geometry. This covered winglet sweep from 30° forward to 60° aft, area, length, taper ratio and cant. This last study was interesting in that the cant was studied both at constant span and variable span. Figure 31 shows the variation in induced drag produced by these two approaches. At constant span the vertical winglet is optimum although not significantly better than the winglet canted at 60° . With variable span the improvement due to the vertical winglet is almost doubled with a cant angle of 90° (span extension).

The winglet selected for test had a root chord equal to 60% of the wing tip chord, a taper ratio of 0.338, leading edge sweep of 37° outward cant of 6° and a height of 0.135 wing semispan. It was positioned chordwise so that the trailing edge of its root section was at the trailing edge of the wing. This minimized the adverse pressure gradients in the junction between wing and winglet.

Wind tunnel tests at high and low speeds were conducted at the NASA-Langley Research Center in the 8-foot transonic wind tunnel. This facility is a pressure tunnel with a 2.2 meter square test section and a Mach number range from 0 to 1.3. At high speeds the winglet behaved satisfactorily with no flow separation within the flight envelope of the KC-135 aircraft. As expected, the first signs of difficulty appeared in the junction on the upper surface. The winglet increased lateral stability directional stability and side force due to sideslip. These changes indicated a significant favorable effect on the unaugmented Dutch roll characteristics. There was an aft shift of about 2% chord in aerodynamic center and no significant change in Mach tuck characteristics.

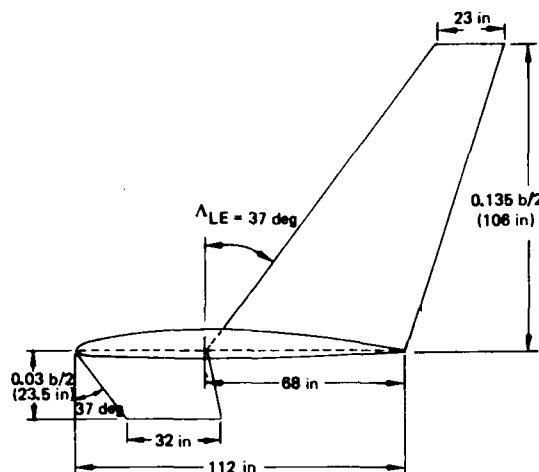


Figure 29. Upper and Lower Winglets Analyzed in TEA-230

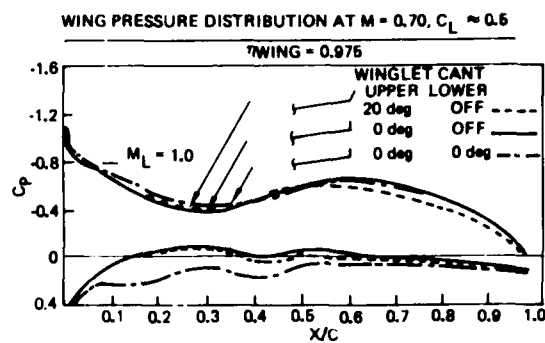


Figure 30. Effect of Cant and Lower Winglet on Wing Pressure Distribution

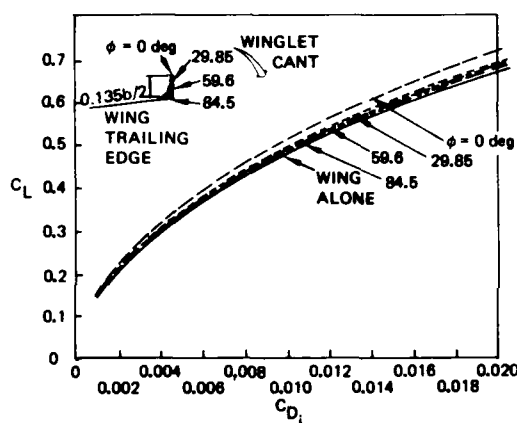


Figure 31(a). Induced Drag—Constant Span

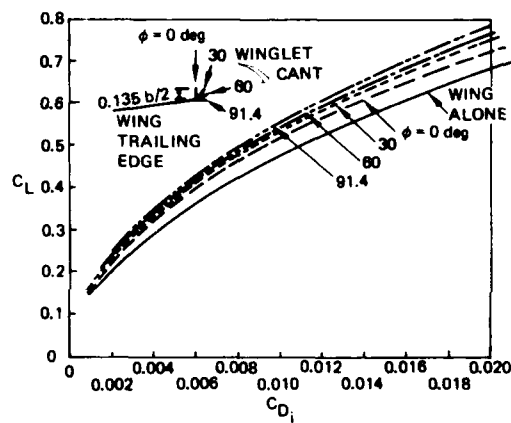


Figure 31(b). Induced Drag—Variable Span

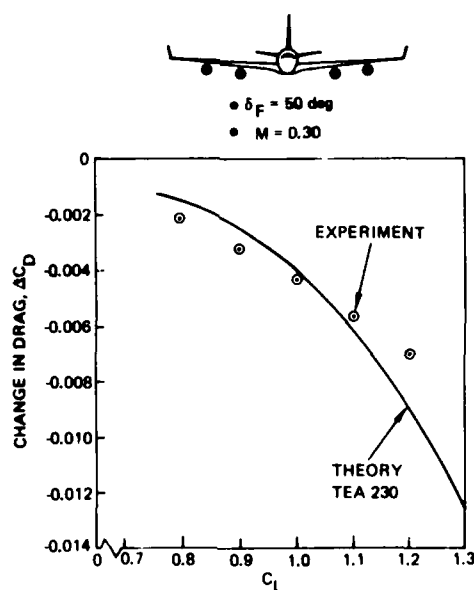


Figure 32. Flaps 50-deg Reduction in Drag With High-Speed AFFDL/Boeing Winglets

At low speeds tests were carried out at 30° and 50° flap deflections. There were negligible effects on longitudinal handling characteristics but a small deterioration in unaugmented Dutch roll damping and cross wind capability. At low speeds the winglet lift coefficients are much higher than in cruise. With wing flaps extended there were signs of incipient separation on the winglet inboard surface. It was suspected that the high speed design had insufficient camber near the leading edge for best low speed characteristics and it was decided to study a compromise design which would incur lesser risk.

Theoretical calculations were used throughout to support the development work. Figure 32 shows the drag improvement obtained at low speeds, flaps deflected 50°, with the initial winglet designed for operation at high speeds. Agreement with the theoretical model is fairly good. However in a critical case at takeoff with 30° flaps the theoretical pressure distributions showed high suction peaks and large adverse pressure gradients near the leading edge. It was decided to reduce these by increasing the camber of the winglet sections in order to reduce leading edge incidence. The effects of this are shown in Figure 33. That this was to some extent an iterative process is apparent from the notation Z5 of the modification which is compared with the original design Z2. This modified winglet was run through the high speed computation with the results shown in Figure 34. Comparisons of drag improvements at takeoff and at high speed for the two winglets are shown in Figure 35. The differences between increments in drag due to the original winglet and to the revised winglet are small. A satisfactory low risk design had thus been achieved.

Another interesting feature of the study was the trade between tip extension and winglet. Tip extensions and winglets of equal area and length were compared on the basis of performance improvement and bending moment increase. Figure 36 shows that for a given reduction in induced drag the winglet produces a significantly lower increment in bending moment.

The final comparison of interest here is shown in Figure 37 where improvements in both drag divergence Mach number and buffet onset are shown for the winglet. These are based on wind tunnel test data on examining breaks in lift and drag curves. The high speed test data are summarized in Figure 38 showing overall drag and bending moment increments in terms of Mach number and lift coefficient. At the design point (0.78M and 200,000 lb) an improvement of 6.3% was established.

Flight testing of the aircraft is currently in progress and results are substantiating the performance and operational characteristics predicted during the study phase.

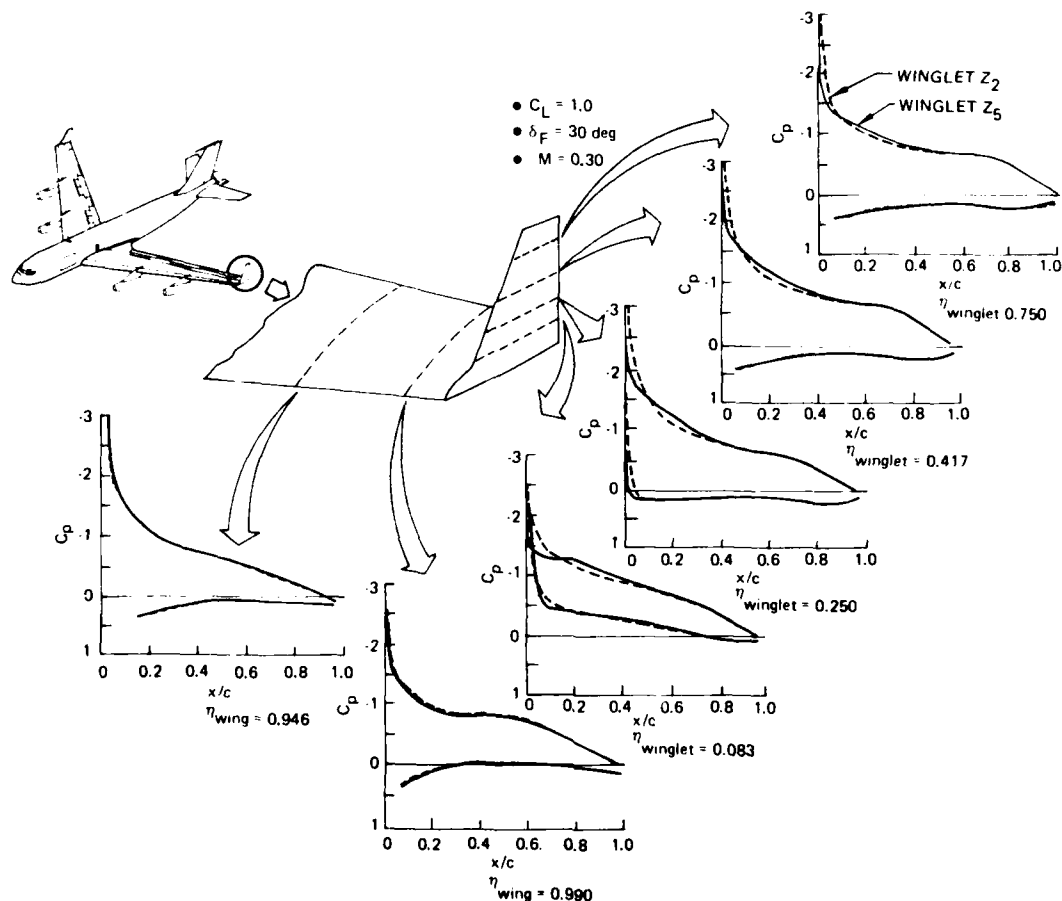
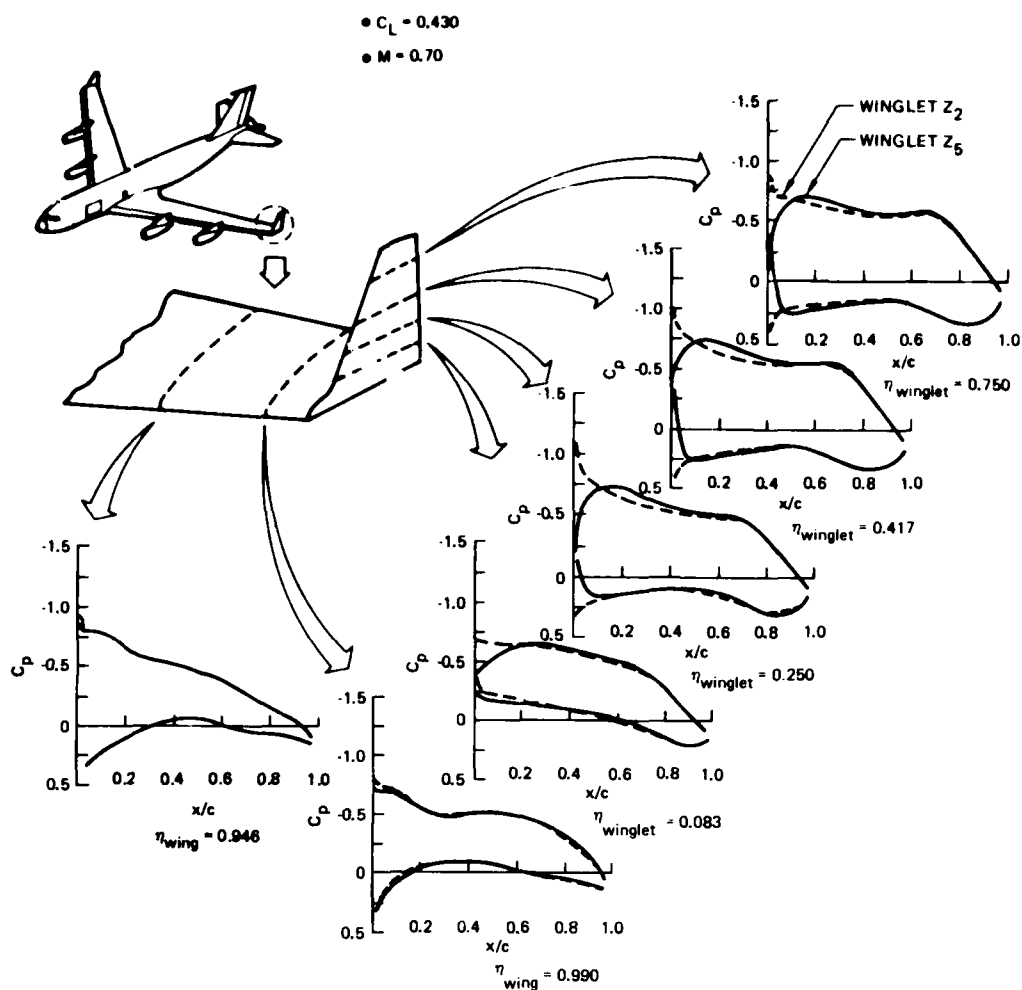
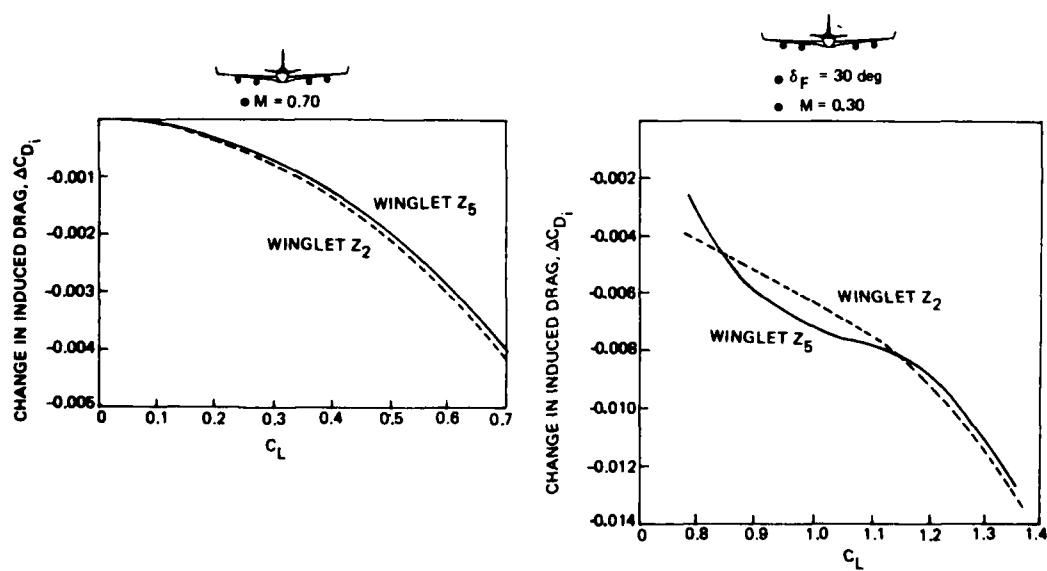


Figure 33. Low-Speed Surface Pressures With Compromise Winglet Z5

Figure 34. High-Speed Surface Pressures With Compromise Winglet Z_5 Figure 35. Reduction in Induced Drag With Compromise Winglet Z_5

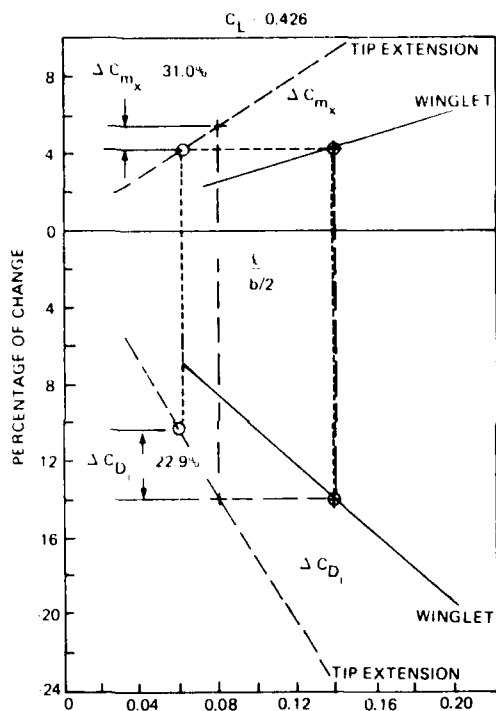


Figure 36. Comparison of Induced Drag and Wing-Root Bending Moment Increments Between Winglets and Tip Extensions

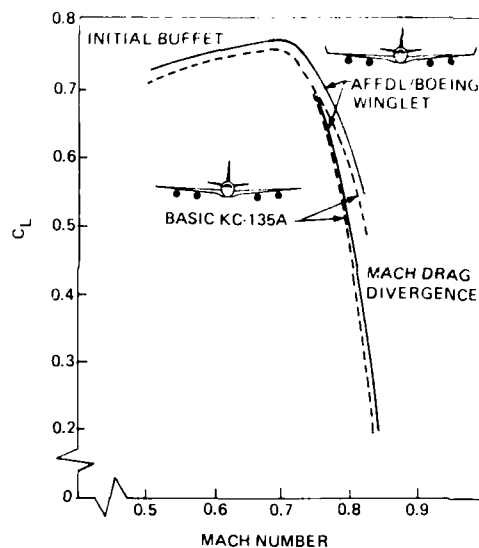


Figure 37. Effect of AFFDL/Boeing Winglets on KC-135A Initial Buffet and Drag Divergence Boundaries

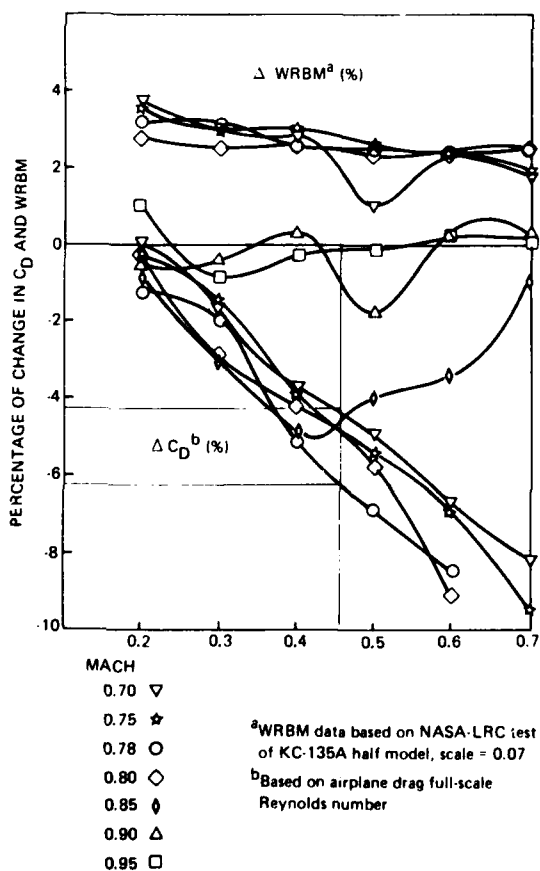


Figure 38. Effect of AFFDL/Boeing Winglets on KC-135A Aerodynamic Performance

CONCLUSION

Favorable aerodynamic interference effects have been identified and demonstrated in configurations of high current interest. These are the installation of slipper-type nacelles on a swept wing for upper surface blowing and of winglets at the tips of a swept and unswept wing for reduced induced drag. The ability of modern computing techniques to predict flow characteristics and assist in design for low drag has been demonstrated in these cases.

REFERENCES

1. Rubbert, P. E. et al., "A General Method for Determining the Aerodynamic Characteristics of Fan-in-Wing Configurations," Vol. 1-Theory and Application, Technical Report 67-61A, USAAVLABS, 1967.
2. Rubbert, P. E. and Saaris, G. R., "A General Three-Dimensional Potential Flow Method Applied to V/STOL Aerodynamics," presented at the SAE Air Transport Meeting, New York, April-May, 1968 and SAE Journal, Vol. 77, September 1969.
3. Rubbert, P. E. and Saaris, G. R., "Review and Evaluation of a Three-Dimensional Lifting Potential Flow Analysis Method for Arbitrary Configurations," AIAA Paper No. 72-188, January 1972.
4. Johnson, F. T. and Rubbert, P. E., "Advanced Panel-Type Influence Coefficient Methods Applied to Subsonic Flows," AIAA Paper No. 75-50, January 1975.
5. Gillette, W. B., Mohn, L. W., Ridley, G. H., and Nark, T. C., "Upper-Surface Blowing Nacelle Design Study for a Swept Wing Airplane at Cruise Conditions," NASA CR-2427, September 1974.
6. Mohn, L. W., "Comparison of Wind-Tunnel Test Results at $M = 0.7$ with Results from the Boeing TEA-230 Subsonic Flow Method," NASA CR-2554, July 1975.
7. Baullinger, N. C., "Design and Analysis of Winglets for the AMST Prototype Aircraft," AFFDL-TR-77 (unreleased) September 1977.
8. Ishimitzu, K. K., "Design and Analysis of Winglets for Military Aircraft," AFFDL-TR-76-6, February 1976.
9. Ishimitzu, K. K., Zanton, P. F., "Design and Analysis of Winglets for Military Aircraft: Phase II," AFFDL-TR-77-23, May 1977.

ACKNOWLEDGEMENT

The work reported here was funded by USAF (winglets) and NASA (nacelles) through contracts awarded to The Boeing Company. Contract monitors were W. C. Sleeman for overwing nacelles, and G. W. Loptien for YC-14 and KC-135 winglets. Thanks are due to these gentlemen and to D. P. LeMasters of the AMST SPO for their encouragement and for permission to release this publication.

DATA BASE FOR THE PREDICTION OF INLET EXTERNAL DRAG

by

O. J. McMillan, E. W. Perkins, and S. C. Perkins, Jr.
Nielsen Engineering & Research, Inc.
510 Clyde Avenue, Mountain View, CA 94043, U.S.A.

SUMMARY

Results are presented from a study to define and evaluate the data base for predicting an airframe/propulsion system interference effect shown to be of considerable importance, inlet external drag. The study is focused on supersonic tactical aircraft with highly integrated jet propulsion systems, although some information is included for supersonic strategic aircraft and for transport aircraft designed for high-subsonic or low-supersonic cruise. The data base for inlet external drag is considered to consist of the theoretical and empirical prediction methods as well as the experimental data identified in an extensive literature search.

The state of the art in the subsonic and transonic speed regimes is evaluated. The experimental data base is organized and presented in a series of tables in which the test article, the quantities measured and the ranges of test conditions covered are described for each set of data; in this way, the breadth of coverage and gaps in the existing experimental data are evident. Prediction methods are categorized by method of solution, type of inlet and speed range to which they apply, major features are given, and their accuracy is assessed by means of comparison to experimental data.

NOMENCLATURE

A	area
A_C	inlet capture area - the frontal area of an inlet, projected in the free-stream velocity vector direction; for axisymmetric inlets, the area is bounded by the cowl leading edge, for others it is bounded by the cowl leading edge, side plate leading edges and initial ramp leading edge
A_{MI}	maximum projected frontal area of inlet
A_P	projected frontal area
A_W	wing reference area
C_{DA}	additive drag coefficient, $D_{add}/q_\infty A_C$
C_{DC}, \hat{C}_{DC}	cowl drag coefficient based on A_C and A_{MI} , respectively (see fig. 1)
$C_{D_{EXT}}$	inlet external drag coefficient, based on A_C (see fig. 1)
C_{DI}	inlet external drag coefficient, based on A_W
C_{DSP}	side-plate drag coefficient, based on A_C
C_{DSPIL}	spillage drag coefficient, based on A_C (see fig. 1)
C_{LS}	lip suction coefficient, based on A_C (see fig. 1)
C_p	pressure coefficient, $(p - p_\infty)/q_\infty$
D_{add}	additive drag, $\int_{\infty}^{\text{cowl lip}} (p - p_\infty) dA_p$
K_{add}	additive drag correction factor [see Eq. (3)]
M	Mach number
MFR	mass flow ratio - mass flow entering the inlet ratioed to free-stream flow through A_C
p	static pressure
q	dynamic pressure
V	velocity
α	angle of attack

Subscripts

crit	critical value (terminal normal shock at the inlet throat)
c	cowl lip plane
ref	reference value
∞	free stream

1. INTRODUCTION

In advanced tactical aircraft, the airframe and propulsion system are closely coupled for reasons of both structural and aerodynamic efficiency. This high degree of integration leads to large flow interference effects which significantly affect the ability of the aircraft to perform its assigned task. Because the missions of these aircraft tend to involve combinations of supersonic and subsonic portions, the optimizations afforded a point-design aircraft are not available and the problem is all the more acute.

The inability to accurately estimate airframe/propulsion system interference effects at an early stage of the design cycle has contributed in an important way to the difficulties encountered in developing aircraft that successfully achieve the performance predicted for them. Part of the problem is that these effects are typically three-dimensional and highly configuration dependent, making their analytical prediction extremely difficult, at best. This leads to a high reliance on experimental data derived from existing configurations. However, these experimental data were generated for the most part in the course of development programs for specific aircraft; in these programs, the usual course followed was that of empirically "optimizing" the configuration with respect to the criteria judged most important in the particular program in question. The broad mission requirements for high performance for these aircraft in the subsonic, transonic, and supersonic speed ranges, at high and low altitudes, have led to an extensive body of experimental data, but there has been no attempt to make the experimental coverage complete, uniform, or widely available.

In ref. 1, from which this paper is drawn, a study is described to improve on this situation of an uncertain predictive capability and a disorganized, fragmented data base. The purpose of that study was to identify, categorize, and evaluate the suitability for preliminary design of the prediction methods and experimental data available for the aerodynamic interference effects associated with airframe/propulsion system integration. The study was focused on interference effects affecting the external aerodynamics of supersonic tactical aircraft with highly integrated jet propulsion systems, although some information was included for supersonic strategic aircraft and for transport aircraft designed for high-subsonic or low-supersonic cruise. Experimental data and prediction methods for all the interference effects were identified and classified, and an evaluation was made of the state of the art for three of the most important: the effects of the airframe on inlet flow fields, afterbody drag, and inlet external drag.

In the present paper, we focus on inlet external drag in the subsonic and transonic speed regimes. Although it is not a phenomenon that arises solely from the installation of the propulsion system into the airframe (an inlet operating completely isolated from airframe structures exhibits external drag), it is conventionally regarded as an interference effect in the thrust-drag bookkeeping systems in common use. For supersonic tactical aircraft designed for mixed missions, inlet external drag is of considerable importance. For example, it is shown in ref. 2 that differences in inlet drag for candidate inlet designs for such an aircraft result in differences in range of up to 200 n.mi. In ref. 3, a 30 percent increase in inlet drag is shown to reduce the mission range for such an aircraft by about 10 percent if the drag increase occurs in a transonic portion of a mission which includes subsonic, transonic, and supersonic portions. In the following, based on an extensive literature search and contacts with those active in the field, the available existing experimental data are identified and classified, and the state of the art is assessed by presenting comparisons with data of the prediction methods in the open literature. While we have attempted to be thorough, our collection of data and methods is doubtless not exhaustive; in particular, we do not include proprietary information. We offer our apologies to anyone we have overlooked.

Inlet external drag ($C_{D_{EXT}}$) is a portion of the drag attributable to an inlet operating at an arbitrary Mach number and mass flow ratio (MFR). It is defined to be the sum of the drag on the stagnation streamtube (additive drag, C_{D_A}), the drag on the external surfaces of the cowl (C_{D_C}), and for two-dimensional inlets, the drag on the external surfaces of the sideplates ($C_{D_{SP}}$). C_{D_C} and $C_{D_{SP}}$ are usually taken to be integrated pressure drag although some investigators include skin friction. The relationships of these quantities with the commonly used terms spillage drag and cowl lip suction are schematically illustrated in fig. 1 for an axisymmetric inlet (thereby avoiding the complication of sideplate drag). Spillage drag ($C_{D_{SPILL}}$) is shown to be the change in external drag as the mass flow ratio is decreased from the reference value appropriate for the Mach number in question. Cowl lip suction (C_{L_S}) is the decrease in C_{D_C} as the mass flow ratio is decreased from this reference value. The experimental data for inlet external drag and related terms are presented and categorized in Section 2, while the

applicable prediction methods are discussed in Section 3. Conclusions drawn from this work are presented in Section 4.

2. INLET EXTERNAL DRAG - EXPERIMENTAL DATA

As previously shown in fig. 1, inlet external drag consists of the sum of integrated cowl pressure drag and additive drag:

$$C_{D_{EXT}} = C_{D_C} + C_{D_A} \quad (1)$$

For a nonaxisymmetric inlet, the drag on surfaces such as sideplates is usually treated separately, but for simplicity in this discussion we include it as part of C_{D_C} . Referring to fig. 1 and the following definitions:

$$C_{D_{SPIL}} = C_{D_{EXT}} - \left(C_{D_{EXT}} \right)_{ref} \quad (2)$$

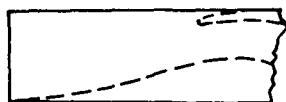
$$K_{add} = C_{D_{SPIL}} / \left[C_{D_A} - \left(C_{D_A} \right)_{ref} \right] \quad (3)$$

equation (1) can also be written

$$\left. \begin{aligned} C_{D_{EXT}} &= C_{D_A} - C_{LS} + \left(C_{D_C} \right)_{ref} \\ &= \left(C_{D_{EXT}} \right)_{ref} + \left\{ \frac{MFR}{MFR_{ref}} \frac{\partial C_{D_{EXT}}}{\partial (MFR)} d(MFR) \right\} \\ &= \left(C_{D_{EXT}} \right)_{ref} + K_{add} \left[C_{D_A} - \left(C_{D_A} \right)_{ref} \right] \end{aligned} \right\} \quad (4)$$

In compiling the experimental data base for inlet external drag in the subsonic and transonic speed regimes, we have included measurements of any of the quantities in Eqs. (1) - (4). The references comprising this data base are listed in Table I; in this table, the type of inlet, the test configuration, the data acquired, and the range of test conditions are given for each data set.

Each inlet in Table I is described by a string of characters, some of them subscripted, which represent the main characteristics of the inlet. These descriptors, and the characteristics they represent, are listed in Table II. Absence of a particular descriptor for a given inlet means that characteristic is not applicable to that inlet, or, as in the case of the design Mach number, that it was not reported. The items in Table II are self-explanatory, with the exception of the conventions for sideplate shape. These are schematically illustrated in the following sketches of the upstream portion of two-dimensional, external-compression inlets with two fixed horizontal ramps and a design Mach number of 2.4. Note that the absence of the descriptors for a bypass system and a boundary-layer-control system implies that these systems do not exist in these inlets.



$E_r H_{2f} S_r 2.4$



$E_r H_{2f} S_t 2.4$



$E_r H_{2f} S_n 2.4$

Other examples of this system are: the string $M_c C_{10} B_p B P 2.5$ which describes an axisymmetric mixed-compression inlet with three conical external compression surfaces, two of which are variable, a boundary-layer-control system consisting of porous elements, an operational bypass system, and a design Mach number of 2.5; and the string P_0 which describes a pitot inlet whose capture area is neither circular nor rectangular.

The column in Table I after the inlet characterization identifies the drag component(s) presented for that inlet in the reference in question. The next column shows the test configuration: that is, whether the inlet was tested alone or in the presence of a forebody, mounted on an entire fuselage, etc. Next come a series of columns containing the ranges of Mach number, unit Reynolds number, angle of attack and angle of sideslip covered for each inlet. Finally, the remaining columns show whether sufficient data exist to evaluate the separate effects of cowl shape, sideplate shape, ramp angle, etc., on the drag component presented. Special circumstances are identified in the notes following Table I.

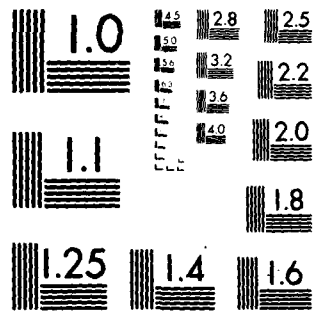
AD-A094 086 ADVISORY GROUP FOR AEROSPACE RESEARCH AND DEVELOPMENT--ETC F/G 20/4
SUBSONIC/TRANSONIC CONFIGURATION AERODYNAMICS.(U)
SEP 80

UNCLASSIFIED AGARD-CP-285

NL

5
ML
204

END
DATE
FILMED
DTIC



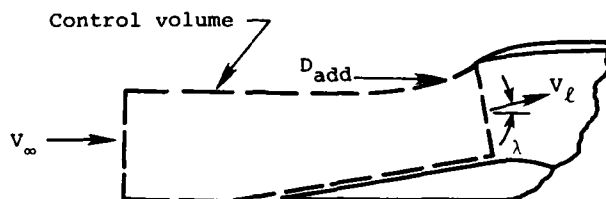
MICROCOPY RESOLUTION TEST CHART
NATIONAL BUREAU OF STANDARDS-1963-A

3. INLET EXTERNAL DRAG - PREDICTION METHODS

3.1 Methods for a Component of $C_{D_{EXT}}$

In this section, we deal with methods which result in the prediction of one or more of the components of $C_{D_{EXT}}$ indicated in Eqs. (1) - (4) (e.g., C_{LS} or C_{DA}). Methods of this type have been categorized in Table III by the inlet type and the speed range to which they apply. Inlet type in this table refers to a pitot inlet of either axisymmetric or two-dimensional shape, or an inlet which is either of two-dimensional or axisymmetric geometry with an external compression surface. Application of prediction methods of this class to an inlet of more complicated shape (e.g., "kidney", or "chin", half-axisymmetric) must be done on an ad hoc basis; the methods are, in general, derived for the simple inlet shapes just described. Further, it should be noted that these methods are in general derived for use at zero angles of attack and sideslip in a uniform free stream. Adaptation to more complicated situations is required, of course, and schemes for accomplishing this exist (see, for example, ref. 44), but the approximations involved are over and above those fundamental to the methods themselves. The following comparisons between data and predictions made using these methods are for a uniform free stream at zero angles of attack and sideslip because published comparisons have not been found for the more general situation.

The first methods from Table III to be discussed are those for additive drag. In the subsonic and transonic speed regimes, this calculation is typically done (refs. 27, 44-48) using a one-dimensional momentum analysis on a control volume encompassing the captured airflow and extending from free-stream conditions to the cowl lip plane. Such a control volume is illustrated in the following sketch for a two-dimensional inlet. For simplicity, viscous forces have been neglected and the inlet is shown at zero angle of attack.



One-dimensional momentum analysis for this control volume gives

$$C_{DA} = \frac{(p_l - p_\infty) A_l \cos \lambda}{q_\infty A_c} + \int_{\text{ramp}} \frac{(p - p_\infty)}{q_\infty A_c} dA_p + 2(MFR) \left(\frac{v_l}{v_\infty} \cos \lambda - 1 \right) \quad (5)$$

Calculation of C_{DA} using this approach thus requires estimation of conditions in the cowl lip plane as well as the pressure force on the external compression surface. This latter contribution is usually treated empirically.

There are relatively few reported comparisons with data for additive drag calculated in this way, and the comparisons which do exist lead to somewhat contradictory conclusions. For example, for pitot inlets, in refs. 9 and 57 it is shown that additive drag is accurately predicted using one-dimensional momentum analysis, although in ref. 9 the use of the experimental stagnation point location was required. In ref. 58, however, values calculated in this way are generally lower than the presumably more accurate values from two-dimensional incompressible potential flow theory with the Lieblein-Stockman compressibility correction (fig. 2). However, because no comparison with data for C_{DA} was made in this reference, no definitive conclusion relative to the accuracy of either prediction method can be drawn.

For a two-dimensional inlet, the version of the momentum analysis given in ref. 27 is shown in ref. 43 to give very poor results (fig. 3). Measured ramp pressures are presented in ref. 43 indicating a complicated flow which is obviously not well represented by inviscid one-dimensional theory. While more comparisons with data for inlets with external compression surfaces would be desirable, there is an additional consideration which reflects adversely on the potential accuracy of the method in this case. At a given M_∞ and MFR, this method would predict the same additive drag for an axisymmetric inlet with conical centerbody of cone half-angle θ as for a two-dimensional inlet with the same throat-capture area ratio and a wedge angle of θ (excluding allowance for sidespill). However, it is well known (e.g., ref. 39) that the additive drag for two-dimensional inlets is higher than that for axisymmetric ones in this circumstance. This is due to the higher pressure force on the external compression surface caused by sharper curvature of the flow in the two-dimensional case. Inclusion of an allowance for sidespill in the prediction for a two-dimensional inlet (which lowers the predicted C_{DA}) does not help the situation.

The other methods for C_{DA} in Table III are those from refs. 49-52. An empirical correlation for pitot-inlet additive drag is given in ref. 49 and is shown to result in adequate predictions for some cases. However, no evaluation of the bounds of applicability of this method was conducted. In ref. 50, a method for two-dimensional inlets is given where C_{DAcrit} is calculated from one-dimensional momentum analysis with an experimental data correlation used for the ramp contribution, but $\partial C_{DA}/\partial(MFR)$ is determined as a function of M_∞ from a correlation of data. No comparisons with data are given, however. In refs. 51 and 52, solutions are given for C_{DAcrit} for inlets utilizing right circular cones at zero angle of attack using inviscid conical flow theory; again, no comparisons with data are given.

The next set of methods in Table III deals with the estimation of change in cowl drag with reduced mass flow (C_{LS}) by means of empirical correlations. The treatment in ref. 53 is one-dimensional and because it is specified by the author to be inapplicable to realistic lip shapes, it is not considered further. Three of the remaining methods, those of refs. 47, 54, and 56, have a reference mass flow ratio of unity. This presents special problems and these methods will be discussed together.

Cowl lip suction in these methods is defined as

$$C_{LS} = C_{DC} (MFR = 1) - C_{DC} \quad (6)$$

In ref. 54, correlations for the quantity C_{LS}/C_{DA} are presented as a function of (local) free-stream Mach number with C_{DA} as a parameter. Two correlations are given, one for two-dimensional inlets, the other for axisymmetric inlets. The two-dimensional correlation is assumed to include the effects of suction on the lips of the sideplates. The data used to generate these correlations are neither identified nor shown. Implicit in this approach is the idea that inlets exhibiting the same levels of additive drag at a given Mach number will have the same C_{LS} . That is, all the dependence of C_{LS} on detailed geometry is in this method contained in C_{DA} . A number of investigators, however, have shown that additive drag is in fact relatively insensitive to variations in cowl geometry, while the variation in cowl drag with mass flow ratio is not. Based on these considerations, one would not expect particularly good agreement of this method with data. Nonetheless, it is very convenient to apply.

This point is investigated in fig. 4 by comparing C_{LS}/C_{DA} as a function of C_{DA} for two different Mach numbers from the correlations for two-dimensional inlets in ref. 54 with data for two different cowl designs from ref. 27 (uniform free stream, angle of attack = angle of sideslip = 0). Agreement of the correlation with the data is seen to be poor in both level and trend. As expected, the effect of cowl geometry is clearly not adequately represented by its effect on additive drag.

In the process of reducing the data in ref. 27 to the form shown in fig. 4, a major disadvantage of the representation of Eq. (6) became apparent. That disadvantage is the choice of unity as the reference mass flow ratio. Because inlets with external compression surfaces cannot in general achieve $MFR = 1$, extrapolations of data for C_{DC} ($C_{DC} + C_{Dsp}$ for two-dimensional inlets) are required to allow evaluation of C_{LS} . The extrapolations required for one of the Mach numbers in fig. 4 are shown in fig. 5. The uncertainties introduced into C_{LS} by this process can be substantial, making comparisons with data extremely difficult to interpret, or to put it another way, making correlations formulated in this way inherently inaccurate.

The correlation method of ref. 47 differs from that of ref. 54 in that the effects of two geometric quantities are explicitly included. These quantities (defined in detail in ref. 47) are effective cowl lip slope and capture-area ratio. C_{LS}/C_{DA} is given as a function of these quantities and the (local) free-stream Mach number. However, because the reference mass flow ratio is unity for this method, the preceding remarks apply here as well and comparisons with data become moot. Similar comments apply to the method of ref. 56, where C_{LS}/C_{DA} is a function of cowl lip angle, camber, leading edge radius, local free-stream Mach number and C_{DA} .

The difficulties resulting from the use of a reference mass flow ratio of unity are avoided in ref. 55. This method is applicable to two-dimensional inlets and employs curve-fits of the lip-suction data from ref. 27. The independent variable is a parameter depending on mass flow ratio, throat Mach number, capture-to-throat area ratio and the contraction ratio required to bring a reference flow to sonic velocity isentropically (A/A^*). For subsonic flows, the reference flow is at the free-stream Mach number; for supersonic flows, A/A^* is evaluated at the Mach number to which the flow is assumed to expand at the end of the cowl area change. The reference value of the independent variable (where lip suction is zero) is taken to be 0.8 for all Mach numbers. For subsonic, isentropic inlet flows, this implies that the reference state is that for which the throat Mach number is approximately 0.82. No such simple statement of the reference condition can be made for supersonic flows.

The dependent variable is expressed in terms of the cowl lip-suction coefficient, the effective thickness-to-chord ratios for the cowl and the ramp (each ratio raised to an exponent which is a function of free-stream Mach number), and the ratio of capture area to maximum projected inlet area, also raised to a Mach-number-dependent exponent. The curves relating the dependent and independent variables also have Mach number as a parameter. Bands are displayed on these mean curves to show the limits within which about 95 percent of the data from ref. 27 fall. This scatter represents among other things,

the effects of different sideplate geometry which is not explicitly treated in this approach.

This method is applied to a two-dimensional inlet with three different cowls and two different sideplate shapes (ref. 26) in fig. 6. The comparisons are for a single external ramp (angle = 5°) at zero angle of attack for a free-stream Mach number of 0.8. The cowl drag measurements shown were derived in a uniform free stream and are normalized on maximum projected inlet area. The data in fig. 6(a) are for an elliptical cowl with a leading-edge radius which is ~ 1 percent of the capture height and with full rectangular sideplates (see ref. 26 for details). The reference mass flow ratio shown is calculated using the criterion in ref. 55 and is in excellent agreement with the maximum mass flow ratio from the data. Cowl-drag coefficients were calculated at two mass flow ratios by the method of ref. 55 by applying the lip suction from that method to the extrapolated experimental cowl-drag coefficient at the reference mass flow ratio. Note that the extrapolation required by the reference mass flow ratio of this method is of a much more reasonable extent than for the methods previously mentioned with $MFR_{ref} = 1$. The predicted cowl drag at the high mass flow ratio is in excellent agreement with the data, but this is mostly due to the fact that a very small amount of lip suction is involved and the experimental reference cowl drag was used. At the lower mass flow ratio, where there is more lip suction, the agreement is not as good. A band is shown on the predicted value, reflecting the bands on the correlation bounding ~ 95 percent of the data from which it was derived. At this low mass flow ratio, the correlation considerably underpredicts the lip suction.

A possible contributing factor to this underprediction is the fact that the data from ref. 26 came from a model with full rectangular sideplates which would essentially eliminate sidespill, enhancing the suction effects on the cowl. Although ref. 27 includes some data for full rectangular sideplates, it is not clear if those geometries are included in the correlation of ref. 55 (indeed it is not clear if the correlated data is for suction on the lips of the cowl or on the lips of the cowl and sideplates). If the correlation only includes the triangular-sideplate geometries of ref. 27, and if it is for lip suction on the cowl only, an underprediction for lip suction would be expected for the case of fig. 6(a).

A portion of this uncertainty is eliminated for the case of fig. 6(b), where the data are for the same cowl as fig. 6(a), but where triangular sideplates were used. Note that the lip suction prediction, which differs from that for fig. 6(a) only by being applied to a different reference cowl drag, is still less than that measured, although at the low mass flow ratio the agreement is improved.

Figure 6(c) shows the agreement for a cowl of the same shape as in fig. 6(a), but for an increased leading-edge radius (2 percent of the capture height). The comparison is again for the full rectangular sideplates because that is the only case for which data exist in ref. 26. The agreement is essentially the same as in fig. 6(a) and the same comments apply. Figure 6(d) is for a cowl with the same leading-edge radius as fig. 6(c), but of different shape (although it is still elliptical, the point of tangency with the leading-edge circle is different). Agreement is improved in fig. 6(d). Although the experimental data show a considerable effect of the detailed cowl shape, predictions from the correlation do not: the lip-suction predictions for the cases of figs. 6(c) and (d) are essentially the same.

The final set of methods in Table III deal with the change in external drag with varying MFR through the K_{add} factor. Use of this factor is advantageous if some freedom from geometric detail is gained by presentation of spillage drag data in this form; that is, if K_{add} is a correlating parameter which achieves some "collapse" of the original data into a more generalized form. Note that such generality of K_{add} would require differences in spillage drag to be reflected in additive drag, just as in the lip suction methods discussed above. If, on the other hand, a different K_{add} is required for each inlet geometry, no real advantage exists for this approach as compared to using the original spillage drag data. This point is examined using the primary source for K_{add} factors, the previously mentioned systematic investigation of ref. 27.

In this investigation, K_{add} was evaluated as in Eq. (3), using experimentally determined spillage drag and the additive drag increment as calculated using the theory presented in ref. 27. Data are shown at six Mach numbers for external-compression, two-dimensional, two-ramp inlets with various combinations of ramp angles, four different sideplate shapes and six cowl designs, all measured in a uniform free stream at zero angles of attack and sideslip. The K_{add} factors determined for an inlet with a design Mach number of 3 tested at a Mach number of 0.7 are shown as functions of mass flow ratio in fig. 7. The band identified as being due to variations in cowl shape is for constant inlet geometry except for variations in the cowl external profile. The other K_{add} curves reflect changes in second-ramp angle and sideplate shape. It is clear that independence from geometric detail is not achieved. If a correlation were to be forced onto these data (e.g., by using some average K_{add} to represent all the geometries), the deviations from this mean must clearly represent sizable uncertainty in evaluating the effects of inlet drag on airplane performance for applications where spillage is at all significant in comparison to total airframe drag.

3.2 Flow-Field Methods

These methods provide a complete description of the flow field in the vicinity of the inlet; external drag and its components are available by a straightforward integration of the calculated pressure distribution. Methods of this type are shown in Table IV, where they are categorized by general approach and the geometry to which they apply; all of these methods are applicable in the subsonic and transonic speed regimes. All of the methods listed as applicable to two-dimensional geometries can handle non-zero angle of attack, but only two of the methods for other geometries (refs. 63 and 64) can do so. This is so because only these methods (intended for use with subsonic design-point inlets) are designed to handle a three-dimensional flow field. Calculation of three-dimensional inlet flow fields is only just beginning, and descriptions of this work are very scarce in the open literature. Additionally, all of the methods except that of ref. 65 are inviscid, whereas in ref. 65 the inviscid streamtube curvature method is coupled to a boundary-layer analysis. This is obviously an option available for use with all of the other methods, but this refinement is a separate problem not discussed in the published accounts nor in this paper. Analysis of the boundary-layer methods available for use in inlet calculations and an evaluation of their success is clearly beyond the scope of the present work.

These methods provide considerably more information than the "partial" methods of the last section. The price is, of course, a computational cost that is increased substantially over that for the simple methods; in fact, in most of these methods, the computational requirements are clearly in excess of what is reasonable for preliminary design purposes. In this section, a selection of the available comparisons with experimental data is presented to allow evaluation of the accuracy of the methods. Note that while it is not likely that every implementation of the general approaches listed in Table IV that exists is included there, it is felt that the specific implementations shown are representative. To take account of the trade-off with computational costs that exists with these flow-field methods, computer run times are given where they were reported. Because the numerical analysis and computer programming techniques used play a very important role in the implementation of these methods, the accuracy and the computer cost demonstrated for a particular implementation may not apply to others of the same general approach, and the conclusions drawn may be generalized only with care.

The first solution method shown in Table IV is the numerical integration of the unsteady Euler equations. Both of the references listed in this category (refs. 29 and 59) are applicable to two-dimensional and axisymmetric geometries in all speed regimes, although ref. 59 has only been applied in the supersonic regime to date. Reference 29 presents an explicit finite-difference method, while ref. 59 uses an implicit formulation to realize the computational efficiency this affords. In both methods, the solutions are advanced in time until they asymptotically converge on the steady-state, and automatic generation of interior mesh points is employed.

In ref. 29, solutions are presented and compared with data at two values of MFR for a two-dimensional, three-ramp, external-compression inlet at $M_\infty = 0.7$. Because the essential features of the comparison with data in both cases were the same, only one value of MFR (MFR = 0.5) will be discussed here. The geometry considered is shown in fig. 8(a). Comparisons of calculated values with measured pressures on the ramp [fig. 8(b)], on the cowl external surface [fig. 8(c)], and on the cowl-lip internal surface [fig. 8(d)] are shown.

In these figures, good qualitative agreement is evident, but in ref. 29 it is concluded that pressure level is not satisfactorily predicted. Drag computed from these pressure distributions would be considerably in error, particularly on the cowl external surface; the authors of ref. 29 feel that improvement in this area would require a refined mesh structure. However, for the solutions shown, the full storage capacity of the available machine (a CDC 6600) was used, and approximately 5.6 hours of computer time were spent in the evolution of the flow field from the prescribed initial free-stream conditions. Although the solutions shown are not considered to be steady state (an additional 1.5 hours of computer time was estimated for full convergence), the calculated pressures are estimated to be near their final values; major improvement is felt to depend on mesh refinement.

The next solution method shown in Table IV involves the finite-difference solution of the full potential equation. This type of method is valid up to free-stream speeds which result in local supersonic regions terminating in strong shocks. Various implementations of the basic approach have been made for pitot inlets and axisymmetric and two-dimensional inlets with external compression surfaces. Reference 63 is an example of an implementation of the general scheme valid for axisymmetric pitot inlets at angle of attack in a uniform subsonic free stream; note that this is one of the two flow-field methods we have acquired which can deal with a three-dimensional flow field. In ref. 63, the solution method is described (including special handling of the circumferential derivatives), as are the boundary conditions and the initial field. Comparisons with measured surface Mach number are given for five pitot inlets operating in low-speed free streams ($M_\infty \leq .2$) at a variety of angles of attack and mass flow ratios (throat Mach numbers ≤ 0.86 ; at 0.86, the inlet was observed to be choked). Very good agreement with the measurements is demonstrated. No integrated drags were calculated. Typical run times for a converged solution are from 12 to 15 minutes on a CDC 6600 computer.

Another implementation of this method is that of ref. 60 (also described in ref. 12). This version allows solution of flow fields for inlets of either two-dimensional

or axisymmetric geometry with external compression surfaces; $\alpha = 0$ for the axisymmetric case, but $\alpha \neq 0$ is allowed for the two-dimensional solution of inlets with two-dimensional geometry. The method is applied to two-dimensional inlets and is compared to data in refs. 31 and 33. Examples of these comparisons are given in fig. 9 which is reproduced from ref. 31. In this figure, fair agreement is shown for the drag slope but poor agreement is achieved for drag level. In ref. 31, the disagreement is attributed to the existence of three-dimensional effects and shocks, and to inadequate grid resolution in the computation in regions of high gradients. Application of this technique to an axisymmetric inlet is shown in fig. 10, taken from ref. 60. Here, the level of CDEXT has been adjusted by calculating additive drag using momentum analysis on the entering streamtube and replacing the stream thrusts generated by the method with one-dimensional values. The approach more typical in flow-field methods of integrating the pressure distribution on the stagnation streamline leads to erroneous C_{pA} in this implementation. The discrepancy in level of additive drag observed here is claimed not to exist in the calculation for two-dimensional geometries. However, in the analysis of two-dimensional inlets, a problem with mass conservation in the calculation is indicated. This problem is obviously attributable to this specific implementation of the potential-equation method. That is, it is not a general characteristic of this solution method. However, because the implementation described in refs. 60 and 12 is the only application of the full potential equation to inlets with external compression surfaces we have been able to discover in the published literature, it is not clear whether or not the problem with additive drag level described above is a general one. Computational run times on the order of 15 seconds on a CDC 6400 computer are claimed.

The next solution method shown in Table IV is the finite-difference solution of the incompressible potential equation with a compressibility correction. One implementation of this method is described in ref. 12, where the Douglas-Neumann incompressible flow program (refs. 66-68) is coupled with either the Prandtl-Glauert, Kármán-Tseien, Laitone, or Krahn compressibility correction. The method is applied to two-dimensional and axisymmetric inlets with centerbodies; in ref. 12, surface pressure on the cowl and centerbody are compared to data at $M_\infty = 0.7, 0.9$ and several mass flow ratios for the axisymmetric inlet shown schematically in fig. 10. No integrated values of drag are given. The calculated pressure coefficients agree best using the Laitone correction.

The other implementation of this solution method shown in Table IV is that of ref. 64. This is the second of the two flow-field methods we have acquired which can deal with a three-dimensional flow field. In this approach, the incompressible flow about a pitot inlet with or without a centerbody is solved using the superposition principle and panel methods. Solutions for unit onset flows parallel to each of the coordinate axes are combined with a solution for static operation to result in a rigorous incompressible solution for an inlet at arbitrary angles of attack and yaw with arbitrary mass flow rate. The Lieblein-Stockman compressibility correction (ref. 69) is applied. The method is applicable for subsonic free streams, although local regions of the flow may be supersonic but shock free. The geometry may be three-dimensional but it must exhibit a plane of symmetry. In ref. 64, the method is applied to a subsonic-design-point axisymmetric pitot inlet at 75° angle of attack in a situation where the throat Mach number is 0.603 (the free-stream velocity is not reported). Excellent agreement with data at one unspecified circumferential position is shown for pressures on the internal cowl surface, and on the initial portion of the cowl external surface. Drag is not calculated. It is observed in ref. 64 that panel methods usually require considerably less computer time than finite-difference methods; the superposition technique and compressibility correction used also lead to computational efficiency. Thus, it is claimed that the method of ref. 64 is faster than a finite-difference method by two orders of magnitude.

The final solution method in Table IV uses streamtube curvature (STC) analysis. This approach, as explained in ref. 65, basically uses one-dimensional compressible flow analysis in a number of adjacent streamtubes; when taken together the entire flow field is simulated. Streamline positions are refined iteratively. In each iteration the momentum equation normal to the streamlines is integrated using calculated values of streamline curvature to obtain velocity, and the continuity equation is used to define a new streamline position. The iterative process is continued until streamline movement is less than a specified amount.

A characteristic of streamtube curvature methods, as discussed in ref. 19, is that the method is extremely sensitive to input geometry. As stated therein, "The difference between an aborted run and a successful run is usually a minute change in the geometric data." This extreme sensitivity is due to the need to calculate surface curvatures from input geometry and can make the method very troublesome to use. The method is applied to the pitot inlet shown in fig. 11(a) for several Mach numbers and mass flow ratios in ref. 65. The integral boundary-layer method of Stratford and Beavers (ref. 70) is used to account for viscous effects. Sample comparisons with data are shown in figs. 11(b)-(d). In fig. 11(b), a fully subsonic case is shown and excellent agreement is obtained. At a higher value of free-stream Mach number, fig. 11(c), increasing the number of grid points in the STC solution led to local oscillations in the inviscid solution which were claimed to be eliminated in the physical situation by "viscous effects." At a still higher Mach number, fig. 11(d), predictions are shown with and without the boundary-layer analysis (labeled STC-SAB and STC, respectively). It is seen that neither one is in agreement with the data; separation over the initial portion of the cowl lip was observed experimentally at this Mach number and mass flow combination, and the integral boundary-layer method is inadequate in this situation. Cowl pressure drag forces resulting from integration of the predictions and the data are in reasonably good

agreement (within .01 for \hat{C}_{DC}), but at least in the case of fig. 11(d), this must be attributable to compensating errors.

In ref. 19, application of the streamtube curvature method to the external-compression inlet shown in fig. 12(a) is made for free-stream Mach numbers of 0.7 and 0.85 for values of MFR of 0.55 and 0.75 and several positions of the variable ramps. Sample comparisons with data are shown in figs. 12(b)-(d). All of these figures are for the ramp positions $R_B = 7.2^\circ$, $H_L = 27.3$, and for $M_\infty = 0.85$. Figures 12(b) and (c) show the ramp and cowl pressures, respectively, for MFR = 0.55. Additive drag over a range of mass flow ratios is shown in fig. 12(d) for this Mach number and geometry. The experimental data of fig. 12 were obtained for an inlet mounted on a fuselage and stub wing assembly. The angle of attack of the model was 2.5° . Allowance for the angularity of the local inlet flow field was made by running the STC program using various incidence angles and selecting the incidence at each value of M_∞ that gave best agreement with the measured ramp pressures. Reasonable values of flow incidence resulted from this procedure and the agreement for ramp pressures in fig. 12(a) is fairly good. Predicted cowl pressures agree poorly with the measurements, as shown in fig. 12(b). This poor agreement is likely due to some combination of inadequate grid resolution and viscous effects, but further work would be required to ascertain this. However, additive drag is predicted with reasonable accuracy, as seen in fig. 12(d); this positive result is possible because of the high degree of two-dimensionality of the inlet flow field indicated by the transverse taps in figs. 12(b) and (c).

4. CONCLUSIONS

Because the sensitivity of airplane performance to inlet external drag is a strong function of the airplane's mission, the required accuracy for preliminary design methods cannot be stated in general. However, for aircraft with missions consisting of significant subsonic and supersonic portions, inlet external drag exerts a powerful influence on the aircraft's performance, and accurate predictions are required to allow for rational configuration definition.

The experimental data base for this effect has been identified and classified. Ranges of geometry and test parameters covered have been shown. Although a few systematic studies exist, the experimental data consist mostly of specialized studies of particular inlets. Because inlet external drag depends in an important way on geometrical details, this portion of the data base is adequate for prediction only for inlets not substantially different than those previously tested.

Several methods which result in the prediction of a component of C_{DEXT} have been identified and evaluated by comparison with experimental data. It has been shown that prediction of additive drag using a one-dimensional momentum analysis leads to acceptable agreement with data only for the simplest possible configuration, i.e., a pitot inlet. Predictions in other situations are in general poor, although methods containing additional empiricism can give reasonable agreement in limited classes of geometries. It is shown that calculation of cowl lip suction by methods with a reference mass flow ratio of unity are inaccurate because of the large extrapolation of data usually entailed. A method without this assumption, that of ref. 55, has been applied to inlets reasonably similar to those from which the correlation was derived. Resulting values of lip suction are in only fair agreement with data at low mass flow ratios. Because of its formulation, this method cannot predict experimentally demonstrated differences in lip suction resulting from changes in detailed cowl shape. Finally, it is shown that the K_{add} factor does not exhibit freedom from geometric detail. Its use is equivalent to using the original experimental data.

Several methods are discussed which predict the detailed flow field about an inlet, allowing calculation of C_{DEXT} and its components by simple integration. Some of these methods discussed herein yield adequate results although the comparisons with data available do not allow for comprehensive evaluation of their limits of applicability. For those methods applicable to supersonic design-point inlets, the large computers and long run times required to achieve satisfactory agreement result in their being of limited usefulness for preliminary design.

5. REFERENCES

1. McMillan, O. J., Perkins, E. W., Kuhn, G. D., and Perkins, S. C., Jr.: Data Base for the Prediction of Airframe/Propulsion System Interference Effects. NASA CR-152316, Nov. 1979.
2. Antonatos, P. P., Surber, L. E., and Stava, D. J.: Inlet/Airplane Interference and Integration. AGARD LS-53, Airframe/Engine Integration, May 1972.
3. Callahan, C. J.: An Experimental Investigation of the Component Drag Composition of a 2-D Inlet at Transonic and Supersonic Speeds. AGARD CP-150, Airframe/Propulsion Interference, Mar. 1975.
4. Mossman, E. A. and Anderson, W. E.: The Effect of Lip Shape on a Nose-Inlet Installation at Mach Numbers from 0 to 1.5 and a Method for Optimizing Engine-Inlet Combinations. NACA RM A54B09, May 1954.

5. Bencze, D. P.: Experimental Evaluation of Nacelle-Airframe Interference Forces and Pressures at Mach Numbers of 0.9 to 1.4. NASA TM X-3321, Mar. 1977.
6. Steffen, F. W.: Cruise Performance of an Isolated 1.15 Pressure Ratio Turbofan Propulsion System Simulator at Mach Numbers from 0.6 to 0.85. NASA TM X-3064, June 1974.
7. Re, R. J.: An Investigation of Several NACA 1-Series Axisymmetric Inlets at Mach Numbers from 0.4 to 1.29. NASA TM X-2917, Mar. 1974.
8. Re, R. J.: An Investigation of Several NACA 1-Series Inlets at Mach Numbers from 0.4 to 1.29 and Mass-Flow Ratios Near 1.0. NASA TM X-3324, Dec. 1975.
9. Motycka, D. L., Disabato, V. J., and Anderson, L. Q.: The Use of a Powered Model for Subsonic Nacelle Optimization. ASME Paper No. 72-GT-14, Gas Turbines and Fluids Engineering Conference and Products Show. Mar. 1972.
10. Sears, R. I., Merlet, C. F., and Putland, L. W.: Flight Determination of Drag Normal-Shock Nose Inlets with Various Cowling Profiles at Mach Numbers from .9 to 1.5. NACA TR 1281, 1953.
11. Dobson, M. D.: The External Drag of Fuselage Side Intakes: Semi-Circular Configurations Both With and Without Half Cone Compression Surfaces. RAE TR-72203, Feb. 1973.
12. McVey, F. D., Rejeske, J. V., and Phillip, J. V.: Experimental Evaluation of Inlet Drag Characteristics in the Transonic Mach Number Regime. AFAPL-TR-68-119, Nov. 1968.
13. Watne, D. A.: Determination of the Supersonic Additive Drag of Several Similar Inlet Configurations of the Type Used in the F-111. ASD TR-68-50, Nov. 1968.
14. Dobson, M. D.: The External Drag of Fuselage Side Intakes: Rectangular Intakes with Compression Surfaces Vertical. ARC CP-1269, 1974.
15. McVey, F. D., Rejeske, J. V., and Phillips, E. J.: Experimental Evaluation of Inlet Drag Characteristics in the Transonic Mach Number Regime. AFAPL-TR-68-119, Supplement 1, Nov. 1969.
16. Black, J. A.: A Wind Tunnel Test of a 0.07-Scale Inlet Drag Model of the B-1 Aircraft at Mach Numbers from 0.60 to 1.60. AEDC-TR-73-188, Nov. 1973.
17. Robertson, J. P.: B-1 Status Propulsion System Installation Effects - October 1972. North American Rockwell Rept. TFD-72-1425, Nov. 1972.
18. Johnson, T. J.: IP-9 Performance Characteristics for the B-1 External Compression Inlet. Rockwell International Rept. TFD-74-1091, Nov. 1974.
19. Schoelen, F. J., Kiser, C. E., and Mitchell, C. E.: Eleventh Interim Technical Report, Inlet/Nozzle Flight Performance Determination (Wind Tunnel Test Program). Rockwell International NA-76-7, Vol. II, June 1976.
20. Kiser, C. E., Johnson, T. J., Manzoku, R. T., and Schoelen, F. J.: Transonic Wind Tunnel Test Results of the 0.07-Scale B-1 Inlet Drag Model (AEDC-TF-305). Rockwell International Corp. Rept. No. NA-74-158, Sept. 1974.
21. Kostin, L.: Wind Tunnel Data Analysis, March 1975 Test, 0.06 Scale Nozzle Afterbody Model. Vol. II - Inlet/Nozzle Flight Performance Determination. Rockwell International Rept. NA-75-809, Feb. 1976.
22. Kiser, C. E. and Johnson, T. J.: Results of the B-1 .07-Scale External Compression Inlet Drag Model Wind Tunnel Test, TWT 269. North American Rockwell Rept. NA-73-42, Mar. 1973.
23. Keeney, F. J.: Inlet-Drag Characteristics of a 7.5-Percent Scale Model of the McDonnell Douglas F-15 Tactical Aircraft at Mach Numbers from 0.60 to 2.20. AEDC TR-70-263, Dec. 1970.
24. Tindell, R. H.: Advanced Inlet-Engine Matching Technology, Volume I - Aircraft Mission Analysis. Grumman Aerospace Corp. Rept. GAD-321-RT, Nov. 1976.
25. Brown, N.: Advanced Inlet-Engine Matching Technology, Volume II - High-Flow Inlet Wind Tunnel Results. Grumman Aerospace Corp. Rept. GAD-321-RT, Nov. 1976.
26. Fuller, D. E.: Pressure Distributions for a Rectangular Supersonic Inlet at Subsonic Speeds. NASA TM X-3305, Feb. 1976.
27. Petersen, M. W. and Tamplin, G. C.: Experimental Review of Transonic Spillage Drag of Rectangular Inlets. AFAPL-TR-66-30, May 1966.
28. Johnson, T. J. and Huff, J. N., Jr.: Propulsion System Integration and Test Program (Steady State). Part IV. AFAPL-TR-69-44, June 1969.

29. Hawkins, J. E., Kirkland, F. P., and Turner, R. L.: Inlet Spillage Drag Tests and Numerical Flow-Field Analysis at Subsonic and Transonic Speeds of a 1/8-Scale, Two Dimensional, External-Compression, Variable-Geometry, Supersonic Inlet Configuration. General Dynamics/Convair Rept. No. FZA-467, May 1974.
30. Brown, N., Tindell, R., and Stevens, C.: F-14A 1/7th Scale Inlet-Forebody Wind Tunnel Test Report, Phase IIIA and IIIB. Grumman Rept. No. ASI-33B-R-70-1, Apr. 1970.
31. Rejeske, J. V. and Porter, J. L.: Inlet/Aircraft Drag Investigation. AFFDL-TR-74-34, Apr. 1974.
32. Sonntag, A. H., Laffay, P. J., and Southerland, T. L.: Wind Tunnel Test on the 7.5 Percent Scale F-15 Aerodynamic Drag Model in the AEDC 16 Foot Transonic and Supersonic Facility. Series I, Test TF240 and SF129. McDonnell Douglas Corp. Rept. No. MDC A0624, Oct. 1970.
33. Kamman, J. H. and Wallace, H. W.: Assessment of Installed Inlet Forces and Inlet/Airframe Interactions. McDonnell Douglas Corp., AFFDL-TR-76-62, July 1976.
34. Burchfield, C. G.: An Investigation of Inlet and Aircraft Drag on a 7.5-Percent Scale Model of a Twin-Engine High-Speed Fighter Aircraft at Transonic Mach Numbers. AEDC TR-76-79, July 1976.
35. Sorensen, N. E. and Smeltzer, D. B.: Investigation of a Large-Scale Mixed-Compression Axisymmetric Inlet System Capable of High Performance at Mach Numbers 0.6 to 3.0. NASA TM X-1507, Feb. 1968.
36. Smeltzer, D. B. and Sorensen, N. E.: Investigation of a Nearly Isentropic Mixed-Compression Axisymmetric Inlet System at Mach Numbers 0.6 to 3.2. NASA TN D-4557, May 1968.
37. Woollett, R. R., Meleason, E. T., and Choby, D. A.: Transonic Off-Design Drag and Performance of Three Mixed-Compression Axisymmetric Inlets. NASA TM X-3215, June 1975.
38. Woollett, R. R., Meleason, E. T., and Choby, D. A.: Transonic Off-Design Drag and Performance of an Axisymmetric Inlet with 40-Percent Internal Contraction on Design. NASA TM X-3042, Aug. 1974.
39. Muller, G. L. and Gasko, W. F.: Subsonic-Transonic Drag of Supersonic Inlets. J. Aircraft, Vol. 4, No. 3, May-June 1967, pp. 231-236.
40. Hartill, W. R., Schoelen, F. J., and Kiser, C. E.: Test Results of an .07 Scale B-1 Mixed Compression Inlet Drag Model, NASA Ames Test (97,11)640. North American Rockwell Rept. NA-72-775, Nov. 1972.
41. Wilhelm, G. A. and Matthews, J. P.: Trisonic Wind Tunnel Tests of the B-1 0.07-Scale Inlet Drag Model I (Test 1, TWT 242). Vols. I, II, III, IV, and V. North American Rockwell Rept. NA-71-721, Aug. 1971.
42. Johnson, T. J.: Test Results of the 0.07-Scale B-1 Inlet Drag Model (TWT 242). North American Rockwell Rept. NA-71-1082, Dec. 1971.
43. Wong, N. D. and Anderson, W. E.: Experimental Investigation of a Large-Scale, Two-Dimensional, Mixed Compression Inlet System. NASA TN D-7445, Oct. 1973.
44. Ball, W. H.: Propulsion System Installation Corrections. Vols. I, II, III, and IV. AFFDL-TR-72-147, Dec. 1972.
45. Ball, W. H.: Rapid Calculation of Propulsion System Installation Corrections. AIAA Paper No. 74-1174, AIAA/SAE 10th Propulsion Conf., Oct. 1974.
46. Brazier, M. E. and Ball, W. H.: Accounting of Aerodynamic Forces on Airframe/Propulsion Systems. AGARD CP-150, Airframe/Propulsion Interference, Mar. 1975.
47. Crosthwait, E. L., Kennon, I. G., Jr., Roland, H. L., et al.: Preliminary Design Methodology for Air-Induction Systems. SEG-TR-67-1, Jan. 1967.
48. Mount, J. S.: Effect of Inlet Additive Drag on Aircraft Performance. J. Aircraft, Vol. 2, No. 5, Sept.-Oct. 1965, pp. 374-378.
49. Crosthwait, E. L.: Pitot Inlet Additive Drag. J. Aircraft, Vol. 7, No. 6, Nov.-Dec. 1970, pp. 569-570.
50. Sharp, B. M. and Howe, J. P.: Procedures for Estimating Inlet External and Internal Performance. NWC TP-5555, Apr. 1974.
51. Mascitti, V. R.: Charts of Additive Drag Coefficient and Mass-Flow Ratio for Inlets Utilizing Right Circular Cones at Zero Angle of Attack. NASA TN D-3434, 1966.

52. Mascitti, V. R.: An Approximate Solution of Additive-Drag Coefficient and Mass-Flow Ratio for Inlets Utilizing Right Circular Cones at Zero Angle of Attack. NASA TN D-5537, Nov. 1969.
53. Moeckel, W. E.: Estimation of Inlet Lip Forces at Subsonic and Supersonic Speeds. NACA TN-3457, June 1955.
54. Cawthon, J. A., Crosthwait, E. L., et al.: Supersonic Inlet Design and Airframe-Inlet Integration Program (Project Tailor-Mate). Vols. I, II, and III. AFFDL-TR-71-124, May 1973.
55. Osmon, R. V.: Improved Method of Spillage Drag Prediction for Two Dimensional Supersonic Inlets. AIAA Paper No. 67-449, AIAA 3rd Propulsion Joint Specialist Conf., July 1967. Also, J. Aircraft, Vol. 5, No. 3, May-June 1968, pp. 254-260.
56. Smith, O. W.: Generalized Method of Predicting Lip-Suction and Spillage Drag Force Coefficients of Isolated Axisymmetric Inlets. General Dynamics AIM No. 185, May 1969.
57. Sibulkin, M.: Theoretical and Experimental Investigation of Additive Drag. NACA Rept. 1187, 1954.
58. Bober, L. J.: Use of Potential Flow Theory to Evaluate Subsonic Inlet Data from a Simulator-Powered Nacelle at Cruise Conditions. NASA TN D-7850, Dec. 1974.
59. Biringen, S. and McMillan, O. J.: Calculation of Inlet Flow Fields by an Implicit Technique. AIAA Paper 80-0031, Jan. 1980.
60. Rochow, T. C., Sharp, B. M., and Spong, E. D.: Calculation of Subsonic Inlet Drag. AFAPL-TR-69-103, June 1970.
61. Caughey, D. A. and Jameson, A.: Accelerated Iterative Calculation of Transonic Nacelle Flowfields. AIAA Paper No. 76-100, AIAA 14th Aerospace Sciences Meeting, Jan. 1976.
62. Arlinger, B. G.: Calculation of Transonic Flow Around Axisymmetric Inlets. AIAA Paper No. 75-80, AIAA 13th Aerospace Sciences Meeting, Jan. 1975.
63. Reyhner, T. A.: Transonic Potential Flow Around Axisymmetric Inlets and Bodies at Angle of Attack. AIAA Paper No. 77-145, AIAA 15th Aerospace Sciences Meeting, Jan. 1977.
64. Hess, J. L. and Stockman, N. O.: An Efficient User-Oriented Method for Calculating Compressible Flow About Three-Dimensional Inlets. AIAA Paper No. 79-0081, Jan. 1979.
65. Keith, J. S., Ferguson, D. R., Merkle, C. L., Heek, P. H., and Lahti, D. J.: Analytical Method for Predicting the Pressure Distribution about Nacelles at Transonic Speeds. NASA CR-2217, July 1973.
66. Smith, A. and Pierce, J.: Exact Solution of the Neumann Problem - Calculation of Non-Circulatory Plane and Axially Symmetric Flows About or Within Arbitrary Boundaries. Douglas Rept. No. ES26988, Apr. 1958.
67. Hess, J.: Calculation of Potential Flow About Bodies of Revolution Having Axes Perpendicular to the Free Stream Direction. Douglas Rept. No. ES29812, Oct. 1960.
68. Hess, J. and Smith, A.: Calculation of Non-Lifting Potential Flow About Arbitrary Three-Dimensional Bodies. Douglas Rept. No. ES40622, Mar. 1962.
69. Lieblein, S. and Stockman, N. O.: Compressibility Correction for Internal Flow Solutions. J. of Aircraft, Vol. 9, No. 4., Apr. 1972.
70. Stratford, B. S. and Beavers, G. S.: The Calculation of the Compressible Turbulent Boundary Layer in an Arbitrary Pressure Gradient - A Correlation of Certain Previous Methods. ARC R&M No. 3207, Sept. 1959.

6. ACKNOWLEDGEMENTS

The work described in this article was sponsored by NASA/Ames Research Center under Contracts NAS2-8874 and NAS2-9513. Messrs. Leroy L. Presley and Daniel C. Bencze were the Technical Monitors.

TABLE I.- DATA FOR INLET EXTERNAL DRAG

Reference Number	Inlet	Drag Component Presented	Test Configuration	Mach Number	Reynolds No. Per Meter ($\times 10^{-6}$)	Angle of Attack, Deg.	Angle of Sideslip, Deg.	Data Showing Separate Effects of						
								Coil Shape	Side Plate Shape	Ramp Angle	Capture Area	Varying A.L.	Varying Plate	Coil Ratio
4	P _o	C _D EXT	I ¹	0.7-1.5	10.3-12.5	0 to 5	0	✓						
5	P _o	2	I ³	0.9-1.4	9.8	0	0	✓						
6	P _c	C _D C	I	0.75, 0.85	12.3-14.3	0	0							
7	P _c	C _D C, C _D EXT	I	0.6-1.29	9.6-12.2	0	0	✓			✓			✓
8	P _c	C _D C	I	0.4-1.29	7.5-12.9	0	0	✓			✓			✓
9	P _c	C _D A, C _D C	I	0.7-0.9	N.R. ⁴	0	0	✓						
10	P _c	5	6	0.9-1.5	14.1-30.8	0	0	✓						
	P _c	7,8	9	0.6-2.0	0.29-0.8 ¹⁰	0	0	✓						
11	E _c Clvl	7,8	9	0.6-2.0	0.29-0.8 ¹⁰	0	0	✓		✓				
12	P _c	C _D EXT, C _D C	I	0.7-1.25	N.R.	0	0	✓						
	E _c Clvl 2.3	C _D EXT, C _D C	I	0.7-1.05	N.R.	0	0	✓						
	E _c Clvl 2.7	C _D EXT, C _D C	I	0.7-2.0	N.R.	0	0	✓			✓			
	E _c Clvl 3.1	C _D EXT, C _D C	I	0.7-1.05	N.R.	0	0	✓						
	E _v Clvl 2.4	C _D EXT	11	0.7-1.05	N.R.	0 to 6	0			✓				
	E _v Clvl 5	C _D EXT	I	0.6-2.2	N.R.	0 to 6	0	✓	✓	✓				
13	E _v Clvl 2.2	C _D A	9,12	1.2, 2.2	N.R.	2,5,5	0	✓	✓					
14	E _v Clvl 2.4	7	9	0.6-2.0	8.5-22.8	0	0	✓	✓					
	E _v Clvl 2.7	7	9	0.7-0.9	8.5	0	0	✓						
15	E _v Clvl 2.7	C _D A, C _D C	I	0.7-2.0	N.R.	0	0							
	E _v Clvl 2.4	C _D EXT	11	0.7, 0.9	N.R.	0,6	0							
	E _v Clvl 2.0	C _D EXT	I	0.7, 0.9	N.R.	0	0			✓				
16	E _v Clvl 2.2	13	14	0.6-1.6	N.R.	0.5 to 3.5	0	✓	✓	✓		✓		
17	E _v Clvl 2.2	C _D A, C _D BP, C _D BL	15	0.2-2.2	N.R.	N.R.	N.R.						✓	
18	E _v Clvl 2.2	C _D BP	14	0.2-2.2	N.R.	N.R.	N.R.						✓	
19	E _v Clvl 2.2	C _D EXT, C _D BL, C _D A, C _D BLD, C _D BP	14	0.7-1.4	1.64-2.4	1 to 4	0			✓		✓	✓	
20	E _v Clvl 2.2	17	14	0.6-1.4	N.R.	0.5 to 3.5	0			✓	✓		✓	
21	E _v Clvl 2.2	18	19	0.7-1.4	3.28-16.4	-2 to 6	0							
22	E _v Clvl 2.2	20	14	0.55-1.3	N.R.	2	0	✓	✓			✓		
	E _v Clvl 2.2	21	14	0.55-0.85	N.R.	2	0							
23	E _v Clvl 2.2	22, C _D EXT, C _D A	23	0.6-2.2	4.1-8.7	-4 to 20	0				✓			
24	E _v Clvl 1.6	24	I	0.85	N.R.	0	0							
	E _v Clvl 1.6	24	125	0.85	N.R.	0	0	✓						
25	E _v Clvl 1.6	5	125	0.85	N.R.	0	0	✓		✓				
26	E _v Clvl 3.3	C _D A, C _D C	I	0.6-0.8	N.R.	0 to 8	0	✓	✓	✓				
27	E _v Clvl 3.0	C _D A, C _D C	I	0.7-1.7	N.R.	0	0	✓		✓				
28	E _v Clvl 2.5	13	11	0.6-2.2	N.R.	2 to 10	0	✓		✓			✓	
29	E _v Clvl 2.2	C _D EXT	I	0.55-1.39	4.9-11.5	0	0			✓				
30	E _v Clvl 2.4	26	27	0.6-2.4	7.4-13.1	-4 to 20	-10 to 10	✓						
31	E _v Clvl 2.5	C _D A, C _D C, C _D SP, C _D EXT	23,28	0.6-0.9	10.8-12.9	0 to 9	0			✓	✓			
32	E _v Clvl 2.5	22	23	0.6-2.2	4.0-8.7	-4 to 20	0			✓	✓			
33	E _v Clvl 2.5	C _D A, C _D C, C _D SP, C _D EXT	23,28	0.6-1.5	5.25-15.74	-1 to 17	0			✓	✓	✓		
34	E _v Clvl 2.5	22,24	23,28	0.6-1.5	8.2-13.1	0 to 17	0			✓	✓			
35	E _v Clvl 3.0	C _D A	I	0.6-1.2	N.R.	0	0							✓
36	E _v Clvl 3.0	C _D A	I	0.6-1.3	N.R.	0	0							
37	E _v Clvl 2.5 (30/70) 29	C _D A, C _D C	I	0.8-1.27	13.8-15.4	0	0						✓	
	E _v Clvl 2.5 (60/40)	C _D A, C _D C	I	0.8-1.27	13.8-15.4	0	0						✓	
	E _v Clvl 2.5 (40/60)	C _D A, C _D C	I	0.8-1.27	13.8-15.4	0	0						✓	
38	E _v Clvl 2.5	C _D A, C _D C	30	0.8-1.27	13.8-15.4	0	0						✓	
39	E _v Clvl 1.5	C _D A	I	0.5-1.3	19.4-45.0	0	0							✓
	E _v Clvl 1.5	C _D A	I	0.5-1.3	19.4-45.0	0	0							✓
40	E _v Clvl 2.2	21	14	0.55-2.2	13.4, 20.0	2,2,5	0	✓	✓	✓	✓	✓	✓	
41	E _v Clvl 2.2	31	14	0.55-2.20	N.R.	0 to 5	0	✓		✓				
42	E _v Clvl 2.2	31	14	0.55-1.7	N.R.	2,2,5	0	✓		✓				
43	E _v Clvl 3.0	C _D A, C _D EXT	I	0.6-1.28	11.2-14.1	0	0					✓		✓

NOTES TO TABLE I

1. I denotes isolated inlet test
2. External drag on a nacelle configuration
3. Nacelle configuration
4. N.R. denotes quantity not reported
5. Additive drag plus pressure and friction drag of entire model
6. Flight test of rocket models having common afterbodies
7. Sum of external and forebody drag
8. Sum of external drag, forebody drag, and boundary-layer-diverter drag
9. Tested with metric forebody
10. Reynolds number range given based on inlet radius; inlet radius not reported
11. Inlet tested in isolated configuration and with non-metric forebody
12. Quarter-round inlet of F-111 type
13. Sum of external drag, drag due to the bypass and boundary-layer control systems, and drag of partial fuselage and wing stub
14. Partial fuselage and stub wing included
15. Type of configuration tested with inlet is not known
16. Sum of additive and bleed drag
17. Sum of external drag, drag due to the bypass and boundary-layer control systems, and the drag of the partial fuselage and wing stub, measured relative to a "propulsion reference inlet"
18. Inlet cowl and ramp integrated pressure-area chord force coefficient
19. Full B-1 aircraft model with balance installed in one inlet. Metric portion included nozzles and part of wing. Inlet configurations included are: flow through inlet, faired-over inlet w/BLC and bypass, flow through inlet w/ramps installed.
20. Sum of external drag, drag due to the boundary-layer control system, drag of the partial fuselage and stub wing, measured relative to a "propulsion reference inlet"
21. Sum of external drag and drag of partial fuselage and stub wing, measured relative to a "propulsion reference inlet"
22. Drag of entire airplane model
23. Model of entire F-15
24. Sum of external drag and bleed/bypass system drag
25. Inlet design includes auxiliary airflow system
26. Sum of external drag, boundary-layer control drag, forebody and external-store drag
27. Tested with forebody, with and without various external stores.
28. Full aircraft model with full aircraft on one force balance, one inlet on another
29. Numbers in parenthesis indicate percentage of external/internal contraction
30. Inlet tested in isolated configuration and with non-metric wing simulator
31. Sum of external drag, drag due to boundary-layer control system, and drag of the partial fuselage and stub wing

TABLE II.- MAIN CHARACTERISTICS OF INLETS

Characteristic	Descriptor	Subscript
Inlet Type	P = Pitot (Normal Shock) E = External Compression M = Mixed Compression	Refers to capture area shape c = circular r = rectangular o = other
Orientation of Compression Surfaces (relative to pitch plane of aircraft)	C = Conical centerbody for axisymmetric inlet H = Horizontal V = Vertical	Refers to numbers of surfaces Either i f or i v j, where i = total number of external surfaces f = fixed v = variable j = number of variable external surfaces
Side Plate Geometry	S = Side Plates present	Refers to shape r = rectangular t = triangular n = notched or cut-back
Boundary-Layer Control	B = Boundary-Layer Control present	Refers to type d = discrete elements e.g., slots or scoops p = porous elements
Bypass System	BP = Bypass system present	None
Design Mach Number	Value given	None

TABLE III.- CLASSIFICATION OF PREDICTION METHODS FOR A COMPONENT OF $C_{D_{EXT}}$ BY GEOMETRY AND SPEED RANGE

Quantity Predicted	Inlet Type	Speed Range	
		Subsonic	Transonic
C_{DA}	Pitot	44,45,46,47,48,49	44,45,46,47,48,49
	2-D	27,44,45,46,47	27,44,45,46,47,50
	Axi	44,45,46,47	44,45,46,47,51,52
C_{LS}	Pitot	47,53	47,53
	2-D	47,54,55	47,54,55
	Axi	47,54,56	47,54,56
K_{add}	Pitot	44,48	44,48
	2-D	27,44	27,44
	Axi	44	

TABLE IV.- CLASSIFICATION OF FLOW-FIELD PREDICTION METHODS BY SOLUTION METHOD AND GEOMETRY

Solution Method	References	Applicable Geometry		
		Pitot	2-D	Axi
Numerical solution of the unsteady Euler equation	29,59		✓	✓
Finite-difference solution of full potential equation	12,60 61,62,63	✓	✓	✓
Finite-difference solution of incompressible potential equation with compressibility correction	12 64	✓	✓	✓
Streamtube curvature	65	✓	✓	✓

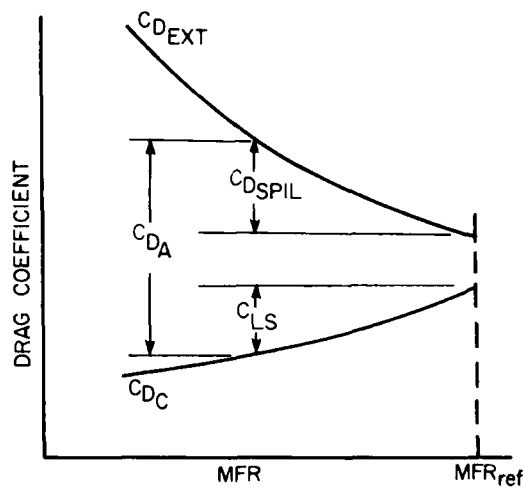


Figure 1.- Inlet external drag terms.

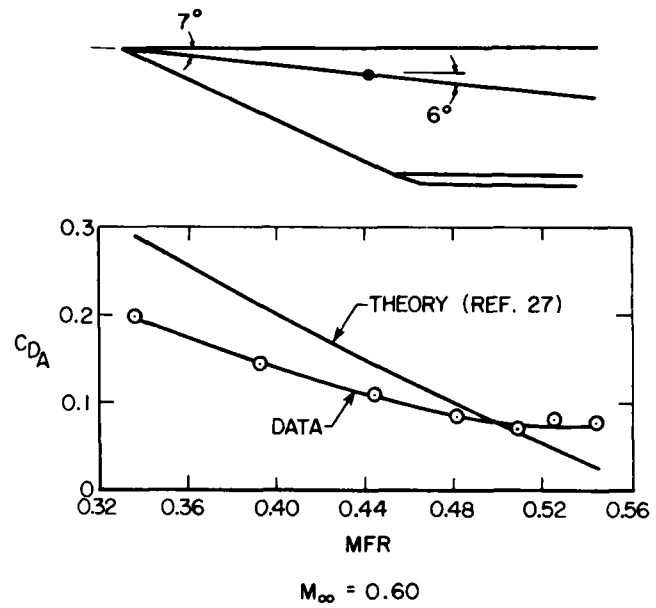


Figure 3.- Comparison of experimental and theoretical additive drag from ref. 43.

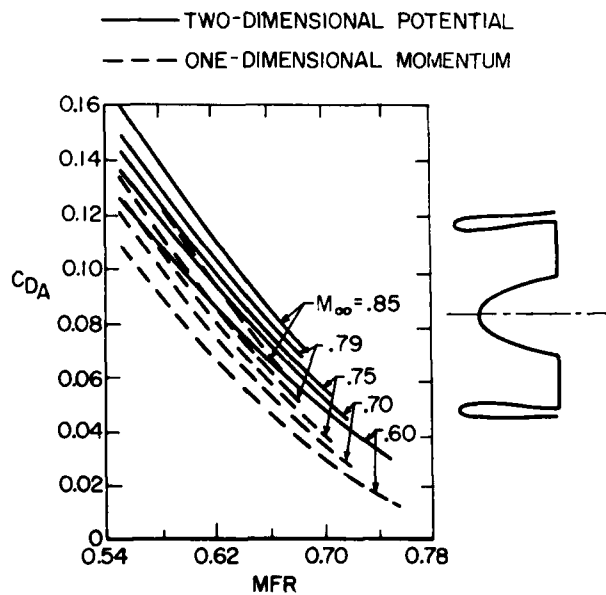


Figure 2.- Comparison of theoretical additive drag values from ref. 58.

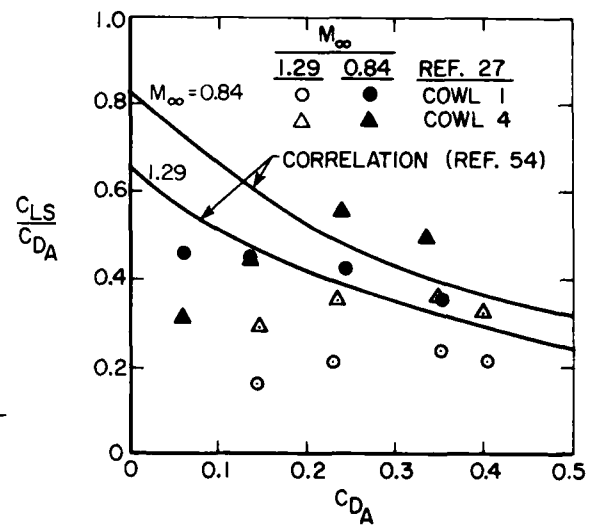


Figure 4.- Comparison of the lip suction correlation of ref. 54 with data from ref. 27.

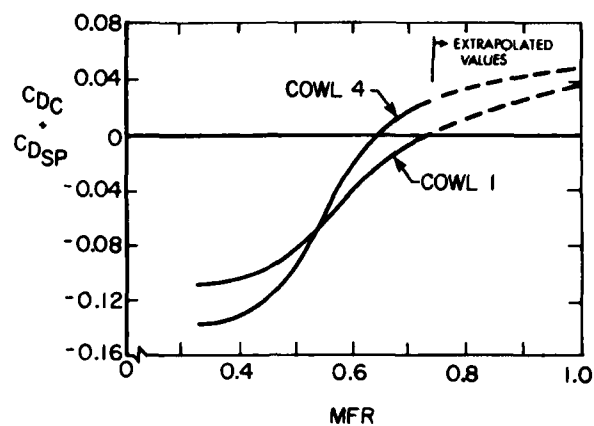
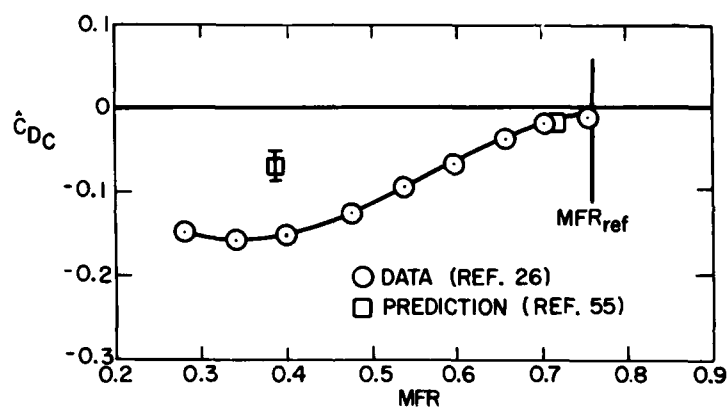
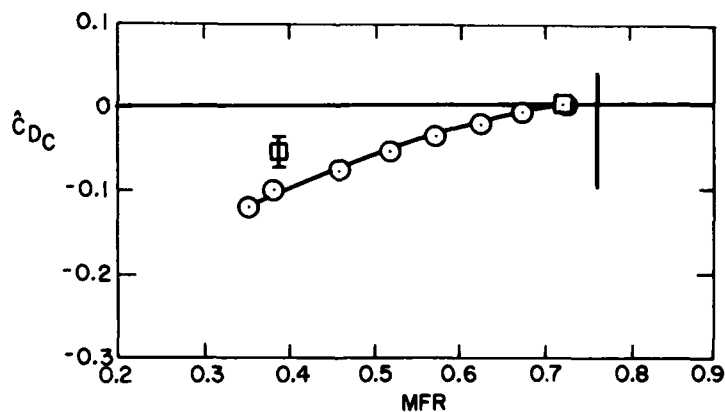


Figure 5.- Extrapolations required to calculate C_{LS} from data of ref. 27 ($M_\infty = 0.84$).

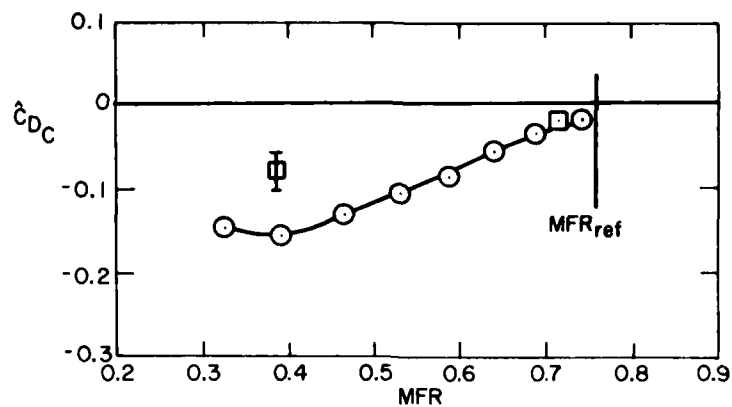


(a) COWL 90-1, RECTANGULAR SIDE PLATES.

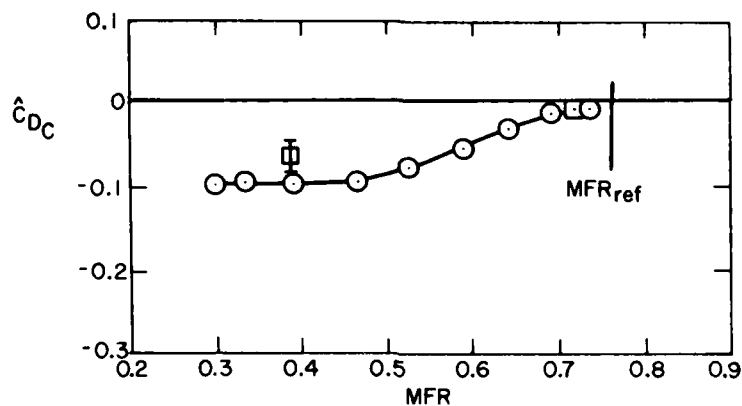


(b) COWL 90-1, TRIANGULAR SIDE PLATES.

Figure 6.- Comparison of lip suction from the method of ref. 55 with the data of ref. 26; $\alpha = 0$, $M_\infty = 0.8$.

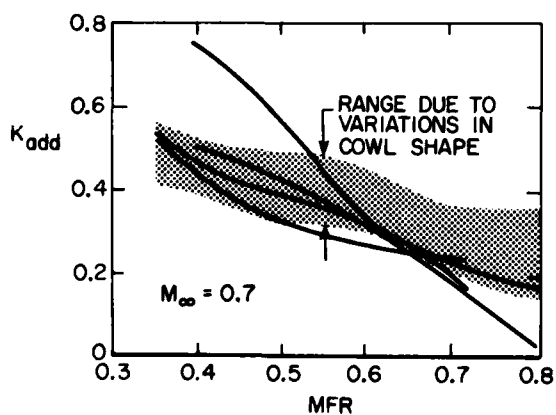
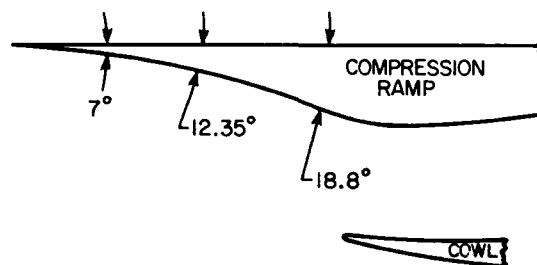


(c) COWL 90-2, RECTANGULAR SIDE PLATES.



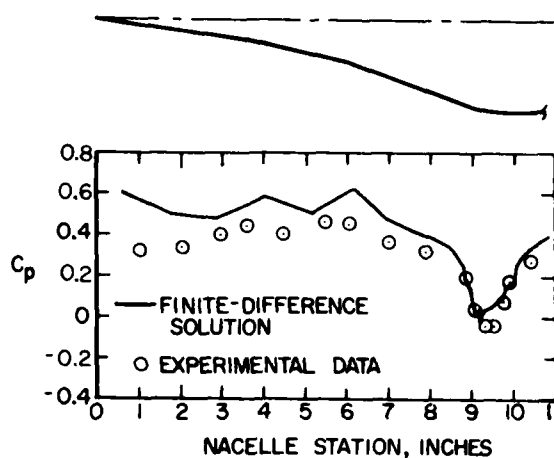
(d) COWL 20-2, RECTANGULAR SIDE PLATES.

Figure 6.- Concluded.

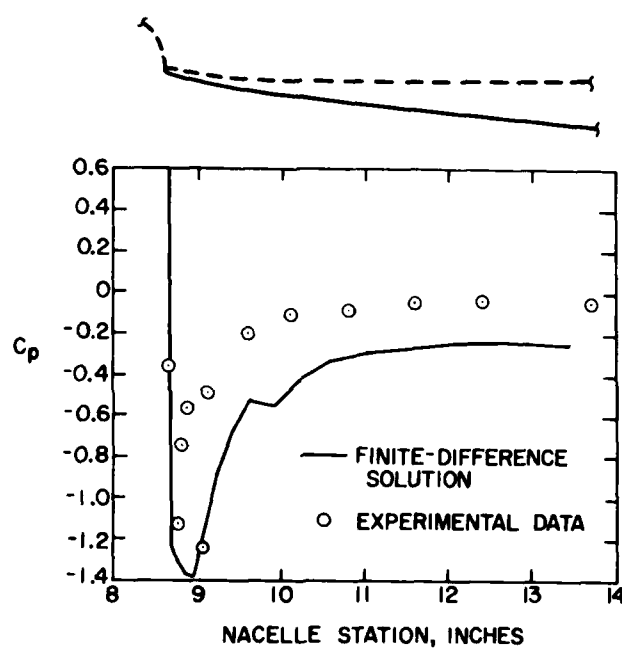
Figure 7.- Variation of K_{add} with mass flow ratio from ref. 27; two-dimensional, two-ramp, external compression inlets with design Mach number = 3.0.

(a) INLET GEOMETRY.

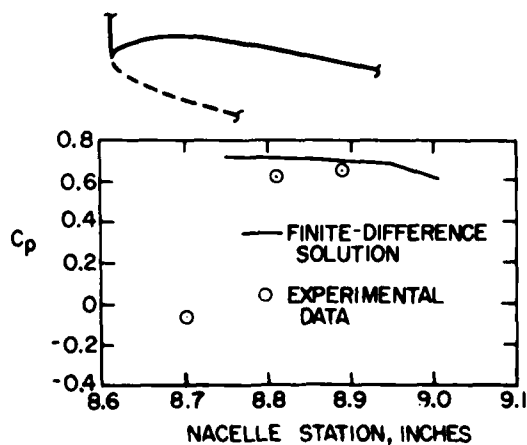
Figure 8.- Comparison of experimental and theoretical surface pressures at $M_\infty = 0.7$, $MFR = 0.5$ from ref. 29.



(b) RAMP PRESSURES.

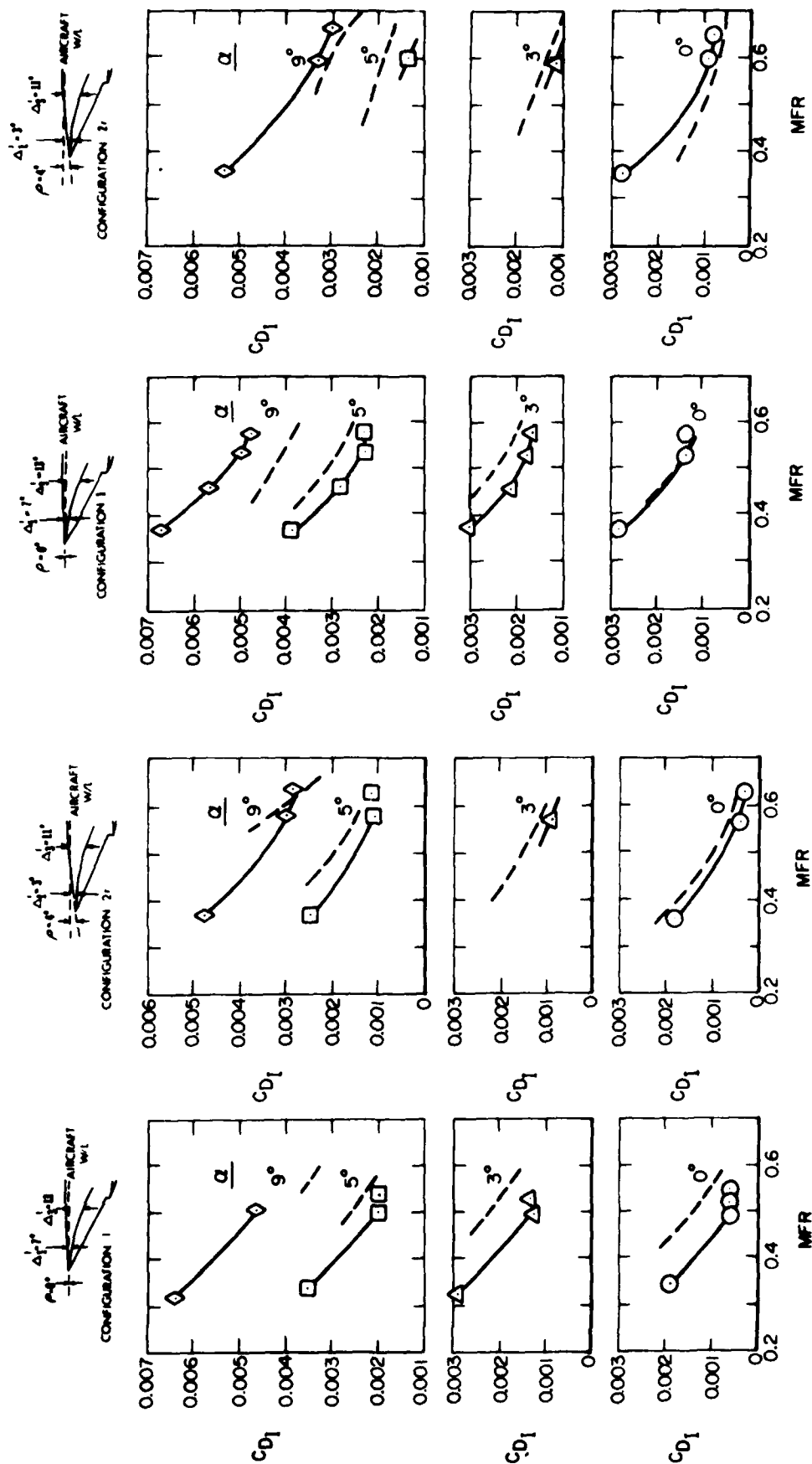


(c) COWL EXTERNAL PRESSURES.



(d) COWL LIP INTERNAL PRESSURES.

— INLET BALANCE DATA
 --- THEORETICAL PERFORMANCE
 (REF. 60)



(a) $M_{\infty} = 0.6$

(b) $M_{\infty} = 0.9$

Figure 9.- Comparison of experimental and theoretical inlet drag for a 2-D inlet; from ref. 31.

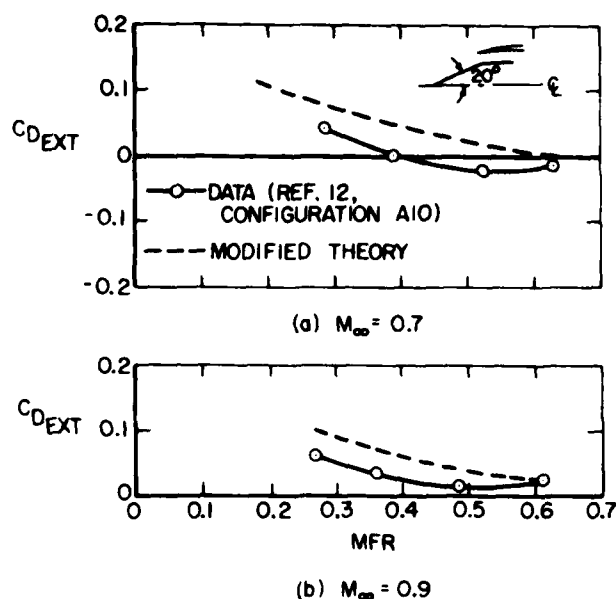
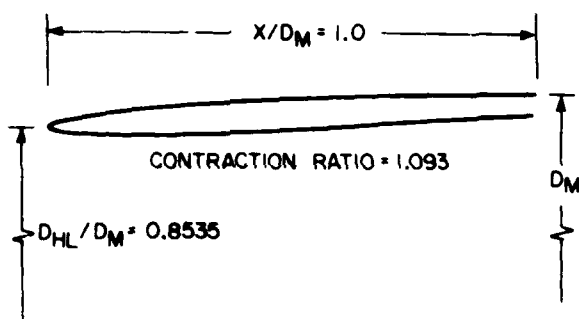


Figure 10.- Comparison of experimental and theoretical inlet drag for an axisymmetric inlet (config. A10, ref. 12); from ref. 60.



(a) PITOT INLET GEOMETRY FROM REF. 65.
(NASA 1-85-100 NO. 8 INLET, NACA-1 SERIES CONTOUR)

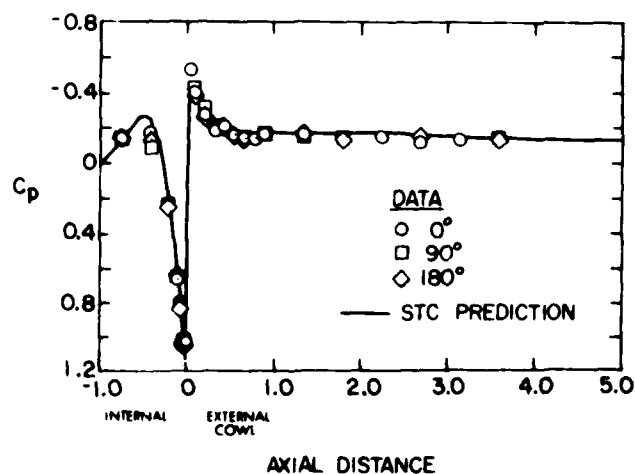
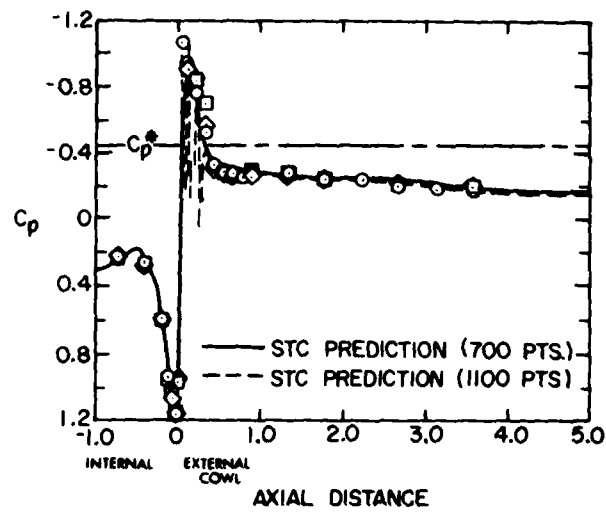
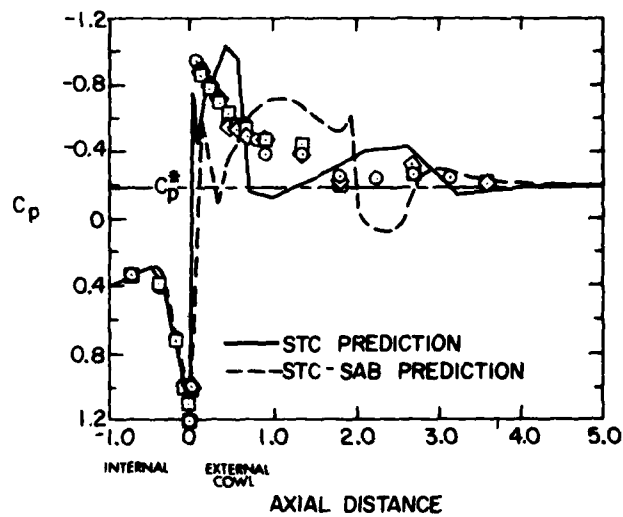


Figure 11.- Comparisons of experimental and theoretical surface pressures for the pitot inlet from ref. 65.

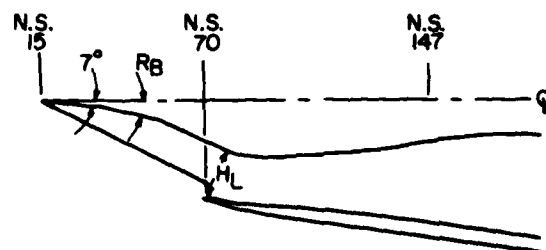


(c) $M_{\infty} = 0.8008$, $MFR = 0.8093$.



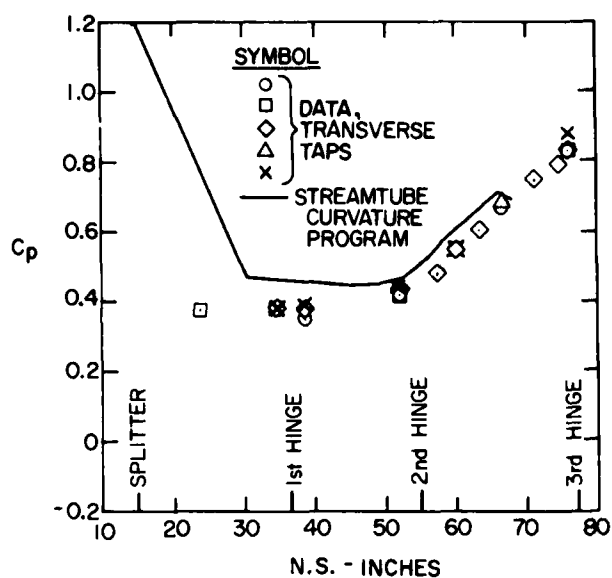
(d) $M_{\infty} = 0.900$, $MFR = 0.8073$.

Figure 11.- Concluded.

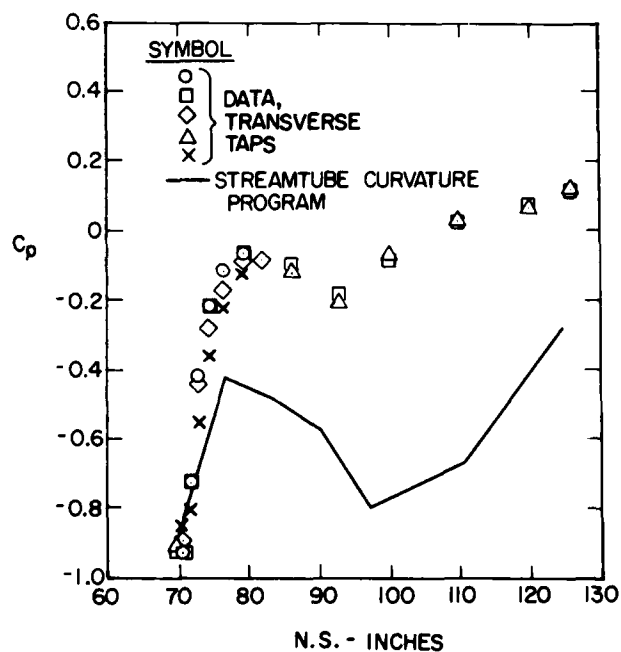


(a) EXTERNAL COMPRESSION INLET GEOMETRY.

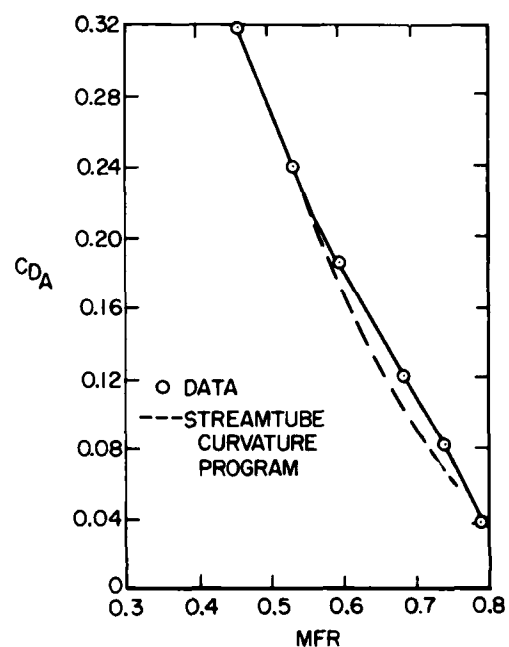
Figure 12.- Comparison of experiment and streamtube curvature analysis from ref. 19; $M_{\infty} = 0.85$, $\alpha = 2.5^\circ$.



(b) RAMP SURFACE PRESSURES, MFR = 0.55.



(c) COWL SURFACE PRESSURES, MFR = 0.55.



(d) ADDITIVE DRAG.

Figure 12.- Concluded.

Figure 12.- Continued.

**PHILOSOPHY AND RESULTS OF STEADY AND UNSTEADY TEST TECHNIQUES
ON A LARGE SCALE TRANSPORT AIRCRAFT MODEL
IN THE ONERA TRANSONIC TUNNEL S1 MA**

Part 1: PHILOSOPHY AND RESULTS OF STEADY TESTS

G. Anders

Vereinigte Flugtechnische Werke GmbH, D-2800 Bremen, FRG

A. Giacchetto

Office National d'Etude et de Recherches Aeronautiques (ONERA),
Centre d'Essais de Modane-Avrieux, FRANCE

Part 2: INTEREST OF LARGE MODELS IN UNSTEADY AERODYNAMICS

A. Gravelle

Office National d'Etude et de Recherches Aeronautiques (ONERA),
Chatillon, FRANCE

SUMMARY

Steady and unsteady wind tunnel tests with a large scale half model have been performed in the large ONERA transonic wind tunnel S1 MA in 1979 within the German technology program ZKP and the development phase of the A 310 Airbus.

The contribution is composed of two chapters. Part 1 concerns with the fundamental concept on the subject "Wind tunnel tests with large models". Various test techniques are introduced, their advantages and problems are discussed. The test arrangement concept is described and typical results for each of the investigated items are presented. Furthermore, comparison with test results on a complete model at lower Reynolds Numbers is drawn.

Whereas in part 1 mainly stationary measurements are described and discussed, chapter 2 primarily deals with unsteady tests. Reasons are given for the advantage of a large model. Test methods, data pick up and processing systems are pointed out. Characteristic results are presented and correlations are shown.

This contribution, prepared by VFW and ONERA, is based on a common work, performed by VFW, MBB, DFVLR and ONERA recently. Domier was associated in the program.

Part 1: PHILOSOPHY AND RESULTS OF STEADY TESTS

NOTATION

A_e	$[m^2]$	nacelle exit area	D_N	$[N]$	nacelle drag
A_i	$[m^2]$	nacelle intake area	$D 1$	$[-]$	nacelle throttle condition
c	$[m]$	local wing chord	$D 5$	$[-]$	
\bar{c}	$[m]$	mean aerodynamic chord (MAC)	$K I$	$[-]$	contour disturbance - slat position -
C_D	$[-]$	drag coefficient	$K III$	$[-]$	
C_{DN}	$[-]$	nacelle drag coefficient	$K 5$	$[-]$	contour disturbance - spoiler position -
C_L	$[-]$	lift coefficient	$K 7$	$[-]$	
C_{m25}	$[-]$	local pitching moment coefficient on the wing	M	$[-]$	Mach Number
C_n	$[-]$	local normal force coefficient on the wing	q	$[Pa]$	free - stream dynamic pressure
C_p	$[-]$	local pressure coefficient	Re	$[-]$	Reynolds Number
C_x	$[-]$	non-corrected drag coefficient	S	$[m^2]$	wing reference area
ΔC_D	$[-]$	drag increment coefficient	s	$[m]$	wing semi span
			$T.S.$	$[-]$	transition strip

v	[m/s]	free - stream velocity		
x	[m]	coordinates		
y	[m]			
z	[m]			
α	[°]	angle of attack	ν	[m ² /s] kinematic viscosity
δ	[%]	wing thickness	ξ	[-] non-dimensional x-coordinate
ϵ_v	[°]	twist	ξ	[°] aileron deflection angle
η	[-]	non-dimensional wing span	ψ_{25}	[°] wing sweep (25 % - line)
Λ	[-]	aspect ratio		

1. INTRODUCTION

The development of the new generation of transport aircrafts is essentially characterized by application of modern wing technology. The necessarily increasing wing loads are achieved by taking advantage of the potential of the transonically profiled wing. For this purpose theoretic calculation- and design-methods are applied, which were successfully developed recently [1].

With increasing loads and local supersonic flow on the wing, sensitivity against interferences and non-stationary effects rises. The wing flow tends to separate. Disturbances on the wing contour, caused by manufacture tolerances and deformations under load conditions, have to be considered with respect of their consequences on the wing flow. Unsteady effects on the wing will result in flow separations, leading to early buffeting.

Usually as a first step theoretical methods and design results are checked out with small models in the wind tunnel, however, application of such results to high Reynolds numbers is uncertain. Experimental proof in the high Re-Number range is necessary. The significance of such experimental proof is evident by the enormous investments carried out for wind tunnel facilities in Europe and all over the world (DNW, RAE 5 x 4.5 m² tunnel, ONERA F1, ETW, cryogenic technology).

In the course of the technology program ZKP under the sponsorship of the German Ministry of Research and Technology, theoretical calculation methods for the design of 2-D-airfoils and 3-D-wings at transonic speeds were developed by the partners [2] [3] [4] [5]. As an output of these activities, several small scale models were produced and tested in the NLR-HST and DFVLR transonic wind tunnel respectively. Results and analysis of these tests led to the choice of the VFW wing design as the basis for a large scale model to be tested in the ONERA S1 MA.

2. MODEL AND TEST ARRANGEMENT CONCEPT

2.1 GENERAL ASPECTS

High demands were made on the model and the test arrangement capability. Influences of various parameters on performance and buffet onset characteristics should be investigated at maximum possible Re-Numbers in the whole Mach Number range:

- o engine and pylon interferences on the wing
- o influence of throttled nacelle intake flow
- o effects of engine position variation relative to the wing
- o aileron deflection effects
- o interaction of wing-fuselage-fairings
- o influence of contour disturbances in the region of spoiler and slat positions
- o nonstationary effects due to unsteady aerodynamic flow.

These requirements led to the design, construction and manufacture of a large wind tunnel half model, consisting of the main components:

- o semi fuselage
- o port side wing
- o flow through nacelle with remotely controlled mass flow
- o external remotely controlled nacelle suspension facility.

Design criteria were defined by certain restrictions:

- o stationary force and pressure distribution measurements were required;
- o unsteady measurements should be possible (local unsteady pressures, strain gauge signals, accelerations);
- o flow pattern on the model should be visible;
- o the necessary geometric configuration and parameter variations should be feasible.

In order to correlate origin and response of nonstationary effects, excitation of moving control surfaces on the wing, either in periodic or in random motion, was necessary. Actuator installation and sufficient instrumentation had to be provided.

The requirements and the ambition to utilize the model also for future purposes led to the philosophy of a manufacturing system of standardized units in a model scale of 1 : 5.4 referring to the A 310 - project.

2.2 MODEL COMPONENTS

2.2.1 Wing

The wing B10.3V was designed by VFW on the basis of the supercritical 2-D-VFW-airfoil Va 2. The wing system is represented in Fig. 1. Main dimensions are given in Fig. 2. The wing structure consists of aluminium panels, screwed to a steel box with cutting lines in the region of leading and trailing edges on the upper and lower surfaces. The final wing contour was milled numerically controlled in the final one piece assembly.

The wing was equipped with 9 static pressure plotting sections with 45 orifices each, distributed on the upper and lower surface. 3 further sections were furnished with a total of 68 unsteady pressure pick ups. In order to correlate wing movement and unsteady pressures, 12 accelerometers were installed. 3 strain gauge bridges were glued to the structure for buffeting investigation and load control purpose. An outboard aileron was installed and connected to a hydraulic actuator to be excited during the nonstationary tests or stationary deflected by the same system. An angle deflection indicator and a hinge moment balance were supplied.

During cruise flight conditions protrusion of retracted slat trailing edges out of the wing contour due to suction forces on the wing nose and disturbances at spoiler trailing edges may occur. To investigate the effects of such phenomena on a transonically airfoiled wing, simulation of several combinations of contour disturbances was provided (Fig. 3). Trailing edge thickness was determined by a similarity calculation under consideration of model scale, Re-Number and theoretical boundary layer. Spoiler trailing edges were consciously overdesigned, to produce measurable effects.

Finally, a tubing system with 42 orifices was installed into the wing, to enable a coloured flow visualization during the tests.

2.2.2 Fuselage

The required stiffness of the 8 m long fuselage was achieved by a construction of an iron frame-work, covered with a fibre glas skin. The conventional solution to seal the semi fuselage force-free with the tunnel floor by a labyrinth system was not sufficient, because of forces contact due to arrangement deformation under loads. The problem was solved by a construction of a brushes system as shown in Fig. 4 [6].

About 270 static pressure orifices were distributed on the fuselage, mainly in the wing-fuselage region, on the boundary layer skirt and in the brushes-covered space between fuselage and tunnel floor, to discover possible internal flow. Two sets of wing-fuselage-fairings were provided.

2.2.3 Flow Through Nacelle

A single bodied flow through nacelle with remotely controlled mass flow was developed in order to simulate engine intake and fan cowl effects during the tests. The axial symmetrical intake and the outer contour correspond to the CF 6-50 engine contour in the pylon section. Mass flow is controlled by a plug with an infinite variable diameter in the nacelle exit area. The principle of this design is presented in Fig. 5. Intake and outer contour are supplied with static pressure orifices in 5 streamwise sections. Mass flow is calibrated and controlled by a rake of total and static pressure probes in the nacelle intake face.

2.2.4 External Nacelle Attachment Device

The flow through nacelle could either be attached together with a pylon directly to the wing or - by means of a special nacelle attachment device - externally brought up into different positions relative to the wing. A remotely controlled hydraulic facility was designed especially for these tests, to synchronize a selected relative nacelle position with varying model incidence by displacements of angle- and x-z-coordinates (Fig. 6). This device can be used for future tests as an engine simulator carrier.

2.3 TEST ARRANGEMENT

The whole test arrangement was designed for the large ONERA transonic wind tunnel S1 in Modane, France. A principle of the model set up in the test section No. 1 is shown in Fig. 7 and Fig. 8. The wing-fuselage unit was attached to the 3-component under floor balance 7 [8]. All electric wiring, pneumatic and hydraulic tubing left the model on its wing base in the under floor section of the tunnel. From here it was distributed to the various power supply and measuring facilities:

- o to an independent measuring and data processing system, designed and assembled by VFW, which controls static pressure distribution measurements, produces and displays the results in on-line and off-line mode;
- o to a combined ONERA-DFVLR measuring station, which controls the hydraulic system for aileron excitation and where all nonstationary data are recorded and analysed;
- o finally to the wind tunnel measuring system, where all aerodynamic and force-data were processed and converted.

3. TESTS

3.1 PREPARATION, PRETESTS, CALIBRATIONS

Installation and adjustment of a test arrangement with such dimensions and weights - model and equipment weight amount to an order of 4 t - require certain effort.

Apart from conventional preparations and calibrations additional preparatory work and pretests are necessary:

- o coupling, synchronization and check out of the different measuring systems
- o static load tests on the model arrangement, to determine stiffness and deformations
- o static vibration tests and analysis to guarantee flutter freedom under all test conditions
- o nacelle flow through calibration
- o tests to ensure a force free sealing between the model and tunnel floor
- o determination of the hysteresis due to forces transferred by the sealing brushes
- o identification of the flow transition laminar/turbulent
- o transition fixing by transition strips.

3.2 TEST TECHNIQUES

3.2.1 Stationary Testing Points

During conventional steady tests forces, stationary pressure distribution and nonstationary measurements were conducted simultaneously under stabilized geometric and wind tunnel conditions. Possible interferences due to stiffness and friction of the tubes and wires were found to be negligible. During a 30 seconds test period all measured informations were recorded and computed on the various facilities. Quick look analysis and a selection of displayed results was available before the following testing point. Thus the carpet of polars at constant Mach Numbers was produced.

3.2.2 Continuous Incidence Polar

At a continually varying test condition measurement signals were recorded and computed quasi-analogous. This technique offers maximum information in a minimum of testing time. Application of this method for continuous polar determination excludes simultaneous pressure distribution measurements with a scanning system. The procedure of continuous incidence variation causes Mach Number increase respectively decrease due to tunnel blockage change. Simultaneous speed readjustment in large wind tunnels is difficult. So polars were produced, where Mach Number changes with angle of attack. By the aid of a 2-dimensional interpolation program a carpet of incidence polars at constant Mach Numbers can be computed, provided that a sufficient number of input data is measured.

3.2.3 Continuous Mach Number Polars

The technique of continuous Mach Number polar is recommended to investigate buffet onset and drag rise behaviour. At a fixed geometric model configuration flow is slowly accelerated to the maximum desired velocity. Force and buffet onset data are observed and recorded against Mach Number. The degree of acceleration is restricted by the time lag of the measuring system. Measuring data collection of various incidence conditions allows

interpolations to constant lift. This method is especially suggested, when effects of relatively small model modifications are to be determined.

3.2.4 Flow Through Throttling under Minimum Internal Loss Conditions

The advantage of the applied principle of throttling the mass flow through the nacelle is obvious, because except for friction no internal losses are produced due to throttle position. This results in the fact, that nacelle drag is kept to a minimum under throttle conditions. Drag rise and changes in the measured characteristics indicate spillage and Mach Number effects.

3.2.5 Determination of Model Deformations under Aerodynamic Loads

Deformations of the test arrangement consist of the attachment-elasticity (balance) and the bending of the model. The balance stiffness was determined by static calibrations. In order to determine model deformations, optical reference screens were installed in several planes of the model and on the tunnel floor. Photographs were taken during static calibrations and at test conditions from optimal camera positions. First evaluations gave reasonable results.

3.2.6 Flow Visualization

Model wing and fairing was provided with a pressurized tubing system by which either different coloured oil was pressed through the orifices on the surface or alternately kerosene, to clean up the wing for a further test, without stopping the tunnel. Coloured photos were taken as well as movies and video recordings.

3.2.7 Unsteady Test Techniques

Unsteady test techniques are described in part 2 of this paper.

3.3. TEST PROGRAM

In 1979 3 test series were carried out with the large model arrangement. Forces, steady and unsteady pressure distribution measurements were performed. On the basic wing-fuselage-configuration the influence of various parameters was investigated:

- o engine intake interference, simulated by the flow through nacelle and pylon
- o influence of externally mounted nacelle in different relative wing positions
- o effect of throttled nacelle mass flow
- o aileron deflection efficiency
- o influence of wing-fuselage-fairings
- o impact of contour disturbances in the region of slats and spoilers
- o nonstationary effects, induced by periodic and random excited aileron.

Generally, the tests were conducted in the Mach Number range $0.3 < M < 0.85$. Maximum speed of $M = 0.87$ was achieved with certain configurations. Incidence range was restricted by load respectively buffeting limitations.

4. RESULTS

4.1 REYNOLDS NUMBER RANGE

Due to the fact, that the ONERA S1 wind tunnel is an atmospheric tunnel, Re-Number varies with Mach Number. Referring to the MAC of the wing, Re-Numbers up to $Re = 11.5 \cdot 10^6$ were achieved with the test configuration. The possible Re-range, depending on Mach Number is shown in Fig. 9.

4.2 DRAG CHARACTERISTICS OF THE FLOW THROUGH THROTTLING PRINCIPLE

Results, obtained by small scale model tests are plotted in Fig. 10. As mentioned before, the aim was, to throttle the mass flow at minimum nacelle drag. It is remarkable, that at moderate Mach Numbers nacelle drag decreases with the degree of throttling due to less internal friction. However at higher flow velocity, drag characteristic changes. Thus spillage and interference effects are indicated [10].

4.3 STATIONARY FORCE TESTS

Compared with small scale complete model tests, Re-effects are evident in the maximum lift and buffet onset behaviour, shown in Fig. 11 for the basic wing-fuselage-configuration. Differences in the slope seem to be caused by the half model test technique.

The phenomena in drag characteristic Fig. 12 have not been explained for the time being. In fact, the induced drag decreases at higher Re-Numbers, compared with small scale model tests. But drag behaviour against Mach Number (Fig. 13) is in opposition to theory and complete model test results. The order of this discrepancy cannot be explained by a lack of tunnel correction quality. Experimental research work on this subject has been carried out at the NLR in Amsterdam recently. First results indicate similar phenomena. Additional current analysis and calculations are performed at ONERA.

Repeatability and accuracy was proved by several tests.

4.4 STATIONARY PRESSURE DISTRIBUTION ON THE WING

As an example local pressure distribution on 4 wing sections is compared with results of small scale complete model tests, thus at two different Re-Numbers in Fig. 14. This comparison is drawn at similar lift coefficients without transition fixing. It is noticed that the double shock tendency on the inner wing is more pronounced at higher Re-Numbers, the type of pressure distribution however remains similar. The supercritical pressure distribution in the front part of the wing recompresses without flow separations on the trailing edge.

Fig. 15 gives an impression of the development of the pressure distribution profile in the critical wing section up to buffet onset and maximum lift conditions. Shock position remains rather constant, even in the stall range.

Certainly, pressure distribution profile and shock position varies with speed. The evaluation of the characteristics on a wing section at constant incidence is shown in Fig. 16. With increasing Mach Number the shock moves rearwards. Speed induced flow separations appear together with shock formation on the lower wing surface.

4.5 NACELLE EFFECTS

The wing fixed nacelle induces remarkable lift reduction in connection with forward shifted shock (Fig. 17). However contrary effects are noticed, when the nacelle is externally attached without pylon (Fig. 18). At extreme close nacelle positions, shocks appear on the lower wing surface, caused by interactions. It must be mentioned that there is a remarkable influence on the results, caused by the addition blockage of the suspension facility. This effect must be eliminated for final analysis.

Due to mass flow throttling, super velocity on the wing is initiated with the corresponding influence on flow distribution (Fig. 19).

4.6 AILERON EFFECTS

Normal force and pitching moment distribution, derived from sectional pressure integrations, plotted over the wing span, illustrate aileron efficiency in Fig. 20 and Fig. 21.

4.7 CONTOUR DISTURBANCE INFLUENCE

The advantage of a large model is especially evident, when relatively small geometric details and modifications are to be simulated and investigated. In the case of contour disturbance simulation the possible high impact of such sources is demonstrated.

In Fig. 22 the local static pressure distribution on a representative wing section is shown as an example. In presence of the slat contour disturbance the shock is reinforced and its position is moved rearwards. Such a type of pressure distribution tends to early flow separation and thus the sensitivity against buffet onset grows.

A shock in a position in front of a spoiler induced contour disturbance is only slightly influenced with respect of its location and strength (Fig. 23).

Rather high effects are detected in the drag behaviour against lift and Mach Number, as documented in Fig. 24 to Fig. 26.

4.8 CONTINUOUS TEST PROCEDURES

Sensitivity of the wing against contour disturbances becomes more evident by the analysis of the results derived from the continuous Mach Number polar technique. Even the relatively small irregularity, caused by only one simulated spoiler, results in distinct measurable effects, demonstrated in Fig. 27, where the uncorrected axial force coefficient is plotted against Mach Number.

As a typical example the technique of buffet onset determination is presented in Fig. 28. Comparison of lift behaviour depending on Mach Number shows:

- o general lift reduction due to contour disturbance
- o lift maximum, which indicates local flow separations, appears at lower Mach Number with a contour disturbance on the wing, i.e. reduction of buffet boundary due to slat simulation by ΔM .

4.9 FLOW VISUALIZATION RESULTS

The technique of flow visualization by means of pressing different coloured liquids through the wing surface, allows the production of flow pictures during varying test conditions, as shown in Fig. 29 as an example.

4.10 DATA HANDLING AND DOCUMENTATION

Special documentation had to be established to handle and analyse the high quantity of data and results, which are produced during a test series of such a degree of complexity. It is not worth-while, to copy and distribute 10 thousands of diagrams and listings. Instead of producing conventional result documentation, it is suggested to provide a test report, which contains:

- o model specification
- o test program
- o introduction of data display and storage
- o example of characteristic results
- o catalogue of data documentation.

Users then require in detail those data only which they are specifically interested in [9] .

5. FUTURE PROSPECTS

This model design of standardized units allows to utilize the model itself, the external remotely controlled suspension facility, and the data processing system for further test purposes.

In particular the model wing can be modified and equipped with:

- o high lift devices
- o new airfoil
- o module systems, containing movable surfaces (excited, ailerons, flapperons, spoilers)
- o additional measuring equipment.

The external nacelle attachment device can be used as remotely controlled

- o engine simulator support
- o sensor support.

Special attention shall be directed to use the model system in connection with engine simulation tests in the wind tunnel. It is planned to adapt a TPS-system (turbine powered simulator) to the model.

The use of the model arrangement is generally not restricted to the large transonic tunnel S1 MA in Modane. After certain modifications it can be installed into comparable large test sections of other wind tunnels for testing.

Transonic tests with model arrangements of such dimensions are not free from risk. Strength limits are reached rather soon on critical model components. It must be realized, that loads on this test installation were achieved, which are by a factor 5 higher than the design wing loads on the full scale aircraft. In addition, usually wind tunnel tests are required beyond flight range. In those cases unpredictable unsteady effects occur on top of that and situations can arise, where loads cannot be kept under control. Monitoring of security devices helps to avoid an accident.

The advantage, to utilize a large scale wind tunnel model is clearly demonstrated by evaluating and analysing the test results. Because of sufficient internal space, the model can be equipped with a high amount of various transducers and pick ups. This leads to accurate and detailed results. Furthermore, on a large scale model even small geometric details and variations can be simulated and their measurable effects can be shown.

Although the fundamental problems, to judge test results and transfer them to the full scale aircraft, generally are not solved by a larger model scale (application of wind tunnel corrections and disadvantages due to half model technique are to be considered), it is however possible to determine experimentally especially interference effects on the basis of differences and reference tests.

[1]	G. Krenz (VFW)	Transonic wing design for transport aircraft. Presentation for the AIAA, Atlantic Aeronautical Conference "Advancing Technology Williamsburg, Virginia, USA (March 1979)
[2]	R. Hilbig (VFW)	Transsonischer Flügelentwurf. ZKP-Report No. 23 (November 1979)
[3]	B. Kiekebusch (MBB-UH)	Flügelentwurf F3. ZKP-Report No. 24
[4]	Dr. G. Redeker Dr. N. Schmidt Dr. H. Hansen (DFVLR)	Entwurf eines Tragflügels (F 4) für den transsonischen Geschwindigkeitsbereich im Rahmen der ZKP-Aufgabe "Flügelsektion". ZKP-Report No. 22 (December 1977)
[5]	G. Binder H. Buers H.-J. Proksch (Dornier)	Untersuchung zur Auslegung eines superkritischen Tragflügels (F 2) für Verkehrsflugzeuge (ZKP). Report No. 78/10 B (August 1978)
[6]	U. Gross (MBB-UF)	A.N. zum ZKP-Modell (1 : 5,4) betreffend Boden-Rumpf-Abdichtung. FE 123/52 (March 1980)
[7]	Marcel Pierre (ONERA)	Caractéristiques et Possibilités de la Grande Soufflerie Sanique de Modane-Avrieux. (March 1969)
[8]	A. Giacchetto (ONERA)	Essai, à S1 Ma, de la demi-maquette à grande echelle d' un avion civil VFW-MBB. Proces-Verbal No. 3/0493 GN (October 1979)
[9]	G. Anders (VFW)	Versuche mit dem ZKP-Großmodell im S1 MA. ZKP-Report No. 39 (March 1980)
[10]	J. Rohde (VFW)	Voruntersuchungen am Prinzipmodell der Triebwerks-Durchfluß-Simulation für das ZKP-Großmodell. ZKP-Report No. 38 (July 1979)

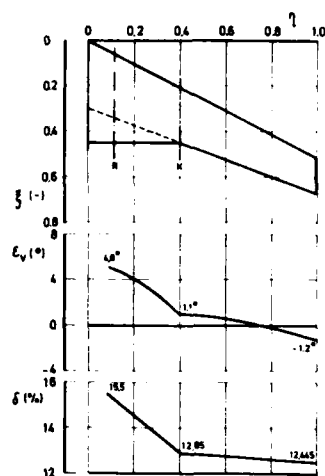


FIG. 1: Wing System B10.3V

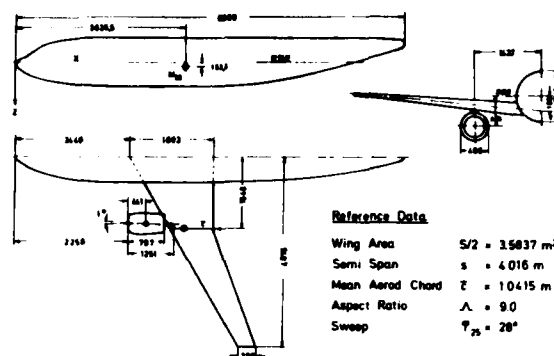


FIG. 2: Large Halfmodel Main Dimensions

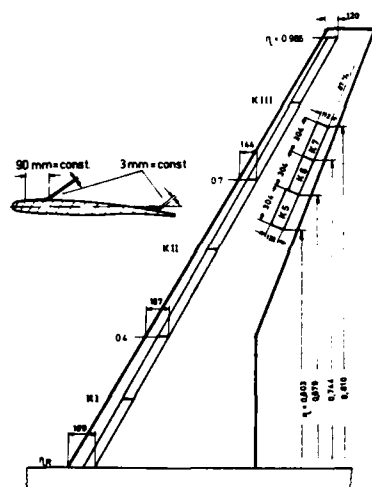


FIG. 3: Contour Disturbances



FIG. 6: Test Arrangement

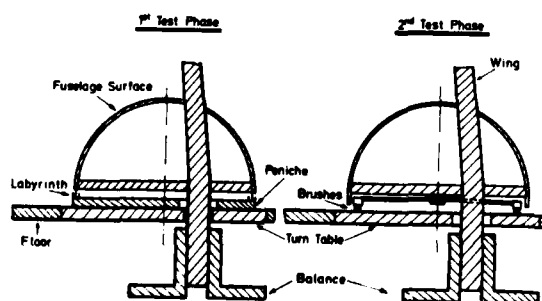


FIG. 4: Halfmodel Arrangement

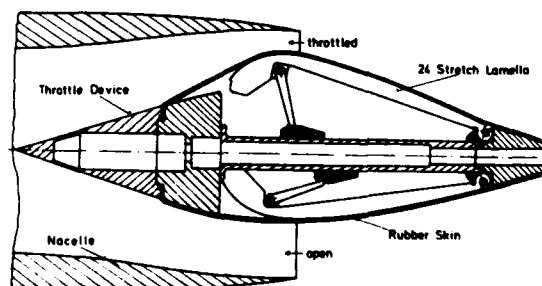


FIG. 5: Throttle Mechanism of Flow Through Nacelle

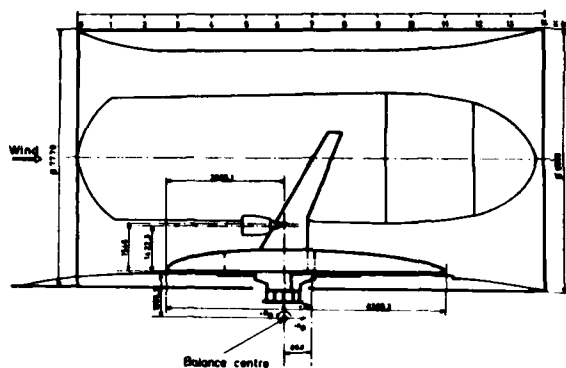
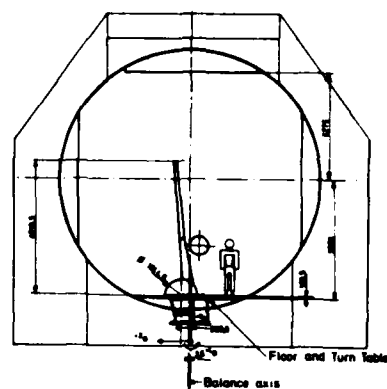


FIG. 7: Large Halfmodel in Test Section No. 1 of S1 MA



**FIG. 8: Large Halfmodel in Test
Section No. 1 of S1 MA**

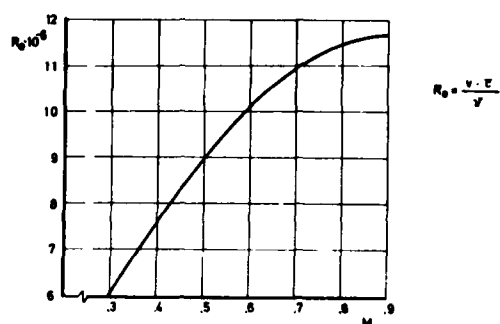


FIG. 9: Large Halfmodel Re-Number Range

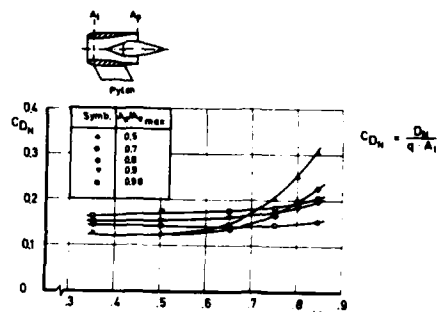


FIG. 10: Drag Characteristic of Nacelle and Pylon

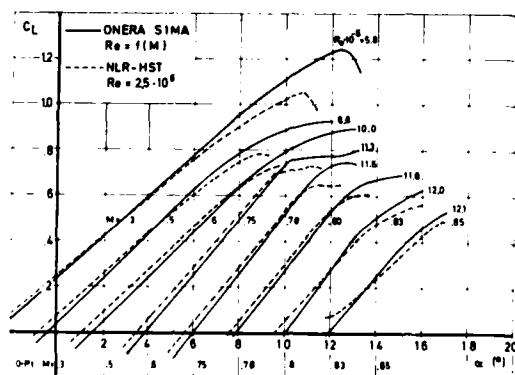


FIG. 11: Influence of Re-Number on Lift

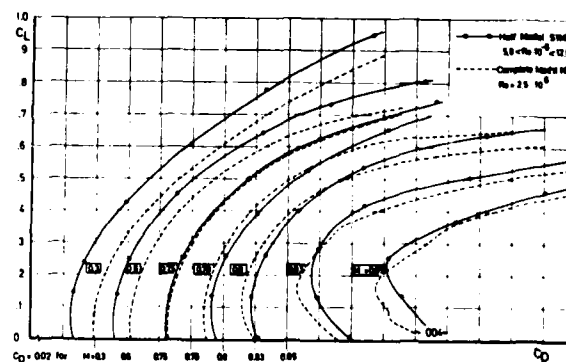


FIG. 12: Drag Comparison Half/Complete Model, Influence of Re-Number

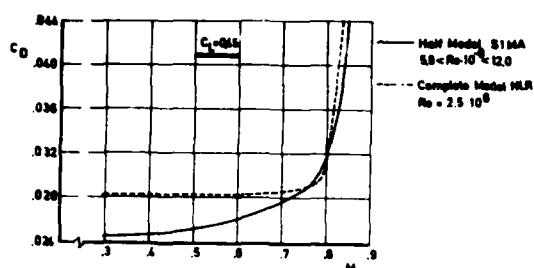


FIG. 13: Drag Comparison Half/Complete Model

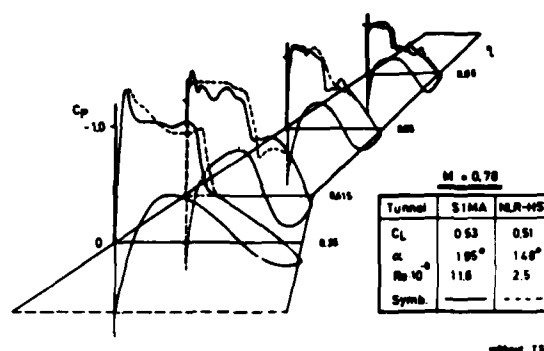


FIG. 14: Influence of Re-Number on Local Pressure Distribution

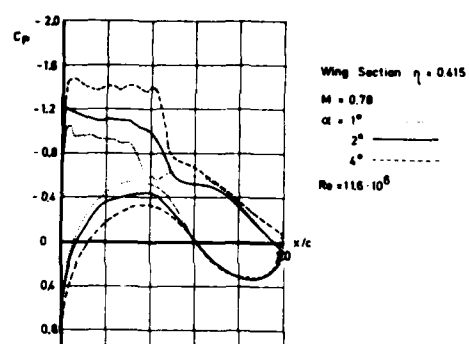


FIG. 15: Incidence Effect on Local Pressure Distribution

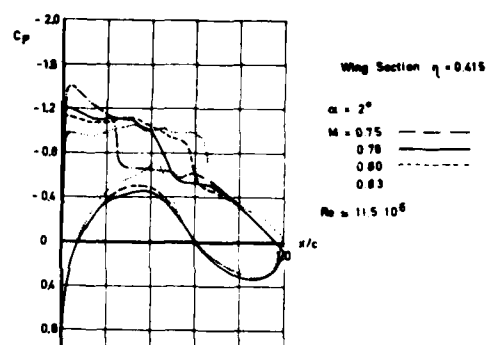


FIG. 16: Mach Number Effect on Local Pressure Distribution

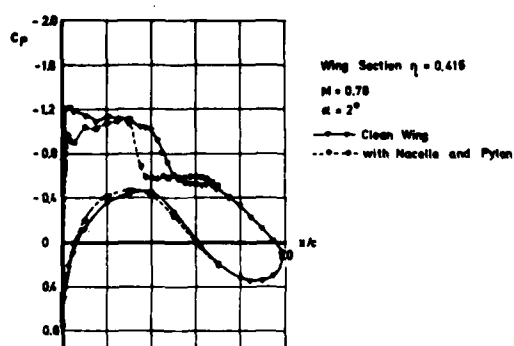


FIG. 17: Effect of Wing fixed Flow Through Nacelle on Local Pressure Distribution

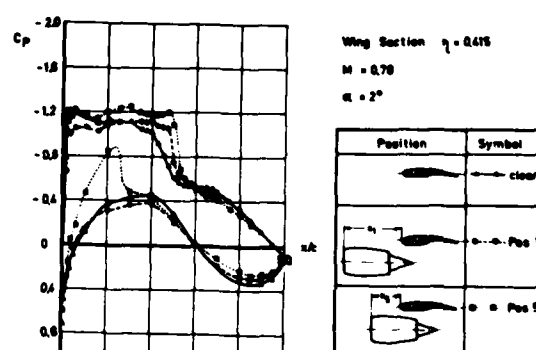


FIG. 18: Effect of Externally attached Flow Through Nacelle on Local Pressure Distribution

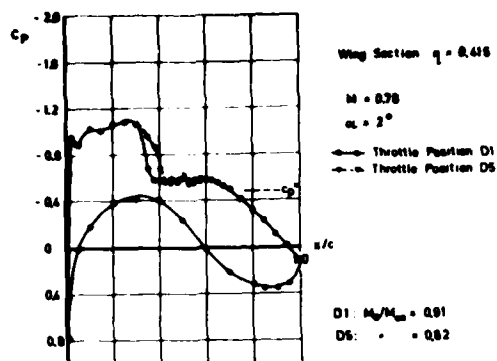


FIG. 19: Effect of throttled Mass Flow on Local Pressure Distribution

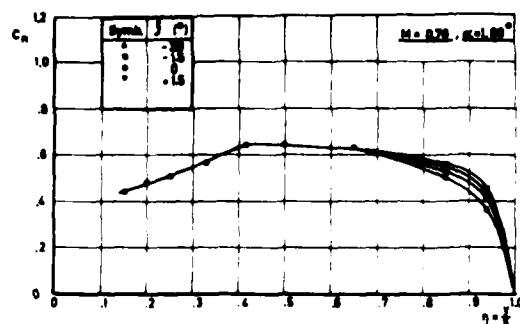


FIG. 20: Effect of Aileron Deflection on Normal Force Distribution

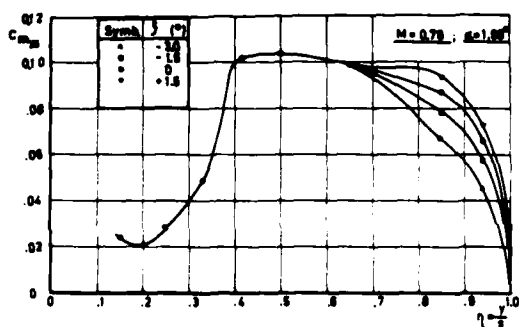


FIG. 21: Effect of Aileron Deflection on Pitching Moment Distribution

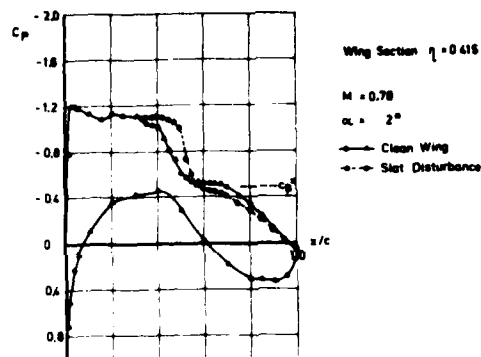


FIG. 22: Influence of Contour Disturbance on Local Pressure Distribution

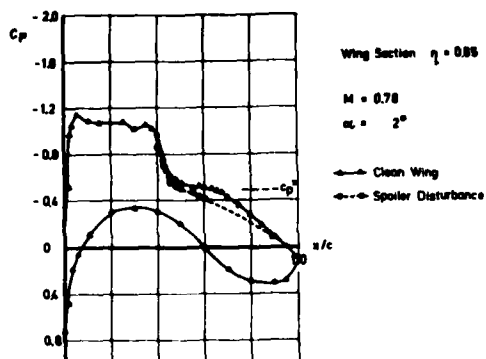


FIG. 23: Influence of Contour Disturbance on Local Pressure Distribution

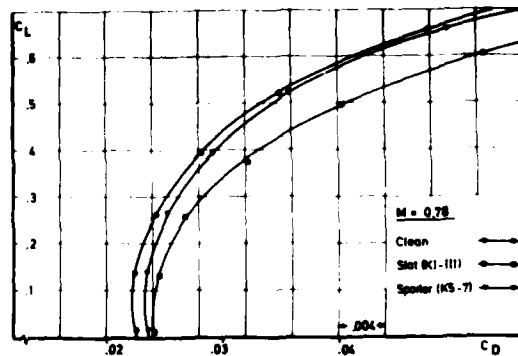


FIG. 24: Effect of Contour Disturbance on Drag

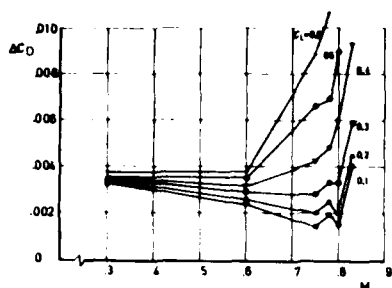


FIG. 25: Effect of Contour Disturbance K I + II + III on Drag

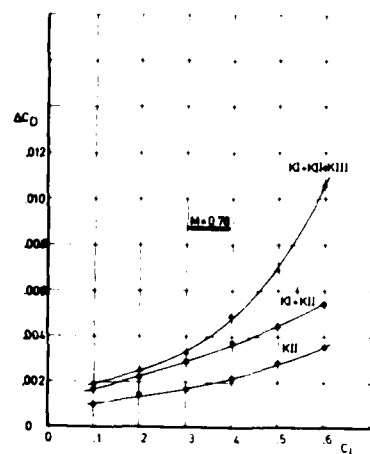


FIG. 26: Effect of Slat Contour Disturbance on Drag

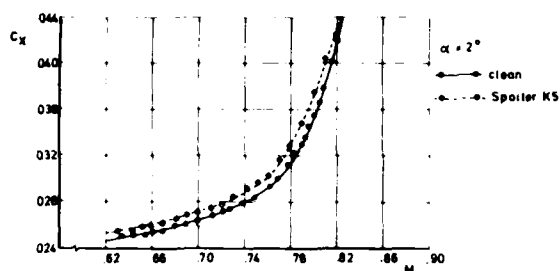


FIG. 27: Drag Determination from Continuous M-Number Polar Technique

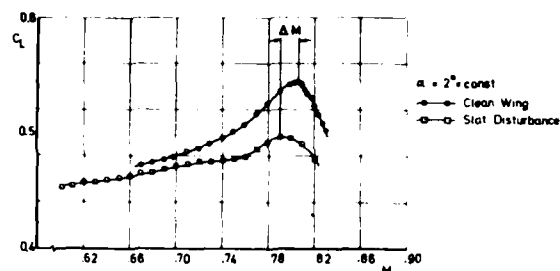


FIG. 28: Test Technique for Buffet Determination



FIG. 29: Oil Flow Pattern

PHILOSOPHIE ET RESULTATS DES TECHNIQUES D'ESSAIS STATIONNAIRE ET INSTATIONNAIRE
 SUR UNE MAQUETTE A GRANDE ECHELLE D'UN AVION DE TRANSPORT
 DANS LA SOUFFLERIE TRANSSONIQUE S1 MA DE L'ONERA

2ème partie : Aspects Aérodynamiques instationnaires

par A. Gravelle

Office National d'Etudes et de Recherches Aérospatiales (ONERA)
 92320 Châtillon (France)

NOTATIONS

$C_p = \frac{p_o (\cos \psi + j \sin \psi)}{q \delta_{io}}$: coefficient de pression instationnaire

f : fréquence d'excitation

M : nombre de Mach

$p = p_o \sin (\omega t + \psi)$: pression en un point induite par le mouvement de la gouverne

q : pression dynamique de l'écoulement

α : incidence de la maquette

δ : braquage statique de la gouverne

$\delta i = \delta_{io} \sin \omega t$: angle dynamique de la gouverne

I - INTRODUCTION

L'utilisation de maquettes de grandes dimensions présente des avantages communs aux problèmes stationnaires et instationnaires, tels que :

- des nombres de Reynolds élevés
- la meilleure précision relative des profils
- la plus grande intensité des forces et des moments à mesurer
- la meilleure logeabilité pour les équipements.

L'obtention de grands nombres de Reynolds peut être réalisée par d'autres moyens que les grandes maquettes : dans les souffleries pressurisées ou, à l'avenir, dans les souffleries cryogéniques.

Nous nous bornerons à décrire dans cette partie de l'exposé les seuls avantages spécifiques fournis par ces maquettes en ce qui concerne les études instationnaires, sans négliger toutefois le problème des équipements qui est alors particulièrement ardu.

Nous désignons par grandes maquettes des maquettes de plusieurs mètres d'envergure destinées aux souffleries telles que S1 Modane, F1 Le Fauga, DNW, RAE 5m

II - MAQUETTES DE MESURE DE COEFFICIENTS INSTATIONNAIRES

II.1 - Généralités

Ces maquettes sont utilisées pour mesurer soit des coefficients globaux, coefficients de portance (C_L) ou coefficients de moment (C_M), soit des coefficients locaux, les coefficients de pression (C_p), en présence d'un mouvement harmonique de tout ou partie de la structure (gouvernes, spoilers ...).

Dans le cas des mesures globales, les valeurs des forces et des moments sont beaucoup plus grandes, donc plus aisément mesurables pour des maquettes de grande dimension.

Dans le cas des mesures locales, on utilise des capteurs de pression miniatures répartis à l'intérieur de la maquette. Plus de place disponible permet de multiplier le nombre des capteurs dans une même zone, donc d'obtenir un réseau plus fin qui augmentera la précision de localisation d'un choc, ou de l'intégration des pressions sur la surface.

Le volume disponible à l'intérieur d'une maquette est également un élément déterminant en ce qui concerne les possibilités d'installation de vérins hydrauliques miniatures permettant l'excitation d'éléments tels que ailerons, spoilers et flapperons, permettant également le braquage statique des éléments non excités dans le cas de configurations complexes. Par exemple des flapperons mobiles s'étendant sur 10 à 15 % de la corde d'une aile sont irréalisables sur des maquettes de 1 mètre d'envergure, et faisables sur des maquettes de 2 à 4 mètres.

II.2 - Essai ZKP

La maquette ZKP, qui a été décrite dans la première partie de cet exposé, a été équipée d'un aileron externe mobile, pouvant être animé d'un mouvement aléatoire (bruit blanc), ou sinusoïdal, au moyen d'un vérin hydraulique miniature (figure 1).

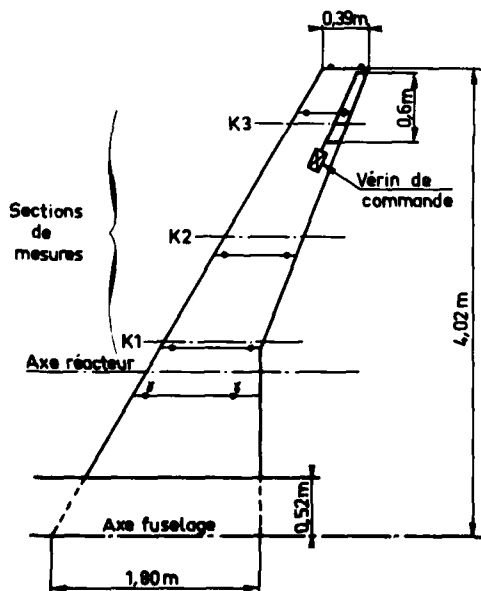


Figure n° 1 Aile ZKP Position des cordes de mesure en envergure.

Les essais instationnaires étaient destinés à apprécier l'efficacité de cet aileron dans différentes conditions de Mach, d'incidence et de braquage statique. Outre le moment de charnière donné par un pont de jauges de torsion sur l'axe de la gouverne, ces essais comportaient essentiellement la mesure du premier harmonique de pression en 68 points de l'aile, dont 32 étaient répartis dans une corde située sensiblement au quart interne de l'aileron. Le mouvement de l'aile elle-même était contrôlé au moyen de 12 accéléromètres.

Les résultats présentés ici concernant des essais réalisés en présence de haubans immobilisant l'extrémité de l'aile, le seul mouvement étant alors l'oscillation de l'aileron. D'autres essais ont été réalisés sans haubans, avec excitation à la fréquence de flexion de l'aile. Les répartitions de pression dues à l'effet combiné du mouvement de l'aileron et de la flexion de l'aile sont moins aisément interprétables.

L'influence du braquage statique δ de l'aileron sur les coefficients de pression à l'extrados est montré (figure 2) dans un cas subcritique, pour un nombre de Mach M de 0,73 et une incidence de l'aile α de 0° . Le moment de charnière stationnaire de l'aileron est nul pour le braquage δ de -6° , l'efficacité de la gouverne est alors maximum. Lorsque δ varie de -6° à $+1,5^\circ$, l'efficacité décroît, alors que le déphasage augmente sensiblement.

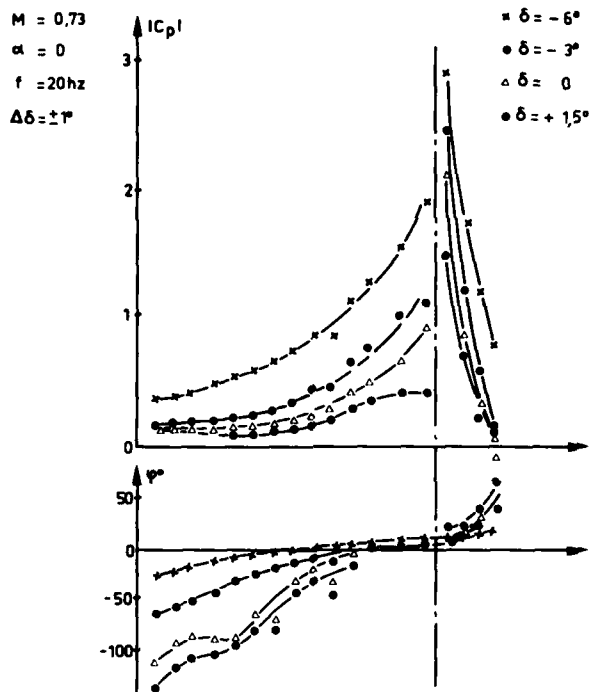


Figure n° 2 Effet du braquage statique de l'aileron

L'augmentation du nombre de Mach (figure 3) provoque également une perte d'efficacité, particulièrement en amont de la charnière, une zone légèrement supersonique se manifestant déjà pour $M = 0,78$, et un choc apparaissant vers 40 % de la corde pour $M = 0,83$. Les très grandes valeurs du coefficient dans cette dernière zone témoignent de l'oscillation de l'onde de choc, en corrélation avec le mouvement de l'aileron. Les ondes de pression ne peuvent traverser ce choc, aussi le C_p est pratiquement nul en amont de celui-ci.

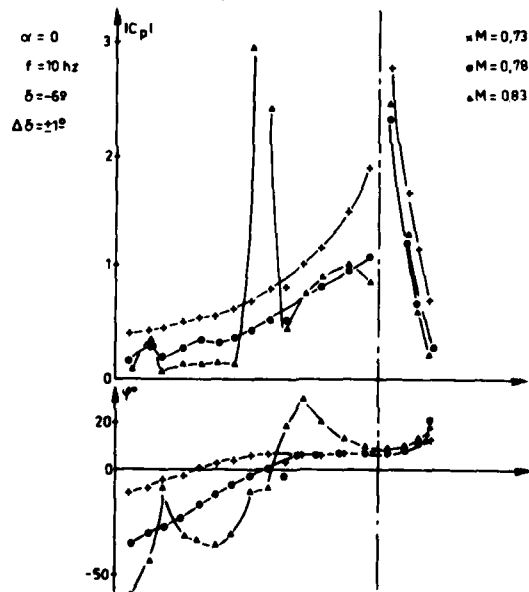


Figure n° 3 Effet du nombre de Mach

Une variation de l'incidence de l'aile de 2 degrés (figure 4), pour un nombre de Mach de 0,78 fait également apparaître une onde de choc à 30 % de la corde, mise en évidence par la grande amplitude, ainsi que la variation de phase rapide du C_p .

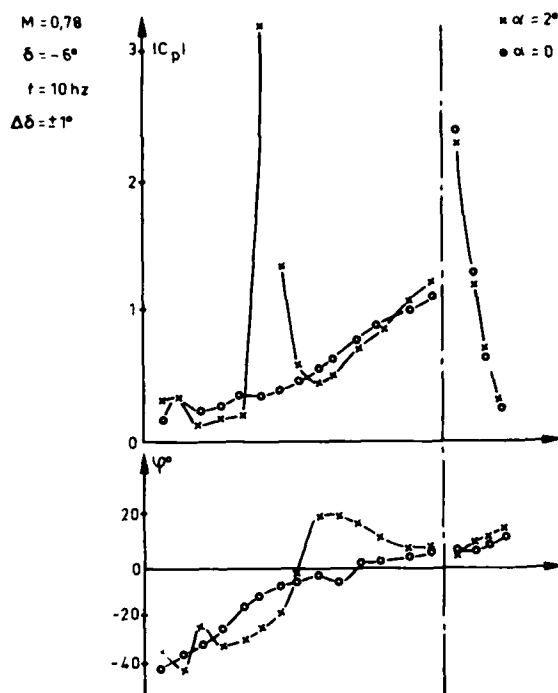


Figure n° 4 Effet de l'incidence de la maquette

L'amplitude des C_p n'est pas notablement affectée par un accroissement de la fréquence d'oscillation de 10 à 30 Hertz (figure 5), le déphasage augmentant de façon sensiblement proportionnelle.

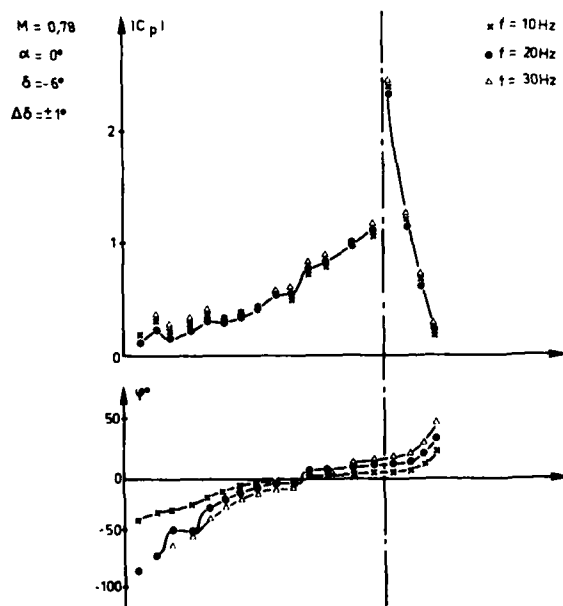


Figure n° 5 Effet de la fréquence d'excitation

II.3 - Projets récents

Il existe actuellement plusieurs projets, soit déjà réalisés, soit en cours d'étude et de fabrication, de maquettes de grandes dimensions, tendant à exploiter au maximum les possibilités offertes en matière d'équipement tant en ce qui concerne les mesures que le nombre de surfaces oscillantes.

Ainsi a été développé à l'ONERA en 1978 une étude d'efficacité de gouverne en présence d'un profil supercritique, au moyen d'essai sur une demi-aile droite, la maquette RA16SC1, mesurant 1,20 mètre d'envergure.

Celle-ci était munie d'une gouverne oscillante pouvant être située soit en extrémité d'aile, soit à la moitié de l'envergure ; elle était équipée de 148 capteurs de pression instationnaire, dont 124 au voisinage immédiat de la tranche concernant la gouverne. Les premiers essais ont été effectués sur cette maquette en avril 1979.

La SNIAS en coopération avec l'ONERA effectuait également l'étude d'une demi-maquette du projet A200 de 2,28 mètres d'envergure équipée de 3 flapperons mobiles et contenant environ 400 capteurs de pression dont 50 dans une même corde. Les 3 flapperons pourront être excités séparément ou simultanément.

Enfin le projet ZKP II (figure 6) consiste à équiper la maquette décrite précédemment de 3 spoilers avec et sans fente, puis de 3 flapperons mobiles, avec également la possibilité d'exciter séparément ou simultanément soit les 3 spoilers, soit les 3 flapperons. Le nombre de capteurs sera augmenté de telle sorte que l'on devra mesurer et traiter simultanément environ 400 signaux de pression sinusoïdaux.

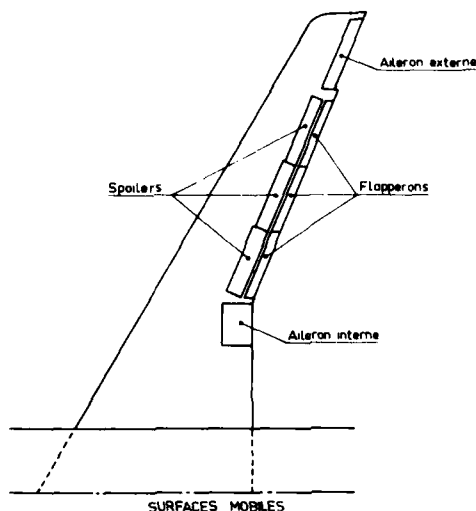


Figure n° 6 Maquette SKP II

11.4 - Méthodes de mesure et de traitement

La chaîne de traitement utilisée lors des essais ZKPI était une chaîne analogique de l'ONERA et dont le dernier développement avait été effectué lors des essais NORA [1] en coopération avec le RAE, le DFVLR et le NLR.

Cette chaîne comportait (figure 7) pour chaque capteur, outre l'alimentation en tension, une amplification réglable et le filtrage de la composante continue. Puis une commutation automatique permettait de réduire le nombre de signaux simultanés à 10, ceux-ci étant multipliés analogiquement par deux signaux de référence en phase et en quadrature avec le déplacement et ensuite intégrés pendant une durée d'environ 100 périodes avant d'être numérisés. Les coefficients de pression étaient calculés par un ordinateur et présentés sous forme de tableaux ou de tracés.

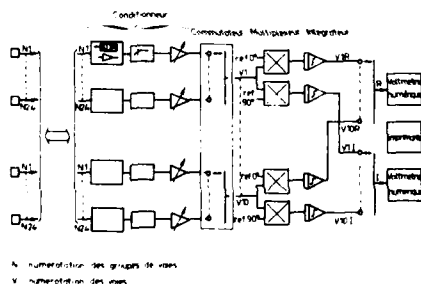


Figure n° 7 Chaîne d'acquisition et de traitement des Cp analogique

Cette chaîne était capable de traiter un maximum de 80 capteurs dans la configuration existant en 1979.

Le nombre croissant de capteurs à traiter nous a conduit à développer une chaîne de mesure permettant de réduire au maximum les éléments analogiques qui restent très coûteux [2]. Le principe retenu est de numériser les signaux sinusoïdaux immédiatement après amplification, puis d'en extraire la réponse harmonique à la fréquence d'excitation, et éventuellement aux multiples de cette fréquence, au moyen d'un analyseur de Fourier (figure 8). Le calcul des coefficients de pression et la présentation des résultats s'effectuant de la même façon que précédemment.

Dans ce cas, chaque capteur ne nécessite plus qu'une alimentation et une pré-amplification de gain fixe séparées. Une commutation conduit ensuite à l'amplification et au filtrage par groupes de 16 ou de 32 voies.

Cette chaîne a été utilisée pour la première fois en 1979, lors des essais de la maquette RA16SC1, avec une capacité de 150 voies ; elle est actuellement en cours d'extension pour atteindre une capacité de 400 voies fin 1980, dans le cas de l'analyse du seul coefficient fondamental de la série de Fourier. Une version permettant l'étude de 3 ou 4 harmoniques sur 100 voies est également prévue pour la même époque.

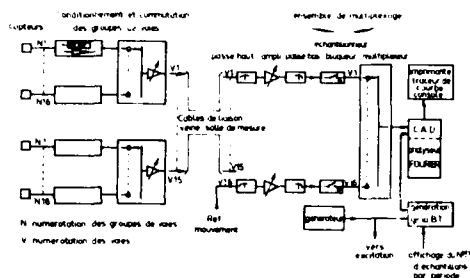


Figure n° 8 Chaîne d'acquisition et de traitement des C_p numérique

III - MAQUETTES DE FLOTTEMENT

La difficulté dans le cas des maquettes de similitude aéroélastique réside dans le fait que les lois de similitude imposent une efficacité de la structure égale, et quelque fois supérieure, à celle des avions [3]. Ceci conduit à un rapport rigidité-masse élevé et dans le cas des échelles réduites, à des épaisseurs de structure extrêmement faibles, donc très difficiles à réaliser, nécessitant l'emploi de matériaux à haut module élastique tels que les fibres de carbone ou de bore. En outre, l'équipement de ces maquettes est réduit à l'extrême, tout apport de masse étant prohibitif.

Il est donc nécessaire d'augmenter soit le rapport d'échelle des longueurs, soit le rapport d'échelle des masses, et ceci peut être réalisé de trois façon différentes :

- dans les souffleries de grandes dimensions
- dans les souffleries pressurisées
- dans les souffleries cryogéniques

Dans les trois cas on obtiendra également un nombre de Reynolds élevé.

Cependant, seules les maquettes à grande échelle permettent de représenter correctement certains éléments.

Il en est ainsi des gouvernes, dont on ne peut, dans des maquettes complètes dimensionnées pour la soufflerie S2 de Modane, c'est-à-dire ne dépassant guère 1 mètre d'envergure, représenter ni les modes propres, ni les fonctions de transfert des servo-mécanismes qui sont en général d'un ordre élevé. Par exemple dans le cas de la maquette à l'échelle 1/38 de l'Airbus A300, les ailerons externes, qui n'étaient représentés qu'en tant que masse et inertie, pesaient 2,1 grammes, les rigidités de liaison étant réalisées au moyen de simples lames métalliques. Une maquette complète de ce même avion, destinée à la soufflerie S1, serait à l'échelle 1/9, et la masse de l'aileron externe serait de 130 grammes. Mais la soufflerie n'étant pas pressurisée elle ne permettrait pas d'étudier aussi complètement le domaine de vol.

Cependant, si des maquettes complètes sont indispensables pour la représentation d'un grand nombre de modes et particulièrement des modes rigides et des modes antisymétriques de l'avion, certains problèmes peuvent être étudiés sur des demi-maquettes montées à la paroi, de dimensions plus grandes, avec une suspension souple qui permet d'obtenir une partie des modes rigides.

Un autre avantage des grandes maquettes pour les aéroélasticiens concerne la fatigue des matériaux. En effet, dans la similitude de Mach, l'échelle des fréquences étant sensiblement inversement proportionnelle à l'échelle des longueurs, des dimensions plus grandes conduisent à un nombre de cycles plus faible dans un temps donné, avec un niveau de contrainte comparable, ce qui a pour effet d'augmenter la durée de vie en fatigue.

IV - MAQUETTES POUR ETUDES DE CONTROLES AUTOMATIQUES GENERALISES (CAG)

Les CAG comprennent les systèmes de contrôle actif de flottement, les systèmes absorbeurs de rafale, les contrôles de portance Ils nécessitent la mise en mouvement d'ailerons, de spoilers, de flapperons, ou de surfaces additionnelles, donc la présence de servo-mécanismes. En outre, mettant en jeu les premiers modes de déformation de la structure, ils doivent être étudiés sur des maquettes dynamiquement semblables.

Les caractéristiques d'une maquette CAG regroupent donc celles des deux types de maquette décrits ci-dessus. En particulier la commande des surfaces de contrôle est réalisée par des vérins hydrauliques qui ne peuvent avoir une action que dans une bande de fréquence limitée.

Ce problème est résolu à ce jour dans la bande 0 - 50 Hz.

D'autre part, les maquettes étant dynamiquement semblables il est nécessaire que la masse locale additionnelle due à ces vérins soit négligeable devant la masse de la structure, or cette masse dépend peu de la dimension des éléments à mouvoir.

Les maquettes doivent donc être suffisamment volumineuses, de masse importante, et présenter des modes de déformation à basse fréquence. Le choix se portera naturellement sur des demi-maquettes de type S1.

L'ONERA étudie actuellement l'implantation d'un générateur de rafale dans la soufflerie S1, qui permettra de telles études sur des maquettes équipées de plusieurs surfaces mobiles.

V - CONCLUSION

Les maquettes de grandes dimensions présentent des avantages appréciables tant pour les mesures stationnaires que les mesures instationnaires. Ces avantages résident principalement dans la possibilité de réalisation d'éléments de petite dimension à l'échelle de l'avion (flapperons, spoilers) et dans le volume disponible pour loger les éléments nécessaires à la motorisation de ces éléments ainsi que dans l'instrumentation de mesure.

Ceci conduit à la multiplication très rapide du nombre de voies de mesure, problèmes qui a été résolu à l'ONERA par une évolution parallèle des chaînes d'acquisition et de mesure.

Le coût de ces maquettes est certainement plus élevé que celui de maquettes plus petites, mais ce coût correspond à des résultats que l'on ne pourrait en aucun cas obtenir sur ces dernières, et on peut penser qu'à performances égales le prix de revient d'une grande maquette ne serait pas plus élevé.

En outre, la motorisation de différents éléments contribue à réduire la durée des essais, les changements de configuration pouvant s'effectuer sans arrêter la soufflerie.

REFERENCES

- [1] - N. Lambourne, R. Destuynder, K. Kienappel, R. Roos
Comparative measurements in four European wind-tunnel of the unsteady pressures on an oscillating model.
AGARD-R-673 (Octobre 1979).
- [2] - C. Christoux, A. Gravelle
Chaîne de mesure numérique de coefficients de pression instationnaire.
La Recherche Aéronautique n° 1980-1 (Janvier 1980).
- [3] - R. Destuynder, R. Labourdette
Maquettes de soufflerie dynamiquement semblables pour études aérodynamiques en transsonique.
La Recherche Aéronautique n° 1972-2 (Mars 1972).

La voilure, sur laquelle est boulonné le demi-fuselage, est fixée sur la partie tournante d'une balance solidaire de la veine ; cette balance assure donc la mise en incidence de l'ensemble ainsi défini et sa pesée en axes aérodynamiques ; un espace de 125 mm environ est aménagé entre le plancher et la demi-maquette, de façon à maintenir celle-ci hors de la couche limite.

Pour la première série d'essais, cet espace était obturé par un élément non pesé appelé "péniche", fixé à une tourelle dont le mouvement en incidence est synchronisé avec celui de la partie tournante de la balance ; un labyrinthe, placé le long du périmètre du demi-fuselage réduisait l'écoulement de l'air sous celui-ci, comme l'indique la figure 3a ; cette configuration dut cependant être abandonnée car les déformations de la balance sous les charges aérodynamiques stationnaires et instationnaires exercées par la voilure, nécessitaient un réajustement du labyrinthe difficile à réaliser.

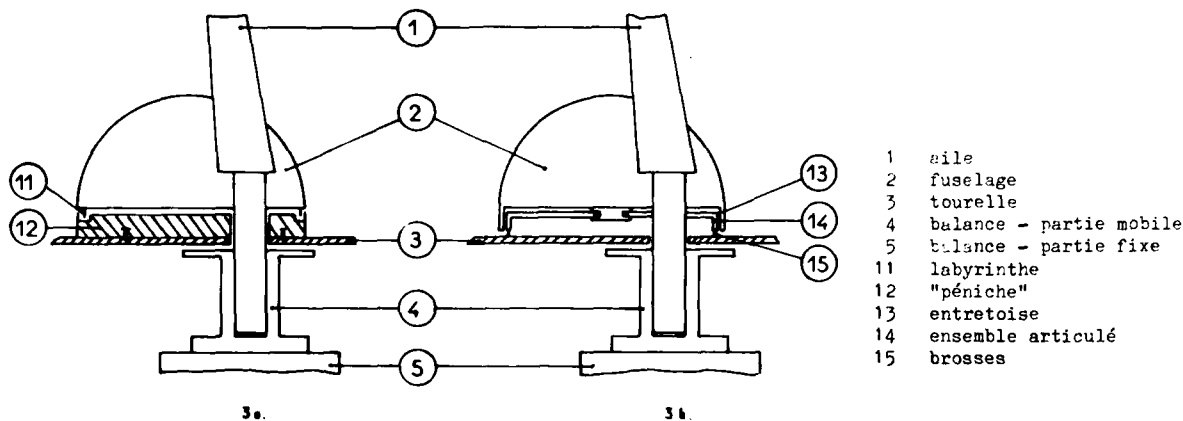


Fig. 3 - Etanchéité entre la demi-maquette et la veine.

Une nouvelle configuration, représentée sur la figure 3b, a été utilisée dès la seconde série d'essais ; le fuselage est ici prolongé par une entretoise jusqu'à 15 mm environ du plancher ; à ce niveau, des broches montées sur des ensembles articulés assurent l'étanchéité sous la demi-maquette. Un tel montage réduit l'écoulement d'air entre partie pesée et non pesée de façon certainement plus efficace que la configuration avec labyrinthe, mais présente deux inconvénients :

- la pesée ne concerne plus une demi-maquette réelle mais permet néanmoins de mettre en évidence les écarts sur les coefficients aérodynamiques provoqués par les modifications de configuration. Des corrections partielles sont aussi possibles, à partir des pressions mesurées sur l'entretoise pour se rapprocher du cas de la demi-maquette.
- les broches introduisent une interaction entre partie pesée et non pesée se traduisant inévitablement par un accroissement de la dispersion des résultats.

2 - MONTAGE POUR ESSAIS INSTATIONNAIRES

Une partie de la seconde série d'essais a été consacrée à l'étude de l'effet d'un aileron excité harmoniquement sur des répartitions de pressions statiques en plusieurs sections de la voilure.

Ces pressions étant également sensibles aux déplacements dynamiques de l'aile, il a été nécessaire, pour les mesures, de brider cette dernière, par un haubanage utilisant deux boucles de câble ; ce haubanage est représenté sur les photographies des figures 4 et 5.

Comme le montre la figure 6, chaque boucle passe par le bout d'aile, s'enroule sur deux électrofreins 3 et parvient au-dessus de la veine à un tendeur 1 et à un dynamomètre à jauges de contraintes 2 permettant de régler sa tension à 20.10^3 N environ.

Lorsque les électrofreins sont desserrés, une mise en incidence de la demi-maquette est possible sans arrêt de la soufflerie, mais pour une plage angulaire réduite (de 0° à 2°) ; le blocage s'effectue par serrage simultané des quatre électrofreins ; la surveillance de la tenue mécanique de l'ensemble se fait à partir des indications de la balance et de jauges de contrainte collées sur la structure de l'aile.



Fig. 4 – Photographie du haubanage.

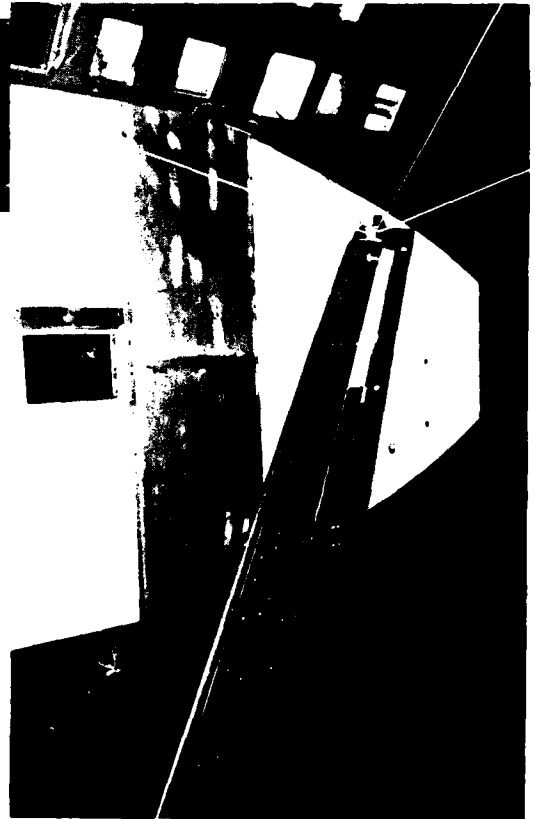


Fig. 5 – Photographie de la fixation des haubans en bout d'aile.

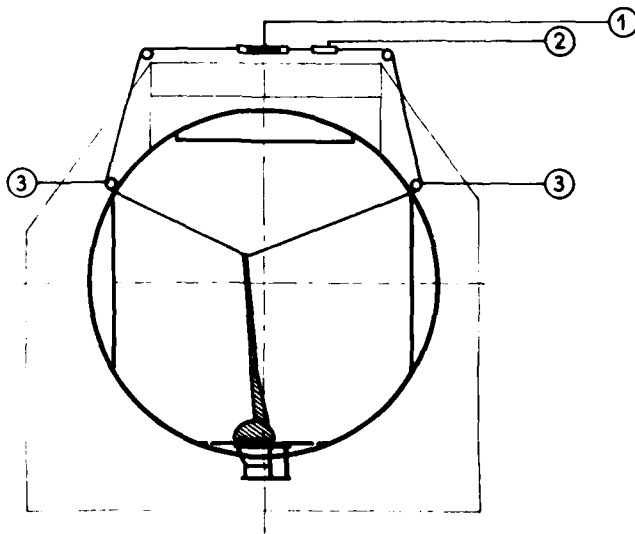


Fig. 6 – Schéma du haubanage de l'aile.

3 - CARACTERISTIQUES DE LA BALANCE-CAPACITE-PRECISION

La balance de la veine n° 1 (42,6 m²) est une balance à 6 composantes dont seuls les ponts X, Z, M fournissent des mesures d'efforts très précises (trainée - portance - moment de tangage). Le diagramme de capacité portance - moment de tangage initial de la balance (traits pointillés de la figure 7) a dû être déplacé de 32 500 N en portance par mise en place de contrepoids, de façon à englober le domaine d'efforts aérodynamiques exercés sur la maquette (partie hachurée de la figure 7).

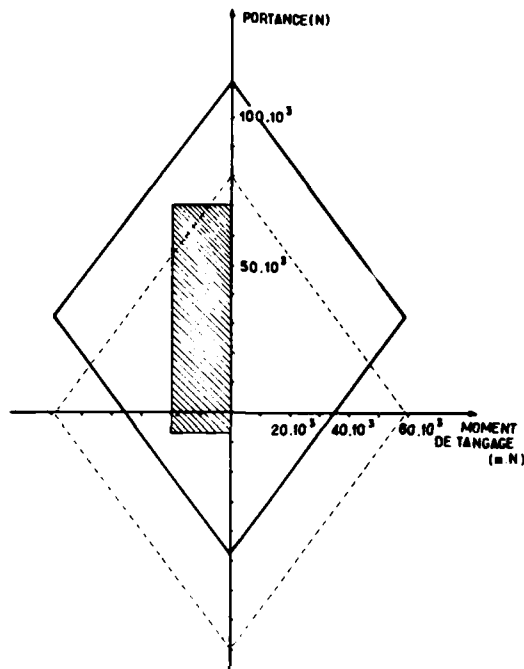


Fig. 7 - Diagramme de capacité portance-moment de tangage de la balance de la veine n° 1 (42,6 m²).

Le tableau ci-dessous fournit la précision théorique de la balance.

	valeur maxi mesurable (voir Fig.7)	précision théorique	précision en % par rapport à la valeur maxi mesurable
trainée	25 000 N	± 20 N	$\pm 0,08$ %
portance	110 000 N	± 100 N	$\pm 0,09$ %
moment de tangage	59 000 Nm	± 50 Nm	$\pm 0,08$ %

En pratique, la dispersion maximale des mesures constatée en essai atteint trois fois (trainée) et 5 fois (portance et moment de tangage) les valeurs citées ci-dessus, en partie en raison de la dispersion de la mesure de l'incidence ($\pm 0,02^\circ$), et en partie en raison de l'interaction provoquée entre la partie non pesée et la partie pesée par les brosses. La dispersion d'ensemble reste néanmoins acceptable vis à vis des effets aérodynamiques appliqués, notamment en subsonique élevé.

4 - EVALUATION DES DEFORMATIONS DE LA DEMI-MAQUETTE EN ESSAI

La maquette étant placée à 3° d'incidence, des prises de vue ont été effectuées par des appareils photographiques installés au plafond de la veine, sans vent, puis pour des nombres de Mach compris entre 0,3 et 0,8 ; ces photographies concernent deux repères placés sur le saumon et sur le bord d'attaque de l'aile à 35 % environ d'envergure.

Les déplacements des repères à partir de la position de référence sans vent sont mesurés sur les photographies pour chaque nombre de Mach ; une vue avec échelle permet d'en déduire les déplacements réels, qui sont essentiellement dus à la flexion de la voilure et à la déformation en roulis de la balance ; cette dernière peut facilement être calculée à partir du moment de roulis et de la raideur de la balance déterminée par essais statiques.

La figure 8 donne la valeur des déplacements constatés en fonction du nombre de Mach, pour une incidence de 3° de la demi-maquette ; étant donné l'imprécision de la méthode de mesure, ces valeurs ne sont à considérer que comme des ordres de grandeur.

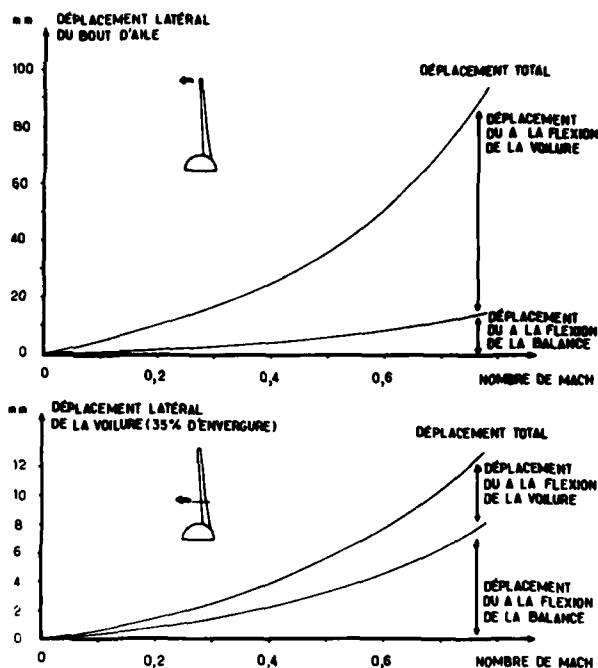


Fig. 8 — Déformations de la voilure et de la balance
(incidence demi-maquette : 3°).

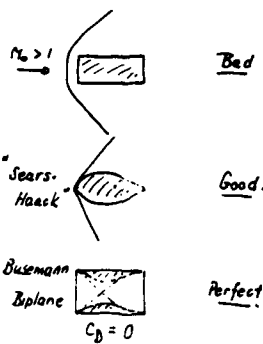
ROUND TABLE DISCUSSION

Dr. Yoshihara

We have four real old-timers here, who have hundreds of years of experience. I am going to have them reflect upon the happenings of this meeting, and perhaps make other comments regarding the future. To begin with, I would like to tell you what favorable interference is. That is what this meeting is all about. Just to remind you of what is really meant, I have five viewgraphs.

1. What is Favorable Interference?Supersonic Example

Given: $M_\infty > 1$, C_L , Volume, Length
Minimize C_D for $Re \rightarrow \infty$



Do we have "Busemann
Biplanes" in Transonics?

The first example of Slide 1 has nothing at all to do with our meeting, but it is one case which illustrates favorable interference. This is a case which is purely supersonic. You recognize that I consider the case of infinite Reynolds number, and the lift is zero. You then pose the problem: How must I shape the body of a given volume to have minimum drag. If you get any suggestions from the factory, they will suggest a circular cylinder shown at the top of Slide 1. We all know you obtain a nice detached shock wave. To be sure, it is easy to make. If you go to someone who has had calculus of variations, he can pose this particular problem in a nice clean-cut fashion, and obtain the Sears-Haack type body. If you are really imaginative, you come up with the solution shown at the bottom of Slide 1 that has zero drag. You can't do any better than that. This is the so-called Busemann biplane. This is an excellent example of what is meant by a global minimum. In a local minimum, as the Sears-Haack body, you look at several neighboring solutions or cases and you pick out the one which has the lowest drag. The global minimum is the lowest of such local minimums.

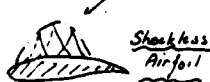
The question of course arises, perhaps getting a little more relevant into the transonic region, "Do we have a Busemann biplane in the transonic area?" With tongue in cheek I say, "Sort of, yes". The answer is yes, and the case as you all know is the shockless airfoil. For this particular case we can pose again an isoperimetric problem as shown in the left side of Slide 2: given certain bulk features of the airfoil and a given lift, determine the shape for minimum drag. It happens that this case does not admit a solution. The shockless airfoil is a degenerate case.

2. Planar Airfoils (Chordwise Interference)Transonic Problem

Given: M_∞ , C_L , (C_M) , t/c , $Re \rightarrow \infty$

Minimize C_D

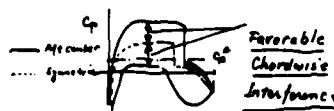
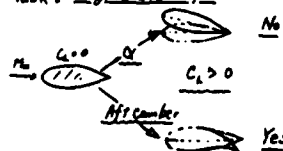
Transonic Busemann
Biplane



$C_D = 0$

- Existence limits in M_∞ - C_L space
- Off-design performance.

Task: To generate Lift



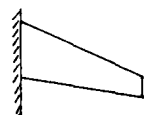
Is shockless Airfoil better
than airfoil with "tolerable"
shock?

If you look at the shockless solution, there are two obvious questions that are raised. You certainly know that if you push the Mach number high enough towards one, you are going to have an increasingly difficult task of determining the shockless solutions. In the same token, at a given Mach number, if you increase the lift, it is also going to be a terrible problem. What is then the practical range in the Mach number/lift space that you can evolve a shockless aerofoil? The second obvious question is what are the off-design penalties?

Quite apart from the shockless solution, you can take an alternate more pragmatic approach without ever having heard of isoperimetric problems. How can I, by cut and try in a windtunnel evolve an airfoil shape having a given lift with a tolerable shock. Let me direct you to the right side of Slide 2. Let's say that we start with a symmetric airfoil at zero angle of attack and we ask ourselves what is the best way to generate lift? The answer will differ depending on how much lift you desire. For the first step, let's ask for a very modest amount. You can try the route of angle of attack, inclining the entire airfoil. In general, this is not a good way because you are creating a significant increase in the transverse projection of the airfoil on which the pressure can create drag. Perhaps a better way is to keep the front end of the airfoil fixed and just bend down the back end. The resulting aft camber induces a loading on the forward portion of the airfoil which you have not changed. This is what you might term favorable chordwise interference. Now, you can push this until you run out of effective aft camber; that is, until the back end starts to separate.

There is another question people have argued about, sometimes in an emotional way. That is, is a shockless airfoil better or worse than an airfoil with a tolerable shock? I am not going to define precisely what a tolerable shock is, except to say that it is one in which you are not too unhappy with the drag which it produces. Next we shall progress to greater complexity. The last slide was an airfoil; in the next slide (Slide 3)

3. Swept Wings (Chordwise & Spanwise Interference)



Questions

- Is shockless wing possible and is it desirable?

$$C_D \rightarrow \frac{C_L^2}{\pi A R} \quad ? \quad \text{Is "Shockless" distribution possible?}$$

Given: $M_\infty, C_L, (C_H)$

$$A \leq b/c \leq B$$

Planform: (AR, S, etc)

$$Re_N \rightarrow \infty$$

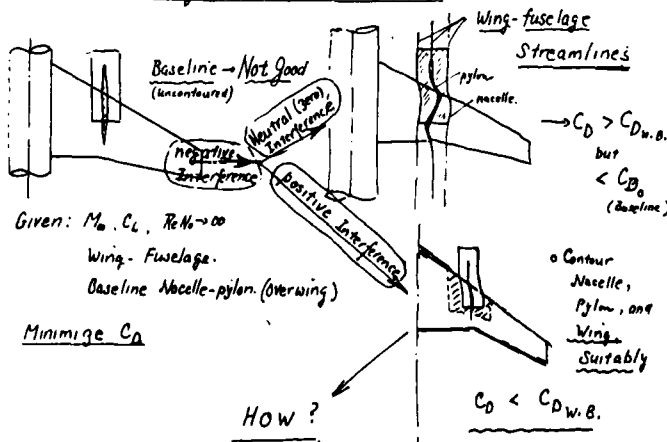
- With shock: is optimal spanloading elliptic?

- What is penalty of planform constraint?

Minimize C_D

we consider a finite wing. First of all, one can ask, can you make a 3-D wing shockless? I don't think that anyone really knows the answer to that. I don't think that there is any obvious reason why you couldn't. In this case for a given lift, the minimum drag is the $C_L^2/\pi AR$. Let's take one further step and say that you don't like shockless airfoils, and permit a tolerable shock. Now, under this condition is the minimum drag compatible with an elliptic loading? If you try to force an elliptic loading, would you foul up the shock system. This is another interesting question. Finally, in most problems that we consider, the poor aerodynamicist is stuck with a planform given to him by other people on the design team. How much then is the constraint on the planform penalizing you in terms of minimum drag? I am posing these questions for our experts to comment upon.

4. Wing-Nacelle-Pylon Interference



Slide 4 is as far in complexity as I will go; that is, given a wing-body, I want now to add a nacelle and pylon. From the point of view of noise, I will put the engine on top of the wing. Such a configuration might have to be considered also in an existing low wing airplane if there isn't enough space below the wing to attach new high bypass engines. The question then is what must I do to optimize the configuration? Now there are three levels of interference. If you use a conventional uncontoured nacelle-pylon, that is an axisymmetric nacelle with a symmetric pylon, this certainly is a case of negative interference. This configuration is very bad. Most of us are generally happy with what I define as zero interference or neutral interference. This case was described by Mr. Rettie. Here you calculate the wing-body and determine the streamlines in the vicinity of where you want to put the nacelle-pylon. You then warp the nacelle-pylon to fit these streamlines. This approach is not fully satisfactory since the finite thickness and the powered internal flow are not compatible with the flow on the wing body.

In the case of a wing design, when you try to design for uniform isobars to recover as much of the sweepback benefits as possible, this is again neutral interference. However, we can do better, and that is the philosophy that we must promote. For positive interference, which I show on the lower right of Slide 4, one must be prepared to change the wing as well. That is, in the region where the nacelle-pylon affects the flow on the wing, you must be prepared to tailor that part of the wing. For example, you may want to incorporate a nose-down camber. Also, you must shape the nacelle-pylon in a manner different than that described above. I don't know what the best way is, but it will require a lot of physical intuition. Unfortunately this is the only way at present to tackle this problem. One thing we can obviously do is to eliminate anything bad that we diagnose in the experiments.

5. Status of Transonic Design.

Tools

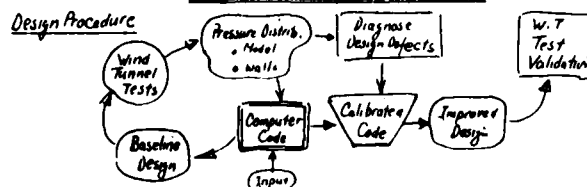
1. Wind Tunnels

- Wall interference
- Reynolds No. Simulation
- Configuration Variations difficult (Models)
- Diagnostics (Pressure measurements) Difficult
- Etc.

Very
Expensive

2. Computers

- Mesh Generation → Complex Configurations
- Incorporation of Viscous Interactions



In the last slide (Slide 5) we show our two basic tools - the windtunnel and computers. We all know the deficiencies of both. I need not remind you that the windtunnels have wall interference, we don't simulate the Reynolds number, sting support, interference, etc. With computers there are two basic problems facing us today. We must be able to compute whole airplanes. That's what Charlie Boppe undertook. We must compute wings, wing-bodies, pod-pylons, winglets, etc. If you use the exact potential or Euler equations, the most important task is to fulfill the boundary conditions correctly. The best way to do this is to generate a mesh system which conforms to the configuration. Therefore the big problem today is mesh generation. For wing-bodies today, this is almost trivial. It is only when we add the nacelle-pylons, components which are topologically not sympathetic to the wing-body components, that we have problems. Today, this is the area that requires a great deal of thought and sweat.

Secondly, we must incorporate the viscous effects. We must be able to treat separated flows, the wake, and we must be able to do this in 3-D. Maybe we should first start out with a quasi 2-D treatment normal to the sweep which will take us to at least a 30 degree sweep. But as you consider higher lifts and greater sweeps with increased spanwise flow, you must use fully 3-D viscous equations.

How do we use these two imperfect tools? First, one must evolve the baseline configuration in the best way one can. Then build the windtunnel model, putting as many pressure taps into it as possible, and then test it. At the same time I would certainly recommend putting pressure taps at key locations along the tunnel wall to measure the wall interference. By the way, I would suggest solid deformable walls as a preferred alternative to perforated and slotted walls. With a solid wall at least you know what is happening to the flow along the wall. The transonic walls need be deformable only mildly without excessive precision requirements.

Now with the fully diagnosed test results on the baseline configuration, we can tailor the theoretical method, as for example the modeling of the viscous interactions. If you have a small disturbance theory this will help you select the mesh around the nose region to compensate for the small disturbance approximation. Finally, the test results will tell you what is wrong with your preliminary design. Here you must have some experience, first to recognize what is wrong, and secondly to know what to do about it. The tailored code is used to evolve a better design, which must be finally validated in the windtunnel. If you have enough money, and if you are ahead of schedule, you may repeat the above design cycle once more.

I think in the past we have been conservative in our optimization when kerosene was fairly inexpensive, but in the future we must design the airplane with much more imagination and innovation. We must do this more efficiently.

Now I would like to turn the discussion over to our experts. Our first expert is Dick Whitcomb. I think we all know him. He has been in charge of the 8 foot transonic tunnel for many years. He has helped to develop quite a few weapon systems and commercial airplanes for many of which he received no recognition. He is a fellow who has real gut feelings on this subject. I would like Dick to talk about his general reactions in the overall area of favorable interference.

Dr. Whitcomb

I am going to concentrate on a discussion of the commercial aircraft. We have been working quite a bit on military aircraft - particularly on the forward swept wing, but I don't have time to cover both, and most of my effort has been with commercial airplanes in recent years. First of all, I would like to recognize the very high quality of work which is represented by the papers presented at this meeting. I am well aware of most of the work presented by the American authors, but I was particularly impressed with the work that the European community was doing. I was at Williamsburg recently and heard some of the papers given by Europeans, but I have heard so much more today. It was all very good. I believe that this work is the basis for the apparent successful challenge of the Europeans to the mighty Boeing organizations' dominance of the commercial aircraft market. I don't know how you will be doing in time, but you seem to be doing pretty well so far. Of course, never count Boeing out though. Let's go through some of these things that were discussed.

The subject of viscous effects, on the first day, I thought I was going to have to say something about, but I think that that has been pretty well covered since then. I would like to make the comment though, that in the United States, a number of people have tried to design wings before the viscous effects were applied to the theory, and many of them were total disasters, because they designed wings with gradients on the rear portion and the boundary layer separated. But on the basis of what I heard the last few days, you Europeans, as well as we in America, now recognize that the boundary layers must be in the theory.

The next point I would like to discuss, I wouldn't have brought it up, except that Yoshihara challenged me several days ago, and then actually put a viewgraph up there to challenge me again, so let's get into this discussion of shockless airfoils vs. airfoils with a small shock. I told him they are the same airfoils. In your printed versions, in the paper by Redeker, Schmidt and Muller, paper 13, figure 14; I think that shows what I am going to talk about. They point out that they started with a shockless airfoil and if you look at their design point which is the little circle, then they also have a contour of the highest L/D and you will notice that the design point is down at the bottom of their optimum region. This is the point I want to make. If you design a shockless airfoil, you will always get a somewhat better L/D if you increase the lift coefficient a little bit and take a little shock loss, because the gain in lift you get is greater than the increase in drag you get. Now, you can push that too far. The onset for the strength of the shock wave is not a linear function, it's about a cubic function, depending on the mach number ahead of it. So with the first little increase in mach number you get, you can get very little drag associated with it. I don't want to continue much more on that, because I want to get on to some of the other points.

The other point that was made strongly by some of the other speakers, is that the fuselage...has a great effect and that is what we found in the United States. In fact, very slight changes in the shape of the fuselage can have pronounced effects on the pressure distribution over the entire span of the wing when you are dealing with supercritical flow. And that was particularly pointed out by Treadgold, and he pointed out that that change that he put on there is not necessarily optimum. He was using it to show the very sensitive nature of supercritical flows to the fuselage shape. Then I would like to mention while we are talking about the fuselage, the effect of the fillets. That was discussed by several people. Here we come to the combined effect of the fuselage and the boundary layer. The reason that that fillet is so important is that it is effecting the interacting boundary layer of the fuselage and the wing. We are a long way from handling that theoretically, but experimentally, we have found that a fillet is a great help, forward as well as rearward.

We have tested winglets on many configurations. In almost every case they are effective. It was pointed out by Mr. Rettie that you get a greater reduction in induced drag by just extending the tip by something equal to the winglet height. But, as he also pointed out you have more bending moment. So the principle advantage of a winglet is to get more in performance with less bending moment. Our general conclusion is somewhat different than the one that Mr. Rettie pointed out. For a given gain in performance, the winglet produces half the bending moment of a tip extension. Or, for a given bending moment, you can get twice the gain in performance. Something more on flight tests. We measured in the windtunnel, after we tuned the winglet, a 7% gain in the L/D, and we are measuring that in flight. I think that Mr. Rettie mentioned 6%. That was before we had done the final tuning in the windtunnel. He said that you don't have to go into a windtunnel, because the theory is so good, but again, the theory that he was using did not have the boundary layer in it. Until you can get the boundary layer into that theory, you must go to the windtunnel for the final answer.

Now, turning to a subject that was discussed later in the conference, one which we are working on intensely ourselves, that is the installation of engines on the next generation of aircraft. We know that there are a number of airplanes flying today with engines on them, so why do we have to continue to worry about the interference effects of engines again. Why do we have to worry about the interference effects again? We are now dealing with supercritical wings. One of the things which we did when we designed the supercritical wing was to transfer some of the problems which were on the upper surface to the lower surface. What I am saying is that we reduced the induced velocities on the upper surface, but with a given thickness ratio we increased the induced velocities on the lower surface. This was alright as long as you were dealing with the wing alone. Then you put an engine under there, and the interference effects are much worse for a supercritical wing than they are for a conventional wing. We have been fighting that for a year. Now several papers were given today or yesterday on what you Europeans are doing. I think that you are probably running into some of the same problems that we are.

Dr. Yoshihara had a picture up there and I want to emphasize that the problem cannot be solved by a simple symmetrical "plain-Jane" pylon. We are working with pylons that have very complex contoured shapes. It is the only way that we can keep the supercritical velocities down in the junction regions. That pretty well covers the various subjects that were discussed.

Dr. Yoshihara

I think what the engine people will have to do is to learn how to build an engine which has a curved shaft. The next speaker is Monsieur Poisson-Quinton, a member of the Flight Mechanics Panel. He is now the Director of International Cooperation at ONERA. But he was a real expert from way back on powered jet effects. This includes jet flaps and blowing over the wing. He will concentrate his comments on airframe/propulsion integration to enhance aircraft lift.

Mr. Poisson-Quinton

I shall give my comments in broken English because it is easier for this R.T. discussion. I want to make some remarks about jet/wing interference. During this meeting we had a variety of good papers dealing firstly with transport aircraft configurations and then with combat aircraft configurations for which propulsive aerodynamics, or "Powered lift" is used to enhance their lifting capability; now, I shall summarize some expected goals and short comings.

As you know, since about twenty five years, a considerable amount of research was carried out on blowing technology for high lift systems, at first to maintain attached flow on wings and flaps through the Boundary Layer Control (BLC), and then to increase the wing circulation (supercirculation of "jet flap" effect); more recently a third application; the spanwise blowing, has been explored to enhance the vortex lift at high angles of attack.

With my first slide (Fig. 1), I have tried to illustrate how to use a jet-engine to induce this powered lift, either by the full engine exhaust, or by a small bleed taken on the compressor flow or on the turbine flow.

Up to now, the main problem for BLC or spanwise blowing applications is the large thrust losses due to the use of compressor bleed from current technology engines; and the engine manufacturers are still reluctant to design a well organized bleeding system on their compressor to avoid these thrust losses.

An alternate solution would be the development of some compact Auxiliary Power Unit (APU) driving a compressed air generator used for various blowing systems (BLC, "jet-flap" controls, spanwise blowing,...) and for other purposes (pressurization, cooling of electronic systems, etc.).

It seems interesting for the FDP to push some AGARD cooperative study with the Propulsion Panel on these two sources of compressed air needed for future high performance combat and transport aircraft.

On the other hand, the use of a very hot bleeding flow taken on the turbine exhaust is only attractive for a spanwise blowing emerging directly from the fuselage to generate or to enhance a vortex sheet on a combat aircraft wing at large angles of attack.

At this stage, you must recall the order of magnitude of the jet momentum coefficients needed at low speed flight for the various blowing concepts:

- BLC on flaps, L.E. slats, : $C_{\mu} = q_m V_j / q_{0.5} \sim 0.02$
- "jet-flap" controls: $C_{\mu} \sim 0.02$ to 0.2
- spanwise blowing: $C_{\mu} \sim 0.1$ to 0.2
- circulation control with the full engine exhaust flow on the wing: $C_{\mu} = C_T \approx 1$ to 2 .

This later concept, very simple because avoiding a large and heavy plumbing installation inside the wing, has been extensively tested for both transport and combat aircraft configurations, using directly the full flow of high by-pass ratio engines or turbo-jet engines respectively, as illustrated on Figure 1: the two first sketches illustrate the Externally Blown Flap (EBF) and the Upper Surface Blowing (USB) concepts flown on the McDonnell-Douglas YC-15 and on the Boeing YC-14 during the US Air Force AMST program; both have demonstrated spectacular high lift capabilities and very short field STOL performance; however, some drawbacks have appeared with these configurations:

- for the EBF concept, some structural fatigue on the multi-element flaps due to the high velocity jet exhaust flow impinging the flaps, and large fly-over noise (these drawbacks would be minimized with some larger by-pass fan engines);
- for the USB concept, quite large cruise parasitic drag due to interactions between the propulsive nacelles and the wing upper-surface, with supercritical flow and shock waves; but such problems can be minimized by careful theoretical and experimental approaches (as illustrated in the Rettie paper Nr 27);
- an effective - but expensive - engine-out procedure has been developed by Boeing for this two-engine configuration; more recently, an experimental four-engine aircraft, the QSRA, built by Boeing for NASA-Ames was very successfully flown to demonstrate ultra-STOL capability (C_L max. around 9) and very low noise around civilian STOL-ports.

A third configuration, a podded upper-surface nacelle, seems also quite attractive to take advantage of some exhaust flow vectoring towards the deflected flaps to induce a supercirculation on the wing; furthermore, this concept allows a very small ground clearance compared with under-wing podded engines, which is mandatory for future huge cargo projects (spanloaders using air-cushion landing systems); and, for this configuration, the shielding effect of the wing allows a reduction of the fly-over noise.

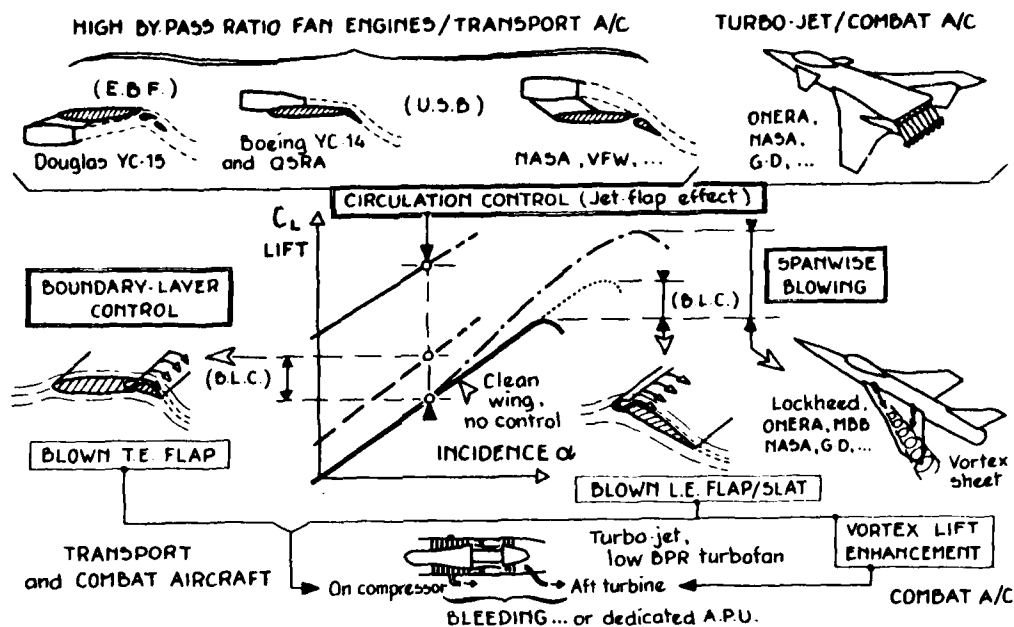


Fig. 1 : HOW TO USE A JET-ENGINE TO INDUCE AERODYNAMIC LIFT

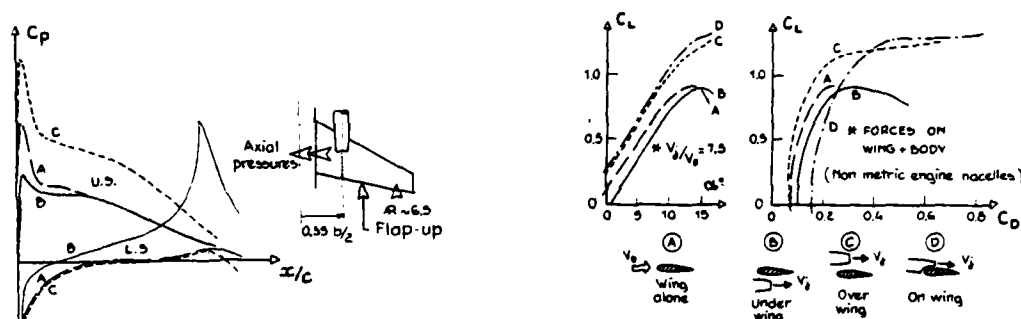


Fig. 2 : V.F.W. RESEARCH ON JET-WING INTERFERENCE AT LOW SPEED

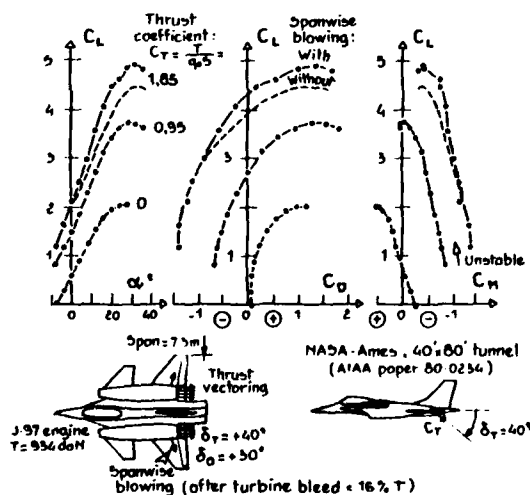


Fig. 3 : NASA LARGE SCALE POWERED FIGHTER MODEL WITH VECTORED THRUST AND SPANWISE BLOWING

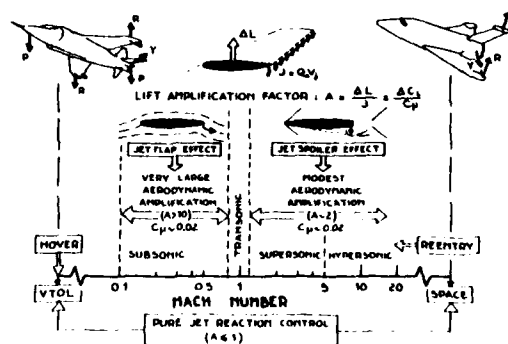


Fig. 4 : LIFT CONTROL BY JET-FLAP AND JET-SPOILER EFFECTS

To illustrate the very different jet/wing interference between these three last configurations, I have made a copy (Fig. 2) of some results from V.F.W. obtained on a transport model in a cruise configuration (flap-up): the wing pressure distribution in the jet plane for under-wing and over-wing concepts are very different; the exhaust jet on the upper surface side (c) develops a large supersonic velocity at the leading-edge, i.e., a thrust effect, meanwhile the conventional under-surface location of the propulsive nacelle leads to a large supersonic velocity on the rear part of the lower-surface, i.e., a drag effect; both configurations (B and C) enjoy a substantial induced circulation lift; in both cases the engine pylon shape and twist must be optimized, together with the local wing and nacelle shape, for minimum cruise drag (not so easy in the case (c)).

For the tangential jet (D) of the USB concept the supercirculation is even better but the drag penalty is quite large in this preliminary test with a non-optimized nozzle shape; Boeing analysis have shown that for a USB configuration, it is mandatory to compromise this nozzle shape between high lift capability at low speed and minimum parasitic drag at cruise regime.

Turning now to the vectored thrust at the rear of a combat aircraft wing, a large amount of experimental research has been conducted to use the supercirculation effect for both low speed capability and transonic manoeuvre enhancement.

Again such concept needs a very careful integration of the 2-Dim. vectored nozzle in the airframe, but even more important is the longitudinal trim of a very large nose-down pitching moment due to the jet flap effect; that is why for such a concept, a canard configuration is generally proposed, combined with some degree of longitudinal instability (authorized with a convenient active control system).

To illustrate this very attractive configuration, I have reproduced (Fig. 3) a typical result obtained on a large powered model recently tested in the 40' x 80' NASA/Ames tunnel.

The combination of the supercirculation effect due to thrust vectoring, and of vortex lift enhancement by the spanwise blowing, gives very large maximum lift increments:

at $C_T = 1.85$, with vectored thrust: $C_L \text{ max.} \sim 4.5$

at $C_T = 1.85$, with vectored thrust and spanwise blowing: $C_L \text{ max.} \sim 5$, to be compared with $C_L \text{ max.} = 2$ without propulsion ($C_T = 0$).

Of course, the close-coupled canard provides a large lift gain at high angles of attack due to the favourable vortex interference on the wing and also a better polar curve (just like the spanwise blowing effect); in this particular test, the negative static margin (-23 %) seems too large and the canard deflection (+20°) is not sufficient to trim the large nose-down pitching moment: some spanwise blowing on the canard itself would be a good way to generate enough positive ΔC_m . Nevertheless, such a large powered model testing is most interesting to understand, evaluate and optimize the complex propulsion/airframe interactions; and it appears mandatory to push the development of a better engine simulation on smaller wind-tunnel model, when it becomes impossible to install an actual small engine; such compact engine simulators, using compressed air turbines, must simulate either a reheated turbo-jet or a turbo-fan, and necessitate a very careful calibration bench to have precise mass flow and thrust data.

My last comment about powered lift and integration of a blowing system to aircraft will be on the pure jet-flap effect obtained by a simple jet sheet emerging from the wing trailing-edge.

A highly successful flight demonstration of the Circulation Control Wing concept (CCW) has been performed recently on a US Navy A-6 aircraft modified by Grumman for the DTNSRDC: with a simple trailing-edge blowing slot installed all along the span, a trimmed $C_L \text{ max.}$ of about 3.7 was obtained for a C_μ of 0.2 only ($\alpha = 16^\circ$, $V_0 = 67 \text{ Kts}$); this maximum lift must be compared to a $C_L \text{ max.}$ of about 2.1 for the standard A-6 with a 30° flap deflection.

Such trailing-edge blowing schemes can be used also as a "pneumatic" control with much smaller lifting performance but with an even better lift amplification ($A = \Delta C_L / C_\mu \cdot \sin \theta$): my last slide (Fig. 4) illustrates some results obtained at ONERA on such pneumatic lift control (trailing-edge jet sheet vectored at 90°); the main idea is to use this jet control in the whole flight domain, from hovering to space conditions; of course for these two limits, there is no aerodynamic effect and the jet is used as a pure reaction control; but at subsonic regime, the lift generated by the jet-flap effect can reach ten or fifteen times the jet momentum for very low C_μ values ($C_\mu \sim 0.02$); near Mach 1 the amplification factor strongly decreases, due to shockwaves development; then, at supersonic and hypersonic speeds, the jet sheet acts as a "spoiler" and the amplification factor remains around $A = 2$; this value is still attractive for a very simple pneumatic control system installed on the three axis of a spacecraft or a missile.

On the other side of the flight domain, there are certainly some interesting applications for the control of VTOL configurations, during hover, transition and cruise regimes. And, of course, everybody is thinking about some application in a future active control system using simple quick air valve instead of complicated mechanical actuator/control surface scheme. Thank you.

Dr. Yoshihara

The next speaker will be Dr. Wolfgang Schmidt, and I have asked him to comment on the role of computers, also with respect to how the computer can be used by the applied aerodynamicist.

Dr. Schmidt

Before I start with my comments I would like to go back to two questions that came up in earlier discussions. The first is the question of the Kutta condition. In the early days most people applied the transonic methods and the Kutta condition in such a way that at the trailing edge they had a mesh point. They said in the wake the jump in potential is exactly that one right at the trailing edge. If you apply this condition you would see that with central differences for the velocities ϕ_x , these velocities are not equal. You don't fulfill the exact Kutta condition. It is easy to overcome that by saying that the jump in potential at the wake is equal to the jump that you have just one point ahead of the trailing edge. If you do that, you can be sure that the velocity right at the trailing edge is exactly the same on upper and lower surface. So it is a very easy way to make sure that you have the right Kutta condition.

The second point was with respect to questions that Professor Young asked more than once. They were never really answered. The question is, "What is happening if I have a wing-body combination and I try to compute the lift. Do I really get the right lift if I do an inviscid analysis and I do not take into account the vortex system emanating from the fuselage aft end and intersecting with the wake coming from the wing?" I think we should be aware of this problem. Separation on the aft end of the body and the circulation that is being created by means of this separated flow has to be taken into account to get the correct lift prediction.

Let's go back to my main comments. First slide. The task that we have is to simulate full aircraft in real flight. That is what we have to do to build more efficient aircraft and better fighters. It is the same with missiles, if you are interested in missile design. The most standard procedure is almost like applying Darwinism - take the windtunnel, test, change, go back, change. If you go into the windtunnel, the first thing you have to do is to build a windtunnel model. We are all aware of the fact that the windtunnel model is not the exact aircraft. We also have to use different windtunnel models depending on the problem that we have to study, such as afterbody problems or jet interference problems or clean aircraft problems, etc. The real aircraft is flexible in general, the model is very stiff.

The second problem comes from the test facility itself. You have tunnel walls - we do not know what they are doing to your results. You also have freestream turbulence, and we saw some papers which clearly indicated that transition location is giving a very large influence on the final result. We are also all aware of the problem of simulating Reynolds number, but we have some hope that we will have facilities in the future that might enable us to overcome that. Hopefully they will not introduce additional problems.

The next problem is that you have to use fast equipment, that is, you have to use a sting, you have to use balances and a lot of other things. They are never the optimum, they will always cause some problems.

You will end up with something finally, which we call windtunnel results. There are a lot of people who believe that this is the best answer we can get and that this fully represents the real aircraft in free flight.

For some years now, more and more people are relying on the other side, that is they are using the computer. I would like to stress that it makes sense to use the computer only if you are fully aware of the limitations on the physical models which you are using. You are restricted to physical models, you cannot solve the whole thing. You must make sure that you have the right physical models, and you must be aware of the limitations of those models.

The next step is that we would like to solve this problem described by the physical model. That means that we have to formulate the mathematical problem, we have to form the differential equations which describe the problem. Most of this work has been done in the past by people like Prandtl, etc. Those equations are however, nasty. They are highly non-linear and are difficult to solve. So, we have to go back to approximations which are based on finite difference or finite volume or finite element techniques. They introduce additional problems because they add up to a set of algebraic equations, and those equations have truncation errors, additional terms, and you don't know what they do. But, even if you have done a fine job up until now, you have to put into the computer the real configuration. You have to discretize what this configuration looks like. You have heard quite a bit about mesh generation during the last few days. We have seen some nice examples of this in the past few days, but we have a great deal of work to do on this in the future. Finally, we end up with something which we call the computed flow field.

The worst point is that now everyone is comparing this computed flow field with the windtunnel result which we have on the right-hand side. They all blame the theory if there is not perfect agreement. I sometimes wonder if it would not be better to compare with free-flight results, for which, however, there is not a great deal of information available. We need more. Furthermore, I hope that computer and windtunnel people will use each others capabilities to improve their own results and understanding.

Next slide. Let us go back to the conclusions that I drew yesterday morning. We saw at least two examples of papers in which computational results can do just as good a job as those prepared by experienced design engineers. One by the DFVLR on the transport wing and the other from the FFA in Sweden, showing those results on the fighter wing. Both wings were almost as good as those being designed by very experienced project engineers in aircraft companies.

We still must make these methods easy to use for design engineers. I said yesterday that we have to do more on the complex configurations. I think that since all of us saw this excellent paper by Charlie Boepe, we must say that a lot of things have been done in this area already. There is still a lack of simulation of three-dimensional separated flows. I think it is partly because we really don't understand what a separated 3-D flow is, and we need a lot of experimental information to build up the right physical model. Since we don't have the physical model, we must be aware of the fact that we can't simulate these flows by purely numerical models. The numerical method cannot provide the physics, it can only simulate what you know.

What I missed in this meeting was a paper on unsteady flow problems influencing the manoeuvre boundaries. This is the pacing element for the future to solve problems dealing with the manoeuvre limits of combat aircraft and for the ultimate drag counts for transport configurations.

Next slide. This is just to recall the results that Charlie Boppe showed us. It is possible these days to compute very complex fighter configurations, including nacelles, stores, pylons, canards, etc. We saw that those results are really quite promising. Nevertheless there are still limitations as far as separated flow is concerned and as well as drag level is concerned.

Next slide. This slide recalls the fascinating agreement between measurement and theory on such a complex configuration as the space shuttle orbiter.

Next slide. This brings us back to the question of the different physical models which we are applying. In this case you see that the viscous effects play a fairly important role. I would like to recall that this is a simulation at Reynolds number 1 million. We did the same case at a Reynolds number of 20 million, and I can say that the pressures do not differ significantly from those for the inviscid solution in that particular case. This raises a question as to what is the ultimate inviscid solution, because if we don't start with the right inviscid solution, which has the right shock position, we will never end up with the correct viscous solution. So as the flow model becomes more complex, the more confident we need to be about the specific components that we are using.

Next slide. To emphasize this point, I would like to go back to the comparison between the three-dimensional Euler solutions, three-dimensional full potential and the three-dimensional small disturbance theory. They all show very different shock positions. In these cases the Reynolds number is very small, but what do you believe will be the right solution at very high Reynolds numbers? Thank you.

Dr. Yoshihara

Last, but certainly not least, we have Barry Haines, and he being a fine applied aerodynamicist. He is going to tell us about the proper role of the computer in applied aerodynamics.

Mr. Haines

Coming fourth, a lot of the things that I wanted to say have already been said, but I will do my best. I think that I would like to start by referring to the fact that 10 years ago there was another AGARD conference on aerodynamic interference, and if you look back at the proceedings for that conference, I think that there are some quite definite differences from the one which we have just been having. Ten years ago, the theoretical people were arguing fairly violently among themselves about what theoretical method you should use. Quite a few of the theoretical methods about which they were arguing are no longer in use today. Theoretical methods have advanced a great deal over the last ten years, and they have gone a long way to dominate this conference. Dare I say that they have almost dominated it too much in the sense that we have been turning ourselves into various other conferences that are held to discuss the validity of the various theoretical methods. It is very exciting to talk about this, but in this conference where we are discussing aerodynamic interference, we have been in danger at times of forgetting our prime aim. I am going to talk from the point of view of a person who has to use the theoretical methods to design configurations and to improve those designs with theoretical methods. Ten years ago, a wing designer was designing a two-dimensional airfoil. Five years ago he would have been designing a three-dimensional wing with the aid of these methods. Then he learned, and we saw papers today on this, how important it was to design a wing-body combination. Now he is trying to design a complete configuration. Looking to the future, the paper for me which undoubtedly held the most promise, was the one by Charles Boppe this morning. While he may not be using the very latest and most refined theoretical methods, he is certainly attempting to do the job which the aircraft designer wants. As a last comment on the theoretical methods, I think that I have about 40 years of experience as a windtunnel engineer, and I just don't believe in a theoretical method which gives good agreement with experiment, if the theoretical method is inviscid.

Now before the theoretical method developers get at me, I ought to recognize that the experimentalists also have problems with these viscous effects, and as a slight aside, but I think it is important to say this, I am still somewhat disturbed about some of the papers that have been written about the tunnel test techniques for getting the right answer when viscous effects are involved. In debating whether you should or should not fix transition, I think that there are certain principles that you should follow. You should ensure that you have a turbulent boundary layer at the shock, but if you find that to achieve a turbulent boundary layer at the shock you have to use a transition fix which clearly gives a rear separation that would not be present full scale, then the results are wrong. You may say, "but how can I know that the separation would not be there full scale?". Well, that is just where the theoretical method may help you. I think that these two pictures we had up of the computer and the windtunnel were wrong. I think that the computer and the windtunnel should be integrated. You should be using the computer to help in your interpretation of the tunnel data. If I understood the Chairman in the beginning, I think he said that he wanted to do away with all slotted and perforated wall tunnels! I presume he wants to use a solid adaptive wall. He will need his computer to know what shape that adaptive wall should be. I don't think he can have a solid wall if he wants to go above Mach number 1. So, I assume that he is talking about Mach numbers less than 1.

To come back to the question of fixing of transition, it is wrong to conclude that there is a general conclusion about whether you should test transition free or transition fixed. What you should do depends on the Mach number, the Reynolds number and the wing that you are testing. If you have to have a turbulent boundary layer at the shock with the most representative boundary layer thickness relative to what you calculated full scale - if you can do that transition free, all well and good provided you know where transition is and provided you allow for the extent of the laminar flow in the interpretation of your drag data. However, you may decide that you are not satisfied with any of the results however you fix or do not fix; that is why we are building cryogenic tunnels. Viscous effects are thus at the kernel of our problem whether we are in the computer or whether we are in the windtunnel.

Going back to the aircraft designer who is using these theoretical methods, I think it is worth saying just a little about design programs and optimization programs. For design programs I think the significant question was asked by Dr. Schmidt yesterday. How do you choose the pressure distribution to get the right answer. That is where the art still comes in. It is all within your experience. I will tell you a very brief story from my own establishment recently. We have got an inverse design program for supercritical flow. We were trying to move the shock rearward to generate more lift. We were also trying to modify the lower surface pressure distribution. The design program devised a shape to do this and achieved its objective, but at the same time, it gave peak suction near the leading edge that were so high that when you went into an off design condition, they were clearly too high and separated flow was obviously going to occur. After trying to solve this anomaly for quite a time, the designer went back to his past and started with a subcritical design program and very quickly got the answer he wanted. In fact, checking back supercritically, he got the shape that he wanted. The significant point is that the shape near the leading edge relative to the original datum was in the exact opposite direction to the shape which had come out of the inverse supercritical program, being wrongly used because the designer didn't appreciate that the pressure distribution that he was asking for was an impossibility. Obviously that particular mistake will not be made again, and in five weeks' time, or should it be five years' time, the designer will have the experience to use his supercritical design program.

Optimization programs that have been propagandized in certain quarters, we have heard very little of in this conference. I myself feel that at transonic speeds we are very far from being able to exploit optimization programs. I will quote just a few examples. Any aerodynamicist that is optimizing wants to know the drag, so that ultimately an optimization program must have the ability to predict drag. I appreciate that in certain theoretical papers today, there have been attempts to predict drag from theoretical considerations. But, I think that everyone in the room would be at least somewhat sceptical as to whether they will give the right answers. If you go to a military aircraft where you have many design points, you have a very complex configuration, these may be the dominant issues - getting good flying qualities near and even beyond separation onset - very difficult to quantify for an optimisation program. Such programs have been produced for two-dimensional airfoils, but it is arguable that an optimum airfoil will not necessarily be the optimal starting point for the design of the complete configuration, and that is what the designer wants.

Let me turn from theoretical methods to favorable interference, the theme of the conference. I would like to pick up one point which has been mentioned several times and which I think is very important. One of the best ways of obtaining favorable interference effects, which is what we strive for, is to carry more lift on a part of the configuration that can stand having extra lift on it without any adverse consequences. This is why Mr. Jupp showed when he liked a particular sort of flaptrack fairing. I am sure that he could have said the same thing about wing root fillets. I am sure that people could and have said the same thing about nacelles. Cases of an aft fuselage nacelle which have given favorable interference have done so because they have redistributed the load over the wing and taken it away from the point at which the shock strength was greatest. It is an example of the same thing. Going back to one of the questions asked by the Chairman: should one design for shock free flow or for a weak shock. Here, I completely agree with what Dr. Whitcomb has said. With a weak shock, you get better performance with a little extra lift: a further example of the same principle. Regarding spanwise loading, the best load distribution on the wing is unlikely to be elliptic. You should consider the full configuration, including the tail plane. You should consider that one is trying to strike a balance between buffet and drag and all of this goes to show that you want to load the inner wing more than you would on an elliptic load basis. To reiterate, one way of getting favorable interference is to add lift. The wing tip carrying the load of the missile is another example adding lift where you can avoid having an adverse effect. Another way is to use side force in a direction relative to the local flows that it gives a thrust component, such as winglets, pylons, etc.

Another method is to apply area rule or shaping - both have their place. You may have tangible examples of how to exploit that. There were many examples that we looked at in the AGARD working panel on stores. The best configurations were those that gave the best longitudinal distribution of cross-sectional areas or shaping the body by following the local streamline as we heard this morning. In the store carriage area, I gave illustrations in my lecture, e.g., tandem and staggered carriage, of adding together flow fields in a manner such that the final flowfield is better than the flow around the individual components. I made the point very much on the basis of drag, but it is relevant to point out that our ability to predict the drag of these configurations is very limited. We do have to rely on experiment and probably will have to do so for some considerable time. It is not just drag, and this is where research is needed. You may have thought it was ill balanced. I did refer to loads, I did refer to release disturbances, but a lot of the promising radical ideas are coming forward on the basis of performance. It is an urgent requirement to look at the release characteristics of such arrangements. In passing, I should note that from our experience in the U.K. the Nielsen method, even without the transonic extensions that was talked about on Monday, works remarkably well up to a remarkably high Mach number. On the other hand, it is very difficult to predict the installed loads by any theoretical method. You have got to look at all of these things before you can persuade people to accept radical schemes.

A slight disappointment of the conference to me is that radical schemes of obtaining favorable interference have not been much mentioned. On the stores front for example, at another conference, there was a scheme put forward by I think it was Grummans, where they were carrying the stores, for reasons unconnected with aerodynamics, on top of the fuselage. They moved them longitudinally along the fuselage according to the Mach number in flight trying to get the right longitudinal area distribution to suit the Mach number. You may say that that sounds complicated and very costly, but I think that the research people have to find and publicize what can be done to induce someone to look at the practical implications of what you are doing.

Incidentally, we should have some sympathy for the person who is having the research pumped at him. If he is doing what we hope he is doing, he is reading the proceedings of all AGARD conferences. This year for very good reasons, I have suggested that there are advantages for mounting weapons at the wing tip, but last year again for very good reasons, someone else was wanting to rotate the tips by about $\pm 70^\circ$. This year, we advocate stores below the fuselage, but next year in Toulouse, somebody will be having his jet nozzles for VSTOL along the bottom of the fuselage. The designer has to weigh up the relative merits of all of these different schemes. Perhaps we should have had a paper in this area at this conference, since it is a conference on configuration aerodynamics.

My last point is, don't think that the computer can do it all for you. Remember that the real optimization has to be done by human beings thinking of all of the problems and with a proper understanding of what makes for favorable interference.

Dr. Yoshihara

Thank you Barry. I think that your comments were very interesting and will be the basis for further comments and questions from the audience. We now open the discussion to members of the audience. Are there any questions?

Mr. DePonte

I have a comment on your remark to make measurements on pressure. You need to measure other things. It is not sufficient to just measure pressure if you want insight into for example the separation region. I don't think we can conclude something by only measuring pressures. I think that we need to measure some other things like flow field velocities, and probably turbulence. We do not have a physical insight and you cannot obtain this from only pressure measurements.

Dr. Yoshihara

Are you referring to the windtunnel walls or to the model? Let me start with the windtunnel walls. If I measure the pressures there, I can prescribe them as boundary conditions in a calculation to tailor the method. In the tailored method I can replace the wall conditions by free stream conditions to obtain finally the free flight results.

Dr. Whitcomb

When Dr. Yoshira put his list up there, I wanted to say the same thing. We not only use pressures, we also use a fluorescent oil film. Remember that this whole meeting has been talking about the fact that we have to have the viscous effects as well as the potential effects.

Pressure distributions give a little bit of both, but the oil flow is primarily viscous. We can immediately see viscous problems with the oil film that we would never see with the pressure distribution.

Mr. Jupp

With reference to the comments made by Dr. Whitcomb, I want to say how much I agree with a lot of what he said. I think there were four points. I am not sure of the order in which he mentioned them: wing root fillets, cambered pylons, designing an airfoil with an acceptable shock, and winglets. Fillets and cambered pylons were mentioned in my paper and need no further comment.

Our philosophy is also to design an airfoil for an acceptable shock: Mr. Haines commented on this, and we would agree that you can get the maximum L/D with some wave drag present. On the fourth point, winglets, there is a widely held view in England, I am not sure it is a majority view, that we rather agree with Mr. Rettie's point of view. I think that looking to the future it is dangerous to think of an equivalent planar wing in terms of a wing tip extension. One must think of an optimized planar wing. When one does that, it reduces the benefits of winglets quite considerably. It would be our position that there is a gain with winglets, but that it is a small one when compared with the optimum planar wing. This must be balanced against the added complications of the design of the winglet and perhaps low speed problems which might require high lift devices on the winglet itself.

Dr. Whitcomb

I think that what you said, I am not sure, "with an acceptable shock wave". I thought I heard you say unacceptable, but I am not sure. I want to emphasize with regard to those three points, I was merely pointing out what I had heard and what I agreed with. I wasn't saying that you guys ought to think about those things. All of those points were covered here today. With regard to winglets, I guess we obviously have our disagreements, but you do have a point. All of our comparisons were made with fairly elementary wing tips, and there may be a tip somewhere that may be better than an elementary tip that will reduce the advantage of a winglet. Over the years we have tried some of those fancy tips and it didn't give as much as we had hoped for.

Mr. Haines

I merely wanted to say very briefly to the last speaker, Mr. Jupp, that if he was suggesting that the generally held view in England is that winglets are unattractive when compared on a fair basis, I do not want to be associated with those particular words. I think that there will be practical cases where one can see good practical reasons for the winglet. It is certainly true that the usefulness of the winglet depends very much on the particular wing on which you are putting it, it depends on the loading on the outer part of the wing and it depends on the taper of the wing. I think that it is still true that we do not completely understand the physics but the results are remarkably good when we test one.

Dr. Hackett

My comment concerns the optimization of non-planar configurations. One may consider the flow in the cross-flow plane, aft of the aircraft and determine drag, lift, root-bending moment, etc. via appropriate trailing vorticity integrations. To optimize, it follows that we should do what our forefathers did when determining the spanload for minimum drag: look at the wake and determine how its velocities and vorticity should be distributed. In the case of non-planar devices, pylons, winglets, flap-track fairings and whatever, one may imagine a "cloud" of trailing vorticity and attempt to optimize its distribution subject to certain practical constraints. These might include not only drag minimization, but also various lift and bending moment trades as well as perturbations on the overall configuration - numbers of pylons or flap tracks, presence or not of winglets or similar devices - and so forth. We should look to the theoreticians for help in determining how to find such optima.

There exists a parallel question regarding the distribution of the axial velocity perturbations which an aircraft leaves in its wake. For current aircraft, we see highly localized "puffs" of high energy air aft of the engines and a widely distributed wake deficit flow. Should these be mixed together in some way, and if so, how? Again, this is a question for the theoreticians.

Mr. Mavriplis

I would like to comment on the remarks made on nacelle interference and on the comparison between wind tunnel and flight test results, that is, test results obtained during the development of the Canadair Challenger, which is a business jet awaiting certification at the moment. This slide (Fig. 1) shows the configuration that I am going to speak about. It has a wide-body fuselage which has quite an effect on the wing pressure distribution. We did design the wing using the Jameson transonic wing method. However, when we got our first wing pressure distributions from the wind tunnel, we were very disappointed. Later on, we did some improvements, some modifications of the Jameson method, using a panel method to calculate the flow due to the body at a vertical plane through the wing root and superimposing that on the Jameson method to get the effect of the body, which showed good agreement with the test. Another effect is that of the nacelles. These nacelles are really big, and they affect the wing pressure distribution quite a bit, and if you don't have a good method to compute this kind of effect, then you are in trouble and you must spend a lot of time in the wind tunnel. The nacelles are positioned quite high, but the intake is at the wing trailing edge, so they don't overlap with the wing.

On the next slide (Fig. 2) we see a superposition of the pressure distributions of two configurations obtained in the wind tunnel at Mach Number .8 at a constant angle of attack of .9 degrees. The black lines are the wing-body pressure distributions, while the red ones are for the complete configuration at the same angle of attack. Now, you see that the shock has moved well forward and that there is a tremendous loss of lift. In order to regain the lift you have to increase the angle of attack from .9 degrees to 2 1/2 degrees. On the next slide (Fig. 3), the same pressure distribution of the wing-body that we saw before is compared with that of the complete configuration after increasing the angle of attack to achieve the same C_L as the wing-body, and you can still see the effects of the nacelle. The shock has moved forward on the inboard wing and back at the tip, and you can see a change in the span loading. The outboard wing is now more loaded than it was with nacelles off. So it is important that these effects can be computed.

Now this slide (Fig. 4), shows a comparison between wind tunnel data and flight test results from a wing pressure survey. The wind tunnel data are joined by lines while the flight test data are marked by squares on the top surface and triangles on the bottom surface. Only three stations were instrumented with external flexible tubing at 40%, 67 1/2 % and 85 % of semispan. The outboard station is right over the aileron. You see that the comparison is so it was really very satisfactory from the point of view of loads. The purpose of the survey was to prove that the wing pressure distributions during flight agree well with those obtained in wind tunnel tests. A good correlation was to confirm the estimated loads at supercritical speeds which were derived from wind tunnel pressure distributions.

However, one can see some differences between flight and wind tunnel test data. For instance during flight, the shock is slightly further back at the wing break section ($\alpha = 40\%$) and further forward at the outboard section. Also there is a little more lift at the inboard station and a little less lift at the outboard station. Finally, the shock appears to be weaker at the outboard station. We think that these effects are due to the difference in Reynolds number. The wind tunnel tests were done at 3.8 million without transition, while the flight Reynolds number was at 15.8 million.

Thank you.

Mr. Persen

I just want to know whether the panel will agree with me when we discuss the viscous effects. It seems to me from the experiences that we had last week, where we were discussing theories of turbulence, where we were discussing boundary layers and all kinds of numerical schemes, that we seem to understand more or less adequately the boundary layer as we saw this morning in a rather comprehensive numerical scheme. We saw that Bradshaw's 2-D strip approach was used. My feeling is that the thing that really matters will be to get a good physical understanding of separation and not only just where separation is located, but also what is happening to the flow in the wake region, that is, in that region where the flow has separated. It is my feeling, that this especially may be of importance when you have a separated region on your wing which may be changing drastically during maneuvers. This is the point where our physical understanding is lacking the most. I want to ask the panel if they agree with me.

Dr. Yoshihara

May I first make a small comment. A separated flow is a very unsteady flow. It is a condition under which half the time you have patches of reverse flow. So it is really the kind of thing in which you have to take a time average. As far as the wake is concerned, you can certainly have a reattachment point beyond the trailing edge. That is certainly a buffeting situation. Again it is very highly unsteady.



Fig. 1 Canadair Challenger

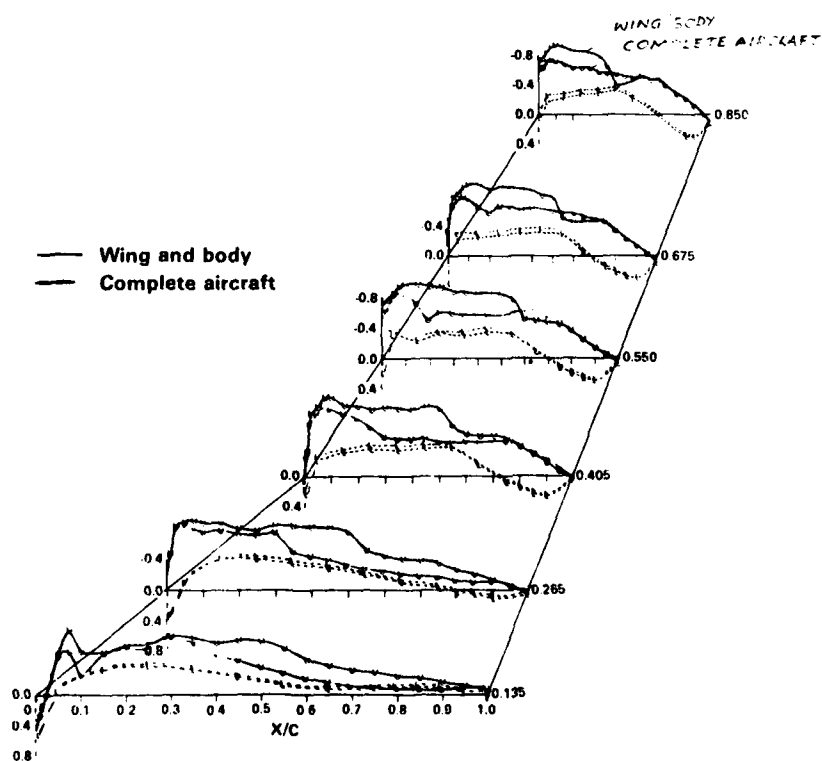


Fig. 2 Nacelle Interference on Wing Pressure Distribution
 $M = 0.8$, $\alpha \approx 0.9^\circ$

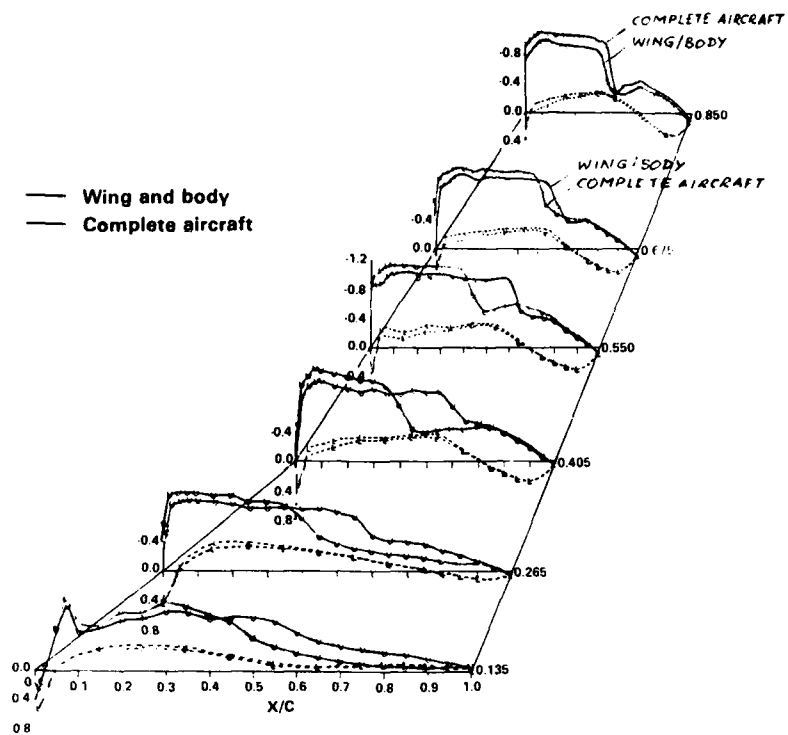


Fig. 3 Nacelle Interference on Wing Pressure Distribution
 $M = 0.8$, $C_L = 0.5$

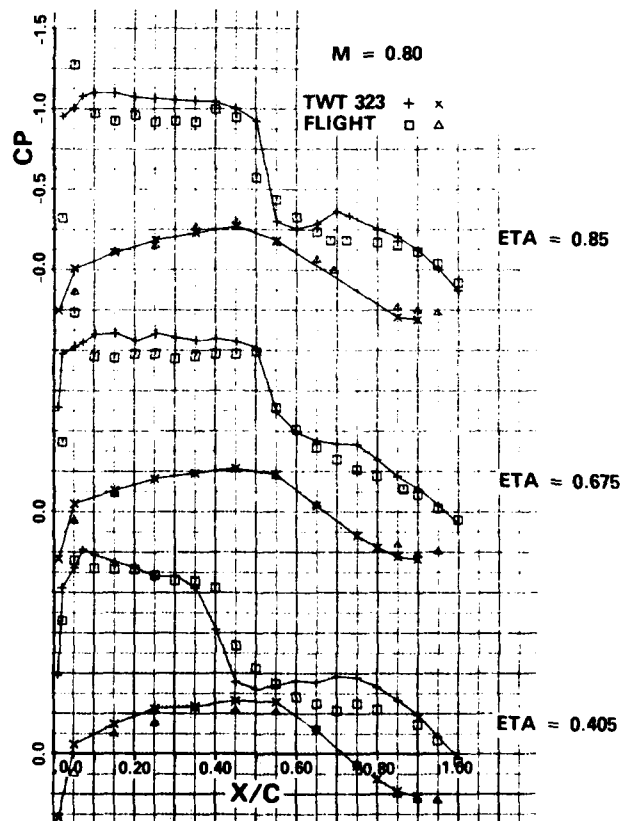


Fig. 4 Wing Pressure Survey Pressure Distributions
 - flight vs wind tunnel

Dr. Schmidt

I completely agree with what you have said, and I would also like to mention that this comparison between strip theory and three-dimensional theory should not be overstressed. We did very careful comparisons on different kinds of pressures using this type of strip theory and a fully 3-d theory. The final conclusion is that as long as the pressure distribution in the spanwise direction does not have large gradients, then strip theory, almost independent of the sweep and of the taper ratio, can give very nice results, but as soon as you have strong pressure gradients in the spanwise direction, as soon as you have delta type wings, then strip theory is lost.

Dr. Zonars

I would like to temper the enthusiasm of the individuals who try to blend the engine-air system with the aircraft. I think that this technology is going to come forward with great enthusiasm in the future, but we did see in both cases where individuals were banking on a high degree of negative stability margin. Fly by wire systems are great. They are a tremendous advance in our technology and permit us to fly at negative margins, but please recognize that a fly by wire system has a stick with a transducer installed in it. It incorporates a sensor system and a computer which sends a signal back into the actuator of the control surface. There are no push rods or cables between that particular stick and the surface. So, you can easily find yourself in circumstances where the pilot may be pulling 40 or 50 lbs of backpressure during a maneuver with the control surface going in the opposite direction, because that is what the sensor and what the computer is commanding. You can easily run out of control surface capability or potential if you are too unstable. Now I think that if you blend the exhaust system with the computer, with the feedback system, then you are o.k., but I think that you are asking for trouble if you go to as much as 17% or 23% negative margin. I would strongly suggest that you contract with some very bold and unmarried pilots if you insist on high degrees of negative margin..

Dr. Orlik-Rüchemann

Most if not all of the presentations and discussions we have had so far have dealt with static aerodynamics. I would like to take up one of the points I think Dr. Schmidt has made, about the need for more data and more information that could be used to predict and determine the maneuvering boundaries of combat aircraft. Of course, as you well know, the information we need for such a prediction, in addition to all kinds of static data, requires also great many dynamic data. Such data are at the present time difficult, but not impossible, to obtain in wind tunnels, but are not yet obtainable at all from numerical methods. This is of special interest, but not exclusively so, to flight at high angles of attack of complete aircraft configurations. Even in wind tunnels the situation is not yet completely satisfactory, since, in addition to the usual problems of simulating the correct Reynolds number, we still experience difficulties in dealing with problems such as the static and the dynamic sting interference and wind-tunnel wall interference, to name but a few. There is a lot to be done in this subject both with the numerical techniques and wind tunnel techniques. If we want to fly efficiently and safely at high angles of attack, this work must be done. I would not like to let a discussion like the present one pass without at least a reminder that we need a lot more work in this area.

Dr. Yoshihara

I would like to remind Dr. Orlik-Rüchemann that there were two recent symposia on high angle of attack aerodynamics and controls, and of course, we have to restrict this meeting to what we have covered. Otherwise, we would be here until Friday.

Dr. Orlik-Rüchemann

I agree, but I was talking not only about the high angle of attack situation, but also in general about the need for more dynamic and unsteady data, which are of interest at any angle of attack.

Prof. Young

I would like to just spend a minute on a point Dr. Schmidt made when he threw up on the screen my badly written comments on the Kutta condition and the fact that we don't have a Kutta condition for fuselages. It seems to me that we will always have a question mark over any kind of modelling on wing body combinations until we are able to predict more accurately the loading distribution on the bodies and the associated boundary layer development. Since at this stage we lack an adequate experimental background, I would like to make a plea that those who are concerned with windtunnel work should consider very seriously making more measurements on bodies and fuselages particularly towards the rear. These measurements should include pressure distributions, boundary layer development and wake development. I think you will find, and I am basing this comment on my own limited experience, that there are things happening there which one would not normally have expected and which may help us, if not to provide a rigorous equivalent of the Kutta condition, at least to formulate a useful substitute for it, and so help us to do better modelling.

Dr. Whitcomb

I am not sure how detailed you want the measurements, for example, did you want vorticity, and so forth? About five years ago, recognizing the problem, we got a very thorough survey of the boundary layer development as it flows in on the back end of a fuselage. In order to get the right answer, we didn't have it sting supported, of course. We had it on a strut. So, there is some data available, and I am sure others have some too. Incidentally we were getting that data to see if we could have some basis for taking the boundary layer of the fuselage into the fan of a rear mounted engine to get this boot strap operation that one can get by doing that. Incidentally, we had Douglas do that and do an analysis on that, and it doesn't appear to be economically practical.

Dr. McCroskey

Rotary wing applications were notably absent from the program, probably partly by design. Just to keep my benefactors happy, I would like to make a few brief comments. It might interest you to know that there are several topics here which would be of interest to the helicopter community, such as 3-D transonic computational programs, drag of external stores and the trajectories of stores leaving in non-uniform flow fields. A fourth topic is wake distortion; it's very important in helicopter aerodynamics to have a real distorted wake, instead of just straight lines of vorticity which leave the wing and the tip. Another is Dr. Drougge's talk this morning about airfoil design for multiple operating conditions: high maximum lift on the one hand at low mach number, good transonic drag divergence mach number at low lift - these things are very relevant to our problems. The most important of all is the general concept of favorable aerodynamic interference between lifting and non-lifting components. There is a tremendous potential in this area for helicopter aerodynamics, and I hope that in the years ahead we will see more done in that area.

Mr. Metcalfe

We have just heard about helicopter interference. Would anyone like to make some comments on the effect of propeller interference on the wing? Do the panel see how the effects of propeller slip stream interference could be built into these computational methods?

Mr. Haines

I would think that most subcritical panel methods would have the facility to include the propeller slip stream, but it is a very good question. Propellers are often being suggested as a means of saving fuel, and one of the crucial questions there is to what extent we can marry the propeller slip stream and an advanced wing design, bearing in mind the appreciable difference in Mach number in the slip stream and outside of it. In general, putting a wing into a propeller slip stream is an effective means of straightening the flow and recovering some of the rotational losses which would occur with the propeller in isolation. This has been known for many years, but the new question is whether you can still achieve this favorable effect with an advanced supercritical wing. A paper at a recent conference is the U.S. was reassuring on this point.

Dr. Schmidt

I would like to stress your comment a little more, because I think it is an important one. If you think of a straight wing, two propellers rotating in the same direction, and if you try to understand the high lift capabilities of such a configuration you will see that you get lost, because there is no way that you can predict or compute the stall characteristics under the slip stream condition. Therefore, I think it is a very basic task, really, to be able to understand and to compute the effects of a propeller slip stream due to the rotating flow, the direction of the rotation and the effects on high lift. What you do actually, is you put some fences or vortex generators to control stall, but at the same time you increase drag. But this is not the ultimate solution if you have to design an efficient transport wing in cruise.

Dr. Roberts

On that last subject, there is work going on in the United States at the Ames Research Center, particularly on trying to optimize a supercritical wing in the presence of a propeller slip stream. The first results do suggest that swirl recovery - although the work is just beginning - looks promising. I would like to take the opportunity to pick up on some remarks that Mr. Haines made regarding the importance of making available to the designer the best tools, both computational and experimental. Certainly future aircraft will need both of those kinds of tools, and the incentive for using the best kind of calculation is very great. If you just take a few order of magnitude numbers to calculate some simple costs for a fleet of 100 aircraft over a 10 year life, the operational fuel cost of that fleet is typically \$10 billion. A 10% reduction in drag would reduce the fuel bill by \$1 billion. Those are large numbers. Typically a wing design program, that is, windtunnel plus computer programming, in the development of a wing costs the order of \$1 million. So there is a leverage there of 1000. I think that it is useless to talk about whether you can save money in a test program by substituting computation for experiment or experiment for computation. That doesn't really face the problem. The problem is to make the best use of both of those capabilities and to spend more on both, with the possibility of a large return.

Dr. Yoshihara

I would like to thank our panel, and I would also like to thank the many excellent speakers during this Symposium, as well as the chairmen. Now I think Dr. Orlik-Rüchemann has a few words to say to end this Symposium.

Dr. Orlik-Rüchemann

I think we have had a most enjoyable, instructive and, I hope, profitable three days and, of course, we are all eager to leave now. I understand that there is a nice reception awaiting us in a few minutes. However, as you well know, successful meetings like this one do not just happen by themselves. Many people are involved in the different stages of preparation and in the conducting of the meeting. A lot of time and effort goes into this, and it is my pleasant duty now to express our thanks to all these people. First of all, I think, we should all thank Professor Laschka, Dr. Yoshihara and the members of the Program Committee for the clever choice of the scope of the symposium, for the careful selection of papers and for the efficient chairing of the various sessions. Next, we should express our thanks to all the local coordinators, with Professor Hindelang Hr. Steckel, Frau Hirsch, and the technical assistants who operated the audio-visual systems. We should also express our appreciation to the interpreters; Madame Vrydach, Mrs. Radison, Mrs. Stewart. They showed a lot of patience and understanding while dealing with the customary technical and human imperfections. Without them this meeting could not have been such a success.

REPORT DOCUMENTATION PAGE

1. Recipient's Reference	2. Originator's Reference AGARD-CP-285	3. Further Reference ISBN 92-835-0276-0	4. Security Classification of Document UNCLASSIFIED								
5. Originator	Advisory Group for Aerospace Research and Development North Atlantic Treaty Organization 7 rue Ancelle, 92200 Neuilly sur Seine, France										
6. Title	SUBSONIC/TRANSONIC CONFIGURATION AERODYNAMICS										
7. Presented at	the Hochschule Bundeswehr, Munich Neubiberg, Germany, 5-7 May 1980.										
8. Author(s)/Editor(s) Various	9. Date September 1980										
10. Author's/Editor's Address Various	11. Pages 462										
12. Distribution Statement	This document is distributed in accordance with AGARD policies and regulations, which are outlined on the Outside Back Covers of all AGARD publications.										
13. Keywords/Descriptors	<table border="0"> <tr> <td>Aerodynamic interference</td> <td>Aircraft protuberances</td> </tr> <tr> <td>Aerodynamic characteristics</td> <td>Subsonic flow</td> </tr> <tr> <td>Wing body configurations</td> <td>Transonic flow</td> </tr> <tr> <td>External stores</td> <td></td> </tr> </table>			Aerodynamic interference	Aircraft protuberances	Aerodynamic characteristics	Subsonic flow	Wing body configurations	Transonic flow	External stores	
Aerodynamic interference	Aircraft protuberances										
Aerodynamic characteristics	Subsonic flow										
Wing body configurations	Transonic flow										
External stores											
14. Abstract	<p>During the past decade, there has been significant progress in the development of transonic wind tunnel test techniques and computational methods. Employing these techniques, the aerodynamicist has developed many imaginative design concepts that have added to the optimization data base. It was the purpose of the symposium to review and assess these developments and project the future.</p> <p>Twenty nine papers comprised the meeting with three invited review papers. There was a relatively even mixture of theoretical and experimental papers with many providing test/theory comparisons. Subject matter ranged from simple wing-fuselage interference for both fighter and airlift configurations to those involving additional components such as nacelle and pylons, powered jets, winglets, and most importantly stores and weapons. The symposium was concluded by a Round Table discussion with invited introductory comments.</p>										

Last, but not least, we should recognize our hard-working Panel staff from AGARD Headquarters, Mr. Bob Rollins and Mlle. Rivault, without whose efforts this meeting would simply not have been possible at all.

In my opening remarks Monday morning, I described to you some of the past activities of our Panel. I think it may be appropriate to conclude this meeting with some indication of our future plans. You may find it convenient to know these plans in advance, so that you can start thinking at an early date about your possible participation. The next meeting will be on the subject of "Computation of Viscous-Inviscid Interactions and will be held in Colorado Springs, U.S.A. from 29 September to 1 October of this year. Our spring 1981 meeting will be on "Aerodynamics of Power Plant Installations; it will be held in Toulouse, France from 11 to 14 May 1981. Finally, the fall 1981 meeting will deal with the "Fluid Dynamics of Jets with Applications to VSTOL Aircraft" and will be held in Portugal. The exact dates are not yet established. I sincerely hope to be able to see as many of you as possible on at least some of these occasions. With that, I now declare this meeting adjourned.

<p>AGARD Conference Proceedings No.285 Advisory Group for Aerospace Research and Development, NATO SUBSONIC/TRANSONIC CONFIGURATION AERODYNAMICS Published September 1980 462 pages</p> <p>During the past decade, there has been significant progress in the development of transonic wind tunnel test techniques and computational methods. Employing these techniques, the aerodynamicist has developed many imaginative design concepts that have added to the optimization data base. It was the purpose of the symposium to review and assess these developments and project the future.</p> <p>P.T.O.</p>	<p>AGARD-CP-285</p> <p>Aerodynamic interference Aerodynamic characteristics Wing body configurations External stores Aircraft protuberances Subsonic flow Transonic flow</p>	<p>AGARD Conference Proceedings No.285 Advisory Group for Aerospace Research and Development, NATO SUBSONIC/TRANSONIC CONFIGURATION AERODYNAMICS Published September 1980 462 pages</p> <p>During the past decade, there has been significant progress in the development of transonic wind tunnel test techniques and computational methods. Employing these techniques, the aerodynamicist has developed many imaginative design concepts that have added to the optimization data base. It was the purpose of the symposium to review and assess these developments and project the future.</p> <p>P.T.O.</p>	<p>AGARD-CP-285</p> <p>Aerodynamic interference Aerodynamic characteristics Wing body configurations External stores Aircraft protuberances Subsonic flow Transonic flow</p>
<p>AGARD Conference Proceedings No.285 Advisory Group for Aerospace Research and Development, NATO SUBSONIC/TRANSONIC CONFIGURATION AERODYNAMICS Published September 1980 462 pages</p> <p>During the past decade, there has been significant progress in the development of transonic wind tunnel test techniques and computational methods. Employing these techniques, the aerodynamicist has developed many imaginative design concepts that have added to the optimization data base. It was the purpose of the symposium to review and assess these developments and project the future.</p> <p>P.T.O.</p>	<p>AGARD-CP-285</p> <p>Aerodynamic interference Aerodynamic characteristics Wing body configurations External stores Aircraft protuberances Subsonic flow Transonic flow</p>	<p>AGARD Conference Proceedings No.285 Advisory Group for Aerospace Research and Development, NATO SUBSONIC/TRANSONIC CONFIGURATION AERODYNAMICS Published September 1980 462 pages</p> <p>During the past decade, there has been significant progress in the development of transonic wind tunnel test techniques and computational methods. Employing these techniques, the aerodynamicist has developed many imaginative design concepts that have added to the optimization data base. It was the purpose of the symposium to review and assess these developments and project the future.</p> <p>P.T.O.</p>	<p>AGARD-CP-285</p> <p>Aerodynamic interference Aerodynamic characteristics Wing body configurations External stores Aircraft protuberances Subsonic flow Transonic flow</p>

<p>Twenty nine papers comprised the meeting with three invited review papers. There was a relatively even mixture of theoretical and experimental papers with many providing test/theory comparisons. Subject matter ranged from simple wing-fuselage interference for both fighter and airlift configurations to those involving additional components such as nacelle and pylons, powered jets, winglets, and most importantly stores and weapons. The symposium was concluded by a Round Table discussion with invited introductory comments.</p> <p>Papers presented and discussions held at the Fluid Dynamics Panel Symposium held at the Hochschule Bundeswehr, Munich Neubiberg, Germany, 5-7 May 1980.</p> <p>ISBN 92-835-0276-0</p>	<p>Twenty nine papers comprised the meeting with three invited review papers. There was a relatively even mixture of theoretical and experimental papers with many providing test/theory comparisons. Subject matter ranged from simple wing-fuselage interference for both fighter and airlift configurations to those involving additional components such as nacelle and pylons, powered jets, winglets, and most importantly stores and weapons. The symposium was concluded by a Round Table discussion with invited introductory comments.</p> <p>Papers presented and discussions held at the Fluid Dynamics Panel Symposium held at the Hochschule Bundeswehr, Munich Neubiberg, Germany, 5-7 May 1980.</p> <p>ISBN 92-835-0276-0</p>
<p>Twenty nine papers comprised the meeting with three invited review papers. There was a relatively even mixture of theoretical and experimental papers with many providing test/theory comparisons. Subject matter ranged from simple wing-fuselage interference for both fighter and airlift configurations to those involving additional components such as nacelle and pylons, powered jets, winglets, and most importantly stores and weapons. The symposium was concluded by a Round Table discussion with invited introductory comments.</p> <p>Papers presented and discussions held at the Fluid Dynamics Panel Symposium held at the Hochschule Bundeswehr, Munich Neubiberg, Germany, 5-7 May 1980.</p> <p>ISBN 92-835-0276-0</p>	<p>Twenty nine papers comprised the meeting with three invited review papers. There was a relatively even mixture of theoretical and experimental papers with many providing test/theory comparisons. Subject matter ranged from simple wing-fuselage interference for both fighter and airlift configurations to those involving additional components such as nacelle and pylons, powered jets, winglets, and most importantly stores and weapons. The symposium was concluded by a Round Table discussion with invited introductory comments.</p> <p>Papers presented and discussions held at the Fluid Dynamics Panel Symposium held at the Hochschule Bundeswehr, Munich Neubiberg, Germany, 5-7 May 1980.</p> <p>ISBN 92-835-0276-0</p>